a number of aspects of the interaction, and in particular—by marked contrast, for example, with ribonuclease—shows that the entry of the substrate provokes appreciable local changes in disposition of side chains. There is no evidence of specific interactions between any groups in the enzyme and the C-terminal side chain of the substrate, which fits easily into the cavity. However, the terminal carboxylate group is brought into contact with an arginine side chain, which moves 2 Å in the process. It is tentatively suggested, moreover, that the oxygen atom of the substrate peptide bond may become a ligand for the zinc atom. It was previously observed by Vallee and co-workers that certain tyrosine residues seem to be involved in enzymatic activity, and indeed it is found that one tyrosine moves a distance of no less than 14 Å when the substrate is introduced so as to bring up the phenolic hydroxyl group close to the substrate peptide bond. The motion occurs in a non-helical part of the chain, and evidently involves a considerable disturbance of the backbone conformation as well as rotation about side chain carbon–carbon bonds. A carboxylate group also seems to form part of the active site.

The details so far available are consistent with chemical data: whether a more precise delineation of the interaction between the active centre and the substrate will immediately suggest a catalytic mechanism remains to be seen. There are grounds for optimism, despite the remarkable failure of known protein structures so far to reveal the mechanism of their function unequivocably.

Observation of a Rapidly Pulsating Radio Source

by

A. HEWISH
S. J. BELL
J. D. H. PILKINGTON
P. F. SCOTT
R. A. COLLINS

Mullard Radio Astronomy Observatory,
Cavendish Laboratory,
University of Cambridge

Unusual signals from pulsating radio sources have been recorded at the Mullard Radio Astronomy Observatory. The radiation seems to come from local objects within the galaxy, and may be associated with oscillations of white dwarf or neutron stars.

In July 1967, a large radio telescope operating at a frequency of 81·5 MHz was brought into use at the Mullard Radio Astronomy Observatory. This instrument was designed to investigate the angular structure of compact radio sources by observing the scintillation caused by the irregular structure of the interplanetary medium[1]. The initial survey includes the whole sky in the declination range $-08° < \delta < 44°$ and this area is scanned once a week. A large fraction of the sky is thus under regular surveillance. Soon after the instrument was brought into operation it was noticed that signals which appeared at first to be weak sporadic interference were repeatedly observed at a fixed declination and right ascension; this result showed that the source could not be terrestrial in origin.

Systematic investigations were started in November and high speed records showed that the signals, when present, consisted of a series of pulses each lasting $\sim 0·3$ s and with a repetition period of about 1·337 s which was soon found to be maintained with extreme accuracy. Further observations have shown that the true period is constant to better than 1 part in 10^7 although there is a systematic variation which can be ascribed to the orbital motion of the Earth. The impulsive nature of the recorded signals is caused by the periodic passage of a signal of descending frequency through the 1 MHz pass band of the receiver.

The remarkable nature of these signals at first suggested an origin in terms of man-made transmissions which might arise from deep space probes, planetary radar or the reflexion of terrestrial signals from the Moon. None of these interpretations can, however, be accepted because the absence of any parallax shows that the source lies far outside the solar system. A preliminary search for further pulsating sources has already revealed the presence of three others having remarkably similar properties which suggests that this type of source may be relatively common at a low flux density. A tentative explanation of these unusual sources in terms of the stable oscillations of white dwarf or neutron stars is proposed.

Position and Flux Density

The aerial consists of a rectangular array containing 2,048 full-wave dipoles arranged in sixteen rows of 128 elements. Each row is 470 m long in an E.–W. direction and the N.–S. extent of the array is 45 m. Phase-scanning is employed to direct the reception pattern in declination and four receivers are used so that four different declinations may be observed simultaneously. Phase-switching receivers are employed and the two halves of the aerial are combined as an E.–W. interferometer. Each row of dipole elements is backed by a tilted reflecting screen so that maximum sensitivity is obtained at a declination of approximately $+30°$, the overall sensitivity being reduced by more than one-half when the beam is scanned to declinations above $+90°$ and below $-5°$. The beamwidth of the array to half intensity is about $\pm\frac{1}{2}°$ in right ascension and $\pm 3°$ in declination; the phasing arrangement is designed to produce beams at roughly 3° intervals in declination. The receivers have a bandwidth of 1 MHz centred at a frequency of 81·5 MHz and routine recordings are made with a time constant of 0·1 s; the r.m.s. noise fluctuations correspond to a flux density of $0·5 \times 10^{-26}$ W m^{-2} Hz^{-1}. For detailed studies of the pulsating source a time constant of 0·05 s was usually employed and the signals were displayed on a multi-channel 'Rapidgraph' pen recorder with a time constant of 0·03 s. Accurate timing of the pulses was achieved by recording second pips derived from the *MSF* Rugby time transmissions.

A record obtained when the pulsating source was un-

© 1968 Nature Publishing Group

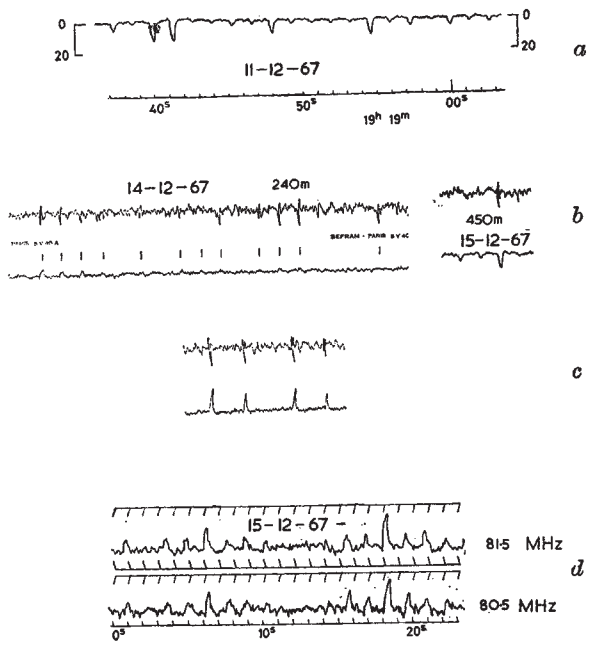

Fig. 1. *a*, A record of the pulsating radio source in strong signal conditions (receiver time constant 0·1 s). Full scale deflexion corresponds to 20×10^{-26} W m^{-2} Hz^{-1}. *b*, Upper trace: records obtained with additional paths (240 m and 450 m) in one side of the interferometer. Lower trace: normal interferometer records. (The pulses are small for $l = 240$ m because they occurred near a null in the interference pattern; this modifies the phase but not the amplitude of the oscillatory response on the upper trace.) *c*, Simulated pulses obtained using a signal generator. *d*, Simultaneous reception of pulses using identical receivers tuned to different frequencies. Pulses at the lower frequency are delayed by about 0·2 s.

usually strong is shown in Fig. 1*a*. This clearly displays the regular periodicity and also the characteristic irregular variation of pulse amplitude. On this occasion the largest pulses approached a peak flux density (averaged over the 1 MHz pass band) of 20×10^{-26} W m^{-2} Hz^{-1}, although the mean flux density integrated over one minute only amounted to approximately $1{\cdot}0 \times 10^{-26}$ W m^{-2} Hz^{-1}. On a more typical occasion the integrated flux density would be several times smaller than this value. It is therefore not surprising that the source has not been detected in the past, for the integrated flux density falls well below the limit of previous surveys at metre wavelengths.

The position of the source in right ascension is readily obtained from an accurate measurement of the "cross-over" points of the interference pattern on those occasions when the pulses were strong throughout an interval embracing such a point. The collimation error of the instrument was determined from a similar measurement on the neighbouring source 3*C* 409 which transits about 52 min later. On the routine recordings which first revealed the source the reading accuracy was only ± 10 s and the earliest record suitable for position measurement was obtained on August 13, 1967. This and all subsequent measurements agree within the error limits. The position in declination is not so well determined and relies on the relative amplitudes of the signals obtained when the reception pattern is centred on declinations of 20°, 23° and 26°. Combining the measurements yields a position

$$\alpha_{1950} = 19\text{h } 19\text{m } 38\text{s} \pm 3\text{s}$$

$$\delta_{1950} = 22^\circ\ 00' \pm 30'$$

As discussed here, the measurement of the Doppler shift in the observed frequency of the pulses due to the Earth's orbital motion provides an alternative estimate of the declination. Observations throughout one year should yield an accuracy of $\pm 1'$. The value currently attained from observations during December–January is $\delta = 21^\circ\ 58' \pm 30'$, a figure consistent with the previous measurement.

Time Variations

It was mentioned earlier that the signals vary considerably in strength from day to day and, typically, they are only present for about 1 min, which may occur quite randomly within the 4 min interval permitted by the reception pattern. In addition, as shown in Fig. 1*a*, the pulse amplitude may vary considerably on a time-scale of seconds. The pulse to pulse variations may possibly be explained in terms of interplanetary scintillation[1], but this cannot account for the minute to minute variation of mean pulse amplitude. Continuous observations over periods of 30 min have been made by tracking the source with an E.–W. phased array in a 470 m × 20 m reflector normally used for a lunar occultation programme. The peak pulse amplitude averaged over ten successive pulses for a period of 30 min is shown in Fig. 2*a*. This plot suggests the possibility of periodicities of a few minutes duration, but a correlation analysis yields no significant result. If the signals were linearly polarized, Faraday rotation in the ionosphere might cause the random variations, but the form of the curve does not seem compatible with this mechanism. The day to day variations since the source was first detected are shown in Fig. 2*b*. In this analysis the daily value plotted is the peak flux density of the greatest pulse. Again the variation from day to day is irregular and no systematic changes are clearly evident, although there is a suggestion that the source was significantly weaker during October to November. It therefore appears that, despite the regular occurrence of the pulses, the magnitude of the power emitted exhibits variations over long and short periods.

Instantaneous Bandwidth and Frequency Drift

Two different experiments have shown that the pulses are caused by a narrow-band signal of descending frequency sweeping through the 1 MHz band of the receiver. In the first, two identical receivers were used, tuned to frequencies of 80·5 MHz and 81·5 MHz. Fig. 1*d*, which illustrates a record made with this system, shows that the lower frequency pulses are delayed by about 0·2 s. This corresponds to a frequency drift of ~ -5 MHz s^{-1}. In the second method a time delay was introduced into the signals reaching the receiver from one-half of the aerial by incorporating an extra cable of known length l. This cable introduces a phase shift proportional to frequency so that, for a signal the coherence length of which exceeds l, the output of the receiver will oscillate with period

$$t_0 = \frac{c}{l}\left(\frac{d\nu}{dt}\right)^{-1}$$

where $d\nu/dt$ is the rate of change of signal frequency. Records obtained with $l = 240$ m and 450 m are shown in Fig. 1*b* together with a simultaneous record of the pulses derived from a separate phase-switching receiver operating with equal cables in the usual fashion. Also shown, in Fig. 1*c*, is a simulated record obtained with exactly the same arrangement but using a signal generator, instead of the source, to provide the swept frequency. For observation with $l > 450$ m the periodic oscillations were slowed down to a low frequency by an additional phase shifting device in order to prevent severe attenuation of the output signal by the time constant of the receiver. The rate of change of signal frequency has been deduced from the additional phase shift required and is $d\nu/dt = -4{\cdot}9 \pm 0{\cdot}5$ MHz s^{-1}. The direction of the frequency drift can be obtained from the phase of the oscillation on the record and is found to be from high to low frequency in agreement with the first result.

© 1968 Nature Publishing Group

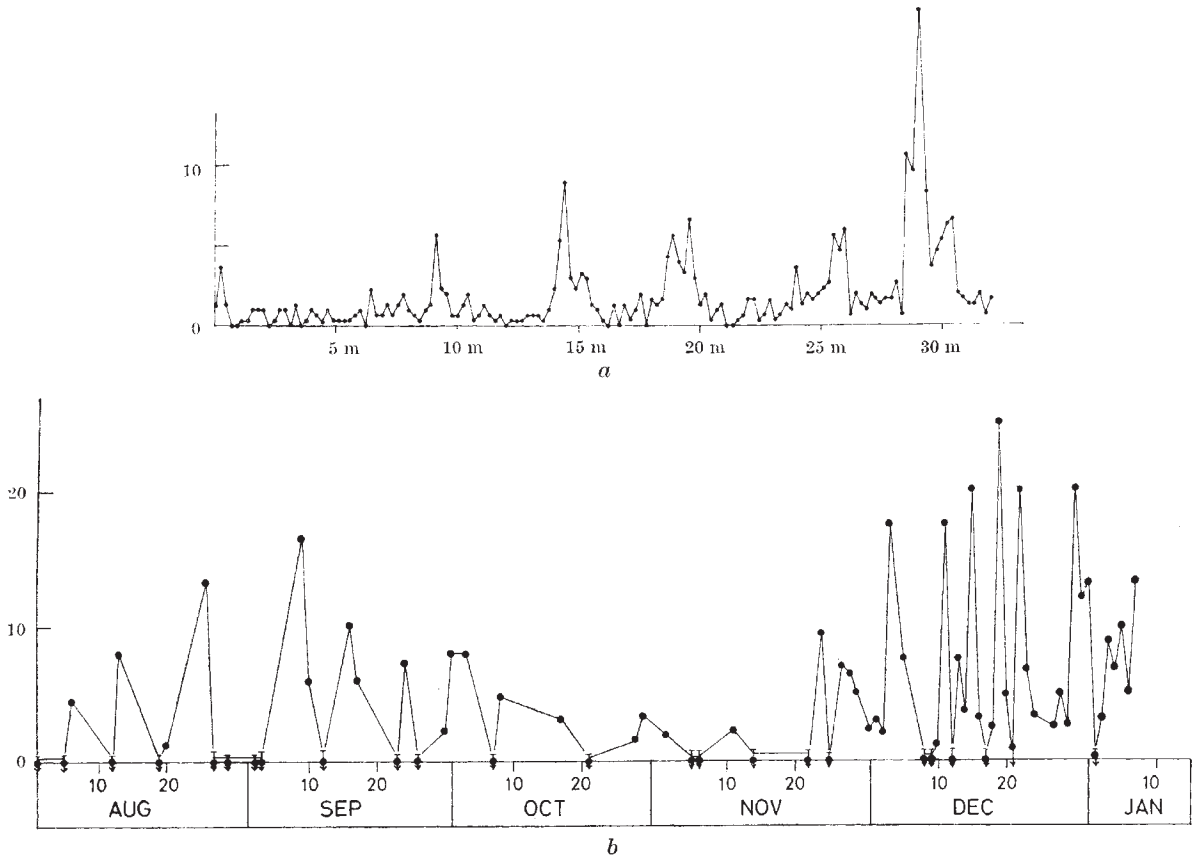

Fig. 2. *a*, The time variation of the smoothed (over ten pulses) pulse amplitude. *b*, Daily variation of peak pulse amplitude. (Ordinates are in units of $W\ m^{-2}\ Hz^{-1} \times 10^{-26}$.)

The instantaneous bandwidth of the signal may also be obtained from records of the type shown in Fig. 1*b* because the oscillatory response as a function of delay is a measure of the autocorrelation function, and hence of the Fourier transform, of the power spectrum of the radiation. The results of the measurements are displayed in Fig. 3 from which the instantaneous bandwidth of the signal to exp (-1), assuming a Gaussian energy spectrum, is estimated to be 80 ± 20 kHz.

Pulse Recurrence Frequency and Doppler Shift

By displaying the pulses and time pips from *MSF* Rugby on the same record the leading edge of a pulse of reasonable size may be timed to an accuracy of about 0·1 s. Observations over a period of 6 h taken with the tracking system mentioned earlier gave the period between pulses as $P_{obs} = 1{\cdot}33733 \pm 0{\cdot}00001$ s. This represents a mean value centred on December 18, 1967, at 14 h 18 m UT. A study of the systematic shift in the frequency of the pulses was obtained from daily measurements of the time interval T between a standard time and the pulse immediately following it as shown in Fig. 4. The standard time was chosen to be 14 h 01 m 00 s UT on December 11 (corresponding to the centre of the reception pattern) and subsequent standard times were at intervals of 23 h 56 m 04 s (approximately one sidereal day). A plot of the variation of T from day to day is shown in Fig. 4. A constant pulse recurrence frequency would show a linear increase or decrease in T if care was taken to add or subtract one period where necessary. The observations, however, show a marked curvature in the sense of a steadily increasing frequency. If we assume a Doppler shift due to the Earth alone, then the number of pulses received per day is given by

$$N = N_0 \left(1 + \frac{v}{c} \cos \varphi \sin \frac{2\pi n}{366{\cdot}25}\right)$$

where N_0 is the number of pulses emitted per day at the source, v the orbital velocity of the Earth, φ the ecliptic latitude of the source and n an arbitrary day number obtained by putting $n = 0$ on January 17, 1968, when the Earth has zero velocity along the line of sight to the source. This relation is approximate since it assumes a circular orbit for the Earth and the origin $n = 0$ is not exact, but it serves to show that the increase of N observed can be explained by the Earth's motion alone within the accuracy currently attainable. For this purpose it is convenient to estimate the values of n for which $\delta T/\delta n = 0$, corresponding to an exactly integral value of N. These occur at $n_1 = 15{\cdot}8 \pm 0{\cdot}1$ and $n_2 = 28{\cdot}7 \pm 0{\cdot}1$, and since N

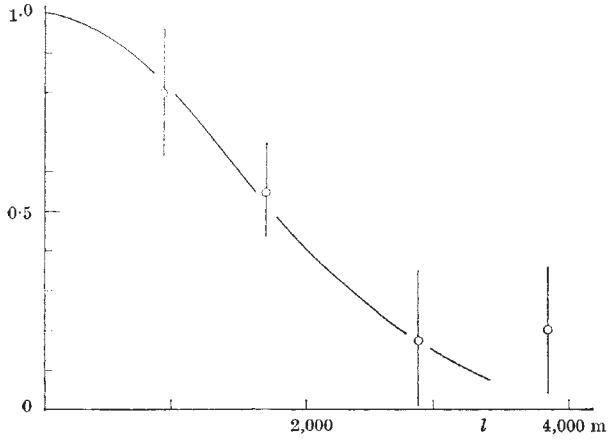

Fig. 3. The response as a function of added path in one side of the interferometer.

© 1968 Nature Publishing Group

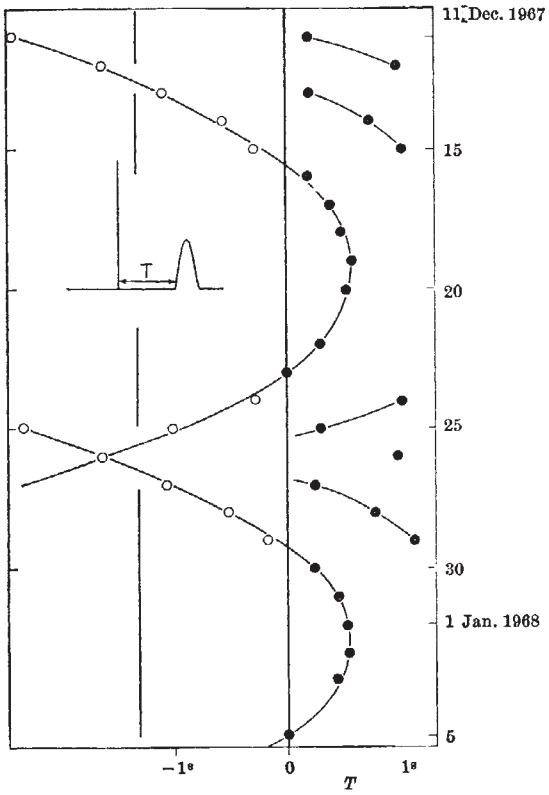

Fig. 4. The day to day variation of pulse arrival time.

is increased by exactly one pulse between these dates we have

$$1=\frac{N_0 v}{c}\cos\varphi\left[\sin\frac{2\pi n_2}{366\cdot25}-\sin\frac{2\pi n_1}{366\cdot25}\right]$$

This yields $\varphi=43°\ 36'\pm30'$ which corresponds to a declination of $21°\ 58'\pm30'$, a value consistent with the declination obtained directly. The true periodicity of the source, making allowance for the Doppler shift and using the integral condition to refine the calculation, is then

$$P_0=1\cdot3372795\pm0\cdot0000020\ \text{s}$$

By continuing observations of the time of occurrence of the pulses for a year it should be possible to establish the constancy of N_0 to about 1 part in 3×10^8. If N_0 is indeed constant, then the declination of the source may be estimated to an accuracy of $\pm1'$; this result will not be affected by ionospheric refraction.

It is also interesting to note the possibility of detecting a variable Doppler shift caused by the motion of the source itself. Such an effect might arise if the source formed one component of a binary system, or if the signals were associated with a planet in orbit about some parent star. For the present, the systematic increase of N is regular to about 1 part in 2×10^7 so that there is no evidence for an additional orbital motion comparable with that of the Earth.

The Nature of the Radio Source

The lack of any parallax greater than about 2′ places the source at a distance exceeding 10^3 A.U. The energy emitted by the source during a single pulse, integrated over 1 MHz at 81·5 MHz, therefore reaches a value which must exceed 10^{17} erg if the source radiates isotropically. It is also possible to derive an upper limit to the physical dimension of the source. The small instantaneous bandwidth of the signal (80 kHz) and the rate of sweep ($-4\cdot9$ MHz s^{-1}) show that the duration of the emission at any given frequency does not exceed 0·016 s. The source size therefore cannot exceed $4\cdot8\times10^3$ km.

An upper limit to the distance of the source may be derived from the observed rate of frequency sweep since impulsive radiation, whatever its origin, will be dispersed during its passage through the ionized hydrogen in interstellar space. For a uniform plasma the frequency drift caused by dispersion is given by

$$\frac{d\nu}{dt}=-\frac{c}{L}\frac{\nu^3}{\nu_p^2}$$

where L is the path and ν_p the plasma frequency. Assuming a mean density of 0·2 electron cm^{-3} the observed frequency drift ($-4\cdot9$ MHz s^{-1}) corresponds to $L\sim65$ parsec. Some frequency dispersion may, of course, arise in the source itself; in this case the dispersion in the interstellar medium must be smaller so that the value of L is an upper limit. While the interstellar electron density in the vicinity of the Sun is not well known, this result is important in showing that the pulsating radio sources so far detected must be local objects on a galactic distance scale.

The positional accuracy so far obtained does not permit any serious attempt at optical identification. The search area, which lies close to the galactic plane, includes two twelfth magnitude stars and a large number of weaker objects. In the absence of further data, only the most tentative suggestion to account for these remarkable sources can be made.

The most significant feature to be accounted for is the extreme regularity of the pulses. This suggests an origin in terms of the pulsation of an entire star, rather than some more localized disturbance in a stellar atmosphere. In this connexion it is interesting to note that it has already been suggested[2,3] that the radial pulsation of neutron stars may play an important part in the history of supernovae and supernova remnants.

A discussion of the normal modes of radial pulsation of compact stars has recently been given by Meltzer and Thorne[4], who calculated the periods for stars with central densities in the range 10^5 to 10^{19} g cm^{-3}. Fig. 4 of their paper indicates two possibilities which might account for the observed periods of the order 1 s. At a density of 10^7 g cm^{-3}, corresponding to a white dwarf star, the fundamental mode reaches a minimum period of about 8 s; at a slightly higher density the period increases again as the system tends towards gravitational collapse to a neutron star. While the fundamental period is not small enough to account for the observations the higher order modes have periods of the correct order of magnitude. If this model is adopted it is difficult to understand why the fundamental period is not dominant; such a period would have readily been detected in the present observations and its absence cannot be ascribed to observational effects. The alternative possibility occurs at a density of 10^{13} g cm^{-3}, corresponding to a neutron star; at this density the fundamental has a period of about 1 s, while for densities in excess of 10^{13} g cm^{-3} the period rapidly decreases to about 10^{-3} s.

If the radiation is to be associated with the radial pulsation of a white dwarf or neutron star there seem to be several mechanisms which could account for the radio emission. It has been suggested that radial pulsation would generate hydromagnetic shock fronts at the stellar surface which might be accompanied by bursts of X-rays and energetic electrons[2,3]. The radiation might then be likened to radio bursts from a solar flare occurring over the entire star during each cycle of the oscillation. Such a model would be in fair agreement with the upper limit of $\sim5\times10^3$ km for the dimension of the source, which compares with the mean value of 9×10^3 km quoted for white dwarf stars by Greenstein[5]. The energy requirement for this model may be roughly estimated by noting that the total energy emitted in a 1 MHz band by a type III solar burst would produce a radio flux of the right order if the source were at a distance of $\sim10^3$ A.U. If it

© 1968 Nature Publishing Group

is assumed that the radio energy may be related to the total flare energy ($\sim 10^{32}$ erg)[6] in the same manner as for a solar flare and supposing that each pulse corresponds to one flare, the required energy would be $\sim 10^{39}$ erg yr^{-1}; at a distance of 65 pc the corresponding value would be $\sim 10^{47}$ erg yr^{-1}. It has been estimated that a neutron star may contain $\sim 10^{51}$ erg in vibrational modes so the energy requirement does not appear unreasonable, although other damping mechanisms are likely to be important when considering the lifetime of the source[4].

The swept frequency characteristic of the radiation is reminiscent of type II and type III solar bursts, but it seems unlikely that it is caused in the same way. For a white dwarf or neutron star the scale height of any atmosphere is small and a travelling disturbance would be expected to produce a much faster frequency drift than is actually observed. As has been mentioned, a more likely possibility is that the impulsive radiation suffers dispersion during its passage through the interstellar medium.

More observational evidence is clearly needed in order to gain a better understanding of this strange new class of radio source. If the suggested origin of the radiation is confirmed further study may be expected to throw valuable light on the behaviour of compact stars and also on the properties of matter at high density.

We thank Professor Sir Martin Ryle, Dr J. E. Baldwin, Dr P. A. G. Scheuer and Dr J. R. Shakeshaft for helpful discussions and the Science Research Council who financed this work. One of us (S. J. B.) thanks the Ministry of Education of Northern Ireland and another (R. A. C.) the SRC for a maintenance award; J. D. H. P. thanks ICI for a research fellowship.

Received February 9, 1968.

1 Hewish, A., Scott, P. F., and Wills, D., *Nature*, **203**, 1214 (1964).
2 Cameron, A. G. W., *Nature*, **205**, 787 (1965).
3 Finzi, A., *Phys. Rev. Lett.*, **15**, 599 (1965).
4 Meltzer, D. W., and Thorne, K. S., *Ap. J.*, **145**, 514 (1966).
5 Greenstein, J. L., in *Handbuch der Physik*, *L.*, 161 (1958).
6 Fichtel, C. E., and McDonald, F. B., in *Annual Review of Astronomy and Astrophysics*, **5**, 351 (1967).

Action Potentials induced in Biomolecular Lipid Membranes

by
PAUL MUELLER
DONALD O. RUDIN
Department of Basic Research,
Eastern Pennsylvania Psychiatric Institute,
Philadelphia, Pennsylvania

Alamethicin, a cyclopeptide, can induce action potentials in biomolecular lipid membranes.

ALAMETHICIN, a cyclopeptide antibiotic from *Trichoderma viride* containing the amino-acids $(GluN)_2$, $(Glu)_1$, $(Pro)_2$, $(Gly)_1$, $(Ala)_2$, (Methyl Ala)$_3$, $(Val)_2$ and $(Leu)_1$ (ref. 1), develops a cationic conductance in experimental bilayers which can be controlled by a factor of 10^4 either chemically or by changing the membrane potential using applied voltages or ionic gradients. When it is brought together with an ionic gradient and a few μg/ml. of protamine, polylysine or spermine in the aqueous phase, the membranes develop characteristics of negative slope resistance (Fig. 1), delayed rectification (Fig. 2), bistable changes of EMF (Fig. 3*A*) and single or rhythmic action potentials (Fig. 3*B* and *C*). These changes resemble those occurring in excitable algae or those produced in bilayers by an unidentified proteinaceous material obtained from *Enterobacter cloacae* called excitability inducing material (EIM)[2,3]. As shown in Fig. 4, alamethicin structurally resembles other macrocyclic compounds like the depsipeptides and macrolids which develop extreme K^+/Na^+ selective conductances of an ohmic nature in experimental bilayers[4]. Alamethicin, however, is a pure peptide containing functional side groups.

The electrokinetic and chemical data suggest that six or more alamethicin molecules form either carriers or tubular channels through which ions flow across the membrane and that assembly and dissembly of these aggregates by the voltage or chemical factors regulate the conductance. The kinetic and chemical characteristics of alamethicin apparently fulfil the criteria of an allosteric protein specifically designed to form complexes of ionic co-ordination within lipid membranes. We discuss the possibility that related compounds could generate active ion transport and act as high energy intermediates in oxidative phosphorylation.

Bilayer membranes separating two aqueous phases were made by published methods[2,3,5]. Alamethicin acts on membranes made from mixed brain lipids and tocopherol, lecithin and decane, sphingomyelin and tocopherol[2,3] or oxidized cholesterol and octane[6], although the sensitivity to alamethicin and to protamine varies from one lipid type to another. Best results were obtained with membranes made from oxidized cholesterol (1 per cent), dodecyl acid phosphate (0·25 per cent), cholesterol (0·42 per cent in octane : dodecane, 1 : 3[6]) and with membranes made from purified lecithin (10 per cent in decane–squalene, 2 : 1). In the presence of adsorbates the life of the membrane lasts from a few minutes to several hours according to the type of lipid. Alamethicin can be introduced either by dissolving it in the bulk lipid solution or by adding it to the aqueous phase after bilayer formation.

Fig. 1 presents three steady state current–voltage, I(V), curves in the presence of 10^{-7} g/ml. of alamethicin on one side of the membrane. With 0·1 M sodium chloride on both sides, the membrane shows strong and more or less symmetrical rectification (Fig. 1*A*). The conductance decreases 10^4 times between zero and 100 mV and attains a maximum change of *e*-fold/5 mV. An ionic gradient generates a cationic resting potential of 10–30 mV/decade without intracationic selectivity. This acts like an applied potential to drive the system into its high conductance state although it does not deliver a net current. As shown in Fig. 1*B*, the resting potential shifts the I(V) curve along the voltage axis, raises the resting conductance and, for analytical reasons given elsewhere[3], transforms the rectification characteristic in one quadrant into a characteristic of negative slope resistance. If protamine is added to either aqueous phase under zero ion gradient there is a similar effect as shown in Fig. 1*C*. The resting conductance is increased and a negative resistance arises in the absence of a resting potential. This is the first of three distinct effects produced by protamine, histone or spermine acting as secondary adsorbates. Because this particular effect resembles that of

© 1968 Nature Publishing Group

WIKIPEDIA
The Free Encyclopedia

WIKIPEDIA

Hulse–Taylor pulsar

The **Hulse–Taylor pulsar** (known as **PSR B1913+16**, **PSR J1915+1606** or **PSR 1913+16**) is a binary star system composed of a neutron star and a pulsar which orbit around their common center of mass. It is the first binary pulsar ever discovered.

The pulsar was discovered by Russell Alan Hulse and Joseph Hooton Taylor Jr., of the University of Massachusetts Amherst in 1974. Their discovery of the system and analysis of it earned them the 1993 Nobel Prize in Physics "for the discovery of a new type of pulsar, a discovery that has opened up new possibilities for the study of gravitation."[8]

PSR B1913+16

Observation data		
	Epoch B1950.0	Equinox B1950.0
Constellation	Aquila[1]	
Right ascension	$19^h\ 13^m\ 12.4655^s$	
Declination	16° 01′ 08.189″	
Astrometry		
Distance	21,000 ly (6,400 pc)	
Details[2]		
Mass	1.441 $M_\odot$	
Rotation	59.02999792988 ms	
Other designations		
PSR B1913+16,[3] PSR J1915+1606,[3] Hulse–Taylor binary pulsar,[4] Hulse–Taylor system,[5] Hulse–Taylor binary, Hulse–Taylor pulsar,[6] Hulse–Taylor PSR[3]		
Database references		
SIMBAD	data (https://simbad.cds.unistra.fr/simbad/sim-id?Ident=PSR+J1915%2B1606)	

Discovery

Using the Arecibo 305 m dish, Hulse and Taylor detected pulsed radio emissions and thus identified the source as a pulsar, a rapidly rotating, highly magnetized neutron star. The neutron star rotates on its axis 17 times per second; thus the pulse period is 59 milliseconds.

After timing the radio pulses for some time, Hulse and Taylor noticed that there was a systematic variation in the arrival time of the pulses. Sometimes, the pulses were received a little sooner than expected; sometimes, later than expected. These variations changed in a smooth and repetitive manner, with a period of 7.75 hours. They realized that such behavior is predicted if the pulsar were in a binary orbit with another star, later confirmed to be another neutron star.[9]

Star system

The pulsar and its neutron star companion both follow elliptical orbits around their common center of mass. The period of the orbital motion is 7.75 hours, and the two neutron stars are believed to be nearly equal in mass, about 1.4 solar masses. Radio emissions have been detected from only one of the

two neutron stars.

The minimum separation at periastron is about 1.1 solar radii; the maximum separation at apastron is 4.8 solar radii. The orbit is inclined at about 45 degrees with respect to the plane of the sky. The orientation of periastron changes by about 4.2 degrees per year in direction of the orbital motion (relativistic precession of periastron). In January 1975, it was oriented so that periastron occurred perpendicular to the line of sight from Earth.[2][10]

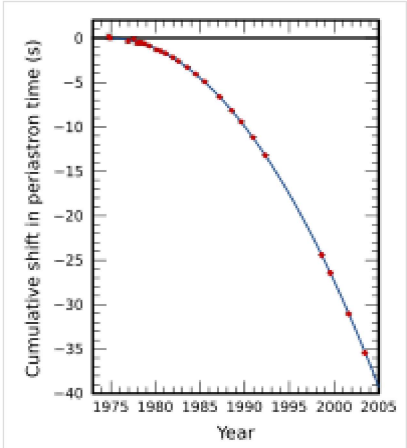

Evidence of orbital decay in PSR B1913+16.[7] The data points indicate the observed change in the time of periastron with date, relative to a system not undergoing decay. The parabola illustrates the theoretically expected change according to general relativity.

Use as a test of general relativity

The orbit has decayed since the binary system was initially discovered, in precise agreement with the loss of energy due to gravitational waves described by Albert Einstein's general theory of relativity.[2][10][11][12] The ratio of observed to predicted rate of orbital decay is calculated to be 0.997 ± 0.002.[12] The total power of the gravitational waves emitted by this system presently is calculated to be 7.35×10^{24} watts. For comparison, this is 1.9% of the power radiated in light by the Sun. The Solar System radiates only about 5,000 watts in gravitational waves, due to the much larger distances and orbit times, particularly between the Sun and Jupiter, and the relatively small mass of the planets.

With this comparatively large energy loss due to gravitational radiation, the rate of decrease of orbital period is 76.5 microseconds per year, the rate of decrease of semimajor axis is 3.5 meters per year, and the calculated lifetime to final inspiral is 300 million years.[2][12]

In 2004, Taylor and Joel M. Weisberg published a new analysis of the experimental data to date, concluding that the 0.2% disparity between the data and the predicted results is due to poorly known galactic constants, including the Sun's distance from the Galactic Center, the pulsar's proper motion and its distance from Earth. While there are efforts underway for better measurement of the first two quantities, they saw "little prospect for a significant improvement in knowledge of the pulsar distance," so tighter bounds will be difficult to attain. Taylor and Weisberg also mapped the pulsar's two-dimensional beam structure using the fact that the system's precession leads to varying pulse shapes. They found that the beam shape is latitudinally elongated, and pinched longitudinally near the centre, leading to an overall shape like a figure eight.[7]

In 2016, Weisberg and Huang published further results, still with a 0.16% disparity, finding that the ratio of the observed value compared to the predicted value was 0.9983 ± 0.0016.[13] They name the main driver of this improvement, from 1.8σ to 1σ discrepancy, as being improved galactic constants published in 2014.

Characteristics

- Mass of companion: 1.387 $M_\odot$
- Total mass of the system: 2.828378(7) $M_\odot$
- Orbital period: 7.751938773864 hr
- Eccentricity: 0.6171334
- Semi-major axis: 1,950,100 km
- Periastron separation: 746,600 km
- Apastron separation: 3,153,600 km
- Orbital velocity of stars at periastron (relative to center of mass): 450 km/s
- Orbital velocity of stars at apastron (relative to center of mass): 110 km/s

See also

- Binary pulsar
- PSR J0737−3039
- Square Kilometre Array
- Tests of general relativity
- Quadrupole formula

Astronomy portal

Physics portal

References

1. wikisky.org SKY-MAP for 19:15:28 / +16:06:27 (J2000 position) (http://server1.wikisky.org/v2?ra=19.25777778&de=16.10761206&zoom=5&show_grid=1&show_constellation_lines=1&show_constellation_boundaries=1&show_const_names=1)
2. Weisberg, J. M.; Taylor, J. H.; Fowler, L. A. (October 1981). "Gravitational waves from an orbiting pulsar". *Scientific American*. **245** (4): 74–82. Bibcode:1981SciAm.245d..74W (https://ui.adsabs.harvard.edu/abs/1981SciAm.245d..74W). doi:10.1038/scientificamerican1081-74 (https://doi.org/10.1038%2Fscientificamerican1081-74).
3. "PSR J1915+1606" (http://simbad.u-strasbg.fr/simbad/sim-basic?Ident=PSR+J1915%2B1606). *SIMBAD*. Centre de données astronomiques de Strasbourg.
4. Ramaswami, Ashwin. "Pulsars" (https://web.archive.org/web/20160308044739/http://enscience.me/pulsar/). *Encyclopedia of Science*. Enscience. Archived from the original (http://enscience.me/pulsar/) on 2016-03-08.
5. Wanjek, Christopher (2005-05-30). "Orbiting Stars Flooding Space With Exotic Gravitational Waves" (https://web.archive.org/web/20220125171545/https://www.nasa.gov/vision/universe/starsgalaxies/collide_whitedwarf_prt.htm). NASA. Archived from the original (https://www.nasa.gov/vision/universe/starsgalaxies/collide_whitedwarf_prt.htm) on 2022-01-25. Retrieved 2020-12-07.
6. "Hulse-Taylor Pulsar (PSR 1913+16)" (http://www.daviddarling.info/encyclopedia/H/HulseTaylor.html). *Encyclopedia of Science*. The Worlds of David Darling.

7. Weisberg, J.M.; Taylor, J.H. (July 2005). "The Relativistic Binary Pulsar B1913+16: Thirty Years of Observations and Analysis" (http://aspbooks.org/custom/publications/paper/328-0025.html). Written at Aspen, Colorado, United States. In F.A. Rasio; I.H. Stairs (eds.). *Binary Radio Pulsars*. ASP Conference Series. Vol. 328. San Francisco: Astronomical Society of the Pacific. p. 25. arXiv:astro-ph/0407149 (https://arxiv.org/abs/astro-ph/0407149). Bibcode:2005ASPC..328...25W (https://ui.adsabs.harvard.edu/abs/2005ASPC..328...25W).
8. "The Nobel Prize in Physics 1993" (https://www.nobelprize.org/prizes/physics/1993/press-release/). Nobel Foundation. Retrieved 2018-10-27. "for the discovery of a new type of pulsar, a discovery that has opened up new possibilities for the study of gravitation"
9. Weisberg, J. M.; Nice, D. J.; Taylor, J. H. (20 October 2010). "Timing Measurements of the Relativistic Binary Pulsar PSR B1913+16". *The Astrophysical Journal*. **722** (2): 1030–1034. arXiv:1011.0718 (https://arxiv.org/abs/1011.0718). Bibcode:2010ApJ...722.1030W (https://ui.adsabs.harvard.edu/abs/2010ApJ...722.1030W). doi:10.1088/0004-637X/722/2/1030 (https://doi.org/10.1088%2F0004-637X%2F722%2F2%2F1030). S2CID 118573183 (https://api.semanticscholar.org/CorpusID:118573183).
10. Taylor, J. H.; Weisberg, J. M. (1982). "A new test of general relativity – Gravitational radiation and the binary pulsar PSR 1913+16". *Astrophysical Journal*. **253**: 908–920. Bibcode:1982ApJ...253..908T (https://ui.adsabs.harvard.edu/abs/1982ApJ...253..908T). doi:10.1086/159690 (https://doi.org/10.1086%2F159690).
11. Taylor, J. H.; Weisberg, J. M. (1989). "Further experimental tests of relativistic gravity using the binary pulsar PSR 1913 + 16". *Astrophysical Journal*. **345**: 434–450. Bibcode:1989ApJ...345..434T (https://ui.adsabs.harvard.edu/abs/1989ApJ...345..434T). doi:10.1086/167917 (https://doi.org/10.1086%2F167917). S2CID 120688730 (https://api.semanticscholar.org/CorpusID:120688730).
12. Weisberg, J. M.; Nice, D. J.; Taylor, J. H. (2010). "Timing Measurements of the Relativistic Binary Pulsar PSR B1913+16". *Astrophysical Journal*. **722** (2): 1030–1034. arXiv:1011.0718 (https://arxiv.org/abs/1011.0718). Bibcode:2010ApJ...722.1030W (https://ui.adsabs.harvard.edu/abs/2010ApJ...722.1030W). doi:10.1088/0004-637X/722/2/1030 (https://doi.org/10.1088%2F0004-637X%2F722%2F2%2F1030). S2CID 118573183 (https://api.semanticscholar.org/CorpusID:118573183).
13. Weisberg, J. M.; Huang, Y. (21 September 2016). "Relativistic measurements from timing the binary pulsar PSR B1913+16" (https://doi.org/10.3847%2F0004-637X%2F829%2F1%2F55). *The Astrophysical Journal*. **829** (1): 55. arXiv:1606.02744 (https://arxiv.org/abs/1606.02744). Bibcode:2016ApJ...829...55W (https://ui.adsabs.harvard.edu/abs/2016ApJ...829...55W). doi:10.3847/0004-637X/829/1/55 (https://doi.org/10.3847%2F0004-637X%2F829%2F1%2F55). S2CID 119283147 (https://api.semanticscholar.org/CorpusID:119283147).

Retrieved from "https://en.wikipedia.org/w/index.php?title=Hulse–Taylor_pulsar&oldid=1267827363"

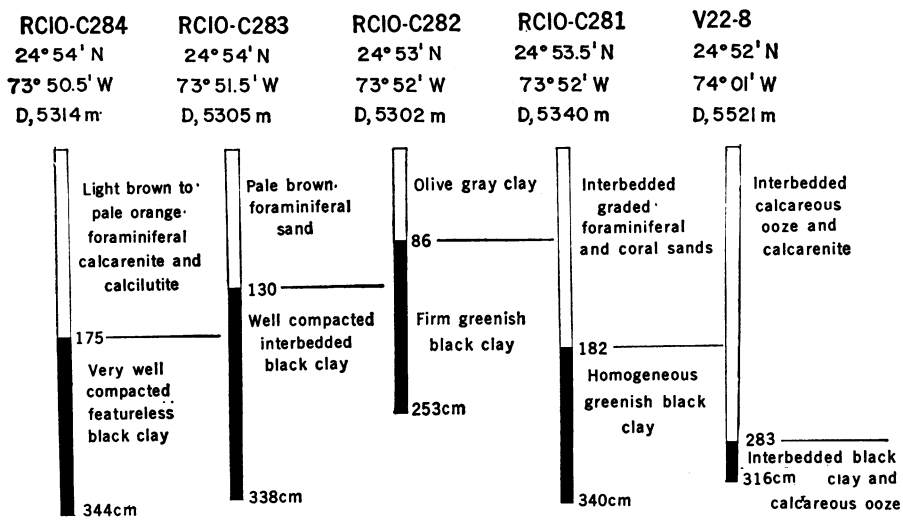

Fig. 2. Lithologic description of cores.

ranging from Upper Jurassic through Lower Cretaceous.

The probability of the assemblages being younger, reworked, marine deposits is small, on the basis of the following evidence: (i) lack of spore and pollen taxa characteristic of younger assemblages, at both the generic and species levels; (ii) occurrence of dinoflagellate and acritarch assemblages that have a closer affinity to older Cretaceous assemblages rather than younger; (iii) close quantitative identity with nonmarine and marine Middle Cretaceous assemblages on the continents; and (iv) evidence from Cretaceous coccoliths and Cenomanian foraminifers.

Study of the distribution of modern land-plant spores and pollen in the ocean basins, especially by Groot (*11*), Stanley (*12*), and Koreneva (*13*), has led to the conclusion that they are deposited relatively close to the continents. Koreneva concluded, moreover, that by 200 to 500 km offshore, the concentration of grains drops sharply from hundreds of specimens per gram to only a few, and that, by sorting or other processes, they lose all quantitative identity with the source area.

On the basis of this and other data obtained thus far from these studies, the assemblages occurring in the five cores suggest deposition in an oceanic environment much nearer a land source than is now indicated, a phenomenon that may be explained by some vertical or lateral tectonic displacement since deposition. The occurrence of thousands of grains per gram of sediment of well-preserved and quantitatively well-defined Middle Cretaceous assemblages, at considerable distance from shore, strongly supports this view. If the continental shelf were submerged through the Middle Cretaceous, the nearest source for these land-derived particles would have been at least 800 km distant.

In conclusion, palynology is held to be a valuable new tool in pre-Pleistocene deep-sea studies.

DANIEL HABIB

Department of Geology, Queens College of City University of New York, and Lamont Geological Observatory, Palisades, New York

References and Notes

1. J. Ewing, J. L. Worzel, M. Ewing, C. C. Windisch, *Science* **154**, 1125 (1966). See also C. C. Windisch, R. J. Leyden, J. L. Worzel, T. Saito, J. Ewing, *ibid.*, this issue.
2. T. Saito, L. H. Burckle, M. Ewing, *ibid.* **154**, 1173 (1966).
3. G. J. Brenner, *Maryland Board Natur. Resour. Dept. Geol. Mines Water Resour. Bull.*, No. 27 (1963), p. 215.
4. G. J. Brenner, *Rev. Paleobot. Palynol.* **1**, 219 (1967).
5. R. A. Couper, *Palaeontographica* **103**, 75 (1958).
6. D. Habib, *Micropaleontology*, in press.
7. R. L. Pierce, *Minnesota Geol. Surv. Bull.*, No. 42 (1961), p. 86.
8. I. C. Cookson and N. F. Hughes, *Palaeontology* **7**, 37 (1964).
9. I. C. Cookson and A. Eisenack, *Proc. Roy. Soc. Victoria* **70**, 19 (1958).
10. E. B. Leopold and H. M. Pakiser, *U.S. Geol. Surv. Bull.*, No. 1160–E (1964), p. 71.
11. J. J. Groot and C. R. Groot, *Marine Geol.* **4**, 387 (1966).
12. E. A. Stanley, *Southeastern Geol.* **7**, 25 (1965).
13. E. V. Koreneva, *Marine Geol.* **4**, 565 (1966).
14. Supported by grants from National Science Foundation (NSF–GA–1193) and from the Office of Naval Research [ONR-to-4(N00014-67-A-0108-0004)]. I thank M. Ewing, J. Ewing, C. Windisch, R. J. Leyden, T. Saito, L. Burckle, A. McIntyre, and J. D. Hays for reading the manuscript. R. J. Leyden was chief scientist when the *Conrad* cores were collected. Anne Riley and Martine Dreyfus typed the final manuscript. Lamont Geological Observatory contribution No. 1262.

26 September 1968

Pulsating Radio Sources near the Crab Nebula

Abstract. *Two new pulsating radio sources, designated NP 0527 and NP 0532, were found near the Crab Nebula and could be coincident with it. Both sources are sporadic, and no periodicities are evident. The pulse dispersions indicate that 1.58 ± 0.03 and 1.74 ± 0.02 × 10^{20} electrons per square centimeter lie in the direction of NP 0527 and NP 0532, respectively.*

During a general search for dispersed periodic signals, an unusual pair of pulsating sources was found in the vicinity of the Crab Nebula. They have been tentatively designated NP 0527 and NP 0532, pending more accurate measurements of position. The search was prompted by the discovery of periodic pulsed radio sources by Hewish *et al.* (*1*). The antenna was the 300-foot (90-m) transit telescope of the National Radio Astronomy Observatory (*2*), Green Bank, West Virginia. The receiver monitored the band between 110 and 115 Mhz with 50 channels, each 0.1 Mhz wide. The time constant of the receiver was 0.05 second, and all channels were sampled every 0.6 second. The output was recorded in digital form on magnetic tape.

The sources were observed during normal drift scans on 17, 19, and 21 October 1968. The beam width of the antenna (2.5°) permitted observations for 15 minutes each day. The sources become more evident when displayed in a time-frequency diagram (Fig. 1). A series of four pulses from NP 0532 and a single pulse from NP 0527 are shown; both the linear and second-order terms of the dispersion relation and also some narrow-band interference can be seen.

The apparent variations in pulse duration indicate variations in pulse strength and result primarily from the 50-msec time constant and the threshold method of display. The absence of strong variations with frequency, despite the strong variations with time, is one of the unusual characteristics of these sources, and it suggests that most of the variations may originate in the immediate vicinity of the sources. The illustrated pulses were observed with circular polarization to minimize the effects of Faraday rotation.

The stability of the pulse dispersion

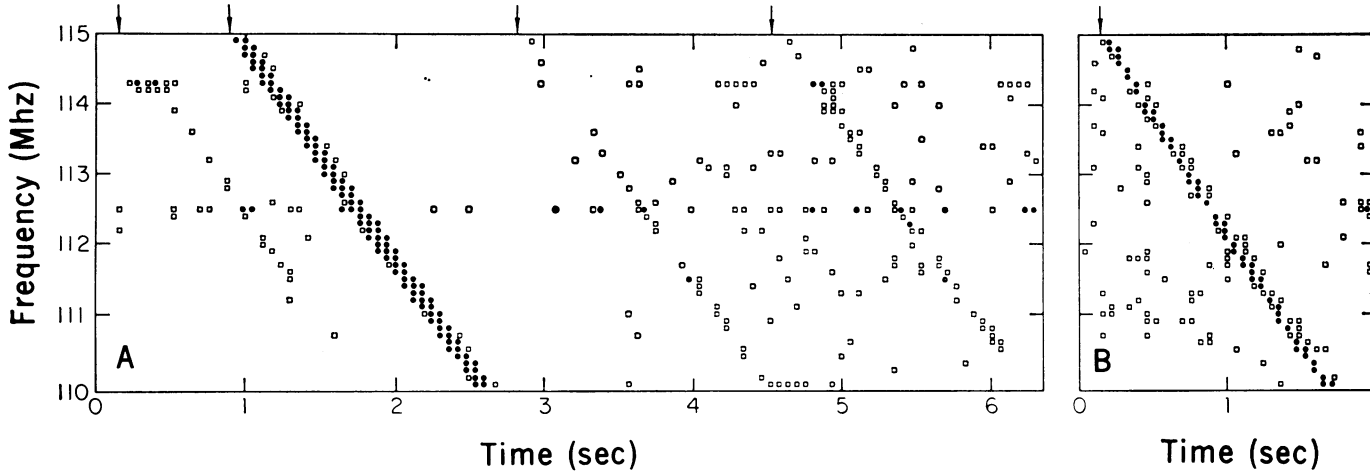

Fig. 1. Time-frequency diagram of radio pulses observed with circular polarization. (A) One strong and three weak pulses received from NP 0532 on 21 October 1968; (B) one typical pulse received from NP 0527 on 19 October 1968. Open squares and closed circles represent deviations from the mean of 4.2 and 8.3 standard deviations, respectively.

is indicated in the histogram (Fig. 2). The smaller maximum appears to be real. The separation between the two peaks is several times the experimental error, and pulses at both values of the dispersion were observed on all 3 days. The dispersion was determined for each pulse with a root-mean-square accuracy corresponding to less than 0.03×10^{20} electron cm^{-2}. The centers of the two peaks correspond to 1.58 ± 0.03 and $1.74 \pm 0.02 \times 10^{20}$ electron cm^{-2}.

Two values of dispersion could originate either from one source which has two emission modes with different ray paths, or from two separate sources. Under the assumption that the two sources are separate, they have tentatively been designated NP 0527 and NP 0532; the latter source is more active and more dispersed. The observed 1950.0 positions of NP 0527 are $\alpha = 5^h\ 27^m \pm 6^m$, $\delta = 22°30' \pm 2°$; those of NP 0532 are $\alpha = 5^h\ 32^m \pm 3^m$, $\delta = 22°30' \pm 2°$. The positions of both sources could be coincident with the Crab Nebula, located at $\alpha = 5^h\ 31^m$, $\delta = 21°58'$. An association of a pulsating radio source with a known celestial object would be very informative, and the determination of a more precise position for these sources is very important. The small angular size of the Crab Nebula would make accidental coincidence of the positions of the sources with that of the nebula highly unlikely. Such an association would support the view that pulsating radio sources may be neutron stars formed in explosions of supernovas (*3*). Scintillation mechanisms may also be responsible. If one or both of these sources are within the nebula, then still more precise measurements of position may permit one to ascertain whether there are any associations with the x-ray source (*4*), small low-frequency radio source (*5*), or central stars.

The observed dispersion of the pulsating sources is consistent with the

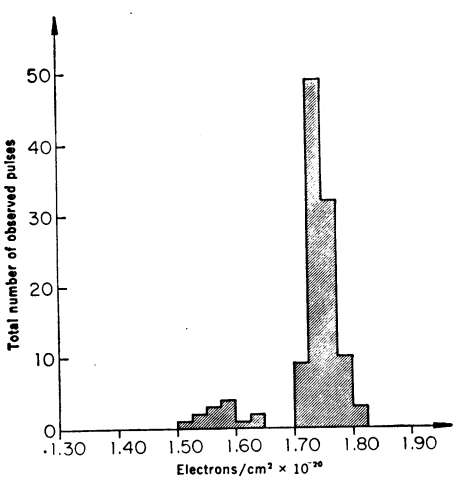

Fig. 2. Number of observed pulses at each value of dispersion. The lower dispersion peak corresponds to NP 0527; the other corresponds to NP 0532.

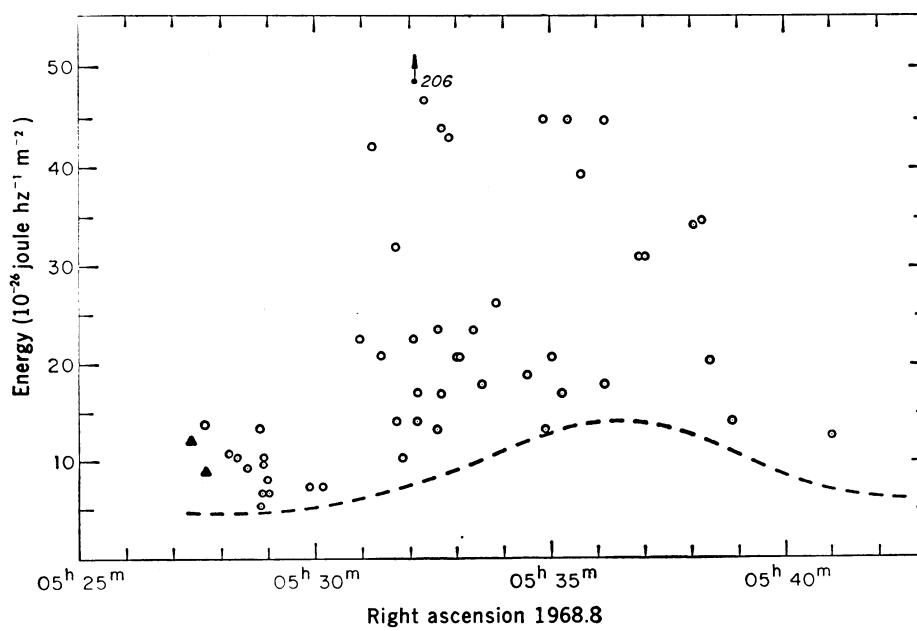

Fig. 3. Pulse energies of all pulses observed on 21 October 1968. The triangles and circles represent pulses from NP 0527 and NP 0532, respectively. The dashed line represents a detection threshold which varies with receiver noise and interference, and which was chosen to be approximately 5 standard deviations above the mean.

estimated distance to the Crab Nebula of 2 kparsec (*6*). If the sources are at this distance, then the average electron density in the interstellar medium is ≤ 0.028 electron cm^{-3} (*7*). If most of the electrons are close to the sources, then the interstellar electron density is even less.

The time variations of the sources are also unusual. The pulses tend to be isolated, although in NP 0532 they have been observed as close together as 0.21 second; NP 0527 is further distinguished by the brevity of its active periods, generally lasting no more than a few minutes during the observing period (15 minutes).

If the sources each have a unique period, then these periods must be less than 0.25 and 0.13 second for NP 0527 and NP 0532, respectively. These limits were determined by checking whether the time intervals between adjacent pulses were consistent with any single period. The upper limits on the source periods were constrained by the time resolution of the observations. If observations with greater time resolution fail to yield unique periods for these sources, they then constitute a new class of radio sources distinct from the highly periodic pulsars. In Fig. 3 are shown those pulses that were observed on 21 October 1968. No pattern is evident.

DAVID H. STAELIN*
EDWARD C. REIFENSTEIN III
National Radio Astronomy Observatory, Edgemont Road, Charlottesville, Virginia

References and Notes

1. A. Hewish, S. J. Bell, J. D. H. Pilkington, P. F. Scott, R. A. Collins, *Nature* **217**, 709 (1968).
2. Operated by Associated Universities, Inc., under tract with NSF.
3. M. J. Large, A. E. Vaughan, B. Y. Mills, *Nature* **220**, 340 (1968).
4. S. Bowyer, E. T. Bryam, T. A. Chubb, H. Friedman, *ibid.* **201**, 1307 (1964).
5. A. Hewish and S. E. Okoye, *ibid.* **207**, 59 (1965).
6. V. Trimble, *Astron. J.* **73**, 535 (1968).
7. H. J. Habing and S. R. Pottasch, *Astrophys. J. Lett.* **149**, L119 (1967).
8. We are grateful for the assistance of W. D. Brundage and K. A. Braly and for the support of the National Radio Astronomy Observatory.
* On leave of absence from the Department of Electrical Engineering, Massachusetts Institute of Technology.

27 November 1968

Surface Structure of Polymers: Glancing-Angle Electron Diffraction Study of Polyethylene

Abstract. *The surface regions of polyethylene nucleated and crystallized in contact with both a high-energy surface (gold) and a low-energy surface (fluorinated ethylene-propylene copolymer Teflon) have been examined by means of glancing-angle electron-diffraction techniques. Examination of these surfaces has been confined to a maximum depth of 120 angstroms. The surface region of the polyethylene generated in contact with the gold is considerably more crystalline than the surface generated in contact with the fluorinated ethylene-propylene copolymer Teflon. These results tend to corroborate recent wettability and infrared studies. Apparently, the surface structure of polyethylene is highly dependent upon the method of preparation.*

Wettability (*1*) and infrared (*2*) examination [attenuated total internal reflection (ATR)] of polymer surfaces, particularly polyethylene, have indicated that when a polymer is nucleated and crystallized in contact with a low-surface-energy phase [for example, vapor, fluorinated ethylene-propylene copolymer (FEP) Teflon, and so forth] an amorphous surface layer is generated, and when a high-surface-energy phase (for example, gold, metal oxide, and so forth) is used, a crystalline interfacial region is produced in the polymer when the melted polymer solidifies. In the above experiments, it was important to (i) provide for extensive wetting of the substrate by the melted polymer, (ii) maximize the area of the solid-liquid interface, and (iii) minimize the contribution of the liquid-vapor interface.

Since wettability determinations are confined to the outermost surface layer, the change in wettability when nucleation is initiated by a high-energy surface is attributed to a variation in surface density. Although an increase in the density of the surface layer may be interpreted as an increase in the extent of crystallinity, no direct evidence for crystallinity can be obtained from a wettability measurement. The evidence obtained from a detailed analysis of the infrared reflection of the absorption bands at 720 and 730 cm^{-1} offers firm proof that crystallinity in the surface region of polyethylene is enhanced when nucleated in contact with a high-surface-energy phase. However, since the depth of penetration of the infrared reflection experiments (*2*) is about 2 μ (*3*), considerably thicker than the surface layer (about 10 to 100 Å), we explored the possibility of using other nondestructive techniques which are confined to the surface layer (< 100 Å) to corroborate the wettability results. With glancing-angle electron diffraction, we examined the surface layer structure (about 60 to 300 Å in depth) to ascertain the extent of crystallinity.

A detailed account of the experimental variables and an analysis of the glancing-angle electron-diffraction technique is found elsewhere (*4*). An RCA-EMD-2 electron-diffraction unit operated at 50 kv was used. During glancing-angle electron diffraction, the beam is incident at angles of 0.02 to 0.1 radian. In order to eliminate prolonged exposure of the polymer film to the electron beam, we determined a proper angle of tilt on trial samples (the beam being stationary while the holder has 3 degrees of freedom). This enabled a diffraction pattern to be obtained in 2 (maximum 3) seconds.

The structure of the surface region of a high density (0.95 g cm^{-3}) polyethylene compound (Marlex 5003, Phillips Petroleum Co.) was examined. Two distinct types of surfaces were prepared. One specimen (treated) was nucleated and crystallized in contact with a high-energy surface (gold), whereas the other specimen (untreated) was nucleated and crystallized in contact with a low-energy surface (FEP Teflon). Both polymer films were prepared by being placed in contact with these surfaces for ½ hour at 200°C in nitrogen, and then being cooled slowly (1°C min^{-1}). It is important that the substrates be removed from the polyethylene by nonmechanical means so as not to damage the surface region which was generated by contact with the substrate. The gold was effectively removed by amalgamation with mercury.

The effectiveness of this method of removal is shown by the complete absence of any diffraction pattern due to gold. The FEP Teflon–polyethylene composite fell apart when cooled to room temperature. Both ATR and wet-

diabetes, phenylketonuria there will be genetic therapy. The appropriate DNA will be provided in the appropriate dose")[20] are justified. If, however, as I have tried to show, the specificity transmitted in inheritance is determined by a multimolecular system vastly more complex than a DNA molecule, any promise to control inheritance by chemical manipulation of DNA is likely to be illusory and, in certain social circumstances, harmful to the welfare of man.

Biologists have confronted successively—like a nest of Chinese boxes—levels of complexity ranging from the ecosystem to the internal chemistry of the cell. The last box has now been opened. According to the Watson–Crick theory, it should have contained the single source of all the inherited specificity of living organisms—DNA. It is my view that we now know that the last box is empty and that the inherited specificity of life is derived from nothing less than life itself.

This article reflects, in part, work supported by a grant from the US Public Health Service.

Received July 2; revised August 16, 1968.

1 Crick, F. H. C., *Cold Spring Harbor Symp. Quant. Biol.*, **31**, 3 (1966).
2 Commoner, B., *Nature*, **203**, 486 (1964).
3 Commoner, B., *Amer. Sci.*, **52**, 365 (1964).
4 Commoner, B., in *Horizons in Biochemistry* (Academic Press, New York, 1962).
5 *Nature*, **218**, 317 (1968).
6 Crick, F. H. C., *Symp. Exp. Biol.*, **12**, 138 (1958).
7 Kornberg, A., *Enzymatic Synthesis of DNA* (Wiley, New York, 1961).
8 Speyer, J. F., Karam, J. D., and Lenny, A. B., *Cold Spring Harbor Symp. Quant. Biol.*, **31**, 693 (1966).
9 Freese, B., and Freese, E., *Proc. US Nat. Acad. Sci.*, **57**, 650 (1967).
10 Marshall, R. E., Caskey, C. T., and Nirenberg, M., *Science*, **155**, 820 (1967).
11 Parisi, B., Milanesi, G., Van Etten, J. L., Perani, A., and Ciferri, O., *J. Mol. Biol.*, **28**, 295 (1967).
12 Gorini, L., Jacoby, G. A., and Breckenridge, L., *Cold Spring Harbor Symp. Quant. Biol.*, **31**, 687 (1966).
13 Barnett, W. E., Brown, David H., and Epler, J. L., *Proc. US Nat. Acad. Sci.*, **57**, 1775 (1967).
14 Barnett, W. E., and Epler, J. L., *Cold Spring Harbor Symp. Quant. Biol.*, **31**, 549 (1966).
15 Arca, M., Frontali, L., Sapora, O., and Tecce, G., *Biochim. Biophys Acta*, **145**, 284 (1967).
16 Commoner, B., *Nature*, **202**, 960 (1964).
17 Bennett, J. M., thesis, Washington Univ. (1968).
18 Britten, R. J., and Kohne, D. E., *Science*, **161**, 529 (1968).
19 Alper, T., Cramp, W. A., Haig, D. A., and Clarke, M. C., *Nature*, **214**, 764 (1967).
20 Sinsheimer, R., *Bull. Atomic Scientists*, **23** (No. 2), 9 (1967).

A Pulsar Supernova Association?

by
M. I. LARGE
A. E. VAUGHAN
B. Y. MILLS

Cornell-Sydney University Astronomy Centre,
School of Physics,
University of Sydney

A pulsar with a very short period (0·089 s) has been discovered at the position of a suspected supernova remnant, raising several interesting consequences.

In a search for southern pulsars at the Molonglo Radio Observatory, a very short period pulsar has been discovered at the position of a suspected supernova remnant. The estimates of distance are also compatible. The apparent coincidence of the pulsar and the supernova may be fortuitous, so it is premature to draw any far reaching conclusions. But it is interesting to explore the possibility of a physical association and to assume tentatively that the pulsar represents the final collapsed stage of a star which exploded. A number of deductions can then be made and some further observations suggested.

Following the scheme of Turtle and Vaughan[1] the pulsar is designated *PSR* 0833–45. The measured parameters are given in Table 1. The position given in the table was measured with the east–west arm of the telescope. The full cross shows a "point" source at $\alpha(1950.0) = 08^h\ 33^m\ 39.0^s \pm 1^s$ and $\delta(1950.0) = -45°\ 00'\ 05'' \pm 15''$. This source is of the correct flux density and close enough in position to be identified with the pulsar. Because of the short period of the pulsar (the shortest yet found) and the comparative constancy of the pulse amplitudes, the pulsar would be expected to appear as an ordinary "point" radio source when recorded with the normal 3 s time constant of the full cross (see Turtle and Vaughan[2]). We have therefore adopted the much more precise declination of the point source as that of the pulsar.

The pulsar is situated in a region of complex emission which has recently been discussed by Milne[3]. It lies within the boundaries of the extended radio source Vela *X* (*MSH* 0833–45) which Milne has shown to be part of a supernova shell some 4 or 5 degrees in diameter. The shell includes also the sources Vela *Y* and Vela *Z* and the filamentary nebula Stromlo 16. Milne suggests that the shell is at a distance of 500 ± 100 pc, which is in good agreement with the distance of the pulsar based on the dispersion measurement. The approximate centre of the emission region (as defined by Milne's outer contour 5 at 635 MHz) is at $\alpha(1950{\cdot}0)$ $08^h\ 38^m$, $\delta(1950{\cdot}0)$ $-45°$. The shell shows evidence of distortion, presumably due to interaction with the interstellar gas, so that the original supernova might well be considerably displaced from the centre of the radio emission region. *PSR* 0833–45 is situated less than 1° (20 per cent of the shell diameter) from the radio centre. An identification of the pulsar with the stellar remnant of the supernova thus seems to be a reasonable working hypothesis. In the following discussion we examine some of the interesting consequences of such an identification.

Table 1. MEASURED PARAMETERS OF *PSR* 0833–45

$\alpha(1950{\cdot}0)$	$08^h\ 33^m\ 38{\cdot}9^s \pm 1^s$
$\delta(1950{\cdot}0)$	$-45{\cdot}4° \pm 0{\cdot}3°$
l^{II}	$263{\cdot}5°$
b^{II}	$-2{\cdot}8°$
P(s)	$0{\cdot}0892 \pm 0{\cdot}0002$
$-\frac{d\nu}{dt}$ (at 408 MHz) MHz s^{-1}	155 ± 15
Distance (assuming $\bar{n}_e = 0{\cdot}1$ cm^{-3}) pc	500
Mean flux density (at 408 MHz) 10^{-26} W m^{-2} Hz^{-1}	$1{\cdot}7 \pm 0{\cdot}4$
Pulse length ms	~10

By comparison of the Faraday rotation of the polarized radio emission from Vela *X* with the dispersion measurements on the pulsar it is possible to obtain directly the mean longitudinal component of the interstellar magnetic field. There is some uncertainty about the rotation measure because, according to Milne, a large part of the Faraday rotation occurs within the radio emitting regions.

© 1968 Nature Publishing Group

In particular, he notes large differences of rotation measure for points only 0·25° apart near the peak of Vela *X*. If Milne's estimate of 46 rad m^{-2} for the component of rotation measure introduced between the source and the Sun is combined with the figure of 155 MHz s^{-1} for the dispersion of the pulsar at 408 MHz, we find that the mean longitudinal field is equal to 10^{-6} gauss. The mean absolute value for the field would obviously be greater. The mean electron density of 0·1 cm^{-3} initially assumed is also consistent with the astronomical distance to the supernova derived by Milne.

The short period of *PSR* 0833–45 and the low optical luminosity of other pulsars[1,2,4] makes it most unlikely that they can be associated with rotating or pulsating white dwarf stars. The most reasonable hypothesis is that they are neutron stars as originally suggested by Hewish *et al.*[5]. The radially pulsating model suggested by them would, however, be very difficult to reconcile with the long period of 1·96 s found for *PSR* 2045–16 (see Thorne and Ipser[6]). It is more plausible to invoke rotation as the basic modulation mechanism.

It seems most likely that the Vela supernova was of type II, resulting from an explosion of a massive star. Milne's data are compatible with either a type I or a type II, but Kesteven[7] has shown that the strong non-thermal galactic radio sources are typically associated with type II supernovae. If neutron stars are formed at every type II supernova explosion, and these have been continuing at their present rate of the order of one per 100 yr over the whole age of the galaxy, then there will be about 10^8 neutron stars in the galaxy, with a space density of the order of 10^{-3} pc^{-3}. While the statistics of pulsars is not yet well established, their space density must be of the order of 10^{-6} pc^{-3}. Thus on the hypothesis that all pulsars are neutron stars, the probability of a neutron star exhibiting pulsar characteristics is of the order of 10^{-3}, with an uncertainty of about two orders of magnitude. One possibility is that all neutron stars pass through a pulsar stage lasting for a time of the order of 10^7 yr (shortly after their formation if the suggested identification is correct). Alternatively, a fraction of neutron stars may be pulsars of longer lifetime. The limiting case is when one neutron star in 10^3 is a pulsar with an active lifetime at least as long as the age of the galaxy. A pulsar phase of long duration seems possible in view of the necessarily slow evolution of neutron stars, although the chance then of detecting the ephemeral gaseous remnant would be rather small. Pulsars probably exist with periods appreciably shorter than those already detected. It is not impossible that some pulsars are included as point sources in radio catalogues.

It is obviously necessary to examine all known and suspected supernova remnants with the greatest possible sensitivity. A preliminary search at the Molonglo Radio Observatory of fifteen possible remnants listed by Kesteven[7] has yielded no further pulsars. This is not surprising because most of the objects are more than 1 kpc distant and the resulting low flux densities and large dispersions would hinder discovery. Although the sensitivity of the east–west arm of the Molonglo Cross is high, the time of observation at each transit is limited to about 10 s. It would be more promising to track these and similar objects with a large steerable reflector with a fairly wide beam and to examine the output for periodicities, using averaging techniques extended over several hours. A range of frequencies and bandwidths should be used because the optimum receiver characteristics depend on the spectrum, rate of frequency drift, inherent pulse length and pulsar period. Frequencies of a few hundred megahertz with bandwidths in the range 0·1 MHz to 1 MHz seem promising on the present evidence.

If the age of most pulsars is very great an appreciable slowing down of the rotation rate might be expected due to the transfer of angular momentum to the interstellar medium. One might expect the older and more numerous pulsars to have significantly longer average periods than the newer and rarer pulsars. Such an effect would appear as a negative correlation between pulsar period and distance. For the eleven pulsars known at present, the correlation coefficient between these parameters is 0·53, a value which is statistically significant at the 10 per cent level. Several times the present number of pulsars is required to establish any such correlation. Indeed, systematic surveys to detect more pulsars are one of the most pressing requirements at present.

To conclude, the possible association between *PSR* 0833–45 and the Vela supernova remnant opens several interesting lines of enquiry. The hypothesis that pulsars are rotating neutron stars formed in the explosion of massive supernovae receives considerable support. If the identification is correct, however, it seems clear that it was made possible by fortunate astronomical circumstances. Verification of the idea that supernovae and pulsars are associated may require a great deal of further radio and optical observations. Details of the instrumentation used in the pulsar search and more accurate parameters of this and other pulsars already detected in the programme will be given in a later publication.

We thank Dr R. Wielebinski for his help in providing recording facilities used during the observations. This research was supported by grants from the Australian Research Grants Committee and the US National Science Foundation.

Received October 17, 1968.

1 Turtle, A. J., and Vaughan, A. E., *Nature*, **219**, 689 (1968).
2 Turtle, A. J., and Vaughan, A. E., *Nature*, **219**, 845 (1968).
3 Milne, D. K., *Austral. J. Phys.*, **21**, 201 (1968).
4 Bailey, J. A., and Mackay, C. D., *Nature*, **218**, 129 (1968).
5 Hewish, A., Bell, S. J., Pilkington, J. D. H., Scott, P. F., and Collins, R. A., *Nature*, **217**, 709 (1968).
6 Thorne, K. S., and Ipser, J. R., *Astrophys. J. Lett.*, **152**, L71 (1968).
7 Kesteven, M. J. L., *Austral. J. Phys.*, **21**, 369 (1968).

East Pacific Rise and Westward Drift of North America

by

HAROLD PALMER

Dames and Moore,
Los Angeles, California

There is some evidence for an ancestral East Pacific Rise which was overridden by North America in Mesozoic time.

THE conformity of the Mid-Atlantic Ridge system to a position midway between North America and Europe, and South America and Africa, and its magnetic, thermal and seismic characteristics lend credence to the seafloor spreading hypothesis. Hurley's recent review[1] of matching structural, lithologic and radiometric data which cross

© 1968 Nature Publishing Group

Table 6. DRUG-RESISTANT STRAINS OF *Staph. aureus* ISOLATED FROM THE SKIN AND NOSE OF PIGS AND FOWLS (MODIFIED FROM SMITH AND CRABB[19])

Animals	Drug fed	No. strains examined	Percentage of strains resistant to: Tetracyclines only	Penicillin only	Both tetracyclines and penicillin
Pigs	Tetracyclines	453 (160)	92·6	0	0
	Penicillin	109 (40)	0	30·3	0
	Neither	380 (160)	4·5	0	0
Fowls	Tetracyclines and penicillin	492 (100)	9·1	41·3	19·5
	Neither	246 (100)	2·8	2·8	1·2

The figures in brackets were the numbers of animals examined, ten from each herd or flock.

Table 7. DRUG-SENSITIVITY OF *Staph. aureus* STRAINS ISOLATED FROM THE NOSE OR SKIN OF THE ATTENDANTS OF ANIMALS FED DIETS CONTAINING LOW LEVELS OF ANTI-MICROBIAL DRUGS (MODIFIED FROM SMITH AND CRABB[19])

Type of strains	Percentage of carriers among attendants of: Tetracycline-fed pigs (35*)	Pigs not fed drugs (50*)	Tetracycline- and penicillin-fed fowls (37*)
Tetracycline-resistant only	34·2	0	14
Tetracycline- and penicillin-resistant	2·9	0	4
Penicillin-resistant only	11·3	5·4	30
Sensitive to both drugs	25·7	32·4	26
No *Staph. aureus* isolated	42·8	64·8	52

Where possible, twelve strains from the nose and twelve from the skin were examined.
* Number of attendants examined.

farms on which these mixtures were not fed was only 3·6 per cent.

The impact of the common policy in Britain of feeding fowls continuously on diets containing "nutritional" levels of penicillin and/or tetracyclines on the incidence of outbreaks of infection in poultry caused by drug-resistant strains of *Staph. aureus* is shown in Table 8. Penicillin and the tetracyclines now have little application in the treatment of this disease, a situation quite different from that which existed at the commencement of the antibiotic era.

Table 8. DRUG SENSITIVITY OF *Staph. aureus* STRAINS CAUSING STAPHYLOCOCCOSIS IN FOWLS

Fowls	No. of strains examined	Percentage of strains that were resistant to: Penicillin only	Tetracyclines only	Penicillin and tetracyclines	Streptomycin
Not fed drugs	30	0	0	0	0
Fed drugs*	40	35	0	60	2·5

*At "nutritional" levels only, penicillin and/or tetracyclines.

Conclusions

The widespread use of anti-microbial drugs in animals has led to the emergence of drug-resistant strains of pathogenic bacteria and these resistant strains are now causing a considerable proportion of the disease hitherto caused by sensitive strains. This complicates the satisfactory treatment of animal disease and the position is worsening. It also has implications for human health. There is no evidence that the resistant strains are any more, or any less, virulent than their sensitive counterparts. Neither is the character of animal disease altering in any observable way—other than in its chemotherapy—that can be attributed to the increased incidence of resistant strains.

There is little doubt that the continuous feeding of animals on drug-containing diets for "nutritional" purposes has contributed significantly to the present position. The more a drug is used in diets the less its value in the treatment of clinical disease. Moreover, as the variety of drugs used for "nutritional" purposes increases, so the variety of drug-resistant strains that are incriminated in outbreaks of disease increases and the number of drugs that can be used with confidence in the treatment of these outbreaks decreases. A strong case therefore exists for limiting the number of different kinds of drugs that can be used for "nutritional" purposes. Ideally, only drugs that are unsuitable or not usually used for the treatment of disease in animals and man, and that do not produce cross-resistance with ones that are, should be used in animal feeds. Such antibiotics are now available. Finally, the information now available calls into question the rationale of the so-called preventive use of drugs, whether as food additives or in any other form, against diseases caused by bacterial species in which drug resistance of the infective type can occur. The use of drugs in this manner may well give rise to the very situations they are intended to prevent.

1 Smith, H. W., *NZ Vet. J.*, **15** (9), 153 (1967).
2 Watanabe, T., *Bact. Rev.*, **27**, 87 (1963).
3 Smith, H. W., and Crabb, W. E., *Vet. Rec.*, **69**, 24 (1957).
4 Harry, E. G., *Res. Vet. Sci.*, **3**, 85 (1962).
5 Smith, H. W., and Halls, S., *Brit. Med. J.*, i, 266 (1966).
6 Sojka, W. J., and Carnaghan, R. B. A., *Res. Vet. Sci.*, **2**, 340 (1961).
7 Smith, H. W., *J. Hyg. Camb.*, **60**, 301 (1966).
8 Huey, C. R., and Edwards, P. R., *Proc. Soc. Exp. Biol. NY*, **97**, 550 (1958).
9 Ramsey, C. H., and Edwards, P. R., *Appl. Microbiol.*, **9**, 389 (1961).
10 McWhorter, A. C., Murrell, M. C., and Edwards, P. R., *Appl. Microbiol.*, **11**, 368 (1963).
11 Manten, A., Kampelmacher, E. H., and Guinée, P. A. M., *Antonie van Leeuwenhoek., J. Microbiol.*, **27**, 103 (1961).
12 Manten, A., Kampelmacher, E. H., and Guinée, P. A. M., *Antonie van Leeuwenhoek., J. Microbiol.*, **27**, 461 (1961).
13 Manten, A., Kampelmacher, E. H., and Guinée, P. A. M., *Tijrschr. Dier. geneesk.*, **88**, 1858 (1963).
14 Manten, A., Guinée, P. A. M., and Kampelmacher, E. H., *Zent. für. Bakt-Paras. Infekt. Hyg., 1, Orig.*, **200**, 13 (1966).
15 Anderson, E. S., *Brit. Med. J.*, ii, 1289 (1965).
16 Anderson, E. S., and Datta, N., *Lancet*, i, 407 (1965).
17 Anderson, E. S., and Lewis, M. J., *Nature*, **206**, 579 (1965).
18 Smith, H. W., *J. Path. Bact.*, **77**, 79 (1959).
19 Smith, H. W., and Crabb, W. E., *J. Path. Bact.*, **79**, 243 (1960).
20 Pogorzelska, A., and Wencel, Z., *Med. Dosw. i. Mikrob. Warsaw*, **17**, 213 (1965).

Rotating Neutron Stars as the Origin of the Pulsating Radio Sources

by

T. GOLD

Center for Radiophysics and Space Research, Cornell University, Ithaca, New York

The constancy of frequency in the recently discovered pulsed radio sources can be accounted for by the rotation of a neutron star. Because of the strong magnetic fields and high rotation speeds, relativistic velocities will be set up in any plasma in the surrounding magnetosphere, leading to radiation in the pattern of a rotating beacon.

THE case that neutron stars are responsible for the recently discovered pulsating radio sources[1–6] appears to be a strong one. No other theoretically known astronomical object would possess such short and accurate periodicities as those observed, ranging from 1·33 to 0·25 s. Higher harmonics of a lower fundamental frequency that may be possessed by a white dwarf have been mentioned; but the detailed fine structure of several short pulses

© 1968 Nature Publishing Group

repeating in each repetition cycle makes any such explanation very unlikely. Since the distances are known approximately from interstellar dispersion of the different radio frequencies, it is clear that the emission per unit emitting volume must be very high; the size of the region emitting any one pulse can, after all, not be much larger than the distance light travels in the few milliseconds that represent the lengths of the individual pulses. No such concentrations of energy can be visualized except in the presence of an intense gravitational field.

The great precision of the constancy of the intrinsic period also suggests that we are dealing with a massive object, rather than merely with some plasma physical configuration. Accuracies of one part in 10^8 belong to the realm of celestial mechanics of massive objects, rather than to that of plasma physics.

It is a consequence of the virial theorem that the lowest mode of oscillation of a star must always have a period which is of the same order of magnitude as the period of the fastest rotation it may possess without rupture. The range of 1·5 s to 0·25 s represents periods that are all longer than the periods of the lowest modes of neutron stars. They would all be periods in which a neutron star could rotate without excessive flattening. It is doubtful that the fundamental frequency of pulsation of a neutron star could ever be so long (ref. 7 and unpublished work of A. G. W. Cameron). If the rotation period dictates the repetition rate, the fine structure of the observed pulses would represent directional beams rotating like a lighthouse beacon. The different types of fine structure observed in the different sources would then have to be attributed to the particular asymmetries of each star (the "sunspots", perhaps). In such a model, time variations in the intensity of emission will have no effect on the precise phase in the repetition period where each pulse appears; and this is indeed a striking observational fact. A fine structure of pulses could be generated within the repetition period, depending only on the distribution of emission regions around the circumference of the star. Similarly, a fine structure in polarization may be generated, for each region may produce a different polarization or be overlaid by a different Faraday-rotating medium. A single pulsating region, on the other hand, could scarcely generate a repetitive fine structure in polarization as seems to have been observed now[8].

There are as yet not really enough clues to identify the mechanism of radio emission. It could be a process deriving its energy from some source of internal energy of the star, and thus as difficult to analyse as solar activity. But there is another possibility, namely, that the emission derives its energy from the rotational energy of the star (very likely the principal remaining energy source), and is a result of relativistic effects in a co-rotating magnetosphere.

In the vicinity of a rotating star possessing a magnetic field there would normally be a co-rotating magnetosphere. Beyond some distance, external influences would dominate, and co-rotation would cease. In the case of a fast rotating neutron star with strong surface fields, the distance out to which co-rotation would be enforced may well be close to that at which co-rotation would imply motion at the speed of light. The mechanism by which the plasma will be restrained from reaching the velocity of light will be that of radiation of the relativistically moving plasma, creating a radiation reaction adequate to overcome the magnetic force. The properties of such a relativistic magnetosphere have not yet been explored, and indeed our understanding of relativistic magnetohydrodynamics is very limited. In the present case the coupling to the electromagnetic radiation field would assume a major role in the bulk dynamical behaviour of the magnetosphere.

The evidence so far shows that pulses occupy about 1/30 of the time of each repetition period. This limits the region responsible to dimensions of the order of 1/30 of the circumference of the "velocity of light circle". In the radial direction equally, dimensions must be small; one would suspect small enough to make the pulse rise-times comparable with or larger than the flight time of light across the region that is responsible. This would imply that the radiation emanates from the plasma that is moving within 1 per cent of the velocity of light. That is the region of velocity where radiation effects would in any case be expected to become important.

The axial asymmetry that is implied needs further comment. A magnetic field of a neutron star may well have a strength of 10^{12} gauss at the surface of the 10 km object. At the "velocity of light circle", the circumference of which for the observed periods would range from 4×10^{10} to $0{\cdot}75 \times 10^{10}$ cm, such a field will be down to values of the order of 10^3–10^4 gauss (decreasing with distance slower than the inverse cube law of an undisturbed dipole field. A field pulled out radially by the stress of the centrifugal force of a whirling plasma would decay as an inverse square law with radius). Asymmetries in the radiation could arise either through the field or the plasma content being non-axially symmetric. A skew and non-dipole field may well result from the explosive event that gave rise to the neutron star; and the access to plasma of certain tubes of force may be dependent on surface inhomogeneities of the star where sufficiently hot or energetic plasma can be produced to lift itself away from the intense gravitational field (10–100 MeV for protons; much less for space charge neutralized electron-positron beams).

The observed distribution of amplitudes of pulses makes it very unlikely that a modulation mechanism can be responsible for the variability (unpublished results of P. A. G. Scheuer and observations made at Cornell's Arecibo Ionospheric Observatory) but rather the effect has to be understood in a variability of the emission mechanism. In that case the observed very sharp dependence of the instantaneous intensity on frequency (1 MHz change in the observation band gives a substantially different pulse amplitude) represents a very narrow-band emission mechanism, much narrower than synchrotron emission, for example. A coherent mechanism is then indicated, as is also necessary to account for the intensity of the emission per unit area that can be estimated from the lengths of the sub-pulses. Such a coherent mechanism would represent non-uniform static configurations of charges in the relativistically rotating region. Non-uniform distributions at rest in a magnetic field are more readily set up and maintained than in the case of high individual speeds of charges, and thus the configuration discussed here may be particularly favourable for the generation of a coherent radiation mechanism.

If this basic picture is the correct one it may be possible to find a slight, but steady, slowing down of the observed repetition frequencies. Also, one would then suspect that more sources exist with higher rather than lower repetition frequency, because the rotation rates of neutron stars are capable of going up to more than 100/s, and the observed periods would seem to represent the slow end of the distribution.

Work in this subject at Cornell is supported by a contract from the US Office of Naval Research.

Received May 20, 1968.

[1] Hewish, A., Bell, S. J., Pilkington, J. D. H., Scott, P. F., and Collins, R. A., *Nature*, **217**, 709 (1968).
[2] Pilkington, J. D. H., Hewish, A., Bell, S. J., and Cole, T. W., *Nature*, **218**, 126 (1968).
[3] Drake, F. D., Gundermann, E. J., Jauncey, D. L., Comella, J. M., Zeissig, G. A., and Craft, jun., H. D., *Science*, **160**, 503 (1968).
[4] Drake, F. D., *Science* (in the press).
[5] Drake, F. D., and Craft, jun., H. D., *Science*, **160**, 758 (1968).
[6] Tanenbaum, B. S., Zeissig, G. A., and Drake, F. D., *Science* (in the press).
[7] Thorne, K. S., and Ipser, J. R., *Ap. J.* (in the press).
[8] Lyne, A. G., and Smith, F. G., *Nature*, **218**, 124 (1968).

© 1968 Nature Publishing Group

doi:10.1038/nature09466

A two-solar-mass neutron star measured using Shapiro delay

P. B. Demorest[1], T. Pennucci[2], S. M. Ransom[1], M. S. E. Roberts[3] & J. W. T. Hessels[4,5]

Neutron stars are composed of the densest form of matter known to exist in our Universe, the composition and properties of which are still theoretically uncertain. Measurements of the masses or radii of these objects can strongly constrain the neutron star matter equation of state and rule out theoretical models of their composition[1,2]. The observed range of neutron star masses, however, has hitherto been too narrow to rule out many predictions of 'exotic' non-nucleonic components[3–6]. The Shapiro delay is a general-relativistic increase in light travel time through the curved space-time near a massive body[7]. For highly inclined (nearly edge-on) binary millisecond radio pulsar systems, this effect allows us to infer the masses of both the neutron star and its binary companion to high precision[8,9]. Here we present radio timing observations of the binary millisecond pulsar J1614-2230[10,11] that show a strong Shapiro delay signature. We calculate the pulsar mass to be $(1.97 \pm 0.04)M_{\odot}$, which rules out almost all currently proposed[2–5] hyperon or boson condensate equations of state ($M_{\odot}$, solar mass). Quark matter can support a star this massive only if the quarks are strongly interacting and are therefore not 'free' quarks[12].

In March 2010, we performed a dense set of observations of J1614-2230 with the National Radio Astronomy Observatory Green Bank Telescope (GBT), timed to follow the system through one complete 8.7-d orbit with special attention paid to the orbital conjunction, where the Shapiro delay signal is strongest. These data were taken with the newly built Green Bank Ultimate Pulsar Processing Instrument (GUPPI). GUPPI coherently removes interstellar dispersive smearing from the pulsar signal and integrates the data modulo the current apparent pulse period, producing a set of average pulse profiles, or flux-versus-rotational-phase light curves. From these, we determined pulse times of arrival using standard procedures, with a typical uncertainty of ~1 μs.

We used the measured arrival times to determine key physical parameters of the neutron star and its binary system by fitting them to a comprehensive timing model that accounts for every rotation of the neutron star over the time spanned by the fit. The model predicts at what times pulses should arrive at Earth, taking into account pulsar rotation and spin-down, astrometric terms (sky position and proper motion), binary orbital parameters, time-variable interstellar dispersion and general-relativistic effects such as the Shapiro delay (Table 1). We compared the observed arrival times with the model predictions, and obtained best-fit parameters by χ^2 minimization, using the TEMPO2 software package[13]. We also obtained consistent results using the original TEMPO package. The post-fit residuals, that is, the differences between the observed and the model-predicted pulse arrival times, effectively measure how well the timing model describes the data, and are shown in Fig. 1. We included both a previously recorded long-term data set and our new GUPPI data in a single fit. The long-term data determine model parameters (for example spin-down rate and astrometry) with characteristic timescales longer than a few weeks, whereas the new data best constrain parameters on timescales of the orbital period or less. Additional discussion of the long-term data set, parameter covariance and dispersion measure variation can be found in Supplementary Information.

As shown in Fig. 1, the Shapiro delay was detected in our data with extremely high significance, and must be included to model the arrival times of the radio pulses correctly. However, estimating parameter values and uncertainties can be difficult owing to the high covariance between many orbital timing model terms[14]. Furthermore, the χ^2 surfaces for the Shapiro-derived companion mass (M_2) and inclination angle (i) are often significantly curved or otherwise non-Gaussian[15]. To obtain robust error estimates, we used a Markov chain Monte Carlo (MCMC) approach to explore the post-fit χ^2 space and derive posterior probability distributions for all timing model parameters (Fig. 2). Our final results for the model

Table 1 | Physical parameters for PSR J1614-2230

Parameter	Value
Ecliptic longitude (λ)	245.78827556(5)°
Ecliptic latitude (β)	−1.256744(2)°
Proper motion in λ	9.79(7) mas yr^{-1}
Proper motion in β	−30(3) mas yr^{-1}
Parallax	0.5(6) mas
Pulsar spin period	3.1508076534271(6) ms
Period derivative	$9.6216(9) \times 10^{-21}$ s s^{-1}
Reference epoch (MJD)	53,600
Dispersion measure*	34.4865 pc cm^{-3}
Orbital period	8.6866194196(2) d
Projected semimajor axis	11.2911975(2) light s
First Laplace parameter ($e \sin \omega$)	$1.1(3) \times 10^{-7}$
Second Laplace parameter ($e \cos \omega$)	$-1.29(3) \times 10^{-6}$
Companion mass	$0.500(6)M_{\odot}$
Sine of inclination angle	0.999894(5)
Epoch of ascending node (MJD)	52,331.1701098(3)
Span of timing data (MJD)	52,469–55,330
Number of TOAs†	2,206 (454, 1,752)
Root mean squared TOA residual	1.1 μs
Right ascension (J2000)	16 h 14 min 36.5051(5) s
Declination (J2000)	−22° 30′ 31.081(7)′′
Orbital eccentricity (e)	$1.30(4) \times 10^{-6}$
Inclination angle	89.17(2)°
Pulsar mass	$1.97(4)M_{\odot}$
Dispersion-derived distance‡	1.2 kpc
Parallax distance	>0.9 kpc
Surface magnetic field	1.8×10^{8} G
Characteristic age	5.2 Gyr
Spin-down luminosity	1.2×10^{34} erg s^{-1}
Average flux density* at 1.4 GHz	1.2 mJy
Spectral index, 1.1–1.9 GHz	−1.9(1)
Rotation measure	−28.0(3) rad m^{-2}

Timing model parameters (top), quantities derived from timing model parameter values (middle) and radio spectral and interstellar medium properties (bottom). Values in parentheses represent the 1σ uncertainty in the final digit, as determined by MCMC error analysis. The fit included both 'long-term' data spanning seven years and new GBT–GUPPI data spanning three months. The new data were observed using an 800-MHz-wide band centred at a radio frequency of 1.5 GHz. The raw profiles were polarization- and flux-calibrated and averaged into 100-MHz, 7.5-min intervals using the PSRCHIVE software package[25], from which pulse times of arrival (TOAs) were determined. MJD, modified Julian date.

* These quantities vary stochastically on $\gtrsim$1-d timescales. Values presented here are the averages for our GUPPI data set.

† Shown in parentheses are separate values for the long-term (first) and new (second) data sets.

‡ Calculated using the NE2001 pulsar distance model[26].

[1]National Radio Astronomy Observatory, 520 Edgemont Road, Charlottesville, Virginia 22093, USA. [2]Astronomy Department, University of Virginia, Charlottesville, Virginia 22094-4325, USA. [3]Eureka Scientific, Inc., Oakland, California 94602, USA. [4]Netherlands Institute for Radio Astronomy (ASTRON), Postbus 2, 7990 AA Dwingeloo, The Netherlands. [5]Astronomical Institute "Anton Pannekoek", University of Amsterdam, 1098 SJ Amsterdam, The Netherlands.

©2010 Macmillan Publishers Limited. All rights reserved

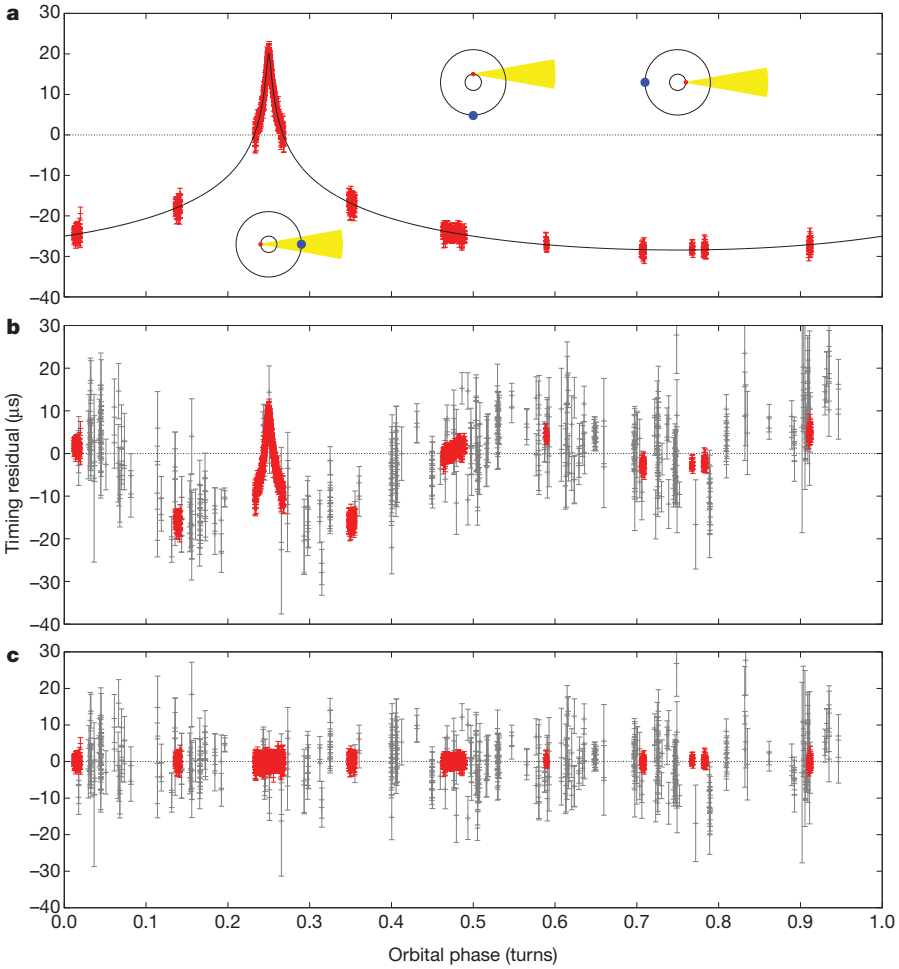

Figure 1 | Shapiro delay measurement for PSR J1614-2230. Timing residual—the excess delay not accounted for by the timing model—as a function of the pulsar's orbital phase. **a**, Full magnitude of the Shapiro delay when all other model parameters are fixed at their best-fit values. The solid line shows the functional form of the Shapiro delay, and the red points are the 1,752 timing measurements in our GBT–GUPPI data set. The diagrams inset in this panel show top-down schematics of the binary system at orbital phases of 0.25, 0.5 and 0.75 turns (from left to right). The neutron star is shown in red, the white dwarf companion in blue and the emitted radio beam, pointing towards Earth, in yellow. At orbital phase of 0.25 turns, the Earth–pulsar line of sight passes nearest to the companion (~240,000 km), producing the sharp peak in pulse delay. We found no evidence for any kind of pulse intensity variations, as from an eclipse, near conjunction. **b**, Best-fit residuals obtained using an orbital model that does not account for general-relativistic effects. In this case, some of the Shapiro delay signal is absorbed by covariant non-relativistic model parameters. That these residuals deviate significantly from a random, Gaussian distribution of zero mean shows that the Shapiro delay must be included to model the pulse arrival times properly, especially at conjunction. In addition to the red GBT–GUPPI points, the 454 grey points show the previous 'long-term' data set. The drastic improvement in data quality is apparent. **c**, Post-fit residuals for the fully relativistic timing model (including Shapiro delay), which have a root mean squared residual of 1.1 μs and a reduced χ^2 value of 1.4 with 2,165 degrees of freedom. Error bars, 1σ.

parameters, with MCMC error estimates, are given in Table 1. Owing to the high significance of this detection, our MCMC procedure and a standard χ^2 fit produce similar uncertainties.

From the detected Shapiro delay, we measure a companion mass of $(0.500 \pm 0.006)M_{\odot}$, which implies that the companion is a helium–carbon–oxygen white dwarf[16]. The Shapiro delay also shows the binary system to be remarkably edge-on, with an inclination of $89.17^{\circ} \pm 0.02^{\circ}$. This is the most inclined pulsar binary system known at present. The amplitude and sharpness of the Shapiro delay increase rapidly with increasing binary inclination and the overall scaling of the signal is linearly proportional to the mass of the companion star. Thus, the unique combination of the high orbital inclination and massive white dwarf companion in J1614-2230 cause a Shapiro delay amplitude orders of magnitude larger than for most other millisecond pulsars. In addition, the excellent timing precision achievable from the pulsar with the GBT and GUPPI provide a very high signal-to-noise ratio measurement of both Shapiro delay parameters within a single orbit.

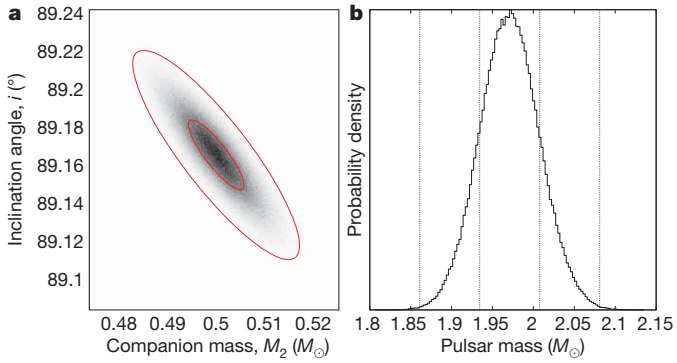

Figure 2 | Results of the MCMC error analysis. **a**, Grey-scale image shows the two-dimensional posterior probability density function (PDF) in the M_2–i plane, computed from a histogram of MCMC trial values. The ellipses show 1σ and 3σ contours based on a Gaussian approximation to the MCMC results. **b**, PDF for pulsar mass derived from the MCMC trials. The vertical lines show the 1σ and 3σ limits on the pulsar mass. In both cases, the results are very well described by normal distributions owing to the extremely high signal-to-noise ratio of our Shapiro delay detection. Unlike secular orbital effects (for example precession of periastron), the Shapiro delay does not accumulate over time, so the measurement uncertainty scales simply as $T^{-1/2}$, where T is the total observing time. Therefore, we are unlikely to see a significant improvement on these results with currently available telescopes and instrumentation.

The standard Keplerian orbital parameters, combined with the known companion mass and orbital inclination, fully describe the dynamics of a 'clean' binary system—one comprising two stable compact objects—under general relativity and therefore also determine the pulsar's mass. We measure a pulsar mass of $(1.97 \pm 0.04)M_{\odot}$, which is by far the highest precisely measured neutron star mass determined to date. In contrast with X-ray-based mass/radius measurements[17], the Shapiro delay provides no information about the neutron star's radius. However, unlike the X-ray methods, our result is nearly model independent, as it depends only on general relativity being an adequate description of gravity. In addition, unlike statistical pulsar mass determinations based on measurement of the advance of periastron[18–20], pure Shapiro delay mass measurements involve no assumptions about classical contributions to periastron advance or the distribution of orbital inclinations.

The mass measurement alone of a $1.97M_{\odot}$ neutron star significantly constrains the nuclear matter equation of state (EOS), as shown in Fig. 3. Any proposed EOS whose mass–radius track does not intersect the J1614-2230 mass line is ruled out by this measurement. The EOSs that produce the lowest maximum masses tend to be those which predict significant softening past a certain central density. This is a

©2010 Macmillan Publishers Limited. All rights reserved

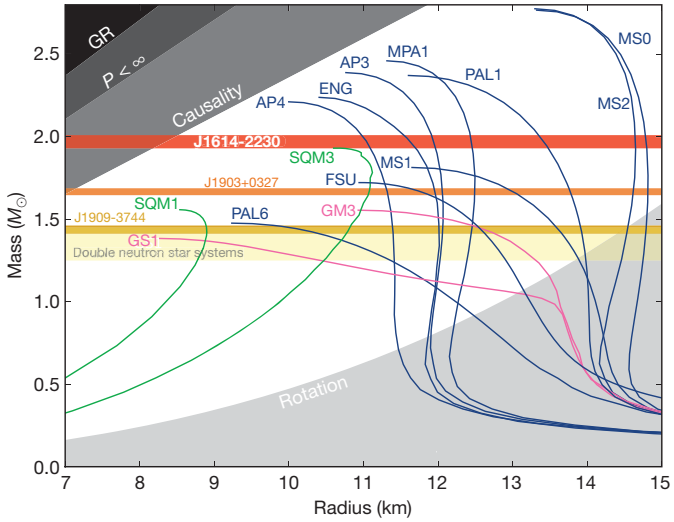

Figure 3 | Neutron star mass–radius diagram. The plot shows non-rotating mass versus physical radius for several typical EOSs[27]: blue, nucleons; pink, nucleons plus exotic matter; green, strange quark matter. The horizontal bands show the observational constraint from our J1614-2230 mass measurement of $(1.97 \pm 0.04)M_\odot$, similar measurements for two other millisecond pulsars[8,28] and the range of observed masses for double neutron star binaries[2]. Any EOS line that does not intersect the J1614-2230 band is ruled out by this measurement. In particular, most EOS curves involving exotic matter, such as kaon condensates or hyperons, tend to predict maximum masses well below $2.0M_\odot$ and are therefore ruled out. Including the effect of neutron star rotation increases the maximum possible mass for each EOS. For a 3.15-ms spin period, this is a $\lesssim 2\%$ correction[29] and does not significantly alter our conclusions. The grey regions show parameter space that is ruled out by other theoretical or observational constraints[2]. GR, general relativity; P, spin period.

common feature of models that include the appearance of 'exotic' hadronic matter such as hyperons[4,5] or kaon condensates[3] at densities of a few times the nuclear saturation density (n_s), for example models GS1 and GM3 in Fig. 3. Almost all such EOSs are ruled out by our results. Our mass measurement does not rule out condensed quark matter as a component of the neutron star interior[6,21], but it strongly constrains quark matter model parameters[12]. For the range of allowed EOS lines presented in Fig. 3, typical values for the physical parameters of J1614-2230 are a central baryon density of between $2n_s$ and $5n_s$ and a radius of between 11 and 15 km, which is only 2–3 times the Schwarzschild radius for a $1.97M_\odot$ star. It has been proposed that the Tolman VII EOS-independent analytic solution of Einstein's equations marks an upper limit on the ultimate density of observable cold matter[22]. If this argument is correct, it follows that our mass measurement sets an upper limit on this maximum density of $(3.74 \pm 0.15) \times 10^{15}\,\mathrm{g\,cm^{-3}}$, or $\sim 10n_s$.

Evolutionary models resulting in companion masses $>0.4M_\odot$ generally predict that the neutron star accretes only a few hundredths of a solar mass of material, and result in a mildly recycled pulsar[23], that is one with a spin period >8 ms. A few models resulting in orbital parameters similar to those of J1614-2230[23,24] predict that the neutron star could accrete up to $0.2M_\odot$, which is still significantly less than the $\gtrsim 0.6M_\odot$ needed to bring a neutron star formed at $1.4M_\odot$ up to the observed mass of J1614-2230. A possible explanation is that some neutron stars are formed massive ($\sim 1.9M_\odot$). Alternatively, the transfer of mass from the companion may be more efficient than current models predict. This suggests that systems with shorter initial orbital periods and lower companion masses—those that produce the vast majority of the fully recycled millisecond pulsar population[23]—may experience even greater amounts of mass transfer. In either case, our mass measurement for J1614-2230 suggests that many other millisecond pulsars may also have masses much greater than $1.4M_\odot$.

Received 7 July; accepted 1 September 2010.

1. Lattimer, J. M. & Prakash, M. The physics of neutron stars. *Science* **304,** 536–542 (2004).
2. Lattimer, J. M. & Prakash, M. Neutron star observations: prognosis for equation of state constraints. *Phys. Rep.* **442,** 109–165 (2007).
3. Glendenning, N. K. & Schaffner-Bielich, J. Kaon condensation and dynamical nucleons in neutron stars. *Phys. Rev. Lett.* **81,** 4564–4567 (1998).
4. Lackey, B. D., Nayyar, M. & Owen, B. J. Observational constraints on hyperons in neutron stars. *Phys. Rev. D* **73,** 024021 (2006).
5. Schulze, H., Polls, A., Ramos, A. & Vidaña, I. Maximum mass of neutron stars. *Phys. Rev. C* **73,** 058801 (2006).
6. Kurkela, A., Romatschke, P. & Vuorinen, A. Cold quark matter. *Phys. Rev. D* **81,** 105021 (2010).
7. Shapiro, I. I. Fourth test of general relativity. *Phys. Rev. Lett.* **13,** 789–791 (1964).
8. Jacoby, B. A., Hotan, A., Bailes, M., Ord, S. & Kulkarni, S. R. The mass of a millisecond pulsar. *Astrophys. J.* **629,** L113–L116 (2005).
9. Verbiest, J. P. W. *et al.* Precision timing of PSR J0437–4715: an accurate pulsar distance, a high pulsar mass, and a limit on the variation of Newton's gravitational constant. *Astrophys. J.* **679,** 675–680 (2008).
10. Hessels, J. *et al.* in *Binary Radio Pulsars* (eds Rasio, F. A. & Stairs, I. H.) 395 (ASP Conf. Ser. 328, Astronomical Society of the Pacific, 2005).
11. Crawford, F. *et al.* A survey of 56 midlatitude EGRET error boxes for radio pulsars. *Astrophys. J.* **652,** 1499–1507 (2006).
12. Özel, F., Psaltis, D., Ransom, S., Demorest, P. & Alford, M. The massive pulsar PSR J1614−2230: linking quantum chromodynamics, gamma-ray bursts, and gravitational wave astronomy. *Astrophys. J.* (in the press).
13. Hobbs, G. B., Edwards, R. T. & Manchester, R. N. TEMPO2, a new pulsar-timing package - I. An overview. *Mon. Not. R. Astron. Soc.* **369,** 655–672 (2006).
14. Damour, T. & Deruelle, N. General relativistic celestial mechanics of binary systems. II. The post-Newtonian timing formula. *Ann. Inst. Henri Poincaré Phys. Théor.* **44,** 263–292 (1986).
15. Freire, P. C. C. & Wex, N. The orthometric parameterisation of the Shapiro delay and an improved test of general relativity with binary pulsars. *Mon. Not. R. Astron. Soc.* (in the press).
16. Iben, I. Jr & Tutukov, A. V. On the evolution of close binaries with components of initial mass between 3 solar masses and 12 solar masses. *Astrophys. J Suppl. Ser.* **58,** 661–710 (1985).
17. Özel, F. Soft equations of state for neutron-star matter ruled out by EXO 0748 - 676. *Nature* **441,** 1115–1117 (2006).
18. Ransom, S. M. *et al.* Twenty-one millisecond pulsars in Terzan 5 using the Green Bank Telescope. *Science* **307,** 892–896 (2005).
19. Freire, P. C. C. *et al.* Eight new millisecond pulsars in NGC 6440 and NGC 6441. *Astrophys. J.* **675,** 670–682 (2008).
20. Freire, P. C. C., Wolszczan, A., van den Berg, M. & Hessels, J. W. T. A massive neutron star in the globular cluster M5. *Astrophys. J.* **679,** 1433–1442 (2008).
21. Alford, M. *et al.* Astrophysics: quark matter in compact stars? *Nature* **445,** E7–E8 (2007).
22. Lattimer, J. M. & Prakash, M. Ultimate energy density of observable cold baryonic matter. *Phys. Rev. Lett.* **94,** 111101 (2005).
23. Podsiadlowski, P., Rappaport, S. & Pfahl, E. D. Evolutionary sequences for low- and intermediate-mass X-ray binaries. *Astrophys. J.* **565,** 1107–1133 (2002).
24. Podsiadlowski, P. & Rappaport, S. Cygnus X-2: the descendant of an intermediate-mass X-Ray binary. *Astrophys. J.* **529,** 946–951 (2000).
25. Hotan, A. W., van Straten, W. & Manchester, R. N. PSRCHIVE and PSRFITS: an open approach to radio pulsar data storage and analysis. *Publ. Astron. Soc. Aust.* **21,** 302–309 (2004).
26. Cordes, J. M. & Lazio, T. J. W. NE2001.I. A new model for the Galactic distribution of free electrons and its fluctuations. Preprint at ⟨http://arxiv.org/abs/astro-ph/0207156⟩ (2002).
27. Lattimer, J. M. & Prakash, M. Neutron star structure and the equation of state. *Astrophys. J.* **550,** 426–442 (2001).
28. Champion, D. J. *et al.* An eccentric binary millisecond pulsar in the Galactic plane. *Science* **320,** 1309–1312 (2008).
29. Berti, E., White, F., Maniopoulou, A. & Bruni, M. Rotating neutron stars: an invariant comparison of approximate and numerical space-time models. *Mon. Not. R. Astron. Soc.* **358,** 923–938 (2005).

Supplementary Information is linked to the online version of the paper at www.nature.com/nature.

Acknowledgements P.B.D. is a Jansky Fellow of the National Radio Astronomy Observatory. J.W.T.H. is a Veni Fellow of The Netherlands Organisation for Scientific Research. We thank J. Lattimer for providing the EOS data plotted in Fig. 3, and P. Freire, F. Özel and D. Psaltis for discussions. The National Radio Astronomy Observatory is a facility of the US National Science Foundation, operated under cooperative agreement by Associated Universities, Inc.

Author Contributions All authors contributed to collecting data, discussed the results and edited the manuscript. In addition, P.B.D. developed the MCMC code, reduced and analysed data, and wrote the manuscript. T.P. wrote the observing proposal and created Fig. 3. J.W.T.H. originally discovered the pulsar. M.S.E.R. initiated the survey that found the pulsar. S.M.R. initiated the high-precision timing proposal.

Author Information Reprints and permissions information is available at www.nature.com/reprints. The authors declare no competing financial interests. Readers are welcome to comment on the online version of this article at www.nature.com/nature. Correspondence and requests for materials should be addressed to P.B.D. (pdemores@nrao.edu).

©2010 Macmillan Publishers Limited. All rights reserved

A Massive Pulsar in a Compact Relativistic Binary

John Antoniadis,* Paulo C. C. Freire, Norbert Wex, Thomas M. Tauris, Ryan S. Lynch, Marten H. van Kerkwijk, Michael Kramer, Cees Bassa, Vik S. Dhillon, Thomas Driebe, Jason W. T. Hessels, Victoria M. Kaspi, Vladislav I. Kondratiev, Norbert Langer, Thomas R. Marsh, Maura A. McLaughlin, Timothy T. Pennucci, Scott M. Ransom, Ingrid H. Stairs, Joeri van Leeuwen, Joris P. W. Verbiest, David G. Whelan

Introduction: Neutron stars with masses above 1.8 solar masses ($M_\odot$), possess extreme gravitational fields, which may give rise to phenomena outside general relativity. Hitherto, these strong-field deviations have not been probed by experiment, because they become observable only in tight binaries containing a high-mass pulsar and where orbital decay resulting from emission of gravitational waves can be tested. Understanding the origin of such a system would also help to answer fundamental questions of close-binary evolution.

Methods: We report on radio-timing observations of the pulsar J0348+0432 and phase-resolved optical spectroscopy of its white-dwarf companion, which is in a 2.46-hour orbit. We used these to derive the component masses and orbital parameters, infer the system's motion, and constrain its age.

Results: We find that the white dwarf has a mass of 0.172 ± 0.003 $M_\odot$, which, combined with orbital velocity measurements, yields a pulsar mass of 2.01 ± 0.04 $M_\odot$. Additionally, over a span of 2 years, we observed a significant decrease in the orbital period, $\dot{P}_b^{obs} = -8.6 \pm 1.4$ μs year^{-1} in our radio-timing data.

Discussion: Pulsar J0348+0432 is only the second neutron star with a precisely determined mass of 2 $M_\odot$ and independently confirms the existence of such massive neutron stars in nature. For these masses and orbital period, general relativity predicts a significant orbital decay, which matches the observed value, $\dot{P}_b^{obs}/\dot{P}_b^{GR} = 1.05 \pm 0.18$.

The pulsar has a gravitational binding energy 60% higher than other known neutron stars in binaries where gravitational-wave damping has been detected. Because the magnitude of strong-field deviations generally depends nonlinearly on the binding energy, the measurement of orbital decay transforms the system into a gravitational laboratory for an as-yet untested gravity regime. The consistency of the observed orbital decay with general relativity therefore supports its validity, even for such extreme gravity-matter couplings, and rules out strong-field phenomena predicted by physically well-motivated alternatives. Moreover, our result supports the use of general relativity–based templates for the detection of gravitational waves from merger events with advanced ground-based detectors.

Lastly, the system provides insight into pulsar-spin evolution after mass accretion. Because of its short merging time scale of 400 megayears, the system is a direct channel for the formation of an ultracompact x-ray binary, possibly leading to a pulsar-planet system or the formation of a black hole.

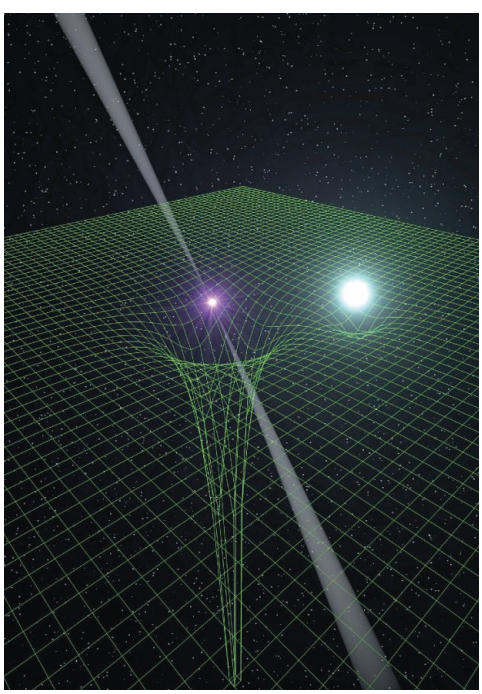

Artist's impression of the PSR J0348+0432 system. The compact pulsar (with beams of radio emission) produces a strong distortion of spacetime (illustrated by the green mesh). Conversely, spacetime around its white dwarf companion (in light blue) is substantially less curved. According to relativistic theories of gravity, the binary system is subject to energy loss by gravitational waves.

The list of author affiliations is available in the full article online.
*Corresponding author. E-mail: jantoniadis@mpifr-bonn.mpg.de

READ THE FULL ARTICLE ONLINE
http://dx.doi.org/10.1126/science.1233232

Cite this article as J. Antoniadis *et al.*, *Science* **340**, 1233232 (2013). DOI: 10.1126/science.1233232

FIGURES AND TABLE IN THE FULL ARTICLE

Fig. 1. Radial velocities and spectrum of the white dwarf companion to PSR J0348+0432

Fig. 2. Mass measurement of the white dwarf companion to PSR J0348+0432

Fig. 3. System masses and orbital-inclination constraints

Fig. 4. Probing strong field gravity with PSR J0348+0432

Fig. 5. Constraints on the phase offset in gravitational wave cycles in the LIGO/VIRGO bands

Fig. 6. Past and future orbital evolution of PSR J0348+0432

Fig. 7. Possible formation channels and final fate of PSR J0348+0432

Table 1. Observed and derived parameters for the PSR J0348+0432 system

SUPPLEMENTARY MATERIALS

Supplementary Text
Figs. S1 to S11
Tables S1 to S3
References

ADDITIONAL RESOURCES

Fundamental Physics in Radio Astronomy group at the Max-Planck-Institut für Radioastronomie, www3.mpifr-bonn.mpg.de/div/fundamental/

The European Southern Observatory, www.eso.org/public/

D. R. Lorimer, Binary and millisecond pulsars. *Living Rev. Relativ.* **11**, 8 (2008). http://dx.doi.org/10.12942/lrr-2008-8

T. Damour, "Binary systems as test-beds of gravity theories," in *Physics of Relativistic Objects in Compact Binaries: From Birth to Coalescence*, M. Colpi, P. Casella, V. Gorini, U. Moschella, A. Possenti, Eds. (Astrophysics and Space Science Library, Springer, Dordrecht, Netherlands, 2009), vol. 359, pp. 1–41.

Downloaded from https://www.science.org at Inter-University Centre for Astronomy and Astrophysics on January 07, 2025

Published by AAAS

A Massive Pulsar in a Compact Relativistic Binary

John Antoniadis,[1*] Paulo C. C. Freire,[1] Norbert Wex,[1] Thomas M. Tauris,[2,1] Ryan S. Lynch,[3] Marten H. van Kerkwijk,[4] Michael Kramer,[1,5] Cees Bassa,[5] Vik S. Dhillon,[6] Thomas Driebe,[7] Jason W. T. Hessels,[8,9] Victoria M. Kaspi,[3] Vladislav I. Kondratiev,[8,10] Norbert Langer,[2] Thomas R. Marsh,[11] Maura A. McLaughlin,[12] Timothy T. Pennucci,[13] Scott M. Ransom,[14] Ingrid H. Stairs,[15] Joeri van Leeuwen,[8,9] Joris P. W. Verbiest,[1] David G. Whelan[13]

Many physically motivated extensions to general relativity (GR) predict substantial deviations in the properties of spacetime surrounding massive neutron stars. We report the measurement of a 2.01 ± 0.04 solar mass ($M_\odot$) pulsar in a 2.46-hour orbit with a 0.172 ± 0.003 $M_\odot$ white dwarf. The high pulsar mass and the compact orbit make this system a sensitive laboratory of a previously untested strong-field gravity regime. Thus far, the observed orbital decay agrees with GR, supporting its validity even for the extreme conditions present in the system. The resulting constraints on deviations support the use of GR-based templates for ground-based gravitational wave detectors. Additionally, the system strengthens recent constraints on the properties of dense matter and provides insight to binary stellar astrophysics and pulsar recycling.

Neutron stars (NSs) with masses above 1.8 solar mass ($M_\odot$) manifested as radio pulsars are valuable probes of fundamental physics in extreme conditions unique in the observable universe and inaccessible to terrestrial experiments. Their high masses are directly linked to the equation-of-state (EOS) of matter at supranuclear densities (*1*, *2*) and constrain the lower mass limit for production of astrophysical black holes (BHs). Furthermore, they possess extreme internal gravitational fields, which result in gravitational binding energies substantially higher than those found in more common, 1.4-$M_\odot$ NSs. Modifications to general relativity (GR), often motivated by the desire for a unified model of the four fundamental forces, can generally imprint measurable signatures in the gravitational waves (GWs) radiated by systems containing such objects, even if deviations from GR vanish in the solar system and in less-massive NSs (*3*–*5*).

However, the most massive NSs known today reside in long-period binaries or other systems unsuitable for GW radiation tests. Identifying a massive NS in a compact, relativistic binary is thus of key importance for understanding gravity-matter coupling under extreme conditions. Furthermore, the existence of a massive NS in a relativistic orbit can also be used to test current knowledge of close binary evolution.

Results

PSR J0348+0432 and Optical Observations of Its Companion

PSR J0348+0432, a pulsar spinning at 39 ms in a 2.46-hour orbit with a low-mass companion, was detected by a recent survey (*6*, *7*) conducted with the Robert C. Byrd Green Bank Telescope (GBT). Initial timing observations of the binary yielded an accurate astrometric position, which allowed us to identify its optical counterpart in the Sloan Digital Sky Survey (SDSS) archive (*8*). The colors and flux of the counterpart are consistent with a low-mass white dwarf (WD) with a helium core at a distance of $d \sim 2.1$ kpc. Its relatively high apparent brightness ($g' = 20.71 \pm 0.03$ mag) allowed us to resolve its spectrum by using the Apache Point Optical Telescope. These observations revealed deep hydrogen lines, typical of low-mass WDs, confirming our preliminary identification. The radial velocities of the WD mirrored that of PSR J0348+0432, also verifying that the two stars are gravitationally bound.

In December 2011, we obtained phase-resolved spectra of the optical counterpart by using the FORS2 spectrograph of the Very Large Telescope (VLT). For each spectrum, we measured the radial velocity, which we then folded modulo the system's orbital period. Our orbital fit to the velocities constrains the semiamplitude of their modulation to be $K_{WD} = 351 \pm 4$ km s^{-1} (1-σ confidence interval) (Fig. 1; see also Materials and Methods). Similarly, the orbital solution from radio-pulsar timing yields $K_{PSR} = 30.008235 \pm 0.000016$ km s^{-1} for the pulsar. Combined, these constraints imply a mass ratio, $q = M_{PSR}/M_{WD} = K_{WD}/K_{PSR} = 11.70 \pm 0.13$.

Modeling of the Balmer-series lines in a high signal-to-noise average spectrum formed by the coherent addition of individual spectra (Fig. 1B) shows that the WD has an effective temperature of $T_{eff} = 10{,}120 \pm 47_{stat} \pm 90_{sys}$ K and a surface gravity of $\log_{10}[g\ (\text{cm s}^{-2})] = 6.035 \pm 0.032_{stat} \pm 0.060_{sys}$ dex. Here, the systematic error is an overall estimate of uncertainties resulting from our fitting technique and flux calibration (*8*). We found no correlation of this measurement with orbital phase and no signs of rotationally induced broadening in the spectral lines (*8*). Furthermore, we searched for variability by using the ULTRACAM instrument (*9*) on the 4.2-m William-Herschel Telescope in La Palma, Spain. The light curves (fig. S3), spanning 3 hours in total, have a root-mean-square (rms) scatter of ~0.53, 0.07, and 0.08 mag in u', g', and r', respectively, and show no evidence for variability over the course of the observations. The phase-folded light curve shows no variability either. Additionally, our calibrated magnitudes are consistent with the SDSS catalog magnitudes, implying that the WD shone at a constant flux over this ~5 year time scale (*8*).

Mass of the White Dwarf

The surface gravity of the WD scales with its mass and the inverse square of its radius ($g \equiv GM_{WD}/R_{WD}^2$, where G is Newton's gravitational constant). Thus, the observational constraints combined with a theoretical finite-temperature mass-radius relation for low-mass WDs yield a unique solution for the mass of the companion (*10*). Numerous such models exist in the literature, the most detailed of which are in good agreement for very-low-mass WDs (<0.17 to 0.18 $M_\odot$) but differ substantially for higher masses [e.g., (*11*–*13*)]. The main reason for this is the difference in the predicted size of the hydrogen envelope, which determines whether the main energy source of the star is residual hydrogen burning (for "thick" envelopes) or the latent heat of the core (for "thin" envelopes).

In the most widely accepted scenario, WDs lose their thick hydrogen envelope only if their mass exceeds a threshold. The exact location of the latter is still uncertain but estimated to be around 0.17 to 0.22 $M_\odot$ [e.g., (*11*–*13*)]. Two other pulsars with WD companions, studied in the literature, strongly suggest that this transition threshold is indeed most likely close to 0.2 $M_\odot$ (*10*, *14*). In particular, PSR J1909−3744 has a large characteristic age of several gigayears (Gy) and a WD

[1]Max-Planck-Institut für Radioastronomie, Auf dem Hügel 69, 53121 Bonn, Germany. [2]Argelander Institut für Astronomie, Auf dem Hügel 71, 53121 Bonn, Germany. [3]Department of Physics, McGill University, 3600 University Street, Montreal, QC H3A 2T8, Canada. [4]Department of Astronomy and Astrophysics, University of Toronto, 50 St. George Street, Toronto, ON M5S 3H4, Canada. [5]Jodrell Bank Centre for Astrophysics, The University of Manchester, Alan Turing Building, Manchester M13 9PL, UK. [6]Department of Physics and Astronomy, University of Sheffield, Sheffield S3 7RH, UK. [7]Deutsches Zentrum für Luft- und Raumfahrt e.V. (DLR), Raumfahrtmanagement, Königswinterer Str. 522-524, 53227 Bonn, Germany. [8]ASTRON, the Netherlands Institute for Radio Astronomy, Postbus 2, 7990 AA Dwingeloo, Netherlands. [9]Astronomical Institute Anton Pannekoek, University of Amsterdam, Science Park 904, 1098 XH Amsterdam, Netherlands. [10]Astro Space Center of the Lebedev Physical Institute, Profsoyuznaya str. 84/32, Moscow 117997, Russia. [11]Department of Physics, University of Warwick, Coventry CV4 7AL, UK. [12]Department of Physics, West Virginia University, 111 White Hall, Morgantown, WV 26506, USA. [13]Department of Astronomy, University of Virginia, Post Office Box 400325, Charlottesville, VA 22904, USA. [14]National Radio Astronomy Observatory, 520 Edgemont Road, Charlottesville, VA 22903, USA. [15]Department of Physics and Astronomy, University of British Columbia, 6224 Agricultural Road, Vancouver, BC V6T 1Z1, Canada.

*Corresponding author. E-mail: jantoniadis@mpifr-bonn.mpg.de

Downloaded from https://www.science.org at Inter-University Centre for Astronomy and Astrophysics on January 07, 2025

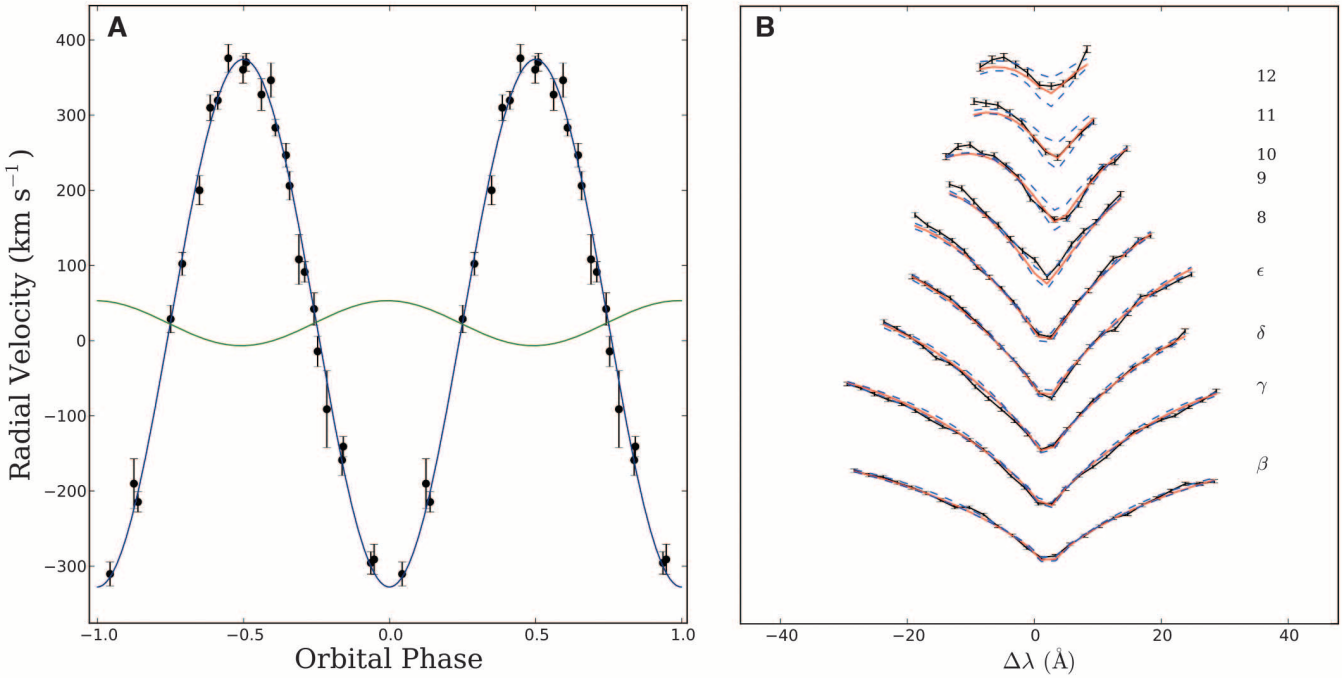

Fig. 1. Radial velocities and spectrum of the white dwarf companion to PSR J0348+0432. (**A**) Radial velocities of the WD companion to PSR J0348+0432 plotted against the orbital phase (shown twice for clarity). Overplotted is the best-fit orbit of the WD (blue line) and the mirror orbit of the pulsar (green). Error bars indicate 1-σ confidence intervals. (**B**) Details of the fit to the Balmer lines (Hβ to H12) in the average spectrum of the WD companion to PSR J0348+0432 created by the coherent addition of 26 individual spectra shifted to zero velocity. Lines from Hβ (bottom) to H12 are shown. The red solid lines are the best-fit atmospheric model (see text). Two models, one with T_{eff} = 9900 K and $\log_{10} g$ = 5.70 and one with T_{eff} = 10,200 K and $\log_{10} g$ = 6.30, each ~ 3-σ off from the best-fit central value (including systematics), are shown for comparison (dashed blue lines).

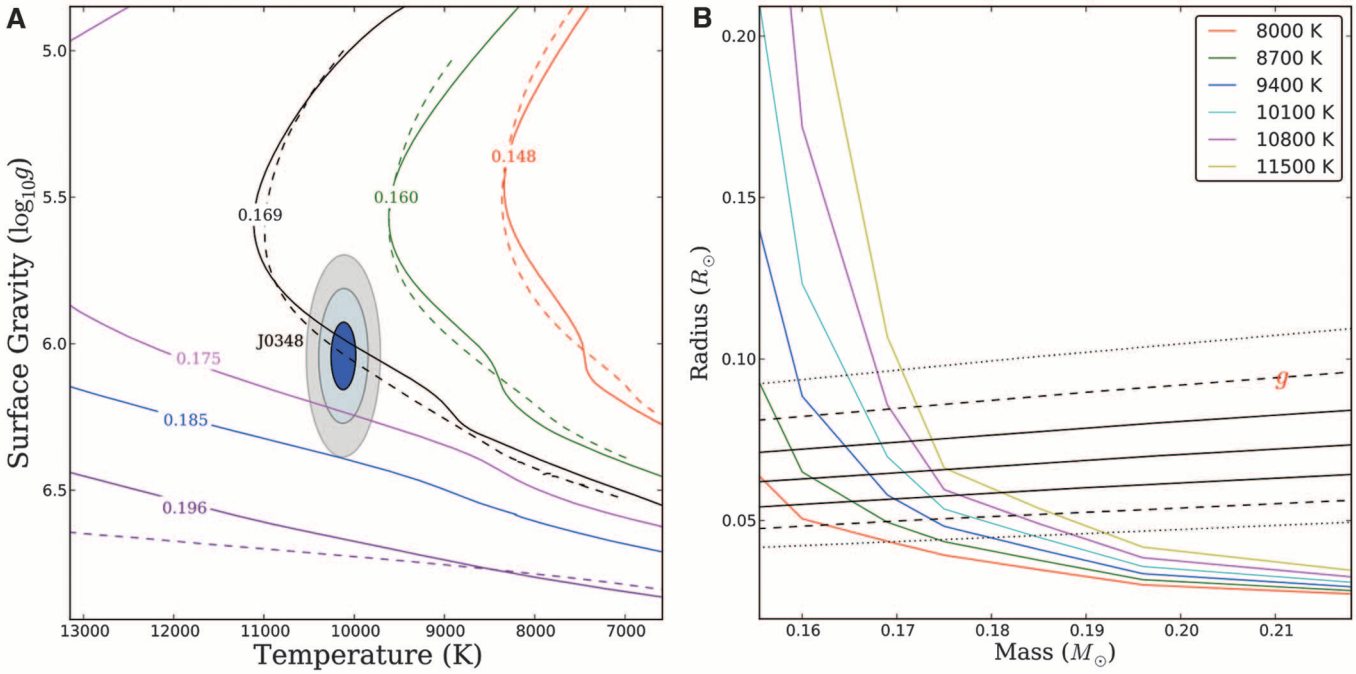

Fig. 2. Mass measurement of the white dwarf companion to PSR J0348+0432. (**A**) Constraints on T_{eff} and g for the WD companion to PSR J0348+0432 compared with theoretical WD models. The shaded areas depict the $\chi^2 - \chi^2_{\mathrm{min}}$ = 2.3, 6.2, and 11.8 intervals (equivalent to 1-, 2-, and 3-σ) of our fit to the average spectrum. Dashed lines show the detailed theoretical cooling models of (*11*). Continuous lines depict tracks with thick envelopes for masses up to ~0.2 $M_\odot$ that yield the most conservative constraints for the mass of the WD. (**B**) Finite-temperature mass-radius relations for our models together with the constraints imposed from modeling of the spectrum. Low mass–high temperature points are an extrapolation from lower temperatures.

Downloaded from https://www.science.org at Inter-University Centre for Astronomy and Astrophysics on January 07, 2025

companion with a well-determined mass of 0.20 $M_\odot$ (*15*) that appears to be hot (*10*), suggesting that its envelope is thick. For this reason, we base the WD mass estimate on cooling tracks with thick hydrogen atmospheres for masses up to 0.2 $M_\odot$, which we constructed by using the MESA stellar evolution code (*8*, *16*). Initial models were built for masses identical to the ones in (*11*), for which previous comparisons have yielded good agreement with observations (*14*), with the addition of tracks with 0.175 and 0.185 $M_\odot$ for finer coverage (Fig. 2). For masses up to 0.169 $M_\odot$, our models show excellent agreement with (*11*); however, our 0.196 $M_\odot$ model is quite different, because it has a thick envelope instead of a thin one. Being closer to the constraints for the WD companion to PSR J0348+0432, it yields a more conservative mass constraint, $M_{\rm WD}$ = 0.165 to 0.185 at 99.73% confidence (Fig. 3 and Table 1), which we adopt. The corresponding radius is $R_{\rm WD}$ = 0.046 to 0.092 $R_\odot$ at 99.73% confidence. Our models yield a cooling age of $\tau_{\rm cool} \sim 2$ Gy.

Pulsar Mass

The derived WD mass and the observed mass ratio q imply a NS mass in the range from 1.97 to 2.05 $M_\odot$ at 68.27% or 1.90 to 2.18 $M_\odot$ at 99.73% confidence. Hence, PSR J0348+0432 is only the second NS with a precisely determined mass around 2 $M_\odot$, after PSR J1614−2230 (*2*). It has a 3-σ lower mass limit 0.05 $M_\odot$ higher than the latter and therefore provides a verification, using a different method, of the constraints on the EOS of superdense matter present in NS interiors (*2*, *17*). For these masses and the known orbital period, GR predicts that the orbital period should decrease at the rate of $\dot{P}_{\rm b}^{\rm GR} = (-2.58^{+0.07}_{-0.11}) \times 10^{-13}$ s s^{-1} (68.27% confidence) because of energy loss through GW emission.

Radio Observations

Since April 2011, we have been observing PSR J0348+0432 with the 1.4-GHz receiver of the 305-m radio telescope at the Arecibo Observatory by using its four wide-band pulsar processors (*18*). In order to verify the Arecibo data, we have been independently timing PSR J0348+0432 at 1.4 GHz by using the 100-m radio telescope in Effelsberg, Germany. The two timing data sets produce consistent rotational models, providing added confidence in both. Combining the Arecibo and Effelsberg data with the initial GBT observations (*7*), we derived the timing solution presented in Table 1. To match the arrival times, the solution requires a significant measurement of orbital decay, $\dot{P}_{\rm b} = -2.73 \times 10^{-13} \pm 0.45 \times 10^{-13}$ s s^{-1} (68.27% confidence).

The total proper motion and distance estimate (Table 1) allowed us to calculate the kinematic corrections to $\dot{P}_{\rm b}$ from its motion in the Galaxy, plus any contribution from possible variations of G: $\delta\dot{P}_{\rm b} = 0.016 \times 10^{-13} \pm 0.003 \times 10^{-13}$ s s^{-1}. This is negligible compared to the measurement uncertainty. Similarly, the small rate of rotational energy loss of the pulsar (Table 1) excludes any substantial contamination resulting from mass loss from the system; furthermore, we can exclude substantial contributions to $\dot{P}_{\rm b}$ from tidal effects [see (*8*) for details]. Therefore, the observed $\dot{P}_{\rm b}$ is caused by GW emission, and its magnitude is entirely consistent with the one predicted by GR: $\dot{P}_{\rm b}/\dot{P}_{\rm b}^{\rm GR} = 1.05 \pm 0.18$ (Fig. 3).

If we assume that GR is the correct theory of gravity, we can then derive the component masses from the intersection of the regions allowed by q and $\dot{P}_{\rm b}$ (Fig. 3): $M_{\rm WD} = 0.177^{+0.017}_{-0.018}$ $M_\odot$ and $M_{\rm PSR} = 2.07^{+0.20}_{-0.21}$ $M_\odot$ (68.27% confidence). These values are not too constraining yet. However, the uncertainty of the measurement of $\dot{P}_{\rm b}$ decreases with $T_{\rm baseline}^{-5/2}$ (where $T_{\rm baseline}$ is the timing baseline); therefore, this method will yield very precise mass measurements within a couple of years.

Discussion

PSR J0348+0432 as a Testbed for Gravity

There are strong arguments for GR not to be valid beyond a (yet unknown) critical point, like its incompatibility with quantum theory and its prediction of the formation of spacetime singularities. Therefore, it remains an open question whether GR is the final description of macroscopic gravity. This strongly motivates testing gravity regimes that have not been tested before, in particular regimes where gravity is strong and highly nonlinear. Presently, binary pulsars provide the best high-precision experiments to probe strong-field deviations from GR and the best tests of the radiative properties of gravity (*19*–*23*). The orbital period of PSR J0348+0432 is only 15 s longer than that of the double pulsar system PSR J0737–3039, but it has ~two times more fractional gravitational binding energy than each of the double-pulsar NSs. This places it far outside the presently tested binding energy range (Fig. 4A) (*8*). Because the magnitude of strong-field effects generally depends nonlinearly on the binding energy, the measurement of orbital decay transforms the

Downloaded from https://www.science.org at Inter-University Centre for Astronomy and Astrophysics on January 07, 2025

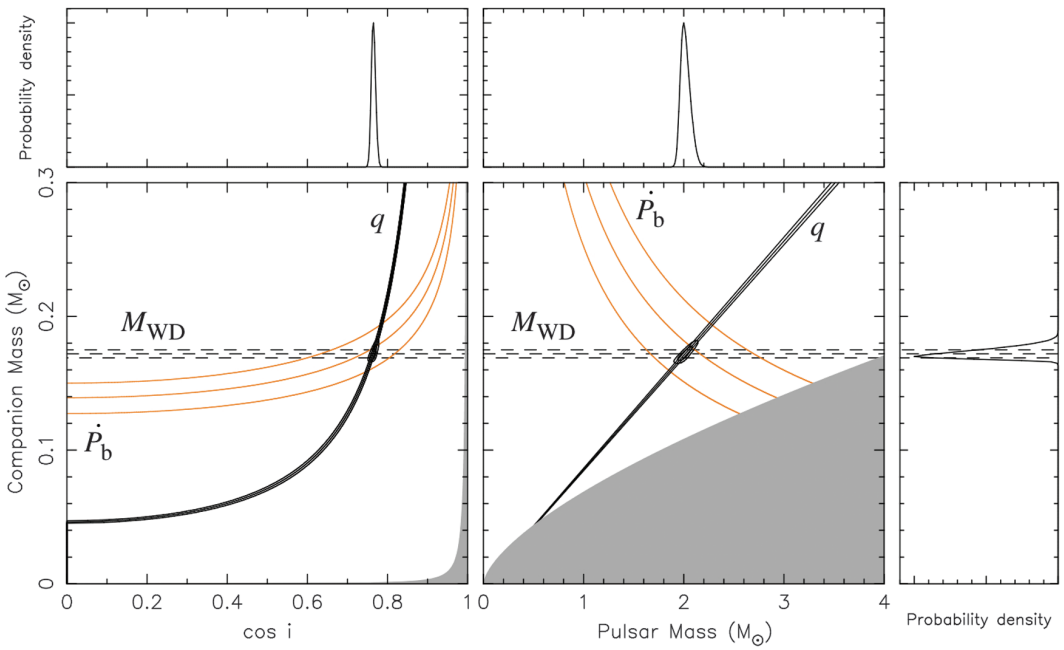

Fig. 3. System masses and orbital-inclination constraints. Constraints on system masses and orbital inclination from radio and optical measurements of PSR J0348+0432 and its WD companion. Each triplet of curves corresponds to the most likely value and standard deviations (68.27% confidence) of the respective parameters. Of these, two (q and $M_{\rm WD}$) are independent of specific gravity theories (in black). The contours contain the 68.27 and 95.45% of the two-dimensional probability distribution. The constraints from the measured intrinsic orbital decay ($\dot{P}_{\rm b}^{\rm int}$, in orange) are calculated assuming that GR is the correct theory of gravity. All curves intersect in the same region, meaning that GR passes this radiative test (*8*). (**Bottom left**) cos$i$-$M_{\rm WD}$ plane. The gray region is excluded by the condition $M_{\rm PSR} > 0$. (**Bottom right**) $M_{\rm PSR}$-$M_{\rm WD}$ plane. The gray region is excluded by the condition sin$i \leq 1$. The lateral graphs depict the one-dimensional probability-distribution function for the WD mass (**right**), pulsar mass (**top right**), and inclination (**top left**) based on the mass function, $M_{\rm WD}$, and q.

system into a gravitational laboratory for a previously untested regime, qualitatively very different from what was accessible in the past.

In physically consistent and extensively studied alternatives, gravity is generally mediated by extra fields (e.g., scalar) in addition to the tensor field of GR (5). A dynamical coupling between matter and these extra fields can lead to prominent deviations from GR that only occur at the high gravitational binding energies of massive NSs. One of the prime examples is the strong-field scalarization discovered in (3). If GR is not valid, in the PSR J0348+0432 system where such an object is closely orbited by a weakly self-gravitating body, one generally expects a violation of the strong equivalence principle that in turn leads to a modification in the emission of GWs. Although in GR the lowest source multipole that generates gravitational radiation is the quadrupole, alternative gravity theories generally predict the presence of monopole and dipole radiation on top of a modification of the other multipoles (5). For a binary system, the leading change in the orbital period is then given by the dipole contribution, which for a (nearly) circular orbit reads (8)

$$\dot{P}_b^{\text{dipolar}} \simeq -\frac{4\pi^2 G}{c^3 P_b}\frac{M_{PSR}M_{WD}}{M_{PSR}+M_{WD}}(\alpha_{PSR}-\alpha_{WD})^2 \quad (1)$$

where α_{PSR} is the effective coupling strength between the NS and the ambient fields responsible for the dipole moment (e.g., scalar fields in scalar-tensor gravity) and α_{WD} is the same parameter for the WD companion. The WD companion to PSR J0348+0432 has a fractional gravitational binding energy ($E_{grav}/M_{WD}c^2$) of just -1.2×10^{-5} and is therefore a weakly self-gravitating object. Consequently, α_{WD} is practically identical to the linear field-matter coupling α_0, which is well constrained ($|\alpha_0| < 0.004$) in solar system experiments (20, 24).

For α_{PSR}, the situation is very different. Even if α_0 is vanishingly small, α_{PSR} can have values close to unity, because of a nonlinear behavior of gravity in the interaction between matter and the gravitational fields in the strong-gravity regime inside NSs (3, 4). A significant α_{PSR} for NSs up to 1.47 $M_\odot$ has been excluded by various binary pulsar experiments (8, 23). The consistency of the observed GW damping ($\dot{P}_b$) with the GR predictions for PSR J0348+0432 (Table 1) implies $|\alpha_{PSR} - \alpha_0| < 0.005$ (95% confidence) and consequently excludes significant strong-field deviations, even for massive NSs of ~2 $M_\odot$.

To demonstrate in some detail the implications of our results for possible strong-field deviations of gravity from Einstein's theory, we confront our limits on dipolar radiation with a specific class of scalar-tensor theories, in which gravity is mediated by a symmetric second-rank tensor field, $g_{\mu\nu}^*$, and by a long-range (massless) scalar field, φ. Scalar-tensor theories are well motivated and consistent theories of gravity, extensively studied in the literature [e.g., (25, 26)]. For this reason, they are the most natural framework for us to illustrate the gravitational phenomena that can be probed with PSR J0348+0432.

Concerning the EOS of NS matter, in our calculations we use the rather stiff EOS ".20" of (27) that supports (in GR) NSs of up to 2.6 $M_\odot$. We make this choice for two reasons: (i) A stiffer EOS generally leads to more conservative limits when constraining alternative gravity theories, and (ii) it is able to support even more massive NSs than PSR J0348+0432, which are likely to exist (28–30). Furthermore, in most of our conclusions a specific EOS is used only for illustrative purposes, and the obtained generic results are EOS independent.

Figure 4B illustrates how PSR J0348+0432 probes a nonlinear regime of gravity that has not been tested before. A change in EOS and gravity theory would lead to a modified functional shape for α_{PSR}. However, this would not change the general picture: Even in the strong gravitational

Table 1. Observed and derived parameters for the PSR J0348+0432 system. Timing parameters for the PSR J0348+0432 system, indicated with their 1-σ uncertainties as derived by tempo2 where appropriate (numbers in parentheses refer to errors on the last digits). The timing parameters are calculated for the reference epoch modified Julian date (MJD) 56000 and are derived from TOAs in the range MJD 54872 to 56208.

Optical parameters	
Effective temperature, T_{eff} (K)	$10120 \pm 47_{stat} \pm 90_{sys}$
Surface gravity, $\log_{10}[g(\text{cm s}^{-1})]$	$6.035 \pm 0.032_{stat} \pm 0.060_{sys}$
Semiamplitude of orbital radial velocity, K_{WD} (km s^{-1})	351 ± 4
Systemic radial velocity relative to the Sun, γ (km s^{-1})	−1 ± 20
Timing parameters	
Right ascension, α (J2000)	$03^h\ 48^m\ 43^s.639000(4)$
Declination, δ (J2000)	+04° 32′ 11.″4580(2)
Proper motion in right ascension, μ_α (mas year^{-1})	+4.04(16)
Proper motion in declination, μ_δ (mas year^{-1})	+3.5(6)
Parallax, π_d (mas)	0.47*
Spin frequency, ν (Hz)	25.5606361937675(4)
First derivative of ν, $\dot{\nu}$ (10^{-15} Hz s^{-1})	−0.15729(3)
Dispersion measure, DM (cm^{-3} pc)	40.46313(11)
First derivative of DM, DM1 (cm^{-3} pc year^{-1})	−0.00069(14)
Orbital period, P_b (day)	0.102424062722(7)
Time of ascending node, T_{asc} (MJD)	56000.084771047(11)
Projected semimajor axis of the pulsar orbit, x (lt-s)	0.14097938(7)
$\eta \equiv e\sin\omega$	$+1.9 \times 10^{-6} \pm 1.0 \times 10^{-6}$
$\kappa \equiv e\cos\omega$	$+1.4 \times 10^{-6} \pm 1.0 \times 10^{-6}$
First derivative of P_b, $\dot{P}_b$ (10^{-12} s s^{-1})	−0.273(45)
Derived parameters	
Galactic longitude, l	183.°3368
Galactic latitude, b	−36.°7736
Distance, d (kpc)	2.1(2)
Total proper motion, μ (mas year^{-1})	5.3(4)
Spin period, P (ms)	39.1226569017806(5)
First derivative of P, $\dot{P}$ (10^{-18} s s^{-1})	0.24073(4)
Characteristic age, τ_c (Gy)	2.6
Transverse magnetic field at the poles, B_0 (10^9 G)	~2
Rate or rotational energy loss, $\dot{E}$ (10^{32} erg s^{-1})	~1.6
Mass function, f ($M_\odot$)	0.000286778(4)
Mass ratio, $q \equiv M_{PSR}/M_{WD}$	11.70(13)
White dwarf mass, M_{WD} ($M_\odot$)	0.172(3)
Pulsar mass, M_{PSR} ($M_\odot$)	2.01(4)
"Range" parameter of Shapiro delay, r (μs)	0.84718*
"Shape" parameter of Shapiro delay, $s \equiv \sin i$	0.64546*
White dwarf radius, R_{WD} ($R_\odot$)	0.065(5)
Orbital separation, a (10^9 m)	0.832
Orbital separation, a ($R_\odot$)	1.20
Orbital inclination, i	40.°2(6)
$\dot{P}_b$ predicted by GR, $\dot{P}_b^{GR}$ (10^{-12} s s^{-1})	$-0.258^{+0.008}_{-0.011}$
$\dot{P}_b/\dot{P}_b^{GR}$	1.05 ± 0.18
Time until coalescence, τ_m (My)	~400

*For these timing parameters, we adopted the optically derived parameters (see text for details).

Downloaded from https://www.science.org at Inter-University Centre for Astronomy and Astrophysics on January 07, 2025

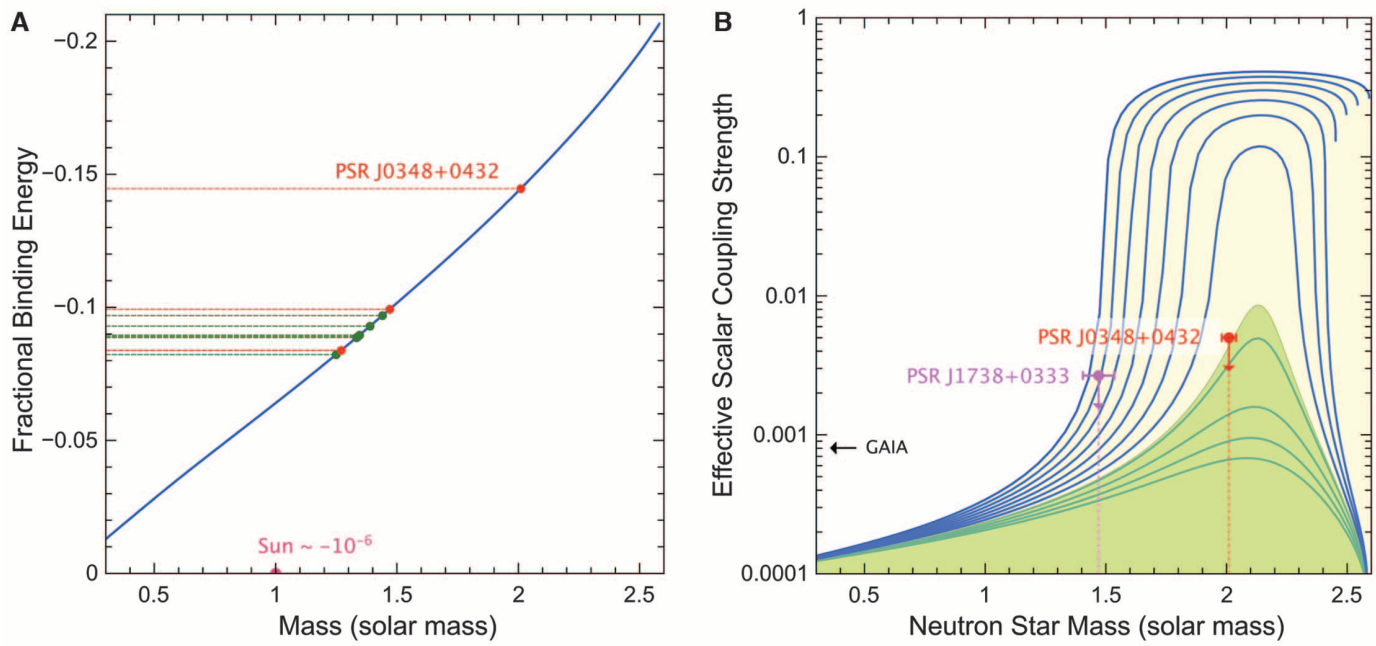

Fig. 4. Probing strong field gravity with PSR J0348+0432. (**A**) Fractional gravitational binding energy as a function of the inertial mass of a NS in GR (blue curve). The dots indicate the NSs of relativistic NS-NS (in green) and NS-WD (in red) binary-pulsar systems currently used for precision gravity tests (*8*). (**B**) Effective scalar coupling as a function of the NS mass, in the "quadratic" scalar-tensor theory of (*4*). For the linear coupling of matter to the scalar field, we have chosen $\alpha_0 = 10^{-4}$, a value well below the sensitivity of any near-future solar system experiment [e.g., GAIA (*62*)]. The solid curves correspond to stable NS configurations for different values of the quadratic coupling β_0: −5 to −4 (top to bottom) in steps of 0.1. The yellow area indicates the parameter space allowed by the best current limit on $|\alpha_{PSR} - \alpha_0|$ (*23*), whereas only the green area is in agreement with the limit presented here.

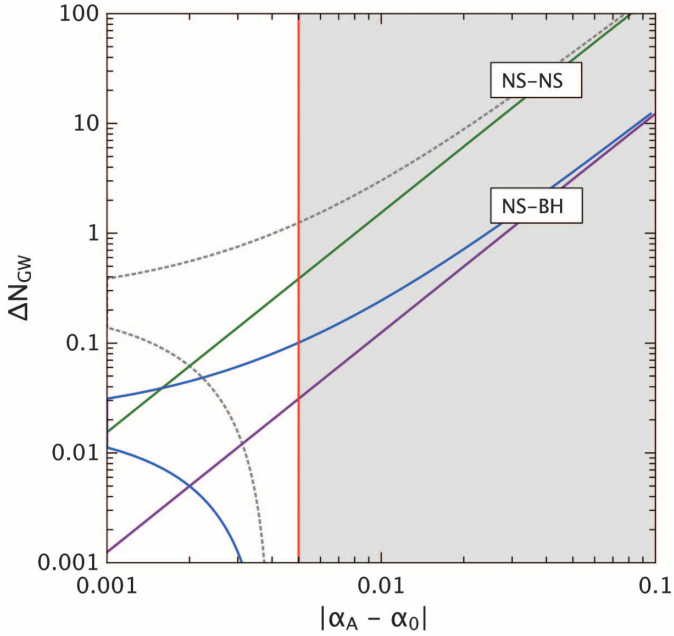

Fig. 5. Constraints on the phase offset in gravitational wave cycles in the LIGO/VIRGO bands. Maximum offset in GW cycles in the LIGO/VIRGO band (20 Hz to a few kHz) between the GR template and the true phase evolution of the in-spiral in the presence of dipolar radiation as a function of the effective coupling of the massive NS for two different system configurations: a 2 $M_\odot$ NS with a 1.25 $M_\odot$ NS (NS-NS) and a merger of a 2 $M_\odot$ NS with a 10 $M_\odot$ BH (NS-BH). In the NS-NS case, the green line is for $\alpha_B = \alpha_0$, and the gray dotted line represents the most conservative, rather unphysical, assumption $\alpha_0 = 0.004$ and $\alpha_B = 0$ (*8*). In the NS-BH case, α_B is set to zero (from the assumption that no-hair theorems hold). The blue line is for $\alpha_0 = 0.004$ (solar system limit for scalar-tensor theories), and the purple line represents $\alpha_0 = 0$. The gray area to the right of the red line is excluded by PSR J0348+0432. In this plot, there is no assumption concerning the EOS.

field of a 2 $M_\odot$ NS, gravity seems to be well described by GR, and there is little space for any deviations, at least in the form of long-range fields, which influence the binary dynamics. Short-range interactions, like massive Brans-Dicke gravity (*31*) with a sufficiently large scalar mass (heavier than ~10^{-19} eV/c^2), cannot be excluded by PSR J0348+0432.

Constraints on the Phase Evolution of Neutron Star Mergers

One of the most promising sources of GWs that might be detected by ground-based laser interferometers like the LIGO [Laser Interferometer Gravitational Wave Observatory (*32*)] and the VIRGO (*33*) projects (*34*) are in-spiraling compact binaries, consisting of NSs and BHs, whose orbits are decaying toward a final coalescence because of GW damping. As the signal sweeps in frequency through the detectors' typical sensitive bandwidth between about 20 Hz and a few kHz, the GW signal will be deeply buried in the broadband noise of the detectors (*34*). To detect it, one will have to apply a matched filtering technique, that is, correlate the output of the detector with a template wave form. Consequently, it is crucial to know the binary's orbital phase with high accuracy for searching and analyzing the signals from in-spiraling compact binaries. Typically, one aims to lose less than one GW cycle in a signal with ~10^4 cycles. For this reason, within GR such calculations have been conducted with great effort by various groups up to the 3.5 post-Newtonian order, that is, all (nonvanishing) terms up to order $(v/c)^7$ (where v is relative orbital velocity of the binary's components), providing sufficient accuracy for a detection (*35*–*37*).

If the gravitational interaction between two compact masses is different from GR, the phase evolution over the last few thousand cycles, which fall into the bandwidth of the detectors, might be too different from the (GR) template to extract

Downloaded from https://www.science.org at Inter-University Centre for Astronomy and Astrophysics on January 07, 2025

the signal from the noise. In scalar-tensor gravity, for instance, the evolution of the phase is driven by radiation reaction, which is modified because the system loses energy to scalar GWs (38, 39). Depending on the difference between the effective scalar couplings of the two bodies, α_A and α_B, the 1.5 post-Newtonian dipolar contribution to the phase evolution could drive the GW signal many cycles away from the GR template. For this reason, it is desirable that potential deviations from GR in the interaction of two compact objects can be tested and constrained before the start of the advanced GW detectors. For "canonical" 1.4 $M_\odot$ NSs and long-range gravitational fields, this has already been achieved to a high degree in binary pulsar experiments, for example, (39). So far, the best constraints on dipolar gravitational wave damping in compact binaries come from the observations of the millisecond pulsar PSR J1738+0333 (23). However, as discussed in detail above, these timing experiments are insensitive to strong-field deviations that might only become relevant in the strong gravitational fields associated with high-mass NSs. Consequently, the dynamics of a merger of a 2 $M_\odot$ NS with a "canonical" NS or a BH might have a significant contribution from dipolar GWs. With our constraints on dipolar radiation damping from the timing observations of PSR J0348+0432, given above, we can already exclude a deviation of more than ~0.5 cycles from the GR template during the observable in-spiral caused by additional long-range gravitational fields for the whole range of NS masses observed in nature [see Fig. 5 and (8) for the details of the calculation]. This compares to the precision of GR templates based on the 3.5 post-Newtonian approximation (35, 37). Furthermore, in an extension of the arguments in (38, 39) to massive NSs, our result implies that binary pulsar experiments are already more sensitive for testing such deviations than the upcoming advanced GW detectors.

Lastly, as mentioned before, our results on PSR J0348+0432 cannot exclude dipolar radiation from short-range fields. Hence, if the range of the additional field in the gravitational interaction happens to lie between the wavelength of the GWs of PSR J0348+0432 and the wavelength of the merger signal (~10^9 cm; ~10^{-13} eV/c^2), then the considerations concerning the applicability of the GR template given here do not apply. On the other hand, in such a case the combination of binary pulsar and LIGO/VIRGO experiments can be used to constrain the mass of this extra field.

Formation and Past and Future Evolution of the System

The measured spin period, P, and spin-period derivative $\dot{P}$ of PSR J0348+0432, combined with the masses and orbital period of the system (Table 1), form a peculiar set of parameters that gives insight to binary stellar evolution. The short 2.46-hour orbital period is best understood from evolution via a common envelope where the NS is captured in the envelope of the WD progenitor, leading to efficient removal of orbital angular momentum on a short time scale of ~10^3 years (40). This implies that the NS was born with an initial mass close to its current mass of 2.01 $M_\odot$, because very little accretion was possible. Whereas the slow spin period of ~39 ms and the unusually strong magnetic field (8) of a few 10^9 G (Table 1) provide further support for this scenario, the low WD mass contradicts the standard common-envelope hypothesis by requiring a progenitor star mass smaller than 2.2 $M_\odot$, because more massive stars would leave behind more massive cores (8, 41). For such low donor star masses, however, the mass ratio of the binary components is close to unity, leading to dynamically stable mass transfer without forming a common envelope (42, 43). One potential solution to this mass discrepancy for common-envelope evolution is to assume that the original mass of the WD was ≥0.4 $M_\odot$ and that it was subsequently evaporated by the pulsar wind (44) when PSR J0348+0432 was young and energetic, right after its recycling phase (8). Such an evolution could also help explain the formation of another puzzling system, PSR J1744−3922 (45). However, we find that this scenario is quite unlikely given that the observed spectrum of the WD in PSR J0348+0432 only displays hydrogen lines, which is not expected if the WD was indeed a stripped remnant of a much more massive helium or carbon-oxygen WD. Furthermore, it is unclear why this evaporation process should have come to a complete stop when the WD reached its current mass of 0.17 $M_\odot$. A speculative hypothesis to circumvent the above-mentioned problems would be a common-envelope evolution with hypercritical accretion, where ~0.6 $M_\odot$ of material was efficiently transferred to a 1.4 $M_\odot$ NS (8, 46).

An alternative, and more promising, formation scenario is evolution via a close-orbit low-mass x-ray binary (LMXB) with a 1.0 to 1.6 $M_\odot$ donor star that suffered from loss of orbital angular momentum because of magnetic braking (43, 47, 48). This requires a finely tuned truncation of the mass-transfer process, which is not yet understood in detail but which is also required for other known recycled pulsars (8) with short orbital periods of $P_b \leq 8$ hours and low-mass helium WD companions with $M_{WD} \approx 0.14$ to 0.18 $M_\odot$. The interplay between magnetic braking, angular momentum loss from stellar winds (possibly caused by irradiation), and mass ejected from the vicinity of the NS is poorly understood, and current stellar evolution models have difficulties reproducing these binary pulsar systems. One issue is that the converging LMXBs most often do not detach but keep evolving with continuous mass transfer to more and more compact systems with $P_b \leq 1$ hour and ultralight donor masses smaller than 0.08 $M_\odot$.

By using the Langer stellar evolution code (8), we have attempted to model the formation of the PSR J0348+0432 system via LMXB evolution (Fig. 6). To achieve this, we forced the donor star to detach its Roche lobe at $P_b \sim 5$ hours, such that the system subsequently shrinks in size to its present value of $P_b \cong 2.46$ hours because of GW radiation within 2 Gy, the estimated cooling age of the WD. An illustration of the past and future evolution of PSR J0348+0432 from the two different formation channels is shown in Fig. 7.

An abnormality of PSR J0348+0432 in view of the LMXB model is its slow spin period of $P \sim 39$ ms and, in particular, the high value for the spin period derivative, $\dot{P} = 2.41 \times 10^{-19}$ s s^{-1}. These values correspond to an inferred surface magnetic flux density of $B \sim 2 \times 10^9$ G, which is high compared with most other recycled pulsars (49). However, a high B value naturally explains the slow spin period of PSR J0348+0432 from a combination of spin-down during the Roche-lobe decoupling phase (50) and subsequent magnetic dipole radiation from this high-magnetic-field pulsar (8, 49). Another intriguing question concerning this evolutionary channel is the spread in NS masses. In the five currently known NS-WD systems with $P_b \leq 8$ hours, the NS masses span a large range of values, ranging from ~ 1.4 up to 2.0 $M_\odot$. The lower masses imply that the mass

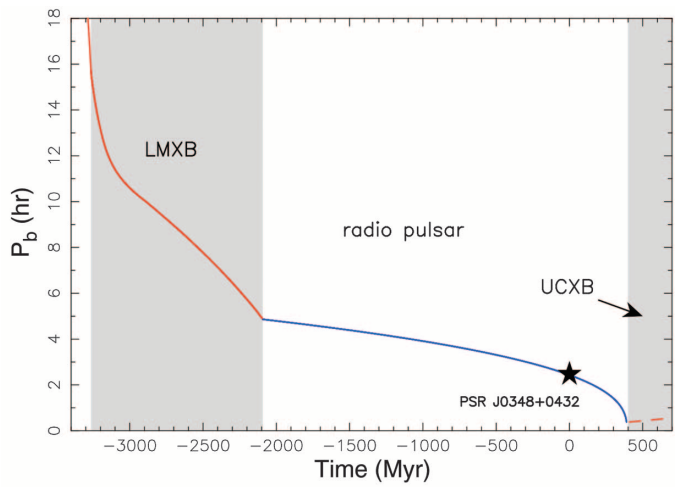

Fig. 6. Past and future orbital evolution of PSR J0348+0432. Formation of PSR J0348+0432 from our converging LMXB model calculation. The plot shows orbital period as a function of time (calibrated to present day). The progenitor detached from its Roche lobe about 2 Gy ago (according to the estimated cooling age of the WD) when $P_b \cong 5$ hours, and since then GW damping reduced the orbital period to its present value of 2.46 hours (marked with a star). UCXB, ultracompact x-ray binary.

Downloaded from https://www.science.org at Inter-University Centre for Astronomy and Astrophysics on January 07, 2025

transfer during the LMXB phase is extremely inefficient: Only about 30% of the material leaving the donor is accreted by the NS (*14*, *15*). If this is indeed the case and if one assumes that the physical processes that lead to the formation of these systems are similar, it is likely that PSR J0348+0432 was born with an initial mass of $1.7 \pm 0.1\ M_\odot$, providing further support for a nonnegligible fraction of NSs born massive (*41*).

Emission of GWs will continue to shrink the orbit of PSR J0348+0432, and in 400 My (when $P_b \cong 23$ min) the WD will fill its Roche lobe and possibly leave behind a planet orbiting the pulsar (*51*, *52*). Alternatively, if PSR J0348+0432 is near the upper-mass limit for NSs, then a BH might form via accretion-induced collapse of the massive NS in a cataclysmic, γ-ray burst–like event (*53*).

Materials and Methods

Radial Velocities and Atmospheric Parameters

A detailed log of the VLT observations can be found in (*8*) (fig. S1 and table S1). We extracted the spectra following closely the method used in (*14*) and compared them with template spectra to measure the radial velocities. Our best fits for the WD had reduced χ^2 minimum values of $\chi^2_{\mathrm{red,\ min}} = 1.0$ to 1.5 (*8*). Uncertainties were taken to be the difference in velocity over which χ^2 increases by $\chi^2_{\mathrm{red,\ min}}$ to account for the fact that $\chi^2_{\mathrm{red,\ min}}$ is not equal to unity (*14*). After transforming the measurements to the reference frame of the solar system barycenter (SSB), we folded them by using the radio-timing ephemeris described below. We then fitted for the semiamplitude of the radial velocity modulation, K_{WD}, and the systemic radial velocity with respect to the SSB, γ, assuming a circular orbit and keeping the time of passage through the ascending node, T_{asc}, fixed to the best-fit value of the radio-timing ephemeris. Our solution yields $K_{\mathrm{WD}} = 351 \pm 4$ km s^{-1} and $\gamma = -1 \pm 20$ km s^{-1} (*8*).

Details of the Balmer lines in the average spectrum of PSR J0348+0432, created by the coherent addition of the individual spectra shifted to zero velocity, are shown in Fig. 1B. We modeled the spectrum by using a grid of detailed hydrogen atmospheres (*54*). These models incorporate the improved treatment of pressure broadening of the absorption lines presented in (*55*). As mentioned above, our fit yields $T_{\mathrm{eff}} = 10{,}120 \pm 35_{\mathrm{stat}} \pm 90_{\mathrm{sys}}$ K for the effective temperature and $\log_{10} g = 6.042 \pm 0.032_{\mathrm{stat}} \pm 0.060_{\mathrm{sys}}$ for the surface gravity (*8*). The χ^2 map shown in Fig. 2A is inflated to take into account systematic uncertainties. The average spectrum was also searched for rotational broadening. By using the analytic profile of (*56*) to convolve the model atmospheres, we scanned the grid of velocities $0 \le v_r \sin i \le 2000$ km s^{-1} with a step size of 100 km s^{-1}. The result is consistent with no rotation and our 1-σ upper limit is $v_r \sin i \le 430$ km s^{-1}.

Modeling of the White Dwarf Mass

Low-mass WDs are thought to form naturally within the age of the universe via mass transfer in a binary, either through Roche-lobe overflow or common-envelope evolution. In both cases, the WD forms when the envelope mass drops below a critical limit, which depends primarily on the mass of the stellar core, forcing the star to contract and detach from its Roche lobe. After the contraction, the mass of the relic envelope is fixed for a given core mass, but further reduction of its size may occur shortly before the star enters the final cooling branch because of hydrogen-shell flashes that force the star to reexpand to giant dimensions. Additional mass removal via Roche-lobe overflow, as well as rapid hydrogen-shell burning through the CNO cycle, may then lead to a decrease of the envelope size and affect the cooling history and atmospheric parameters. To investigate the consequence of a reduced envelope size for the WD companion to PSR J0348+0432, we constructed WD models in which we treat the envelope mass as a free parameter (*8*). For the WD companion to PSR J0348+0432, an envelope mass below the critical limit for hydrogen fusion is not likely for two main reasons.

First, for a pure helium composition, the observed surface gravity translates to a WD mass of ~0.15 $M_\odot$ and a cooling age of ~ 20 My, which is anomalously small. Such a small age would also imply a large increase in the birth and in-spiral rate of similar relativistic NS-WD systems (*57*). Furthermore, postcontraction flash episodes on the WD are not sufficient to remove the entire envelope. Therefore, creation of a pure helium WD requires large mass loss rates before the progenitor contracts, which is unlikely. For small progenitor masses (≤1.5 $M_\odot$), large mass loss prevents contraction, and the star evolves to a semidegenerate companion on a nuclear time scale that exceeds the age of the universe. For more massive progenitors (>1.5 $M_\odot$), the core grows beyond ~0.17 $M_\odot$ in a short time scale and ultimately leaves a too-massive WD.

Second, even for envelope hydrogen fractions as low as $X_{\mathrm{avg}} = 10^{-6}$, the observed temperature and surface gravity cannot be explained simultaneously: The low surface gravity would again require a small mass of ~0.15 $M_\odot$. However, in this case the surface hydrogen acts like an insulator, preventing the heat of the core from reaching the stellar surface. As a result, temperatures as high as 10,000 K can only be reached for masses above ~0.162 $M_\odot$.

Past a critical envelope mass, the pressure at the bottom of the envelope becomes high enough to initiate hydrogen-shell burning. The latter then becomes the dominant energy source, and the

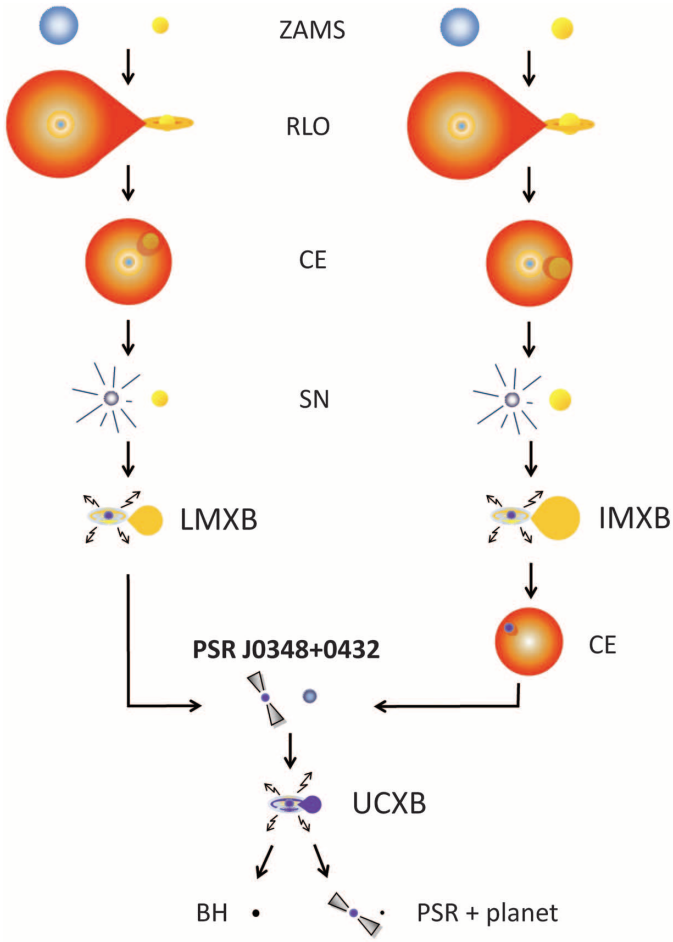

Fig. 7. Possible formation channels and final fate of PSR J0348+0432. An illustration of the formation and evolution of PSR J0348+0432. The zero-age main sequence (ZAMS) mass of the NS progenitor is likely to be 20 to 25 $M_\odot$, whereas the WD progenitor had a mass of 1.0 to 1.6 $M_\odot$ (LMXB) or 2.2 to 5 $M_\odot$ (common envelope, CE), depending on its formation channel. In ~400 My (when P_b ~ 23 min), the WD will fill its Roche lobe, and the system becomes an UCXB, leading to the formation of a BH or a pulsar with a planet. RLO, Roche-lobe overflow; SN, supernova; IMXB, intermediate-mass x-ray binary.

Downloaded from https://www.science.org at Inter-University Centre for Astronomy and Astrophysics on January 07, 2025

evolutionary time scale increases; the radius of the star grows by ~50% (depending on the mass), expanding further for larger envelopes. The dependence of the surface gravity on the radius implies that the observed value translates to a higher mass as the envelope mass increases. Therefore, the most conservative lower limit for the WD mass (and thus for PSR J0348+0432, given the fixed mass ratio) is obtained if one considers models with the absolute minimum envelope mass required for hydrogen burning. In this scenario, the mass of the WD is in the range from 0.162 to 0.181 $M_\odot$ at 99.73% confidence (*8*). Despite this constraint being marginally consistent with our observations (*8*), it is not likely correct because of the high degree of fine-tuning.

For these reasons, we have adopted the assumption that the WD companion to PSR J0348+0432 has a thick envelope, as generally expected for WDs with such low surface gravity and high temperature.

Radio Timing Analysis

The Arecibo observing setup (*8*) and data reduction are similar to the well-tested ones described in (*23*). Special care was taken with saving raw search data, which allows for iterative improvement of the ephemeris and eliminates orbital phase–dependent smearing of the pulse profiles, which might contaminate the measurement of $\dot{P}_b$ (*58*). From this analysis, we derived 7773 independent measurements of pulse times of arrival (TOAs) with a rms uncertainty smaller than 10 μs. Similarly the Effelsberg observations yield a total of 179 TOAs with uncertainties smaller than 20 μs.

We used the tempo2 timing package (*59*) and 8121 available TOAs from GBT (*7*), Arecibo, and Effelsberg to derive the timing solution presented in Table 1. The motion of the radiotelescopes relative to the barycenter of the Solar System was computed by using the DE/LE 421 solar system ephemeris (*60*) published by the Jet Propulsion Laboratory. The orbit of PSR J0348+0432 has a very low eccentricity; therefore, we use the ELL1 orbital model (*61*) to describe the motion of the pulsar.

For the best fit, the reduced χ^2 of the timing residuals (TOA minus model prediction) is 1.66, a result similar to what was obtained in timing observations of other millisecond pulsars. The overall weighted residual rms is 4.6 μs. There are no unmodeled systematic trends in the residuals, either as a function of orbital phase or as a function of time. Therefore $\chi^2 > 1$ is most likely produced by underestimated TOA uncertainties. We increased our estimated TOA uncertainties for each telescope and receiver to produce a reduced χ^2 of unity on short time scales; for our dominant data set (Arecibo), the errors were multiplied by a factor of 1.3.

This produces more conservative estimates of the uncertainties of the timing parameters; these have been verified by using the Monte Carlo statistical method described in (*23*): When all parameters are fitted, the Monte Carlo uncertainty ranges are very similar to those estimated by tempo2. As an example, tempo2 estimates $\dot{P}_b = -2.73 \times 10^{-13} \pm 0.45 \times 10^{-13}$ s s^{-1} (68.27% confidence), and the Monte Carlo method yields $\dot{P}_b = -2.72 \times 10^{-13} \pm 0.45 \times 10^{-13}$ s s^{-1} (68.27% confidence), in excellent agreement. The observed orbital decay appears to be stable; no higher derivatives of the orbital period are detected (*8*).

References and Notes

1. J. M. Lattimer, M. Prakash, The physics of neutron stars. *Science* **304**, 536 (2004). doi: 10.1126/science.1090720
2. P. B. Demorest, T. Pennucci, S. M. Ransom, M. S. Roberts, J. W. Hessels, A two-solar-mass neutron star measured using Shapiro delay. *Nature* **467**, 1081 (2010). doi: 10.1038/nature09466; pmid: 20981094
3. T. Damour, G. Esposito-Farèse, Nonperturbative strong-field effects in tensor-scalar theories of gravitation. *Phys. Rev. Lett.* **70**, 2220 (1993). doi: 10.1103/PhysRevLett.70.2220; pmid: 10053506
4. T. Damour, G. Esposito-Farèse, Tensor-scalar gravity and binary-pulsar experiments. *Phys. Rev. D Part. Fields* **54**, 1474 (1996). doi: 10.1103/PhysRevD.54.1474; pmid: 10020822
5. C. M. Will, *Theory and Experiment in Gravitational Physics* (Cambridge Univ. Press, Cambridge, 1993).
6. J. Boyles *et al.*, The Green Bank Telescope 350 MHz drift-scan survey. I. Survey observations and the discovery of 13 pulsars. *Astrophys. J.* **763**, 80 (2013). doi: 10.1088/0004-637X/763/2/80
7. R. S. Lynch *et al.*, The Green Bank Telescope 350 MHz drift-scan survey. II: Data analysis and the timing of 10 new pulsars, including a relativistic binary. *Astrophys. J.* **763**, 81 (2013). doi: 10.1088/0004-637X/763/2/81
8. Supplementary materials are available on *Science* Online.
9. V. S. Dhillon *et al.*, ULTRACAM: an ultrafast, triple-beam CCD camera for high-speed astrophysics. *Mon. Not. R. Astron. Soc.* **378**, 825 (2007). doi: 10.1111/j.1365-2966.2007.11881.x
10. M. van Kerkwijk, C. G. Bassa, B. A. Jacoby, P. G. Jonker, in *Binary Radio Pulsars*, F. Rasio, I. H. Stairs, Eds. (Astronomical Society of the Pacific Conference Series, San Francisco, CA, 2005) vol. 328, pp. 357–370.
11. A. M. Serenelli, L. G. Althaus, R. D. Rohrmann, O. G. Benvenuto, The ages and colours of cool helium-core white dwarf stars. *Mon. Not. R. Astron. Soc.* **325**, 607 (2001). doi: 10.1046/j.1365-8711.2001.04449.x
12. J. A. Panei, L. G. Althaus, X. Chen, Z. Han, Full evolution of low-mass white dwarfs with helium and oxygen cores. *Mon. Not. R. Astron. Soc.* **382**, 779 (2007). doi: 10.1111/j.1365-2966.2007.12400.x
13. M. Kilic, W. R. Brown, C. Allende Prieto, S. J. Kenyon, J. A. Panei, The discovery of bianry white dwarfs that will merge within 500 Myr. *Astrophys. J.* **716**, 122 (2010). doi: 10.1088/0004-637X/716/1/122
14. J. Antoniadis *et al.*, The relativistic pulsar-white dwarf binary PSR J1738+0333 - I. Mass determination and evolutionary history. *Mon. Not. R. Astron. Soc.* **423**, 3316 (2012). doi: 10.1111/j.1365-2966.2012.21124.x
15. B. A. Jacoby, A. Hotan, M. Bailes, S. Ord, S. R. Kulkarni, The Mass of a Millisecond Pulsar. *Astrophys. J.* **629**, L113 (2005). doi: 10.1086/449311
16. B. Paxton *et al.*, Modules for Experiments in Stellar Astrophysics (MESA). *Astrophys. J.* **192** (suppl.), 3 (2011). doi: 10.1088/0067-0049/192/1/3
17. F. Özel, D. Psaltis, S. Ransom, P. Demorest, M. Alford, The massive pulsar PSR J1614–2230: linking quantum chromodynamics, gamma-ray bursts, and gravitational wave astronomy. *Astrophys. J.* **724**, L199 (2010). doi: 10.1088/2041-8205/724/2/L199
18. A. Dowd, W. Sisk, J. Hagen, *Pulsar Astronomy - 2000 and Beyond, IAU Colloquium 177*, M. Kramer, N. Wex, R. Wielebinski, Eds. (Astronomical Society of the Pacific Conference Series, San Francisco, CA, 2000), vol. 202, pp. 275–276.
19. T. Damour, J. H. Taylor, Strong-field tests of relativistic gravity and binary pulsars. *Phys. Rev. D Part. Fields* **45**, 1840 (1992). doi: 10.1103/PhysRevD.45.1840; pmid: 10014561
20. T. Damour, "Binary systems as test-beds of gravity theories," in *Physics of Relativistic Objects in Compact Binaries: From Birth to Coalescence*, M. Colpi, P. Casella, V. Gorini, U. Moschella, A. Possenti, Eds. (Astrophysics and Space Science Library, Springer, Dordrecht, Netherlands, 2009), vol. 359, pp. 1–41.
21. I. H. Stairs, *Living Rev. Relativ.* **6**, 5 (2003), www.livingreviews.org/lrr-2003-5.
22. M. Kramer *et al.*, Tests of general relativity from timing the double pulsar. *Science* **314**, 97 (2006). doi: 10.1126/science.1132305
23. P. C. C. Freire *et al.*, The relativistic pulsar-white dwarf binary PSR J1738+0333 - II. The most stringent test of scalar-tensor gravity. *Mon. Not. R. Astron. Soc.* **423**, 3328 (2012). doi: 10.1111/j.1365-2966.2012.21253.x
24. C. M. Will, *Living Rev. Relativ.* **9**, 3 (2006), www.livingreviews.org/lrr-2006-3.
25. Y. Fujii, K.-I. Maeda, *The Scalar-Tensor Theory of Gravitation* (Cambridge University Press, Cambridge, 2003).
26. H. Goenner, Some remarks on the genesis of scalar-tensor theories. *Gen. Relativ. Gravit.* **44**, 2077 (2012). doi: 10.1007/s10714-012-1378-8
27. M. Haensel, M. Prószyski, M. Kutschera, *Astron. Astrophys.* **102**, 299 (1981).
28. P. C. C. Freire *et al.*, Eight New Millisecond Pulsars in NGC 6440 and NGC 6441. *Astrophys. J.* **675**, 670 (2008). doi: 10.1086/526338
29. M. H. van Kerkwijk, R. P. Breton, S. R. Kulkarni, Evidence for a massive neutron star from a radial-velocity study of the companion to the black-window pulsar PSR B1957 +20. *Astrophys. J.* **728**, 95 (2011). doi: 10.1088/0004-637X/728/2/95
30. R. W. Romani *et al.*, PSR J1311–3430: A heavyweight neutron star with a flyweight helium companion. *Astrophys. J.* **760**, L36 (2012). doi: 10.1088/2041-8205/760/2/L36
31. J. Alsing, E. Berti, C. M. Will, H. Zaglauer, Gravitational radiation from compact binary systems in the massive Brans-Dicke theory of gravity. *Phys. Rev. D Part. Fields Gravit. Cosmol.* **85**, 064041 (2012). doi: 10.1103/PhysRevD.85.064041
32. www.ligo.org.
33. www.cascina.virgo.infn.it.
34. B. S. Sathyaprakash, B. F. Schutz, *Living Rev. Relativ.* **12**, 2 (2009), www.livingreviews.org/lrr-2009-2.
35. L. Blanchet, *Living Rev. Relativ.* **9**, 4 (2006), www.livingreviews.org/lrr-2006-4.
36. C. M. Will, On the unreasonable effectiveness of the post-Newtonian approximation in gravitational physics. *Proc. Natl. Acad. Sci. U.S.A.* **108**, 5938 (2011). doi: 10.1073/pnas.1103127108; pmid: 21447714
37. M. Maggiore, *Gravitational Waves. Volume 1: Theory and Experiments* (Oxford Univ. Press, Oxford, 2008).
38. C. M. Will, Testing scalar-tensor gravity with gravitational-wave observations of inspiralling compact binaries. *Phys. Rev. D Part. Fields* **50**, 6058 (1994). doi: 10.1103/PhysRevD.50.6058; pmid: 10017576
39. T. Damour, G. Esposito-Farèse, *Phys. Rev. D Part. Fields* **58**, 1 (1998).
40. I. J. Iben, M. Livio, *Publ. Astron. Soc. Pac.* **105**, 1373 (1993).
41. T. M. Tauris, N. Langer, M. Kramer, Formation of millisecond pulsars with CO white dwarf companions - I. PSR J1614–2230: evidence for a neutron star born massive. *Mon. Not. R. Astron. Soc.* **416**, 2130 (2011). doi: 10.1111/j.1365-2966.2011.19189.x
42. T. M. Tauris, G. J. Savonije, *Astron. Astrophys.* **350**, 928 (1999).
43. P. Podsiadlowski, S. Rappaport, E. D. Pfahl, Evolutionary Sequences for Low- and Intermediate-Mass X-Ray Binaries. *Astrophys. J.* **565**, 1107 (2002). doi: 10.1086/324686
44. A. S. Fruchter, J. E. Gunn, T. R. Lauer, A. Dressler, Optical detection and characterization of the eclipsing pulsar's companion. *Nature* **334**, 686 (1988). doi: 10.1038/334686a0

Downloaded from https://www.science.org at Inter-University Centre for Astronomy and Astrophysics on January 07, 2025

45. R. P. Breton *et al.*, The Unusual Binary Pulsar PSR J1744–3922: Radio Flux Variability, Near-Infrared Observation, and Evolution. *Astrophys. J.* **661**, 1073 (2007). doi: 10.1086/515392
46. R. A. Chevalier, Neutron star accretion in a stellar envelope. *Astrophys. J.* **411**, L33 (1993). doi: 10.1086/186905
47. E. Pylyser, G. J. Savonije, *Astron. Astrophys.* **208**, 52 (1989).
48. M. V. van der Sluys, F. Verbunt, O. R. Pols, Reduced magnetic braking and the magnetic capture model for the formation of ultra-compact binaries. *Astron. Astrophys.* **440**, 973 (2005). doi: 10.1051/0004-6361:20052696
49. T. M. Tauris, N. Langer, M. Kramer, Formation of millisecond pulsars with CO white dwarf companions - II. Accretion, spin-up, true ages and comparison to MSPs with He white dwarf companions. *Mon. Not. R. Astron. Soc.* **425**, 1601 (2012). doi: 10.1111/j.1365-2966.2012.21446.x
50. T. M. Tauris, Spin-down of radio millisecond pulsars at genesis. *Science* **335**, 561 (2012). doi: 10.1126/science.1216355
51. M. Bailes *et al.*, Transformation of a star into a planet in a millisecond pulsar binary. *Science* **333**, 1717 (2011). doi: 10.1126/science.1208890
52. L. M. van Haaften, G. Nelemans, R. Voss, P. G. Jonker, Formation of the planet around the millisecond pulsar J1719–1438. *Astron. Astrophys.* **541**, A22 (2012). doi: 10.1051/0004-6361/201218798
53. C. D. Dermer, A. Atoyan, Collapse of Neutron Stars to Black Holes in Binary Systems: A Model for Short Gamma-Ray Bursts. *Astrophys. J.* **643**, L13 (2006). doi: 10.1086/504895
54. D. Koester (2008), http://arxiv.org/abs/0812.0482.
55. P.-E. Tremblay, P. Bergeron, Spectroscopic analysis of DA white dwarfs: Stark broadening of hydrogen lines including nonideal effects. *Astrophys. J.* **696**, 1755 (2009). doi: 10.1088/0004-637X/696/2/1755
56. D. F. Gray, *The Observation and Analysis of Stellar Photospheres* (Cambridge Univ. Press, Cambridge, 2005).
57. C. Kim, V. Kalogera, D. R. Lorimer, T. White, The Probability Distribution Of Binary Pulsar Coalescence Rates. II. Neutron Star–White Dwarf Binaries. *Astrophys. J.* **616**, 1109 (2004). doi: 10.1086/424954
58. D. J. Nice, I. H. Stairs, L. E. Kasian, in *40 Years of Pulsars: Millisecond Pulsars, Magnetars and More*, C. Bassa, Z. Wang, A. Cumming, V. M. Kaspi, Eds. (American Institute of Physics Conference Series, Springer, Dordrecht, 2008), vol. 983, pp. 453–458.
59. G. B. Hobbs, R. T. Edwards, R. N. Manchester, tempo2, a new pulsar-timing package - I. An overview. *Mon. Not. R. Astron. Soc.* **369**, 655 (2006). doi: 10.1111/j.1365-2966.2006.10302.x
60. W. M. Folkner, J. G. Williams, D. H. Boggs, *Interplanet. Network Prog. Rep.* **178**, C1 (2009).
61. C. Lange *et al.*, Precision timing measurements of PSR J1012+5307. *Mon. Not. R. Astron. Soc.* **326**, 274 (2001). doi: 10.1046/j.1365-8711.2001.04606.x
62. D. Hobbs *et al.*, in *Relativity in Fundamental Astronomy: Dynamics, Reference Frames, and Data Analysis, IAU Symposium 261*, S. A. Klioner, P. K. Seidelmann, M. H. Soffel, Eds. (Cambridge Univ. Press, Cambridge, 2010), pp. 315–319.
63. I. Appenzeller *et al.*, *Messenger* **94**, 1 (1998).

Acknowledgments: J.A. is a member of the International Max Planck research school for Astronomy and Astrophysics at the Universities of Bonn and Cologne. P.C.C.F. and J.P.W.V. gratefully acknowledge financial support by the European Research Council for the ERC Starting Grant BEACON under contract no. 279702. M.A.M. acknowledges support from a West Virginia Experimental Program to Stimulate Competitive Research Challenge Grant. J.W.T.H. is a Veni Fellow of the Netherlands Foundation for Scientific Research. V.M.K. holds the Lorne Trottier Chair in Astrophysics and Cosmology, a Canada Research Chair, and a Killam Research Fellowship and acknowledges additional support from a Natural Sciences and Engineering Research Council of Canada (NSERC) Discovery Grant, from Fonds Québécois de la Recherche sur la Nature et les Technologies via le Centre de Recherche Astrophysique du Québec and the Canadian Institute for Advanced Research. M.H.v.K. and I.H.S. acknowledge support from NSERC Discovery Grants. V.S.D., T.R.M., and ULTRACAM are supported by the Science and Technology Facilities Council. This work is based on data collected with the VLT of the European Southern Observatory (ESO) under program 088.D-0138A and observations with the 100-m Effelsberg telescope of the Max Planck Institute for Radioastronomy. The Arecibo Observatory is operated by SRI International under a cooperative agreement with the NSF (AST-1100968) and in alliance with Ana G. Méndez-Universidad Metropolitana and the Universities Space Research Association. The National Radio Astronomy Observatory is a facility of the NSF operated under cooperative agreement by Associated Universities, Incorporated. We are grateful to D. Koester and J. Panei *et al.* for providing models presented in their publications. We are obliged to J. Smoker (ESO) for his help during the VLT observations and D. Champion for assistance with the Effelsberg observations and useful discussions. We also thank D. Lorimer, J. Bell-Burnell, G. Esposito-Farèse, E. Keane, P. Podsiadlowski, and B. Schutz for helpful discussions. This research made use of NASA's Astrophysics Data System and M. T. Flanagan's Java Scientific Library (www.ee.ucl.ac.uk/~mflanaga).

Supplementary Materials

www.sciencemag.org/content/340/6131/1233232/suppl/DC1
Supplementary Text
Figs. S1 to S11
Tables S1 to S3
References (*63*–*112*)

27 November 2012; accepted 6 March 2013
10.1126/science.1233232

Downloaded from https://www.science.org at Inter-University Centre for Astronomy and Astrophysics on January 07, 2025

LETTERS
https://doi.org/10.1038/s41550-019-0880-2

nature astronomy

Relativistic Shapiro delay measurements of an extremely massive millisecond pulsar

H. T. Cromartie[1*], E. Fonseca[2], S. M. Ransom[3], P. B. Demorest[4], Z. Arzoumanian[5], H. Blumer[6,7], P. R. Brook[6,7], M. E. DeCesar[8], T. Dolch[9], J. A. Ellis[10], R. D. Ferdman[11], E. C. Ferrara[12,13], N. Garver-Daniels[6,7], P. A. Gentile[6,7], M. L. Jones[6,7], M. T. Lam[6,7], D. R. Lorimer[6,7], R. S. Lynch[14], M. A. McLaughlin[6,7], C. Ng[15,16], D. J. Nice[8], T. T. Pennucci[17], R. Spiewak[18], I. H. Stairs[15], K. Stovall[4], J. K. Swiggum[19] and W. W. Zhu[20]

Despite its importance to our understanding of physics at supranuclear densities, the equation of state (EoS) of matter deep within neutron stars remains poorly understood. Millisecond pulsars (MSPs) are among the most useful astrophysical objects in the Universe for testing fundamental physics, and place some of the most stringent constraints on this high-density EoS. Pulsar timing—the process of accounting for every rotation of a pulsar over long time periods—can precisely measure a wide variety of physical phenomena, including those that allow the measurement of the masses of the components of a pulsar binary system[1]. One of these, called relativistic Shapiro delay[2], can yield precise masses for both an MSP and its companion; however, it is only easily observed in a small subset of high-precision, highly inclined (nearly edge-on) binary pulsar systems. By combining data from the North American Nanohertz Observatory for Gravitational Waves (NANOGrav) 12.5-yr data set with recent orbital-phase-specific observations using the Green Bank Telescope, we have measured the mass of the MSP J0740+6620 to be $2.14^{+0.10}_{-0.09}\,M_\odot$ (68.3% credibility interval; the 95.4% credibility interval is $2.14^{+0.20}_{-0.18}\,M_\odot$). It is highly likely to be the most massive neutron star yet observed, and serves as a strong constraint on the neutron star interior EoS.

Relativistic Shapiro delay, which is observable when a pulsar passes behind its stellar companion during orbital conjunction, manifests as a small delay in pulse arrival times induced by the curvature of spacetime in the vicinity of the companion star. For a highly inclined MSP–white dwarf binary, the full delay is on the order of ~10 μs. The relativistic effect is characterized by two parameters, 'shape' and 'range'. In general relativity, shape (s) is the sine of the angle of inclination of the binary orbit (i), while range (r) is proportional to the mass of the companion, m_c. When combined with the Keplerian mass function, measurements of r and s also constrain the pulsar mass (m_p; ref. [3] provides a detailed overview and an alternative parameterization).

Precise neutron star mass measurements are an effective way to constrain the EoS of the ultradense matter in neutron star interiors. Although radio pulsar timing cannot directly determine neutron star radii, the existence of pulsars with masses exceeding the maximum mass allowed by a given model can straightforwardly rule out that EoS.

In 2010, Demorest et al. reported the discovery of a $2\,M_\odot$ MSP, J1614−2230 (ref. [4]) (though the originally reported mass was $1.97 \pm 0.04\,M_\odot$, continued timing has led to a more precise mass measurement of $1.928 \pm 0.017\,M_\odot$ by Fonseca et al.[5]). This Shapiro-delay-enabled measurement disproved the plausibility of some hyperon, boson and free quark models in nuclear-density environments. In 2013, Antoniadis et al. used optical techniques in combination with pulsar timing to yield a mass measurement of $2.01 \pm 0.04\,M_\odot$ for the pulsar J0348+0432 (ref. [6]). These two observational results (along with others[7]) encouraged a reconsideration of the canonical $1.4\,M_\odot$ neutron star. Gravitational-wave astrophysics has also begun to provide EoS constraints; for example, the Laser Interferometer Gravitational-Wave Observatory (LIGO) detection of a double neutron star merger constrains permissible EoSs, suggesting that the upper limit on neutron star mass is $2.17\,M_\odot$ (90% credibility[8]). Though the existence of extremely massive ($>2.4\,M_\odot$) neutron stars has been suggested through optical spectroscopic and photometric observations (for example ref. [9]), radio timing can provide much more precise constraints on the existence of $\gtrsim 2\,M_\odot$ neutron stars.

NANOGrav employs pulsar timing for an important general relativistic application: the detection of low-frequency gravitational waves primarily from supermassive black hole binaries. The collaboration's observing programme consists of high-cadence, multifrequency radio observations of ~75 MSPs using the Green Bank and Arecibo telescopes (GBT and AO; see ref. [10] and the upcoming 12.5-yr data release). Additionally, NANOGrav has begun using the Karl G. Jansky Very Large Array as the third

[1]Department of Astronomy, University of Virginia, Charlottesville, VA, USA. [2]Department of Physics, McGill University, Montreal, QC, Canada. [3]National Radio Astronomy Observatory, Charlottesville, VA, USA. [4]National Radio Astronomy Observatory, Socorro, NM, USA. [5]X-ray Astrophysics Laboratory, Code 662, NASA Goddard Space Flight Center, Greenbelt, MD, USA. [6]Department of Physics and Astronomy, West Virginia University, Morgantown, WV, USA. [7]Center for Gravitational Waves and Cosmology, West Virginia University, Morgantown, WV, USA. [8]Department of Physics, Lafayette College, Easton, PA, USA. [9]Department of Physics, Hillsdale College, Hillsdale, MI, USA. [10]Infinia ML, Durham, NC, USA. [11]School of Chemistry, University of East Anglia, Norwich, UK. [12]NASA Goddard Space Flight Center, Greenbelt, MD, USA. [13]Department of Astronomy, University of Maryland, College Park, MD, USA. [14]Green Bank Observatory, Green Bank, WV, USA. [15]Department of Physics and Astronomy, University of British Columbia, Vancouver, BC, Canada. [16]Dunlap Institute, University of Toronto, Toronto, ON, Canada. [17]Hungarian Academy of Sciences MTA-ELTE 'Extragalactic Astrophysics Research Group', Institute of Physics, Eötvös Loránd University, Budapest, Hungary. [18]Centre for Astrophysics and Supercomputing, Swinburne University of Technology, Hawthorn, VIC, Australia. [19]Center for Gravitation, Cosmology and Astrophysics, Department of Physics, University of Wisconsin—Milwaukee, Milwaukee, WI, USA. [20]CAS Key Laboratory of FAST, NAOC, Chinese Academy of Sciences, Beijing, China. *e-mail: thankful@virginia.edu

observatory in its pulsar-timing programme. Using the GBT, NANOGrav regularly observes J1614−2230 and another high-mass radio MSP, J0740+6620.

PSR J0740+6620 (period = 2.89 ms) was discovered in the Green Bank Northern Celestial Cap 350 MHz survey (GBNCC) in 2012 (ref. [11]). It is in a nearly circular (eccentricity = 5×10^{-6}), 4.77-day orbit (Lynch et al. presented a recent GBNCC timing solution in 2018; ref. [12]). Recent optical and near-infrared observations by Beronya et al. (2019) revealed that its companion is probably the coolest white dwarf ever measured in orbit with an MSP[13].

Here we present timing observations of the pulsar with the GBT taken between 2014 and 2019. We observed the pulsar regularly throughout this period as part of the NANOGrav timing programme[10]. This section of our data set includes ~70 epochs (occurring approximately monthly and at random orbital phases) during which the pulsar was observed at both 1.4 GHz and 820 MHz for ~20 min each. We were awarded additional time for two concentrated campaigns over superior conjunction (that is, when the pulsar is behind its companion star), as probing the minima and maxima of the Shapiro delay signal is the best way to improve the signal's detectability (see the absorbed or 'detectable' signal in the second panel of Fig. 1).

After the second concentrated campaign consisting of two 5 h observations at orbital phases 0.15 and 0.25 (GBT 18B-372), the timing analysis (see details in Methods) yielded a pulsar mass of $2.14^{+0.10}_{-0.09}\,M_\odot$ at 68.3% credibility (Fig. 2). Methods describes our rationale for choosing these two orbital phases, as well as the progression of mass measurements and precisions as more observations were added. Our final fits with and without Shapiro delay as a function of orbital phase are presented in Fig. 1, and the top panel of Fig. 3 shows timing residuals spanning the entire data set. Although our measured relative uncertainty is higher than, for example, the original relative error reported by Demorest et al. for J1614−2230 (5% versus 2%), J0740+6620 is a remarkably high-mass MSP. This measurement will help constrain high-density nuclear physics, as there are very few examples of $\gtrsim 2\ M_\odot$ neutron stars. PSR J0740+6620 is 98% and 90% likely to be more massive than J1614−2230 and J0348+0432, respectively, and is therefore likely to be the most massive well measured neutron star so far.

Taken together, these three massive MSPs serve as a strong validation of the existence of high-mass neutron stars. Due to the asymptotic nature of the relationship between maximum neutron star mass and nearly all EoSs, even small increases in the measured mass of the most massive neutron stars force a reconsideration of the fundamental physics at play in their interiors (for example, see Fig. 2 in ref. [14]). Non-nucleonic solutions to the EoS problem, such as quark matter, hyperons or Bose–Einstein meson condensates, yield softer EoSs (that is, relatively compressible matter); however, more massive neutron stars necessitate stiffer EoSs, which allow for higher maximum masses (see ref. [15] for a review). The measurement of a $2.14\,M_\odot$ neutron star is therefore in extreme tension with these non-nucleonic proposals, and underlines the necessity of untangling existing theoretical paradoxes. The most prominent of these may be the hyperon problem, which proposes that, although the extreme densities inside neutron stars would favour the conversion of nucleons to hyperons, the presence of hyperons softens the EoS and excludes the possibility of high-mass neutron stars (see, for example, ref. [16]). In addition, the mass measurement of J0740+6620 may have implications for the nature of neutron star mergers as detected by LIGO. Because several neutron stars with masses close to or greater than $\sim 2\,M_\odot$ are now known, it may be the case that more mass-asymmetric neutron star mergers will occur than previously supposed.

Constraining the mass of J0740+6620 carries additional astrophysical benefits. Recent evidence from Antoniadis et al.[17] suggests that the distribution of MSP masses may be bimodal, implying

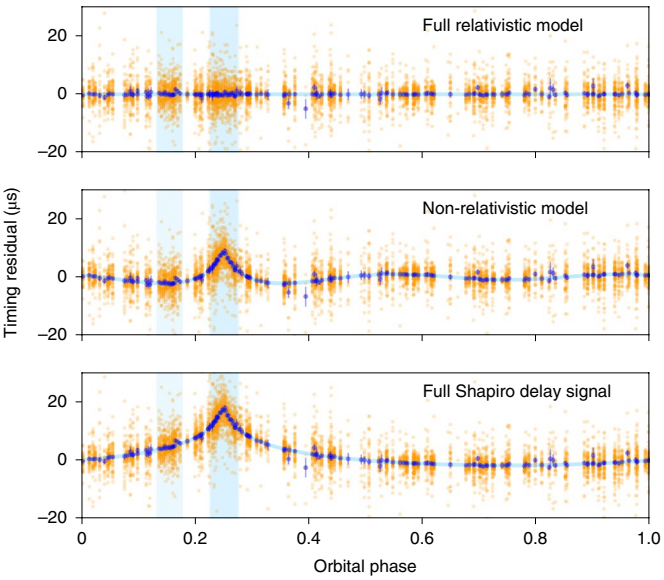

Fig. 1 | Timing residuals from all observations of J0740+6620 as a function of orbital phase, with superior conjunction at orbital phase = 0.25. Orange points are multifrequency timing residuals, while dark-blue points are averages of each group (timing epoch) of these points with 1σ error bars. Averages were taken over a minimum of four data points to avoid showing misleading residuals from faint observations. Blue boxes indicate the orbital phases over which each of the three supplemental observations was taken (the box over conjunction is slightly darker because we made two superior conjunction observations). The top panel shows the full fit (including Shapiro delay parameters and all dispersion measure (DM) parameters—that is, the full timing solution). The middle panel is the best fit with the measurable Shapiro delay signal added; this is the signal to which we are actually sensitive. The bottom panel is the 'full' Shapiro delay signal. Both the second and third panels are calculated on the basis of the orbital and system parameters determined from the full fit. The lighter-blue line represents the theoretical measurable and full Shapiro delay in the middle and bottom panels, respectively (and marks a 0 μs residual in the top panel). The width of the line in each panel is equal to the root mean square error of the averaged points.

that many more neutron stars with masses greater than $\sim 1.6\,M_\odot$ may exist than previously supposed (see also ref. [15]). Not only is it becoming clear that high-mass neutron stars make up a sizeable portion of the population, but also their existence carries substantial implications for our understanding of MSP binary evolution. Because many fully recycled pulsars have been measured to have masses less than or equal to $1.4\,M_\odot$, we know that recycling can be accomplished with only a small amount of mass transfer. We must therefore consider the possibility that some MSPs are not formed near the Chandrasekhar mass and increase to high masses through accretion; rather, they are born massive in the first place (see refs. [18] and [19] for earlier evidence of this phenomenon).

There exists a well known relationship between the mass of a pulsar's white dwarf companion and the binary system's orbital period[20,21]. For our measured orbital period of ~4.77 days, the predicted white dwarf companion masses (from equations (20) and (21) in ref. [21]) are $\sim 0.24\,M_\odot$ for a mid-metallicity (Pop I+II) donor star and $\sim 0.25\,M_\odot$ for a low-metallicity, Pop II star. Our measured mass of J0740+6620's helium white dwarf companion is $0.260^{+0.008}_{-0.007}\,M_\odot$ (at 68.3% credibility). Given the stated uncertainties in convective mixing length, this discrepancy of 5–10% is not an indication that J0740+6620 is an exception to the orbital period versus white dwarf mass relationship; however, it may indicate that this system was born in a relatively low-metallicity environment. There exist

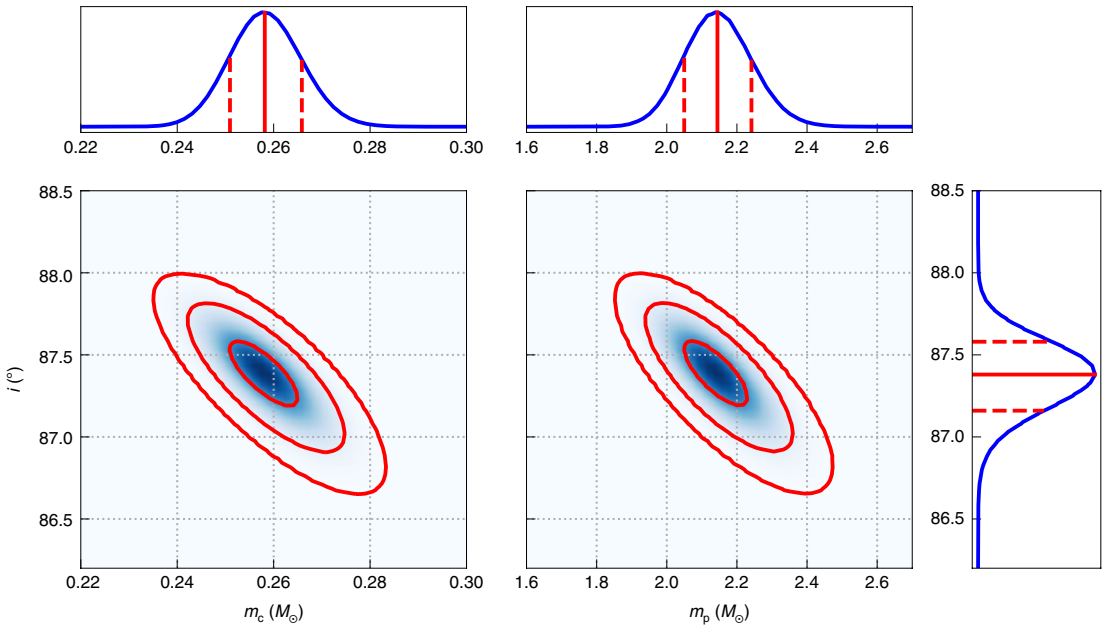

Fig. 2 | Map of fitted χ^2 distributions and corresponding probability density functions for m_p, m_c and i. The left-hand heat map was generated by computing χ^2 values for different combinations of m_c and i; the right-hand heat map was calculated by translating the m_c–i probability density function to the m_p–i phase space using the binary mass function. Darker-blue regions correspond to lower χ^2 values. The three red circles correspond to 1, 2 and 3σ significance cut-offs. Each of the three probability density functions (blue lines plotted above and beside the heat maps) is a projection of the χ^2 distributions. The solid red lines mark median values of each of the three parameters, while red dashed lines denote the upper and lower bounds of the 68.3% (1σ) credibility interval.

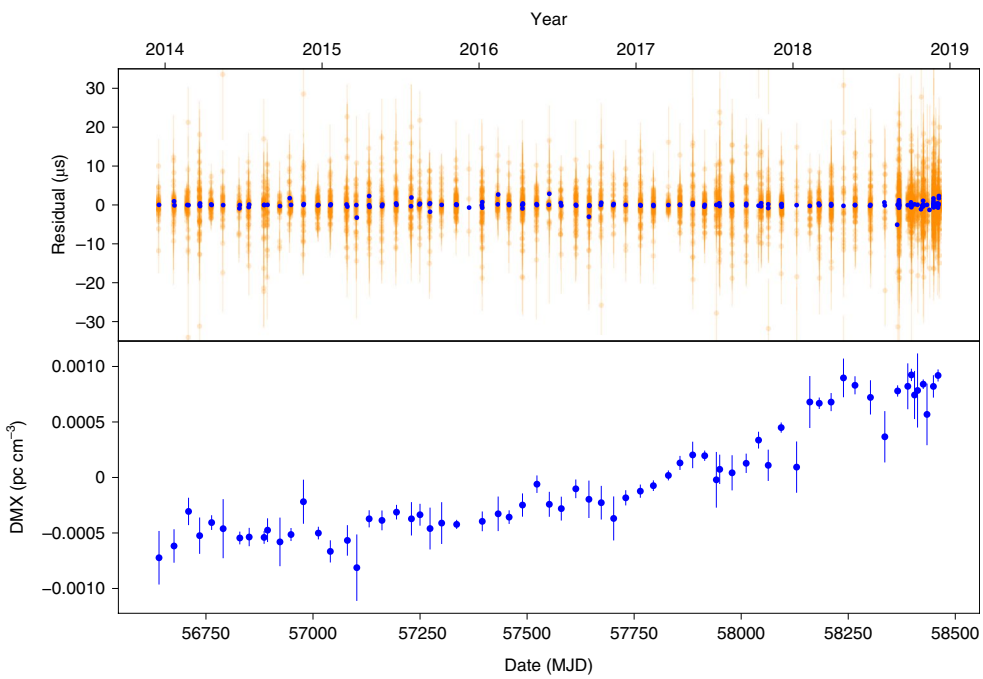

Fig. 3 | Timing residuals and DMX for all epochs of J0740+6620 data. Top: timing residuals from all epochs of J0740+6620 data, including both NANOGrav and superior conjunction-specific observations at all frequencies, are shown in orange (with 1σ error bars). The superimposed blue points represent an average over each epoch (root mean square = 1.5 μs; note that some days have two separately calculated averages from dual-frequency data). Bottom: blue points indicate DMX values calculated for each epoch of data with 1σ error bars, where DMX is a piecewise constant approximation to the DM. The DMX trend is fairly simple (that is, roughly quadratic); however, linear modelling is strongly disfavoured. A single averaged epoch (one dark-blue point) was removed from these plots, as its error bar was ~8 μs due to a faint detection from which only one time of arrival (TOA) could be extracted. MJD, modified Julian date.

at least three other examples of MSP–helium white dwarf binaries with minimum companion masses greater than the Pop II masses predicted by Tauris and Savonije (J1125−6014, J1903−7051 and J1933−6211). Finally, if J0740+6620 is measured to be at the high end of our mass credibility interval, it may provide evidence that the creation of a stable, high-mass neutron star is possible through the

merger of two low-mass neutron stars (in a LIGO-like gravitational-wave event).

Though it will require considerable additional observing time to improve on our J0740+6620 measurement, high-cadence monitoring of the pulsar is a promising strategy. Daily observations with the Canadian Hydrogen Intensity Mapping Experiment (CHIME[22]) telescope, in conjunction with the present data set, have the potential to determine the mass of J0740+6620 with 2–3% precision within a year. Additionally, the Neutron Star Interior Composition Explorer (NICER) is observing J0740+6620 at X-ray wavelengths (https://heasarc.gsfc.nasa.gov/docs/nicer/science_team_investigations). Modelling the thermal pulse profile of this MSP at X-ray energies will aid in constraining the mass and radius of J0740+6620. Continued collaboration with multifrequency observing programmes will guarantee the steady improvement of this pulsar mass measurement in the long term.

Methods

GBT observations. Both NANOGrav and targeted observations were conducted using the Green Bank Ultimate Pulsar Processing Instrument (GUPPI[23]). Observations at 1.5 GHz were acquired with 800 MHz of bandwidth split into 512 frequency channels (which were summed to 64 channels before analysis), sampling every 0.64 μs. At an observing frequency of 820 MHz, 200 MHz of bandwidth over 128 channels was acquired with an identical sampling rate (and later also summed to 64 channels). These dual-polarization observations at both frequencies were coherently dedispersed at the known DM of 15.0 pc cm^{-3}. Data were processed using NANOGrav pipelines for consistency with the existing 4-yr-long NANOGrav J0740+6620 data set (see ref. [24] for a thorough description of NANOGrav observing procedures, and ref. [25] for a description of NANOGrav's main data processing pipeline, `nanopipe`).

Generation of TOAs and the timing model. The measurement and modelling of pulse TOAs closely mirrors the procedure described by Arzoumanian et al.[10]. We provide a summary of the analysis procedure in this section.

During offline processing, total-intensity profile data were integrated over ~20–30 min intervals to yield one or two TOAs per downsampled frequency interval for a normal NANOGrav observation, and ~10 min for the long scans near or during conjunction. We extracted TOAs from each of the 64 integrated channels over the entire observing bandwidth through cross-correlation between the data and a smoothed profile template using the software package `PSRCHIVE` (source code in ref. [26]; see http://psrchive.sourceforge.net).

We used standard pulsar-timing analysis tools, namely `TEMPO` (http://tempo.sourceforge.net) and `TEMPO2` (source code in ref. [27]; see https://www.atnf.csiro.au/research/pulsar/tempo2) for modelling TOA variation in terms of many physical mechanisms. `TEMPO` and `TEMPO2`, while not fully independent timing packages, yield consistent results. For J0740+6620, fitted parameters include celestial (ecliptic) coordinates, proper motion, spin frequency and its first derivative, and binary orbital parameters (see Table 1, which lists best-fit values for these parameters as determined with `TEMPO`).

We used the DE436 (https://naif.jpl.nasa.gov/pub/naif/JUNO/kernels/spk/de436s.bsp.lbl) Solar System ephemeris, maintained by the NASA Jet Propulsion Laboratory, for correction to the barycentric reference frame. The time standard used was BIPM2017. The overall root mean square timing residual value for the timing model presented in this work is 1.5 μs. The χ^2 of our fit is 7,314.35 with 7,334 degrees of freedom, yielding a reduced-χ^2 value of 0.997; note that the noise modelling (Assessment of timing noise) will always yield a χ^2 of ~1.

We employed the ELL1 binary timing model[28] in describing the nearly circular orbital dynamics of the J0740+6620 system. Parameters of the ELL1 binary model consist of the projected semi-major axis, orbital period, epoch of passage through the ascending orbital node, and two 'Laplace–Lagrange parameters' (ϵ_1 and ϵ_2; the orbital eccentricity multiplied by the sine and cosine of periastron longitude, respectively[28]) that quantify departures from perfectly circular orbits.

Assessment of timing noise. MSP rotation often exhibits a limit in achievable precision due to the presence of stochastic processes that act as noise in timing measurements. Examples of timing noise include systematic errors from cross-correlation template matching and 'spin noise' due to irregular rotation of the neutron star. We use a noise model similar to those developed in the NANOGrav 9-yr and 11-yr data releases to quantify these noise terms in the J0740+6620 data set.

The noise model consists of white-noise components that combine to form additive Gaussian noise. For each of the two front-end receivers used in this work, we use three parameters to describe the white-noise contribution to timing noise: a scaling factor applied to all raw TOA uncertainties ('EFAC'), a term added in quadrature to the TOA uncertainties ('EQUAD') and a noise term that quantifies TOA correlations purely across observing frequency ('ECORR').

Table 1 | PSR J0740+6620 best-fit parameters

Pulsar name	J0740+6620
Dates of observations (MJD)	56640–58462
Number of TOAs	7,419
Measured quantities	
Ecliptic longitude, λ (°)	103.75913607(1)
Ecliptic latitude, β (°)	44.10248468(2)
Epoch of position and period (MJD)	57551.0
Proper motion in ecliptic longitude (mas yr^{-1})	−2.75(3)
Proper motion in ecliptic latitude (mas yr^{-1})	−32.43(4)
Parallax (mas)	0.5(3)
Spin frequency, ν (Hz)	346.5319964932129(6)
Spin frequency derivative, $\dot{\nu}$ (s^{-2})	$-1.46389(2)\times10^{-15}$
Dispersion measure, DM (pc cm^{-3})[a]	14.961787
Profile frequency dependency parameter, FD1	$-1.17(4)\times10^{-5}$
Binary model	ELL1
Projected semi-major axis of orbit, x (lt-s)	3.9775561(2)
Binary orbital period, P_b (days)	4.7669446191(1)
Epoch of ascending node, TASC (MJD)	57552.08324415(2)
EPS1 (first Laplace–Lagrange parameter), $e\sin\omega$	$-5.70(4)\times10^{-6}$
EPS2 (second Laplace–Lagrange parameter), $e\cos\omega$	$-1.89(3)\times10^{-6}$
Sine of inclination angle i	0.9990(2)
Companion mass, m_c ($M_\odot$)	0.258(8)
Derived parameters	
Orbital eccentricity, e	$5.10(3)\times10^{-6}$
Longitude of periastron, ω (°)	244.4(3)
Epoch of periastron, T_0 (MJD)	57550.543(5)
Binary mass function ($M_\odot$)	0.0029733870(4)
Pulsar mass (68.3% credibility interval, $M_\odot$)	$2.14^{+0.10}_{-0.09}$
Pulsar mass (95.4% credibility interval, $M_\odot$)	$2.14^{+0.20}_{-0.18}$
Companion mass (68.3% credibility interval, $M_\odot$)	$0.260^{+0.008}_{-0.007}$
Companion mass (95.4% credibility interval, $M_\odot$)	$0.260^{+0.016}_{-0.014}$
Inclination angle (68.3% credibility interval, °)	$87.38^{+0.20}_{-0.22}$
Inclination angle (95.4% credibility interval, °)	$87.38^{+0.39}_{-0.45}$

[a]Because this DM is an unfitted reference value, no error is reported. Values of DMX for each of the ~70 epochs are available on request.

We used the `Enterprise` (https://enterprise.readthedocs.io/en/latest) modelling suite for estimation of the white components of the noise model using a Markov chain Monte Carlo (MCMC)-based algorithm. `Enterprise` uses the `TEMPO(2)` fit as the maximum-likelihood fit for the timing parameters and the basis of the fit for the red-noise parameters, should they be found to be significant. In our `TEMPO(2)` fits, we include an EFAC of 1.036 for L-band (1,500 MHz) TOAs and 1.013 for 820 MHz TOAs. EQUAD is 0.00610 μs for the L band, and 0.18310 μs for 820 MHz. ECORR values for L-band and 820 MHz TOAs are 0.00511 μs and 0.00871 μs, respectively. Bayesian model selection via an `Enterprise` MCMC run disfavours the inclusion of red noise; therefore, the noise model includes only white-noise components.

DM modelling. The complexity of modelling DM variations arising from a dynamic interstellar medium has been discussed at length in previous works (see, for example, refs. [29,30]). We have adopted the standard NANOGrav piecewise-constant model for DM trends wherein each epoch of data is fitted with a constant DMX value; in other words, each of these parameters is a deviation from some nominal DM and is fixed over a single epoch. The observation that J0740+6620's DM behaviour is fairly smooth over the duration of our data set (see Fig. 3) led us to attempt alternatively modelling the entire data set by fitting for only the first and second derivatives of DM. In theory, this approach could be advantageous given the ability of DMX to absorb Shapiro delay signals (thanks to the similar duration of conjunction and a DMX epoch). While this strategy does reduce the formal parameter uncertainties from the fit, both an F-test and an Akaike information criterion test strongly favour the DMX model over the quadratic DM fit. This indicates that the DM variation is not fully characterized by a quadratic model, and parameter values (including pulsar mass) derived from this model are likely to have systematic biases not reflected in their formal uncertainties.

Simulations. Analysis of the NANOGrav 12.5-yr data set without supplemental data yielded $m_p = 2.00 \pm 0.20\,M_\odot$. After the initial 6 h supplemental observation, we measured the mass of J0740+6620 to be $2.18 \pm 0.15\,M_\odot$. We conducted simulations of future observations both to predict the constraining power of a concentrated Director's Discretionary Time campaign and to determine how our mass measurement may improve with additional observations going forward. For these simulations, we first generated an arbitrary array of TOAs that mirror the desired observing cadence, starting date and so on. The TOAs were then fitted (with pulsar-timing software such as `TEMPO` or `PINT`; https://github.com/nanograv/PINT) using the known parameters for J0740+6620. Residuals from this fit were then subtracted from the original TOAs to create 'perfect' TOAs, to which stochastic noise was then added. Two notable types of simulation were conducted. The first was an estimation of the improvement in our measurement of m_p given random orbital sampling (the 'NANOGrav-only observation' scenario); this solidified our conclusion that the concentrated GBT campaigns were necessary. The second served to optimize our observing strategy during a targeted orbital-phase campaign by trying various permutations of orbital phase, number of observing sessions and observing session lengths. The results of this simulation informed our GBT Director's Discretionary Time request for 5 h over conjunction and 5 h in one of the Shapiro 'troughs' (we were awarded time in the first trough—around orbital phase 0.15—in addition to conjunction). To ensure that obtaining data in this asymmetric fashion would not bias our mass measurement, we ran 10,000 simulations of a 5 h conjunction observation plus 5 h in either the first or second Shapiro trough. The averages of the 10,000 mass measurements obtained from each of these troughs were consistent within 1%, implying that our orbital sampling is not biasing our results (as one would expect, given that the Shapiro delay response curve is symmetric about superior conjunction).

Data availability

PSR J0740+6620 TOAs from both the 12.5-yr data set and from the two supplemental GBT observations will be available at https://data.nanograv.org on publication of this manuscript.

Code availability

All code mentioned in this work is open source and available at the links provided in the manuscript.

Received: 13 April 2019; Accepted: 31 July 2019;
Published online: 16 September 2019

References

1. Lorimer, D. R. & Kramer, M. *Handbook of Pulsar Astronomy* (Cambridge University Press, 2005).
2. Shapiro, I. I. Fourth test of general relativity. *Phys. Rev. Lett.* **13**, 789–791 (1964).
3. Freire, P. C. C. & Wex, N. The orthometric parametrization of the Shapiro delay and an improved test of general relativity with binary pulsars. *Mon. Not. R. Astron. Soc.* **409**, 199–212 (2010).
4. Demorest, P. B., Pennucci, T., Ransom, S. M., Roberts, M. S. E. & Hessels, J. W. T. A two-solar-mass neutron star measured using Shapiro delay. *Nature* **467**, 1081–1083 (2010).
5. Fonseca, E. et al. The NANOGrav nine-year data set: mass and geometric measurements of binary millisecond pulsars. *Astrophys. J.* **832**, 167 (2016).
6. Antoniadis, J. et al. A massive pulsar in a compact relativistic binary. *Science* **340**, 448 (2013).
7. Friere, P. C. C. et al. On the nature and evolution of the unique binary pulsar J1903+0327. *Mon. Not. R. Astron. Soc.* **412**, 2763–2780 (2011).
8. Margalit, B. & Metzger, B. D. Constraining the maximum mass of neutron stars from multi-messenger observations of GW170817. *Astrophys. J. Lett.* **850**, L19 (2017).
9. Linares, M., Shahbaz, T. & Casares, J. Peering into the dark side: magnesium lines establish a massive neutron star in PSR J2215+5135. *Astrophys. J.* **859**, 54 (2018).
10. Arzoumanian, Z. et al. The NANOGrav 11-year data set: pulsar-timing constraints on the stochastic gravitational-wave background. *Astrophys. J.* **859**, 47 (2018).
11. Stovall, K. et al. The Green Bank Northern Celestial Cap pulsar survey. I. Survey description, data analysis, and initial results. *Astrophys. J.* **791**, 67 (2014).
12. Lynch, R. S. et al. The Green Bank North Celestial Cap pulsar survey. III. 45 new pulsar timing solutions. *Astrophys. J.* **859**, 93 (2018).
13. Beronya, D. M. et al. The ultracool helium-atmosphere white dwarf companion of PSR J0740+6620?. *Mon. Not. R. Astron. Soc.* **485**, 3715–3720 (2019).
14. Watts, A. et al. Probing the neutron star interior and the Equation of State of cold dense matter with the SKA. *Proc. Sci.* **215**, 43 (2015).
15. Özel, F. & Freire, P. Masses, radii, and the equation of state of neutron stars. *Annu. Rev. Astron. Astrophys.* **54**, 401–440 (2016).
16. Bedaque, P. F. & Steiner, A. W. Hypernuclei and the hyperon problem in neutron stars. *Phys. Rev. C* **92**, 025803 (2015).
17. Antoniadis, J. et al. The millisecond pulsar mass distribution: Evidence for bimodality and constraints on the maximum neutron star mass. Preprint at https://arxiv.org/abs/1605.01665 (2016).
18. Tauris, T. M., Langer, N. & Kramer, M. Formation of millisecond pulsars with CO white dwarf companions—I. PSR J1614-2230: evidence for a neutron star born massive. *Mon. Not. R. Astron. Soc.* **416**, 2130–2142 (2011).
19. Cognard, I. et al. A massive-born neutron star with a massive white dwarf companion. *Astrophys. J.* **844**, 128 (2017).
20. Rappaport, S., Podsiadlowski, P., Joss, P. C., Di Stefano, R. & Han, Z. The relation between white dwarf mass and orbital period in wide binary radio pulsars. *Mon. Not. R. Astron. Soc.* **273**, 731–741 (1995).
21. Tauris, T. M. & Savonije, G. J. Formation of millisecond pulsars. I. Evolution of low-mass X-ray binaries with $P_{orb} > 2$ days. *Astron. Astrophys.* **350**, 928–944 (1999).
22. Ng, C. Pulsar science with the CHIME telescope. In *Proc. International Astronomical Union Vol. 13, Symp. 337: Pulsar Astrophysics —The Next Fifty Years* (eds Weltevrede, P. et al.) 179–182 (Cambridge University Press, 2018).
23. DuPlain, R. et al. Launching GUPPI: the Green Bank Ultimate Pulsar Processing Instrument. *Proc. SPIE* **7019**, 70191D (2008).
24. Arzoumanian, Z. et al. The NANOGrav nine-year data set: observations, arrival time measurements, and analysis of 37 millisecond pulsars. *Astrophys. J.* **813**, 65 (2015).
25. Demorest, P. B. nanopipe: calibration and data reduction pipeline for pulsar timing. *Astrophysics Source Code Library* ascl:1803.004 (2018).
26. van Straten, W. et al. PSRCHIVE: development library for the analysis of pulsar astronomical data. *Astrophysics Source Code Library* ascl:1105.014 (2011).
27. Hobbs, G. & Edwards, R. Tempo2: pulsar timing package. *Astrophysics Source Code Library* ascl:1210.015 (2012).
28. Lange, Ch et al. Precision timing measurements of PSR J1012+5307. *Mon. Not. R. Astron. Soc.* **326**, 274–282 (2001).
29. Lam, M. T. et al. Systematic and stochastic variations in pulsar dispersion measures. *Astrophys. J.* **821**, 66 (2015).
30. Jones, M. L. et al. The NANOGrav nine-year data set: measurement and interpretation of variations in dispersion measures. *Astrophys. J.* **841**, 125 (2017).

Acknowledgements

The NANOGrav Project receives support from NSF Physics Frontiers Center award no. 1430284. Pulsar research at UBC is supported by an NSERC Discovery Grant and by the Canadian Institute for Advanced Research (CIFAR). The National Radio Astronomy Observatory and the Green Bank Observatory are facilities of the National Science Foundation operated under cooperative agreement by Associated Universities, Inc. S.M.R is a CIFAR Senior Fellow. W.W.Z. is supported by the CAS Pioneer Hundred Talents Program, the Strategic Priority Research Program of the Chinese Academy of Sciences grant no. XDB23000000 and the National Natural Science Foundation of China grant nos. 11690024, 11743002 and 11873067. Supplementary Green Bank conjunction-phase observing project codes were 18B-289 and 18B-372 (DDT).

Author contributions

The creation of the NANOGrav 12.5-yr data set was made possible through extensive observations and pulsar-timing activities conducted by all the authors. H.T.C. was responsible for the NANOGrav-adjacent concentrated observing campaigns and the majority of this manuscript's contents. H.T.C., E.F., S.M.R. and P.B.D. were responsible for the extended J0740+6620 data analysis (the merging of NANOGrav and conjunction-phase observations) and modelling effort. E.F. was responsible for much of the initial work on J0740+6620 that informed the supplementary observing proposals, and for the development of the gridding code that yielded both the mass and inclination credibility intervals and Fig. 2.

Competing interests

The authors declare no competing interests.

Additional information

Reprints and permissions information is available at www.nature.com/reprints.

Correspondence and requests for materials should be addressed to H.T.C.

Peer review information *Nature Astronomy* thanks John Antoniadis and the other, anonymous, reviewer(s) for their contribution to the peer review of this work.

Publisher's note Springer Nature remains neutral with regard to jurisdictional claims in published maps and institutional affiliations.

© The Author(s), under exclusive licence to Springer Nature Limited 2019

The Astrophysical Journal Letters, 934:L17 (6pp), 2022 August 1 https://doi.org/10.3847/2041-8213/ac8007
© 2022. The Author(s). Published by the American Astronomical Society.
OPEN ACCESS

PSR J0952−0607: The Fastest and Heaviest Known Galactic Neutron Star

Roger W. Romani[1], D. Kandel[1], Alexei V. Filippenko[2], Thomas G. Brink[2], and WeiKang Zheng[2]
[1] Department of Physics/KIPAC, Stanford University, Stanford, CA 94305, USA; rwr@astro.stanford.edu
[2] Department of Astronomy, University of California, Berkeley, CA 94720-3411, USA
Received 2022 May 12; revised 2022 June 24; accepted 2022 July 4; published 2022 July 26

Abstract

We describe Keck-telescope spectrophotometry and imaging of the companion of the "black widow" pulsar PSR J0952−0607, the fastest known spinning neutron star (NS) in the disk of the Milky Way. The companion is very faint at minimum brightness, presenting observational challenges, but we have measured multicolor light curves and obtained radial velocities over the illuminated "day" half of the orbit. The model fits indicate system inclination $i = 59\overset{\circ}{.}8 \pm 1\overset{\circ}{.}9$ and a pulsar mass $M_{\rm NS} = 2.35 \pm 0.17\,M_\odot$, the largest well-measured mass found to date. Modeling uncertainties are small, since the heating is not extreme; the companion lies well within its Roche lobe and a simple direct-heating model provides the best fit. If the NS started at a typical pulsar birth mass, nearly $1\,M_\odot$ has been accreted; this may be connected with the especially low intrinsic dipole surface field, estimated at 6×10^7 G. Joined with reanalysis of other black widow and redback pulsars, we find that the minimum value for the maximum NS mass is $M_{\rm max} > 2.19\,M_\odot$ ($2.09\,M_\odot$) at 1σ (3σ) confidence. This is $\sim 0.15\,M_\odot$ heavier than the lower limit on $M_{\rm max}$ implied by the white dwarf–pulsar binaries measured via radio Shapiro-delay techniques.

Unified Astronomy Thesaurus concepts: Pulsars (1306)

Supporting material: data behind figure

1. Introduction

Pulsar PSR J0952−0607 (hereafter J0952) was discovered by Bassa et al. (2017) with a spin period of $P_s = 1.41$ ms, making it the fastest-spinning pulsar in the disk of the Milky Way. It is a "black widow" (BW) pulsar with a low-mass (substellar) companion being irradiated and evaporated by the pulsar luminosity. Nieder et al. (2019) subsequently detected it as a gamma-ray pulsar, and obtained additional radio timing and optical photometry that allowed initial fits for the system properties. In particular, they measure a low period derivative $\dot{P}_{\rm obs} = 4.6 \times 10^{-21}$ s s^{-1}, which places an upper limit on the surface dipole field of 8.2×10^7 G, among the 15 lowest-known pulsar magnetic fields (B), even before the Shklovskii (1970) correction. Since in addition their optical photometry suggests a large (>5 kpc) distance, and timing data gave a best-fit (albeit low-significance) proper motion of $\sim$10 mas yr^{-1}, the correction to find the intrinsic $\dot{P}$,

$$\dot{P} = \dot{P}_{\rm obs} - 2.43 \times 10^{-21} P\, \mu^2_{\rm mas/yr} d_{\rm kpc}, \quad (1)$$

may be substantial, reducing $\dot{P}$ to 2.0×10^{-21} s s^{-1} and thus B to $B_i \approx 6.1 \times 10^7$ G. Not all pulsars have a proper motion allowing an intrinsic B_i estimate, but only 10 pulsars have a lower B_i in the ATNF catalog[3] (Manchester et al. 2005).

The measurement of high neutron star (NS) masses in some white dwarf (WD)–NS millisecond-pulsar binaries, via radio-measured Shapiro delay, has been very influential in driving thinking about the dense-matter equation of state. Two systems have best-estimate masses barely exceeding $2.0\,M_\odot$: J0348+0432 at $2.01 \pm 0.04\,M_\odot$ (Antoniadis et al. 2013) and PSR J0740+6620 at $2.08 \pm 0.07\,M_\odot$ (Fonseca et al. 2021), both 1σ uncertainties. However, the maximum mass that an NS can reach must depend on its binary evolutionary history. For example, inspection of the double NS–NS binaries alone would lead one to conclude that the typical NS mass is $\sim 1.35\,M_\odot$, with a maximum of $\sim 1.45\,M_\odot$; the millisecond pulsars in these systems are only mildly recycled, with spin periods of tens of milliseconds and moderate magnetic fields. One must therefore examine a variety of pulsar binary classes in a quest to find the most massive NSs.

It has long been argued (e.g., Bisnovatyi-Kogan & Komberg 1974; Romani 1990) that binary accretion may reduce young pulsar terraGauss fields to millisecond-pulsar values. While the mechanism is unclear, ranging from simple burial to heating-driven ohmic decay (see Mukherjee 2017 for a review), it seems likely that the amount of mass accretion or its duration play a role in controlling the degree of field reduction. Thus, it is interesting to measure the masses of millisecond pulsars, and the fastest-spinning lowest-field pulsars are good candidates for substantial accretion and high NS mass. Since evolution is driven by angular momentum loss and irradiation bloating, rather than by nuclear evolution, long periods of sub-Eddington rate accretion are expected for the progenitors of "spider" (BW and "redback" (RB) millisecond-pulsar) binaries before the start of the pulsar-driven evaporation phase; these short-period binaries may host very massive NSs.

Thus, J0952 is a particularly attractive candidate for further investigation. However, Nieder et al. (2019) state, "Unfortunately, the optical counterpart of PSR J0952−0607 is too faint ($r \approx 23$ at quadrature when the radial velocity is highest) for spectroscopic radial-velocity measurements to be feasible even with 10 m class 'telescopes.'" This is nearly true, but the exceptional P_s and B inspired our intensive campaign of J0952 Keck LRIS imaging and spectroscopy. Modeling these data, we find that the NS mass is indeed the largest well-measured value to date. Combining this mass with those from new modeling of other spider binaries, we show that these objects put a strong

[3] http://www.atnf.csiro.au/research/pulsar/psrcat

Original content from this work may be used under the terms of the Creative Commons Attribution 4.0 licence. Any further distribution of this work must maintain attribution to the author(s) and the title of the work, journal citation and DOI.

Table 1
Keck LRIS Observations

Session	Spec. Exp. (s)	MJD Range	Phase Range
2018A Im	9 gi + 3 gr	58455.50562–.57691	0.92–1.20
2020A Im	18 gi	58932.36032–.47731	0.07–0.51
2018A Spec	12 × 900	58454.52711–.63543	0.53–0.94
2019A Spec	5 × 900	58577.39244–.43654	0.91–1.08
2020A Spec	13 × 600	58932.22869–.33973	0.61–1.00
2021B Spec	21 × 900	59610.45450–.62940	0.39–1.04
2022A Spec	10 × 900	59637.27289–.37235	0.66–1.03
2022A2 Spec	11 × 900	59641.26374–.37420	0.58–0.99

lower bound on the maximum NS mass, appreciably above the values inferred from radio Shapiro-delay measurements. This should have deep implications for the dense-matter equation of state.

2. Observations

With its $P_b = 6.42$ hr orbital period and faint magnitude, the effective study of J0952 requires substantial amounts of large-telescope time, ideally with superior seeing. Our campaign uses the Keck-I 10 m telescope and the Low Resolution Imaging Spectrometer (LRIS; Oke et al. 1995). We report here on two dual-color (typically g/i with a few r/i pairs) imaging runs and six spectroscopy campaigns (Table 1). For the latter we used the 5600 Å dichroic, the 600 l/4000 Å blue grism, and the 400 l/8500 Å red grating, covering ∼3300–10500 Å with dispersions of 0.63 Å pixel^{-1} (blue side) and 1.2 Å pixel^{-1} (red side). Typical exposures were 600–900 s. All spectra were processed with the `LPipe` reduction software (Perley 2019). The LRIS red-arm thick chip collects many cosmic rays, so additional editing was needed to clean the red-arm spectra. All companion and comparison star spectra are available in a TAR archive as the data behind Figure 1.

With the atmospheric dispersion corrector (ADC) being used, we could rotate the 1″-wide slit away from the parallactic angle (Filippenko 1982) to simultaneously measure a nearby brighter G1 star with known Pan-STARRS2 (PS2) magnitudes. This allows us to monitor the system throughput and wavelength solution among frames. In particular, since this PS2 star has known and stable magnitudes, we integrate the spectra over the Sloan Digital Sky Survey (SDSS) standard *ugriz* filter bands using the `sbands IRAF` script, and calibrate with the comparison star's catalog magnitudes (converted to the SDSS system using the prescription of Finkbeiner et al. 2016) to obtain light curves with absolute fluxes, up to small gray shifts from differential slit losses.

Our spectroscopic strategy was to observe J0952 for half-nights ideally covering optical maximum brightness. To cover the critical phases at low airmass under dark moon conditions required a careful selection of observing nights. Unfortunately, none of the nights had particularly good seeing; indeed, several additional half-nights requested for this program were completely lost to weather and COVID-19 shutdowns. Nevertheless, the night-to-night consistency in the flux scale and radial-velocity (RV) scale, aided by the comparison star, has let us make combined fits of all the data, allowing good model constraints.

As noted, imperfect position angle (PA) and slit placement can give small differential slit losses. These we correct via gray shifts to the `sbands` magnitudes, matching the imaging fluxes in the overlap regions and between epochs. These $\leqslant -0.2$ mag shifts increase the companion flux; this is sensible, as one tends to ensure that the (brighter) comparison star is well covered by the slit.

In the phase window $\phi_B = 0.1$–0.4 the companion is too faint to determine spectrophotometric colors. We therefore collected LRIS dual-band (g/i with a few g/r) direct images covering minimum brightness. We established a reference grid of PS2 catalog stars, with positions set relative to the pulsar companion, measured near maximum brightness, and extracted forced aperture photometry at these fixed positions. PS2 magnitudes were converted to the SDSS scale and used to determine the companion magnitude. Direct photometric errors were combined in quadrature with zero-point systematic errors determined from scatter in the catalog star residuals; near minimum the photometric errors strongly dominate the final uncertainty. The resulting light curve (Figure 1) covers a large (>5 mag) range, an observational challenge. Image artifacts seem to produce a few modest outliers, and companion flare activity may occasionally brighten the source. We discuss trimming such points below.

We measure the RV amplitude by IRAF `rvsao` (Kurtz & Mink 1998) cross-correlation with a G1 template, using the 3800–9500 Å range, excluding wavelengths near strong telluric features. The spectra were resampled to 8192 wavelengths and filtered in Fourier space with a lower cosine-bell filter cutoff from 20 to 100 and the upper cutoff running from 1000 to 1800. The average companion spectrum near $\phi_B = 0.75$ is shown in Figure 2. The pulsar and companion star were correlated using identical parameters. For the first two epochs (2018B and 2019A), a different slit PA led to the use of a cooler (∼K5) comparison star. A small velocity offset was found between these data and the G1 comparison-star correlations used for the other epochs. In practice, the red K5 star produced poorer RV solutions, and lacked sufficient flux for good g and u calibration; thus, the 2018B and 2019A data do not contribute spectrophotometric points to Figure 1. The G1 comparison-star velocity was always measured to $\sigma_v <$ 5 km s^{-1}, but pulsar companion velocity uncertainties varied greatly from as little as 10 km s^{-1} near "midday" ($\phi_B = 0.75$) to 30–50 km s^{-1} toward the "dawn" and "dusk" phases. In addition, spurious correlation peaks appeared well outside the plausible companion-velocity range for many lower signal-to-noise-ratio (S/N) spectra.

Thus, we measured in two passes, first correlating all spectra over a broad velocity range, and fitting the results with a simple sinusoid RV of amplitude K and offset Γ at the radio ephemeris orbital phasing. We then correlated again, accepting only results within ±100 km s^{-1} of the preliminary fit. This greatly decreased the number of outlier points, and allowed us to recover several weaker RV measurements near the plausible companion solution. For each spectrum the velocity was referenced to that of the comparison star, which varied between exposures, evidently driven by details of the pipeline wavelength solution and extraction aperture. We confirm that these variations are in the pulsar as well; the scatter in the final RVs increases significantly if the points are not referenced to the comparison star. Small overall RV zero-point shifts were also found in several epochs, again likely owing to differences in the apertures. Figure 3 shows all RV values with a finite correlation coefficient ($R > 0$). The point size is scaled to R; a number of obvious outliers with very small R remain.

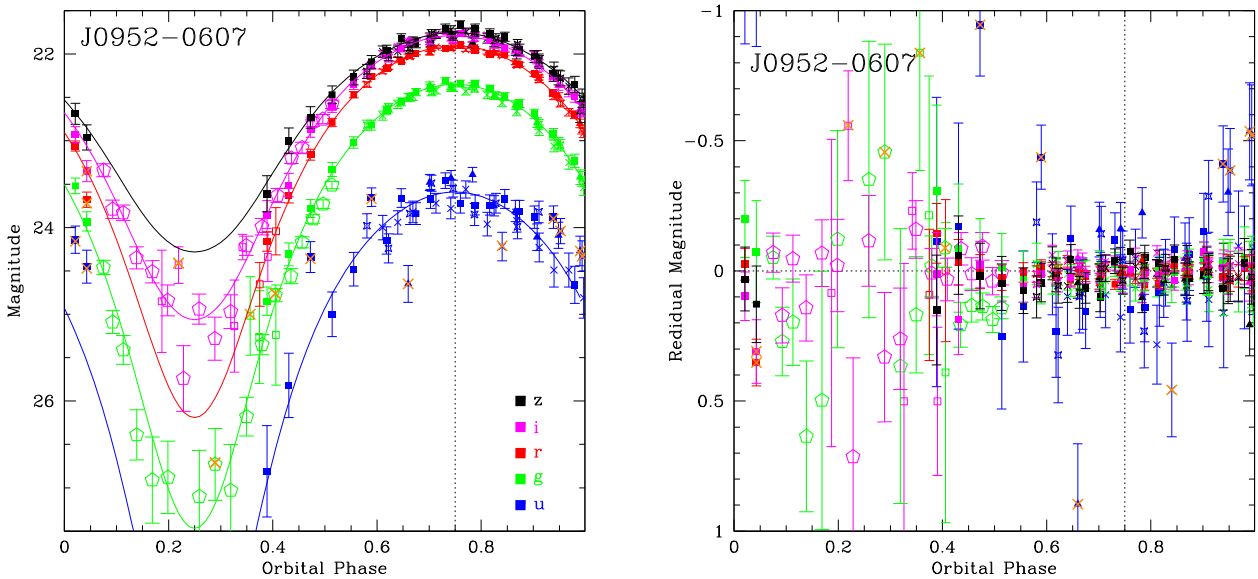

Figure 1. Left: calibrated *ugriz* light curves from Keck LRIS spectrophotometry (filled dots) and direct imaging (open dots). Outlier points excluded in the "trimmed" model fitting are indicated by orange crosses. The curves show the best-fit *ugriz* models and the dotted line marks pulsar inferior conjunction. Right: residuals to the best model fit. Optionally excluded points are again marked by orange crosses. The spectra used for Figures 1–3 are available as data behind the Figure.

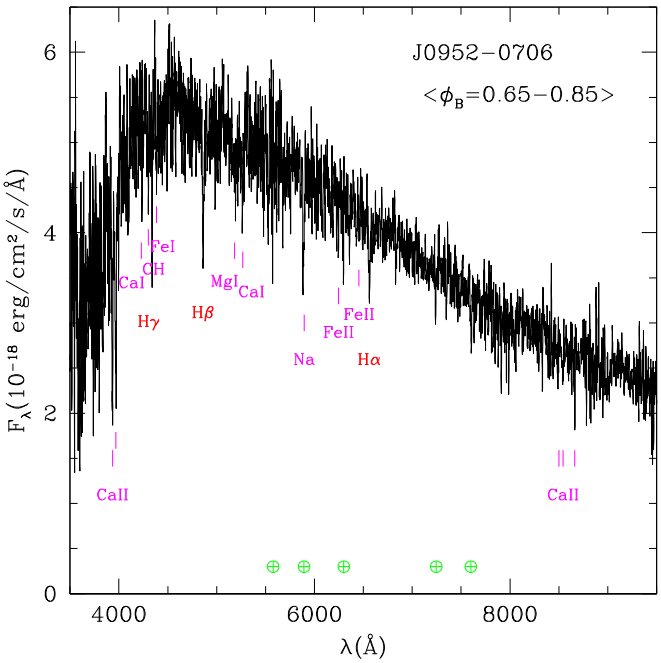

Figure 2. Spectrum of the heated face. S/N-weighted average of 27 individual spectra, Doppler corrected to zero velocity, using the best-fit RV model. Select lines are indicated.

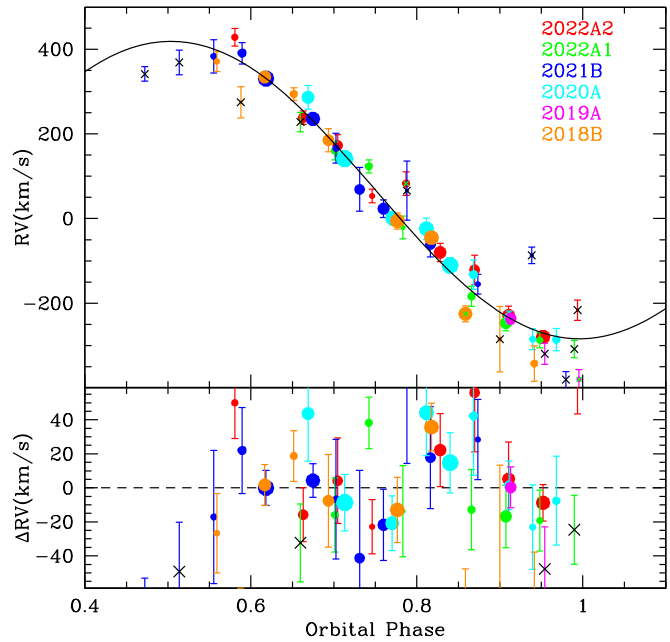

Figure 3. RV measurements for J0952. Dot size is proportional to the correlation coefficient R; low-significance correlations with $R < 2$ are marked with black crosses and are excluded from all fits. Three higher-significance points marked with green crosses appear as outliers and are optionally excluded for the "trimmed" fit. The background curve is the best-fit RV curve for the heating model fit to the light curve in Figure 1. The lower panel shows the fit residuals.

3. Photometric/Radial-velocity Fitting

Our light-curve fits are performed with an outgrowth of the `ICARUS` light-curve model (Breton et al. 2012) with the additions described by Kandel & Romani (2020) and Romani et al. (2021); the main parameters of interest are the orbital inclination i, the companion Roche-lobe filling factor f_1, the heating luminosity L_H, the companion's nightside temperature T_N, and the system distance d. In addition we can fit for the extinction A_V to the source and a set of "bandpass calibrations," for possible imperfections in the photometric zero-points.

The Markov Chain Monte Carlo (MCMC) fits and Bayesian parameter estimation are performed by Multinest sampling (Feroz et al. 2009) using its `Python` implementation `pymultinest` (Buchner 2016). In addition to the photometry, the fits use the pulsar kinematic parameters of Nieder et al. (2019). The light-curve fit is also (weakly) dependent on the companion center-of-mass RV $K_{\rm CoM}$. We do not fit for this with `ICARUS`; instead, we initially fit light curves using the

Table 2
Light-curve/RV-fit Results for J0952[a]

Parameters	Trimmed	All
i (deg)	$59.8^{+2.0}_{-1.9}$	$58.5^{+1.9}_{-1.8}$
f_1	0.79 ± 0.01	0.77 ± 0.01
$L_{\rm H}$ /10^{34} (erg s^{-1})	$3.81^{+0.46}_{-0.43}$	$6.22^{+0.88}_{-0.77}$
$T_{\rm N}$(K)	3085^{+85}_{-80}	3206^{+100}_{-95}
$d_{\rm kpc}$	$6.26^{+0.36}_{-0.40}$	$7.60^{+0.74}_{-0.82}$
χ^2/DoF	286/(298-11)[1.00]	451/(314-11)[1.49]
$K_{\rm CoM}$ (km s^{-1})	376.1 ± 5.1	379.1 ± 6.8
$M_{\rm NS}(M_\odot)$	2.35 ± 0.17	2.50 ± 0.20
$M_{\rm C}(M_\odot)$	0.032 ± 0.002	0.034 ± 0.002
χ^2/DoF	55/(40-2)[1.4]	90/(43-2)[2.2]

Note.
[a] Also fitted: A_V, Δu, Δg, Δr, Δi, and Δz. See the text.

observed spectroscopic K and then refit with $K_{\rm CoM}$ determined from the spectroscopic fit (below), iterating to convergence.

The fit χ^2 is increased by a handful of measurements several σ from the models. The synthesized u photometry has several such points owing to the very low S/N (per resolution element) of the spectra in this band. The most important outliers are a few bright g and i direct-imaging points during the "night" phase. Many spider binaries exhibit occasional short-term ($\sim$1000 s) light-curve flares. Since the quiescence light curve is needed for the light-curve fits, we optionally excise the few points well above the model curves (marked in Figure 1). Table 2 gives the fit values with these points first excluded, and then included. Note that inclusion slightly decreases the fit i and increases the mass (by $\sim 0.7\sigma$), while giving much larger χ^2. We therefore adopt the fit to the "trimmed" data set as conservative.

Extinction in the direction of J0952 is estimated from the three-dimensional dust map of Green et al. (2018), reaching its maximal $E(g-r) = 0.05^{+0.03}_{-0.02}$ mag ($A_V = 0.14^{+0.08}_{-0.05}$ mag) by 0.3 kpc. Treating A_V as a free parameter in the MCMC fits, we find 0.16 ± 0.04 mag, consistent with the dust-map value. Since we rely on the PS2 *griz* catalog magnitudes of our comparison star, there are $\sim$0.02 mag zero-point uncertainties (lacking PS2 u, we rely on the extrapolation of Finkbeiner et al. 2016). Leaving the passband calibrations free in the ICARUS fit to the trimmed data set, we find $\Delta u = +0.07^{+0.08}_{-0.10}$, $\Delta g = +0.05^{+0.05}_{-0.06}$, $\Delta r = +0.02 \pm 0.04$, $\Delta i = -0.02 \pm 0.04$, and $\Delta z = -0.02 \pm 0.04$ mag, all consistent with zero. We therefore believe that our initial calibration was quite good. For the untrimmed data, the outliers produce a large χ^2/degrees of freedom (DoF) and drive these color terms to larger values, notably $\Delta ugriz = +0.27$, $+0.23$, $+0.03$, -0.12, and -0.15 mag. While including these passband shifts does not strongly change either χ^2 or the fit parameters, it does slightly increase the MCMC uncertainty ranges of other parameters (most notably d and L_H); we thus retain these in the fit, although we omit them from Figure 4.

The fits all find $i \leqslant 60°$, with $f_1 = 0.79$ (companion underfilling its Roche lobe), $T_N \approx 3000$ K, dayside heated to $\sim$6200 K, and $d \approx 6$ kpc, larger than the dispersion-measure estimates. These values are very similar to those of Nieder et al. (2019), but with substantially higher precision. Interestingly, simple direct-heating models always provide the best statistical fit; adding additional effects required for many other spider binaries, such as companion

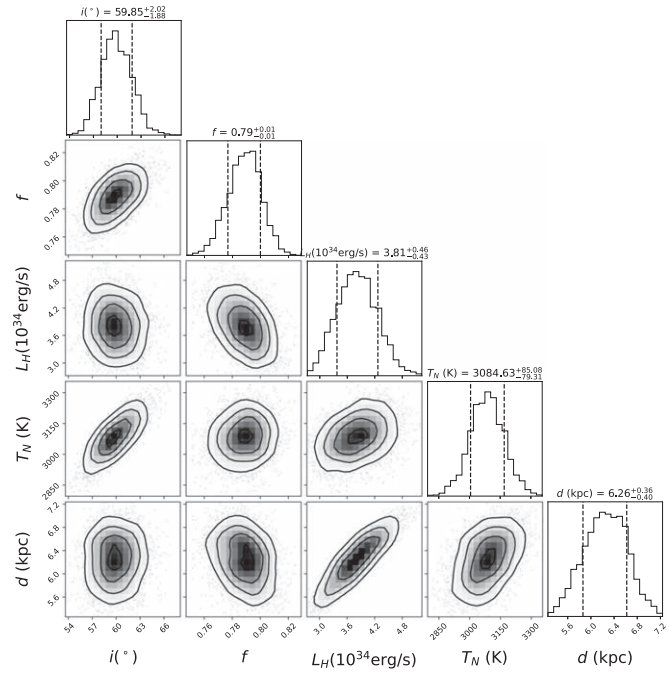

Figure 4. Corner plot from the MCMC light-curve fit to the "trimmed" photometry points. Contours are at 0.5σ, 1.0σ, 1.5σ, and 2σ.

hot spots and surface winds, does not significantly improve the fit. This means that our results are particularly immune to model-dependant systematics, and the fit-parameter errors (Table 2) are dominated by measurement uncertainties.

We next compare the Keck spectroscopy with model RVs computed from photometric-fit companion models. As emphasized by Linares et al. (2018) and discussed by KR20, different species' temperature sensitivities cause varying line equivalent widths (EWs) across the face of the companion. As the model parameters change, the surface heating changes and the line EWs vary. For J0952, metal lines dominate the cross-correlation signal (as appropriate for our G1 correlation spectrum); we apply metal line equivalent width EW(T) weighting to correct center-of-mass RVs to observed center-of-light values (see KR20). If we (inappropriately) apply Balmer EW(T) weighting, the RV amplitude increases to 384 ± 5 km s^{-1}, so again our choice is conservative.

We always exclude the low-significance correlations with $R < 2$ in the RV MCMC fits (marked with black crosses in Figure 3; note that some crossed points follow the expected curve, but many are quite discrepant). The remaining χ^2 is in fact dominated by three outlier points with small uncertainties (marked with green crosses in Figure 3). In our "trimmed" fit for the mass we exclude these three points. Again, this is conservative, as with them the K increases slightly (by 0.4σ). The lower section of Table 2 gives the RV fit parameters and their uncertainties. The mass difference in the "All" column is dominated by the smaller i of the "All" photometric fit.

4. Mass Implications and Conclusions

In the quest for precision mass measurements from spider binaries, J0952 has the advantage that the complex modeling effects required to fit other spiders (hot spots, wind flows, extreme gravity darkening) are not needed. This is a natural consequence of its relatively large P_b, weak pulsar heating, and low Roche-lobe filling factor. On the other hand, the large

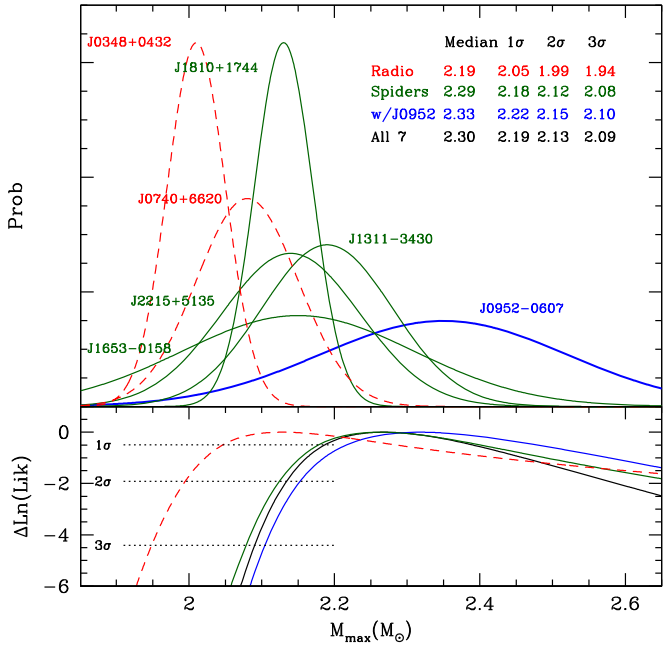

Figure 5. Mass estimates for heavy NSs. The dashed curves show the two heaviest WD–pulsar binaries with masses measured from radio pulse timing (supplemented by WD atmosphere modeling for J0348). The solid curves show the best mass estimates from companion spectroscopy and light-curve fitting for four BWs (J1810, J1653, J1311, and J0952) and one RB (J2215). The bottom panel shows the normalized Ln(Likelihood) for various combinations of these measurements, assuming a flat distribution of masses from 1.8 $M_\odot$ up to some $M_{\rm max}$. The inset legend gives the median estimator for $M_{\rm max}$ as well as the 1σ, 2σ, and 3σ lower bounds on its value, for various data subsets.

distance, weak heating, and low f_1 mean that the companion is quite faint, barely bright enough for measurement with present 10 m telescope systems. Our intensive Keck campaign has managed to measure the binary properties, constraining the masses with sufficient precision that the lower limit on $M_{\rm NS}$ contributes to equation-of-state constraints.

We can examine the minimum required $M_{\rm max}$ by plotting the Gaussian probability distribution functions with M_i, σ_i for observed heavy NSs in Figure 5. Here we compare the latest measurements of the $>2\,M_\odot$ "radio selected" WD–NS MSP J0348+0432 and J0740+6620 with the measurements extracted from light-curve and RV measurements of spider pulsar (BW and RB) companions. For the latter we use the most conservative (best-fit) models with all heating effects as summarized by D. Kandel & R. W. Romani (2022, in preparation). To estimate the minimum value of $M_{\rm max}$ required by these observations, we assume that the NS mass distribution is flat M^0 above $M_1 = 1.8\,M_\odot$ to some cutoff value (for this $>2\,M_\odot$ sample, results are insensitive to the underlying distribution; values change by $< 0.01\,M_\odot$ for M^{-1}). The log (likelihood) for n measurements is

$$\ln \mathcal{L} = -n \ln(M_{\rm max} - M_1) + \Sigma_{i=1}^{n} \ln\left[\mathrm{erf}\left(\frac{M_i - M_1}{2^{1/2}\sigma_i}\right) - \mathrm{erf}\left(\frac{M_i - M_{\rm max}}{2^{1/2}\sigma_i}\right)\right].$$

These curves are plotted in the lower panel of Figure 5. We list the medians and lower bounds at various confidence levels on $M_{\rm max}$, from the likelihood ratio, for the different sample sets.

Since the spiders are appreciably heavier than the WD–NS binaries, the 1σ $M_{\rm max}$ bound increases by $\sim 0.13\,M_\odot$, or $\sim 0.17\,M_\odot$ with J0952. We have checked these bounds with several different estimators. For example a bias-corrected, accelerated bootstrap analysis (kindly supplied by B. Efron) of the seven masses gives $M_{\rm max} = 2.34\,M_\odot$ with a 2σ lower bound of $2.17\,M_\odot$. Numerical simulations with random draws and our observed errors give similar values. Of course, J0952 would constrain $M_{\rm max}$ even more strongly if its mass uncertainty could be reduced; with $\sigma = 0.05\,M_\odot$, we would infer $M_{\rm max} > 2.30\,M_\odot(1\sigma)$ and $>2.20\,M_\odot(3\sigma)$.

From studies of the millisecond-pulsar population, it seems that the *initial* masses M_i of these pulsars are bimodal, with a dominant component of $M_i \leqslant 1.4\,M_\odot$ and a 20% subpopulation with $M_i \approx 1.8\,M_\odot$ (Antoniadis et al. 2016, and references therein). This complicates use of the present mass to constrain mass accretion and test evolutionary models (e.g., of magnetic field reduction). For J0952 at our 1σ lower limit we infer that at least $0.5\,M_\odot$ and more likely $\sim 1\,M_\odot$ has been accreted. Assuming a start from $1.4\,M_\odot$, three of our BWs have particularly high accreted mass (J0952, $\Delta M \approx 0.95\,M_\odot$; J1653−0158, $\Delta M \approx 0.77\,M_\odot$; J1810+1740, $\Delta M \approx 0.73\,M_\odot$). After the Shklovskii (1970) corrections, these have some of the lowest pulsar dipole fields known (estimated as 6.1×10^7 G, 3.9×10^7 G, and 7.7×10^7 G, respectively). More M and B_i measurements, as well as additional analysis, are needed to see if this is coincidental or causal.

Finally, we note that with a central value of $2.35\,M_\odot$, J0952 provides the most severe constraints on the dense-matter equation of state. This remains true even considering the lower bound, and this bound can be adopted with high confidence given the strong preference for a simple heating model. Of course, we would like an even tighter mass measurement of this especially important system. Improved photometry in blue filters at optical minimum may be feasible with 10 m–class telescopes and excellent conditions, but improved RVs likely await the 30 m telescope era.

We thank B. Efron for a discussion of bounds from a data sample and for the bootstrap analysis, and the anonymous referee whose probing questions led to some improvements in the paper. The data presented herein were obtained at the W. M. Keck Observatory, which is operated as a scientific partnership among the California Institute of Technology, the University of California, and NASA; it was made possible by the generous financial support of the W. M. Keck Foundation. We are grateful for the excellent assistance of the observatory staff, as well as the Keck Time Allocation Committee and Keck scheduler for accommodating our requests for specific half-nights. D.K. and R.W.R. were supported in part by NASA grants 80NSSC17K0024 and 80NSSC21K0896. A.V.F.'s group received generous financial assistance from the Christopher R. Redlich Fund, the TABASGO Foundation, and the U.C. Berkeley Miller Institute for Basic Research in Science (where A.V.F. was a Miller Senior Fellow).

ORCID iDs

Roger W. Romani https://orcid.org/0000-0001-6711-3286
D. Kandel https://orcid.org/0000-0002-5402-3107
Alexei V. Filippenko https://orcid.org/0000-0003-3460-0103
Thomas G. Brink https://orcid.org/0000-0001-5955-2502
WeiKang Zheng https://orcid.org/0000-0002-2636-6508

References

Antoniadis, J., Freire, P. C., Wex, N., et al. 2013, Sci, 340, 448
Antoniadis, J., Tauris, T. M., Ozel, F., et al. 2016, arXiv:1605.01665
Bassa, C. G., Pleunis, Z., Hessels, J. W. T., et al. 2017, ApJL, 846, L20
Bisnovatyi-Kogan, G. S., & Komberg, B. V. 1974, SvA, 18, 217
Breton, R. P., Rappaport, S. A., van Kerkwijk, M. H., & Carter, J. A. 2012, ApJ, 748, 115
Buchner, J. 2016, ascl.soft:1606.005
Feroz, F., Hobson, M., & Bridges, M. 2009, MNRAS, 398, 1601
Filippenko, A. V. 1982, PASP, 94, 715
Finkbeiner, D. P., Schlafly, E. F., Schlegel, D. J., et al. 2016, ApJ, 822, 66
Fonseca, E., Cromartie, H. T., Pennucci, T. T., et al. 2021, ApJL, 915, L12
Green, G. M., Schlafly, E. F., Finkbeiner, D., et al. 2018, MNRAS, 478, 651
Kandel, D., & Romani, R. W. 2020, ApJ, 892, 101
Kurtz, M. J., & Mink, D. J. 1998, PASP, 110, 934
Linares, M., Shahbaz, T., & Casares, J. 2018, ApJ, 859, 54
Manchester, R. N., Hobbs, G. B., Teoh, A., & Hobbs, M. 2005, AJ, 129, 1993
Mukherjee, D. 2017, JApA, 38, 48
Nieder, L., Clark, C. J., Bassa, C. G., et al. 2019, ApJ, 883, 42
Oke, J., Cohen, J., Carr, M., et al. 1995, PASP, 107, 375
Perley, D. A. 2019, PASP, 131, 084503
Romani, R. W. 1990, Natur, 347, 741
Romani, R. W., Kandel, D., Filippenko, A. V., Brink, T. G., & Zheng, W. 2021, ApJL, 908, L46
Shklovskii, I. S. 1970, SvA, 13, 562

The Astrophysical Journal Letters, 934:L17 (6pp), 2022 August 1 https://doi.org/10.3847/2041-8213/ac8007
© 2022. The Author(s). Published by the American Astronomical Society.
OPEN ACCESS

PSR J0952−0607: The Fastest and Heaviest Known Galactic Neutron Star

Roger W. Romani[1], D. Kandel[1], Alexei V. Filippenko[2], Thomas G. Brink[2], and WeiKang Zheng[2]
[1] Department of Physics/KIPAC, Stanford University, Stanford, CA 94305, USA; rwr@astro.stanford.edu
[2] Department of Astronomy, University of California, Berkeley, CA 94720-3411, USA
Received 2022 May 12; revised 2022 June 24; accepted 2022 July 4; published 2022 July 26

Abstract

We describe Keck-telescope spectrophotometry and imaging of the companion of the "black widow" pulsar PSR J0952−0607, the fastest known spinning neutron star (NS) in the disk of the Milky Way. The companion is very faint at minimum brightness, presenting observational challenges, but we have measured multicolor light curves and obtained radial velocities over the illuminated "day" half of the orbit. The model fits indicate system inclination $i = 59\overset{\circ}{.}8 \pm 1\overset{\circ}{.}9$ and a pulsar mass $M_{\rm NS} = 2.35 \pm 0.17\,M_\odot$, the largest well-measured mass found to date. Modeling uncertainties are small, since the heating is not extreme; the companion lies well within its Roche lobe and a simple direct-heating model provides the best fit. If the NS started at a typical pulsar birth mass, nearly $1\,M_\odot$ has been accreted; this may be connected with the especially low intrinsic dipole surface field, estimated at 6×10^7 G. Joined with reanalysis of other black widow and redback pulsars, we find that the minimum value for the maximum NS mass is $M_{\rm max} > 2.19\,M_\odot$ ($2.09\,M_\odot$) at 1σ (3σ) confidence. This is $\sim 0.15\,M_\odot$ heavier than the lower limit on $M_{\rm max}$ implied by the white dwarf–pulsar binaries measured via radio Shapiro-delay techniques.

Unified Astronomy Thesaurus concepts: Pulsars (1306)

Supporting material: data behind figure

1. Introduction

Pulsar PSR J0952−0607 (hereafter J0952) was discovered by Bassa et al. (2017) with a spin period of $P_s = 1.41$ ms, making it the fastest-spinning pulsar in the disk of the Milky Way. It is a "black widow" (BW) pulsar with a low-mass (substellar) companion being irradiated and evaporated by the pulsar luminosity. Nieder et al. (2019) subsequently detected it as a gamma-ray pulsar, and obtained additional radio timing and optical photometry that allowed initial fits for the system properties. In particular, they measure a low period derivative $\dot{P}_{\rm obs} = 4.6 \times 10^{-21}$ s s^{-1}, which places an upper limit on the surface dipole field of 8.2×10^7 G, among the 15 lowest-known pulsar magnetic fields (B), even before the Shklovskii (1970) correction. Since in addition their optical photometry suggests a large (>5 kpc) distance, and timing data gave a best-fit (albeit low-significance) proper motion of $\sim$10 mas yr^{-1}, the correction to find the intrinsic $\dot{P}$,

$$\dot{P} = \dot{P}_{\rm obs} - 2.43 \times 10^{-21} P\, \mu^2_{\rm mas/yr} d_{\rm kpc}, \quad (1)$$

may be substantial, reducing $\dot{P}$ to 2.0×10^{-21} s s^{-1} and thus B to $B_i \approx 6.1 \times 10^7$ G. Not all pulsars have a proper motion allowing an intrinsic B_i estimate, but only 10 pulsars have a lower B_i in the ATNF catalog[3] (Manchester et al. 2005).

The measurement of high neutron star (NS) masses in some white dwarf (WD)–NS millisecond-pulsar binaries, via radio-measured Shapiro delay, has been very influential in driving thinking about the dense-matter equation of state. Two systems have best-estimate masses barely exceeding $2.0\,M_\odot$: J0348+0432 at $2.01 \pm 0.04\,M_\odot$ (Antoniadis et al. 2013) and PSR J0740+6620 at $2.08 \pm 0.07\,M_\odot$ (Fonseca et al. 2021), both 1σ uncertainties. However, the maximum mass that an NS can reach must depend on its binary evolutionary history. For example, inspection of the double NS–NS binaries alone would lead one to conclude that the typical NS mass is $\sim 1.35\,M_\odot$, with a maximum of $\sim 1.45\,M_\odot$; the millisecond pulsars in these systems are only mildly recycled, with spin periods of tens of milliseconds and moderate magnetic fields. One must therefore examine a variety of pulsar binary classes in a quest to find the most massive NSs.

It has long been argued (e.g., Bisnovatyi-Kogan & Komberg 1974; Romani 1990) that binary accretion may reduce young pulsar terraGauss fields to millisecond-pulsar values. While the mechanism is unclear, ranging from simple burial to heating-driven ohmic decay (see Mukherjee 2017 for a review), it seems likely that the amount of mass accretion or its duration play a role in controlling the degree of field reduction. Thus, it is interesting to measure the masses of millisecond pulsars, and the fastest-spinning lowest-field pulsars are good candidates for substantial accretion and high NS mass. Since evolution is driven by angular momentum loss and irradiation bloating, rather than by nuclear evolution, long periods of sub-Eddington rate accretion are expected for the progenitors of "spider" (BW and "redback" (RB) millisecond-pulsar) binaries before the start of the pulsar-driven evaporation phase; these short-period binaries may host very massive NSs.

Thus, J0952 is a particularly attractive candidate for further investigation. However, Nieder et al. (2019) state, "Unfortunately, the optical counterpart of PSR J0952−0607 is too faint ($r \approx 23$ at quadrature when the radial velocity is highest) for spectroscopic radial-velocity measurements to be feasible even with 10 m class 'telescopes.'" This is nearly true, but the exceptional P_s and B inspired our intensive campaign of J0952 Keck LRIS imaging and spectroscopy. Modeling these data, we find that the NS mass is indeed the largest well-measured value to date. Combining this mass with those from new modeling of other spider binaries, we show that these objects put a strong

[3] http://www.atnf.csiro.au/research/pulsar/psrcat

Original content from this work may be used under the terms of the Creative Commons Attribution 4.0 licence. Any further distribution of this work must maintain attribution to the author(s) and the title of the work, journal citation and DOI.

Table 1
Keck LRIS Observations

Session	Spec. Exp. (s)	MJD Range	Phase Range
2018A Im	9 gi + 3 gr	58455.50562–.57691	0.92–1.20
2020A Im	18 gi	58932.36032–.47731	0.07–0.51
2018A Spec	12 × 900	58454.52711–.63543	0.53–0.94
2019A Spec	5 × 900	58577.39244–.43654	0.91–1.08
2020A Spec	13 × 600	58932.22869–.33973	0.61–1.00
2021B Spec	21 × 900	59610.45450–.62940	0.39–1.04
2022A Spec	10 × 900	59637.27289–.37235	0.66–1.03
2022A2 Spec	11 × 900	59641.26374–.37420	0.58–0.99

lower bound on the maximum NS mass, appreciably above the values inferred from radio Shapiro-delay measurements. This should have deep implications for the dense-matter equation of state.

2. Observations

With its $P_b = 6.42$ hr orbital period and faint magnitude, the effective study of J0952 requires substantial amounts of large-telescope time, ideally with superior seeing. Our campaign uses the Keck-I 10 m telescope and the Low Resolution Imaging Spectrometer (LRIS; Oke et al. 1995). We report here on two dual-color (typically g/i with a few r/i pairs) imaging runs and six spectroscopy campaigns (Table 1). For the latter we used the 5600 Å dichroic, the 600 l/4000 Å blue grism, and the 400 l/8500 Å red grating, covering ∼3300–10500 Å with dispersions of 0.63 Å pixel^{-1} (blue side) and 1.2 Å pixel^{-1} (red side). Typical exposures were 600–900 s. All spectra were processed with the `LPipe` reduction software (Perley 2019). The LRIS red-arm thick chip collects many cosmic rays, so additional editing was needed to clean the red-arm spectra. All companion and comparison star spectra are available in a TAR archive as the data behind Figure 1.

With the atmospheric dispersion corrector (ADC) being used, we could rotate the 1″-wide slit away from the parallactic angle (Filippenko 1982) to simultaneously measure a nearby brighter G1 star with known Pan-STARRS2 (PS2) magnitudes. This allows us to monitor the system throughput and wavelength solution among frames. In particular, since this PS2 star has known and stable magnitudes, we integrate the spectra over the Sloan Digital Sky Survey (SDSS) standard *ugriz* filter bands using the `sbands IRAF` script, and calibrate with the comparison star's catalog magnitudes (converted to the SDSS system using the prescription of Finkbeiner et al. 2016) to obtain light curves with absolute fluxes, up to small gray shifts from differential slit losses.

Our spectroscopic strategy was to observe J0952 for half-nights ideally covering optical maximum brightness. To cover the critical phases at low airmass under dark moon conditions required a careful selection of observing nights. Unfortunately, none of the nights had particularly good seeing; indeed, several additional half-nights requested for this program were completely lost to weather and COVID-19 shutdowns. Nevertheless, the night-to-night consistency in the flux scale and radial-velocity (RV) scale, aided by the comparison star, has let us make combined fits of all the data, allowing good model constraints.

As noted, imperfect position angle (PA) and slit placement can give small differential slit losses. These we correct via gray shifts to the `sbands` magnitudes, matching the imaging fluxes in the overlap regions and between epochs. These $\leqslant -0.2$ mag shifts increase the companion flux; this is sensible, as one tends to ensure that the (brighter) comparison star is well covered by the slit.

In the phase window $\phi_B = 0.1$–0.4 the companion is too faint to determine spectrophotometric colors. We therefore collected LRIS dual-band (g/i with a few g/r) direct images covering minimum brightness. We established a reference grid of PS2 catalog stars, with positions set relative to the pulsar companion, measured near maximum brightness, and extracted forced aperture photometry at these fixed positions. PS2 magnitudes were converted to the SDSS scale and used to determine the companion magnitude. Direct photometric errors were combined in quadrature with zero-point systematic errors determined from scatter in the catalog star residuals; near minimum the photometric errors strongly dominate the final uncertainty. The resulting light curve (Figure 1) covers a large (>5 mag) range, an observational challenge. Image artifacts seem to produce a few modest outliers, and companion flare activity may occasionally brighten the source. We discuss trimming such points below.

We measure the RV amplitude by IRAF `rvsao` (Kurtz & Mink 1998) cross-correlation with a G1 template, using the 3800–9500 Å range, excluding wavelengths near strong telluric features. The spectra were resampled to 8192 wavelengths and filtered in Fourier space with a lower cosine-bell filter cutoff from 20 to 100 and the upper cutoff running from 1000 to 1800. The average companion spectrum near $\phi_B = 0.75$ is shown in Figure 2. The pulsar and companion star were correlated using identical parameters. For the first two epochs (2018B and 2019A), a different slit PA led to the use of a cooler (∼K5) comparison star. A small velocity offset was found between these data and the G1 comparison-star correlations used for the other epochs. In practice, the red K5 star produced poorer RV solutions, and lacked sufficient flux for good g and u calibration; thus, the 2018B and 2019A data do not contribute spectrophotometric points to Figure 1. The G1 comparison-star velocity was always measured to $\sigma_v <$ 5 km s^{-1}, but pulsar companion velocity uncertainties varied greatly from as little as 10 km s^{-1} near "midday" ($\phi_B = 0.75$) to 30–50 km s^{-1} toward the "dawn" and "dusk" phases. In addition, spurious correlation peaks appeared well outside the plausible companion-velocity range for many lower signal-to-noise-ratio (S/N) spectra.

Thus, we measured in two passes, first correlating all spectra over a broad velocity range, and fitting the results with a simple sinusoid RV of amplitude K and offset Γ at the radio ephemeris orbital phasing. We then correlated again, accepting only results within ±100 km s^{-1} of the preliminary fit. This greatly decreased the number of outlier points, and allowed us to recover several weaker RV measurements near the plausible companion solution. For each spectrum the velocity was referenced to that of the comparison star, which varied between exposures, evidently driven by details of the pipeline wavelength solution and extraction aperture. We confirm that these variations are in the pulsar as well; the scatter in the final RVs increases significantly if the points are not referenced to the comparison star. Small overall RV zero-point shifts were also found in several epochs, again likely owing to differences in the apertures. Figure 3 shows all RV values with a finite correlation coefficient ($R > 0$). The point size is scaled to R; a number of obvious outliers with very small R remain.

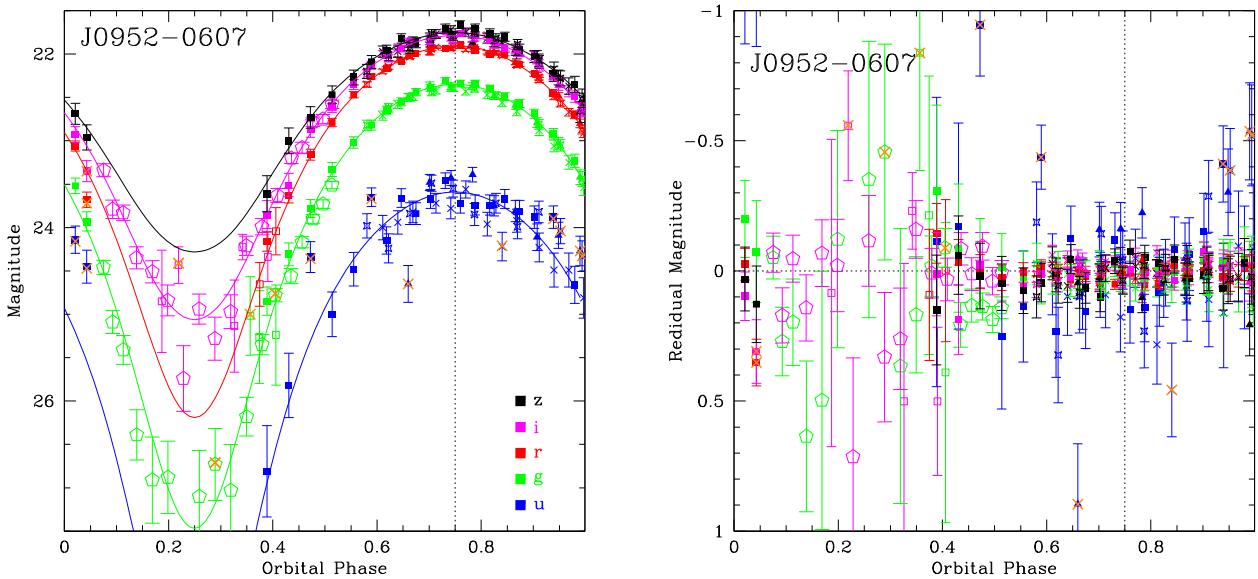

Figure 1. Left: calibrated *ugriz* light curves from Keck LRIS spectrophotometry (filled dots) and direct imaging (open dots). Outlier points excluded in the "trimmed" model fitting are indicated by orange crosses. The curves show the best-fit *ugriz* models and the dotted line marks pulsar inferior conjunction. Right: residuals to the best model fit. Optionally excluded points are again marked by orange crosses. The spectra used for Figures 1–3 are available as data behind the Figure.

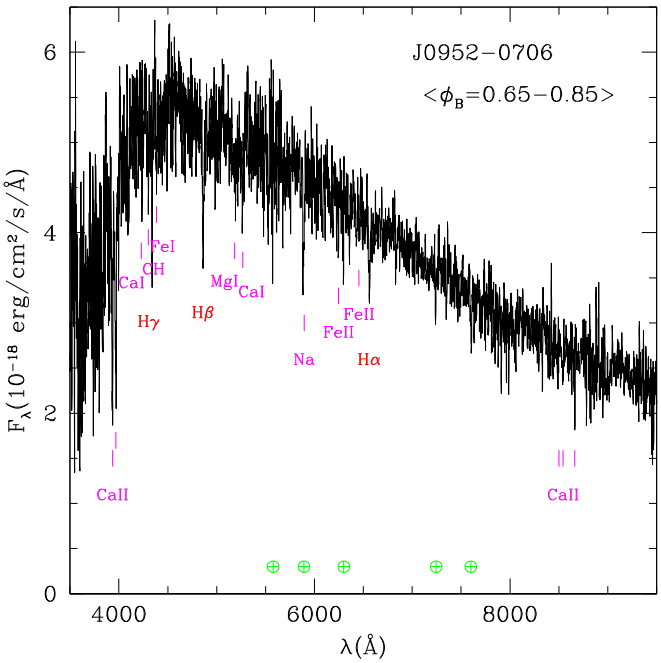

Figure 2. Spectrum of the heated face. S/N-weighted average of 27 individual spectra, Doppler corrected to zero velocity, using the best-fit RV model. Select lines are indicated.

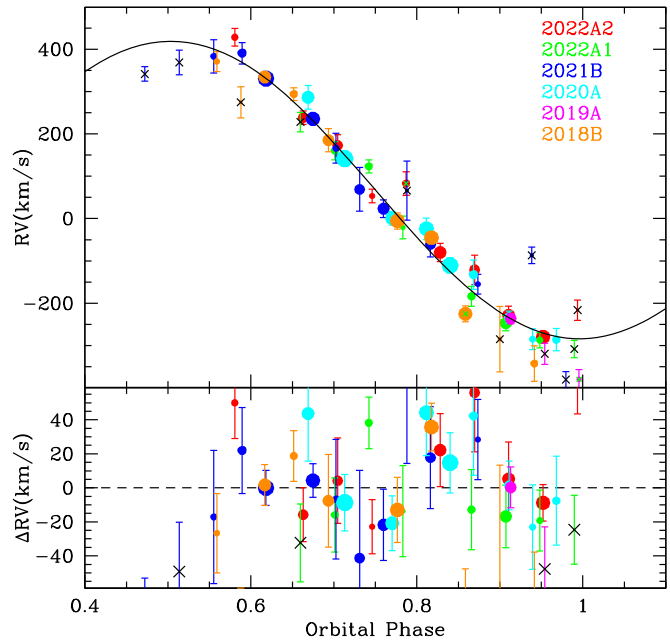

Figure 3. RV measurements for J0952. Dot size is proportional to the correlation coefficient R; low-significance correlations with $R < 2$ are marked with black crosses and are excluded from all fits. Three higher-significance points marked with green crosses appear as outliers and are optionally excluded for the "trimmed" fit. The background curve is the best-fit RV curve for the heating model fit to the light curve in Figure 1. The lower panel shows the fit residuals.

3. Photometric/Radial-velocity Fitting

Our light-curve fits are performed with an outgrowth of the `ICARUS` light-curve model (Breton et al. 2012) with the additions described by Kandel & Romani (2020) and Romani et al. (2021); the main parameters of interest are the orbital inclination i, the companion Roche-lobe filling factor f_1, the heating luminosity L_H, the companion's nightside temperature T_N, and the system distance d. In addition we can fit for the extinction A_V to the source and a set of "bandpass calibrations," for possible imperfections in the photometric zero-points.

The Markov Chain Monte Carlo (MCMC) fits and Bayesian parameter estimation are performed by Multinest sampling (Feroz et al. 2009) using its `Python` implementation `pymultinest` (Buchner 2016). In addition to the photometry, the fits use the pulsar kinematic parameters of Nieder et al. (2019). The light-curve fit is also (weakly) dependent on the companion center-of-mass RV $K_{\rm CoM}$. We do not fit for this with `ICARUS`; instead, we initially fit light curves using the

Table 2
Light-curve/RV-fit Results for J0952[a]

Parameters	Trimmed	All
i (deg)	$59.8^{+2.0}_{-1.9}$	$58.5^{+1.9}_{-1.8}$
f_1	0.79 ± 0.01	0.77 ± 0.01
$L_{\rm H}$ /10^{34} (erg s^{-1})	$3.81^{+0.46}_{-0.43}$	$6.22^{+0.88}_{-0.77}$
$T_{\rm N}$(K)	3085^{+85}_{-80}	3206^{+100}_{-95}
$d_{\rm kpc}$	$6.26^{+0.36}_{-0.40}$	$7.60^{+0.74}_{-0.82}$
χ^2/DoF	286/(298-11)[1.00]	451/(314-11)[1.49]
$K_{\rm CoM}$ (km s^{-1})	376.1 ± 5.1	379.1 ± 6.8
$M_{\rm NS}(M_\odot)$	2.35 ± 0.17	2.50 ± 0.20
$M_{\rm C}(M_\odot)$	0.032 ± 0.002	0.034 ± 0.002
χ^2/DoF	55/(40-2)[1.4]	90/(43-2)[2.2]

Note.
[a] Also fitted: A_V, Δu, Δg, Δr, Δi, and Δz. See the text.

observed spectroscopic K and then refit with $K_{\rm CoM}$ determined from the spectroscopic fit (below), iterating to convergence.

The fit χ^2 is increased by a handful of measurements several σ from the models. The synthesized u photometry has several such points owing to the very low S/N (per resolution element) of the spectra in this band. The most important outliers are a few bright g and i direct-imaging points during the "night" phase. Many spider binaries exhibit occasional short-term ($\sim$1000 s) light-curve flares. Since the quiescence light curve is needed for the light-curve fits, we optionally excise the few points well above the model curves (marked in Figure 1). Table 2 gives the fit values with these points first excluded, and then included. Note that inclusion slightly decreases the fit i and increases the mass (by $\sim 0.7\sigma$), while giving much larger χ^2. We therefore adopt the fit to the "trimmed" data set as conservative.

Extinction in the direction of J0952 is estimated from the three-dimensional dust map of Green et al. (2018), reaching its maximal $E(g-r) = 0.05^{+0.03}_{-0.02}$ mag ($A_V = 0.14^{+0.08}_{-0.05}$ mag) by 0.3 kpc. Treating A_V as a free parameter in the MCMC fits, we find 0.16 ± 0.04 mag, consistent with the dust-map value. Since we rely on the PS2 *griz* catalog magnitudes of our comparison star, there are $\sim$0.02 mag zero-point uncertainties (lacking PS2 u, we rely on the extrapolation of Finkbeiner et al. 2016). Leaving the passband calibrations free in the ICARUS fit to the trimmed data set, we find $\Delta u = +0.07^{+0.08}_{-0.10}$, $\Delta g = +0.05^{+0.05}_{-0.06}$, $\Delta r = +0.02 \pm 0.04$, $\Delta i = -0.02 \pm 0.04$, and $\Delta z = -0.02 \pm 0.04$ mag, all consistent with zero. We therefore believe that our initial calibration was quite good. For the untrimmed data, the outliers produce a large χ^2/degrees of freedom (DoF) and drive these color terms to larger values, notably $\Delta ugriz = +0.27$, $+0.23$, $+0.03$, -0.12, and -0.15 mag. While including these passband shifts does not strongly change either χ^2 or the fit parameters, it does slightly increase the MCMC uncertainty ranges of other parameters (most notably d and L_H); we thus retain these in the fit, although we omit them from Figure 4.

The fits all find $i \leqslant 60°$, with $f_1 = 0.79$ (companion underfilling its Roche lobe), $T_N \approx 3000$ K, dayside heated to $\sim$6200 K, and $d \approx 6$ kpc, larger than the dispersion-measure estimates. These values are very similar to those of Nieder et al. (2019), but with substantially higher precision. Interestingly, simple direct-heating models always provide the best statistical fit; adding additional effects required for many other spider binaries, such as companion

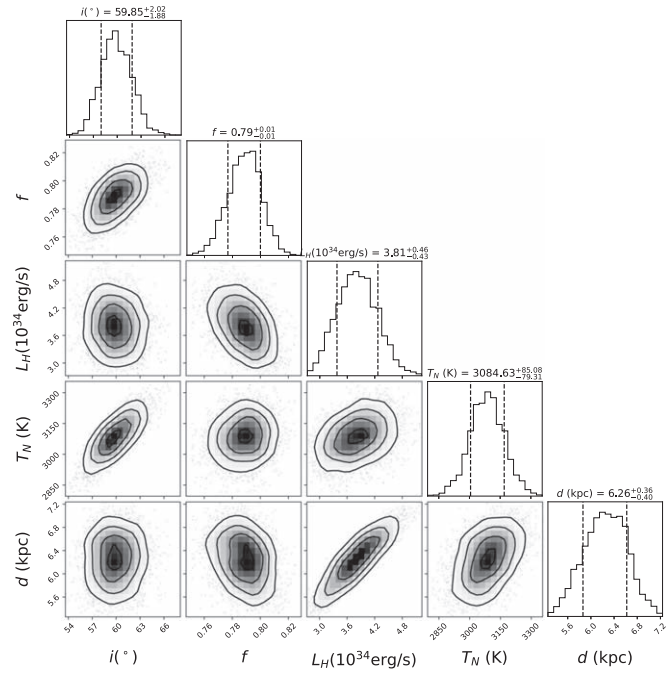

Figure 4. Corner plot from the MCMC light-curve fit to the "trimmed" photometry points. Contours are at 0.5σ, 1.0σ, 1.5σ, and 2σ.

hot spots and surface winds, does not significantly improve the fit. This means that our results are particularly immune to model-dependant systematics, and the fit-parameter errors (Table 2) are dominated by measurement uncertainties.

We next compare the Keck spectroscopy with model RVs computed from photometric-fit companion models. As emphasized by Linares et al. (2018) and discussed by KR20, different species' temperature sensitivities cause varying line equivalent widths (EWs) across the face of the companion. As the model parameters change, the surface heating changes and the line EWs vary. For J0952, metal lines dominate the cross-correlation signal (as appropriate for our G1 correlation spectrum); we apply metal line equivalent width EW(T) weighting to correct center-of-mass RVs to observed center-of-light values (see KR20). If we (inappropriately) apply Balmer EW(T) weighting, the RV amplitude increases to 384 ± 5 km s^{-1}, so again our choice is conservative.

We always exclude the low-significance correlations with $R < 2$ in the RV MCMC fits (marked with black crosses in Figure 3; note that some crossed points follow the expected curve, but many are quite discrepant). The remaining χ^2 is in fact dominated by three outlier points with small uncertainties (marked with green crosses in Figure 3). In our "trimmed" fit for the mass we exclude these three points. Again, this is conservative, as with them the K increases slightly (by 0.4σ). The lower section of Table 2 gives the RV fit parameters and their uncertainties. The mass difference in the "All" column is dominated by the smaller i of the "All" photometric fit.

4. Mass Implications and Conclusions

In the quest for precision mass measurements from spider binaries, J0952 has the advantage that the complex modeling effects required to fit other spiders (hot spots, wind flows, extreme gravity darkening) are not needed. This is a natural consequence of its relatively large P_b, weak pulsar heating, and low Roche-lobe filling factor. On the other hand, the large

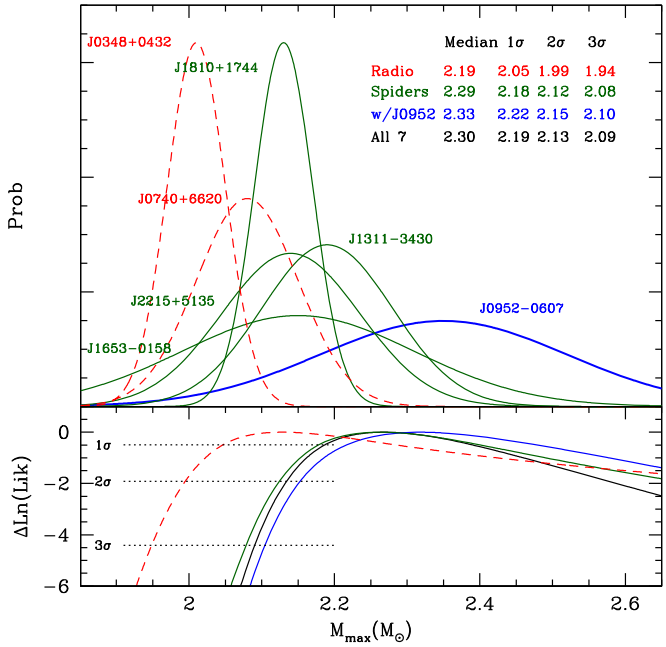

Figure 5. Mass estimates for heavy NSs. The dashed curves show the two heaviest WD–pulsar binaries with masses measured from radio pulse timing (supplemented by WD atmosphere modeling for J0348). The solid curves show the best mass estimates from companion spectroscopy and light-curve fitting for four BWs (J1810, J1653, J1311, and J0952) and one RB (J2215). The bottom panel shows the normalized Ln(Likelihood) for various combinations of these measurements, assuming a flat distribution of masses from 1.8 $M_\odot$ up to some $M_{\rm max}$. The inset legend gives the median estimator for $M_{\rm max}$ as well as the 1σ, 2σ, and 3σ lower bounds on its value, for various data subsets.

distance, weak heating, and low f_1 mean that the companion is quite faint, barely bright enough for measurement with present 10 m telescope systems. Our intensive Keck campaign has managed to measure the binary properties, constraining the masses with sufficient precision that the lower limit on $M_{\rm NS}$ contributes to equation-of-state constraints.

We can examine the minimum required $M_{\rm max}$ by plotting the Gaussian probability distribution functions with M_i, σ_i for observed heavy NSs in Figure 5. Here we compare the latest measurements of the $>2\,M_\odot$ "radio selected" WD–NS MSP J0348+0432 and J0740+6620 with the measurements extracted from light-curve and RV measurements of spider pulsar (BW and RB) companions. For the latter we use the most conservative (best-fit) models with all heating effects as summarized by D. Kandel & R. W. Romani (2022, in preparation). To estimate the minimum value of $M_{\rm max}$ required by these observations, we assume that the NS mass distribution is flat M^0 above $M_1 = 1.8\,M_\odot$ to some cutoff value (for this $>2\,M_\odot$ sample, results are insensitive to the underlying distribution; values change by $< 0.01\,M_\odot$ for M^{-1}). The log (likelihood) for n measurements is

$$\ln \mathcal{L} = -n \ln(M_{\rm max} - M_1) + \Sigma_{i=1}^{n} \ln\left[\mathrm{erf}\left(\frac{M_i - M_1}{2^{1/2}\sigma_i}\right) - \mathrm{erf}\left(\frac{M_i - M_{\rm max}}{2^{1/2}\sigma_i}\right)\right].$$

These curves are plotted in the lower panel of Figure 5. We list the medians and lower bounds at various confidence levels on $M_{\rm max}$, from the likelihood ratio, for the different sample sets.

Since the spiders are appreciably heavier than the WD–NS binaries, the 1σ $M_{\rm max}$ bound increases by $\sim 0.13\,M_\odot$, or $\sim 0.17\,M_\odot$ with J0952. We have checked these bounds with several different estimators. For example a bias-corrected, accelerated bootstrap analysis (kindly supplied by B. Efron) of the seven masses gives $M_{\rm max} = 2.34\,M_\odot$ with a 2σ lower bound of $2.17\,M_\odot$. Numerical simulations with random draws and our observed errors give similar values. Of course, J0952 would constrain $M_{\rm max}$ even more strongly if its mass uncertainty could be reduced; with $\sigma = 0.05\,M_\odot$, we would infer $M_{\rm max} > 2.30\,M_\odot(1\sigma)$ and $>2.20\,M_\odot(3\sigma)$.

From studies of the millisecond-pulsar population, it seems that the *initial* masses M_i of these pulsars are bimodal, with a dominant component of $M_i \leqslant 1.4\,M_\odot$ and a 20% subpopulation with $M_i \approx 1.8\,M_\odot$ (Antoniadis et al. 2016, and references therein). This complicates use of the present mass to constrain mass accretion and test evolutionary models (e.g., of magnetic field reduction). For J0952 at our 1σ lower limit we infer that at least $0.5\,M_\odot$ and more likely $\sim 1\,M_\odot$ has been accreted. Assuming a start from $1.4\,M_\odot$, three of our BWs have particularly high accreted mass (J0952, $\Delta M \approx 0.95\,M_\odot$; J1653−0158, $\Delta M \approx 0.77\,M_\odot$; J1810+1740, $\Delta M \approx 0.73\,M_\odot$). After the Shklovskii (1970) corrections, these have some of the lowest pulsar dipole fields known (estimated as 6.1×10^7 G, 3.9×10^7 G, and 7.7×10^7 G, respectively). More M and B_i measurements, as well as additional analysis, are needed to see if this is coincidental or causal.

Finally, we note that with a central value of $2.35\,M_\odot$, J0952 provides the most severe constraints on the dense-matter equation of state. This remains true even considering the lower bound, and this bound can be adopted with high confidence given the strong preference for a simple heating model. Of course, we would like an even tighter mass measurement of this especially important system. Improved photometry in blue filters at optical minimum may be feasible with 10 m–class telescopes and excellent conditions, but improved RVs likely await the 30 m telescope era.

We thank B. Efron for a discussion of bounds from a data sample and for the bootstrap analysis, and the anonymous referee whose probing questions led to some improvements in the paper. The data presented herein were obtained at the W. M. Keck Observatory, which is operated as a scientific partnership among the California Institute of Technology, the University of California, and NASA; it was made possible by the generous financial support of the W. M. Keck Foundation. We are grateful for the excellent assistance of the observatory staff, as well as the Keck Time Allocation Committee and Keck scheduler for accommodating our requests for specific half-nights. D.K. and R.W.R. were supported in part by NASA grants 80NSSC17K0024 and 80NSSC21K0896. A.V.F.'s group received generous financial assistance from the Christopher R. Redlich Fund, the TABASGO Foundation, and the U.C. Berkeley Miller Institute for Basic Research in Science (where A.V.F. was a Miller Senior Fellow).

ORCID iDs

Roger W. Romani https://orcid.org/0000-0001-6711-3286
D. Kandel https://orcid.org/0000-0002-5402-3107
Alexei V. Filippenko https://orcid.org/0000-0003-3460-0103
Thomas G. Brink https://orcid.org/0000-0001-5955-2502
WeiKang Zheng https://orcid.org/0000-0002-2636-6508

References

Antoniadis, J., Freire, P. C., Wex, N., et al. 2013, Sci, 340, 448
Antoniadis, J., Tauris, T. M., Ozel, F., et al. 2016, arXiv:1605.01665
Bassa, C. G., Pleunis, Z., Hessels, J. W. T., et al. 2017, ApJL, 846, L20
Bisnovatyi-Kogan, G. S., & Komberg, B. V. 1974, SvA, 18, 217
Breton, R. P., Rappaport, S. A., van Kerkwijk, M. H., & Carter, J. A. 2012, ApJ, 748, 115
Buchner, J. 2016, ascl.soft:1606.005
Feroz, F., Hobson, M., & Bridges, M. 2009, MNRAS, 398, 1601
Filippenko, A. V. 1982, PASP, 94, 715
Finkbeiner, D. P., Schlafly, E. F., Schlegel, D. J., et al. 2016, ApJ, 822, 66
Fonseca, E., Cromartie, H. T., Pennucci, T. T., et al. 2021, ApJL, 915, L12
Green, G. M., Schlafly, E. F., Finkbeiner, D., et al. 2018, MNRAS, 478, 651
Kandel, D., & Romani, R. W. 2020, ApJ, 892, 101
Kurtz, M. J., & Mink, D. J. 1998, PASP, 110, 934
Linares, M., Shahbaz, T., & Casares, J. 2018, ApJ, 859, 54
Manchester, R. N., Hobbs, G. B., Teoh, A., & Hobbs, M. 2005, AJ, 129, 1993
Mukherjee, D. 2017, JApA, 38, 48
Nieder, L., Clark, C. J., Bassa, C. G., et al. 2019, ApJ, 883, 42
Oke, J., Cohen, J., Carr, M., et al. 1995, PASP, 107, 375
Perley, D. A. 2019, PASP, 131, 084503
Romani, R. W. 1990, Natur, 347, 741
Romani, R. W., Kandel, D., Filippenko, A. V., Brink, T. G., & Zheng, W. 2021, ApJL, 908, L46
Shklovskii, I. S. 1970, SvA, 13, 562

GW170817: Observation of Gravitational Waves from a Binary Neutron Star Inspiral

B. P. Abbott *et al.*[*]
(LIGO Scientific Collaboration and Virgo Collaboration)

(Received 26 September 2017; revised manuscript received 2 October 2017; published 16 October 2017)

On August 17, 2017 at 12:41:04 UTC the Advanced LIGO and Advanced Virgo gravitational-wave detectors made their first observation of a binary neutron star inspiral. The signal, GW170817, was detected with a combined signal-to-noise ratio of 32.4 and a false-alarm-rate estimate of less than one per 8.0×10^4 years. We infer the component masses of the binary to be between 0.86 and 2.26 $M_\odot$, in agreement with masses of known neutron stars. Restricting the component spins to the range inferred in binary neutron stars, we find the component masses to be in the range 1.17–1.60 $M_\odot$, with the total mass of the system $2.74^{+0.04}_{-0.01} M_\odot$. The source was localized within a sky region of 28 deg^2 (90% probability) and had a luminosity distance of 40^{+8}_{-14} Mpc, the closest and most precisely localized gravitational-wave signal yet. The association with the γ-ray burst GRB 170817A, detected by Fermi-GBM 1.7 s after the coalescence, corroborates the hypothesis of a neutron star merger and provides the first direct evidence of a link between these mergers and short γ-ray bursts. Subsequent identification of transient counterparts across the electromagnetic spectrum in the same location further supports the interpretation of this event as a neutron star merger. This unprecedented joint gravitational and electromagnetic observation provides insight into astrophysics, dense matter, gravitation, and cosmology.

DOI: 10.1103/PhysRevLett.119.161101

I. INTRODUCTION

On August 17, 2017, the LIGO-Virgo detector network observed a gravitational-wave signal from the inspiral of two low-mass compact objects consistent with a binary neutron star (BNS) merger. This discovery comes four decades after Hulse and Taylor discovered the first neutron star binary, PSR B1913+16 [1]. Observations of PSR B1913+16 found that its orbit was losing energy due to the emission of gravitational waves, providing the first indirect evidence of their existence [2]. As the orbit of a BNS system shrinks, the gravitational-wave luminosity increases, accelerating the inspiral. This process has long been predicted to produce a gravitational-wave signal observable by ground-based detectors [3–6] in the final minutes before the stars collide [7].

Since the Hulse-Taylor discovery, radio pulsar surveys have found several more BNS systems in our galaxy [8]. Understanding the orbital dynamics of these systems inspired detailed theoretical predictions for gravitational-wave signals from compact binaries [9–13]. Models of the population of compact binaries, informed by the known binary pulsars, predicted that the network of advanced gravitational-wave detectors operating at design sensitivity will observe between one BNS merger every few years to hundreds per year [14–21]. This detector network currently includes three Fabry-Perot-Michelson interferometers that measure spacetime strain induced by passing gravitational waves as a varying phase difference between laser light propagating in perpendicular arms: the two Advanced LIGO detectors (Hanford, WA and Livingston, LA) [22] and the Advanced Virgo detector (Cascina, Italy) [23].

Advanced LIGO's first observing run (O1), from September 12, 2015, to January 19, 2016, obtained 49 days of simultaneous observation time in two detectors. While two confirmed binary black hole (BBH) mergers were discovered [24–26], no detections or significant candidates had component masses lower than $5M_\odot$, placing a 90% credible upper limit of 12 600 Gpc^{-3} yr^{-1} on the rate of BNS mergers [27] (credible intervals throughout this Letter contain 90% of the posterior probability unless noted otherwise). This measurement did not impinge on the range of astrophysical predictions, which allow rates as high as ~10 000 Gpc^{-3} yr^{-1} [19].

The second observing run (O2) of Advanced LIGO, from November 30, 2016 to August 25, 2017, collected 117 days of simultaneous LIGO-detector observing time. Advanced Virgo joined the O2 run on August 1, 2017. At the time of this publication, two BBH detections have been announced [28,29] from the O2 run, and analysis is still in progress.

Toward the end of the O2 run a BNS signal, GW170817, was identified by matched filtering [7,30–33] the data against post-Newtonian waveform models [34–37]. This gravitational-wave signal is the loudest yet observed, with a combined signal-to-noise ratio (SNR) of 32.4 [38]. After

[*]Full author list given at the end of the Letter.

Published by the American Physical Society under the terms of the Creative Commons Attribution 4.0 International license. Further distribution of this work must maintain attribution to the author(s) and the published article's title, journal citation, and DOI.

~100 s (calculated starting from 24 Hz) in the detectors' sensitive band, the inspiral signal ended at 12:41:04.4 UTC. In addition, a γ-ray burst was observed 1.7 s after the coalescence time [39–45]. The combination of data from the LIGO and Virgo detectors allowed a precise sky position localization to an area of 28 deg^2. This measurement enabled an electromagnetic follow-up campaign that identified a counterpart near the galaxy NGC 4993, consistent with the localization and distance inferred from gravitational-wave data [46–50].

From the gravitational-wave signal, the best measured combination of the masses is the chirp mass [51] $\mathcal{M} = 1.188^{+0.004}_{-0.002} M_\odot$. From the union of 90% credible intervals obtained using different waveform models (see Sec. IV for details), the total mass of the system is between 2.73 and 3.29 $M_\odot$. The individual masses are in the broad range of 0.86 to 2.26 $M_\odot$, due to correlations between their uncertainties. This suggests a BNS as the source of the gravitational-wave signal, as the total masses of known BNS systems are between 2.57 and 2.88 $M_\odot$ with components between 1.17 and ~1.6 $M_\odot$ [52]. Neutron stars in general have precisely measured masses as large as 2.01 ± 0.04 $M_\odot$ [53], whereas stellar-mass black holes found in binaries in our galaxy have masses substantially greater than the components of GW170817 [54–56].

Gravitational-wave observations alone are able to measure the masses of the two objects and set a lower limit on their compactness, but the results presented here do not exclude objects more compact than neutron stars such as quark stars, black holes, or more exotic objects [57–61]. The detection of GRB 170817A and subsequent electromagnetic emission demonstrates the presence of matter. Moreover, although a neutron star–black hole system is not ruled out, the consistency of the mass estimates with the dynamically measured masses of known neutron stars in binaries, and their inconsistency with the masses of known black holes in galactic binary systems, suggests the source was composed of two neutron stars.

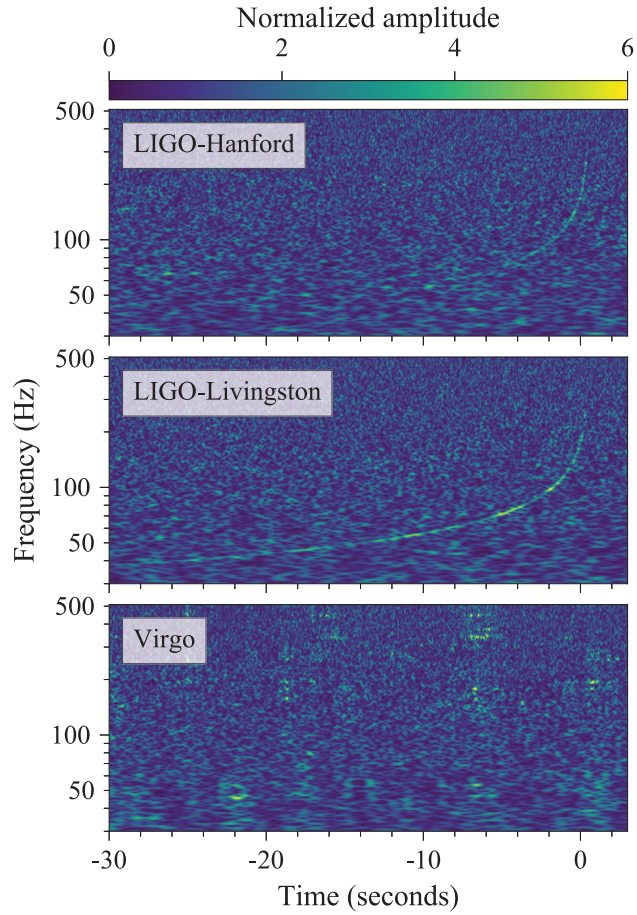

FIG. 1. Time-frequency representations [65] of data containing the gravitational-wave event GW170817, observed by the LIGO-Hanford (top), LIGO-Livingston (middle), and Virgo (bottom) detectors. Times are shown relative to August 17, 2017 12:41:04 UTC. The amplitude scale in each detector is normalized to that detector's noise amplitude spectral density. In the LIGO data, independently observable noise sources and a glitch that occurred in the LIGO-Livingston detector have been subtracted, as described in the text. This noise mitigation is the same as that used for the results presented in Sec. IV.

II. DATA

At the time of GW170817, the Advanced LIGO detectors and the Advanced Virgo detector were in observing mode. The maximum distances at which the LIGO-Livingston and LIGO-Hanford detectors could detect a BNS system (SNR = 8), known as the detector horizon [32,62,63], were 218 Mpc and 107 Mpc, while for Virgo the horizon was 58 Mpc. The GEO600 detector [64] was also operating at the time, but its sensitivity was insufficient to contribute to the analysis of the inspiral. The configuration of the detectors at the time of GW170817 is summarized in [29].

A time-frequency representation [65] of the data from all three detectors around the time of the signal is shown in Fig 1. The signal is clearly visible in the LIGO-Hanford and LIGO-Livingston data. The signal is not visible in the Virgo data due to the lower BNS horizon and the direction of the source with respect to the detector's antenna pattern.

Figure 1 illustrates the data as they were analyzed to determine astrophysical source properties. After data collection, several independently measured terrestrial contributions to the detector noise were subtracted from the LIGO data using Wiener filtering [66], as described in [67–70]. This subtraction removed calibration lines and 60 Hz ac power mains harmonics from both LIGO data streams. The sensitivity of the LIGO-Hanford detector was particularly improved by the subtraction of laser pointing noise; several broad peaks in the 150–800 Hz region were effectively removed, increasing the BNS horizon of that detector by 26%.

Additionally, a short instrumental noise transient appeared in the LIGO-Livingston detector 1.1 s before the coalescence time of GW170817 as shown in Fig. 2. This transient noise, or glitch [71], produced a very brief (less than 5 ms) saturation in the digital-to-analog converter of the feedback signal controlling the position of the test masses. Similar glitches are registered roughly once every few hours in each of the LIGO detectors with no temporal correlation between the LIGO sites. Their cause remains unknown. To mitigate the effect on the results presented in Sec. III, the search analyses applied a window function to zero out the data around the glitch [72,73], following the treatment of other high-amplitude glitches used in the O1 analysis [74]. To accurately determine the properties of GW170817 (as reported in Sec. IV) in addition to the noise subtraction described above, the glitch was modeled with a time-frequency wavelet reconstruction [75] and subtracted from the data, as shown in Fig. 2.

Following the procedures developed for prior gravitational-wave detections [29,78], we conclude there is no environmental disturbance observed by LIGO environmental sensors [79] that could account for the GW170817 signal.

The Virgo data, used for sky localization and an estimation of the source properties, are shown in the bottom panel of Fig. 1. The Virgo data are nonstationary above 150 Hz due to scattered light from the output optics modulated by alignment fluctuations and below 30 Hz due to seismic noise from anthropogenic activity. Occasional noise excess around the European power mains frequency of 50 Hz is also present. No noise subtraction was applied to the Virgo data prior to this analysis. The low signal amplitude observed in Virgo significantly constrained the sky position, but meant that the Virgo data did not contribute significantly to other parameters. As a result, the estimation of the source's parameters reported in Sec. IV is not impacted by the nonstationarity of Virgo data at the time of the event. Moreover, no unusual disturbance was observed by Virgo environmental sensors.

Data used in this study can be found in [80].

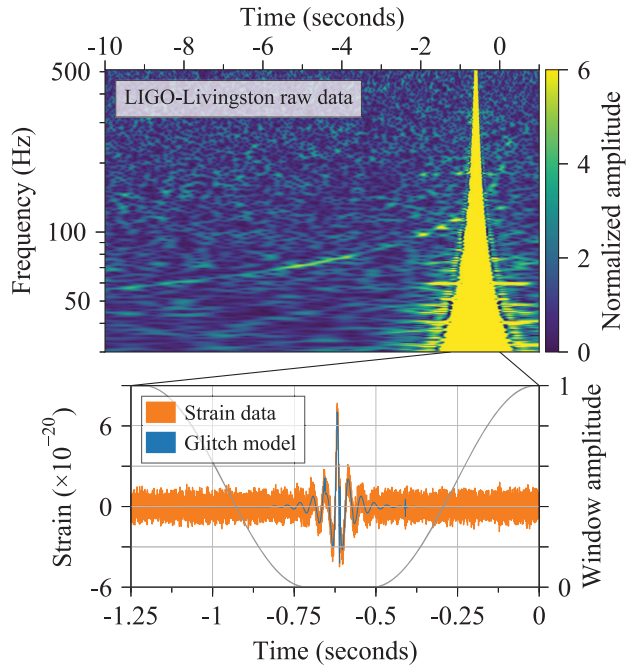

FIG. 2. Mitigation of the glitch in LIGO-Livingston data. Times are shown relative to August 17, 2017 12:41:04 UTC. *Top panel*: A time-frequency representation [65] of the raw LIGO-Livingston data used in the initial identification of GW170817 [76]. The coalescence time reported by the search is at time 0.4 s in this figure and the glitch occurs 1.1 s before this time. The time-frequency track of GW170817 is clearly visible despite the presence of the glitch. *Bottom panel*: The raw LIGO-Livingston strain data (orange curve) showing the glitch in the time domain. To mitigate the glitch in the rapid reanalysis that produced the sky map shown in Fig. 3 [77], the raw detector data were multiplied by an inverse Tukey window (gray curve, right axis) that zeroed out the data around the glitch [73]. To mitigate the glitch in the measurement of the source's properties, a model of the glitch based on a wavelet reconstruction [75] (blue curve) was subtracted from the data. The time-series data visualized in this figure have been bandpassed between 30 Hz and 2 kHz so that the detector's sensitive band is emphasized. The gravitational-wave strain amplitude of GW170817 is of the order of 10^{-22} and so is not visible in the bottom panel.

III. DETECTION

GW170817 was initially identified as a single-detector event with the LIGO-Hanford detector by a low-latency binary-coalescence search [81–83] using template waveforms computed in post-Newtonian theory [11,13,36,84]. The two LIGO detectors and the Virgo detector were all taking data at the time; however, the saturation at the LIGO-Livingston detector prevented the search from registering a simultaneous event in both LIGO detectors, and the low-latency transfer of Virgo data was delayed.

Visual inspection of the LIGO-Hanford and LIGO-Livingston detector data showed the presence of a clear, long-duration chirp signal in time-frequency representations of the detector strain data. As a result, an initial alert was generated reporting a highly significant detection of a binary neutron star signal [85] in coincidence with the independently observed γ-ray burst GRB 170817A [39–41].

A rapid binary-coalescence reanalysis [86,87], with the time series around the glitch suppressed with a window function [73], as shown in Fig. 2, confirmed the presence of a significant coincident signal in the LIGO detectors. The source was rapidly localized to a region of 31 deg^2, shown in Fig. 3, using data from all three detectors [88]. This sky map was issued to observing partners, allowing the identification of an electromagnetic counterpart [46,48,50,77].

The combined SNR of GW170817 is estimated to be 32.4, with values 18.8, 26.4, and 2.0 in the LIGO-Hanford,

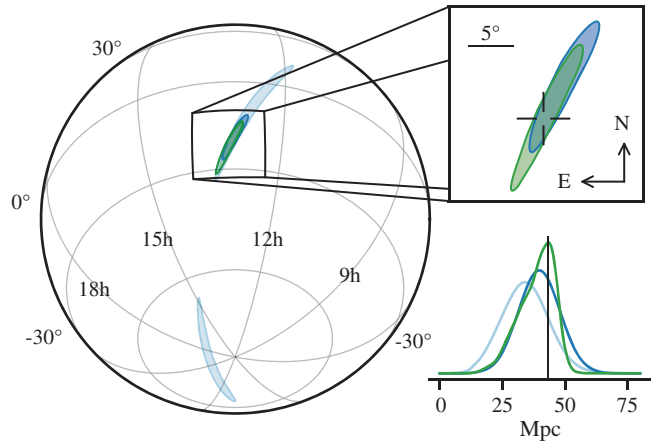

FIG. 3. Sky location reconstructed for GW170817 by a rapid localization algorithm from a Hanford-Livingston (190 deg^2, light blue contours) and Hanford-Livingston-Virgo (31 deg^2, dark blue contours) analysis. A higher latency Hanford-Livingston-Virgo analysis improved the localization (28 deg^2, green contours). In the top-right inset panel, the reticle marks the position of the apparent host galaxy NGC 4993. The bottom-right panel shows the *a posteriori* luminosity distance distribution from the three gravitational-wave localization analyses. The distance of NGC 4993, assuming the redshift from the NASA/IPAC Extragalactic Database [89] and standard cosmological parameters [90], is shown with a vertical line.

LIGO-Livingston, and Virgo data respectively, making it the loudest gravitational-wave signal so far detected. Two matched-filter binary-coalescence searches targeting sources with total mass between 2 and 500 $M_\odot$ in the detector frame were used to estimate the significance of this event [9,12,30,32,73,81–83,86,87,91–97]. The searches analyzed 5.9 days of LIGO data between August 13, 2017 02:00 UTC and August 21, 2017 01:05 UTC. Events are assigned a detection-statistic value that ranks their probability of being a gravitational-wave signal. Each search uses a different method to compute this statistic and measure the search background—the rate at which detector noise produces events with a detection-statistic value equal to or higher than the candidate event.

GW170817 was identified as the most significant event in the 5.9 days of data, with an estimated false alarm rate of one in 1.1×10^6 years with one search [81,83], and a consistent bound of less than one in 8.0×10^4 years for the other [73,86,87]. The second most significant signal in this analysis of 5.9 days of data is GW170814, which has a combined SNR of 18.3 [29]. Virgo data were not used in these significance estimates, but were used in the sky localization of the source and inference of the source properties.

IV. SOURCE PROPERTIES

General relativity makes detailed predictions for the inspiral and coalescence of two compact objects, which may be neutron stars or black holes. At early times, for low orbital and gravitational-wave frequencies, the chirplike time evolution of the frequency is determined primarily by a specific combination of the component masses m_1 and m_2, the chirp mass $\mathcal{M} = (m_1 m_2)^{3/5}(m_1 + m_2)^{-1/5}$. As the orbit shrinks and the gravitational-wave frequency grows rapidly, the gravitational-wave phase is increasingly influenced by relativistic effects related to the mass ratio $q = m_2/m_1$, where $m_1 \geq m_2$, as well as spin-orbit and spin-spin couplings [98].

The details of the objects' internal structure become important as the orbital separation approaches the size of the bodies. For neutron stars, the tidal field of the companion induces a mass-quadrupole moment [99,100] and accelerates the coalescence [101]. The ratio of the induced quadrupole moment to the external tidal field is proportional to the tidal deformability (or polarizability) $\Lambda = (2/3)k_2[(c^2/G)(R/m)]^5$, where k_2 is the second Love number and R is the stellar radius. Both R and k_2 are fixed for a given stellar mass m by the equation of state (EOS) for neutron-star matter, with $k_2 \simeq 0.05$–0.15 for realistic neutron stars [102–104]. Black holes are expected to have $k_2 = 0$ [99,105–109], so this effect would be absent.

As the gravitational-wave frequency increases, tidal effects in binary neutron stars increasingly affect the phase and become significant above $f_{\mathrm{GW}} \simeq 600$ Hz, so they are potentially observable [103,110–116]. Tidal deformabilities correlate with masses and spins, and our measurements are sensitive to the accuracy with which we describe the point-mass, spin, and tidal dynamics [113,117–119]. The point-mass dynamics has been calculated within the post-Newtonian framework [34,36,37], effective-one-body formalism [10,120–125], and with a phenomenological approach [126–131]. Results presented here are obtained using a frequency domain post-Newtonian waveform model [30] that includes dynamical effects from tidal interactions [132], point-mass spin-spin interactions [34,37,133,134], and couplings between the orbital angular momentum and the orbit-aligned dimensionless spin components of the stars χ_z [92].

The properties of gravitational-wave sources are inferred by matching the data with predicted waveforms. We perform a Bayesian analysis in the frequency range 30–2048 Hz that includes the effects of the 1σ calibration uncertainties on the received signal [135,136] ($< 7\%$ in amplitude and 3° in phase for the LIGO detectors [137] and 10% and 10° for Virgo at the time of the event). Unless otherwise specified, bounds on the properties of GW170817 presented in the text and in Table I are 90% posterior probability intervals that enclose systematic differences from currently available waveform models.

To ensure that the applied glitch mitigation procedure previously discussed in Sec. II (see Fig. 2) did not bias the estimated parameters, we added simulated signals with known parameters to data that contained glitches analogous

TABLE I. Source properties for GW170817: we give ranges encompassing the 90% credible intervals for different assumptions of the waveform model to bound systematic uncertainty. The mass values are quoted in the frame of the source, accounting for uncertainty in the source redshift.

	Low-spin priors ($\lvert\chi\rvert \leq 0.05$)	High-spin priors ($\lvert\chi\rvert \leq 0.89$)
Primary mass m_1	1.36–1.60 $M_\odot$	1.36–2.26 $M_\odot$
Secondary mass m_2	1.17–1.36 $M_\odot$	0.86–1.36 $M_\odot$
Chirp mass $\mathcal{M}$	$1.188^{+0.004}_{-0.002} M_\odot$	$1.188^{+0.004}_{-0.002} M_\odot$
Mass ratio m_2/m_1	0.7–1.0	0.4–1.0
Total mass $m_{\rm tot}$	$2.74^{+0.04}_{-0.01} M_\odot$	$2.82^{+0.47}_{-0.09} M_\odot$
Radiated energy $E_{\rm rad}$	$> 0.025 M_\odot c^2$	$> 0.025 M_\odot c^2$
Luminosity distance $D_{\rm L}$	40^{+8}_{-14} Mpc	40^{+8}_{-14} Mpc
Viewing angle Θ	$\leq 55°$	$\leq 56°$
Using NGC 4993 location	$\leq 28°$	$\leq 28°$
Combined dimensionless tidal deformability $\tilde{\Lambda}$	≤ 800	≤ 700
Dimensionless tidal deformability $\Lambda(1.4 M_\odot)$	≤ 800	≤ 1400

to the one observed at the LIGO-Livingston detector during GW170817. After applying the glitch subtraction technique, we found that the bias in recovered parameters relative to their known values was well within their uncertainties. This can be understood by noting that a small time cut out of the coherent integration of the phase evolution has little impact on the recovered parameters. To corroborate these results, the test was also repeated with a window function applied, as shown in Fig. 2 [73].

The source was localized to a region of the sky 28 deg^2 in area, and 380 Mpc^3 in volume, near the southern end of the constellation Hydra, by using a combination of the timing, phase, and amplitude of the source as observed in the three detectors [138,139]. The third detector, Virgo, was essential in localizing the source to a single region of the sky, as shown in Fig. 3. The small sky area triggered a successful follow-up campaign that identified an electromagnetic counterpart [50].

The luminosity distance to the source is 40^{+8}_{-14} Mpc, the closest ever observed gravitational-wave source and, by association, the closest short γ-ray burst with a distance measurement [45]. The distance measurement is correlated with the inclination angle $\cos\theta_{JN} = \hat{\mathbf{J}} \cdot \hat{\mathbf{N}}$, where $\hat{\mathbf{J}}$ is the unit vector in the direction of the total angular momentum of the system and $\hat{\mathbf{N}}$ is that from the source towards the observer [140]. We find that the data are consistent with an antialigned source: $\cos\theta_{JN} \leq -0.54$, and the viewing angle $\Theta \equiv \min(\theta_{JN}, 180° - \theta_{JN})$ is $\Theta \leq 56°$. Since the luminosity distance of this source can be determined independently of the gravitational wave data alone, we can use the association with NGC 4993 to break the distance degeneracy with $\cos\theta_{JN}$. The estimated Hubble flow velocity near NGC 4993 of 3017 ± 166 km s^{-1} [141] provides a redshift, which in a flat cosmology with $H_0 = 67.90 \pm 0.55$ km s^{-1} Mpc^{-1} [90], constrains $\cos\theta_{JN} < -0.88$ and $\Theta < 28°$. The constraint varies with the assumptions made about H_0 [141].

From the gravitational-wave phase and the ~3000 cycles in the frequency range considered, we constrain the chirp mass in the detector frame to be $\mathcal{M}^{\rm det} = 1.1977^{+0.0008}_{-0.0003} M_\odot$ [51]. The mass parameters in the detector frame are related to the rest-frame masses of the source by its redshift z as $m^{\rm det} = m(1+z)$ [142]. Assuming the above cosmology [90], and correcting for the motion of the Solar System Barycenter with respect to the Cosmic Microwave Background [143], the gravitational-wave distance measurement alone implies a cosmological redshift of $0.008^{+0.002}_{-0.003}$, which is consistent with that of NGC 4993 [50,141,144,145]. Without the host galaxy, the uncertainty in the source's chirp mass $\mathcal{M}$ is dominated by the uncertainty in its luminosity distance. Independent of the waveform model or the choice of priors, described below, the source-frame chirp mass is $\mathcal{M} = 1.188^{+0.004}_{-0.002} M_\odot$.

While the chirp mass is well constrained, our estimates of the component masses are affected by the degeneracy between mass ratio q and the aligned spin components χ_{1z} and χ_{2z} [38,146–150]. Therefore, the estimates of q and the component masses depend on assumptions made about the admissible values of the spins. While $\chi < 1$ for black holes, and quark stars allow even larger spin values, realistic NS equations of state typically imply more stringent limits. For the set of EOS studied in [151] $\chi < 0.7$, although other EOS can exceed this bound. We began by assuming $\lvert\chi\rvert \leq 0.89$, a limit imposed by available rapid waveform models, with an isotropic prior on the spin direction. With these priors we recover $q \in (0.4, 1.0)$ and a constraint on the effective aligned spin of the system [127,152] of $\chi_{\rm eff} \in (-0.01, 0.17)$. The aligned spin components are consistent with zero, with stricter bounds than in previous BBH observations [26,28,29]. Analysis using the effective precessing phenomenological waveforms of [128], which do not contain tidal effects, demonstrates that spin components in the orbital plane are not constrained.

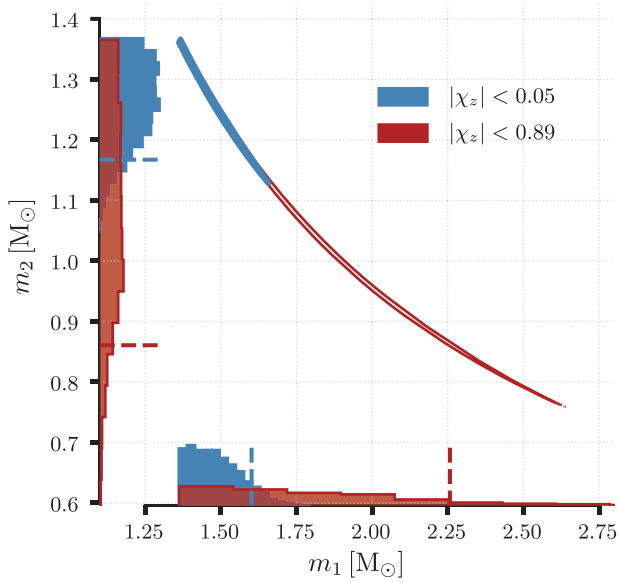

FIG. 4. Two-dimensional posterior distribution for the component masses m_1 and m_2 in the rest frame of the source for the low-spin scenario ($|\chi| < 0.05$, blue) and the high-spin scenario ($|\chi| < 0.89$, red). The colored contours enclose 90% of the probability from the joint posterior probability density function for m_1 and m_2. The shape of the two dimensional posterior is determined by a line of constant $\mathcal{M}$ and its width is determined by the uncertainty in $\mathcal{M}$. The widths of the marginal distributions (shown on axes, dashed lines enclose 90% probability away from equal mass of $1.36M_\odot$) is strongly affected by the choice of spin priors. The result using the low-spin prior (blue) is consistent with the masses of all known binary neutron star systems.

From $\mathcal{M}$ and q, we obtain a measure of the component masses $m_1 \in (1.36, 2.26)M_\odot$ and $m_2 \in (0.86, 1.36)M_\odot$, shown in Fig. 4. As discussed in Sec. I, these values are within the range of known neutron-star masses and below those of known black holes. In combination with electromagnetic observations, we regard this as evidence of the BNS nature of GW170817.

The fastest-spinning known neutron star has a dimensionless spin $\lesssim 0.4$ [153], and the possible BNS J1807-2500B has spin $\lesssim 0.2$ [154], after allowing for a broad range of equations of state. However, among BNS that will merge within a Hubble time, PSR J0737-3039A [155] has the most extreme spin, less than ~ 0.04 after spin-down is extrapolated to merger. If we restrict the spin magnitude in our analysis to $|\chi| \leq 0.05$, consistent with the observed population, we recover the mass ratio $q \in (0.7, 1.0)$ and component masses $m_1 \in (1.36, 1.60)M_\odot$ and $m_2 \in (1.17, 1.36)M_\odot$ (see Fig. 4). We also recover $\chi_{\rm eff} \in (-0.01, 0.02)$, where the upper limit is consistent with the low-spin prior.

Our first analysis allows the tidal deformabilities of the high-mass and low-mass component, Λ_1 and Λ_2, to vary independently. Figure 5 shows the resulting 90% and 50% contours on the posterior distribution with the post-Newtonian waveform model for the high-spin and low-spin priors. As a comparison, we show predictions coming from a set of candidate equations of state for neutron-star matter [156–160], generated using fits from [161]. All EOS support masses of $2.01 \pm 0.04M_\odot$. Assuming that both components are neutron stars described by the same equation of state, a single function $\Lambda(m)$ is computed from the static $\ell = 2$ perturbation of a Tolman-Oppenheimer-Volkoff solution [103]. The shaded regions in Fig. 5 represent the values of the tidal deformabilities Λ_1 and Λ_2 generated using an equation of state from the 90% most probable fraction of the values of m_1 and m_2, consistent with the posterior shown in Fig. 4. We find that our constraints on Λ_1 and Λ_2 disfavor equations of state that predict less compact stars, since the mass range we recover generates Λ values outside the 90% probability region. This is consistent with radius constraints from x-ray observations of neutron stars [162–166]. Analysis methods, in development, that *a priori* assume the same EOS governs both stars should improve our constraints [167].

To leading order in Λ_1 and Λ_2, the gravitational-wave phase is determined by the parameter

$$\tilde{\Lambda} = \frac{16}{13}\frac{(m_1 + 12m_2)m_1^4\Lambda_1 + (m_2 + 12m_1)m_2^4\Lambda_2}{(m_1 + m_2)^5} \quad (1)$$

[101,117]. Assuming a uniform prior on $\tilde{\Lambda}$, we place a 90% upper limit of $\tilde{\Lambda} \leq 800$ in the low-spin case and $\tilde{\Lambda} \leq 700$ in the high-spin case. We can also constrain the function $\Lambda(m)$ more directly by expanding $\Lambda(m)$ linearly about $m = 1.4M_\odot$ (as in [112,115]), which gives $\Lambda(1.4M_\odot) \leq 1400$ for the high-spin prior and $\Lambda(1.4M_\odot) \leq 800$ for the low-spin prior. A 95% upper bound inferred with the low-spin prior, $\Lambda(1.4M_\odot) \leq 970$, begins to compete with the 95% upper bound of 1000 derived from x-ray observations in [168].

Since the energy emitted in gravitational waves depends critically on the EOS of neutron-star matter, with a wide range consistent with constraints above, we are only able to place a lower bound on the energy emitted before the onset of strong tidal effects at $f_{\rm GW} \sim 600$ Hz as $E_{\rm rad} > 0.025M_\odot c^2$. This is consistent with $E_{\rm rad}$ obtained from numerical simulations and fits for BNS systems consistent with GW170817 [114,169–171].

We estimate systematic errors from waveform modeling by comparing the post-Newtonian results with parameters recovered using an effective-one-body model [124] augmented with tidal effects extracted from numerical relativity with hydrodynamics [172]. This does not change the 90% credible intervals for component masses and effective spin under low-spin priors, but in the case of high-spin priors, we obtain the more restrictive $m_1 \in (1.36, 1.93)M_\odot$, $m_2 \in (0.99, 1.36)M_\odot$, and $\chi_{\rm eff} \in (0.0, 0.09)$. Recovered tidal deformabilities indicate shifts in the posterior distributions towards smaller values, with upper bounds for $\tilde{\Lambda}$ and $\Lambda(1.4M_\odot)$ reduced by a factor of roughly (0.8, 0.8) in the

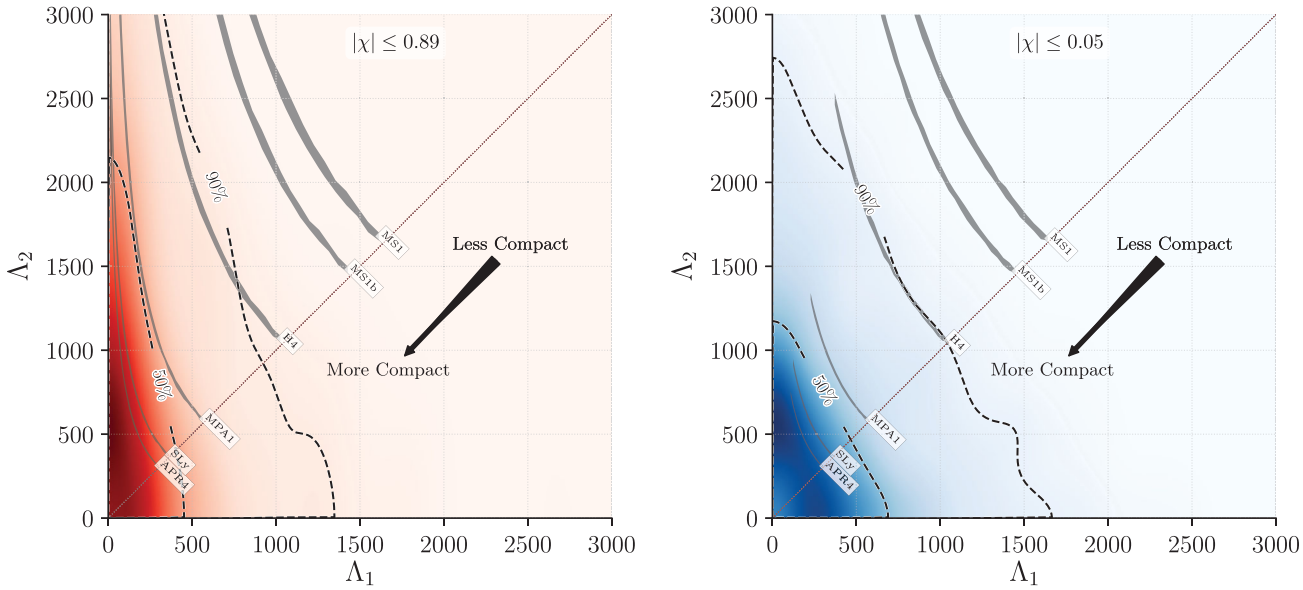

FIG. 5. Probability density for the tidal deformability parameters of the high and low mass components inferred from the detected signals using the post-Newtonian model. Contours enclosing 90% and 50% of the probability density are overlaid (dashed lines). The diagonal dashed line indicates the $\Lambda_1 = \Lambda_2$ boundary. The Λ_1 and Λ_2 parameters characterize the size of the tidally induced mass deformations of each star and are proportional to $k_2(R/m)^5$. Constraints are shown for the high-spin scenario $|\chi| \leq 0.89$ (left panel) and for the low-spin $|\chi| \leq 0.05$ (right panel). As a comparison, we plot predictions for tidal deformability given by a set of representative equations of state [156–160] (shaded filled regions), with labels following [161], all of which support stars of $2.01 M_\odot$. Under the assumption that both components are neutron stars, we apply the function $\Lambda(m)$ prescribed by that equation of state to the 90% most probable region of the component mass posterior distributions shown in Fig. 4. EOS that produce less compact stars, such as MS1 and MS1b, predict Λ values outside our 90% contour.

low-spin case and (1.0, 0.7) in the high-spin case. Further analysis is required to establish the uncertainties of these tighter bounds, and a detailed study of systematics is a subject of ongoing work.

Preliminary comparisons with waveform models under development [171,173–177] also suggest the post-Newtonian model used will systematically overestimate the value of the tidal deformabilities. Therefore, based on our current understanding of the physics of neutron stars, we consider the post-Newtonian results presented in this Letter to be conservative upper limits on tidal deformability. Refinements should be possible as our knowledge and models improve.

V. IMPLICATIONS

A. Astrophysical rate

Our analyses identified GW170817 as the only BNS-mass signal detected in O2 with a false alarm rate below 1/100 yr. Using a method derived from [27,178,179], and assuming that the mass distribution of the components of BNS systems is flat between 1 and 2 $M_\odot$ and their dimensionless spins are below 0.4, we are able to infer the local coalescence rate density R of BNS systems. Incorporating the upper limit of 12600 $\mathrm{Gpc}^{-3}\,\mathrm{yr}^{-1}$ from O1 as a prior, $R = 1540^{+3200}_{-1220}\ \mathrm{Gpc}^{-3}\,\mathrm{yr}^{-1}$. Our findings are consistent with the rate inferred from observations of galactic BNS systems [19,20,155,180].

From this inferred rate, the stochastic background of gravitational wave s produced by unresolved BNS mergers throughout the history of the Universe should be comparable in magnitude to the stochastic background produced by BBH mergers [181,182]. As the advanced detector network improves in sensitivity in the coming years, the total stochastic background from BNS and BBH mergers should be detectable [183].

B. Remnant

Binary neutron star mergers may result in a short- or long-lived neutron star remnant that could emit gravitational waves following the merger [184–190]. The ringdown of a black hole formed after the coalescence could also produce gravitational waves, at frequencies around 6 kHz, but the reduced interferometer response at high frequencies makes their observation unfeasible. Consequently, searches have been made for short (tens of ms) and intermediate duration (≤ 500 s) gravitational-wave signals from a neutron star remnant at frequencies up to 4 kHz [75,191,192]. For the latter, the data examined start at the time of the coalescence and extend to the end of the observing run on August 25, 2017. With the time scales and methods considered so far [193], there is no evidence of a postmerger signal of

astrophysical origin. However, upper limits placed on the strength of gravitational-wave emission cannot definitively rule out the existence of a short- or long-lived postmerger neutron star. The implications of various postmerger scenarios are explored in [45,193].

C. Tests of gravity

GRB 170817A was observed 1.7 s after GW170817. Combining this delay with the knowledge of the source luminosity distance, strong constraints are placed on the fundamental physics of gravity. The observed arrival times are used to investigate the speed of gravity, Lorentz invariance, and tests of the equivalence principle through the Shapiro time delay, as reported in [45].

We also expect the much longer duration of the BNS signal compared to previous BBH gravitational-wave sources to yield significantly improved constraints when testing for waveform deviations from general relativity using a parametrized waveform expansion [194], especially at low post-Newtonian orders. Placing these bounds requires a deep understanding of the systematic uncertainties resulting from waveform modeling and data conditioning, and is the subject of ongoing investigations.

D. Cosmology

The gravitational-wave signal gives a direct measurement of the luminosity distance of the source, which, along with a redshift measurement, can be used to infer cosmological parameters independently of the cosmic distance ladder [141,195]. Using the association with the galaxy NGC 4993 and the luminosity distance directly measured from the gravitational-wave signal, the Hubble constant is inferred to be $H_0 = 70^{+12}_{-8}\ \mathrm{km\,s^{-1}\,Mpc^{-1}}$ [141] (most probable value and minimum 68.3% probability range, which can be compared to the value from Planck $H_0 = 67.90 \pm 0.55\ \mathrm{km\,s^{-1}\,Mpc^{-1}}$ [90]). Alternatively, we may assume the cosmology is known and use the association with NGC 4993 to constrain the luminosity distance of the source, in which case the gravitational-wave measurement of the inclination angle of the source is significantly improved, with consequences for the γ-ray burst opening angle and related physics [45].

VI. CONCLUSIONS

In this Letter we have presented the first detection of gravitational waves from the inspiral of a binary neutron star system. Gravitational-wave event GW170817, observed and localized by the two Advanced LIGO detectors and the Advanced Virgo detector, is the loudest gravitational-wave signal detected to date. This coalescence event was followed by a short burst of γ rays observed with the *Fermi* Gamma-Ray Burst Monitor [39–42] and *INTEGRAL* [43,44]. The coincident observation of a gravitational-wave signal and a γ-ray burst appears to confirm the long-held hypothesis that BNS mergers are linked to short-γ-ray bursts [196,197]. Subsequent observations have determined the location of the source and followed its evolution through the electromagnetic spectrum [50].

Detailed analyses of the gravitational-wave data, together with observations of electromagnetic emissions, are providing new insights into the astrophysics of compact binary systems and γ-ray bursts, dense matter under extreme conditions, the nature of gravitation, and independent tests of cosmology. Less than two years after the debut of gravitational-wave astronomy, GW170817 marks the beginning of a new era of discovery.

ACKNOWLEDGMENTS

The authors gratefully acknowledge the support of the United States National Science Foundation (NSF) for the construction and operation of the LIGO Laboratory and Advanced LIGO as well as the Science and Technology Facilities Council (STFC) of the United Kingdom, the Max-Planck-Society (MPS), and the State of Niedersachsen, Germany for support of the construction of Advanced LIGO and construction and operation of the GEO600 detector. Additional support for Advanced LIGO was provided by the Australian Research Council. The authors gratefully acknowledge the Italian Istituto Nazionale di Fisica Nucleare (INFN), the French Centre National de la Recherche Scientifique (CNRS), and the Foundation for Fundamental Research on Matter supported by the Netherlands Organisation for Scientific Research, for the construction and operation of the Virgo detector and the creation and support of the EGO consortium. The authors also gratefully acknowledge research support from these agencies as well as by the Council of Scientific and Industrial Research of India, the Department of Science and Technology, India, the Science & Engineering Research Board (SERB), India, the Ministry of Human Resource Development, India, the Spanish Agencia Estatal de Investigación, the Vicepresidència i Conselleria d'Innovació, Recerca i Turisme and the Conselleria d'Educació i Universitat del Govern de les Illes Balears, the Conselleria d'Educació, Investigació, Cultura i Esport de la Generalitat Valenciana, the National Science Centre of Poland, the Swiss National Science Foundation (SNSF), the Russian Foundation for Basic Research, the Russian Science Foundation, the European Commission, the European Regional Development Funds (ERDF), the Royal Society, the Scottish Funding Council, the Scottish Universities Physics Alliance, the Hungarian Scientific Research Fund (OTKA), the Lyon Institute of Origins (LIO), the National Research, Development and Innovation Office Hungary (NKFI), the National Research Foundation of Korea, Industry Canada and the Province of Ontario through the Ministry of Economic Development and Innovation, the Natural Science and Engineering Research Council Canada, the Canadian Institute for Advanced Research, the Brazilian

Ministry of Science, Technology, Innovations, and Communications, the International Center for Theoretical Physics South American Institute for Fundamental Research (ICTP-SAIFR), the Research Grants Council of Hong Kong, the National Natural Science Foundation of China (NSFC), the Leverhulme Trust, the Research Corporation, the Ministry of Science and Technology (MOST), Taiwan and the Kavli Foundation. The authors gratefully acknowledge the support of the NSF, STFC, MPS, INFN, CNRS and the State of Niedersachsen, Germany for provision of computational resources. This research has made use of the NASA/IPAC Extragalactic Database (NED) which is operated by the Jet Propulsion Laboratory, California Institute of Technology, under contract with the National Aeronautics and Space Administration.

[1] R. A. Hulse and J. H. Taylor, Astrophys. J. **195**, L51 (1975).
[2] J. H. Taylor and J. M. Weisberg, Astrophys. J. **253**, 908 (1982).
[3] R. Weiss, MIT Technical Report No. LIGO-P720002, 1972.
[4] R. W. P. Drever, in *Gravitational Radiation*, edited by N. Deruelle and T. Piran (North-Holland, Amsterdam, 1983), p. 321.
[5] A. Brillet *et al.* (Virgo Collaboration), Technical Report No. VIR-0517A-15, 1989 [https://tds.virgo-gw.eu/?content=3&r=12122].
[6] J. Hough *et al.*, MPQ Technical Report No. 147, 1989 [GWD/137/JH(89)].
[7] K. Thorne, *Three Hundred Years of Gravitation*, edited by S. W. Hawking and W. Israel (Cambridge University Press, Cambridge, U.K., 1987), pp. 330–458.
[8] R. N. Manchester, G. B. Hobbs, A. Teoh, and M. Hobbs, Astron. J. **129**, 1993 (2005).
[9] L. Blanchet, Thibault Damour, Bala R. Iyer, Clifford M. Will, and Alan G. Wiseman, Phys. Rev. Lett. **74**, 3515 (1995).
[10] A. Buonanno and T. Damour, Phys. Rev. D **59**, 084006 (1999).
[11] T. Damour, P. Jaranowski, and G. Schäfer, Phys. Lett. B **513**, 147 (2001).
[12] L. Blanchet, T. Damour, G. Esposito-Farese, and B. R. Iyer, Phys. Rev. Lett. **93**, 091101 (2004).
[13] W. D. Goldberger and I. Z. Rothstein, Phys. Rev. D **73**, 104029 (2006).
[14] B. P. Flannery and E. P. J. van den Heuvel, Astron. Astrophys. **39**, 61 (1975).
[15] A. G. Massevitch, A. V. Tutukov, and L. R. Yungelson, Astrophys. Space Sci. **40**, 115 (1976).
[16] J. P. A. Clark, E. P. J. van den Heuvel, and W. Sutantyo, Astron. Astrophys. **72**, 120 (1979).
[17] E. S. Phinney, Astrophys. J. Lett. **380**, L17 (1991).
[18] V. Kalogera *et al.*, Astrophys. J. Lett. **601**, L179 (2004). V. Kalogera *et al.*, Astrophys. J. Lett. **614**, L137(E) (2004).
[19] J. Abadie *et al.* (LIGO Scientific Collaboration and Virgo Collaboration), Classical Quantum Gravity **27**, 173001 (2010).
[20] C. Kim, B. B. P. Perera, and M. A. McLaughlin, Mon. Not. R. Astron. Soc. **448**, 928 (2015).
[21] B. P. Abbott *et al.* (KAGRA Collaboration, LIGO Scientific Collaboration, Virgo Collaboration), Living Rev. Relativity **19**, 1 (2016).
[22] J. Aasi *et al.* (LIGO Scientific Collaboration), Classical Quantum Gravity **32**, 074001 (2015).
[23] F. Acernese *et al.* (Virgo Collaboration), Classical Quantum Gravity **32**, 024001 (2015).
[24] B. P. Abbott *et al.* (LIGO Scientific Collaboration and Virgo Collaboration), Phys. Rev. Lett. **116**, 061102 (2016).
[25] B. P. Abbott *et al.* (LIGO Scientific Collaboration and Virgo Collaboration), Phys. Rev. Lett. **116**, 241103 (2016).
[26] B. P. Abbott *et al.* (LIGO Scientific Collaboration and Virgo Collaboration), Phys. Rev. X **6**, 041015 (2016).
[27] B. P. Abbott *et al.* (LIGO Scientific Collaboration and Virgo Collaboration), Astrophys. J. Lett. **832**, L21 (2016).
[28] B. P. Abbott *et al.* (LIGO Scientific Collaboration and Virgo Collaboration), Phys. Rev. Lett. **118**, 221101 (2017).
[29] B. P. Abbott *et al.* (LIGO Scientific Collaboration and Virgo Collaboration), Phys. Rev. Lett. **119**, 141101 (2017).
[30] B. S. Sathyaprakash and S. V. Dhurandhar, Phys. Rev. D **44**, 3819 (1991).
[31] C. Cutler *et al.*, Phys. Rev. Lett. **70**, 2984 (1993).
[32] B. Allen, W. G. Anderson, P. R. Brady, D. A. Brown, and J. D. E. Creighton, Phys. Rev. D **85**, 122006 (2012).
[33] D. A. Brown, P. Kumar, and A. H. Nitz, Phys. Rev. D **87**, 082004 (2013).
[34] K. G. Arun, A. Buonanno, G. Faye, and E. Ochsner, Phys. Rev. D **79**, 104023 (2009); **84**, 049901(E) (2011).
[35] A. Buonanno, B. R. Iyer, E. Ochsner, Y. Pan, and B. S. Sathyaprakash, Phys. Rev. D **80**, 084043 (2009).
[36] L. Blanchet, Living Rev. Relativity **17**, 2 (2014).
[37] C. K. Mishra, A. Kela, K. G. Arun, and G. Faye, Phys. Rev. D **93**, 084054 (2016).
[38] C. Cutler and E. E. Flanagan, Phys. Rev. D **49**, 2658 (1994).
[39] A. G. A. von Kienlin, C. Meegan, and the Fermi GBM Team, GCN **21520**, 1 (2017).
[40] V. Connaughton *et al.*, GCN **21506**, 1 (2017).
[41] A. Goldstein *et al.*, GCN **21528**, 1 (2017).
[42] A. Goldstein *et al.*, Astrophys. J. Lett. **848**, L14 (2017).
[43] V. Savchenko *et al.*, GCN **21507**, 1 (2017).
[44] V. Savchenko *et al.*, Astrophys. J. Lett. **848**, L15 (2017).
[45] B. P. Abbott *et al.* (LIGO Scientific Collaboration and Virgo Collaboration), Astrophys. J. Lett. **848**, L13 (2017);
[46] D. A. Coulter *et al.*, GCN **21529**, 1 (2017).
[47] R. J. Foley *et al.*, GCN **21536**, 1 (2017).
[48] D. A. Coulter *et al.*, Science, in press (2017), DOI: 10.1126/science.aap9811.
[49] Y.-C. Pan *et al.*, Astrophys. J. Lett. **848**, L30 (2017).
[50] B. P. Abbott *et al.* (LIGO Scientific Collaboration and Virgo Collaboration), Astrophys. J. Lett. **848**, L12 (2017).
[51] P. C. Peters and J. Mathews, Phys. Rev. **131**, 435 (1963).
[52] T. M. Tauris *et al.*, Astrophys. J. **846**, 170 (2017).
[53] J. Antoniadis *et al.*, Science **340**, 1233232 (2013).

[54] F. Özel, D. Psaltis, R. Narayan, and J. E. McClintock, Astrophys. J. **725**, 1918 (2010).
[55] L. Kreidberg, C. D. Bailyn, W. M. Farr, and V. Kalogera, Astrophys. J. **757**, 36 (2012).
[56] R. Narayan and J. E. McClintock, in *General Relativity and Gravitation: A Centennial Perspective*, edited by A. Ashtekar, B. K. Berger, J. Isenberg, and M. MacCallum (Cambridge University Press, Cambridge, U.K., 2015), Chap. 3.3, pp. 133–147.
[57] D. J. Kaup, Phys. Rev. **172**, 1331 (1968).
[58] P. O. Mazur and E. Mottola, Proc. Natl. Acad. Sci. U.S.A. **101**, 9545 (2004).
[59] N. Itoh, Prog. Theor. Phys. **44**, 291 (1970).
[60] V. Cardoso, S. Hopper, C. F. B. Macedo, C. Palenzuela, and P. Pani, Phys. Rev. D **94**, 084031 (2016).
[61] V. Cardoso, E. Franzin, A. Maselli, P. Pani, and G. Raposo, Phys. Rev. D **95**, 084014 (2017); **95**, 089901 (2017).
[62] L. S. Finn and D. F. Chernoff, Phys. Rev. D **47**, 2198 (1993).
[63] H.-Y. Chen, D. E. Holz, J. Miller, M. Evans, S. Vitale, and J. Creighton, arXiv:1709.08079.
[64] K. L. Dooley *et al.*, Classical Quantum Gravity **33**, 075009 (2016).
[65] S. Chatterji, L Blackburn, G Martin, and E Katsavounidis, Classical Quantum Gravity **21**, S1809 (2004).
[66] R. G. Brown and P. Y. C. Hwang, *Introduction to Random Signals and Applied Kalman Filtering with Matlab Exercises* (Wiley, New York, 2012).
[67] J. C. Driggers *et al.*, Technical Report No. LIGO-P1700260, 2017.
[68] J. C. Driggers, M. Evans, K. Pepper, and R. Adhikari, Rev. Sci. Instrum. **83**, 024501 (2012).
[69] G. D. Meadors, K. Kawabe, and K. Riles, Classical Quantum Gravity **31**, 105014 (2014).
[70] V. Tiwari *et al.*, Classical Quantum Gravity **32**, 165014 (2015).
[71] L. Nuttall *et al.*, Classical Quantum Gravity **32**, 245005 (2015).
[72] B. P. Abbott *et al.* (LIGO Scientific Collaboration and Virgo Collaboration), Phys. Rev. D **93**, 122003 (2016).
[73] S. A. Usman *et al.*, Classical Quantum Gravity **33**, 215004 (2016).
[74] B. P. Abbott *et al.* (LIGO Scientific Collaboration and Virgo Collaboration), Technical Report No. LIGO-P1600110, 2017.
[75] N. J. Cornish and T. B. Littenberg, Classical Quantum Gravity **32**, 135012 (2015).
[76] LIGO Scientific Collaboration and Virgo Collaboration, GCN **21509**, 1 (2017).
[77] LIGO Scientific Collaboration and Virgo Collaboration, GCN **21513**, 1 (2017).
[78] B. P. Abbott *et al.* (LIGO Scientific Collaboration and Virgo Collaboration), Classical Quantum Gravity **33**, 134001 (2016).
[79] A. Effler, R M S Schofield, V V Frolov, G González, K Kawabe, J R Smith, J Birch, and R McCarthy, Classical Quantum Gravity **32**, 035017 (2015).
[80] LIGO Scientific Collaboration and Virgo Collaboration, LIGO Open Science Center (LOSC), 2017 [https://doi.org/10.7935/K5B8566F].
[81] K. Cannon *et al.*, Astrophys. J. **748**, 136 (2012).
[82] S. Privitera, S. R. P. Mohapatra, P. Ajith, K. Cannon, N. Fotopoulos, M. A. Frei, C. Hanna, A. J. Weinstein, and J. T. Whelan, Phys. Rev. D **89**, 024003 (2014).
[83] C. Messick *et al.*, Phys. Rev. D **95**, 042001 (2017).
[84] A. Einstein, L. Infeld, and B. Hoffmann, Ann. Math. **39**, 65 (1938).
[85] LIGO Scientific Collaboration and Virgo Collaboration, GCN **21505**, 1 (2017).
[86] A. H. Nitz, T. Dent, T. Dal Canton, S. Fairhurst, and D. A. Brown, arXiv:1705.01513.
[87] A. Nitz *et al.*, ligo-cbc/pycbc: O2 production release 20, 2017.
[88] L. P. Singer and L. R. Price, Phys. Rev. D **93**, 024013 (2016).
[89] NASA/IPAC Extragalactic Database.
[90] P. A. R. Ade *et al.* (Planck Collaboration), Astron. Astrophys. **594**, A13 (2016).
[91] L. Blanchet, A. Buonanno, and G. Faye, Phys. Rev. D **74**, 104034 (2006); **75**, 049903(E) (2007); **81**, 089901(E) (2010).
[92] A. Bohé, S. Marsat, and L. Blanchet, Classical Quantum Gravity **30**, 135009 (2013).
[93] B. J. Owen and B. S. Sathyaprakash, Phys. Rev. D **60**, 022002 (1999).
[94] D. A. Brown, I. Harry, A. Lundgren, and A. H. Nitz, Phys. Rev. D **86**, 084017 (2012).
[95] T. Dal Canton and I. W. Harry, arXiv:1705.01845.
[96] B. Allen, Phys. Rev. D **71**, 062001 (2005).
[97] A. H. Nitz, arXiv:1709.08974.
[98] C. Cutler, T. A. Apostolatos, L. Bildsten, L. S. Finn, E. E. Flanagan, D. Kennefick, D. M. Markovic, A. Ori, E. Poisson, G. J. Sussman, and K. S. Thorne, Phys. Rev. Lett. **70**, 2984 (1993).
[99] T. Damour, Lect. Notes Phys., **124**, 59 (1983).
[100] T. Damour, M. Soffel, and C.-m. Xu, Phys. Rev. D **45**, 1017 (1992).
[101] E. E. Flanagan and T. Hinderer, Phys. Rev. D **77**, 021502 (2008).
[102] T. Hinderer, Astrophys. J. **677**, 1216 (2008).
[103] T. Hinderer, B. D. Lackey, R. N. Lang, and J. S. Read, Phys. Rev. D **81**, 123016 (2010).
[104] S. Postnikov, M. Prakash, and J. M. Lattimer, Phys. Rev. D **82**, 024016 (2010).
[105] T. Damour and A. Nagar, Phys. Rev. D **80**, 084035 (2009).
[106] T. Binnington and E. Poisson, Phys. Rev. D **80**, 084018 (2009).
[107] B. Kol and M. Smolkin, J. High Energy Phys. 02 (2012) 010.
[108] P. Pani, L. Gualtieri, A. Maselli, and V. Ferrari, Phys. Rev. D **92**, 024010 (2015).
[109] P. Landry and E. Poisson, Phys. Rev. D **91**, 104018 (2015).
[110] J. S. Read, C. Markakis, M. Shibata, K. Uryu, J. D. E. Creighton, and J. L. Friedman, Phys. Rev. D **79**, 124033 (2009).
[111] T. Damour, A. Nagar, and L. Villain, Phys. Rev. D **85**, 123007 (2012).
[112] W. Del Pozzo, T. G. F. Li, M. Agathos, C. Van Den Broeck, and S. Vitale, Phys. Rev. Lett. **111**, 071101 (2013).

[113] L. Wade, J. D. E. Creighton, E. Ochsner, B. D. Lackey, B. F. Farr, T. B. Littenberg, and V. Raymond, Phys. Rev. D **89**, 103012 (2014).
[114] S. Bernuzzi, A. Nagar, S. Balmelli, T. Dietrich, and M. Ujevic, Phys. Rev. Lett. **112**, 201101 (2014).
[115] M. Agathos, J. Meidam, W. Del Pozzo, T. G. F. Li, M. Tompitak, J. Veitch, S. Vitale, and C. Van Den Broeck, Phys. Rev. D **92**, 023012 (2015).
[116] K. Hotokezaka, K. Kyutoku, Y.-i. Sekiguchi, and M. Shibata, Phys. Rev. D **93**, 064082 (2016).
[117] M. Favata, Phys. Rev. Lett. **112**, 101101 (2014).
[118] K. Yagi and N. Yunes, Phys. Rev. D **89**, 021303 (2014).
[119] T. Cullen, I. Harry, J. Read, and E. Flynn, arXiv: 1708.04359.
[120] A. Buonanno and T. Damour, Phys. Rev. D **62**, 064015 (2000).
[121] T. Damour, P. Jaranowski, and G. Schäfer, Phys. Rev. D **78**, 024009 (2008).
[122] T. Damour and A. Nagar, Phys. Rev. D **79**, 081503 (2009).
[123] E. Barausse and A. Buonanno, Phys. Rev. D **81**, 084024 (2010).
[124] A. Bohé *et al.*, Phys. Rev. D **95**, 044028 (2017).
[125] A. Nagar, G. Riemenschneider, and G. Pratten, arXiv:1703.06814 [Phys. Rev. D (to be published)].
[126] P. Ajith *et al.*, Classical Quantum Gravity **24**, S689 (2007).
[127] P. Ajith *et al.*, Phys. Rev. Lett. **106**, 241101 (2011).
[128] M. Hannam, Patricia Schmidt, Alejandro Bohé, Leïla Haegel, Sascha Husa, Frank Ohme, Geraint Pratten, and Michael Pürrer, Phys. Rev. Lett. **113**, 151101 (2014).
[129] S. Husa, S. Khan, M. Hannam, M. Purrer, F. Ohme, X. J. Forteza, and A. Bohe, Phys. Rev. D **93**, 044006 (2016).
[130] S. Khan, S. Husa, M. Hannam, F. Ohme, M. Purrer, X. J. Forteza, and A. Bohe, Phys. Rev. D **93**, 044007 (2016).
[131] R. Smith, S. E. Field, K. Blackburn, C.-J. Haster, M. Pürrer, V. Raymond, and P. Schmidt, Phys. Rev. D **94**, 044031 (2016).
[132] J. Vines, E. E. Flanagan, and T. Hinderer, Phys. Rev. D **83**, 084051 (2011).
[133] B. Mikoczi, M. Vasuth, and L. A. Gergely, Phys. Rev. D **71**, 124043 (2005).
[134] A. Bohé, G. Faye, S. Marsat, and E. K. Porter, Classical Quantum Gravity **32**, 195010 (2015).
[135] J. Veitch *et al.*, Phys. Rev. D **91**, 042003 (2015).
[136] B. P. Abbott *et al.* (LIGO Scientific Collaboration and Virgo Collaboration), Phys. Rev. Lett. **116**, 241102 (2016).
[137] C. Cahillane *et al.*, arXiv:1708.03023.
[138] L. P. Singer, H.-Y. Chen, D. E. Holz, W. M. Farr, L. R. Price, V. Raymond, S. B. Cenko, N. Gehrels, J. Cannizzo, M. M. Kasliwal, S. Nissanke, M. Coughlin, B. Farr, A. L. Urban, S. Vitale, J. Veitch, P. Graff, C. P. L. Berry, S. Mohapatra, and I. Mandel, Astrophys. J. Lett. **829**, L15 (2016).
[139] H.-Y. Chen and D. E. Holz, arXiv:1612.01471.
[140] T. A. Apostolatos, C. Cutler, G. J. Sussman, and K. S. Thorne, Phys. Rev. D **49**, 6274 (1994).
[141] B. P. Abbott *et al.* (LIGO Scientific Collaboration, Virgo Collaboration, IM2H Collaboration, Dark Energy Camera GW-EM Collaboration, DES Collaboration, DLT40 Collaboration, Las Cumbres Observatory Collaboration, VINROUGE Collaboration, and MASTER Collaboration), Nature (London), in press (2017), DOI: 10.1038/nature24471.
[142] A. Krolak and B. F. Schutz, Gen. Relativ. Gravit. **19**, 1163 (1987).
[143] D. J. Fixsen, Astrophys. J. **707**, 916 (2009).
[144] A. C. Crook, J. P. Huchra, N. Martimbeau, K. L. Masters, T. Jarrett, and L. M. Macri, Astrophys. J. **655**, 790 (2007).
[145] A. C. Crook, J. P. Huchra, N. Martimbeau, K. L. Masters, T. Jarrett, and L. M. Macri, Astrophys. J. **685**, 1320 (2008).
[146] M. Hannam, D. A. Brown, S. Fairhurst, C. L. Fryer, and I. W. Harry, Astrophys. J. Lett. **766**, L14 (2013).
[147] F. Ohme, A. B. Nielsen, D. Keppel, and A. Lundgren, Phys. Rev. D **88**, 042002 (2013).
[148] C. P. L. Berry *et al.*, Astrophys. J. **804**, 114 (2015).
[149] M. Pürrer, M. Hannam, and F. Ohme, Phys. Rev. D **93**, 084042 (2016).
[150] B. Farr *et al.*, Astrophys. J. **825**, 116 (2016).
[151] K.-W. Lo and L.-M. Lin, Astrophys. J. **728**, 12 (2011).
[152] E. Racine, Phys. Rev. D **78**, 044021 (2008).
[153] J. W. T. Hessels, S. M. Ransom, I. H. Stairs, P. C. C. Freire, V. M. Kaspi, and F. Camilo, Science **311**, 1901 (2006).
[154] R. S. Lynch, P. C. C. Freire, S. M. Ransom, and B. A. Jacoby, Astrophys. J. **745**, 109 (2012).
[155] M. Burgay *et al.*, Nature (London) **426**, 531 (2003).
[156] H. Müther, M. Prakash, and T. L. Ainsworth, Phys. Lett. B **199**, 469 (1987).
[157] H. Mueller and B. D. Serot, Nucl. Phys. A **A606**, 508 (1996).
[158] F. Douchin and P. Haensel, Astron. Astrophys. **380**, 151 (2001).
[159] A. Akmal, V. R. Pandharipande, and D. G. Ravenhall, Phys. Rev. C **58**, 1804 (1998).
[160] B. D. Lackey, M. Nayyar, and B. J. Owen, Phys. Rev. D **73**, 024021 (2006).
[161] J. S. Read, B. D. Lackey, B. J. Owen, and J. L. Friedman, Phys. Rev. D **79**, 124032 (2009).
[162] J. M. Lattimer and M. Prakash, Phys. Rep. **621**, 127 (2016).
[163] F. Ozel and P. Freire, Annu. Rev. Astron. Astrophys. **54**, 401 (2016).
[164] A. L. Watts *et al.*, Rev. Mod. Phys. **88**, 021001 (2016).
[165] A. W. Steiner, C. O. Heinke, S. Bogdanov, C. Li, W. C. G. Ho, A. Bahramian, and S. Han, arXiv:1709.05013.
[166] J. Nättilä, M. C. Miller, A. W. Steiner, J. J. E. Kajava, V. F. Suleimanov, and J. Poutanen, arXiv:1709.09120.
[167] B. D. Lackey and L. Wade, Phys. Rev. D **91**, 043002 (2015).
[168] A. W. Steiner, S. Gandolfi, F. J. Fattoyev, and W. G. Newton, Phys. Rev. C **91**, 015804 (2015).
[169] R. De Pietri, A. Feo, F. Maione, and F. Löffler, Phys. Rev. D **93**, 064047 (2016).
[170] T. Dietrich, M. Ujevic, W. Tichy, S. Bernuzzi, and B. Brügmann, Phys. Rev. D **95**, 024029 (2017).
[171] T. Dietrich and T. Hinderer, Phys. Rev. D **95**, 124006 (2017).
[172] T. Dietrich, S. Bernuzzi, and W. Tichy, arXiv:1706.02969.
[173] T. Damour and A. Nagar, Phys. Rev. D **81**, 084016 (2010).
[174] B. D. Lackey, S. Bernuzzi, C. R. Galley, J. Meidam, and C. Van Den Broeck, Phys. Rev. D **95**, 104036 (2017).

[175] S. Bernuzzi, A. Nagar, T. Dietrich, and T. Damour, Phys. Rev. Lett. **114**, 161103 (2015).
[176] T. Hinderer *et al.*, Phys. Rev. Lett. **116**, 181101 (2016).
[177] J. Steinhoff, T. Hinderer, A. Buonanno, and A. Taracchini, Phys. Rev. D **94**, 104028 (2016).
[178] B. P. Abbott *et al.* (LIGO Scientific Collaboration and Virgo Collaboration), Astrophys. J. Lett. **833**, L1 (2016).
[179] B. P. Abbott *et al.* (LIGO Scientific Collaboration and Virgo Collaboration), Astrophys. J. Suppl. Ser. **227**, 14 (2016).
[180] C. Kim, V. Kalogera, and D. R. Lorimer, Astrophys. J. **584**, 985 (2003).
[181] B. P. Abbott *et al.* (LIGO Scientific Collaboration and Virgo Collaboration), Phys. Rev. Lett. **118**, 121101 (2017).
[182] B. P. Abbott *et al.* (LIGO Scientific Collaboration and Virgo Collaboration), Phys. Rev. Lett. **116**, 131102 (2016).
[183] LIGO Scientific Collaboration and Virgo Collaboration, Technical Report No. LIGO-P170272, 2017.
[184] N. Andersson, Classical Quantum Gravity **20**, R105 (2003).
[185] A. L. Piro, B. Giacomazzo, and R. Perna, Astrophys. J. **844**, L19 (2017).
[186] J. A. Clark, A. Bauswein, N. Stergioulas, and D. Shoemaker, Classical Quantum Gravity **33**, 085003 (2016).
[187] P. D. Lasky and K. Glampedakis, Mon. Not. R. Astron. Soc. **458**, 1660 (2016).
[188] S. Bose, K. Chakravarti, L. Rezzolla, B. S. Sathyaprakash, and K. Takami, arXiv:1705.10850.
[189] M. Shibata and K. Uryū, Phys. Rev. D **61**, 064001 (2000).
[190] L. Baiotti and L. Rezzolla, Rep. Prog. Phys. **80**, 096901 (2017).
[191] S. Klimenko *et al.*, Phys. Rev. D **93**, 042004 (2016).
[192] B. P. Abbott *et al.* (LIGO Scientific Collaboration and Virgo Collaboration), Phys. Rev. D **93**, 042005 (2016).
[193] LIGO Scientific Collaboration and Virgo Collaboration *et al.*, Technical Report No. LIGO-P1700318, 2017.
[194] B. P. Abbott *et al.* (LIGO Scientific Collaboration and Virgo Collaboration), Phys. Rev. Lett. **116**, 221101 (2016).
[195] B. F. Schutz, Nature (London) **323**, 310 (1986).
[196] D. Eichler, M. Livio, T. Piran, and D. N. Schramm, Nature (London) **340**, 126 (1989).
[197] P. D'Avanzo, J. High Energy Astrophys. **7**, 73 (2015).

B. P. Abbott,[1] R. Abbott,[1] T. D. Abbott,[2] F. Acernese,[3,4] K. Ackley,[5,6] C. Adams,[7] T. Adams,[8] P. Addesso,[9] R. X. Adhikari,[1] V. B. Adya,[10] C. Affeldt,[10] M. Afrough,[11] B. Agarwal,[12] M. Agathos,[13] K. Agatsuma,[14] N. Aggarwal,[15] O. D. Aguiar,[16] L. Aiello,[17,18] A. Ain,[19] P. Ajith,[20] B. Allen,[10,21,22] G. Allen,[12] A. Allocca,[23,24] P. A. Altin,[25] A. Amato,[26] A. Ananyeva,[1] S. B. Anderson,[1] W. G. Anderson,[21] S. V. Angelova,[27] S. Antier,[28] S. Appert,[1] K. Arai,[1] M. C. Araya,[1] J. S. Areeda,[29] N. Arnaud,[28,30] K. G. Arun,[31] S. Ascenzi,[32,33] G. Ashton,[10] M. Ast,[34] S. M. Aston,[7] P. Astone,[35] D. V. Atallah,[36] P. Aufmuth,[22] C. Aulbert,[10] K. AultONeal,[37] C. Austin,[2] A. Avila-Alvarez,[29] S. Babak,[38] P. Bacon,[39] M. K. M. Bader,[14] S. Bae,[40] M. Bailes,[41] P. T. Baker,[42] F. Baldaccini,[43,44] G. Ballardin,[30] S. W. Ballmer,[45] S. Banagiri,[46] J. C. Barayoga,[1] S. E. Barclay,[47] B. C. Barish,[1] D. Barker,[48] K. Barkett,[49] F. Barone,[3,4] B. Barr,[47] L. Barsotti,[15] M. Barsuglia,[39] D. Barta,[50] S. D. Barthelmy,[51] J. Bartlett,[48] I. Bartos,[52,5] R. Bassiri,[53] A. Basti,[23,24] J. C. Batch,[48] M. Bawaj,[54,44] J. C. Bayley,[47] M. Bazzan,[55,56] B. Bécsy,[57] C. Beer,[10] M. Bejger,[58] I. Belahcene,[28] A. S. Bell,[47] B. K. Berger,[1] G. Bergmann,[10] S. Bernuzzi,[59,60] J. J. Bero,[61] C. P. L. Berry,[62] D. Bersanetti,[63] A. Bertolini,[14] J. Betzwieser,[7] S. Bhagwat,[45] R. Bhandare,[64] I. A. Bilenko,[65] G. Billingsley,[1] C. R. Billman,[5] J. Birch,[7] I. A. Birney,[66] O. Birnholtz,[10] S. Biscans,[1,15] S. Biscoveanu,[67,6] A. Bisht,[22] M. Bitossi,[30,24] C. Biwer,[45] M. A. Bizouard,[28] J. K. Blackburn,[1] J. Blackman,[49] C. D. Blair,[1,68] D. G. Blair,[68] R. M. Blair,[48] S. Bloemen,[69] O. Bock,[10] N. Bode,[10] M. Boer,[70] G. Bogaert,[70] A. Bohe,[38] F. Bondu,[71] E. Bonilla,[53] R. Bonnand,[8] B. A. Boom,[14] R. Bork,[1] V. Boschi,[30,24] S. Bose,[72,19] K. Bossie,[7] Y. Bouffanais,[39] A. Bozzi,[30] C. Bradaschia,[24] P. R. Brady,[21] M. Branchesi,[17,18] J. E. Brau,[73] T. Briant,[74] A. Brillet,[70] M. Brinkmann,[10] V. Brisson,[28] P. Brockill,[21] J. E. Broida,[75] A. F. Brooks,[1] D. A. Brown,[45] D. D. Brown,[76] S. Brunett,[1] C. C. Buchanan,[2] A. Buikema,[15] T. Bulik,[77] H. J. Bulten,[78,14] A. Buonanno,[38,79] D. Buskulic,[8] C. Buy,[39] R. L. Byer,[53] M. Cabero,[10] L. Cadonati,[80] G. Cagnoli,[26,81] C. Cahillane,[1] J. Calderón Bustillo,[80] T. A. Callister,[1] E. Calloni,[82,4] J. B. Camp,[51] M. Canepa,[83,63] P. Canizares,[69] K. C. Cannon,[84] H. Cao,[76] J. Cao,[85] C. D. Capano,[10] E. Capocasa,[39] F. Carbognani,[30] S. Caride,[86] M. F. Carney,[87] G. Carullo,[23,24] J. Casanueva Diaz,[28] C. Casentini,[32,33] S. Caudill,[21,14] M. Cavaglià,[11] F. Cavalier,[28] R. Cavalieri,[30] G. Cella,[24] C. B. Cepeda,[1] P. Cerdá-Durán,[88] G. Cerretani,[23,24] E. Cesarini,[89,33] S. J. Chamberlin,[67] M. Chan,[47] S. Chao,[90] P. Charlton,[91] E. Chase,[92] E. Chassande-Mottin,[39] D. Chatterjee,[21] K. Chatziioannou,[93] B. D. Cheeseboro,[42] H. Y. Chen,[94] X. Chen,[68] Y. Chen,[49] H.-P. Cheng,[5] H. Chia,[5] A. Chincarini,[63] A. Chiummo,[30] T. Chmiel,[87] H. S. Cho,[95] M. Cho,[79] J. H. Chow,[25] N. Christensen,[75,70] Q. Chu,[68] A. J. K. Chua,[13] S. Chua,[74] A. K. W. Chung,[96] S. Chung,[68] G. Ciani,[5,55,56] R. Ciolfi,[97,98] C. E. Cirelli,[53] A. Cirone,[83,63] F. Clara,[48] J. A. Clark,[80] P. Clearwater,[99] F. Cleva,[70] C. Cocchieri,[11] E. Coccia,[17,18] P.-F. Cohadon,[74] D. Cohen,[28] A. Colla,[100,35] C. G. Collette,[101] L. R. Cominsky,[102] M. Constancio Jr.,[16] L. Conti,[56] S. J. Cooper,[62] P. Corban,[7] T. R. Corbitt,[2] I. Cordero-Carrión,[103] K. R. Corley,[52] N. Cornish,[104] A. Corsi,[86] S. Cortese,[30]

C. A. Costa,[16] M. W. Coughlin,[75,1] S. B. Coughlin,[92] J.-P. Coulon,[70] S. T. Countryman,[52] P. Couvares,[1] P. B. Covas,[105] E. E. Cowan,[80] D. M. Coward,[68] M. J. Cowart,[7] D. C. Coyne,[1] R. Coyne,[86] J. D. E. Creighton,[21] T. D. Creighton,[106] J. Cripe,[2] S. G. Crowder,[107] T. J. Cullen,[29,2] A. Cumming,[47] L. Cunningham,[47] E. Cuoco,[30] T. Dal Canton,[51] G. Dálya,[57] S. L. Danilishin,[22,10] S. D'Antonio,[33] K. Danzmann,[22,10] A. Dasgupta,[108] C. F. Da Silva Costa,[5] V. Dattilo,[30] I. Dave,[64] M. Davier,[28] D. Davis,[45] E. J. Daw,[109] B. Day,[80] S. De,[45] D. DeBra,[53] J. Degallaix,[26] M. De Laurentis,[17,4] S. Deléglise,[74] W. Del Pozzo,[62,23,24] N. Demos,[15] T. Denker,[10] T. Dent,[10] R. De Pietri,[59,60] V. Dergachev,[38] R. De Rosa,[82,4] R. T. DeRosa,[7] C. De Rossi,[26,30] R. DeSalvo,[110] O. de Varona,[10] J. Devenson,[27] S. Dhurandhar,[19] M. C. Díaz,[106] T. Dietrich,[38] L. Di Fiore,[4] M. Di Giovanni,[111,98] T. Di Girolamo,[52,82,4] A. Di Lieto,[23,24] S. Di Pace,[100,35] I. Di Palma,[100,35] F. Di Renzo,[23,24] Z. Doctor,[94] V. Dolique,[26] F. Donovan,[15] K. L. Dooley,[11] S. Doravari,[10] I. Dorrington,[36] R. Douglas,[47] M. Dovale Álvarez,[62] T. P. Downes,[21] M. Drago,[10] C. Dreissigacker,[10] J. C. Driggers,[48] Z. Du,[85] M. Ducrot,[8] R. Dudi,[36] P. Dupej,[47] S. E. Dwyer,[48] T. B. Edo,[109] M. C. Edwards,[75] A. Effler,[7] H.-B. Eggenstein,[38,10] P. Ehrens,[1] J. Eichholz,[1] S. S. Eikenberry,[5] R. A. Eisenstein,[15] R. C. Essick,[15] D. Estevez,[8] Z. B. Etienne,[42] T. Etzel,[1] M. Evans,[15] T. M. Evans,[7] M. Factourovich,[52] V. Fafone,[32,33,17] H. Fair,[45] S. Fairhurst,[36] X. Fan,[85] S. Farinon,[63] B. Farr,[94] W. M. Farr,[62] E. J. Fauchon-Jones,[36] M. Favata,[112] M. Fays,[36] C. Fee,[87] H. Fehrmann,[10] J. Feicht,[1] M. M. Fejer,[53] A. Fernandez-Galiana,[15] I. Ferrante,[23,24] E. C. Ferreira,[16] F. Ferrini,[30] F. Fidecaro,[23,24] D. Finstad,[45] I. Fiori,[30] D. Fiorucci,[39] M. Fishbach,[94] R. P. Fisher,[45] M. Fitz-Axen,[46] R. Flaminio,[26,113] M. Fletcher,[47] H. Fong,[93] J. A. Font,[88,114] P. W. F. Forsyth,[25] S. S. Forsyth,[80] J.-D. Fournier,[70] S. Frasca,[100,35] F. Frasconi,[24] Z. Frei,[57] A. Freise,[62] R. Frey,[73] V. Frey,[28] E. M. Fries,[1] P. Fritschel,[15] V. V. Frolov,[7] P. Fulda,[5] M. Fyffe,[7] H. Gabbard,[47] B. U. Gadre,[19] S. M. Gaebel,[62] J. R. Gair,[115] L. Gammaitoni,[43] M. R. Ganija,[76] S. G. Gaonkar,[19] C. Garcia-Quiros,[105] F. Garufi,[82,4] B. Gateley,[48] S. Gaudio,[37] G. Gaur,[116] V. Gayathri,[117] N. Gehrels,[51,†] G. Gemme,[63] E. Genin,[30] A. Gennai,[24] D. George,[12] J. George,[64] L. Gergely,[118] V. Germain,[8] S. Ghonge,[80] Abhirup Ghosh,[20] Archisman Ghosh,[20,14] S. Ghosh,[69,14,21] J. A. Giaime,[2,7] K. D. Giardina,[7] A. Giazotto,[24] K. Gill,[37] L. Glover,[110] E. Goetz,[119] R. Goetz,[5] S. Gomes,[36] B. Goncharov,[6] G. González,[2] J. M. Gonzalez Castro,[23,24] A. Gopakumar,[120] M. L. Gorodetsky,[65] S. E. Gossan,[1] M. Gosselin,[30] R. Gouaty,[8] A. Grado,[121,4] C. Graef,[47] M. Granata,[26] A. Grant,[47] S. Gras,[15] C. Gray,[48] G. Greco,[122,123] A. C. Green,[62] E. M. Gretarsson,[37] P. Groot,[69] H. Grote,[10] S. Grunewald,[38] P. Gruning,[28] G. M. Guidi,[122,123] X. Guo,[85] A. Gupta,[67] M. K. Gupta,[108] K. E. Gushwa,[1] E. K. Gustafson,[1] R. Gustafson,[119] O. Halim,[18,17] B. R. Hall,[72] E. D. Hall,[15] E. Z. Hamilton,[36] G. Hammond,[47] M. Haney,[124] M. M. Hanke,[10] J. Hanks,[48] C. Hanna,[67] M. D. Hannam,[36] O. A. Hannuksela,[96] J. Hanson,[7] T. Hardwick,[2] J. Harms,[17,18] G. M. Harry,[125] I. W. Harry,[38] M. J. Hart,[47] C.-J. Haster,[93] K. Haughian,[47] J. Healy,[61] A. Heidmann,[74] M. C. Heintze,[7] H. Heitmann,[70] P. Hello,[28] G. Hemming,[30] M. Hendry,[47] I. S. Heng,[47] J. Hennig,[47] A. W. Heptonstall,[1] M. Heurs,[10,22] S. Hild,[47] T. Hinderer,[69] W. C. G. Ho,[126] D. Hoak,[30] D. Hofman,[26] K. Holt,[7] D. E. Holz,[94] P. Hopkins,[36] C. Horst,[21] J. Hough,[47] E. A. Houston,[47] E. J. Howell,[68] A. Hreibi,[70] Y. M. Hu,[10] E. A. Huerta,[12] D. Huet,[28] B. Hughey,[37] S. Husa,[105] S. H. Huttner,[47] T. Huynh-Dinh,[7] N. Indik,[10] R. Inta,[86] G. Intini,[100,35] H. N. Isa,[47] J.-M. Isac,[74] M. Isi,[1] B. R. Iyer,[20] K. Izumi,[48] T. Jacqmin,[74] K. Jani,[80] P. Jaranowski,[127] S. Jawahar,[66] F. Jiménez-Forteza,[105] W. W. Johnson,[2] N. K. Johnson-McDaniel,[13] D. I. Jones,[126] R. Jones,[47] R. J. G. Jonker,[14] L. Ju,[68] J. Junker,[10] C. V. Kalaghatgi,[36] V. Kalogera,[92] B. Kamai,[1] S. Kandhasamy,[7] G. Kang,[40] J. B. Kanner,[1] S. J. Kapadia,[21] S. Karki,[73] K. S. Karvinen,[10] M. Kasprzack,[2] W. Kastaun,[10] M. Katolik,[12] E. Katsavounidis,[15] W. Katzman,[7] S. Kaufer,[22] K. Kawabe,[48] F. Kéfélian,[70] D. Keitel,[47] A. J. Kemball,[12] R. Kennedy,[109] C. Kent,[36] J. S. Key,[128] F. Y. Khalili,[65] I. Khan,[17,33] S. Khan,[10] Z. Khan,[108] E. A. Khazanov,[129] N. Kijbunchoo,[25] Chunglee Kim,[130] J. C. Kim,[131] K. Kim,[96] W. Kim,[76] W. S. Kim,[132] Y.-M. Kim,[95] S. J. Kimbrell,[80] E. J. King,[76] P. J. King,[48] M. Kinley-Hanlon,[125] R. Kirchhoff,[10] J. S. Kissel,[48] L. Kleybolte,[34] S. Klimenko,[5] T. D. Knowles,[42] P. Koch,[10] S. M. Koehlenbeck,[10] S. Koley,[14] V. Kondrashov,[1] A. Kontos,[15] M. Korobko,[34] W. Z. Korth,[1] I. Kowalska,[77] D. B. Kozak,[1] C. Krämer,[10] V. Kringel,[10] B. Krishnan,[10] A. Królak,[133,134] G. Kuehn,[10] P. Kumar,[93] R. Kumar,[108] S. Kumar,[20] L. Kuo,[90] A. Kutynia,[133] S. Kwang,[21] B. D. Lackey,[38] K. H. Lai,[96] M. Landry,[48] R. N. Lang,[135] J. Lange,[61] B. Lantz,[53] R. K. Lanza,[15] S. L. Larson,[92] A. Lartaux-Vollard,[28] P. D. Lasky,[6] M. Laxen,[7] A. Lazzarini,[1] C. Lazzaro,[56] P. Leaci,[100,35] S. Leavey,[47] C. H. Lee,[95] H. K. Lee,[136] H. M. Lee,[137] H. W. Lee,[131] K. Lee,[47] J. Lehmann,[10] A. Lenon,[42] E. Leon,[29] M. Leonardi,[111,98] N. Leroy,[28] N. Letendre,[8] Y. Levin,[6] T. G. F. Li,[96] S. D. Linker,[110] T. B. Littenberg,[138] J. Liu,[68] X. Liu,[21] R. K. L. Lo,[96] N. A. Lockerbie,[66] L. T. London,[36] J. E. Lord,[45] M. Lorenzini,[17,18] V. Loriette,[139] M. Lormand,[7] G. Losurdo,[24] J. D. Lough,[10] C. O. Lousto,[61] G. Lovelace,[29] H. Lück,[22,10] D. Lumaca,[32,33] A. P. Lundgren,[10] R. Lynch,[15] Y. Ma,[49] R. Macas,[36] S. Macfoy,[27] B. Machenschalk,[10] M. MacInnis,[15] D. M. Macleod,[36] I. Magaña Hernandez,[21] F. Magaña-Sandoval,[45] L. Magaña Zertuche,[45] R. M. Magee,[67] E. Majorana,[35] I. Maksimovic,[139] N. Man,[70] V. Mandic,[46] V. Mangano,[47]

G. L. Mansell,[25] M. Manske,[21,25] M. Mantovani,[30] F. Marchesoni,[54,44] F. Marion,[8] S. Márka,[52] Z. Márka,[52] C. Markakis,[12] A. S. Markosyan,[53] A. Markowitz,[1] E. Maros,[1] A. Marquina,[103] P. Marsh,[128] F. Martelli,[122,123] L. Martellini,[70] I. W. Martin,[47] R. M. Martin,[112] D. V. Martynov,[15] J. N. Marx,[1] K. Mason,[15] E. Massera,[109] A. Masserot,[8] T. J. Massinger,[1] M. Masso-Reid,[47] S. Mastrogiovanni,[100,35] A. Matas,[46] F. Matichard,[1,15] L. Matone,[52] N. Mavalvala,[15] N. Mazumder,[72] R. McCarthy,[48] D. E. McClelland,[25] S. McCormick,[7] L. McCuller,[15] S. C. McGuire,[140] G. McIntyre,[1] J. McIver,[1] D. J. McManus,[25] L. McNeill,[6] T. McRae,[25] S. T. McWilliams,[42] D. Meacher,[67] G. D. Meadors,[38,10] M. Mehmet,[10] J. Meidam,[14] E. Mejuto-Villa,[9] A. Melatos,[99] G. Mendell,[48] R. A. Mercer,[21] E. L. Merilh,[48] M. Merzougui,[70] S. Meshkov,[1] C. Messenger,[47] C. Messick,[67] R. Metzdorff,[74] P. M. Meyers,[46] H. Miao,[62] C. Michel,[26] H. Middleton,[62] E. E. Mikhailov,[141] L. Milano,[82,4] A. L. Miller,[5,100,35] B. B. Miller,[92] J. Miller,[15] M. Millhouse,[104] M. C. Milovich-Goff,[110] O. Minazzoli,[70,142] Y. Minenkov,[33] J. Ming,[38] C. Mishra,[143] S. Mitra,[19] V. P. Mitrofanov,[65] G. Mitselmakher,[5] R. Mittleman,[15] D. Moffa,[87] A. Moggi,[24] K. Mogushi,[11] M. Mohan,[30] S. R. P. Mohapatra,[15] I. Molina,[29] M. Montani,[122,123] C. J. Moore,[13] D. Moraru,[48] G. Moreno,[48] S. Morisaki,[84] S. R. Morriss,[106] B. Mours,[8] C. M. Mow-Lowry,[62] G. Mueller,[5] A. W. Muir,[36] Arunava Mukherjee,[10] D. Mukherjee,[21] S. Mukherjee,[106] N. Mukund,[19] A. Mullavey,[7] J. Munch,[76] E. A. Muñiz,[45] M. Muratore,[37] P. G. Murray,[47] A. Nagar,[89,144,145] K. Napier,[80] I. Nardecchia,[32,33] L. Naticchioni,[100,35] R. K. Nayak,[146] J. Neilson,[110] G. Nelemans,[69,14] T. J. N. Nelson,[7] M. Nery,[10] A. Neunzert,[119] L. Nevin,[1] J. M. Newport,[125] G. Newton,[47,‡] K. K. Y. Ng,[96] P. Nguyen,[73] T. T. Nguyen,[25] D. Nichols,[69] A. B. Nielsen,[10] S. Nissanke,[69,14] A. Nitz,[10] A. Noack,[10] F. Nocera,[30] D. Nolting,[7] C. North,[36] L. K. Nuttall,[36] J. Oberling,[48] G. D. O'Dea,[110] G. H. Ogin,[147] J. J. Oh,[132] S. H. Oh,[132] F. Ohme,[10] M. A. Okada,[16] M. Oliver,[105] P. Oppermann,[10] Richard J. Oram,[7] B. O'Reilly,[7] R. Ormiston,[46] L. F. Ortega,[5] R. O'Shaughnessy,[61] S. Ossokine,[38] D. J. Ottaway,[76] H. Overmier,[7] B. J. Owen,[86] A. E. Pace,[67] J. Page,[138] M. A. Page,[68] A. Pai,[117,148] S. A. Pai,[64] J. R. Palamos,[73] O. Palashov,[129] C. Palomba,[35] A. Pal-Singh,[34] Howard Pan,[90] Huang-Wei Pan,[90] B. Pang,[49] P. T. H. Pang,[96] C. Pankow,[92] F. Pannarale,[36] B. C. Pant,[64] F. Paoletti,[24] A. Paoli,[30] M. A. Papa,[38,21,10] A. Parida,[19] W. Parker,[7] D. Pascucci,[47] A. Pasqualetti,[30] R. Passaquieti,[23,24] D. Passuello,[24] M. Patil,[134] B. Patricelli,[149,24] B. L. Pearlstone,[47] M. Pedraza,[1] R. Pedurand,[26,150] L. Pekowsky,[45] A. Pele,[7] S. Penn,[151] C. J. Perez,[48] A. Perreca,[1,111,98] L. M. Perri,[92] H. P. Pfeiffer,[93,38] M. Phelps,[47] O. J. Piccinni,[100,35] M. Pichot,[70] F. Piergiovanni,[122,123] V. Pierro,[9] G. Pillant,[30] L. Pinard,[26] I. M. Pinto,[9] M. Pirello,[48] M. Pitkin,[47] M. Poe,[21] R. Poggiani,[23,24] P. Popolizio,[30] E. K. Porter,[39] A. Post,[10] J. Powell,[47,41] J. Prasad,[19] J. W. W. Pratt,[37] G. Pratten,[105] V. Predoi,[36] T. Prestegard,[21] M. Prijatelj,[10] M. Principe,[9] S. Privitera,[38] R. Prix,[10] G. A. Prodi,[111,98] L. G. Prokhorov,[65] O. Puncken,[10] M. Punturo,[44] P. Puppo,[35] M. Pürrer,[38] H. Qi,[21] V. Quetschke,[106] E. A. Quintero,[1] R. Quitzow-James,[73] F. J. Raab,[48] D. S. Rabeling,[25] H. Radkins,[48] P. Raffai,[57] S. Raja,[64] C. Rajan,[64] B. Rajbhandari,[86] M. Rakhmanov,[106] K. E. Ramirez,[106] A. Ramos-Buades,[105] P. Rapagnani,[100,35] V. Raymond,[38] M. Razzano,[23,24] J. Read,[29] T. Regimbau,[70] L. Rei,[63] S. Reid,[66] D. H. Reitze,[1,5] W. Ren,[12] S. D. Reyes,[45] F. Ricci,[100,35] P. M. Ricker,[12] S. Rieger,[10] K. Riles,[119] M. Rizzo,[61] N. A. Robertson,[1,47] R. Robie,[47] F. Robinet,[28] A. Rocchi,[33] L. Rolland,[8] J. G. Rollins,[1] V. J. Roma,[73] J. D. Romano,[106] R. Romano,[3,4] C. L. Romel,[48] J. H. Romie,[7] D. Rosińska,[152,58] M. P. Ross,[153] S. Rowan,[47] A. Rüdiger,[10] P. Ruggi,[30] G. Rutins,[27] K. Ryan,[48] S. Sachdev,[1] T. Sadecki,[48] L. Sadeghian,[21] M. Sakellariadou,[154] L. Salconi,[30] M. Saleem,[117] F. Salemi,[10] A. Samajdar,[146] L. Sammut,[6] L. M. Sampson,[92] E. J. Sanchez,[1] L. E. Sanchez,[1] N. Sanchis-Gual,[88] V. Sandberg,[48] J. R. Sanders,[45] B. Sassolas,[26] B. S. Sathyaprakash,[67,36] P. R. Saulson,[45] O. Sauter,[119] R. L. Savage,[48] A. Sawadsky,[34] P. Schale,[73] M. Scheel,[49] J. Scheuer,[92] J. Schmidt,[10] P. Schmidt,[1,69] R. Schnabel,[34] R. M. S. Schofield,[73] A. Schönbeck,[34] E. Schreiber,[10] D. Schuette,[10,22] B. W. Schulte,[10] B. F. Schutz,[36,10] S. G. Schwalbe,[37] J. Scott,[47] S. M. Scott,[25] E. Seidel,[12] D. Sellers,[7] A. S. Sengupta,[155] D. Sentenac,[30] V. Sequino,[32,33,17] A. Sergeev,[129] D. A. Shaddock,[25] T. J. Shaffer,[48] A. A. Shah,[138] M. S. Shahriar,[92] M. B. Shaner,[110] L. Shao,[38] B. Shapiro,[53] P. Shawhan,[79] A. Sheperd,[21] D. H. Shoemaker,[15] D. M. Shoemaker,[80] K. Siellez,[80] X. Siemens,[21] M. Sieniawska,[58] D. Sigg,[48] A. D. Silva,[16] L. P. Singer,[51] A. Singh,[38,10,22] A. Singhal,[17,35] A. M. Sintes,[105] B. J. J. Slagmolen,[25] B. Smith,[7] J. R. Smith,[29] R. J. E. Smith,[1,6] S. Somala,[156] E. J. Son,[132] J. A. Sonnenberg,[21] B. Sorazu,[47] F. Sorrentino,[63] T. Souradeep,[19] A. P. Spencer,[47] A. K. Srivastava,[108] K. Staats,[37] A. Staley,[52] M. Steinke,[10] J. Steinlechner,[34,47] S. Steinlechner,[34] D. Steinmeyer,[10] S. P. Stevenson,[62,41] R. Stone,[106] D. J. Stops,[62] K. A. Strain,[47] G. Stratta,[122,123] S. E. Strigin,[65] A. Strunk,[48] R. Sturani,[157] A. L. Stuver,[7] T. Z. Summerscales,[158] L. Sun,[99] S. Sunil,[108] J. Suresh,[19] P. J. Sutton,[36] B. L. Swinkels,[30] M. J. Szczepańczyk,[37] M. Tacca,[14] S. C. Tait,[47] C. Talbot,[6] D. Talukder,[73] D. B. Tanner,[5] M. Tápai,[118] A. Taracchini,[38] J. D. Tasson,[75] J. A. Taylor,[138] R. Taylor,[1] S. V. Tewari,[151] T. Theeg,[10] F. Thies,[10] E. G. Thomas,[62] M. Thomas,[7] P. Thomas,[48] K. A. Thorne,[7] K. S. Thorne,[49] E. Thrane,[6] S. Tiwari,[17,98] V. Tiwari,[36] K. V. Tokmakov,[66] K. Toland,[47] M. Tonelli,[23,24] Z. Tornasi,[47] A. Torres-Forné,[88] C. I. Torrie,[1] D. Töyrä,[62] F. Travasso,[30,44] G. Traylor,[7] J. Trinastic,[5] M. C. Tringali,[111,98]

L. Trozzo,[159,24] K. W. Tsang,[14] M. Tse,[15] R. Tso,[1] L. Tsukada,[84] D. Tsuna,[84] D. Tuyenbayev,[106] K. Ueno,[21] D. Ugolini,[160] C. S. Unnikrishnan,[120] A. L. Urban,[1] S. A. Usman,[36] H. Vahlbruch,[22] G. Vajente,[1] G. Valdes,[2] M. Vallisneri,[49] N. van Bakel,[14] M. van Beuzekom,[14] J. F. J. van den Brand,[78,14] C. Van Den Broeck,[14] D. C. Vander-Hyde,[45] L. van der Schaaf,[14] J. V. van Heijningen,[14] A. A. van Veggel,[47] M. Vardaro,[55,56] V. Varma,[49] S. Vass,[1] M. Vasúth,[50] A. Vecchio,[62] G. Vedovato,[56] J. Veitch,[47] P. J. Veitch,[76] K. Venkateswara,[153] G. Venugopalan,[1] D. Verkindt,[8] F. Vetrano,[122,123] A. Viceré,[122,123] A. D. Viets,[21] S. Vinciguerra,[62] D. J. Vine,[27] J.-Y. Vinet,[70] S. Vitale,[15] T. Vo,[45] H. Vocca,[43,44] C. Vorvick,[48] S. P. Vyatchanin,[65] A. R. Wade,[1] L. E. Wade,[87] M. Wade,[87] R. Walet,[14] M. Walker,[29] L. Wallace,[1] S. Walsh,[38,10,21] G. Wang,[17,123] H. Wang,[62] J. Z. Wang,[67] W. H. Wang,[106] Y. F. Wang,[96] R. L. Ward,[25] J. Warner,[48] M. Was,[8] J. Watchi,[101] B. Weaver,[48] L.-W. Wei,[10,22] M. Weinert,[10] A. J. Weinstein,[1] R. Weiss,[15] L. Wen,[68] E. K. Wessel,[12] P. Weßels,[10] J. Westerweck,[10] T. Westphal,[10] K. Wette,[25] J. T. Whelan,[61] S. E. Whitcomb,[1] B. F. Whiting,[5] C. Whittle,[6] D. Wilken,[10] D. Williams,[47] R. D. Williams,[1] A. R. Williamson,[69] J. L. Willis,[1,161] B. Willke,[22,10] M. H. Wimmer,[10] W. Winkler,[10] C. C. Wipf,[1] H. Wittel,[10,22] G. Woan,[47] J. Woehler,[10] J. Wofford,[61] K. W. K. Wong,[96] J. Worden,[48] J. L. Wright,[47] D. S. Wu,[10] D. M. Wysocki,[61] S. Xiao,[1] H. Yamamoto,[1] C. C. Yancey,[79] L. Yang,[162] M. J. Yap,[25] M. Yazback,[5] Hang Yu,[15] Haocun Yu,[15] M. Yvert,[8] A. Zadrożny,[133] M. Zanolin,[37] T. Zelenova,[30] J.-P. Zendri,[56] M. Zevin,[92] L. Zhang,[1] M. Zhang,[141] T. Zhang,[47] Y.-H. Zhang,[61] C. Zhao,[68] M. Zhou,[92] Z. Zhou,[92] S. J. Zhu,[38,10] X. J. Zhu,[6] A. B. Zimmerman,[93] M. E. Zucker,[1,15] and J. Zweizig[1]

(LIGO Scientific Collaboration and Virgo Collaboration)

[1]*LIGO, California Institute of Technology, Pasadena, California 91125, USA*
[2]*Louisiana State University, Baton Rouge, Louisiana 70803, USA*
[3]*Università di Salerno, Fisciano, I-84084 Salerno, Italy*
[4]*INFN, Sezione di Napoli, Complesso Universitario di Monte S.Angelo, I-80126 Napoli, Italy*
[5]*University of Florida, Gainesville, Florida 32611, USA*
[6]*OzGrav, School of Physics & Astronomy, Monash University, Clayton 3800, Victoria, Australia*
[7]*LIGO Livingston Observatory, Livingston, Louisiana 70754, USA*
[8]*Laboratoire d'Annecy-le-Vieux de Physique des Particules (LAPP), Université Savoie Mont Blanc, CNRS/IN2P3, F-74941 Annecy, France*
[9]*University of Sannio at Benevento, I-82100 Benevento, Italy and INFN, Sezione di Napoli, I-80100 Napoli, Italy*
[10]*Max Planck Institute for Gravitational Physics (Albert Einstein Institute), D-30167 Hannover, Germany*
[11]*The University of Mississippi, University, Mississippi 38677, USA*
[12]*NCSA, University of Illinois at Urbana-Champaign, Urbana, Illinois 61801, USA*
[13]*University of Cambridge, Cambridge CB2 1TN, United Kingdom*
[14]*Nikhef, Science Park, 1098 XG Amsterdam, Netherlands*
[15]*LIGO, Massachusetts Institute of Technology, Cambridge, Massachusetts 02139, USA*
[16]*Instituto Nacional de Pesquisas Espaciais, 12227-010 São José dos Campos, São Paulo, Brazil*
[17]*Gran Sasso Science Institute (GSSI), I-67100 L'Aquila, Italy*
[18]*INFN, Laboratori Nazionali del Gran Sasso, I-67100 Assergi, Italy*
[19]*Inter-University Centre for Astronomy and Astrophysics, Pune 411007, India*
[20]*International Centre for Theoretical Sciences, Tata Institute of Fundamental Research, Bengaluru 560089, India*
[21]*University of Wisconsin-Milwaukee, Milwaukee, Wisconsin 53201, USA*
[22]*Leibniz Universität Hannover, D-30167 Hannover, Germany*
[23]*Università di Pisa, I-56127 Pisa, Italy*
[24]*INFN, Sezione di Pisa, I-56127 Pisa, Italy*
[25]*OzGrav, Australian National University, Canberra, Australian Capital Territory 0200, Australia*
[26]*Laboratoire des Matériaux Avancés (LMA), CNRS/IN2P3, F-69622 Villeurbanne, France*
[27]*SUPA, University of the West of Scotland, Paisley PA1 2BE, United Kingdom*
[28]*LAL, Univ. Paris-Sud, CNRS/IN2P3, Université Paris-Saclay, F-91898 Orsay, France*
[29]*California State University Fullerton, Fullerton, California 92831, USA*
[30]*European Gravitational Observatory (EGO), I-56021 Cascina, Pisa, Italy*
[31]*Chennai Mathematical Institute, Chennai 603103, India*
[32]*Università di Roma Tor Vergata, I-00133 Roma, Italy*
[33]*INFN, Sezione di Roma Tor Vergata, I-00133 Roma, Italy*
[34]*Universität Hamburg, D-22761 Hamburg, Germany*
[35]*INFN, Sezione di Roma, I-00185 Roma, Italy*

[36]Cardiff University, Cardiff CF24 3AA, United Kingdom
[37]Embry-Riddle Aeronautical University, Prescott, Arizona 86301, USA
[38]Max Planck Institute for Gravitationalphysik (Albert Einstein Institute), D-14476 Potsdam-Golm, Germany
[39]APC, AstroParticule et Cosmologie, Université Paris Diderot, CNRS/IN2P3, CEA/Irfu, Observatoire de Paris, Sorbonne Paris Cité, F-75205 Paris Cedex 13, France
[40]Korea Institute of Science and Technology Information, Daejeon 34141, Korea
[41]OzGrav, Swinburne University of Technology, Hawthorn VIC 3122, Australia
[42]West Virginia University, Morgantown, West Virginia 26506, USA
[43]Università di Perugia, I-06123 Perugia, Italy
[44]INFN, Sezione di Perugia, I-06123 Perugia, Italy
[45]Syracuse University, Syracuse, New York 13244, USA
[46]University of Minnesota, Minneapolis, Minnesota 55455, USA
[47]SUPA, University of Glasgow, Glasgow G12 8QQ, United Kingdom
[48]LIGO Hanford Observatory, Richland, Washington 99352, USA
[49]Caltech CaRT, Pasadena, California 91125, USA
[50]Wigner RCP, RMKI, H-1121 Budapest, Konkoly Thege Miklós út 29-33, Hungary
[51]NASA Goddard Space Flight Center, Greenbelt, Maryland 20771, USA
[52]Columbia University, New York, New York 10027, USA
[53]Stanford University, Stanford, California 94305, USA
[54]Università di Camerino, Dipartimento di Fisica, I-62032 Camerino, Italy
[55]Università di Padova, Dipartimento di Fisica e Astronomia, I-35131 Padova, Italy
[56]INFN, Sezione di Padova, I-35131 Padova, Italy
[57]Institute of Physics, Eötvös University, Pázmány P. s. 1/A, Budapest 1117, Hungary
[58]Nicolaus Copernicus Astronomical Center, Polish Academy of Sciences, 00-716, Warsaw, Poland
[59]Dipartimento di Scienze Matematiche, Fisiche e Informatiche, Università di Parma, I-43124 Parma, Italy
[60]INFN, Sezione di Milano Bicocca, Gruppo Collegato di Parma, I-43124 Parma, Italy
[61]Rochester Institute of Technology, Rochester, New York 14623, USA
[62]University of Birmingham, Birmingham B15 2TT, United Kingdom
[63]INFN, Sezione di Genova, I-16146 Genova, Italy
[64]RRCAT, Indore MP 452013, India
[65]Faculty of Physics, Lomonosov Moscow State University, Moscow 119991, Russia
[66]SUPA, University of Strathclyde, Glasgow G1 1XQ, United Kingdom
[67]The Pennsylvania State University, University Park, Pennsylvania 16802, USA
[68]OzGrav, University of Western Australia, Crawley, Western Australia 6009, Australia
[69]Department of Astrophysics/IMAPP, Radboud University Nijmegen, P.O. Box 9010, 6500 GL Nijmegen, Netherlands
[70]Artemis, Université Côte d'Azur, Observatoire Côte d'Azur, CNRS, CS 34229, F-06304 Nice Cedex 4, France
[71]Institut FOTON, CNRS, Université de Rennes 1, F-35042 Rennes, France
[72]Washington State University, Pullman, Washington 99164, USA
[73]University of Oregon, Eugene, Oregon 97403, USA
[74]Laboratoire Kastler Brossel, UPMC-Sorbonne Universités, CNRS, ENS-PSL Research University, Collège de France, F-75005 Paris, France
[75]Carleton College, Northfield, Minnesota 55057, USA
[76]OzGrav, University of Adelaide, Adelaide, South Australia 5005, Australia
[77]Astronomical Observatory Warsaw University, 00-478 Warsaw, Poland
[78]VU University Amsterdam, 1081 HV Amsterdam, Netherlands
[79]University of Maryland, College Park, Maryland 20742, USA
[80]Center for Relativistic Astrophysics, Georgia Institute of Technology, Atlanta, Georgia 30332, USA
[81]Université Claude Bernard Lyon 1, F-69622 Villeurbanne, France
[82]Università di Napoli "Federico II", Complesso Universitario di Monte S.Angelo, I-80126 Napoli, Italy
[83]Dipartimento di Fisica, Università degli Studi di Genova, I-16146 Genova, Italy
[84]RESCEU, University of Tokyo, Tokyo, 113-0033, Japan
[85]Tsinghua University, Beijing 100084, China
[86]Texas Tech University, Lubbock, Texas 79409, USA
[87]Kenyon College, Gambier, Ohio 43022, USA
[88]Departamento de Astronomía y Astrofísica, Universitat de València, E-46100 Burjassot, València, Spain
[89]Museo Storico della Fisica e Centro Studi e Ricerche Enrico Fermi, I-00184 Roma, Italy
[90]National Tsing Hua University, Hsinchu City, 30013 Taiwan, Republic of China
[91]Charles Sturt University, Wagga Wagga, New South Wales 2678, Australia
[92]Center for Interdisciplinary Exploration & Research in Astrophysics (CIERA), Northwestern University, Evanston, Illinois 60208, USA

[93]Canadian Institute for Theoretical Astrophysics, University of Toronto, Toronto, Ontario M5S 3H8, Canada
[94]University of Chicago, Chicago, Illinois 60637, USA
[95]Pusan National University, Busan 46241, Korea
[96]The Chinese University of Hong Kong, Shatin, NT, Hong Kong
[97]INAF, Osservatorio Astronomico di Padova, I-35122 Padova, Italy
[98]INFN, Trento Institute for Fundamental Physics and Applications, I-38123 Povo, Trento, Italy
[99]OzGrav, University of Melbourne, Parkville, Victoria 3010, Australia
[100]Università di Roma "La Sapienza", I-00185 Roma, Italy
[101]Université Libre de Bruxelles, Brussels 1050, Belgium
[102]Sonoma State University, Rohnert Park, California 94928, USA
[103]Departamento de Matemáticas, Universitat de València, E-46100 Burjassot, València, Spain
[104]Montana State University, Bozeman, Montana 59717, USA
[105]Universitat de les Illes Balears, IAC3—IEEC, E-07122 Palma de Mallorca, Spain
[106]The University of Texas Rio Grande Valley, Brownsville, Texas 78520, USA
[107]Bellevue College, Bellevue, Washington 98007, USA
[108]Institute for Plasma Research, Bhat, Gandhinagar 382428, India
[109]The University of Sheffield, Sheffield S10 2TN, United Kingdom
[110]California State University, Los Angeles, 5151 State University Drive, Los Angeles, California 90032, USA
[111]Università di Trento, Dipartimento di Fisica, I-38123 Povo, Trento, Italy
[112]Montclair State University, Montclair, New Jersey 07043, USA
[113]National Astronomical Observatory of Japan, 2-21-1 Osawa, Mitaka, Tokyo 181-8588, Japan
[114]Observatori Astronòmic, Universitat de València, E-46980 Paterna, València, Spain
[115]School of Mathematics, University of Edinburgh, Edinburgh EH9 3FD, United Kingdom
[116]University and Institute of Advanced Research, Koba Institutional Area, Gandhinagar Gujarat 382007, India
[117]IISER-TVM, CET Campus, Trivandrum Kerala 695016, India
[118]University of Szeged, Dóm tér 9, Szeged 6720, Hungary
[119]University of Michigan, Ann Arbor, Michigan 48109, USA
[120]Tata Institute of Fundamental Research, Mumbai 400005, India
[121]INAF, Osservatorio Astronomico di Capodimonte, I-80131, Napoli, Italy
[122]Università degli Studi di Urbino "Carlo Bo" I-61029 Urbino, Italy
[123]INFN, Sezione di Firenze, I-50019 Sesto Fiorentino, Firenze, Italy
[124]Physik-Institut, University of Zurich, Winterthurerstrasse 190, 8057 Zurich, Switzerland
[125]American University, Washington, DC 20016, USA
[126]University of Southampton, Southampton SO17 1BJ, United Kingdom
[127]University of Biał ystok, 15-424 Biał ystok, Poland
[128]University of Washington Bothell, 18115 Campus Way NE, Bothell, Washington 98011, USA
[129]Institute of Applied Physics, Nizhny Novgorod, 603950, Russia
[130]Korea Astronomy and Space Science Institute, Daejeon 34055, Korea
[131]Inje University Gimhae, South Gyeongsang 50834, Korea
[132]National Institute for Mathematical Sciences, Daejeon 34047, Korea
[133]NCBJ, 05-400 Świerk-Otwock, Poland
[134]Institute of Mathematics, Polish Academy of Sciences, 00656 Warsaw, Poland
[135]Hillsdale College, Hillsdale, Michigan 49242, USA
[136]Hanyang University, Seoul 04763, Korea
[137]Seoul National University, Seoul 08826, Korea
[138]NASA Marshall Space Flight Center, Huntsville, Alabama 35811, USA
[139]ESPCI, CNRS, F-75005 Paris, France
[140]Southern University and A&M College, Baton Rouge, Louisiana 70813, USA
[141]College of William and Mary, Williamsburg, Virginia 23187, USA
[142]Centre Scientifique de Monaco, 8 quai Antoine Ier, MC-98000, Monaco
[143]Indian Institute of Technology Madras, Chennai 600036, India
[144]INFN Sezione di Torino, I-10125 Torino, Italy
[145]Institut des Hautes Etudes Scientifiques, F-91440 Bures-sur-Yvette, France
[146]IISER-Kolkata, Mohanpur, West Bengal 741252, India
[147]Whitman College, 345 Boyer Avenue, Walla Walla, Washington 99362 USA
[148]Indian Institute of Technology Bombay, Powai, Mumbai, Maharashtra 400076, India
[149]Scuola Normale Superiore, Piazza dei Cavalieri 7, I-56126 Pisa, Italy
[150]Université de Lyon, F-69361 Lyon, France
[151]Hobart and William Smith Colleges, Geneva, New York 14456, USA
[152]Janusz Gil Institute of Astronomy, University of Zielona Góra, 65-265 Zielona Góra, Poland

[153]University of Washington, Seattle, Washington 98195, USA
[154]King's College London, University of London, London WC2R 2LS, United Kingdom
[155]Indian Institute of Technology, Gandhinagar Ahmedabad Gujarat 382424, India
[156]Indian Institute of Technology Hyderabad, Sangareddy, Khandi, Telangana 502285, India
[157]International Institute of Physics, Universidade Federal do Rio Grande do Norte, Natal RN 59078-970, Brazil
[158]Andrews University, Berrien Springs, Michigan 49104, USA
[159]Università di Siena, I-53100 Siena, Italy
[160]Trinity University, San Antonio, Texas 78212, USA
[161]Abilene Christian University, Abilene, Texas 79699, USA
[162]Colorado State University, Fort Collins, Colorado 80523, USA

[†]Deceased, February 2017.
[‡]Deceased, December 2016.

Properties of the Binary Neutron Star Merger GW170817

B. P. Abbott *et al.*[*]
(LIGO Scientific Collaboration and Virgo Collaboration)

(Received 6 June 2018; revised manuscript received 20 September 2018; published 2 January 2019; corrected 30 April 2019)

On August 17, 2017, the Advanced LIGO and Advanced Virgo gravitational-wave detectors observed a low-mass compact binary inspiral. The initial sky localization of the source of the gravitational-wave signal, GW170817, allowed electromagnetic observatories to identify NGC 4993 as the host galaxy. In this work, we improve initial estimates of the binary's properties, including component masses, spins, and tidal parameters, using the known source location, improved modeling, and recalibrated Virgo data. We extend the range of gravitational-wave frequencies considered down to 23 Hz, compared to 30 Hz in the initial analysis. We also compare results inferred using several signal models, which are more accurate and incorporate additional physical effects as compared to the initial analysis. We improve the localization of the gravitational-wave source to a 90% credible region of 16 deg^2. We find tighter constraints on the masses, spins, and tidal parameters, and continue to find no evidence for nonzero component spins. The component masses are inferred to lie between 1.00 and 1.89 $M_\odot$ when allowing for large component spins, and to lie between 1.16 and 1.60 $M_\odot$ (with a total mass $2.73^{+0.04}_{-0.01}$ $M_\odot$) when the spins are restricted to be within the range observed in Galactic binary neutron stars. Using a precessing model and allowing for large component spins, we constrain the dimensionless spins of the components to be less than 0.50 for the primary and 0.61 for the secondary. Under minimal assumptions about the nature of the compact objects, our constraints for the tidal deformability parameter $\tilde{\Lambda}$ are (0,630) when we allow for large component spins, and 300^{+420}_{-230} (using a 90% highest posterior density interval) when restricting the magnitude of the component spins, ruling out several equation-of-state models at the 90% credible level. Finally, with LIGO and GEO600 data, we use a Bayesian analysis to place upper limits on the amplitude and spectral energy density of a possible postmerger signal.

DOI: 10.1103/PhysRevX.9.011001 Subject Areas: Astrophysics, Gravitation

I. INTRODUCTION

On August 17, 2017, the advanced gravitational-wave (GW) detector network, consisting of the two Advanced LIGO detectors [1] and Advanced Virgo [2], observed the compact binary inspiral event GW170817 [3] with a total mass less than any previously observed binary coalescence and a matched-filter signal-to-noise ratio (SNR) of 32.4, louder than any signal to date. Follow-up Bayesian parameter inference allowed GW170817 to be localized to a relatively small sky area of 28 deg^2 and revealed component masses consistent with those of binary neutron star (BNS) systems. In addition, 1.7 s after the binary's coalescence time, the Fermi and INTEGRAL gamma-ray telescopes observed the gamma-ray burst GRB 170817A with an inferred sky location consistent with that measured for GW170817 [4], providing initial evidence that the binary system contained neutron star (NS) matter.

Astronomers followed up on the prompt alerts produced by this signal, and within 11 hours the transient SSS17a/AT 2017gfo was discovered [5,6] and independently observed by multiple instruments [7–11], localizing the source of GW170817 to the galaxy NGC 4993. The identification of the host galaxy drove an extensive follow-up campaign [12], and analysis of the fast-evolving optical, ultraviolet, and infrared emission was consistent with that predicted for a kilonova [13–17] powered by the radioactive decay of *r*-process nuclei synthesized in the ejecta (see Refs. [18–28] for early analyses). The electromagnetic (EM) signature, observed throughout the entire spectrum, provides further evidence that GW170817 was produced by the merger of a BNS system (see, e.g., Refs. [29–31]).

According to general relativity, the gravitational waves emitted by inspiraling compact objects in a quasicircular orbit are characterized by a chirplike time evolution in their frequency that depends primarily on a combination of the component masses called the chirp mass [32] and secondarily on the mass ratio and spins of the components. In contrast to binary black hole (BBH) systems, the internal structure of the NS also impacts the waveform and needs to

[*]Full author list given at the end of the article.

Published by the American Physical Society under the terms of the Creative Commons Attribution 4.0 International license. Further distribution of this work must maintain attribution to the author(s) and the published article's title, journal citation, and DOI.

be included for a proper description of the binary evolution. The internal structure can be probed primarily through attractive tidal interactions that lead to an accelerated inspiral. These tidal interactions are small at lower GW frequencies but increase rapidly in strength during the final tens of GW cycles before merger. Although tidal effects are small relative to other effects, their distinct behavior makes them potentially measurable from the GW signal [33–37], providing additional evidence for a BNS system and insight into the internal structure of NSs.

In this work, we present improved constraints on the binary parameters first presented in Ref. [3]. These improvements are enabled by (i) recalibrated Virgo data [38], (ii) a broader frequency band of 23–2048 Hz as compared to the original 30–2048 Hz band used in Ref. [3], (iii) a wider range of more sophisticated waveform models (see Table I), and (iv) knowledge of the source location from EM observations. By extending the bandwidth from 30–2048 Hz to 23–2048 Hz, we gain access to an additional about 1500 waveform cycles compared to the about 2700 cycles in the previous analysis. Overall, our results for the parameters of GW170817 are consistent with, but more precise than, those in the initial analysis [3]. The main improvements are (i) improved 90% sky localization from 28 deg^2 to 16 deg^2 without use of EM observations, (ii) improved constraint on inclination angle enabled by independent measurements of the luminosity distance to NGC 4993, (iii) limits on precession from a new waveform model that includes both precession and tidal effects, and (iv) evidence for a nonzero tidal deformability parameter that is seen in all waveform models. Finally, we analyze the potential postmerger signal with an unmodeled Bayesian inference method [39] using data from the Advanced LIGO detectors and the GEO600 detector [40]. This method allows us to place improved upper bounds on the amount of postmerger GW emission from GW170817 [41].

As in the initial analysis of GW170817 [3], we infer the binary parameters from the inspiral signal while making minimal assumptions about the nature of the compact objects, in particular, allowing the tidal deformability of each object to vary independently. We allow for a large range of tidal deformabilities in our analysis, including zero, which means that our analysis includes the possibility of phase transitions within the stars and allows for exotic compact objects or even for black holes as binary components. In a companion paper [42], we present a complementary analysis assuming that both compact objects are NSs obeying a common equation of state (EOS). This analysis results in stronger constraints on the tidal deformabilities of the NSs than we can make under our minimal assumptions, and it allows us to constrain the radii of the NSs and make for novel inferences about the equation of state of cold matter at supranuclear densities.

This paper is organized as follows. Section II details the updated analysis, including improvements to the instrument calibration, improved waveform models, and additional constraints on the source location. Section III reports the improved constraints on the binary's sky location, inclination angle, masses, spins, and tidal parameters. Section IV provides upper limits on possible GW emission after the binary merger. Finally, Sec. V summarizes the results and highlights remaining work such as inference of the NS radius and EOS. Additional results from a range of waveform models are reported in Appendix A, and an injection and recovery study investigating the systematic errors in our waveform models is given in Appendix B.

II. METHODS

A. Bayesian method

All available information about the source parameters $\vec{\vartheta}$ of GW170817 can be expressed as a posterior probability density function (PDF) $p(\vec{\vartheta}|d(t))$ given the data $d(t)$ from the GW detectors. Through application of Bayes' theorem, this posterior PDF is proportional to the product of the likelihood $\mathcal{L}(d(t)|\vec{\vartheta})$ of observing data $d(t)$ given the waveform model described by $\vec{\vartheta}$ and the prior PDF $p(\vec{\vartheta})$ of observing those parameters. Marginalized posteriors are computed through stochastic sampling using an implementation of Markov-chain Monte Carlo algorithm [43,44] available in the LALInference package [45] as part of the LSC Algorithm Library (LAL) [46]. By marginalizing over all but one or two parameters, it is then possible to generate credible intervals or credible regions for those parameters.

B. Data

For each detector, we assume that the noise is additive, i.e., a data stream $d(t) = h^M(t;\vec{\vartheta}) + n(t)$ where $h^M(t;\vec{\vartheta})$ is the measured gravitational-wave strain and $n(t)$ is Gaussian and stationary noise characterized by the one-sided power spectral densities (PSDs) shown in Fig. 1. The PSD is defined as $S_n \equiv (2/T)\langle|\tilde{n}(f)|^2\rangle$, where $\tilde{n}(f)$ is the Fourier transform of $n(t)$ and the angle brackets indicate a time average over the duration of the analysis T, in this case the 128 s containing the $d(t)$ used for all results presented in Sec. III. This PSD is modeled as a cubic spline for the broadband structure and a sum of Lorentzians for the line features, using the BayesWave package [39,47], which produces a posterior PDF of PSDs. Here, we approximate the full structure and variation of these posteriors as a point estimate by using a median PSD, defined separately at each frequency.

The analyses presented here use the same data and calibration model for the LIGO detectors as Ref. [3], including subtraction of the instrumental glitch present in LIGO-Livingston (cf. Fig. 2 of Ref. [3]) and of other independently measured noise sources as described in

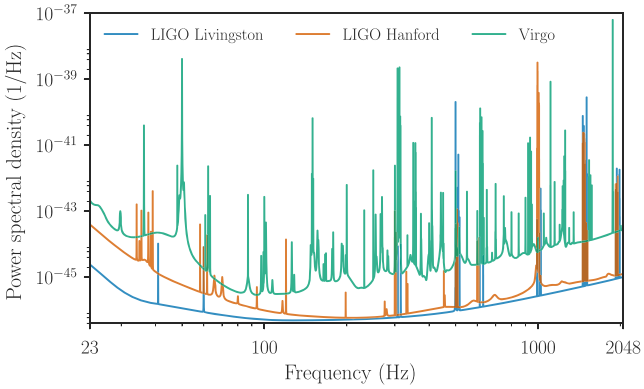

FIG. 1. PSDs of the Advanced LIGO–Advanced Virgo network. Shown, for each detector, is the median PSD computed from a posterior distribution of PSDs as estimated by BayesWave [39,47] using 128 s of data containing the signal GW170817.

Refs. [48–51]. The method used for subtracting the instrumental glitch leads to unbiased parameter recovery when applied to simulated signals injected on top of similar glitches in detector data [52]. The data from Virgo has been recalibrated since the publication of Ref. [3], including the subtraction of known noise sources during postprocessing of the data, following the procedure of Ref. [38] (the same as described in Sec. II of Ref. [53]). While the assumption of stationary, Gaussian noise in the detectors is not expected to hold over long timescales, our subtraction of the glitch, known noise sources, and recalibration of the Virgo data helps bring the data closer to this assumption. Applying the Anderson-Darling test to the data whitened by the on-source PSDs generated by BayesWave, we do not reject the null hypothesis that the whitened data are consistent with zero-mean, unit-variance, Gaussian noise $\mathcal{N}(0,1)$. The test returns p-values > 0.1 for the LIGO detectors' data. Meanwhile, the test is marginal when applied to the Virgo data, with $p \sim 0.01$. However, the information content of the data is dominated by the LIGO detectors, as they contained the large majority of the recovered signal power. The results of the Anderson-Darling tests support the use of the likelihood function as described in Ref. [45] for the signal characterization analyses reported in this paper.

The measured strain $h^M(t;\vec{\vartheta})$ may differ from the true GW strain $h(t;\vec{\vartheta})$ due to measured uncertainties in the detector calibration [54,55]. We relate the measured strain to the true GW strain with the expression [56,57]

$$\tilde{h}^M(f;\vec{\vartheta}) = \tilde{h}(f;\vec{\vartheta})[1+\delta A(f;\vec{\theta}^{\rm cal})]\exp[i\delta\phi(f;\vec{\theta}^{\rm cal})], \quad (1)$$

where $\tilde{h}^M(f;\vec{\vartheta})$ and $\tilde{h}(f;\vec{\vartheta})$ are the Fourier transforms of $h^M(t;\vec{\vartheta})$ and $h(t;\vec{\vartheta})$, respectively. The terms $\delta A(f;\vec{\theta}^{\rm cal})$ and $\delta\phi(f;\vec{\theta}^{\rm cal})$ are the frequency-dependent amplitude correction factor and phase correction factor, respectively, and are each modeled as cubic splines. For each detector, the parameters are the values of δA and $\delta\phi$ at each of ten spline nodes spaced uniformly in $\log f$ [58] between 23 and 2048 Hz.

For the LIGO detectors, the calibration parameters $\vec{\theta}^{\rm cal}$ are informed by direct measurements of the calibration uncertainties [54] and are modeled in the same way as in Ref. [3] with 1σ uncertainties of less than 7% in amplitude and less than 3 degrees in phase for LIGO Hanford and less than 5% in amplitude and less than 2 degrees in phase for LIGO Livingston, all allowing for a nonzero mean offset. The corresponding calibration parameters for Virgo follow Ref. [38], with a 1σ amplitude uncertainty of 8% and a 1σ phase uncertainty of 3 degrees. This is supplemented with an additional uncertainty in the time stamping of the data of 20 μs (to be compared to the LIGO timing uncertainty of less than 1 μs [59] already included in the phase correction factor). At each of the spline nodes, a Gaussian prior is used with these 1σ uncertainties and their corresponding means. By sampling these calibration parameters in addition to the waveform parameters, the calibration uncertainty is marginalized over. This marginalization broadens the localization posterior (Sec. III A) but

TABLE I. Waveform models employed to measure the source properties of GW170817. The models differ according to how they treat the inspiral in the absence of tidal corrections [i.e., the BBH-baseline—in particular, the point particle (PP), spin-orbit (SO), and spin-spin (SS) terms], the manner in which tidal corrections are applied, whether the spin-induced quadrupoles of the neutron stars [67–70,79] are incorporated, and whether the model allows for precession or only treats aligned spins. Our standard model, PhenomPNRT, incorporates effective-one-body (EOB)- and numerical relativity (NR)-tuned tidal effects, the spin-induced quadrupole moment, and precession.

Model name	Name in LALSuite	BBH baseline	Tidal effects	Spin-induced quadrupole effects	Precession
TaylorF2	TaylorF2	3.5PN (PP [60–65], SO [66] SS [67–70])	6PN [71]	None	✗
SEOBNRT	SEOBNRv4_ROM_NRTidal	SEOBNRv4_ROM [72,73]	NRTidal [74,75]	None	✗
PhenomDNRT	IMRPhenomD_NRTidal	IMRPhenomD [76,77]	NRTidal [74,75]	None	✗
PhenomPNRT	IMRPhenomPv2_NRTidal	IMRPhenomPv2 [78]	NRTidal [74,75]	3PN [67–70,79]	✓

does not significantly affect the recovered masses, spins, or tidal deformability parameters.

C. Waveform models for binary neutron stars

In this paper, we use four different frequency-domain waveform models which are fast enough to be used as templates in LALInference. These waveforms incorporate point-particle, spin, and tidal effects in different ways. We briefly describe them below. Each waveform's key features are stated in detail in Table I, and further tests of the performance of the waveform models can be found in Ref. [75]. In addition to these frequency domain models, we employ two state-of-the-art time-domain tidal EOB models that also include spin and tidal effects [80,81]. These tidal EOB models have shown good agreement in comparison with NR simulations [80–83] in the late inspiral and improve on the post-Newtonian (PN) dynamics in the early inspiral. However, these implementations are too slow for use in LALInference. We describe these models in Sec. III D when we discuss an alternative parameter-estimation code [84,85].

The TaylorF2 model used in previous work is a purely analytic PN model. It includes point-particle and aligned-spin terms to 3.5PN order as well as leading-order (5PN) and next-to-leading-order (6PN) tidal effects [34,60–71,86–88]. The other three waveform models begin with point-particle models and add a fit to the phase evolution from tidal effects, labeled NRTidal [74,75], that fit the high-frequency region to both an analytic EOB model [80] and NR simulations [74,89]. The SEOBNRT model is based on the aligned-spin point-particle EOB model presented in Ref. [72] using methods presented in Ref. [73] to allow fast evaluation in the frequency domain. PhenomDNRT is based on an aligned-spin point-particle model [76,77] calibrated to untuned EOB waveforms [90] and NR hybrids [76,77]. Finally, PhenomPNRT is based on the point-particle model presented in Ref. [78], which includes an effective description of precession effects. In addition to tidal effects, PhenomPNRT also includes the spin-induced quadrupole moment that enters in the phasing at 2PN order [91]. For aligned-spin systems, PhenomPNRT differs from PhenomDNRT only in the inclusion of the spin-induced quadrupole moment. We include the EOS dependence of each NS's spin-induced quadrupole moment by relating it to the tidal parameter of each NS using the quasi-universal relations of Ref. [92]. Although this 2PN effect can have a large phase contribution, even for small spins [37], it enters at similar PN order as many other terms. We therefore expect it to be degenerate with the mass ratio and spins.

These four waveform models have been compared to waveforms constructed by hybridizing BNS EOB inspiral waveforms [80,83] with NR waveforms [74,80,82,89] of the late inspiral and merger. Since only the PhenomPNRT model includes the spin-induced quadrupole moment, it was found that it has smaller mismatches than PhenomDNRT and SEOBNRT [75]. In addition, because PhenomPNRT is the only model that includes precession effects, we use it as our reference model throughout this paper.

In Fig. 2, we show differences in the amplitude and phase evolution between the four models for an equal-mass, nonspinning BNS system. The top panel shows the fractional difference in the amplitude $\Delta A/A$ between each model and PhenomPNRT, while the bottom panel shows the absolute phase difference $|\Delta\Phi|$ between each model and PhenomPNRT. Because none of the models have amplitude corrections from tidal effects, the amplitude differences between the models are entirely due to the underlying point-particle models. For the nonprecessing system shown here, PhenomPNRT and PhenomDNRT agree by construction, and the difference with SEOBNRT is also small. On the other hand, the purely analytic TaylorF2 model that has not been tuned to NR simulations deviates by up to 30% from the other models. For the phase evolution of nonspinning systems, PhenomDNRT, PhenomPNRT, and SEOBNRT have the same tidal prescription, so the small $\lesssim 2$ rad phase differences are due to the underlying point-particle models. For nonspinning systems PhenomDNRT and PhenomPNRT are the same, but for spinning systems, the spin-induced quadrupole moment included in PhenomPNRT but not in PhenomDNRT will cause an additional phase difference. For TaylorF2 the difference with respect to PhenomPNRT is due

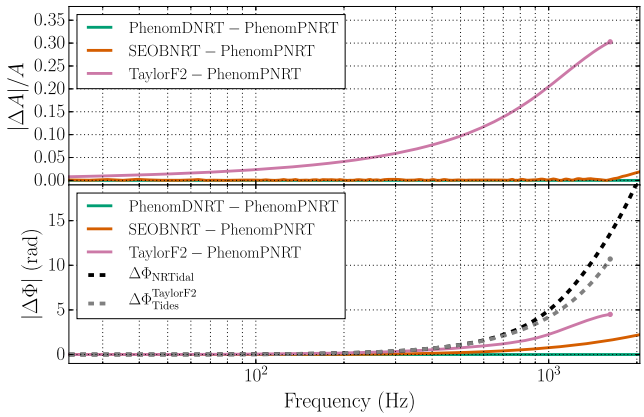

FIG. 2. Relative amplitude and phase of the employed waveform models starting at 23 Hz (see Table I) with respect to PhenomPNRT after alignment within the frequency interval [30, 30.25] Hz. Note that, in particular, the alignment between SEOBNRT and PhenomPNRT is sensitive to the chosen interval due to the difference in the underlying BBH-baseline models at early frequencies. We show, as an example, an equal-mass, nonspinning system with a total mass of 2.706 $M_\odot$ and a tidal deformability of $\tilde{\Lambda} = 400$. In the bottom panel, we also show the tidal contribution to the phasing for the TaylorF2 and the NRTidal models. This contribution can be interpreted as the phase difference between the tidal waveform models and the corresponding BBH models. The TaylorF2 waveform terminates at the frequency of the innermost stable circular orbit, which is marked by a small dot.

to both the underlying point-particle model and the tidal prescription, and it is about 5 rad for nonspinning systems.

For reference, we also show in Fig. 2 the tidal contribution to the phase for the NRTidal models ($\Delta\Phi_{\mathrm{NRTidal}}$) and the TaylorF2 model ($\Delta\Phi_{\mathrm{Tides}}^{\mathrm{TaylorF2}}$). For the system here with tidal deformability $\tilde{\Lambda} = 400$ [Eq. (5)], the tidal contribution is larger than the differences due to the underlying point-particle models.

D. Source parameters and choice of priors

The signal model for the quasicircular inspiral of compact binaries is described by intrinsic parameters that describe the components of the binary and extrinsic parameters that determine the location and orientation of the binary with respect to the observer. The intrinsic parameters include the component masses m_1 and m_2, where we choose the convention $m_1 \geq m_2$. The best measured parameter for systems displaying a long inspiral is the chirp mass [32,61,93,94],

$$\mathcal{M} = \frac{(m_1 m_2)^{3/5}}{(m_1 + m_2)^{1/5}}. \tag{2}$$

Meanwhile, ground-based GW detectors actually measure redshifted (detector-frame) masses, and these are the quantities we state our prior assumptions on. Detector-frame masses are related to the astrophysically relevant source-frame masses by $m^{\mathrm{det}} = (1+z)m$, where z is the redshift of the binary [93,95]. Dimensionless quantities such as the ratio of the two masses, $q = m_2/m_1 \leq 1$, are thus the same in the detector frame and the source frame. When exploring the parameter space $\vec{\vartheta}$, we assume a prior PDF $p(\vec{\vartheta})$ uniform in the detector-frame masses, with the constraint that $0.5\ \mathrm{M}_\odot \leq m_1^{\mathrm{det}},\ m_2^{\mathrm{det}} \leq 7.7\ \mathrm{M}_\odot$, where $m_1^{\mathrm{det}} \geq m_2^{\mathrm{det}}$, and with an additional constraint on the chirp mass, $1.184\ \mathrm{M}_\odot \leq \mathcal{M}^{\mathrm{det}} \leq 2.168\ \mathrm{M}_\odot$. These limits were chosen to mimic the settings in Ref. [3] to allow for easier comparisons and were originally selected for technical reasons. The posterior does not have support near those limits. Despite correlations with the prior on the distance to the source, the source masses also have an effectively uniform prior in the region of parameter space relevant to this analysis.

When converting from detector-frame to source-frame quantities, we use the MUSE/VLT measurement of the heliocentric redshift of NGC 4993, $z_{\mathrm{helio}} = 0.0098$, reported in Refs. [96,97]. We convert this into a geocentric redshift using the known time of the event, yielding $z = 0.0099$.

The spin angular momenta of the two binary components $\mathbf{S}_i$ represent six additional intrinsic parameters and are usually represented in their dimensionless forms $\boldsymbol{\chi}_i = c\mathbf{S}_i/(Gm_i^2)$. For these parameters, we have, following Ref. [3], implemented two separate priors for the magnitudes of the dimensionless spins, $|\boldsymbol{\chi}| = \chi$, of the two objects. In both cases, we assume isotropic and uncorrelated orientations for the spins, and we use a uniform prior for the spin magnitudes, up to a maximum magnitude. In the first case, we enforce $\chi \leq 0.89$ to be consistent with the value used in Ref. [3]. This allows us to explore the possibility of exotic binary systems. The exact value of this upper limit does not significantly affect the results. Meanwhile, observations of pulsars indicate that, while the fastest-spinning neutron star has an observed $\chi \lesssim 0.4$ [98], the fastest-spinning BNSs capable of merging within a Hubble time, PSR J0737–3039A [99] and PSR J1946+2052 [100], will have at most dimensionless spins of $\chi \sim 0.04$ or $\chi \sim 0.05$ when they merge. Consistent with this population of BNS systems, in the second case we restrict $\chi \leq 0.05$.

For the waveforms in Table I that do not support spin precession, the components of the spins aligned with the orbital angular momentum χ_{1z} and χ_{2z} still follow the same prior distributions, which are marginalized over the unsupported spin components. We use the labels "high-spin" and "low-spin" to refer to analyses that use the prior $\chi \leq 0.89$ and $\chi \leq 0.05$, respectively.

The dimensionless parameters Λ_i governing the tidal deformability of each component, discussed in greater detail in Sec. III D, are given a prior distribution uniform within $0 \leq \Lambda_i \leq 5000$, where no correlation between Λ_1, Λ_2, and the mass parameters is assumed. If we assume the two components are NSs that obey the same EOS, then Λ_1 and Λ_2 must have similar values when m_1 and m_2 have similar values [101–103]. This additional constraint is discussed in a companion paper that focuses on the NS EOS [42].

The remaining signal parameters in $\vec{\vartheta}$ are extrinsic parameters that give the localization and orientation of the binary. When we infer the location of the binary from GW information alone (in Sec. III A), we use an isotropic prior PDF for the location of the source on the sky. For most of the results presented here, we restrict the sky location to the known position of SSS17a/AT 2017gfo as determined by electromagnetic observations [12]. In every case, we use a prior on the distance which assumes a homogeneous rate density in the nearby Universe, with no cosmological corrections applied; in other words, the distance prior grows with the square of the luminosity distance. Meanwhile, we use EM observations to reweight our distance posteriors when investigating the inclination of the binary in Sec. III A, and we use the measured redshift factor to the host galaxy NGC 4993 in order to infer source-frame masses from detector-frame masses in Sec. III B. For the angle $\cos\theta_{JN} = \hat{\mathbf{J}} \cdot \hat{\mathbf{N}}$, defined for the total angular momentum $\mathbf{J}$ and the line of sight $\mathbf{N}$, we assume a prior distribution uniform in $\cos\theta_{JN}$ [104]. To improve the convergence rate of the stochastic samplers, the analyses with the nonprecessing waveform models implement a likelihood function where the phase at coalescence is analytically marginalized out [45].

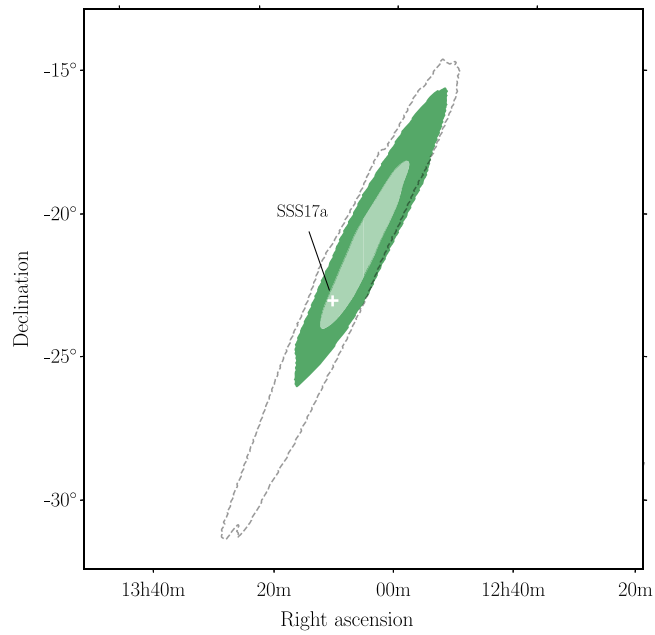

FIG. 3. The improved localization of GW170817, with the location of the associated counterpart SSS17a/AT 2017gfo. The darker and lighter green shaded regions correspond to 50% and 90% credible regions, respectively, and the gray dashed line encloses the previously derived 90% credible region presented in Ref. [3].

III. PROPERTIES INFERRED FROM INSPIRAL AND MERGER

A. Localization

For most of the analyses in this work, we assume *a priori* that the source of GW170817 is in NGC 4993. However, the improved calibration of Virgo data enables better localization of the source of GW170817 from GW data alone. To demonstrate the improved localization, we use results from the updated TaylorF2 analysis (the choice of model does not meaningfully affect localization [105]), shown in Fig. 3. We find a reduction in the 90% localization region from $28\,\mathrm{deg}^2$ [3] to $16\,\mathrm{deg}^2$. This improved localization is still consistent with the associated counterpart SSS17a/AT 2017gfo (see Fig. 3).

For the remainder of this work, we incorporate our knowledge of the location of the event.

While fixing the position of the event to the known location within NGC 4993, we infer the luminosity distance from the GW data alone. Using the PhenomPNRT waveform model, we find that the luminosity distance is $D_L = 41^{+6}_{-12}$ Mpc in the high-spin case and $D_L = 39^{+7}_{-14}$ Mpc in the low-spin case. Combining this distance information with the redshift associated with the Hubble flow at NGC 4993, we measure the Hubble parameter as in Ref. [106]. We find that $H_0 = 70^{+13}_{-7}\ \mathrm{km\,s^{-1}\,Mpc^{-1}}$ (we use maximum *a posteriori* and 68.3% credible interval for only H_0 in this work) in the high-spin case and $H_0 = 70^{+19}_{-8}\ \mathrm{km\,s^{-1}\,Mpc^{-1}}$ in the low-spin case; both measurements are within the uncertainties seen in Extended Data Table I and Extended Data Fig. 2 of Ref. [106]. As noted in Refs. [106,107], when only measuring one polarization of GW radiation from a binary merger, in the absence of strong precession there is a degeneracy between distance and inclination of the binary. When using GW170817 to measure the Hubble constant, this degeneracy is the main source of uncertainty. The slightly stronger constraints on H_0 in the high-spin case arise because, under that prior, our weak constraint on precession (see Sec. III C) helps to rule out binary inclinations that are closer to edge-on (i.e., $\theta_{JN} = 90$ deg) and where precession effects would be measurable, and hence increases the lower bound on the luminosity distance. Meanwhile, the upper bound on the luminosity distance is achieved with face-off (i.e., $\theta_{JN} = 180$ deg) binary inclinations and is nearly the same for both high-spin and low-spin cases.

This same weak constraint on precession leads to a tighter constraint on the inclination angle in the high-spin case when using the precessing signal model PhenomPNRT, $\theta_{JN} = 152^{+21}_{-27}$ deg, as compared to the low-spin case. The inclination measurement in the low-spin case, $\theta_{JN} = 146^{+25}_{-27}$ deg, agrees with the inferred values for both the high- and low-spin cases of our three waveform models that treat only aligned spins (see Table IV in Appendix A). This agreement gives further evidence that it is the absence of strong precession effects in the signal, which can only occur in the high-spin case of the precessing model, that leads to tighter constraints on θ_{JN}. These tighter constraints are absent for systems restricted to the lower spins expected from Galactic NS binaries.

Conversely, EM measurements of the distance to the host galaxy can be used to reduce the effect of this degeneracy, improving constraints on the luminosity distance of the binary and its inclination, which may be useful for constraining emission mechanisms. Figure 4 compares our posterior estimates for distance and inclination with no *a priori* assumptions regarding the distance to the binary (i.e., using a uniform-in-volume prior) to the improved constraints from an EM-informed prior for the distance to the binary. For the EM-informed results, we have reweighted the posterior distribution to use a prior in distance following a normal distribution with mean 40.7 Mpc and standard deviation 2.36 Mpc [108]. This leads to improved measurements of the inclination angle $\theta_{JN} = 151^{+15}_{-11}$ deg (low spin) and $\theta_{JN} = 153^{+15}_{-11}$ deg (high spin). This measurement is consistent for both the high-spin and low-spin cases since the EM measurements constrain the source of GW170817 to higher luminosity distances and correspondingly more face-off inclination values. They are also consistent with the limits reported in previous studies using afterglow measurements [109] and combined

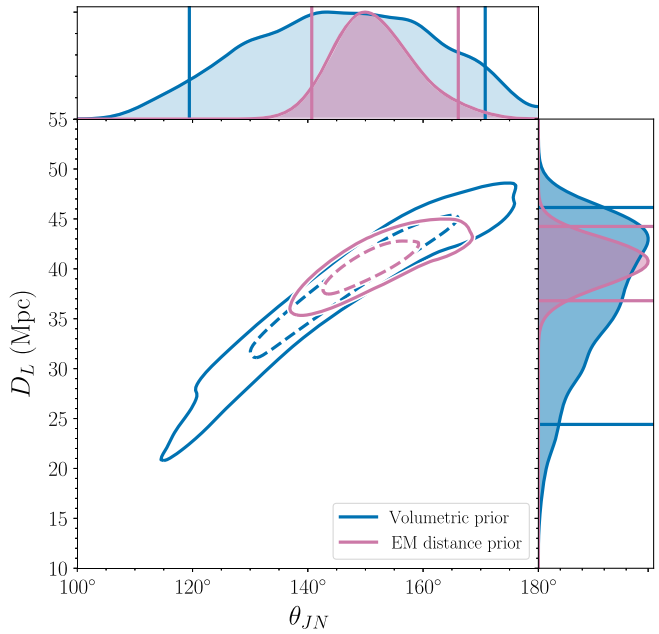

FIG. 4. Marginalized posteriors for the binary inclination (θ_{JN}) and luminosity distance (D_L) using a uniform-in-volume prior (blue) and EM-constrained luminosity distance prior (purple) [108]. The dashed and solid contours enclose the 50% and 90% credible regions, respectively. Both analyses use a low-spin prior and make use of the known location of SSS17a. The 1D marginal distributions have been renormalized to have equal maxima to facilitate comparison, and the vertical and horizontal lines mark 90% credible intervals.

GW and EM constraints [108,110,111] to infer the inclination of the binary.

B. Masses

Owing to its low mass, most of the SNR for GW170817 comes from the inspiral phase, while the merger and postmerger phases happen at frequencies above 1 kHz, where LIGO and Virgo are less sensitive (Fig. 1). This case is different than the BBH systems detected so far, e.g., GW150914 [112–115] or GW170814 [53]. The inspiral phase evolution of a compact binary coalescence can be written as a PN expansion, a power series in v/c, where v is the characteristic velocity within the system [65]. The intrinsic parameters on which the system depends enter the expansion at different PN orders. Generally speaking, parameters that enter at lower orders have a large impact on the phase evolution and are thus easier to measure using the inspiral portion of the signal.

The chirp mass $\mathcal{M}$ enters the phase evolution at the lowest order; thus, we expect it to be the best constrained among the source parameters [32,61,93,94]. The mass ratio q, and consequently the component masses, are instead harder to measure due to two main factors: (1) They are higher-order corrections in the phase evolution, and (2) the mass ratio is partially degenerate with the component of the spins aligned with the orbital angular momentum [93,94,116], as discussed further below.

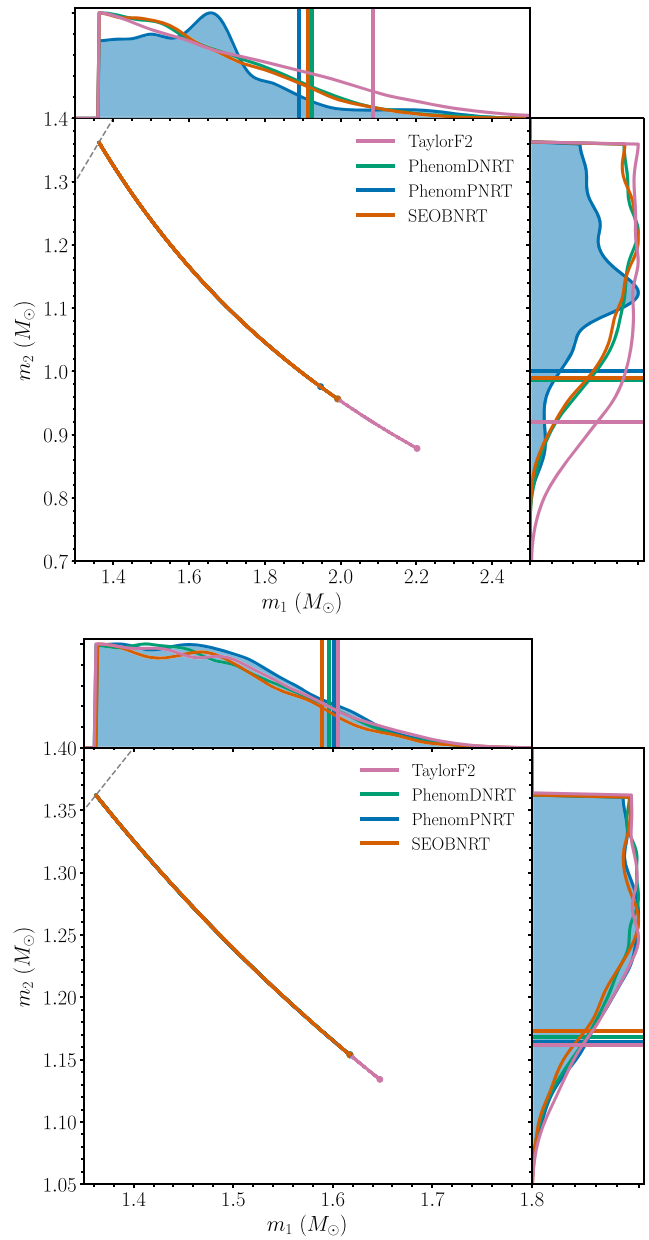

FIG. 5. The 90% credible regions for component masses using the four waveform models for the high-spin prior (top panel) and low-spin prior (bottom panel). The true thickness of the contour, determined by the uncertainty in the chirp mass, is too small to show. The points mark the edge of the 90% credible regions. The 1D marginal distributions have been renormalized to have equal maxima, and the vertical and horizontal lines give the 90% upper and lower limits on m_1 and m_2, respectively.

In Fig. 5, we show one-sided 90% credible intervals of the joint posterior distribution of the two component masses in the source frame. We obtain $m_1 \in (1.36, 1.89)\ \mathrm{M}_\odot$ and $m_2 \in (1.00, 1.36)\ \mathrm{M}_\odot$ in the high-spin case, and

TABLE II. Properties for GW170817 inferred using the PhenomPNRT waveform model. All properties are source properties except for the detector-frame chirp mass $\mathcal{M}^{\rm det} = \mathcal{M}(1+z)$. Errors quoted as x^{+z}_{-y} represent the median, 5% lower limit, and 95% upper limit. Errors quoted as (x, y) are one-sided 90% lower or upper limits, and they are used when one side is bounded by a prior. For the masses, m_1 is bounded from below and m_2 is bounded from above by the equal-mass line. The mass ratio is bounded by $q \leq 1$. For the tidal parameter $\tilde{\Lambda}$, we quote results using a constant (flat) prior in $\tilde{\Lambda}$. In the high-spin case, we quote a 90% upper limit for $\tilde{\Lambda}$, while in the low-spin case, we report both the symmetric 90% credible interval and the 90% highest posterior density (HPD) interval, which is the smallest interval that contains 90% of the probability.

	Low-spin prior ($\chi \leq 0.05$)	High-spin prior ($\chi \leq 0.89$)
Binary inclination θ_{JN}	146^{+25}_{-27} deg	152^{+21}_{-27} deg
Binary inclination θ_{JN} using EM distance constraint [108]	151^{+15}_{-11} deg	153^{+15}_{-11} deg
Detector-frame chirp mass $\mathcal{M}^{\rm det}$	$1.1975^{+0.0001}_{-0.0001}$ $\mathrm{M}_\odot$	$1.1976^{+0.0004}_{-0.0002}$ $\mathrm{M}_\odot$
Chirp mass $\mathcal{M}$	$1.186^{+0.001}_{-0.001}$ $\mathrm{M}_\odot$	$1.186^{+0.001}_{-0.001}$ $\mathrm{M}_\odot$
Primary mass m_1	$(1.36, 1.60)$ $\mathrm{M}_\odot$	$(1.36, 1.89)$ $\mathrm{M}_\odot$
Secondary mass m_2	$(1.16, 1.36)$ $\mathrm{M}_\odot$	$(1.00, 1.36)$ $\mathrm{M}_\odot$
Total mass m	$2.73^{+0.04}_{-0.01}$ $\mathrm{M}_\odot$	$2.77^{+0.22}_{-0.05}$ $\mathrm{M}_\odot$
Mass ratio q	(0.73, 1.00)	(0.53, 1.00)
Effective spin $\chi_{\rm eff}$	$0.00^{+0.02}_{-0.01}$	$0.02^{+0.08}_{-0.02}$
Primary dimensionless spin χ_1	(0.00, 0.04)	(0.00, 0.50)
Secondary dimensionless spin χ_2	(0.00, 0.04)	(0.00, 0.61)
Tidal deformability $\tilde{\Lambda}$ with flat prior	300^{+500}_{-190}(symmetric)/300^{+420}_{-230}(HPD)	(0, 630)

tighter constraints of $m_1 \in (1.36, 1.60)$ $\mathrm{M}_\odot$ and $m_2 \in (1.16, 1.36)$ $\mathrm{M}_\odot$ in the low-spin case. These estimates are consistent with, and generally more precise than, those presented in Ref. [3]. The inferred masses for the components are also broadly consistent with the known masses of Galactic neutron stars observed in BNS systems (see, e.g., Ref. [117]).

As expected, the detector-frame chirp mass is measured with much higher precision, with $\mathcal{M}^{\rm det} = 1.1976^{+0.0004}_{-0.0002}$ $\mathrm{M}_\odot$ (high spin) and $\mathcal{M}^{\rm det} = 1.1975^{+0.0001}_{-0.0001}$ $\mathrm{M}_\odot$ (low spin). These uncertainties are decreased by nearly a factor of 2 as compared to the value reported in Ref. [3] for the detector-frame chirp mass, while the median remains consistent with the 90% credible intervals previously reported. The main source of uncertainty in the source-frame chirp mass comes from the unknown velocity of the source: The line-of-sight velocity dispersion $\sigma_v = 170$ km s^{-1} of NGC 4993 reported in Ref. [96] translates into an uncertainty on the geocentric redshift of the source $z = 0.0099 \pm 0.0009$, and thereby onto the chirp mass. This uncertainty dominates over the statistical uncertainty in $\mathcal{M}$ and over the subpercent level uncertainty in the redshift measurement of NGC 4993 reported in Ref. [97]. The use of the velocity dispersion to estimate the uncertainty in the radial velocity of the source is consistent with the impact of the second supernova on the center-of-mass velocity of the progenitor of GW170817 being relatively small [96,118], especially given that the probable delay time of GW170817 is much longer than the dynamical time of its host galaxy. Both sources of uncertainty are incorporated into the values reported in Table II, which still correspond to a subpercent level of precision on the measurement of $\mathcal{M}$. This method of determining $\mathcal{M}$ from the detector-frame chirp mass differs from the original method used in Ref. [3], and the resulting median value of $\mathcal{M}$ lies at the edge of the 90% credible interval reported there, with uncertainties reduced by a factor of 2 or more. The fact that chirp mass is estimated much better than the individual masses is the reason why, in Fig. 5, the two-dimensional posteriors are so narrow in one direction [119]. Meanwhile, the unknown velocity of the progenitor of GW170817 impacts the component masses at a subpercent level and is neglected in the bounds reported above and in Table II.

C. Spins

The spins of compact objects directly impact the phasing and amplitude of the GW signal through gravitomagnetic interactions (e.g., Refs. [120–122]) and through additional contributions to the mass- and current-multipole moments, which are the sources of GWs (e.g., Ref. [65]). This result allows for the measurement of the spins of the compact objects from their GW emission. The spins produce two qualitatively different effects on the waveform.

First, the components of spins along the orbital angular momentum $\mathbf{L}$ have the effect of slowing down or speeding up the overall rate of inspiral, for aligned-spin components and anti-aligned spin components, respectively [123]. The most important combination of spin components along $\mathbf{L}$ is a mass-weighted combination called the effective spin, $\chi_{\rm eff}$ [124–126], defined as

$$\chi_{\rm eff} = \frac{m_1\chi_{1z} + m_2\chi_{2z}}{m_1 + m_2}. \tag{3}$$

This combination contributes to the gravitational-wave phase evolution at 1.5PN order, together with $\mathcal{M}$, q, and an additional spin degree of freedom [93,127]. This leads to a degeneracy among these quantities, especially between q and $\chi_{\rm eff}$, which complicates the measurement of both of these parameters from the GW phase. The remaining aligned-spin degree of freedom at 1.5PN order is more important for systems with lower mass ratios [128], while the perpendicular components of the spins first contribute to the phasing at 2PN order [61,127,129].

Second, the components of the spins perpendicular to the instantaneous direction of $\mathbf{L}$ precess due to spin-orbit and spin-spin interactions. This leads to the precession of the orbital plane itself in order to approximately conserve the direction of the total angular momentum, which modulates the GW phasing and signal amplitude measured by a fixed observer [104]. One benefit of considering the effective spin $\chi_{\rm eff}$ is that it is approximately conserved throughout inspiral, even as the other components of spins undergo complicated precessional dynamics [130].

The precession-induced modulations of the GW amplitude and phase occur on timescales that span many orbital periods. They are most measurable for systems with large spin components perpendicular to $\mathbf{L}$, for systems with smaller mass ratios q, and for systems viewed close to edge-on [131,132], where precession of the orbital plane strongly modulates the observed signal [104]. Precession effects are commonly quantified by an effective spin-precession parameter χ_p, which is defined as [133]

$$\chi_p = \max\left(\chi_{1\perp}, \frac{3+4q}{4+3q} q\chi_{2\perp}\right), \tag{4}$$

where $\chi_{i\perp}$ are the magnitudes of the components of the dimensionless spins which are perpendicular to $\mathbf{L}$. When considering precessing binaries, we must specify a reference frequency at which spin-related quantities such as χ_p and the individual spins are extracted. For the precessing waveform PhenomPNRT used in this work, we use 100 Hz.

As discussed previously, we use two choices for priors on component spins, a prior that allows for high spins ($\chi \leq 0.89$) and one that restricts to lower spin magnitudes ($\chi \leq 0.05$). The choice of prior has a strong impact on our spin inferences, which in turn influences the inferred component masses through the q–$\chi_{\rm eff}$ degeneracy.

Figure 6 shows the marginalized posterior probability distributions for $\chi_{\rm eff}$ from the four waveform models, along with the high-spin and low-spin priors. For the high-spin case, we find that negative values of $\chi_{\rm eff}$ are mostly excluded for all of the models, although small negative $\chi_{\rm eff}$ and negligible values are still allowed. Large values of $\chi_{\rm eff}$ are also excluded, and the 90% credible interval for

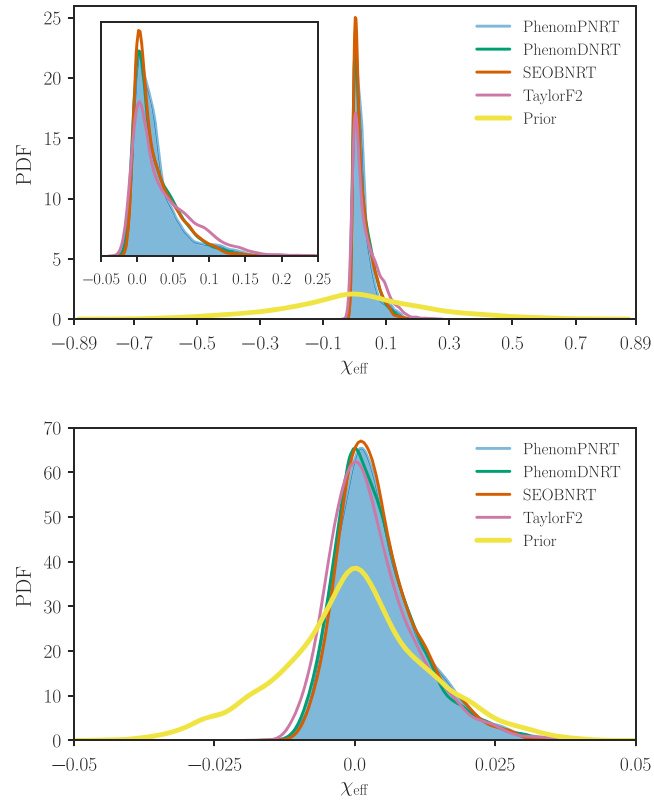

FIG. 6. Posterior PDF for the effective spin parameter $\chi_{\rm eff}$ using the high-spin prior (top panel) and low-spin prior (bottom panel). The four waveform models used are TaylorF2, PhenomDNRT, PhenomPNRT, and SEOBNRT.

PhenomPNRT is $\chi_{\rm eff} \in (-0.00, 0.10)$. The uncertainty in $\chi_{\rm eff}$ is reduced by nearly a factor of 2 as compared with the more conservative constraint $\chi_{\rm eff} \in (-0.01, 0.17)$ reported in Ref. [3] for this prior, and it remains consistent with negligibly small spins. For the low-spin prior, the constraints on negative values of $\chi_{\rm eff}$ are nearly identical, but in this case, the upper end of the $\chi_{\rm eff}$ marginal posterior is shaped by the prior distribution. The 90% credible interval in the low-spin case for PhenomPNRT is $\chi_{\rm eff} \in (-0.01, 0.02)$, which is the same range as reported in Ref. [3] for the low-spin case.

Figure 7 shows two-dimensional marginalized posteriors for q and $\chi_{\rm eff}$ for PhenomPNRT, illustrating the degeneracy between these parameters. The two-dimensional posterior distributions are truncated at the boundary $q = 1$, and when combined with the degeneracy, this causes a positive skew in the marginalized $\chi_{\rm eff}$ posteriors, as seen in Fig. 6 [134]. Compared to the high-spin priors, the low-spin prior on $\chi_{\rm eff}$ cuts off smaller values of q, favoring nearly equal-mass systems.

While all of the models provide constraints on the effective spin, only the PhenomPNRT model provides constraints on the spin precession of the binary. The top panel of Fig. 8 shows the inferred component spin magnitudes and orientations for the high-spin case. In the high-spin case, Fig. 8

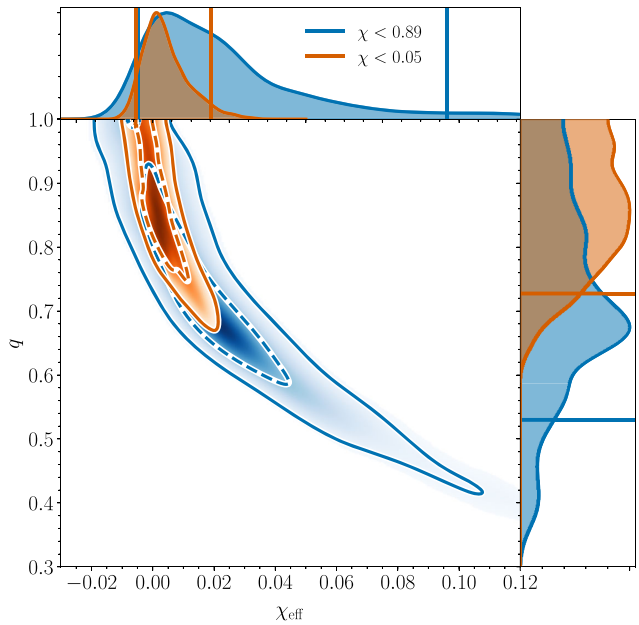

FIG. 7. Marginalized two-dimensional posteriors for the effective spin $\chi_{\rm eff}$ and mass ratio q using the PhenomPNRT model for the high-spin prior (blue) and low-spin prior (orange). The 50% (dashed line) and 90% (solid line) credible regions are shown for the joint posterior. The 90% credible interval for $\chi_{\rm eff}$ is shown by vertical lines, and the 90% lower limit for q is shown by horizontal lines. The 1D marginal distributions have been renormalized to have equal maxima.

shows that we rule out large spin components aligned or anti-aligned with $\mathbf{L}$, but the constraints on in-plane spin components are weaker. As such, we can only rule out large values for the effective precession parameter χ_p, as seen in the bottom panel of Fig 8, with the upper 90th percentile at 0.53. Nevertheless, in this case, we can place bounds on the magnitudes of the component spins; we find that the 90% upper bounds are $\chi_1 \leq 0.50$ and $\chi_2 \leq 0.61$, still well above the range of spins inferred for Galactic binary neutron stars.

Figure 9 shows the same quantities as Fig. 8 using the low-spin prior. In this case, we primarily constrain the spins to lie in or above the orbital plane at the reference frequency. This is consistent with the inferences on $\chi_{\rm eff}$, which rule out large negative values of $\chi_{\rm eff}$ but whose upper bounds are controlled by the prior distribution. Meanwhile, for χ_p, the upper 90th percentile is at 0.04, which is nearly unchanged between the prior and posterior distributions. The inability to place strong constraints on precession is consistent with an analysis reported in Ref. [3] using a precessing model that neglects tidal effects [78].

D. Tidal parameters

In the post-Newtonian formalism, matter effects for nonspinning objects first enter the waveform phase at 5PN order through the tidally induced quadrupolar ($\ell = 2$) deformation [135]. The amount of deformation

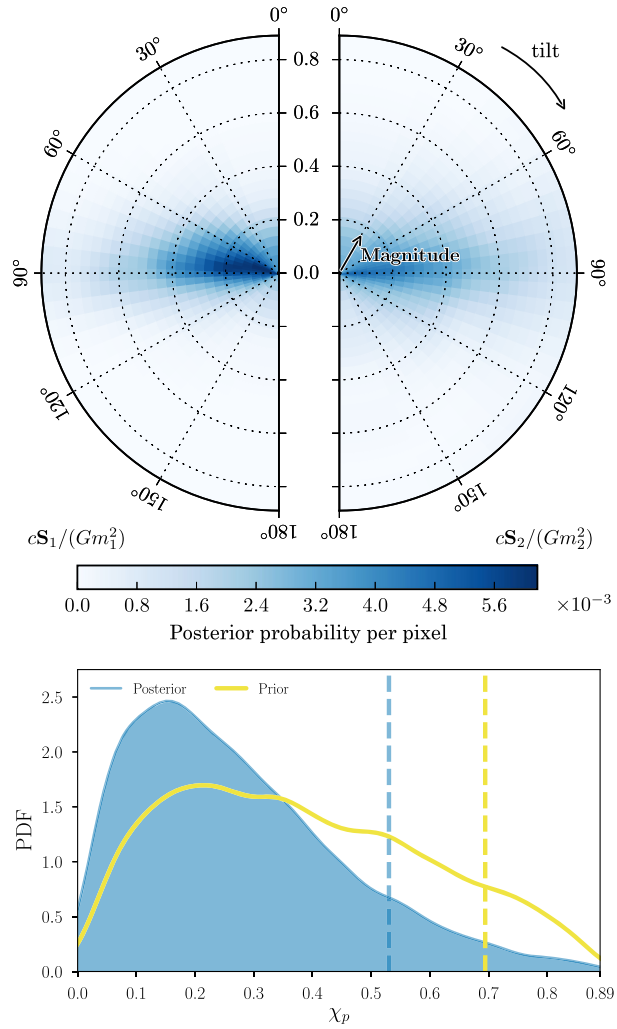

FIG. 8. Top panel: Inferred spin parameters using the PhenomPNRT model in the high-spin case, where the dimensionless component spin magnitudes $\chi < 0.89$. Plotted are the probability densities for the dimensionless spin components $\boldsymbol{\chi}_1$ and $\boldsymbol{\chi}_2$ relative to the orbital angular momentum $\mathbf{L}$, plotted at the reference gravitational-wave frequency of $f = 100$ Hz. A tilt angle of 0° indicates alignment with $\mathbf{L}$. Each pixel has equal prior probability. Bottom panel: The posterior for the precession parameter χ_p, plotted together with its prior distribution, also plotted at the reference frequency of $f = 100$ Hz. The vertical lines represent the 90th percentile for each distribution.

is described by the dimensionless tidal deformability of each NS, defined by $\Lambda = (2/3)k_2[(c^2/G)(R/m)]^5$, where k_2 is the dimensionless $\ell = 2$ Love number and R is the NS radius. These quantities depend on the NS mass m and EOS. For spinning NSs, matter effects also enter at 2PN due to the spin-induced quadrupole moment as discussed in Sec. II C, and of the models considered here, only PhenomPNRT implements this effect.

We show marginalized posteriors for the tidal parameters Λ_1 and Λ_2 in Fig. 10 for the four waveform models. For TaylorF2, the results in this work are in general agreement

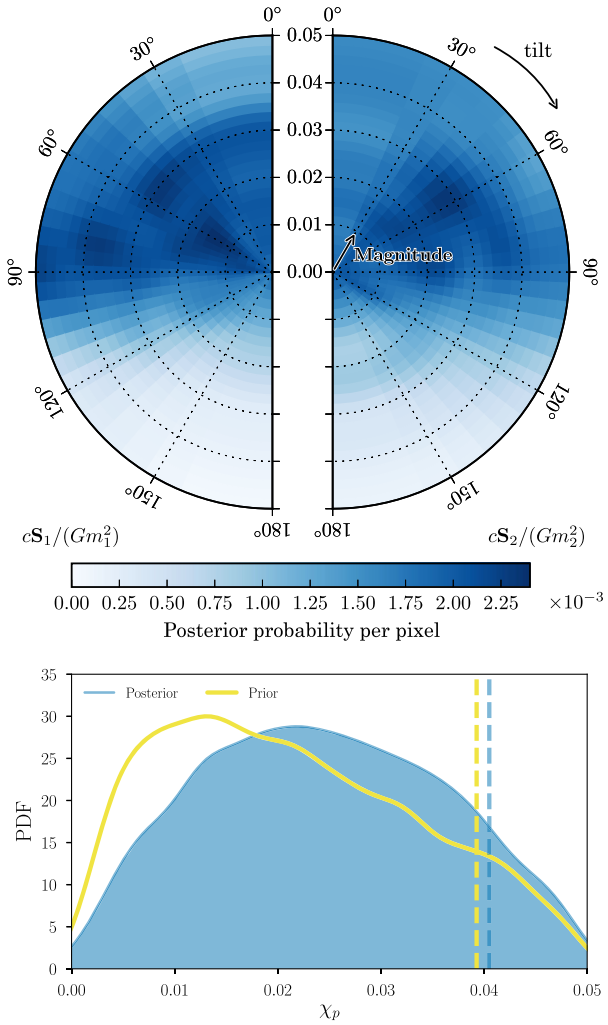

FIG. 9. Inferred spin parameters using the PhenomPNRT model as in Fig. 8, but in the low-spin case where the dimensionless component spin magnitudes $\chi < 0.05$. The posterior probability densities for the dimensionless spin components and for χ_p are plotted at the reference gravitational-wave frequency of $f = 100$ Hz.

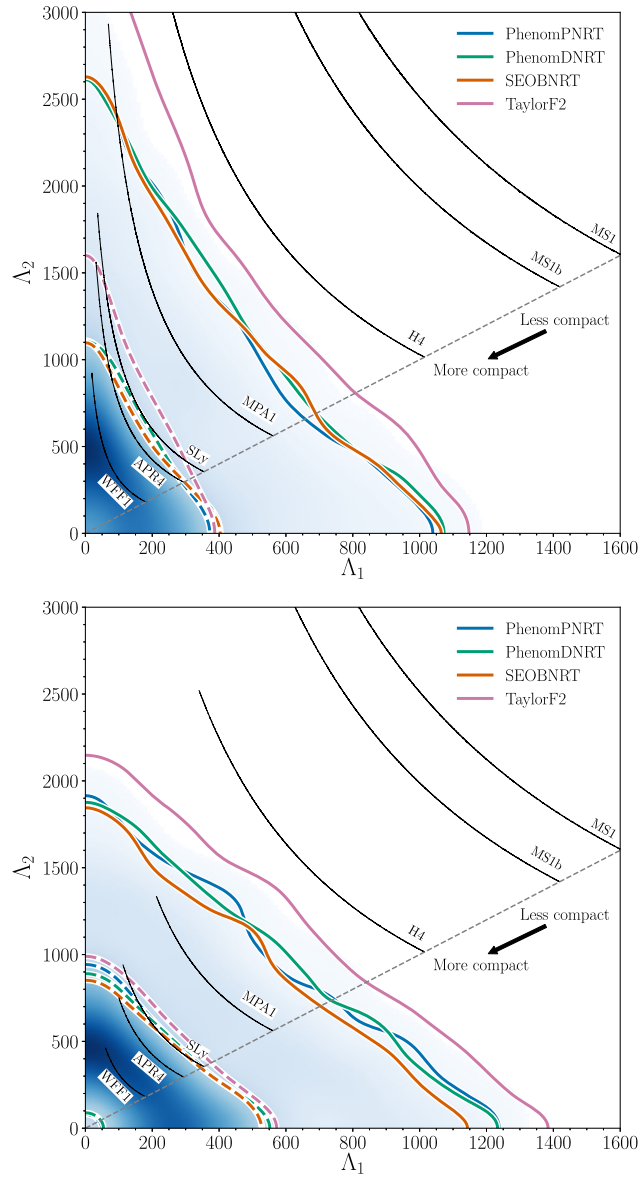

FIG. 10. PDFs for the tidal deformability parameters Λ_1 and Λ_2 using the high-spin (top panel) and low-spin (bottom panel) priors. The blue shading is the PDF for the precessing waveform PhenomPNRT. The 50% (dashed lines) and 90% (solid lines) credible regions are shown for the four waveform models. The seven black curves are the tidal parameters for the seven representative EOS models using the masses estimated with the PhenomPNRT model, ending at the $\Lambda_1 = \Lambda_2$ boundary.

with the values reported in Ref. [3], which also used the TaylorF2 model. However, here we use a lower starting frequency of 23 Hz instead of 30 Hz, resulting in upper bounds on Λ_1 and Λ_2 that are about 10% (for the high-spin prior) and about 20% (for the low-spin prior) smaller than in Ref. [3]. This improvement occurs because, although most of the tidal effects occur above several hundred Hz as shown in Fig. 2, the tidal parameters still have a weak correlation with the other parameters. Using more low-frequency information improves the measurement of the other parameters and thus decreases correlated uncertainties in the tidal parameters.

The three waveform models that use the same NRTidal prescription produce nearly identical 90% upper limits that are about 10% smaller than those of TaylorF2. The reason for this result is that the tidal effect for these models is larger than for TaylorF2, as shown in Fig. 2, so the tidal parameters that best fit the data will be smaller in order to compensate. Including precession and the spin-induced quadrupole moment in the PhenomPNRT model does not noticeably change the results for the tidal parameters compared to the other two models with the NRTidal prescription. Overall, as already found in Ref. [3] the NRTidal models have 90% upper limits that are about 20%–30% lower than the TaylorF2 results presented.

For reference, we also show Λ_1–Λ_2 contours for a representative subset of theoretical EOS models that span the range of plausible tidal parameters using piecewise-polytrope fits from Refs. [136,137]. The values of Λ_1 and Λ_2 are calculated using the samples for the source-frame masses m_1 and m_2 contained in the 90% credible region for PhenomPNRT. The widths of these bands are determined by the small uncertainty in chirp mass. The lengths of these bands are determined by the uncertainty in mass ratio. Most of their support is near the $\Lambda_1 = \Lambda_2$ line corresponding to the equal-mass case and ends at the 90% lower limit for the mass ratio. The predicted values of the tidal parameters for the EOSs MS1, MS1b, and H4 lie well outside of the 90% credible region for both the low-spin and high-spin priors, and for all waveform models. This can be compared to Fig. 5 of Ref. [3], where H4 was still marginally consistent with the 90% credible region.

The leading tidal contribution to the GW phase evolution is a mass-weighted linear combination of the two tidal parameters $\tilde{\Lambda}$ [138]. It first appears at 5PN order and is defined such that $\tilde{\Lambda} = \Lambda_1 = \Lambda_2$ when $m_1 = m_2$:

$$\tilde{\Lambda} = \frac{16}{13}\frac{(m_1 + 12m_2)m_1^4\Lambda_1 + (m_2 + 12m_1)m_2^4\Lambda_2}{(m_1 + m_2)^5}. \quad (5)$$

In Fig. 11, we show marginalized posteriors of $\tilde{\Lambda}$ for the two spin priors and four waveform models. Because there is only one combination of the component tidal deformabilities that gives $\tilde{\Lambda} = 0$, namely, $\Lambda_1 = \Lambda_2 = 0$, when using flat priors in Λ_1 and Λ_2, the prior distribution for $\tilde{\Lambda}$ falls to zero as $\tilde{\Lambda} \to 0$. This means that the posterior for $\tilde{\Lambda}$ must also fall to zero as $\tilde{\Lambda} \to 0$. To avoid the misinterpretation that there is no evidence for $\tilde{\Lambda} = 0$, we reweight the posterior for $\tilde{\Lambda}$ by dividing by the prior used, effectively imposing a flat prior in $\tilde{\Lambda}$. In practice, this is done by dividing a histogram of the posterior by a histogram of the prior. The resulting histogram is then resampled and smoothed with kernel density estimation. We have verified the validity of the reweighting procedure by comparing the results to runs where we fix $\Lambda_2 = 0$ and use a flat prior in $\tilde{\Lambda}$. This differs from the reweighting procedure only in the small, next-to-leading-order tidal effect.

After reweighting, there is still some support at $\tilde{\Lambda} = 0$. For the high-spin prior, we can only place a 90% upper limit on the tidal parameter, shown in Fig. 11 and listed in Tables II and IV. For the TaylorF2 model, this 90% upper limit can be directly compared to the value reported in Ref. [3]. We note, however, that due to a bookkeeping error, the value reported in Ref. [3] should have been 800 instead of 700. Our improved value of 730 is about 10% less than this corrected value. As with the Λ_1–Λ_2 posterior (Fig. 10), the three models with the NRTidal prescription predict 90% upper limits that are consistent with each other and less than the TaylorF2 results by about 10%. For the low-spin prior,

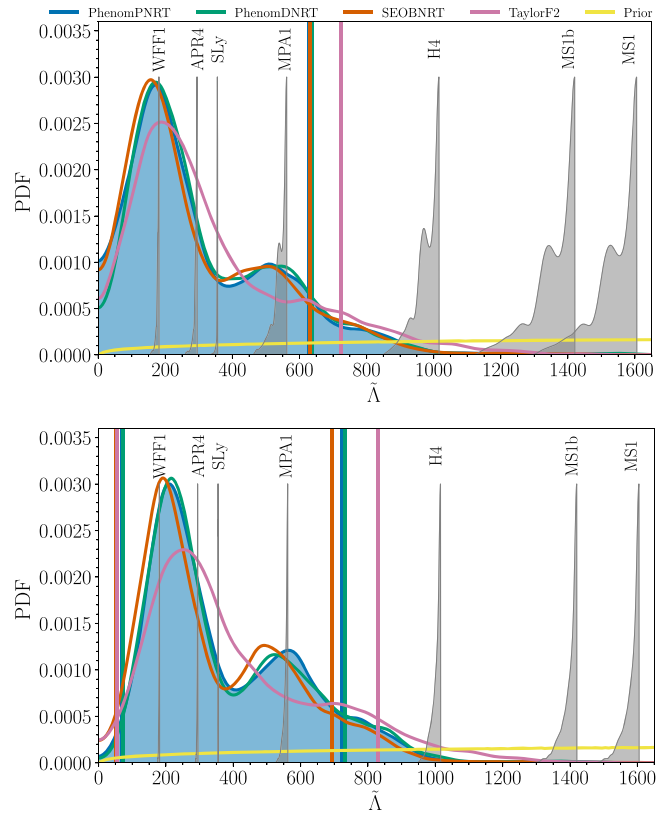

FIG. 11. PDFs of the combined tidal parameter $\tilde{\Lambda}$ for the high-spin (top panel) and low-spin (bottom panel) priors. Unlike in Fig. 6, the PDFs have been reweighted by dividing by the original prior for $\tilde{\Lambda}$ (also shown). The 90% HPD credible intervals are represented by vertical lines for each of the four waveform models: TaylorF2, PhenomDNRT, SEOBNRT, and PhenomPNRT. For the high-spin prior, the lower limit on the credible interval is $\tilde{\Lambda} = 0$. The seven gray PDFs are those for the seven representative EOSs using the masses estimated with the PhenomPNRT model. Their normalization constants have been rescaled to fit in the figure. For these EOSs, a 1.36 $M_\odot$ NS has a radius of 10.4 km (WFF1), 11.3 km (APR4), 11.7 km (SLy), 12.4 km (MPA1), 14.0 km (H4), 14.5 km (MS1b), and 14.9 km (MS1).

we can now place a two-sided 90% HPD credible interval on $\tilde{\Lambda}$ that does not contain $\tilde{\Lambda} = 0$. This 90% HPD interval is the smallest interval that contains 90% of the probability.

The PDFs for the NRTidal waveform models are bimodal. The secondary peak's origin is the subject of further investigation, but it may result from a specific noise realization, as similar results have been seen with injected waveforms with simulated Gaussian noise (see Fig. 4 of Ref. [138]).

In Fig. 11, we also show posteriors of $\tilde{\Lambda}$ (gray PDFs) predicted by the same (EOSs) as in Fig. 10, evaluated using the masses m_1 and m_2 sampled from the posterior. The sharp cutoff to the right of each EOS posterior corresponds to the equal-mass-ratio boundary. Again, as in Fig. 10, the

EOSs MS1, MS1b, and H4 lie outside the 90% credible upper limit and are therefore disfavored.

The differences between the high-spin prior and low-spin prior can be better understood from the joint posterior for $\tilde{\Lambda}$ and the mass ratio q. Figure 12 shows these posteriors for the PhenomPNRT model without reweighting by the prior. For mass ratios near $q = 1$, the two posteriors are similar. However, the high-spin prior allows for a larger range of mass ratios, and for smaller values of q, there is more support for small values of $\tilde{\Lambda}$. If we restrict the mass ratio to $q \gtrsim 0.5$, or equivalently $m_2 \gtrsim 1\ \mathrm{M}_\odot$, we find that there is less support for small values of $\tilde{\Lambda}$, and the two posteriors for $\tilde{\Lambda}$ are nearly identical.

To verify that we have reliably measured the tidal parameters, we supplement the four waveforms used in this paper with two time-domain EOB waveform models: SEOBNRv4T [81,139] and TEOBResumS [80]. SEOBNRv4T includes dynamical tides and the effects of the spin-induced quadrupole moment. TEOBResumS incorporates a gravitational-self-force resummed tidal potential and the spin-induced quadrupole moment. Both models are compatible with state-of-the-art BNS numerical simulations up to merger [83,140].

Unfortunately, these waveform models are too expensive to be used for parameter estimation with LALInference.

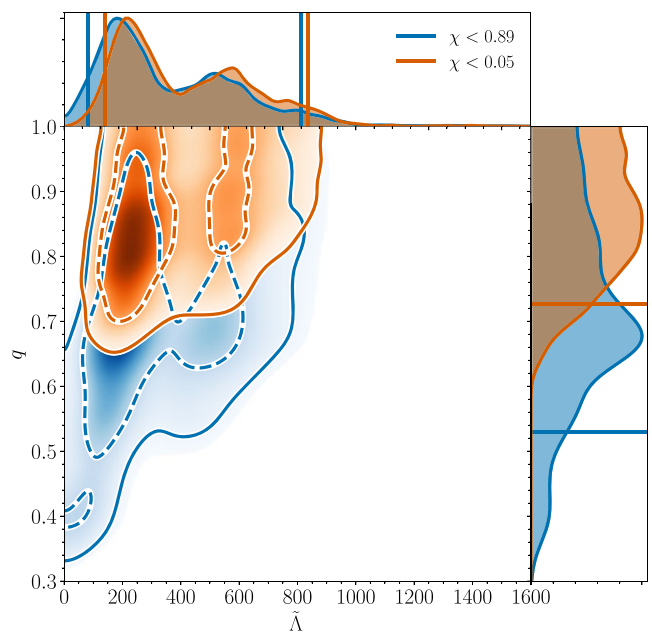

FIG. 12. PDFs for the tidal parameter $\tilde{\Lambda}$ and mass ratio q using the PhenomPNRT model for the high-spin (blue) and low-spin (orange) priors. Unlike Fig. 11, the posterior is not reweighted by the prior, so the support that is seen at $\tilde{\Lambda} = 0$ is due to smoothing from the kernel density estimator (KDE) that approximates the distribution from the discrete samples. The 50% (dashed lines) and 90% (solid lines) credible regions are shown for the joint posterior. The 90% credible interval for $\tilde{\Lambda}$ is shown by vertical lines, and the 90% lower limit for q is shown by horizontal lines.

We therefore use the parallelized but less validated parameter estimation code RapidPE [84,85]. This code uses a different procedure from the standard LALInference code for generating posterior samples and allows for parameter estimation with significantly more expensive waveform models. For each point in the intrinsic parameter space, RapidPE marginalizes over the extrinsic parameters with Monte Carlo integration. For aligned-spin models, the resulting six-dimensional intrinsic marginalized posterior is then adaptively sampled and fit with Gaussian process regression. Samples from this fitted posterior are then drawn using a Markov-chain Monte Carlo algorithm.

We perform runs with RapidPE using the low-spin prior for three waveform models. The first run uses the PhenomDNRT waveform for a direct comparison with the LALInference result. The 90% highest posterior density credible interval for $\tilde{\Lambda}$ is shifted downward from (70,730) using LALInference to (20,690) using RapidPE. Although these differences are not negligible, they are still smaller than the differences between different waveform models. The main difference, however, is that $\tilde{\Lambda}$ has a bimodal structure using LALInference that is not seen with RapidPE. There are several possible reasons for this difference. One possibility is over-smoothing from the Gaussian process regression fit used in RapidPE. Another possibility is the difference in data processing when evaluating the likelihood functions for the two codes. In addition, RapidPE does not marginalize over detector calibration uncertainties. However, comparisons using LALInference with and without calibration error marginalization show that this cannot account for the differences between LALInference and RapidPE. Unfortunately, we have not been able to resolve the differences in the shape of the posterior. Given its extensive previous use and testing, we use LALInference for our main results, and we only use RapidPE for exploratory studies, leaving detailed comparisons to future work. For the two EOB waveforms, the 90% highest posterior density credible interval for $\tilde{\Lambda}$ is (0,560) for SEOBNRv4T and (10,690) for TEOBResumS. For SEOBNRv4T, the posterior for $\tilde{\Lambda}$ has a peak away from $\tilde{\Lambda} = 0$, and the lower bound of $\tilde{\Lambda} = 0$ is not simply due to the prior bound. In fact, the value of the posterior distribution is the same at both the upper and lower limits of the 90% credible interval, indicating that the peak is resolved.

Recently, De *et al.* performed an independent analysis of the GW data to measure the tidal parameters [141]. Their results are broadly consistent with those presented here but are made under the assumption that the two merging NSs have the same EOS. They assume that the two NSs have identical radii and that the tidal deformabilities of the individual stars are related by the approximate relation $\Lambda_1 = q^6 \Lambda_2$, whereas we allow the tidal parameters to vary independently. A more direct comparison of the results is made in our companion paper, where we assume a

common EOS using approximate universal relations as well as directly sampling a parametrized EOS [42,101–103,142,143].

IV. LIMITS ON POSTMERGER SIGNAL

Having used the inspiral phase of the GW signal to constrain the properties of the component bodies, we now place limits on the signal content after the two stars merged to make inferences about the remnant object. The outcome of a BNS coalescence depends on the progenitor masses and the NS EOS. Soft EOSs and large masses result in the prompt formation of a black hole immediately after the merger [144]. Stiffer EOS and lower masses result in the formation of a stable or quasistable NS remnant [145,146]. A hypermassive NS, whose mass exceeds the maximum mass of a uniformly rotating star but is supported by differential rotation and possibly thermal gradients [145], will survive for $\lesssim$1s, after which time the NS collapses into a black hole [147,148]. A supramassive star, whose mass is lower but still exceeds the threshold for nonrotating NSs, will spin down on longer timescales before forming a black hole [149]. Finally, extremely stiff EOSs and low masses will result in a stable NS.

We use the BayesWave algorithm [39] to form frequency-dependent upper limits on the strain amplitude and radiated energy by following the approach described in Ref. [150]. BayesWave models GWs as a superposition of an arbitrary number of elliptically polarized Morlet-Gabor wavelets. This signal model has been found to be capable of accurate waveform reconstruction for a variety of signal morphologies, including short-duration postmerger signals [150]. The priors of this analysis are expressed in terms of the individual wavelet parameters and on the SNR of each wavelet. Consequently, the priors on the signal amplitude and waveform morphology are derived from the individual wavelet priors, rather than being directly specified. The priors on the wavelet quality factor and phase are flat in (0,200) and $(0, 2\pi)$, respectively. The priors on the central frequency and time are determined by the analysis duration and bandwidth described below, while the amplitude prior is determined through the SNR of each wavelet and discussed in more detail in Ref. [39].

We use the analysis described in Ref. [150] to estimate an upper bound on the amplitude of a putative GW signal assumed to be present but at insufficiently high SNR to generate a statistically significant detection candidate. We use coincident data from the two LIGO detectors and from GEO600 [40], which has comparable sensitivity to Virgo at high frequency. Indeed, the sky location of GW170817 is particularly favorable for the GEO600 antenna response so that any high-frequency signal component observed by GEO600 will have a SNR greater than or equal to that expected in Virgo. During this period, the Virgo data above 2 kHz suffer from an abundance of spectral lines and transient noise and, therefore, are not included in this analysis. It should also be noted that GEO600 was not in science mode due to investigations into a degraded squeezer phase error point signal leading to a reduced level of squeezing. At the time of the event, the investigations were passive observations. Otherwise, GEO600 was in nominal running condition. The calibration of the LIGO detectors is more uncertain above 2 kHz than at lower frequencies, but it is still within 8% in amplitude and 4 deg in phase [54]. The GEO600 calibration uncertainty is estimated to be within 15% in amplitude and 15 deg in phase in the 1–4 kHz band. GEO600 was not used in a previous search for high-frequency GW emission due to an insufficient characterization of data quality and analysis tuning, which would have been required for accurate background estimation [41]. The analysis reported in this work, by contrast, is a Bayesian characterization of an underlying signal, and it involves only the 1 s of data around the coalescence time of the merger, which relaxes the data quality requirements somewhat. Furthermore, the analysis configuration has been chosen based on studies of the expected signal (i.e., Ref. [150]), and it is not optimized to eliminate statistical outliers in a background distribution.

We use a 1-s segment of data centered around the time of coalescence, and we restrict the analysis to waveforms whose peak amplitude lies within a 250-ms window at the center of the segment. This window is sufficient to account for statistical or systematic uncertainties in the time-of-coalescence measurement inferred from the inspiral signal, and the total length of segment used encompasses the duration of postmerger signals predicted by numerical simulations for hypermassive NSs that eventually collapse to black holes. The analysis is performed over the 1024–4096-Hz band, which is sufficient to contain the full postmerger spectrum.

We determine the relative evidence for two models: that the on-source data are described by Gaussian noise only, or by Gaussian noise plus a GW signal as described in Refs. [151,152]. We find that the Gaussian noise model is strongly preferred, with a Bayes factor (evidence ratio) of 256.79 over the signal model. This result is consistent with both prompt collapse to a BH and with a postmerger signal that is too weak to be measurable with our current sensitivity. We further characterize the absence of a detectable signal by forming 90% credible upper limits on three measures of signal strength: (i) the network SNR, evaluated over 1–4 kHz, (ii) the strain amplitude spectral density (ASD), and (iii) the spectral energy density (SED).

We compute the 90% credible upper limit on the network SNR directly using the reconstructed waveform posterior. We exclude signal power in our analysis band with $\rho_{\mathrm{net}} >$ 6.7 at the 90% level. The top panel of Fig. 13 reports the upper limits and expectations for the strain ASD induced in the LIGO-Hanford instrument. These limits are formed directly from the posterior probability distribution for the reconstructed waveform in the 1 s of data around the

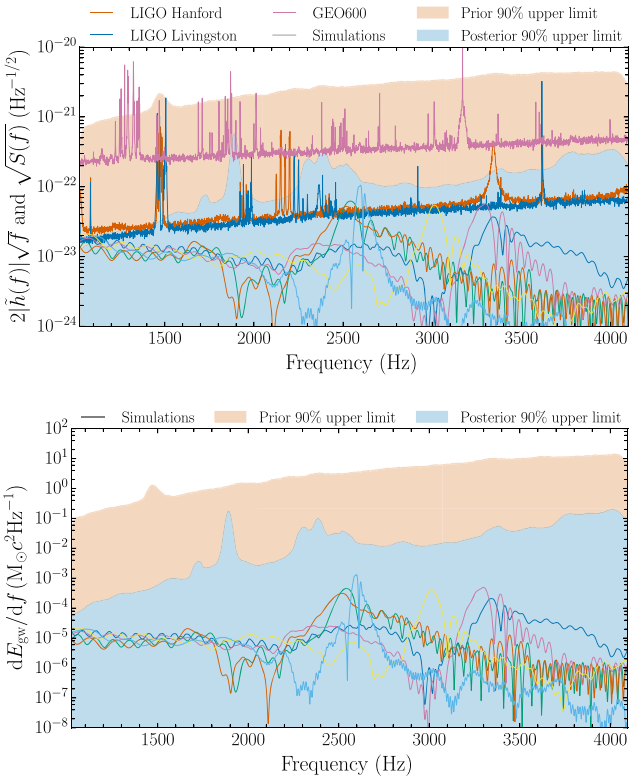

FIG. 13. The 90% credible upper limits on GW strain induced in the Hanford detector (top panel) and radiated energy (bottom panel). Both results are derived from a coherent analysis across the detector network. The noise ASDs for each instrument used in this analysis are shown for comparison top panel). Results from selected numerical simulations are also shown.

merger time measured from the premerger observations using a coherent analysis of data from all three detectors. The noise ASDs for each instrument are shown for comparison. As one would expect in the absence of a signal, the upper limits on strain amplitude approximately follow the shape of the noise spectrum. We also overlay a small set of spectra obtained from simulations of BNS mergers using different EOSs with extrinsic parameters (i.e., sky location, inclination, and distance) determined from the premerger analysis. Information about the simulations used is presented in Table III. Depending on the EOS, the analysis frequency band might contain significant contributions from the inspiral and merger phases of the coalescence. If the simulated waveforms are truncated at peak amplitude such that we only include the postmerger phase, the network SNR of each waveform is about 0.5.

Finally, the peaklike structures evident in the posterior upper limit are due to low-significance instrumental artefacts and, particularly around 2.4 kHz, a nonstationary spectral line in LIGO-Livingston. The low end of the strain ASD posterior extends to include zero, consistent with the nondetection of a postmerger signal.

We apply a similar procedure to form a frequency-dependent 90% credible upper limit on GW energy (see Ref. [150] for details). The bottom panel of Fig. 13 shows the 90% credible upper limits on the SED. As with the reconstructed amplitude, the prior on the SED is imposed by the priors on individual wavelet parameters rather than any specific astrophysical argument. SEDs derived from BNS simulations in which the source is held at the distance, sky location, and orientation of GW170817 are shown for comparison with our upper limits. Our 90% credible upper limit is still too large to make any inference about the EOSs from this part of the signal. Instead, we characterize the sensitivity improvement required to begin to probe astrophysically interesting energy regimes by comparing the peaks of the simulated SEDs to the 90% credible upper limit on the energy radiated at that frequency.

We find that our upper limits on energy are 12–215 times larger than expectations based on our choice of EOS and simulations, shown in Table III. We therefore require amplitude sensitivity to improve by a factor of about 3.5–15 compared to our current results in order to probe realistic energy scales for an equivalent event. This should be regarded as a rather conservative estimate of the upgrade required before we can start probing the astrophysically interesting energy regime, as a number of improvements can increase the sensitivity of our analysis. The current methodology described in Ref. [150] is agnostic when it comes to the morphology of the postmerger signal. Additional information about the signal, such as its broadband structure or the finite extent of the postmerger peak, could increase the sensitivity of our analysis, making it easier to detect and characterize the postmerger signal.

As stated earlier, the analysis described here complements the previous, more generic, high-frequency search in Ref. [41]. The upper limits here are given by the 90% credible interval of the posterior probability distribution on the signal amplitude spectrum and its power spectral density. The analysis in Ref. [41], by contrast, reports the root-sum-squared amplitude that a number of numerical simulations would require in order that 50% of a population of those signals would produce a ranking statistic with false alarm probability of 10^{-4}. Nonetheless, one can compare the amplitude sensitivity improvement required such that each analysis begins to probe astrophysically interesting energy scales. The two analyses share a subset of simulated signals: those with the H4, SLy, and SFHx EOSs reported in Table III. In Ref. [41], sensitivities are quoted in terms of the root-sum-squared amplitude, which scales with the square root of the gravitational-wave energy. The energy scales probed by Ref. [41] for the H4, SLy, and SFHx waveforms are, respectively, 169, 144, and 121 times higher than the values expected from merger simulations with extrinsic parameters of GW170817. In this analysis, the best energy upper limits for the same waveforms are 70, 64, and 31 times greater than the peak energies of those waveforms. With the caveat that

we are free to compare our limits with the dominant postmerger frequency, the analysis reported here effectively probes a factor of about 2–4 smaller energies.

Sensitivity improvements may come from more stringent and accurate waveform models, serendipitously located sources, as well as improved instrumental high-frequency sensitivity. The Advanced LIGO design sensitivity, e.g., is expected to be 3 times better at high frequencies than what has been achieved to date [1,153], while squeezing is expected to improve the sensitivity by another factor of 2 [154]. Similarly, the high-frequency sensitivity of Virgo may see as much as a factor of about 40 improvement when design sensitivity is achieved [2,153]. The postmerger SNR of the simulated waveforms is about 6–8 times smaller than the SNR required for marginal reconstruction of the postmerger signal [150] depending on the EOS and its energy content [155]. A similar event observed with the full LIGO-Virgo network operating at design sensitivity would, therefore, offer an opportunity to probe an astrophysically interesting energy regime and may even provide an estimate of the dominant postmerger oscillation frequency and corresponding constraints on the NS EOS.

V. CONCLUSIONS

This work provides the most constraining measurements of the source of GW170817 to date. Without imposing strong astrophysical priors on the masses or spins, we show that the GW data constrains the masses to the range expected for BNS systems and constrains spin components parallel to the orbital angular momentum to be small. The GW data, however, do not significantly constrain the spin components perpendicular to the orbital angular momentum. If there is significant spin, it must lie near the orbital plane of the binary. Imposing a prior on the distance to GW170817 from the known distance to the host NGC 4993 allows us to constrain the inclination angle of the binary, providing insight into the nature of gamma-ray bursts.

Our improved constraints on the tidal deformation of the binary components reduce the upper bounds on this deformation, further ruling out some of the stiffest equation-of-state models. In addition, we find evidence for finite-size effects by establishing a lower bound for the tidal deformation parameter $\tilde{\Lambda}$ when we restrict the spins to be within the ranges observed in Galactic binaries. However, when we allow for large component spins, we are still unable to rule out the possibility of no tidal deformation of the component stars, as would occur, e.g., in a surprisingly low-mass binary black hole merger. While the measured properties are consistent with what we expect for binary neutron star systems, we cannot definitively say from GW measurements alone that both components of the binary were indeed neutron stars.

Comparing results from four different waveform models provides assurance that systematic uncertainties are small compared to statistical uncertainties. Improved waveform models, as well as optimizations to the models and parameter estimation codes that allow them to be used, will further reduce systematic uncertainties. We have shown initial results with the RapidPE code and SEOBNRv4T and TEOBResumS waveform models, and found that the measured tidal parameters are consistent with the main results of the paper. Furthermore, updated instrumental calibration could improve constraints further. However, we do not expect these improvements to change the conclusions obtained here.

We have also placed new, morphology-agnostic bounds on the postmerger signal and argue that the Advanced LIGO-Virgo network at design sensitivity could have potentially reconstructed the postmerger signal.

There is still significant potential for improved constraints on GW170817 in the use of additional information in the priors for tidal deformation. In this work, we allow the component tidal parameters to vary independently, implicitly allowing each neutron star to have a different equation of state. One can require that the two neutron stars obey the same EOS through the use of binary universal

TABLE III. Numerical simulations of the 1.35 $M_\odot$–1.35 $M_\odot$ binary neutron star mergers with different EOSs shown in Fig. 13. We report the value of the SED from each simulation at the peak frequency $f_{\rm peak}$ and our 90% credible upper limit on the SED at that frequency. The distance $D_L = 44.74$ Mpc and inclination $\theta_{JN} = 166.05$ deg are determined from the point of maximum posterior probability sampled from the PhenomPNRT model. Note that this is the maximum posterior probability sample drawn from the full posterior probability distribution, and it does not necessarily correspond to the maxima of the 1D and 2D marginal distributions shown in Fig. 4.

EOS	Simulation	$f_{\rm peak}$ (Hz)	SED (10^{-4} $M_\odot c^2$ Hz^{-1})	SED_{90} (10^{-4} $M_\odot c^2$ Hz^{-1})
APR4 [156]	[157]	3342	2.1	450
H4 [158]	[157]	2541	4.5	320
GNH3 [159]	[160]	2522	3.1	380
SLy [161]	[160]	3299	5.0	320
SFHx [162]	[163]	3012	4.1	130
DD2 [164,165]	[163]	2598	13.1	160

relations [101–103] or a parametrized EOS [142,143]. This assumption also allows one to place bounds on the radii of the two neutron stars, and results are discussed in a companion paper [42].

Data associated with the figures in this article, including posterior samples generated using the PhenomPNRT model, can be found in Ref. [166].

ACKNOWLEDGMENTS

The authors gratefully acknowledge the support of the United States National Science Foundation (NSF) for the construction and operation of the LIGO Laboratory and Advanced LIGO, as well as the Science and Technology Facilities Council (STFC) of the United Kingdom, the Max-Planck-Society (MPS), and the State of Niedersachsen/Germany for support of the construction of Advanced LIGO and construction and operation of the GEO600 detector. Additional support for Advanced LIGO was provided by the Australian Research Council. The authors gratefully acknowledge the Italian Istituto Nazionale di Fisica Nucleare (INFN), the French Centre National de la Recherche Scientifique (CNRS) and the Foundation for Fundamental Research on Matter supported by the Netherlands Organisation for Scientific Research, for the construction and operation of the Virgo detector and the creation and support of the EGO consortium. The authors also gratefully acknowledge research support from these agencies as well as by the Council of Scientific and Industrial Research of India; the Department of Science and Technology, India; the Science & Engineering Research Board (SERB), India; the Ministry of Human Resource Development, India; the Spanish Agencia Estatal de Investigación; the Vicepresidència i Conselleria d'Innovació; Recerca i Turisme and the Conselleria d'Educació i Universitat del Govern de les Illes Balears; the Conselleria d'Educació, Investigació, Cultura i Esport de la Generalitat Valenciana; the National Science Centre of Poland; the Swiss National Science Foundation (SNSF); the Russian Foundation for Basic Research; the Russian Science Foundation; the European Commission; the European Regional Development Funds (ERDF); the Royal Society; the Scottish Funding Council; the Scottish Universities Physics Alliance; the Hungarian Scientific Research Fund (OTKA); the Lyon Institute of Origins (LIO); the Paris Île-de-France Region; the National Research, Development and Innovation Office Hungary (NKFI); the National Research Foundation of Korea; Industry Canada and the Province of Ontario through the Ministry of Economic Development and Innovation; the Natural Science and Engineering Research Council Canada; the Canadian Institute for Advanced Research; the Brazilian Ministry of Science, Technology, Innovations, and Communications; the International Center for Theoretical Physics South American Institute for Fundamental Research (ICTP-SAIFR); the Research Grants Council of Hong Kong; the National Natural Science Foundation of China (NSFC); the Leverhulme Trust; the Research Corporation; the Ministry of Science and Technology (MOST), Taiwan; and the Kavli Foundation. The authors gratefully acknowledge the support of the NSF, STFC, Max-Planck-Society (MPS), INFN, CNRS, and the State of Niedersachsen/Germany for provision of computational resources. The GW strain data for this event are available at the LIGO Open Science Center [167]. This article has been assigned the document number LIGO-P1800061.

APPENDIX A: SOURCE PROPERTIES FROM ADDITIONAL WAVEFORM MODELS

In this Appendix, we present additional results for the source properties of GW170817. Table IV presents the same inferred parameters quoted in Table II for the three additional waveform models TaylorF2, PhenomDNRT, and SEOBNRT. As expected from Figs. 5, 6, 10, and 11, the results among the four waveform models are largely consistent with each other.

One exception is the binary inclination angle θ_{JN}: In the high-spin case, the precessing waveform PhenomPNRT achieves tighter bounds centered around a more face-off ($\theta_{JN} = 180$ deg) orientation than for the low-spin case. As discussed in Sec. III A, we attribute the tighter constraints on θ_{JN} to the fact that we disfavor configurations where strong precession effects would be observable; hence, we prefer values of θ_{JN} closer to face-off. Meanwhile, the other three waveform models only treat aligned spins, so the absence of strong precession does not help improve their inclination measurements. For all four waveforms, in the small-spin case, the spins are constrained to sufficiently small values so that there can be no strong precession effects; thus, again, the inclination measurements for the small-spin case are consistent with the aligned-spin measurements in the high-spin case. Finally, when we incorporate EM information about the distance to the source of GW170817, we eliminate the portion of the posteriors at closer distances and lower θ_{JN}, achieving consistent inclination constraints across all cases.

The upper bounds on the spin magnitudes χ_1 and χ_2 are also lower for the waveforms that treat aligned spins only. This result is as expected, given that only the components $\chi_{i,z}$ contribute to the spin magnitudes for the aligned-spin runs, and these spin components are constrained by $\chi_{\rm eff}$ in the high-spin case and by our prior in the low-spin case. The differences between the remaining inferred parameters among the four waveforms give a sense of the possible size of systematic errors from our signal modeling, although PhenomPNRT includes the greatest number of relevant physical effects, as seen in Table I.

Table V presents the inferred intrinsic parameters of the binary as produced by RapidPE.

TABLE IV. Source properties for GW170817 using the additional waveform models TaylorF2, PhenomDNRT, and SEOBNRT. Conventions are the same as in Table II. The TaylorF2 results here can be directly compared with those from Ref. [3]. Note that the 90% upper limits for $\tilde{\Lambda}$ reported in Table I of Ref. [3] for TaylorF2 are incorrect (see Sec. III D). In Ref. [3], for the high-spin prior, it should be ≤ 800 and not ≤ 700, while for the low-spin prior, it should be ≤ 900 and not ≤ 800.

High-spin prior, $\chi_i \leq 0.89$	TaylorF2	SEOBNRT	PhenomDNRT
Binary inclination θ_{JN}	146^{+25}_{-28} deg	146^{+24}_{-28} deg	146^{+26}_{-28} deg
Binary inclination θ_{JN} using EM distance constraint [108]	149^{+13}_{-10} deg	152^{+14}_{-11} deg	151^{+15}_{-10} deg
Detector-frame chirp mass $\mathcal{M}^{\mathrm{det}}$	$1.1976^{+0.0004}_{-0.0002}$ $\mathrm{M}_\odot$	$1.1976^{+0.0003}_{-0.0002}$ $\mathrm{M}_\odot$	$1.1976^{+0.0003}_{-0.0002}$ $\mathrm{M}_\odot$
Chirp mass $\mathcal{M}$	$1.186^{+0.001}_{-0.001}$ $\mathrm{M}_\odot$	$1.186^{+0.001}_{-0.001}$ $\mathrm{M}_\odot$	$1.186^{+0.001}_{-0.001}$
Primary mass m_1	$(1.36, 2.09)$ $\mathrm{M}_\odot$	$(1.36, 1.92)$ $\mathrm{M}_\odot$	$(1.36, 1.92)$ $\mathrm{M}_\odot$
Secondary mass m_2	$(0.92, 1.36)$ $\mathrm{M}_\odot$	$(0.99, 1.36)$ $\mathrm{M}_\odot$	$(0.99, 1.36)$ $\mathrm{M}_\odot$
Total mass m	$2.79^{+0.30}_{-0.06}$ $\mathrm{M}_\odot$	$2.76^{+0.20}_{-0.04}$ $\mathrm{M}_\odot$	$2.77^{+0.20}_{-0.04}$ $\mathrm{M}_\odot$
Mass ratio q	(0.44, 1.00)	(0.52, 1.00)	(0.51, 1.00)
Effective spin χ_{eff}	$0.02^{+0.10}_{-0.03}$	$0.01^{+0.07}_{-0.02}$	$0.01^{+0.07}_{-0.02}$
Primary dimensionless spin χ_1	(0.00, 0.25)	(0.00, 0.25)	(0.00, 0.25)
Secondary dimensionless spin χ_2	(0.00, 0.39)	(0.00, 0.36)	(0.00, 0.35)
Tidal deformability $\tilde{\Lambda}$ with flat prior	(0, 730)	(0, 630)	(0, 640)
Low-spin prior, $\chi_i \leq 0.05$	**TaylorF2**	**SEOBNRT**	**PhenomDNRT**
Binary inclination θ_{JN}	146^{+24}_{-28} deg	146^{+24}_{-28} deg	147^{+24}_{-28} deg
Binary inclination θ_{JN} using EM distance constraint [108]	149^{+13}_{-10} deg	152^{+14}_{-11} deg	151^{+14}_{-10} deg
Detector-frame chirp mass $\mathcal{M}^{\mathrm{det}}$	$1.1975^{+0.0001}_{-0.0001}$ $\mathrm{M}_\odot$	$1.1976^{+0.0001}_{-0.0001}$ $\mathrm{M}_\odot$	$1.1975^{+0.0001}_{-0.0001}$ $\mathrm{M}_\odot$
Chirp mass $\mathcal{M}$	$1.186^{+0.001}_{-0.001}$ $\mathrm{M}_\odot$	$1.186^{+0.001}_{-0.001}$ $\mathrm{M}_\odot$	$1.186^{+0.001}_{-0.001}$
Primary mass m_1	$(1.36, 1.61)$ $\mathrm{M}_\odot$	$(1.36, 1.59)$ $\mathrm{M}_\odot$	$(1.36, 1.60)$ $\mathrm{M}_\odot$
Secondary mass m_2	$(1.16, 1.36)$ $\mathrm{M}_\odot$	$(1.17, 1.36)$ $\mathrm{M}_\odot$	$(1.17, 1.36)$ $\mathrm{M}_\odot$
Total mass m	$2.73^{+0.05}_{-0.01}$ $\mathrm{M}_\odot$	$2.73^{+0.04}_{-0.01}$ $\mathrm{M}_\odot$	$2.73^{+0.04}_{-0.01}$ $\mathrm{M}_\odot$
Mass ratio q	(0.72, 1.00)	(0.74, 1.00)	(0.73, 1.00)
Effective spin χ_{eff}	$0.00^{+0.02}_{-0.01}$	$0.00^{+0.02}_{-0.01}$	$0.00^{+0.02}_{-0.01}$
Primary dimensionless spin χ_1	(0.00, 0.02)	(0.00, 0.02)	(0.00, 0.02)
Secondary dimensionless spin χ_2	(0.00, 0.02)	(0.00, 0.02)	(0.00, 0.02)
Tidal deformability $\tilde{\Lambda}$ with flat prior (symmetric/HPD)	$340^{+580}_{-240}/340^{+490}_{-290}$	$280^{+490}_{-190}/280^{+410}_{-230}$	$300^{+520}_{-190}/300^{+430}_{-230}$

TABLE V. Source properties for GW170817 produced using RapidPE for the additional waveform models SEOBNRv4T and TEOBResumS. Conventions are the same as in Table II.

Low-spin prior, $\chi_i \leq 0.05$	SEOBNRv4T	TEOBResumS	PhenomDNRT
Detector-frame chirp mass $\mathcal{M}^{\mathrm{det}}$	$1.1975^{+0.0001}_{-0.0001}$ $\mathrm{M}_\odot$	$1.1975^{+0.0001}_{-0.0001}$ $\mathrm{M}_\odot$	$1.1975^{+0.0001}_{-0.0001}$ $\mathrm{M}_\odot$
Chirp mass $\mathcal{M}$	$1.186^{+0.001}_{-0.001}$ $\mathrm{M}_\odot$	$1.186^{+0.001}_{-0.001}$ $\mathrm{M}_\odot$	$1.186^{+0.001}_{-0.001}$
Primary mass m_1	$(1.36, 1.56)$ $\mathrm{M}_\odot$	$(1.36, 1.53)$ $\mathrm{M}_\odot$	$(1.36, 1.57)$ $\mathrm{M}_\odot$
Secondary mass m_2	$(1.19, 1.36)$ $\mathrm{M}_\odot$	$(1.22, 1.36)$ $\mathrm{M}_\odot$	$(1.19, 1.36)$ $\mathrm{M}_\odot$
Total mass m	$2.73^{+0.04}_{-0.01}$ $\mathrm{M}_\odot$	$2.73^{+0.03}_{-0.01}$ $\mathrm{M}_\odot$	$2.73^{+0.04}_{-0.01}$ $\mathrm{M}_\odot$
Mass ratio q	(0.76, 1.00)	(0.79, 1.00)	(0.76, 1.00)
Effective spin χ_{eff}	$0.00^{+0.02}_{-0.01}$	$0.00^{+0.01}_{-0.01}$	$0.00^{+0.02}_{-0.01}$
Primary dimensionless spin χ_1	(0.00, 0.03)	(0.00, 0.02)	(0.00, 0.03)
Secondary dimensionless spin χ_2	(0.00, 0.03)	(0.00, 0.03)	(0.00, 0.03)
Tidal deformability $\tilde{\Lambda}$ with flat prior (symmetric/HPD)	$280^{+430}_{-220}/280^{+280}_{-280}$	$340^{+520}_{-260}/340^{+350}_{-330}$	$310^{+510}_{-240}/310^{+380}_{-290}$

TABLE VI. Parameters used for the injected SEOBNRv4T waveform. The chosen masses and spins are consistent with the measured posteriors for GW170817. The tidal parameters are calculated from the mass and chosen EOS.

Injection	(m_1, m_2) $(M_\odot)$	(χ_1, χ_2)	EOS	(Λ_1, Λ_2)	$\tilde{\Lambda}$
i	(1.38, 1.37)	(0, 0)	APR4	(275, 309)	292
ii	(1.68, 1.13)	(0, 0)	APR4	(77, 973)	303
iii	(1.38, 1.37)	(0.04, 0)	APR4	(275, 309)	292
iv	(1.38, 1.37)	(0, 0)	H	(1018, 1063)	1040

APPENDIX B: INJECTION AND RECOVERY STUDY

The reliability of the parameter estimation techniques used here was studied in detail for the first BBH detection by injecting state-of-the-art numerical waveform models into the data and verifying that the waveform templates correctly recover the injected parameters [115]. We perform a similar analysis for GW170817 by injecting a state-of-the-art BNS waveform model using parameters consistent with the data and then verifying that our waveform templates reliably recover the injected values. For BNS systems, we focus on the additional tidal parameters that are particularly sensitive to errors in the waveform models [138,168–171]. We use as our injected waveform model the time-domain aligned-spin SEOBNRv4T model [81,139] discussed in Sec. III D. The version used in this study did not include the spin-induced quadrupole moment, but later implementations of SEOBNRv4T such as the one used for the results in Table V include this effect.

We inject SEOBNRv4T with the following parameters in Table VI, which are consistent with the measured posterior for GW170817: (i) an approximately equal-mass, nonspinning case, (ii) an unequal-mass-ratio ($q = 0.67$), nonspinning case, and (iii) an approximately equal-mass case with a small spin for the primary star. For these systems, we choose a reference EOS that is near the peak of the tidal parameter $\tilde{\Lambda}$ in Fig. 11, APR4, from which we calculate the tidal parameters Λ_1 and Λ_2. Finally, we also choose (iv) a stiffer parametrized EOS that is sometimes used in NR simulations, H [172], which is near the maximum allowed value of $\tilde{\Lambda}$. We use the high-spin prior ($\chi_i \leq 0.89$) and the three aligned-spin waveform models (TaylorF2, PhenomDNRT, and SEOBNRT) as templates. In all four cases, we use the same PSD used in the analysis of GW170817 and inject the waveform with a network SNR of 32, consistent with GW170817. While the PSD is nonzero, we inject these waveforms into a zero-noise realization of the data. In other words, we assume the noise is zero at all frequencies. This has the advantage of making the results independent on possible large fluctuations of the Gaussian noise. Results obtained with zero noise are statistically equivalent to averaging results obtained with Gaussian noise over a large number of random realizations of Gaussian noise, and they are routinely presented in gravitational-wave literature [115,173–176].

We show in Fig. 14 the recovered tidal parameter $\tilde{\Lambda}$ when using the soft APR4 EOS. The posteriors for the three templates are peaked near the injected value of $\tilde{\Lambda}$. As with Fig. 11, the 90% upper limits are nearly the same for the two waveforms that use the NRTidal description, while the 90% upper limit for TaylorF2 is about 100 units higher.

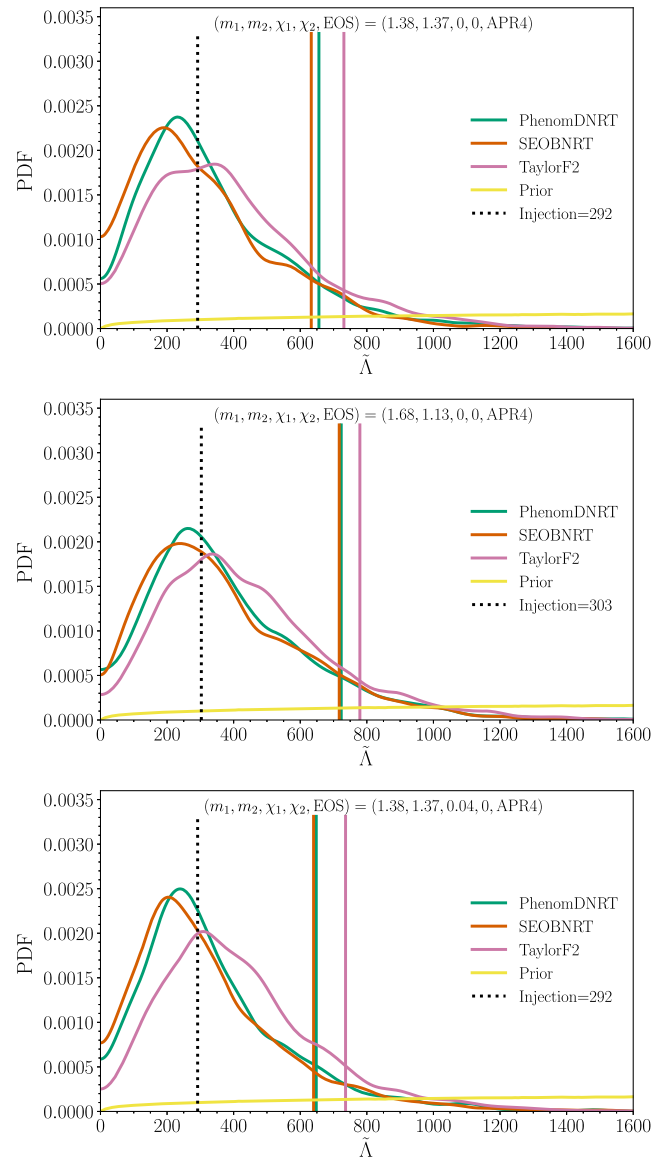

FIG. 14. Marginalized PDF of $\tilde{\Lambda}$ for the three aligned-spin waveform models using the high-spin prior of $\chi_i < 0.89$. As in Fig. 11, the PDF is reweighted by the prior. The SEOBNRv4T model was injected into zero-noise data with a network SNR of 32. The injected tidal parameter shown by the dotted vertical line was calculated with the APR4 EOS. Top panel: Approximately equal mass and nonspinning. Middle panel: Unequal mass and nonspinning. Bottom panel: Approximately equal mass and primary component spinning. Solid vertical lines represent the 90% upper limit for each waveform.

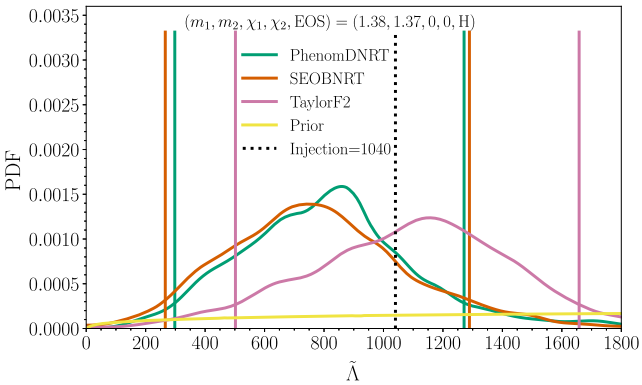

FIG. 15. Same as Fig. 14 but with injection (iv) using the H EOS. Solid vertical lines represent the 90% HPD credible interval for each waveform.

Because the TaylorF2 tidal effect is smaller than that for the NRTidal models, the TaylorF2 model will estimate a larger tidal parameter to compensate for the smaller tidal effect, cf. Fig. 2.

In Fig. 15, we show the recovered tidal parameter using the stiffer H EOS. The width of the posteriors, distance of the peaks from the injected value, and spread in the 90% credible intervals between the waveform models are larger than in Fig. 14, indicating that the statistical error and systematic waveform errors scale with the true tidal parameter. As with the APR4 injections, the credible interval for the NRTidal waveforms agree fairly well with each other, while the credible interval for the TaylorF2 waveform is about 400 units larger.

For GW170817 with a network SNR of 32, waveform systematic errors are important but do not dominate over statistical errors. However, as the detectors improve and results from multiple BNS observations are combined, the statistical errors will decrease. In this case, systematic waveform errors may become the dominant source of error, and improved waveform modeling will be needed.

[1] J. Aasi *et al.* (LIGO Scientific Collaboration), *Advanced LIGO*, Classical Quantum Gravity **32**, 115012 (2015).

[2] F. Acernese *et al.* (Virgo Collaboration), *Advanced Virgo: A Second-Generation Interferometric Gravitational Wave Detector*, Classical Quantum Gravity **32**, 024001 (2015).

[3] B. P. Abbott *et al.* (LIGO Scientific Collaboration and Virgo Collaboration), *GW170817: Observation of Gravitational Waves from a Binary Neutron Star Inspiral*, Phys. Rev. Lett. **119**, 161101 (2017).

[4] B. P. Abbott *et al.* (LIGO Scientific Collaboration, Virgo Collaboration, Fermi-GBM, and INTEGRAL), *Gravitational Waves and Gamma-Rays from a Binary Neutron Star Merger: GW170817 and GRB 170817A*, Astrophys. J. **848**, L13 (2017).

[5] D. A. Coulter *et al.*, *LIGO/Virgo G298048: Potential Optical Counterpart Discovered by Swope Telescope*, GCN **21529**, 1 (2017).

[6] D. A. Coulter *et al.*, *Swope Supernova Survey 2017a (SSS17a), the Optical Counterpart to a Gravitational Wave Source*, Science **358**, 1556 (2017).

[7] S. Allam *et al.*, *LIGO/Virgo G298048: DECam Optical Candidate*, GCN **21530**, 1 (2017).

[8] S. Yang *et al.*, *LIGO/Virgo G298048: DLT40 Optical Candidate*, GCN **21531**, 1 (2017).

[9] I. Arcavi *et al.*, *LIGO/Virgo G298048: Las Cumbres Observatory Detection of the Possible Optical Counterpart in NGC 4993*, GCN **21538**, 1 (2017).

[10] N. R. Tanvir *et al.*, *LIGO/Virgo G298048: VISTA/VIRCAM Detection of Candidate Counterpart*, GCN **21544**, 1 (2017).

[11] V. M. Lipunov *et al.*, *LIGO/Virgo G298048: Master Observations of the NGC 4993*, GCN **21546**, 1 (2017).

[12] B. P. Abbott *et al.* [GROND, SALT Group, OzGrav, CAASTROs, DFN, DES, INTEGRAL, Virgo, Insight-HXMT, MAXI Team, J-GEM, RATIR, ATLAS, IceCube, LWA, ePESSTO, GRAWITA, RIMAS, SKA South Africa/MeerKAT, H.E.S.S., Fermi Large Area Telescope, 1M2H Team, IKI-GW Follow-up, Fermi GBM, Pi of Sky, DWF (Deeper Wider Faster Program), MASTER, AstroSat Cadmium Zinc Telluride Imager Team, Swift, Pierre Auger, ASKAP, VINROUGE, JAGWAR, Chandra Team at McGill University, TTU-NRAO, GROWTH, AGILE Team, MWA, ATCA, AST3, TOROS, Pan-STARRS, NuSTAR, BOOTES, CaltechNRAO, LIGO Scientific, High Time Resolution Universe Survey, Nordic Optical Telescope, Las Cumbres Observatory Group, TZAC Consortium, LOFAR, IPN, DLT40, Texas Tech University, HAWC, ANTARES, KU, Dark Energy Camera GW-EM, CALET, Euro VLBI Team, ALMA], *Multi-messenger Observations of a Binary Neutron Star Merger*, Astrophys. J. **848**, L12 (2017).

[13] Li-Xin Li and B. Paczynski, *Transient Events from Neutron Star Mergers*, Astrophys. J. **507**, L59 (1998).

[14] B. D. Metzger, G. Martinez-Pinedo, S. Darbha, E. Quataert, A. Arcones, D. Kasen, R. Thomas, P. Nugent, I. V. Panov, and N. T. Zinner, *Electromagnetic Counterparts of Compact Object Mergers Powered by the Radioactive Decay of r-Process Nuclei*, Mon. Not. R. Astron. Soc. **406**, 2650 (2010).

[15] J. Barnes and D. Kasen, *Effect of a High Opacity on the Light Curves of Radioactively Powered Transients from Compact Object Mergers*, Astrophys. J. **775**, 18 (2013).

[16] M. Tanaka and K. Hotokezaka, *Radiative Transfer Simulations of Neutron Star Merger Ejecta*, Astrophys. J. **775**, 113 (2013).

[17] D. Grossman, O. Korobkin, S. Rosswog, and T. Piran, *The Long-Term Evolution of Neutron Star Merger Remnants II. Radioactively Powered Transients*, Mon. Not. R. Astron. Soc. **439**, 757 (2014).

[18] P. A. Evans *et al.*, *Swift and NuSTAR Observations of GW170817: Detection of a Blue Kilonova*, Science **358**, 1565 (2017).

[19] C. D. Kilpatrick *et al.*, *Electromagnetic Evidence that SSS17a Is the Result of a Binary Neutron Star Merger*, Science **358**, 1583 (2017).
[20] E. Pian *et al.*, *Spectroscopic Identification of r-Process Nucleosynthesis in a Double Neutron Star Merger*, Nature (London) **551**, 67 (2017).
[21] S. J. Smartt *et al.*, *A Kilonova as the Electromagnetic Counterpart to a Gravitational-Wave Source*, Nature (London) **551**, 75 (2017).
[22] N. R. Tanvir *et al.*, *The Emergence of a Lanthanide-Rich Kilonova Following the Merger of Two Neutron Stars*, Astrophys. J. **848**, L27 (2017).
[23] I. Arcavi *et al.*, *Optical Emission from a Kilonova Following a Gravitational-Wave-Detected Neutron-Star Merger*, Nature (London) **551**, 64 (2017).
[24] P. S. Cowperthwaite *et al.*, *The Electromagnetic Counterpart of the Binary Neutron Star Merger LIGO/Virgo GW170817. II. UV, Optical, and Near-Infrared Light Curves and Comparison to Kilonova Models*, Astrophys. J. **848**, L17 (2017).
[25] M. R. Drout *et al.*, *Light Curves of the Neutron Star Merger GW170817/SSS17a: Implications for r-Process Nucleosynthesis*, Science **358**, 1570 (2017).
[26] C. McCully *et al.*, *The Rapid Reddening and Featureless Optical Spectra of the Optical Counterpart of GW170817, AT 2017gfo, During the First Four Days*, Astrophys. J. **848**, L32 (2017).
[27] S. Valenti, D. J. Sand, S. Yang, E. Cappellaro, L. Tartaglia, A. Corsi, S. W. Jha, D. E. Reichart, J. Haislip, and V. Kouprianov, *The Discovery of the Electromagnetic Counterpart of GW170817: Kilonova AT 2017gfo/DLT17ck*, Astrophys. J. **848**, L24 (2017).
[28] I. Andreoni *et al.*, *Follow-up of GW170817 and Its Electromagnetic Counterpart by Australian-led Observing Programs*, Pub. Astron. Soc. Aust. **34**, e069 (2017).
[29] M. Nicholl *et al.*, *The Electromagnetic Counterpart of the Binary Neutron Star Merger LIGO/VIRGO GW170817. III. Optical and UV Spectra of a Blue Kilonova from Fast Polar Ejecta*, Astrophys. J. **848**, L18 (2017).
[30] V. A. Villar *et al.*, *The Combined Ultraviolet, Optical, and Near-Infrared Light Curves of the Kilonova Associated with the Binary Neutron Star Merger GW170817: Unified Data Set, Analytic Models, and Physical Implications*, Astrophys. J. **851**, L21 (2017).
[31] A. Perego, D. Radice, and S. Bernuzzi, *AT 2017gfo: An Anisotropic and Three-Component Kilonova Counterpart of GW170817*, Astrophys. J. **850**, L37 (2017).
[32] L. S. Finn and D. F. Chernoff, *Observing Binary Inspiral in Gravitational Radiation: One Interferometer*, Phys. Rev. D **47**, 2198 (1993).
[33] T. Hinderer, B. D. Lackey, R. N. Lang, and J. S. Read, *Tidal Deformability of Neutron Stars with Realistic Equations of State and Their Gravitational Wave Signatures in Binary Inspiral*, Phys. Rev. D **81**, 123016 (2010).
[34] T. Damour, A. Nagar, and L. Villain, *Measurability of the Tidal Polarizability of Neutron Stars in Late-Inspiral Gravitational-Wave Signals*, Phys. Rev. D **85**, 123007 (2012).
[35] W. Del Pozzo, T. G. F. Li, M. Agathos, C. Van Den Broeck, and S. Vitale, *Demonstrating the Feasibility of Probing the Neutron Star Equation of State with Second-Generation Gravitational Wave Detectors*, Phys. Rev. Lett. **111**, 071101 (2013).
[36] M. Agathos, J. Meidam, W. Del Pozzo, T. G. F. Li, M. Tompitak, J. Veitch, S. Vitale, and C. Van Den Broeck, *Constraining the Neutron Star Equation of State with Gravitational Wave Signals from Coalescing Binary Neutron Stars*, Phys. Rev. D **92**, 023012 (2015).
[37] I. Harry and T. Hinderer, *Observing and Measuring the Neutron-Star Equation-of-State in Spinning Binary Neutron Star Systems*, Classical Quantum Gravity **35**, 145010 (2018).
[38] F. Acernese *et al.* (Virgo Collaboration) *Calibration of Advanced Virgo and Reconstruction of the Gravitational Wave Signal h(t) during the Science Run O2*, arXiv:1807.03275.
[39] N. J. Cornish and T. B. Littenberg, *BayesWave: Bayesian Inference for Gravitational Wave Bursts and Instrument Glitches*, Classical Quantum Gravity **32**, 135012 (2015).
[40] K. L. Dooley *et al.*, *GEO 600 and the GEO-HF Upgrade Program: Successes and Challenges*, Classical Quantum Gravity **33**, 075009 (2016).
[41] B. P. Abbott *et al.* (LIGO Scientific Collaboration and Virgo Collaboration), *Search for Post-merger Gravitational Waves from the Remnant of the Binary Neutron Star Merger GW170817*, Astrophys. J. **851**, L16 (2017).
[42] B. P. Abbott *et al.* (LIGO Scientific Collaboration and Virgo Collaboration), *GW170817: Measurements of Neutron Star Radii and Equation of State*, Phys. Rev. Lett. **121**, 161101 (2018).
[43] C. Röver, R. Meyer, and N. Christensen, *Bayesian Inference on Compact Binary Inspiral Gravitational Radiation Signals in Interferometric Data*, Classical Quantum Gravity **23**, 4895 (2006).
[44] M. van der Sluys, V. Raymond, I. Mandel, C. Röver, N. Christensen, V. Kalogera, R. Meyer, and A. Vecchio, *Parameter Estimation of Spinning Binary Inspirals Using Markov-Chain Monte Carlo*, Classical Quantum Gravity **25**, 184011 (2008).
[45] J. Veitch *et al.*, *Parameter Estimation for Compact Binaries with Ground-based Gravitational-Wave Observations Using the LALInference Software Library*, Phys. Rev. D **91**, 042003 (2015).
[46] LIGO Scientific Collaboration and Virgo Collaboration, LALSuite, https://git.ligo.org/lscsoft/lalsuite/tree/lalinference_o2 (2017).
[47] T. B. Littenberg and N. J. Cornish, *Bayesian Inference for Spectral Estimation of Gravitational Wave Detector Noise*, Phys. Rev. D **91**, 084034 (2015).
[48] J. C. Driggers *et al.*, *Improving Astrophysical Parameter Estimation via Offline Noise Subtraction for Advanced LIGO*, arXiv:1806.00532.
[49] J. C. Driggers, M. Evans, K. Pepper, and R. Adhikari, *Active Noise Cancellation in a Suspended Interferometer*, Rev. Sci. Instrum. **83**, 024501 (2012).
[50] G. D. Meadors, K. Kawabe, and K. Riles, *Increasing LIGO Sensitivity by Feedforward Subtraction of Auxiliary*

Length Control Noise, Classical Quantum Gravity **31**, 105014 (2014).

[51] V. Tiwari *et al.*, *Regression of Environmental Noise in LIGO Data*, Classical Quantum Gravity **32**, 165014 (2015).

[52] C. Pankow *et al.*, *Mitigation of the Instrumental Noise Transient in Gravitational-Wave Data Surrounding GW170817*, Phys. Rev. D **98**, 084016 (2018).

[53] B. P. Abbott *et al.* (LIGO Scientific Collaboration and Virgo Collaboration), *GW170814: A Three-Detector Observation of Gravitational Waves from a Binary Black Hole Coalescence*, Phys. Rev. Lett. **119**, 141101 (2017).

[54] C. Cahillane *et al.* (LIGO Scientific Collaboration), *Calibration Uncertainty for Advanced LIGO's First and Second Observing Runs*, Phys. Rev. D **96**, 102001 (2017).

[55] A. Viets *et al.*, *Reconstructing the Calibrated Strain Signal in the Advanced LIGO Detectors*, Classical Quantum Gravity **35**, 095015 (2018).

[56] B. P. Abbott *et al.* (LIGO Scientific), *Calibration of the Advanced LIGO Detectors for the Discovery of the Binary Black-Hole Merger GW150914*, Phys. Rev. D **95**, 062003 (2017).

[57] S. Vitale, W. Del Pozzo, T. G. F. Li, C. Van Den Broeck, I. Mandel, B. Aylott, and J. Veitch, *Effect of Calibration Errors on Bayesian Parameter Estimation for Gravitational Wave Signals from Inspiral Binary Systems in the Advanced Detectors Era*, Phys. Rev. D **85**, 064034 (2012).

[58] W. M. Farr, B. Farr, and T. Littenberg, Modelling Calibration Errors in CBC Waveforms, Technical Report No. LIGO-T1400682(LIGO Project, 2015).

[59] I. Bartos, R. Bork, M. Factourovich, J. Heefner, S. Marka, Z. Marka, Z. Raics, P. Schwinberg, and D. Sigg, *The Advanced LIGO Timing System*, Classical Quantum Gravity **27**, 084025 (2010).

[60] B. S. Sathyaprakash and S. V. Dhurandhar, *Choice of Filters for the Detection of Gravitational Waves from Coalescing Binaries*, Phys. Rev. D **44**, 3819 (1991).

[61] L. Blanchet, T. Damour, B. R. Iyer, C. M. Will, and A. G. Wiseman, *Gravitational Radiation Damping of Compact Binary Systems to Second Post-Newtonian Order*, Phys. Rev. Lett. **74**, 3515 (1995).

[62] T. Damour, P. Jaranowski, and G. Schaefer, *Dimensional Regularization of the Gravitational Interaction of Point Masses*, Phys. Lett. B **513**, 147 (2001).

[63] W. D. Goldberger and I. Z. Rothstein, *An Effective Field Theory of Gravity for Extended Objects*, Phys. Rev. D **73**, 104029 (2006).

[64] L. Blanchet, T. Damour, G. Esposito-Farese, and B.R. Iyer, *Dimensional Regularization of the Third Post-Newtonian Gravitational Wave Generation from Two Point Masses*, Phys. Rev. D **71**, 124004 (2005).

[65] L. Blanchet, *Gravitational Radiation from Post-Newtonian Sources and Inspiralling Compact Binaries*, Living Rev. Relativity **17**, 2 (2014).

[66] A. Boh, S. Marsat, and L. Blanchet, *Next-to-Next-to-Leading Order Spin-Orbit Effects in the Gravitational Wave Flux and Orbital Phasing of Compact Binaries*, Classical Quantum Gravity **30**, 135009 (2013).

[67] K. G. Arun, A. Buonanno, G. Faye, and E. Ochsner, *Higher-Order Spin Effects in the Amplitude and Phase of Gravitational Waveforms Emitted by Inspiraling Compact Binaries: Ready-to-use Gravitational Waveforms*, Phys. Rev. D **79**, 104023 (2009).

[68] B. Mikoczi, M. Vasuth, and L. A. Gergely, *Self-interaction Spin Effects in Inspiralling Compact Binaries*, Phys. Rev. D **71**, 124043 (2005).

[69] A. Boh, G. Faye, S. Marsat, and E. K. Porter, *Quadratic-in-Spin Effects in the Orbital Dynamics and Gravitational-Wave Energy Flux of Compact Binaries at the 3PN Order*, Classical Quantum Gravity **32**, 195010 (2015).

[70] C. K. Mishra, A. Kela, K. G. Arun, and G. Faye, *Ready-to-Use Post-Newtonian Gravitational Waveforms for Binary Black Holes with Nonprecessing Spins: An Update*, Phys. Rev. D **93**, 084054 (2016).

[71] J. Vines, É. É. Flanagan, and T. Hinderer, *Post-1-Newtonian Tidal Effects in the Gravitational Waveform from Binary Inspirals*, Phys. Rev. D **83**, 084051 (2011).

[72] A. Bohé *et al.*, *Improved Effective-One-Body Model of Spinning, Nonprecessing Binary Black Holes for the Era of Gravitational-Wave Astrophysics with Advanced Detectors*, Phys. Rev. D **95**, 044028 (2017).

[73] M. Pürrer, *Frequency Domain Reduced Order Models for Gravitational Waves from Aligned-Spin Compact Binaries*, Classical Quantum Gravity **31**, 195010 (2014).

[74] T. Dietrich, S. Bernuzzi, and W. Tichy, *Closed-form Tidal Approximants for Binary Neutron Star Gravitational Waveforms Constructed from High-Resolution Numerical Relativity Simulations*, Phys. Rev. D **96**, 121501 (2017).

[75] T. Dietrich *et al.*, *Matter Imprints in Waveform Models for Neutron Star Binaries: Tidal and Self-spin Effects*, arXiv: 1804.02235.

[76] S. Husa, S. Khan, M. Hannam, M. Pürrer, F. Ohme, X. J. Forteza, and A. Bohé, *Frequency-Domain Gravitational Waves from Nonprecessing Black-Hole Binaries. I. New Numerical Waveforms and Anatomy of the Signal*, Phys. Rev. D **93**, 044006 (2016).

[77] S. Khan, S. Husa, M. Hannam, F. Ohme, M. Pürrer, X. J. Forteza, and A. Bohé, *Frequency-Domain Gravitational Waves from Non-precessing Black-Hole Binaries. II. A Phenomenological Model for the Advanced Detector Era*, Phys. Rev. D **93**, 044007 (2016).

[78] M. Hannam, P. Schmidt, A. Bohé, L. Haegel, S. Husa, F. Ohme, G. Pratten, and M. Pürrer, *Simple Model of Complete Precessing Black-Hole-Binary Gravitational Waveforms*, Phys. Rev. Lett. **113**, 151101 (2014).

[79] E. Poisson, *Gravitational Waves from Inspiraling Compact Binaries: The Quadrupole-Moment Term*, Phys. Rev. D **57**, 5287 (1998).

[80] S. Bernuzzi, A. Nagar, T. Dietrich, and T. Damour, *Modeling the Dynamics of Tidally Interacting Binary Neutron Stars up to the Merger*, Phys. Rev. Lett. **114**, 161103 (2015).

[81] Tanja Hinderer *et al.*, *Effects of Neutron-Star Dynamic Tides on Gravitational Waveforms within the Effective-One-Body Approach*, Phys. Rev. Lett. **116**, 181101 (2016).

[82] T. Dietrich and T. Hinderer, *Comprehensive Comparison of Numerical Relativity and Effective-One-Body Results to Inform Improvements in Waveform Models for Binary Neutron Star Systems*, Phys. Rev. D **95**, 124006 (2017).

[83] A. Nagar *et al.*, *Time-Domain Effective-One-Body Gravitational Waveforms for Coalescing Compact Binaries with Nonprecessing Spins, Tides and Self-spin Effects*, Phys. Rev. D **98**, 104052 (2018).
[84] C. Pankow, P. Brady, E. Ochsner, and R. O'Shaughnessy, *Novel Scheme for Rapid Parallel Parameter Estimation of Gravitational Waves from Compact Binary Coalescences*, Phys. Rev. D **92**, 023002 (2015).
[85] J. Lange, R. O'Shaughnessy, and M. Rizzo, *Rapid and Accurate Parameter Inference for Coalescing, Precessing Compact Binaries*, arXiv:1805.10457.
[86] L. Blanchet, T. Damour, G. Esposito-Farèse, and B. R. Iyer, *Gravitational Radiation from Inspiralling Compact Binaries Completed at the Third Post-Newtonian Order*, Phys. Rev. Lett. **93**, 091101 (2004).
[87] T. Damour and A. Nagar, *Effective One Body Description of Tidal Effects in Inspiralling Compact Binaries*, Phys. Rev. D **81**, 084016 (2010).
[88] D. Bini, T. Damour, and G. Faye, *Effective Action Approach to Higher-Order Relativistic Tidal Interactions in Binary Systems and Their Effective One Body Description*, Phys. Rev. D **85**, 124034 (2012).
[89] T. Dietrich, S. Bernuzzi, B. Brügmann, and W. Tichy, *High-Resolution Numerical Relativity Simulations of Spinning Binary Neutron Star Mergers*, arXiv:1803.07965.
[90] A. Taracchini *et al.*, *Effective-One-Body Model for Black-Hole Binaries with Generic Mass Ratios and Spins*, Phys. Rev. D **89**, 061502 (2014).
[91] E. Poisson, *Gravitational Waves from Inspiraling Compact Binaries: The Quadrupole Moment Term*, Phys. Rev. D **57**, 5287 (1998).
[92] K. Yagi and N. Yunes, *Approximate Universal Relations for Neutron Stars and Quark Stars*, Phys. Rep. **681**, 1 (2017).
[93] C. Cutler and É. É. Flanagan, *Gravitational Waves from Merging Compact Binaries: How Accurately Can One Extract the Binary's Parameters from the Inspiral Wave Form?*, Phys. Rev. D **49**, 2658 (1994).
[94] E. Poisson and C. M. Will, *Gravitational Waves from Inspiraling Compact Binaries: Parameter Estimation Using Second Post-Newtonian Wave Forms*, Phys. Rev. D **52**, 848 (1995).
[95] A. Krolak and B. F. Schutz, *Coalescing Binaries–Probe of the Universe*, Gen. Relativ. Gravit. **19**, 1163 (1987).
[96] A. J. Levan *et al.*, *The Environment of the Binary Neutron Star Merger GW170817*, Astrophys. J. **848**, L28 (2017).
[97] J. Hjorth, A. J. Levan, N. R. Tanvir, J. D. Lyman, R. Wojtak, S. L. Schrøder, I. Mandel, C. Gall, and S. H. Bruun, *The Distance to NGC 4993: The Host Galaxy of the Gravitational-Wave Event GW170817*, Astrophys. J. **848**, L31 (2017).
[98] J. W. T. Hessels, S. M. Ransom, I. H. Stairs, P. C. C. Freire, V. M. Kaspi, and F. Camilo, *A Radio Pulsar Spinning at 716 Hz*, Science **311**, 1901 (2006).
[99] M. Burgay *et al.*, *An Increased Estimate of the Merger Rate of Double Neutron Stars from Observations of a Highly Relativistic System*, Nature (London) **426**, 531 (2003).
[100] K. Stovall *et al.*, *PALFA Discovery of a Highly Relativistic Double Neutron Star Binary*, Astrophys. J. **854**, L22 (2018).
[101] K. Yagi and N. Yunes, *Binary Love Relations*, Classical Quantum Gravity **33**, 13LT01 (2016).
[102] K. Yagi and N. Yunes, *Approximate Universal Relations Among Tidal Parameters for Neutron Star Binaries*, Classical Quantum Gravity **34**, 015006 (2017).
[103] K. Chatziioannou, C.-J. Haster, and A. Zimmerman, *Measuring the Neutron Star Tidal Deformability with Equation-of-State-Independent Relations and Gravitational Waves*, Phys. Rev. D **97**, 104036 (2018).
[104] T. A. Apostolatos, C. Cutler, G. J. Sussman, and K. S. Thorne, *Spin Induced Orbital Precession and Its Modulation of the Gravitational Wave Forms from Merging Binaries*, Phys. Rev. D **49**, 6274 (1994).
[105] B. Farr *et al.*, *Parameter Estimation on Gravitational Waves from Neutron-Star Binaries with Spinning Components*, Astrophys. J. **825**, 116 (2015).
[106] B. P. Abbott *et al.* (LIGO Scientific Collaboration, VINROUGE, Las Cumbres Observatory, DES, DLT40, Virgo Collaboration, 1M2H, Dark Energy Camera GW-E, and MASTER), *A Gravitational-Wave Standard Siren Measurement of the Hubble Constant*, Nature (London) **551**, 85 (2017).
[107] S. Nissanke, D. E. Holz, S. A. Hughes, N. Dalal, and J. L. Sievers, *Exploring Short Gamma-Ray Bursts as Gravitational-Wave Standard Sirens*, Astrophys. J. **725**, 496 (2010).
[108] M. Cantiello *et al.*, *A Precise Distance to the Host Galaxy of the Binary Neutron Star Merger GW170817 Using Surface Brightness Fluctuations*, Astrophys. J. **854**, L31 (2018).
[109] C. Guidorzi *et al.*, *Improved Constraints on H_0 from a Combined Analysis of Gravitational-Wave and Electromagnetic Emission from GW170817*, Astrophys. J. **851**, L36 (2017).
[110] I. Mandel, *The Orbit of GW170817 Was Inclined by Less Than 28 to the Line of Sight*, Astrophys. J. **853**, L12 (2018).
[111] D. Finstad, S. De, D. A. Brown, E. Berger, and C. M. Biwer, *Measuring the Viewing Angle of GW170817 with Electromagnetic and Gravitational Waves*, Astrophys. J. **860**, L2 (2018).
[112] B. P. Abbott *et al.* (LIGO Scientific Collaboration and Virgo Collaboration), *Observation of Gravitational Waves from a Binary Black Hole Merger*, Phys. Rev. Lett. **116**, 061102 (2016).
[113] B. P. Abbott *et al.* (LIGO Scientific Collaboration and Virgo Collaboration), *Properties of the Binary Black Hole Merger GW150914*, Phys. Rev. Lett. **116**, 241102 (2016).
[114] B. P. Abbott *et al.* (LIGO Scientific Collaboration and Virgo Collaboration), *Binary Black Hole Mergers in the First Advanced LIGO Observing Run*, Phys. Rev. X **6**, 041015 (2016).
[115] B. P. Abbott *et al.* (LIGO Scientific Collaboration and Virgo Collaboration), *Effects of Waveform Model Systematics on the Interpretation of GW150914*, Classical Quantum Gravity **34**, 104002 (2017).
[116] E. Baird, S. Fairhurst, M. Hannam, and P. Murphy, *Degeneracy between Mass and Spin in Black-Hole-Binary Waveforms*, Phys. Rev. D **87**, 024035 (2013).

[117] J. Antoniadis, T. M. Tauris, F. Özel, E. Barr, D. J. Champion, and P. C. C. Freire, *The Millisecond Pulsar Mass Distribution: Evidence for Bimodality and Constraints on the Maximum Neutron Star Mass*, arXiv:1605.01665.

[118] B. P. Abbott *et al.* (LIGO Scientific Collaboration and Virgo Collaboration), *On the Progenitor of Binary Neutron Star Merger GW170817*, Astrophys. J. **850**, L40 (2017).

[119] A similar contour as that displayed in Fig. 4 of Ref. [3] was broader as a result of not using the full information about the redshift to the source to calculate the source-frame masses.

[120] J. Lense and H. Thirring, *Über den Einflußder Eigenrotation der Zentralkörper auf die Bewegung der Planeten und Monde nach der Einsteinschen Gravitationstheorie*, Phys. Z. **19**, 156 (1918).

[121] B. Mashhoon, F. W. Hehl, and D. S. Theiss, *On the Gravitational Effects of Rotating Masses—The Thirring-Lense Papers*, Gen. Relativ. Gravit. **16**, 711 (1984).

[122] J. D. Kaplan, D. A. Nichols, and K. S. Thorne, *Post-Newtonian Approximation in Maxwell-like Form*, Phys. Rev. D **80**, 124014 (2009).

[123] M. Campanelli, C. O. Lousto, and Y. Zlochower, *Spinning-Black-Hole Binaries: The Orbital Hang Up*, Phys. Rev. D **74**, 041501 (2006).

[124] T. Damour, *Coalescence of Two Spinning Black Holes: An Effective One-Body Approach*, Phys. Rev. D **64**, 124013 (2001).

[125] P. Ajith *et al.*, *Inspiral-Merger-Ringdown Waveforms for Black-Hole Binaries with Non-precessing Spins*, Phys. Rev. Lett. **106**, 241101 (2011).

[126] L. Santamaría, F. Ohme, P. Ajith, B. Brügmann, N. Dorband *et al.*, *Matching Post-Newtonian and Numerical Relativity Waveforms: Systematic Errors and a New Phenomenological Model for Non-precessing Black Hole Binaries*, Phys. Rev. D **82**, 064016 (2010).

[127] L. E. Kidder, C. M. Will, and A. G. Wiseman, *Spin Effects in the Inspiral of Coalescing Compact Binaries*, Phys. Rev. D **47**, R4183 (1993).

[128] P. Ajith, *Addressing the Spin Question in Gravitational-Wave Searches: Waveform Templates for Inspiralling Compact Binaries with Nonprecessing Spins*, Phys. Rev. D **84**, 084037 (2011).

[129] L. Blanchet, T. Damour, and B. R. Iyer, *Gravitational Waves from Inspiralling Compact Binaries: Energy Loss and Wave Form to Second Post-Newtonian Order*, Phys. Rev. D **51**, 5360 (1995); **54**, 1860 (1996).

[130] E. Racine, *Analysis of Spin Precession in Binary Black Hole Systems Including Quadrupole-Monopole Interaction*, Phys. Rev. D **78**, 044021 (2008).

[131] S. Vitale, R. Lynch, J. Veitch, V. Raymond, and R. Sturani, *Measuring the Spin of Black Holes in Binary Systems Using Gravitational Waves*, Phys. Rev. Lett. **112**, 251101 (2014).

[132] S. Vitale, R. Lynch, V. Raymond, R. Sturani, J. Veitch, and P. Graff, *Parameter Estimation for Heavy Binary-Black Holes with Networks of Second-Generation Gravitational-Wave Detectors*, Phys. Rev. D **95**, 064053 (2017).

[133] P. Schmidt, F. Ohme, and M. Hannam, *Towards Models of Gravitational Waveforms from Generic Binaries II: Modelling Precession Effects with a Single Effective Precession Parameter*, Phys. Rev. D **91**, 024043 (2015).

[134] K. K. Y. Ng, S. Vitale, A. Zimmerman, K. Chatziioannou, D. Gerosa, and C.-J. Haster, *Gravitational-Wave Astrophysics with Effective-Spin Measurements: Asymmetries and Selection Biases*, Phys. Rev. D **98**, 083007 (2018).

[135] É. É. Flanagan and T. Hinderer, *Constraining Neutron-Star Tidal Love Numbers with Gravitational-Wave Detectors*, Phys. Rev. D **77**, 021502 (2008).

[136] J. S. Read, B. D. Lackey, B. J. Owen, and J. L. Friedman, *Constraints on a Phenomenologically Parametrized Neutron-Star Equation of State*, Phys. Rev. D **79**, 124032 (2009).

[137] Reference [3] connected these high-density EOS fits to a single, low-density polytrope. Here, we use the four-piece low-density polytrope fit described in Ref. [136]. The choice of low-density EOS can change the curves shown here by about 5%.

[138] L. Wade, J. D. E. Creighton, E. Ochsner, B. D. Lackey, B. F. Farr, T. B. Littenberg, and V. Raymond, *Systematic and Statistical Errors in a Bayesian Approach to the Estimation of the Neutron-Star Equation of State Using Advanced Gravitational Wave Detectors*, Phys. Rev. D **89**, 103012 (2014).

[139] J. Steinhoff, T. Hinderer, A. Buonanno, and A. Taracchini, *Dynamical Tides in General Relativity: Effective Action and Effective-One-Body Hamiltonian*, Phys. Rev. D **94**, 104028 (2016).

[140] T. Dietrich and T. Hinderer, *Comprehensive Comparison of Numerical Relativity and Effective-One-Body Results to Inform Improvements in Waveform Models for Binary Neutron Star Systems*, Phys. Rev. D **95**, 124006 (2017).

[141] S. De, D. Finstad, J. M. Lattimer, D. A. Brown, E. Berger, and C. M. Biwer, *Constraining the Nuclear Equation of State with GW170817*, Phys. Rev. Lett. **121**, 091102 (2018).

[142] B. D. Lackey and L. Wade, *Reconstructing the Neutron-Star Equation of State with Gravitational-Wave Detectors from a Realistic Population of Inspiralling Binary Neutron Stars*, Phys. Rev. D **91**, 043002 (2015).

[143] M. F. Carney, L. E. Wade, and B. S. Irwin, *Comparing Two Models for Measuring the Neutron Star Equation of State from Gravitational-Wave Signals*, Phys. Rev. D **98**, 063004 (2018).

[144] M. Shibata and K. Taniguchi, *Merger of Binary Neutron Stars to a Black Hole: Disk Mass, Short Gamma-Ray Bursts, and Quasinormal Mode Ringing*, Phys. Rev. D **73**, 064027 (2006).

[145] T. W. Baumgarte, S. L. Shapiro, and M. Shibata, *On the Maximum Mass of Differentially Rotating Neutron Stars*, Astrophys. J. Lett. **528**, L29 (2000).

[146] B. Giacomazzo and R. Perna, *Formation of Stable Magnetars from Binary Neutron Star Mergers*, Astrophys. J. **771**, L26 (2013).

[147] S. L. Shapiro, *Differential Rotation in Neutron Stars: Magnetic Braking and Viscous Damping*, Astrophys. J. **544**, 397 (2000).

[148] K. Hotokezaka, K. Kiuchi, K. Kyutoku, T. Muranushi, Y.-i. Sekiguchi, M. Shibata, and K. Taniguchi, *Remnant Massive Neutron Stars of Binary Neutron Star Mergers:*

Evolution Process and Gravitational Waveform, Phys. Rev. D **88**, 044026 (2013).
[149] V. Ravi and P. D. Lasky, *The Birth of Black Holes: Neutron Star Collapse Times, Gamma-Ray Bursts and Fast Radio Bursts*, Mon. Not. R. Astron. Soc. **441**, 2433 (2014).
[150] K. Chatziioannou, J. A. Clark, A. Bauswein, M. Millhouse, T. B. Littenberg, and N. Cornish, *Inferring the Post-merger Gravitational Wave Emission from Binary Neutron Star Coalescences*, Phys. Rev. D **96**, 124035 (2017).
[151] B. P. Abbott *et al.* (LIGO Scientific Collaboration and Virgo Collaboration), *Tests of General Relativity with GW150914*, Phys. Rev. Lett. **116**, 221101 (2016).
[152] B. P. Abbott *et al.* (LIGO Scientific Collaboration and Virgo Collaboration), *GW170104: Observation of a 50-Solar-Mass Binary Black Hole Coalescence at Redshift 0.2*, Phys. Rev. Lett. **118**, 221101 (2017).
[153] B. P. Abbott *et al.* (LIGO Scientific Collaboration and Virgo Collaboration), *Prospects for Observing and Localizing Gravitational-Wave Transients with Advanced LIGO, Advanced Virgo and KAGRA*, Living Rev. Relativity **19**, 1 (2016); **21**, 3 (2018).
[154] J. Miller, L. Barsotti, S. Vitale, P. Fritschel, M. Evans, and D. Sigg, *Prospects for Doubling the Range of Advanced LIGO*, Phys. Rev. D **91**, 062005 (2015).
[155] F. Zappa, S. Bernuzzi, D. Radice, A. Perego, and T. Dietrich, *Gravitational-Wave Luminosity of Binary Neutron Stars Mergers*, Phys. Rev. Lett. **120**, 111101 (2018).
[156] A. Akmal, V. R. Pandharipande, and D. G. Ravenhall, *Equation of State of Nucleon Matter and Neutron Star Structure*, Phys. Rev. C **58**, 1804 (1998).
[157] R. Ciolfi, W. Kastaun, B. Giacomazzo, A. Endrizzi, D. M. Siegel, and R. Perna, *General Relativistic Magnetohydrodynamic Simulations of Binary Neutron Star Mergers Forming a Long-lived Neutron Star*, Phys. Rev. D **95**, 063016 (2017).
[158] N. K. Glendenning and S. A. Moszkowski, *Reconciliation of Neutron Star Masses and Binding of the Lambda in Hypernuclei*, Phys. Rev. Lett. **67**, 2414 (1991).
[159] N. K. Glendenning, *Neutron Stars Are Giant Hypernuclei?*, Astrophys. J. **293**, 470 (1985).
[160] K. Takami, L. Rezzolla, and L. Baiotti, *Spectral Properties of the Post-merger Gravitational-Wave Signal from Binary Neutron Stars*, Phys. Rev. D **91**, 064001 (2015).
[161] F. Douchin and P. Haensel, *A Unified Equation of State of Dense Matter and Neutron Star Structure*, Astron. Astrophys. **380**, 151 (2001).
[162] A. W. Steiner, M. Hempel, and T. Fischer, *Core-Collapse Supernova Equations of State Based on Neutron Star Observations*, Astrophys. J. **774**, 17 (2013).
[163] A. Bauswein, T. W. Baumgarte, and H.-T. Janka, *Prompt Merger Collapse and the Maximum Mass of Neutron Stars*, Phys. Rev. Lett. **111**, 131101 (2013).
[164] M. Hempel and J. Schaffner-Bielich, *Statistical Model for a Complete Supernova Equation of State*, Nucl. Phys. **A837**, 210 (2010).
[165] S. Typel, G. Röpke, T. Klähn, D. Blaschke, and H. H. Wolter, *Composition and Thermodynamics of Nuclear Matter with Light Clusters*, Phys. Rev. C **81**, 015803 (2010).
[166] https://dcc.ligo.org/LIGO-P1800061/public.
[167] LIGO Open Science Center (LOSC), https://doi.org/10.7935/K5B8566F.
[168] M. Favata, *Systematic Parameter Errors in Inspiraling Neutron Star Binaries*, Phys. Rev. Lett. **112**, 101101 (2014).
[169] K. Yagi and N. Yunes, *Love Number Can Be Hard to Measure*, Phys. Rev. D **89**, 021303 (2014).
[170] B. D. Lackey and L. Wade, *Reconstructing the Neutron-Star Equation of State with Gravitational-Wave Detectors from a Realistic Population of Inspiralling Binary Neutron Stars*, Phys. Rev. D **91**, 043002 (2015).
[171] R. Dudi, F. Pannarale, T. Dietrich, M. Hannam, S. Bernuzzi, F. Ohme, and B. Bruegmann, *Relevance of Tidal Effects and Post-merger Dynamics for Binary Neutron Star Parameter Estimation*, Phys. Rev. D **98**, 084061 (2018).
[172] J. S. Read, C. Markakis, M. Shibata, K. Uryu, J. D. E. Creighton, and J. L. Friedman, *Measuring the Neutron Star Equation of State with Gravitational Wave Observations*, Phys. Rev. D **79**, 124033 (2009).
[173] M. Vallisneri, *Use and Abuse of the Fisher Information Matrix in the Assessment of Gravitational-Wave Parameter-Estimation Prospects*, Phys. Rev. D **77**, 042001 (2008).
[174] C. L. Rodriguez, B. Farr, V. Raymond, W. M. Farr, T. B. Littenberg, D. Fazi, and V. Kalogera, *Basic Parameter Estimation of Binary Neutron Star Systems by the Advanced LIGO/Virgo Network*, Astrophys. J. **784**, 119 (2014).
[175] S. M. Gaebel and J. Veitch, *How Would GW150914 Look with Future Gravitational Wave Detector Networks?*, Classical Quantum Gravity **34**, 174003 (2017).
[176] S. Vitale and H.-Y. Chen, *Measuring the Hubble Constant with Neutron Star Black Hole Mergers*, Phys. Rev. Lett. **121**, 021303 (2018).

Correction: The wrong author-affiliation list was used and has now been fixed.

B. P. Abbott,[1] R. Abbott,[1] T. D. Abbott,[2] F. Acernese,[3,4] K. Ackley,[5] C. Adams,[6] T. Adams,[7] P. Addesso,[8] R. X. Adhikari,[1] V. B. Adya,[9,10] C. Affeldt,[9,10] B. Agarwal,[11] M. Agathos,[12] K. Agatsuma,[13] N. Aggarwal,[14] O. D. Aguiar,[15] L. Aiello,[16,17] A. Ain,[18] P. Ajith,[19] B. Allen,[9,20,10] G. Allen,[11] A. Allocca,[21,22] M. A. Aloy,[23] P. A. Altin,[24] A. Amato,[25] A. Ananyeva,[1] S. B. Anderson,[1] W. G. Anderson,[20] S. V. Angelova,[26] S. Antier,[27] S. Appert,[1] K. Arai,[1] M. C. Araya,[1] J. S. Areeda,[28] M. Arène,[29] N. Arnaud,[27,30] K. G. Arun,[31] S. Ascenzi,[32,33] G. Ashton,[5] M. Ast,[34]

S. M. Aston,[6] P. Astone,[35] D. V. Atallah,[36] F. Aubin,[7] P. Aufmuth,[10] C. Aulbert,[9] K. AultONeal,[37] C. Austin,[2] A. Avila-Alvarez,[28] S. Babak,[38,29] P. Bacon,[29] F. Badaracco,[16,17] M. K. M. Bader,[13] S. Bae,[39] P. T. Baker,[40] F. Baldaccini,[41,42] G. Ballardin,[30] S. W. Ballmer,[43] S. Banagiri,[44] J. C. Barayoga,[1] S. E. Barclay,[45] B. C. Barish,[1] D. Barker,[46] K. Barkett,[47] S. Barnum,[14] F. Barone,[3,4] B. Barr,[45] L. Barsotti,[14] M. Barsuglia,[29] D. Barta,[48] J. Bartlett,[46] I. Bartos,[49] R. Bassiri,[50] A. Basti,[21,22] J. C. Batch,[46] M. Bawaj,[51,42] J. C. Bayley,[45] M. Bazzan,[52,53] B. Bécsy,[54] C. Beer,[9] M. Bejger,[55] I. Belahcene,[27] A. S. Bell,[45] D. Beniwal,[56] M. Bensch,[9,10] B. K. Berger,[1] G. Bergmann,[9,10] S. Bernuzzi,[57,58] J. J. Bero,[59] C. P. L. Berry,[60] D. Bersanetti,[61] A. Bertolini,[13] J. Betzwieser,[6] R. Bhandare,[62] I. A. Bilenko,[63] S. A. Bilgili,[40] G. Billingsley,[1] C. R. Billman,[49] J. Birch,[6] I. A. Birney,[26] O. Birnholtz,[59] S. Biscans,[1,14] S. Biscoveanu,[5] A. Bisht,[9,10] M. Bitossi,[30,22] M. A. Bizouard,[27] J. K. Blackburn,[1] J. Blackman,[47] C. D. Blair,[6] D. G. Blair,[64] R. M. Blair,[46] S. Bloemen,[65] O. Bock,[9] N. Bode,[9,10] M. Boer,[66] Y. Boetzel,[67] G. Bogaert,[66] A. Bohe,[38] F. Bondu,[68] E. Bonilla,[50] R. Bonnand,[7] P. Booker,[9,10] B. A. Boom,[13] C. D. Booth,[36] R. Bork,[1] V. Boschi,[30] S. Bose,[69,18] K. Bossie,[6] V. Bossilkov,[64] J. Bosveld,[64] Y. Bouffanais,[29] A. Bozzi,[30] C. Bradaschia,[22] P. R. Brady,[20] A. Bramley,[6] M. Branchesi,[16,17] J. E. Brau,[70] T. Briant,[71] F. Brighenti,[72,73] A. Brillet,[66] M. Brinkmann,[9,10] V. Brisson,[27,a] P. Brockill,[20] A. F. Brooks,[1] D. D. Brown,[56] S. Brunett,[1] C. C. Buchanan,[2] A. Buikema,[14] T. Bulik,[74] H. J. Bulten,[75,13] A. Buonanno,[38,76] D. Buskulic,[7] C. Buy,[29] R. L. Byer,[50] M. Cabero,[9] L. Cadonati,[77] G. Cagnoli,[25,78] C. Cahillane,[1] J. Calderón Bustillo,[77] T. A. Callister,[1] E. Calloni,[79,4] J. B. Camp,[80] M. Canepa,[81,61] P. Canizares,[65] K. C. Cannon,[82] H. Cao,[56] J. Cao,[83] C. D. Capano,[9] E. Capocasa,[29] F. Carbognani,[30] S. Caride,[84] M. F. Carney,[85] G. Carullo,[21] J. Casanueva Diaz,[22] C. Casentini,[32,33] S. Caudill,[13,20] M. Cavaglià,[86] F. Cavalier,[27] R. Cavalieri,[30] G. Cella,[22] C. B. Cepeda,[1] P. Cerdá-Durán,[23] G. Cerretani,[21,22] E. Cesarini,[87,33] O. Chaibi,[66] S. J. Chamberlin,[88] M. Chan,[45] S. Chao,[89] P. Charlton,[90] E. Chase,[91] E. Chassande-Mottin,[29] D. Chatterjee,[20] K. Chatziioannou,[92] B. D. Cheeseboro,[40] H. Y. Chen,[93] X. Chen,[64] Y. Chen,[47] H.-P. Cheng,[49] H. Y. Chia,[49] A. Chincarini,[61] A. Chiummo,[30] T. Chmiel,[85] H. S. Cho,[94] M. Cho,[76] J. H. Chow,[24] N. Christensen,[95,66] Q. Chu,[64] A. J. K. Chua,[47] S. Chua,[71] K. W. Chung,[96] S. Chung,[64] G. Ciani,[52,53,49] A. A. Ciobanu,[56] R. Ciolfi,[97,98] F. Cipriano,[66] C. E. Cirelli,[50] A. Cirone,[81,61] F. Clara,[46] J. A. Clark,[77] P. Clearwater,[99] F. Cleva,[66] C. Cocchieri,[86] E. Coccia,[16,17] P.-F. Cohadon,[71] D. Cohen,[27] A. Colla,[100,35] C. G. Collette,[101] C. Collins,[60] L. R. Cominsky,[102] M. Constancio Jr.,[15] L. Conti,[53] S. J. Cooper,[60] P. Corban,[6] T. R. Corbitt,[2] I. Cordero-Carrión,[103] K. R. Corley,[104] N. Cornish,[105] A. Corsi,[84] S. Cortese,[30] C. A. Costa,[15] R. Cotesta,[38] M. W. Coughlin,[1] S. B. Coughlin,[36,91] J.-P. Coulon,[66] S. T. Countryman,[104] P. Couvares,[1] P. B. Covas,[106] E. E. Cowan,[77] D. M. Coward,[64] M. J. Cowart,[6] D. C. Coyne,[1] R. Coyne,[107] J. D. E. Creighton,[20] T. D. Creighton,[108] J. Cripe,[2] S. G. Crowder,[109] T. J. Cullen,[2] A. Cumming,[45] L. Cunningham,[45] E. Cuoco,[30] T. Dal Canton,[80] G. Dálya,[54] S. L. Danilishin,[10,9] S. D'Antonio,[33] K. Danzmann,[9,10] A. Dasgupta,[110] C. F. Da Silva Costa,[49] V. Dattilo,[30] I. Dave,[62] M. Davier,[27] D. Davis,[43] E. J. Daw,[111] B. Day,[77] D. DeBra,[50] M. Deenadayalan,[18] J. Degallaix,[25] M. De Laurentis,[79,4] S. Deléglise,[71] W. Del Pozzo,[21,22] N. Demos,[14] T. Denker,[9,10] T. Dent,[9] R. De Pietri,[57,58] J. Derby,[28] V. Dergachev,[9] R. De Rosa,[79,4] C. De Rossi,[25,30] R. DeSalvo,[112] O. de Varona,[9,10] S. Dhurandhar,[18] M. C. Díaz,[108] T. Dietrich,[13,38] L. Di Fiore,[4] M. Di Giovanni,[113,98] T. Di Girolamo,[79,4] A. Di Lieto,[21,22] B. Ding,[101] S. Di Pace,[100,35] I. Di Palma,[100,35] F. Di Renzo,[21,22] A. Dmitriev,[60] Z. Doctor,[93] V. Dolique,[25] F. Donovan,[14] K. L. Dooley,[36,86] S. Doravari,[9,10] I. Dorrington,[36] M. Dovale Álvarez,[60] T. P. Downes,[20] M. Drago,[9,16,17] C. Dreissigacker,[9,10] J. C. Driggers,[46] Z. Du,[83] R. Dudi,[36] P. Dupej,[45] S. E. Dwyer,[46] P. J. Easter,[5] T. B. Edo,[111] M. C. Edwards,[95] A. Effler,[6] H.-B. Eggenstein,[9,10] P. Ehrens,[1] J. Eichholz,[1] S. S. Eikenberry,[49] M. Eisenmann,[7] R. A. Eisenstein,[14] R. C. Essick,[93] H. Estelles,[106] D. Estevez,[7] Z. B. Etienne,[40] T. Etzel,[1] M. Evans,[14] T. M. Evans,[6] V. Fafone,[32,33,16] H. Fair,[43] S. Fairhurst,[36] X. Fan,[83] S. Farinon,[61] B. Farr,[70] W. M. Farr,[60] E. J. Fauchon-Jones,[36] M. Favata,[114] M. Fays,[36] C. Fee,[85] H. Fehrmann,[9] J. Feicht,[1] M. M. Fejer,[50] F. Feng,[29] A. Fernandez-Galiana,[14] I. Ferrante,[21,22] E. C. Ferreira,[15] F. Ferrini,[30] F. Fidecaro,[21,22] I. Fiori,[30] D. Fiorucci,[29] M. Fishbach,[93] R. P. Fisher,[43] J. M. Fishner,[14] M. Fitz-Axen,[44] R. Flaminio,[7,115] M. Fletcher,[45] H. Fong,[92] J. A. Font,[23,116] P. W. F. Forsyth,[24] S. S. Forsyth,[77] J.-D. Fournier,[66] S. Frasca,[100,35] F. Frasconi,[22] Z. Frei,[54] A. Freise,[60] R. Frey,[70] V. Frey,[27] P. Fritschel,[14] V. V. Frolov,[6] P. Fulda,[49] M. Fyffe,[6] H. A. Gabbard,[45] B. U. Gadre,[18] S. M. Gaebel,[60] J. R. Gair,[117] L. Gammaitoni,[41] M. R. Ganija,[56] S. G. Gaonkar,[18] A. Garcia,[28] C. García-Quirós,[106] F. Garufi,[79,4] B. Gateley,[46] S. Gaudio,[37] G. Gaur,[118] V. Gayathri,[119] G. Gemme,[61] E. Genin,[30] A. Gennai,[22] D. George,[11] J. George,[62] L. Gergely,[120] V. Germain,[7] S. Ghonge,[77] Abhirup Ghosh,[19] Archisman Ghosh,[13] S. Ghosh,[20] B. Giacomazzo,[113,98] J. A. Giaime,[2,6] K. D. Giardina,[6] A. Giazotto,[22,b] K. Gill,[37] G. Giordano,[3,4] L. Glover,[112] E. Goetz,[46] R. Goetz,[49] B. Goncharov,[5] G. González,[2] J. M. Gonzalez Castro,[21,22] A. Gopakumar,[121] M. L. Gorodetsky,[63] S. E. Gossan,[1]

M. Gosselin,[30] R. Gouaty,[7] A. Grado,[122,4] C. Graef,[45] M. Granata,[25] A. Grant,[45] S. Gras,[14] C. Gray,[46] G. Greco,[72,73] A. C. Green,[60] R. Green,[36] E. M. Gretarsson,[37] P. Groot,[65] H. Grote,[36] S. Grunewald,[38] P. Gruning,[27] G. M. Guidi,[72,73] H. K. Gulati,[110] X. Guo,[83] A. Gupta,[88] M. K. Gupta,[110] K. E. Gushwa,[1] E. K. Gustafson,[1] R. Gustafson,[123] O. Halim,[17,16] B. R. Hall,[69] E. D. Hall,[14] E. Z. Hamilton,[36] H. F. Hamilton,[124] G. Hammond,[45] M. Haney,[67] M. M. Hanke,[9,10] J. Hanks,[46] C. Hanna,[88] M. D. Hannam,[36] O. A. Hannuksela,[96] J. Hanson,[6] T. Hardwick,[2] J. Harms,[16,17] G. M. Harry,[125] I. W. Harry,[38] M. J. Hart,[45] C.-J. Haster,[92] K. Haughian,[45] J. Healy,[59] A. Heidmann,[71] M. C. Heintze,[6] H. Heitmann,[66] P. Hello,[27] G. Hemming,[30] M. Hendry,[45] I. S. Heng,[45] J. Hennig,[45] A. W. Heptonstall,[1] F. J. Hernandez,[5] M. Heurs,[9,10] S. Hild,[45] T. Hinderer,[65] D. Hoak,[30] S. Hochheim,[9,10] D. Hofman,[25] N. A. Holland,[24] K. Holt,[6] D. E. Holz,[93] P. Hopkins,[36] C. Horst,[20] J. Hough,[45] E. A. Houston,[45] E. J. Howell,[64] A. Hreibi,[66] E. A. Huerta,[11] D. Huet,[27] B. Hughey,[37] M. Hulko,[1] S. Husa,[106] S. H. Huttner,[45] T. Huynh-Dinh,[6] A. Iess,[32,33] N. Indik,[9] C. Ingram,[56] R. Inta,[84] G. Intini,[100,35] H. N. Isa,[45] J.-M. Isac,[71] M. Isi,[1] B. R. Iyer,[19] K. Izumi,[46] T. Jacqmin,[71] K. Jani,[77] P. Jaranowski,[126] D. S. Johnson,[11] W. W. Johnson,[2] D. I. Jones,[127] R. Jones,[45] R. J. G. Jonker,[13] L. Ju,[64] J. Junker,[9,10] C. V. Kalaghatgi,[36] V. Kalogera,[91] B. Kamai,[1] S. Kandhasamy,[6] G. Kang,[39] J. B. Kanner,[1] S. J. Kapadia,[20] S. Karki,[70] K. S. Karvinen,[9,10] M. Kasprzack,[2] W. Kastaun,[9] M. Katolik,[11] S. Katsanevas,[30] E. Katsavounidis,[14] W. Katzman,[6] S. Kaufer,[9,10] K. Kawabe,[46] N. V. Keerthana,[18] F. Kéfélian,[66] D. Keitel,[45] A. J. Kemball,[11] R. Kennedy,[111] J. S. Key,[128] F. Y. Khalili,[63] B. Khamesra,[77] H. Khan,[28] I. Khan,[16,33] S. Khan,[9] Z. Khan,[110] E. A. Khazanov,[129] N. Kijbunchoo,[24] Chunglee Kim,[130] J. C. Kim,[131] K. Kim,[96] W. Kim,[56] W. S. Kim,[132] Y.-M. Kim,[133] E. J. King,[56] P. J. King,[46] M. Kinley-Hanlon,[125] R. Kirchhoff,[9,10] J. S. Kissel,[46] L. Kleybolte,[34] S. Klimenko,[49] T. D. Knowles,[40] P. Koch,[9,10] S. M. Koehlenbeck,[9,10] S. Koley,[13] V. Kondrashov,[1] A. Kontos,[14] M. Korobko,[34] W. Z. Korth,[1] I. Kowalska,[74] D. B. Kozak,[1] C. Krämer,[9] V. Kringel,[9,10] B. Krishnan,[9] A. Królak,[134,135] G. Kuehn,[9,10] P. Kumar,[136] R. Kumar,[110] S. Kumar,[19] L. Kuo,[89] A. Kutynia,[134] S. Kwang,[20] B. D. Lackey,[38] K. H. Lai,[96] M. Landry,[46] P. Landry,[93] R. N. Lang,[137] J. Lange,[59] B. Lantz,[50] R. K. Lanza,[14] A. Lartaux-Vollard,[27] P. D. Lasky,[5] M. Laxen,[6] A. Lazzarini,[1] C. Lazzaro,[53] P. Leaci,[100,35] S. Leavey,[9,10] C. H. Lee,[94] H. K. Lee,[138] H. M. Lee,[130] H. W. Lee,[131] K. Lee,[45] J. Lehmann,[9,10] A. Lenon,[40] M. Leonardi,[9,10,115] N. Leroy,[27] N. Letendre,[7] Y. Levin,[5] J. Li,[83] T. G. F. Li,[96] X. Li,[47] S. D. Linker,[112] T. B. Littenberg,[139] J. Liu,[64] X. Liu,[20] R. K. L. Lo,[96] N. A. Lockerbie,[26] L. T. London,[36] A. Longo,[140,141] M. Lorenzini,[16,17] V. Loriette,[142] M. Lormand,[6] G. Losurdo,[22] J. D. Lough,[9,10] C. O. Lousto,[59] G. Lovelace,[28] H. Lück,[9,10] D. Lumaca,[32,33] A. P. Lundgren,[9] R. Lynch,[14] Y. Ma,[47] R. Macas,[36] S. Macfoy,[26] B. Machenschalk,[9] M. MacInnis,[14] D. M. Macleod,[36] I. Magaña Hernandez,[20] F. Magaña-Sandoval,[43] L. Magaña Zertuche,[86] R. M. Magee,[88] E. Majorana,[35] I. Maksimovic,[142] N. Man,[66] V. Mandic,[44] V. Mangano,[45] G. L. Mansell,[24] M. Manske,[20,24] M. Mantovani,[30] F. Marchesoni,[51,42] F. Marion,[7] S. Márka,[104] Z. Márka,[104] C. Markakis,[11] A. S. Markosyan,[50] A. Markowitz,[1] E. Maros,[1] A. Marquina,[103] F. Martelli,[72,73] L. Martellini,[66] I. W. Martin,[45] R. M. Martin,[114] D. V. Martynov,[14] K. Mason,[14] E. Massera,[111] A. Masserot,[7] T. J. Massinger,[1] M. Masso-Reid,[45] S. Mastrogiovanni,[100,35] A. Matas,[44] F. Matichard,[1,14] L. Matone,[104] N. Mavalvala,[14] N. Mazumder,[69] J. J. McCann,[64] R. McCarthy,[46] D. E. McClelland,[24] S. McCormick,[6] L. McCuller,[14] S. C. McGuire,[143] J. McIver,[1] D. J. McManus,[24] T. McRae,[24] S. T. McWilliams,[40] D. Meacher,[88] G. D. Meadors,[5] M. Mehmet,[9,10] J. Meidam,[13] E. Mejuto-Villa,[8] A. Melatos,[99] G. Mendell,[46] D. Mendoza-Gandara,[9,10] R. A. Mercer,[20] L. Mereni,[25] E. L. Merilh,[46] M. Merzougui,[66] S. Meshkov,[1] C. Messenger,[45] C. Messick,[88] R. Metzdorff,[71] P. M. Meyers,[44] H. Miao,[60] C. Michel,[25] H. Middleton,[99] E. E. Mikhailov,[144] L. Milano,[79,4] A. L. Miller,[49] A. Miller,[100,35] B. B. Miller,[91] J. Miller,[14] M. Millhouse,[105] J. Mills,[36] M. C. Milovich-Goff,[112] O. Minazzoli,[66,145] Y. Minenkov,[33] J. Ming,[9,10] C. Mishra,[146] S. Mitra,[18] V. P. Mitrofanov,[63] G. Mitselmakher,[49] R. Mittleman,[14] D. Moffa,[85] K. Mogushi,[86] M. Mohan,[30] S. R. P. Mohapatra,[14] M. Montani,[72,73] C. J. Moore,[12] D. Moraru,[46] G. Moreno,[46] S. Morisaki,[82] B. Mours,[7] C. M. Mow-Lowry,[60] G. Mueller,[49] A. W. Muir,[36] Arunava Mukherjee,[9,10] D. Mukherjee,[20] S. Mukherjee,[108] N. Mukund,[18] A. Mullavey,[6] J. Munch,[56] E. A. Muñiz,[43] M. Muratore,[37] P. G. Murray,[45] A. Nagar,[87,147,148] K. Napier,[77] I. Nardecchia,[32,33] L. Naticchioni,[100,35] R. K. Nayak,[149] J. Neilson,[112] G. Nelemans,[65,13] T. J. N. Nelson,[6] M. Nery,[9,10] A. Neunzert,[123] L. Nevin,[1] J. M. Newport,[125] K. Y. Ng,[14] S. Ng,[56] P. Nguyen,[70] T. T. Nguyen,[24] D. Nichols,[65] A. B. Nielsen,[9] S. Nissanke,[65,13] A. Nitz,[9] F. Nocera,[30] D. Nolting,[6] C. North,[36] L. K. Nuttall,[36] M. Obergaulinger,[23] J. Oberling,[46] B. D. O'Brien,[49] G. D. O'Dea,[112] G. H. Ogin,[150] J. J. Oh,[132] S. H. Oh,[132] F. Ohme,[9] H. Ohta,[82] M. A. Okada,[15] M. Oliver,[106] P. Oppermann,[9,10] Richard J. Oram,[6] B. O'Reilly,[6] R. Ormiston,[44] L. F. Ortega,[49] R. O'Shaughnessy,[59] S. Ossokine,[38] D. J. Ottaway,[56] H. Overmier,[6] B. J. Owen,[84] A. E. Pace,[88] G. Pagano,[21,22] J. Page,[139] M. A. Page,[64] A. Pai,[119] S. A. Pai,[62] J. R. Palamos,[70] O. Palashov,[129] C. Palomba,[35] A. Pal-Singh,[34] Howard Pan,[89]

Huang-Wei Pan,[89] B. Pang,[47] P. T. H. Pang,[96] C. Pankow,[91] F. Pannarale,[36] B. C. Pant,[62] F. Paoletti,[22] A. Paoli,[30] M. A. Papa,[9,20,10] A. Parida,[18] W. Parker,[6] D. Pascucci,[45] A. Pasqualetti,[30] R. Passaquieti,[21,22] D. Passuello,[22] M. Patil,[135] B. Patricelli,[151,22] B. L. Pearlstone,[45] C. Pedersen,[36] M. Pedraza,[1] R. Pedurand,[25,152] L. Pekowsky,[43] A. Pele,[6] S. Penn,[153] C. J. Perez,[46] A. Perreca,[113,98] L. M. Perri,[91] H. P. Pfeiffer,[92,38] M. Phelps,[45] K. S. Phukon,[18] O. J. Piccinni,[100,35] M. Pichot,[66] F. Piergiovanni,[72,73] V. Pierro,[8] G. Pillant,[30] L. Pinard,[25] I. M. Pinto,[8] M. Pirello,[46] M. Pitkin,[45] R. Poggiani,[21,22] P. Popolizio,[30] E. K. Porter,[29] L. Possenti,[154,73] A. Post,[9] J. Powell,[155] J. Prasad,[18] J. W. W. Pratt,[37] G. Pratten,[106] V. Predoi,[36] T. Prestegard,[20] M. Principe,[8] S. Privitera,[38] G. A. Prodi,[113,98] L. G. Prokhorov,[63] O. Puncken,[9,10] M. Punturo,[42] P. Puppo,[35] M. Pürrer,[38] H. Qi,[20] V. Quetschke,[108] E. A. Quintero,[1] R. Quitzow-James,[70] F. J. Raab,[46] D. S. Rabeling,[24] H. Radkins,[46] P. Raffai,[54] S. Raja,[62] C. Rajan,[62] B. Rajbhandari,[84] M. Rakhmanov,[108] K. E. Ramirez,[108] A. Ramos-Buades,[106] Javed Rana,[18] P. Rapagnani,[100,35] V. Raymond,[36] M. Razzano,[21,22] J. Read,[28] T. Regimbau,[66,7] L. Rei,[61] S. Reid,[26] D. H. Reitze,[1,49] W. Ren,[11] F. Ricci,[100,35] P. M. Ricker,[11] G. Riemenschneider,[147,156] K. Riles,[123] M. Rizzo,[59] N. A. Robertson,[1,45] R. Robie,[45] F. Robinet,[27] T. Robson,[105] A. Rocchi,[33] L. Rolland,[7] J. G. Rollins,[1] V. J. Roma,[70] R. Romano,[3,4] C. L. Romel,[46] J. H. Romie,[6] D. Rosińska,[157,55] M. P. Ross,[158] S. Rowan,[45] A. Rüdiger,[9,10] P. Ruggi,[30] G. Rutins,[159] K. Ryan,[46] S. Sachdev,[1] T. Sadecki,[46] M. Sakellariadou,[160] L. Salconi,[30] M. Saleem,[119] F. Salemi,[9] A. Samajdar,[149,13] L. Sammut,[5] L. M. Sampson,[91] E. J. Sanchez,[1] L. E. Sanchez,[1] N. Sanchis-Gual,[23] V. Sandberg,[46] J. R. Sanders,[43] N. Sarin,[5] B. Sassolas,[25] B. S. Sathyaprakash,[88,36] P. R. Saulson,[43] O. Sauter,[123] R. L. Savage,[46] A. Sawadsky,[34] P. Schale,[70] M. Scheel,[47] J. Scheuer,[91] P. Schmidt,[65] R. Schnabel,[34] R. M. S. Schofield,[70] A. Schönbeck,[34] E. Schreiber,[9,10] D. Schuette,[9,10] B. W. Schulte,[9,10] B. F. Schutz,[36,9] S. G. Schwalbe,[37] J. Scott,[45] S. M. Scott,[24] E. Seidel,[11] D. Sellers,[6] A. S. Sengupta,[161] D. Sentenac,[30] V. Sequino,[32,33,16] A. Sergeev,[129] Y. Setyawati,[9] D. A. Shaddock,[24] T. J. Shaffer,[46] A. A. Shah,[139] M. S. Shahriar,[91] M. B. Shaner,[112] L. Shao,[38] B. Shapiro,[50] P. Shawhan,[76] H. Shen,[11] D. H. Shoemaker,[14] D. M. Shoemaker,[77] K. Siellez,[77] X. Siemens,[20] M. Sieniawska,[55] D. Sigg,[46] A. D. Silva,[15] L. P. Singer,[80] A. Singh,[9,10] A. Singhal,[16,35] A. M. Sintes,[106] B. J. J. Slagmolen,[24] T. J. Slaven-Blair,[64] B. Smith,[6] J. R. Smith,[28] R. J. E. Smith,[5] S. Somala,[162] E. J. Son,[132] B. Sorazu,[45] F. Sorrentino,[61] T. Souradeep,[18] A. P. Spencer,[45] A. K. Srivastava,[110] K. Staats,[37] M. Steinke,[9,10] J. Steinlechner,[34,45] S. Steinlechner,[34] D. Steinmeyer,[9,10] B. Steltner,[9,10] S. P. Stevenson,[155] D. Stocks,[50] R. Stone,[108] D. J. Stops,[60] K. A. Strain,[45] G. Stratta,[72,73] S. E. Strigin,[63] A. Strunk,[46] R. Sturani,[163] A. L. Stuver,[164] T. Z. Summerscales,[165] L. Sun,[99] S. Sunil,[110] J. Suresh,[18] P. J. Sutton,[36] B. L. Swinkels,[13] M. J. Szczepańczyk,[37] M. Tacca,[13] S. C. Tait,[45] C. Talbot,[5] D. Talukder,[70] D. B. Tanner,[49] M. Tápai,[120] A. Taracchini,[38] J. D. Tasson,[95] J. A. Taylor,[139] R. Taylor,[1] S. V. Tewari,[153] T. Theeg,[9,10] F. Thies,[9,10] E. G. Thomas,[60] M. Thomas,[6] P. Thomas,[46] K. A. Thorne,[6] E. Thrane,[5] S. Tiwari,[16,98] V. Tiwari,[36] K. V. Tokmakov,[26] K. Toland,[45] M. Tonelli,[21,22] Z. Tornasi,[45] A. Torres-Forné,[23] C. I. Torrie,[1] D. Töyrä,[60] F. Travasso,[30,42] G. Traylor,[6] J. Trinastic,[49] M. C. Tringali,[113,98] L. Trozzo,[166,22] K. W. Tsang,[13] M. Tse,[14] R. Tso,[47] D. Tsuna,[82] L. Tsukada,[82] D. Tuyenbayev,[108] K. Ueno,[20] D. Ugolini,[167] A. L. Urban,[1] S. A. Usman,[36] H. Vahlbruch,[9,10] G. Vajente,[1] G. Valdes,[2] N. van Bakel,[13] M. van Beuzekom,[13] J. F. J. van den Brand,[75,13] C. Van Den Broeck,[13,168] D. C. Vander-Hyde,[43] L. van der Schaaf,[13] J. V. van Heijningen,[13] A. A. van Veggel,[45] M. Vardaro,[52,53] V. Varma,[47] S. Vass,[1] M. Vasúth,[48] A. Vecchio,[60] G. Vedovato,[53] J. Veitch,[45] P. J. Veitch,[56] K. Venkateswara,[158] G. Venugopalan,[1] D. Verkindt,[7] F. Vetrano,[72,73] A. Viceré,[72,73] A. D. Viets,[20] S. Vinciguerra,[60] D. J. Vine,[159] J.-Y. Vinet,[66] S. Vitale,[14] T. Vo,[43] H. Vocca,[41,42] C. Vorvick,[46] S. P. Vyatchanin,[63] A. R. Wade,[1] L. E. Wade,[85] M. Wade,[85] R. Walet,[13] M. Walker,[28] L. Wallace,[1] S. Walsh,[20,9] G. Wang,[16,22] H. Wang,[60] J. Z. Wang,[123] W. H. Wang,[108] Y. F. Wang,[96] R. L. Ward,[24] J. Warner,[46] M. Was,[7] J. Watchi,[101] B. Weaver,[46] L.-W. Wei,[9,10] M. Weinert,[9,10] A. J. Weinstein,[1] R. Weiss,[14] F. Wellmann,[9,10] L. Wen,[64] E. K. Wessel,[11] P. Weßels,[9,10] J. Westerweck,[9] K. Wette,[24] J. T. Whelan,[59] B. F. Whiting,[49] C. Whittle,[14] D. Wilken,[9,10] D. Williams,[45] R. D. Williams,[1] A. R. Williamson,[59,65] J. L. Willis,[1,124] B. Willke,[9,10] M. H. Wimmer,[9,10] W. Winkler,[9,10] C. C. Wipf,[1] H. Wittel,[9,10] G. Woan,[45] J. Woehler,[9,10] J. K. Wofford,[59] W. K. Wong,[96] J. Worden,[46] J. L. Wright,[45] D. S. Wu,[9,10] D. M. Wysocki,[59] S. Xiao,[1] W. Yam,[14] H. Yamamoto,[1] C. C. Yancey,[76] L. Yang,[169] M. J. Yap,[24] M. Yazback,[49] Hang Yu,[14] Haocun Yu,[14] M. Yvert,[7] A. Zadrożny,[134] M. Zanolin,[37] T. Zelenova,[30] J.-P. Zendri,[53] M. Zevin,[91] J. Zhang,[64] L. Zhang,[1] M. Zhang,[144] T. Zhang,[45] Y.-H. Zhang,[9,10] C. Zhao,[64] M. Zhou,[91] Z. Zhou,[91] S. J. Zhu,[9,10] X. J. Zhu,[5] A. B. Zimmerman,[92] Y. Zlochower,[59] M. E. Zucker,[1,14] and J. Zweizig[1]

(LIGO Scientific Collaboration and Virgo Collaboration)

[1]LIGO, California Institute of Technology, Pasadena, California 91125, USA
[2]Louisiana State University, Baton Rouge, Louisiana 70803, USA
[3]Università di Salerno, Fisciano, I-84084 Salerno, Italy
[4]INFN, Sezione di Napoli, Complesso Universitario di Monte S. Angelo, I-80126 Napoli, Italy
[5]OzGrav, School of Physics & Astronomy, Monash University, Clayton 3800, Victoria, Australia
[6]LIGO Livingston Observatory, Livingston, Louisiana 70754, USA
[7]Laboratoire d'Annecy de Physique des Particules (LAPP), Univ. Grenoble Alpes, Université Savoie Mont Blanc, CNRS/IN2P3, F-74941 Annecy, France
[8]University of Sannio at Benevento, I-82100 Benevento, Italy and INFN, Sezione di Napoli, I-80100 Napoli, Italy
[9]Max Planck Institute for Gravitational Physics (Albert Einstein Institute), D-30167 Hannover, Germany
[10]Leibniz Universität Hannover, D-30167 Hannover, Germany
[11]NCSA, University of Illinois at Urbana-Champaign, Urbana, Illinois 61801, USA
[12]University of Cambridge, Cambridge CB2 1TN, United Kingdom
[13]Nikhef, Science Park 105, 1098 XG Amsterdam, Netherlands
[14]LIGO, Massachusetts Institute of Technology, Cambridge, Massachusetts 02139, USA
[15]Instituto Nacional de Pesquisas Espaciais, 12227-010 Sáo José dos Campos, São Paulo, Brazil
[16]Gran Sasso Science Institute (GSSI), I-67100 L'Aquila, Italy
[17]INFN, Laboratori Nazionali del Gran Sasso, I-67100 Assergi, Italy
[18]Inter-University Centre for Astronomy and Astrophysics, Pune 411007, India
[19]International Centre for Theoretical Sciences, Tata Institute of Fundamental Research, Bengaluru 560089, India
[20]University of Wisconsin-Milwaukee, Milwaukee, Wisconsin 53201, USA
[21]Università di Pisa, I-56127 Pisa, Italy
[22]INFN, Sezione di Pisa, I-56127 Pisa, Italy
[23]Departamento de Astronomía y Astrofísica, Universitat de València, E-46100 Burjassot, València, Spain
[24]OzGrav, Australian National University, Canberra, Australian Capital Territory 0200, Australia
[25]Laboratoire des Matériaux Avancés (LMA), CNRS/IN2P3, F-69622 Villeurbanne, France
[26]SUPA, University of Strathclyde, Glasgow G1 1XQ, United Kingdom
[27]LAL, Univ. Paris-Sud, CNRS/IN2P3, Université Paris-Saclay, F-91898 Orsay, France
[28]California State University Fullerton, Fullerton, California 92831, USA
[29]APC, AstroParticule et Cosmologie, Université Paris Diderot, CNRS/IN2P3, CEA/Irfu, Observatoire de Paris, Sorbonne Paris Cité, F-75205 Paris Cedex 13, France
[30]European Gravitational Observatory (EGO), I-56021 Cascina, Pisa, Italy
[31]Chennai Mathematical Institute, Chennai 603103, India
[32]Università di Roma Tor Vergata, I-00133 Roma, Italy
[33]INFN, Sezione di Roma Tor Vergata, I-00133 Roma, Italy
[34]Universität Hamburg, D-22761 Hamburg, Germany
[35]INFN, Sezione di Roma, I-00185 Roma, Italy
[36]Cardiff University, Cardiff CF24 3AA, United Kingdom
[37]Embry-Riddle Aeronautical University, Prescott, Arizona 86301, USA
[38]Max Planck Institute for Gravitational Physics (Albert Einstein Institute), D-14476 Potsdam-Golm, Germany
[39]Korea Institute of Science and Technology Information, Daejeon 34141, Korea
[40]West Virginia University, Morgantown, West Virginia 26506, USA
[41]Università di Perugia, I-06123 Perugia, Italy
[42]INFN, Sezione di Perugia, I-06123 Perugia, Italy
[43]Syracuse University, Syracuse, New York 13244, USA
[44]University of Minnesota, Minneapolis, Minnesota 55455, USA
[45]SUPA, University of Glasgow, Glasgow G12 8QQ, United Kingdom
[46]LIGO Hanford Observatory, Richland, Washington 99352, USA
[47]Caltech CaRT, Pasadena, California 91125, USA
[48]Wigner RCP, RMKI, H-1121 Budapest, Konkoly Thege Miklós út 29-33, Hungary
[49]University of Florida, Gainesville, Florida 32611, USA
[50]Stanford University, Stanford, California 94305, USA
[51]Università di Camerino, Dipartimento di Fisica, I-62032 Camerino, Italy
[52]Università di Padova, Dipartimento di Fisica e Astronomia, I-35131 Padova, Italy
[53]INFN, Sezione di Padova, I-35131 Padova, Italy
[54]MTA-ELTE Astrophysics Research Group, Institute of Physics, Eötvös University, Budapest 1117, Hungary

[55]Nicolaus Copernicus Astronomical Center, Polish Academy of Sciences, 00-716, Warsaw, Poland
[56]OzGrav, University of Adelaide, Adelaide, South Australia 5005, Australia
[57]Dipartimento di Scienze Matematiche, Fisiche e Informatiche, Università di Parma, I-43124 Parma, Italy
[58]INFN, Sezione di Milano Bicocca, Gruppo Collegato di Parma, I-43124 Parma, Italy
[59]Rochester Institute of Technology, Rochester, New York 14623, USA
[60]University of Birmingham, Birmingham B15 2TT, United Kingdom
[61]INFN, Sezione di Genova, I-16146 Genova, Italy
[62]RRCAT, Indore, Madhya Pradesh 452013, India
[63]Faculty of Physics, Lomonosov Moscow State University, Moscow 119991, Russia
[64]OzGrav, University of Western Australia, Crawley, Western Australia 6009, Australia
[65]Department of Astrophysics/IMAPP, Radboud University Nijmegen, P.O. Box 9010, 6500 GL Nijmegen, Netherlands
[66]Artemis, Université Côte d'Azur, Observatoire Côte d'Azur, CNRS, CS 34229, F-06304 Nice Cedex 4, France
[67]Physik-Institut, University of Zurich, Winterthurerstrasse 190, 8057 Zurich, Switzerland
[68]Univ Rennes, CNRS, Institut FOTON - UMR6082, F-3500 Rennes, France
[69]Washington State University, Pullman, Washington 99164, USA
[70]University of Oregon, Eugene, Oregon 97403, USA
[71]Laboratoire Kastler Brossel, Sorbonne Université, CNRS, ENS-Université PSL, Collège de France, F-75005 Paris, France
[72]Università degli Studi di Urbino 'Carlo Bo', I-61029 Urbino, Italy
[73]INFN, Sezione di Firenze, I-50019 Sesto Fiorentino, Firenze, Italy
[74]Astronomical Observatory Warsaw University, 00-478 Warsaw, Poland
[75]VU University Amsterdam, 1081 HV Amsterdam, Netherlands
[76]University of Maryland, College Park, Maryland 20742, USA
[77]School of Physics, Georgia Institute of Technology, Atlanta, Georgia 30332, USA
[78]Université Claude Bernard Lyon 1, F-69622 Villeurbanne, France
[79]Università di Napoli 'Federico II', Complesso Universitario di Monte S. Angelo, I-80126 Napoli, Italy
[80]NASA Goddard Space Flight Center, Greenbelt, Maryland 20771, USA
[81]Dipartimento di Fisica, Università degli Studi di Genova, I-16146 Genova, Italy
[82]RESCEU, University of Tokyo, Tokyo 113-0033, Japan
[83]Tsinghua University, Beijing 100084, China
[84]Texas Tech University, Lubbock, Texas 79409, USA
[85]Kenyon College, Gambier, Ohio 43022, USA
[86]The University of Mississippi, University, Mississippi 38677, USA
[87]Museo Storico della Fisica e Centro Studi e Ricerche "Enrico Fermi", I-00184 Roma, Italyrico Fermi, I-00184 Roma, Italy
[88]The Pennsylvania State University, University Park, Pennsylvania 16802, USA
[89]National Tsing Hua University, Hsinchu City, 30013 Taiwan, Republic of China
[90]Charles Sturt University, Wagga Wagga, New South Wales 2678, Australia
[91]Center for Interdisciplinary Exploration & Research in Astrophysics (CIERA), Northwestern University, Evanston, Illinois 60208, USA
[92]Canadian Institute for Theoretical Astrophysics, University of Toronto, Toronto, Ontario M5S 3H8, Canada
[93]University of Chicago, Chicago, Illinois 60637, USA
[94]Pusan National University, Busan 46241, Korea
[95]Carleton College, Northfield, Minnesota 55057, USA
[96]The Chinese University of Hong Kong, Shatin, NT, Hong Kong
[97]INAF, Osservatorio Astronomico di Padova, I-35122 Padova, Italy
[98]INFN, Trento Institute for Fundamental Physics and Applications, I-38123 Povo, Trento, Italy
[99]OzGrav, University of Melbourne, Parkville, Victoria 3010, Australia
[100]Università di Roma 'La Sapienza', I-00185 Roma, Italy
[101]Université Libre de Bruxelles, Brussels 1050, Belgium
[102]Sonoma State University, Rohnert Park, California 94928, USA
[103]Departamento de Matemáticas, Universitat de València, E-46100 Burjassot, València, Spain
[104]Columbia University, New York, New York 10027, USA
[105]Montana State University, Bozeman, Montana 59717, USA
[106]Universitat de les Illes Balears, IAC3—IEEC, E-07122 Palma de Mallorca, Spain
[107]University of Rhode Island, 45 Upper College Road, Kingston, Rhode Island 02881, USA

[108]The University of Texas Rio Grande Valley, Brownsville, Texas 78520, USA
[109]Bellevue College, Bellevue, Washington 98007, USA
[110]Institute for Plasma Research, Bhat, Gandhinagar 382428, India
[111]The University of Sheffield, Sheffield S10 2TN, United Kingdom
[112]California State University, Los Angeles, 5151 State University Drive, Los Angeles, California 90032, USA
[113]Università di Trento, Dipartimento di Fisica, I-38123 Povo, Trento, Italy
[114]Montclair State University, Montclair, New Jersey 07043, USA
[115]National Astronomical Observatory of Japan, 2-21-1 Osawa, Mitaka, Tokyo 181-8588, Japan
[116]Observatori Astronòmic, Universitat de València, E-46980 Paterna, València, Spain
[117]School of Mathematics, University of Edinburgh, Edinburgh EH9 3FD, United Kingdom
[118]University and Institute of Advanced Research, Koba Institutional Area, Gandhinagar Gujarat 382007, India
[119]Indian Institute of Technology, Main Gate Rd, IIT Area, Powai, Mumbai, Maharashtra 400076, India
[120]University of Szeged, Dóm tér 9, Szeged 6720, Hungary
[121]Tata Institute of Fundamental Research, Mumbai 400005, India
[122]INAF, Osservatorio Astronomico di Capodimonte, I-80131, Napoli, Italy
[123]University of Michigan, Ann Arbor, Michigan 48109, USA
[124]Abilene Christian University, Abilene, Texas 79699, USA
[125]American University, Washington, DC 20016, USA
[126]University of Białystok, 15-424 Białystok, Poland
[127]University of Southampton, Southampton SO17 1BJ, United Kingdom
[128]University of Washington Bothell, 18115 Campus Way NE, Bothell, Washington 98011, USA
[129]Institute of Applied Physics, Nizhny Novgorod, 603950, Russia
[130]Korea Astronomy and Space Science Institute, Daejeon 34055, Korea
[131]Inje University Gimhae, South Gyeongsang 50834, Korea
[132]National Institute for Mathematical Sciences, Daejeon 34047, Korea
[133]Ulsan National Institute of Science and Technology, 50 UNIST-gil, Eonyang-eup, Ulju-gun, Ulsan, South Korea
[134]NCBJ, 05-400 Świerk-Otwock, Poland
[135]Institute of Mathematics, Polish Academy of Sciences, 00656 Warsaw, Poland
[136]Cornell Universtiy, Ithaca, New York, USA
[137]Hillsdale College, Hillsdale, Michigan 49242, USA
[138]Hanyang University, Seoul 04763, Korea
[139]NASA Marshall Space Flight Center, Huntsville, Alabama 35811, USA
[140]Dipartimento di Fisica, Università degli Studi Roma Tre, I-00154 Roma, Italy
[141]INFN, Sezione di Roma Tre, I-00154 Roma, Italy
[142]ESPCI, CNRS, F-75005 Paris, France
[143]Southern University and A&M College, Baton Rouge, Louisiana 70813, USA
[144]College of William and Mary, Williamsburg, Virginia 23187, USA
[145]Centre Scientifique de Monaco, 8 quai Antoine Ier, MC-98000, Monaco
[146]Indian Institute of Technology Madras, Chennai 600036, India
[147]INFN Sezione di Torino, Via P. Giuria 1, I-10125 Torino, Italy
[148]Institut des Hautes Etudes Scientifiques, F-91440 Bures-sur-Yvette, France
[149]IISER-Kolkata, Mohanpur, West Bengal 741252, India
[150]Whitman College, 345 Boyer Avenue, Walla Walla, Washington 99362, USA
[151]Scuola Normale Superiore, Piazza dei Cavalieri 7, I-56126 Pisa, Italy
[152]Université de Lyon, F-69361 Lyon, France
[153]Hobart and William Smith Colleges, Geneva, New York 14456, USA
[154]Università degli Studi di Firenze, I-50121 Firenze, Italy
[155]OzGrav, Swinburne University of Technology, Hawthorn VIC 3122, Australia
[156]Dipartimento di Fisica, Università di Torino, via P. Giuria 1, I-10125 Torino, Italy
[157]Janusz Gil Institute of Astronomy, University of Zielona Góra, 65-265 Zielona Góra, Poland
[158]University of Washington, Seattle, Washington 98195, USA
[159]SUPA, University of the West of Scotland, Paisley PA1 2BE, United Kingdom
[160]King's College London, University of London, London WC2R 2LS, United Kingdom
[161]Indian Institute of Technology, Gandhinagar Ahmedabad Gujarat 382424, India
[162]Indian Institute of Technology Hyderabad, Sangareddy, Khandi, Telangana 502285, India
[163]International Institute of Physics, Universidade Federal do Rio Grande do Norte, Natal RN 59078-970, Brazil

[164]*Villanova University, 800 Lancaster Ave, Villanova, Pennsylvania 19085, USA*
[165]*Andrews University, Berrien Springs, Michigan 49104, USA*
[166]*Università di Siena, I-53100 Siena, Italy*
[167]*Trinity University, San Antonio, Texas 78212, USA*
[168]*Van Swinderen Institute for Particle Physics and Gravity, University of Groningen, Nijenborgh 4, 9747 AG Groningen, Netherlands*
[169]*Colorado State University, Fort Collins, Colorado 80523, USA*

[a]Deceased, February 2018.
[b]Deceased, November 2017.

This is the accepted manuscript made available via CHORUS. The article has been published as:

GW170817: Measurements of Neutron Star Radii and Equation of State

B. P. Abbott *et al.* (The LIGO Scientific Collaboration and the Virgo Collaboration)

Phys. Rev. Lett. **121**, 161101 — Published 15 October 2018

DOI: 10.1103/PhysRevLett.121.161101

GW170817: Measurements of neutron star radii and equation of state

The LIGO Scientific Collaboration and The Virgo Collaboration

On August 17, 2017, the LIGO and Virgo observatories made the first direct detection of gravitational waves from the coalescence of a neutron star binary system. The detection of this gravitational wave signal, GW170817, offers a novel opportunity to directly probe the properties of matter at the extreme conditions found in the interior of these stars. The initial, minimal-assumption analysis of the LIGO and Virgo data placed constraints on the tidal effects of the coalescing bodies, which were then translated to constraints on neutron star radii. Here, we expand upon previous analyses by working under the hypothesis that both bodies were neutron stars that are described by the same equation of state and have spins within the range observed in Galactic binary neutron stars. Our analysis employs two methods: the use of equation-of-state-insensitive relations between various macroscopic properties of the neutron stars and the use of an efficient parameterization of the defining function $p(\rho)$ of the equation of state itself. From the LIGO and Virgo data alone and the first method, we measure the two neutron star radii as $R_1 = 10.8^{+2.0}_{-1.7}$ km for the heavier star and $R_2 = 10.7^{+2.1}_{-1.5}$ km for the lighter star at the 90% credible level. If we additionally require that the equation of state supports neutron stars with masses larger than $1.97\,\mathrm{M}_\odot$ as required from electromagnetic observations and employ the equation of state parametrization, we further constrain $R_1 = 11.9^{+1.4}_{-1.4}$ km and $R_2 = 11.9^{+1.4}_{-1.4}$ km at the 90% credible level. Finally, we obtain constraints on $p(\rho)$ at supranuclear densities, with pressure at twice nuclear saturation density measured at $3.5^{+2.7}_{-1.7} \times 10^{34}\,\mathrm{dyn\,cm^{-2}}$ at the 90% level.

INTRODUCTION

Since September 2015, the Advanced LIGO [1] and Advanced Virgo [2] observatories have opened a window on the gravitational-wave (GW) Universe [3, 4]. A new type of astrophysical source of GWs was detected on the 17th of August 2017, when the GW signal emitted by a low-mass coalescing compact binary was observed [5]. This observation coincided with the detection of a gamma ray burst, GRB 170817A [6, 7], verifying that the source binary contained matter, which was further corroborated by a series of observations that followed across the electromagnetic spectrum, e.g. [8–12]. The measured masses of the bodies and the variety of electromagnetic observations are consistent with neutron stars (NSs).

Neutron stars are unique natural laboratories for studying the behavior of cold, high-density nuclear matter. Such behavior is governed by the equation of state (EOS), which prescribes a relationship between pressure and density. This determines the relation between NS mass and radius, as well as other macroscopic properties such as the stellar moment of inertia and the tidal deformability (see e.g. [13]). While terrestrial experiments are able to test and constrain the cold EOS at densities below and near the saturation density of nuclei $\rho_{\rm nuc} = 2.8 \times 10^{14}$ g cm^{-3} (see e.g. [14–17] for a review), currently they cannot probe the extreme conditions in the deep core of NSs. Astrophysical measurements of NS masses, radii, moments of inertia and tidal effects, on the other hand, have the potential to offer information about whether the EOS is soft or stiff and what the pressure is at several times the nuclear saturation density [16, 18–20].

GWs offer another opportunity for such astrophysical measurements to be performed, as the GW signal emitted by merging NS binaries differs from that of two merging black holes (BHs). The most prominent effect of matter during the observed binary inspiral comes from the tidal deformation that each star's gravitational field induces on its companion. This deformation enhances GW emission and thus accelerates the decay of the quasi-circular inspiral [21–23]. In the post-Newtonian (PN) expansion of the inspiral dynamics [24–32], this effect causes the phase of the GW signal to differ from that of a binary BH from the fifth PN order onwards [21, 33, 34]. The leading-order contribution is proportional to each star's tidal deformability parameter, $\Lambda = (2/3)k_2 C^{-5}$, an EOS-sensitive quantity that describes how much a star is deformed in the presence of a tidal field. Here k_2 is the $l = 2$ relativistic Love number [35–39], $C \equiv Gm/(c^2 R)$ is the compactness, R is the areal radius, and m is the mass of the NS. The deformation of each NS due to its own spin also modifies the waveform and depends on the EOS. This effect enters the post-Newtonian expansion as a contribution to the (lowest order) spin-spin term at the second order in the GW phase [40, 41]. The EOS also affects the waveform at merger, the merger outcome and its lifetime, as well as the post-merger emission (see e.g. [42]). Finally, other stellar modes can couple to the tidal field and affect the GW signal [21, 43–45].

Among the various EOS-dependent effects, the tidal deformation is the one most readily measurable with GW170817. The spin-induced quadrupole has a larger effect on the orbital evolution for systems with large NS spin [46–49] but is also largely degenerate with the mass ratio and the NS spins, making it difficult to measure independently [50]. The post-merger signal, while rich in content, is also difficult to observe, with current detector sensitivities being limited due to photon shot noise [1] at the high frequencies of interest. The merger and post-merger

signal make a negligible contribution to our inference for GW170817 [51, 52].

In [5], we presented the first measurements of the properties of GW170817, including a first set of constraints on the tidal deformabilities of the two compact objects, from which inferences about the EOS can be made. An independent analysis further exploring how well the gravitational-wave data can be used to constrain the tidal deformabilites, and, from that, the NS radii, has also been performed recently [53]. Our initial bounds have facilitated a large number of studies, e.g. [54–64], aiming to translate the measurements of masses and tidal deformabilities into constraints on the EOS of NS matter. In a companion paper [52], we perform a more detailed analysis focusing on the source properties, improving upon the original analysis of [5] by using Virgo data with reduced calibration uncertainty, extending the analysis to lower frequencies, employing more accurate waveform models, and fixing the location of the source in the sky to the one identified by the electromagnetic observations.

Here we complement the analysis of [52], and work under the hypothesis that GW170817 was the result of a coalescence of two NSs whose masses and spins are consistent with astrophysical observations and expectations. Moreover since NSs represent equilibrium ground-state configurations, we assume that their properties are described by the same EOS. By making these additional assumptions, we are able to further improve our measurements of the tidal deformabilities of GW170817, and constrain the radii of the two NSs. Moreover, we use an efficient parametrization of the EOS to place constraints on the pressure of cold matter at supranuclear densities using GW observations. This direct measurement of the pressure takes into account physical and observational constraints on the NS EOS, namely causality, thermodynamic stability, and a lower limit on the maximum NS mass supported by the EOS to be $M_{\rm max} > 1.97\,{\rm M}_\odot$. The latter is chosen as a 1-σ conservative estimate, based on the observation of PSR J0348+0432 with $M = 2.01 \pm 0.04\,{\rm M}_\odot$ [65], the heaviest NS known to date.

The radii measurements presented here improve upon existing results (e.g. [58, 62]) which had used the initial tidal measurements reported in [5]. We also verify that our radii measurements are consistent with the result of the methodologies presented in these studies when applied to our improved tidal measurements. Moreover, we obtain a more precise estimate of the NS radius than [53].

METHODS

In this section we describe the details of the analysis. We use the same LIGO and Virgo data and calibration model analyzed in [52]. The data can be dowloaded from the LIGO Open Science Center (LOSC) [66]. The data include the subtraction of an instrumental artifact occurring at LIGO-Livingston within 2 s of the GW170817 merger [5, 67], as well as the subtraction of independently measurable noise sources [68–71].

Bayesian methods

We employ a coherent Bayesian analysis to estimate the source parameters $\vec{\vartheta}$ as described in [72, 73]. The goal is to determine the posterior probability density function (PDF), $p(\vec{\vartheta}|d)$, given the LIGO and Virgo data d. Given a prior PDF $p(\vec{\vartheta})$ on the parameter space (quantifying our prior belief in observing a source with properties $\vec{\vartheta}$), the posterior PDF is given by Bayes' Theorem $p(\vec{\vartheta}|d) \propto p(\vec{\vartheta})p(d|\vec{\vartheta})$, where $p(d|\vec{\vartheta})$ is the likelihood of obtaining the data d given that a signal with parameters $\vec{\vartheta}$ is present in the data. Evaluating the multi-dimensional $p(\vec{\vartheta}|d)$ analytically is computationally prohibitive so we resort to sampling techniques to efficiently draw samples from the underlying distribution. We make use of the Markov-chain Monte Carlo algorithm as implemented in the `LALInference` package [72], which is part of the publicly available LSC Algorithm Library (`LAL`) [74]. For the likelihood calculation, we use 128 s of data around GW170817 over a frequency range of 23-2048 Hz, covering both the time and frequency ranges where there was appreciable signal above the detector noise, and we estimate the likelihood for our waveform templates up to merger. The power spectral density (PSD) of the noise is computed on-source [52, 75, 76], and we marginalize over the detectors' calibration uncertainties as described in [52, 73, 77].

In the analysis of a GW signal from a binary NS coalescence, the source parameters $\vec{\vartheta}$ on which the signal depends can be decomposed as $\vec{\vartheta} = (\vec{\vartheta}_{\rm PM}, \vec{\vartheta}_{\rm EOS})$, into parameters that would be present if the two bodies behaved like point-masses $\vec{\vartheta}_{\rm PM}$, and EOS-sensitive parameters $\vec{\vartheta}_{\rm EOS}$ that arise due to matter effects of the two finite-sized bodies (e.g. tidal deformabilities). The priors on the point-mass parameters that we use are described in Sec. II D of [52] and we do not repeat them here. We also use the same convention for the component masses, i.e. $m_1 \geq m_2$. We only consider the "low-spin" prior of [52] where the dimensionless NS spin parameter is restricted to $\chi \leq 0.05$, in agreement with expectations from Galactic binary NS spin measurements [78], and we fix the location of the source in the sky to the one given by EM observations. Regarding the EOS-related part of the parameter space and the corresponding priors, we consider two physically motivated parameterizations of different dimensionalities, which we describe in detail in the following sections. The first method requires the sampling of tidal deformability parameters, whereas the second method directly samples the EOS function $p(\rho)$ from a 4-dimensional family of functions. In both cases, the assumption that the binary consists of two NSs that are

described by the same EOS is implicit in the parametrization of matter effects (in contrast with the analysis of [52], where minimal assumptions are made about the nature of the source).

Waveform models and matter effects

The measurement process described above requires a waveform model that maps the source parameters $\vec{\vartheta}$ to a signal $h(t;\vec{\vartheta})$ that would be observed in the detector. The publicly available `LALSimulation` software package of `LAL` [74] contains several such waveform models obtained with different theoretical approaches. The impact of varying the models among several choices [21, 22, 41, 79–94] is analyzed in detail in [52], showing that for GW170817 the systematic uncertainties due to the modeling of matter effects or the underlying point-particle description are smaller than the statistical errors in the measurement. We perform a similar analysis here by varying the BBH baseline model or using a post-Newtonian waveform prescription and find results consistent with those presented in Sec. III D and Table IV of [52]. Moreover, the study of Appendix A of [52] (Table V) suggests that varying the tidal description in the waveforms also leads to broadly consistent tidal measurements. Since the net effect of varying waveform models is very different for each of the source properties, we refer to the tables and figures in [52] for quantitative statements to assess the impact of modeling uncertainties.

In the GW170817 discovery paper [5] the results for the inferred tidal deformabilities were obtained with the model TaylorF2 that is based solely on post-Newtonian results for both the BBH baseline model [41, 90–94] and for tidal effects [21, 22], as this model led to the conservatively largest bounds. In this paper, we use a more realistic waveform model PhenomPNRT [79–83], which is also used as the reference model in our detailed analysis of the properties of GW170817 [52]. The BBH baseline in this model, constructed based on [24, 91–93, 95–98], is calibrated to numerical relativity data and describes relativistic point-mass, spin, and the dominant precession effects. The model further includes tidal effects in the phase from combining analytical information [22, 23, 86, 99] with results from numerical-relativity simulations of binary NSs as described in [84, 100], and matter effects in the spin-induced quadrupole based post-Newtonian results [40, 41, 92–94]. The characteristic rotational quadrupole deformation parameters are computed from Λ through EOS-insensitive relations [101, 102] as described in [48, 103]. Other matter effects with non-zero spins are not taken into account in our analysis.

EOS-insensitive relations

Despite the microscopic complexity of NSs, some of their macroscopic properties are linked by EOS-insensitive relations that depend only weakly on the EOS [104]. We use two such relations to ensure that the two NSs obey the same EOS and to translate NS tidal deformabilities to NS radii.

The first such relation we employ was constructed in [105] and studied in the context of realistic GW inference in [106]. It combines the mass ratio of the binary $q \equiv m_2/m_1 \leq 1$, the symmetric tidal deformability $\Lambda_s \equiv (\Lambda_2+\Lambda_1)/2$ and the antisymmetric tidal deformability $\Lambda_a \equiv (\Lambda_2-\Lambda_1)/2$ in a relation of the form $\Lambda_a(\Lambda_s, q)$. Fitting coefficients and an estimate of the relation's intrinsic error were obtained by tuning to a large set of EOS models [104, 106], ensuring that the relation gives pairs of tidal deformabilities that correspond to realistic EOS models. We sample uniformly in the symmetric tidal deformability $\Lambda_s \in [0, 5000]$, use the EOS-insensitive relation to compute Λ_a, and then obtain Λ_1 and Λ_2, which are used to generate a waveform template. The sampling of tidal parameters also involves a marginalization over the intrinsic error in the relation, which is also a function of Λ_s and q. This procedure leads to unbiased estimation of the tidal parameters for a wide range of EOSs and mass ratios [106].

The second relation we employ is between NS tidal deformability Λ and NS compactness C [107, 108]. We employ this Λ–C relation with the coefficients given in Sec. (4.4) of [104] to compute the posterior for the radius and the mass of each binary component. Reference [104] reports a maximum 6.5% relative error in the relation when compared to a large set of EOS models. We assume that the relative error is constant across the parameter space and distributed according to a zero-mean Gaussian with a standard deviation of $(6.5/3)\%$ and marginalize over it. We verified that our results are not sensitive to this choice of error estimate by comparing to the more conservative choice of a uniform distribution in $[-6.5\%, 6.5\%]$.

Parameterized EOS

Instead of sampling macroscopic EOS-related parameters such as tidal deformabilities, one may instead sample the defining function $p(\rho)$ of the EOS directly. A number of parametrizations of different degrees of complexity and fidelity to realistic EOS models have been proposed (see [109] for a review), and here we employ the spectral parametrization constructed and validated in [110–112]. This parameterization expresses the logarithm of the adiabatic index of the EOS $\Gamma(p;\gamma_i)$, as a polynomial of the pressure p, where $\gamma_i = (\gamma_0, \gamma_1, \gamma_2, \gamma_3)$ are the free EOS parameters. The adiabatic index is then used to compute the energy $\epsilon(p;\gamma_i)$ and rest-mass density $\rho(p;\gamma_i)$, which are inverted to give the EOS. The pa-

rameterized high-density EOS is then stitched to the SLy EOS [113] below about half the nuclear saturation density. This is chosen because such low densities do not significantly impact the global properties of the NS [114]. Different low density EOSs can produce a difference in radius, for a given m, of order 0.1 km. Though use of a specific parametrization makes our results model-dependent, we have checked that they are consistent with another common EOS parametrization, the piecewise polytropic one [115, 116], as also found in [117].

In this analysis, we follow the methodology detailed in [117], developed from the work of [118], to sample directly in an EOS parameter space. We sample uniformly in all EOS parameters within the following ranges: $\gamma_0 \in [0.2, 2]$, $\gamma_1 \in [-1.6, 1.7]$, $\gamma_2 \in [-0.6, 0.6]$, and $\gamma_3 \in [-0.02, 0.02]$ and additionally impose that the adiabatic index $\Gamma(p) \in [0.6, 4.5]$. This choice of prior ranges for the EOS parameters was chosen such that our parametrization encompasses a wide range of candidate EOSs [110] and leads to NSs with a compactness below 0.33 and a tidal deformability above about 10. Then for each sample, the four EOS parameters and the masses are mapped to a (Λ_1, Λ_2) pair through the Tolman-Oppenheimer-Volkoff (TOV) equations describing the equilibrium configuration of a spherical star [119]. The two tidal deformabilities are then used to compute the waveform template.

Sampling directly in the EOS parameter space allows for certain prior constraints to be conveniently incorporated in the analysis. In our analysis, we impose the following criteria on all EOS and mass samples: (i) causality, the speed of sound in the NS ($\sqrt{dp/d\epsilon}$) must be less than the speed of light (plus 10% to allow for imperfect parameterization) up to the central pressure of the heaviest star supported by the EOS; (ii) internal consistency, the EOS must support the proposed masses of each component; and (iii) observational consistency, the EOS must have a maximum mass at least as high as previously observed NS masses, specifically $1.97\,\mathrm{M}_\odot$. Another condition the EOS must obey is that of thermodynamic stability; the EOS must be monotonically increasing ($d\epsilon/dp > 0$). This condition is built into the parametrization [110], so we do not need to explicitly impose it.

RESULTS

We begin by demonstrating the improvement in the measurement of the tidal deformability parameters due to imposing a common but unknown EOS for the two NSs. In Fig. 1 we show the marginalized joint posterior PDF for the individual tidal deformabilities. We show results from our analysis using the $\Lambda_a(\Lambda_s, q)$ relation in green and the parametrized EOS without a maximum mass constraint in blue. These are compared to results from [52], where the two tidal deformability parameters are sampled independently, in orange. The shaded region marks the $\Lambda_2 < \Lambda_1$ region that is naturally excluded when a common realistic EOS is assumed, but is not excluded from the analysis of [52]. In both cases imposing a common EOS leads to a smaller uncertainty in the tidal deformability measurement. The area of the 90% credible region for the Λ_1–Λ_2 posterior shrinks by a factor of ~ 3, which is consistent with the results of [106] for soft EOSs and NSs with similar masses. The tidal deformability of a $1.4\,\mathrm{M}_\odot$ NS can be estimated through a linear expansion of $\Lambda(m)m^5$ around $1.4\,\mathrm{M}_\odot$ as in [5, 48, 120] to be $\Lambda_{1.4} = 190^{+390}_{-120}$ at the 90% level when a common EOS is imposed (here and throughout this paper we quote symmetric credible intervals). Our results suggest that "soft" EOSs such as APR4, which predict smaller values of the tidal deformability parameter, are favored over "stiff" EOSs such as H4 or MS1, which predict larger values of the tidal deformability parameter and lie outside the 90% credible region.

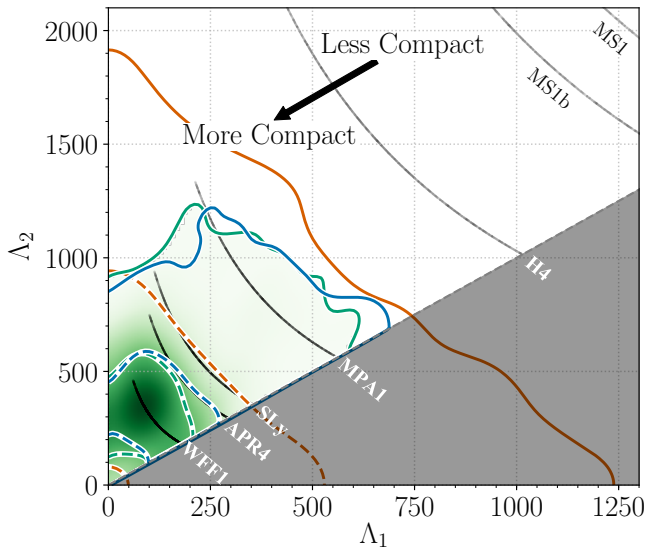

FIG. 1. Marginalized posterior for the tidal deformabilities of the two binary components of GW170817. The green shading shows the posterior obtained using the $\Lambda_a(\Lambda_s, q)$ EOS-insensitive relation to impose a common EOS for the two bodies, while the green, blue, and orange lines denote 50% (dashed) and 90% (solid) credible levels for the posteriors obtained using EOS-insensitive relations, a parameterized EOS without a maximum mass requirement, and independent EOSs (taken from [52]), respectively. The grey shading corresponds to the unphysical region $\Lambda_2 < \Lambda_1$ while the seven black scatter regions give the tidal parameters predicted by characteristic EOS models for this event [113, 115, 121–125].

We next explore what inferences we can make about the structure of NSs. We do this using the spectral EOS parameterization described above in combination with the requirement that the EOS must support NSs up to at least $1.97\,\mathrm{M}_\odot$, a conservative estimate based on the heaviest known pulsar [65]. From this we obtain a posterior for the NS interior pressure as a function of rest-mass density. The

result is shown in Fig. 2, along with marginalized posteriors for central densities and central pressures and predictions of the pressure-density relationship from various EOS models. The pressure posterior is shifted from the 90% credible prior region (marked by the purple dashed lines) and towards the soft floor of the parameterized family of EOS. This means that the posterior is indicating more support for softer EOS than the prior. The solid vertical lines denote the nuclear saturation density and two more rest-mass density values that are known to approximately correlate with bulk macroscopic properties of NSs [19]. The pressure at twice (six times) the nuclear saturation density is measured to be $3.5^{+2.7}_{-1.7}\times10^{34}$ ($9.0^{+7.9}_{-2.6}\times10^{35}$) $\mathrm{dyn/cm^2}$ at the 90% level.

The pressure posterior appears to show minor signs of a bend above a density of $\sim 5\rho_{\rm nuc}$. Evidence of such behavior at high densities would be an indication of extra degrees of freedom, though this is not an outcome of the GW data alone. Indeed in the top (right) panel, the vertical (horizontal) lines denote the 90% confidence intervals for the central densities (pressures) of the two stars, suggesting that our data are not informative for densities (pressures) above those intervals. The bend is an outcome of two competing effects: the GW data point toward a lower pressure, while the requirement that the EOS supports masses above $1.97\,\mathrm{M}_\odot$ demands a high pressure at large densities. The result is a precise pressure estimate at around $5\rho_{\rm nuc}$ and a broadening above that, giving the impression of a bend in the pressure. We have verified that the bend is absent if we remove the maximum mass constraint from our analysis.

Finally we place constraints in the 2-dimensional parameter space of the NS mass and areal radius for each binary component. This posterior is shown in Fig. 3. The left panel is obtained by first using the $\Lambda_a(\Lambda_s, q)$ relation to obtain tidal deformability samples assuming a common EOS and then using the Λ–C relation to compute the NS radii. The right panel is computed by integrating the TOV equation to compute the radius for each sample in the spectral EOS parametrization after imposing a maximum mass of at least $1.97\,\mathrm{M}_\odot$. At the 90% level, the radii of the two NSs are $R_1 = 10.8^{+2.0}_{-1.7}$ km and $R_2 = 10.7^{+2.1}_{-1.5}$ km from the left panel and $R_1 = 11.9^{+1.4}_{-1.4}$ km and $R_2 = 11.9^{+1.4}_{-1.4}$ km from the right panel. The one-sided 90% lower [upper] limit on $m_2[m_1]$ is $(1.15, 1.36)M_\odot[(1.36, 1.62)M_\odot]$ from the left panel and $(1.18, 1.36)M_\odot[(1.36, 1.58)M_\odot]$ from the right panel, consistent with the results of Ref. [52]. We note that the Λ–C relation has not been established to values of Λ less than 20 [104]. In order to check the validity of our EoS-insensitive results in this regime, we first verify that the parametrized-EoS results without a maximum mass constraint satisfy the Λ–C relation to the required accuracy, even for $\Lambda_1 < 20$. Furthermore, we find that our radius and mass estimates are unaffected if we discard all $\Lambda_1 < 10$ samples.

The difference between the two radius estimates is mainly due to different physical information included in

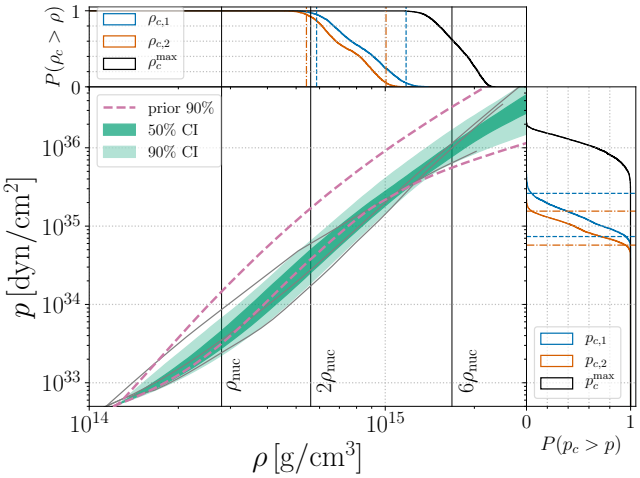

FIG. 2. Marginalized posterior (green bands) and prior (purple dashed) for the pressure p as a function of the rest-mass density ρ of the NS interior using the spectral EOS parametrization and imposing a lower limit on the maximum NS mass supported by the EOS of $1.97\,\mathrm{M}_\odot$. The dark (light) shaded region corresponds to the 50% (90%) posterior credible level and the purple dashed lines show the 90% prior credible interval. Vertical lines correspond to once, twice, and six times the nuclear saturation density. Overplotted in grey are representative EOS models [121, 122, 124], using data taken from [19]; from top to bottom at $2\rho_{\rm nuc}$ we show H4, APR4, and WFF1. The corner plots show cumulative posteriors of central densities ρ_c (top) and central pressures p_c (right) for the two NSs (blue and orange), as well as for the heaviest NS that the EOS supports (black). The 90% credible intervals for ρ_c and p_c are denoted by vertical and horizontal lines respectively for the heavier (blue dashed) and lighter (orange dot-dashed) NS.

each analysis. The EOS-insensitive-relations analysis (left panel) is based on GW data alone, while the parametrized-EOS analysis (right panel) imposes an additional observational constraint, namely that the EOS must support NSs of at least $1.97\,\mathrm{M}_\odot$. This has a large effect on the radii priors as shown in the 1-dimensional plots of Fig. 3, since small radii are typically predicted by soft EOSs, which cannot support large NS masses. In the case of EOS-insensitive relations (left panel), the prior allows for smaller values of the radius than in the parametrized-EOS case (right panel), something that is reflected in the posteriors since the GW data alone cannot rule out radii below $\sim 10\,\mathrm{km}$. Therefore the lower radius limit in the EOS-insensitive-relations analysis is determined by the GW measurement, while in the case of the parametrized-EOS analysis it is determined by the mass of the heaviest observed pulsar and its implications for NS radii [65]. Additionally, we verified that the parametrized-EOS analysis without the maximum mass constraint leads to similar results to the EOS-insensitive-relations analysis.

To quantify the improvement from assuming that both NSs obey the same EOS, we apply the Λ–C relation to

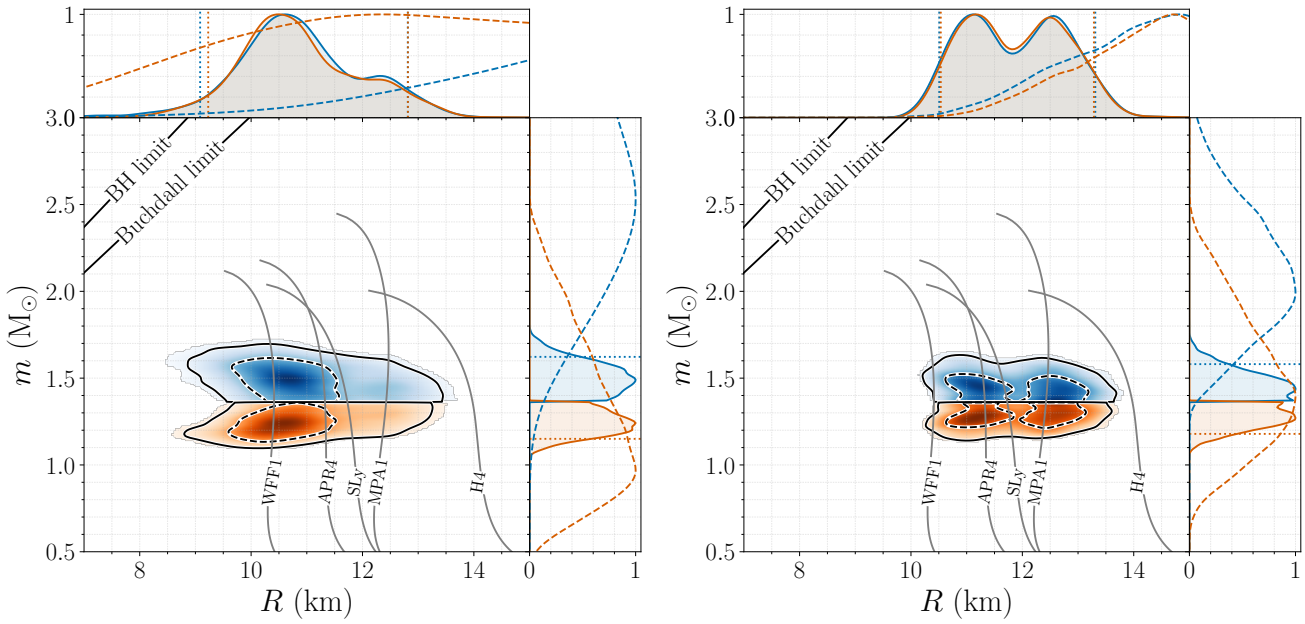

FIG. 3. Marginalized posterior for the mass m and areal radius R of each binary component using EOS-insensitive relations (left panel) and a parametrized EOS where we impose a lower limit on the maximum mass of $1.97\,M_\odot$ (right panel). The top blue (bottom orange) posterior corresponds to the heavier (lighter) NS. Example mass-radius curves for selected EOSs are overplotted in grey. The lines in the top left denote the Schwarzschild BH ($R = 2m$) and Buchdahl ($R = 9m/4$) limits. In the one-dimensional plots, solid lines are used for the posteriors, while dashed lines are used for the corresponding parameter priors. Dotted vertical lines are used for the bounds of the 90% credible intervals.

tidal deformability samples calculated without assuming the $\Lambda_a(\Lambda_s, q)$ relation (the orange posterior of Fig. 1) and obtain $R_1 = 11.8^{+2.7}_{-3.3}$ km and $R_2 = 10.8^{+2.9}_{-3.0}$ km at the 90% level. This suggests that imposing a common EOS for the two binary components leads to a reduction of the 90% credible interval width for the radius measurement of almost a factor of two from 5.9 km to 3.6 km.

DISCUSSION

In this letter, we complement our analysis of the tidal effects of GW170817 in [52] with a targeted analysis that assumes astrophysically plausible NS spins and tidal parameters, as well as the same EOS for both NSs. This additional prior information enables us to measure NS radii with an uncertainty less than 2.8 km if consistency with observed pulsar masses is enforced, and 3.6 km using GW data alone at the 90% credible level. We observe that, in both cases, the data are informative and drive the upper bounds on the NS radii and the stiffness of the EOS. Simultaneously, the pressure at twice the nuclear saturation density is measured to be $p(2\rho_{\rm nuc}) = 3.5^{+2.7}_{-1.7} \times 10^{34}\,{\rm dyn/cm^2}$. Our results are consistent with X-ray binary observations (e.g. [19, 20, 126, 127]) and suggest that NS radii are not large. Additionally, our results can be compared to tidal inference based on the electromagnetic emission of GW170817 [128–130].

Our results are comparable and consistent with studies that use the tidal measurement from [5] to obtain bounds on NS radii. Using our bound of $\Lambda_{1.4} < 800$ (the only tidal parameter in [5], which assumed a common EOS for both NSs) and different EOS parametrizations, several studies found $R_{1.4} \lesssim 13.5$ km [56, 58, 62, 64]. Reference [63] arrives at a similar conclusion using our $\tilde{\Lambda} < 800$ constraint [5] (though see [52] for an amended $\tilde{\Lambda}$ bound) and the observation that $\tilde{\Lambda}$ is almost insensitive to the binary mass ratio [99]. Our improved estimate of $\Lambda_{1.4} = 190^{+390}_{-120}$, and $R_1 = 10.8^{+2.0}_{-1.7}$ km and $R_2 = 10.7^{+2.1}_{-1.5}$ km for the EOS-insensitive-relation analysis is roughly consistent with these estimates (see for example Fig. 1 of [62] and [58]). If we additionally enforce the heaviest observed pulsar to be supported by placing direct constraints on the EOS parameter space, we get further improvement in the radius measurement, with $R_1 = 11.9^{+1.4}_{-1.4}$ km and $R_2 = 11.9^{+1.4}_{-1.4}$ km.

A recent analysis of the GW170817 data was performed in De et al. [53] using the TaylorF2 model, imposing that the two NSs have the same radii which, under the additional assumption that $\Lambda \propto C^{-6}$ (an alternative to the Λ–C relation used here [104]), directly relates the two tidal deformabilities as $\Lambda_1 = q^6\Lambda_2$. After our paper appeared as a preprint, De et al. obtained a revised estimate of the common NS radius $8.9\,{\rm km} < \hat{R} < 13.2\,{\rm km}$. Despite using a lower low frequency cut off - and hence more data

- than our study, the result of De et al. corresponds to a width of $4.3\,\mathrm{km}$, which is wider than the uncertainty on radii computed under our EoS-insensitive analysis. There are differences in several details of the set-up of the two analyses (most notably, frequency range, data calibration, the noise PSD estimation, waveform model, parameter priors, assumed relations between radii and Λs and treatment of corresponding uncertainties), each of which may be responsible for part of the observed discrepancies.

Our results, and specifically the lower radius limit, do not constitute observational proof of tidal effects in GW170817, as our analysis has explicitly assumed that the coalescing bodies were NSs both in terms of their spins and tidal deformabilities. In particular, the spins are restricted to small values typical for galactic NSs in binaries, and the tidal deformabilites are calculated consistently assuming a common typical NS EoS. Moreover, the Λ–C map diverges as Λ approaches zero (BH), and therefore the lower bounds obtained for the radii do not imply lower bounds on the tidal deformabilities. Meanwhile, the analysis of [52] assumes independent tidal parameters and finds a lower bound on $\tilde{\Lambda}$ only under the small-spin assumption but not if spins larger than 0.05 are allowed.

The detection of GW170817 has opened new avenues in astrophysics and in the study of matter at conditions currently unattainable in terrestrial laboratories. As the network of GW observatories expands and improves in sensitivity, we expect many more observations of BNS mergers [4]. Each new observation will yield additional information about the properties of NSs, and the increasing precision of our measurements will simultaneously raise new challenges. As statistical uncertainties shrink, systematic uncertainties that are naturally introduced by our models and the underlying assumptions of our methods may begin to dominate. Improved waveform models and data analysis techniques are an area of active research for the GW community, and will be required to achieve our most complete understanding of these extreme systems.

ACKNOWLEDGMENTS

The authors gratefully acknowledge the support of the United States National Science Foundation (NSF) for the construction and operation of the LIGO Laboratory and Advanced LIGO as well as the Science and Technology Facilities Council (STFC) of the United Kingdom, the Max-Planck-Society (MPS), and the State of Niedersachsen/Germany for support of the construction of Advanced LIGO and construction and operation of the GEO600 detector. Additional support for Advanced LIGO was provided by the Australian Research Council. The authors gratefully acknowledge the Italian Istituto Nazionale di Fisica Nucleare (INFN), the French Centre National de la Recherche Scientifique (CNRS) and the Foundation for Fundamental Research on Matter supported by the Netherlands Organisation for Scientific Research, for the construction and operation of the Virgo detector and the creation and support of the EGO consortium. The authors also gratefully acknowledge research support from these agencies as well as by the Council of Scientific and Industrial Research of India, the Department of Science and Technology, India, the Science & Engineering Research Board (SERB), India, the Ministry of Human Resource Development, India, the Spanish Agencia Estatal de Investigación, the Vicepresidència i Conselleria d'Innovació, Recerca i Turisme and the Conselleria d'Educació i Universitat del Govern de les Illes Balears, the Conselleria d'Educació, Investigació, Cultura i Esport de la Generalitat Valenciana, the National Science Centre of Poland, the Swiss National Science Foundation (SNSF), the Russian Foundation for Basic Research, the Russian Science Foundation, the European Commission, the European Regional Development Funds (ERDF), the Royal Society, the Scottish Funding Council, the Scottish Universities Physics Alliance, the Hungarian Scientific Research Fund (OTKA), the Lyon Institute of Origins (LIO), the Paris Île-de-France Region, the National Research, Development and Innovation Office Hungary (NKFI), the National Research Foundation of Korea, Industry Canada and the Province of Ontario through the Ministry of Economic Development and Innovation, the Natural Science and Engineering Research Council Canada, the Canadian Institute for Advanced Research, the Brazilian Ministry of Science, Technology, Innovations, and Communications, the International Center for Theoretical Physics South American Institute for Fundamental Research (ICTP-SAIFR), the Research Grants Council of Hong Kong, the National Natural Science Foundation of China (NSFC), the Leverhulme Trust, the Research Corporation, the Ministry of Science and Technology (MOST), Taiwan and the Kavli Foundation. The authors gratefully acknowledge the support of the NSF, STFC, MPS, INFN, CNRS and the State of Niedersachsen/Germany for provision of computational resources. Data associated with the figures in this article, including posterior samples generated using the PhenomPNRT model, can be found at dcc.ligo.org/LIGO-P1800115/public. The GW strain data for this event are available at the LIGO Open Science Center [131]. This article has been assigned the document number LIGO-P1800115.

[1] J. Aasi *et al.* (LIGO Scientific Collaboration), Class. Quant. Grav. **32**, 074001 (2015).

[2] F. Acernese *et al.* (The Virgo Collaboration), Class. Quantum Grav. **32**, 024001 (2015), arXiv:1408.3978 [gr-qc].

[3] B. P. Abbott, R. Abbott, T. D. Abbott, M. R. Abernathy, F. Acernese, K. Ackley, C. Adams, T. Adams, P. Addesso, R. X. Adhikari, and et al., Physical Review Letters **116**, 061102 (2016), arXiv:1602.03837 [gr-qc].

[4] B. P. Abbott *et al.* (LIGO Scientific Collaboration, Virgo Collaboration, KAGRA Collaboration), Living Rev. Rel. **21**, 3 (2018), arXiv:1304.0670 [gr-qc].

[5] B. Abbott *et al.* (LIGO Scientific Collaboration, Virgo Collaboration), Phys. Rev. Lett. **119**, 161101 (2017), arXiv:1710.05832 [gr-qc].

[6] B. P. Abbott *et al.* (Virgo, Fermi-GBM, INTEGRAL, LIGO Scientific Collaboration), Astrophys. J. **848**, L13 (2017), arXiv:1710.05834 [astro-ph.HE].

[7] A. Goldstein *et al.*, Astrophys. J. **848**, L14 (2017), arXiv:1710.05446 [astro-ph.HE].

[8] B. P. Abbott *et al.* (GROND, SALT Group, OzGrav, CAASTROs, DFN, DES, INTEGRAL, Virgo, Insight-HXMT, MAXI Team, J-GEM, RATIR, ATLAS, IceCube, LWA, ePESSTO, GRAWITA, RIMAS, SKA South Africa/MeerKAT, H.E.S.S., Fermi Large Area Telescope, 1M2H Team, IKI-GW Follow-up, Fermi GBM, Pi of Sky, DWF (Deeper Wider Faster Program), MASTER, AstroSat Cadmium Zinc Telluride Imager Team, Swift, Pierre Auger, ASKAP, VINROUGE, JAGWAR, Chandra Team at McGill University, TTU-NRAO, GROWTH, AGILE Team, MWA, ATCA, AST3, TOROS, Pan-STARRS, NuSTAR, BOOTES, CaltechNRAO, LIGO Scientific Collaboration, High Time Resolution Universe Survey, Nordic Optical Telescope, Las Cumbres Observatory Group, TZAC Consortium, LOFAR, IPN, DLT40, Texas Tech University, HAWC, ANTARES, KU, Dark Energy Camera GW-EM, CALET, Euro VLBI Team, ALMA), Astrophys. J. **848**, L12 (2017), arXiv:1710.05833 [astro-ph.HE].

[9] D. A. Coulter *et al.*, Science **358**, 1556 (2017), arXiv:1710.05452 [astro-ph.HE].

[10] E. Troja *et al.*, Nature **551**, 71 (2017), arXiv:1710.05433 [astro-ph.HE].

[11] D. Haggard, M. Nynka, J. J. Ruan, V. Kalogera, S. Bradley Cenko, P. Evans, and J. A. Kennea, Astrophys. J. **848**, L25 (2017), arXiv:1710.05852 [astro-ph.HE].

[12] G. Hallinan *et al.*, Science **358**, 1579 (2017), arXiv:1710.05435 [astro-ph.HE].

[13] A. W. Steiner, S. Gandolfi, F. J. Fattoyev, and W. G. Newton, Phys. Rev. C **91**, 015804 (2015), arXiv:1403.7546 [nucl-th].

[14] M. B. Tsang, J. R. Stone, F. Camera, P. Danielewicz, S. Gandolfi, K. Hebeler, C. J. Horowitz, J. Lee, W. G. Lynch, Z. Kohley, R. Lemmon, P. Möller, T. Murakami, S. Riordan, X. Roca-Maza, F. Sammarruca, A. W. Steiner, I. Vidaña, and S. J. Yennello, Phys. Rev. C **86**, 015803 (2012), arXiv:1204.0466 [nucl-ex].

[15] M. Baldo and G. F. Burgio, Progress in Particle and Nuclear Physics **91**, 203 (2016), arXiv:1606.08838 [nucl-th].

[16] J. M. Lattimer and M. Prakash, Phys. Rep. **621**, 127 (2016), arXiv:1512.07820 [astro-ph.SR].

[17] M. Oertel, M. Hempel, T. Klähn, and S. Typel, Reviews of Modern Physics **89**, 015007 (2017), arXiv:1610.03361 [astro-ph.HE].

[18] K. Hebeler, J. M. Lattimer, C. J. Pethick, and A. Schwenk, Astrophys. J. **773**, 11 (2013), arXiv:1303.4662 [astro-ph.SR].

[19] F. Özel and P. Freire, Ann. Rev. Astron. Astrophys. **54**, 401 (2016), arXiv:1603.02698 [astro-ph.HE].

[20] A. W. Steiner, C. O. Heinke, S. Bogdanov, C. Li, W. C. G. Ho, A. Bahramian, and S. Han, Mon. Not. Roy. Astron. Soc. **476**, 421 (2018), arXiv:1709.05013 [astro-ph.HE].

[21] E. E. Flanagan and T. Hinderer, Phys. Rev. D **77**, 021502 (2008).

[22] J. Vines, E. E. Flanagan, and T. Hinderer, Phys. Rev. D **83**, 084051 (2011), arXiv:1101.1673 [gr-qc].

[23] T. Damour, A. Nagar, and L. Villain, Phys. Rev. D **85**, 123007 (2012), arXiv:1203.4352 [gr-qc].

[24] A. Buonanno, B. R. Iyer, E. Ochsner, Y. Pan, and B. S. Sathyaprakash, Phys. Rev. D **80**, 084043 (2009), arXiv:0907.0700 [gr-qc].

[25] L. Blanchet, Living Rev. Rel. **17**, 2 (2014), arXiv:1310.1528 [gr-qc].

[26] W. D. Goldberger and I. Z. Rothstein, Phys. Rev. D **73**, 104029 (2006), arXiv:hep-th/0409156 [hep-th].

[27] W. D. Goldberger, in *Les Houches Summer School - Session 86: Particle Physics and Cosmology: The Fabric of Spacetime Les Houches, France, July 31-August 25, 2006* (2007) arXiv:hep-ph/0701129 [hep-ph].

[28] T. Damour, B. R. Iyer, and B. S. Sathyaprakash, Phys. Rev. D **63**, 044023 (2001).

[29] L. Blanchet, T. Damour, B. R. Iyer, C. M. Will, and A. G. Wiseman, Phys. Rev. Lett. **74**, 3515 (1995), arXiv:9501027 [gr-qc].

[30] L. Blanchet, T. Damour, G. Esposito-Farèse, and B. R. Iyer, Phys. Rev. Lett. **93**, 091101 (2004), arXiv:0406012 [gr-qc].

[31] T. Damour, P. Jaranowski, and G. Schaefer, Phys. Lett. B **513**, 147 (2001), arXiv:gr-qc/0105038 [gr-qc].

[32] E. E. Flanagan, Phys. Rev. D **58**, 124030 (1998), arXiv:gr-qc/9706045 [gr-qc].

[33] T. Damour, in *Les Houches Summer School on Gravitational Radiation Les Houches, France, June 2-21, 1982* (1982).

[34] S. E. Gralla, Class. Quant. Grav. **35**, 085002 (2018), arXiv:1710.11096 [gr-qc].

[35] T. Damour, in *Gravitational Radiation*, edited by N. Deruelle and T. Piran (North-Holland, Amsterdam, 1983) pp. 59–144.

[36] T. Hinderer, Astrophys. J. **677**, 1216 (2008), arXiv:0711.2420 [astro-ph].

[37] T. Hinderer, B. D. Lackey, R. N. Lang and J. S. Read, Phys. Rev. D **81**, 123016 (2010), arXiv:0911.3535 [astro-ph].

[38] T. Binnington and E. Poisson, Phys. Rev. D **80**, 084018 (2009), arXiv:0906.1366 [gr-qc].

[39] T. Damour and A. Nagar, Phys. Rev. D **80**, 084035 (2009), arXiv:0906.0096 [gr-qc].

[40] E. Poisson, Phys. Rev. D **57**, 5287 (1998), arXiv:gr-qc/9709032 [gr-qc].

[41] A. Bohé, G. Faye, S. Marsat, and E. K. Porter, Class. Quant. Grav. **32**, 195010 (2015), arXiv:1501.01529 [gr-qc].

[42] L. Baiotti and L. Rezzolla, Rept. Prog. Phys. **80**, 096901 (2017), arXiv:1607.03540 [gr-qc].

[43] D. Lai, Monthly Notices of the Royal Astronomical Society **270**, 611 (1994), astro-ph/9404062.

[44] T. Hinderer, A. Taracchini, F. Foucart, A. Buonanno, J. Steinhoff, M. Duez, L. E. Kidder, H. P. Pfeiffer, M. A. Scheel, B. Szilagyi, K. Hotokezaka, K. Kyutoku, M. Shibata, and C. W. Carpenter, Physical Review Letters **116**, 181101 (2016), arXiv:1602.00599 [gr-qc].

[45] N. Andersson and W. C. G. Ho, Phys. Rev. D **97**, 023016 (2018), arXiv:1710.05950 [astro-ph.HE].
[46] W. G. Laarakkers and E. Poisson, Astrophys. J. **512**, 282 (1999), arXiv:gr-qc/9709033 [gr-qc].
[47] G. Pappas and T. A. Apostolatos, (2012), arXiv:1211.6299 [gr-qc].
[48] M. Agathos, J. Meidam, W. Del Pozzo, T. G. F. Li, M. Tompitak, J. Veitch, S. Vitale, and C. Van Den Broeck, Phys. Rev. D **92**, 023012 (2015).
[49] I. Harry and T. Hinderer, (2018), arXiv:1801.09972 [gr-qc].
[50] N. V. Krishnendu, K. G. Arun, and C. K. Mishra, Phys. Rev. Lett. **119**, 091101 (2017), arXiv:1701.06318 [gr-qc].
[51] B. P. Abbott *et al.* (LIGO Scientific Collaboration, Virgo Collaboration), Astrophys. J. **851**, L16 (2017), arXiv:1710.09320 [astro-ph.HE].
[52] B. P. Abbott *et al.* (Virgo, LIGO Scientific), (2018), LIGO-P1800061, https://dcc.ligo.org/LIGO-P1800061/public, arXiv:1805.11579 [gr-qc].
[53] S. De, D. Finstad, J. M. Lattimer, D. A. Brown, E. Berger, and C. M. Biwer, Phys. Rev. Lett. **121**, 091102 (2018), arXiv:1804.08583 [astro-ph.HE].
[54] B. Margalit and B. D. Metzger, The Astrophysical Journal Letters **850**, L19 (2017).
[55] A. Bauswein, O. Just, H.-T. Janka, and N. Stergioulas, The Astrophysical Journal Letters **850**, L34 (2017).
[56] E.-P. Zhou, X. Zhou, and A. Li, Phys. Rev. D **97**, 083015 (2018), arXiv:1711.04312 [astro-ph.HE].
[57] L. Rezzolla, E. R. Most, and L. R. Weih, The Astrophysical Journal Letters **852**, L25 (2018).
[58] F. J. Fattoyev, J. Piekarewicz, and C. J. Horowitz, Phys. Rev. Lett. **120**, 172702 (2018).
[59] R. Nandi and P. Char, Astrophys. J. **857**, 12 (2018), arXiv:1712.08094 [astro-ph.HE].
[60] V. Paschalidis, K. Yagi, D. Alvarez-Castillo, D. B. Blaschke, and A. Sedrakian, Phys. Rev. D **97**, 084038 (2018), arXiv:1712.00451 [astro-ph.HE].
[61] M. Ruiz, S. L. Shapiro, and A. Tsokaros, Phys. Rev. D **97**, 021501 (2018).
[62] E. Annala, T. Gorda, A. Kurkela, and A. Vuorinen, Phys. Rev. Lett. **120**, 172703 (2018).
[63] C. Raithel, F. Özel, and D. Psaltis, (2018), arXiv:1803.07687 [astro-ph.HE].
[64] E. R. Most, L. R. Weih, L. Rezzolla, and J. Schaffner-Bielich, (2018), arXiv:1803.00549 [gr-qc].
[65] J. Antoniadis, P. C. Freire, N. Wex, T. M. Tauris, R. S. Lynch, *et al.*, Science **340**, 1233232 (2013), arXiv:1304.6875 [astro-ph.HE].
[66] LIGO Open Science Center (LOSC), https://losc.ligo.org.
[67] C. Pankow *et al.*, (2018), arXiv:1808.03619 [gr-qc].
[68] J. C. Driggers *et al.* (LIGO Scientific), (2018), arXiv:1806.00532 [astro-ph.IM].
[69] J. C. Driggers, M. Evans, K. Pepper, and R. Adhikari, Rev. Sci. Instrum. **83**, 024501 (2012), arXiv:1112.2224 [gr-qc].
[70] G. D. Meadors, K. Kawabe, and K. Riles, Class. Quantum. Grav. **31**, 105014 (2014), arXiv:1311.6835 [astro-ph.IM].
[71] V. Tiwari *et al.*, Class. Quantum. Grav. **32**, 165014 (2015), arXiv:1503.07476 [gr-qc].
[72] J. Veitch, V. Raymond, B. Farr, W. Farr, P. Graff, S. Vitale, B. Aylott, K. Blackburn, N. Christensen, M. Coughlin, W. Del Pozzo, F. Feroz, J. Gair, C.-J. Haster, V. Kalogera, T. Littenberg, I. Mandel, R. O'Shaughnessy, M. Pitkin, C. Rodriguez, C. Röver, T. Sidery, R. Smith, M. Van Der Sluys, A. Vecchio, W. Vousden, and L. Wade, Phys. Rev. D **91**, 042003 (2015), arXiv:1409.7215 [gr-qc].
[73] B. P. Abbott *et al.* (LIGO Scientific Collaboration, Virgo Collaboration), Phys. Rev. Lett. **116**, 241102 (2016), arXiv:1602.03840 [gr-qc].
[74] LIGO Scientific Collaboration and Virgo Collaboration, "LALSuite, https://git.ligo.org/lscsoft/lalsuite/tree/lalinference_o2," (2017).
[75] T. B. Littenberg and N. J. Cornish, Phys. Rev. D **91**, 084034 (2015), arXiv:1410.3852 [gr-qc].
[76] N. J. Cornish and T. B. Littenberg, Class. Quant. Grav. **32**, 135012 (2015).
[77] W. M. Farr, B. Farr, and T. Littenberg, *Modelling Calibration Errors In CBC Waveforms*, Tech. Rep. LIGO-T1400682 (LIGO Project, 2015).
[78] T. M. Tauris *et al.*, Astrophys. J. **846**, 170 (2017), arXiv:1706.09438 [astro-ph.HE].
[79] P. Schmidt, M. Hannam, and S. Husa, Phys. Rev. D **86**, 104063 (2012), arXiv:1207.3088 [gr-qc].
[80] M. Hannam, P. Schmidt, A. Bohé, L. Haegel, S. Husa, F. Ohme, G. Pratten, and M. Pürrer, Phys. Rev. Lett. **113**, 151101 (2014), arXiv:1308.3271 [gr-qc].
[81] P. Schmidt, F. Ohme, and M. Hannam, Phys. Rev. D **91**, 024043 (2015), arXiv:1408.1810 [gr-qc].
[82] S. Husa, S. Khan, M. Hannam, M. Pürrer, F. Ohme, X. J. Forteza, and A. Bohé, Phys. Rev. D **93**, 044006 (2016), arXiv:1508.07250 [gr-qc].
[83] S. Khan, S. Husa, M. Hannam, F. Ohme, M. Pürrer, X. J. Forteza, and A. Bohé, Phys. Rev. D **93**, 044007 (2016), arXiv:1508.07253 [gr-qc].
[84] T. Dietrich, S. Bernuzzi, and W. Tichy, Phys. Rev. D **96**, 121501 (2017), arXiv:1706.02969 [gr-qc].
[85] A. Bohé *et al.*, Phys. Rev. D **95**, 044028 (2017), arXiv:1611.03703 [gr-qc].
[86] S. Bernuzzi, A. Nagar, T. Dietrich, and T. Damour, Phys. Rev. Lett. **114**, 161103 (2015), arXiv:1412.4553 [gr-qc].
[87] B. D. Lackey, S. Bernuzzi, C. R. Galley, J. Meidam, and C. Van Den Broeck, Phys. Rev. D **95**, 104036 (2017), arXiv:1610.04742 [gr-qc].
[88] T. Hinderer *et al.*, Phys. Rev. Lett. **116**, 181101 (2016), arXiv:1602.00599 [gr-qc].
[89] J. Steinhoff, T. Hinderer, A. Buonanno, and A. Taracchini, Phys. Rev. D **94**, 104028 (2016), arXiv:1608.01907 [gr-qc].
[90] B. S. Sathyaprakash and S. V. Dhurandhar, Phys. Rev. D **44**, 3819 (1991).
[91] A. Bohé, S. Marsat, and L. Blanchet, Class. Quant. Grav. **30**, 135009 (2013), arXiv:1303.7412 [gr-qc].
[92] K. Arun, A. Buonanno, G. Faye, and E. Ochsner, Phys. Rev. D **79**, 104023 (2009), arXiv:0810.5336 [gr-qc].
[93] B. Mikoczi, M. Vasuth, and L. A. Gergely, Phys. Rev. D **71**, 124043 (2005), arXiv:astro-ph/0504538 [astro-ph].
[94] C. K. Mishra, A. Kela, K. G. Arun, and G. Faye, Phys. Rev. D **93**, 084054 (2016), arXiv:1601.05588 [gr-qc].

[95] A. Taracchini, A. Buonanno, Y. Pan, T. Hinderer, M. Boyle, D. A. Hemberger, L. E. Kidder, G. Lovelace, A. H. Mroué, H. P. Pfeiffer, M. A. Scheel, B. Szilágyi, N. W. Taylor, and A. Zenginoglu, Phys. Rev. D **89**, 061502 (2014), arXiv:1311.2544 [gr-qc].

[96] E. Barausse and A. Buonanno, Phys. Rev. D **81**, 084024 (2010), arXiv:0912.3517 [gr-qc].

[97] A. Buonanno and T. Damour, Phys. Rev. D **62**, 064015 (2000), arXiv:gr-qc/0001013 [gr-qc].

[98] A. Buonanno and T. Damour, Phys. Rev. D **59**, 084006 (1999), arXiv:gr-qc/9811091 [gr-qc].

[99] L. Wade, J. D. E. Creighton, E. Ochsner, B. D. Lackey, B. F. Farr, T. B. Littenberg, and V. Raymond, Phys. Rev. D **89**, 103012 (2014), arXiv:1402.5156 [gr-qc].

[100] T. Dietrich *et al.*, (2018), arXiv:1804.02235 [gr-qc].

[101] K. Yagi and N. Yunes, Science **341**, 365 (2013), arXiv:1302.4499 [gr-qc].

[102] K. Yagi and N. Yunes, Phys. Rev. D **88**, 023009 (2013), arXiv:1303.1528 [gr-qc].

[103] K. Chatziioannou, K. Yagi, A. Klein, N. Cornish, and N. Yunes, Phys. Rev. D **92**, 104008 (2015), arXiv:1508.02062 [gr-qc].

[104] K. Yagi and N. Yunes, Phys. Rept. **681**, 1 (2017), arXiv:1608.02582 [gr-qc].

[105] K. Yagi and N. Yunes, Class. Quant. Grav. **33**, 13LT01 (2016), arXiv:1512.02639 [gr-qc].

[106] K. Chatziioannou, C.-J. Haster, and A. Zimmerman, Phys. Rev. D **97**, 104036 (2018), arXiv:1804.03221 [gr-qc].

[107] A. Maselli, V. Cardoso, V. Ferrari, L. Gualtieri, and P. Pani, Phys. Rev. D **88**, 023007 (2013), arXiv:1304.2052 [gr-qc].

[108] M. Urbanec, J. C. Miller, and Z. Stuchlik, Mon. Not. Roy. Astron. Soc. **433**, 1903 (2013), arXiv:1301.5925 [astro-ph.SR].

[109] L. Lindblom, (2018), arXiv:1804.04072 [astro-ph.HE].

[110] L. Lindblom, Phys. Rev. D **82**, 103011 (2010).

[111] L. Lindblom and N. M. Indik, Phys. Rev. D **86**, 084003 (2012), arXiv:1207.3744 [astro-ph.HE].

[112] L. Lindblom and N. M. Indik, Phys. Rev. D **89**, 064003 (2014), [Erratum: Phys. Rev.D93,no.12,129903(2016)], arXiv:1310.0803 [astro-ph.HE].

[113] F. Douchin and P. Haensel, Astron. Astrophys **380**, 151 (2001), arXiv:astro-ph/0111092.

[114] J. M. Lattimer and M. Prakash, Astrophys. J. **550**, 426 (2001), arXiv:astro-ph/0002232 [astro-ph].

[115] J. S. Read, B. D. Lackey, B. J. Owen, and J. L. Friedman, Phys. Rev. D **79**, 124032 (2009), arXiv:0812.2163 [astro-ph].

[116] G. Raaijmakers, T. E. Riley, and A. L. Watts, (2018), arXiv:1804.09087 [astro-ph.HE].

[117] M. F. Carney, L. E. Wade, and B. S. Irwin, (2018), arXiv:1805.11217 [gr-qc].

[118] B. D. Lackey and L. Wade, Phys. Rev. D **91**, 043002 (2015), arXiv:1410.8866 [gr-qc].

[119] S. L. Shapiro and S. A. Teukolsky, *Black holes, white dwarfs, and neutron stars: They physics of compact objects. New York, Wiley-Interscience, 1983, 663 p.* (1983).

[120] W. Del Pozzo, T. G. F. Li, M. Agathos, C. Van Den Broeck, and S. Vitale, Phys. Rev. Lett. **111**, 071101 (2013).

[121] R. B. Wiringa, V. Fiks, and A. Fabrocini, Phys. Rev. C **38**, 1010 (1988).

[122] A. Akmal, V. R. Pandharipande, and D. G. Ravenhall, Phys. Rev. C **58**, 1804 (1998), arXiv:nucl-th/9804027.

[123] H. Müther, M. Prakash, and T. L. Ainsworth, Phys. Lett. B **199**, 469 (1987).

[124] B. D. Lackey, M. Nayyar, and B. J. Owen, Phys. Rev. D **73**, 024021 (2006), arXiv:astro-ph/0507312.

[125] H. Müller and B. D. Serot, Nucl. Phys. **A606**, 508 (1996), arXiv:nucl-th/9603037 [nucl-th].

[126] A. W. Steiner, J. M. Lattimer, and E. F. Brown, Astrophys. J. **722**, 33 (2010), arXiv:1005.0811 [astro-ph.HE].

[127] J. Nattila, M. C. Miller, A. W. Steiner, J. J. E. Kajava, V. F. Suleimanov, and J. Poutanen, Astron. Astrophys. **608**, A31 (2017), arXiv:1709.09120 [astro-ph.HE].

[128] M. Shibata, S. Fujibayashi, K. Hotokezaka, K. Kiuchi, K. Kyutoku, Y. Sekiguchi, and M. Tanaka, Phys. Rev. **D96**, 123012 (2017), arXiv:1710.07579 [astro-ph.HE].

[129] D. Radice, A. Perego, F. Zappa, and S. Bernuzzi, Astrophys. J. **852**, L29 (2018), arXiv:1711.03647 [astro-ph.HE].

[130] M. W. Coughlin *et al.*, (2018), arXiv:1805.09371 [astro-ph.HE].

[131] LIGO Open Science Center (LOSC), https://doi.org/10.7935/K5B8566F (2017).

Authors

B. P. Abbott,[1] R. Abbott,[1] T. D. Abbott,[2] F. Acernese,[3,4] K. Ackley,[5] C. Adams,[6] T. Adams,[7] P. Addesso,[8] R. X. Adhikari,[1] V. B. Adya,[9,10] C. Affeldt,[9,10] B. Agarwal,[11] M. Agathos,[12] K. Agatsuma,[13] N. Aggarwal,[14] O. D. Aguiar,[15] L. Aiello,[16,17] A. Ain,[18] P. Ajith,[19] B. Allen,[9,20,10] G. Allen,[11] A. Allocca,[21,22] M. A. Aloy,[23] P. A. Altin,[24] A. Amato,[25] A. Ananyeva,[1] S. B. Anderson,[1] W. G. Anderson,[20] S. V. Angelova,[26] S. Antier,[27] S. Appert,[1] K. Arai,[1] M. C. Araya,[1] J. S. Areeda,[28] M. Arène,[29] N. Arnaud,[27,30] K. G. Arun,[31] S. Ascenzi,[32,33] G. Ashton,[5] M. Ast,[34] S. M. Aston,[6] P. Astone,[35] D. V. Atallah,[36] F. Aubin,[7] P. Aufmuth,[10] C. Aulbert,[9] K. AultONeal,[37] C. Austin,[2] A. Avila-Alvarez,[28] S. Babak,[38,29] P. Bacon,[29] F. Badaracco,[16,17] M. K. M. Bader,[13] S. Bae,[39] P. T. Baker,[40] F. Baldaccini,[41,42] G. Ballardin,[30] S. W. Ballmer,[43] S. Banagiri,[44] J. C. Barayoga,[1] S. E. Barclay,[45] B. C. Barish,[1] D. Barker,[46] K. Barkett,[47] S. Barnum,[14] F. Barone,[3,4] B. Barr,[45] L. Barsotti,[14] M. Barsuglia,[29] D. Barta,[48] J. Bartlett,[46] I. Bartos,[49] R. Bassiri,[50] A. Basti,[21,22] J. C. Batch,[46] M. Bawaj,[51,42] J. C. Bayley,[45] M. Bazzan,[52,53] B. Bécsy,[54] C. Beer,[9] M. Bejger,[55] I. Belahcene,[27] A. S. Bell,[45] D. Beniwal,[56] M. Bensch,[9,10] B. K. Berger,[1] G. Bergmann,[9,10] S. Bernuzzi,[57,58] J. J. Bero,[59] C. P. L. Berry,[60] D. Bersanetti,[61] A. Bertolini,[13] J. Betzwieser,[6] R. Bhandare,[62] I. A. Bilenko,[63] S. A. Bilgili,[40] G. Billingsley,[1] C. R. Billman,[49] J. Birch,[6] R. Birney,[26] O. Birnholtz,[59] S. Biscans,[1,14] S. Biscoveanu,[5] A. Bisht,[9,10] M. Bitossi,[30,22] M. A. Bizouard,[27] J. K. Blackburn,[1] J. Blackman,[47] C. D. Blair,[6] D. G. Blair,[64] R. M. Blair,[46] S. Bloemen,[65] O. Bock,[9] N. Bode,[9,10] M. Boer,[66] Y. Boetzel,[67] G. Bogaert,[66] A. Bohe,[38] F. Bondu,[68] E. Bonilla,[50] R. Bonnand,[7] P. Booker,[9,10] B. A. Boom,[13] C. D. Booth,[36] R. Bork,[1] V. Boschi,[30] S. Bose,[69,18] K. Bossie,[6] V. Bossilkov,[64] J. Bosveld,[64] Y. Bouffanais,[29] A. Bozzi,[30] C. Bradaschia,[22] P. R. Brady,[20] A. Bramley,[6] M. Branchesi,[16,17] J. E. Brau,[70] T. Briant,[71] F. Brighenti,[72,73] A. Brillet,[66] M. Brinkmann,[9,10] V. Brisson,[27,*] P. Brockill,[20] A. F. Brooks,[1] D. D. Brown,[56] S. Brunett,[1] C. C. Buchanan,[2] A. Buikema,[14] T. Bulik,[74] H. J. Bulten,[75,13] A. Buonanno,[38,76] D. Buskulic,[7] C. Buy,[29] R. L. Byer,[50] M. Cabero,[9] L. Cadonati,[77] G. Cagnoli,[25,78] C. Cahillane,[1] J. Calderón Bustillo,[77] T. A. Callister,[1] E. Calloni,[79,4] J. B. Camp,[80] M. Canepa,[81,61] P. Canizares,[65] K. C. Cannon,[82] H. Cao,[56] J. Cao,[83] C. D. Capano,[9] E. Capocasa,[29] F. Carbognani,[30] S. Caride,[84] M. F. Carney,[85] G. Carullo,[21] J. Casanueva Diaz,[22] C. Casentini,[32,33] S. Caudill,[13,20] M. Cavaglià,[86] F. Cavalier,[27] R. Cavalieri,[30] G. Cella,[22] C. B. Cepeda,[1] P. Cerdá-Durán,[23] G. Cerretani,[21,22] E. Cesarini,[87,33] O. Chaibi,[66] S. J. Chamberlin,[88] M. Chan,[45] S. Chao,[89] P. Charlton,[90] E. Chase,[91] E. Chassande-Mottin,[29] D. Chatterjee,[20] K. Chatziioannou,[92] B. D. Cheeseboro,[40] H. Y. Chen,[93] X. Chen,[64] Y. Chen,[47] H.-P. Cheng,[49] H. Y. Chia,[49] A. Chincarini,[61] A. Chiummo,[30] T. Chmiel,[85] H. S. Cho,[94] M. Cho,[76] J. H. Chow,[24] N. Christensen,[95,66] Q. Chu,[64] A. J. K. Chua,[47] S. Chua,[71] K. W. Chung,[96] S. Chung,[64] G. Ciani,[52,53,49] A. A. Ciobanu,[56] R. Ciolfi,[97,98] F. Cipriano,[66] C. E. Cirelli,[50] A. Cirone,[81,61] F. Clara,[46] J. A. Clark,[77] P. Clearwater,[99] F. Cleva,[66] C. Cocchieri,[86] E. Coccia,[16,17] P.-F. Cohadon,[71] D. Cohen,[27] A. Colla,[100,35] C. G. Collette,[101] C. Collins,[60] L. R. Cominsky,[102] M. Constancio Jr.,[15] L. Conti,[53] S. J. Cooper,[60] P. Corban,[6] T. R. Corbitt,[2] I. Cordero-Carrión,[103] K. R. Corley,[104] N. Cornish,[105] A. Corsi,[84] S. Cortese,[30] C. A. Costa,[15] R. Cotesta,[38] M. W. Coughlin,[1] S. B. Coughlin,[36,91] J.-P. Coulon,[66] S. T. Countryman,[104] P. Couvares,[1] P. B. Covas,[106] E. E. Cowan,[77] D. M. Coward,[64] M. J. Cowart,[6] D. C. Coyne,[1] R. Coyne,[107] J. D. E. Creighton,[20] T. D. Creighton,[108] J. Cripe,[2] S. G. Crowder,[109] T. J. Cullen,[2] A. Cumming,[45] L. Cunningham,[45] E. Cuoco,[30] T. Dal Canton,[80] G. Dálya,[54] S. L. Danilishin,[10,9] S. D'Antonio,[33] K. Danzmann,[9,10] A. Dasgupta,[110] C. F. Da Silva Costa,[49] V. Dattilo,[30] I. Dave,[62] M. Davier,[27] D. Davis,[43] E. J. Daw,[111] B. Day,[77] D. DeBra,[50] M. Deenadayalan,[18] J. Degallaix,[25] M. De Laurentis,[79,4] S. Deléglise,[71] W. Del Pozzo,[21,22] N. Demos,[14] T. Denker,[9,10] T. Dent,[9] R. De Pietri,[57,58] J. Derby,[28] V. Dergachev,[9] R. De Rosa,[79,4] C. De Rossi,[25,30] R. DeSalvo,[112] O. de Varona,[9,10] S. Dhurandhar,[18] M. C. Díaz,[108] T. Dietrich,[13,38] L. Di Fiore,[4] M. Di Giovanni,[113,98] T. Di Girolamo,[79,4] A. Di Lieto,[21,22] B. Ding,[101] S. Di Pace,[100,35] I. Di Palma,[100,35] F. Di Renzo,[21,22] A. Dmitriev,[60] Z. Doctor,[93] V. Dolique,[25] F. Donovan,[14] K. L. Dooley,[36,86] S. Doravari,[9,10] I. Dorrington,[36] M. Dovale Álvarez,[60] T. P. Downes,[20] M. Drago,[9,16,17] C. Dreissigacker,[9,10] J. C. Driggers,[46] Z. Du,[83] P. Dupej,[45] S. E. Dwyer,[46] P. J. Easter,[5] T. B. Edo,[111] M. C. Edwards,[95] A. Effler,[6] H.-B. Eggenstein,[9,10] P. Ehrens,[1] J. Eichholz,[1] S. S. Eikenberry,[49] M. Eisenmann,[7] R. A. Eisenstein,[14] R. C. Essick,[93] H. Estelles,[106] D. Estevez,[7] Z. B. Etienne,[40] T. Etzel,[1] M. Evans,[14] T. M. Evans,[6] V. Fafone,[32,33,16] H. Fair,[43] S. Fairhurst,[36] X. Fan,[83] S. Farinon,[61] B. Farr,[70] W. M. Farr,[60] E. J. Fauchon-Jones,[36] M. Favata,[114] M. Fays,[36] C. Fee,[85] H. Fehrmann,[9] J. Feicht,[1] M. M. Fejer,[50] F. Feng,[29] A. Fernandez-Galiana,[14] I. Ferrante,[21,22] E. C. Ferreira,[15] F. Ferrini,[30] F. Fidecaro,[21,22] I. Fiori,[30] D. Fiorucci,[29] M. Fishbach,[93] R. P. Fisher,[43] J. M. Fishner,[14] M. Fitz-Axen,[44] R. Flaminio,[7,115] M. Fletcher,[45] H. Fong,[92] J. A. Font,[23,116] P. W. F. Forsyth,[24] S. S. Forsyth,[77] J.-D. Fournier,[66] S. Frasca,[100,35] F. Frasconi,[22] Z. Frei,[54] A. Freise,[60] R. Frey,[70] V. Frey,[27] P. Fritschel,[14] V. V. Frolov,[6] P. Fulda,[49] M. Fyffe,[6] H. A. Gabbard,[45] B. U. Gadre,[18] S. M. Gaebel,[60] J. R. Gair,[117] L. Gammaitoni,[41] M. R. Ganija,[56] S. G. Gaonkar,[18] A. Garcia,[28]

C. García-Quirós,[106] F. Garufi,[79,4] B. Gateley,[46] S. Gaudio,[37] G. Gaur,[118] V. Gayathri,[119] G. Gemme,[61] E. Genin,[30] A. Gennai,[22] D. George,[11] J. George,[62] L. Gergely,[120] V. Germain,[7] S. Ghonge,[77] Abhirup Ghosh,[19] Archisman Ghosh,[13] S. Ghosh,[20] B. Giacomazzo,[113,98] J. A. Giaime,[2,6] K. D. Giardina,[6] A. Giazotto,[22,†] K. Gill,[37] G. Giordano,[3,4] L. Glover,[112] E. Goetz,[46] R. Goetz,[49] B. Goncharov,[5] G. González,[2] J. M. Gonzalez Castro,[21,22] A. Gopakumar,[121] M. L. Gorodetsky,[63] S. E. Gossan,[1] M. Gosselin,[30] R. Gouaty,[7] A. Grado,[122,4] C. Graef,[45] M. Granata,[25] A. Grant,[45] S. Gras,[14] C. Gray,[46] G. Greco,[72,73] A. C. Green,[60] R. Green,[36] E. M. Gretarsson,[37] P. Groot,[65] H. Grote,[36] S. Grunewald,[38] P. Gruning,[27] G. M. Guidi,[72,73] H. K. Gulati,[110] X. Guo,[83] A. Gupta,[88] M. K. Gupta,[110] K. E. Gushwa,[1] E. K. Gustafson,[1] R. Gustafson,[123] O. Halim,[17,16] B. R. Hall,[69] E. D. Hall,[14] E. Z. Hamilton,[36] H. F. Hamilton,[124] G. Hammond,[45] M. Haney,[67] M. M. Hanke,[9,10] J. Hanks,[46] C. Hanna,[88] M. D. Hannam,[36] O. A. Hannuksela,[96] J. Hanson,[6] T. Hardwick,[2] J. Harms,[16,17] G. M. Harry,[125] I. W. Harry,[38] M. J. Hart,[45] C.-J. Haster,[92] K. Haughian,[45] J. Healy,[59] A. Heidmann,[71] M. C. Heintze,[6] H. Heitmann,[66] P. Hello,[27] G. Hemming,[30] M. Hendry,[45] I. S. Heng,[45] J. Hennig,[45] A. W. Heptonstall,[1] F. J. Hernandez,[5] M. Heurs,[9,10] S. Hild,[45] T. Hinderer,[65] W. C. G. Ho,[126] D. Hoak,[30] S. Hochheim,[9,10] D. Hofman,[25] N. A. Holland,[24] K. Holt,[6] D. E. Holz,[93] P. Hopkins,[36] C. Horst,[20] J. Hough,[45] E. A. Houston,[45] E. J. Howell,[64] A. Hreibi,[66] E. A. Huerta,[11] D. Huet,[27] B. Hughey,[37] M. Hulko,[1] S. Husa,[106] S. H. Huttner,[45] T. Huynh-Dinh,[6] A. Iess,[32,33] N. Indik,[9] C. Ingram,[56] R. Inta,[84] G. Intini,[100,35] B. S. Irwin,[85] H. N. Isa,[45] J.-M. Isac,[71] M. Isi,[1] B. R. Iyer,[19] K. Izumi,[46] T. Jacqmin,[71] K. Jani,[77] P. Jaranowski,[127] D. S. Johnson,[11] W. W. Johnson,[2] D. I. Jones,[126] R. Jones,[45] R. J. G. Jonker,[13] L. Ju,[64] J. Junker,[9,10] C. V. Kalaghatgi,[36] V. Kalogera,[91] B. Kamai,[1] S. Kandhasamy,[6] G. Kang,[39] J. B. Kanner,[1] S. J. Kapadia,[20] S. Karki,[70] K. S. Karvinen,[9,10] M. Kasprzack,[2] M. Katolik,[11] S. Katsanevas,[30] E. Katsavounidis,[14] W. Katzman,[6] S. Kaufer,[9,10] K. Kawabe,[46] N. V. Keerthana,[18] F. Kéfélian,[66] D. Keitel,[45] A. J. Kemball,[11] R. Kennedy,[111] J. S. Key,[128] F. Y. Khalili,[63] B. Khamesra,[77] H. Khan,[28] I. Khan,[16,33] S. Khan,[9] Z. Khan,[110] E. A. Khazanov,[129] N. Kijbunchoo,[24] Chunglee Kim,[130] J. C. Kim,[131] K. Kim,[96] W. Kim,[56] W. S. Kim,[132] Y.-M. Kim,[133] E. J. King,[56] P. J. King,[46] M. Kinley-Hanlon,[125] R. Kirchhoff,[9,10] J. S. Kissel,[46] L. Kleybolte,[34] S. Klimenko,[49] T. D. Knowles,[40] P. Koch,[9,10] S. M. Koehlenbeck,[9,10] S. Koley,[13] V. Kondrashov,[1] A. Kontos,[14] M. Korobko,[34] W. Z. Korth,[1] I. Kowalska,[74] D. B. Kozak,[1] C. Krämer,[9] V. Kringel,[9,10] B. Krishnan,[9] A. Królak,[134,135] G. Kuehn,[9,10] P. Kumar,[136] R. Kumar,[110] S. Kumar,[19] L. Kuo,[89] A. Kutynia,[134] S. Kwang,[20] B. D. Lackey,[38] K. H. Lai,[96] M. Landry,[46] P. Landry,[93] R. N. Lang,[137] J. Lange,[59] B. Lantz,[50] R. K. Lanza,[14] A. Lartaux-Vollard,[27] P. D. Lasky,[5] M. Laxen,[6] A. Lazzarini,[1] C. Lazzaro,[53] P. Leaci,[100,35] S. Leavey,[9,10] C. H. Lee,[94] H. K. Lee,[138] H. M. Lee,[130] H. W. Lee,[131] K. Lee,[45] J. Lehmann,[9,10] A. Lenon,[40] M. Leonardi,[9,10,115] N. Leroy,[27] N. Letendre,[7] Y. Levin,[5] J. Li,[83] T. G. F. Li,[96] X. Li,[47] S. D. Linker,[112] T. B. Littenberg,[139] J. Liu,[64] X. Liu,[20] R. K. L. Lo,[96] N. A. Lockerbie,[26] L. T. London,[36] A. Longo,[140,141] M. Lorenzini,[16,17] V. Loriette,[142] M. Lormand,[6] G. Losurdo,[22] J. D. Lough,[9,10] C. O. Lousto,[59] G. Lovelace,[28] H. Lück,[9,10] D. Lumaca,[32,33] A. P. Lundgren,[9] R. Lynch,[14] Y. Ma,[47] R. Macas,[36] S. Macfoy,[26] B. Machenschalk,[9] M. MacInnis,[14] D. M. Macleod,[36] I. Magaña Hernandez,[20] F. Magaña-Sandoval,[43] L. Magaña Zertuche,[86] R. M. Magee,[88] E. Majorana,[35] I. Maksimovic,[142] N. Man,[66] V. Mandic,[44] V. Mangano,[45] G. L. Mansell,[24] M. Manske,[20,24] M. Mantovani,[30] F. Marchesoni,[51,42] F. Marion,[7] S. Márka,[104] Z. Márka,[104] C. Markakis,[11] A. S. Markosyan,[50] A. Markowitz,[1] E. Maros,[1] A. Marquina,[103] F. Martelli,[72,73] L. Martellini,[66] I. W. Martin,[45] R. M. Martin,[114] D. V. Martynov,[14] K. Mason,[14] E. Massera,[111] A. Masserot,[7] T. J. Massinger,[1] M. Masso-Reid,[45] S. Mastrogiovanni,[100,35] A. Matas,[44] F. Matichard,[1,14] L. Matone,[104] N. Mavalvala,[14] N. Mazumder,[69] J. J. McCann,[64] R. McCarthy,[46] D. E. McClelland,[24] S. McCormick,[6] L. McCuller,[14] S. C. McGuire,[143] J. McIver,[1] D. J. McManus,[24] T. McRae,[24] S. T. McWilliams,[40] D. Meacher,[88] G. D. Meadors,[5] M. Mehmet,[9,10] J. Meidam,[13] E. Mejuto-Villa,[8] A. Melatos,[99] G. Mendell,[46] D. Mendoza-Gandara,[9,10] R. A. Mercer,[20] L. Mereni,[25] E. L. Merilh,[46] M. Merzougui,[66] S. Meshkov,[1] C. Messenger,[45] C. Messick,[88] R. Metzdorff,[71] P. M. Meyers,[44] H. Miao,[60] C. Michel,[25] H. Middleton,[99] E. E. Mikhailov,[144] L. Milano,[79,4] A. L. Miller,[49] A. Miller,[100,35] B. B. Miller,[91] J. Miller,[14] M. Millhouse,[105] J. Mills,[36] M. C. Milovich-Goff,[112] O. Minazzoli,[66,145] Y. Minenkov,[33] J. Ming,[9,10] C. Mishra,[146] S. Mitra,[18] V. P. Mitrofanov,[63] G. Mitselmakher,[49] R. Mittleman,[14] D. Moffa,[85] K. Mogushi,[86] M. Mohan,[30] S. R. P. Mohapatra,[14] M. Montani,[72,73] C. J. Moore,[12] D. Moraru,[46] G. Moreno,[46] S. Morisaki,[82] B. Mours,[7] C. M. Mow-Lowry,[60] G. Mueller,[49] A. W. Muir,[36] Arunava Mukherjee,[9,10] D. Mukherjee,[20] S. Mukherjee,[108] N. Mukund,[18] A. Mullavey,[6] J. Munch,[56] E. A. Muñiz,[43] M. Muratore,[37] P. G. Murray,[45] A. Nagar,[87,147,148] K. Napier,[77] I. Nardecchia,[32,33] L. Naticchioni,[100,35] R. K. Nayak,[149] J. Neilson,[112] G. Nelemans,[65,13] T. J. N. Nelson,[6] M. Nery,[9,10] A. Neunzert,[123] L. Nevin,[1] J. M. Newport,[125] K. Y. Ng,[14] S. Ng,[56] P. Nguyen,[70] T. T. Nguyen,[24] D. Nichols,[65] A. B. Nielsen,[9] S. Nissanke,[65,13] A. Nitz,[9] F. Nocera,[30] D. Nolting,[6] C. North,[36] L. K. Nuttall,[36] M. Obergaulinger,[23] J. Oberling,[46] B. D. O'Brien,[49] G. D. O'Dea,[112] G. H. Ogin,[150] J. J. Oh,[132] S. H. Oh,[132]

F. Ohme,[9] H. Ohta,[82] M. A. Okada,[15] M. Oliver,[106] P. Oppermann,[9,10] Richard J. Oram,[6] B. O'Reilly,[6] R. Ormiston,[44] L. F. Ortega,[49] R. O'Shaughnessy,[59] S. Ossokine,[38] D. J. Ottaway,[56] H. Overmier,[6] B. J. Owen,[84] A. E. Pace,[88] G. Pagano,[21,22] J. Page,[139] M. A. Page,[64] A. Pai,[119] S. A. Pai,[62] J. R. Palamos,[70] O. Palashov,[129] C. Palomba,[35] A. Pal-Singh,[34] Howard Pan,[89] Huang-Wei Pan,[89] B. Pang,[47] P. T. H. Pang,[96] C. Pankow,[91] F. Pannarale,[36] B. C. Pant,[62] F. Paoletti,[22] A. Paoli,[30] M. A. Papa,[9,20,10] A. Parida,[18] W. Parker,[6] D. Pascucci,[45] A. Pasqualetti,[30] R. Passaquieti,[21,22] D. Passuello,[22] M. Patil,[135] B. Patricelli,[151,22] B. L. Pearlstone,[45] C. Pedersen,[36] M. Pedraza,[1] R. Pedurand,[25,152] L. Pekowsky,[43] A. Pele,[6] S. Penn,[153] A. Perego,[154,58] C. J. Perez,[46] A. Perreca,[113,98] L. M. Perri,[91] H. P. Pfeiffer,[92,38] M. Phelps,[45] K. S. Phukon,[18] O. J. Piccinni,[100,35] M. Pichot,[66] F. Piergiovanni,[72,73] V. Pierro,[8] G. Pillant,[30] L. Pinard,[25] I. M. Pinto,[8] M. Pirello,[46] M. Pitkin,[45] R. Poggiani,[21,22] P. Popolizio,[30] E. K. Porter,[29] L. Possenti,[155,73] A. Post,[9] J. Powell,[156] J. Prasad,[18] J. W. W. Pratt,[37] G. Pratten,[106] V. Predoi,[36] T. Prestegard,[20] M. Principe,[8] S. Privitera,[38] G. A. Prodi,[113,98] L. G. Prokhorov,[63] O. Puncken,[9,10] M. Punturo,[42] P. Puppo,[35] M. Pürrer,[38] H. Qi,[20] V. Quetschke,[108] E. A. Quintero,[1] R. Quitzow-James,[70] F. J. Raab,[46] D. S. Rabeling,[24] H. Radkins,[46] P. Raffai,[54] S. Raja,[62] C. Rajan,[62] B. Rajbhandari,[84] M. Rakhmanov,[108] K. E. Ramirez,[108] A. Ramos-Buades,[106] Javed Rana,[18] P. Rapagnani,[100,35] V. Raymond,[36] M. Razzano,[21,22] J. Read,[28] T. Regimbau,[66,7] L. Rei,[61] S. Reid,[26] D. H. Reitze,[1,49] W. Ren,[11] F. Ricci,[100,35] P. M. Ricker,[11] G. M. Riemenschneider,[147,157] K. Riles,[123] M. Rizzo,[59] N. A. Robertson,[1,45] R. Robie,[45] F. Robinet,[27] T. Robson,[105] A. Rocchi,[33] L. Rolland,[7] J. G. Rollins,[1] V. J. Roma,[70] R. Romano,[3,4] C. L. Romel,[46] J. H. Romie,[6] D. Rosińska,[158,55] M. P. Ross,[159] S. Rowan,[45] A. Rüdiger,[9,10] P. Ruggi,[30] G. Rutins,[160] K. Ryan,[46] S. Sachdev,[1] T. Sadecki,[46] M. Sakellariadou,[161] L. Salconi,[30] M. Saleem,[119] F. Salemi,[9] A. Samajdar,[149,13] L. Sammut,[5] L. M. Sampson,[91] E. J. Sanchez,[1] L. E. Sanchez,[1] N. Sanchis-Gual,[23] V. Sandberg,[46] J. R. Sanders,[43] N. Sarin,[5] B. Sassolas,[25] B. S. Sathyaprakash,[88,36] P. R. Saulson,[43] O. Sauter,[123] R. L. Savage,[46] A. Sawadsky,[34] P. Schale,[70] M. Scheel,[47] J. Scheuer,[91] P. Schmidt,[65] R. Schnabel,[34] R. M. S. Schofield,[70] A. Schönbeck,[34] E. Schreiber,[9,10] D. Schuette,[9,10] B. W. Schulte,[9,10] B. F. Schutz,[36,9] S. G. Schwalbe,[37] J. Scott,[45] S. M. Scott,[24] E. Seidel,[11] D. Sellers,[6] A. S. Sengupta,[162] D. Sentenac,[30] V. Sequino,[32,33,16] A. Sergeev,[129] Y. Setyawati,[9] D. A. Shaddock,[24] T. J. Shaffer,[46] A. A. Shah,[139] M. S. Shahriar,[91] M. B. Shaner,[112] L. Shao,[38] B. Shapiro,[50] P. Shawhan,[76] H. Shen,[11] D. H. Shoemaker,[14] D. M. Shoemaker,[77] K. Siellez,[77] X. Siemens,[20] M. Sieniawska,[55] D. Sigg,[46] A. D. Silva,[15] L. P. Singer,[80] A. Singh,[9,10] A. Singhal,[16,35] A. M. Sintes,[106] B. J. J. Slagmolen,[24] T. J. Slaven-Blair,[64] B. Smith,[6] J. R. Smith,[28] R. J. E. Smith,[5] S. Somala,[163] E. J. Son,[132] B. Sorazu,[45] F. Sorrentino,[61] T. Souradeep,[18] A. P. Spencer,[45] A. K. Srivastava,[110] K. Staats,[37] M. Steinke,[9,10] J. Steinlechner,[34,45] S. Steinlechner,[34] D. Steinmeyer,[9,10] B. Steltner,[9,10] S. P. Stevenson,[156] D. Stocks,[50] R. Stone,[108] D. J. Stops,[60] K. A. Strain,[45] G. Stratta,[72,73] S. E. Strigin,[63] A. Strunk,[46] R. Sturani,[164] A. L. Stuver,[165] T. Z. Summerscales,[166] L. Sun,[99] S. Sunil,[110] J. Suresh,[18] P. J. Sutton,[36] B. L. Swinkels,[13] M. J. Szczepańczyk,[37] M. Tacca,[13] S. C. Tait,[45] C. Talbot,[5] D. Talukder,[70] D. B. Tanner,[49] M. Tápai,[120] A. Taracchini,[38] J. D. Tasson,[95] J. A. Taylor,[139] R. Taylor,[1] S. V. Tewari,[153] T. Theeg,[9,10] F. Thies,[9,10] E. G. Thomas,[60] M. Thomas,[6] P. Thomas,[46] K. A. Thorne,[6] E. Thrane,[5] S. Tiwari,[16,98] V. Tiwari,[36] K. V. Tokmakov,[26] K. Toland,[45] M. Tonelli,[21,22] Z. Tornasi,[45] A. Torres-Forné,[23] C. I. Torrie,[1] D. Töyrä,[60] F. Travasso,[30,42] G. Traylor,[6] J. Trinastic,[49] M. C. Tringali,[113,98] A. Trovato,[29] L. Trozzo,[167,22] K. W. Tsang,[13] M. Tse,[14] R. Tso,[47] D. Tsuna,[82] L. Tsukada,[82] D. Tuyenbayev,[108] K. Ueno,[20] D. Ugolini,[168] A. L. Urban,[1] S. A. Usman,[36] H. Vahlbruch,[9,10] G. Vajente,[1] G. Valdes,[2] N. van Bakel,[13] M. van Beuzekom,[13] J. F. J. van den Brand,[75,13] C. Van Den Broeck,[13,169] D. C. Vander-Hyde,[43] L. van der Schaaf,[13] J. V. van Heijningen,[13] A. A. van Veggel,[45] M. Vardaro,[52,53] V. Varma,[47] S. Vass,[1] M. Vasúth,[48] A. Vecchio,[60] G. Vedovato,[53] J. Veitch,[45] P. J. Veitch,[56] K. Venkateswara,[159] G. Venugopalan,[1] D. Verkindt,[7] F. Vetrano,[72,73] A. Viceré,[72,73] A. D. Viets,[20] S. Vinciguerra,[60] D. J. Vine,[160] J.-Y. Vinet,[66] S. Vitale,[14] T. Vo,[43] H. Vocca,[41,42] C. Vorvick,[46] S. P. Vyatchanin,[63] A. R. Wade,[1] L. E. Wade,[85] M. Wade,[85] R. Walet,[13] M. Walker,[28] L. Wallace,[1] S. Walsh,[20,9] G. Wang,[16,22] H. Wang,[60] J. Z. Wang,[123] W. H. Wang,[108] Y. F. Wang,[96] R. L. Ward,[24] J. Warner,[46] M. Was,[7] J. Watchi,[101] B. Weaver,[46] L.-W. Wei,[9,10] M. Weinert,[9,10] A. J. Weinstein,[1] R. Weiss,[14] F. Wellmann,[9,10] L. Wen,[64] E. K. Wessel,[11] P. Weßels,[9,10] J. Westerweck,[9] K. Wette,[24] J. T. Whelan,[59] B. F. Whiting,[49] C. Whittle,[14] D. Wilken,[9,10] D. Williams,[45] R. D. Williams,[1] A. R. Williamson,[59,65] J. L. Willis,[1,124] B. Willke,[9,10] M. H. Wimmer,[9,10] W. Winkler,[9,10] C. C. Wipf,[1] H. Wittel,[9,10] G. Woan,[45] J. Woehler,[9,10] J. K. Wofford,[59] W. K. Wong,[96] J. Worden,[46] J. L. Wright,[45] D. S. Wu,[9,10] D. M. Wysocki,[59] S. Xiao,[1] W. Yam,[14] H. Yamamoto,[1] C. C. Yancey,[76] L. Yang,[170] M. J. Yap,[24] M. Yazback,[49] Hang Yu,[14] Haocun Yu,[14] M. Yvert,[7] A. Zadrożny,[134] M. Zanolin,[37] T. Zelenova,[30] J.-P. Zendri,[53] M. Zevin,[91] J. Zhang,[64] L. Zhang,[1] M. Zhang,[144] T. Zhang,[45] Y.-H. Zhang,[9,10] C. Zhao,[64] M. Zhou,[91] Z. Zhou,[91] S. J. Zhu,[9,10] X. J. Zhu,[5] A. B. Zimmerman,[92] Y. Zlochower,[59] M. E. Zucker,[1,14] and J. Zweizig[1]

(The LIGO Scientific Collaboration and the Virgo Collaboration)

[1]*LIGO, California Institute of Technology, Pasadena, CA 91125, USA*
[2]*Louisiana State University, Baton Rouge, LA 70803, USA*
[3]*Università di Salerno, Fisciano, I-84084 Salerno, Italy*
[4]*INFN, Sezione di Napoli, Complesso Universitario di Monte S.Angelo, I-80126 Napoli, Italy*
[5]*OzGrav, School of Physics & Astronomy, Monash University, Clayton 3800, Victoria, Australia*
[6]*LIGO Livingston Observatory, Livingston, LA 70754, USA*
[7]*Laboratoire d'Annecy de Physique des Particules (LAPP), Univ. Grenoble Alpes, Université Savoie Mont Blanc, CNRS/IN2P3, F-74941 Annecy, France*
[8]*University of Sannio at Benevento, I-82100 Benevento, Italy and INFN, Sezione di Napoli, I-80100 Napoli, Italy*
[9]*Max Planck Institute for Gravitational Physics (Albert Einstein Institute), D-30167 Hannover, Germany*
[10]*Leibniz Universität Hannover, D-30167 Hannover, Germany*
[11]*NCSA, University of Illinois at Urbana-Champaign, Urbana, IL 61801, USA*
[12]*University of Cambridge, Cambridge CB2 1TN, United Kingdom*
[13]*Nikhef, Science Park 105, 1098 XG Amsterdam, The Netherlands*
[14]*LIGO, Massachusetts Institute of Technology, Cambridge, MA 02139, USA*
[15]*Instituto Nacional de Pesquisas Espaciais, 12227-010 São José dos Campos, São Paulo, Brazil*
[16]*Gran Sasso Science Institute (GSSI), I-67100 L'Aquila, Italy*
[17]*INFN, Laboratori Nazionali del Gran Sasso, I-67100 Assergi, Italy*
[18]*Inter-University Centre for Astronomy and Astrophysics, Pune 411007, India*
[19]*International Centre for Theoretical Sciences, Tata Institute of Fundamental Research, Bengaluru 560089, India*
[20]*University of Wisconsin-Milwaukee, Milwaukee, WI 53201, USA*
[21]*Università di Pisa, I-56127 Pisa, Italy*
[22]*INFN, Sezione di Pisa, I-56127 Pisa, Italy*
[23]*Departamento de Astronomía y Astrofísica, Universitat de València, E-46100 Burjassot, València, Spain*
[24]*OzGrav, Australian National University, Canberra, Australian Capital Territory 0200, Australia*
[25]*Laboratoire des Matériaux Avancés (LMA), CNRS/IN2P3, F-69622 Villeurbanne, France*
[26]*SUPA, University of Strathclyde, Glasgow G1 1XQ, United Kingdom*
[27]*LAL, Univ. Paris-Sud, CNRS/IN2P3, Université Paris-Saclay, F-91898 Orsay, France*
[28]*California State University Fullerton, Fullerton, CA 92831, USA*
[29]*APC, AstroParticule et Cosmologie, Université Paris Diderot, CNRS/IN2P3, CEA/Irfu, Observatoire de Paris, Sorbonne Paris Cité, F-75205 Paris Cedex 13, France*
[30]*European Gravitational Observatory (EGO), I-56021 Cascina, Pisa, Italy*
[31]*Chennai Mathematical Institute, Chennai 603103, India*
[32]*Università di Roma Tor Vergata, I-00133 Roma, Italy*
[33]*INFN, Sezione di Roma Tor Vergata, I-00133 Roma, Italy*
[34]*Universität Hamburg, D-22761 Hamburg, Germany*
[35]*INFN, Sezione di Roma, I-00185 Roma, Italy*
[36]*Cardiff University, Cardiff CF24 3AA, United Kingdom*
[37]*Embry-Riddle Aeronautical University, Prescott, AZ 86301, USA*
[38]*Max Planck Institute for Gravitational Physics (Albert Einstein Institute), D-14476 Potsdam-Golm, Germany*
[39]*Korea Institute of Science and Technology Information, Daejeon 34141, Korea*
[40]*West Virginia University, Morgantown, WV 26506, USA*
[41]*Università di Perugia, I-06123 Perugia, Italy*
[42]*INFN, Sezione di Perugia, I-06123 Perugia, Italy*
[43]*Syracuse University, Syracuse, NY 13244, USA*
[44]*University of Minnesota, Minneapolis, MN 55455, USA*
[45]*SUPA, University of Glasgow, Glasgow G12 8QQ, United Kingdom*
[46]*LIGO Hanford Observatory, Richland, WA 99352, USA*
[47]*Caltech CaRT, Pasadena, CA 91125, USA*
[48]*Wigner RCP, RMKI, H-1121 Budapest, Konkoly Thege Miklós út 29-33, Hungary*
[49]*University of Florida, Gainesville, FL 32611, USA*
[50]*Stanford University, Stanford, CA 94305, USA*
[51]*Università di Camerino, Dipartimento di Fisica, I-62032 Camerino, Italy*
[52]*Università di Padova, Dipartimento di Fisica e Astronomia, I-35131 Padova, Italy*
[53]*INFN, Sezione di Padova, I-35131 Padova, Italy*
[54]*MTA-ELTE Astrophysics Research Group, Institute of Physics, Eötvös University, Budapest 1117, Hungary*
[55]*Nicolaus Copernicus Astronomical Center, Polish Academy of Sciences, 00-716, Warsaw, Poland*
[56]*OzGrav, University of Adelaide, Adelaide, South Australia 5005, Australia*
[57]*Dipartimento di Scienze Matematiche, Fisiche e Informatiche, Università di Parma, I-43124 Parma, Italy*
[58]*INFN, Sezione di Milano Bicocca, Gruppo Collegato di Parma, I-43124 Parma, Italy*

[59]*Rochester Institute of Technology, Rochester, NY 14623, USA*
[60]*University of Birmingham, Birmingham B15 2TT, United Kingdom*
[61]*INFN, Sezione di Genova, I-16146 Genova, Italy*
[62]*RRCAT, Indore, Madhya Pradesh 452013, India*
[63]*Faculty of Physics, Lomonosov Moscow State University, Moscow 119991, Russia*
[64]*OzGrav, University of Western Australia, Crawley, Western Australia 6009, Australia*
[65]*Department of Astrophysics/IMAPP, Radboud University Nijmegen, P.O. Box 9010, 6500 GL Nijmegen, The Netherlands*
[66]*Artemis, Université Côte d'Azur, Observatoire Côte d'Azur, CNRS, CS 34229, F-06304 Nice Cedex 4, France*
[67]*Physik-Institut, University of Zurich, Winterthurerstrasse 190, 8057 Zurich, Switzerland*
[68]*Univ Rennes, CNRS, Institut FOTON - UMR6082, F-3500 Rennes, France*
[69]*Washington State University, Pullman, WA 99164, USA*
[70]*University of Oregon, Eugene, OR 97403, USA*
[71]*Laboratoire Kastler Brossel, Sorbonne Université, CNRS, ENS-Université PSL, Collège de France, F-75005 Paris, France*
[72]*Università degli Studi di Urbino 'Carlo Bo,' I-61029 Urbino, Italy*
[73]*INFN, Sezione di Firenze, I-50019 Sesto Fiorentino, Firenze, Italy*
[74]*Astronomical Observatory Warsaw University, 00-478 Warsaw, Poland*
[75]*VU University Amsterdam, 1081 HV Amsterdam, The Netherlands*
[76]*University of Maryland, College Park, MD 20742, USA*
[77]*School of Physics, Georgia Institute of Technology, Atlanta, GA 30332, USA*
[78]*Université Claude Bernard Lyon 1, F-69622 Villeurbanne, France*
[79]*Università di Napoli 'Federico II,' Complesso Universitario di Monte S.Angelo, I-80126 Napoli, Italy*
[80]*NASA Goddard Space Flight Center, Greenbelt, MD 20771, USA*
[81]*Dipartimento di Fisica, Università degli Studi di Genova, I-16146 Genova, Italy*
[82]*RESCEU, University of Tokyo, Tokyo, 113-0033, Japan.*
[83]*Tsinghua University, Beijing 100084, China*
[84]*Texas Tech University, Lubbock, TX 79409, USA*
[85]*Kenyon College, Gambier, OH 43022, USA*
[86]*The University of Mississippi, University, MS 38677, USA*
[87]*Museo Storico della Fisica e Centro Studi e Ricerche "Enrico Fermi", I-00184 Roma, Italyrico Fermi, I-00184 Roma, Italy*
[88]*The Pennsylvania State University, University Park, PA 16802, USA*
[89]*National Tsing Hua University, Hsinchu City, 30013 Taiwan, Republic of China*
[90]*Charles Sturt University, Wagga Wagga, New South Wales 2678, Australia*
[91]*Center for Interdisciplinary Exploration & Research in Astrophysics (CIERA), Northwestern University, Evanston, IL 60208, USA*
[92]*Canadian Institute for Theoretical Astrophysics, University of Toronto, Toronto, Ontario M5S 3H8, Canada*
[93]*University of Chicago, Chicago, IL 60637, USA*
[94]*Pusan National University, Busan 46241, Korea*
[95]*Carleton College, Northfield, MN 55057, USA*
[96]*The Chinese University of Hong Kong, Shatin, NT, Hong Kong*
[97]*INAF, Osservatorio Astronomico di Padova, I-35122 Padova, Italy*
[98]*INFN, Trento Institute for Fundamental Physics and Applications, I-38123 Povo, Trento, Italy*
[99]*OzGrav, University of Melbourne, Parkville, Victoria 3010, Australia*
[100]*Università di Roma 'La Sapienza,' I-00185 Roma, Italy*
[101]*Université Libre de Bruxelles, Brussels 1050, Belgium*
[102]*Sonoma State University, Rohnert Park, CA 94928, USA*
[103]*Departamento de Matemáticas, Universitat de València, E-46100 Burjassot, València, Spain*
[104]*Columbia University, New York, NY 10027, USA*
[105]*Montana State University, Bozeman, MT 59717, USA*
[106]*Universitat de les Illes Balears, IAC3—IEEC, E-07122 Palma de Mallorca, Spain*
[107]*University of Rhode Island*
[108]*The University of Texas Rio Grande Valley, Brownsville, TX 78520, USA*
[109]*Bellevue College, Bellevue, WA 98007, USA*
[110]*Institute for Plasma Research, Bhat, Gandhinagar 382428, India*
[111]*The University of Sheffield, Sheffield S10 2TN, United Kingdom*
[112]*California State University, Los Angeles, 5151 State University Dr, Los Angeles, CA 90032, USA*
[113]*Università di Trento, Dipartimento di Fisica, I-38123 Povo, Trento, Italy*
[114]*Montclair State University, Montclair, NJ 07043, USA*
[115]*National Astronomical Observatory of Japan, 2-21-1 Osawa, Mitaka, Tokyo 181-8588, Japan*
[116]*Observatori Astronòmic, Universitat de València, E-46980 Paterna, València, Spain*

[117]*School of Mathematics, University of Edinburgh, Edinburgh EH9 3FD, United Kingdom*
[118]*University and Institute of Advanced Research, Koba Institutional Area, Gandhinagar Gujarat 382007, India*
[119]*Indian Institute of Technology Bombay*
[120]*University of Szeged, Dóm tér 9, Szeged 6720, Hungary*
[121]*Tata Institute of Fundamental Research, Mumbai 400005, India*
[122]*INAF, Osservatorio Astronomico di Capodimonte, I-80131, Napoli, Italy*
[123]*University of Michigan, Ann Arbor, MI 48109, USA*
[124]*Abilene Christian University, Abilene, TX 79699, USA*
[125]*American University, Washington, D.C. 20016, USA*
[126]*University of Southampton, Southampton SO17 1BJ, United Kingdom*
[127]*University of Białystok, 15-424 Białystok, Poland*
[128]*University of Washington Bothell, 18115 Campus Way NE, Bothell, WA 98011, USA*
[129]*Institute of Applied Physics, Nizhny Novgorod, 603950, Russia*
[130]*Korea Astronomy and Space Science Institute, Daejeon 34055, Korea*
[131]*Inje University Gimhae, South Gyeongsang 50834, Korea*
[132]*National Institute for Mathematical Sciences, Daejeon 34047, Korea*
[133]*Ulsan National Institute of Science and Technology*
[134]*NCBJ, 05-400 Świerk-Otwock, Poland*
[135]*Institute of Mathematics, Polish Academy of Sciences, 00656 Warsaw, Poland*
[136]*Cornell Universtiy*
[137]*Hillsdale College, Hillsdale, MI 49242, USA*
[138]*Hanyang University, Seoul 04763, Korea*
[139]*NASA Marshall Space Flight Center, Huntsville, AL 35811, USA*
[140]*Dipartimento di Fisica, Università degli Studi Roma Tre, I-00154 Roma, Italy*
[141]*INFN, Sezione di Roma Tre, I-00154 Roma, Italy*
[142]*ESPCI, CNRS, F-75005 Paris, France*
[143]*Southern University and A&M College, Baton Rouge, LA 70813, USA*
[144]*College of William and Mary, Williamsburg, VA 23187, USA*
[145]*Centre Scientifique de Monaco, 8 quai Antoine Ier, MC-98000, Monaco*
[146]*Indian Institute of Technology Madras, Chennai 600036, India*
[147]*INFN Sezione di Torino, Via P. Giuria 1, I-10125 Torino, Italy*
[148]*Institut des Hautes Etudes Scientifiques, F-91440 Bures-sur-Yvette, France*
[149]*IISER-Kolkata, Mohanpur, West Bengal 741252, India*
[150]*Whitman College, 345 Boyer Avenue, Walla Walla, WA 99362 USA*
[151]*Scuola Normale Superiore, Piazza dei Cavalieri 7, I-56126 Pisa, Italy*
[152]*Université de Lyon, F-69361 Lyon, France*
[153]*Hobart and William Smith Colleges, Geneva, NY 14456, USA*
[154]*INFN, Sezione di Milano Bicocca, I-20126, Milano, Italy*
[155]*Università degli Studi di Firenze, I-50121 Firenze, Italy*
[156]*OzGrav, Swinburne University of Technology, Hawthorn VIC 3122, Australia*
[157]*Dipartimento di Fisica, Università di Torino, Via P. Giuria 1, I-10125 Torino, Italy*
[158]*Janusz Gil Institute of Astronomy, University of Zielona Góra, 65-265 Zielona Góra, Poland*
[159]*University of Washington, Seattle, WA 98195, USA*
[160]*SUPA, University of the West of Scotland, Paisley PA1 2BE, United Kingdom*
[161]*King's College London, University of London, London WC2R 2LS, United Kingdom*
[162]*Indian Institute of Technology, Gandhinagar Ahmedabad Gujarat 382424, India*
[163]*Indian Institute of Technology Hyderabad, Sangareddy, Khandi, Telangana 502285, India*
[164]*International Institute of Physics, Universidade Federal do Rio Grande do Norte, Natal RN 59078-970, Brazil*
[165]*Villanova University, 800 Lancaster Ave, Villanova, PA 19085, USA*
[166]*Andrews University, Berrien Springs, MI 49104, USA*
[167]*Università di Siena, I-53100 Siena, Italy*
[168]*Trinity University, San Antonio, TX 78212, USA*
[169]*Van Swinderen Institute for Particle Physics and Gravity,*
University of Groningen, Nijenborgh 4, 9747 AG Groningen, The Netherlands
[170]*Colorado State University, Fort Collins, CO 80523, USA*

This is the accepted manuscript made available via CHORUS. The article has been published as:

Tidal Deformabilities and Radii of Neutron Stars from the Observation of GW170817

Soumi De, Daniel Finstad, James M. Lattimer, Duncan A. Brown, Edo Berger, and Christopher M. Biwer

Phys. Rev. Lett. **121**, 091102 — Published 29 August 2018

DOI: 10.1103/PhysRevLett.121.091102

Tidal Deformabilities and Radii of Neutron Stars from the Observation of GW170817

Soumi De[1], Daniel Finstad[1], James M. Lattimer[2], Duncan A. Brown[1], Edo Berger[3], and Christopher M. Biwer[1,4]
[1] *Department of Physics, Syracuse University, Syracuse, NY 13244, USA*
[2] *Department of Physics and Astronomy, Stony Brook University, Stony Brook, NY 11794-3800, USA*
[3] *Harvard-Smithsonian Center for Astrophysics, 60 Garden Street, Cambridge, Massachusetts 02139, USA and*
[4] *Applied Computer Science (CCS-7), Los Alamos National Laboratory, Los Alamos, NM, 87545, USA*

We use gravitational-wave observations of the binary neutron star merger GW170817 to explore the tidal deformabilities and radii of neutron stars. We perform Bayesian parameter estimation with the source location and distance informed by electromagnetic observations. We also assume that the two stars have the same equation of state; we demonstrate that for stars with masses comparable to the component masses of GW170817, this is effectively implemented by assuming that the stars' dimensionless tidal deformabilities are determined by the binary's mass ratio q by $\Lambda_1/\Lambda_2 = q^6$. We investigate different choices of prior on the component masses of the neutron stars. We find that the tidal deformability and 90% credible interval is $\tilde{\Lambda} = 222^{+420}_{-138}$ for a uniform component mass prior, $\tilde{\Lambda} = 245^{+453}_{-151}$ for a component mass prior informed by radio observations of Galactic double neutron stars, and $\tilde{\Lambda} = 233^{+448}_{-144}$ for a component mass prior informed by radio pulsars. We find a robust measurement of the common areal radius of the neutron stars across all mass priors of $8.9 \leq \hat{R} \leq 13.2$ km, with a mean value of $\langle \hat{R} \rangle = 10.8$ km. Our results are the first measurement of tidal deformability with a physical constraint on the star's equation of state and place the first lower bounds on the deformability and areal radii of neutron stars using gravitational waves.

PACS numbers: 95.85.Sz, 26.60.Kp, 97.80.-d

Introduction—On August 17, 2017 LIGO and Virgo observed gravitational waves from a binary neutron star coalescence, GW170817 [1]. This observation can be used to explore the equation of state (EOS) of matter at supernuclear densities [2, 3]. This information is encoded as a change in gravitational-wave phase evolution caused by the tidal deformation of the neutron stars [4]. At leading order, the tidal effects are imprinted in the gravitational-wave signal through the binary tidal deformability [4, 5]

$$\tilde{\Lambda} = \frac{16}{13}\frac{(12q+1)\Lambda_1 + (12+q)q^4\Lambda_2}{(1+q)^5}, \qquad (1)$$

where $q = m_2/m_1 \leq 1$ is the binary's mass ratio (c.f. Eq. (34) of Ref. [6]). The deformability of each star is

$$\Lambda_{1,2} = \frac{2}{3}k_2\left(\frac{R_{1,2}c^2}{Gm_{1,2}}\right)^5, \qquad (2)$$

where k_2 is the tidal Love number [4, 5], which depends on the star's mass and the EOS. $R_{1,2}$ and $m_{1,2}$ are the areal radii and masses of the neutron stars, respectively.

In the results of Ref. [1], the priors on $\Lambda_{1,2}$ are taken to be completely uncorrelated, which is equivalent to assuming that each star may have a different EOS. Here, we re-analyze the gravitational-wave data using Bayesian inference [7-9] to measure the tidal deformability, using a correlation between Λ_1 and Λ_2 which follows from the assumption that both stars have the same EOS. We repeat our analysis without the common EOS constraint and calculate the Bayes factor that compares the evidences for these two models. We also fix the sky position and distance from electromagnetic observations [10, 11]. We study the effect of the prior for the component masses by performing analyses with three different priors: the first is uniform between 1 and $2M_\odot$, the second is informed by radio observations of double neutron star binaries, and the third is informed by the masses of isolated pulsars [12].

The common equation of state constraint—To explore imposing a common EOS constraint, we employ a piecewise polytrope scheme [13] to simulate thousands of equations of state. Each EOS obeys causality, connects at low densities to the well-known EOS of neutron star crusts [14], is constrained by experimental and theoretical studies of the symmetry properties of matter near the nuclear saturation density, and satisfies the observational constraint for the maximum mass of a neutron star, $m_{\rm max} \geq 2M_\odot$ [15]. Fig. 1 shows the results of Tolman-Oppenheimer-Volkoff (TOV) integrations [16, 17] to determine Λ as functions of m, R, and the EOS. Each configuration is color-coded according to its radius. In the relevant mass range, Λ generally varies as m^{-6}. For a given mass m, there is an inherent spread of about a factor ten in Λ, which is correlated with R^6. We find that the star's tidal deformability is related to its compactness parameter $\beta = Gm/(Rc^2)$ by the relation $\Lambda \simeq a\beta^{-6}$. We find that $a = 0.0093 \pm 0.0007$ bounds this relation if $1.1M_\odot \leq m \leq 1.6M_\odot$ (note that this is a bound, not a confidence interval). The additional power of β^{-1} in the $\Lambda-\beta$ relation, relative to β^{-5} in Eq. (2), originates because the dimensionless tidal Love number, k_2, varies roughly as β^{-1} for masses $\geq 1M_\odot$, although this is not the case for all masses [17]. For $m \to 0$ we see that $k_2 \to 0$ so that k_2 is proportional to β with a positive power, but since neutron stars with $m < 1\,M_\odot$ are physically unrealistic, that domain is not pertinent in our study.

We observed that, for nearly every specific EOS, the range of stellar radii in the mass range of interest for

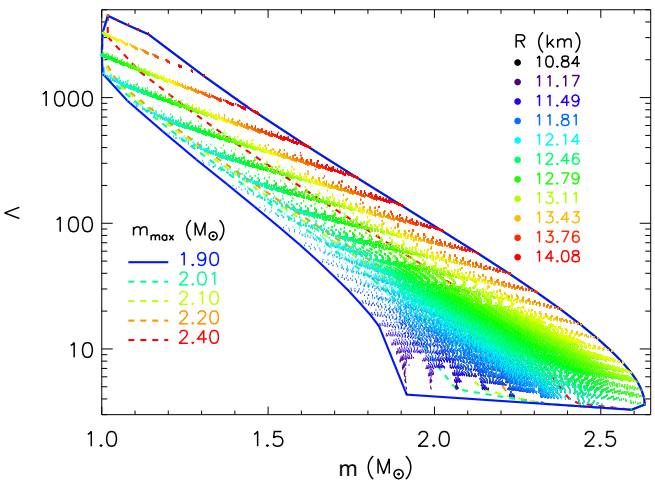

FIG. 1. The tidal deformability Λ as a function of mass for physically realistic polytropes. A TOV integration with each EOS parameter set results in a series of values of $\Lambda(m)$ that are shown as points colored by their radii R. Dashed curves are lower bounds to Λ for a given mass m which vary depending on the assumed lower limit to the neutron star maximum mass, $m_{\rm max}$. All values of $m_{\rm max}$ produce the same upper bound.

GW170817 is typically small. As long as $m_{\rm max} \geq 2M_\odot$, the piecewise polytrope study reveals $\langle \Delta R \rangle = -0.070$ km and $\sqrt{\langle (\Delta R)^2 \rangle} = 0.11$ km, where $\Delta R \equiv R_{1.6} - R_{1.1}$ with $R_{1.1,1.6}$ the radii of stars with $m = 1.1M_\odot$ and $m = 1.6M_\odot$, respectively. Therefore, for masses relevant for GW170817, each EOS assigns a common value of $\hat{R}$ to stellar radii with little sensitivity to the mass. We can combine the relations $\Lambda \simeq a\beta^{-6}$ and $R_1 = R_2$ to find the simple prescription $\Lambda_1 = q^6 \Lambda_2$. We impose the common EOS constraint in our analysis using this relation. The exponent of q changes with chirp mass $\mathcal{M}$ and for $\mathcal{M} > 1.5\,M_\odot$ this relation has to be modified. However, this is not relevant for the study of GW170817.

Implications for the neutron star radius—The common EOS constraint allows us to show that the binary tidal deformability $\tilde{\Lambda}$ is essentially a function of the chirp mass $\mathcal{M}$, the common radius $\hat{R}$, and the mass ratio q, but that its dependence on q is very weak. Substituting the expressions $\Lambda \simeq a\beta^{-6}$ and $R = \hat{R}$ into Eq. (1), we find

$$\tilde{\Lambda} = \frac{16a}{13}\left(\frac{\hat{R}c^2}{G\mathcal{M}}\right)^6 f(q). \tag{3}$$

where $f(q)$ is very weakly dependent on q:

$$f(q) = q^{8/5}(12 - 11q + 12q^2)(1+q)^{-26/5}. \tag{4}$$

For example, if we compare a binary with $q = 0.75$ to an equal mass binary, we find $f(0.75)/f(1) = 1.021$. As long as $q \geq 0.6$, valid for $1M_\odot \leq m \leq 1.6M_\odot$ for both stars, we infer from Eq. (3),

$$\tilde{\Lambda} = a'\left(\frac{\hat{R}c^2}{G\mathcal{M}}\right)^6, \tag{5}$$

where $a' = 0.0042 \pm 0.0004$. The supplemental material [56] shows TOV integrations for a range of EOS that validate this relationship. For stars with masses comparable to GW170817, the common radius $\hat{R}$ can be found from the inversion of Eq. (5),

$$\hat{R} \simeq R_{1.4} \simeq (11.2 \pm 0.2)\frac{\mathcal{M}}{M_\odot}\left(\frac{\tilde{\Lambda}}{800}\right)^{1/6} \text{ km}. \tag{6}$$

The quoted errors originate from the uncertainties in a and q, and amount in total to 2%.

Parameter Estimation Methods— We use Bayesian inference to measure the parameters of GW170817 [18]. We calculate the posterior probability density function, $p(\vec{\theta}|\vec{d}(t), H)$, for the set of parameters $\vec{\theta}$ for the gravitational-waveform model, H, given the LIGO Hanford, LIGO Livingston, and Virgo data $\vec{d}(t)$ [19, 20]

$$p(\vec{\theta}|\vec{d}(t), H) = \frac{p(\vec{\theta}|H)p(\vec{d}(t)|\vec{\theta}, H)}{p(\vec{d}(t)|H)}. \tag{7}$$

The prior, $p(\vec{\theta}|H)$, is the set of assumed probability distributions for the waveform parameters. The likelihood $p(\vec{d}(t)|\vec{\theta}, H)$ assumes a Gaussian model for the detector noise [21]. Marginalization of the likelihood to obtain the posterior probabilities is performed using Markov Chain Monte Carlo (MCMC) techniques using the *PyCBC Inference* software [7, 8] and the parallel-tempered *emcee* sampler [9, 22, 23]. We fix the sky location and distance to GW170817 [10, 11] and calculate the posterior probabilities for the remaining source parameters. Following Ref. [1], the waveform model H is the restricted TaylorF2 post-Newtonian aligned-spin model [24–29]. Technical details of our parameter estimation and a comparison to Fig. 5 of Ref [1] are provided as supplemental material [56].

To implement the common EOS constraint we construct the priors on $\Lambda_{1,2}$ according to

$$\Lambda_1 = q^3\Lambda_s, \qquad \Lambda_2 = q^{-3}\Lambda_s, \tag{8}$$

where $\Lambda_s \sim U[0, 5000]$. We discard draws with $\tilde{\Lambda} > 5000$, since these values are beyond the range of all plausible EOS. The resulting prior on $\tilde{\Lambda}$ is uniform between 0 and 5000. We also perform analyses that do not assume the common EOS constraint where we allow completely uncorrelated priors for $\Lambda_{1,2}$. This allows us to compare the evidences between these hypotheses. For the uncorrelated $\Lambda_{1,2}$ analyses, the prior for $\Lambda_1 \sim U[0, 1000]$ and $\Lambda_2 \sim U[0, 5000]$ with these intervals set by the range of plausible equations of state in the mass range of interest, our convention of $m_1 \geq m_2$, and discarding draws with $\tilde{\Lambda} > 5000$.

The choice of mass prior can have an impact on the recovery of the tidal deformability [30]. To investigate this, we carry out our parameter estimation analyses using three different priors on the binary's component masses. We first

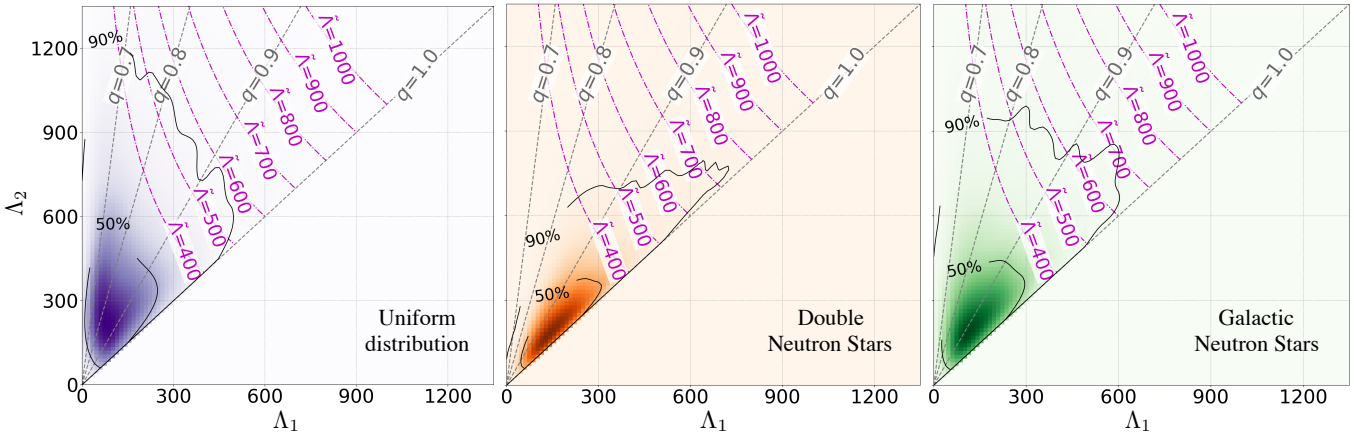

FIG. 2. Posterior probability densities for $\Lambda_{1,2}$ with the common EOS constraint using Uniform (left), Double Neutron Stars (middle), and Galactic Neutron Stars (right) component mass priors. The 50% and 90% credible region contours are shown as solid curves. Overlaid are contours of $\tilde{\Lambda}$ (in magenta) and q (in gray). The values of Λ_1 and Λ_2 forbidden by causality have been excluded from the posteriors.

assume a uniform prior on each star's mass, with $m_{1,2} \sim U[1,2]\,M_\odot$. We then assume a Gaussian prior on the component masses $m_{1,2} \sim N(\mu = 1.33, \sigma = 0.09)\,M_\odot$, which is a fit to masses of neutron stars observed in double neutron star systems [12]. The third prior assumes that the component masses are drawn from a fit to the observed mass distributions of recycled and slow pulsars in the Galaxy with $m_1 \sim N(\mu = 1.54, \sigma = 0.23)\,M_\odot$ and $m_2 \sim N(\mu = 1.49, \sigma = 0.19)\,M_\odot$ [12]. We impose the constraint $m_1 \geq m_2$ which leads to $\Lambda_2 \geq \Lambda_1$. For all our analyses, the prior on the component spins is $\chi_{1,2} \sim U[-0.05, 0.05]$, consistent with the expected spins of field binaries when they enter the LIGO-Virgo sensitive band [31].

Results—We perform parameter estimation for each mass prior with and without the common EOS constraint and calculate the Bayes factor—the ratio of the evidences $p(\vec{d}(t)|H)$—between the common EOS constrained and unconstrained analyses. We find Bayes factors $\mathcal{B}$ of 369, 125, and 612 for the three mass priors, respectively, indicating that the data strongly favors the common EOS constraint in all cases. The full posterior probability densities of the parameters $p(\vec{\theta}|\vec{d}(t), H)$ for the common EOS runs are shown in the supplemental material [56] and are available for download at Ref. [32]. Fig. 2 shows the posterior probability densities for Λ_1 and Λ_2 with 90% and 50% credible region contours. Overlaid are q contours and $\tilde{\Lambda}$ contours obtained from Eq. (1), $\Lambda \simeq a\beta^{-6}$, and $R_1 \simeq R_2 \simeq \hat{R}$ as

$$\Lambda_1(\tilde{\Lambda}, q) = \frac{13}{16}\tilde{\Lambda}\frac{q^2(1+q)^4}{12q^2 - 11q + 12}, \quad \Lambda_2(\tilde{\Lambda}, q) = q^{-6}\Lambda_1 \tag{9}$$

Due to our constraint $\Lambda_2 \geq \Lambda_1$, our credible contours are confined to the region where $q \leq 1$. One can easily demonstrate that $\Lambda_2 \geq \Lambda_1$ is valid unless $(c^2/G)dR/dm > 1$, which is impossible for realistic equations of state. For the entire set of piecewise polytropes satisfying $m_{\max} > 2M_\odot$ we considered, $(c^2/G)dR/dm$ never exceeded 0.26. Even if a first order phase transition appeared in stars with masses between m_2 and m_1, it would be necessarily true that $dR/dm < 0$ across the transition. Due to the q dependence of Λ_1, Λ_2, the credible region enclosed by the contours broadens from the double neutron star (most restricted), to the pulsar, to the uniform mass (least restricted) priors. However, the upper bound of the credible region is robust.

We find $\tilde{\Lambda} = 205^{+415}_{-167}$ for the uniform component mass prior, $\tilde{\Lambda} = 234^{+452}_{-180}$ for the prior informed by double neutron star binaries in the Galaxy, and $\tilde{\Lambda} = 218^{+445}_{-173}$ for the prior informed by all Galactic neutron star masses (errors represent 90% credible intervals). Our measurement of $\tilde{\Lambda}$ appears to be robust to the choice of component mass prior, within the (relatively large) statistical errors on its measurement. The Bayes factors comparing the evidence from the three mass priors are of order unity, so we cannot claim any preference between the mass priors.

The 90% credible intervals on $\tilde{\Lambda}$ obtained from the gravitational-wave observations include regions forbidden by causality. Applying a constraint to our posteriors for the causal lower limit of Λ as a function of m [55], we obtain $\tilde{\Lambda} = 222^{+420}_{-138}$ for the uniform component mass prior, $\tilde{\Lambda} = 245^{+453}_{-151}$ for the prior informed by double neutron star binaries in the Galaxy, and $\tilde{\Lambda} = 233^{+448}_{-144}$ for the prior informed by all Galactic neutron star masses (errors represent 90% credible intervals). Using Eq. 6, we map our $\mathcal{M}$ posteriors and $\tilde{\Lambda}$ posteriors (with the causal lower limit applied) to $\hat{R} \simeq R_{1.4}$ posteriors, allowing us to estimate the common radius of the neutron stars for GW170817 for each mass prior. Fig. 3 shows the posterior probability distribution for the binary tidal deformation $\tilde{\Lambda}$ and the common radius $\hat{R}$ of the neutron stars in the binary. Our results

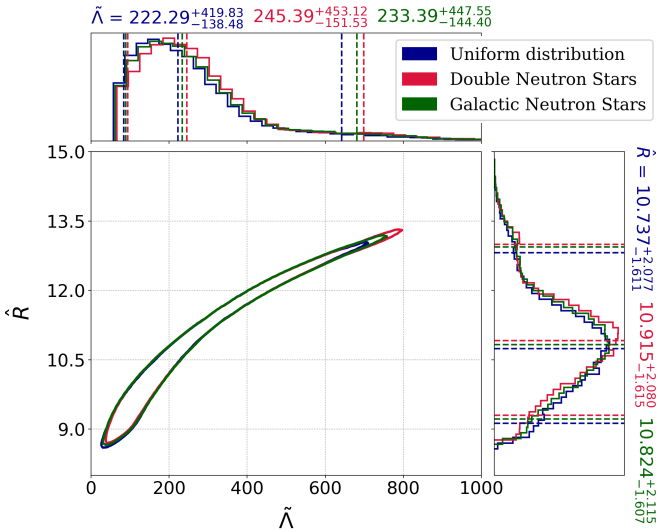

FIG. 3. The 90% credible region of the posterior probability for the common radius $\hat{R}$ and binary tidal deformability $\tilde{\Lambda}$ with the common EOS constraint for the three mass priors. The posteriors for the individual parameters are shown with dotted lines at the 5%, 50% and 95% percentiles. The values of $\tilde{\Lambda}$, and hence $\hat{R}$ forbidden by causality have been excluded from the posteriors.

suggest a radius $\hat{R} = 10.7^{+2.1}_{-1.6} \pm 0.2$ km (90% credible interval, statistical and systematic errors) for the uniform mass prior, $\hat{R} = 10.9^{+2.1}_{-1.6} \pm 0.2$ km for double neutron star mass prior, and $\hat{R} = 10.8^{+2.1}_{-1.6} \pm 0.2$ km for the prior based on all neutron star masses.

For the uniform mass prior, we computed the Bayes factor comparing a model with a prior $\Lambda_s \sim U[0, 5000]$ to a model with a prior $\Lambda_s \sim U[0, 100]$. We find $\log_{10}(\mathcal{B}) \sim 1$, suggesting that the data favors a model that includes measurement of tidal deformability $\tilde{\Lambda} \gtrsim 100$. However, the evidences were calculated using thermodynamic integration of the MCMC chains [9]. We will investigate model selection using e.g. nested sampling [33] in a future work.

Finally, we note the post-Newtonian waveform family used will result in systematic errors in our measurement of the tidal deformability [34, 35]. However, this waveform family allows a direct comparison to the results of Ref. [1]. Accurate modeling of the waveform is challenging, as the errors in numerical simulations are comparable to the size of the matter effects that we are trying to measure [36]. Waveform systematics and comparison of other waveform models (e.g. [37]) will be investigated in a future work.

Discussion—Using Bayesian parameter estimation we have measured the tidal deformability and common radius of the neutron stars in GW170817. Table I summarizes our findings. To compare to Ref. [1], which reports a 90% upper limit on $\tilde{\Lambda} \leq 800$ under the assumption of a uniform prior on $\tilde{\Lambda}$, we integrate the posterior for $\tilde{\Lambda}$ to obtain 90% upper limits on $\tilde{\Lambda}$. For the common EOS analyses these are 485, 521, and 516 for the uniform, double neutron star, and Galactic neutron star component mass priors, respectively.

Mass prior	$\tilde{\Lambda}$	$\hat{R}$ (km)	$\mathcal{B}$	$\tilde{\Lambda}_{90\%}$
Uniform	222^{+420}_{-138}	$10.7^{+2.1}_{-1.6} \pm 0.2$	369	< 485
Double neutron star	245^{+453}_{-151}	$10.9^{+2.1}_{-1.6} \pm 0.2$	125	< 521
Galactic neutron star	233^{+448}_{-144}	$10.8^{+2.1}_{-1.6} \pm 0.2$	612	< 516

TABLE I. Results from parameter estimation analyses using three different mass prior choices with the common EOS constraint, and applying the causal minimum constraint to $\Lambda(m)$. We show 90% credible intervals for $\tilde{\Lambda}$, 90% credible intervals and systematic errors for $\hat{R}$, Bayes factors $\mathcal{B}$ comparing our common EOS to the unconstrained results, and the 90% upper limits on $\tilde{\Lambda}$.

We find that in comparison to the unconstrained analysis, the common EOS assumption significantly reduces the median value and 90% confidence upper bound of $\tilde{\Lambda}$ by about 28% and 19% respectively for all three mass priors. The difference between our common EOS results for the three mass priors is consistent with the physics of the gravitational waveform. At constant $\mathcal{M}$, decreasing q causes the binary to inspiral more quickly [38]. At constant $\mathcal{M}$ and constant q, increasing $\tilde{\Lambda}$ also causes the binary to inspiral more quickly, so there is a mild degeneracy between q and $\tilde{\Lambda}$. The uniform mass prior allows the largest range of mass ratios, so we can fit the data with a larger q and smaller $\tilde{\Lambda}$. The double neutron star mass prior allows the smallest range of mass ratios and so a larger $\tilde{\Lambda}$ is required to fit the data, with the Galactic neutron star mass prior lying between these two cases.

Nevertheless, considering all analyses we performed with different mass prior choices, we find a relatively robust measurement of the common neutron star radius with a mean value $\langle \hat{R} \rangle$ = 10.8 km bounded above by $\hat{R} <$ 13.2 km and below by $\hat{R} >$ 8.9 km. Nuclear theory and experiment currently predict a somewhat smaller range by 2 km, but with approximately the same centroid as our results [14, 39]. A minimum radius 10.5–11 km is strongly supported by neutron matter theory [40–42], the unitary gas [43], and most nuclear experiments [14, 39, 44]. The only major nuclear experiment that could indicate radii much larger than 13 km is the PREX neutron skin measurement, but this has published error bars much larger than previous analyses based on anti-proton data, charge radii of mirror nuclei, and dipole resonances. Our results are consistent with photospheric radius expansion measurements of X-ray binaries which obtain $R \approx$ 10–12 km [12, 45, 46]. Ref. [47] found from an analysis of 5 neutron stars in quiescent low-mass X-ray binaries a common neutron star radius 9.4 ± 1.2 km, but systematic effects including uncertainties in interstellar absorption and the neutron stars' atmospheric compositions are large. Other analyses have inferred 12 ± 0.7 km [48] and 12.3 ± 1.8 km [49] for the radii of $1.4 M_\odot$ quiescent sources.

We have found that the relation $q^{7.48} < \Lambda_1/\Lambda_2 < q^{5.76}$ in fact completely bounds the uncertainty for the range of $\mathcal{M}$ relevant to GW170817, assuming $m_2 > 1 M_\odot$ [55]

and that no strong first-order phase transitions occur near the nuclear saturation density (i.e., the case in which m_1 is a hybrid star and m_2 is not). Analyses using this prescription instead of the q^6 correlation produce insignificant differences in our results [54]. Since models with the common EOS assumption are highly favored over those without this assumption, our results support the absence of a strong first-order phase transition in this mass range.

In this *letter*, we have shown that for binary neutron star mergers consistent with observed double neutron star systems [50], assuming a common EOS implies that $\Lambda_1/\Lambda_2 \simeq q^6$. We find evidence from GW170817 that favors the common EOS interpretation compared to uncorrelated deformabilities. Although previous studies have suggested that measurement of the tidal deformability is sensitive to the choice of mass prior [30], we find that varying the mass priors does not significantly influence our conclusions suggesting that our results are robust to the choice of mass prior. Our results support the conclusion that we find the first evidence for finite size effects using gravitational-wave observations.

After our *letter* was submitted, the LIGO/Virgo collaborations have placed new constraints on the radii of the neutron stars using GW170817 [51]. The most direct comparison is between our uniform mass prior result ($\hat{R} = 10.7^{+2.1}_{-1.6} \pm 0.2$) and the LIGO/Virgo method that uses equation-of-state-insensitive relations [52, 53] ($R_1 = 10.8^{+2.0}_{-1.7}$ km and $R_2 = 10.7^{+2.1}_{-1.5}$ km). This result validates our approximation $R_1 = R_2$ used to motivate the prescription $\Lambda_1 = q^6\Lambda_2$, and Eqs. 3, 5. Our statistical errors are comparable to the error reported by LIGO/Virgo. Systematic errors from EOS physics of ± 0.2 km are added as conservative bounds to our statistical errors, broadening our measurement error, whereas Ref. [51] marginalized over these errors in the analysis. Ref. [51] also investigates a method of directly measuring the parameters of the EOS which results in smaller measurement errors. Investigation of these differences between our analysis and the latter approach will be pursued in a future paper.

Observations of future binary neutron star mergers will allow further constraints to be placed on the deformability and radius, especially if these binaries have chirp masses similar to GW170817 as radio observations suggest. As more observations improve our knowledge of the neutron star mass distribution, more precise mass–deformability correlations can be used to further constrain the star's radius.

Acknowledgements—We thank Stefan Ballmer, Swetha Bhagwat, Steven Reyes, Andrew Steiner, and Douglas Swesty for helpful discussions. We particularly thank Collin Capano and Alexander Nitz for contributing to the development of PyCBC Inference. This work was supported by NSF awards PHY-1404395 (DAB, CMB), PHY-1707954 (DAB, SD), PHY-1607169 (SD), AST-1559694 (DF), AST-1714498 (EB), and DOE Award DE-FG02-87ER40317 (JML). Computations were supported by Syracuse University and NSF award OAC-1541396. DAB, EB, SD, and JML thank Kavli Institute for Theoretical Physics which is supported by the NSF award PHY-1748958. The gravitational-wave data used in this work was obtained from the LIGO Open Science Center.

[1] B. Abbott *et al.*, Phys. Rev. Lett. **119**, 161101 (2017).
[2] K. S. Thorne, in *Three hundred years of gravitation*, edited by S. W. Hawking and W. Israel (Cambridge University Press, Cambridge, 1987) Chap. 9, pp. 330–458.
[3] J. S. Read *et al.*, Phys. Rev. **D79**, 124033 (2009).
[4] E. E. Flanagan and T. Hinderer, Phys. Rev. **D77**, 021502 (2008).
[5] T. Hinderer, Astrophys. J. **677**, 1216 (2008).
[6] S. E. Gralla, Class. Quant. Grav. **35**, 085002 (2018).
[7] C. M. Biwer, C. D. Capano, S. De, M. Cabero, D. A. Brown, A. H. Nitz, and V. Raymond, (2018), arXiv:1807.10312 [astro-ph.IM].
[8] A. Nitz *et al.*, *PyCBC v1.9.4* (2018).
[9] D. Foreman-Mackey *et al.*, PASP **125**, 306 (2013).
[10] M. Soares-Santos *et al.*, Astrophys. J. **848**, L16 (2017).
[11] M. Cantiello *et al.*, Astrophys. J. **854**, L31 (2018).
[12] F. Özel and P. Freire, Ann. Rev. Astron. Astrophys. **54**, 401 (2016).
[13] J. M. Lattimer and M. Prakash, Phys. Rept. **621**, 127 (2016).
[14] J. M. Lattimer, Ann. Rev. Nucl. Part. Sci. **62**, 485 (2012).
[15] J. Antoniadis *et al.*, Science **340**, 6131 (2013).
[16] J. R. Oppenheimer and G. M. Volkoff, Phys. Rev. **55**, 374 (1939).
[17] S. Postnikov, M. Prakash, and J. M. Lattimer, Phys. Rev. **D82**, 024016 (2010).
[18] N. Christensen and R. Meyer, Phys. Rev. **D64**, 022001 (2001).
[19] M. Vallisneri *et al.*, J. Phys. Conf. Ser. **610**, 012021 (2015).
[20] K. Blackburn *et al.*, *LOSC CLN Data Products for GW170817* (2017).
[21] C. Rover *et al.*, Phys. Rev. **D75**, 062004 (2007).
[22] W. D. Vousden, W. M. Farr, and I. Mandel, Monthly Notices of the Royal Astronomical Society **455**, 1919 (2016).
[23] W. J. Goodman J., Commun. Appl. Math. Comput. Sci. **5**, 65 (2010).
[24] B. S. Sathyaprakash and S. V. Dhurandhar, Phys. Rev. **D44**, 3819 (1991).
[25] A. Buonanno *et al.*, Phys. Rev. **D80**, 084043 (2009).
[26] K. G. Arun *et al.*, Phys. Rev. **D79**, 104023 (2009), [Erratum: Phys. Rev.D84,049901(2011)].
[27] B. Mikoczi, M. Vasuth, and L. A. Gergely, Phys. Rev. **D71**, 124043 (2005).
[28] A. Bohe, S. Marsat, and L. Blanchet, Class. Quant. Grav. **30**, 135009 (2013).
[29] J. Vines, E. E. Flanagan, and T. Hinderer, Phys. Rev. **D83**, 084051 (2011).
[30] M. Agathos *et al.*, Phys. Rev. **D92**, 023012 (2015).
[31] D. A. Brown *et al.*, Phys. Rev. **D86**, 084017 (2012).
[32] S. De *et al.*, *SUGWG GitHub Repository* (2018).
[33] J. Skilling, Bayesian Anal. **1**, 833 (2006).
[34] L. Wade *et al.*, Phys. Rev. **D89**, 103012 (2014).

[35] B. D. Lackey and L. Wade, Phys. Rev. **D91**, 043002 (2015).
[36] K. Barkett *et al.*, Phys. Rev. **D93**, 044064 (2016).
[37] S. Bernuzzi *et al.*, Phys. Rev. Lett. **114**, 161103 (2015).
[38] M. Hannam *et al.*, Astrophys. J. **766**, L14 (2013).
[39] J. M. Lattimer and Y. Lim, Astrophys. J. **771**, 51 (2013).
[40] S. Gandolfi, J. Carlson, and S. Reddy, Phys. Rev. **C85**, 032801 (2012).
[41] J. E. Lynn *et al.*, Phys. Rev. Lett. **116**, 062501 (2016).
[42] C. Drischler, K. Hebeler, and A. Schwenk, Phys. Rev. **C93**, 054314 (2016).
[43] I. Tews, J. M. Lattimer, A. Ohnishi, and E. E. Kolomeitsev, Astrophys. J. **848**, 105 (2017).
[44] I. Tews, T. Krger, K. Hebeler, and A. Schwenk, Phys. Rev. Lett. **110**, 032504 (2013).
[45] A. W. Steiner, J. M. Lattimer, and E. F. Brown, Astrophys. J. **722**, 33 (2010).
[46] N. Degenaar and V. F. Suleimanov, (2018), arXiv:1806.02833 [astro-ph.HE].
[47] S. Guillot and R. E. Rutledge, Astrophys. J. **796**, L3 (2014).
[48] J. M. Lattimer and A. W. Steiner, Astrophys. J. **784**, 123 (2014).
[49] A. W. Shaw *et al.*, (2018), 10.1093/mnras/sty582.
[50] T. M. Tauris *et al.*, Astrophys. J. **846**, 170 (2017).
[51] B. P. Abbott *et al.* (Virgo, LIGO Scientific), (2018), arXiv:1805.11581 [gr-qc].
[52] K. Yagi and N. Yunes, Class. Quant. Grav. **34**, 015006 (2017).
[53] K. Chatziioannou, C.-J. Haster, and A. Zimmerman, Phys. Rev. **D97**, 104036 (2018).
[54] S. De *et al.*, (in preparation) .
[55] T. Zhao and J. M. Lattimer, (In preparation) .
[56] See Supplemental Material for descriptions supporting our implementation of the common radius and causal constraints, technical details of the parameter estimation analysis, full posterior distributions from the common EOS runs, and comparison of results to Ref [1]. The Supplemental Material includes Refs. [57–63] in addition to some of the references included in this letter.
[57] J. Driggers, S. Vitale, A. Lundgren, M. Evans, K. Kawabe, S. Dwyer, K. Izumi, and P. Fritschel, "Offline noise subtraction for Advanced LIGO," (2017), https://dcc.ligo.org/LIGO-P1700260/public.
[58] P. Welch, IEEE Transactions on Audio and Electroacoustics **15**, 70 (1967).
[59] B. Allen, W. G. Anderson, P. R. Brady, D. A. Brown, and J. D. E. Creighton, Phys. Rev. **D85**, 122006 (2012).
[60] T. Damour, A. Nagar, and L. Villain, Phys. Rev. **D85**, 123007 (2012).
[61] T. B. Littenberg and N. J. Cornish, Phys. Rev. **D91**, 084034 (2015).
[62] R. A. Mercer *et al.*, "LIGO Algorithm Library," (2017), https://git.ligo.org/lscsoft/lalsuite.
[63] F. Pérez and B. E. Granger, Computing in Science and Engineering **9**, 21 (2007).

Constraint on the maximum mass of neutron stars using GW170817 event

Masaru Shibata,[1,2] Enping Zhou,[1] Kenta Kiuchi,[1,2] and Sho Fujibayashi[1]

[1] *Max Planck Institute for Gravitational Physics (Albert Einstein Institute), Am Muhlenberg 1, Potsdam-Golm 14476, Germany*

[2] *Yukawa Institute for Theoretical Physics, Kyoto University, Kyoto, 606-8502, Japan*

(Dated: June 25, 2019)

We revisit the constraint on the maximum mass of cold spherical neutron stars coming from the observational results of GW170817. We develop a new framework for the analysis by employing both energy and angular momentum conservation laws as well as solid results of latest numerical-relativity simulations and of neutron stars in equilibrium. The new analysis shows that the maximum mass of cold spherical neutron stars can be only weakly constrained as $M_{\rm max} \lesssim 2.3 M_\odot$. Our present result illustrates that the merger remnant neutron star at the onset of collapse to a black hole is not necessarily rapidly rotating and shows that we have to take into account the angular momentum conservation law to impose the constraint on the maximum mass of neutron stars.

PACS numbers: 04.25.D-, 04.30.-w, 04.40.Dg

arXiv:1905.03656v3 [astro-ph.HE] 24 Jun 2019

I. INTRODUCTION

The first direct detection of gravitational waves from the coalescence of binary neutron stars (GW170817) [1] was accompanied with a wide variety of the observations of electromagnetic counterparts [2]. These observations give us new constraints for the properties of neutron stars. Gravitational-wave observation for the late inspiral phase of the binary neutron stars constrains the binary tidal deformability in the range of $100 \lesssim \Lambda \lesssim 800$ [3, 4]. This suggests that the radius of the $1.4 M_\odot$ neutron star would be in the range between ~ 10.5 km and ~ 13.5 km.

Electromagnetic observations, in particular a possible observation of a gamma-ray burst [5] and ultraviolet-optical-infrared observation [2, 6], are also used for constraining the maximum mass of neutron stars. If we assume that the gamma-ray burst was driven from a remnant black hole surrounded by a torus, the black hole might have to be formed in a short timescale after the merger. In this hypothesis, Ref. [7] suggests that the maximum mass of neutron stars would be fairly small central value of $\approx 2.17 M_\odot$. Reference [8] suggests that the maximum mass of neutron stars would be 2.16–$2.28 M_\odot$, supposing that the merger remnant neutron star has the same mass as that of the inspiraling binary neutron star and is a rapidly rotating state (note that the actual mass of the remnant neutron star should be smaller: see Sec. II). The optical and infrared counterparts also suggest that the remnant massive neutron star would survive at least for several hundreds ms [9–12], while the absence of an extremely bright emission in the ultraviolet and optical bands at $\lesssim 1$ d suggests that the remnant formed after the merger would collapse to a black hole within a timescale of ~ 100 s after the merger [9, 10, 13]. This speculation could also give a constraint on the maximum mass of neutron stars, and Refs [9, 10] suggest a fairly small value of the maximum mass as $\lesssim 2.2 M_\odot$. However, these constraints are imposed in the assumption that the merger remnant neutron star is rapidly rotating at the onset of collapse; the constraint is imposed without taking into account details of angular momentum dissipation process in the post-merger stage self-consistently.

In this paper, we revisit the constraint on the maximum mass of cold spherical neutron stars imposed by the observational results of GW170817. The analysis is done taking into account the evolution process in the post-merger phase of binary neutron stars, by carefully analyzing both energy and angular momentum conservation laws and by employing solid results of latest numerical-relativity simulations and of rotating neutron stars in equilibrium. In particular, we show that it is essential to take into account the angular momentum conservation for this kind of analysis. We then find that the maximum mass of cold spherical neutron stars could be as large as $\sim 2.3 M_\odot$: that is, the upper bound may be by $\sim 0.1 M_\odot$ larger than in our previous analysis [10]. We thus conclude that a simplified analysis and an inappropriate assumption lead to an inaccurate constraint on the maximum mass.

The paper is organized as follows. In Sec. II, we describe assumptions imposed in our present analysis and resulting basic equations. In Sec. III, we derive the constraint on the maximum mass of cold spherical neutron stars. Section IV is devoted to a summary. Throughout this paper, G and c denote the gravitational constant and speed of light, respectively.

II. ASSUMPTIONS AND BASIC EQUATIONS

In this paper, we postulate or assume the following interpretation for the observational results of neutron-star merger event GW170817. First, we postulate that a remnant neutron star was formed after the merger and survived temporarily as a quasi-steady strong neutrino emitter. This is supported by the observations of electromagnetic (ultraviolet-optical-infrared) counterparts for the merger event [6], because the neutrino irradiation from the remnant neutron stars would play an important role

for reducing the neutron richness and lanthanide fraction of the ejecta (e.g., Refs. [6, 10–12]). Second, we postulate that the remnant neutron star collapsed to a black hole within the dissipation timescale of its kinetic energy via electromagnetic radiation like the magnetic dipole radiation (i.e., within $\sim 100\,$sec). This is because after the merger of binary neutron stars, magnetic fields are likely to be significantly amplified in the remnant neutron star [14] and in the presence of a strong energy injection comparable to the rest-mass energy of the ejecta by the electromagnetic radiation associated with large kinetic energy of the remnant, the ultra-violate-optical-infrared counterparts for GW170817 would be much brighter than the observational results [9, 10]. However, it should be noted that if the rotational kinetic energy of the remnant neutron star is dissipated by gravitational radiation and/or carried away by mass ejection in a short timescale (e.g., $\sim 10\,$s), we may accept the formation of a stable neutron star, although this possibility is not very likely (see Sec. III D for a discussion). Third, we *assume* that the remnant neutron star at the onset of collapse was rigidly rotating. This could be a reasonable assumption for the case that the remnant neutron star was long-lived, because the degree of the differential rotation is likely to be reduced sufficiently via long-term angular momentum transport process (e.g., Ref. [15]). Thus, we suppose that the collapse of the remnant neutron star should occur at a turning point (a marginally stable state) along an equilibrium sequence of rigidly rotating supramassive neutron stars [16, 17] (see Fig. 1 for turning points). Fourth, we postulate that an appreciable fraction of the baryon of mass $\gtrsim 0.05 M_\odot$ was located outside the black hole at its formation because the ultraviolet-optical-infrared observations for the GW170817 event indicate that the ejecta mass was likely to be $\gtrsim 0.03 M_\odot$ [6]. Finally, in this paper, we assume that neutron stars are described by simple nuclear matter equations of state (see Appendix A) and do not suppose other exotic possibilities like quark stars, twin stars, and hybrid stars (e.g., Ref. [18]). We also postulate that general relativity is a high-precision theory for neutron stars and binary neutron star mergers.

The quantities which are referred to in this paper are as follows; the baryon rest mass and gravitational mass at the formation of the binary neutron stars, M_* and M, respectively; the torus mass around the remnant neutron star and ejecta mass at the formation of a black hole, $M_{\rm out}$ and $M_{\rm eje}$, respectively; the total energy radiated by gravitational waves throughout the inspiral to post-merger phases, $E_{\rm GW}$; total energy radiated by neutrinos throughout the merger to post-merger phases, E_ν; and the maximum mass for cold spherical neutron stars, $M_{\rm max}$. Here, we know that $M = 2.74^{+0.04}_{-0.01} M_\odot$ with the 90% credible level [1, 3]. In $M_{\rm out}$, we include mass of an atmosphere surrounding the central object. $E_{\rm GW}$ can be divided into two parts: One is that emitted in the inspiral phase, $E_{\rm GW,i}$, and the other is that in the merger and post-merger phases, $E_{\rm GW,p}$. The subject of this paper is to constrain the value of $M_{\rm max}$ by using the relations

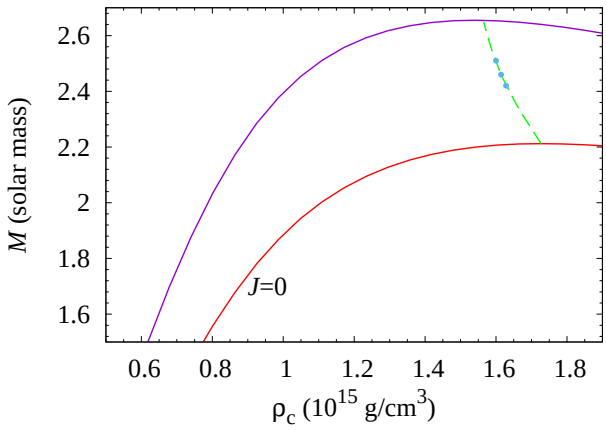

FIG. 1. Several important curves for rigidly rotating neutron stars in the plane of the gravitational mass (M) as a function of the central density ($\rho_{\rm c}$). In this example, we employ EOS-6 (see Sec. III) as the neutron-star equation of state. The lower and upper solid curves show the sequences of non-rotating neutron stars (labeled by $J = 0$) and rigidly rotating neutron stars at mass shedding limits. The dashed curve shows the sequence of neutron stars that are marginally stable to gravitational collapse (the sequence of the turning points); the neutron stars in the lower-density side of this dashed curve are stable, otherwise they are unstable. The filled circles denote the predicted points at the onset of collapse for GW170817 in this model equation of state with $M_{\rm out} + M_{\rm eje} = 0.048$, 0.096, and $0.150 M_\odot$ (from higher to lower mass: see Sec. III).

satisfied among these quantities.

The first relation employed is the energy conservation law together with the rest-mass conservation law, which gives

$$M_{*f} := M_* - M_{\rm out} - M_{\rm eje} = f_{\rm MS} M_f, \qquad (2.1)$$

where

$$M_f := M - E_{\rm GW} c^{-2} - E_\nu c^{-2} - M_{\rm out} - M_{\rm eje}, \quad (2.2)$$

and M_{*f} and M_f denote the rest mass and gravitational mass at the onset of collapse of the remnant neutron star, respectively. In Eq. (2.2), we assumed that the thermal, kinetic, and gravitational binding energy of the matter outside the remnant neutron star is much smaller than (at most $\sim 10\%$ of) its rest-mass energy. This could affect the values of M_f, $M_{\rm out}$, and $M_{\rm eje}$ only by $\sim 0.01 M_\odot$. We ignore the dissipation by electromagnetic radiation like the magnetic dipole radiation because in a short timescale of $\lesssim 10\,$s which we consider here, the effect is likely to be negligible.

In Eq. (2.1), we denoted the ratio of the baryon rest mass to the gravitational mass for the remnant neutron star at the onset of collapse by $f_{\rm MS}$ ($:= M_{*f}/M_f$). For cold spherical neutron stars at a marginally stable state to collapse, the ratio of the baryon rest mass to the gravitational mass is $\approx 1.19 \pm 0.05$ (see Appendix A). For rigidly rotating neutron stars near the marginally stable state, this value is smaller by a factor of up to ~ 0.02,

and thus, it depends only weakly on angular momentum (cf. Fig. 2 of Sec. III).

We also denote the ratio of M_* to M as $f_0 := M_*/M$. Since the ratio of the baryon rest mass to the gravitational mass is ~ 1.08–1.14 for realistic neutron stars with mass 1.2–$1.6 M_\odot$, f_0 should be also $\approx 1.11 \pm 0.03$ (see Appendix A).

For larger radii of neutron stars, f_0 and $f_{\rm MS}$ are in general smaller. It should be cautioned that the values of f_0 and $f_{\rm MS}$ depend on the equation of state and their deviation is not negligible for imposing the constraint to $M_{\rm max}$ within an error of $0.1 M_\odot$. Thus, in the analysis for constraining $M_{\rm max}$, we must not use particular values for them.

By eliminating M_* from Eqs. (2.1) and (2.2), we finally obtain

$$M\left(1-\frac{f_0}{f_{\rm MS}}\right) = E_{\rm GW}c^{-2} + E_\nu c^{-2} + (M_{\rm out}+M_{\rm eje})\left(1-\frac{1}{f_{\rm MS}}\right). \quad (2.3)$$

From Eqs. (2.2) and (2.3), we also obtain the gravitational mass at the onset of collapse as

$$M_f = \frac{f_0}{f_{\rm MS}}M - \frac{M_{\rm out}+M_{\rm eje}}{f_{\rm MS}}. \quad (2.4)$$

As we show in Appendix A, for cold spherical neutron stars of a variety of equations of state with the constraint that the tidal deformability of $1.35 M_\odot$ neutron stars, $\Lambda_{1.35}$, is smaller than 1000, the value of $f_0/f_{\rm MS}$ is approximately 0.920 ± 0.025. For this range, the left-hand side of Eq. (2.3) is found to be in a wide range as

$$M\left(1-\frac{f_0}{f_{\rm MS}}\right) = 0.219^{+0.073}_{-0.069} M_\odot, \quad (2.5)$$

and also,

$$M_f = 2.521^{+0.106}_{-0.077} M_\odot - \frac{M_{\rm out}+M_{\rm eje}}{f_{\rm MS}}. \quad (2.6)$$

We note that $f_{\rm MS}$ depends only weakly on the angular momentum, as we find in Sec. III. Equations (2.5) and (2.6) clearly illustrate that the dissipated energy and the gravitational mass at the onset of collapse have uncertain of approximately $\pm 0.1 M_\odot$ because the equation of state is not well constrained. As we show in Appendix A, the values of $f_0/f_{\rm MS}$ are correlated with $M_{\rm max}^{-1}$. Thus, smaller values of $M_{\rm max}$ lead to larger values of M_f and to smaller energy dissipated from the system (see Sec. III).

The electromagnetic (ultraviolet-optical-infrared) counterpart observations for GW170817 show that the ejecta mass would be approximately $M_{\rm eje} \approx 0.03$–$0.05 M_\odot$ (e.g., Ref. [6]). This value is also supported by numerical simulations for a neutron star surrounded by a torus [15, 19, 20]. Numerical simulations (e.g., Refs. [10, 15, 21]) also indicate that the mass of the torus around the remnant neutron star would be ~ 0.1–$0.2 M_\odot$ for its early stage, and reduce to ~ 0.02–$0.05 M_\odot$ for its late stage $\tau \gtrsim 1\,$s due to the mass ejection and mass accretion onto the remnant neutron star. Thus, $M_{\rm out}$ depends on the lifetime, τ, of the remnant neutron star. Also, at the formation of a black hole, it is decreased by $\gtrsim 50\%$ because a substantial fraction of the torus matter in the vicinity of the central object is swallowed by the black hole at its formation. Thus, we suppose $0.02 M_\odot \le M_{\rm out} \le 0.10 M_\odot$ at the collapse of the remnant neutron star in the following. For $M_{\rm out} = 0.06 \pm 0.04 M_\odot$, $(M_{\rm out}+M_{\rm eje})/f_{\rm MS}$ is approximately $(0.083 \pm 0.042) M_\odot$ and $(M_{\rm out}+M_{\rm eje})(1-1/f_{\rm MS})$ is $(0.016 \pm 0.008) M_\odot$, which is much smaller than the value of Eq. (2.5). Using this result, we approximately obtain

$$M_f = 2.44^{+0.15}_{-0.12} M_\odot, \quad (2.7)$$

and

$$\begin{aligned}&(E_{\rm GW}+E_\nu)c^{-2}\\ &= M\left(1-\frac{f_0}{f_{\rm MS}}\right) - (M_{\rm out}+M_{\rm eje})\left(1-\frac{1}{f_{\rm MS}}\right)\\ &= (0.20 \pm 0.08) M_\odot. \end{aligned} \quad (2.8)$$

Here the large (small) side of the uncertainty in M_f comes basically from the large (small) values of $f_0/f_{\rm MS}$, i.e., for small (large) values of $E_{\rm GW}+E_\nu$. Taking into account the uncertainty in these unknown values enlarges the uncertainty in the estimate of M_f compared with our previous estimation [10]. It should be also mentioned that the central value of M_f is by $\sim 0.15 M_\odot$ smaller than the value estimated in our previous paper [10]. The reason for this is that we underestimated the values of $E_{\rm GW}+E_\nu$ in the previous paper.

$(E_{\rm GW}+E_\nu)c^{-2}$ is found to be typically $\sim 0.2 M_\odot$ and at least larger than $\approx 0.12 M_\odot$. Numerical relativity simulations (e.g., Ref. [22]) have shown that $E_{\rm GW,i}$ is well constrained to be 0.035–$0.045 M_\odot c^2$ for $\Lambda_{1.35} \le 1000$. On the other hand, they show that $E_{\rm GW,p}$ depends strongly on the equation of state. It could be $\sim 0.125 M_\odot c^2 \approx 2.5 \times 10^{53}\,$erg for the maximum case [22]. Note that $E_{\rm GW,p}$ should be smaller than the rotational kinetic energy of the remnant neutron star (see also Table II of Sec. III),

$$T = \frac{1}{2} I \Omega^2 \approx 2.3 \times 10^{53}\,{\rm erg} \left(\frac{M_{\rm MNS}}{2.6 M_\odot}\right)\left(\frac{R_{\rm MNS}}{15\,{\rm km}}\right)^2 \times \left(\frac{\Omega}{10^4\,{\rm rad/s}}\right)^2, \quad (2.9)$$

where $M_{\rm MNS}$, $R_{\rm MNS}$, and Ω are the gravitational mass, equatorial circumferential radius, and angular velocity of the remnant neutron star, and we assumed that it is rigidly rotating (and hence its angular momentum is written as $2T/\Omega$). We note that the maximum angular

velocity is approximately written as (see also Table II)

$$\Omega_K \approx \sqrt{GM_{\rm MNS}/R_{\rm MNS}^3} \approx 1.01\times 10^4\,{\rm rad/s}\left(\frac{M_{\rm MNS}}{2.6M_\odot}\right)^{1/2}\left(\frac{R_{\rm MNS}}{15\,{\rm km}}\right)^{-3/2}. \quad (2.10)$$

As we find in the following, one of the key parameters for determining the angular momentum at the onset of collapse of the remnant neutron star is $E_{\rm GW,p}$. While $E_{\rm GW,p}$ could be $\sim 0.125M_\odot c^2$ if most of the rotational kinetic energy is dissipated by gravitational radiation, the post-merger evolution process is highly uncertain. If an efficient angular momentum transport works in the remnant neutron star and the degree of its non-axisymmetric deformation is reduced quickly, $E_{\rm GW,p}$ would be of order $0.01M_\odot c^2$ [23]. These facts together with Eq. (2.5) suggest that an appreciable amount of energy of $\sim 0.1M_\odot c^2 \approx 2\times 10^{53}$ erg would be dissipated by the emission of neutrinos until the onset of collapse to a black hole, unless the remnant neutron star radiates gravitational waves of energy comparable to T. Note that the value of $E_\nu \sim 10^{53}$ erg is quite natural if the remnant neutron star is long-lived with its lifetime $\tau \sim 1$ s because numerical-relativity simulations have shown that the neutrino luminosity from the remnant neutron star, L_ν, is of order 10^{53} erg/s (e.g., Refs. [24–26]). By contrast, if the remnant neutron star is relatively short-lived with $\tau \sim 100$ ms, E_ν would be of $O(10^{52}$ erg) (i.e., $\lesssim 0.01M_\odot c^2$) and for this case, we have to employ a large value of $E_{\rm GW,p}$ to satisfy Eq. (2.8) (see Sec. III for more specific examples).

Since the remnant neutron star is rotating, the gravitational mass at the onset of collapse has to be larger than the maximum mass, $M_{\rm max}$, for cold spherical neutron stars by a factor of $f_r = M_f/M_{\rm max} > 1$. Here, the value of f_r is determined at a turning point along an equilibrium sequence of rigidly rotating neutron stars. If we could obtain the value of f_r together with M_f, we can determine the value of $M_{\rm max}$. For the change of f_r by 0.1, $M_{\rm max}$ could be changed by $\approx 0.2M_\odot$. Thus, for constraining $M_{\rm max}$, e.g., within the $0.1M_\odot$ error, we have to determine the value of f_r within an error of ~ 0.05. For the maximally rotating neutron star along the turning point sequence, the value of f_r is known to be ~ 1.2 [17, 27] (see also Fig. 2 of Sec. III) and this value has been often used for guessing the maximum mass of cold spherical neutron stars [7–10]. However, the remnant neutron star is not always rotating in such a high rotation speed as shown in Sec. III. In setting $f_r \approx 1.2$, one would assume a particular angular momentum of the remnant neutron star neglecting the angular momentum conservation. In addition, the maximum value of f_r depends on the equation of state (see Fig. 2 of Sec. III). It should be cautioned again that in the analysis for constraining the value of $M_{\rm max}$, we must not a priori employ a particular value for f_r.

For inferring the angular momentum of the remnant neutron star at the onset of collapse, we have to seriously analyze the dissipation of angular momentum in the post-merger phase. Let J_0 and J_f be the angular momentum at the onset of merger and at the onset of collapse of the remnant neutron star to a black hole, respectively. Then, we obtain

$$J_f = J_0 - J_{\rm GW,p} - J_\nu - J_{\rm out} - J_{\rm eje}, \quad (2.11)$$

where $J_{\rm GW,p}$, J_ν, $J_{\rm out}$, and $J_{\rm eje}$ are the angular momentum carried away (after the merger) by gravitational radiation, by neutrinos, angular momentum of the torus surrounding the remnant black hole at its formation, and angular momentum of ejecta (at the black-hole formation). In the following, we give or determine these quantities based on the results of numerical-relativity simulations. We also note that by angular momentum transport processes from the remnant neutron star to the surrounding matter, the angular momentum of torus and ejecta in general increases with time in the post-merger phase.

Since gravitational waves emitted in the post-merger phase are dominated by a fundamental mode of its frequency $f = 2$–4 kHz [28, 29], $J_{\rm GW}$ is approximately written as

$$J_{\rm GW,p} \approx \frac{E_{\rm GW,p}}{\pi f} \approx 9.5\times 10^{48}\,{\rm erg\,s}\left(\frac{E_{\rm GW,p}}{0.05M_\odot c^2}\right)\left(\frac{f}{3.0\,{\rm kHz}}\right)^{-1}. \quad (2.12)$$

Our latest numerical-relativity simulation confirms that this relation is satisfied within 1% accuracy [30]. Here, for the binaries of total mass $\approx 2.7M_\odot$, $f \approx 3.6$, 3.1, and 2.5 kHz for $R_{1.60} \approx 11$, 12, and 13.5 km [28, 29] with R_M the radius of a spherical neutron star of its gravitational mass M (in units of $M_\odot$). Thus, for $R_{1.35} \approx R_{1.60} \lesssim 13.5$ km (this constraint was given from the observational result of the tidal deformability of GW170817 [1, 3]), $f \gtrsim 2.5$ kHz. In this paper, we infer the value of f by using the relation of Eq. (3) of Ref. [28].

Since the angular momentum of neutrinos are dissipated due to the fact that the emitter (remnant neutron star) is rotating, J_ν is written approximately by $J_\nu \approx (2/3)c^{-2}R_{\rm MNS}^2\Omega E_\nu$ [31], and thus,

$$J_\nu \approx 3.0\times 10^{48}\,{\rm erg\,s}\left(\frac{E_\nu}{0.1M_\odot c^2}\right)\left(\frac{R_{\rm MNS}}{15\,{\rm km}}\right)^2 \times\left(\frac{\Omega}{10^4\,{\rm rad/s}}\right). \quad (2.13)$$

We note that the value of J_ν described here agrees with the results of a numerical-relativity simulation within a factor of 2 [21]. Equation (2.13), in comparison with Eq. (2.12), illustrates that this is a non-negligible but minor effect for dissipating the angular momentum (thus, the error would be also a minor effect).

$J_{\rm out}$ is associated with the typical radius of the torus surrounding the remnant neutron star (at the onset of

collapse). Denoting it by $R_{\rm out}$, it is approximated by $J_{\rm out} \approx M_{\rm out}\sqrt{GM_{\rm MNS}R_{\rm out}}$, and thus,

$$J_{\rm out} \approx 5.8\times 10^{48}\,{\rm erg\,s}\left(\frac{M_{\rm out}}{0.05M_\odot}\right)\left(\frac{R_{\rm out}}{100\,{\rm km}}\right)^{1/2} \times \left(\frac{M_{\rm MNS}}{2.6M_\odot}\right)^{1/2}. \quad (2.14)$$

Here $R_{\rm out}$ would be fairly small ~ 50 km in the early evolution stage of the accretion torus. However, during its long-term viscous evolution as well as angular momentum transport from the remnant neutron star, the typical radius increases to be $\gtrsim 100$ km for $\tau \gtrsim 300$ ms [15] which shows $R_{\rm out} \approx 40 + 100(\tau/1\,{\rm s})^{1/2}$ km for $\tau \lesssim 1.5$ s and for a longer term, $R_{\rm out}$ approaches ~ 200 km.

$J_{\rm eje}$ is associated with the location at which the mass ejection occurs. Denoting the typical location by $R_{\rm eje}$, it is approximated by $J_{\rm eje} \approx M_{\rm eje}\sqrt{GM_{\rm MNS}R_{\rm eje}}$, and thus,

$$J_{\rm eje} \approx 6.9\times 10^{48}\,{\rm erg\,s}\left(\frac{M_{\rm eje}}{0.05M_\odot}\right)\left(\frac{R_{\rm eje}}{140\,{\rm km}}\right)^{1/2} \times \left(\frac{M_{\rm MNS}}{2.6M_\odot}\right)^{1/2}. \quad (2.15)$$

For long-lived remnant neutron stars which we consider in this paper, mass ejection mainly occurs through the long-term viscous process in the post-merger stage from an accretion torus [15, 19, 20] with mass $\sim 0.05M_\odot$, while for dynamical mass ejection that occurs at merger, the matter would be ejected at $R_{\rm eje} \sim 30$ km with mass $\lesssim 0.01M_\odot$. (Note that in $M_{\rm eje}$ both contributions are included.) Thus, for $J_{\rm eje}$, only the post-merger mass ejection could contribute dominantly to the angular momentum loss. Since this mass ejection is driven from the torus, we simply set $R_{\rm out} = R_{\rm eje}$ in this paper; that is, we employ a relation as $J_{\rm out} + J_{\rm eje} = (M_{\rm out} + M_{\rm eje})\sqrt{GM_{\rm MNS}R_{\rm out}}$. Here, we may overestimate $J_{\rm eje}$ because the dynamical ejecta would have smaller angular momentum than the post-merger one. However, since the mass of the dynamical ejecta would be much smaller than the post-merger ejecta, the degree of the overestimation would be minor.

We note that the error for the estimate in $J_{\rm out} + J_{\rm eje}$ associated with the uncertainty in $R_{\rm out}$ would be of order 10%. This error will be reflected in $M_{\rm out} + M_{\rm eje}$ for determining it (see Sec. III). However, its error size does not affect our final conclusion.

Thus, besides J_0, the quantities in the right-hand side of Eq. (2.11) is related to $E_{\rm GW}$, E_ν, $M_{\rm out}$, and $M_{\rm eje}$ with f, Ω, $M_{\rm MNS}$, and $R_{\rm out}$ as given parameters.

In addition, we have an important relation. From the definitions already shown, we obtain

$$f_r M_{\rm max} = M_f = \frac{f_0}{f_{\rm MS}}M - \frac{M_{\rm out}+M_{\rm eje}}{f_{\rm MS}}. \quad (2.16)$$

Thus, for a given value of f_r and $(M_{\rm out} + M_{\rm eje})/f_{\rm MS}$, $f_0/f_{\rm MS}$ becomes a linear function of $M_{\rm max}$ as

$$\frac{f_0}{f_{\rm MS}} = \frac{M_{\rm out}+M_{\rm eje}}{f_{\rm MS}M} + \frac{f_r M_{\rm max}}{M}. \quad (2.17)$$

This becomes a condition that determines a particular state of the remnant neutron star at the onset of collapse for a given equation of state. This equation plays an important role in Sec. III.

Note that for larger values of M_f, $E_{\rm GW,p} + E_\nu$ should be smaller, and thus, the value of f_r should be larger because the collapse to a black hole should occur before a substantial fraction of angular momentum (and energy) is dissipated. Remembering the fact that M_f is correlated with $M_{\rm max}^{-1}$ for plausible equations of state (see Appendix A), we then find that for the larger value of $M_{\rm max}$, the required value of f_r is smaller. This fact clarifies that we cannot a priori give the value of f_r for constraining $M_{\rm max}$.

III. ANALYSIS BASED ON NUMERICAL MODELING OF NEUTRON STARS AND BINARY NEUTRON STAR MERGERS

A. Preparation

In the analysis of Sec. II, we have several unknown parameters; f_0, $f_{\rm MS}$, $E_{\rm GW,i}$, $E_{\rm GW,p}$, E_ν, f, Ω, $M_{\rm MNS}$, $M_{\rm out}$, $M_{\rm eje}$, $R_{\rm MNS}$, $R_{\rm out}$, and J_0. Among them, f_0, $f_{\rm MS}$, Ω, $M_{\rm MNS}$, and $R_{\rm MNS}$ for a given equation of state are calculated (at least with good approximation) by constructing equilibrium states of non-rotating and rotating neutron stars. Also, $E_{\rm GW,i}$, f, $M_{\rm out}$, $M_{\rm eje}$, and $R_{\rm out}$ are approximately obtained with the help of numerical-relativity simulations as already mentioned in Sec. II. J_0 is also obtained accurately with the help of numerical relativity. The dependence of J_0 on total binary mass m_0, symmetric mass ratio (hereafter referred to as $\eta\,(\le 1/4)$), and $R_{1.35}$ is determined by the results by numerical relativity simulations [30] as

$$J_0 \approx Gc^{-1}m_0^2\eta\left[a_1 - a_2\delta\eta + a_3\bar{R}_{1.35}^3\left(1+a_4\delta\eta\right)\right], \quad (3.1)$$

where $\bar{R}_{1.35}$ denotes $R_{1.35}$ in units of 10 km, $\delta\eta = \eta - 1/4(\le 0)$, $a_1 \approx 3.32$, $a_2 \approx 31$, $a_3 \approx 0.137$, and $a_4 \approx 27$. We note that J_0 increases with the increase of $R_{1.35}$ and with the decrease of η because the merger occurs at a more distant orbit for larger stellar radii and for more asymmetric binaries.

Equation (3.1) shows that J_0 is in the range between $\approx 5.8\times 10^{49}$ erg s and $\approx 6.3\times 10^{49}$ erg s for neutron stars with $R_{1.35} = 10.5$–14 km, total mass $m_0 \approx 2.74M_\odot$, and $\eta = 0.244$–0.250 (i.e., mass ratio 0.73–1.00). The value of J_0 is by $\sim 1\times 10^{49}$ erg s larger than the maximum angular momentum of rigidly rotating neutron stars (see Fig. 2) and $2T/\Omega$ for $\Omega \approx \Omega_K$ (see Eq. (2.9)), and this fact suggests that the remnant neutron star would initially have a differentially rotating state with the maximum angular velocity slightly larger than Ω_K, as has been found in many numerical-relativity simulations since Ref. [32].

In contrast to J_0 and $E_{\rm GW,i}$, $E_{\rm GW,p}$ and E_ν are not determined into a narrow range although $E_{\rm GW,p} + E_\nu$ is constrained by Eq. (2.8) for given values of $f_0/f_{\rm MS}$,

TABLE I. Selected piecewise polytropic equations of state and important quantities for spherical neutron stars. The units of the mass and radius are $M_\odot$ and kilometer, and that of p is dyn/cm^2. $f_{\rm MS}$ is the ratio of the baryon rest mass to $M_{\rm max}$ for the maximum mass neutron star. f_0 shown here is M_*/M for binaries of mass $1.35M_\odot$ and $1.40M_\odot$. f denotes the dominant frequency of post-merger gravitational waves predicted approximately by the formula in Ref. [28].

Model	Γ_2	Γ_3	$\log_{10} p$	$M_{\rm max}$	$f_{\rm MS}$	$R_{1.60}$	$R_{1.35}$	$\Lambda_{1.35}$	f_0	f (kHz)
EOS-1	3.15	2.81	34.350	2.075	1.200	11.27	11.30	366.6	1.113	3.45
EOS-2	2.60	2.84	34.550	2.106	1.172	12.67	12.94	746.0	1.092	2.71
EOS-3	3.45	2.70	34.300	2.113	1.208	11.17	11.12	348.2	1.117	3.50
EOS-4	3.80	2.80	34.200	2.147	1.221	10.91	10.80	302.8	1.122	3.62
EOS-5	2.70	2.78	34.575	2.176	1.177	12.88	13.06	821.9	1.092	2.65
EOS-6	3.00	2.80	34.500	2.212	1.196	12.21	12.25	599.0	1.102	3.01
EOS-7	3.15	2.81	34.475	2.246	1.204	12.06	12.04	555.7	1.105	3.08
EOS-8	3.65	2.78	34.325	2.252	1.222	11.39	11.27	395.2	1.116	3.40
EOS-9	3.05	2.80	34.550	2.306	1.200	12.57	12.56	720.7	1.099	2.74
EOS-10	2.85	2.85	34.625	2.328	1.189	13.24	13.29	967.6	1.092	2.55
EOS-11	3.80	2.50	34.375	2.353	1.229	11.66	11.50	459.7	1.113	3.27
EOS-12	3.25	2.78	34.575	2.433	1.212	12.68	12.60	757.8	1.100	2.70

$E_{\rm GW,i}$, and $(M_{\rm out}+M_{\rm eje})/f_{\rm MS}$ fairly well. We note that E_ν is associated with the lifetime of the remnant neutron star of GW170817, τ, as $E_\nu \approx L_\nu \tau$. Here, the neutrino luminosity is $L_\nu \gtrsim 10^{53}$ erg/s [21] but τ is not very clear. Thus, we consider $E_{\rm GW,p}$ and E_ν as values to be determined in the present analysis.

In the following, we constrain the value of $M_{\rm max}$ by analysing rigidly rotating neutron stars at marginally stable states (at turning points) for several equations of state. For computing rigidly rotating neutron stars in equilibrium, we employ a piecewise polytropic equation of state, for which the details are described in Appendix A. The selected equations of state used in this section are listed in Table I. We selected many equations of state rather randomly for each range of $M_{\rm max}$. For the analysis, we only employ the equations of state with which $2M_\odot$ neutron stars [33] are reproduced, $\Lambda_{1.35} \le 1000$, and the sound speed is always smaller than the speed of light for stable neutron stars. We ignore the thermal effect of the remnant neutron star for constructing equilibrium rotating neutron stars because it is a minor contribution to the neutron-star properties if we consider its age to be of order 0.1–1 s [34].

Figure 2 displays several key quantities as functions of the angular momentum, J, along the sequences of the marginally stable neutron stars (cf. the dashed curve of Fig. 1). Here, the neutron stars with $J=0$ denote the marginally stable state for the spherical neutron stars of mass $M_{\rm max}$, and at $J=J_{\rm max}$, the neutron stars are at the mass-shedding limit; the angular velocity at the equatorial surface is equal to the Keplerian one. Table II also lists several quantities of rigidly rotating neutron star at a turning point and mass shedding limit.

Figure 3 displays the relation between $f_0/f_{\rm MS}$ and $M_{\rm max}$ for marginally-stable rigidly-rotating neutron stars with several piecewise polytropic equations of state. Here, f_0 is calculated for binaries of mass $(1.35_\odot, 1.40M_\odot)$ and $(1.20_\odot, 1.55M_\odot)$, but the values for two cases are different only by 0.2–0.3% (see Fig. 5), and thus, the difference in f_0 is not very important in the following. The uncertainty in Fig. 3 reflects the variation of $f_{\rm MS}$ for the different angular momentum of the marginally stable rotating neutron stars: As found from Fig. 2, $f_0/f_{\rm MS}$ is smallest for $J=0$ and largest for $J=J_{\rm max}$. The tilted lines show the relation of Eq. (2.17) for $f_r = 1.20 - 0.02\times i$ up to 1.00 (from left to right) with $(M_{\rm out}+M_{\rm eje})/f_{\rm MS} = 0.04M_\odot$ and $0.08M_\odot$, while M is fixed to be $2.74M_\odot$. We note that for a given value of $M_{\rm max}$, the value of $f_0/f_{\rm MS}$ is in general larger for the larger values of $\Lambda_{1.35}$, and hence, the upper bound is determined by the constraint for $\Lambda_{1.35}$ (see Appendix A).

For rigidly rotating neutron stars, the upper limit of f_r is approximately 1.2 as found from Fig. 2 (see also Table II). Thus, the left region of the line of $f_r = 1.2$ in Fig. 3 is prohibited in our model. That is, for the equations of state with small values of $M_{\rm max} = 2.0$–$2.1M_\odot$, the remnant neutron star cannot achieve the rigidly rotating state at the onset of collapse (we show the examples in Sec. III C). For such equations of state, the remnant neutron star would collapse before the rigidly rotating state is achieved, i.e., its lifetime is shorter than the angular momentum transport timescale in the remnant neutron star. It is natural to consider that the lifetime of the remnant neutron star with such equations of state is fairly short $\ll 1$ s.

For the right region of the line of $f_r = 1$, on the other hand, the collapse cannot occur, because the mass of the remnant neutron star is smaller than $M_{\rm max}$. Thus, for such equations of state, a stable neutron star should be the final outcome. As mentioned in the first paragraph of Sec. II, if such a stable remnant is formed in GW170817 and has large rotational kinetic energy $\gtrsim 10^{52}$ erg, an energy injection to ejecta through electromagnetic radiation like the magnetic dipole radiation would occur and

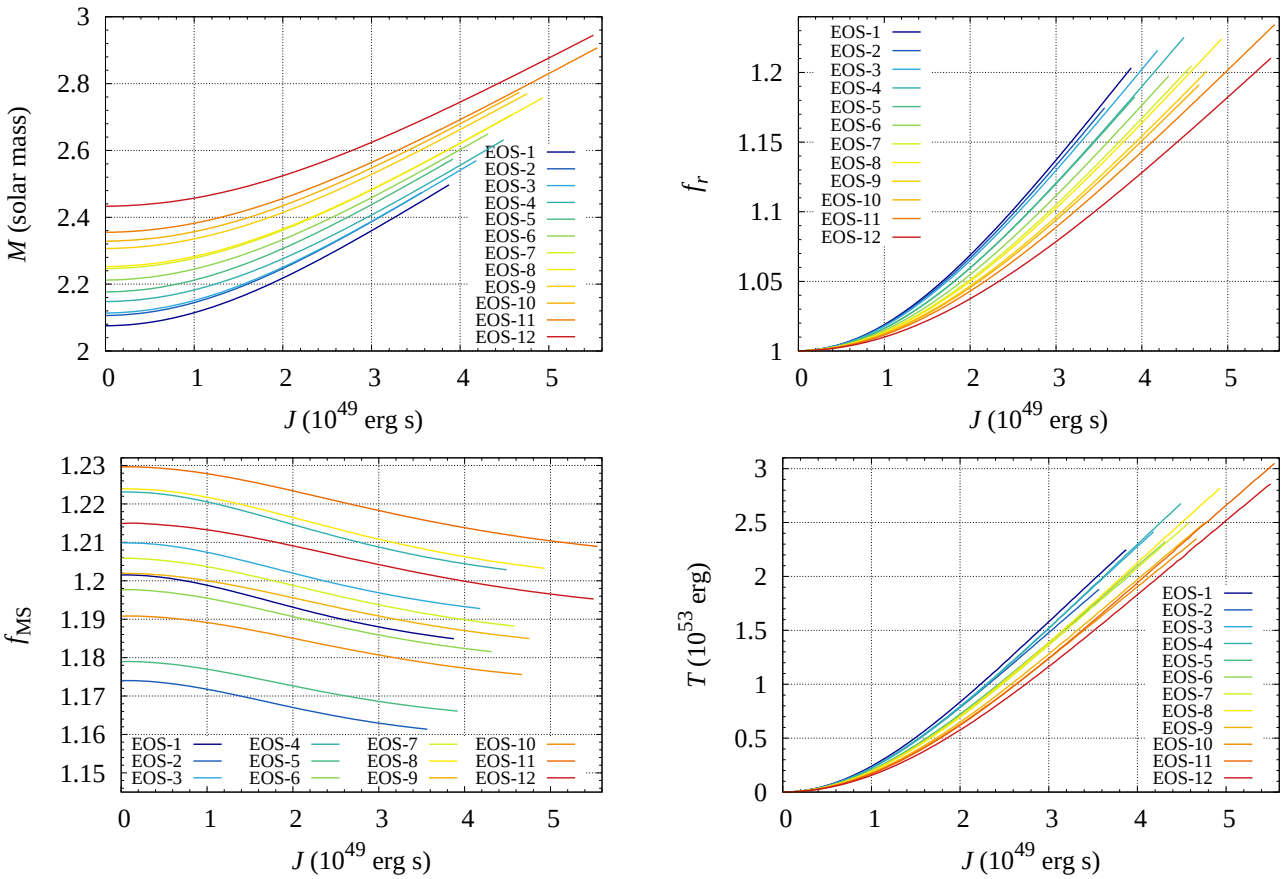

FIG. 2. Gravitational mass, M, ratio of M to $M_{\rm max}$ (f_r), ratio of baryon rest mass to the gravitational mass, $f_{\rm MS}$, and rotational kinetic energy $T = J\Omega/2$ as functions of J for rigidly rotating neutron stars along the marginally stable sequence (i.e., along the turning point sequence) with selected equations of state (see Table I). Note that M at $J = 0$ is $M_{\rm max}$.

be inconsistent with the observational results for the electromagnetic counterparts of GW170817 [9, 10]. However, if the rotational kinetic energy is dissipated or removed in a short timescale ($\lesssim 100\,$s), e.g., by gravitational radiation and neutrino emission, we may accept the formation of a stable neutron star [35].

Figure 3 shows an important fact as follows: If the maximum mass of spherical neutron stars in nature is relatively small $\lesssim 2.1 M_\odot$, the collapse would occur for the remnant neutron star in a rapidly rotating state with $f_r \approx 1.2$. On the other hand, if the maximum mass of spherical neutron stars is relatively large $\gtrsim 2.3 M_\odot$, the collapse would not occur for rapidly rotating remnant neutron star but for $f_r \lesssim 1.05$. Then the next issue is whether we can find a self-consistent solution for such collapses, because f_r is determined by the angular momentum dissipation process in the post-merger stage. In the following, we show several realistic scenarios for this process in some of equations of state that we select.

B. Method

For each equation of state, we try to find a solution that satisfies the conservation relations of energy and angular momentum self-consistently. We will have a brief summary of our model by analyzing the degree of freedoms of all unknown variables here. There are in total 14 variables in the conservation law of rest mass, energy and angular momentum (cf. Eq. (2.1), (2.2) and (2.11)). Nevertheless, M is determined by observation and M_* is related to M by factor f_0 which could be determined once a model equation of state is assumed. Similarly, according to the marginally stable solution results, M_f and J_f are fixed once M_{*f} is fixed and an equation of state is given. Hence, there is only one degree of freedom among M_f, M_{*f} and J_f. J_0 is given by Eq. (3.1). There are 8 other variables left: E_ν and J_ν are related by Eq. (2.13), $E_{\rm GW,p}$ and $J_{\rm GW,p}$ are related by Eq. (2.12), $M_{\rm eje} + M_{\rm out}$ and $J_{\rm eje} + J_{\rm out}$ are related by Eq. (2.15) and (2.14). As a consequence, there are only 3 degrees of freedom in the remaining 8 variables. In total, there are 4 degrees of freedom and we have 3 equations (laws of conservation). Once we have input one parameter, such

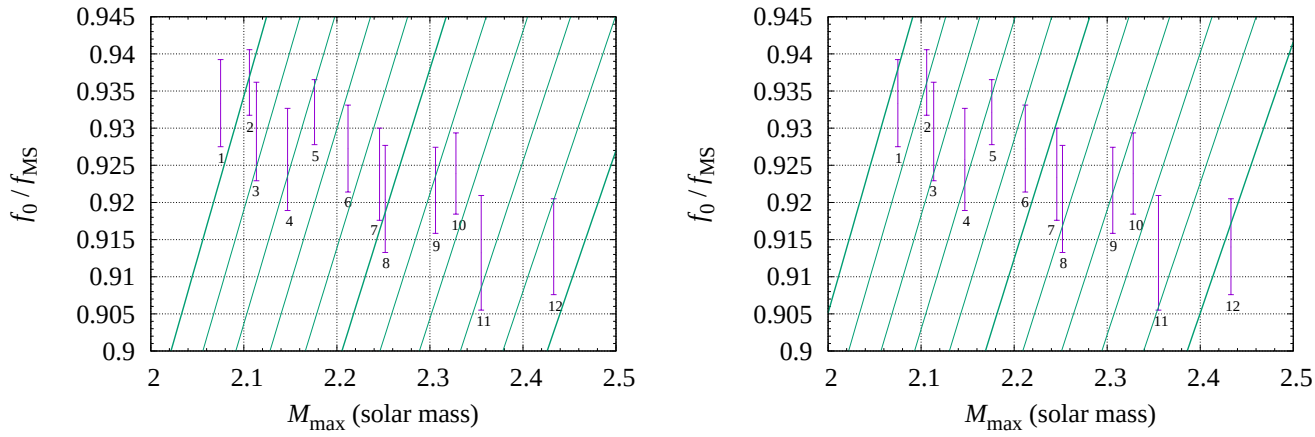

FIG. 3. Relation between $f_0/f_{\rm MS}$ and $M_{\rm max}$ for marginally-stable rigidly-rotating neutron stars with several equations of state listed in Table I. The lower and upper ends of each uncertainty range correspond to $J = 0$ and $J = J_{\rm max}$, respectively. The numbers attached in each data denote the model equations of state. The tilted lines show the relation of Eq. (2.17) for $f_r = 1.20$, 1.18, 1.16, $\cdots$, 1.04, 1.02, and 1.00 (from left to right) with $(M_{\rm out} + M_{\rm eje})/f_{\rm MS} = 0.04M_\odot$ (left panel) and $0.08M_\odot$ (right panel) and with $M = 2.74M_\odot$. The thick lines are for $f_r = 1.20$, 1.10, and 1.00.

TABLE II. Key quantities for rigidly rotating neutron stars at the maximum mass along the marginally stable sequences for selected equations of state listed in Table I. $M_{\rm MS,R}$: gravitational mass, $M_{*\rm MS,R}$: baryon rest mass, $J_{\rm MS,R}$: angular momentum, $\Omega_{\rm MS,R}$: angular velocity, $T_{\rm MS,R}$: rotational kinetic energy, and $R_{\rm MS,R}$: circumferential radius at the equatorial surface.

Model	$M_{\rm MS,R}$ ($M_\odot$)	$M_{*\rm MS,R}/M_{\rm MS,R}$	$M_{\rm MS,R}/M_{\rm max}$	$J_{\rm MS,R}$ (10^{49} erg s)	$\Omega_{\rm MS,R}$ (10^4 rad/s)	$T_{\rm MS,R}$ (10^{53} erg)	$R_{\rm MS,R}$ (km)
EOS-1	2.497	1.185	1.203	3.875	1.160	2.247	13.04
EOS-2	2.474	1.161	1.175	3.567	1.055	1.880	13.74
EOS-3	2.570	1.193	1.216	4.183	1.155	2.415	13.15
EOS-4	2.631	1.203	1.225	4.492	1.192	2.677	13.11
EOS-5	2.574	1.167	1.183	3.919	1.028	2.014	14.19
EOS-6	2.649	1.182	1.198	4.315	1.077	2.323	13.87
EOS-7	2.707	1.188	1.205	4.580	1.090	2.496	13.93
EOS-8	2.757	1.203	1.224	4.932	1.143	2.819	13.73
EOS-9	2.770	1.185	1.208	4.756	1.049	2.494	14.33
EOS-10	2.774	1.176	1.191	4.668	1.007	2.349	14.79
EOS-11	2.907	1.209	1.234	5.548	1.099	3.049	14.26
EOS-12	2.945	1.195	1.210	5.504	1.039	2.858	14.77

as $M_{\rm eje} + M_{\rm out}$, and a model equation of state is given, all the other quantities related to the properties of the star at the moment of collapse, the total energy of neutrino emission and gravitational wave in the post-merger phase could be solved (cf. Table. III). With this analysis we can tell whether the assumed equation of state model is consistent with the observation, for instance, the obtained values of E_ν and $E_{\rm GW,p}$ have to be positive and within a plausible range.

In this analysis, we employ M_f, $R_{\rm MS}$ (circumferential radius), and $\Omega_{\rm MS}$ (angular velocity) for rigidly rotating neutron stars at turning points as $M_{\rm MNS}$, $R_{\rm MNS}$, and $\Omega_{\rm MNS}$, respectively. $f_{\rm MS}$ is also found from a solution of rigidly rotating neutron stars at turning points. f_0 is calculated from the solutions of spherical neutron stars of mass 1.35-1.40$M_\odot$ or 1.20-1.55$M_\odot$. $E_{\rm GW,i}$ is set to be $(0.040 \pm 0.005)M_\odot c^2$. J_0 is determined by Eq. (3.1) for a given value of $R_{1.35}$ and η. Here the variation in η by ± 0.003 systematically changes the values of $E_{\rm GW,p}$ and E_ν only by at most $\pm 0.007M_\odot$ and $\mp 0.007M_\odot$. Hence, we only show the results with $\eta = 0.247$. Since the dependence of $J_{\rm out} + J_{\rm eje}$ on $R_{\rm out}$ is not very strong (compared with the dependence on $M_{\rm out} + M_{\rm eje}$), we fix $R_{\rm out}$ to be 140 km. On the other hand, $M_{\rm out} + M_{\rm eje}$ has a strong effect on the solution. Thus, we vary it in a wide range (e.g., see Fig. 4).

With these preparations, Eq. (2.17) can be considered as a relation between f_r and $f_{\rm MS}$. Here, in Eq. (2.17), M is given ($2.74M_\odot$), f_0 is determined for a given equation of state and each mass of binary, and $M_{\rm out} + M_{\rm eje}$ is an input parameter. An equilibrium sequence of rigidly rotating neutron stars along the turning points for a given equation of state also gives another monotonic relation between these two variables as found in Fig. 2. Thus,

we first determine f_r and $f_{\rm MS}$ by solving a simultaneous equation composed of two independent relations and specify a model for the rigidly rotating neutron star at a turning point. (We note that for some equations of state, e.g., EOS-12, the solution does not exist.) We can then obtain J_f, M_f, $\Omega_{\rm MS}$, and $R_{\rm MS}$ for this model using the monotonic relations of $f_{\rm MS}(J_f)$, $M_f(J_f)$, $\Omega_{\rm MS}(J_f)$, and $R_{\rm MS}(J_f)$: cf. Fig. 2.

We can subsequently determine $E_{\rm GW,p} + E_\nu$ and $J_{\rm GW,p} + J_\nu$ from Eqs. (2.8) and (2.11). For Eq. (2.11), we employ J_0, $M_{\rm MNS}(= M_f)$, $R_{\rm out}$, $R_{\rm MNS}(= R_{\rm MS})$, f, and $\Omega(= \Omega_{\rm MS})$ for each equation of state. Then these two relations, $E_{\rm GW,p} + E_\nu$ =const and $J_{\rm GW,p} + J_\nu$ =const, constitute a simultaneous equation for $E_{\rm GW,p}$ and E_ν because we have already given the values of $R_{\rm MNS}$, Ω, and f, which are necessary to relate $J_{\rm GW,p}$ and J_ν to $E_{\rm GW,p}$ and E_ν, respectively. Thus, these two quantities are immediately determined, if the solution exists. (Again we note that for some equations of state, a physical solution does not exist: see below.)

C. Results

Table III shows the solutions that self-consistently satisfy the conservation relations of energy and angular momentum for each equation of state with the selected values of $M_{\rm out} + M_{\rm eje}$; $0.048 M_\odot$, $0.096 M_\odot$, and $0.150 M_\odot$. Figure 4 also shows representative results: The top-left, top-right, and bottom-left panels display $E_{\rm GW,p}$ and E_ν as functions of $M_{\rm out} + M_{\rm eje}$ for EOS-3, 6, and 9, respectively, and the bottom-right panel shows f_r as a function of $M_{\rm out} + M_{\rm eje}$ for EOS-1, 3, 6, 9, and 11. Here, associated with the uncertainties in J_0 and $E_{\rm GW,i}$ by $\pm 0.1 \times 10^{49}$ erg s, and $0.005 M_\odot c^2$, respectively, an uncertainty, typically, of $\pm 0.007 M_\odot c^2$ and $\mp 0.012 M_\odot c^2$, exists in $E_{\rm GW,p}$ and E_ν, respectively. The three curves for each plot in the the top-left, top-right, and bottom-left panels of Fig. 4 denote the upper and lower bounds as well as the central value for $E_{\rm GW,p}$ and E_ν. In addition, the change of f_0 from the 1.35-1.40$M_\odot$ case to the 1.20-1.55$M_\odot$ case varies $E_{\rm GW,p}$ and E_ν typically by $-0.003 M_\odot c^2$ for both quantities.

For EOS-12, no solution is found for given parameters. The reason for this is that (i) for large values of $M_{\rm out} + M_{\rm eje}$, the predicted final mass of the remnant neutron star, M_f, becomes smaller than $M_{\rm max}$, and hence, no solution with $f_r \geq 1$ is present and (ii) for $M_{\rm out} + M_{\rm eje} \lesssim 0.057 M_\odot$, the value of f_r is determined but physical (positive) values for the set of $(E_{\rm GW,p}, E_\nu)$ are not found. If this type of equation of state with $M_{\rm max} \gtrsim 2.4 M_\odot$ would be the real one, the final outcome should be a stable neutron star in the GW170817 event. However, this is not likely as we discuss in Sec. III D.

For EOS-1 and 2 for which $M_{\rm max}$ is rather small, $\lesssim 2.1 M_\odot$, we often fail to find a solution. The reason for this is that Eq. (2.17) can be satisfied only for a high value of $f_r \sim 1.2$, and thus, for small values of $M_{\rm out} +$

TABLE III. Predicted states of rigidly rotating neutron stars at the onset of collapse for the GW170817 event with several equations of state. The given values of $M_{\rm out} + M_{\rm eje}$ are $0.048 M_\odot$ (upper), $0.096 M_\odot$ (middle), and $0.150 M_\odot$ (lower), respectively. M_f and J_f are shown in units of $M_\odot$ and 10^{49} erg s, respectively. The units of $E_{\rm GW,p}$ and E_ν are $M_\odot c^2$. "—" means that no solution of f_r and $f_0/f_{\rm MS}$ exists for the corresponding equations of state. Associated with the uncertainties in J_0 and $E_{\rm GW,i}$ by $\pm 0.1 \times 10^{49}$ erg s, and $0.005 M_\odot c^2$, respectively, an uncertainty, typically, of $\pm 0.007 M_\odot c^2$ and $\mp 0.012 M_\odot c^2$, exists in $E_{\rm GW,p}$ and E_ν, respectively. * shows that only solutions with negative values of E_ν are obtained. For EOS-12, no solution for f_r and $f_0/f_{\rm MS}$ exists for $M_{\rm out} + M_{\rm eje} \gtrsim 0.058 M_\odot$ and no solution with the positive value of E_ν exists for $M_{\rm out} + M_{\rm eje} \leq 0.15 M_\odot$, so that we do not describe the results.

Model	$f_0/f_{\rm MS}$	f_r	M_f	J_f	$E_{\rm GW,p}$	E_ν
EOS-1	—	—	—	—	—	—
EOS-2	—	—	—	—	—	—
EOS-3	0.935	1.194	2.52	3.89	0.076	0.053
EOS-4	0.931	1.169	2.51	3.71	0.091	0.049
EOS-5	0.936	1.160	2.52	3.59	0.082	0.047
EOS-6	0.930	1.134	2.51	3.35	0.102	0.043
EOS-7	0.926	1.111	2.50	3.11	0.118	0.038
EOS-8	0.921	1.103	2.48	3.01	0.130	0.037
EOS-9	0.922	1.077	2.49	2.65	0.130	0.037
EOS-10	0.923	1.069	2.49	2.51	0.130	0.034
EOS-11	0.910	1.042	2.45	1.98	0.194	0.004
EOS-1	0.939	1.201	2.49	3.84	0.034	0.078
EOS-2	—	—	—	—	—	—
EOS-3	0.935	1.174	2.48	3.62	0.051	0.072
EOS-4	0.930	1.150	2.47	3.43	0.067	0.068
EOS-5	0.935	1.140	2.48	3.30	0.064	0.059
EOS-6	0.929	1.114	2.46	3.04	0.083	0.057
EOS-7	0.924	1.092	2.45	2.78	0.100	0.051
EOS-8	0.920	1.084	2.44	2.67	0.112	0.051
EOS-9	0.920	1.058	2.44	2.26	0.118	0.045
EOS-10	0.921	1.050	2.44	2.09	0.120	0.040
EOS-11	0.908	1.023	2.41	1.44	0.188	0.006
EOS-1	0.938	1.178	2.44	3.54	0.008	0.098
EOS-2	0.940	1.162	2.45	3.39	0.024	0.079
EOS-3	0.934	1.151	2.43	3.31	0.025	0.092
EOS-4	0.929	1.127	2.42	3.10	0.041	0.088
EOS-5	0.935	1.118	2.43	2.96	0.046	0.071
EOS-6	0.928	1.092	2.42	2.68	0.064	0.070
EOS-7	0.923	1.070	2.40	2.38	0.083	0.063
EOS-8	0.918	1.062	2.39	2.25	0.094	0.064
EOS-9	0.918	1.037	2.39	1.75	0.109	0.051
EOS-10	0.920	1.028	2.39	1.54	0.114	0.043
EOS-11*	—	—	—	—	—	—

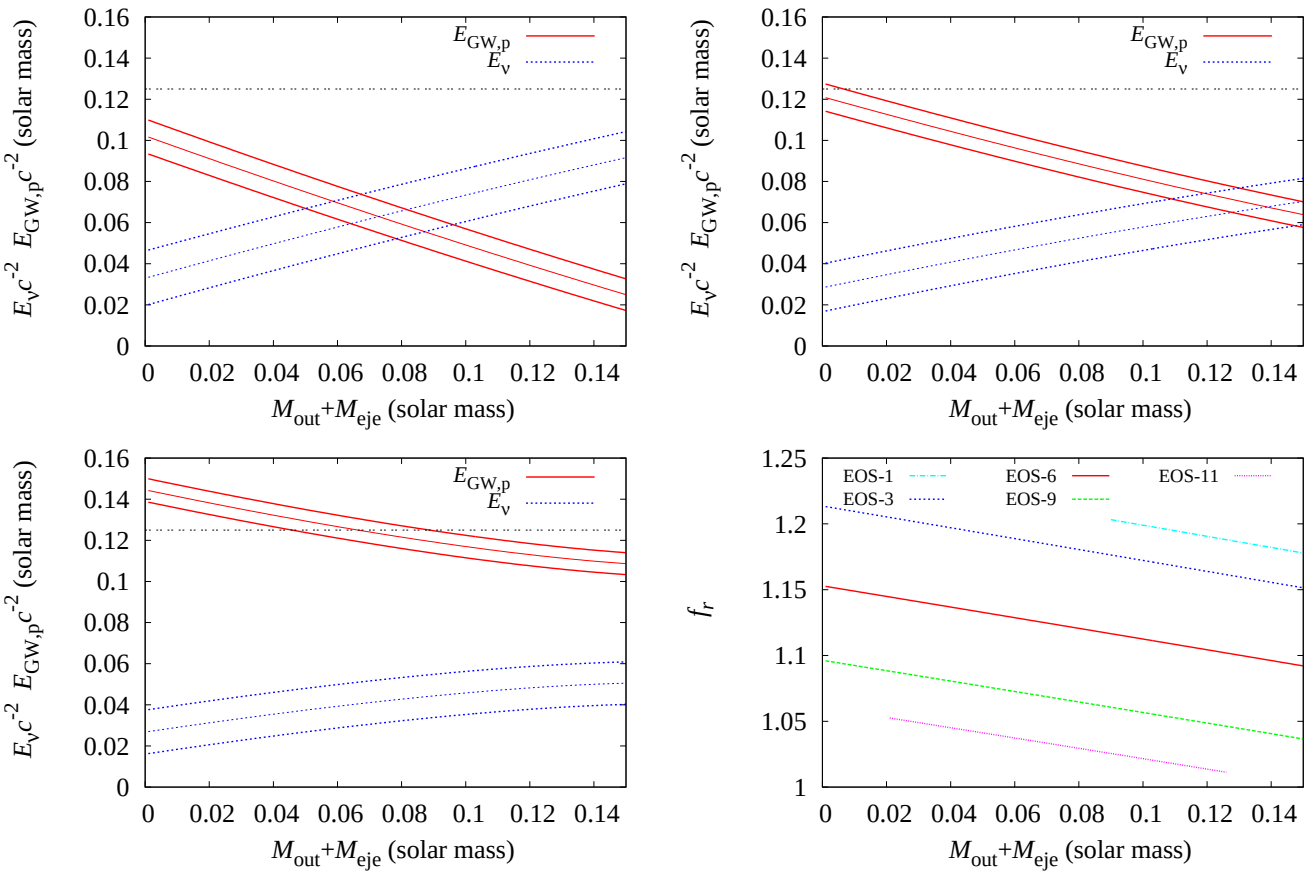

FIG. 4. Top-left, top-right, and bottom-left panels display $E_{\rm GW,p}$ and E_ν as functions of $M_{\rm out} + M_{\rm eje}$ for EOS-3, 6, and 9, respectively, and for the 1.35-1.40$M_\odot$ case. Associated with the uncertainties in J_0 and $E_{\rm GW,i}$, an uncertainty exists in $E_{\rm GW,p}$ and E_ν. The three curves for each plot in the the top-left, top-right, and bottom-left panels denote the upper and lower bounds (thick curves) as well as the central value (thin curve) for $E_{\rm GW,p}$ and E_ν. The horizontal dot-dot line shows $E_{\rm GW,p} = 0.125 M_\odot c^2$ (plausible upper limit of $E_{\rm GW,p}$ [22]). Bottom-right panel shows f_r as a function of $M_{\rm out} + M_{\rm eje}$ for EOS-1, 3, 6, 9, and 11. For EOS-1, the solution for f_r does not exist for small value of $M_{\rm out} + M_{\rm eje}$. For EOS-11, E_ν becomes negative for $M_{\rm out} + M_{\rm eje} \le 0.02 M_\odot$ and $\ge 0.127 M_\odot$, and thus, we do not plot the solution for these ranges.

$M_{\rm eje} \lesssim 0.09 M_\odot$, any solution cannot be present (cf. Fig. 3 and the bottom-right panel of Fig. 4). However, this fact does not imply that these equations of state with $M_{\rm max} \lesssim 2.1 M_\odot$ cannot be accepted. It is still possible that our assumption described in the first paragraph of Sec. II might be inappropriate (i.e., the collapse of the remnant neutron star to a black hole might occur before a rigidly rotating state was reached). If the equation of state with a low value of $M_{\rm max}$ would be the real one, the collapse to a black hole could occur in a stage that the remnant neutron star is differentially rotating for the GW170817 event. If so, the value of f_r is larger than $\gtrsim 1.2$, and thus, the collapse would occur within the angular momentum transport timescale of the remnant neutron star.

Table III and Fig. 4 show that for EOS-3–7 for which $M_{\rm max} = 2.10$–$2.25 M_\odot$, we find solutions with plausible values of $E_{\rm GW,p}$ and E_ν as $0.03 M_\odot c^2 \lesssim E_{\rm GW,p} \lesssim 0.11 M_\odot c^2$ and $0.03 M_\odot c^2 \lesssim E_\nu \lesssim 0.10 M_\odot c^2$ for plausible values of $M_{\rm out} + M_{\rm eje}$. Also, as Fig. 4 illustrates for EOS-3 and 6, reasonable solutions exist for a wide range of $M_{\rm out} + M_{\rm eje}$ for this class of the equations of state. Here, the value of E_ν indicates that the predicted lifetime of the remnant neutron star in these equations of state is of order 0.1 s to 1 s, which is also quite reasonable. Thus, we conclude that we do not have any reason to exclude equations of state with $2.10 M_\odot \lesssim M_{\rm max} \lesssim 2.25 M_\odot$. It should be emphasized that for these cases, the value of f_r is not always close to ~ 1.2 but in a wide range between 1.07 and 1.20 (see the bottom-right panel of Fig. 4). Thus, $f_r \approx 1.2$ does not always hold for many candidate equations of state.

For EOS-9 and 10 for which $M_{\rm max} \approx 2.30 M_\odot$–$2.33 M_\odot$, we can also find solutions. However, for these cases, a highly efficient energy dissipation by gravitational radiation with $E_{\rm GW,p} \gtrsim 0.11 M_\odot$ is necessary in particular for small values of $M_{\rm out} + M_{\rm eje}$ (see the bottom-left panel of Fig. 4). As found from Table II, the maximum rotational kinetic energy of the rigidly rotating neutron stars is $T_{\rm MS,R} \approx 2.5 \times 10^{53}$ erg $\approx 0.125 M_\odot c^2$. This implies

that the energy dissipated by gravitational radiation has to be comparable to the rotational kinetic energy of the remnant neutron star. To know if this class of equations of state is really viable, we have to perform a numerical-relativity simulation to check whether such efficient gravitational radiation is possible or not. However, this is beyond the scope of this paper and is left for our future study. The bottom-right panel of Fig. 4 illustrates that for this class of equations of state, the value of f_r has to be small (≤ 1.1). That is, an efficient angular momentum dissipation is supposed.

For EOS-8 of $M_{\rm max} \approx 2.25 M_\odot$, we also find solutions with high values of $E_{\rm GW,p}$. However, for this case, with high values of $M_{\rm out} + M_{\rm eje}$, the required value of $E_{\rm GW,p}$ can be reduced. Also, the maximum rotational kinetic energy of the rigidly rotating neutron stars for this equation of state is relatively high, $T_{\rm MS,R} \approx 2.8 \times 10^{53}\,{\rm erg} \approx 0.14 M_\odot c^2$. Thus, the restriction for this equation of state is not as strong as for EOS-9 and 10.

For EOS-11 for which $M_{\rm max} \approx 2.35 M_\odot$, the required energy dissipated by gravitational radiation, $E_{\rm GW,p}$, far exceeds $0.125 M_\odot c^2$ that is a plausible maximum value [22]. Moreover, for this case, $E_{\rm GW,p}$ required exceeds the maximum rotational kinetic energy of the rigidly rotating neutron stars, $T_{\rm MS,R}$. The reason why the required value of $E_{\rm GW,p}$ is very large is that for this case the value of f_r is quite small, ≤ 1.05, and thus, a large fraction of the angular momentum dissipation, $\sim 4 \times 10^{49}\,{\rm erg\,s}$, is necessary to reach a marginally stable state. However, for such significant angular momentum dissipation, unrealistically large dissipation by gravitational radiation is necessary. Therefore it is reasonable to exclude these equations of state.

To conclude, it is easy to find model equations of state with $M_{\rm max} \leq 2.25 M_\odot$ that satisfy the conservation laws of energy and angular momentum self-consistently. Also it is not impossible to find model equations of state with $M_{\rm max} \lesssim 2.3 M_\odot$ that satisfy the required laws. For these cases, f_r is not always ≈ 1.2. By contrast, it would not be easy to find an equation of state with $M_{\rm max} \geq 2.35 M_\odot$ that satisfy the required laws.

D. Stable neutron star formation: not likely

For $M_{\rm max} \gtrsim 2.4 M_\odot$, a stable neutron star could be the final outcome (e.g., EOS-12) as already mentioned above. For this case to be viable, its angular momentum (and rotational kinetic energy) has to be sufficiently small, since the observational results for the electromagnetic counterparts of GW170817 do not show the evidence for the energy injection to ejecta from strong electromagnetic radiation like the magnetic dipole radiation associated with the rotational kinetic energy of the remnant neutron star [9]. If we require that the resulting rotational kinetic energy of the stable neutron star at its age of $\sim 100\,{\rm s}$ is smaller than $10^{52}\,{\rm erg}$ (i.e., by one order of magnitude smaller than the rest-mass energy of ejecta of mass $\sim 0.05 M_\odot$), we need $J_f < 0.5 \times 10^{49}\,{\rm erg\,s}$ (see Fig. 2). Because $J_0 \approx 6.0 \times 10^{49}\,{\rm erg\,s}$ for stiff equations of state like EOS-12, we obtain a constraint as

$$J_{\rm GW,p} + J_\nu + J_{\rm out} + J_{\rm eje} \gtrsim 5.5 \times 10^{49}\,{\rm erg\,s} \approx 0.9 J_0. \tag{3.2}$$

Thus, it is necessary for the remnant neutron star to relax to a fairly slow rotation state close to a spherical star.

Figure 5 shows $f_0/f_{\rm MS} \geq 0.90$ ($f_{\rm MS} \sim 1.2$) for spherical neutron stars of $M_{\rm max} \approx 2.4 M_\odot$. Then we also obtain the following conditions from Eq. (2.8) and $E_{\rm GW,i} = (0.040 \pm 0.005) M_\odot$:

$$(E_{\rm GW,p} + E_\nu) c^{-2} + (M_{\rm out} + M_{\rm eje}) \left(1 - \frac{1}{f_{\rm MS}}\right) \leq (0.234 \pm 0.005) M_\odot. \tag{3.3}$$

Here, we supposed that the remnant neutron star would be located along a stable branch near the marginally stable sequence, and hence, we employed the equations derived in Sec. II.

In the hypothesis of this subsection, the remnant is long-lived and it is natural to suppose that $E_\nu \sim 0.1 M_\odot c^2 \approx 2 \times 10^{53}\,{\rm erg}$ or more [21]. Note that it is often mentioned that the total energy dissipated by the neutrino emission from a protoneutron star formed in each supernova would be $\sim$ (2–3) $\times 10^{53}\,{\rm erg}$ (e.g., Ref. [36]). Here, the value is larger for larger mass of the protoneutron stars. The remnant neutron star of binary neutron star mergers is more massive and hotter than the protoneutron star, and hence, it is natural to consider $E_\nu \gtrsim 3 \times 10^{53}\,{\rm erg}$. In the following, we conservatively assume that $E_\nu = 3 \times 10^{53}\,{\rm erg} \approx 0.15 M_\odot c^2$. For this case, we can estimate as $J_\nu \sim 0.5 \times 10^{49}\,{\rm erg\,s}$ using Eq. (2.13).

We also suppose $M_{\rm out} \ll M_{\rm eje}$ for $\tau \gtrsim 100\,{\rm s}$ in the following because the torus matter would accrete onto the neutron star or be ejected from the system by viscous angular momentum transport and/or propeller effect [37].

Equation (3.3) with $M_{\rm out} = 0$ gives a constraint as $(E_{\rm GW,p} + E_\nu) c^{-2} + M_{\rm eje}(1 - 1/f_{\rm MS}) \leq 0.24 M_\odot$. For $E_\nu = 0.15 M_\odot c^2$, we obtain

$$E_{\rm GW,p} c^{-2} + M_{\rm eje} \left(1 - \frac{1}{f_{\rm MS}}\right) \leq 0.09 M_\odot. \tag{3.4}$$

Now we consider two extreme cases (assume $f_{\rm MS} = 1.2$): $E_{\rm GW,p} = 0.085 M_\odot c^2$ and $M_{\rm eje} = 0.03 M_\odot$ (minimum ejecta mass required for the GW170817 event), and $E_{\rm GW,p} = 0.055 M$ and $M_{\rm eje} = 0.15 M_\odot$. Here, for the GW170817 event, the value of $M_{\rm eje}$ would be smaller than $0.15 M_\odot$.

For $E_{\rm GW,p} = 0.085 M_\odot c^2$ and $f = 2.5\,{\rm kHz}$ (which would be the possible lowest value), $J_{\rm GW,p} \approx 1.9 \times 10^{49}\,{\rm erg\,s}$. For $M_{\rm eje} = 0.03 M_\odot$, the ejection of the angular momentum would be $\approx 0.5 \times 10^{49}\,{\rm erg\,s}$ for $R_{\rm eje} \approx 200\,{\rm km}$ (cf. Eq. (2.15)). Since $J_\nu \approx 0.5 \times 10^{49}\,{\rm erg\,s}$, the constraint of Eq. (3.2) cannot be satisfied in this model at all.

For $M_{\rm eje} = 0.15 M_\odot$, the ejection of the angular momentum would be $\approx 2.5 \times 10^{49}\,{\rm erg\,s}$ for $R_{\rm eje} \approx 200\,{\rm km}$ (e.g., Eq. (2.15)). With $E_{\rm GW,p} = 0.055 M_\odot c^2$ and $f = 2.5\,{\rm Hz}$, $J_{\rm GW,p} \approx 1.3 \times 10^{49}\,{\rm erg\,s}$. For $J_\nu \approx 0.5 \times 10^{49}\,{\rm erg\,s}$, it is found that the constraint of Eq. (3.2) cannot be also satisfied in this model.

As found from the above analysis, for a larger value of $M_{\rm eje}$, $J_{\rm GW,p} + J_\nu + J_{\rm eje}$ increases. However, for the GW170817 event, $M_{\rm eje}$ is not very likely to be larger than $0.15 M_\odot$. If f is smaller than $2.5\,{\rm kHz}$, $J_{\rm GW,p}$ would be larger. However, a number of numerical-relativity simulations have shown $f \geq 2\,{\rm kHz}$ [28, 29, 38]; $J_{\rm GW,p}$ could be increased only by 20%. Thus, we conclude that it is quite difficult to find a mechanism of the angular momentum dissipation by $\approx 0.9 J_0$ in a short timescale of $\sim 100\,{\rm s}$.

Since the values of E_ν, $R_{\rm eje}$, $M_{\rm eje}$, and f have uncertainty, it is not possible to fully exclude the possibility of forming a stable neutron star. In particular, in case that E_ν could be much smaller than $3 \times 10^{53}\,{\rm erg}$, the angular momentum of the remnant neutron star could be smaller than $0.1 J_0$, e.g., by setting $E_{\rm GW,p} = 0.125 M_\odot c^2$, $E_\nu = 0.09 M_\odot c^2$, and $M_{\rm eje} = 0.15 M_\odot$ with $f = 2.5\,{\rm kHz}$ and $R_{\rm eje} = 200\,{\rm km}$. However, we need a (unphysical) fine tuning, and hence, such a possibility would not be very likely.

IV. SUMMARY

We study the constraint on the maximum mass of cold spherical neutron stars coming from the observational results of GW170817 more strictly than our previous study. We develop a framework which employs not only energy conservation law but also angular momentum conservation one, as well as solid results of latest numerical-relativity simulations and of neutron stars in equilibrium.

In this framework, we postulate that a massive neutron star was formed as a remnant after the merger in the GW170817 event, and the collapse occurred after the remnant neutron star relaxes to a rigidly rotating state. Thus, we construct several rigidly rotating neutron stars in equilibrium as models of the remnant neutron stars at the onset of collapse. In the analysis, we first give plausible values for $M_{\rm out} + M_{\rm eje}$ taking into account the observational results of electromagnetic counterparts of GW170817. Then, the energy conservation law gives a relation between the maximum mass, $M_{\rm max}$, and angular momentum of the remnant neutron star at the onset of collapse. This relation indicates that for smaller values of $M_{\rm max}$, the collapse occurs at higher angular momentum (i.e., at larger values of f_r: cf. Fig. 3). We also find that the correlation between $M_{\rm max}$ and M_f: the gravitational mass at the onset of collapse. Thus, for smaller values of $M_{\rm max}$, M_f has to be larger, i.e., less energy and angular momentum have to be dissipated prior to the onset of collapse.

We find that the energy conservation laws can be satisfied for a wide range of equations of state with various values of $f_r = 1.0$–1.2. Also, it is found that the combination of energy and angular momentum conservation laws gives plausible values of $E_{\rm GW,p}$ and E_ν for the equations of state in which $M_{\rm max}$ is between $\sim 2.1 M_\odot$ and $\sim 2.3 M_\odot$. In particular, the cases of $M_{\rm max} \lesssim 2.25 M_\odot$ result in quite plausible values of $E_{\rm GW,p}$ and E_ν. For $M_{\rm max} = 2.30 M_\odot$–$2.35 M_\odot$, it is still possible to find solutions although for such a case, we need to require large energy dissipation by gravitational radiation, $E_{\rm GW,p} \gtrsim 0.11 M_\odot c^2$. It is also found that if the value of $M_{\rm max}$ is not very high, i.e., $M_{\rm max} \leq 2.1 M_\odot$, the collapse is likely to occur before the velocity profile of the remnant neutron star relaxes to a rigidly rotating state. Thus, we infer that if $M_{\rm max} \lesssim 2.1 M_\odot$, the remnant neutron star collapses to a black hole in the timescale of angular momentum transport inside it.

The previous analysis often assumes $f_r \approx 1.2$ [7–10], i.e., the collapse occurs at a rapidly rotating stage of the remnant neutron star. As Fig. 3 shows, this assumption together with the energy conservation law would automatically leads to an inaccurate conclusion that the value of $M_{\rm max}$ is small, $\lesssim 2.1 M_\odot$ (i.e., the conclusion is derived from the assumption). The lesson obtained from our present analysis is that inappropriate assumptions could lead to an inaccurate constraint on the maximum mass.

The framework of our analysis for the maximum mass of neutron stars developed in this paper will be applied for future events, in which the remnant after the mergers is a massive neutron star that eventually collapses to a black hole, by simply replacing the values of M and $M_{\rm out} + M_{\rm eje}$. This analysis will be in particular interesting if post-merger gravitational waves are observed in future. For this case, $E_{\rm GW,p}$ and $J_{\rm GW,p}$ will be constrained, and then, the constraint for the equation of state and the value of $M_{\rm max}$ will be better imposed. Furthermore, it will be also feasible to infer how much energy is carried away by neutrinos.

ACKNOWLEDGMENTS

We thank Koutarou Kyutoku for helpful discussions. This work was in part supported by Grant-in-Aid for Scientific Research (Grant Nos. 16H02183 and 18H01213) of Japanese MEXT/JSPS. We also thank the participants of a workshop entitled "Nucleosynthesis and electromagnetic counterparts of neutron-star mergers" at Yukawa Institute for Theoretical Physics, Kyoto University (No. YITP-T-18-06) for many useful discussions. Numerical computations were performed at Oakforest-PACS at Information Technology Center of the University of Tokyo, XC50 at National Astronomical Observatory of Japan, and XC30 at Yukawa Institute for Theoretical Physics.

Appendix A: Model equations of state

To model the neutron-star equation of state with a small number of parameters, we employ a piecewise polytrope introduced by Read et al. [39]. It is a phenomenologically parametrized equation of state of the form

$$P(\rho) = \kappa_i \rho^{\Gamma_i} \quad \text{for} \quad \rho_{i-1} \le \rho < \rho_i \quad (1 \le i \le n), \qquad \text{(A1)}$$

where n is the number of the pieces used to parametrize an equation of state, ρ_i is the rest-mass density at the boundary of two neighboring ith and $(i+1)$th pieces, κ_i is the polytropic constant for the ith piece, and Γ_i is the adiabatic index for the ith piece. Here, $\rho_0 = 0$, and other parameters $(\rho_i, \kappa_i, \Gamma_i)$ are freely chosen. Requiring the continuity of the pressure at each value of ρ_i, $2n$ free parameters, (κ_i, Γ_i), determine the equation of state completely. The specific internal energy, ε, is determined by the first law of thermodynamics and continuity of each variable at ρ_i.

In this paper we employ the case of $n = 3$ and fix $\rho_2 = 10^{15}\,\mathrm{g/cm^3}$ (and $\rho_3 = \infty$). The lowest-density piece models the crust equation of state and the other two do the core equation of state. Following Ref. [39], the equation of state for the crust region is fixed by $\Gamma_1 = 1.35692395$ and $\kappa_1/c^2 = 3.99873692 \times 10^{-8}\,(\mathrm{g/cm^3})^{1-\Gamma_1}$. The equation of state for the core region is determined by two adiabatic indices, Γ_2 and Γ_3, and the pressure, p, at a fiducial density $\rho_f = 10^{14.7}\,\mathrm{g/cm^3}$. Here, p is closely related to the radius and tidal deformability of neutron stars [40]. For Γ_2, we employ a wide range of values between 2.10–5.00. Γ_3 is chosen to be small values in a narrow range between 2.00–2.91 because for the large values, the sound speed exceeds the speed of light even for stable neutron stars while for the small values, the maximum mass for given equations of state cannot exceed $2M_\odot$ [33]. The value of $\log_{10} p$ is varied between 33.8 and 34.8. Here, for large values of Γ_2, only small values of p is accepted (e.g., for $\Gamma_2 = 4.0$ and 5.0, $p \lesssim 10^{34.35}\,\mathrm{dyn/cm^2}$ and $p \lesssim 10^{33.9}\,\mathrm{dyn/cm^2}$, respectively). If this condition is not satisfied, the sound velocity exceeds the speed of light near $\rho \sim 10^{15}\,\mathrm{g/cm^3}$. With the given values of Γ_2, Γ_3, and p, κ_2, κ_3, and ρ_1 are determined as $\kappa_2 = p\rho_f^{-\Gamma_2}$, $\kappa_3 = \kappa_2 \rho_2^{\Gamma_2 - \Gamma_3}$, and $\rho_1 = (\kappa_1/\kappa_2)^{1/(\Gamma_2 - \Gamma_1)}$.

We analyzed the values of f_0 and $f_{\rm MS}$ for spherical neutron stars with the piecewise polytropes. Figure 5 displays a result. In this figure, we plot the data in the piecewise polytropes with which $2M_\odot$ neutron stars are reproduced and dimensionless tidal deformability of $1.35M_\odot$ neutron stars satisfies $\Lambda_{1.35} \le 1000$ taking into account the results of GW170817 [1]. It is found that f_0 and $f_{\rm MS}$ are in a wide range approximately between 1.08 and 1.14 and between 1.14 and 1.24, respectively. Because f_0 and $f_{\rm MS}$ are weakly correlated, $f_0/f_{\rm MS}$ is not distributed as widely as $f_{\rm MS}$, but it is still in a fairly wide range as 0.895–0.945. This value depends weakly on each mass of binaries: For 1.20–$1.55M_\odot$ binaries, the values of $f_0/f_{\rm MS}$ is 0.2–0.3% larger than that for 1.35–$1.40M_\odot$ binaries for a given equation of state.

One interesting and key fact for the context of the present paper is that $f_0/f_{\rm MS}$ is correlated with $M_{\rm max}$; for larger value of $f_0/f_{\rm MS}$, the maximum mass of neutron stars is smaller. The reason for this is that for the equations of state with smaller maximum mass, the neutron star at the maximum mass is less compact and thus has smaller value of $f_{\rm MS}$. This fact implies that for smaller maximum mass, the mass of the remnant neutron-star mass at the onset of collapse, $M_f = M f_0/f_{\rm MS} - (M_{\rm out} + M_{\rm eje})/f_{\rm MS}$, is larger (see Eq. (2.4)), and hence, the merger remnant is more subject to gravitational collapse. We note that the upper boundary of $f_0/f_{\rm MS}$ for a give value of $M_{\rm max}$ is determined by the condition of $\Lambda_{1.35} \le 1000$.

[1] B. P. Abbott et al., Phys. Rev. Lett. **119**, 116101 (2017).
[2] B. P. Abbott et al., Astrophys. J. **848**, L12 (2017).
[3] B. P. Abbott et al., Phys. Rev. Lett. **121**, 161101 (2018); Phys. Rev. D **9**, 011001 (2019).
[4] S. De, D. Finstad, J. M. Lattimer, D. A. Brown, E. Berger, and C. M. Biwer, Phys. Rev. Lett. **121**, 091102 (2018).
[5] B. P. Abbott et al., Astrophys. J. **848**, L13 (2017).
[6] M. Tanaka et al., Pub. Astro. Soc. Japan **69**, 102 (2017); D. Kasen, B. D. Metzger, J. Barnes, E. Quataert, and E. Ramirez-Ruiz, Nature **551**, 80 (2017).
[7] L. Rezzolla, E. R. Most, and L. R. Weih, Astrophys. J. **852**, L25 (2018).
[8] M. Ruiz, S. L. Shapiro, and A. Tsokaros, Phys. Rev. D **97**, 021501 (2018).
[9] B. Margalit and B. D. Metzger, Astrophys. J. **850**, L19 (2017).
[10] M. Shibata et al., Phys. Rev. D **96** (2017).
[11] A. Perego, D. Radice, and S. Bernuzzi, Astrophys. J. **850**, L37 (2017).
[12] J. Lippuner, R. Fernández, L. Robert, F. Foucart, D. Kasen, B. D. Metzger, and C. D. Ott, Mon. Not. R. Soc. Astron. **472**, 904 (2017).
[13] B. D. Metzger and A. L. Piro, Mon. Not. Roy. Astron. Soc. **439**, 3916 (2014).
[14] D. J. Price and S. Rosswog, Science **312**, 719 (2006); K. Kiuchi, K. Kyutoku, Y. Sekiguchi, M. Shibata, and T. Wada, Phys. Rev. D **90**, 041502 (2014); K. Kiuchi, P. Cerda-Duran, K. Kyutoku, Y. Sekiguchi, and M. Shibata, Phys. Rev. D **92**, 124034 (2015).
[15] S. Fujibayashi, K. Kiuchi, N. Nishimura, Y. Sekiguchi, and M. Shibata, Astrophys. J **860**, 64 (2018).
[16] J. L. Friedman, J. R. Ipser, and R. Sorkin, Astrophys. J. **325**, 722 (1988).
[17] G.B. Cook, S.L. Shapiro, and S.A Teukolsky, Astrophys. J. **423**, 823 (1994).
[18] C. Alcock, E. Farhi, and A. Olinto, Astrophys. J **310**, 261 (1986); A. Drago, A. Lavagno, and G. Pagliara, Phys.

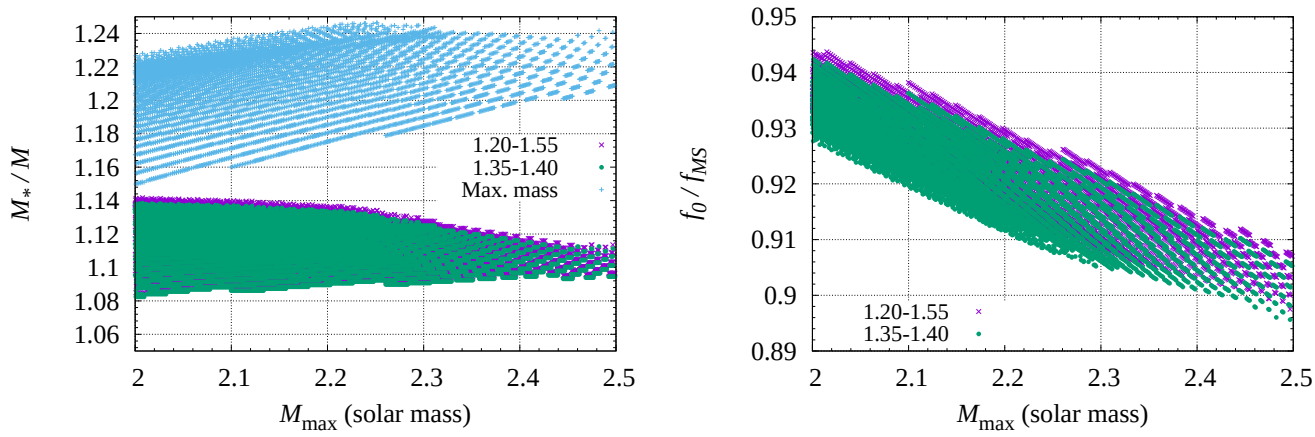

FIG. 5. Left panel: f_0 for the case of 1.20-1.55$M_\odot$ and 1.35-1.40$M_\odot$ binary neutron stars and $f_{\rm MS}$ for spherical maximum-mass stars as a function of the maximum mass for a variety of equations of state. Right panel: The same as the left panel but for $f_0/f_{\rm MS}$. We plot the data with equations of state by which $2M_\odot$ neutron stars are reproduced and dimensionless tidal deformability of $1.35M_\odot$ star, $\Lambda_{1.35}$, is smaller than 1000.

Rev. D **89**, 043014 (2014); M. G. Alford, S. Han, and M. Prakash, Phys. Rev. D **88**, 083013 (2013); G. Bozzola, P. L. Espino, C. D. Lewin, and V. Paschalidis, arxiv: 1905.00028; E. Zhou, A. Tsokaros, K. Uryū, R. X. Xu, and M. Shibata, arXiv:1902.09361; R. D. Pietri, A. Drago, A. Feo, G. Pagliara, M. Pasquali, S. Traversi, and G. Wiktorow- icz, arXiv:1904.01545.

[19] B. D. Metzger and R. Fernández, Mon. Not. Royal Astron. Soc. **441**, 3444 (2014).

[20] A. Perego., et al. on Not. R. Rstron. Aoc. **443**, 3134 (2014).

[21] S. Fujibayashi, K. Kiuchi, K. Kyutoku, N. Nishimura, Y. Sekiguchi, M. Shibata, and S. Wanajo, in preparation

[22] F. Zappa, S. Bernuzzi, D. Radice, A. Perego, and T. Dietrich, Phys. Rev. Lett. **120**, 111101 (2018).

[23] M. Shibata and K. Kiuchi, Phys. Rev. D **95**, 123003 (2017).

[24] Y. Sekiguchi, K. Kiuchi, K. Kyutoku, and M. Shibata, Phys. Rev. Lett. **107**, 051102 (2011); Phys. Rev. D **91**, 064059 (2015); Phys. Rev. D **93**, 124046 (2016).

[25] F. Foucart, R. Haas, M. D. Duez, E. O'Connor, C. D. Ott, L. Roberts, L. E. Kidder, J. Lippuner, H. P. Pfeiffer, and M. A. Scheel, Phys. Rev. D **93**, 044019 (2016).

[26] D. Radice, F. Galeazzi, J. Lippuner, L. F. Roberts, C. D. Ott, and L. Rezzolla, Mon. Not. R. Soc. Astron. **460**, 3255 (2016).

[27] C. Breu and L. Rezzolla, Mon. Not. R. Astro. Soc. **459**, 646 (2016).

[28] A. Bauswein, H.-T. Janka, K. Hebeler, and A. Schwenk, Phys. Rev. D **86**, 063001 (2012).

[29] K. Hotokezaka, K. Kiuchi, K. Kyutoku, T. Muranushi, Y. Sekiguchi, M. Shibata, and K. Taniguchi, Phys. Rev. D **88**, 044026 (2013).

[30] K. Kiuchi, K. Kawaguchi, K. Kyutoku, et al., in preparation.

[31] T. W. Baumgarte and S. L. Shapiro, Astrophys. J. **504**, 431 (1998).

[32] M. Shibata and K. Uryū, Phys. Rev. D **61**, 064001 (2000); M. Shibata, K. Taniguchi, and K. Uryū, Phys. Rev. D **71**, 084021 (2005).

[33] P. Demorest, T. Pennucci, S. Ransom, M. Roberts, and J. Hessels, Nature **467**, 1081 (2010); J. Antoniadis et al., Science, **340**, 448 (2013); H. T. Cromartie, et al., arXiv;: 1904.06759.

[34] J. D. Kaplan et al., Astrophys. J. **790**, 19 (2014).

[35] S.-Z. Li, L.-D. Liu, Y.-W. Yu, and B. Zhang, Astrophys. J. **861**, L12 (2018).

[36] Y. Suwa et al., arXiv: 1904.09996.

[37] A. L. Piro and C. D. Ott, Astrophys. J. **736**, 108 (2011).

[38] K. Takami, L. Rezzolla, and L. Baiotti, Phys. Rev. D **91**, 064001 (2015).

[39] J. Read, B. Lackey, J. L. Friedman, and B. Owen, Phys. Rev. D **79**, 124032 (2009).

[40] J. M. Lattimer and M. Prakash, Astrophys. J. **550**, 426 (2001).

The Astrophysical Journal Letters, 896:L44 (20pp), 2020 June 20 https://doi.org/10.3847/2041-8213/ab960f
© 2020. The American Astronomical Society.
OPEN ACCESS

GW190814: Gravitational Waves from the Coalescence of a 23 Solar Mass Black Hole with a 2.6 Solar Mass Compact Object

R. Abbott[1], T. D. Abbott[2], S. Abraham[3], F. Acernese[4,5], K. Ackley[6], C. Adams[7], R. X. Adhikari[1], V. B. Adya[8], C. Affeldt[9,10], M. Agathos[11,12], K. Agatsuma[13], N. Aggarwal[14], O. D. Aguiar[15], A. Aich[16], L. Aiello[17,18], A. Ain[3], P. Ajith[19], S. Akcay[11,20], G. Allen[21], A. Allocca[22], P. A. Altin[8], A. Amato[23], S. Anand[1], A. Ananyeva[1], S. B. Anderson[1], W. G. Anderson[24], S. V. Angelova[25], S. Ansoldi[26,27], S. Antier[28], S. Appert[1], K. Arai[1], M. C. Araya[1], J. S. Areeda[29], M. Arène[28], N. Arnaud[30,31], S. M. Aronson[32], K. G. Arun[33], Y. Asali[34], S. Ascenzi[17,35], G. Ashton[6], S. M. Aston[7], P. Astone[36], F. Aubin[37], P. Aufmuth[10], K. AultONeal[38], C. Austin[2], V. Avendano[39], S. Babak[28], P. Bacon[28], F. Badaracco[17,18], M. K. M. Bader[40], S. Bae[41], A. M. Baer[42], J. Baird[28], F. Baldaccini[43,44], G. Ballardin[31], S. W. Ballmer[45], A. Bals[38], A. Balsamo[42], G. Baltus[46], S. Banagiri[47], D. Bankar[3], R. S. Bankar[3], J. C. Barayoga[1], C. Barbieri[48,49], B. C. Barish[1], D. Barker[50], K. Barkett[51], P. Barneo[52], F. Barone[5,53], B. Barr[54], L. Barsotti[55], M. Barsuglia[28], D. Barta[56], J. Bartlett[50], I. Bartos[32], R. Bassiri[57], A. Basti[22,58], M. Bawaj[44,59], J. C. Bayley[54], M. Bazzan[60,61], B. Bécsy[62], M. Bejger[63], I. Belahcene[30], A. S. Bell[54], D. Beniwal[64], M. G. Benjamin[38], R. Benkel[65], J. D. Bentley[13], F. Bergamin[9], B. K. Berger[57], G. Bergmann[9,10], S. Bernuzzi[11], C. P. L. Berry[14], D. Bersanetti[66], A. Bertolini[40], J. Betzwieser[7], R. Bhandare[67], A. V. Bhandari[3], J. Bidler[29], E. Biggs[24], I. A. Bilenko[68], G. Billingsley[1], I. A. Birney[69], O. Birnholtz[70,71], S. Biscans[1,55], M. Bischi[72,73], S. Biscoveanu[55], A. Bisht[10], G. Bissenbayeva[16], M. Bitossi[22,31], M. A. Bizouard[74], J. K. Blackburn[1], J. Blackman[51], C. D. Blair[7], D. G. Blair[75], R. M. Blair[50], F. Bobba[76,77], N. Bode[9,10], M. Boer[74], Y. Boetzel[78], G. Bogaert[74], F. Bondu[79], E. Bonilla[57], R. Bonnand[37], P. Booker[9,10], B. A. Boom[40], R. Bork[1], V. Boschi[22], S. Bose[3], V. Bossilkov[75], J. Bosveld[75], Y. Bouffanais[60,61], A. Bozzi[31], C. Bradaschia[22], P. R. Brady[24], A. Bramley[7], M. Branchesi[17,18], J. E. Brau[80], M. Breschi[11], T. Briant[81], J. H. Briggs[54], F. Brighenti[72,73], A. Brillet[74], M. Brinkmann[9,10], R. Brito[36,65,82], P. Brockill[24], A. F. Brooks[1], J. Brooks[31], D. D. Brown[64], S. Brunett[1], G. Bruno[83], R. Bruntz[42], A. Buikema[55], T. Bulik[84], H. J. Bulten[40,85], A. Buonanno[65,86], D. Buskulic[37], R. L. Byer[57], M. Cabero[9,10], L. Cadonati[87], G. Cagnoli[88], C. Cahillane[1], J. Calderón Bustillo[6], J. D. Callaghan[54], T. A. Callister[1], E. Calloni[5,89], J. B. Camp[90], M. Canepa[66,91], K. C. Cannon[92], H. Cao[64], J. Cao[93], G. Carapella[76,77], F. Carbognani[31], S. Caride[94], M. F. Carney[14], G. Carullo[22,58], J. Casanueva Diaz[22], C. Casentini[35,95], J. Castañeda[52], S. Caudill[40], M. Cavaglià[96], F. Cavalier[30], R. Cavalieri[31], G. Cella[22], P. Cerdá-Durán[97], E. Cesarini[35,98], O. Chaibi[74], K. Chakravarti[3], C. Chan[92], M. Chan[54], S. Chao[99], P. Charlton[100], E. A. Chase[14], E. Chassande-Mottin[28], D. Chatterjee[24], M. Chaturvedi[67], K. Chatziioannou[101,102], H. Y. Chen[103], X. Chen[75], Y. Chen[51], H.-P. Cheng[32], C. K. Cheong[104], H. Y. Chia[32], F. Chiadini[77,105], R. Chierici[106], A. Chincarini[66], A. Chiummo[31], G. Cho[107], H. S. Cho[108], M. Cho[86], N. Christensen[74], Q. Chu[75], S. Chua[81], K. W. Chung[104], S. Chung[75], G. Ciani[60,61], P. Ciecielag[63], M. Cieślar[63], A. A. Ciobanu[64], R. Ciolfi[61,109], F. Cipriano[74], A. Cirone[66,91], F. Clara[50], J. A. Clark[87], P. Clearwater[110], S. Clesse[83], F. Cleva[74], E. Coccia[17,18], P.-F. Cohadon[81], D. Cohen[30], M. Colleoni[111], C. G. Collette[112], C. Collins[13], M. Colpi[48,49], M. Constancio, Jr.[15], L. Conti[61], S. J. Cooper[13], P. Corban[7], T. R. Corbitt[2], I. Cordero-Carrión[113], S. Corezzi[43,44], K. R. Corley[34], N. Cornish[62], D. Corre[30], A. Corsi[94], S. Cortese[31], C. A. Costa[15], R. Cotesta[65], M. W. Coughlin[1], S. B. Coughlin[14,114], J.-P. Coulon[74], S. T. Countryman[34], P. Couvares[1], P. B. Covas[111], D. M. Coward[75], M. J. Cowart[7], D. C. Coyne[1], R. Coyne[115], J. D. E. Creighton[24], T. D. Creighton[16], J. Cripe[2], M. Croquette[81], S. G. Crowder[116], J.-R. Cudell[46], T. J. Cullen[2], A. Cumming[54], R. Cummings[54], L. Cunningham[54], E. Cuoco[31], M. Curylo[84], T. Dal Canton[65], G. Dálya[117], A. Dana[57], L. M. Daneshgaran-Bajastani[118], B. D'Angelo[66,91], S. L. Danilishin[9,10], S. D'Antonio[35], K. Danzmann[9,10], C. Darsow-Fromm[119], A. Dasgupta[120], L. E. H. Datrier[54], V. Dattilo[31], I. Dave[67], M. Davier[30], G. S. Davies[121], D. Davis[45], E. J. Daw[122], D. DeBra[57], M. Deenadayalan[3], J. Degallaix[23], M. De Laurentis[5,89], S. Deléglise[81], M. Delfavero[70], N. De Lillo[54], W. Del Pozzo[22,58], L. M. DeMarchi[14], V. D'Emilio[114], N. Demos[55], T. Dent[121], R. De Pietri[123,124], R. De Rosa[5,89], C. De Rossi[31], R. DeSalvo[125], O. de Varona[9,10], S. Dhurandhar[3], M. C. Díaz[16], M. Diaz-Ortiz, Jr.[32], T. Dietrich[40], L. Di Fiore[5], C. Di Fronzo[13], C. Di Giorgio[76,77], F. Di Giovanni[97], M. Di Giovanni[126,127], T. Di Girolamo[5,89], A. Di Lieto[22,58], B. Ding[112], S. Di Pace[36,82], I. Di Palma[36,82], F. Di Renzo[22,58], A. K. Divakarla[32], A. Dmitriev[13], Z. Doctor[103], F. Donovan[55], K. L. Dooley[114], S. Doravari[3], I. Dorrington[114], T. P. Downes[24], M. Drago[17,18], J. C. Driggers[50], Z. Du[93], J.-G. Ducoin[30], P. Dupej[54], O. Durante[76,77], D. D'Urso[128,129], S. E. Dwyer[50], P. J. Easter[6], G. Eddolls[54], B. Edelman[80], T. B. Edo[122], O. Edy[130], A. Effler[7], P. Ehrens[1], J. Eichholz[8], S. S. Eikenberry[32], M. Eisenmann[37], R. A. Eisenstein[55], A. Ejlli[114], L. Errico[5,89], R. C. Essick[103], H. Estelles[111], D. Estevez[37], Z. B. Etienne[131], T. Etzel[1], M. Evans[55], T. M. Evans[7], B. E. Ewing[132], V. Fafone[17,35,95], S. Fairhurst[114], X. Fan[93], S. Farinon[66], B. Farr[80], W. M. Farr[101,102], E. J. Fauchon-Jones[114], M. Favata[39], M. Fays[122], M. Fazio[133], J. Feicht[1], M. M. Fejer[57], F. Feng[28], E. Fenyvesi[56,134], D. L. Ferguson[87], A. Fernandez-Galiana[55], I. Ferrante[22,58], E. C. Ferreira[15], T. A. Ferreira[15], F. Fidecaro[22,58], I. Fiori[31], D. Fiorucci[17,18], M. Fishbach[103], R. P. Fisher[42], R. Fittipaldi[77,135], M. Fitz-Axen[47], V. Fiumara[77,136], R. Flaminio[37,137], E. Floden[47], E. Flynn[29], H. Fong[92], J. A. Font[97,138], P. W. F. Forsyth[8], J.-D. Fournier[74], S. Frasca[36,82], F. Frasconi[22], Z. Frei[117], A. Freise[13], R. Frey[80], V. Frey[30], P. Fritschel[55], V. V. Frolov[7], G. Fronzè[139], P. Fulda[32], M. Fyffe[7], H. A. Gabbard[54], B. U. Gadre[65], S. M. Gaebel[13], J. R. Gair[65], S. Galaudage[6], D. Ganapathy[55], A. Ganguly[19], S. G. Gaonkar[3], C. García-Quirós[111], F. Garufi[5,89], B. Gateley[50], S. Gaudio[38], V. Gayathri[140], G. Gemme[66], E. Genin[31], A. Gennai[22], D. George[21], J. George[67], L. Gergely[141], S. Ghonge[87], Abhirup Ghosh[65], Archisman Ghosh[40,142,143,144], S. Ghosh[24], B. Giacomazzo[126,127], J. A. Giaime[2,7], K. D. Giardina[7],

D. R. Gibson[69], C. Gier[25], K. Gill[34], J. Glanzer[2], J. Gniesmer[119], P. Godwin[132], E. Goetz[2,96], R. Goetz[32], N. Gohlke[9,10], B. Goncharov[6], G. González[2], A. Gopakumar[145], S. E. Gossan[1], M. Gosselin[22,31,58], R. Gouaty[37], B. Grace[8], A. Grado[5,146], M. Granata[23], A. Grant[54], S. Gras[55], P. Grassia[1], C. Gray[50], R. Gray[54], G. Greco[72,73], A. C. Green[32], R. Green[114], E. M. Gretarsson[38], H. L. Griggs[87], G. Grignani[43,44], A. Grimaldi[126,127], S. J. Grimm[17,18], H. Grote[114], S. Grunewald[65], P. Gruning[30], G. M. Guidi[72,73], A. R. Guimaraes[2], G. Guixé[52], H. K. Gulati[120], Y. Guo[40], A. Gupta[132], Anchal Gupta[1], P. Gupta[40], E. K. Gustafson[1], R. Gustafson[147], L. Haegel[111], O. Halim[17,18], E. D. Hall[55], E. Z. Hamilton[114], G. Hammond[54], M. Haney[78], M. M. Hanke[9,10], J. Hanks[50], C. Hanna[132], M. D. Hannam[114], O. A. Hannuksela[104], T. J. Hansen[38], J. Hanson[7], T. Harder[74], T. Hardwick[2], K. Haris[19], J. Harms[17,18], G. M. Harry[148], I. W. Harry[130], R. K. Hasskew[7], C.-J. Haster[55], K. Haughian[54], F. J. Hayes[54], J. Healy[70], A. Heidmann[81], M. C. Heintze[7], J. Heinze[9,10], H. Heitmann[74], F. Hellman[149], P. Hello[30], G. Hemming[31], M. Hendry[54], I. S. Heng[54], E. Hennes[40], J. Hennig[9,10], M. Heurs[9,10], S. Hild[54,150], T. Hinderer[40,142,144], S. Y. Hoback[29,148], S. Hochheim[9,10], E. Hofgard[57], D. Hofman[23], A. M. Holgado[21], N. A. Holland[8], K. Holt[7], D. E. Holz[103], P. Hopkins[114], C. Horst[24], J. Hough[54], E. J. Howell[75], C. G. Hoy[114], Y. Huang[55], M. T. Hübner[6], E. A. Huerta[21], D. Huet[30], B. Hughey[38], V. Hui[37], S. Husa[111], S. H. Huttner[54], R. Huxford[132], T. Huynh-Dinh[7], B. Idzkowski[84], A. Iess[35,95], H. Inchauspe[32], C. Ingram[64], G. Intini[36,82], J.-M. Isac[81], M. Isi[55], B. R. Iyer[19], T. Jacqmin[81], S. J. Jadhav[151], S. P. Jadhav[3], A. L. James[114], K. Jani[87], N. N. Janthalur[151], P. Jaranowski[152], D. Jariwala[32], R. Jaume[111], A. C. Jenkins[153], J. Jiang[32], G. R. Johns[42], N. K. Johnson-McDaniel[12], A. W. Jones[13], D. I. Jones[154], J. D. Jones[50], P. Jones[13], R. Jones[54], R. J. G. Jonker[40], L. Ju[75], J. Junker[9,10], C. V. Kalaghatgi[114], V. Kalogera[14], B. Kamai[1], S. Kandhasamy[3], G. Kang[41], J. B. Kanner[1], S. J. Kapadia[19], S. Karki[80], R. Kashyap[19], M. Kasprzack[1], W. Kastaun[9,10], S. Katsanevas[31], E. Katsavounidis[55], W. Katzman[7], S. Kaufer[10], K. Kawabe[50], F. Kéfélian[74], D. Keitel[130], A. Keivani[34], R. Kennedy[122], J. S. Key[155], S. Khadka[57], F. Y. Khalili[68], I. Khan[17,35], S. Khan[9,10], Z. A. Khan[93], E. A. Khazanov[156], N. Khetan[17,18], M. Khursheed[67], N. Kijbunchoo[8], Chunglee Kim[157], G. J. Kim[87], J. C. Kim[158], K. Kim[104], W. Kim[64], W. S. Kim[159], Y.-M. Kim[160], C. Kimball[14], P. J. King[50], M. Kinley-Hanlon[54], R. Kirchhoff[9,10], J. S. Kissel[50], L. Kleybolte[119], S. Klimenko[32], T. D. Knowles[131], E. Knyazev[55], P. Koch[9,10], S. M. Koehlenbeck[9,10], G. Koekoek[40,150], S. Koley[40], V. Kondrashov[1], A. Kontos[161], N. Koper[9,10], M. Korobko[119], W. Z. Korth[1], M. Kovalam[75], D. B. Kozak[1], V. Kringel[9,10], N. V. Krishnendu[33], A. Królak[162,163], N. Krupinski[24], G. Kuehn[9,10], A. Kumar[151], P. Kumar[164], Rahul Kumar[50], Rakesh Kumar[120], S. Kumar[19], L. Kuo[99], A. Kutynia[162], B. D. Lackey[65], D. Laghi[22,58], E. Lalande[165], T. L. Lam[104], A. Lamberts[74,166], M. Landry[50], P. Landry[29], B. B. Lane[55], R. N. Lang[167], J. Lange[70], B. Lantz[57], R. K. Lanza[55], I. La Rosa[37], A. Lartaux-Vollard[30], P. D. Lasky[6], M. Laxen[7], A. Lazzarini[1], C. Lazzaro[61], P. Leaci[36,82], S. Leavey[9,10], Y. K. Lecoeuche[50], C. H. Lee[108], H. M. Lee[168], H. W. Lee[158], J. Lee[107], K. Lee[57], J. Lehmann[9,10], N. Leroy[30], N. Letendre[37], Y. Levin[6], A. K. Y. Li[104], J. Li[93], K. li[104], T. G. F. Li[104], X. Li[51], F. Linde[40,169], S. D. Linker[118], J. N. Linley[54], T. B. Littenberg[170], J. Liu[9,10], X. Liu[24], M. Llorens-Monteagudo[97], R. K. L. Lo[1], A. Lockwood[171], L. T. London[55], A. Longo[172,173], M. Lorenzini[17,18], V. Loriette[174], M. Lormand[7], G. Losurdo[22], J. D. Lough[9,10], C. O. Lousto[70], G. Lovelace[29], H. Lück[9,10], D. Lumaca[35,95], A. P. Lundgren[130], Y. Ma[51], R. Macas[114], S. Macfoy[25], M. MacInnis[55], D. M. Macleod[114], I. A. O. MacMillan[148], A. Macquet[74], I. Magaña Hernandez[24], F. Magaña-Sandoval[32], R. M. Magee[132], E. Majorana[36], I. Maksimovic[174], A. Malik[67], N. Man[74], V. Mandic[47], V. Mangano[36,54,82], G. L. Mansell[50,55], M. Manske[24], M. Mantovani[31], M. Mapelli[60,61], F. Marchesoni[44,59,175], F. Marion[37], S. Márka[34], Z. Márka[34], C. Markakis[12], A. S. Markosyan[57], A. Markowitz[1], E. Maros[1], A. Marquina[113], S. Marsat[28], F. Martelli[72,73], I. W. Martin[54], R. M. Martin[39], V. Martinez[88], D. V. Martynov[13], H. Masalehdan[119], K. Mason[55], E. Massera[122], A. Masserot[37], T. J. Massinger[55], M. Masso-Reid[54], S. Mastrogiovanni[28], A. Matas[65], F. Matichard[1,55], N. Mavalvala[55], E. Maynard[2], J. J. McCann[75], R. McCarthy[50], D. E. McClelland[8], S. McCormick[7], L. McCuller[55], S. C. McGuire[176], C. McIsaac[130], J. McIver[1], D. J. McManus[8], T. McRae[8], S. T. McWilliams[131], D. Meacher[24], G. D. Meadors[6], M. Mehmet[9,10], A. K. Mehta[19], E. Mejuto Villa[77,125], A. Melatos[110], G. Mendell[50], R. A. Mercer[24], L. Mereni[23], K. Merfeld[80], E. L. Merilh[50], J. D. Merritt[80], M. Merzougui[74], S. Meshkov[1], C. Messenger[54], C. Messick[177], R. Metzdorff[81], P. M. Meyers[110], F. Meylahn[9,10], A. Mhaske[3], A. Miani[126,127], H. Miao[13], I. Michaloliakos[32], C. Michel[23], H. Middleton[110], L. Milano[5,89], A. L. Miller[32,36,82], M. Millhouse[110], J. C. Mills[114], E. Milotti[27,178], M. C. Milovich-Goff[118], O. Minazzoli[74,179], Y. Minenkov[35], A. Mishkin[32], C. Mishra[180], T. Mistry[122], S. Mitra[3], V. P. Mitrofanov[68], G. Mitselmakher[32], R. Mittleman[55], G. Mo[55], K. Mogushi[96], S. R. P. Mohapatra[55], S. R. Mohite[24], M. Molina-Ruiz[149], M. Mondin[118], M. Montani[72,73], C. J. Moore[13], D. Moraru[50], F. Morawski[63], G. Moreno[50], S. Morisaki[92], B. Mours[181], C. M. Mow-Lowry[13], S. Mozzon[130], F. Muciaccia[36,82], Arunava Mukherjee[54], D. Mukherjee[132], S. Mukherjee[16], Subroto Mukherjee[120], N. Mukund[9,10], A. Mullavey[7], J. Munch[64], E. A. Muñiz[45], P. G. Murray[54], A. Nagar[98,139,182], I. Nardecchia[35,95], L. Naticchioni[36,82], R. K. Nayak[183], B. F. Neil[75], J. Neilson[77,125], G. Nelemans[40,184], T. J. N. Nelson[7], M. Nery[9,10], A. Neunzert[147], K. Y. Ng[55], S. Ng[64], C. Nguyen[28], P. Nguyen[80], D. Nichols[40,144], S. A. Nichols[2], S. Nissanke[40,144], F. Nocera[31], M. Noh[55], C. North[114], D. Nothard[185], L. K. Nuttall[130], J. Oberling[50], B. D. O'Brien[32], G. Oganesyan[17,18], G. H. Ogin[186], J. J. Oh[159], S. H. Oh[159], F. Ohme[9,10], H. Ohta[92], M. A. Okada[15], M. Oliver[111], C. Olivetto[31], P. Oppermann[9,10], Richard J. Oram[7], B. O'Reilly[7], R. G. Ormiston[47], L. F. Ortega[32], R. O'Shaughnessy[70], S. Ossokine[65], C. Osthelder[1], D. J. Ottaway[64], H. Overmier[7], B. J. Owen[94], A. E. Pace[132], G. Pagano[22,58], M. A. Page[75], G. Pagliaroli[17,18], A. Pai[140], S. A. Pai[67], J. R. Palamos[80], O. Palashov[156], C. Palomba[36], H. Pan[99], P. K. Panda[151], P. T. H. Pang[40], C. Pankow[14], F. Pannarale[36,82], B. C. Pant[67], F. Paoletti[22], A. Paoli[31], A. Parida[3], W. Parker[7,176], D. Pascucci[40,54], A. Pasqualetti[31], R. Passaquieti[22,58], D. Passuello[22], B. Patricelli[22,58], E. Payne[6], B. L. Pearlstone[54], T. C. Pechsiri[32], A. J. Pedersen[45], M. Pedraza[1], A. Pele[7], S. Penn[187], A. Perego[126,127], C. J. Perez[50], C. Périgois[37], A. Perreca[126,127], S. Perriès[106], J. Petermann[119], H. P. Pfeiffer[65],

M. Phelps[9,10], K. S. Phukon[3,40,169], O. J. Piccinni[36,82], M. Pichot[74], M. Piendibene[22,58], F. Piergiovanni[72,73], V. Pierro[77,125], G. Pillant[31], L. Pinard[23], I. M. Pinto[77,98,125], K. Piotrzkowski[83], M. Pirello[50], M. Pitkin[188], W. Plastino[172,173], R. Poggiani[22,58], D. Y. T. Pong[104], S. Ponrathnam[3], P. Popolizio[31], E. K. Porter[28], J. Powell[189], A. K. Prajapati[120], K. Prasai[57], R. Prasanna[151], G. Pratten[13], T. Prestegard[24], M. Principe[77,98,125], G. A. Prodi[126,127], L. Prokhorov[13], M. Punturo[44], P. Puppo[36], M. Pürrer[65], H. Qi[114], V. Quetschke[16], P. J. Quinonez[38], F. J. Raab[50], G. Raaijmakers[40,144], H. Radkins[50], N. Radulesco[74], P. Raffai[117], H. Rafferty[190], S. Raja[67], C. Rajan[67], B. Rajbhandari[94], M. Rakhmanov[16], K. E. Ramirez[16], A. Ramos-Buades[111], Javed Rana[3], K. Rao[14], P. Rapagnani[36,82], V. Raymond[114], M. Razzano[22,58], J. Read[29], T. Regimbau[37], L. Rei[66], S. Reid[25], D. H. Reitze[1,32], P. Rettegno[139,191], F. Ricci[36,82], C. J. Richardson[38], J. W. Richardson[1], P. M. Ricker[21], G. Riemenschneider[139,191], K. Riles[147], M. Rizzo[14], N. A. Robertson[1,54], F. Robinet[30], A. Rocchi[35], R. D. Rodriguez-Soto[38], L. Rolland[37], J. G. Rollins[1], V. J. Roma[80], M. Romanelli[79], R. Romano[4,5], C. L. Romel[50], I. M. Romero-Shaw[6], J. H. Romie[7], C. A. Rose[24], D. Rose[29], K. Rose[185], D. Rosińska[84], S. G. Rosofsky[21], M. P. Ross[171], S. Rowan[54], S. J. Rowlinson[13], P. K. Roy[16], Santosh Roy[3], Soumen Roy[192], P. Ruggi[31], G. Rutins[69], K. Ryan[50], S. Sachdev[132], T. Sadecki[50], M. Sakellariadou[153], O. S. Salafia[48,49,193], L. Salconi[31], M. Saleem[33], F. Salemi[126], A. Samajdar[40], E. J. Sanchez[1], L. E. Sanchez[1], N. Sanchis-Gual[194], J. R. Sanders[195], K. A. Santiago[39], E. Santos[74], N. Sarin[6], B. Sassolas[23], B. S. Sathyaprakash[114,132], O. Sauter[37], R. L. Savage[50], V. Savant[3], D. Sawant[140], S. Sayah[23], D. Schaetzl[1], P. Schale[80], M. Scheel[51], J. Scheuer[14], P. Schmidt[13], R. Schnabel[119], R. M. S. Schofield[80], A. Schönbeck[119], E. Schreiber[9,10], B. W. Schulte[9,10], B. F. Schutz[114], O. Schwarm[186], E. Schwartz[7], J. Scott[54], S. M. Scott[8], E. Seidel[21], D. Sellers[7], A. S. Sengupta[192], N. Sennett[65], D. Sentenac[31], V. Sequino[66], A. Sergeev[156], Y. Setyawati[9,10], D. A. Shaddock[8], T. Shaffer[50], M. S. Shahriar[14], A. Sharma[17,18], P. Sharma[67], P. Shawhan[86], H. Shen[21], M. Shikauchi[92], R. Shink[165], D. H. Shoemaker[55], D. M. Shoemaker[87], K. Shukla[149], S. ShyamSundar[67], K. Siellez[87], M. Sieniawska[63], D. Sigg[50], L. P. Singer[90], D. Singh[132], N. Singh[84], A. Singha[54], A. Singhal[17,36], A. M. Sintes[111], V. Sipala[128,129], V. Skliris[114], B. J. J. Slagmolen[8], T. J. Slaven-Blair[75], J. Smetana[13], J. R. Smith[29], R. J. E. Smith[6], S. Somala[196], E. J. Son[159], S. Soni[2], B. Sorazu[54], V. Sordini[106], F. Sorrentino[66], T. Souradeep[3], E. Sowell[94], A. P. Spencer[54], M. Spera[14,60,61], A. K. Srivastava[120], V. Srivastava[45], K. Staats[14], C. Stachie[74], M. Standke[9,10], D. A. Steer[28], J. Steinhoff[65], M. Steinke[9,10], J. Steinlechner[54,119], S. Steinlechner[119], D. Steinmeyer[9,10], S. Stevenson[189], D. Stocks[57], D. J. Stops[13], M. Stover[185], K. A. Strain[54], G. Stratta[73,197], A. Strunk[50], R. Sturani[198], A. L. Stuver[199], S. Sudhagar[3], V. Sudhir[55], T. Z. Summerscales[200], L. Sun[1], S. Sunil[120], A. Sur[63], J. Suresh[92], P. J. Sutton[114], B. L. Swinkels[40], M. J. Szczepańczyk[32], M. Tacca[40], S. C. Tait[54], C. Talbot[6], A. J. Tanasijczuk[83], D. B. Tanner[32], D. Tao[1], M. Tápai[141], A. Tapia[29], E. N. Tapia San Martin[40], J. D. Tasson[201], R. Taylor[1], R. Tenorio[111], L. Terkowski[119], M. P. Thirugnanasambandam[3], M. Thomas[7], P. Thomas[50], J. E. Thompson[114], S. R. Thondapu[67], K. A. Thorne[7], E. Thrane[6], C. L. Tinsman[6], T. R. Saravanan[3], Shubhanshu Tiwari[78,126,127], S. Tiwari[145], V. Tiwari[114], K. Toland[54], M. Tonelli[22,58], Z. Tornasi[54], A. Torres-Forné[65], C. I. Torrie[1], I. Tosta e Melo[128,129], D. Töyrä[8], E. A. Trail[2], F. Travasso[44,59], G. Traylor[7], M. C. Tringali[84], A. Tripathee[147], A. Trovato[28], R. J. Trudeau[1], K. W. Tsang[40], M. Tse[55], R. Tso[51], L. Tsukada[92], D. Tsuna[92], T. Tsutsui[92], M. Turconi[74], A. S. Ubhi[13], K. Ueno[92], D. Ugolini[190], C. S. Unnikrishnan[145], A. L. Urban[2], S. A. Usman[103], A. C. Utina[54], H. Vahlbruch[10], G. Vajente[1], G. Valdes[2], M. Valentini[126,127], N. van Bakel[40], M. van Beuzekom[40], J. F. J. van den Brand[40,85,150], C. Van Den Broeck[40,202], D. C. Vander-Hyde[45], L. van der Schaaf[40], J. V. Van Heijningen[75], A. A. van Veggel[54], M. Vardaro[40,169], V. Varma[51], S. Vass[1], M. Vasúth[56], A. Vecchio[13], G. Vedovato[61], J. Veitch[54], P. J. Veitch[64], K. Venkateswara[171], G. Venugopalan[1], D. Verkindt[37], D. Veske[34], F. Vetrano[72,73], A. Viceré[72,73], A. D. Viets[203], S. Vinciguerra[13], D. J. Vine[69], J.-Y. Vinet[74], S. Vitale[55], Francisco Hernandez Vivanco[6], T. Vo[45], H. Vocca[43,44], C. Vorvick[50], S. P. Vyatchanin[68], A. R. Wade[8], L. E. Wade[185], M. Wade[185], R. Walet[40], M. Walker[29], G. S. Wallace[25], L. Wallace[1], S. Walsh[24], J. Z. Wang[147], S. Wang[21], W. H. Wang[16], R. L. Ward[8], Z. A. Warden[38], J. Warner[50], M. Was[37], J. Watchi[112], B. Weaver[50], L.-W. Wei[9,10], M. Weinert[9,10], A. J. Weinstein[1], R. Weiss[55], F. Wellmann[9,10], L. Wen[75], P. Weßels[9,10], J. W. Westhouse[38], K. Wette[8], J. T. Whelan[70], B. F. Whiting[32], C. Whittle[55], D. M. Wilken[9,10], D. Williams[54], J. L. Willis[1], B. Willke[9,10], W. Winkler[9,10], C. C. Wipf[1], H. Wittel[9,10], G. Woan[54], J. Woehler[9,10], J. K. Wofford[70], C. Wong[104], J. L. Wright[54], D. S. Wu[9,10], D. M. Wysocki[70], L. Xiao[1], H. Yamamoto[1], L. Yang[133], Y. Yang[32], Z. Yang[47], M. J. Yap[8], M. Yazback[32], D. W. Yeeles[114], Hang Yu[55], Haocun Yu[55], S. H. R. Yuen[104], A. K. Zadrożny[16], A. Zadrożny[162], M. Zanolin[38], T. Zelenova[31], J.-P. Zendri[61], M. Zevin[14], J. Zhang[75], L. Zhang[1], T. Zhang[54], C. Zhao[75], G. Zhao[112], M. Zhou[14], Z. Zhou[14], X. J. Zhu[6], A. B. Zimmerman[177], M. E. Zucker[1,55], and J. Zweizig[1]

LIGO Scientific Collaboration and Virgo Collaboration

[1] LIGO, California Institute of Technology, Pasadena, CA 91125, USA
[2] Louisiana State University, Baton Rouge, LA 70803, USA
[3] Inter-University Centre for Astronomy and Astrophysics, Pune 411007, India
[4] Dipartimento di Farmacia, Università di Salerno, I-84084 Fisciano, Salerno, Italy
[5] INFN, Sezione di Napoli, Complesso Universitario di Monte S. Angelo, I-80126 Napoli, Italy
[6] OzGrav, School of Physics & Astronomy, Monash University, Clayton 3800, Victoria, Australia
[7] LIGO Livingston Observatory, Livingston, LA 70754, USA
[8] OzGrav, Australian National University, Canberra, Australian Capital Territory 0200, Australia
[9] Max Planck Institute for Gravitational Physics (Albert Einstein Institute), D-30167 Hannover, Germany
[10] Leibniz Universität Hannover, D-30167 Hannover, Germany
[11] Theoretisch-Physikalisches Institut, Friedrich-Schiller-Universität Jena, D-07743 Jena, Germany
[12] University of Cambridge, Cambridge CB2 1TN, UK
[13] University of Birmingham, Birmingham B15 2TT, UK
[14] Center for Interdisciplinary Exploration & Research in Astrophysics (CIERA), Northwestern University, Evanston, IL 60208, USA
[15] Instituto Nacional de Pesquisas Espaciais, 12227-010 São José dos Campos, São Paulo, Brazil

[16] The University of Texas Rio Grande Valley, Brownsville, TX 78520, USA
[17] Gran Sasso Science Institute (GSSI), I-67100 L'Aquila, Italy
[18] INFN, Laboratori Nazionali del Gran Sasso, I-67100 Assergi, Italy
[19] International Centre for Theoretical Sciences, Tata Institute of Fundamental Research, Bengaluru 560089, India
[20] University College Dublin, Dublin 4, Ireland
[21] NCSA, University of Illinois at Urbana-Champaign, Urbana, IL 61801, USA
[22] INFN, Sezione di Pisa, I-56127 Pisa, Italy
[23] Laboratoire des Matériaux Avancés (LMA), IP2I—UMR 5822, CNRS, Université de Lyon, F-69622 Villeurbanne, France
[24] University of Wisconsin-Milwaukee, Milwaukee, WI 53201, USA
[25] SUPA, University of Strathclyde, Glasgow G1 1XQ, UK
[26] Dipartimento di Matematica e Informatica, Università di Udine, I-33100 Udine, Italy
[27] INFN, Sezione di Trieste, I-34127 Trieste, Italy
[28] APC, AstroParticule et Cosmologie, Université Paris Diderot, CNRS/IN2P3, CEA/Irfu, Observatoire de Paris, Sorbonne Paris Cité, F-75205 Paris Cedex 13, France
[29] California State University Fullerton, Fullerton, CA 92831, USA
[30] LAL, Univ. Paris-Sud, CNRS/IN2P3, Université Paris-Saclay, F-91898 Orsay, France
[31] European Gravitational Observatory (EGO), I-56021 Cascina, Pisa, Italy
[32] University of Florida, Gainesville, FL 32611, USA
[33] Chennai Mathematical Institute, Chennai 603103, India
[34] Columbia University, New York, NY 10027, USA
[35] INFN, Sezione di Roma Tor Vergata, I-00133 Roma, Italy
[36] INFN, Sezione di Roma, I-00185 Roma, Italy
[37] Laboratoire d'Annecy de Physique des Particules (LAPP), Univ. Grenoble Alpes, Université Savoie Mont Blanc, CNRS/IN2P3, F-74941 Annecy, France
[38] Embry-Riddle Aeronautical University, Prescott, AZ 86301, USA
[39] Montclair State University, Montclair, NJ 07043, USA
[40] Nikhef, Science Park 105, 1098 XG Amsterdam, The Netherlands
[41] Korea Institute of Science and Technology Information, Daejeon 34141, Republic of Korea
[42] Christopher Newport University, Newport News, VA 23606, USA
[43] Università di Perugia, I-06123 Perugia, Italy
[44] INFN, Sezione di Perugia, I-06123 Perugia, Italy
[45] Syracuse University, Syracuse, NY 13244, USA
[46] Université de Liège, B-4000 Liège, Belgium
[47] University of Minnesota, Minneapolis, MN 55455, USA
[48] Università degli Studi di Milano-Bicocca, I-20126 Milano, Italy
[49] INFN, Sezione di Milano-Bicocca, I-20126 Milano, Italy
[50] LIGO Hanford Observatory, Richland, WA 99352, USA
[51] Caltech CaRT, Pasadena, CA 91125, USA
[52] Departament de Física Quàntica i Astrofísica, Institut de Ciències del Cosmos (ICCUB), Universitat de Barcelona (IEEC-UB), E-08028 Barcelona, Spain
[53] Dipartimento di Medicina, Chirurgia e Odontoiatria "Scuola Medica Salernitana," Università di Salerno, I-84081 Baronissi, Salerno, Italy
[54] SUPA, University of Glasgow, Glasgow G12 8QQ, UK
[55] LIGO, Massachusetts Institute of Technology, Cambridge, MA 02139, USA
[56] Wigner RCP, RMKI, H-1121 Budapest, Konkoly Thege Miklós út 29-33, Hungary
[57] Stanford University, Stanford, CA 94305, USA
[58] Università di Pisa, I-56127 Pisa, Italy
[59] Università di Camerino, Dipartimento di Fisica, I-62032 Camerino, Italy
[60] Università di Padova, Dipartimento di Fisica e Astronomia, I-35131 Padova, Italy
[61] INFN, Sezione di Padova, I-35131 Padova, Italy
[62] Montana State University, Bozeman, MT 59717, USA
[63] Nicolaus Copernicus Astronomical Center, Polish Academy of Sciences, 00-716, Warsaw, Poland
[64] OzGrav, University of Adelaide, Adelaide, South Australia 5005, Australia
[65] Max Planck Institute for Gravitational Physics (Albert Einstein Institute), D-14476 Potsdam-Golm, Germany
[66] INFN, Sezione di Genova, I-16146 Genova, Italy
[67] RRCAT, Indore, Madhya Pradesh 452013, India
[68] Faculty of Physics, Lomonosov Moscow State University, Moscow 119991, Russia
[69] SUPA, University of the West of Scotland, Paisley PA1 2BE, UK
[70] Rochester Institute of Technology, Rochester, NY 14623, USA
[71] Bar-Ilan University, Ramat Gan 5290002, Israel
[72] Università degli Studi di Urbino "Carlo Bo," I-61029 Urbino, Italy
[73] INFN, Sezione di Firenze, I-50019 Sesto Fiorentino, Firenze, Italy
[74] Artemis, Université Côte d'Azur, Observatoire Côte d'Azur, CNRS, CS 34229, F-06304 Nice Cedex 4, France
[75] OzGrav, University of Western Australia, Crawley, Western Australia 6009, Australia
[76] Dipartimento di Fisica "E.R. Caianiello," Università di Salerno, I-84084 Fisciano, Salerno, Italy
[77] INFN, Sezione di Napoli, Gruppo Collegato di Salerno, Complesso Universitario di Monte S. Angelo, I-80126 Napoli, Italy
[78] Physik-Institut, University of Zurich, Winterthurerstrasse 190, 8057 Zurich, Switzerland
[79] Univ Rennes, CNRS, Institut FOTON—UMR6082, F-3500 Rennes, France
[80] University of Oregon, Eugene, OR 97403, USA
[81] Laboratoire Kastler Brossel, Sorbonne Université, CNRS, ENS-Université PSL, Collège de France, F-75005 Paris, France
[82] Università di Roma "La Sapienza," I-00185 Roma, Italy
[83] Université catholique de Louvain, B-1348 Louvain-la-Neuve, Belgium
[84] Astronomical Observatory Warsaw University, 00-478 Warsaw, Poland
[85] VU University Amsterdam, 1081 HV Amsterdam, The Netherlands
[86] University of Maryland, College Park, MD 20742, USA
[87] School of Physics, Georgia Institute of Technology, Atlanta, GA 30332, USA
[88] Université de Lyon, Université Claude Bernard Lyon 1, CNRS, Institut Lumière Matière, F-69622 Villeurbanne, France
[89] Università di Napoli "Federico II," Complesso Universitario di Monte S.Angelo, I-80126 Napoli, Italy
[90] NASA Goddard Space Flight Center, Greenbelt, MD 20771, USA

[91] Dipartimento di Fisica, Università degli Studi di Genova, I-16146 Genova, Italy
[92] RESCEU, University of Tokyo, Tokyo, 113-0033, Japan
[93] Tsinghua University, Beijing 100084, People's Republic of China
[94] Texas Tech University, Lubbock, TX 79409, USA
[95] Università di Roma Tor Vergata, I-00133 Roma, Italy
[96] Missouri University of Science and Technology, Rolla, MO 65409, USA
[97] Departamento de Astronomía y Astrofísica, Universitat de València, E-46100 Burjassot, València, Spain
[98] Museo Storico della Fisica e Centro Studi e Ricerche "Enrico Fermi," I-00184 Roma, Italy
[99] National Tsing Hua University, Hsinchu City, 30013 Taiwan, Republic of China
[100] Charles Sturt University, Wagga Wagga, New South Wales 2678, Australia
[101] Physics and Astronomy Department, Stony Brook University, Stony Brook, NY 11794, USA
[102] Center for Computational Astrophysics, Flatiron Institute, 162 5th Avenue, New York, NY 10010, USA
[103] University of Chicago, Chicago, IL 60637, USA
[104] The Chinese University of Hong Kong, Shatin, NT, Hong Kong, People's Republic of China
[105] Dipartimento di Ingegneria Industriale (DIIN), Università di Salerno, I-84084 Fisciano, Salerno, Italy
[106] Institut de Physique des 2 Infinis de Lyon (IP2I) - UMR 5822, Université de Lyon, Université Claude Bernard, CNRS, F-69622 Villeurbanne, France
[107] Seoul National University, Seoul 08826, Republic of Korea
[108] Pusan National University, Busan 46241, Republic of Korea
[109] INAF, Osservatorio Astronomico di Padova, I-35122 Padova, Italy
[110] OzGrav, University of Melbourne, Parkville, Victoria 3010, Australia
[111] Universitat de les Illes Balears, IAC3—IEEC, E-07122 Palma de Mallorca, Spain
[112] Université Libre de Bruxelles, Brussels B-1050, Belgium
[113] Departamento de Matemáticas, Universitat de València, E-46100 Burjassot, València, Spain
[114] Cardiff University, Cardiff CF24 3AA, UK
[115] University of Rhode Island, Kingston, RI 02881, USA
[116] Bellevue College, Bellevue, WA 98007, USA
[117] MTA-ELTE Astrophysics Research Group, Institute of Physics, Eötvös University, Budapest 1117, Hungary
[118] California State University, Los Angeles, 5151 State University Dr, Los Angeles, CA 90032, USA
[119] Universität Hamburg, D-22761 Hamburg, Germany
[120] Institute for Plasma Research, Bhat, Gandhinagar 382428, India
[121] IGFAE, Campus Sur, Universidade de Santiago de Compostela, 15782 Spain
[122] The University of Sheffield, Sheffield S10 2TN, UK
[123] Dipartimento di Scienze Matematiche, Fisiche e Informatiche, Università di Parma, I-43124 Parma, Italy
[124] INFN, Sezione di Milano Bicocca, Gruppo Collegato di Parma, I-43124 Parma, Italy
[125] Dipartimento di Ingegneria, Università del Sannio, I-82100 Benevento, Italy
[126] Università di Trento, Dipartimento di Fisica, I-38123 Povo, Trento, Italy
[127] INFN, Trento Institute for Fundamental Physics and Applications, I-38123 Povo, Trento, Italy
[128] Università degli Studi di Sassari, I-07100 Sassari, Italy
[129] INFN, Laboratori Nazionali del Sud, I-95125 Catania, Italy
[130] University of Portsmouth, Portsmouth, PO1 3FX, UK
[131] West Virginia University, Morgantown, WV 26506, USA
[132] The Pennsylvania State University, University Park, PA 16802, USA
[133] Colorado State University, Fort Collins, CO 80523, USA
[134] Institute for Nuclear Research (Atomki), Hungarian Academy of Sciences, Bem tér 18/c, H-4026 Debrecen, Hungary
[135] CNR-SPIN, c/o Università di Salerno, I-84084 Fisciano, Salerno, Italy
[136] Scuola di Ingegneria, Università della Basilicata, I-85100 Potenza, Italy
[137] National Astronomical Observatory of Japan, 2-21-1 Osawa, Mitaka, Tokyo 181-8588, Japan
[138] Observatori Astronòmic, Universitat de València, E-46980 Paterna, València, Spain
[139] INFN Sezione di Torino, I-10125 Torino, Italy
[140] Indian Institute of Technology Bombay, Powai, Mumbai 400 076, India
[141] University of Szeged, Dóm tér 9, Szeged 6720, Hungary
[142] Delta Institute for Theoretical Physics, Science Park 904, 1090 GL Amsterdam, The Netherlands
[143] Lorentz Institute, Leiden University, P.O. Box 9506, Leiden 2300 RA, The Netherlands
[144] GRAPPA, Anton Pannekoek Institute for Astronomy and Institute for High-Energy Physics, University of Amsterdam, Science Park 904, 1098 XH Amsterdam, The Netherlands
[145] Tata Institute of Fundamental Research, Mumbai 400005, India
[146] INAF, Osservatorio Astronomico di Capodimonte, I-80131 Napoli, Italy
[147] University of Michigan, Ann Arbor, MI 48109, USA
[148] American University, Washington, D.C. 20016, USA
[149] University of California, Berkeley, CA 94720, USA
[150] Maastricht University, P.O. Box 616, 6200 MD Maastricht, The Netherlands
[151] Directorate of Construction, Services & Estate Management, Mumbai 400094 India
[152] University of Białystok, 15-424 Białystok, Poland
[153] King's College London, University of London, London WC2R 2LS, UK
[154] University of Southampton, Southampton SO17 1BJ, UK
[155] University of Washington Bothell, Bothell, WA 98011, USA
[156] Institute of Applied Physics, Nizhny Novgorod, 603950, Russia
[157] Ewha Womans University, Seoul 03760, Republic of Korea
[158] Inje University Gimhae, South Gyeongsang 50834, Republic of Korea
[159] National Institute for Mathematical Sciences, Daejeon 34047, Republic of Korea
[160] Ulsan National Institute of Science and Technology, Ulsan 44919, Republic of Korea
[161] Bard College, 30 Campus Rd, Annandale-On-Hudson, NY 12504, USA
[162] NCBJ, 05-400 Świerk-Otwock, Poland
[163] Institute of Mathematics, Polish Academy of Sciences, 00656 Warsaw, Poland
[164] Cornell University, Ithaca, NY 14850, USA
[165] Université de Montréal/Polytechnique, Montreal, Quebec H3T 1J4, Canada

[166] Lagrange, Université Côte d'Azur, Observatoire Côte d'Azur, CNRS, CS 34229, F-06304 Nice Cedex 4, France
[167] Hillsdale College, Hillsdale, MI 49242, USA
[168] Korea Astronomy and Space Science Institute, Daejeon 34055, Republic of Korea
[169] Institute for High-Energy Physics, University of Amsterdam, Science Park 904, 1098 XH Amsterdam, The Netherlands
[170] NASA Marshall Space Flight Center, Huntsville, AL 35811, USA
[171] University of Washington, Seattle, WA 98195, USA
[172] Dipartimento di Matematica e Fisica, Università degli Studi Roma Tre, I-00146 Roma, Italy
[173] INFN, Sezione di Roma Tre, I-00146 Roma, Italy
[174] ESPCI, CNRS, F-75005 Paris, France
[175] Center for Phononics and Thermal Energy Science, School of Physics Science and Engineering, Tongji University, 200092 Shanghai, People's Republic of China
[176] Southern University and A&M College, Baton Rouge, LA 70813, USA
[177] Department of Physics, University of Texas, Austin, TX 78712, USA
[178] Dipartimento di Fisica, Università di Trieste, I-34127 Trieste, Italy
[179] Centre Scientifique de Monaco, 8 quai Antoine Ier, MC-98000, Monaco
[180] Indian Institute of Technology Madras, Chennai 600036, India
[181] Université de Strasbourg, CNRS, IPHC UMR 7178, F-67000 Strasbourg, France
[182] Institut des Hautes Etudes Scientifiques, F-91440 Bures-sur-Yvette, France
[183] IISER-Kolkata, Mohanpur, West Bengal 741252, India
[184] Department of Astrophysics/IMAPP, Radboud University Nijmegen, P.O. Box 9010, 6500 GL Nijmegen, The Netherlands
[185] Kenyon College, Gambier, OH 43022, USA
[186] Whitman College, 345 Boyer Avenue, Walla Walla, WA 99362 USA
[187] Hobart and William Smith Colleges, Geneva, NY 14456, USA
[188] Department of Physics, Lancaster University, Lancaster, LA1 4 YB, UK
[189] OzGrav, Swinburne University of Technology, Hawthorn VIC 3122, Australia
[190] Trinity University, San Antonio, TX 78212, USA
[191] Dipartimento di Fisica, Università degli Studi di Torino, I-10125 Torino, Italy
[192] Indian Institute of Technology, Gandhinagar Ahmedabad Gujarat 382424, India
[193] INAF, Osservatorio Astronomico di Brera sede di Merate, I-23807 Merate, Lecco, Italy
[194] Centro de Astrofísica e Gravitação (CENTRA), Departamento de Física, Instituto Superior Técnico, Universidade de Lisboa, 1049-001 Lisboa, Portugal
[195] Marquette University, 11420 W. Clybourn Street, Milwaukee, WI 53233, USA
[196] Indian Institute of Technology Hyderabad, Sangareddy, Khandi, Telangana 502285, India
[197] INAF, Osservatorio di Astrofisica e Scienza dello Spazio, I-40129 Bologna, Italy
[198] International Institute of Physics, Universidade Federal do Rio Grande do Norte, Natal RN 59078-970, Brazil
[199] Villanova University, 800 Lancaster Avenue, Villanova, PA 19085, USA
[200] Andrews University, Berrien Springs, MI 49104, USA
[201] Carleton College, Northfield, MN 55057, USA
[202] Department of Physics, Utrecht University, 3584CC Utrecht, The Netherlands
[203] Concordia University Wisconsin, 2800 N Lake Shore Drive, Mequon, WI 53097, USA
Received 2020 May 2; revised 2020 May 21; accepted 2020 May 22; published 2020 June 23

Abstract

We report the observation of a compact binary coalescence involving a 22.2–24.3 $M_\odot$ black hole and a compact object with a mass of 2.50–2.67 $M_\odot$ (all measurements quoted at the 90% credible level). The gravitational-wave signal, GW190814, was observed during LIGO's and Virgo's third observing run on 2019 August 14 at 21:10:39 UTC and has a signal-to-noise ratio of 25 in the three-detector network. The source was localized to 18.5 deg^2 at a distance of 241^{+41}_{-45} Mpc; no electromagnetic counterpart has been confirmed to date. The source has the most unequal mass ratio yet measured with gravitational waves, $0.112^{+0.008}_{-0.009}$, and its secondary component is either the lightest black hole or the heaviest neutron star ever discovered in a double compact-object system. The dimensionless spin of the primary black hole is tightly constrained to $\leqslant 0.07$. Tests of general relativity reveal no measurable deviations from the theory, and its prediction of higher-multipole emission is confirmed at high confidence. We estimate a merger rate density of 1–23 Gpc^{-3} yr^{-1} for the new class of binary coalescence sources that GW190814 represents. Astrophysical models predict that binaries with mass ratios similar to this event can form through several channels, but are unlikely to have formed in globular clusters. However, the combination of mass ratio, component masses, and the inferred merger rate for this event challenges all current models of the formation and mass distribution of compact-object binaries.

Unified Astronomy Thesaurus concepts: Gravitational wave astronomy (675); Gravitational wave sources (677); Astrophysical black holes (98); Compact binary stars (283); Gravitational waves (678); Gravitational wave detectors (676)

1. Introduction

The first two observing runs (O1 and O2) with Advanced LIGO (Aasi et al. 2015) and Advanced Virgo (Acernese et al. 2015) opened up the field of gravitational-wave astrophysics with the detection of the first binary black hole (BBH) coalescence signal, GW150914 (Abbott et al. 2016a). Another nine such events (Abbott et al. 2016b, 2019a) were discovered by the LIGO Scientific and Virgo Collaborations (LVC) during this period, and additional events were reported by independent groups (Venumadhav et al. 2020; Zackay et al. 2019a, 2019b; Nitz

Original content from this work may be used under the terms of the Creative Commons Attribution 3.0 licence. Any further distribution of this work must maintain attribution to the author(s) and the title of the work, journal citation and DOI.

et al. 2020). The first binary neutron star (BNS) coalescence signal, GW170817, was discovered during the second of these observing campaigns (Abbott et al. 2017a, 2019b). It proved to be a multmessenger source with emission across the electromagnetic spectrum (Abbott et al. 2017b), with implications for the origin of short gamma-ray bursts (Abbott et al. 2017c), the formation of heavy elements (Abbott et al. 2017d; Chornock et al. 2017; Tanvir et al. 2017; Rosswog et al. 2018; Kasliwal et al. 2019; Watson et al. 2019), cosmology (Abbott et al. 2017e, 2019c), and fundamental physics (Abbott et al. 2017c, 2019d).

The first six months of the third observing run (O3) were completed between 2019 April 1 and September 30. The LVC recently reported on the discovery of GW190425, the coalescence signal of what is most likely a BNS with unusually large chirp mass and total mass compared to the Galactic BNSs known from radio pulsar observations (Abbott et al. 2020a). Another discovery from O3 is that of GW190412, the first BBH coalescence with an unequivocally unequal mass ratio $q = m_2/m_1$ of $0.28^{+0.12}_{-0.06}$ (all measurements are reported as symmetric 90% credible intervals around the median of the marginalized posterior distribution, unless otherwise specified). It is also the first event for which higher-multipole gravitational radiation was detected with high significance (Abbott et al. 2020d).

Here we report on another O3 detection, GW190814, the signal of a compact binary coalescence with the most unequal mass ratio yet measured with gravitational waves: $q = 0.112^{+0.008}_{-0.009}$. The signal was first identified in data from two detectors, LIGO Livingston and Virgo, on 2019 August 14, 21:11:00 UTC. Subsequent analysis of data from the full three-detector network revealed a merger signal with signal-to-noise ratio (S/N) of $\simeq$25.

The primary component of GW190814 is conclusively a black hole (BH) with mass $m_1 = 23.2^{+1.1}_{-1.0}\,M_\odot$. Its dimensionless spin magnitude is constrained to $\chi_1 \leqslant 0.07$. The nature of the $2.59^{+0.08}_{-0.09}$ $M_\odot$ secondary component is unclear. The lack of measurable tidal deformations and the absence of an electromagnetic counterpart are consistent with either a neutron star (NS) or a BH given the event's asymmetric masses and distance of 241^{+41}_{-45} Mpc. However, we show here that comparisons with the maximum NS mass predicted by studies of GW170817's remnant, by current knowledge of the NS equation of state, and by electromagnetic observations of NSs in binary systems indicate that the secondary is likely too heavy to be an NS. Either way, this is an unprecedented source because the secondary's well-constrained mass of 2.50–2.67 $M_\odot$ makes it either the lightest BH or the heaviest NS ever observed in a double compact-object system.

As in the case of GW190412, we are able to measure the presence of higher multipoles in the gravitational radiation, and a set of tests of general relativity with the signal reveal no deviations from the theory. Treating this event as a new class of compact binary coalescences, we estimate a merger rate density of 1–23 $\mathrm{Gpc^{-3}\,yr^{-1}}$ for GW190814-like events. Forming coalescing compact binaries with this unusual combination of masses at such a rate challenges our current understanding of astrophysical models.

We report on the status of the detector network and the specifics of the detection in Sections 2 and 3. In Section 4, we estimate physical source properties with a set of waveform models, and we assess statistical and systematic uncertainties. Tests of general relativity are described in Section 5. In Section 6, we calculate the merger rate density and discuss implications for the nature of the secondary component, compact binary formation, and cosmology. Section 7 summarizes our findings.

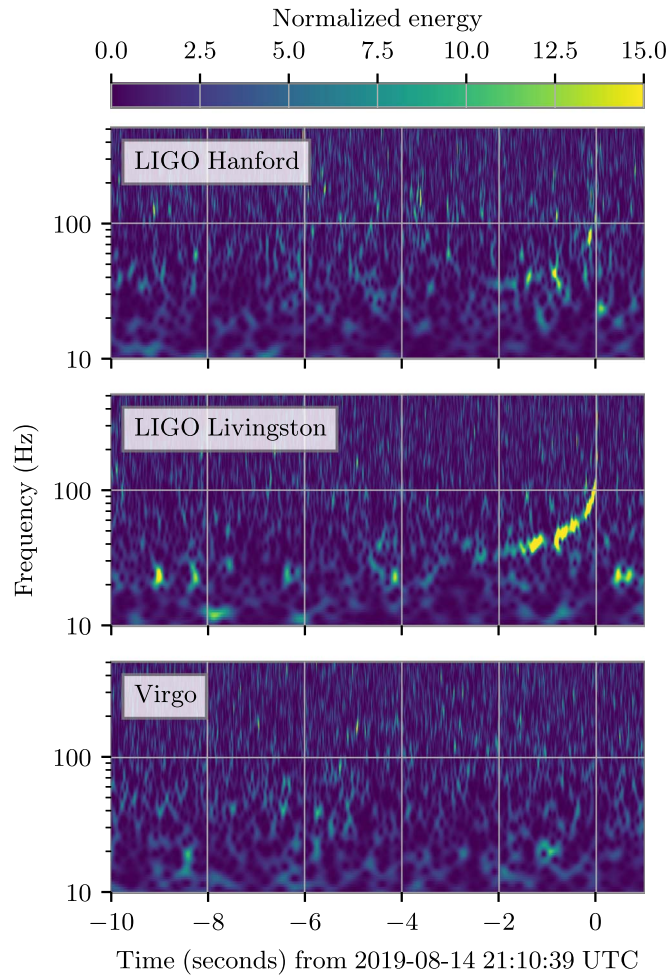

Figure 1. Time–frequency representations (Chatterji et al. 2004) of data containing GW190814, observed by LIGO Hanford (top), LIGO Livingston (middle), and Virgo (bottom). Times are shown relative to 2019 August 14, 21:10:39 UTC. Each detector's data are whitened by their respective noise amplitude spectral density and a Q-transform is calculated. The colorbar displays the normalized energy reported by the Q-transform at each frequency. These plots are not used in our detection procedure and are for visualization purposes only.

2. Detector Network

At the time of GW190814, LIGO Hanford, LIGO Livingston, and Virgo were operating with typical O3 sensitivities (Abbott et al. 2020a). Although LIGO Hanford was in a stable operating configuration at the time of GW190814, the detector was not in observing mode due to a routine procedure to minimize angular noise coupling to the strain measurement (Kasprzack & Yu 2017). This same procedure took place at LIGO Hanford around the time of GW170608; we refer the reader to Abbott et al. (2017f) for details of this procedure. Within a 5 minute window around GW190814, this procedure was not taking place; therefore, LIGO Hanford data for GW190814 are usable in the nominal range of analyzed frequencies. A time–frequency representation (Chatterji et al. 2004) of the data from all three detectors around the time of the signal is shown in Figure 1.

We used validation procedures similar to those used to vet previous gravitational-wave events (Abbott et al. 2016c, 2019a). Overall we found no evidence that instrumental or environmental disturbances (Effler et al. 2015) could account for GW190814. However, we did identify low-frequency transient noise due to scattered light at LIGO Livingston, a common source of noise in

all three interferometers (Nuttall 2018). Scattered light features in the strain data are produced when a small fraction of the main laser beam reflects off a moving surface and is phase modulated before recombining with the main beam. This recombination can result in excess noise with the morphology of arches in the time–frequency plane; the frequency of this noise is determined by the velocity of the moving surface (Accadia et al. 2010). Thunderstorms near LIGO Livingston around the time of GW190814 resulted in acoustic noise coupling to the detector and caused features in the strain data associated with scattered light (Abbott et al. 2019a). In this instance, this form of noise affects frequencies up to 30 Hz from roughly 22 s to 8 s before and 0.2 s to 1.5 s after the detected time of GW190814, as seen in the middle panel of Figure 1. Since this noise could bias the estimation of GW190814's source parameters, we used a starting frequency of 30 Hz to analyze LIGO Livingston data. Virgo was operating nominally and there are no quality issues in the Virgo data.

The LIGO and Virgo detectors are calibrated by photon pressure from modulated auxiliary lasers inducing test-mass motion (Karki et al. 2016; Acernese et al. 2018; Viets et al. 2018). Over the frequency range of 20–2048 Hz, the maximum 1σ calibration uncertainties for strain data used in the analysis of GW190814 were 6% in amplitude and 4 deg in phase for LIGO data, and 5% in amplitude and 7 deg in phase for Virgo data. These calibration uncertainties are propagated into the parameter estimation reported in Section 4 via marginalization.

3. Detection

3.1. Low-latency Identification of a Candidate Event

GW190814 was first identified on 2019 August 14, 21:11:00 UTC as a loud two-detector event in LIGO Livingston and Virgo data (S/N 21.4 and 4.3) by the low-latency GstLAL matched-filtering search pipeline for coalescing binaries (Cannon et al. 2012; Privitera et al. 2014; Messick et al. 2017; Sachdev et al. 2019; Hanna et al. 2020). Matched-filtering searches use banks (Sathyaprakash & Dhurandhar 1991; Blanchet et al. 1995; Owen 1996; Owen & Sathyaprakash 1999; Damour et al. 2001; Blanchet et al. 2005; Cokelaer 2007; Harry et al. 2009; Brown et al. 2013; Ajith et al. 2014; Harry et al. 2014; Capano et al. 2016b; Roy et al. 2017, 2019a; Indik et al. 2018) of modeled gravitational waveforms (Buonanno & Damour 1999; Arun et al. 2009; Blanchet 2014; Bohé et al. 2017; Pürrer 2016) as filter templates. A Notice was issued through NASA's Gamma-ray Coordinates Network (GCN) 20 minutes later (LIGO Scientific Collaboration & Virgo Collaboration 2019a) with a two-detector source localization computed using the rapid Bayesian algorithm BAYESTAR (Singer & Price 2016) that is shown in Figure 2. The event was initially classified as "MassGap"(Kapadia et al. 2020; LIGO Scientific Collaboration & Virgo Collaboration 2019b), implying that at least one of the binary merger components was found to have a mass between 3 and 5 $M_\odot$ in the low-latency analyses.

Other low-latency searches, including the matched-filtering based MBTA (Adams et al. 2016) and PyCBC (Nitz et al. 2017, 2018, 2019; Usman et al. 2016) pipelines, could not detect the event at the time as its S/N in Virgo data was below their single-detector detection thresholds. Test versions of MBTA and the additional matched-filtering pipeline SPIIR (Hooper et al. 2012; Liu et al. 2012; Guo et al. 2018) operating with a lower S/N threshold also identified the event with consistent attributes.

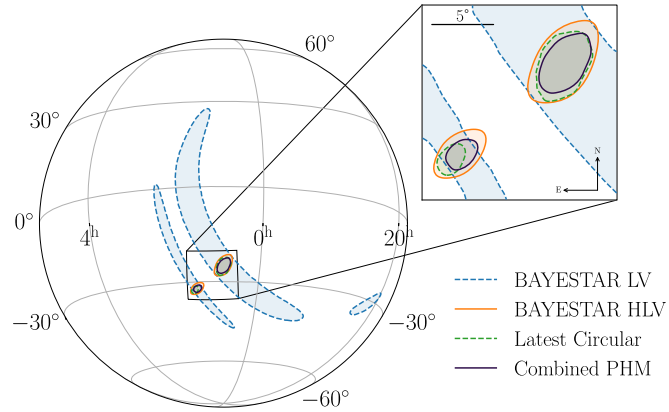

Figure 2. Posterior distributions for the sky location of GW190814. The contours show the 90% credible interval for a LIGO Livingston–Virgo (blue) and LIGO Hanford–LIGO Livingston–Virgo (orange) detector network based on the rapid localization algorithm BAYESTAR (Singer & Price 2016). The sky localization circulated 13.5 hr after the event, based on a LIGO Hanford–LIGO Livingston–Virgo analysis with the LALINFERENCE stochastic sampling software (Veitch et al. 2015), is shown in green. The purple contour indicates the final sky localization as presented in this paper, which constrains the source to within 18.5 deg^2 at 90% probability.

Shortly thereafter, reanalyses including LIGO Hanford data were performed using GstLAL and PyCBC. A coincident gravitational-wave signal was identified in all three detectors by both searches, with S/N 21.6 in LIGO Livingston, 10.6 in LIGO Hanford, and 4.5 in Virgo data (as measured by GstLAL, consistent with S/Ns reported by PyCBC). Results of these three-detector analyses were reported in a GCN Circular within 2.3 hr of the time of the event (LIGO Scientific Collaboration & Virgo Collaboration 2019c, 2019d), providing a three-detector localization (Singer & Price 2016) constraining the distance to 220–330 Mpc and the sky area to 38 deg^2 at the 90% credible level. Another GCN Circular (LIGO Scientific Collaboration & Virgo Collaboration 2019e) sent 13.5 hours after the event updated the source localization to a distance of 215–320 Mpc, the sky area to 23 deg^2, and the source classification to "NSBH" (Kapadia et al. 2020; LIGO Scientific Collaboration & Virgo Collaboration 2019b), indicating that the secondary had a mass below 3 $M_\odot$. These updated sky localizations are also shown in Figure 2. The two disjoint sky localizations arise because the low S/N in the Virgo detector (4.5) means that the data are consistent with two different signal arrival times in that detector.

3.2. Multimessenger Follow-up

Several external groups performed multimessenger follow-up of the source with observations across the electromagnetic spectrum (e.g., Dobie et al. 2019; Gomez et al. 2019; Lipunov et al. 2019; Ackley et al. 2020; Antier et al. 2020; Andreoni et al. 2020; Watson et al. 2020; Vieira et al. 2020) and with neutrino observations (e.g., Ageron et al. 2019; The IceCube Collaboration 2019). No counterpart candidates were reported. The nondetection is consistent with the source's highly unequal mass ratio and low primary spin (LIGO Scientific Collaboration & Virgo Collaboration 2019d, 2019e; Fernández et al. 2020; Morgan et al. 2020). Tentative constraints placed by multi-messenger studies on the properties of the system, such as the ejecta mass and maximum primary spin (Ackley et al. 2020; Andreoni et al. 2020; Coughlin et al. 2020; Kawaguchi et al. 2020) or the circum-merger density (Dobie et al. 2019) assuming

a neutron star–black hole (NSBH) source, may need to be revisited in light of the updated source parameters we present in Section 4.1.

3.3. Significance

The significance of GW190814 was estimated by follow-up searches using improved calibration and refined data-quality information that are not available in low latency. They also used longer stretches of data for better precision (Abbott et al. 2016b, 2016c). With LIGO Hanford data being usable but not in nominal observing mode at the time of GW190814, we used only data from the LIGO Livingston and Virgo detectors for significance estimation. GW190814 was identified as a confident detection in analyses of detector data collected over the period from 2019 August 7 to August 15 by the two independent matched-filtering searches GstLAL and PyCBC, with S/N values consistent with the low-latency analyses. The production version of PyCBC for O3 estimates significance only for events that are coincident in the LIGO Hanford and LIGO Livingston detectors, and therefore an extended version (Davies et al. 2020) was used for GW190814 in order to enable the use of Virgo data in significance estimation.

GstLAL and PyCBC use different techniques for estimating the noise background and methods of ranking gravitational-wave candidates. Both use results from searches over non-time-coincident data to improve their noise background estimation (Privitera et al. 2014; Messick et al. 2017; Usman et al. 2016). Using data from the first six months of O3 and including all events during this period in the estimation of noise background, GstLAL estimated a false-alarm rate (FAR) of 1 in 1.3×10^3 yr for GW190814. Using data from the 8 day period surrounding GW190814 and including this and all quieter events during this period in noise background estimation, the extended PyCBC pipeline (Davies et al. 2020) estimated an FAR for the event of 1 in 8.1 yr. The higher FAR estimate from PyCBC can be attributed to the event being identified by the pipeline as being quieter than multiple noise events in Virgo data. As PyCBC estimates background statistics using noncoincident data from both detectors, these louder noise events in Virgo data can form chance coincidences with the signal in LIGO Livingston data and elevate the noise background estimate for coincident events, especially when considering shorter data periods. All estimated background events that were ranked higher than GW190814 by PyCBC were indeed confirmed to be coincidences of the candidate event itself in LIGO Livingston with random noise events in Virgo. The stated background estimates are therefore conservative (Capano et al. 2016a). We also estimate the background excluding the candidate from the calculation, a procedure that yields a mean-unbiased estimation of the distribution of noise events (Abbott et al. 2016d; Capano et al. 2016a). In this case, with GstLAL we found an FAR of <1 in 10^5 yr while with PyCBC we found an FAR of <1 in 4.2×10^4 yr. With both pipelines identifying GW190814 as more significant than any event in the background, the FARs assigned are upper bounds.

When data from LIGO Hanford were included, GW190814 was also identified by the unmodeled coherent WaveBurst (cWB) search that targets generic gravitational-wave transients with increasing frequency over time without relying on waveform models (Klimenko et al. 2008, 2016; Abbott et al. 2016e). We found an FAR of <1 in 10^3 yr of observing time against the noise background from LIGO Hanford and LIGO Livingston data, consistent with the other searches.

4. Properties of GW190814

We infer the physical properties of GW190814 using a coherent Bayesian analysis of the data from LIGO Livingston, LIGO Hanford, and Virgo following the methodology described in Appendix B of Abbott et al. (2019a). Results presented here are obtained using 16 s of data around the time of detection. We use a low-frequency cutoff of 20 Hz for LIGO Hanford and Virgo and 30 Hz for LIGO Livingston for the likelihood evaluations, and we choose uninformative and wide priors, as defined in Appendix B.1 of Abbott et al. (2019a). The LALINFERENCE stochastic sampling software (Veitch et al. 2015) is the primary tool used to sample the posterior distribution. A parallelized version of the parameter estimation software BILBY (PBILBY; Ashton et al. 2019; Smith & Ashton 2019) is used for computationally expensive signal models. The power spectral density used in the likelihood calculations is a fair draw estimate calculated with BAYESWAVE (Cornish & Littenberg 2015; Littenberg & Cornish 2015).

This signal is analyzed under two different assumptions: that it represents a BBH, or that it represents an NSBH. For the BBH analyses, two different waveform families are used, one based on the effective-one-body approach (EOBNR; Bohé et al. 2017; Babak et al. 2017; Cotesta et al. 2018; Ossokine et al. 2020) and the other on a phenomenological approach (Phenom; Husa et al. 2016; Khan et al. 2016, 2019, 2020; London et al. 2018).

For the NSBH analyses, we use BBH waveform models augmented with tidal effects (Matas et al. 2020; Thompson et al. 2020a). Systematic uncertainties due to waveform modeling are expected to be subdominant compared to statistical errors (Huang et al. 2020). When sampling the parameter space with the SEOBNRV4_ROM_NRTIDALV2_NSBH (Matas et al. 2020) and IMRPHENOMNSBH (Thompson et al. 2020a) waveform models, we obtained posterior distributions for the secondary component's tidal deformability Λ_2 that are uninformative relative to a uniform prior in $\Lambda_2 \in [0, 3000]$. The absence of a measurable tidal signature is consistent with the highly unequal mass ratio (Foucart et al. 2013; Kumar et al. 2017) and with the relatively large secondary mass (Flanagan & Hinderer 2008). The large asymmetry in the masses implies that the binary will merge before the neutron star is tidally disrupted for any expected NS equation of state (Foucart et al. 2013). Given that the signal carries no discernible information about matter effects, here we present quantitative results only from BBH waveform models.

Our primary analyses include the effect of subdominant multipole moments in precessing waveform template models (PHM): IMRPHENOMPV3HM (Phenom PHM; Khan et al. 2019, 2020) from the phenomenological family and SEOBNRV4PHM (EOBNR PHM; Babak et al. 2017; Ossokine et al. 2020) from the EOBNR family.[204] Analyses that assume the spins are aligned with the orbital angular momentum were also performed, either including (Phenom/EOBNR HM) or excluding (Phenom/EOBNR) the effect of subdominant multipole moments.

4.1. Properties

From the ~300 observed cycles above 20 Hz, we are able to tightly constrain the source properties of GW190814. Our analysis shows that GW190814's source is a binary with an

[204] In the coprecessing frame the EOBNR model includes the $(l, m) = (2, \pm 2)$, $(2, \pm 1)$, $(3, \pm 3)$, $(4, \pm 4)$, and $(5, \pm 5)$ multipoles, and the Phenom model includes the $(2, \pm 2)$, $(2, \pm 1)$, $(3, \pm 3)$, $(3, \pm 2)$, $(4, \pm 4)$, and $(4, \pm 3)$ multipoles.

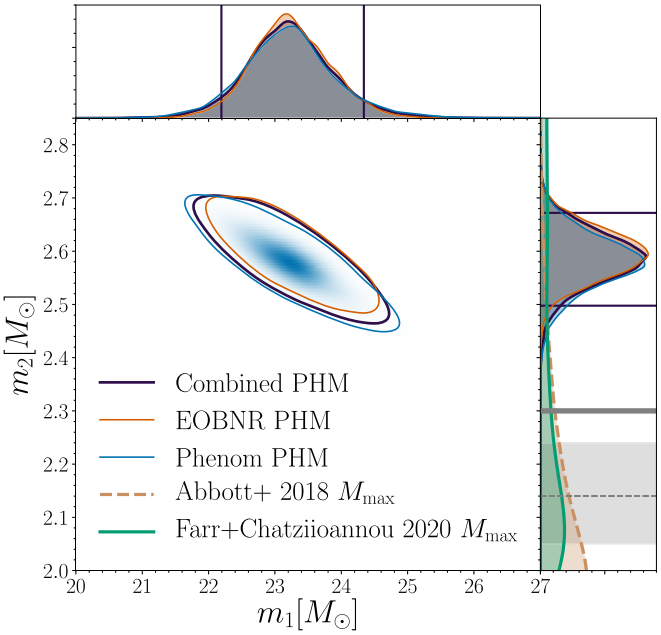

Figure 3. Posterior distribution of the primary and secondary source masses for two waveform models that include precession and subdominant multipole moments. The posterior distribution resulting from combining their samples is also shown. Each contour, as well as the colored horizontal and vertical lines, shows the 90% credible intervals. The right panel compares m_2 to predictions for the maximum NS mass, $M_{\rm max}$ (see Section 6). The posterior distribution for $M_{\rm max}$ from the spectral equation of state analysis of GW170817 (Abbott et al. 2018) is shown in orange, and the empirical $M_{\rm max}$ distribution from the population model of Farr & Chatziioannou (2020) is shown in green. The gray dashed line and shading represent the measured mass of the heaviest pulsar in the Galaxy (median and 68% confidence interval; Cromartie et al. 2019). The solid gray band at 2.3 $M_\odot$ is the upper bound on $M_{\rm max}$ from studies of GW170817's merger remnant.

unequal mass ratio $q = 0.112^{+0.008}_{-0.009}$, with individual source masses $m_1 = 23.2^{+1.1}_{-1.0}\,M_\odot$ and $m_2 = 2.59^{+0.08}_{-0.09}\,M_\odot$, as shown in Figure 3. A summary of the inferred source properties is given in Table 1. We assume a standard flat ΛCDM cosmology with Hubble constant $H_0 = 67.9\ \ \mathrm{km\,s^{-1}\,Mpc^{-1}}$ (Ade et al. 2016).

We report detailed results obtained from the two precessing BBH signal models including subdominant multipole moments: Phenom PHM and EOBNR PHM. In order to compare the template models, we compute their Bayes factor ($\log_{10}\mathcal{B}$). We find no significant evidence that one waveform family is preferred over the other as the Bayes factor between Phenom PHM and EOBNR PHM is $\log_{10}\mathcal{B} \simeq 1.0$. As a result, we combine the posterior samples with equal weight, in effect marginalizing over a discrete set of signal models with a uniform probability. This is shown in the last column of Table 1, and we refer to these values throughout the paper unless stated otherwise.

We find that the secondary mass lies in the range of 2.50–2.67 $M_\odot$. This inferred secondary mass exceeds the bounds of the primary component in GW190425 (1.61–2.52 $M_\odot$; Abbott et al. 2020a) and the most massive known pulsar in the Galaxy: $2.14^{+0.10}_{-0.09}\,M_\odot$ at 68.3% credible interval (Cromartie et al. 2019). Furthermore, the secondary is more massive than bounds on the maximum NS mass from studies of the remnant of GW170817, and from theoretical (Abbott et al. 2018) and observational estimates (Farr & Chatziioannou 2020). The inferred secondary mass is comparable to the putative BH remnant mass of GW170817 (Abbott et al. 2019b).

The primary object is identified as a BH based on its measured mass of $23.2^{+1.1}_{-1.0}\,M_\odot$. Due to accurately observing the frequency evolution over a long inspiral, the chirp mass is well constrained to $6.09^{+0.06}_{-0.06}\,M_\odot$. The inferred mass ratio $q = 0.112^{+0.008}_{-0.009}$ makes GW190814 only the second gravitational-wave observation with a significantly unequal mass ratio (Abbott et al. 2019a, 2020d).

Given that this system is in a region of the parameter space that has not been explored via gravitational-wave emission previously, we test possible waveform systematics by comparing the Phenom and EOB waveform families. Differences in the inferred secondary mass are shown in Figure 4. The results indicate that the inferred secondary mass is robust to possible waveform systematics, with good agreement between the Phenom PHM and EOBNR PHM signal models. Signal models that exclude higher multipoles or precession do not constrain the secondary mass as well.

The time delay of a signal across a network of gravitational wave detectors, together with the relative amplitude and phase at each detector, allows us to measure the location of the GW source on the sky (Abbott et al. 2020b). We localize GW190814's source to within 18.5 deg^2 at 90% probability, as shown in Figure 2. This is comparable to the localization of GW170817 (Abbott et al. 2017a, 2019a).

Spins are a fundamental property of BHs. Their magnitude and orientation carry information regarding the evolution history of the binary. The effective inspiral spin parameter $\chi_{\rm eff}$ (Damour 2001; Racine 2008; Santamaría et al. 2010; Ajith et al. 2011) contains information about the spin components that are perpendicular to the orbital plane. We infer that $\chi_{\rm eff} = -0.002^{+0.060}_{-0.061}$. The tight constraints are consistent with being able to measure the phase evolution from the long inspiral.

Orbital precession occurs when there is a significant spin component in the orbital plane of the binary (Apostolatos et al. 1994). We parameterize precession by the effective precession spin parameter $0 \leqslant \chi_{\rm p} \leqslant 1$ (Schmidt et al. 2015). This effect is difficult to measure for face-on and face-off systems (Apostolatos et al. 1994; Buonanno et al. 2003; Vitale et al. 2014, 2017; Fairhurst et al. 2019a, 2019b). GW190814 constrains the inclination of the binary to be $\Theta = 0.8^{+0.3}_{-0.2}$ rad. Since the system is neither face-on nor face-off, we are able to put strong constraints on the precession of the system: $\chi_{\rm p} = 0.04^{+0.04}_{-0.03}$. This is both the strongest constraint on the amount of precession for any gravitational-wave detection to date, and the first gravitational-wave measurement that conclusively measures near-zero precession (Abbott et al. 2019a, 2020a, 2020d).

By computing the Bayes factor between a precessing and nonprecessing signal model ($\log_{10}\mathcal{B} \sim 0.5$ in favor of precession), we find inconclusive evidence for in-plane spin. This is consistent with the inferred power from precession S/N $\rho_{\rm p}$ (Fairhurst et al. 2019a, 2019b), whose recovered distribution resembles that expected in the absence of any precession in the signal; see Figure 5. The $\rho_{\rm p}$ calculation assumes a signal dominated by the $\ell = 2$ mode; however, we have verified that the contribution of higher harmonics to the measurement of spin precession is subdominant by a factor of 5. The data are therefore consistent with the signal from a nonprecessing system.

Figure 4 shows that signal models including spin-precession effects give tighter constraints on the secondary mass compared to their nonprecessing equivalents. Signal models that include spin-precession effects can constrain $\chi_{\rm p}$, whereas nonprecessing signal models cannot provide information on in-plane spin

Table 1
Source Properties of GW190814: We Report the Median Values Along with the Symmetric 90% Credible Intervals for the SEOBNRv4PHM (EOBNR PHM) and IMRPHENOMPV3HM (PHENOM PHM) Waveform Models

	EOBNR PHM	Phenom PHM	Combined
Primary mass $m_1/M_\odot$	$23.2^{+1.0}_{-0.9}$	$23.2^{+1.3}_{-1.1}$	$23.2^{+1.1}_{-1.0}$
Secondary mass $m_2/M_\odot$	$2.59^{+0.08}_{-0.08}$	$2.58^{+0.09}_{-0.10}$	$2.59^{+0.08}_{-0.09}$
Mass ratio q	$0.112^{+0.008}_{-0.008}$	$0.111^{+0.009}_{-0.010}$	$0.112^{+0.008}_{-0.009}$
Chirp mass $\mathcal{M}/M_\odot$	$6.10^{+0.06}_{-0.05}$	$6.08^{+0.06}_{-0.05}$	$6.09^{+0.06}_{-0.06}$
Total mass $M/M_\odot$	$25.8^{+0.9}_{-0.8}$	$25.8^{+1.2}_{-1.0}$	$25.8^{+1.0}_{-0.9}$
Final mass $M_f/M_\odot$	$25.6^{+1.0}_{-0.8}$	$25.5^{+1.2}_{-1.0}$	$25.6^{+1.1}_{-0.9}$
Upper bound on primary spin magnitude χ_1	0.06	0.08	0.07
Effective inspiral spin parameter $\chi_{\rm eff}$	$0.001^{+0.059}_{-0.056}$	$-0.005^{+0.061}_{-0.065}$	$-0.002^{+0.060}_{-0.061}$
Upper bound on effective precession parameter $\chi_{\rm p}$	0.07	0.07	0.07
Final spin χ_f	$0.28^{+0.02}_{-0.02}$	$0.28^{+0.02}_{-0.03}$	$0.28^{+0.02}_{-0.02}$
Luminosity distance D_L/Mpc	235^{+40}_{-45}	249^{+39}_{-43}	241^{+41}_{-45}
Source redshift z	$0.051^{+0.008}_{-0.009}$	$0.054^{+0.008}_{-0.009}$	$0.053^{+0.009}_{-0.010}$
Inclination angle Θ/rad	$0.9^{+0.3}_{-0.2}$	$0.8^{+0.2}_{-0.2}$	$0.8^{+0.3}_{-0.2}$
Signal-to-noise ratio in LIGO Hanford ρ_H	$10.6^{+0.1}_{-0.1}$	$10.7^{+0.1}_{-0.2}$	$10.7^{+0.1}_{-0.2}$
Signal-to-noise ratio in LIGO Livingston ρ_L	$22.21^{+0.09}_{-0.15}$	$22.16^{+0.09}_{-0.17}$	$22.18^{+0.10}_{-0.17}$
Signal-to-noise ratio in Virgo ρ_V	$4.3^{+0.2}_{-0.5}$	$4.1^{+0.2}_{-0.6}$	$4.2^{+0.2}_{-0.6}$
Network Signal-to-noise ratio ρ_{HLV}	$25.0^{+0.1}_{-0.2}$	$24.9^{+0.1}_{-0.2}$	$25.0^{+0.1}_{-0.2}$

Note. The primary spin magnitude and the effective precession is given as the 90% upper limit. The inclination angle is folded to $[0, \pi/2]$. The last column is the result of combining the posteriors of each model with equal weight. The sky location of GW190814 is shown in Figure 2.

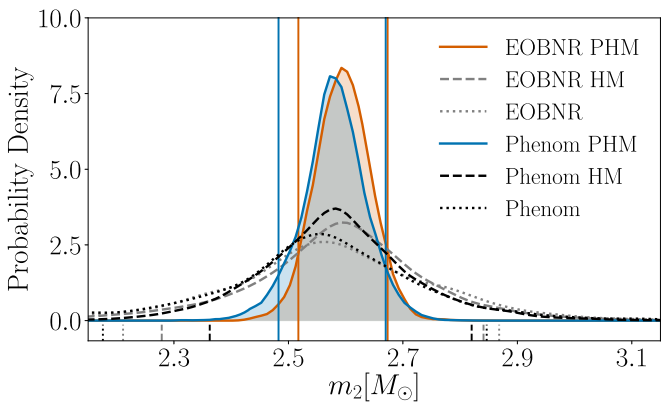

Figure 4. Marginalized posterior distribution for the secondary mass obtained using a suite of waveform models. The vertical lines indicate the 90% credible bounds for each waveform model. The labels Phenom/EOBNR PHM (generic spin directions + higher multipoles), Phenom/EOBNR HM (aligned-spin + higher multipoles), and Phenom/EOBNR (aligned-spin, quadrupole only) indicate the different physical content in each of the waveform models.

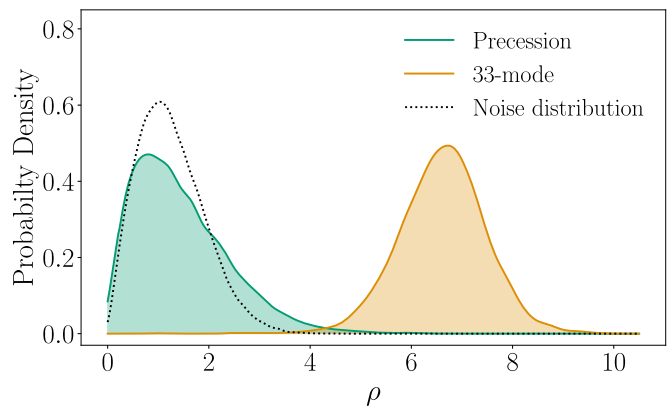

Figure 5. Posterior distributions for the precessing S/N, $\rho_{\rm p}$ (green) and the optimal S/N in the (3, 3) subdominant multipole moment, ρ (orange). The gray dotted line shows the expected distribution for Gaussian noise.

components. In all analyses, we assume a prior equivalent to spin orientations being isotropically distributed. We find that the data are inconsistent with large $\chi_{\rm p}$ and consistent with any secondary spin. Therefore, for precessing signal models the allowed q–$\chi_{\rm eff}$ parameter space is restricted, which helps to break the degeneracy (Poisson & Will 1995; Baird et al. 2013; Farr et al. 2016; Ng et al. 2018). Consequently, the extra information from constraining $\chi_{\rm p}$ to small values enables a more precise measurement of the secondary mass.

The asymmetry in the masses of GW190814 means that the spin of the more massive object dominates contributions to $\chi_{\rm eff}$ and $\chi_{\rm p}$. As both $\chi_{\rm eff}$ and $\chi_{\rm p}$ are tightly constrained, we are able to bound the primary spin of GW190814 to be $\chi_1 \leqslant 0.07$, as shown in Figure 6. This is the strongest constraint on the primary spin for any gravitational-wave event to date (Abbott et al. 2019a, 2020a, 2020d).

The joint posterior probability of the magnitude and orientation of χ_1 and χ_2 are shown in Figure 6. Deviations from uniform shading indicate a spin property measurement. The primary spin is tightly constrained to small magnitudes, but its orientation is indistinguishable from the prior distribution. The spin of the less massive object, χ_2, remains unconstrained; the posterior distribution is broadly consistent with the prior.

The final mass M_f and final dimensionless spin χ_f of the merger remnant are estimated under the assumption that the secondary is a BH. By averaging several fits calibrated to numerical relativity (Hofmann et al. 2016; Johnson-McDaniel et al. 2016; Healy & Lousto 2017; Jiménez-Forteza et al. 2017), we infer the final mass and spin of the remnant BH to be $25.6^{+1.1}_{-0.9}\,M_\odot$ and $0.28^{+0.02}_{-0.02}$, respectively. The final spin is lower than for previous mergers (Abbott et al. 2019a, 2020d), as expected from the low primary spin and smaller orbital contribution due to the asymmetric masses.

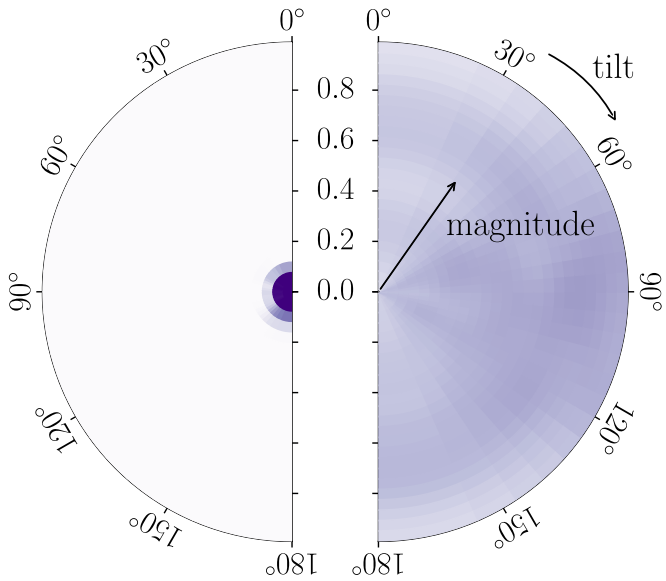

Figure 6. Two-dimensional posterior probability for the tilt-angle and spin-magnitude for the primary object (left) and secondary object (right) based on the combined samples. The tilt angles are 0° for spins aligned and 180° for spins antialigned with the orbital angular momentum. The tiles are constructed linearly in spin magnitude and the cosine of the tilt angles such that each tile contains identical prior probability. The color indicates the posterior probability per pixel. The probabilities are marginalized over the azimuthal angles.

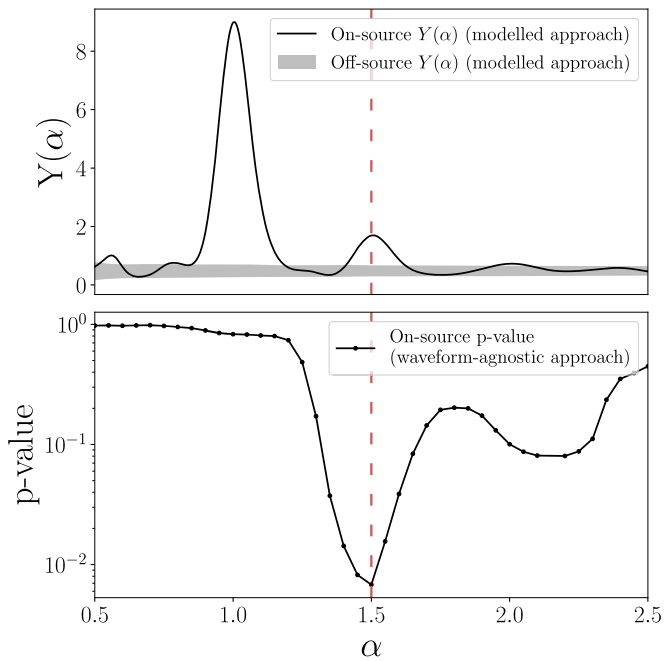

Figure 7. Top panel: variation of $Y(\alpha)$, i.e., the energy in the pixels along the α-th track defined by $f_\alpha(t) = \alpha f_{22}(t)$, using the modeled approach. The peaks at $\alpha = 1$ and 1.5 indicate the energies in the $m = 2$ and $m = 3$ multipoles, respectively. The gray band indicates the 68% confidence interval on the off-source measurements of $Y(\alpha)$. Bottom panel: the variation of p-value of the on-source results, as a function of α, using the waveform-agnostic approach. The dip at $\alpha = 1.5$ is strong evidence of the presence of the $m = 3$ mode in the underlying signal. The red dashed line in both panels corresponds to general relativity's prediction of $\alpha = 1.5$ for the $m = 3$ mode.

4.2. Evidence for Higher-order Multipoles

The relative importance of a subdominant multipole moment increases with mass ratio. Each subdominant multipole moment has a different angular dependence on the emission direction. With significant evidence for multipoles other than the dominant $(\ell, m) = (2, 2)$ quadrupole, we gain an independent measurement of the inclination of the source. This allows for the distance-inclination degeneracy to be broken (Cutler & Flanagan 1994; Abbott et al. 2016f; Kalaghatgi et al. 2020; Usman et al. 2019). Measuring higher-order multipoles therefore gives more precise measurements of source parameters (van den Broeck & Sengupta 2007a, 2007b; Kidder 2008; Blanchet et al. 2008; Mishra et al. 2016; Kumar et al. 2019).

GW190412 was the first event where there was significant evidence for higher-order multipoles (Kumar et al. 2019; Payne et al. 2019; Abbott et al. 2020d). GW190814 exhibits stronger evidence for higher-order multipoles, with $\log_{10}\mathcal{B} \simeq 9.6$ in favor of a higher-multipole versus a pure quadrupole model. The $(\ell, m) = (3, 3)$ is the strongest subdominant multipole, with $\log_{10}\mathcal{B} \simeq 9.1$ in favor of a signal model including both the $(\ell, m) = (2, 2)$ and $(3, 3)$ multipole moments. GW190814's stronger evidence for higher multipoles is expected given its more asymmetric masses and the larger network S/N.

The orthogonal optimal S/N of a subdominant multipole is calculated by decomposing each multipole into components parallel and perpendicular to the dominant harmonic (Abbott et al. 2020d; Mills & Fairhurst 2020). We infer that the orthogonal optimal S/N of the $(\ell, m) = (3, 3)$ multipole is $6.6^{+1.3}_{-1.4}$, as shown in Figure 5. This is the strongest evidence for measuring a subdominant multipole to date (Kumar et al. 2019; Payne et al. 2019; Abbott et al. 2020d).

Finally, we perform two complementary analyses involving time–frequency tracks in the data to provide further evidence for the presence of higher multipoles in the signal. In the first approach (also outlined in Abbott et al. 2020d, Section 4) we predict the time–frequency track of the dominant (2, 2) multipole in the LIGO Livingston detector (as seen in Figure 1, middle panel) from an EOBNR HM parameter estimation analysis. This analysis collects energies along a time–frequency track that is $\alpha \times f_{22}(t)$, the (2, 2) multipole's instantaneous frequency, where α is a dimensionless parameter (Roy et al. 2019b; Abbott et al. 2020d). We find prominent peaks in $Y(\alpha)$, the energy in the pixels along the α-th track defined in Abbott et al. (2020d), at $\alpha = 1$ and 1.5, as can be seen from the on-source curve in the top panel of Figure 7. These peaks correspond to the $m = 2$ and $m = 3$ multipole predictions in the data containing the signal (on-source data). We also compute a detection statistic β (Roy et al. 2019b) of 10.09 for the presence of the $m = 3$ multipole with a p-value of $<2.5 \times 10^{-4}$, compared to a background distribution estimated over 18 hr of data adjacent to the event (off-source data), where the largest background β is 7.59. The significant difference between on- and off-source values provides much stronger evidence for the presence of higher multipoles than what is reported for GW190412 (Abbott et al. 2020d).

The second analysis uses waveform-agnostic methods to reconstruct the signal. It then compares the observed coherent signal energy in the LIGO Hanford–LIGO Livingston–Virgo network of detectors, as identified by the cWB detection pipeline (Klimenko et al. 2016), with the predictions of a waveform model without higher multipoles (EOBNR; Prodi et al. 2020) to investigate if the description of the underlying signal is incomplete if we do not include contributions from the $m = 3$ multipole in our waveform model. We compute a test statistic, the squared sum of the coherent residuals estimated over

selected time–frequency tracks parameterized in terms of the same α parameter defined in the previous analysis (Roy et al. 2019b; Abbott et al. 2020d). Each time–frequency track centered on α includes frequencies within $[\alpha - 0.1,\ \alpha + 0.1] \times f_{22}(t)$, and times within $[t_{\rm merger} - 0.5$ s, $t_{\rm merger} - 0.03$ s], where $f_{22}(t)$ and $t_{\rm merger}$ correspond to the maximum likelihood template from the EOBNR parameter estimation analysis. We further compute a background distribution using simulated signals in off-source data (Prodi et al. 2020), and compute p-values for the on-source results as a function of α (Figure 7, bottom panel). We find a minimum p–value of 6.8×10^{-3} at $\alpha = 1.5$, providing strong evidence that the disagreement between the actual event and the EOBNR prediction is because of the absence of the $m = 3$ multipoles in the waveform model. The local minimum near $\alpha = 2$ is not an indication of the $m = 4$ multipoles, but rather a statistical fluctuation that is consistent with similar behavior seen for studies with simulated signals described in detail in Prodi et al. (2020).

Although the two time–frequency analyses are similar in motivation, the latter differs from the former in that it is not restricted to data from just one detector, but rather uses the coherent signal energy across the three-detector network. Both analyses point to strong evidence for the presence of higher multipoles in the signal.

5. Tests of General Relativity

GW190814 is the gravitational-wave event with the most unequal mass ratio to date, and can therefore be used to test general relativity (GR) in a region of parameter space previously unexplored with strong-field tests of GR (Abbott et al. 2016g, 2019e, 2019d). The asymmetric nature of a system excites the higher multipole moments of the gravitational signal, which allows us to test the multipolar structure of gravity (Kastha et al. 2018, 2019; Dhanpal et al. 2019; Islam et al. 2020). The addition of information from the higher harmonics of a signal also breaks certain degeneracies in the description of the source, and could potentially enable us to place stronger constraints on certain deviations from GR (van den Broeck & Sengupta 2007b, 2007a). We perform several null tests of GR using GW190814. These tests assume GW190814 is a (quasi-circular) BBH merger as described in GR, and look for inconsistencies between the observed signal and predictions of the theory. An inconsistency might arise from an incomplete understanding of the underlying signal (or noise), and could indicate a non-BBH nature of the signal or a potential departure from GR.

First, as a consistency test of the signal reconstruction, we subtract from the data the maximum likelihood compact binary coalescence waveforms, Phenom (Khan et al. 2016), Phenom HM (Kalaghatgi et al. 2020), Phenom PHM (Khan et al. 2020), and EOBNR PHM (Ossokine et al. 2020) and analyze 4 s of the resulting residual data centered around the time of merger with the morphology-independent transient analysis BAYESWAVE (Cornish & Littenberg 2015; Littenberg & Cornish 2015). We measure the 90% credible upper limit on the coherent S/N, ρ_{90}, and compare it to the S/N, ρ_{90}^{N}, recovered by analyzing 175 randomly selected data segments in surrounding time (off–source data) with the same configuration settings. If the residual data are consistent with the noise, we expect ρ_{90} to be consistent with ρ_{90}^{N}. We compute the p-value by comparing the distribution of ρ_{90}^{N} to ρ_{90} through $p = P(\rho_{90}^{N} < \rho_{90})$. We obtain p-values of 0.59, 0.82, 0.82, and 0.75 for Phenom, Phenom HM, Phenom PHM, and EOBNR PHM, respectively. Hence, we find no evidence for deviations in the behavior of the residual data stream.

We also look for deviations in the spin-induced quadrupole moments of the binary components. According to the no-hair conjecture (Carter 1971; Hansen 1974) the multipole moments of a Kerr BH are completely described by its mass and spin angular momentum. At leading order in spin, the spin-induced quadrupole moment scalar is (Hartle 1967; Pappas & Apostolatos 2012), $Q = -\kappa a^2 m^3$, where (m, a) are the mass and dimensionless spin of the compact object, and κ is a dimensionless deformation parameter characterizing deviations in the spin-induced quadrupole moment. Kerr BHs have $\kappa = 1$ (Thorne 1980), while $\kappa \sim 2$–14 for NSs (depending on the equation of state) and $\kappa \sim 10$–150 for spinning boson stars with large self-interaction (Ryan 1997). The deformation parameter can even be negative for (slowly rotating, thin-shelled) gravastars (Uchikata et al. 2016). Hence, an accurate measurement of κ sheds light onto the nature of the compact object. For compact binaries, the spin-induced quadrupole moment terms appear at second post-Newtonian order (Poisson 1998). For Kerr BHs in GR, $\kappa_1 = \kappa_2 = 1$, where κ_1, κ_2 are the individual deformation parameters of the primary and secondary compact objects in the binary. Since κ_1 and κ_2 are strongly degenerate in the gravitational waveform, we instead measure a linear symmetric combination of these quantities, $\kappa_{\rm s} = (\kappa_1 + \kappa_2)/2$, which is 1 for a BBH in GR. The posteriors on $\kappa_{\rm s}$ are relatively uninformative, and nearly span the prior range of [0, 500], with increased support at $\kappa_{\rm s} = 0$ relative to the prior. The upper bound of the prior was chosen to accommodate all the objects listed above. The result shows that GW190814 is consistent with having a BBH source described by GR. However, the broad posterior means that we cannot exclude the possibility that one or both components of the source is not a BH. We can attempt to understand this result in terms of the spin measurements for the binary. The measurements of $\kappa_{\rm s}$ and a nonzero $\chi_{\rm eff}$ are highly correlated (Krishnendu et al. 2019), and for a system with small $\chi_{\rm eff}$ the bounds on the measured value of $\kappa_{\rm s}$ are weak.

Finally, we investigate the source dynamics of the binary through a parameterized test of gravitational waveform generation, where we allow for the coefficients describing the post-Newtonian inspiral of a BBH coalescence to deviate away from their predictions in GR (Arun et al. 2006a, 2006b; Yunes & Pretorius 2009; Mishra et al. 2010; Cornish et al. 2011; Li et al. 2012; Meidam et al. 2018). We use an aligned-spin EOB waveform without higher modes (EOBNR), and find no deviations in the post-Newtonian coefficients from their nominal values in GR. In summary, none of our tests of GR indicate any departure from the predictions of the theory, and GW190814 is consistent with the description of a compact binary merger in GR.

6. Astrophysical Implications

The highly unequal mass ratio of $0.112^{+0.008}_{-0.009}$ and unusual secondary mass of $2.59^{+0.08}_{-0.09}\,M_\odot$ make the source of GW190814 unlike any other compact binary coalescence observed so far. The average mass ratio for BBH coalescences detected by the LVC during O1 and O2 is $\simeq$0.9 (Roulet & Zaldarriaga 2019), and an inference of the underlying population predicted that 99% of detectable BBHs have mass ratios $q \geqslant 0.5$ (Fishbach & Holz 2020). However, the paucity of events from O1 and O2 means that this picture is limited. Indeed, the discovery of GW190412 has already changed the picture substantially (Abbott et al. 2020d).

GW190814's secondary mass lies in the hypothesized lower mass gap of 2.5–5 $M_\odot$ (Bailyn et al. 1998; Özel et al. 2010; Farr et al. 2011; Özel et al. 2012) between known NSs and BHs. It is heavier than the most massive pulsar in the Galaxy (Cromartie et al. 2019), and almost certainly exceeds the mass of the 1.61–2.52 $M_\odot$ primary component of GW190425, which is itself an outlier relative to the Galactic population of BNSs (Abbott et al. 2020a). On the other hand, it is comparable in mass to two BH candidates: the $\simeq$2.7 $M_\odot$ merger remnant of GW170817 (Abbott et al. 2019b) and the 2.6–6.1 $M_\odot$ compact object (95% confidence interval) discovered by Thompson et al. (2019).[205] It is also comparable to the millisecond pulsar PSR J1748−2021B (Freire et al. 2008), whose mass is claimed as $2.74^{+0.21}_{-0.21}\,M_\odot$ at 68% confidence. However, this estimate, obtained via measurement of the periastron advance, could be inaccurate if the system inclination is low or the pulsar's companion is rapidly rotating (Freire et al. 2008). In sum, it is not clear if GW190814's secondary is a BH or an NS.

GW190814 poses a challenge for our understanding of the population of merging compact binaries. In what follows, we estimate the merger rate density of the compact binary subpopulation represented by this source, investigate the nature of its secondary component and possible implications for the NS equation of state, discuss how the system may have formed, and study its implications for cosmology.

6.1. Merger Rate Density

Given the unprecedented combination of component masses found in GW190814, we take the system to represent a new class of compact binary mergers, and use our analysis of its source properties to estimate a merger rate density for GW190814-like events. Following a method described in Kim et al. (2003), we calculate a simple, single-event rate density estimate $\mathcal{R}$ according to our sensitivity to a population of systems drawn from the parameter-estimation posteriors. As in Abbott et al. (2020a), we calculate our surveyed spacetime volume $\langle VT\rangle$ semianalytically, imposing single-detector and network S/N thresholds of 5 and 10, respectively (Tiwari 2018). The semianalytic $\langle VT\rangle$ for GW190814 is then multiplied by a calibration factor to match results from the search pipelines assuming a once-per-century FAR threshold. The sensitivity of a search pipeline is estimated using a set of simulated signals. For computational efficiency, this was done using preexisting search pipeline simulations and the mass properties were not highly optimized. However, given that we are estimating a rate based on a single source, the calibration errors are much smaller than the statistical errors associated with the estimate. The simulated sources were uniformly distributed in comoving volume, component masses, and component spins aligned with the orbital angular momentum. For O1 and O2, the simulated BH mass range was 5–100 $M_\odot$, but for the first part of O3 we are analyzing here, the injected range was 2.5–40 $M_\odot$ (following our updated knowledge of the BH mass distribution); the NS mass range was 1–3 $M_\odot$, and component spins are <0.95. As GW190814 occurred when LIGO Hanford was not in nominal observing mode, it is not included in the production PyCBC results, and we use GstLAL results to calculate the merger rate.

We assume a Poisson likelihood over the astrophysical rate with a single count and we apply a Jeffreys $\mathcal{R}^{-1/2}$ prior to obtain rate posteriors. The analysis was done using samples from the Phenom PHM posterior and separately from the EOBNR PHM posterior, producing the same result in both cases. We find the merger rate density of GW190814-like systems to be 7^{+16}_{-6} Gpc^{-3} yr^{-1}.

As a consistency check, we used the PyCBC search results to calculate an upper limit. Repeating the rate calculation with a PyCBC-based $\langle VT\rangle$ calibration and zero event count, we obtain an upper limit consistent (to within 10%) with the upper limit of the merger rate estimated using GstLAL search results. We conclude that the uncertainty in our estimate of the rate density for the class of mergers represented by GW190814 is primarily dominated by Poisson statistics.

6.2. Nature of the Secondary Component

The primary mass measurement of $23.2^{+1.1}_{-1.0}\,M_\odot$ securely identifies the heavier component of GW190814 as a BH, but the secondary mass of $2.59^{+0.08}_{-0.09}\,M_\odot$ may be compatible with either an NS or a BH depending on the maximum mass supported by the unknown NS equation of state (EOS). The source's asymmetric masses, the nondetection of an electromagnetic counterpart and the lack of a clear signature of tides or spin-induced quadrupole effects in the waveform do not allow us to distinguish between a BBH or an NSBH. Instead, we rely on comparisons between m_2 and different estimates of the maximum NS mass, $M_{\rm max}$, to indicate the source classification preferred by data: if $m_2 > M_{\rm max}$, then the NSBH scenario is untenable.

While some candidate EOSs from nuclear theory can support nonrotating NSs with masses of up to $\sim$3 $M_\odot$ (e.g., Müller & Serot 1996), such large values of $M_{\rm max}$ are disfavored by the relatively small tidal deformabilities measured in GW170817 (Abbott et al. 2017a, 2019b), which correlate with smaller internal pressure gradients as a function of density and hence a lower threshold for gravitational collapse. By adopting a phenomenological model for the EOS, conditioning it on GW170817, and extrapolating the constraints to the high densities relevant for the maximum mass, Lim & Holt (2019) and Essick et al. (2020) place $M_{\rm max} \lesssim 2.3\,M_\odot$. Similarly, the EOS inference reported in Abbott et al. (2018), based on an analysis of GW170817 with a spectral parameterization (Lindblom 2010; Lindblom & Indik 2012, 2014) for the EOS, implies a 90% credible upper bound of $M_{\rm max} \leqslant 2.43\,M_\odot$, with tenuous but nonzero posterior support beyond 2.6 $M_\odot$. We calculate the corresponding $M_{\rm max}$ posterior distribution, shown in the right panel of Figure 3, from the GW170817-informed spectral EOS samples used in Abbott et al. (2018) by reconstructing each EOS from its parameters and computing its maximum mass. Comparison with the m_2 posterior suggests that the secondary component of GW190814 is probably more massive than this prediction for $M_{\rm max}$: the posterior probability of $m_2 \leqslant M_{\rm max}$, marginalized over the uncertainty in m_2 and $M_{\rm max}$, is only 3%. Nevertheless, the maximum mass predictions from these kinds of EOS inferences come with important caveats: their extrapolations are sensitive to the phenomenological model assumed for the EOS; they use hard $M_{\rm max}$ thresholds on the EOS prior to account for the existence of the heaviest Galactic pulsars, which is known to bias the inferred maximum mass distribution toward the threshold (Miller et al. 2020); and they predate the NICER observatory's recent simultaneous mass and radius measurement for J0030+0451,

[205] See van den Heuvel & Tauris (2020) and Thompson et al. (2020b) for discussions about the interpretation of this observation.

which may increase the $M_{\max}$ estimates by a few percent (Landry et al. 2020) because it favors slightly stiffer EOSs than GW170817 (Miller et al. 2019; Raaijmakers et al. 2019; Riley et al. 2019; Jiang et al. 2020).

NS mass measurements also inform bounds on $M_{\max}$ independently of EOS assumptions. Fitting the known population of NSs in binaries to a double-Gaussian mass distribution with a high-mass cutoff, Alsing et al. (2018) obtained an empirical constraint of $M_{\max} \leqslant 2.6\,M_{\odot}$ (one-sided 90% confidence interval). Farr & Chatziioannou (2020) recently updated this analysis to include PSR J0740+6620 (Cromartie et al. 2019), which had not been discovered at the time of the original study. Based on samples from the Farr & Chatziioannou (2020) maximum-mass posterior distribution, which is plotted in the right panel of Figure 3, we find $M_{\max} = 2.25^{+0.81}_{-0.26}\,M_{\odot}$. In this case, the posterior probability of $m_2 \leqslant M_{\max}$ is 29%, again favoring the $m_2 > M_{\max}$ scenario, albeit less strongly because of the distribution's long tail up to $\sim 3\,M_{\odot}$. However, the empirical $M_{\max}$ prediction is sensitive to selection effects that could potentially bias it (Alsing et al. 2018). In particular, masses are only measurable for binary pulsars, and the mass distribution of isolated NSs could be different. Additionally, the discovery of GW190425 (Abbott et al. 2020a) should also be taken into account in the population when predicting $M_{\max}$.

Finally, the NS maximum mass is constrained by studies of the merger remnant of GW170817. Although no postmerger gravitational waves were observed (Abbott et al. 2017g, 2019f), modeling of the associated kilonova (Abbott et al. 2017b, 2017d; Cowperthwaite et al. 2017; Kasen et al. 2017; Villar et al. 2017) suggests that the merger remnant collapsed to a BH after a brief supramassive or hypermassive NS phase during which it was stabilized by uniform or differential rotation. Assuming this ultimate fate for the merger remnant immediately implies that no NS can be stable above $\sim 2.7\,M_{\odot}$, but it places a more stringent constraint on NSs that are not rotationally supported. The precise mapping from the collapse threshold mass of the remnant to $M_{\max}$ depends on the EOS, but by developing approximate prescriptions based on sequences of rapidly rotating stars for a range of candidate EOSs, $M_{\max}$ has been bounded below approximately 2.2–2.3 $M_{\odot}$ (Margalit & Metzger 2017; Rezzolla et al. 2018; Ruiz et al. 2018; Shibata et al. 2019; Abbott et al. 2020c). Although the degree of EOS uncertainty in these results is difficult to quantify precisely, if we take the more conservative 2.3 $M_{\odot}$ bound at face value, then m_2 is almost certainly not an NS: the m_2 posterior distribution has negligible support below 2.3 $M_{\odot}$.

Overall, these considerations suggest that GW190814 is probably not the product of an NSBH coalescence, despite its preliminary classification as such. Nonetheless, the possibility that the secondary component is an NS cannot be completely discounted due to the current uncertainty in $M_{\max}$.

There are two further caveats to this assessment. First, because the secondary's spin is unconstrained, it could conceivably be rotating rapidly enough for m_2 to exceed $M_{\max}$ without triggering gravitational collapse: rapid uniform rotation can stabilize a star up to $\sim$20% more massive than the nonrotating maximum mass (Cook et al. 1994), in which case only the absolute upper bound of $\sim 2.7\,M_{\odot}$ is relevant. However, it is very unlikely that an NSBH system could merge before dissipating such extreme natal NS spin angular momentum.

Second, our discussion has thus far neglected the possibility that the secondary component is an exotic compact object, such as a boson star (Kaup 1968) or a gravastar (Mazur & Mottola 2004), instead of an NS or a BH. Depending on the model, some exotic compact objects can potentially support masses up to and beyond 2.6 $M_{\odot}$ (Cardoso & Pani 2019). Our analysis does not exclude this hypothesis for the secondary.

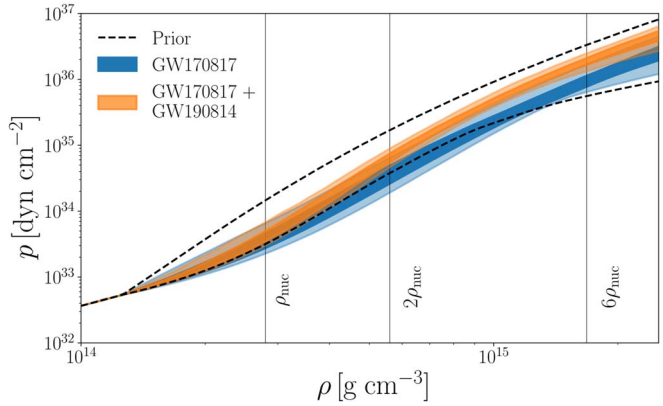

Figure 8. Constraints on the NS EOS assuming GW190814 was produced by a BBH (blue) or an NSBH (orange) coalescence. The 90% and 50% credible contours of the posterior in the pressure-density plane are shown. The constraints are calculated by assuming a spectral decomposition for the EOS, following Abbott et al. (2018). The BBH constraints are identical to those from the analysis of GW170817, while for the NSBH case the posterior is reweighted by the probability that each EOS's maximum mass is at least m_2. The dashed lines indicate the 90% credible region of the prior.

Since the NSBH scenario cannot be definitively ruled out, we examine GW190814's potential implications for the NS EOS, assuming that the secondary proves to be an NS. This would require $M_{\max}$ to be no less than m_2, a condition that severely constrains the distribution of EOSs compatible with existing astrophysical data. The combined constraints on the EOS from GW170817 and this hypothetical maximum mass information are shown in Figure 8. Specifically, we have taken the spectral EOS distribution conditioned on GW170817 from Abbott et al. (2018) and reweighted each EOS by the probability that its maximum mass is at least as large as m_2. The updated posterior favors stiffer EOSs, which translates to larger radii for NSs of a given mass. The corresponding constraints on the radius and tidal deformability of a canonical 1.4 $M_{\odot}$ NS are $R_{1.4} = 12.9^{+0.8}_{-0.7}$ km and $\Lambda_{1.4} = 616^{+273}_{-158}$.

6.3. Origins of GW190814-like Systems

The source of GW190814 represents a previously undetected class of coalescences that has the potential to shed light on the formation of merging compact-object binaries with highly asymmetric masses.

Electromagnetic observations of Galactic NSs and stellar-mass BHs suggest a dearth of compact objects in the $\sim 2.5\,M_{\odot}$ to 5 $M_{\odot}$ range (Bailyn et al. 1998; Özel et al. 2010; Farr et al. 2011; Özel et al. 2012). Observations of a few candidates with masses in this range seem to disfavor the existence of a gap (Freire et al. 2008; Neustroev et al. 2014; Giesers et al. 2018; Thompson et al. 2019; Wyrzykowski & Mandel 2020), but whether the mass gap is physical or caused by selection biases is still a matter of debate (e.g., Kreidberg et al. 2012).

From a theoretical point of view, accurately calculating the masses of compact remnants at formation is challenging, because it depends on the complex physics of the supernova

explosion and the details of stellar evolution, especially for the late evolutionary stages of massive stars (Janka 2012; Müller 2016; Burrows et al. 2018, 2019). Whether the models favor the presence of a gap or a smooth transition between NSs and BHs is still unclear, and in fact some models have been developed with the purpose of reproducing this lower mass gap (Ugliano et al. 2012; Fryer et al. 2012; Kochanek 2014; Sukhbold & Woosley 2014; Ertl et al. 2016). Therefore, our robust discovery of an object with a well-constrained mass in this regime may provide crucial constraints on compact-object formation models. In fact, GW190814 demonstrates the need to adjust remnant mass prescriptions previously designed to produce a perceived mass gap. The combination of mass ratio and component masses challenges most results obtained from population synthesis simulations for isolated binaries (Dominik et al. 2012, 2015; Marchant et al. 2017; Giacobbo & Mapelli 2018; Kruckow et al. 2018; Mapelli & Giacobbo 2018; Mapelli et al. 2019; Neijssel et al. 2019; Spera et al. 2019; Olejak et al. 2020).

Population synthesis models distinguish between NSs and BHs using only a mass threshold, which is generally in the range of 2–3 $M_\odot$. Thus, depending on the adopted threshold and on the adopted supernova explosion model, a GW190814-like event may be labeled as either an NSBH merger or a BBH merger. Most BBH mergers have $q > 0.5$, while the distributions of merging NSBH binaries suggest that systems with $q \lesssim 0.1$ may be up to $\sim 10^3$ times less common than more symmetric ones ($q > 0.1$) and that the mass-ratio distribution peaks at $q \approx 0.2$. Furthermore, models tend to favor mergers of massive ($\gtrsim 1.3\,M_\odot$) NSs with relatively small BHs ($\lesssim 15\,M_\odot$) in environments with subsolar metallicity ($Z \lesssim 0.5\,Z_\odot$). The tendency to disfavor mergers with highly asymmetric masses in isolated binaries may be the consequence of mass transfer (e.g., Postnov & Yungelson 2014) and common envelope episodes (e.g., Ivanova et al. 2013) that cause systems with initially asymmetric masses to evolve toward more symmetric configurations. Overall, producing mergers with such unequal masses, with a secondary in the perceived mass gap, and at the rate implied by this discovery is a challenge for current models.

Nevertheless, particular choices of poorly constrained assumptions within rapid population synthesis models may increase the number of mergers with $q \lesssim 0.1$ so that the latter may be only a few times less common than (or even comparable to) systems with $q \simeq 0.2$ (e.g., Eldridge & Stanway 2016; Eldridge et al. 2017; Giacobbo & Mapelli 2018).

Another possibility is that GW190814 is of dynamical origin. Dynamical exchanges in dense stellar environments tend to pair up massive compact objects with similar masses (e.g., Sigurdsson & Hernquist 1993). This process is effective for globular clusters, where compact-object binaries may undergo tens of exchanges before they get ejected from the cluster (Portegies Zwart & McMillan 2000; Rodriguez et al. 2016, 2019; Askar et al. 2017; Park et al. 2017). For such environments, models predict that most merging BBHs have $q \simeq 1$ (e.g., Rodriguez et al. 2016), and the formation of NSBH binaries is highly suppressed because BHs dynamically dominate the cores over the complete lifetime of the clusters, preventing the interactions between BHs and NSs, with the consequence that the merger rate of NSBH binaries in globular clusters in the local universe is $\sim 10^{-2}$–10^{-1} Gpc^{-3} yr^{-1} (Clausen et al. 2013; Arca Sedda 2020; Ye et al. 2020). The rate for GW190814-like events, with a secondary in the perceived mass gap, is likely even lower. In contrast, the NSBH merger rate may be significantly higher in young star clusters (e.g., Ziosi et al. 2014) and the latter can effectively increase the number of progenitors leading to merging compact-object binaries with $q \lesssim 0.15$ (di Carlo et al. 2019; Rastello et al. 2020). Thus, young star clusters may be promising hosts for GW190814-like events, but the parameter space relevant for GW190814 is mostly unexplored in the context of star clusters.

In dense stellar environments, GW190814-like systems may also form from a low-mass merger remnant that acquires a BH companion via dynamical interactions (Gupta et al. 2020). Gupta et al. (2020) predicts a population of second-generation BHs in the 2.2–3.8 $M_\odot$ range, with a peak in the distribution at 2.6 $M_\odot$, assuming a double-Gaussian mass distribution for the NSs. However, recent dynamical simulations of globular clusters (e.g., Ye et al. 2020) find the subsequent merger of such a second-generation BH with a larger stellar-mass BH to be exceedingly rare. A high component spin could be a distinguishing feature of a second-generation compact object, but the uninformative spin posterior for the lighter component of GW190814 provides no evidence for or against this hypothesis.

A GW190814-like merger may also have originated from a hierarchical triple in the field (e.g., Antonini et al. 2017; Silsbee & Tremaine 2017; Fragione & Loeb 2019), from a wide hierarchical quadruple system (Safarzadeh et al. 2020), or from hierarchical triples in galactic centers, where the tertiary body is a supermassive BH (Antonini & Perets 2012; Petrovich & Antonini 2017; Hoang et al. 2018; Fragione et al. 2019; Stephan et al. 2019). Specifically, Safarzadeh et al. (2020) explore the possibility that a second-generation remnant with mass 3 $M_\odot$ may merge with a 30 $M_\odot$ BH, catalyzed by a 50 $M_\odot$-BH perturber. The mass-ratio distributions of BBH and NSBH mergers from hierarchical systems are similar to those of field binaries and it is unclear whether hierarchies may enhance the formation of merging compact-object binaries with highly asymmetric masses (e.g., Silsbee & Tremaine 2017).

Disks of gas around supermassive BHs in active galactic nuclei may be promising environments for the formation of GW190814-like systems. For such environments, theoretical models show that merging compact-object binaries with asymmetric masses are likely, but cannot necessarily accommodate masses as low as the secondary mass of GW190814 (e.g., Yang et al. 2019). However, McKernan et al. (2020) show that the median mass ratio of NSBH mergers in active galactic nucleus disks may be as low as ~ 0.07.

We conclude that the combination of masses, mass ratio, and inferred rate of GW190814 is challenging to explain, but potentially consistent with multiple formation scenarios. However, it is not possible to assess the validity of models that produce the right properties but do not make quantitative predictions about formation rates, even at some order-of-magnitude level.

Young star clusters and active galactic nucleus disks seem to be more promising hosts for GW190814-like mergers, since both these environments may enhance the formation of either progenitors of or directly merging compact-object binaries with more asymmetric masses to relevant rates. In contrast, globular-cluster models provide more robust predictions, showing that GW190814-like mergers with such asymmetric masses are outliers in the population predictions, even though a revision of the remnant-mass prescription is still needed. Isolated binaries could prove possible progenitors provided similar revisions are

implemented. The importance of field multiples remains to be fully explored. Future gravitational-wave observations will provide further insights into the dominance of different channels.

6.4. Cosmological Implications

Luminosity distances inferred directly from observed gravitational-wave events can be used with measurements of source redshifts in the electromagnetic spectrum to constrain cosmological parameters (Schutz 1986). Redshifts can be either obtained directly from counterparts to the gravitational-wave source (Holz & Hughes 2005), as was the case for GW170817 (Abbott et al. 2017a, 2017b, 2017e), by cross-correlation of the gravitational-wave localization posterior with catalogs of galaxy redshifts (del Pozzo 2012; Chen et al. 2018; Nair et al. 2018; Abbott et al. 2019c; Gray et al. 2020; Fishbach et al. 2019; Soares-Santos et al. 2019), by exploiting information in the neutron star equation of state (Messenger & Read 2012), or by using the redshifted masses inferred from the gravitational wave observation and assumptions about the mass distribution of the sources (Chernoff & Finn 1993; Taylor et al. 2012; Taylor & Gair 2012; Farr et al. 2019). At current sensitivities, the cosmological parameter to which LIGO–Virgo observations are most sensitive is the Hubble constant, H_0. The gravitational-wave observation of GW170817 provided a posterior on H_0 with mode and 68.3% highest posterior density interval of $H_0 = 69^{+22}_{-8}$ km s^{-1} Mpc^{-1} (Abbott et al. 2017e, 2019b, 2019c), assuming a flat prior on H_0.

GW190814 is the best localized dark siren, i.e., gravitational-wave source without an electromagnetic counterpart, observed to date, and so it is a good candidate for the statistical cross-correlation method. For a fixed reference cosmology (Ade et al. 2016), the GLADE galaxy catalog (Dálya et al. 2018) is approximately 40% complete at the distance of GW190814 and contains 472 galaxies within the 90% posterior credible volume of GW190814. To obtain a constrain on H_0, we use the methodology described in Abbott et al. (2019c) and the GLADE catalog. We take a flat prior for $H_0 \in [20, 140]$ km s^{-1} Mpc^{-1} and assign a probability to each galaxy that it is the true host of the event that is proportional to its B-band luminosity. Using the posterior distribution on the distance obtained from the combined PHM samples, we obtain $H_0 = 75^{+59}_{-13}$ km s^{-1} Mpc^{-1} using GW190814 alone (mode and 68.3% highest posterior density interval; the median and 90% symmetric credible interval is $H_0 = 83^{+55}_{-53}$ km s^{-1} Mpc^{-1}), which can be compared to $H_0 = 75^{+40}_{-32}$ km s^{-1} Mpc^{-1} (Soares-Santos et al. 2019) obtained using the dark siren GW170814 alone. The GW190814 result is the most precise measurement from a single dark siren observation to date, albeit comparable to the GW170814 result, which is expected given GW190814's small localization volume ($\sim$39,000 Mpc^3). The result is not very constraining, with the 68.3% highest posterior density interval comprising 60% of the prior range. Combining the result for GW190814 with the result obtained from GW170817, we see an improvement over the GW170817-only result, to $H_0 = 70^{+17}_{-8}$ km s^{-1} Mpc^{-1} (the median and 90% symmetric credible interval is $H_0 = 77^{+33}_{-23}$ km s^{-1} Mpc^{-1}).This result is not yet sufficiently constraining to provide further insight into current tensions in low and high redshift measurements of the Hubble constant (Verde et al. 2019), but these constraints will continue to improve as further gravitational-wave observations are included (e.g., projections in Chen et al. 2018; Vitale & Chen 2018; Gray et al. 2020; Feeney et al. 2019).

7. Conclusions

During their third observing run, on 2019 August 14, 21:10:39 UTC, the LIGO and Virgo detectors observed GW190814, a novel source unlike any other known compact binary coalescence. Thanks in part to the observation of significant power in subdominant multipoles of the gravitational radiation, and the conclusive measurement of little to no spin precession, we obtain precise measurements of its physical source properties that clearly set it apart from other compact binaries.

In particular, (a) its mass ratio of $q = 0.112^{+0.008}_{-0.009}$ is the most unequal ever observed with gravitational waves, (b) the bound $\chi_1 \leqslant 0.07$ on the spin of the $23.2^{+1.1}_{-1.0}\,M_\odot$ BH is the strongest constraint on a primary spin for any gravitational-wave source to date, and (c) the secondary mass measurement of $2.59^{+0.08}_{-0.09}$ $M_\odot$ makes it the lightest BH or the heaviest NS discovered in a double compact-object system. We find no evidence of measurable tidal effects in the signal, and no electromagnetic counterpart to the gravitational waves has been identified.

Comparisons between the secondary mass and several current estimates of the maximum NS mass suggest that GW190814 is unlikely to originate in an NSBH coalescence. Nevertheless, the $M_{\rm max}$ estimates are uncertain enough that improved knowledge of the NS EOS or further observations of the astrophysical population of compact objects could alter this assessment. For this reason, we cannot firmly exclude the possibility that the secondary is an NS, nor can we be certain that it is a BH. Regardless, this event sheds new light on the compact-object mass distribution at the interface between known NSs and BHs.

The unique combination of masses and inferred merger rate for this event is difficult to produce in population synthesis models of multicomponent systems in galactic fields or dense stellar environments. The discovery of GW190814 may therefore reshape our understanding of the processes by which the lightest BHs or the most massive NSs form. Based on our rate density estimate, we may reasonably expect to detect more systems of this kind after a year at design sensitivity. This discovery may prove to be the first hint of a larger population that could change our perspective on the formation and mass spectrum of compact objects.

Segments of data containing the signal from all three interferometers, and samples from the posterior distributions for the source parameters, are available from the Gravitational Wave Open Science Center (https://doi.org/10.7935/zzw5-ak90). The software packages used in our analysis are open source.

The authors gratefully acknowledge the support of the United States National Science Foundation (NSF) for the construction and operation of the LIGO Laboratory and Advanced LIGO as well as the Science and Technology Facilities Council (STFC) of the United Kingdom, the Max-Planck-Society (MPS), and the State of Niedersachsen/Germany for support of the construction of Advanced LIGO and construction and operation of the GEO600 detector. Additional support for Advanced LIGO was provided by the Australian Research Council. The authors gratefully acknowledge the Italian Istituto Nazionale di Fisica Nucleare (INFN), the French Centre National de la Recherche Scientifique (CNRS) and the Netherlands Organization for Scientific Research, for the construction and operation of the Virgo detector and the creation and support of the EGO consortium.

The authors also gratefully acknowledge research support from these agencies as well as by the Council of Scientific and Industrial Research of India, the Department of Science and Technology, India, the Science & Engineering Research Board (SERB), India, the Ministry of Human Resource Development, India, the Spanish Agencia Estatal de Investigación, the Vicepresidència i Conselleria d'Innovació Recerca i Turisme and the Conselleria d'Educació i Universitat del Govern de les Illes Balears, the Conselleria d'Innovació Universitats, Ciència i Societat Digital de la Generalitat Valenciana and the CERCA Programme Generalitat de Catalunya, Spain, the National Science Centre of Poland, the Swiss National Science Foundation (SNSF), the Russian Foundation for Basic Research, the Russian Science Foundation, the European Commission, the European Regional Development Funds (ERDF), the Royal Society, the Scottish Funding Council, the Scottish Universities Physics Alliance, the Hungarian Scientific Research Fund (OTKA), the French Lyon Institute of Origins (LIO), the Belgian Fonds de la Recherche Scientifique (FRS-FNRS), Actions de Recherche Concertées (ARC) and Fonds Wetenschappelijk Onderzoek–Vlaanderen (FWO), Belgium, the Paris Île-de-France Region, the National Research, Development and Innovation Office Hungary (NKFIH), the National Research Foundation of Korea, Industry Canada and the Province of Ontario through the Ministry of Economic Development and Innovation, the Natural Science and Engineering Research Council Canada, the Canadian Institute for Advanced Research, the Brazilian Ministry of Science, Technology, Innovations, and Communications, the International Center for Theoretical Physics South American Institute for Fundamental Research (ICTP-SAIFR), the Research Grants Council of Hong Kong, the National Natural Science Foundation of China (NSFC), the Leverhulme Trust, the Research Corporation, the Ministry of Science and Technology (MOST), Taiwan and the Kavli Foundation. The authors gratefully acknowledge the support of the NSF, STFC, INFN and CNRS for provision of computational resources. Some of the parameter estimation analyses presented in this paper were performed using the supercomputer cluster at the Swinburne University of Technology (OzSTAR and SSTAR).

We would like to thank all of the essential workers who put their health at risk during the COVID-19 pandemic, without whom we would not have been able to complete this work.

Software: The detection of the signal and subsequent significance evaluation were performed with the GSTLAL-based inspiral software pipeline (Cannon et al. 2012; Privitera et al. 2014; Messick et al. 2017; Sachdev et al. 2019; Hanna et al. 2020), built on the LALSUITE software library (LIGO Scientific Collaboration 2018), and with the PYCBC (Nitz et al. 2018, 2019; Usman et al. 2016) and MBTAONLINE (Adams et al. 2016) packages. Parameter estimation was performed with the LALINFERENCE (Veitch et al. 2015) and LALSIMULATION libraries within LALSUITE (LIGO Scientific Collaboration 2018), as well as the BILBY and PBILBY Libraries (Ashton et al. 2019; Smith & Ashton 2019) and the DYNESTY nested sampling package (Speagle 2020). Interpretation and curation of the posterior samples was handled by the PESummary library (Hoy & Raymond 2020). Estimates of the noise spectra were obtained using BAYESWAVE (Cornish & Littenberg 2015; Littenberg & Cornish 2015). Plots were prepared with Matplotlib (Hunter 2007). The sky map plot also used Astropy (http://www.astropy.org) a community-developed core Python package for Astronomy (Astropy Collaboration et al. 2013; Price-Whelan et al. 2018) and `ligo.skymap` (https://lscsoft.docs.ligo.org/ligo.skymap).

ORCID iDs

S. Bernuzzi https://orcid.org/0000-0002-2334-0935
C. P. L. Berry https://orcid.org/0000-0003-3870-7215
M. Cabero https://orcid.org/0000-0003-4059-4512
N. Cornish https://orcid.org/0000-0002-7435-0869
D. E. Holz https://orcid.org/0000-0002-0175-5064
V. Kalogera https://orcid.org/0000-0001-9236-5469
J. S. Key https://orcid.org/0000-0003-0123-7600
K. Lee https://orcid.org/0000-0003-3175-1336
Shubhanshu Tiwari https://orcid.org/0000-0003-1611-6625
K. Ueno https://orcid.org/0000-0003-0424-3045
J. T. Whelan https://orcid.org/0000-0001-5710-6576
Hang Yu https://orcid.org/0000-0002-6011-6190
M. Zevin https://orcid.org/0000-0002-0147-0835

References

Aasi, J., Abbott, B. P., Abbott, R., et al. 2015, CQGra, 32, 074001
Abbott, B. P., Abbott, R., Abbott, T. D., et al. 2016a, PhRvL, 116, 061102
Abbott, B. P., Abbott, R., Abbott, T. D., et al. 2016b, PhRvX, 6, 041015
Abbott, B. P., Abbott, R., Abbott, T. D., et al. 2016c, CQGra, 33, 134001
Abbott, B. P., Abbott, R., Abbott, T. D., et al. 2016d, PhRvD, 93, 122003
Abbott, B. P., Abbott, R., Abbott, T. D., et al. 2016e, PhRvD, 93, 122004
Abbott, B. P., Abbott, R., Abbott, T. D., et al. 2016f, PhRvL, 116, 241102
Abbott, B. P., Abbott, R., Abbott, T. D., et al. 2016g, PhRvL, 116, 221101
Abbott, B. P., Abbott, R., Abbott, T. D., et al. 2017a, PhRvL, 119, 161101
Abbott, B. P., Abbott, R., Abbott, T. D., et al. 2017b, ApJL, 848, L12
Abbott, B. P., Abbott, R., Abbott, T. D., et al. 2017c, ApJL, 848, L13
Abbott, B. P., Abbott, R., Abbott, T. D., et al. 2017d, ApJL, 850, L39
Abbott, B. P., Abbott, R., Abbott, T. D., et al. 2017e, Nat, 551, 85
Abbott, B. P., Abbott, R., Abbott, T. D., et al. 2017f, ApJL, 851, L35
Abbott, B. P., Abbott, R., Abbott, T. D., et al. 2017g, ApJL, 851, L16
Abbott, B. P., Abbott, R., Abbott, T. D., et al. 2018, PhRvL, 121, 161101
Abbott, B. P., Abbott, R., Abbott, T. D., et al. 2019a, PhRvX, 9, 031040
Abbott, B. P., Abbott, R., Abbott, T. D., et al. 2019b, PhRvX, 9, 011001
Abbott, B. P., Abbott, R., Abbott, T. D., et al. 2019c, arXiv:1908.06060
Abbott, B. P., Abbott, R., Abbott, T. D., et al. 2019d, PhRvL, 123, 011102
Abbott, B. P., Abbott, R., Abbott, T. D., et al. 2019e, PhRvD, 100, 104036
Abbott, B. P., Abbott, R., Abbott, T. D., et al. 2019f, ApJ, 875, 160
Abbott, B. P., Abbott, R., Abbott, T. D., et al. 2020a, ApJL, 892, L3
Abbott, B. P., Abbott, R., Abbott, T. D., et al. 2020b, arXiv:1304.0670v10
Abbott, B. P., Abbott, R., Abbott, T. D., et al. 2020c, CQGra, 37, 045006
Abbott, R., Abbott, T. D., Abraham, S., et al. 2020d, arXiv:2004.08342
Accadia, T., Acernese, F., Antonucci, F., et al. 2010, CQGra, 27, 194011
Acernese, F., Adams, T., Agatsuma, K., et al. 2018, CQGra, 35, 205004
Acernese, F., Agathos, M., Agatsuma, K., et al. 2015, CQGra, 32, 024001
Ackley, K., Amati, L., Barbieri, C., et al. 2020, arXiv:2002.01950
Adams, T., Buskulic, D., Germain, V., et al. 2016, CQGra, 33, 175012
Ade, P. A. R., Aghanim, N., Arnaud, M., et al. 2016, A&A, 594, A13
Ageron, M., Baret, B., Coleiro, A., et al. 2019, GCN, 25330, 1
Ajith, P., Fotopoulos, N., Privitera, S., Neunzert, A., & Weinstein, A. J. 2014, PhRvD, 89, 084041
Ajith, P., Hannam, M., Husa, S., et al. 2011, PhRvL, 106, 241101
Alsing, J., Silva, H. O., & Berti, E. 2018, MNRAS, 478, 1377
Andreoni, I., Goldstein, D. A., Kasliwal, M. M., et al. 2020, ApJ, 890, 131
Antier, S., Agayeva, S., Aivazyan, V., et al. 2020, MNRAS, 492, 3904
Antonini, F., & Perets, H. B. 2012, ApJ, 757, 27
Antonini, F., Toonen, S., & Hamers, A. S. 2017, ApJ, 841, 77
Apostolatos, T. A., Cutler, C., Sussman, G. J., & Thorne, K. S. 1994, PhRvD, 49, 6274
Arca Sedda, M. 2020, CmPhy, 3, 43
Arun, K. G., Buonanno, A., Faye, G., & Ochsner, E. 2009, PhRvD, 79, 104023
Arun, K. G., Iyer, B. R., Qusailah, M. S. S., & Sathyaprakash, B. S. 2006a, PhRvD, 74, 024006
Arun, K. G., Iyer, B. R., Qusailah, M. S. S., & Sathyaprakash, B. S. 2006b, CQGra, 23, L37
Ashton, G., Hübner, M., Lasky, P. D., et al. 2019, ApJS, 241, 27
Askar, A., Szkudlarek, M., Gondek-Rosińska, D., Giersz, M., & Bulik, T. 2017, MNRAS, 464, L36

Astropy Collaboration, Robitaille, T. P., Tollerud, E. J., et al. 2013, A&A, 558, A33
Babak, S., Taracchini, A., & Buonanno, A. 2017, PhRvD, 95, 024010
Bailyn, C. D., Jain, R. K., Coppi, P., & Orosz, J. A. 1998, ApJ, 499, 367
Baird, E., Fairhurst, S., Hannam, M., & Murphy, P. 2013, PhRvD, 87, 024035
Blanchet, L. 2014, LRR, 17, 2
Blanchet, L., Damour, T., Esposito-Farèse, G., & Iyer, B. R. 2005, PhRvD, 71, 124004
Blanchet, L., Damour, T., Iyer, B. R., Will, C. M., & Wiseman, A. G. 1995, PhRvL, 74, 3515
Blanchet, L., Faye, G., Iyer, B. R., & Sinha, S. 2008, CQGra, 25, 165003
Bohé, A., Shao, L., Taracchini, A., et al. 2017, PhRvD, 95, 044028
Brown, D. A., Kumar, P., & Nitz, A. H. 2013, PhRvD, 87, 082004
Buonanno, A., & Damour, T. 1999, PhRvD, 59, 084006
Buonanno, A., Chen, Y., & Vallisneri, M. 2003, PhRvD, 67, 104025
Burrows, A., Radice, D., & Vartanyan, D. 2019, MNRAS, 485, 3153
Burrows, A., Vartanyan, D., Dolence, J. C., Skinner, M. A., & Radice, D. 2018, SSRv, 214, 33
Cannon, K., Cariou, R., Chapman, A., et al. 2012, ApJ, 748, 136
Capano, C., Dent, T., Hanna, C., et al. 2016a, PhRvD, 96, 082002
Capano, C., Harry, I., Privitera, S., & Buonanno, A. 2016b, PhRvD, 93, 124007
Cardoso, V., & Pani, P. 2019, LRR, 22, 4
Carter, B. 1971, PhRvL, 26, 331
Chatterji, S., Blackburn, L., Martin, G., & Katsavounidis, E. 2004, CQGra, 21, S1809
Chen, H.-Y., Fishbach, M., & Holz, D. E. 2018, Nat, 562, 545
Chernoff, D. F., & Finn, L. S. 1993, ApJL, 411, L5
Chornock, R., Berger, E., Kasen, D., et al. 2017, ApJL, 848, L19
Clausen, D., Sigurdsson, S., & Chernoff, D. F. 2013, MNRAS, 428, 3618
Cokelaer, T. 2007, PhRvD, 76, 102004
Cook, G. B., Shapiro, S. L., & Teukolsky, S. A. 1994, ApJ, 424, 823
Cornish, N., Sampson, L., Yunes, N., & Pretorius, F. 2011, PhRvD, 84, 062003
Cornish, N. J., & Littenberg, T. B. 2015, CQGra, 32, 135012
Cotesta, R., Buonanno, A., Bohé, A., et al. 2018, PhRvD, 98, 084028
Coughlin, M. W., Dietrich, T., Antier, S., et al. 2020, MNRAS, 492, 863
Cowperthwaite, P. S., Berger, E., Villar, V. A., et al. 2017, ApJL, 848, L17
Cromartie, H. T., Fonseca, E., Ransom, S. M., et al. 2019, NatAs, 4, 72
Cutler, C., & Flanagan, E. E. 1994, PhRvD, 49, 2658
Dálya, G., Galgóczi, G., Dobos, L., et al. 2018, MNRAS, 479, 2374
Damour, T. 2001, PhRvD, 64, 124013
Damour, T., Jaranowski, P., & Schäfer, G. 2001, PhLB, 513, 147
Davies, G. S., Dent, T., Tápai, M., et al. 2020, arXiv:2002.08291
del Pozzo, W. 2012, PhRvD, 86, 043011
Dhanpal, S., Ghosh, A., Mehta, A. K., Ajith, P., & Sathyaprakash, B. 2019, PhRvD, 99, 104056
di Carlo, U. N., Giacobbo, N., Mapelli, M., et al. 2019, MNRAS, 487, 2947
Dobie, D., Stewart, A., Murphy, T., et al. 2019, ApJL, 887, L13
Dominik, M., Belczynski, K., Fryer, C., et al. 2012, ApJ, 759, 52
Dominik, M., Berti, E., O'Shaughnessy, R., et al. 2015, ApJ, 806, 263
Effler, A., Schofield, R. M. S., Frolov, V. V., et al. 2015, CQGra, 32, 035017
Eldridge, J. J., & Stanway, E. R. 2016, MNRAS, 462, 3302
Eldridge, J. J., Stanway, E. R., Xiao, L., et al. 2017, PASA, 34, e058
Ertl, T., Janka, H. T., Woosley, S. E., Sukhbold, T., & Ugliano, M. 2016, ApJ, 818, 124
Essick, R., Landry, P., & Holz, D. E. 2020, PhRvD, 101, 063007
Fairhurst, S., Green, R., Hannam, M., et al. 2019a, arXiv:1908.00555
Fairhurst, S., Green, R., Hoy, C., et al. 2019b, arXiv:1908.05707
Farr, B., Berry, C. P. L., Farr, W. M., et al. 2016, ApJ, 825, 116
Farr, W. M., & Chatziioannou, K. 2020, RNAAS, 4, 65
Farr, W. M., Fishbach, M., Ye, J., & Holz, D. E. 2019, ApJL, 883, L42
Farr, W. M., Sravan, N., Cantrell, A., et al. 2011, ApJ, 741, 103
Feeney, S. M., Peiris, H. V., Williamson, A. R., et al. 2019, PhRvL, 122, 061105
Fernández, R., Foucart, F., & Lippuner, J. 2020, arXiv:2005.14208
Fishbach, M., Gray, R., Magaña Hernandez, I., Qi, H., & Sur, A. 2019, ApJL, 871, L13
Fishbach, M., & Holz, D. E. 2020, ApJL, 891, L27
Flanagan, E. E., & Hinderer, T. 2008, PhRvD, 77, 021502
Foucart, F., Buchman, L., Duez, M. D., et al. 2013, PhRvD, 88, 064017
Fragione, G., Grishin, E., Leigh, N. W. C., Perets, H. B., & Perna, R. 2019, MNRAS, 488, 47
Fragione, G., & Loeb, A. 2019, MNRAS, 486, 4443
Freire, P. C. C., Ransom, S. M., Bégin, S., et al. 2008, ApJ, 675, 670
Fryer, C. L., Belczynski, K., Wiktorowicz, G., et al. 2012, ApJ, 749, 91
Giacobbo, N., & Mapelli, M. 2018, MNRAS, 480, 2011
Giesers, B., Dreizler, S., Husser, T.-O., et al. 2018, MNRAS, 475, L15
Gomez, S., Hosseinzadeh, G., Cowperthwaite, P. S., et al. 2019, ApJL, 884, L55
Gray, R., Magaña Hernandez, I., Qi, H., et al. 2020, PhRvD, 101, 122001
Guo, X., Chu, Q., Chung, S. K., et al. 2018, CoPhC, 231, 62
Gupta, A., Gerosa, D., Arun, K. G., Berti, E., & Sathyaprakash, B. S. 2020, PhRvD, 101, 103036
Hanna, C., Caudill, S., Messick, C., et al. 2020, PhRvD, 101, 022003
Hansen, R. O. 1974, JMP, 15, 46
Harry, I. W., Allen, B., & Sathyaprakash, B. S. 2009, PhRvD, 80, 104014
Harry, I., Nitz, A. H., Brown, D. A., et al. 2014, PhRvD, 89, 024010
Hartle, J. B. 1967, ApJ, 150, 1005
Healy, J., & Lousto, C. O. 2017, PhRvD, 95, 024037
Hoang, B.-M., Naoz, S., Kocsis, B., Rasio, F. A., & Dosopoulou, F. 2018, ApJ, 856, 140
Hofmann, F., Barausse, E., & Rezzolla, L. 2016, ApJL, 825, L19
Holz, D. E., & Hughes, S. A. 2005, ApJ, 629, 15
Hooper, S., Chung, S. K., Luan, J., et al. 2012, PhRvD, 86, 024012
Hoy, C., & Raymond, V. 2020, arXiv:2006.06639
Huang, Y., Haster, C.-J., Vitale, S., et al. 2020, arXiv:2005.11850
Hunter, J. D. 2007, CSE, 9, 90
Husa, S., Khan, S., Hannam, M., et al. 2016, PhRvD, 93, 044006
Indik, N., Fehrmann, H., Harke, F., Krishnan, B., & Nielsen, A. B. 2018, PhRvD, 97, 124008
Islam, T., Mehta, A. K., Ghosh, A., et al. 2020, PhRvD, 101, 024032
Ivanova, N., Justham, S., Chen, X., et al. 2013, A&Ar, 21, 59
Janka, H.-T. 2012, ARNPS, 62, 407
Jiang, J.-L., Tang, S.-P., Wang, Y.-Z., Fan, Y.-Z., & Wei, D.-M. 2020, ApJ, 892, 55
Jiménez-Forteza, X., Keitel, D., Husa, S., et al. 2017, PhRvD, 95, 064024
Johnson-McDaniel, N. K., Gupta, A., Ajith, P., et al. 2016, Determining the final spin of a binary black hole system including in-plane spins: Method and checks of accuracy, Tech. Rep. LIGO-T1600168, https://dcc.ligo.org/T1600168/public
Kalaghatgi, C., Hannam, M., & Raymond, V. 2020, PhRvD, 10, 103004
Kapadia, S. J., Caudill, S., Creighton, J. D. E., et al. 2020, CQGra, 37, 045007
Karki, S., Tuyenbayev, D., Kandhasamy, S., et al. 2016, RScI, 87, 114503
Kasen, D., Metzger, B., Barnes, J., Quataert, E., & Ramirez-Ruiz, E. 2017, Nat, 551, 80
Kasliwal, M. M., Kasen, D., Lau, R. M., et al. 2019, MNRAS Letters, in press
Kasprzack, M., & Yu, H. 2017, Beam Position from Angle to Length Minimization, Tech. Rep. LIGO-T1600397, https://dcc.ligo.org/T1600397/public
Kastha, S., Gupta, A., Arun, K., Sathyaprakash, B., & van den Broeck, C. 2018, PhRvD, 98, 124033
Kastha, S., Gupta, A., Arun, K. G., Sathyaprakash, B. S., & van den Broeck, C. 2019, PhRvD, 100, 044007
Kaup, D. J. 1968, PhRv, 172, 1331
Kawaguchi, K., Shibata, M., & Tanaka, M. 2020, ApJ, 893, 153
Khan, S., Chatziioannou, K., Hannam, M., & Ohme, F. 2019, PhRvD, 100, 024059
Khan, S., Husa, S., Hannam, M., et al. 2016, PhRvD, 93, 044007
Khan, S., Ohme, F., Chatziioannou, K., & Hannam, M. 2020, PhRvD, 101, 024056
Kidder, L. E. 2008, PhRvD, 77, 044016
Kim, C., Kalogera, V., & Lorimer, D. R. 2003, ApJ, 584, 985
Klimenko, S., Yakushin, I., Mercer, A., et al. 2008, CQGra, 25, 114029
Klimenko, S., Vedovato, G., Drago, M., et al. 2016, PhRvD, 93, 042004
Kochanek, C. S. 2014, ApJ, 785, 28
Kreidberg, L., Bailyn, C. D., Farr, W. M., & Kalogera, V. 2012, ApJ, 757, 36
Krishnendu, N. V., Saleem, M., Samajdar, A., et al. 2019, PhRvD, 100, 104019
Kruckow, M. U., Tauris, T. M., Langer, N., Kramer, M., & Izzard, R. G. 2018, MNRAS, 481, 1908
Kumar, P., Blackman, J., Field, S. E., et al. 2019, PhRvD, 99, 124005
Kumar, P., Pürrer, M., & Pfeiffer, H. P. 2017, PhRvD, 95, 044039
Landry, P., Essick, R., & Chatziioannou, K. 2020, PhRvD, 101, 123007
Li, T. G. F., del Pozzo, W., Vitale, S., et al. 2012, PhRvD, 85, 082003
LIGO Scientific CollaborationVirgo Collaboration 2019a, GCN, https://gcn.gsfc.nasa.gov/notices_l/S190814bv.lvc
LIGO Scientific CollaborationVirgo Collaboration 2019b, Public Alerts User Guide, https://emfollow.docs.ligo.org/userguide/content.html
LIGO Scientific CollaborationVirgo Collaboration 2019c, GraceDB, S190814bv, https://gracedb.ligo.org/superevents/S190814bv/
LIGO Scientific CollaborationVirgo Collaboration 2019d, GCN, 25324, 1
LIGO Scientific CollaborationVirgo Collaboration 2019e, GCN, 25333, 1

LIGO Scientific Collaboration 2018, LIGO Algorithm Library, doi:10.7935/GT1W-FZ16
Lim, Y., & Holt, J. W. 2019, EPJA, 55, 209
Lindblom, L. 2010, PhRvD, 82, 103011
Lindblom, L., & Indik, N. M. 2012, PhRvD, 86, 084003
Lindblom, L., & Indik, N. M. 2014, PhRvD, 89, 064003
Lipunov, V., Gorbovskoy, E., Kornilov, V., et al. 2019, GCN, 25354, 1
Littenberg, T. B., & Cornish, N. J. 2015, PhRvD, 91, 084034
Liu, Y., Du, Z., Chung, S. K., et al. 2012, CQGra, 29, 235018
London, L., Khan, S., Fauchon-Jones, E., et al. 2018, PhRvL, 120, 161102
Mapelli, M., & Giacobbo, N. 2018, MNRAS, 479, 4391
Mapelli, M., Giacobbo, N., Santoliquido, F., & Artale, M. C. 2019, MNRAS, 487, 2
Marchant, P., Langer, N., Podsiadlowski, P., et al. 2017, A&A, 604, A55
Margalit, B., & Metzger, B. D. 2017, ApJL, 850, L19
Matas, A., Dietrich, T., Buonanno, A., et al. 2020, arXiv:2004.10001
Mazur, P. O., & Mottola, E. 2004, PNAS, 101, 9545
McKernan, B., Ford, K. E. S., & O'Shaughnessy, R. 2020, arXiv:2002.00046
Meidam, J., Tsang, K. W., Goldstein, J., et al. 2018, PhRvD, 97, 044033
Messenger, C., & Read, J. 2012, PhRvL, 108, 091101
Messick, C., Blackburn, K., Brady, P., et al. 2017, PhRvD, 95, 042001
Miller, M. C., Chirenti, C., & Lamb, F. K. 2020, ApJ, 888, 12
Miller, M. C., Lamb, F. K., Dittmann, A. J., et al. 2019, ApJL, 887, L24
Mills, J. C., & Fairhurst, S. 2020, Measuring gravitational-wave subdominant multipoles, Tech. Rep. LIGO-P2000136, https://dcc.ligo.org/P2000136/public
Mishra, C. K., Arun, K. G., Iyer, B. R., & Sathyaprakash, B. S. 2010, PhRvD, 82, 064010
Mishra, C. K., Kela, A., Arun, K. G., & Faye, G. 2016, PhRvD, 93, 084054
Morgan, R., Soares-Santos, M., Annis, J., et al. 2020, arXiv:2006.07385
Müller, B. 2016, PASA, 33, e048
Müller, H., & Serot, B. D. 1996, NuPhA, 606, 508
Nair, R., Bose, S., & Saini, T. D. 2018, PhRvD, 98, 023502
Neijssel, C. J., Vigna-Gómez, A., Stevenson, S., et al. 2019, MNRAS, 490, 3740
Neustroev, V. V., Veledina, A., Poutanen, J., et al. 2014, MNRAS, 445, 2424
Ng, K. K. Y., Vitale, S., Zimmerman, A., et al. 2018, PhRvD, 98, 083007
Nitz, A., Harry, I., Brown, D., et al. 2019, gwastro/pycbc: PyCBC Release v1.15.2, Zenodo, doi:10.5281/zenodo.3596447
Nitz, A. H., Dal Canton, T., Davis, D., & Reyes, S. 2018, PhRvD, 98, 024050
Nitz, A. H., Dent, T., Dal Canton, T., Fairhurst, S., & Brown, D. A. 2017, ApJ, 849, 118
Nitz, A. H., Dent, T., Davies, G. S., et al. 2020, ApJ, 891, 123
Nuttall, L. K. 2018, RSPTA, 376, 20170286
Olejak, A., Belczynski, K., Holz, D. E., et al. 2020, arXiv:2004.11866
Ossokine, S., Buonanno, A., Marsat, S., et al. 2020, arXiv:2004.09442
Owen, B. J. 1996, PhRvD, 53, 6749
Owen, B. J., & Sathyaprakash, B. S. 1999, PhRvD, 60, 022002
Özel, F., Psaltis, D., Narayan, R., & McClintock, J. E. 2010, ApJ, 725, 1918
Özel, F., Psaltis, D., Narayan, R., & Villarreal, A. S. 2012, ApJ, 757, 55
Pappas, G., & Apostolatos, T. A. 2012, PhRvL, 108, 231104
Park, D., Kim, C., Lee, H. M., Bae, Y.-B., & Belczynski, K. 2017, MNRAS, 469, 4665
Payne, E., Talbot, C., & Thrane, E. 2019, PhRvD, 100, 123017
Petrovich, C., & Antonini, F. 2017, ApJ, 846, 146
Poisson, E. 1998, PhRvD, 57, 5287
Poisson, E., & Will, C. M. 1995, PhRvD, 52, 848
Portegies Zwart, S. F., & McMillan, S. L. W. 2000, ApJL, 528, L17
Postnov, K. A., & Yungelson, L. R. 2014, LRR, 17, 3
Price-Whelan, A. M., Sipőcz, B. M., & Günther, H. M. 2018, AJ, 156, 123
Privitera, S., Mohapatra, S. R. P., Ajith, P., et al. 2014, PhRvD, 89, 024003
Prodi, G., Vedovato, G., Drago, M., et al. 2020, Technical note on the measurement of inspiral higher order modes by coherent WaveBurst in GW190814, Tech. Rep. LIGO-T2000124, https://dcc.ligo.org/T2000124/public
Pürrer, M. 2016, PhRvD, 93, 064041
Raaijmakers, G., Riley, T. E., Watts, A. L., et al. 2019, ApJL, 887, L22
Racine, E. 2008, PhRvD, 78, 044021
Rastello, S., Mapelli, M., di Carlo, U. N., et al. 2020, arXiv:2003.02277
Rezzolla, L., Most, E. R., & Weih, L. R. 2018, ApJL, 852, L25
Riley, T. E., Watts, A. L., Bogdanov, S., et al. 2019, ApJL, 887, L21
Rodriguez, C. L., Chatterjee, S., & Rasio, F. A. 2016, PhRvD, 93, 084029
Rodriguez, C. L., Zevin, M., Amaro-Seoane, P., et al. 2019, PhRvD, 100, 043027
Rosswog, S., Sollerman, J., Feindt, U., et al. 2018, A&A, 615, A132
Roulet, J., & Zaldarriaga, M. 2019, MNRAS, 484, 4216
Roy, S., Sengupta, A. S., & Ajith, P. 2019a, PhRvD, 99, 024048
Roy, S., Sengupta, A. S., & Arun, K. G. 2019b, arXiv:1910.04565
Roy, S., Sengupta, A. S., & Thakor, N. 2017, PhRvD, 95, 104045
Ruiz, M., Shapiro, S. L., & Tsokaros, A. 2018, PhRvD, 97, 021501
Ryan, F. D. 1997, PhRvD, 55, 6081
Sachdev, S., Caudill, S., Fong, H., et al. 2019, arXiv:1901.08580
Safarzadeh, M., Hamers, A. S., Loeb, A., & Berger, E. 2020, ApJL, 888, L3
Santamaría, L., Ohme, F., Ajith, P., et al. 2010, PhRvD, 82, 064016
Sathyaprakash, B., & Dhurandhar, S. 1991, PhRvD, 44, 3819
Schmidt, P., Ohme, F., & Hannam, M. 2015, PhRvD, 91, 024043
Schutz, B. F. 1986, Nat, 323, 310
Shibata, M., Zhou, E., Kiuchi, K., & Fujibayashi, S. 2019, PhRvD, 100, 023015
Sigurdsson, S., & Hernquist, L. 1993, Nat, 364, 423
Silsbee, K., & Tremaine, S. 2017, ApJ, 836, 39
Singer, L. P., & Price, L. 2016, PhRvD, 93, 024013
Smith, R., & Ashton, G. 2019, arXiv:1909.11873
Soares-Santos, M., Palmese, A., Hartley, W., et al. 2019, ApJL, 876, L7
Speagle, J. S. 2020, MNRAS, 493, 3132
Spera, M., Mapelli, M., Giacobbo, N., et al. 2019, MNRAS, 485, 889
Stephan, A. P., Naoz, S., Ghez, A. M., et al. 2019, ApJ, 878, 58
Sukhbold, T., & Woosley, S. E. 2014, ApJ, 783, 10
Tanvir, N. R., Levan, A. J., González-Fernández, C., et al. 2017, ApJL, 848, L27
Taylor, S. R., & Gair, J. R. 2012, PhRvD, 86, 023502
Taylor, S. R., Gair, J. R., & Mandel, I. 2012, PhRvD, 85, 023535
The IceCube Collaboration 2019, GCN, 25557, 1
Thompson, J. E., Fauchon-Jones, E., Khan, S., et al. 2020a, arXiv:2002.08383
Thompson, T. A., Kochanek, C. S., Stanek, K. Z., et al. 2019, Sci, 366, 637
Thompson, T. A., Kochanek, C. S., Stanek, K. Z., et al. 2020b, Sci, 368, eaba4356
Thorne, K. S. 1980, RvMP, 52, 299
Tiwari, V. 2018, CQGra, 35, 145009
Uchikata, N., Yoshida, S., & Pani, P. 2016, PhRvD, 94, 064015
Ugliano, M., Janka, H.-T., Marek, A., & Arcones, A. 2012, ApJ, 757, 69
Usman, S. A., Mills, J. C., & Fairhurst, S. 2019, ApJ, 877, 82
Usman, S. A., Nitz, A. H., Harry, I. W., et al. 2016, CQGra, 33, 215004
van den Broeck, C., & Sengupta, A. S. 2007a, CQGra, 24, 155
van den Broeck, C., & Sengupta, A. S. 2007b, CQGra, 24, 1089
van den Heuvel, E. P. J., & Tauris, T. M. 2020, Sci, 368, eaba3282
Veitch, J., Raymond, V., Farr, B., et al. 2015, PhRvD, 91, 042003
Venumadhav, T., Zackay, B., Roulet, J., Dai, L., & Zaldarriaga, M. 2020, PhRvD, 101, 083030
Verde, L., Treu, T., & Riess, A. G. 2019, NatAs, 3, 891
Vieira, N., Ruan, J. J., Haggard, D., et al. 2020, ApJ, 895, 96
Viets, A. D., Wade, M., Urban, A. L., et al. 2018, CQGra, 35, 095015
Villar, V. A., Guillochon, J., Berger, E., et al. 2017, ApJL, 851, L21
Vitale, S., & Chen, H.-Y. 2018, PhRvL, 121, 021303
Vitale, S., Lynch, R., Raymond, V., et al. 2017, PhRvD, 95, 064053
Vitale, S., Lynch, R., Veitch, J., Raymond, V., & Sturani, R. 2014, PhRvL, 112, 251101
Watson, A. M., Butler, N. R., Lee, W. H., et al. 2020, MNRAS, 492, 5916
Watson, D., Hansen, C. J., Selsing, J., et al. 2019, Nat, 574, 497
Wyrzykowski, Ł., & Mandel, I. 2020, A&A, 636, A20
Yang, Y., Bartos, I., Haiman, Z., et al. 2019, ApJ, 876, 122
Ye, C. S., Fong, W.-F., Kremer, K., et al. 2020, ApJL, 888, L10
Yunes, N., & Pretorius, F. 2009, PhRvD, 80, 122003
Zackay, B., Dai, L., Venumadhav, T., Roulet, J., & Zaldarriaga, M. 2019a, arXiv:1910.09528
Zackay, B., Venumadhav, T., Dai, L., Roulet, J., & Zaldarriaga, M. 2019b, PhRvD, 100, 023007
Ziosi, B. M., Mapelli, M., Branchesi, M., & Tormen, G. 2014, MNRAS, 441, 3703

Monthly Notices of the ROYAL ASTRONOMICAL SOCIETY

MNRAS **505,** 1600–1606 (2021)
Advance Access publication 2021 May 17

https://doi.org/10.1093/mnras/stab1383

GW190814: on the properties of the secondary component of the binary

Bhaskar Biswas,[1★] Rana Nandi,[2★] Prasanta Char,[3] Sukanta Bose[1,4] and Nikolaos Stergioulas[5]

[1]*Inter-University Centre for Astronomy and Astrophysics, Post Bag 4, Ganeshkhind, Pune 411007, India*
[2]*Polba Mahavidyalaya, Hooghly, West Bengal 712148, India*
[3]*Space Sciences, Technologies and Astrophysics Research (STAR) Institute, Université de Liège, Bât. B5a, 4000 Liège, Belgium*
[4]*Department of Physics & Astronomy, Washington State University, 1245 Webster, Pullman, WA 99164-2814, USA*
[5]*Aristotle University of Thessaloniki, Department of Physics, University Campus Laboratory of Astronomy, 54124 Thessaloniki, Greece*

Accepted 2021 May 8. Received 2021 May 1; in original form 2021 February 25

ABSTRACT

We show that the odds of the mass-gap (secondary) object in GW190814 being a neutron star (NS) improve if one allows for a stiff high-density equation of state (EoS) or a large spin. Since its mass is $\in (2.50, 2.67)\,\mathrm{M}_\odot$, establishing its true nature will make it either the heaviest NS or the lightest black hole (BH), and can have far-reaching implications on NS EoS and compact object formation channels. When limiting oneself to the NS hypothesis, we deduce the secondary's properties by using a Bayesian framework with a hybrid EoS formulation that employs a parabolic expansion-based nuclear empirical parametrization around the nuclear saturation density augmented by a generic 3-segment piecewise polytrope (PP) model at higher densities and combining a variety of astrophysical observations. For the slow-rotation scenario, GW190814 implies a very stiff EoS and a stringent constraint on the EoS specially in the high-density region. On the other hand assuming the secondary object is a rapidly rotating NS, we constrain its rotational frequency to be $f = 1170^{+389}_{-495}$ Hz, within a 90 per cent confidence interval (CI). In this scenario, the secondary object in GW190814 would qualify as the fastest rotating NS ever observed. However, for this scenario to be viable, rotational instabilities would have to be suppressed both during formation and the subsequent evolution until merger, otherwise the secondary of GW190814 is more likely to be a BH.

Key words: dense matter – stars: neutron.

1 INTRODUCTION

Recently, the LIGO (Aasi et al. 2015) and Virgo (Acernese et al. 2015) scientific collaborations (LVC) reported the detection of one of the most enigmatic gravitational wave (GW) mergers till date (Abbott et al. 2020a). This event, named GW190814, has been associated with a compact object binary of mass ratio, $q = 0.112^{+0.008}_{-0.009}$, and primary and secondary masses $m_1 = 23.2^{+1.1}_{-1.0}\,\mathrm{M}_\odot$ and $m_2 = 2.59^{+0.08}_{-0.09}$, respectively. Since, an electromagnetic (EM) counterpart has not been found for this particular event and the tidal deformability has not been measurable from the GW signal, the secondary component might well be the lightest BH ever found. However, EM emissions are expected to be observed for only a fraction of NS binaries, and tidal deformabilities are known to be small for massive NSs, hence the secondary in this case cannot be ruled out as an NS. In the latter scenario, it would become the heaviest NS observed in a binary system, given its well-constrained mass. Either hypothesis deserves a deep study owing to its far-reaching implications on the formation channels of such objects and the nature of the densest form of matter in the Universe.

Discoveries of massive pulsars in past decades have severely constrained the EoS of supranuclear matter inside their cores (Demorest et al. 2010; Antoniadis et al. 2013; Fonseca et al. 2016; Arzoumanian et al. 2018; Cromartie et al. 2019). These observations provided a very strong lower bound of $\sim 2\,\mathrm{M}_\odot$ on the maximum mass of non-rotating NSs that all the competing EoS models from nuclear physics must satisfy. Furthermore, GW170817 (Abbott et al. 2017) has prompted several studies predicting an upper bound of ~ 2.2–$2.3\,\mathrm{M}_\odot$ on $M_{\max}$ of non-rotating NSs, based on the mass ejecta, kilonova signal and absence of a prompt collapse (Margalit & Metzger 2017; Shibata et al. 2017; Rezzolla, Most & Weih 2018; Ruiz, Shapiro & Tsokaros 2018; Shibata et al. 2019; Shao et al. 2020). While the simultaneous mass−radius measurements of PSR J0030 + 0451 by NICER collaboration (Miller et al. 2019; Riley et al. 2019) indicate a tilt towards slightly stiffer EoS (Biswas et al. 2020; Landry, Essick & Chatziioannou 2020; Raaijmakers et al. 2020), the distribution of m_2 would require even higher $M_{\max}$. Possible formation channels of GW190814-type binaries have also been studied in some recent works (Kinugawa, Nakamura & Nakano 2020; Safarzadeh & Loeb 2020; Zevin et al. 2020). While there is a general consensus that the fallback of a significant amount of bound supernova ejecta on the secondary compact remnant leads to its formation in the lower mass-gap region, the nature of its state at the time of the merger being a BH or an NS remains unclear. Nevertheless, GW190814 has motivated experts to reevaluate the knowledge of dense matter and stellar structure to determine the possible scenarios in which one can construct such configurations of NSs while satisfying relevant constraints (Dexheimer et al. 2020; Fattoyev et al. 2020; Godzieba, Radice & Bernuzzi 2020; Huang et al. 2020; Li, Sedrakian & Weber 2020; Lim et al. 2020; Most et al. 2020; Sedrakian, Weber & Li 2020; Tsokaros, Ruiz & Shapiro 2020; Zhang & Li 2020; Demircik,

★ E-mail:bhaskarb@iucaa.in (BB); nandi.rana@gmail.com (RN)

© 2021 The Author(s)
Published by Oxford University Press on behalf of Royal Astronomical Society

Downloaded from https://academic.oup.com/mnras/article/505/2/1600/6276725 by guest on 01 June 2025

Ecker & Järvinen 2021; Tews et al. 2021). Most of these works suggest rapid uniform rotation with or without exotic matter, such as hyperons or quark matter, exploiting the caveat that the spin of m_2 is unconstrained. Other possibilities such as m_2 being a primordial BH (Clesse & Garcia-Bellido 2020; Vattis, Goldstein & Koushiappas 2020; Jedamzik 2021), an anisotropic object (Roupas 2021) [see also (Biswas & Bose 2019) for a detailed study on anisotropic object] or a NS in scalar–tensor gravity (Rosca-Mead et al. 2020) have also been considered.

In this article, we investigate the possibility of the GW190814's secondary being a NS within a hybrid nuclear + PP EoS parametrization (Biswas et al. 2020), and study its related properties under assumptions of it being both slowly and rapidly rotating. We also constrain its spin using a universal relation developed by Breu & Rezzolla (2016).

2 A BRIEF REVIEW OF OUR PREVIOUS WORK

In a previous work (Biswas et al. 2020), we have employed Bayesian statistics to constrain the EoS of NS combining multiple astrophysical observations. We have formulated a hybrid nuclear + PP EoS model which uses a parabolic expansion based nuclear empirical parametrization around the nuclear saturation density (ρ_0) and a 3-segment PP parametrization at higher densities. Within the parabolic expansion, the energy per nucleon $e(\rho, \delta)$ of asymmetric nuclear matter can be expressed as

$$e(\rho, \delta) \approx e_0(\rho) + e_{\rm sym}(\rho)\delta^2, \tag{1}$$

where $e_0(\rho)$ is the energy of the symmetric nuclear matter which holds equal number of neutrons and protons. The $e_{\rm sym}(\rho)$ is known as the symmetry energy which characterizes the strength of asymmetry in neutron to proton ratio, and $\delta = (\rho_{\rm n} - \rho_{\rm p})/\rho$ is known as symmetry parameter. $e_0(\rho)$ and $e_{\rm sym}(\rho)$ can be further expanded in a Taylor series around ρ_0:

$$e_0(\rho) = e_0(\rho_0) + \frac{K_0}{2}\chi^2 + \ldots, \tag{2}$$

$$e_{\rm sym}(\rho) = e_{\rm sym}(\rho_0) + L\chi + \frac{K_{\rm sym}}{2}\chi^2 + \ldots, \tag{3}$$

where $\chi \equiv (\rho - \rho_0)/3\rho_0$.

At higher densities the EoS of nuclear matter is completely unknown to us. This is the reason we choose a generic 3-segment PP parametrization after $1.25\rho_0$. This particular transition density is motivated by Bayesian evidence calculation which is detailed in Biswas et al. (2020). Then, we construct the posterior of the EoS parameters using Bayesian statistics based on this hybrid nuclear+PP model by combining astrophysical data from the radio observation of PSR J0740 + 6620, GW170817, GW190425, and NICER observations:

$$P(\theta|d) = \frac{P(d|\theta) \times P(\theta)}{P(d)} = \frac{\Pi_i P(d_i|\theta) \times P(\theta)}{P(d)}, \tag{4}$$

where θ is the set of EoS parameters in the model, $d = (d_{\rm GW}, d_{\rm X\text{-}ray}, d_{\rm Radio})$ is the set of data from the three different types of observations that are used to construct the likelihood. The mathematical expressions to compute each of the individual likelihoods are given in equations (5)–(7) of Biswas et al. (2020), respectively.

In this paper, we make use the methodology built in our previous work and investigate the properties of the secondary object of GW190814 under a variety of assumption.

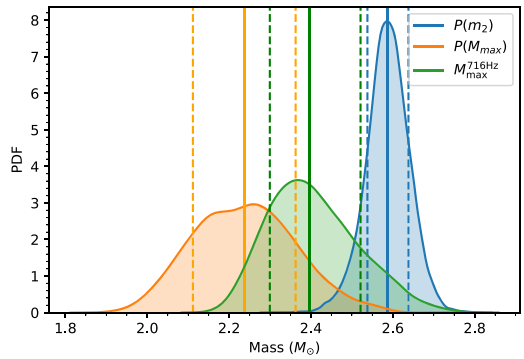

Figure 1. The probability distribution of $M_{\rm max}$ of NSs, obtained from Biswas et al. (2020), is shown in orange. The distribution shown in green is obtained with the same EoS samples as for the orange one, but considering uniform NS rotation at 716 Hz. These two distributions are compared with the probability distribution of the secondary mass m_2 (in blue) deduced from the GW190814 posterior samples in Abbott et al. (2020b).

3 LIGHTEST BH OR HEAVIEST NS?

The mass of the secondary object in GW190814 measured by the LVC falls into the so-called 'mass gap' region (Bailyn et al. 1998; Özel et al. 2010) and therefore demands a careful inspection of its properties before it can be ruled out as a BH or NS.

A non-informative measurement of the tidal deformability or the spin of the secondary, or the absence of an EM counterpart associated with this event, has made it difficult to make a robust statement about the nature of this object. We begin by examining if the GW mass measurement along with hybrid nuclear + PP model alone can rule it out as an NS. In Fig. 1, the posterior distribution of secondary mass m_2 is plotted, in blue, by using publicly available LVC posterior samples (Abbott et al. 2020b) .[1] In orange, the posterior distribution of $M_{\rm max}$ is overlaid from hybrid nuclear + PP model analysis by Biswas et al. (2020) using PSR J0740+6620 (Cromartie et al. 2019), combined GW170817[2] (Abbott et al. 2018) and GW190425 (Abbott et al. 2020a),[3] and NICER[4] data.

Given these two distributions – both for non-rotating stars – we calculate the probability of m_2 being greater than $M_{\rm max}$, i.e. $P(m_2 > M_{\rm max}) = P(m_2 - M_{\rm max})$. This probability can be easily obtained by calculating the convolution of the m_2 and $-M_{\rm max}$ probability distributions, which yields $P(m_2 > M_{\rm max}) = 0.99$. Therefore, the mass measurement implies that the probability that the secondary object in GW190814 is an NS is $\sim$ 1 per cent. However, this type of analysis is highly sensitive to the choice of EoS parametrization as well as on the implementation of the maximum-mass constraint obtained from the heaviest pulsar observations. The LVC analysis (Abbott et al. 2020b) that is based on the spectral EoS parametrization (Lindblom 2010), obtained $\sim$ 3 per cent probability for the secondary to be an NS using GW170817-informed EoS samples from Abbott et al. (2018). The addition of NICER data might increase this probability. Essick & Landry (2020) added NICER data in their analysis of GW observations based on a non-parametric EoS and also examined the impact of different assumptions about the compact object mass distribution. The $P(m_2 > M_{\rm max})$ probabilities technically depend on

[1]LVK collaboration, https://dcc.ligo.org/LIGO-P2000183/public
[2]LVK collaboration, https://dcc.ligo.org/LIGO-P1800115/public
[3]LVK collaboration, https://dcc.ligo.org/LIGO-P2000026/public
[4]PSR J0030 + 0451 mass–radius samples released by Miller et al. (2019), https://zenodo.org/record/3473466#.XrOt1nWlxBc

Downloaded from https://academic.oup.com/mnras/article/505/2/1600/6276725 by guest on 01 June 2025

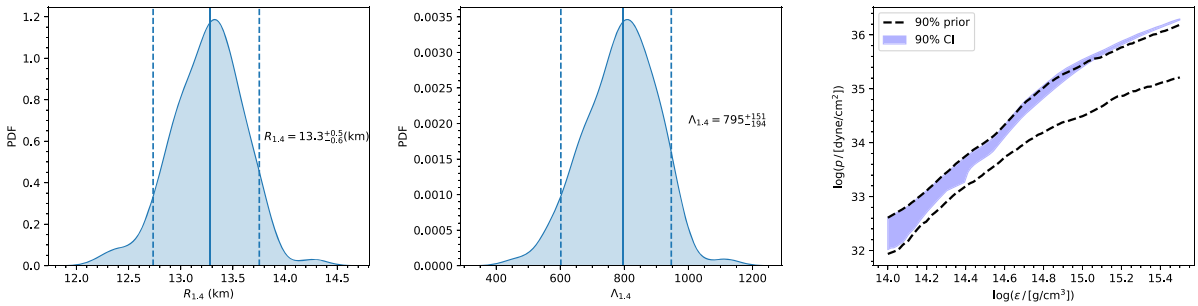

Figure 2. Posterior distributions of $R_{1.4}$ (left-hand panel) and $\Lambda_{1.4}$ (middle panel), as well as the pressure as a function of energy density (right-hand panel) are plotted assuming that the secondary companion of GW190814 is a non-rotating NS. Median and 90 per cent CI are shown by solid and dashed lines, respectively.

the mass prior assumed for the secondary, but Essick et al. (2020) showed that, regardless of assumed population model, there is a less than ~ 6 per cent probability for the GW190814 secondary to be an NS. In the discovery paper, LVC also reported an EoS-independent result using the pulsar mass distribution, following Farr & Chatziioannou (2020), which suggests that there is less than ~ 29 per cent probability that the secondary is an NS. Despite the differences inherent to these studies, they all suggest that there is a small but finite probability of the secondary object in GW190814 to be an NS. It is also important to note that they all assumed the NS to be either non-rotating or slowly rotating ($\chi < 0.05$).

Another possibility is that the secondary object is a rapidly rotating NS (Most et al. 2020; Tsokaros et al. 2020). It is known that uniform rotation can increase the maximum mass of an NS by ~ 20 per cent (Friedman & Ipser 1987; Cook, Shapiro & Teukolsky 1992, 1994). Therefore, rapid rotation may improve the chances that the GW190814 data are consistent with an NS.

From pulsar observations, we know that NSs with spin frequencies as high as $\nu_{\rm max}^{\rm obs} = 716$ Hz exist in nature (Hessels et al. 2006). Using this value for the spin frequency and the EoS samples of Biswas et al. (2020), we can deduce the maximum improvement in probability that the GW190814 secondary is an NS. We used this information in the `RNS` code (Stergioulas & Friedman 1995) and obtained a corresponding distribution of maximum mass denoted as $M_{\rm max}^{716\rm Hz}$. The superscript '716 Hz' emphasizes that all configurations here are computed at that fixed spin frequency. In Fig. 1, the distribution of $M_{\rm max}^{716\rm Hz}$ is shown in green. From the overlap of this distribution with $P(m_2)$, we find there is ~ 8 per cent probability that m_2 is a rapidly rotating NS.

Alternatively, if the GW190814's secondary were indeed an NS, then the LVC mass measurement sets a lower limit on the maximum NS mass for any spin at least up to $\nu_{\rm max}^{\rm obs}$.

We next relax this constraint by considering all theoretically allowed values of the spin frequency, which for some masses and EoSs may exceed the maximum observed value. In the next two sections, we investigate the properties of NSs – for various rotational frequencies – using a Bayesian approach based on hybrid nuclear + PP EoS parametrization.

4 PROPERTIES ASSUMING A SLOWLY ROTATING NS

For slowly rotating NS, a Bayesian methodology was already developed in Biswas et al. (2020) (also briefly described in Section 2) by combining multiple observations based on hybrid nuclear + PP EoS parametrization. In this paper, instead of marginalizing over the mass of PSR J0740+6620 taking into account of its measurement uncertainties (as described in Biswas et al. 2020), we consider the m_2 distribution of GW190814 as the heaviest pulsar mass measurement. We use Gaussian kernel-density to approximate the posterior distribution of m_2. The resulting posteriors of radius ($R_{1.4}$) and tidal deformability ($\Lambda_{1.4}$) obtained from this analysis are plotted in Fig. 2. We find that $R_{1.4} = 13.3^{+0.5}_{-0.6}$ km and $\Lambda_{1.4} = 795^{+151}_{-194}$, at 90 per cent CI, which are in good agreement with previous studies (Abbott et al. 2020a; Essick & Landry 2020; Tews et al. 2021).

The addition of GW190814 makes the EoS stiffer, especially in the high-density region since now a very small subspace of the EoS family can support an $\sim 2.6\,{\rm M}_\odot$ NS. In the right-hand panel of Fig. 2, the 90 per cent CI of posterior of the pressure inside the NS is plotted as a function of energy density in shaded blue colour and the corresponding 90 per cent CI of prior is shown by the black dotted lines. This plot clearly shows that the addition of GW190814 places a very tight constraint on the high-density part of the EoS.

5 PROPERTIES ASSUMING A RAPIDLY ROTATING NS

In this article, for the first time, we develop a Bayesian formalism to constrain the EoS of NS that allows for rapid rotation. We use a universal relation found by Breu & Rezzolla (2016) which relates the maximum mass of a uniformly rotating star ($M_{\rm rmax}^{\rm rot}$) with the maximum mass of a non-rotating star ($M_{\rm max}^{\rm TOV}$) for the same EoS

$$M_{\rm rmax}^{\rm rot} = M_{\rm max}^{\rm TOV}\left[1 + a_1\left(\frac{\chi}{\chi_{\rm kep}}\right)^2 + a_2\left(\frac{\chi}{\chi_{\rm kep}}\right)^4\right], \quad (5)$$

where $a_1 = 0.132$ and $a_2 = 0.071$. χ is the dimensionless spin magnitude of a uniformly rotating star and $\chi_{\rm kep}$ is the maximum allowed dimensionless spin magnitude at the mass-shedding limit. Given a $\chi/\chi_{\rm kep}$ value, we calculate $M_{\rm rmax}^{\rm rot}$ using this universal relation. Its use makes our computation much faster but can cause up to ~ 2 per cent deviation from the exact result, as noted by Breu & Rezzolla (2016). We assume that the error is constant throughout the parameter space; we took it to be distributed uniformly in [−2 per cent, 2 per cent] and marginalized over it to get an unbiased estimate of the properties of the object.

We combine data from PSR J0740 + 6620, two other binary neutron stars, namely GW170817 and GW190425, as well as NICER data assuming non-rotating NS following Biswas et al. (2020). Then, the m_2 distribution of GW190814 is used for the maximum-mass threshold of a uniformly rotating star, i.e. $M_{\rm rmax}^{\rm rot}$. We use a nested sampler algorithm implemented in `Pymultinest` (Buchner et al. 2014) to simultaneously sample the EoS parameters and $\chi/\chi_{\rm kep}$. These posterior samples are then used in the `RNS` code (Stergioulas &

Downloaded from https://academic.oup.com/mnras/article/505/2/1600/6276725 by guest on 01 June 2025

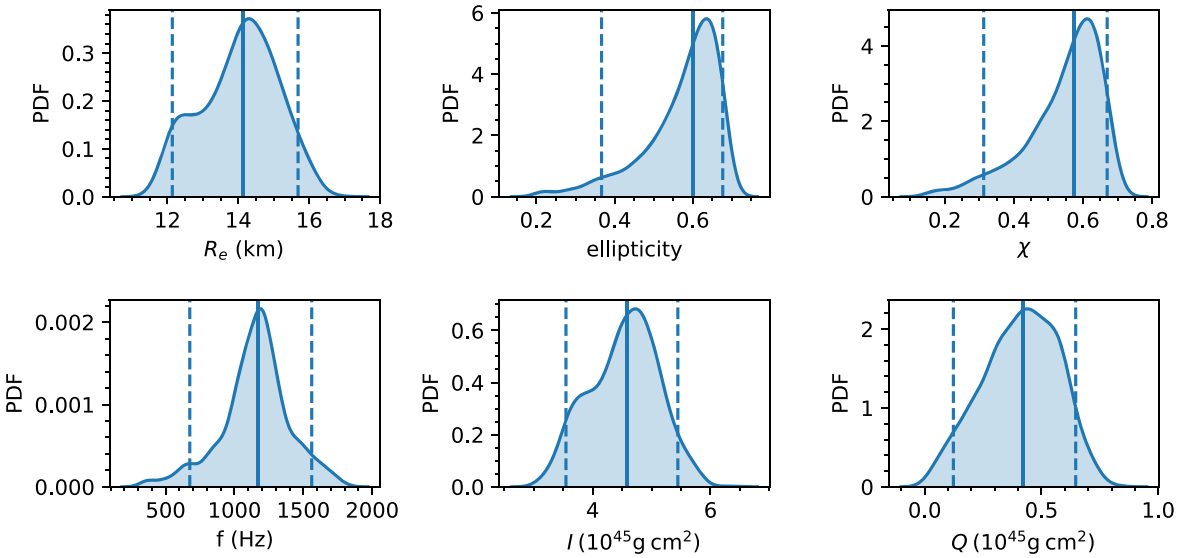

Figure 3. Posterior distribution of various properties of the secondary companion of GW190814 is shown assuming a rapidly rotating NS: Equatorial radius R_e (upper left), ellipticity e (upper middle), dimensionless spin magnitude χ (upper right), rotational frequency f in Hz (lower left), moment of Inertia I (lower middle), and quadrupole moment Q (lower right). Median and 90 per cent CI are shown by solid and dashed lines, respectively.

Friedman 1995) to calculate several properties of the secondary object associated with GW190814.

In the upper left and middle panel of Fig. 3 posterior distributions of equatorial radius (R_e) and ellipticiy (e) are plotted, respectively. Within the 90 per cent CI we find $R_e = 14.1^{+1.5}_{-2.0}$ km and $e = 0.60^{+0.07}_{-0.23}$. Such high values of equatorial radius and ellipticity imply a considerable deviation from a spherically symmetric static configuration. From the distribution of χ shown in the upper left panel of Fig. 3 we find its value to be $\chi = 0.57^{+0.09}_{-0.26}$. Most et al. (2020) have also obtained a similar bound on χ with simpler arguments. In this paper, we provide a distribution for χ employing a Bayesian framework as well as place a more robust bound on this parameter. In the lower left panel of Fig. 3, the posterior distribution of rotational frequency is plotted in Hz. We find its value to be $f = 1170^{+389}_{-495}$ Hz. As noted above, till date PSR J1748−2446a (Hessels et al. 2006) is known as the fastest rotating pulsar, with a rotational frequency of 716 Hz. *Therefore, if the secondary of GW190814 is indeed a rapidly rotating NS, it would definitely be the fastest rotating NS observed so far.* In the lower middle and right-hand panels, the posterior distributions of the moment of inertia and quadrupole moment of the secondary are shown, respectively.

5.1 Maximum spin frequencies and rotational instabilities

EoS constraints derived from the observation of non-rotating NSs also provide an upper bound on the maximum spin of an NS. The maximum spin frequency is given empirically as $f_{\rm lim} \simeq \frac{1}{2\pi}(0.468 + 0.378\chi_s)\sqrt{\frac{GM_{\rm max}}{R_{\rm max}^3}}$, (Lasota, Haensel & Abramowicz 1996; Paschalidis & Stergioulas 2017) where $\chi_s = \frac{2GM_{\rm max}}{R_{\rm max}c^2}$, with $M_{\rm max}$ and $R_{\rm max}$ being the maximum mass and its corresponding radius of a non-rotating NS, respectively. We use $M_{\rm max}$–$R_{\rm max}$ posterior samples that were deduced in Biswas et al. (2020) by using PSR J0740 + 6620, combined GWs, and NICER data to calculate $f_{\rm lim}$. In the left-hand panel of Fig. 4, its distribution is shown by the grey-shaded region. We overlay that distribution with distributions of frequencies of the secondary object of GW190814 and those of a few hypothetical rotating NSs of various masses – all Gaussian distributed, but with medians of 2.4, 2.8, and 3.0 $M_\odot$, respectively, and each having a measurement uncertainty of 0.1 $M_\odot$. We also assume the primary component of GW190425 to be a rapidly rotating NS, since by using a high-spin prior LVC determined its mass to be 1.61–2.52 $M_\odot$. In our calculations, for GW190425 we used the publicly available high-spin posterior of m_1 obtained by using the PhenomPNRT waveform. We find observations like m_1 of GW190425 and simulations like $\mathcal{N}(2.4, 0.1\,M_\odot)$ correspond to posteriors of rotational frequency that are comparatively lower than limiting values of rotational frequencies. However, as the mass increases, the posterior of frequency eventually almost coincides with $f_{\rm lim}$. Therefore, if the secondary of GW190814 was a rapidly rotating NS, it would have to be rotating rather close to the limiting frequency.

Any rotating star is generically unstable through the Chandrasekhar–Friedman–Schutz (CFS) mechanism (Chandrasekhar 1970; Friedman & Schutz 1978). This instability occurs when a certain retrograde mode in the rotating frame becomes prograde in the inertial frame. For example, the f modes of a rotating NS can always be made unstable for a sufficiently large mode number m (not to be confused with component masses $m_{1,2}$) even for low-spin frequencies, but, the instability time-scale increases rapidly with the increase of m. Numerical calculations have shown (Stergioulas & Friedman 1998; Morsink, Stergioulas & Blattnig 1999), that for maximum mass stars $m = 2$ mode changes from retrograde to prograde at $T/|W| \sim 0.06$, where T is the rotional energy and W the gravitational potential energy of the NS. We computed this ratio for all the cases considered in this section and plot the distributions in the right-hand panel of Fig. 4. From this analysis, we find that the secondary of GW190814 should be f mode unstable as for most of the allowed EoSs $T/|W|$ is significantly larger than 0.06. The CFS instability is even more effective for r modes (Lindblom, Owen & Morsink 1998; Andersson, Kokkotas & Schutz 1999) as they are generically unstable for all values of spin frequency. However, an instability can develop, only if its growth time-scale is shorter than the time-scale of the strongest damping mechanism affecting it. A multitude of damping mechanisms, such

Downloaded from https://academic.oup.com/mnras/article/505/2/1600/6276725 by guest on 01 June 2025

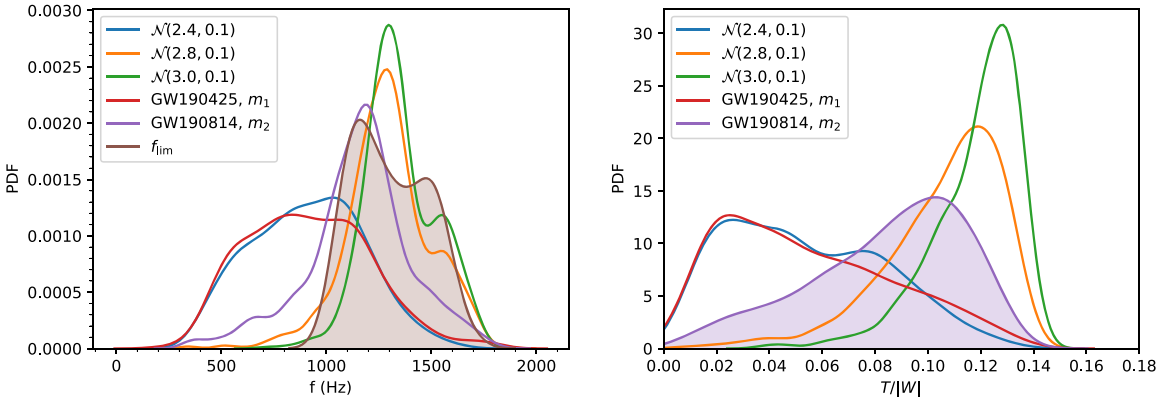

Figure 4. In the left-hand panel, the probability distribution of $f_{\rm lim}$ is shown in brown shade. The distribution of $f_{\rm lim}$ is plotted considering three simulated rapidly rotating NS whose mass measurements are Gaussian distributed with median 2.4, 2.8, and 3.0 $\mathrm{M}_\odot$, respectively, and each having a measurement uncertainty of 0.1 $\mathrm{M}_\odot$. The same has been overlaid using the secondary component of the GW190814 and the primary of the GW190425 events. In the right-hand panel, the corresponding ratio of rotational to gravitational potential energy $T/|W|$ is shown.

as shear viscosity, bulk viscosity, viscous boundary layer, crustal resonances, and superfluid mutual friction (each having each own temperature dependence) have been investigated (see Kokkotas & Schwenzer 2016; Paschalidis & Stergioulas 2017; Andersson 2019; Zhou, Li & Li 2021 and references therein). The spin distribution of millisecond pulsars in accreting systems (Papitto et al. 2014) can be explained, if the r mode instability is effectively damped up to spin frequencies of ~ 700 Hz (Ho, Andersson & Haskell 2011), and operating at higher spin rates. This would not allow for the secondary in GW190814 to be a rapidly rotating NS at the limiting spin frequency.

On the other hand, if the secondary of GW190814 *was* a rapidly rotating NS at the limiting frequency, then the f-mode and r-mode instabilities must be effectively damped both during the spin-up phase in a low-mass X-ray binary, where it acquires rapid rotation, as well as during its subsequent lifetime up to the moment of merger. This might be possible, if both the f-mode and the r-mode instabilities are damped by a particularly strong mutual friction of superfluid vortices below the superfluid transition temperature of $\sim 10^9$ K (see Lindblom & Mendell 2000; Gaertig et al. 2011 and in particular the case of an intermediate drag parameter $\mathcal{R} \sim 1$ in Haskell, Andersson & Passamonti 2009). If this is the case, then the limiting frequency observed in the spin distribution of millisecond pulsars must be explained by other mechanisms (see Gittins & Andersson 2019). A possible presence of rapidly rotating NS in merging binaries thus would have strong implications on the physics of superfluidity in NS matter (in particular constraining the drag parameter $\mathcal{R}$ of mutual friction) and on the astrophysics of accreting systems.

6 CONSTRAINING NS EOS ASSUMING THAT THE GW190814 SECONDARY IS A BH

So far, we have analysed the impact on NS EoS properties arising from the hypothesis that the secondary object in GW190814 is an NS. On the other hand, if that secondary object is a BH, then again novel information about the NS EoS can be obtained, since it will set an upper bound on the NS maximum mass, but only if one were to assume that the NS and BH mass distributions do not overlap.

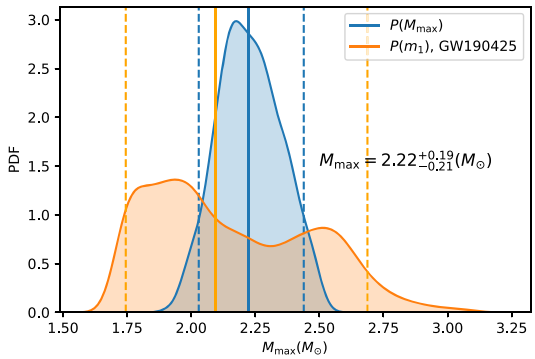

Figure 5. The probability of NS $M_{\rm max}$ is plotted in blue, under the hypothesis that the GW190814 secondary is a BH. Overlaid in orange is the LVC posterior of the primary in GW190425, for the high-spin prior.

In our analysis, we take this value to be 2.5 $\mathrm{M}_\odot$, which is the lowest possible value of the secondary object within 90 per cent CI. Then, using Bayesian inference for non-rotating stars, we combine PSR J0740+6620, GWs, and NICER data to place further constraints on the NS EoS. In Fig. 5, the distribution of the maximum mass for non-rotating NSs is shown in blue using the EoS samples obtained from this analysis. Within the 90 per cent CI we find $M_{\rm max} = 2.22^{+0.19}_{-0.21}\,\mathrm{M}_\odot$, which is the most conservative bound on NS maximum mass obtained so far in this work.

Assuming a high-spin prior, the mass of the primary component of GW190425 is constrained between $1.61-2.52\,\mathrm{M}_\odot$. In Fig. 5, its distribution is overplotted in orange. From the overlap with the newly obtained $M_{\rm max}$ distribution and the m_1 distribution of GW190425, we find that there is ~ 40 per cent probability that the primary of GW190425 is a BH.

7 CONCLUSION

Based on the maximum mass samples obtained from Biswas et al. (2020), we find that there is ~ 1 per cent probability that the secondary object associated with GW190814 is a non-rotating NS. However, such an estimation depends on the choice of EoS parametrization and the maximum mass threshold. Nevertheless,

Downloaded from https://academic.oup.com/mnras/article/505/2/1600/6276725 by guest on 01 June 2025

the possibility of the secondary being a non-rotating NS is not inconsistent with the data. Based on our hybrid nuclear + PP EoS parametrization, we find that the addition of GW190814 as a non-rotating stars provides a very stringent constraint on the EoS specially in the high-density region. We also discussed the alternative that the secondary is a rapidly rotating NS. We find that in order to satisfy the secondary mass estimate of GW190814, its spin magnitude has to be close to the limiting spin frequency for uniform rotation. In fact, it would be the fastest rotating NS ever observed. However, this could be the case, only if gravitational-wave instabilities are effectively damped for rapidly rotating stars, which opens the possibility of constraining physical mechanisms, such as mutual friction in a superfluid interior.

ACKNOWLEDGEMENTS

We thank Philippe Landry and Toni Font for carefully reading the manuscript and making several useful suggestions. We gratefully acknowledge the use of high performance super-computing cluster Pegasus at IUCAA for this work. PC is supported by the Fonds de la Recherche Scientifique-FNRS, Belgium, under grant No. 4.4503.19. This research has made use of data, software and/or web tools obtained from the Gravitational Wave Open Science Center (https://www.gw-openscience.org), a service of the LIGO (Laser Interferometer Gravitational-Wave Observatory) Laboratory, the LIGO Scientific Collaboration and the Virgo Collaboration. LIGO is funded by the U.S. National Science Foundation. The authors gratefully acknowledge the Italian Istituto Nazionale di Fisica Nucleare (INFN), the French Centre National de la Recherche Scientifique (CNRS) and the Netherlands Organization for Scientific Research, for the construction and operation of the Virgo detector and the creation and support of the EGO (European Gravitational Observatory) consortium. We would like to thank all of the essential workers who put their health at risk during the COVID-19 pandemic, without whom we would not have been able to complete this work.

NOTE ADDED IN PROOF

Recently the mass of PSR J0740+6620 was revised slightly downwards – to $2.08^{+0.07}_{-0.07}\,M_\odot$, at 68 per cent CI (Fonseca et al. 2021). This has a marginal effect on the EoS posterior, potentially making some slightly softer EoSs viable (Biswas 2021). Consequently, under the rapidly rotating scenario, the spin of the secondary would become slightly higher than what is reported in this paper.

DATA AVAILABILITY

The data generated in this article will be shared on reasonable request to the corresponding author.

REFERENCES

Aasi J. et al., 2015, Class. Quantum Gravity, 32, 074001
Abbott B. P. et al., 2017, Phys. Rev. Lett., 119, 161101
Abbott B. P. et al., 2018, Phys. Rev. Lett., 121, 161101
Abbott R. et al., 2020a, ApJ, 892, L3
Abbott R. et al., 2020b, ApJ, 896, L44
Acernese F. et al., 2015, Class. Quantum Gravity, 32, 024001
Andersson N., 2019, Gravitational-Wave Astronomy: Exploring the Dark Side of the Universe. Oxford Graduate Texts, Oxford Univ. Press, Oxford
Andersson N., Kokkotas K., Schutz B. F., 1999, ApJ, 510, 846
Antoniadis J. et al., 2013, Science, 340, 6131
Arzoumanian Z. et al., 2018, ApJS, 235, 37
Bailyn C. D., Jain R. K., Coppi P., Orosz J. A., 1998, ApJ, 499, 367
Biswas B., 2021, preprint(arXiv:2105.02886)
Biswas B., Bose S., 2019, Phys. Rev. D, 99, 104002
Biswas B., Char P., Nandi R., Bose S., 2021, Phys. Rev. D, 103, 103015
Breu C., Rezzolla L., 2016, MNRAS, 459, 646
Buchner J. et al., 2014, A&A, 564, A125
Chandrasekhar S., 1970, Phys. Rev. Lett., 24, 611
Clesse S., Garcia-Bellido J., 2020, preprint(arXiv:2007.06481)
Cook G. B., Shapiro S. L., Teukolsky S. A., 1992, ApJ, 398, 203
Cook G. B., Shapiro S. L., Teukolsky S. A., 1994, ApJ, 424, 823
Cromartie H. T. et al., 2019, Nat. Astron., 4, 72
Demircik T., Ecker C., Järvinen M., 2021, ApJ, 907, L37
Demorest P., Pennucci T., Ransom S., Roberts M., Hessels J., 2010, Nature, 467, 1081
Dexheimer V., Gomes R. O., Klähn T., Han S., Salinas M., 2021, Phys. Rev. C, 103, 025808
Essick R., Landry P., 2020, ApJ, 904, 80
Essick R., Tews I., Landry P., Reddy S., Holz D. E., 2020, Phys. Rev. C, 102, 055803
Farr W. M., Chatziioannou K., 2020, Res. Notes Am. Astron. Soc., 4, 65
Fattoyev F. J., Horowitz C. J., Piekarewicz J., Reed B., 2020, Phys. Rev. C, 102, 065805
Fonseca E. et al., 2016, ApJ, 832, 167
Fonseca E. et al., 2021, preprint(arXiv:2104.00880)
Friedman J. L., Ipser J. R., 1987, ApJ, 314, 594
Friedman J. L., Schutz B. F., 1978, ApJ, 222, 281
Gaertig E., Glampedakis K., Kokkotas K. D., Zink B., 2011, Phys. Rev. Lett., 107, 101102
Gittins F., Andersson N., 2019, MNRAS, 488, 99
Godzieba D. A., Radice D., Bernuzzi S., 2020, ApJ, 908, 122
Haskell B., Andersson N., Passamonti A., 2009, MNRAS, 397, 1464
Hessels J. W., Ransom S. M., Stairs I. H., Freire P. C. C., Kaspi V. M., Camilo F., 2006, Science, 311, 1901
Ho W. C. G., Andersson N., Haskell B., 2011, Phys. Rev. Lett., 107, 101101
Huang K., Hu J., Zhang Y., Shen H., 2020, ApJ, 904, 39
Jedamzik K., 2021, Phys. Rev. Lett., 126, 051302
Kinugawa T., Nakamura T., Nakano H., 2021, PTEP, 2021, 021E01
Kokkotas K. D., Schwenzer K., 2016, Eur. Phys. J. A, 52, 38
Landry P., Essick R., Chatziioannou K., 2020, Phys. Rev. D, 101, 123007
Lasota J.-P., Haensel P., Abramowicz M. A., 1996, ApJ, 456, 300
Li J. J., Sedrakian A., Weber F., 2020, Phys. Lett. B, 810, 135812
Lim Y., Bhattacharya A., Holt J. W., Pati D., 2020, preprint(arXiv:2007.06526)
Lindblom L., 2010, Phys. Rev., D82, 103011
Lindblom L., Mendell G., 2000, Phys. Rev. D, 61, 104003
Lindblom L., Owen B. J., Morsink S. M., 1998, Phys. Rev. Lett., 80, 4843
Margalit B., Metzger B. D., 2017, ApJ, 850, L19
Miller M. C. et al., 2019, ApJ, 887, L24
Morsink S. M., Stergioulas N., Blattnig S. R., 1999, ApJ, 510, 854
Most E. R., Papenfort L. J., Weih L. R., Rezzolla L., 2020, MNRAS, 499, L82
Özel F., Psaltis D., Narayan R., McClintock J. E., 2010, ApJ, 725, 1918
Papitto A., Torres D., Rea N., Tauris T., 2014, A&A, 566, A64
Paschalidis V., Stergioulas N., 2017, Living Rev. Rel., 20, 7
Raaijmakers G. et al., 2020, ApJ, 893, L21
Rezzolla L., Most E. R., Weih L. R., 2018, ApJ, 852, L25
Riley T. E. et al., 2019, ApJ, 887, L21
Rosca-Mead R., Moore C. J., Sperhake U., Agathos M., Gerosa D., 2020, Symmetry, 12, 1384
Roupas Z., 2021, Ap&SS, 366, 9
Ruiz M., Shapiro S. L., Tsokaros A., 2018, Phys. Rev. D, 97, 021501
Safarzadeh M., Loeb A., 2020, ApJ, 899, L15
Sedrakian A., Weber F., Li J. J., 2020, Phys. Rev. D, 102, 041301
Shao D.-S., Tang S.-P., Sheng X., Jiang J.-L., Wang Y.-Z., Jin Z.-P., Fan Y.-Z., Wei D.-M., 2020, Phys. Rev. D, 101, 063029

Downloaded from https://academic.oup.com/mnras/article/505/2/1600/6276725 by guest on 01 June 2025

Shibata M., Fujibayashi S., Hotokezaka K., Kiuchi K., Kyutoku K., Sekiguchi Y., Tanaka M., 2017, Phys. Rev. D, 96, 123012
Shibata M., Zhou E., Kiuchi K., Fujibayashi S., 2019, Phys. Rev. D, 100, 023015
Stergioulas N., Friedman J., 1995, ApJ, 444, 306
Stergioulas N., Friedman J. L., 1998, ApJ, 492, 301
Tews I., Pang P. T. H., Dietrich T., Coughlin M. W., Antier S., Bulla M., Heinzel J., Issa L., 2021, ApJ, 908, L1
Tsokaros A., Ruiz M., Shapiro S. L., 2020, ApJ, 905, 48
Vattis K., Goldstein I. S., Koushiappas S. M., 2020, Phys. Rev. D, 102, 061301
Zevin M., Spera M., Berry C. P., Kalogera V., 2020, ApJ, 899, L1
Zhang N.-B., Li B.-A., 2020, ApJ, 902, 38
Zhou X., Li A., Li B.-A., 2021, ApJ, 910, 62

This paper has been typeset from a TEX/LATEX file prepared by the author.

Downloaded from https://academic.oup.com/mnras/article/505/2/1600/6276725 by guest on 01 June 2025

The Astrophysical Journal, 908:122 (5pp), 2021 February 20 https://doi.org/10.3847/1538-4357/abd4dd
© 2021. The American Astronomical Society. All rights reserved.

On the Maximum Mass of Neutron Stars and GW190814

Daniel A. Godzieba[1], David Radice[1,2,3], and Sebastiano Bernuzzi[4]
[1] Department of Physics, The Pennsylvania State University, University Park, PA 16802, USA; dag5611@psu.edu, dur566@psu.edu
[2] Institute for Gravitation & the Cosmos, The Pennsylvania State University, University Park, PA 16802, USA
[3] Department of Astronomy & Astrophysics, The Pennsylvania State University, University Park, PA 16802, USA
[4] Theoretisch-Physikalisches Institut, Friedrich-Schiller-Universität Jena, D-07743, Jena, Germany; sebastiano.bernuzzi@uni-jena.de
Received 2020 August 15; revised 2020 December 13; accepted 2020 December 16; published 2021 February 18

Abstract

Motivated by the recent discovery of a compact object with mass in the range 2.5–2.67 $M_\odot$ in the binary merger GW190814, we revisit the question of the maximum mass of neutron stars (NSs). We use a Markov Chain Monte Carlo approach to generate about two million phenomenological equations of state with and without first-order phase transitions. We fix the crust equation of state and only assume causality at higher densities. We show how a strict upper bound on the maximum NS mass can be inferred from upcoming observation of NS radii and masses. The derived upper bounds depend only on relativity and causality, so it is not affected by nuclear physics uncertainties. We show how a lower limit on the maximum mass of NSs, in combination with upcoming measurements of NS radii by LIGO/Virgo and NICER, would constrain the equation of state of dense matter. Finally, we discuss the implications for GW190814.

Unified Astronomy Thesaurus concepts: Neutron stars (1108); Nuclear astrophysics (1129)

1. Introduction

One of the most striking predictions of general relativity is the existence of a maximum mass for any static matter configuration. The value of the maximum mass for nonrotating neutron stars (NSs; $M_{\rm max}$) is known to be the most important parameter controlling the outcome of binary NS mergers (Shibata & Taniguchi 2006; Sekiguchi et al. 2011; Bauswein et al. 2013; Hotokezaka et al. 2013; Palenzuela et al. 2015; Bernuzzi et al. 2016; Lehner et al. 2016; Dietrich et al. 2017; Piro et al. 2017; Radice et al. 2018b; Köppel et al. 2019), and determines the possible formation of black holes (BHs) in core-collapse supernovae (O'Connor & Ott 2011; Schneider et al. 2020). Moreover, the knowledge of the maximum NS mass would strongly constrain the (poorly known) equation of state (EOS) of matter at several times nuclear density (Hebeler et al. 2010, 2013; Lattimer 2012; Özel & Freire 2016; Annala et al. 2018, 2020; Tews et al. 2018; Miller et al. 2019a).

Recently, the LIGO/Virgo collaboration announced the discovery of a compact binary merger, GW190814, containing a compact object with mass 2.5–2.67 $M_\odot$ (Abbott et al. 2020). This is either the most massive NS, or the least massive BH ever found. Gravitational wave (GW) observations did not reveal the nature of this object. However, understanding whether it was a NS or a BH would have profound implications for our understanding of high-density physics and the formation of compact objects in the universe (Abbott et al. 2020).

The theoretical upper limit on $M_{\rm max}$ is of 3.2 $M_\odot$ (Rhoades & Ruffini 1974). This limit rests on weak assumptions on the nature of nuclear forces at around nuclear saturation density ($\rho_{\rm nuc} \simeq 2.7 \times 10^{14}\,{\rm g\,cm^{-3}}$), and on causality. It can be somewhat reduced if the EOS of matter is assumed to be known (within some uncertainty range) up to some given density (e.g., Kalogera & Baym 1996; Hebeler et al. 2013; Tews & Schwenk 2020). Observationally, only lower bounds on the maximum mass of nonrotating NSs are known with high confidence from mass measurements of slowly rotating NSs. The precise determination of the mass of pulsars J1614−2230 ($1.908 \pm 0.016\,M_\odot$; Demorest et al. 2010; Fonseca et al. 2016; Arzoumanian et al. 2018), J0348+0432 ($2.01 \pm 0.04\,M_\odot$; Antoniadis et al. 2013), J0740+6620 ($2.14 \pm 0.1\,M_\odot$; Cromartie et al. 2019), and J2215+5135 ($2.27 \pm 0.17\,M_\odot$; Linares et al. 2018) show that $M_{\rm max}$ should be of at least 2 $M_\odot$. Multimessenger observations of the binary NS merger GW170817 (Abbott et al. 2017) have been interpreted as an indication of an upper bound on $M_{\rm max}$ of about 2.3 $M_\odot$ (Margalit & Metzger 2017; Shibata et al. 2017, 2019; Rezzolla et al. 2018; Ruiz et al. 2018). However, this interpretation rests on the poor understanding of the long-term postmerger evolution of NS binaries (Radice et al. 2018a, 2020) and is not universally accepted (Ai et al. 2018; Li et al. 2018; Piro et al. 2019). The tidal deformability data from GW170817 also suggests that $M_{\rm max}$ should be of about 2.3 $M_\odot$ (Abbott et al. 2018; Lim & Holt 2018; Essick et al. 2020), but these results are very sensitive to their prior and model choices (Greif et al. 2019; Lim et al. 2020). This is not surprising, since GW170817 does not probe directly the EOS at the densities relevant for NSs close to the maximum mass. Finally, the statistical analysis of the mass distribution of known NSs (Alsing et al. 2018; Farr & Chatziioannou 2020) also provides a plausible range for $M_{\rm max}$, but this analysis suffers from large uncertainties due to the small number of known NSs with high mass and due to possible selection effects. Summarizing, $M_{\rm max}$ is currently only weakly constrained.

The announcement of GW190814 triggered a renewed interest in the possibility of very massive NSs and the possible implications of their existence. Most et al. (2020), Zhang & Li (2020), and Dexheimer et al. (2020) argued that the presence of an NS in GW190814 is compatible with a relatively small $M_{\rm max}$ under the assumption that the NS was rapidly spinning. However, such a scenario requires significantly faster rotation than that of any observed millisecond pulsar. Indeed, in order to significantly exceed the maximum mass, a rotating NS must be endowed with a few times 10^{52} erg in rotational kinetic energy (Margalit & Metzger 2017).[5] More exotic interpretations include anisotropic NSs (Roupas 2020) and primordial BHs (Vattis et al. 2020). Tsokaros et al. (2020) and

[5] See, however, Safarzadeh & Loeb (2020) for a proposed mechanism for the formation of fast spinning compact objects in binaries.

Fattoyev et al. (2020) showed that current EOS models can accommodate present astrophysical constraints on the NS radii and, at the same time, explain a $2.6\,M_\odot$ NS, although the resulting EOS is in tension with constraints from heavy-ion collision experiments (Danielewicz et al. 2002). Finally, the possible implications of the existence of a $2.6\,M_\odot$ NS for the EOS of dense matter have been explored by Tews et al. (2020) and Lim et al. (2020).

Despite the intense theoretical efforts, the nature of the secondary in GW190814 remains unknown. Here, we derive strict upper bounds on $M_{\rm max}$ under the sole assumptions of causality and general relativity. With these assumptions, only bulk properties of NSs factor into the upper bound, and thus the upper bound is independent of nuclear physics uncertainties. We show that current astrophysical constraints on the NS EOS are not in tension with an NS in GW190814, but that future measurements of radii and tidal deformabilities could translate into more stringent upper bounds on $M_{\rm max}$ and exclude that GW190814 was a NS–BH, unless extreme rotation is invoked for the secondary object.

2. Methods

The constraints of causality and general relativity define a space of all possible EOSs, referred to as the EOS band. To probe this space in a computationally efficient manner, we utilize a Markov chain Monte Carlo (MCMC) algorithm. We parameterize the EOSs within the band using a variation on the method developed by Read et al. (2009) that approximates each EOS as a continuous piecewise polytrope with four pieces:

$$p(\rho) = \begin{cases} K_0\rho^{\Gamma_0} & \rho \leqslant \rho_0 \\ K_1\rho^{\Gamma_1} & \rho_0 < \rho \leqslant \rho_1 \\ K_2\rho^{\Gamma_2} & \rho_1 < \rho \leqslant \rho_2 \\ K_3\rho^{\Gamma_3} & \rho > \rho_2. \end{cases} \quad (1)$$

The choice of a piecewise polytropic ansatz does not significantly bias the results compared to other EOS representation schemes (Annala et al. 2018, 2020). The first polytrope piece corresponds to the (presumed known) crust EOS, with $K_0 = 3.59389 \times 10^{13}$ (cgs) and $\Gamma_0 = 1.35692$ (Douchin & Haensel 2001), and is fixed for all EOSs. The choice of the crust EOS does not influence the bulk properties of massive NSs (Rhoades & Ruffini 1974; Most et al. 2018). The last three pieces are specified by six parameters: three transition densities, $\rho_0 \in [0.15\rho_{\rm nuc},\ 1.2\rho_{\rm nuc}]$, $\rho_1 \in [1.5\rho_{\rm nuc}, 8\rho_{\rm nuc}]$, $\rho_2 \in [\rho_1, 8.5\rho_{\rm nuc}]$; and three adiabatic indices, $\Gamma_1 \in [1.4, 5]$, $\Gamma_2 \in [0, 8]$, $\Gamma_3 \in [0.5, 8]$. Nuclear saturation density is taken to be $\rho_{\rm nuc} = 2.7 \times 10^{14}\,{\rm g\,cm^{-3}}$. The polytropic constants K_1, K_2, and K_3 are fixed by requiring the continuity of the EOS. The wide bounds on the possible values for the Γ_i allow for a diverse variety of EOSs with a wide range of softnesses and includes EOSs with and without first-order phase transitions.

The MCMC algorithm will be discussed in detail in a future publication (D. A. Godzieba et al. 2020, in preparation). The basic aspects of the algorithm are as follows. For each trial EOS we compute sequences of solutions of the Tolman–Oppenheimer–Volkoff (TOV) equations using the publicly available `TOVL` code that is described in Bernuzzi & Nagar (2008) and Damour & Nagar (2009). The transition probability is determined by whether the physical properties of the EOS are within three weak physical constraints: (1) causality of the maximum mass NS (sound speed $c_s < c$); (2) $M_{\rm max} > 1.97\,M_\odot$; (3) tidal deformability of the $1.4\,M_\odot$ NS $\Lambda_{1.4} < 800$. We have verified that our results do not change if the upper limit on $\Lambda_{1.4}$ is set to 4000. Here, we report the results from the analysis performed with $\Lambda_{1.4} < 800$, since this allows for a more dense coverage of the relevant portion of the parameter space.

3. Results

We assemble a data set of 1,966,225 phenomenological EOSs. As already mentioned, the maximum value of $M_{\rm max}$ in our data set is $2.9\,M_\odot$. Much larger masses are found if $\Lambda_{1.4}$ is allowed to be larger than 800, however, these EOSs are strongly disfavored in light of GW170817 (Abbott et al. 2019a, 2019b). In any case, our conclusions below would not be altered if we included these more stiff EOSs. Our analysis reveals that the set of all EOSs satisfying certain conditions on the NS radii admits stricter upper bounds on $M_{\rm max}$. To be concrete, we consider cases in which the radii of reference NSs with masses $1.4\,M_\odot$ and $2.14\,M_\odot$—$R_{1.4}$ and $R_{2.14}$—are fixed, and we show that more stringent upper bounds on $M_{\rm max}$ can be derived in these cases.

We consider at first the impact of restricting the range of $R_{1.4}$. The radius of an NS with mass close to $1.4\,M_\odot$, PSR J0030+0451, has been directly measured by NICER (Miller et al. 2019b; Riley et al. 2019). An indirect constraint on $R_{1.4}$ has also been obtained using multimessenger data from GW170817 (Abbott et al. 2018; Annala et al. 2018; De et al. 2018; Most et al. 2018; Radice & Dai 2019; Capano et al. 2020; Essick et al. 2020). More precise constraints are expected as systematics in NICER data are better understood, and when GW observatories will come back online with increased sensitivity. Finally, $R_{1.4}$ is known to correlate strongly with the EOS at around twice nuclear saturation density (Lattimer 2012). This makes $R_{1.4}$ a particularly interesting case.

Figure 1 shows the joint span of $M_{\rm max}$ and $R_{1.4}$ across our data set. We also color each data point according to the maximum value of the sound speed reached in the maximum mass NS predicted by that EOS. As expected in the light of the results of Rhoades & Ruffini (1974), we find that the largest $M_{\rm max}$ values are reached at the boundary of causality, that is when $c_s = c$ at the highest densities. We also find that the range of $M_{\rm max}$ decreases substantially as $R_{1.4}$ decreases. For example, an upper limit on $R_{1.4}$ of 11 km would imply $M_{\rm max} \lesssim 2.35\,M_\odot$. NICER observations of PSR J0030+0451 currently only provide a weak upper bound of $R_{1.4} \lesssim 14$ km (Miller et al. 2019b). This measurement is currently not constraining for $M_{\rm max}$. GW and electromagnetic (EM) observations of the NS merger in GW170817 place a more stringent constraint $R_{1.4} \lesssim 13$ km (Abbott et al. 2018; De et al. 2018; Radice & Dai 2019). However, even this value is still compatible with maximum NS masses of up to $\sim 2.9\,M_\odot$. This is consistent with the findings of Tews & Schwenk (2020) and Fattoyev et al. (2020), who constructed EOS models compatible with GW170817 and reaching maximum masses of ~ 2.6–$2.9\,M_\odot$.

Among the next NICER targets are pulsars J1614−223 ($M \simeq 1.908\,M_\odot$) and J0740+6620 ($M \simeq 2.14\,M_\odot$). The measurement of their radii has the potential to yield very strong constraints on the EOS of dense matter (e.g., Han & Prakash 2020), but also to constrain $M_{\rm max}$, as we show in Figure 2. We find that an upper bound on $R_{2.14}$ of 12 km would be sufficient to confidently rule out a NS in GW190814, unless fast rotation is invoked. Similarly, if $\Lambda_{1.4}$ can be constrained to be less than 400 with future GW

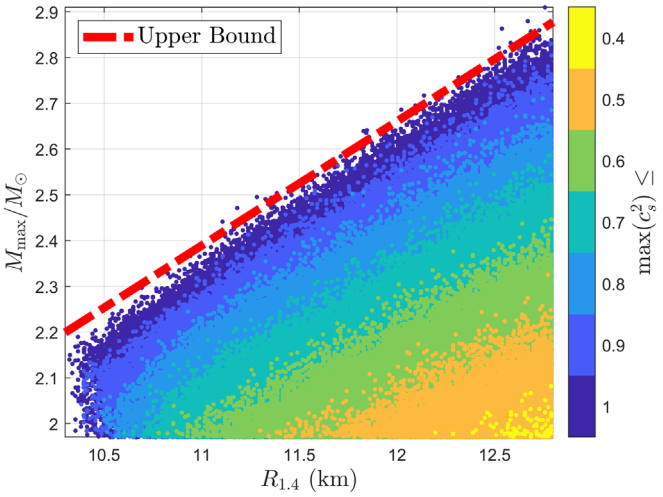

Figure 1. Distribution of $M_{\max}$ and radius of the 1.4 $M_\odot$ NS, $R_{1.4}$ for about two million phenomenological EOSs. Each point is colored according to the value of the sound speed reached in the maximum mass NS (points with smaller $\max(c_s^2)$ are drawn on top). The red dashed line shows an approximate linear ansatz for the boundary of all physical EOSs in the $M_{\max}$–$R_{1.4}$ plane (see main text for the details).

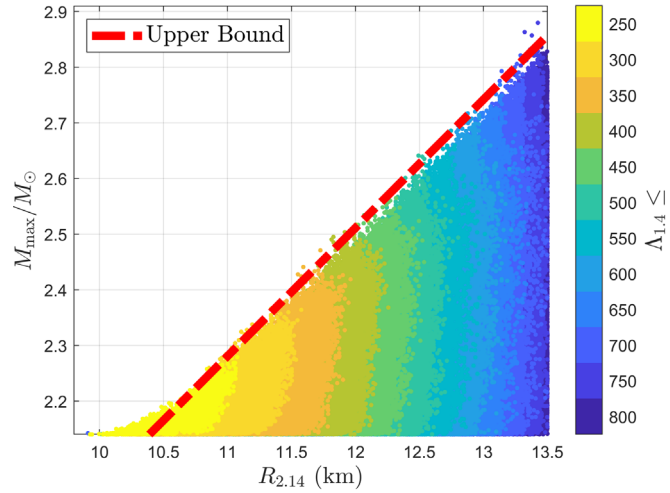

Figure 2. Distribution of $M_{\max}$ and radius of the 2.14 $M_\odot$ NS, $R_{2.14}$ for about two million phenomenological EOSs. Each point is colored according to the tidal deformability of the 1.4 $M_\odot$ NS, $\Lambda_{1.4}$ (points with smaller $\Lambda_{1.4}$ are drawn on top). The red dashed line shows an approximate linear ansatz for the boundary of all physical EOSs in the $M_{\max}$–$R_{2.14}$ plane (see main text for the details).

observations of merging NSs, then $M_{\max}$ would be constrained to be less than $\sim 2.5\,M_\odot$.

In general, we find that the upper bound on $M_{\max}$ can be very well approximated as

$$M_{\max} \leqslant \alpha(M) + \beta(M) R_M, \tag{2}$$

where R_M is the radius in km of a NS of gravitational mass M and

$$\alpha = 0.45\,M_\odot - 1.22\,M,$$
$$\beta = -0.051\,M_\odot\,\mathrm{km}^{-1} + 0.34\,M\,\mathrm{km}^{-1}. \tag{3}$$

These coefficients are obtained by performing a linear fit to a set of data points at the upper edge of the distribution that fall within the range $0.95 < \max(c_s^2) < 1$ for eight values of M. We then add a small shift of $0.04\,M_\odot$ to α, which is sufficient to enclose the vast majority of data points. The quality of these approximate expressions can be appreciated from Figures 1 and 2.

If the secondary in GW190814 is a NS, then the lower bound on the maximum mass is $M_{\max} > 2.5\,M_\odot$. Under this assumption, the measurement of the radius of the $1.4\,M_\odot$ NS would strongly constrain the EOS up to densities of $\sim 3\rho_{\rm nuc}$ ($\log\rho \simeq 14.9$), as shown in Figure 3. We find that an EOS supporting $M_{\max} > 2.5\,M_\odot$ would violate the causal limit if $R_{1.4} \lesssim 11.38$ km, which can be roughly seen in Figure 1. We also find that all EOSs supporting $M_{\max} > 2.5\,M_\odot$ with radii in the range we considered for $R_{1.4}$ must violate the conformal limit of $(c_s/c)^2 < 1/3$ at $\sim 2\rho_{\rm nuc}$ (see Figure 4). The behavior of the sound speed at higher densities depends on $R_{1.4}$. Among these constrained EOSs, those that accommodate small radii (between 11.38 and 11.75 km) must have $\max(c_s^2) \gtrsim 0.86$. So, while there are extreme EOSs very close to the causal limit that lie in the small radius range, there are still EOSs in this range that do not approach the causal limit. Thus, we cannot constrain out non-extreme EOSs with $M_{\max} > 2.5\,M_\odot$ and $R_{1.4} < 11.75$ km. (If we look at EOSs that support $M_{\max} > 2.6\,M_\odot$, we find that the causal limit is violated if $R_{1.4} \lesssim 11.8$ km, which excludes the previous small radius range.) These measurements would still

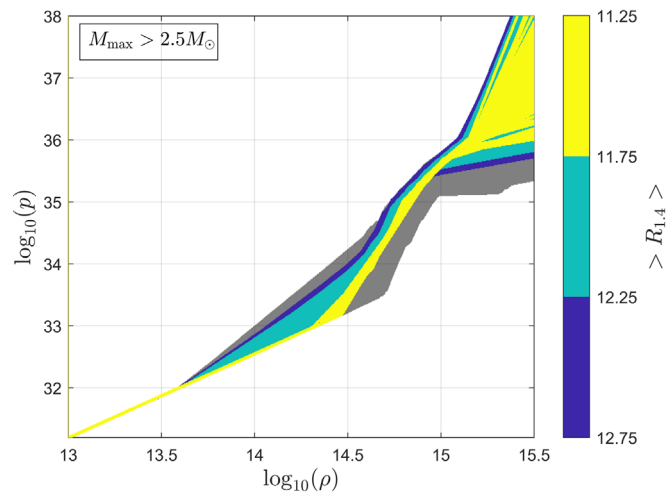

Figure 3. All EOSs with $M_{\max} > 2.5M_\odot$ and 11.25 km $< R_{1.4} <$ 12.75 km plotted as the pressure, p (dyne cm^{-2}), as a function of density, ρ (g cm^{-3}). EOSs with smaller radii are drawn on top, since they cover a smaller region. The gray shaded region beneath the colored layers represents the full data set of 1,966,225 EOSs.

leave the extreme density part of the EOS($\rho > 10^{15}$ g cm^{-3}) relatively unconstrained. This would likely change if we were to enforce a matching to perturbative QCD at high densities (Annala et al. 2020). We leave this analysis to future work.

4. Conclusions

We revisited the problem of determining the maximum mass for nonrotating NSs $M_{\max}$ using minimal assumptions and a nuclear-physics agnostic approach. Differently from other works, our analysis does not attempt to provide a likely value $M_{\max}$ and is not affected by prior or model choices. Instead, we provide strict upper limits based on the sole assumptions of causality and general relativity. Our results confirm that current astrophysical measurements of radii and tidal deformability of NSs with canonical mass $\sim 1.4\,M_\odot$ do not significantly constrain $M_{\max}$. In particular, we find that the presence of a nonrotating or moderately spinning NSs in GW190814 cannot be excluded. However, future

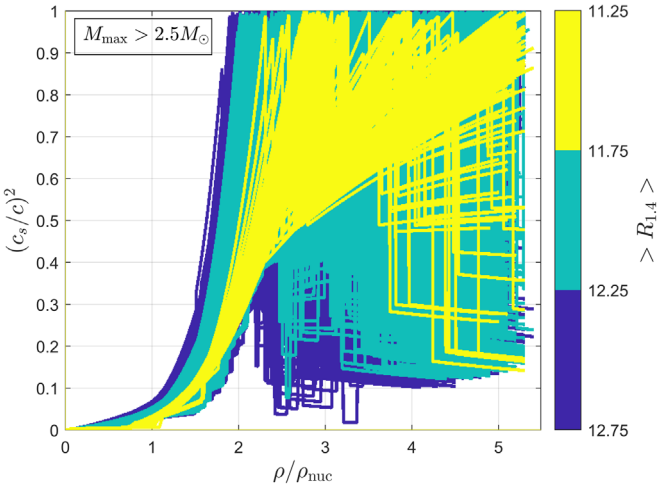

Figure 4. Sound speed squared for the EOSs with $M_{\max} > 2.5M_\odot$ and 11.25 km $< R_{1.4} <$ 12.75 km as a function of density, ρ (normalized to $\rho_{\rm nuc}$). EOSs with smaller radii are drawn on top, since they cover a smaller region. We remark that the sound speed is not assumed to be smooth in our EOSs.

observations constraining the radii of massive NSs have the potential to yield stringent upper bounds on the NS maximum mass and might rule out a nonrotating NSs in GW190814. Our analysis also show that, if the secondary in GW190814 was in fact an NS, then this information, in combination with upcoming measurements of $R_{1.4}$, would strongly constraint the EOS to densities up to $\sim 3\rho_{\rm nuc}$. It would also imply that the conformal limit must be violated at $\sim 2\rho_{\rm nuc}$. However, even a stringent upper limit on $R_{1.4}$ of 11.75 km, together with $M_{\max} > 2.5\ M_\odot$, could still be accommodated by EOSs that are well below the causal limit. If we assume $M_{\max} > 2.5\ M_\odot$, the causal limit is strictly violated for $R_{1.4} \lesssim 11.38$ km, and if we assume $M_{\max} > 2.6\ M_\odot$, the causal limit is strictly violated for $R_{1.4} \lesssim 11.8$ km.

Our analysis did not make use of the knowledge of the EOS of matter at around nuclear density (Gandolfi et al. 2019). Instead, we treated the EOS at densities beyond those of the crust as being unconstrained. It is likely that, with the inclusion of more information from nuclear theory, more stringent upper bounds on $M_{\max}$ could be derived. However, the fact that our results are broadly consistent with those obtained with more sophisticated approaches (Hebeler et al. 2013; Annala et al. 2018; Fattoyev et al. 2020; Tews & Schwenk 2020) suggests that the extent to which the upper bound might be improved will be modest. Indeed, it is well known that $M_{\max}$ depends most strongly on the EOS at densities of several times that of nuclear saturation (Lattimer 2012).

Our analysis did not consider the possibility of strange quark stars, but our EOS parameterization does allow for hybrid stars with hadronic crusts and a first-order QCD phase transition in their interior (e.g., Annala et al. 2020). We leave the determination of upper bounds on the maximum mass for self-bound quark stars to a future work. Future work should also consider the implication of X-ray burst (Steiner et al. 2010; Lattimer 2012; Özel & Freire 2016) and laboratory constraints (Danielewicz et al. 2002) on the high-density EOS on the upper bound of $M_{\max}$.

We thank the anonymous referee for insightful suggestions that improved the quality of this work. Computations for this research were performed on the Pennsylvania State University's Institute for Computational and Data Sciences Advanced CyberInfrastructure (ICDS-ACI). S.B. acknowledges support by the EU H2020 under ERC Starting Grant, no. BinGraSp-714626.

Software Used

TOVL (Bernuzzi & Nagar 2008), Matlab®.

Data Availability

EOS parameters and bulk properties of reference NSs generated for this work are publicly available on Zenodo (Godzieba et al. 2020).

ORCID iDs

Daniel A. Godzieba https://orcid.org/0000-0001-7454-0104
David Radice https://orcid.org/0000-0001-6982-1008
Sebastiano Bernuzzi https://orcid.org/0000-0002-2334-0935

References

Abbott, B. P., Abbott, R., Abbott, T. D., et al. 2017, ApJL, 848, L12
Abbott, B. P., Abbott, R., Abbott, T. D., et al. 2018, PhRvL, 121, 161101
Abbott, B. P., Abbott, R., Abbott, T. D., et al. 2019a, PhRvX, 9, 011001
Abbott, B. P., Abbott, R., Abbott, T. D., et al. 2019b, PhRvX, 9, 031040
Abbott, R., Abbott, T. D., Abraham, S., et al. 2020, ApJL, 896, L44
Ai, S., Gao, H., Dai, Z.-G., et al. 2018, ApJ, 860, 57
Alsing, J., Silva, H. O., & Berti, E. 2018, MNRAS, 478, 1377
Annala, E., Gorda, T., Kurkela, A., Nättilä, J., & Vuorinen, A. 2020, NatPh, 16, 907
Annala, E., Gorda, T., Kurkela, A., & Vuorinen, A. 2018, PhRvL, 120, 172703
Antoniadis, J., Freire, P. C. C., Wex, N., et al. 2013, Sci, 340, 6131
Arzoumanian, Z., Brazier, A., Burke-Spolaor, S., et al. 2018, ApJS, 235, 37
Bauswein, A., Baumgarte, T. W., & Janka, H. T. 2013, PhRvL, 111, 131101
Bernuzzi, S., & Nagar, A. 2008, PhRvD, 78, 024024
Bernuzzi, S., Radice, D., Ott, C. D., et al. 2016, PhRvD, 94, 024023
Capano, C. D., Tews, I., Brown, S. M., et al. 2020, NatAs, 4, 625
Cromartie, H. T., Fonseca, E., Ransom, S., et al. 2019, NatAs, 4, 72
Damour, T., & Nagar, A. 2009, PhRvD, 80, 084035
Danielewicz, P., Lacey, R., & Lynch, W. G. 2002, Sci, 298, 1592
De, S., Finstad, D., Lattimer, J. M., et al. 2018, PhRvL, 121, 091102
Demorest, P., Pennucci, T., Ransom, S., Roberts, M., & Hessels, J. 2010, Natur, 467, 1081
Dexheimer, V., Gomes, R. O., Klähn, T., Han, S., & Salinas, M. 2020, arXiv:2007.08493
Dietrich, T., Ujevic, M., Tichy, W., Bernuzzi, S., & Bruegmann, B. 2017, PhRvD, 95, 024029
Douchin, F., & Haensel, P. 2001, A&A, 380, 151
Essick, R., Landry, P., & Holz, D. E. 2020, PhRvD, 101, 063007
Farr, W. M., & Chatziioannou, K. 2020, RNAAS, 4, 65
Fattoyev, F. J., Horowitz, C. J., Piekarewicz, J., & Reed, B. 2020, PhRvC, 102, 065805
Fonseca, E., Pennucci, T. T., Ellis, J. A., et al. 2016, ApJ, 832, 167
Gandolfi, S., Lippuner, J., Steiner, A., et al. 2019, JPhG, 46, 103001
Godzieba, D. A., Radice, D., & Bernuzzi, S. 2020, Phenomenological EOS Data Set 2, Zenodo, doi:10.5281/zenodo.3954899
Greif, S., Raaijmakers, G., Hebeler, K., Schwenk, A., & Watts, A. 2019, MNRAS, 485, 5363
Han, S., & Prakash, M. 2020, ApJ, 899, 164
Hebeler, K., Lattimer, J. M., Pethick, C. J., & Schwenk, A. 2010, PhRvL, 105, 161102
Hebeler, K., Lattimer, J. M., Pethick, C. J., & Schwenk, A. 2013, ApJ, 773, 11
Hotokezaka, K., Kiuchi, K., Kyutoku, K., et al. 2013, PhRvD, 88, 044026
Kalogera, V., & Baym, G. 1996, ApJL, 470, L61
Köppel, S., Bovard, L., & Rezzolla, L. 2019, ApJL, 872, L16
Lattimer, J. M. 2012, ARNPS, 62, 485
Lehner, L., Liebling, S. L., Palenzuela, C., et al. 2016, CQGra, 33, 184002
Li, S.-Z., Liu, L.-D., Yu, Y.-W., & Zhang, B. 2018, ApJL, 861, L12
Lim, Y., Bhattacharya, A., Holt, J. W., & Pati, D. 2020, arXiv:2007.06526
Lim, Y., & Holt, J. W. 2018, PhRvL, 121, 062701
Linares, M., Shahbaz, T., & Casares, J. 2018, ApJ, 859, 54

Margalit, B., & Metzger, B. D. 2017, ApJL, 850, L19
Miller, M. C., Chirenti, C., & Lamb, F. K. 2019a, ApJ, 888, 12
Miller, M., Lamb, F. K., Dittman, A. J., et al. 2019b, ApJL, 887, L24
Most, E. R., Papenfort, L. J., Weih, L. R., & Rezzolla, L. 2020, MNRAS, 499, L82
Most, E. R., Weih, L. R., Rezzolla, L., & Schaffner-Bielich, J. 2018, PhRvL, 120, 261103
O'Connor, E., & Ott, C. D. 2011, ApJ, 730, 70
Özel, F., & Freire, P. 2016, ARA&A, 54, 401
Palenzuela, C., Liebling, S. L., Neilsen, D., et al. 2015, PhRvD, 92, 044045
Piro, A. L., Giacomazzo, B., & Perna, R. 2017, ApJL, 844, L19
Piro, L., Troja, E., Zhang, B., et al. 2019, MNRAS, 483, 1912
Radice, D., Bernuzzi, S., & Perego, A. 2020, ARNPS, 70, 95
Radice, D., & Dai, L. 2019, EPJA, 55, 50
Radice, D., Perego, A., Bernuzzi, S., & Zhang, B. 2018a, MNRAS, 481, 3670
Radice, D., Perego, A., Zappa, F., & Bernuzzi, S. 2018b, ApJL, 852, L29
Read, J. S., Lackey, B. D., Owen, B. J., & Friedman, J. L. 2009, PhRvD, 79, 124032
Rezzolla, L., Most, E. R., & Weih, L. R. 2018, ApJL, 852, L25
Rhoades, C. E., Jr., & Ruffini, R. 1974, PhRvL, 32, 324
Riley, T. E., Watts, A. L., Bogdanov, S., et al. 2019, ApJL, 887, L21
Roupas, Z. 2020, AP&SS, 366, 9
Ruiz, M., Shapiro, S. L., & Tsokaros, A. 2018, PhRvD, 97, 021501
Safarzadeh, M., & Loeb, A. 2020, ApJL, 899, L15
Schneider, A. S., O'Connor, E., Granqvist, E., Betranhandy, A., & Couch, S. M. 2020, ApJ, 894, 4
Sekiguchi, Y., Kiuchi, K., Kyutoku, K., & Shibata, M. 2011, PhRvL, 107, 051102
Shibata, M., Fujibayashi, S., Hotokezaka, K., et al. 2017, PhRvD, 96, 123012
Shibata, M., & Taniguchi, K. 2006, PhRvD, 73, 064027
Shibata, M., Zhou, E., Kiuchi, K., & Fujibayashi, S. 2019, PhRvD, 100, 023015
Steiner, A. W., Lattimer, J. M., & Brown, E. F. 2010, ApJ, 722, 33
Tews, I., Margueron, J., & Reddy, S. 2018, PhRvC, 98, 045804
Tews, I., Pang, P. T. H., Dietrich, T., et al. 2020, arXiv:2007.06057
Tews, I., & Schwenk, A. 2020, ApJ, 892, 14
Tsokaros, A., Ruiz, M., & Shapiro, S. L. 2020, ApJ, 905, 48
Vattis, K., Goldstein, I. S., & Koushiappas, S. M. 2020, PhRvD, 102, 061301
Zhang, N.-B., & Li, B.-A. 2020, ApJ, 902, 38

arXiv:2007.03799v1 [nucl-th] 7 Jul 2020

GW190814: Impact of a 2.6 solar mass neutron star on nucleonic equations of state

F. J. Fattoyev,[1,*] C. J. Horowitz,[2,†] J. Piekarewicz,[3,‡] and Brendan Reed[4,§]

[1] *Department of Physics, Manhattan College, Riverdale, NY 10471, USA*
[2] *Center for Exploration of Energy and Matter and Department of Physics, Indiana University, Bloomington, IN 47405, USA*
[3] *Department of Physics, Florida State University, Tallahassee, FL 32306, USA*
[4] *Department of Astronomy, Indiana University, Bloomington, Indiana 47405, USA*

(Dated: July 9, 2020)

Is the secondary component of GW190814 the lightest black hole or the heaviest neutron star ever discovered in a double compact-object system [R. Abbott *et al.* ApJ Lett., 896, L44 (2020)]? This is the central question animating this letter. Covariant density functional theory provides a unique framework to investigate both the properties of finite nuclei and neutron stars, while enforcing causality at all densities. By tuning existing energy density functionals we were able to: (a) account for a $2.6\,M_\odot$ neutron star, (b) satisfy the original constraint on the tidal deformability of a $1.4\,M_\odot$ neutron star, and (c) reproduce ground-state properties of finite nuclei. Yet, for the class of models explored in this work, we find that the stiffening of the equation of state required to support super-massive neutron stars is inconsistent with either constraints obtained from energetic heavy-ion collisions or from the low deformability of medium-mass stars. Thus, we speculate that the maximum neutron star mass can not be significantly higher than the existing observational limit and that the $2.6\,M_\odot$ compact object is likely to be the lightest black hole ever discovered.

PACS numbers: 21.60.Jz, 24.10.Jv, 26.60.Kp, 97.60.Jd

The first direct detection of gravitational waves from the binary collision of two black holes launched the new era of gravitational-wave astronomy [1].Two years later, the detection of gravitational waves from GW170817—a binary neutron star merger [2]—in association with its electromagnetic counterpart [3–6], greatly advanced multimessenger astronomy. And two years after GW170817, the LIGO-Virgo collaboration continues to mesmerize the physics community after reporting the detection of gravitational waves from the coalescence of a binary system with the most extreme mass ratio ever observed: a 23 solar mass black hole and a 2.6 solar mass "compact" object [7]. Although data from all three instruments (LIGO-Livingston, LIGO-Hanford, and Virgo) allowed good sky localization of the source, no electromagnetic counterpart has been reported. Moreover, unlike GW170817, no measurable tidal signature was imprinted on the gravitational waveform, which seems consistent with the relatively large mass of the $2.6\,M_\odot$ compact object. Hence, one is left speculating whether the compact object is either the most massive neutron star or the lightest black hole ever discovered [8, 9].

The discovery paper suggests that, based on several current estimates of the maximum neutron star mass, "GW190814 is unlikely to originate in a neutron star-black hole (NSBH) coalescence" [7]. Yet the paper leaves open the possibility that improved knowledge of the equation of state or further observations could alter this assessment. The absence of super-massive neutron stars is consistent with the analysis by Margalit and Metzger who argue against their formation based on the lack of evidence of a large amount of rotational energy in the ejecta during the spin-down phase of GW170817 [10]. Interestingly, the suggested upper limit of $M_{\rm max} \lesssim 2.17\,M_\odot$ [10] is in full agreement with the recent observation by Cromartie and collaborators of the heaviest $2.14^{+0.10}_{-0.09}\,M_\odot$ neutron star to date [11]. However, given that one can not definitively exclude the existence of super-massive neutron stars, we explore here the impact of a $2.6\,M_\odot$ neutron star on nucleonic equations of state, particularly in the framework of covariant density functional theory.

It has been known for more than two decades that the class of covariant energy density functionals (EDFs) used in this work can reproduce nuclear observables at normal nuclear densities and also generate neutron stars with maximum masses that differ by more than one solar mass [12]. Hence, stable neutron stars with $2.6\,M_\odot$—and even higher—can be readily generated. The challenge, however, is not to reconcile super-massive neutron stars with the properties of finite nuclei, but rather, with neutron-star properties that are sensitive to the equation of state (EOS) at two-to-three times nuclear densities, such as stellar radii and tidal deformabilities that favor a rather soft EOS [2, 13].

In particular, GW170817 has provided stringent constraints on the EOS of neutron rich matter at a few times nuclear densities from the determination of the tidal deformability of a $M = 1.4\,M_\odot$ neutron star [13–27]. Constraints from GW170817 seem to favor compact stars with relatively small stellar radii, suggesting a relatively

*Electronic address: ffattoyev01@manhattan.edu
†Electronic address: horowit@indiana.edu
‡Electronic address: jpiekarewicz@fsu.edu
§Electronic address: reedbr@iu.edu

soft EOS. These constraints are consistent with the recent determination of both the mass and radius of PSR J0030+0451 by the Neutron star Interior Composition Explorer (NICER) [28, 29]. Pulse-profile modeling of the thermal emission from the pulsar's hot spots suggest a mass of about $1.4\,M_\odot$ and a radius of nearly 13 km, with a $\pm 10\%$ uncertainty on both quantities [28, 29]. Note that although consistent with GW170817, NICER results can accommodate slightly stiffer equations of state. However, a real tension develops as one aims to reconcile a relatively soft EOS as demanded by GW170817, with the much stiffer EOS required to account for heavy neutron stars with masses in the vicinity of $2M_\odot$ [11, 30, 31]. Based on this combined evidence, suggestions have been made for the existence quark matter cores in massive neutron stars [32]. Although the claim may be premature, after all there are purely nucleonic EOS that satisfy all experimental and observational constraints to date [15], the prospect of identifying an assumed phase transition in the stellar cores is exciting. As shown below, the tension is exacerbated if the EOS must be stiffened even further to account for the possible existence of super-massive neutron stars.

To test the possible existence of a $2.6\,M_\odot$ neutron star we rely on density functional theory [33]. The energy density functional employed here is defined in terms of an underlying Lagrangian density that has been extensively discussed in earlier publications [34–36], so we limit ourselves to highlight those terms of relevance to the high-density component of the equation of state. That is,

$$\mathscr{L} = \ldots + \frac{\zeta}{4!} g_{\rm v}^4 (V_\mu V^\mu)^2 + \Lambda_{\rm v} \Big(g_\rho^2 \, \mathbf{b}_\mu \cdot \mathbf{b}^\mu \Big) \Big(g_{\rm v}^2 V_\nu V^\nu \Big). \quad (1)$$

The basic degrees of freedom of the model are neutrons and protons interacting via the exchange of photons and "mesons". Besides the conventional Yukawa couplings (not shown) the model includes non-linear meson interactions that serve to simulate the complicated many-body dynamics and that are required to improve the predictive power of the model. The two terms shown in Eq. (1) fall into this category and are of critical importance to the behavior of dense, neutron-rich matter. The first term in the expression describes a quartic self-interaction of the isoscalar-vector field V^μ which affects the EOS of symmetric nuclear matter at high densities [12]. In turn, the last term includes a mixed quartic coupling between V^μ and the isovector-vector field $\mathbf{b}^\mu$. This term was introduced to modify the density dependence of the symmetry energy, which plays a critical role in the structure of both neutron-rich nuclei and neutron stars [34]. Note that the symmetry energy is to a very good approximation equal to the difference in the energy per nucleon between pure neutron matter and symmetric nuclear matter. Covariant density functional theory provides a relativistic consistent framework as one extrapolates to dense matter as it ensures—unlike non-relativistic formulations—that the EOS remains causal at all densities. Finally, the structure of neutron stars will be explored by enforcing both charge neutrality and chemical equilibrium. As such, the basic constituents of the model are nucleons and leptons (both electrons and muons). No "exotic" degrees of freedom—such as hyperons, meson condensates, or quarks—will be considered.

As already alluded, tuning the ζ parameter in Eq. (1) allows one to stiffen the symmetric-matter EOS to produce super-massive neutron stars. For example, two of the EDFs used in Ref. [15]—IUFSU [37] and FSUGarnet [38])—that are consistent with both the $2M_\odot$ constraint [11, 30, 31] and the tidal deformability of a $1.4\,M_\odot$ neutron star [2], can be adjusted to produce maximum stellar masses of at least $2.8\,M_\odot$. However, we find no need to strain the model to such an extreme, so we tune ζ to produce a maximum neutron star mass of $2.6\,M_\odot$. Reducing the ζ parameter requires tuning the other model parameters. To do so, we start with the bulk properties predicted by IUFSU—together with the analytical transformation described in [36]—to connect the bulk properties to the model parameters. Next, we slightly decrease the value of the slope of the symmetry energy to obtain a neutron skin of 0.15 fm for ^{208}Pb—and adjusted the value of the incompressibility coefficient to $K = 227$ MeV to maintain agreement with the centroid energy of the giant monopole resonance in ^{208}Pb. Finally, we re-adjust the values of $m_{\rm s}$, the saturation density ρ_0, and the binding energy at saturation ϵ_0 to ensure that the binding energies and charge radii of both ^{40}Ca and ^{208}Pb remain intact. We refer to this nuclear EDF as "BigApple" and display its parameters, as defined in Ref. [36], in Table I alongside the other two covariant EDFs used in this work.

Model	$m_{\rm s}$	$g_{\rm s}^2$	$g_{\rm v}^2$	g_ρ^2	κ	λ	ζ	$\Lambda_{\rm v}$
IUFSU	491.500	99.4266	169.8349	184.6877	3.38081	+0.000296	0.03000	0.046000
FSUGarnet	496.939	110.3492	187.6947	192.9274	3.26018	−0.003551	0.02350	0.043377
BigApple	492.730	93.5074	151.6839	200.5562	5.20326	−0.021739	0.00070	0.047471

TABLE I: Parameters, as in Ref. [36], for the three models discussed in the text. The scalar mass $m_{\rm s}$ and κ are in MeV. The vector-meson masses are fixed at $m_{\rm v} = 782.5$ MeV and $m_\rho = 763.0$ MeV, respectively, and the nucleon mass at $M = 939$ MeV.

Nucleus	B/A(MeV)	$R_{\rm ch}$(fm)	$R_{\rm skin}$(fm)
^{40}Ca	8.552 (8.551)	3.452 (3.478)	−0.050
^{48}Ca	8.536 (8.666)	3.476 (3.477)	0.168
^{68}Ni	8.643 (8.682)	3.875 (3.887)	0.170
^{90}Zr	8.666 (8.710)	4.255 (4.269)	0.061
^{132}Sn	8.294 (8.355)	4.708 (4.709)	0.212
^{208}Pb	7.868 (7.867)	5.503 (5.501)	0.151 $\left(0.33^{+0.16}_{-0.18}\right)$

TABLE II: Theoretical predictions alongside experimental data (in parentheses) for the binding energy per nucleon [40] and charge radii [41] for a representative set of doubly-magic and semi-magic nuclei; the experimental charge radius of ^{68}Ni is from Ref. [42]. The last column displays predictions for the neutron skin thickness. With the exception of ^{208}Pb [43], no electroweak measurements of neutron skins are presently available.

One of the central tenets of nuclear density functional theory is to provide a "universal" EDF that can reproduce nuclear observables over an enormous range of densities and isospin asymmetries. The goal is to build a nuclear EDF that can be used to explore both the properties of finite nuclei as well as the structure of neutron stars—dynamical objects that differ in length scales by more that 18 orders of magnitude. In this context, we display in Table II binding energies and charge radii as predicted by the BigApple. Although the agreement between theory and experiment is fairly good, it is certainly not as good as some modern nuclear EDFs that have been fitted to a host of nuclear observables.

Before moving on to discuss neutron star properties, we display in Table III some bulk properties of infinite neutron-rich matter that encode its behavior in the vicinity of the saturation density; the definitions are as in Ref. [44]. The saturation point of symmetric nuclear matter is defined in terms of the saturation density ρ_0 and the value of the energy per particle ϵ_0. Because the pressure at saturation density vanishes, the rate at which the energy per particle increases is controlled by the incompressibility coefficient K, a quantity that is strongly correlated to the centroid energy of the giant monopole resonance [45]. In turn, J and L are fundamental parameters of the symmetry energy that encode the increase in the energy per particle and its density dependence as the system becomes neutron rich. In particular, given that the pressure of symmetric nuclear matter vanishes at saturation, L is closely related to the pressure of pure neutron matter at saturation density. As such, it is strongly correlated to both the neutron skin thickness of heavy nuclei and the radius of neutron stars [46].

We observe from Table III that, with the exception of L, all three models are in very close agreement. It is important to note that the calibration of FSUGarnet relied exclusively on physical observables that can be either measured in the laboratory or extracted from observation, so

Model	ρ_0	ϵ_0	K	J	L
IUFSU	0.155	−16.397	231.333	31.296	47.205
FSUGarnet	0.153	−16.231	229.628	30.917	50.961
BigApple	0.155	−16.344	227.001	31.315	39.800

TABLE III: Bulk properties of nuclear matter as predicted by three covariant EDFs: IUFSU [37], FSUGarnet [38], and BigApple. The listed properties are the saturation density of symmetric nuclear matter together with the energy per particle and incompressibility coefficient at saturation. Also shown is the value of the symmetry energy J and its slope L at saturation density. All quantities are given in MeV except for ρ_0 which is given in fm^{-3}.

the bulk properties listed in Table III are genuine model predictions.

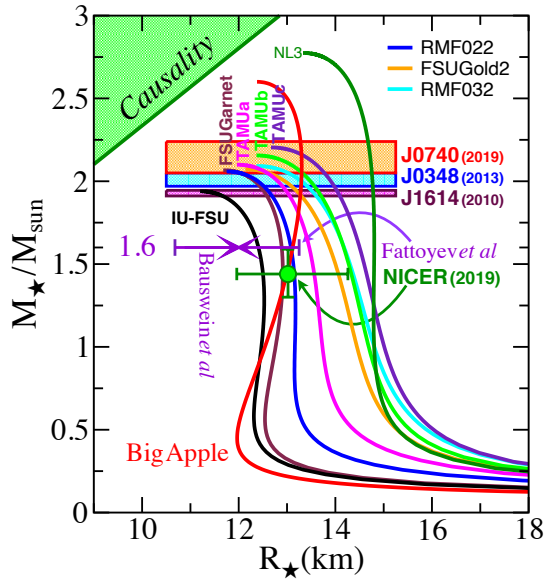

FIG. 1: (Color online). Mass-vs-Radius relation predicted by a variety of covariant EDFs. The figure has been adapted from Ref. [15] and is supplemented by the maximum mass constraint from Ref. [11], NICER constraint on the stellar radius of a $1.4\,M_\odot$ neutron star [28, 29], and our predictions from BigApple.

Displayed in Fig. 1 is the mass-*vs*-radius relation as predicted by a variety of covariant EDFs—including BigApple. The figure has been adapted from Ref. [15] and includes, besides earlier constraints on the maximum neutron star mass [30, 31], the newest constraint from Cromartie et al. [11] as well as the recent NICER result. All models support a $\sim 2\,M_\odot$ neutron star and, with couple of exceptions, agree with the NICER result. Yet, several of these models generate stellar radii for medium mass neutron stars that are inconsistent with the tidal deformability extracted from GW170817 [2]. Note, however, that BigApple—with a maximum neutron-star mass of $2.6\,M_\odot$ satisfies all observational constraints; see also Table IV.

Model	$R_{1.4}$	$\Lambda_{1.4}$	$M_{\rm max}$	$R_{\rm max}$	$\Lambda_{\rm max}$
IUFSU	12.528	499.2	1.939	11.265	20.9
FSUGarnet	12.869	624.8	2.066	11.706	18.2
BigApple	12.960	717.3	2.600	12.417	5.0

TABLE IV: Stellar properties as predicted by the three covariant EDFs used in this work. The maximum mass is given in solar masses, both radii in km, and the tidal deformability is dimensionless.

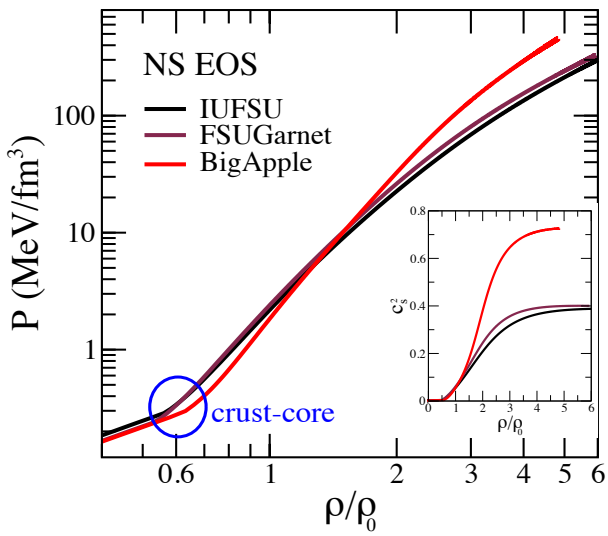

FIG. 2: (Color online) Equation of state—pressure as a function of baryon density—for neutron-star matter in chemical equilibrium. Here $\rho_0 \simeq 0.154\,{\rm fm}^{-3}$ is the density of nuclear matter at saturation (see Table III), and the inset displays the associated speed of sound in units of the speed of light.

We now proceed to examine the microphysics responsible for the macroscopic properties displayed in Fig. 1. The underlying neutron-star matter EOS alongside the square of the speed of sound—defined as the derivative of the pressure with respect to the energy density—is displayed in Fig. 2. The kink in the pressure at around 2/3 saturation density signals the transition from the solid crust to the liquid core. At saturation density (ρ_0) the pressure is generated exclusively by the symmetry energy. This pressure determines the thickness of the neutron skin in neutron-rich nuclei [47–50]. In turn, the pressure at two-to-three times saturation density appears to controls the radius of medium-mass neutron stars [23–25, 51]. Indeed, all three models share the same pressure just below $2\rho_0$ and, as consequence, predict similar radii for a canonical $1.4\,M_\odot$ neutron star. However, the maximum mass of stable neutron stars stars is highly sensitive to the pressure at the highest densities [27]. Indeed, a dramatic rate of increase in the pressure—best reflected in the speed of sound—is required to support a super-massive $2.6\,M_\odot$ neutron star.

Based on the evidence presented so far, there seems to be no compelling argument against the possible existence of a super-massive $2.6\,M_\odot$ neutron star. Note, however, that whereas the relatively large tidal deformability predicted by BigApple is consistent with the limits presented in the discovery paper [2], the revised limit of $\Lambda_{1.4} = 190^{+390}_{-120}$ [13] presents a more serious challenge. However, the most serious evidence against such a stiff EOS comes from laboratory experiments involving the energetic collision between two gold nuclei, a violent encounter that compressed matter to pressures in excess of 10^{34} Pa [52]; note that 1Pa =10 dyn/cm^2= 6.242×10^{-33}MeV/fm^3.

We display in Fig. 3 constraints on the EOS of symmetric nuclear matter as extracted from the analysis of particle flow in heavy-ion collisions [52]. We observe that IUFSU and FSUGarnet—with predictions of $1.94\,M_\odot$ and $2.07\,M_\odot$ for the maximum neutron star mass—already sit near the upper edge of the allowed region. In contrast, the very stiff EOS predicted by the NL3 parametrization [53] was explicitly ruled out by the heavy-ion data [52]. Following a similar trend as NL3, it is clear that the stiff EOS predicted by BigApple and required to account for super-massive neutron stars is also ruled out. Given that FSUGarnet is approaching the upper boundary allowed by the heavy-ion data, it is unlikely that the maximum neutron star mass can go much beyond the present observational limit of $2.14\,M_\odot$ [11].

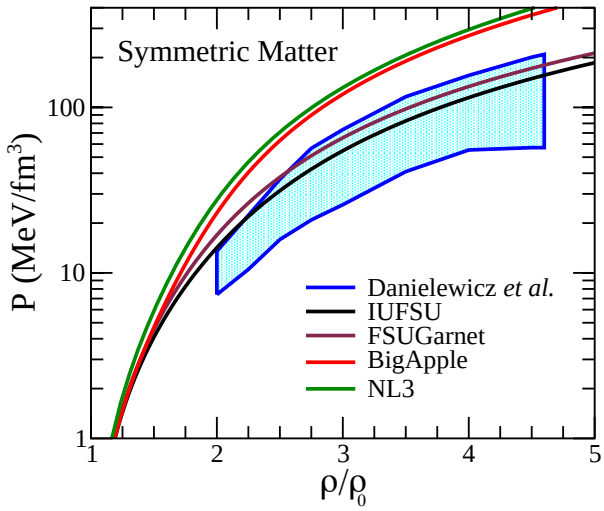

FIG. 3: (Color online) Equation of state—pressure as a function of baryon density—of symmetric nuclear matter. The blue shaded area represents the EOS extracted from the analysis of flow data using a value of $\rho_0 \simeq 0.16\,{\rm fm}^{-3}$ for the saturation density [52].

In summary, motivated by the recent identification of a compact object in the 2.5–5.0 $M_\odot$ mass gap [7], we have explored the possibility that such an object could be a super-massive neutron star. Given the lack of an electromagnetic counterpart to GW190814 and the absence of tidal distortions to the gravitational waveform, it is unlikely that the nature of the $2.6\,M_\odot$ compact object

will ever be resolved by a further analysis of the data. In this letter we have adapted a class of modern covariant EDFs to account for a stable $2.6\,M_\odot$ neutron star, while ensuring that earlier constraints on the structure of neutron stars as well as ground-state properties of finite nuclei are accurately reproduced. Indeed, we demonstrated that such an EDF—dubbed "BigApple"—successfully accounts for the binding energy and charge radii of a representative set of spherical nuclei, is consistent with the bulk properties of infinite nuclear matter, reproduces the recent NICER data, and is compatible with the limits on the tidal deformability of a $1.4\,M_\odot$ neutron star, as reported in the GW170817 discovery paper. In particular, our predictions are well aligned (see Table IV) with the constraints extracted from GW190814 under the NSBH scenario: $R_{1.4}=12.9^{+0.8}_{-0.7}$ and $\Lambda_{1.4}=616^{+273}_{-158}$ [7].

However, despite the considerable success of the model, two sets of data strongly disfavor such a stiff EOS. First, the revised upper limit from GW170817 of $\Lambda_{1.4}=190^{+390}_{-120}$ (at the 90% level) [13] is significantly lower than the $\Lambda_{1.4}\simeq 720$ value predicted by BigApple. This would require a softening of the EOS, particularly of the symmetry energy. Second, constraints on the EOS of symmetric nuclear matter extracted from particle-flow in high-energy nuclear collisions rule out an overly stiff nuclear matter EOS. For example, BigApple predicts a pressure at four times saturation density that is nearly twice as large as the upper limit extracted from the flow data. In principle, by adding additional interactions at high densities one could soften the EOS of symmetric nuclear matter to bring it into agreement with the heavy-ion data at the expense of needing to stiffen the symmetry energy. Whereas such a procedure may still result in an overall EOS that can account for a $2.6\,M_\odot$ neutron star, it may require considerable fine tuning to keep the pressure of nuclear matter and the tidal deformability low enough. Hence, we conclude that the low deformability demanded by GW170817 combined with the heavy-ion data for symmetric nuclear matter make it highly unlikely that the maximum mass could be as large as $2.6\,M_\odot$, at least for the class of models used in this work. So as one is left speculating whether the $2.6\,M_\odot$ compact object in GW190814 is either the most massive neutron star or the lightest black hole ever detected, our analysis points strongly in favor of the latter.

Acknowledgments

This material is based upon work supported by the U.S. Department of Energy Office of Science, Office of Nuclear Physics under Awards DE-FG02-87ER40365 (Indiana University), Number DE-FG02-92ER40750 (Florida State University), and Number desc0008808 (NUCLEI SciDAC Collaboration).

[1] B. P. Abbott et al. (LIGO Scientific Collaboration and Virgo Collaboration), Phys. Rev. Lett. **116**, 061102 (2016).
[2] B. P. Abbott et al. (Virgo, LIGO Scientific), Phys. Rev. Lett. **119**, 161101 (2017).
[3] M. R. Drout et al., Science **358**, 1570 (2017).
[4] P. S. Cowperthwaite et al., Astrophys. J. **848**, L17 (2017).
[5] R. Chornock et al., Astrophys. J. **848**, L19 (2017).
[6] M. Nicholl et al., Astrophys. J. **848**, L18 (2017).
[7] R. Abbott et al. (LIGO Scientific, Virgo), Astrophys. J. **896**, L44 (2020).
[8] E. R. Most, L. J. Papenfort, L. R. Weih, and L. Rezzolla (2020), 2006.14601.
[9] H. Tan, J. Noronha-Hostler, and N. Yunes (2020), 2006.16296.
[10] B. Margalit and B. D. Metzger, Astrophys. J. **850**, L19 (2017).
[11] H. T. Cromartie et al., Nat. Astron. **4**, 72 (2019).
[12] H. Mueller and B. D. Serot, Nucl. Phys. **A606**, 508 (1996).
[13] B. P. Abbott et al. (Virgo, LIGO Scientific), Phys. Rev. Lett. **121**, 161101 (2018).
[14] A. Bauswein, O. Just, H.-T. Janka, and N. Stergioulas, Astrophys. J. **850**, L34 (2017).
[15] F. J. Fattoyev, J. Piekarewicz, and C. J. Horowitz, Phys. Rev. Lett. **120**, 172702 (2018).
[16] E. Annala, T. Gorda, A. Kurkela, and A. Vuorinen, Phys. Rev. Lett. **120**, 172703 (2018).
[17] E. R. Most, L. R. Weih, L. Rezzolla, and J. Schaffner-Bielich, Phys. Rev. Lett. **120**, 261103 (2018).
[18] I. Tews, J. Margueron, and S. Reddy, Phys. Rev. **C98**, 045804 (2018).
[19] T. Malik, N. Alam, M. Fortin, C. Providencia, B. K. Agrawal, T. K. Jha, B. Kumar, and S. K. Patra, Phys. Rev. **C98**, 035804 (2018).
[20] C. Y. Tsang, M. B. Tsang, P. Danielewicz, W. G. Lynch, and F. J. Fattoyev (2018), 1807.06571.
[21] D. Radice, A. Perego, F. Zappa, and S. Bernuzzi, Astrophys. J. Lett. **852**, L29 (2018).
[22] D. Radice and L. Dai, Eur. Phys. J. A **55**, 50 (2019).
[23] I. Tews, J. Margueron, and S. Reddy, Eur. Phys. J. A **55**, 97 (2019).
[24] C. D. Capano, I. Tews, S. M. Brown, B. Margalit, S. De, S. Kumar, D. A. Brown, B. Krishnan, and S. Reddy, Nature Astronomy **4**, 625 (2019).
[25] C. Drischler, J. Melendez, R. Furnstahl, and D. Phillips (2020), 2004.07805.
[26] W.-J. Xie and B.-A. Li (2020), 2005.07216.
[27] K. Chatziioannou (2020), 2006.03168.
[28] T. E. Riley et al., Astrophys. J. Lett. **887**, L21 (2019).
[29] M. C. Miller et al., Astrophys. J. Lett. **887**, L24 (2019).
[30] P. Demorest, T. Pennucci, S. Ransom, M. Roberts, and J. Hessels, Nature **467**, 1081 (2010).
[31] J. Antoniadis, P. C. Freire, N. Wex, T. M. Tauris, R. S. Lynch, et al., Science **340**, 6131 (2013).
[32] E. Annala, T. Gorda, A. Kurkela, J. Nttil, and A. Vuorinen, Nature Phys. (2020).

[33] W. Kohn, Rev. Mod. Phys. **71**, 1253 (1999).
[34] C. J. Horowitz and J. Piekarewicz, Phys. Rev. Lett. **86**, 5647 (2001).
[35] B. G. Todd-Rutel and J. Piekarewicz, Phys. Rev. Lett **95**, 122501 (2005).
[36] W.-C. Chen and J. Piekarewicz, Phys. Rev. **C90**, 044305 (2014).
[37] F. J. Fattoyev, C. J. Horowitz, J. Piekarewicz, and G. Shen, Phys. Rev. **C82**, 055803 (2010).
[38] W.-C. Chen and J. Piekarewicz, Phys. Lett. **B748**, 284 (2015).
[39] J. Piekarewicz, J. Phys. **G37**, 064038 (2010).
[40] M. Wang, G. Audi, A. H. Wapstra, F. G. Kondev, M. MacCormick, X. Xu, and B. Pfeiffer, Chinese Phys. C **36**, 1603 (2012).
[41] I. Angeli and K. Marinova, At. Data Nucl. Data Tables **99**, 69 (2013).
[42] S. Kaufmann et al., Phys. Rev. Lett. **124**, 132502 (2020).
[43] S. Abrahamyan, Z. Ahmed, H. Albataineh, K. Aniol, D. S. Armstrong, et al., Phys. Rev. Lett. **108**, 112502 (2012).
[44] J. Piekarewicz and M. Centelles, Phys. Rev. **C79**, 054311 (2009).
[45] M. N. Harakeh and A. van der Woude, *Giant Resonances-Fundamental High-frequency Modes of Nuclear Excitation* (Clarendon, Oxford, 2001).
[46] C. J. Horowitz and J. Piekarewicz, Phys. Rev. **C64**, 062802 (2001).
[47] B. A. Brown, Phys. Rev. Lett. **85**, 5296 (2000).
[48] R. J. Furnstahl, Nucl. Phys. **A706**, 85 (2002).
[49] M. Centelles, X. Roca-Maza, X. Viñas, and M. Warda, Phys. Rev. Lett. **102**, 122502 (2009).
[50] X. Roca-Maza, M. Centelles, X. Viñas, and M. Warda, Phys. Rev. Lett. **106**, 252501 (2011).
[51] J. M. Lattimer and M. Prakash, Phys. Rept. **442**, 109 (2007).
[52] P. Danielewicz, R. Lacey, and W. G. Lynch, Science **298**, 1592 (2002).
[53] G. A. Lalazissis, J. Konig, and P. Ring, Phys. Rev. **C55**, 540 (1997).

The Astrophysical Journal Letters, 887:L24 (28pp), 2019 December 10 https://doi.org/10.3847/2041-8213/ab50c5
© 2019. The American Astronomical Society. All rights reserved.

PSR J0030+0451 Mass and Radius from *NICER* Data and Implications for the Properties of Neutron Star Matter

M. C. Miller[1], F. K. Lamb[2,3], A. J. Dittmann[1], S. Bogdanov[4], Z. Arzoumanian[5], K. C. Gendreau[5], S. Guillot[6,7], A. K. Harding[8], W. C. G. Ho[9,10], J. M. Lattimer[11], R. M. Ludlam[12,19], S. Mahmoodifar[1,8], S. M. Morsink[13], P. S. Ray[14], T. E. Strohmayer[15], K. S. Wood[16], T. Enoto[17], R. Foster[18], T. Okajima[5], G. Prigozhin[18], and Y. Soong[5]

[1] Department of Astronomy and Joint Space-Science Institute, University of Maryland, College Park, MD 20742-2421 USA; miller@astro.umd.edu
[2] Center for Theoretical Astrophysics and Department of Physics, University of Illinois at Urbana-Champaign, 1110 West Green Street, Urbana, IL 61801-3080, USA
[3] Department of Astronomy, University of Illinois at Urbana-Champaign, 1002 West Green Street, Urbana, IL 61801-3074, USA
[4] Columbia Astrophysics Laboratory, Columbia University, 550 West 120th Street, New York, NY 10027, USA
[5] X-Ray Astrophysics Laboratory, NASA Goddard Space Flight Center, Code 662, Greenbelt, MD 20771, USA
[6] IRAP, CNRS, 9 avenue du Colonel Roche, BP 44346, F-31028 Toulouse Cedex 4, France
[7] Universitié de Toulouse, CNES, UPS-OMP, F-31028 Toulouse, France
[8] Astrophysics Science Division, NASA Goddard Space Flight Center, Greenbelt, MD 20771, USA
[9] Department of Physics and Astronomy, Haverford College, 370 Lancaster Avenue, Haverford, PA 19041, USA
[10] Mathematical Sciences, Physics and Astronomy, and STAG Research Centre, University of Southampton, Southampton SO17 1BJ, UK
[11] Department of Physics and Astronomy, Stony Brook University, Stony Brook, NY 11794-3800, USA
[12] Cahill Center for Astronomy and Astrophysics, California Institute of Technology, Pasadena, CA 91125, USA
[13] Department of Physics, University of Alberta, 4-183 CCIS, Edmonton, AB T6G 2E1, Canada
[14] Space Science Division, U.S. Naval Research Laboratory, Washington, DC 20375, USA
[15] Astrophysics Science Division and Joint Space-Science Institute, NASA Goddard Space Flight Center, Greenbelt, MD 20771, USA
[16] Praxis, resident at the U.S. Naval Research Laboratory, Washington, DC 20375, USA
[17] The Hakubi Center for Advanced Research and Department of Astronomy, Kyoto University, Kyoto 606-8302, Japan
[18] MIT Kavli Institute for Astrophysics and Space Research, Massachusetts Institute of Technology, 70 Vassar Street, Cambridge, MA, USA
Received 2019 August 9; revised 2019 October 9; accepted 2019 October 24; published 2019 December 12

Abstract

Neutron stars are not only of astrophysical interest, but are also of great interest to nuclear physicists because their attributes can be used to determine the properties of the dense matter in their cores. One of the most informative approaches for determining the equation of state (EoS) of this dense matter is to measure both a star's equatorial circumferential radius R_e and its gravitational mass M. Here we report estimates of the mass and radius of the isolated 205.53 Hz millisecond pulsar PSR J0030+0451 obtained using a Bayesian inference approach to analyze its energy-dependent thermal X-ray waveform, which was observed using the *Neutron Star Interior Composition Explorer* (*NICER*). This approach is thought to be less subject to systematic errors than other approaches for estimating neutron star radii. We explored a variety of emission patterns on the stellar surface. Our best-fit model has three oval, uniform-temperature emitting spots and provides an excellent description of the pulse waveform observed using *NICER*. The radius and mass estimates given by this model are $R_e = 13.02^{+1.24}_{-1.06}$ km and $M = 1.44^{+0.15}_{-0.14}\,M_\odot$ (68%). The independent analysis reported in the companion paper by Riley et al. explores different emitting spot models, but finds spot shapes and locations and estimates of R_e and M that are consistent with those found in this work. We show that our measurements of R_e and M for PSR J0030+0451 improve the astrophysical constraints on the EoS of cold, catalyzed matter above nuclear saturation density.

Unified Astronomy Thesaurus concepts: X-ray sources (1822); Millisecond pulsars (1062); Neutron stars (1108); Neutron star cores (1107)

1. Introduction

A key current goal of nuclear physics is to understand the properties of cold catalyzed matter above the saturation density of nuclear matter. Matter at these densities cannot be studied in terrestrial laboratories. Hence observations of neutron stars—which contain large quantities of such matter—play a key role (see, e.g., Lattimer & Prakash 2007). Over the last few years, the discovery of several high-mass neutron stars (Demorest et al. 2010; Antoniadis et al. 2013; Arzoumanian et al. 2018a; Cromartie et al. 2019) and measurement of the binary tidal deformability during a neutron star merger (Abbott et al. 2017, 2018; De et al. 2018) have advanced our knowledge of the properties of cold dense matter, but precise and reliable measurements of neutron star radii would significantly improve our understanding.

Various radius estimates have been made using models of the X-ray emission from quiescent neutron stars (see Steiner et al. 2018 for a recent summary), from neutron stars during thermonuclear X-ray bursts (see Steiner et al. 2010; Özel et al. 2016; and Nättilä et al. 2017 for different perspectives), and from accretion-powered millisecond pulsars (see Salmi et al. 2018), with inferred radii typically ranging from ∼10 km to ∼14 km, consistent with most theoretical predictions. However, these estimates are susceptible to significant systematic errors, in the sense that a model could provide a formally good fit to the data but yield a credible interval for the radius that strongly excludes the true value (Miller 2013; Miller & Lamb 2016).

In contrast, analyses of the soft X-ray pulse waveforms observed using the *Neutron Star Interior Composition Explorer* (*NICER*) are expected to be less susceptible to systematic errors. Analyses of synthetic waveforms carried out prior to the

[19] Einstein Fellow.

launch of *NICER* showed that, for the cases considered, using model assumptions different from the true situation (e.g., different emission or beaming patterns, different spectra, or different surface temperature distributions) did not significantly bias parameter estimates, provided that the fit was formally good (Lo et al. 2013; Miller & Lamb 2015). Simple pulse waveform models have previously been fit to the soft X-ray waveforms of rotation-powered pulsars observed using *ROSAT* and the *Extreme Ultraviolet Explorer* (*EUVE*; Pavlov & Zavlin 1997; Zavlin & Pavlov 1998) and *XMM-Newton* (see, e.g., Bogdanov et al. 2007, 2008; Bogdanov 2013). These fits gave estimates for the radii of these pulsars that were consistent with the expected range of neutron-star radii, but the number of counts available was too small to obtain tight constraints. Nevertheless, these pioneering studies indicated that rotation-powered pulsars are promising targets for such measurements.

Here we present the results of an analysis by *NICER* team members of the currently available data on the 205.53 Hz (Arzoumanian et al. 2018a) millisecond pulsar PSR J0030+0451. The results of an independent analysis of these data by other *NICER* team members are presented in the companion paper by Riley et al. (2019). The analysis presented there uses an independently developed code for computing pulse waveforms, a different approach to modeling the heated regions on the stellar surface, and different sampling methods than the ones used in the analysis presented here. The consistency of the surface temperature distributions and mass–radius posteriors reported there with those reported here suggests that the unavoidable uncertainties in models of the heated areas on the stellar surface have not greatly affected the results of either analysis. In Section 2 we describe how we obtained and processed the *NICER* data on PSR J0030+0451. In Section 3 we discuss our methods, including our modeling of the emission from the stellar surface, our approach to modeling the soft X-ray waveform, our parameter estimation and model evaluation methods, and our treatment of instrumental effects and bias. In Section 4 we describe how we used analyses of synthetic waveforms to verify our parameter estimation codes and procedures, and to evaluate the consequences of our decision to analyze a subset of the *NICER* data on PSR J0030+0451. In Section 5 we present and discuss our best estimates of the radius and mass of PSR J0030+0451 using the currently available *NICER* data on its pulse waveform. In Section 6 we compute and discuss the constraints on two different parameterized models of the equation of state (EoS) of neutron star matter implied by our measurements of the radius and mass of PSR J0030+0451. We summarize our conclusions in Section 7.

2. Observations

2.1. Data Used

Here, we briefly summarize the *NICER* X-ray Timing Instrument (XTI) data set that was used for the parameter estimation analyses presented here. More detailed descriptions of the observations, data reduction, and event folding procedures, and a thorough examination of the properties of the final event data can be found in Bogdanov et al. (2019a).

The *NICER* XTI data on PSR J0030+0451 were collected in a set of short observations (typically lasting a few hundred to ∼2000 s) over the period from 2017 July 24 to 2018 December 9. Due to the exceptional rotational stability of PSR J0030+0451 and the superb absolute timing accuracy of *NICER*, neither the large time span nor the discontinuities in the exposure had any adverse effects, such as smearing due to long-term pulse-phase drifts, on the pulse profile.

2.2. Filtering of the Data and Event Folding

For this analysis, we used products from the calibration database (CALDB) version 20181105 and gain solution version `optmv7`. In addition to the standard pipeline processing event filtering that all *NICER* data undergo, the PSR J0030+0451 data set was subjected to screening criteria tailored to the inference analyses discussed later.

We included only data accumulated when the source subtended an angle greater than 80° from the Sun, in order to minimize the contamination from optical loading in the lowest-energy detector channels. All events from the XTI detector with DET_ID 34 were excised because it frequently exhibits significantly elevated count rates relative to the other detectors (analogous to a "hot pixel" in charge-coupled device detectors).

In the final filtering stage, we constructed a time series with 16 s time bins using the event data in channels 25–800 and then discarded all the events in those time bins that had an average count rate greater than 3 counts s^{-1}. The long-term average count rate during the *NICER* observations of PSR J0030+0451 was ∼0.7 counts s^{-1}. This cut therefore excluded the event data in all the 16 s time bins that had count rates more than four times the long-term average count rate. The purpose of this cut was to improve the signal-to-noise ratio of the measured thermal emission from the pulsar by removing data contaminated by flares that were not filtered out by the standard pipeline processing.

The thermal emission pulse profile that was used to estimate the mass and radius of PSR J0030+0451 was constructed by averaging the data from the roughly 400 million rotation periods observed by *NICER* during more than 18 months of observations. We compared the profile measured during the first third of this observing time with the profile measured during the second third, and also compared the profile measured during the first half of this observing time with the profile measured during the second half. These comparisons showed no statistically significant differences between the compared profiles. We expect that any shorter-term flux variations were averaged out by using such a long data set.

To generate the final X-ray pulse profile as a function of pulsar rotational phase and energy, we used the "photons" plugin for the Tempo2 pulsar timing package (Hobbs et al. 2006) and the best publicly available radio timing solution, obtained by NANOGrav (Arzoumanian et al. 2018b), to assign pulse phases to each event. The number of the "pulse invariant" (PI) detector channel provides an estimate of the photon energy: the photon energy in eV is approximately equal to 10× the PI channel number in which the event occurs.

As discussed in Bogdanov et al. (2019a), the final X-ray pulse profile was cross-verified by comparing it with an independently generated profile in which pulse phases were assigned to events using the PINT pulsar timing software. The pulse phases assigned to individual events by the two procedures differed by $\lesssim 1\ \mu$s, and the differences between the two folded X-ray pulse profiles were negligible. The final event list used in the analysis reported in this Letter is available at https://doi.org/10.5281/zenodo.3524457.

2.3. Calibration of the Instrument

To incorporate the performance of the *NICER* XTI in our model, we used version 1.02 of the redistribution matrix file (RMF), which gives the probability that a photon in a particular energy range is registered by a particular detector channel, and version 1.02 of the ancillary response file (ARF), which provides the effective area of the telescope as a function of energy, as measured on axis.

Spectral calibration of the *NICER* XTI has been carried out primarily using observations of the Crab pulsar and nebula. The response below channel 40 is more uncertain than the response at higher energies, because of current imperfections in the modeling of instrumental effects such as the detector trigger efficiency. Also, because at these low energies the Crab spectrum is strongly attenuated by the interstellar medium, only a relatively small number of counts are available to determine the spectrum at these energies. Fits to *NICER* observations of the Crab pulsar and nebula in the energy channels 40–299 used in this study (see Section 5.2) show systematic residuals, but these are typically $\lesssim$5% (Ludlam et al. 2018). They are likely due to imperfect modeling of the microphysics of the concentrator optics and astrophysical features, such as oxygen edges and emission lines.

3. Methods

In this section, we first describe our modeling of the soft X-ray emission from hot spots on the stellar surface and our approach to modeling the soft X-ray pulses produced by the rotation of these spots. We then present the specific pulse waveform models that we consider in this work and our procedure for constructing and fitting these model waveforms to the *NICER* pulse waveform data on PSR J0030+0451. We end this section by discussing how we deal with the errors in the response of the *NICER* instrument and the evidence that including data from channels below channel 40 would risk biasing our estimates of the mass and radius of PSR J0030+0451. We defer to subsequent sections discussion of our use of synthetic pulse waveform data to verify our parameter estimation procedures, our use of *NICER* pulse waveform data to estimate the mass and radius of PSR J0030+0451, our assessment of the reliability of these estimates, and their implications for the EoS of cold dense matter.

3.1. Modeling the Emission from the Stellar Surface

The soft X-ray pulse waveform of PSR J0030+0451 is thought to be produced by hot regions on its rotating surface created by inward moving particles created in electron-positron pair cascades interacting with the outermost layers of the neutron star (Arons 1981; Harding & Muslimov 2001). Models of global pulsar magnetospheres (see, e.g., Kalapotharakos et al. 2014; Philippov et al. 2015; Brambilla et al. 2018) have delineated the current-closure patterns of pulsars, which show outward currents in the magnetic polar regions balanced by return currents over the outer parts of the polar caps that are connected to the current sheet. Some of the particles that make up the return currents (those that are accelerated in the current sheet) are responsible for the pulsar's γ-ray and nonthermal X-ray emission (Kalapotharakos et al. 2018; Philippov & Spitkovsky 2018). The polar cap pair cascades that take place in both outgoing and return current regions (Timokhin & Arons 2013) supply pairs for radio emission. Some of the particles produced in these pair cascades are accelerated downward and are expected to deposit energy deep in the neutron star's atmosphere (see Tsai 1974 and Bogdanov et al. 2007). This energy is expected to heat the atmosphere at large optical depths, producing thermal soft X-ray emission from the stellar surface (Harding & Muslimov 2001, 2002). The spectrum of this emission is expected to depend on the chemical composition of the star's atmosphere and, possibly, on the strength and orientation of the magnetic field at the locations of the hot spots (Potekhin 2014).

The models of the thermal emission from these hot spots that we have used in the analysis of the soft X-ray waveform of PSR J0030+0451 that we report here assume that the upper atmosphere of the pulsar is fully ionized pure hydrogen and that, for our purposes, the magnetic fields in the hot spots can be neglected. We now discuss these assumptions.

Composition of the upper atmosphere. Our model atmospheres were constructed assuming that the gas in the atmosphere is fully ionized, and hence that the dominant opacity is free–free absorption (Ho & Lai 2001). While opacity tables for partially ionized matter exist (Iglesias & Rogers 1996; Badnell et al. 2005; Colgan et al. 2016), they do not cover the full range of temperatures and energies needed for the present analysis. However, at the temperatures $\sim 10^6$ K that are relevant for the present study, the fraction of hydrogen that is neutral is very low; comparison of the outward specific intensity given by our fully ionized hydrogen atmosphere model differs by at most 1%–2% at 0.5–1 keV from that for an atmosphere with an effective temperature of 10^6 K given by a model constructed using the Opacity Project (OP) opacity table (Badnell et al. 2005), which allows for partial ionization (see Bogdanov et al. 2019b).

Our assumption that the upper atmosphere is pure hydrogen is based primarily on the astrophysical abundance of hydrogen and calculations that show how the lightest element present in a neutron star atmosphere will float to the top within seconds. These calculations are extrapolations of earlier calculations by, for example, Alcock & Illarionov (1980). Given the astrophysical abundance of hydrogen and its tendency to float to the top, we expect it to completely dominate the composition of the upper atmosphere.

If the outer atmosphere of the pulsar were instead dominated by helium, the emission spectrum and beaming pattern in the energy range 0.5–1.0 keV would be expected to be very similar to those for a hydrogen atmosphere, but their normalizations would be slightly smaller than for hydrogen (see Bogdanov et al. 2019b). In particular, hydrogen and helium atmospheres with an effective temperature of 10^6 K (the approximate inferred temperature of the heated regions on the surface of PSR J0030+0451) are predicted to produce specific intensities normal to the surface that differ from each other by $\lesssim$5% in the 0.5–1 keV energy range (again see Bogdanov et al. 2019b). Our current best fit of the zero-field NSX helium atmosphere (Ho & Lai 2001) to the *NICER* data on PSR J0030+0451 appears disfavored relative to our current best fit of the zero-field NSX hydrogen atmosphere (Ho & Lai 2001; see also Ho & Heinke 2009). Specifically, our current fit using the NSX helium model yields a best-fit mass of $2.7\,M_\odot$, with little posterior probability below $2.0\,M_\odot$. Although more work would be needed to completely rule out a helium atmosphere

for PSR J0030+0451, this mass estimate is so large that we interpret it as disfavoring a helium atmosphere.

Thus, while there is at present no direct spectroscopic confirmation that the upper atmosphere of PSR J0030+0451 is pure hydrogen, the fact that the spectrum and beaming pattern predicted by hydrogen atmosphere models agree well with the spectrum and beaming of the soft X-ray emission from PSR J0030+0451 observed using *NICER*, and that the X-ray spectrum and beaming predicted by helium atmosphere models appear disfavored, supports our assumption that the upper atmosphere is hydrogen. Therefore, in computing model waveforms we used the local emission for a given surface gravity, effective temperature, angle from the surface normal, and photon energy that is predicted by the NSX code developed by Ho & Lai (2001; see also Ho & Heinke 2009) for a fully ionized hydrogen atmosphere.

The 205.53 Hz rotation frequency of PSR J0030+0451 (Arzoumanian et al. 2018a) is small enough that the only effects of the rotation that need to be taken into account in computing pulse waveforms are the special relativistic Doppler shift and aberration caused by the motion of the emitting surface and the rotationally induced oblateness of the star; the effect of frame-dragging and the effect on the exterior spacetime of the rotationally induced stellar mass quadrupole are negligible (see Morsink et al. 2007 and Bogdanov et al. 2019b). We therefore used the so-called oblate-star Schwarzschild-spacetime (OS) approximation (Cadeau et al. 2007; Morsink et al. 2007; AlGendy & Morsink 2014) when tracing light rays from the stellar surface to the observer. Computations of pulse waveforms like those used here were verified by members of the *NICER* Lightcurve Working Group, as described in Bogdanov et al. (2019b).

Strength and structure of the stellar magnetic field. We can estimate an approximate lower bound on the strength of the surface magnetic field of PSR J0030+0451 by assuming that the field is a centered dipole and estimating the strength of the dipole moment using the best braking models currently available (see, e.g., Contopoulos & Spitkovsky 2006). The period P of PSR J0030+0451 is 0.00487 seconds and its period derivative $\dot{P}$ is 1.02×10^{-20} (Arzoumanian et al. 2018a). If we use Equation (12) of Contopoulos & Spitkovsky (2006) and, for the sake of argument, choose a magnetic field inclination θ of $\pi/2$ and the field configuration described by $\alpha = 0$, then the inferred strength of the magnetic field at the stellar surface is $B \sim 4 \times 10^8$ G. In principle, this represents an approximate lower bound on the strength of the total magnetic field in the atmospheres of the hot spots. For comparison, the electron cyclotron energy in a magnetic field of this strength is $\hbar\omega_c \approx 4$ eV, which is more than 50 times smaller than the lowest photon energies that can be observed using *NICER* and $\sim$100 times smaller than the lowest energies that we consider in our fits.

We note, however, that the three hot spots in the "southern" rotational hemisphere (we denote the rotational hemisphere that includes the line of sight to the observer as the "northern" rotational hemisphere) that can explain the pulse waveform of PSR J0030+0451 observed using *NICER* suggest that the magnetic field of PSR J0030+0451 is at least an offset dipole, and may have higher moments that dominate the field strength near the stellar surface. A complex field would be consistent with the structures of the magnetic fields of other millisecond rotation-powered pulsars inferred from their radio and γ-ray emission (Ruderman 1991; Ruderman et al. 1998), and the inferred magnetic field configurations of the accretion-powered millisecond pulsars that are thought to be the progenitors of the millisecond rotation-powered pulsars (Lamb et al. 2009a, 2009b).

If the magnetic field of PSR J0030+0451 does have significant higher multipole moments, they may not be negligible at the light cylinder, which is closer to the stellar surface in millisecond pulsars than in pulsars with lower spin rates. Moreover, in some spin-down models (again see Contopoulos & Spitkovsky 2006), the spin-down rate depends on the magnetic flux enclosed by the open-field-line region, which is defined by the boundary of the closed magnetosphere and may not extend all the way out to the light cylinder. The way this flux evolves with spin rate can be affected by the presence of multipolar field components, complicating the relation between the strength of the surface magnetic field and the spin-down rate.

Given this complexity, it is difficult to infer the strength and configuration of the magnetic field on the surface of PSR J0030+0451. In current braking models, the braking torque scales with the strength of the dipole component of the magnetic field at some characteristic distance from the star. For a given strength of the dipole component at this distance, the strength of the magnetic field at the stellar surface scales as $(R_e/d)^3$, where R_e is the circumferential radius of the star and $2d$ is the distance through the star from one magnetic pole to the other. Thus, if the large-scale magnetic field is essentially dipolar and the corresponding magnetic poles are a significant distance south of the rotational equator, the field strength at the surface of the star could be 5–10× greater than it would be for a centered dipole field with the same strength a large distance from the stellar surface. In this case, the indicated strength of the magnetic fields at the hot spots could be as large as $B \sim 4 \times 10^9$ G.

Effect of the magnetic field on the soft X-ray emission from the stellar surface. The model atmospheres that we have used to compute the waveforms that we fitted to the *NICER* waveform data assume that the effects of the stellar magnetic field on the structure and radiative properties of the atmosphere are negligible. This approximation is valid for magnetic field strengths that are less than $B_c = e^3 m_e^2\, c/\hbar^3 = 2 \times 10^9$ G. The upper bound on the strength of the magnetic field that we estimated above by assuming that it is dipolar and using the best currently available braking models is an order of magnitude smaller than B_c, but our estimates of the possible field strengths at the hot spots are a factor of two larger than B_c.

If the magnetic field exceeds B_c, its effect is non-perturbative and dominant (see Lai 2001): the radiation field becomes polarized, the beaming pattern becomes strongly anisotropic, and spectral features associated with the electron cyclotron resonance and bound species become important (Potekhin 2014). The absence of any obvious spectral feature in the spectra observed using *XMM-Newton* (see, e.g., Bogdanov & Grindlay 2009) and in the $\sim$0.3–3 keV spectra obtained using *NICER* rules out $B = (3\text{–}30) \times 10^{10}$ G, assuming a redshift of 20%. In addition, while an electron cyclotron line produced by a magnetic field $B \gg 10^{11}$ G could be hidden at $E > 3$ keV, such fields would produce pencil or fan beams that are unlikely to be able to produce an energy-dependent pulse profile that can match the profile observed using *NICER*.

The changes in the spectrum and the beaming pattern that occur for magnetic fields $B \gtrsim 10^{10}$ G are somewhat larger than the changes in the spectrum and beaming pattern that occur when going from a purely H model atmosphere to a purely He model atmosphere without any magnetic field. While spectra that assume such strong fields might yield statistically acceptable fits to the *NICER* observations of PSR J0030+0451, it is likely, though not certain, that such fits would, as in the case of the He atmosphere models, yield mass and radius estimates that are so extreme that we would consider these models disfavored.

If the total strengths of the magnetic fields in the atmospheres of the hot spots of PSR J0030+0451 are less than B_c, they are expected to have little effect on the spectrum and shape of its soft X-ray waveform. The agreement of our energy-resolved waveform models with the energy-resolved waveform data obtained using *NICER* are consistent with this interpretation.

3.2. Our Approach to Modeling the Soft X-Ray Waveform

In modeling the soft X-ray pulse waveform of PSR J0030+0451, we started with the simplest possible description of the heated region(s) on the stellar surface and then, as necessary, considered more complicated descriptions, guided at each step by the differences between the best-fit simpler pulse waveform models and the waveform observed using *NICER*. Along the way, we verified our parameter estimation algorithms by fitting appropriate models to several synthetic waveforms that were generated using the models of the heated regions on the stellar surface that emerged from our fits to the observed waveform, and then comparing the values of the parameters obtained from these fits with the values of these same parameters that were used to generate the synthetic waveforms.

Visual examination of the PSR J0030+0451 waveform observed using *NICER* shows evidence for two peaks, and waveform models constructed using a single hot spot fail to reproduce the qualitative features of the observed waveform. Consequently, we began our modeling of the observed waveform using models that had two uniform circular hot spots with possibly different locations, areas, and temperatures, but these models did not adequately describe the observed waveform. In particular, the (relatively large) spot sizes that were required to reproduce the weak higher harmonic content of the observed waveform appeared to conflict with the (relatively small) spot areas that were required to reproduce the observed X-ray flux.

We therefore considered models with three and four different uniform-temperature circular hot spots, and finally models with two and three different uniform-temperature oval hot spots. In all cases we allowed the spots to overlap in any way that improved the fit; our procedure for treating overlapping spots is described below. This algorithm allowed the heated regions in the model to evolve toward a variety of different complex shapes as the fitting process proceeded, including multiple separate hot spots, multiple-temperature spots in which each spot has hotter and cooler regions, elongated or more complicated configurations produced by two or more partially or completely overlapping or adjacent circular or oval hot spots, crescent-shaped hot regions produced by cold oval spots partially or completely overlapping hot oval spots, and so on. These explorations found no evidence for different temperatures within the same hot spot and no evidence for more than three heated regions on the stellar surface.

We found that a model with two different, non-overlapping, uniform oval spots is preferred over any models with two overlapping spots, adequately describes the observed waveform, and gives a much better fit to the data than a model with two circular spots. The larger east–west extent of the best-fitting oval spots allows them to reproduce the observed weak higher harmonic content of the waveform, while their smaller north–south extent allows them to have the relatively small areas required to reproduce the observed X-ray flux.

To assess whether a model with two different uniform-temperature oval spots is sufficient, we also considered configurations with three different uniform-temperature oval spots. We found that a model with three different, non-overlapping, uniform oval spots is preferred over any models in which the spots overlap, describes the observed waveform adequately, and gives a fit to the data that is slightly, but not significantly, better than the best-fit model with two non-overlapping, uniform oval spots. The two main spots in the best-fit model with three spots are very similar to the spots in the two-spot model, while the third spot has a much higher temperature but a much smaller area than either of the other two spots, is located close to the rotational pole on the far side of the star from the observer, and makes only a very small contribution to the waveform.

The pulse waveforms and the mass and radius estimates given by the best-fit two- and three-spot models are statistically indistinguishable. We therefore concluded that both models adequately describe the observed waveform, that there is no evidence that a more complicated model is required, and that the mass and radius estimates given by these models are reliable. We slightly prefer the radius and mass estimates given by the model with three oval spots, only because the evidence for this model is slightly—although not significantly—greater than the evidence for the model with two oval spots.

In Section 4, we show and discuss the results of several of the analyses of synthetic waveform data that we performed to gain confidence in the accuracy and reliability of our parameter estimation procedure. Specifically, we show the results that we obtained by fitting a model of the waveform produced by two circular spots to synthetic waveform data generated using this model, and by fitting a model of the waveform produced by two oval spots to synthetic waveform data generated using this more complicated model. In Section 5, we describe in detail our systematic approach to modeling the pulse waveform of PSR J0030+0451 and the evidence that led us to focus on the waveform model with three oval spots that we used to estimate the radius and mass of PSR J0030+0451. But first we detail the various waveform models that we constructed, the modeling procedure that led us to consider these models, and the algorithms that we used to estimate the best-fit values of the parameters in these models. We also describe the procedures that we used to evaluate and compare these models, the motivation for our selection of the *NICER* data we analyzed, and our assessment of the effects of the errors in the *NICER* response.

3.3. Waveform Models

In the analyses that we present here, we used pulse waveform models with the primary parameters listed and defined in Table 1. There are 12 primary parameters in the model that has two circular spots (this model assumes $f_1 = 1 = f_2$ and has no parameters for a third spot), 14 primary

Table 1
Primary Parameters of the Pulse Waveform Models Considered in this Work

Parameter	Definition	Assumed Prior
$GM/(c^2R_e)$	Stellar compactness	0.125–0.3125
M	Gravitational mass	1.0–2.4 $M_\odot$
θ_{c1}	Spot 1 center	0.1–3.1 rad
$\Delta\theta_1$	Spot 1 radius	0–3 rad
f_1	Spot 1 oval ratio	0.1–20
$kT_{\rm eff,1}$	Spot 1 eff. temp.	0.011–0.5 keV
$\Delta\phi_2$	Spot 2 longitude diff.	0–1 cycles
θ_{c2}	Spot 2 center	0.1–3.1 rad
$\Delta\theta_2$	Spot 2 radius	0–3 rad
f_2	Spot 2 oval ratio	0.1–20
$kT_{\rm eff,2}$	Spot 2 eff. temp.	0.011–0.5 keV
$\Delta\phi_3$	Spot 3 longitude diff.	0–1 cycles
θ_{c3}	Spot 3 center	0.1–3.1 rad
$\Delta\theta_3$	Spot 3 radius	0–3 rad
f_3	Spot 3 oval ratio	0.1–20
$kT_{\rm eff,3}$	Spot 3 eff. temp.	0.011–0.5 keV
$\theta_{\rm obs}$	Observer inclination	0.1-$\pi/2$ rad
$N_{\rm H}$	H column density	0–2.5 $\times$ 10^{20} cm^{-2}
D	Distance	$\exp[-(D - 0.325{\rm kpc})^2/2(0.017{\rm kpc})^2]$

Note. We assumed the above priors, which are flat in the indicated range except for the distance D, and a rotation frequency of 205.53 Hz as seen by a distant observer (a) when we analyzed the synthetic PSR J0030+0451 waveform generated using two oval hot spots, which had parameter values (see Table 4) chosen so that it would mimic the waveform observed by *NICER*, and (b) when we analyzed the actual PSR J0030+0451 waveform observed by *NICER*. When we analyzed the synthetic waveform that was generated using two circular hot spots, we used the priors listed above for most of the parameters, but different priors for four parameters. This is because the waveform was constructed to mimic the waveform of PSR J0437−4715 observed by *NICER*, and in generating it we used values for these four parameters that are different from those listed in Table 2. In generating this synthetic waveform, we assumed a rotation frequency of 173.6 Hz and flat priors in the intervals listed for the following four parameters: M: 1.0–1.9$M_\odot$, $\theta_{\rm obs}$: 0.6–0.9 rad, $N_{\rm H}$: 0–2.5 $\times$ 10^{20} cm^2, D: 0.13–0.18 kpc. See the text for further details about the assumed prior probability distributions for each parameter.

parameters in the model that has two oval spots, and 19 primary parameters in the model that has three oval spots.

For the reasons discussed previously, all the waveform models that we present in this report assume that the effective temperature of the emission from a given hot spot does not vary across the spot. The effective temperature listed in Table 1 is the effective temperature that would be measured by a local observer on the stellar surface.

When constructing an oval spot centered at a given colatitude and having a given latitudinal extent, we determined the longitudinal extent it would have if it were instead circular and then multiplied this extent by the colatitude-independent factor f_1 for spot 1, f_2 for spot 2, and f_3 for spot 3. The possible values of f_1, f_2, and f_3 are bounded from above by the requirement that no spot have a longitudinal extent greater than 2π.

We defined the northern hemisphere as the hemisphere containing the sightline to the observer. We defined longitude 0 as the longitude of the center of spot 1; after generating a trial waveform, we rotated its phase to give the best fit to the waveform data (see below).

3.4. Our Waveform Modeling Procedure

As noted earlier, when fitting model waveforms to the observed waveform, we allowed hot spots to overlap one another. This approach allowed the fitting process to create more complicated heated regions, such as multiple isolated spots, spots with hotter cores and cooler annuli, spots with cooler cores and hotter annuli, noncircular heated regions having two different temperatures, and so on, if these configurations were favored by the data. For the reasons described in Section 3.2, we discuss here only our modeling of waveforms with at least two hot spots and at most three.

In the pixels on the stellar surface where spots overlap, our fitting algorithm chooses the temperature of the lowest-numbered spot. For example, if spot 2 and spot 3 overlap, all the pixels in the overlap region are assumed to emit with the effective temperature currently assigned to spot 2. If spot 1, spot 2, and spot 3 all overlap, all pixels in the overlap region are assumed to emit with the effective temperature currently assigned to spot 1.

In addition to the primary parameters listed in Table 1, we introduced two types of ancillary parameters. The first set of ancillary parameters describes the counts in each energy channel that do not come from any of the hot spots. We refer to these as *background* counts. These background counts allow for any unmodulated emission from the star that is not produced by any of the hot spots, any other unmodulated emission from the pulsar system, any emission within the field of view that does not come from the pulsar system, and the instrumental backgrounds. Another ancillary parameter describes the overall starting phase of the pulse waveform. In our fitting procedure, we chose to marginalize over these ancillary parameters, rather than fitting for them explicitly. Separately marginalizing the likelihood over the ancillary parameters is fully justified when, as here, the values of the primary parameters are uncorrelated with the values of the ancillary parameters.

We estimated the number of background counts in each energy channel and marginalized the likelihood with respect to the number of background counts in each channel as follows. We first generated a trial waveform by choosing a trial set of values for all the parameters in the waveform model and a trial starting phase for the waveform. Then, for each energy channel, we independently fit a Gaussian to the curve of the likelihood versus the number of background counts assumed present in that channel. By integrating over each Gaussian, we were able to estimate the number of background counts in each energy channel and marginalize the likelihood over the number of background counts in each energy channel, for each trial waveform. This procedure added one parameter to the waveform model for each energy channel that we considered. As we discuss in detail below, for our final fits to the *NICER* pulse

waveform data we chose to use *NICER* energy channels 40 through 299. This approach therefore added 260 parameters to the waveform model.

We performed a similar procedure to determine the best-fit overall phase of the waveform and marginalize the likelihood over this phase. Namely, for each trial offset of the overall phase (defined as the difference between the longitude of the center of the first spot relative to the longitude of the line of sight to the observer), we computed the likelihood over all energy channels. We then fit a Gaussian to the likelihood as a function of the overall phase, which allowed us to estimate the overall phase. We then marginalized the likelihood with respect to the overall phase by integrating the phase offset over the Gaussian curve, assuming a prior for the overall phase that was uniform from 0 to 1 cycles and zero outside this range. This added one more parameter to the waveform model.

Our procedure for estimating the number of background counts in each *NICER* energy channel assumes that we have no independent knowledge of the number or spectrum of the background counts. In reality, we have some information about astrophysical and sky backgrounds and the backgrounds contributed by solar system, magnetospheric, terrestrial, and International Space Station sources. We have developed codes that can take this information into account, but many of these backgrounds are time-variable and are often not accurately known. The values of the waveform parameters that we derived when we included models of the properties of these backgrounds differ little from the values we found when we used the procedure just described. We have therefore chosen to adopt the conservative approach of using this procedure, which does not rely on any models of the various backgrounds.

3.5. Parameter Estimation and Model Evaluation

Parameter estimation and model comparison. To estimate the values of the parameters in our pulse waveform models and compare the evidence for different models using synthetic or *NICER* data, we used standard Bayesian methods. For a given model $\mathcal{M}$ with parameters $\boldsymbol{\theta}$ that have a normalized prior probability density $q(\boldsymbol{\theta})$, the normalized posterior probability density is given by Bayes' Theorem:

$$P(\mathcal{M}, \boldsymbol{\theta}|\text{data}) = \frac{\mathcal{L}(\text{data}|\mathcal{M}, \boldsymbol{\theta})q(\boldsymbol{\theta})}{P(\mathcal{M}|\text{data})}, \tag{1}$$

where $\mathcal{L}(\text{data}|\mathcal{M}, \boldsymbol{\theta})$ is the likelihood of the data given the model with parameter values $\boldsymbol{\theta}$, and $P(\mathcal{M}|\text{data}) \equiv \int_{\boldsymbol{\theta}} \mathcal{L}(\text{data}|\mathcal{M}, \boldsymbol{\theta})q(\boldsymbol{\theta})d\boldsymbol{\theta}$ is the evidence for model $\mathcal{M}$.

Given a model $\mathcal{M}$, we can compute the joint posterior probability density distribution of the values of any subset of the parameters $\boldsymbol{\theta}$ by marginalizing the other parameters, i.e., by integrating $P(\mathcal{M}, \boldsymbol{\theta} \mid \text{data})$ over the possible values of all parameters except those in the subset. For example, the 1D probability density distribution of the value of any single parameter can be computed by integrating $P(\mathcal{M}, \boldsymbol{\theta} \mid \text{data})$ over the possible values of all the other parameters.

The relative probability of two different models is given by their odds ratio, which is the ratio of their evidences (their Bayes factors) multiplied by the ratio of the prior probabilities of the two models.

Sampling methods. We used three statistical sampling methods to estimate the values of the parameters in our various waveform models and compute the evidence for these models: the publicly available nested sampler MultiNest (MN; Feroz et al. 2009), the parallel-tempering Markov chain Monte Carlo sampler (PT-emcee) that is included in the publicly available emcee package version 2.2.1 (Foreman-Mackey et al. 2013), and a hybrid sampling algorithm (see below) that we call MN +PT-emcee.

The MN and PT-emcee sampling algorithms are complementary: nested samplers are optimized for computing the Bayesian evidence and are therefore well suited for computing the odds ratios of different models, whereas Markov Chain Monte Carlo algorithms are optimized for parameter estimation. We carried out many tests of MN, PT-emcee, and MN +PT-emcee in the context of our waveform-fitting problem, using both synthetic and *NICER* waveform data sets.

For relatively simple waveform models and data sets, such as those with two uniform circular hot spots, we were able to adequately sample the full parameter space using either MN or PT-emcee in a reasonable amount of clock time. For these simpler models and data sets, the posterior probability density distributions given by these two algorithms appeared well converged and were in excellent agreement.

For more complex models and data sets, such as our fits of models with two or three oval spots to synthetic data or to the *NICER* data on PSR J0030+0451, we found that, at least for the values of its sampling parameters that we explored, the MN algorithm abandoned regions of parameter space that contained solutions with log likelihoods comparable to the highest found in previous searches, did not give reproducible results, and—when we used it to analyze synthetic data—produced 1σ and 2σ credible regions that too often did not contain the values of the parameters that had been assumed in generating the synthetic data, even after we ran the code for a very long time.

In contrast, even with poor initial seeds, the PT-emcee algorithm appeared able to sample well the parameter space of complicated models and data sets, gave reproducible results, and produced 1σ and 2σ credible regions that contained the values of the parameters that had been assumed in generating the synthetic data about as often as one would expect, i.e., about 68% of the time for 1σ credible regions and about 95% of the time for 2σ credible regions. We therefore adopted the PT-emcee algorithm for analyzing the more complex models and data sets that we considered. However, with poor initial seeds, PT-emcee took large amounts of clock time to complete each parameter estimation.

In order to speed up parameter estimation using PT-emcee, we sought to choose high likelihood points as initial guesses. Having the MN nested sampling algorithm readily available, we typically used it to provide an initial guess. We tested this hybrid approach, which we refer to as MN+PT-emcee, extensively, and found that it was able to find correct solutions in much less clock time than was required if PT-emcee was not given a high likelihood initial guess. Consequently, we used MN+PT-emcee to estimate the values of the parameters in the models with two and three oval spots, and used the resulting samples to estimate the evidence for these models, given the data.

In our initial MultiNest surveys, we used 1000 active points (essentially the number of parameter combinations being actively updated), an efficiency of 0.01 (the target fraction of new parameter combinations that update the list of active points), and a tolerance of 0.1; for precise definitions of these parameters; see Feroz et al. (2009). Based on our experience

sampling the synthetic and *NICER* waveform data, we limited the number of modes to five for models with two spots and 10 for models with three spots. In our PT-emcee analyses, we used 400 walkers when fitting models with two spots and 1000 walkers when fitting models with three spots, and the default temperature ladder.

Completeness of models. Although our parameter estimations and model comparisons are fully Bayesian, we also performed χ^2 analyses to determine whether our models adequately describe the *NICER* data. In computing χ^2, we use the expression for model variance originally advocated by Pearson (1900), namely,

$$\chi^2 = \sum_i \frac{(m_i - d_i)^2}{m_i}, \tag{2}$$

where m_i is the number of counts in bin i that are expected in the model, and d_i is the observed number of counts in bin i, rather than the common data variance form in which the m_i in the denominator is replaced by d_i. The model variance form has the advantage that if the counts d_i are drawn from a Poisson distribution with expected values m_i, then the expected value of χ^2 is equal to the number of bins for any values of m_i. This is not true for the data variance form. We note that for our purposes the computation of χ^2 is a one-way test: if the value of χ^2 for a given number of degrees of freedom is large enough to be highly improbable then we are warned that our model of the spots and/or the instrument is likely to be incomplete, but if the value of χ^2 is reasonably probable we cannot conclude that the model is correct.

3.6. Treatment of Instrumental Uncertainties and Bias

The method that we used to make the final parameter estimates we report here takes into account the substantially larger uncertainties in the *NICER* response below 0.4 keV (channel 40) and the evidence we found that including data from these channels might bias our results on PSR J0030+045.

As we discuss in Section 5.2, we found that including data from channels below channel 40 biases waveform-based estimates of the distance to PSR J0030+0451 toward values much larger than the independently known distance. The source of this bias is currently unknown. Since its origin is unknown, it could also bias waveform-based estimates of other parameters, including the radius and mass of the star. Given this risk, we judged it important to address this issue.

It might be possible to gain a better understanding of the origin of this distance bias if we also had reliable, independent estimates of the values of other stellar and waveform parameters, but for PSR J0030+0451, we only have a reliable independent estimate of the distance. This provides too little information to identify the source(s) of this bias or to devise sophisticated corrections. We therefore considered only simple ways to address this bias. We also wanted to be careful not to do anything that might bias other, even more important model parameters.

As was mentioned in Section 2.3, the *NICER* response below channel 40 is more uncertain than the response above channel 40. It was therefore natural to explore the effect of ignoring the data in channels below channel 40. As we show in detail in Section 5.2, discarding the data in these low channels eliminates the bias in our waveform-based estimates of the distance to PSR J0030+045. It is our hope that discarding these data also reduces any potential biases in our estimates of the other parameters in the waveform model. Because this data selection procedure is so simple and does not touch the data that we do use, we think it is less likely to bias other waveform parameters than a more complex procedure.

In analyzing the *NICER* data on PSR J0030+0451, we found no detectable modulation in the energy channels above channel 299, and we therefore did not include data from these channels in our analyses of the *NICER* data on PSR J0030+0451.

One would expect that discarding the data in channels 25–39 would reduce the precisions of the parameter estimates. We investigated this possibility by comparing the precisions of the parameter estimates obtained by analyzing the data in channels 40–299 produced by a synthetic waveform that is similar to the PSR J0030+0451 waveform observed by *NICER* with the precisions obtained by analyzing the data in channels 25–299 produced by the same synthetic waveforms and found that discarding the data in channels 25–39 did not significantly reduce the precisions of parameter estimates (see Section 4.2). We also compared the posterior probability distributions for the radius and mass of PSR J0030+0451 obtained using the *NICER* data in channels 40–299 with the probability distributions obtained using the data in channels 25–299 and found no evidence that the precisions of the parameter estimates were reduced by discarding the data in channels 25–39 (see Section 5.2).

A remaining question is whether the fits of our waveform models to the *NICER* waveform data on PSR J0030+0451 are affected by the unavoidable systematic errors present in our model of the *NICER* response in the energy channels 40–299 that we used. As we described in Section 2.3, the *NICER* response in these channels was calibrated by comparing the results of *NICER* observations of the Crab Nebula, which is traditionally assumed to have a power-law spectrum, with the power-law spectrum of the nebula determined by observations made using other instruments. When *NICER* observations of the Crab Nebula spectrum are compared with the spectrum obtained by folding the power law determined by other instruments through the nominal *NICER* response, the residuals in the energy channels we used in this study (channels 40–299) are $\lesssim$5% (Ludlam et al. 2018). As mentioned in Section 2.3, these residuals are likely due to imperfect modeling of the microphysics of the concentrator optics and astrophysical features, such as oxygen edges and emission lines.

We explored the likely effect of deviations of the nominal *NICER* response from the true *NICER* response curve by multiplying the nominal effective area curve of *NICER* by the ratio between the count rate as a function of energy given by the assumed spectrum of the Crab Nebula and the count rate as a function of energy measured by *NICER* (Ludlam et al. 2018). We then used this modified effective area curve to analyze both synthetic waveform data constructed to mimic the *NICER* data on PSR J0030+0451, and the actual *NICER* waveform data on PSR J0030+0451.

We found that modifying the nominal effective area in this way had a negligible effect on the quality of our fits to synthetic waveform data and to the actual waveform data on PSR J0030+0451. For example, the probability of the χ^2 obtained by comparing the energy-resolved waveform given by the best-fit model with two oval spots to the *NICER* data in energy

Table 2
Fits to Synthetic Data Generated Using Two Circular Spots

Parameter	Assumed Value	Median	-1σ	$+1\sigma$	-2σ	$+2\sigma$
R_e (km)	13.0	13.435	12.248	14.722	11.191	15.929
$GM/(c^2R_e)$	0.1636	0.163	0.149	0.174	0.137	0.182
M ($M_\odot$)	1.44	1.472	1.289	1.667	1.151	1.849
θ_{c1} (rad)	0.6283	0.531	0.456	0.608	0.400	0.680
$\Delta\theta_1$ (rad)	0.01	0.011	0.010	0.012	0.009	0.013
$kT_{\rm eff,1}$ (keV)	0.231	0.229	0.223	0.233	0.219	0.237
θ_{c2} (rad)	2.077	2.096	1.959	2.260	1.871	2.401
$\Delta\theta_2$ (rad)	0.33	0.358	0.322	0.397	0.288	0.446
$kT_{\rm eff,2}$ (keV)	0.0578	0.056	0.054	0.059	0.052	0.061
$\Delta\phi_2$ (cycles)	0.5625	0.562	0.556	0.567	0.550	0.571
$\theta_{\rm obs}$ (rad)	0.733	0.774	0.662	0.894	0.583	0.996
$N_{\rm H}$ (10^{20} cm^{-2})	2.0	2.266	2.132	2.398	1.999	2.536
D (kpc)	0.156	0.165	0.146	0.176	0.133	0.179

Note. Results obtained using our MN+PT-emcee sampling algorithm to fit a waveform model with two possibly different and overlapping uniform circular spots to the data in *NICER* energy channels 25–299 from a synthetic waveform generated assuming two different, non-overlapping uniform circular spots.

channels assigned to 32 phase bins changed from 0.105 to 0.112 when we used the modified effective area curve instead of the nominal effective area curve. This indicates that the current systematic errors in the nominal effective area of *NICER* in channels 40–299 have only a minor effect on our fits.

Given these results, we chose to ignore all events in the channels below channel 40 and use the current nominal *NICER* effective area curve for channels 40–299, both when analyzing the actual *NICER* data on PSR J0030+0451 and when analyzing synthetic *NICER* data.

4. Analysis of Synthetic Pulse Waveform Data

In order to verify that our parameter estimation procedures give correct posterior probability distributions for the range of pulse waveform models that we used to analyze the *NICER* waveform data on PSR J0030+0451, we applied these same procedures to synthetic waveform data sets that we created to mimic the *NICER* data on PSR J0030+0451, and checked that our procedures give appropriate parameter estimates and credible regions.

As we explained in the previous section, we chose to discard the data on PSR J0030+0451 in the *NICER* energy channels below channel 40 and above channel 299. In order to verify that discarding the data in the channels below channel 40 would not bias our estimates of the waveform parameters, and to assess the effect of discarding these data on the precisions of our estimates, we first analyzed the data in channels 25–299 given by a particular synthetic waveform and then analyzed only the data in channels 40–299 given by the same synthetic waveform (we did not consider any channels below channel 25, because channel 25 was the lowest channel included in the cleaned *NICER* data set). In each case, we analyzed the synthetic data using the MultiNest sampling algorithm and also using either the PT-emcee sampling algorithm or our hybrid MN+PT-emcee algorithm.

By (1) fitting models having two possibly different and overlapping circular spots to synthetic data generated assuming two different, non-overlapping circular spots and (2) fitting models having two possibly different and overlapping oval spots to synthetic data generated assuming two different, non-overlapping oval spots, we were able to verify that our parameter estimation procedures yield appropriate posterior probability density distributions for these synthetic waveforms. Specifically, for these data sets the MultiNest and MN+PT-emcee sampling algorithms both produced posterior distributions for the waveform parameters that are fully consistent with the values of the parameters that were assumed when the synthetic waveforms were generated. We view the agreement of the results given by these two different sampling algorithms with each other and with the parameters assumed in generating the synthetic data as evidence that both algorithms give correct results when used to analyze synthetic waveforms like these, when the sampling is complete.

By comparing the results we obtained by analyzing the synthetic waveform data in *NICER* energy channels 40–299 with the results that we obtained by analyzing the data in channels 25–299, we were also able to assess the effect on the precisions of our parameter estimates of using only the data in energy channels 40–299. We found that using this reduced data set had a negligible effect on the sizes of the credible regions.

We now provide the details of these tests.

4.1. Analysis of Synthetic Waveforms Generated Using Two Uniform Circular Spots

The first analysis of synthetic data we present here shows the results we obtained by fitting a 12-parameter waveform model with two possibly different and overlapping uniform circular spots to a synthetic waveform generated assuming two different, non-overlapping uniform circular spots, using our MN+PT-emcee sampling algorithm. Table 2 lists the values of

Table 3
Verification of Fits to Synthetic Data Generated by Two Circular Spots

Energy Channels	$\pm1\sigma$ (68.3%)	$\pm2\sigma$ (95.4%)	$\pm3\sigma$ (99.7%)
25–299	10	12	12
40–299	7	11	12

Note. The number of values of the waveform parameters assumed in generating the synthetic waveform that are within the indicated 1D credible intervals derived from our fit of the 12-parameter waveform model with two possibly different and overlapping circular spots to the synthetic waveform generated assuming two different, non-overlapping circular spots, using the data in the indicated energy channels.

the waveform parameters that we assumed when we generated the synthetic waveform data. We note that the temperature we assumed for one of the two spots when we generated this synthetic waveform is substantially less than the temperatures of either of the two main spots we found when we analyzed the *NICER* data on PSR J0030+0451. We show our results for this synthetic waveform because it was the synthetic waveform that was selected—in advance of the analyses of the PSR J0030+0451 waveform—to verify the parameter estimation procedures that would be used by the *NICER* team to analyze pulse waveforms. The results obtained by others on the team when they analyzed this waveform are consistent with the results we obtained when we analyzed it (Bogdanov et al. 2019b).

Table 2 shows the results that we obtained by fitting the waveform model with two possibly different and overlapping uniform circular spots to synthetic waveform data generated assuming two different, non-overlapping uniform circular spots. The table lists the median value of each model parameter computed using its 1D posterior probability distribution and the boundaries of the $\pm1\sigma$ and $\pm2\sigma$ credible intervals for each parameter.

We found that when this waveform model was fit to the synthetic waveform data in *NICER* energy channels 25–299, the values of 10 of the 12 parameters assumed in generating the synthetic waveform are within the relevant $\pm1\sigma$ credible intervals for these parameters while the values of the remaining two parameters (θ_{c1} and $N_{\rm H}$) assumed in generating the synthetic waveform are within their $\pm2\sigma$ credible intervals. We found that when this model was instead fit only to the synthetic data in *NICER* energy channels 40–299, the assumed values of seven of the 12 parameters were within the relevant $\pm1\sigma$ credible intervals, the assumed values of four others were within the relevant $\pm2\sigma$ credible intervals, and the assumed value of the other parameter was within the relevant $\pm3\sigma$ credible interval. Thus, for both energy channel choices, the 1D posterior probability distributions derived for the waveform parameters are consistent with the values of the parameters assumed when the synthetic waveform was generated. These results are summarized in Table 3.

Figure 1 shows that the joint probability density distribution for M and R_e that was obtained by fitting this model to the synthetic waveform data in *NICER* energy channels 25–299 is consistent with the values of the stellar mass and radius assumed when the synthetic waveform was generated.

The panels in the top row of Figure 2 show the 1D probability distributions of M, R_e, and D obtained by fitting this model to the synthetic waveform data in *NICER* energy channels 25–299, whereas the panels in the bottom row show the results obtained by fitting to the data in channels 40–299. This figure illustrates two noteworthy aspects of these distributions.

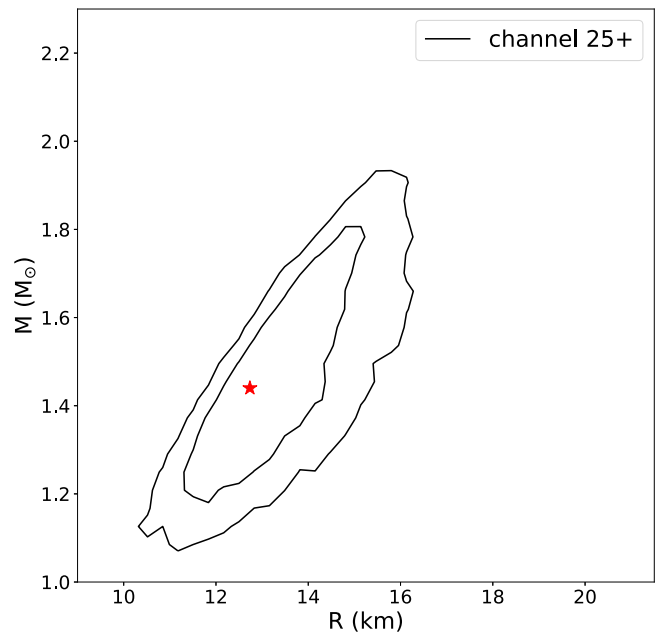

Figure 1. 68% (inner) and 95% (outer) contours of the joint probability density distribution of M and R_e obtained by fitting a model waveform with two possibly different uniform circular hot spots to a synthetic waveform that assumed two different uniform circular hot spots. This analysis used the synthetic waveform data in *NICER* energy channels 25–299. The joint probability density of M and R_e obtained from this fit is consistent with the M and R_e values assumed when the synthetic data were generated, which are indicated by the star.

First, these 1D probability distributions are consistent with each other and with the values of M, R_e, and D that were assumed in generating the synthetic waveform. The widths of the distributions for M and R_e obtained using only the data in channels 40–299 underestimate the true uncertainties in the estimates of these parameters, because the temperature assumed for the lower-temperature spot when generating this synthetic waveform was sufficiently low that discarding the data in energy channels 25–39 narrowed these distributions. Our tests (see, e.g., Figure 4 below) have shown that—in contrast to the reduced widths of the M, R_e, and D distributions obtained from this synthetic waveform when the data in channels 25–39 are discarded—discarding the data in these channels has no significant effect on the distributions of M, R_e, and D obtained by analyzing the *NICER* data on PSR J0030+0451, which has higher-temperature hot spots.

Second, although the 1D probability distributions for D obtained by fitting this model to data selected using both these energy-channel criteria are consistent with the value of D assumed in generating the synthetic waveform data (the cumulative probability near the assumed value of D is substantial for both channel selections and fits with wider priors show that the probability density eventually decreases with increasing distance), these results show that pulse waveform analysis does not determine D very precisely. These analyses demonstrate the importance of using the precise and accurate independent measurement of D that is available for

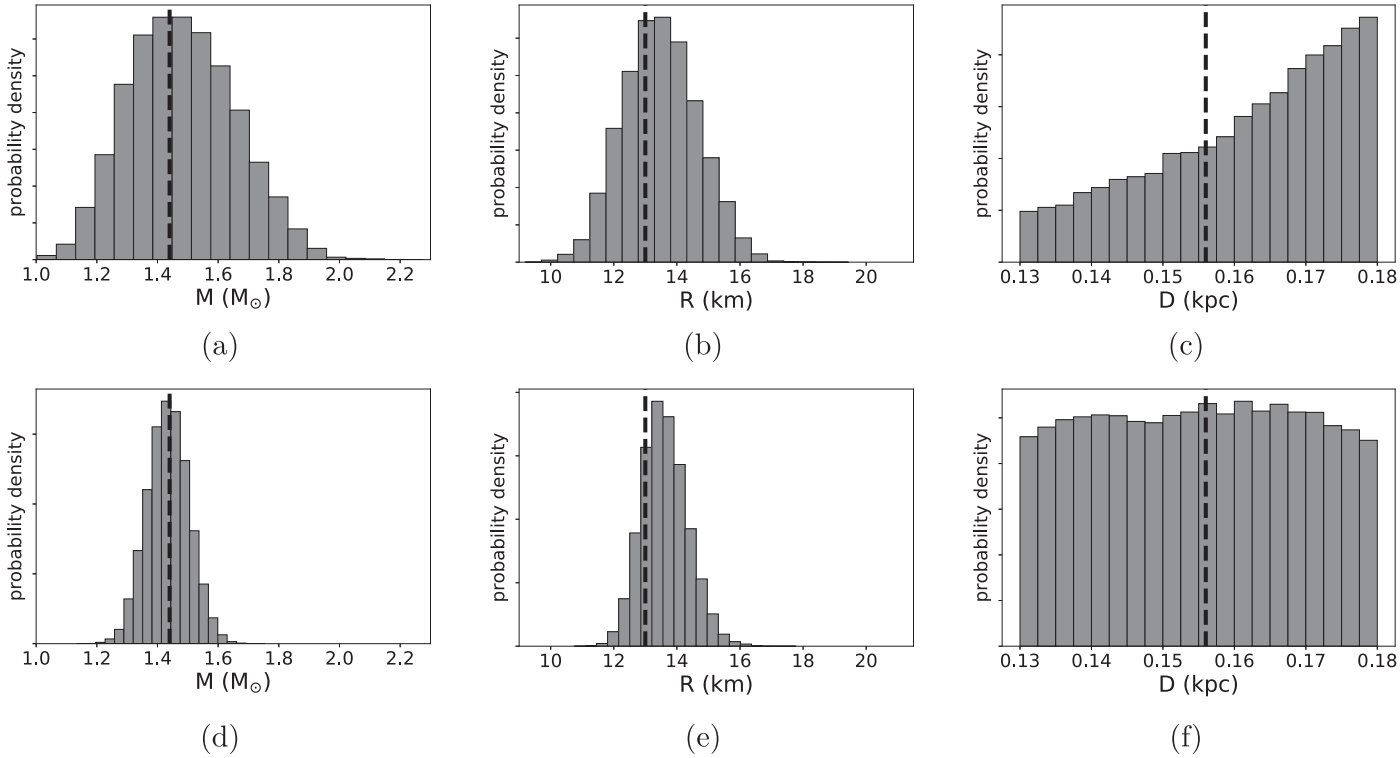

Figure 2. Posterior probability density distributions for M, R_e, and D obtained by fitting the waveform model with two possibly different uniform circular hot spots to synthetic waveform data generated using a model that assumed two different uniform circular hot spots. Top row: results obtained by fitting the data in *NICER* energy channels 25–299. Bottom row: results obtained by fitting the data in *NICER* energy channels 40–299. The vertical dashed line in each panel shows the value of that waveform parameter that was assumed when generating the synthetic waveform data.

Table 4
Fits to Synthetic Data with Two Oval Spots

Parameter	Assumed Value	Median	-1σ	$+1\sigma$	-2σ	$+2\sigma$
R_e (km)	13.49	15.997	14.497	17.471	13.044	18.798
$GM/(c^2R_e)$	0.1503	0.145	0.136	0.153	0.129	0.161
M ($M_\odot$)	1.374	1.565	1.386	1.750	1.225	1.918
θ_{c1} (rad)	2.251	2.247	2.181	2.319	2.113	2.393
$\Delta\theta_1$ (rad)	0.026	0.024	0.021	0.028	0.018	0.033
f_1	9.14	7.356	5.589	9.558	4.603	11.742
$kT_{\rm eff,1}$ (keV)	0.1151	0.114	0.111	0.117	0.109	0.119
θ_{c2} (rad)	2.442	2.459	2.401	2.516	2.336	2.567
$\Delta\theta_2$ (rad)	0.031	0.028	0.025	0.032	0.022	0.038
f_2	16.23	17.465	14.672	19.288	11.941	19.907
$kT_{\rm eff,2}$ (keV)	0.1164	0.115	0.113	0.117	0.111	0.119
$\Delta\phi_2$ (cycles)	0.457	0.455	0.452	0.457	0.450	0.459
$\theta_{\rm obs}$ (rad)	0.939	0.931	0.848	1.003	0.766	1.071
$N_{\rm H}$ (10^{20} cm^{-2})	0.084	0.163	0.051	0.355	0.007	0.654
D (kpc)	0.352	0.350	0.315	0.369	0.284	0.374

Note. Results obtained using our MN+PT-emcee sampling algorithm to fit a waveform model with two possibly different and overlapping uniform oval spots to *NICER* energy channels 40–299 of a synthetic waveform generated assuming two different, non-overlapping uniform oval spots.

Table 5
Verification of Fits to Synthetic Data Generated by Two Oval Spots

Energy Channels	$\pm 1\sigma$ (68.3%)	$\pm 2\sigma$ (95.4%)	$\pm 3\sigma$ (99.7%)
25–299	10	13	14
40–299	12	14	14

Note. The number of values of the waveform parameters assumed in generating the synthetic waveform that are within the indicated 1D credible intervals derived from our fit of the 14-parameter waveform model with two possibly different and overlapping oval spots to the synthetic waveform generated assuming two different, non-overlapping oval spots, using the data in the indicated energy channels.

PSR J0030+0451 (see below) when analyzing the pulse waveform of this pulsar.

4.2. Analysis of Synthetic Waveforms Generated Using Two Uniform Oval Spots

The second analysis of synthetic data we present here shows the results we obtained by fitting a 14-parameter waveform model with two possibly different and overlapping uniform oval spots to a synthetic waveform generated assuming two different, non-overlapping uniform oval spots, using our MN +PT-emcee sampling algorithm. Table 4 lists the values of the waveform parameters that we assumed when we generated the synthetic waveform data.

The results that we obtained by fitting this waveform model to the synthetic waveform data in *NICER* energy channels 25–299 and 40–299 are shown in Table 4, which lists the median value of each model parameter computed using its 1D posterior probability distribution and the boundaries of the $\pm 1\sigma$ and $\pm 2\sigma$ credible intervals for each parameter.

We found that when the model waveform was fit to the synthetic waveform data in *NICER* energy channels 25–299, the values of 10 of the 14 parameters assumed in generating the synthetic waveform are within the $\pm 1\sigma$ credible intervals for these parameters, the values assumed for three others are within the relevant $\pm 2\sigma$ credible intervals, and the value assumed for the remaining parameter is within the relevant $\pm 3\sigma$ credible interval. When this model waveform was fit only to the synthetic data in *NICER* energy channels 40–299, the assumed values of 12 of the 14 parameters fall within their $\pm 1\sigma$ credible intervals and the assumed values of the other two parameters fall within their $\pm 2\sigma$ credible intervals. The waveform parameter values that were assumed when generating the synthetic waveform data are all consistent with the 1D posterior probability densities obtained by analyzing the data using either energy cut. These results are summarized in Table 5.

Figure 3 shows that the joint probability density distribution for M and R_e obtained by fitting this model to the synthetic waveform data in *NICER* energy channels 25–299, and by fitting it to the synthetic data in channels 40–299, are both consistent with the values of the stellar mass and radius assumed when the synthetic data was generated. Figure 3 also demonstrates that discarding the data in *NICER* energy channels 25–39 does not significantly degrade the precision of the M and R_e estimates.

The panels in the top row of Figure 4 show the 1D probability distributions of M, R_e, and D obtained by fitting this model to the synthetic waveform using the data in *NICER* energy channels 25–299, whereas the panels in the bottom row show the results obtained using only the data in energy channels 40–299. We note several aspects of these distributions.

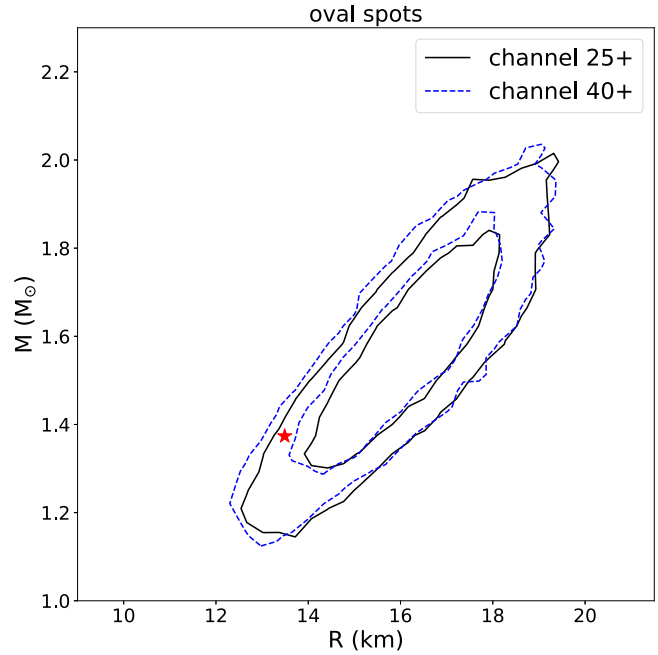

Figure 3. Plot of the 68% (inner) and 95% (outer) contours of the joint probability density distribution of M and R_e obtained by fitting a model waveform with two possibly different and overlapping uniform oval hot spots to a synthetic waveform that assumed two different, non-overlapping uniform oval spots. The solid black lines show the contours obtained when the synthetic waveform data in *NICER* energy channels 25–299 were used, whereas the dashed blue lines show the contours obtained when the synthetic waveform data in energy channels 40–299 were used. Both joint probability distributions are consistent with the M and R_e values assumed when the synthetic data were generated, which are indicated by the star. These results show that using only the data in energy channels 40–299 neither biases the M and R_e estimates nor significantly reduces their precisions.

First, these 1D probability distributions are consistent with each other and with the values of M, R_e, and D that were assumed in generating the synthetic waveform. Second, these distributions are not significantly affected by using only the data in energy channels 40 and above. Finally, although the 1D probability distributions for D obtained by fitting this model to these data are consistent with the value of D assumed in generating the synthetic waveform (the cumulative probability near the assumed value of D is substantial for both energy cuts and fits with wider priors show that the probability density eventually decreases with increasing distance), waveform analysis again does not determine D very precisely. This further emphasizes the value of using the precise and accurate independent measurement of D (see below) when analyzing the *NICER* waveform data on PSR J0030+0451.

5. Analysis of the *NICER* Pulse Waveform Data

In this section we describe our estimation of the radius and mass of PSR J0030+0451 using *NICER* observations of its soft X-ray pulse waveform. We first describe our modeling of this waveform and detail the basis for our decision to use the data in *NICER* energy channels 40–299. We then present our radius and mass estimates, and the evidence for the validity of the model that we used to make these estimates. Finally, we

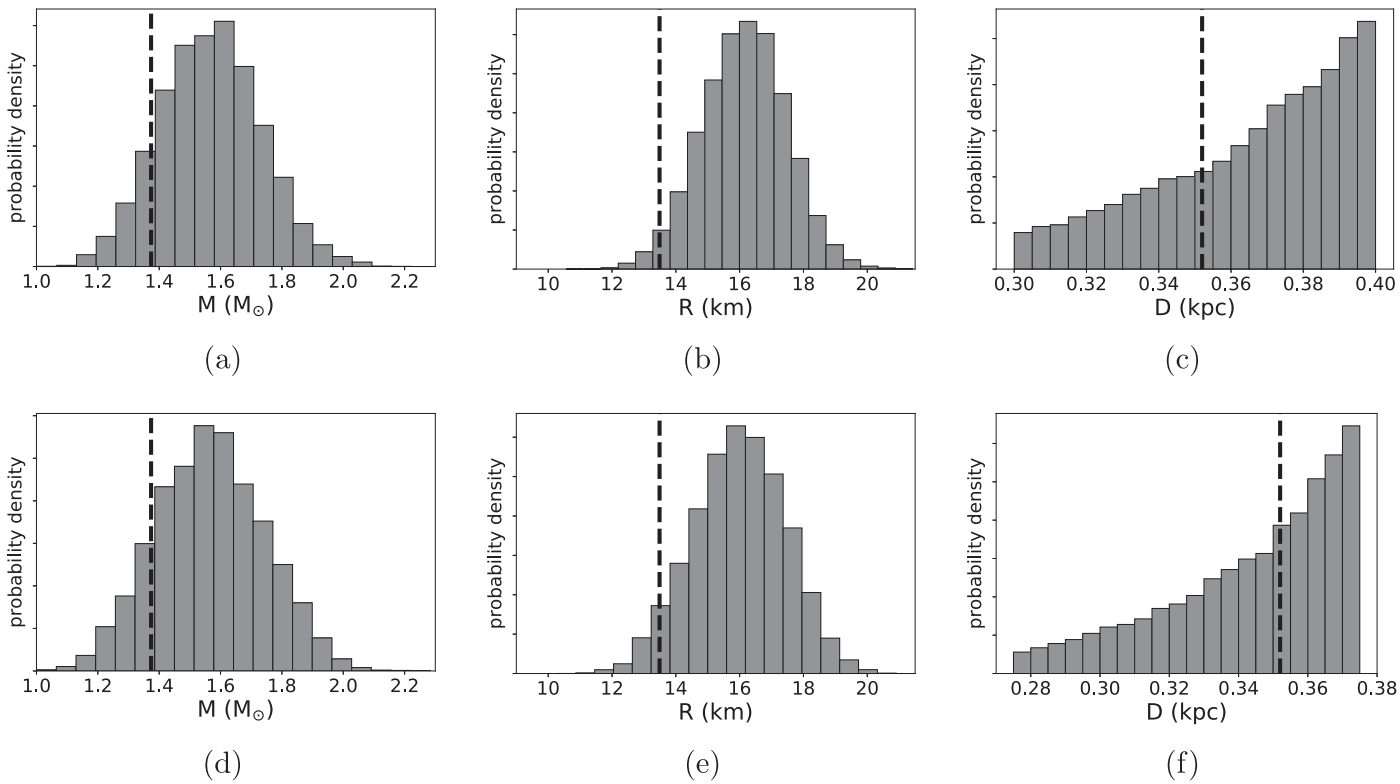

Figure 4. Posterior probability density distributions for the M, R_e, and D estimates obtained by fitting the waveform model with two possibly different and overlapping uniform oval hot spots to synthetic waveform data generated using a model that assumed two different, non-overlapping uniform oval hot spots. Top row: results obtained by fitting the data in *NICER* energy channels 25–299. Bottom row: results obtained by fitting the data in *NICER* energy channels 40–299. The vertical dashed line in each panel shows the value of that waveform parameter that was assumed when generating the synthetic waveform data.

discuss our choices of waveform-phase resolution, the sizes and locations of the hot spots given by our modeling, the best-fit colatitude of the observer, and the combined, waveform- and phase-integrated X-ray spectrum of the hot spots given by our analysis.

As we have previously described in Section 3.5, we explored a variety of algorithms for sampling the parameter space of waveform models but found the best results using the hybrid sampling algorithm that we refer to as MN+PT-emcee. Therefore, in this section we present only results obtained using this algorithm.

5.1. Modeling the Waveform of PSR J0030+0451

Our algorithm for developing a successful model of the heated regions on the surface of PSR J0030+0451 was to proceed systematically from the simplest possible model to more complicated models, guided at each step by the differences between the waveform given by the best-fit simpler models and the waveform observed using *NICER*, and ending when adding additional hot spots or complexity fails to increase significantly the evidence for the model. The sequence of models that we considered in our quantitative modeling is presented in Table 6. We now discuss this sequence.

As mentioned in Section 3.2, visual examination of the PSR J0030+0451 waveform shows evidence for two peaks. As a result, waveform models constructed using a single hot spot fail to reproduce the qualitative features of the observed waveform. We therefore began our quantitative modeling of the observed waveform using models with two uniform circular hot spots, allowing the spots to have different locations, areas, and temperatures. We also allowed the two circular spots to overlap partially or completely. The sampling algorithm therefore explored configurations in which the two circular spots (1) are disjoint, with the same or different temperatures; (2) partially overlap, potentially producing a somewhat oval-shaped uniform-temperature spot if the two component spots have the same temperature, or a spot with a complicated boundary and a complex temperature structure, if the two component spots have different temperatures; or (3) fully overlap, producing (3a) a single, uniform-temperature circular spot, if one of the spots completely covers the other, (3b) a spot with a centered or off-center core-annulus structure in which the core is hotter or colder than the annulus, if the two spots have different temperatures, or (3c) a circular spot partially surrounded by a hotter or colder crescent-shaped region. None of these models produced waveforms that adequately describe the observed waveform. Among other problems, the (relatively large) spot sizes required to reproduce the weak higher harmonic content of the observed waveform appeared to conflict with the (relatively small) spot areas required to reproduce the observed X-ray flux. We therefore considered more complicated heated regions.

In the second step of our exploration of waveform models, we considered models with three and four uniform circular hot spots. In all cases we allowed the spots to overlap in any way that improved the fit. This algorithm allowed the heated regions in the model to evolve toward a variety of different complex shapes as the fitting process proceeded (see Section 3.2). These explorations found no significant evidence for configurations with more than three circular hot spots on the stellar surface, for configurations in which three hot spots were near one another,

Table 6
Summary of Pulse Waveform Models Considered and the Results

Waveform Model	Results
Two circular spots	Strongly disfavored The required areas of the spots appear to conflict with the harmonic structure of the waveform
Three or four circular spots	Disfavored No evidence for overlapping spots No evidence for configurations with more than three spots No evidence for more than one temperature in any of the heated regions The required areas of the spots appear to conflict with the harmonic structure of the waveform
Two oval spots	Strongly favored over models with two circular spots Two different non-overlapping oval spots adequately describe the observed waveform data The best-fit temperatures of the two spots are almost the same One spot is slightly elongated in the east–west direction The other spot is highly elongated in the east–west direction No evidence that a more complicated configuration is needed to describe the observed waveform
Three oval spots	Strongly favored over models with two circular spots Three different non-overlapping oval spots adequately describe the observed waveform data Radius and mass estimates are statistically indistinguishable from the estimates using the model with two oval hot spots Two of the spots are almost identical to the two spots in the best-fit model with two oval spots The third spot makes almost no contribution to the waveform Slightly but not significantly higher evidence than the model with two oval spots No evidence that a more complicated configuration is needed to describe the observed waveform

Note. See the text for details about the assumed prior probability distributions for each parameter.

or for overlapping or adjacent hot spots with significantly different temperatures, such as one would expect if there were spots on the stellar surface that had regions with different temperatures or a significant temperature gradient. We again found that the larger spot sizes required to reproduce the weak higher harmonic content of the waveform appeared to conflict with the smaller sizes required to reproduce the observed X-ray flux. This conflict led us to consider uniform-temperature oval hot spots as the next step in our sequence of trial models.

The first oval hot-spot model that we considered examined heated regions that could be modeled using two uniform-temperature oval spots. We again allowed the two spots to have different properties and to overlap one another, partially or completely. The sampling algorithm could have collapsed this model to a model with two uniform-temperature circular spots, if that was preferred by the data, but it was not. The sampling algorithm therefore explored configurations in which the two oval spots (1) are disjoint, with the same or different temperatures; (2) partially overlap, potentially producing a uniform-temperature spot with a complicated boundary, if both spots have the same temperature, or a spot with a complicated boundary and a complex temperature structure, if the two spots have different temperatures; or (3) fully overlap, producing (3a) a single, uniform-temperature oval spot, if one of the spots completely covers the other, (3b) a possibly oval spot with a potentially oval centered or off-center core-annulus structure in which the core is hotter or colder than the annulus, if the two spots have different temperatures, or (3c) a possibly oval spot partially surrounded by a hotter or colder crescent-shaped region.

Our analysis showed that a configuration with two non-overlapping, uniform oval spots with almost the same temperatures is preferred over any models with two overlapping spots, adequately describes the observed waveform, and is strongly favored over the best-fit model with two circular spots. Indeed, the log evidence for the best-fit model with two oval spots was 11.6 larger than the log evidence for the best-fit model with two circular spots. The fit with two uniform oval spots favors a configuration in which both spots are elongated in the east–west direction and both have almost the same temperature. The larger east–west extent of the best-fitting oval spots allows them to successfully reproduce the observed weak higher harmonic content of the waveform while the smaller north–south extent allows them to have the relatively small areas required to reproduce the observed X-ray flux.

To assess whether a model with two uniform-temperature oval spots is sufficient, we also considered configurations with three, possibly different, uniform-temperature oval spots. We found that a configuration with three different non-overlapping oval spots also describes the observed waveform adequately. This model is again strongly favored over the best-fit model with two uniform circular spots: the log evidence for the best-fit model with three oval spots was 13.3 greater than the log

evidence for the best-fit model with two circular spots. We again found no evidence for more than one temperature in any of the heated regions. Two of the three spots in the best-fitting three-spot model are almost identical to the two spots in the best-fitting two-spot model. Like the two spots in the best-fitting two-spot model, the two larger spots in the best-fitting three-spot model are elongated in the east–west direction and have almost the same temperatures. The third spot in the best-fitting three-spot model has a much higher temperature but a much smaller area than either of the other two spots, is located close to the rotational pole on the far side of the star from the observer, and makes only a very small contribution to the waveform. The waveform produced by the best-fitting model with three oval spots is very similar to the waveform produced by the model with two oval spots.

The best-fitting models with two and three oval spots both provide acceptable fits to the phase-channel and bolometric waveform data in the χ^2 sense, and are not statistically distinguishable from each other. Most importantly, the best-fit values of the stellar radius and mass given by the model with three oval spots are almost identical to, and are statistically indistinguishable from, the best-fit values of the stellar radius and mass given by the model with two oval spots. The evidence for the best-fit model with three oval spots is slightly, but not significantly, greater than the evidence for the model with two oval spots.

Based on these results, we conclude that the models with two and three oval spots both provide adequate descriptions of the observed waveform, that there is no evidence that a more complicated model is required to describe the observed waveform, and that the mass and radius estimates inferred using these two models are reliable. We slightly prefer, and therefore report here, the radius and mass estimates given by the model with three oval spots, only because the evidence for this model is slightly—although not significantly—greater than the evidence for the model with two oval spots.

These considerations and results are summarized in Table 6. We now provide the details.

5.2. Choice of Energy Channels

The lowest-energy *NICER* data that was included in the standard pipeline data set that we analyzed was in energy channel 25 (see Section 2.2). As noted previously (see Section 3.6), we found no detectable modulation of the X-ray flux in *NICER* energy channels 300 and above. We therefore considered in our analyses only the data in channels 25–299.

The calibration errors in the data from energy channels 40–299 are relatively small. For example, the residuals between the Crab Nebula spectrum determined from *NICER* measurements and the Crab Nebula spectrum determined from measurements made using other instruments are $\lesssim$5% for channels 40–299 (see Sections 2.3 and 3.6; see also Ludlam et al. 2018). In contrast, there are still substantial and poorly understood errors in the calibration of energy channels 25–39. We were therefore concerned that including data from channels 25–39 in our analysis would bias our estimates of the mass and radius of PSR J0030+0451.

The distance to PSR J0030+0451 has been accurately measured to be 0.325 ± 0.009 kpc, independent of any waveform analyses (see Arzoumanian et al. 2018a). We therefore decided to investigate the effect of including or not including the data in channels 25–39 on estimates of the distance made using the PSR J0030+0451 waveform. We found that if we used the *NICER* waveform data in channels 25–299, thereby including the data in channels 25–39, and assumed a wide, flat prior for the distance, all our analyses gave posterior probability distributions for the distance that peaked at distances substantially larger than the independently measured distance of 0.325 kpc and excluded 0.325 kpc with high confidence. This is illustrated by panel (c) in Figure 5, which shows the 1D posterior distributions for M, R_e, and D obtained by fitting the waveform model with two possibly different and overlapping uniform oval hot spots to the *NICER* data in channels 25–299. In contrast, when we used only the well-calibrated data in channels 40–299, we found posterior probability distributions for the distance that naturally peak close to the independently measured distance. This is illustrated by panel (f) in Figure 5, which shows the 1D posterior distributions for M, R_e, and D obtained by fitting the waveform model with two possibly different and overlapping uniform oval hot spots to the *NICER* data in channels 40–299.

These results suggested to us that including the poorly calibrated data in channels 25–39 in the analysis was likely to be biasing the distance estimate and could also be biasing the estimates of M and R_e, about which we have no independent information. We therefore thought it was important to address the effects of the apparent calibration errors in channels 25–39, but we wanted to do this in a way that would not itself bias our results. Consequently, we decided that, rather than attempting to correct for the calibration errors in channels 25–39, which are poorly understood at present, the safest approach would be to discard the data in all these channels. This would prevent the calibration errors in these channels from biasing our M and R_e estimates, but it could in principle increase the uncertainties in our estimates of these parameters because the amount of data we used would be reduced.

Comparison of the results obtained by analyzing synthetic waveform data in *NICER* energy channels 25–299 and 40–299 that were generated assuming two different, non-overlapping uniform circular spots (see Section 4.1) shows that using only the data in the reduced energy range does not significantly bias the estimates of M and R_e or decrease the precisions of the estimates (compare panels (a) and (d) and panels (b) and (e) of Figure 2)). (We note that for this synthetic waveform, the temperature assumed for one of the hot spots was substantially lower than any of the temperatures inferred for the hot spots of PSR J0030+0451. Consequently, the cut at channel 40 discarded much more of the spectrum of this waveform than it does for the spectrum of PSR J0030+0451 observed by *NICER*.)

Similarly, comparison of the results obtained by analyzing synthetic waveform data in *NICER* energy channels 25–299 and 40–299 that were generated assuming two different, non-overlapping uniform oval spots (see Section 4.2) shows that using only the data in the reduced energy range does not significantly bias the estimates of M and R_e or decrease the precisions of the estimates (compare panels (a) and (d) and panels (b) and (e) of Figure 4).

Finally, comparison of the results obtained by analyzing the *NICER* data on the waveform of PSR J0030+0451 in energy channels 25–299 and 40–299 shows that using only the data in the reduced energy range does not significantly decrease the precisions of the estimates of M and R_e (compare panels (a) and (d) and panels (b) and (e) of Figure 5).

Taking into account all these results, we decided to use only the data in energy channels 40–299 to estimate the values of the

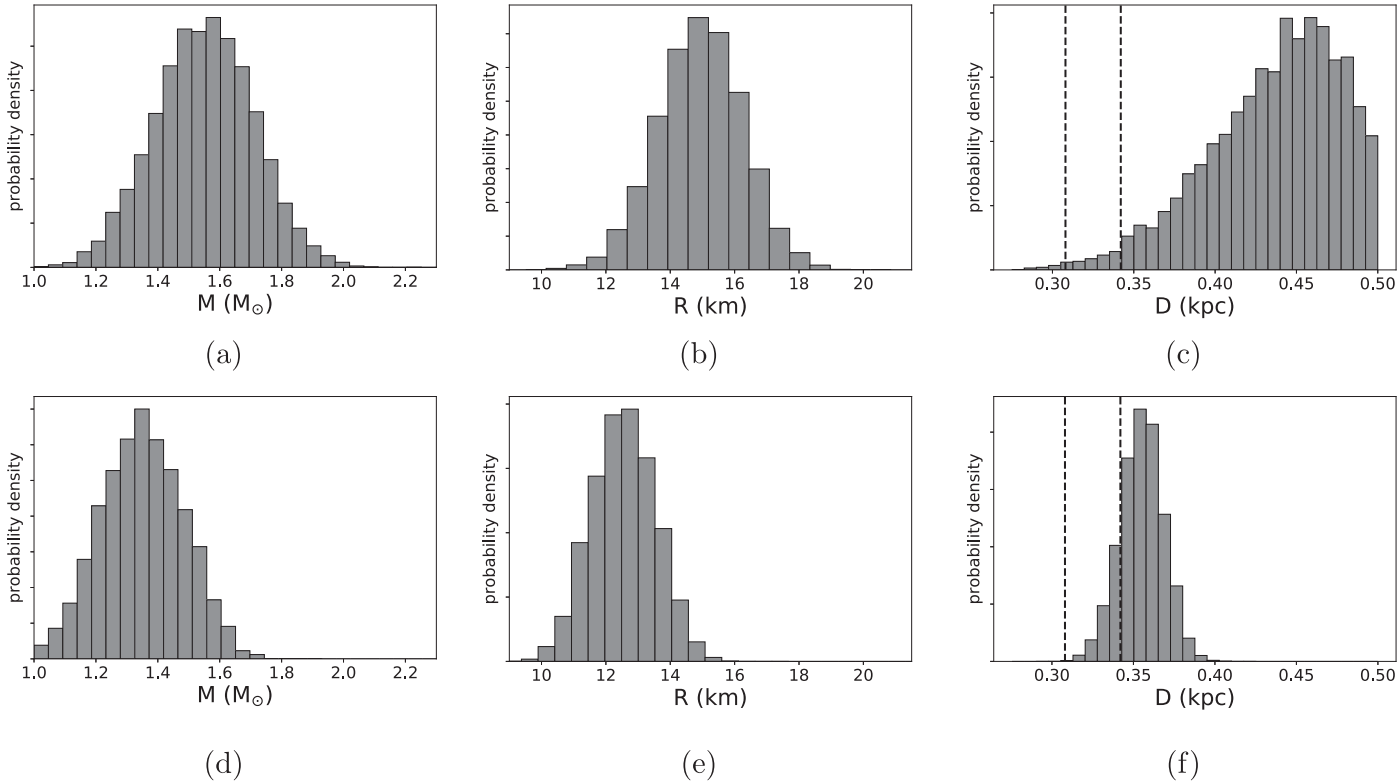

Figure 5. 1D posterior probability distributions for M, R_e, and D estimates obtained by fitting the waveform model with two possibly different uniform oval hot spots to two different sets of *NICER* data on PSR J0030+0451. Both fits assumed a distance prior flat between 0.275 and 0.5 kpc and zero outside this interval. The independently measured distance to PSR J0030+0451 is 0.325 ± 0.009 kpc (see the text). The vertical dashed lines in panels (c) and (f) indicate the uncertainty in D obtained by combining the uncertainty in the measurement of D and the uncertainty in D that corresponds to the uncertainty in the effective area of *NICER* (see the text for details). Top row: posteriors obtained using the data in *NICER* energy channels 25–299. Note that the distance posterior, which is plotted in panel (c), peaks at ∼0.45 kpc and excludes the independently measured distance with high confidence. Bottom row: posteriors obtained using the data in *NICER* energy channels 40–299. In contrast to the distance posterior obtained using the data in *NICER* energy channels 25–299, the distance posterior obtained using this data set, which is plotted in panel (f), peaks at a distance that is close to the independently measured distance.

parameters in our models of the PSR J0030+0451 pulse waveform. Consequently, in the remainder of this Letter we present only results obtained using the data in these energy channels. Given that the independently measured distance of 0.325 ± 0.009 kpc is very precise, we imposed a Gaussian prior on the distance that uses this measurement and an uncertainty that takes into account the uncertainty in this measurement and the global (in energy) uncertainty in the effective area of the *NICER* instrument (see below).

5.3. The Mass and Radius of PSR J0030+0451

In this section, we present and discuss the results of our analysis of the *NICER* data on PSR J0030+0451, focusing on our estimates of its mass and radius. For the reasons described in Section 5.2, we present only the results we obtained by fitting the *NICER* data in energy channels 40–299. When estimating the values of all the parameters except the distance, we assumed prior probability distributions constant within the intervals listed in Table 1 and zero outside these intervals. When estimating the distance, we assumed a Gaussian prior. We chose the width of the Gaussian by combining linearly, rather than quadratically, the 0.009 kpc uncertainty in the measured distance to PSR J0030+0451 (see Arzoumanian et al. 2018a) and the estimated uncertainty in the overall normalization of the *NICER* effective area, converted to an uncertainty in the distance. We assumed a 5% uncertainty in the overall normalization of the *NICER* effective area (see Section 3.6). This translates into a distance uncertainty of 2.5%. The distance to PSR J0030+0451 has been independently measured to be 0.325 kpc (Arzoumanian et al. 2018a). Consequently, a 1σ uncertainty of 2.5% in the distance is ≈0.008 kpc, yielding a total 1σ width for the Gaussian of 0.009 kpc + 0.008 kpc =0.017 kpc.

We considered two waveform models, one with two possibly different and overlapping uniform-temperature oval spots, and one with three possibly different and overlapping uniform-temperature oval spots. The model with two oval spots has 14 primary parameters. These are listed in Table 7, along with their median values and the $\pm1\sigma$ and $\pm2\sigma$ boundaries of their 1D credible regions, computed using the 1D posterior probability density distribution we found for each parameter. The model with three oval spots has 19 primary parameters. These are listed in Table 8, along with their median values and the $\pm1\sigma$ and $\pm2\sigma$ boundaries of their 1D credible regions, computed using the 1D posterior probability density distribution we found for each parameter.[20] Both fits favored models in which the spots do not overlap.

Table 9 compares the median values of R_e and M and the boundaries of the $\pm1\sigma$ credible regions computed from the posterior probability density distributions obtained by fitting the two models described here.

[20] Samples from the full posterior probability distribution obtained by fitting the model with three uniform-temperature oval spots to the waveform data are available at https://zenodo.org/record/3473466.

Table 7
Fits to *NICER* Data with Two Oval Spots

Parameter	Median	-1σ	$+1\sigma$	-2σ	$+2\sigma$	Best Fit
R_e (km)	13.271	12.115	14.578	11.042	15.968	13.643
$GM/(c^2R_e)$	0.160	0.152	0.169	0.143	0.176	0.161
M ($M_\odot$)	1.442	1.282	1.619	1.141	1.802	1.488
θ_{c1} (rad)	2.251	2.165	2.334	2.084	2.419	2.232
$\Delta\theta_1$ (rad)	0.035	0.030	0.041	0.026	0.047	0.031
f_1	5.347	3.950	6.981	3.136	8.362	6.024
$kT_{\rm eff,1}$ (keV)	0.117	0.114	0.120	0.111	0.122	0.119
θ_{c2} (rad)	2.417	2.333	2.495	2.245	2.560	2.394
$\Delta\theta_2$ (rad)	0.033	0.028	0.039	0.025	0.044	0.029
f_2	15.490	12.317	18.396	10.020	19.748	17.744
$kT_{\rm eff,2}$ (keV)	0.117	0.115	0.119	0.112	0.122	0.119
$\Delta\phi_2$ (cycles)	0.459	0.457	0.461	0.455	0.463	0.458
$\theta_{\rm obs}$ (rad)	0.848	0.751	0.951	0.660	1.043	0.827
$N_{\rm H}$ (10^{20} cm^{-2})	0.266	0.072	0.593	0.011	1.08	0.047
D (kpc)	0.327	0.309	0.345	0.293	0.361	0.332

Note. 1D credible regions, and best fit, obtained by fitting the model with two possibly different uniform oval spots to channels 40–299 of the *NICER* data on PSR J0030+0451.

Figure 6 compares the 1D posterior probability density distributions for M, R_e, and D. Note that the waveform data modifies the posterior probability distributions for the distance only slightly compared to the Gaussian prior that we assumed based on the independently measured distance to PSR J0030+0451 and the uncertainty in the *NICER* effective area (see Section 5.2), showing that the distance estimates obtained by fitting both models to the waveform data are consistent with the measured distance.

Figure 7 compares the joint posterior probability density distributions for R_e and M that were obtained by fitting the two models to the *NICER* waveform data.

Figure 8 compares the bolometric waveforms given by the best-fit waveform models with two and three oval spots. The waveform components are very similar for the two models, and the full waveforms are almost identical.

All these comparisons show that the models with two and three uniform-temperature oval spots give mutually consistent credible regions for all the parameters that they have in common, most notably for the mass and radius of the pulsar. The log evidence for the best fit of the model with three oval spots is higher than the log evidence for the best fit of the model with two oval spots, but only by 1.7, which is less than the estimated uncertainty in the log evidence. Thus, both models are comparably good. This consistency suggests that, at least for the types of waveform models considered here, no further complexity is needed to adequately describe the observed waveform. The 68% credible intervals for M and R_e given by the fit of the model with three oval spots to the *NICER* data from PSR J0030+0451 are 1.30–1.59 $M_\odot$ and 11.96–14.26 km.

Our results for mass and radius of PSR J0030+0451 may be compared with the recent results of Steiner et al. (2018), who examined the evidence from neutron stars that are transient X-ray sources and conclude that the radius of a 1.4 $M_\odot$ neutron star is most likely between 10 and 14 km, which is consistent with our estimates of the mass and radius of PSR J0030+0451.

Our results may also be compared with those of Nättilä et al. (2017), who estimated that the mass of the (neutron star) X-ray burst source 4U 1702−429 is between 1.6 and 2.2 $M_\odot$ and that its circumferential radius is between 12.0 and 12.8 km (with 68% credibility). Although this estimate of the mass of 4U 1702−429 is higher than our estimate of the mass of PSR J0030+0451, for most neutron star EoS currently under consideration, the radius of a neutron star depends only weakly on its mass in this mass range, in which case this estimate of the radius of 4U 1702−429 is consistent with our estimate of the radius of PSR J0030+0451.

The full posterior probability density distributions for the parameters in the fit of the model with two oval spots to the *NICER* waveform data are shown in Figure 15 in Appendix A. The full posterior probability density distributions for the parameters in the fit of the model with three oval spots are shown in Figure 16 in Appendix B. Among other things, these "corner" plots show that there is a correlation between estimates of the stellar radius and the distance, but that this correlation is fairly weak. Thus, any errors in the data that bias the estimate of the distance may not significantly bias the estimate of the radius. There are indications that our sampling of the posterior distribution of the stretching parameter for the second oval spot did not explore a wide enough range, but this probably did not significantly affect our results, because there is no correlation between the value of this parameter and the values of the mass, radius, or distance parameters.

5.4. Adequacy of the Models

We performed χ^2 analyses (see Equation (2)) to determine whether the models we have used to estimate the radius and mass

Table 8
Fits to *NICER* Data with Three Oval Spots

Parameter	Median	-1σ	$+1\sigma$	-2σ	$+2\sigma$	Best Fit
R_e(km)	13.019	11.959	14.255	10.938	15.500	13.466
$GM/(c^2R_e)$	0.163	0.154	0.171	0.144	0.179	0.156
M ($M_\odot$)	1.443	1.299	1.594	1.164	1.745	1.423
θ_{c1} (rad)	2.270	2.179	2.357	2.093	2.442	2.330
$\Delta\theta_1$ (rad)	0.036	0.031	0.040	0.028	0.045	0.032
f_1	5.352	4.364	6.502	3.568	7.664	5.335
$kT_{\rm eff,1}$ (keV)	0.117	0.114	0.120	0.110	0.122	0.113
θ_{c2} (rad)	2.417	2.341	2.486	2.252	2.540	2.446
$\Delta\theta_2$ (rad)	0.033	0.029	0.038	0.025	0.043	0.029
f_2	15.769	13.017	18.498	10.923	19.79	16.588
$kT_{\rm eff,2}$ (keV)	0.115	0.112	0.118	0.107	0.121	0.105
$\Delta\phi_2$ (cycles)	0.460	0.458	0.463	0.456	0.466	0.463
θ_{c3}(rad)	2.988	2.865	3.063	2.691	3.094	3.056
$\Delta\theta_3$ (rad)	0.056	0.021	0.103	0.004	0.168	0.087
f_3	1.215	0.493	2.096	0.161	3.511	1.253
$kT_{\rm eff,3}$ (keV)	0.239	0.143	0.354	0.029	0.470	0.209
$\Delta\phi_3$ (cycles)	0.420	0.378	0.534	0.071	0.932	0.427
$\theta_{\rm obs}$ (rad)	0.878	0.769	0.973	0.675	1.051	1.012
$N_{\rm H}$ (10^{20} cm^{-2})	0.244	0.082	0.441	0.011	0.723	0.187
D (kpc)	0.327	0.307	0.347	0.290	0.365	0.317

Note. 1D credible regions, and best fit, obtained by fitting the model with three possibly different uniform oval spots to channels 40–299 of the *NICER* data on PSR J0030+0451.

of PSR J0030+0451 adequately describe the *NICER* data. Specifically, we compared our best-fit energy-resolved model waveforms with the energy-resolved waveform data (i.e., the pulse-phase–energy-channel data) collected by *NICER*, and compared the energy-integrated (bolometric) waveforms given by our best-fit energy-resolved waveform models with the bolometric waveforms observed by *NICER*, using the values of χ^2 given by these comparisons. (In principle, we could also compare the pulse-phase-integrated spectra given by our models with the pulse-phase-integrated spectrum observed by *NICER* by computing the relevant values of χ^2, but our procedure for modeling the observed unmodulated counts—see Section 3.4—guarantees a nearly perfect description of the photon energy spectrum, so this comparison would be uninformative.)

Assigning the *NICER* data to 32 phase bins and 260 energy channels, the best-fit energy-resolved waveform model with two oval spots gives a χ^2 of 8204.68 when compared with this data set, which consists of the number of counts in each of $32 \times 260 = 8320$ phase-energy bins. As discussed in Section 3.3, the model waveform with two oval spots has 14 primary parameters, 260 ancillary parameters related to the non-star emission, and one additional parameter that describes its overall phase, yielding a total of 8320-260-14-1 = 8045 degrees of freedom. The resulting χ^2/degrees of freedom (dof) is therefore 8204.68/8045. If this model is correct, the probability of finding a value of χ^2/dof this large or larger is 0.104. Thus, according to the χ^2 test this model provides an acceptable description of this data set.

Again assigning the *NICER* data to 32 phase bins and 260 energy channels, the best-fit energy-resolved waveform model with three oval spots gives a χ^2 of 8188.99 when compared with the *NICER* data binned in this way. This model has 19 primary parameters, yielding a total of 8040 degrees of freedom. The resulting χ^2/dof is therefore 8188.99/8040. If this model is correct, the probability of finding a χ^2/dof this large or larger by chance is 0.120, so the fit of this model to this data set is also acceptable, according to the χ^2 test. In Figure 9, we show the value of χ in each of the 8320 phase-energy bins, for this fit. No patterns in the values of χ are evident as a function of phase or energy, which is what one would expect for a good fit.

When the bolometric waveforms predicted by the models with two oval spots and three oval spots that best fit the *NICER* phase-channel data with 32 phases are compared with the 32-phase bolometric waveform constructed using the *NICER* data, the values of χ^2/dof are considerably larger. When the bolometric waveform given by the model with two oval spots is compared with the 32-phase bolometric waveform constructed using the *NICER* data, the value of χ^2 is 40.6. There are 32-14-1-1 = 16 dof in this 32-phase bolometric data. The χ^2/dof is therefore 40.6/16, which has a probability 6.3×10^{-4} of occurring by chance. This probability is low enough that it indicates that this

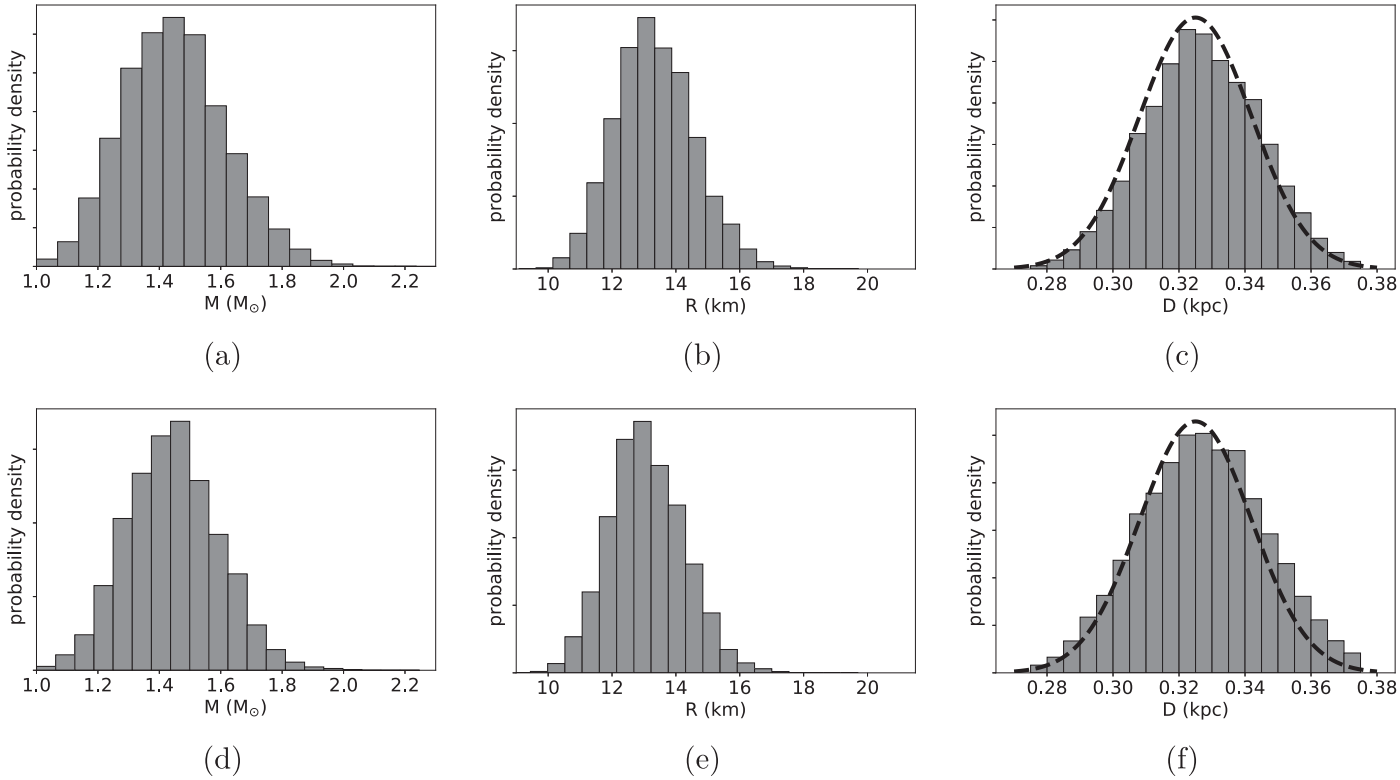

Figure 6. Comparison of the 1D posterior probability density distributions of the stellar mass (panels (a) and (d)), stellar radius (panels (b) and (e)), and the distance to the pulsar (panels (c) and (f)) given by the best fits of the waveform model with two (top row of panels) and three (bottom row of panels) oval spots. Both models were fit to the *NICER* data in energy channels 40–299, assigned to 32 phase bins. The dashed lines in panels (c) and (f) show the Gaussian prior that was used for the distance estimate (see the text). The agreement of the distributions given by the two models is excellent.

Table 9
Comparison between Two-oval and Three-oval Fits to *NICER* Data

Fit	-1σ, R	Median R_e	$+1\sigma$, R	-1σ, M	Median M	$+1\sigma$, M
Two ovals	12.118	13.274	14.582	1.282	1.442	1.619
Three ovals	11.962	13.022	14.259	1.299	1.443	1.594

Note. Comparison of the radius (in km) and mass (in solar masses) estimates given by the fits of the models with two and three oval spots to the *NICER* data on PSR J0030+0451.

model provides a description of this data set that is at least incomplete. When the bolometric waveform given by the model with three oval spots is compared with the 32-phase bolometric waveform constructed using the *NICER* data, the value of χ^2 is 41.7. There are 32-19-1-1 = 11 dof in this 32-phase bolometric data. The χ^2/dof is therefore 41.7/11, which has a probability 2×10^{-5} of occurring by chance. This probability again indicates that this model provides a description of this data set that is at least incomplete.

Noting these low probabilities, we performed exploratory fits specifically designed to minimize the value of χ^2 obtained when the 32-phase bolometric waveforms predicted by these two energy-resolved waveform models are compared with the 32-phase bolometric waveform constructed from the *NICER* data. The probabilities of the models given by these fits were not significantly larger than the values given by the best fits of these models to the full phase-channel data.

Next, we constructed 64-phase bolometric waveforms using the *NICER* data and compared these with the 64-phase bolometric waveforms predicted by the best fit of the 32-phase energy-resolved waveform model with two oval spots to the 32-phase energy-resolved *NICER* waveform data, re-fitting the phase shift and the number of phase-independent background counts in each energy channel. The resulting minimum value of χ^2/dof is 58.64/48, which has a chance probability of 0.140, indicating that this model provides an acceptable description of the 64-phase bolometric waveform data. When the predictions of this model for the 64-phase energy-resolved waveform are compared with 64-phase energy-resolved *NICER* data, the resulting χ^2/dof is 16363.9/16365, which has a probability of 0.501, much higher than the probability we found when we divided the data into only 32 phase bins, and indicating that this energy-resolved waveform model also provides an acceptable description of the energy-resolved *NICER* waveform data with 64 phase bins.

Finally, we compared the 64-phase bolometric waveforms constructed using the *NICER* data with the 64-phase bolometric waveforms predicted by the energy-resolved waveform model with three oval spots that best fits the 32-phase energy-resolved *NICER* waveform data (again re-fitting the phase shift and the number of phase-independent counts in each energy channel).

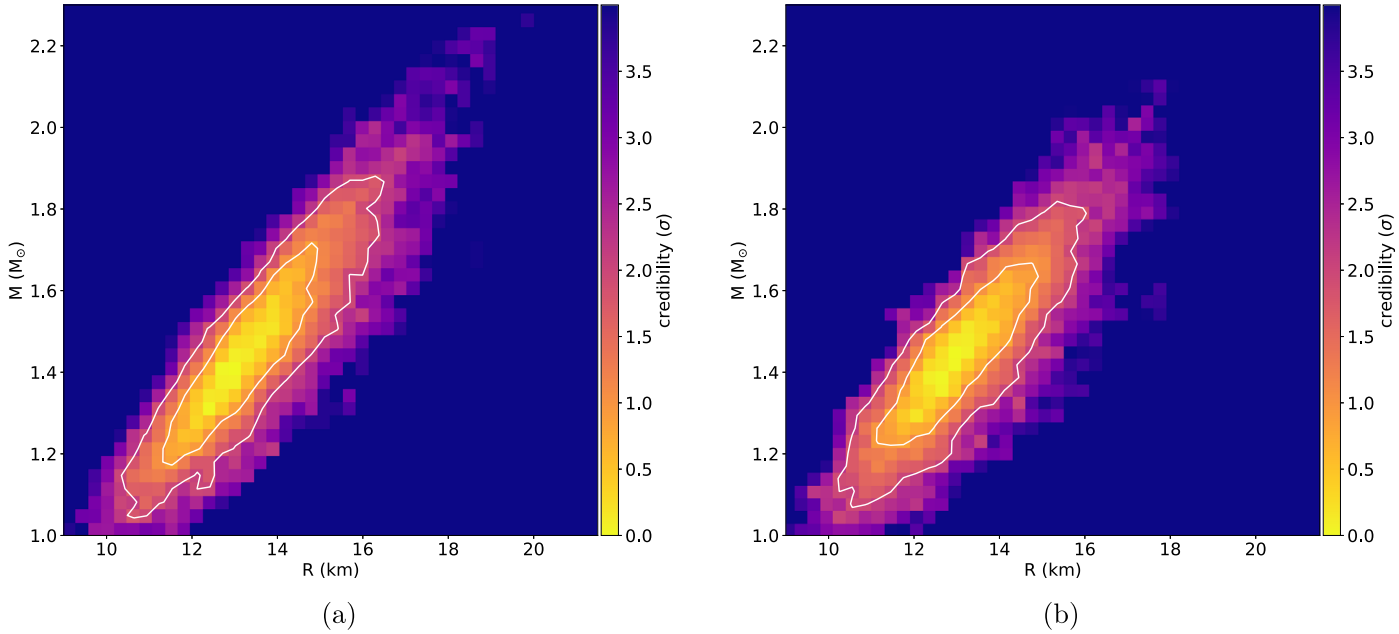

Figure 7. Comparison of the joint posterior probability density distributions for M and R_e given by the best fits of the waveform model with two (panel (a)) and three (panel (b)) uniform-temperature oval spots. The inner contour shown in each panel contains 68.3% of the posterior probability, whereas the outer contour contains 95.4%. The color indicates the credibility in standard deviations of each point in the posterior probability density distribution. Again, the agreement of the distributions given by the two models is excellent.

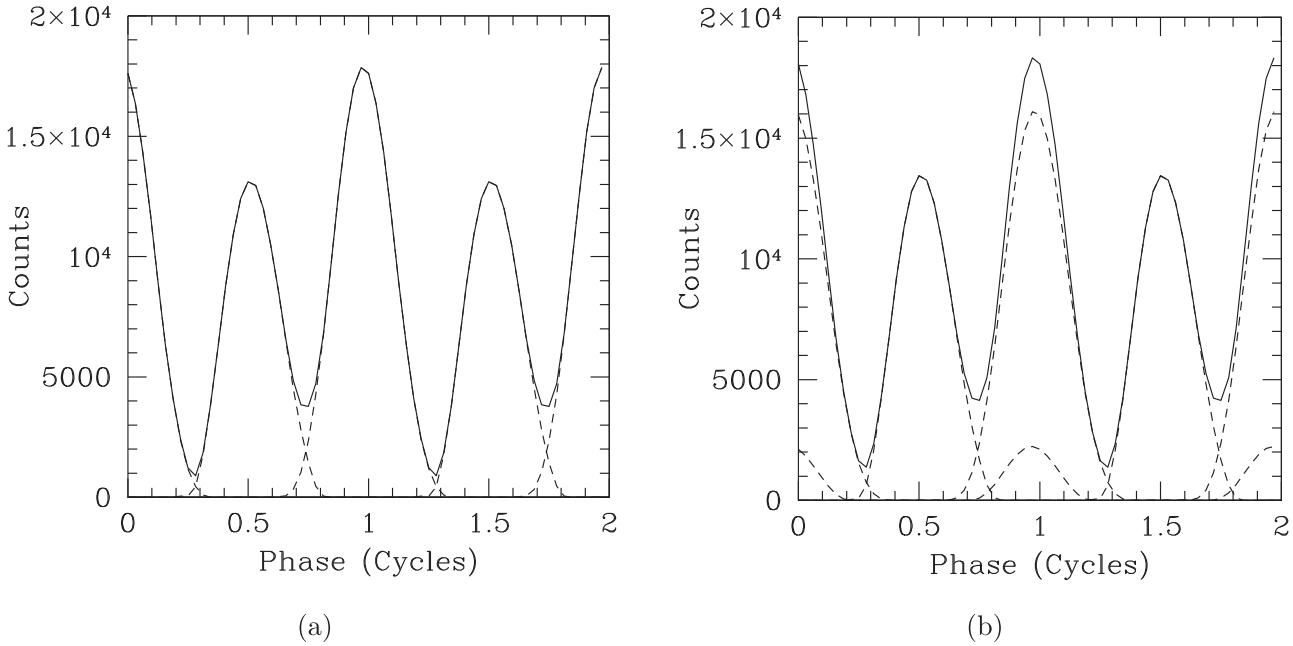

Figure 8. Comparison of the bolometric waveforms given by the best-fit waveform models with two (panel (a)) and three (panel (b)) oval spots. The solid curves show the full waveforms; the dashed curves show the contributions to the full waveform made by the individual hot spots. The components that generate the full waveforms are very similar for the two models.

The results are shown in Figure 10. The minimum value of the bolometric χ^2/dof is 59.6/43, which has a probability of 0.0473, indicating that this 64-phase model also provides an acceptable description of the 64-phase bolometric waveform data. When the predictions of this best-fit model for the energy-resolved waveform with 64 phase bins are compared with the 64-bin energy-resolved *NICER* waveform data, the resulting χ^2/dof is 16347.5/16360, which has a probability of 0.526, again much higher than the probability that we found when we divided the data into only 32 phase bins, and indicating that this energy-resolved waveform model provides an acceptable description of the energy-resolved *NICER* waveform data with 64 phase bins.

These results indicate that our best-fit models with two and three oval spots provide good descriptions of the *NICER* waveform data at high phase resolutions, and that the radius and mass estimates inferred from them are therefore credible. Why the bolometric waveforms given by the models that best fit the 32- and 64-phase energy-resolved *NICER* waveform data differ from the 32-phase bolometric waveforms constructed

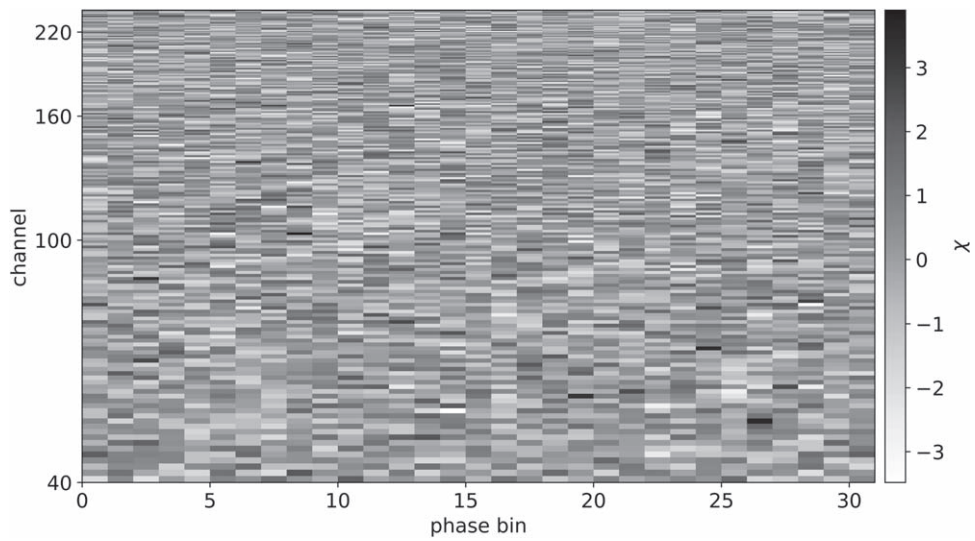

Figure 9. Value of χ in each of the 8320 phase-energy bins (32 phase bins and 260 energy bins), for the best fit of our energy-resolved waveform model with three oval spots to the *NICER* data grouped in 32 phase bins. The energy channel numbers are plotted on a logarithmic scale. No patterns in the values of χ are evident as a function of phase or energy, which is what one would expect for a good fit.

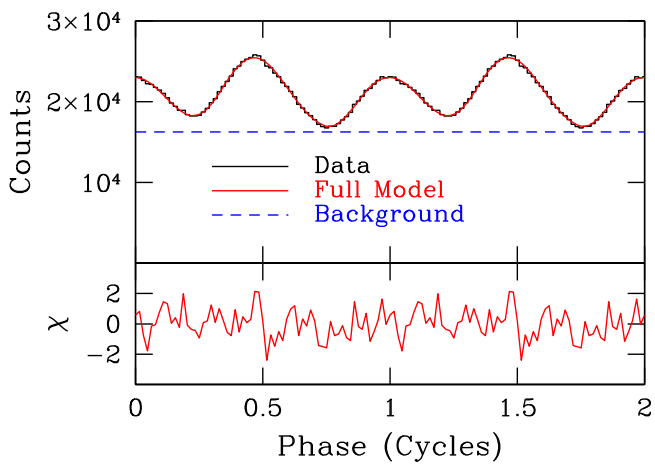

Figure 10. Top: comparison of the 64-phase bolometric waveform constructed using the *NICER* data on PSR J0030+0451 with the 64-phase bolometric waveform model given by the 32-phase energy-resolved waveform model with three oval spots that best fits the 32-phase energy-resolved waveform data. The dashed blue line shows the fitted unmodulated background that was added to the counts produced by the three hot spots as part of the fitting procedure (see Section 3.4). The zero of time of the model bolometric waveform was adjusted to minimize the value of χ^2; this adjustment was +0.49 cycles. Bottom: the resulting value of χ as a function of phase. The χ^2/dof is 59.6/43, which has a probability of 0.0473.

from the *NICER* data but agree with 64-phase bolometric waveforms is unclear, but is most likely due to temporal fluctuations in the *NICER* data that are not yet understood. This question deserves further study.

5.5. Other Aspects of the Models

5.5.1. Locations of the Hot Spots

Figure 11 compares the best-fit locations and shapes of the hot spots obtained by fitting the models with two and three oval spots to the *NICER* waveform data. Both hot spots in the model with two oval spots and all three hot spots in the model with three oval hot spots are located in the southern rotational hemisphere, well away from the sightline to the observer (recall our convention that the sightline to the observer defines the northern hemisphere). Fits that force any of the spots to be in the same hemisphere as the sightline to the observer are strongly disfavored. As we noted earlier, when we discussed the phase-channel χ^2 values for the fits of both models to the *NICER* waveform data, these spot locations provide formally excellent fits.

The fundamental reason spot locations in the southern hemisphere are favored appears to be that the modulation fraction of the waveform observed by *NICER* is high and its harmonic content is substantial. Both waveform properties favor spot locations in the southern hemisphere, because when the spots are visible for only a small fraction of a rotational cycle, both the modulation amplitude of the waveform and the strengths of the higher harmonics of the spin frequency are larger. Spots located in the northern hemisphere are visible for most of each rotational cycle and therefore produce waveforms with smaller modulation amplitudes and weaker high harmonics. In contrast, radio observations as well as joint fitting of radio and γ-ray profiles suggest geometries in which one of the two radio pulses comes from the northern hemisphere (Johnson et al. 2014). However, these studies assume a star-centered dipolar field, whereas the *NICER* results suggest that the magnetic field of PSR J0030+0451 is not a centered dipole (see also Lockhart et al. 2019). Although the locations of the soft, thermal X-ray emission and the nonthermal radio emission need not be the same, this difference should be investigated further.

5.5.2. Colatitude of the Observer

One recent analysis of γ-ray observations of PSR J0030+0451 suggests that the colatitude $\theta_{\rm obs}$ of the observer lies between 0.942 and 1.222 rad (the boundaries of the $\pm 1\sigma$ interval; see Chang & Zhang 2019). The lower end of this interval is consistent with the $\pm 1\sigma$ range of the probability density distributions for $\theta_{\rm obs}$ that we infer from the fit of our model with two oval spots and the fit of our model with three oval spots, which is encouraging.

5.5.3. Spectrum of the Emission from the Hot Spots

An independent estimate of the total X-ray emission from PSR J0030+0451 can be made using observations made with

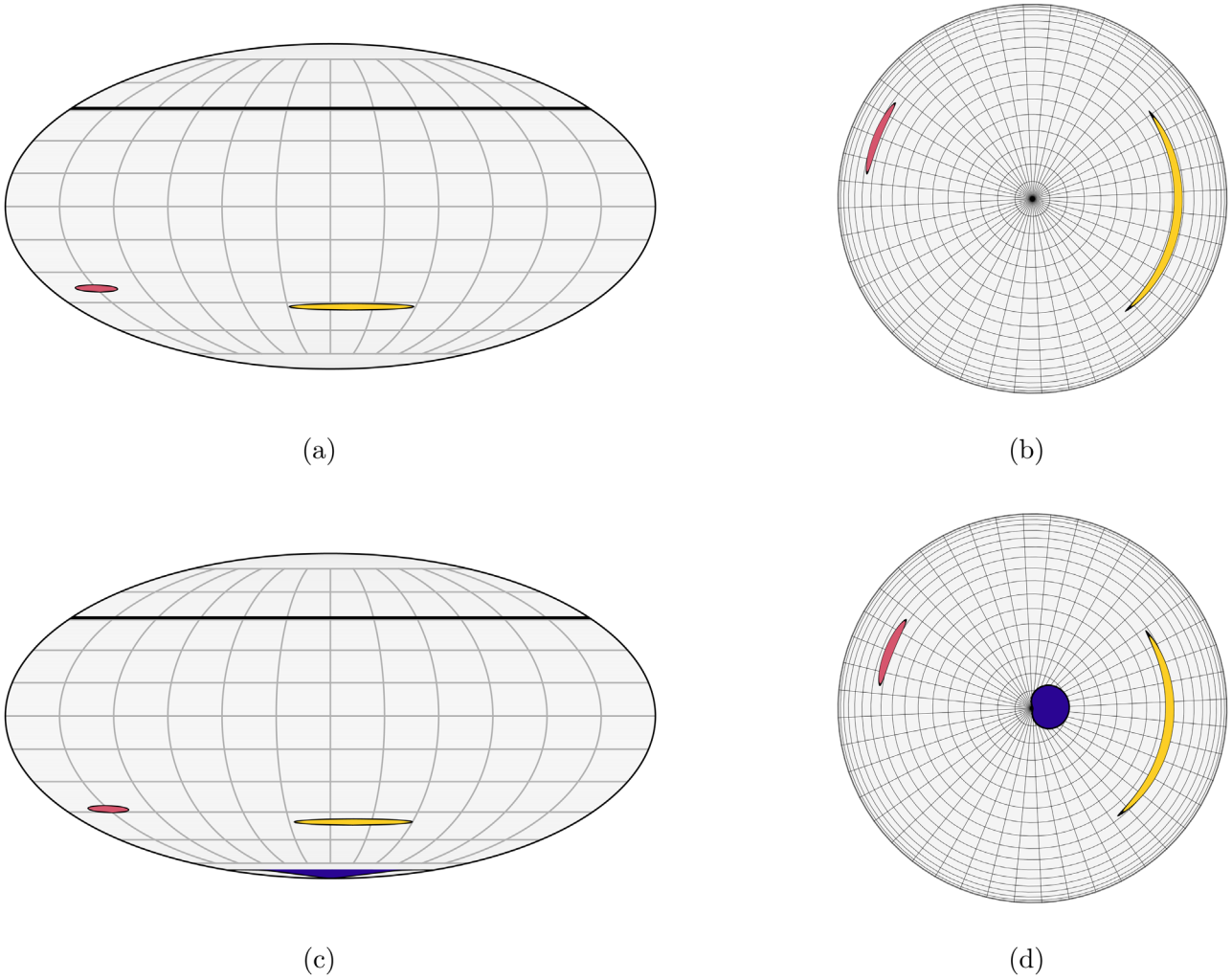

Figure 11. Locations, shapes, and sizes of the hot spots in the best-fit waveform models with two oval spots (panels (a) and (b)) (see Table 7) and three oval spots (panels (c) and (d)) (see Table 8). Panels (a) and (c) show equal-area projections, centered on the rotational equator. Panels (b) and (d) are views from the south pole. The cooler main spot is indicated by yellow, the hotter main spot is indicated by red, and in the three-spot model, the hottest spot is indicated by blue. For both fits, the horizontal line shows the inferred colatitude of the observer. Clearly, both spots in the model with two oval spots and the two main spots in the model with three oval spots are very similar in location, size, and shape; the third spot in the three-spot model has a very small area and makes only a minor contribution to the waveform.

XMM-Newton (Bogdanov & Grindlay 2009). Although the *XMM-Newton* EPIC MOS1/2 observations have substantially fewer source counts, they have a much lower background in the point-source spatial extraction region compared to the non-imaging *NICER* data, which means that to first order all of the counts detected by *XMM-Newton* come from the star rather than from unassociated sources. If the phase-integrated data from *XMM-Newton* are fit using a two-temperature non-magnetic hydrogen atmosphere model (as in Bogdanov & Grindlay 2009) and the predictions of the model are folded through the *NICER* response matrix, then we obtain an estimate for the total number of *NICER* counts from the star and the spectral shape that we expect to see in *NICER*. This predicted spectral flux can be compared with the total spectral flux expected from all the hot spots in our best-fit models of the pulse waveform emission. Figure 12 shows this comparison for our models with two oval spots and three oval spots. In both cases, the combined spectral flux expected from the hot spots at low photon energies falls short of the spectral flux predicted by the *XMM-Newton* observations.

A first thought would be that the missing emission might be unpulsed thermal emission from a substantial fraction of the stellar surface. There are, however, several serious difficulties with such an interpretation. First, the emission would have to be almost exactly axisymmetric around the stellar rotation axis in order to avoid generating detectable pulsed emission. This forces one to consider emission patterns that are highly tuned: filled circular emitting regions around one or both rotation poles, annular emitting regions centered around one or both rotation axes, or some combination of these would be required to avoid producing detectable flux modulation. Second, if the emission is thermal, the total area of the axisymmetric emitting region(s) would have to be a very small fraction of the stellar surface.

We illustrate these difficulties by an example. In order to make up the observed deficit in the flux at low energies and not produce detectable modulation, a circular spot centered on the north rotational pole (the pole nearer the observer), would have to have an angular radius of just 0.075 rad, assuming thermal emission at the best-fit effective temperature of $kT_{\rm eff} \approx 0.075$ keV. Such a spot would also have to be very nearly circular and centered on the north rotational pole: a deviation of more than $\sim$0.01 rad would cause a flux modulation that would be inconsistent with the observed waveform. Because of its smaller projected area, a circular spot centered on the south rotational pole would have to

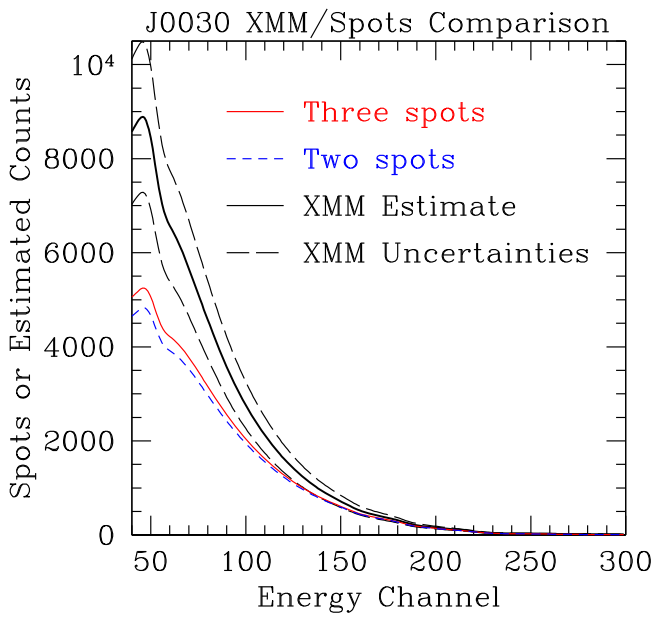

Figure 12. Comparison of the predicted total count spectrum that should be observed from PSR J0030+0451 by *NICER* (solid black line), based on the *XMM-Newton* observations of PSR J0030+0451, with the total count spectrum expected from all the hot spots in the best-fit model with two (dashed blue line) and three (solid red line) oval hot spots. The dashed black lines indicate the $\pm 1\sigma$ uncertainty in the count spectrum predicted from the *XMM-Newton* observations. They are a linear combination of the statistical uncertainty in the *XMM-Newton* observations and an estimate of the systematic error in the *NICER* calibration. The total emission predicted in the lower-energy channels using the emission observed by *XMM-Newton* is greater than the total emission expected from all the hot spots in the best-fit hot spot models. This indicates that the emission provided by the hot spots in these models does not account for all of the emission.

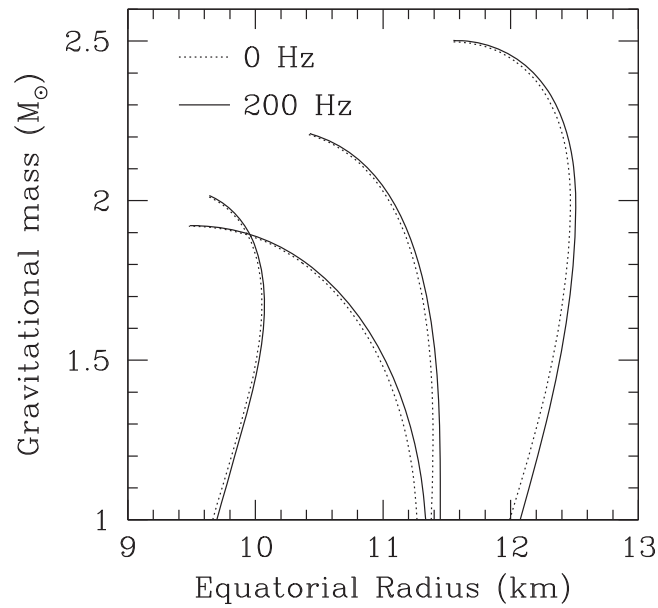

Figure 13. Comparison of the mass–radius relations for a wide variety of EoS computed exactly for a stellar spin rate of 200 Hz (solid curves) and approximately using the TOV equation (dotted curves). The EoS are (in order of increasing radius at 1.5 $M_\odot$) HLPS1 (Hebeler et al. 2013), BBB2 (the higher mass model that uses the Paris two-body interaction potential from Baldo et al. 1997), APR (Model A18+$\delta(v)$+UIX* from Akmal et al. 1998), and HLPS2 (Hebeler et al. 2013). For the $\sim$1.4 $M_\odot$ estimated mass of PSR J0030+0451, the exact radii for a spin rate of 200 Hz differ by less than 1% from the approximate radii given by the TOV equation. This difference is far smaller than the uncertainty in the estimate of the radius of PSR J0030+0451 we have obtained from analyzing its soft X-ray waveform.

have an angular radius $\sim$0.7 rad, about 10 times larger than a spot at the north rotational pole, but would have to be even more precisely circular and centered than a spot at the north rotational pole: a deviation of more than $\sim$0.005 rad would cause a flux modulation inconsistent with the observed waveform.

Other thermal emission geometries with the same projected area are theoretically possible (e.g., one or more very thin axisymmetric annuli), but these seem to us even more fine-tuned. The spectrum could also be produced by processes in which the peak in the spectrum required to make up the deficit does not reflect the temperature of the emitting plasma, but is instead created by a steep decrease of the optical depth of the emitting region with increasing photon energy. High-harmonic cyclotron emission in a region where the optical depth to cyclotron absorption decreases with increasing photon energy is one such possibility (Psaltis & Lamb 1999), but usually requires a population of higher-energy electrons, in which case the optically thick (Rayleigh–Jeans) portion of the spectrum would have to have a very small area, in order to avoid producing too much emission.

It does appear worthwhile to explore other possibilities. For example, the spot pattern is clearly not that of a centered dipole. If this means that the total magnetic field at the surface of the star has significant multipolar components, and is therefore much stronger than the nominal dipole component of $\sim 2 \times 10^8$ G, then perhaps cyclotron emission could contribute to the missing emission.

6. Implications for the Dense Matter EoS

The joint posterior probability distribution we have obtained for the mass and radius of PSR J0030+0451 provides additional constraints on the EoS of cold catalyzed matter, through the effect of the EoS on the stellar structure. The EoS can be expressed as a relation between the pressure p and the total mass-energy density ρ, or a similar relation between p and a different thermodynamic variable.

Here we use the Tolman–Oppenheimer–Volkoff (TOV) structure equation (Tolman 1939; Oppenheimer & Volkoff 1939)

$$\frac{dp}{dr} = -\frac{(\rho c^2 + p)(M(<r) + 4\pi r^3 p/c^2)}{r(c^2 r/G - 2M(<r))}, \tag{3}$$

where r is the circumferential radius and $M(<r)$ is the gravitational mass inside r. The TOV equation assumes that the star is cold enough that its EoS can be treated as barotropic, which is expected to be an excellent approximation for PSR J0030+0451. The TOV equation also assumes that the star is nonrotating and spherically symmetric. Figure 13 shows that this is an excellent approximation for PSR J0030+0451, which has a rotation frequency of 205 Hz. For a given central mass-energy density, the compactness ratio $GM/(R_e c^2)$ is even less sensitive to the rotation rate than either the mass or the radius considered separately.

Given $p(\rho)$ and a central density, the TOV equation can be integrated to yield the gravitational mass M and circumferential radius R_e of a star.

There are numerous papers that apply various Bayesian techniques to the problem of constraining a parameterization of $p(\rho)$ using various astronomical measurements (e.g., Agathos et al. 2015; Lackey & Wade 2015; Alvarez-Castillo et al. 2016; Riley et al. 2018; Greif et al. 2019). Here we use the approach of Miller et al. (2019), who emphasize using full posterior

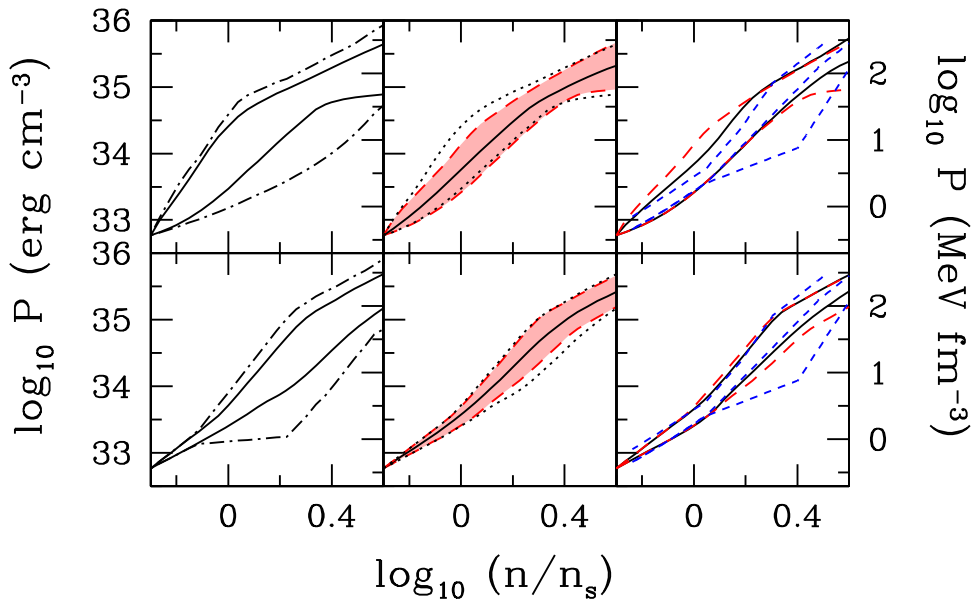

Figure 14. Constraints on the EoS (pressure vs. equivalent number density) of cold, catalyzed matter with and without taking into account the *NICER* measurements of the mass and radius of PSR J0030+0451 described earlier in this Letter, for the two parameterizations of the EoS described in the text. We define the equivalent number density as the rest mass density divided by the mass of a neutron. Top row: constraints on the spectral EoS described in the text. Top left: the vertical separation of the black dashed–dotted lines shows the full range of the assumed prior for the pressure at each equivalent number density, for the spectral EoS; the black solid lines show the 5% (bottom) and 95% (top) credibility contours for the pressure at each number density, when only the priors are used. Top middle: the black dotted lines show the 5% and 95% contours in the credible region when only the prior on the pressure is used, whereas the red shaded region, which is bounded by the red dashed lines, shows the range of pressures between the 5% and 95% contours when the priors are augmented by the mass and radius estimates that we report here; the solid black line shows the median pressure within the credible region at each density. Top right: the red dashed lines are the same as in the middle panel, whereas the blue dashed lines show the soft, intermediate, and hard EoS described in Hebeler et al. (2013); the solid black lines show the 5% and 95% contours when the information provided by the measured masses of PSR J1614−2230 (Arzoumanian et al. 2018a), PSR J0348+0432 (Antoniadis et al. 2013), and PSR J0740+662 (Cromartie et al. 2019), and the tidal deformability estimate from the GW170817 event is added to the information provided by the mass and radius estimates reported here. Bottom row: the same as in the top row, but for the piecewise-polytropic EoS described in the text. These results show that the measurements of the mass and radius of PSR J0030+0451 made using *NICER* definitely tighten the constraints on the EoS of the cold, catalyzed matter in the interiors of neutron stars.

probability distributions rather than strict bounds on the mass or other quantities. They also emphasize that mass–radius measurements such as the ones we report in Section 5.3 need to be incorporated in the constraints on the EoS by fully marginalizing over the central density, rather than (for example) simply picking the point in a mass–radius curve from an EoS that has the highest likelihood from the mass–radius measurement.

There is at present no agreement on the EoS of neutron star matter at the densities expected near the centers of the most massive stars, or even on how best to incorporate the information that is currently available from nuclear and particle physics. A variety of parameterized EoS models are therefore currently being considered (for recent examples, see Tews et al. 2018; Baym et al. 2019; Greif et al. 2019). For this reason, we prefer here to use generic parameterizations to illustrate the new constraints on EoS models that are provided by the new measurements of the mass and radius of PSR J0030+0451 reported above. We caution, though, that as has been emphasized by Greif et al. (2019) and others, the constraints on the EoS derived from a given set of observations depend somewhat on the parameterization chosen for the EoS. Here we present results for the following two parameterizations.

1. The spectral parameterization of Lindblom (2010; see also Lindblom 2018). In this approach, the adiabatic index $\Gamma(p) = [(\rho + p)/p]\,(dp/d\rho)$ is represented using

$$\Gamma(p) = \exp\left(\sum_k \gamma_k x^k\right), \tag{4}$$

where $x \equiv \log(p/p_0)$ and p_0 is the pressure at $\rho_s/2$, where ρ_s is the density of nuclear saturation, which we take to be $\approx 2.7 \times 10^{14}\,\mathrm{g\,cm^{-3}}$. Following Carney et al. (2018) and Abbott et al. (2018), we carry out the expansion up to x^3. The intervals in x that we use and the corresponding uniform priors are $\gamma_0 \in [0.2,\ 2]$, $\gamma_1 \in [-1.6,\ 1.7]$, $\gamma_2 \in [-0.6,\ 0.6]$, and $\gamma_3 \in [-0.02,\ 0.02]$.

2. A piecewise polytrope with transition densities that are also parameters. Here the adiabatic index from $\rho_s/2$ to $\rho_2 \in [3/4,\ 5/4]\rho_s$ is $\Gamma_1 \in [2,\ 3]$; from ρ_2 to $\rho_3 \in [3/2,\ 5/2]\rho_s$ is $\Gamma_2 \in [0,\ 5]$; from ρ_3 to $\rho_4 \in [3,\ 5]\rho_s$ is $\Gamma_3 \in [0,\ 5]$; from ρ_4 to $\rho_5 \in [6,\ 10]\rho_s$ is $\Gamma_4 \in [0,\ 5]$; and from ρ_5 to ∞ is $\Gamma_5 \in [0,\ 5]$ (all priors are uniform in the listed range). The relatively restricted range of Γ_1 is based on the study of Hebeler et al. (2013). Note also that the large number of parameters in this parameterization is intended to give flexibility to our description of the equation of state; we are not attempting to produce a concise fit to realistic microphysics. Unlike the spectral parameterization, the piecewise polytrope can represent phase transitions, in regions where the adiabatic index is close to zero.

For both parameterizations, we use the EoS of Douchin & Haensel (2001) up to $\rho = \rho_s/2$. We also use as a prior the requirement that all candidate EoS be able to support stars with masses of at least $1.4\,M_\odot$. Unlike in Miller et al. (2019), we do not incorporate information about the nuclear symmetry energy, but otherwise we follow their procedure.

For a given EoS, we do not consider densities above the density at which the adiabatic sound speed for that particular

EoS exceeds the speed of light ($dp/d\rho > c^2$). We generate 150,000 random equations of state from each parameterization and then weight them, first, based only on the priors, then using our mass and radius measurement for PSR J0030+0451, and finally also including the high measured masses of PSR J1614−2230 (Arzoumanian et al. 2018a), PSR J0348+0432 (Antoniadis et al. 2013), and PSR J0740+662 (Cromartie et al. 2019), and the tidal deformability constraints from the GW170817 binary neutron star coalescence event (Abbott et al. 2018; De et al. 2018).

In order to perform our analysis, we need a way to turn discrete samples of the (M, R) posterior into an estimate of the continuous posterior probability distribution. We use the standard approach of kernel density estimation (see Rosenblatt 1956; Parzen 1962; Silverman 1986 for details). In kernel density estimation, each point in the sample is replaced by an extended probability distribution (that is, a kernel), and then the probability density at any (M, R) is proportional to the sum of the kernels associated with every point, evaluated at (M, R). One must make a choice for both the shape of the kernel and its width (called its bandwidth in this context). For our kernels we use a Gaussian form, and a bandwidth matrix $\boldsymbol{H}$ based on the covariance matrix. More specifically, our estimate of the probability density at a given point $\boldsymbol{x} = (M, R)$ given $\boldsymbol{H}$ and samples at the points $\boldsymbol{X}_1, \boldsymbol{X}_2, \ldots, \boldsymbol{X}_n$ is

$$\hat{f}_{\boldsymbol{H}}(\boldsymbol{x}) = \frac{1}{n}\sum_{i=1}^{n}\frac{1}{\det(\boldsymbol{H})}\mathcal{K}\{\boldsymbol{H}^{-1}(\boldsymbol{x} - \boldsymbol{X}_i)\}. \tag{5}$$

Here $\mathcal{K}(\boldsymbol{v})$, where $\boldsymbol{v}$ is a column vector, is

$$\mathcal{K}(\boldsymbol{v}) = \exp(-\boldsymbol{v}^T\boldsymbol{v}/2). \tag{6}$$

For $\boldsymbol{H}$ we employ the covariance matrix Σ. To calculate Σ, assume that each sample point in (M, R) is a 2D vector (M_i, R_i). Let μ_M be the mean of M over the sample, let μ_R similarly be the mean of R over the sample, and let $E[(Y_i-\mu_i)\,(Y_j-\mu_j)]$ be the mean of $(Y_i-\mu_i)\,(Y_j-\mu_j)$ over the sample where i and j are M or R. Then the ij element of Σ is

$$\Sigma_{ij} = E[(Y_i - \mu_i)(Y_j - \mu_j)]. \tag{7}$$

The standard rule-of-thumb from Silverman (1986) is that the bandwidth matrix is

$$\boldsymbol{H} = n^{-1/(d+4)}\boldsymbol{\Sigma}^{1/2} \tag{8}$$

where d is the number of dimensions in the data ($d = 2$ in our case) and n is the number of samples from the posterior. This bandwidth is a compromise: if the width is too great then information is lost (an infinitely broad kernel would lead to a constant probability density) whereas if the width is too narrow then the probability density is choppy, with many peaks near the points that happened to be sampled.

We find, however, that our measurement of M and R for PSR J0030+0451 is precise enough that the standard bandwidth produces an inappropriately broadened posterior. For example, using the standard bandwidth we find a smoothed posterior in M/R that is ∼50% broader than the unsmoothed posterior. We therefore multiply the standard bandwidth by 0.1, so that for n samples and two dimensions ($d = 2$),

$$\boldsymbol{H} = 0.1n^{-1/6}\boldsymbol{\Sigma}^{1/2}. \tag{9}$$

This modification yields a smoothed posterior that retains the information without introducing choppiness.

As Figure 14 shows, the measurements of the mass and radius of PSR J0030+0451 made using *NICER* have definitely tightened the constraints on the EoS of the cold, catalyzed matter in the interiors of neutron stars.

7. Conclusions

Our analysis of the *NICER* pulse waveform data on PSR J0030+0451 and the independent analysis by Riley et al. (2019) are the first analyses of this type on data with enough counts to provide a precise and reliable measurement of the mass and radius of a neutron star. The radius and mass estimates given by our analysis are $R_e = 13.02^{+1.24}_{-1.06}$ km and $M = 1.44^{+0.15}_{-0.14}\,M_\odot$ (68%). These estimates imply an allowed range of high-density equations of state that is consistent with previous measurements of neutron star masses (see, e.g., Antoniadis et al. 2013; Arzoumanian et al. 2018a; Cromartie et al. 2019), with the tidal deformability of the neutron stars in GW170817 (see, e.g., Abbott et al. 2018; De et al. 2018), and with general nuclear physics considerations (see, e.g., the discussion in De et al. 2018). The *NICER* measurements have significantly tightened constraints on the EoS. The consistency of our results with those of Riley et al. (2019) adds confidence that the systematic errors in these results are not large, but further pulse waveform modeling and analysis of additional *NICER* data will be helpful.

In summary, our results and those of Riley et al. (2019) provide a new constraint on the radius and mass of PSR J0030+0451, and through them, on the properties of the dense matter in its core (see also Raaijmakers et al. 2019). This work, and future analyses of *NICER* data on other sources, represents an important contribution to the ongoing transition to an era of unprecedented precision in our knowledge of neutron star interiors.

This work was supported by NASA through the *NICER* mission and the Astrophysics Explorers Program. The authors acknowledge the University of Maryland supercomputing resources (http://hpcc.umd.edu) that were made available for conducting the research reported in this Letter. M.C.M. is grateful for the hospitality of the Kavli Institute for Theoretical Physics at the University of California, Santa Barbara, where part of this Letter was written. This Letter was therefore supported in part by the National Science Foundation under grant No. NSF PHY-1748958. M.C.M. was also supported by a Visiting Researcher position at Perimeter Institute for Theoretical Physics in the last stages of this project. W.C.G.H. appreciates the use of computer facilities at the Kavli Institute for Particle Astrophysics and Cosmology. J.M.L. acknowledges support from NASA through grant 80NSSC17K0554 and the U.S. DOE from grant DE-FG02-87ER40317. R.M.L. acknowledges the support of NASA through Hubble Fellowship Program grant *HST*-HF2-51440.001. The authors acknowledge the use of NASA's Astrophysics Data System (ADS) Bibliographic Services and the arXiv.

Facility: NICER (Gendreau et al. 2016).

Software: emcee (Foreman-Mackey et al. 2013), MultiNest (Feroz et al. 2009), Python and NumPy (Oliphant 2007), Matplotlib (Hunter 2007), Cython (Behnel et al. 2011), SuperMongo (https://www.astro.princeton.edu/~rhl/sm/sm.html).

Appendix A
Posterior Distributions for the Model With Two Oval Spots

Figure 15 shows the posterior probability density distributions for each of the parameters in the model pulse waveform produced by two, uniform, oval hot spots that best fits the NICER pulse waveform data on J0030+0451.

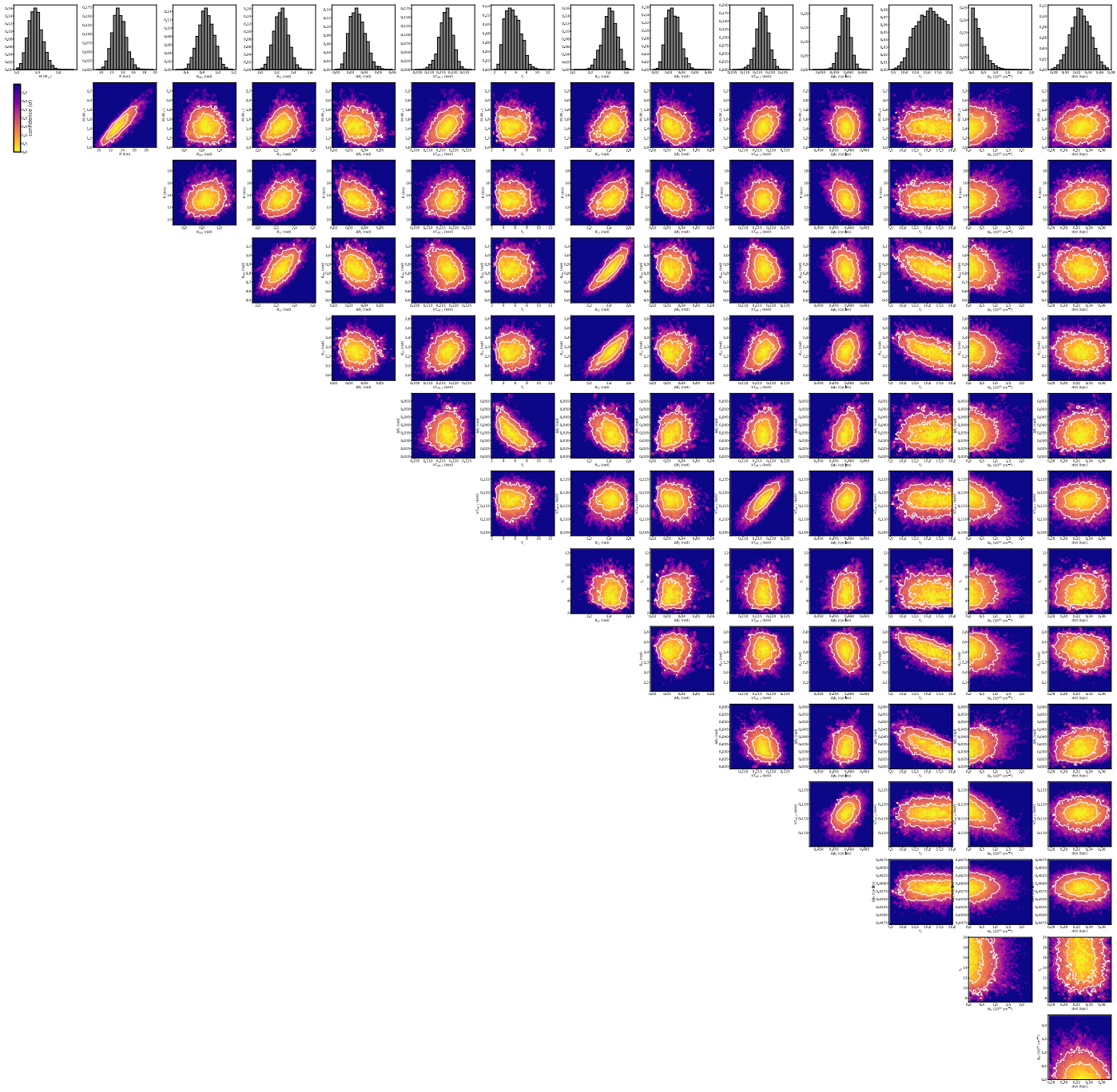

Figure 15. Posterior probability density distributions for the parameters in the best-fitting model pulse waveform produced by two, uniform, oval hot spots.

Appendix B
Posterior Distributions for the Model With Three Oval Spots

Figure 16 shows the posterior probability density distributions for each of the parameters in the model pulse waveform produced by three, uniform, oval hot spots that best fits the NICER pulse waveform data on J0030+0451.

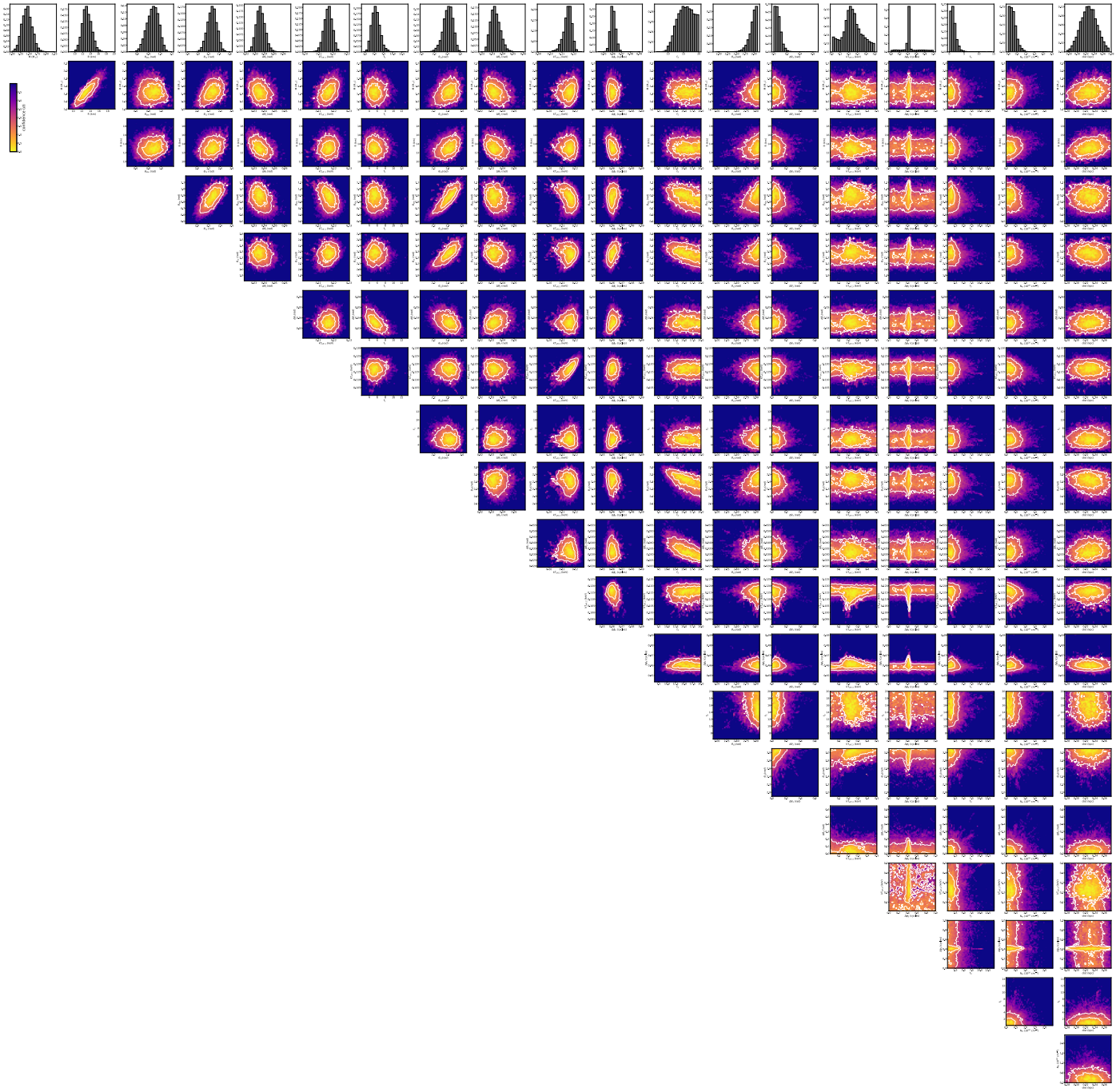

Figure 16. Posterior probability density distributions for the parameters in the best-fitting model pulse waveform produced by three, uniform, oval hot spots.

ORCID iDs

M. C. Miller https://orcid.org/0000-0002-2666-728X
F. K. Lamb https://orcid.org/0000-0002-3862-7402
A. J. Dittmann https://orcid.org/0000-0001-6157-6722
S. Bogdanov https://orcid.org/0000-0002-9870-2742
S. Guillot https://orcid.org/0000-0002-6449-106X
A. K. Harding https://orcid.org/0000-0001-6119-859X
W. C. G. Ho https://orcid.org/0000-0002-6089-6836
J. M. Lattimer https://orcid.org/0000-0002-5907-4552
R. M. Ludlam https://orcid.org/0000-0002-8961-939X
S. Mahmoodifar https://orcid.org/0000-0003-2386-1359
S. M. Morsink https://orcid.org/0000-0003-4357-0575
P. S. Ray https://orcid.org/0000-0002-5297-5278
T. E. Strohmayer https://orcid.org/0000-0001-7681-5845
K. S. Wood https://orcid.org/0000-0002-7376-3151
T. Enoto https://orcid.org/0000-0003-1244-3100
R. Foster https://orcid.org/0000-0002-2731-9295

References

Abbott, B. P., Abbott, R., Abbott, T. D., et al. 2017, PhRvL, 119, 161101
Abbott, B. P., Abbott, R., Abbott, T. D., et al. 2018, PhRvL, 121, 161101
Agathos, M., Meidam, J., Del Pozzo, W., et al. 2015, PhRvD, 92, 023012
Akmal, A., Pandharipande, V. R., & Ravenhall, D. G. 1998, PhRvC, 58, 1804
Alcock, C., & Illarionov, A. 1980, ApJ, 235, 534
AlGendy, M., & Morsink, S. M. 2014, ApJ, 791, 78
Alvarez-Castillo, D., Ayriyan, A., Benic, S., et al. 2016, EPJA, 52, 69
Antoniadis, J., Freire, P. C. C., Wex, N., et al. 2013, Sci, 340, 448
Arons, J. 1981, ApJ, 248, 1099
Arzoumanian, Z., Baker, P. T., Brazier, A., et al. 2018a, ApJ, 859, 47
Arzoumanian, Z., Brazier, A., Burke-Spolaor, S., et al. 2018b, ApJS, 235, 37
Badnell, N. R., Bautista, M. A., Butler, K., et al. 2005, MNRAS, 360, 458
Baldo, M., Bombaci, I., & Burgio, G. F. 1997, A&A, 328, 274
Baym, G., Furusawa, S., Hatsuda, T., Kojo, T., & Togashi, H. 2019, ApJ, 885, 42
Behnel, S., Bradshaw, R., Citro, C., et al. 2011, CSE, 13, 31
Bogdanov, S. 2013, ApJ, 762, 96
Bogdanov, S., & Grindlay, J. E. 2009, ApJ, 703, 1557
Bogdanov, S., Grindlay, J. E., & Rybicki, G. B. 2008, ApJ, 689, 407
Bogdanov, S., Guillot, S., Ray, P. S., et al. 2019a, ApJL, 887, L25
Bogdanov, S., Lamb, F. K., Mahmoodifar, S., et al. 2019b, ApJL, L26
Bogdanov, S., Rybicki, G. B., & Grindlay, J. E. 2007, ApJ, 670, 668
Brambilla, G., Kalapotharakos, C., Timokhin, A. N., Harding, A. K., & Kazanas, D. 2018, ApJ, 858, 81
Cadeau, C., Morsink, S. M., Leahy, D., & Campbell, S. S. 2007, ApJ, 654, 458
Carney, M. F., Wade, L. E., & Irwin, B. S. 2018, PhRvD, 98, 063004
Chang, S., & Zhang, L. 2019, MNRAS, 483, 1796
Colgan, J., Kilcrease, D. P., Magee, N. H., et al. 2016, ApJ, 817, 116
Contopoulos, I., & Spitkovsky, A. 2006, ApJ, 643, 1139
Cromartie, H. T., Fonseca, E., Ransom, S. M., et al. 2019, arXiv:1904.06759
De, S., Finstad, D., Lattimer, J. M., et al. 2018, PhRvL, 121, 091102
Demorest, P. B., Pennucci, T., Ransom, S. M., Roberts, M. S. E., & Hessels, J. W. T. 2010, Nature, 467, 1081
Douchin, F., & Haensel, P. 2001, A&A, 380, 151
Feroz, F., Hobson, M. P., & Bridges, M. 2009, MNRAS, 398, 1601
Foreman-Mackey, D., Hogg, D. W., Lang, D., & Goodman, J. 2013, PASP, 125, 306
Gendreau, K. C., Arzoumanian, Z., Adkins, P. W., et al. 2016, Proc. SPIE, 9905, 99051H
Greif, S. K., Raaijmakers, G., Hebeler, K., Schwenk, A., & Watts, A. L. 2019, MNRAS, 485, 5363
Harding, A. K., & Muslimov, A. G. 2001, ApJ, 556, 987
Harding, A. K., & Muslimov, A. G. 2002, ApJ, 568, 862
Hebeler, K., Lattimer, J. M., Pethick, C. J., & Schwenk, A. 2013, ApJ, 773, 11
Ho, W. C. G., & Heinke, C. O. 2009, Nature, 462, 71
Ho, W. C. G., & Lai, D. 2001, MNRAS, 327, 1081
Hobbs, G. B., Edwards, R. T., & Manchester, R. N. 2006, MNRAS, 369, 655
Hunter, J. D. 2007, CSE, 9, 90
Iglesias, C. A., & Rogers, F. J. 1996, ApJ, 464, 943
Johnson, T. J., Venter, C., Harding, A. K., et al. 2014, ApJS, 213, 6
Kalapotharakos, C., Brambilla, G., Timokhin, A., Harding, A. K., & Kazanas, D. 2018, ApJ, 857, 44
Kalapotharakos, C., Harding, A. K., & Kazanas, D. 2014, ApJ, 793, 97
Lackey, B. D., & Wade, L. 2015, PhRvD, 91, 043002
Lai, D. 2001, RvMP, 73, 629
Lamb, F. K., Boutloukos, S., Van Wassenhove, S. O., et al. 2009a, ApJ, 706, 417
Lamb, F. K., Boutloukos, S., Van Wassenhove, S. O., et al. 2009b, ApJL, 705, L36
Lattimer, J. M., & Prakash, M. 2007, PhR, 442, 109
Lindblom, L. 2010, PhRvD, 82, 103011
Lindblom, L. 2018, PhRvD, 97, 123019
Lo, K. H., Miller, M. C., Bhattacharyya, S., & Lamb, F. K. 2013, ApJ, 776, 19
Lockhart, W., Gralla, S. E., Özel, F., & Psaltis, D. 2019, MNRAS, 490, 1774
Ludlam, R. M., Miller, J. M., Arzoumanian, Z., et al. 2018, ApJL, 858, L5
Miller, M. C. 2013, arXiv:1312.0029
Miller, M. C., Chirenti, C., & Lamb, F. K. 2019, arXiv:1904.08907
Miller, M. C., & Lamb, F. K. 2015, ApJ, 808, 31
Miller, M. C., & Lamb, F. K. 2016, EPJA, 52, 63
Morsink, S. M., Leahy, D. A., Cadeau, C., & Braga, J. 2007, ApJ, 663, 1244
Nättilä, J., Miller, M. C., Steiner, A. W., et al. 2017, A&A, 608, A31
Oliphant, T. E. 2007, CSE, 9, 10
Oppenheimer, J. R., & Volkoff, G. M. 1939, PhRv, 55, 374
Özel, F., Psaltis, D., Güver, T., et al. 2016, ApJ, 820, 28
Parzen, E. 1962, Ann. Math. Statist., 33, 1065
Pavlov, G. G., & Zavlin, V. E. 1997, ApJL, 490, L91
Pearson, K. 1900, The London, Edinburgh, and Dublin Philosophical Magazine and Journal of Science, 50, 157
Philippov, A. A., & Spitkovsky, A. 2018, ApJ, 855, 94
Philippov, A. A., Spitkovsky, A., & Cerutti, B. 2015, ApJL, 801, L19
Potekhin, A. Y. 2014, PhyU, 57, 735
Psaltis, D., & Lamb, F. K. 1999, A&AT, 18, 447
Raaijmakers, G., Riley, T. E., Watts, A. L., et al. 2019, ApJL, 887, L22
Riley, T. E., Raaijmakers, G., & Watts, A. L. 2018, MNRAS, 478, 1093
Riley, T. E., Watts, A. L., Bogdanov, S., et al. 2019, ApJL, 887, L21
Rosenblatt, M. 1956, Ann. Math. Statist., 27, 832
Ruderman, M. 1991, ApJ, 366, 261
Ruderman, M., Zhu, T., & Chen, K. 1998, ApJ, 492, 267
Salmi, T., Nättilä, J., & Poutanen, J. 2018, A&A, 618, A161
Silverman, B. W. 1986, Density Estimation for Statistics and Data Analysis (London, Boca Raton, FL: Chapman and Hall, CRC), http://engineering.purdue.edu/mark/puthesis/
Steiner, A. W., Heinke, C. O., Bogdanov, S., et al. 2018, MNRAS, 476, 421
Steiner, A. W., Lattimer, J. M., & Brown, E. F. 2010, ApJ, 722, 33
Tews, I., Carlson, J., Gandolfi, S., & Reddy, S. 2018, ApJ, 860, 149
Timokhin, A. N., & Arons, J. 2013, MNRAS, 429, 20
Tolman, R. C. 1939, PhRv, 55, 364
Tsai, Y.-S. 1974, RvMP, 46, 815
Zavlin, V. E., & Pavlov, G. G. 1998, A&A, 329, 583

The Astrophysical Journal Letters, 887:L21 (60pp), 2019 December 10 https://doi.org/10.3847/2041-8213/ab481c
© 2019. The American Astronomical Society. All rights reserved.

A *NICER* View of PSR J0030+0451: Millisecond Pulsar Parameter Estimation

T. E. Riley [1], A. L. Watts [1], S. Bogdanov [2], P. S. Ray [3], R. M. Ludlam [4,16], S. Guillot [5,6], Z. Arzoumanian [7], C. L. Baker [8], A. V. Bilous [1], D. Chakrabarty [9], K. C. Gendreau [7], A. K. Harding [10], W. C. G. Ho [11,12], J. M. Lattimer [13], S. M. Morsink [14], and T. E. Strohmayer [15]

[1] Anton Pannekoek Institute for Astronomy, University of Amsterdam, Science Park 904, 1090GE Amsterdam, The Netherlands; T.E.Riley@uva.nl, A.L.Watts@uva.nl
[2] Columbia Astrophysics Laboratory, Columbia University, 550 West 120th Street, New York, NY 10027, USA
[3] Space Science Division, U.S. Naval Research Laboratory, Washington, DC 20375, USA
[4] Cahill Center for Astronomy and Astrophysics, California Institute of Technology, Pasadena, CA 91125, USA
[5] IRAP, CNRS, 9 avenue du Colonel Roche, BP 44346, F-31028 Toulouse Cedex 4, France
[6] Université de Toulouse, CNES, UPS-OMP, F-31028 Toulouse, France
[7] X-Ray Astrophysics Laboratory, NASA Goddard Space Flight Center, Code 662, Greenbelt, MD 20771, USA
[8] Applied Engineering and Technology Directorate, NASA Goddard Space Flight Center, Code 592, Greenbelt, MD 20771, USA
[9] MIT Kavli Institute for Astrophysics and Space Research, Massachusetts Institute of Technology, Cambridge, MA 02139, USA
[10] Astrophysics Science Division, NASA Goddard Space Flight Center, Greenbelt, MD 20771, USA
[11] Department of Physics and Astronomy, Haverford College, 370 Lancaster Avenue, Haverford, PA 19041, USA
[12] Mathematical Sciences, Physics and Astronomy, and STAG Research Centre, University of Southampton, Southampton SO17 1BJ, UK
[13] Department of Physics and Astronomy, Stony Brook University, Stony Brook, NY 11794-3800, USA
[14] Department of Physics, University of Alberta, 4-183 CCIS, Edmonton, AB T6G 2E1, Canada
[15] Astrophysics Science Division and Joint Space-Science Institute, NASA's Goddard Space Flight Center, Greenbelt, MD 20771, USA
Received 2019 July 12; revised 2019 September 24; accepted 2019 September 25; published 2019 December 12

Abstract

We report on Bayesian parameter estimation of the mass and equatorial radius of the millisecond pulsar PSR J0030+0451, conditional on pulse-profile modeling of *Neutron Star Interior Composition Explorer* X-ray spectral-timing event data. We perform relativistic ray-tracing of thermal emission from hot regions of the pulsar's surface. We assume two distinct hot regions based on two clear pulsed components in the phase-folded pulse-profile data; we explore a number of forms (morphologies and topologies) for each hot region, inferring their parameters in addition to the stellar mass and radius. For the family of models considered, the evidence (prior predictive probability of the data) strongly favors a model that permits both hot regions to be located in the same rotational hemisphere. Models wherein both hot regions are assumed to be simply connected circular single-temperature spots, in particular those where the spots are assumed to be reflection-symmetric with respect to the stellar origin, are strongly disfavored. For the inferred configuration, one hot region subtends an angular extent of only a few degrees (in spherical coordinates with origin at the stellar center) and we are insensitive to other structural details; the second hot region is far more azimuthally extended in the form of a narrow arc, thus requiring a larger number of parameters to describe. The inferred mass M and equatorial radius $R_{\rm eq}$ are, respectively, $1.34^{+0.15}_{-0.16}\,M_\odot$ and $12.71^{+1.14}_{-1.19}$ km, while the compactness $GM/R_{\rm eq}c^2 = 0.156^{+0.008}_{-0.010}$ is more tightly constrained; the credible interval bounds reported here are approximately the 16% and 84% quantiles in marginal posterior mass.

Unified Astronomy Thesaurus concepts: Matter density (1014); Rotation powered pulsars (1408); Millisecond pulsars (1062); Pulsars (1306); X-ray stars (1823); Neutron stars (1108); Neutron star cores (1107); Nuclear astrophysics (1129)

Supporting material: figure sets

1. Introduction

Neutron star (NS) cores are thought to harbor nucleonic matter under extreme conditions: high in density, neutron rich, and potentially strange. Stable states of strange matter may either be bound in the form of hyperons, or deconfined as a mixture of up, down, and strange quarks. The density in the stellar core may reach up to several times the nuclear saturation density $\rho_{\rm sat} = 2.8 \times 10^{14}$ g cm^{-3}, a range for which we cannot yet calculate the state of nuclear matter from first principles.[17] Instead, theorists develop phenomenological models of particle interactions and phase transitions, which must be tested by experiment and observation. Heavy ion collision experiments explore the high-temperature and lower-density parts of the nuclear matter phase diagram; but NSs are unique laboratories for the study of strong and weak force physics in cold, dense matter (for recent reviews see Lattimer & Prakash 2016; Oertel et al. 2017; Baym et al. 2018).

The particle interactions on a microphysical scale emerge macroscopically as an equation of state (EOS)—in the context of cold dense matter, a relationship between pressure and (energy) density. The EOS forms part of the relativistic stellar structure equations that enable us, given a central density and a spin rate, to compute model NSs (e.g., Hartle 1967; Hartle & Thorne 1968). An EOS function thus maps to a sequence of stable global spacetime solutions, each controlled in the exterior domain by parameters such as the mass and equatorial radius (at low orders in a small dimensionless spin parameter;

[16] Einstein Fellow.

[17] Although note that calculations at sub-saturation densities (see, e.g., Hebeler et al. 2010), and perturbative quantum chromodynamics (QCD) modeling (valid for densities that are several times higher than the maximum expected in NS cores; see Kurkela et al. 2014) can impose some constraints on the low- and high-density limits of NS core parameter space.

Hartle 1967). In this work we constrain the total mass (sometimes referred to as the gravitational mass) and the equatorial radius of the star, respectively defined as the mass and coordinate radius in the Schwarzschild metric. If we can statistically estimate the masses and radii of a set of stars whose central densities span some sufficiently broad range, we can in principle map out the EOS and hence make inferential statements about the microphysics (Özel & Psaltis 2009; Steiner et al. 2010, 2013; Nättilä et al. 2016; Özel et al. 2016; Raithel et al. 2017; Raaijmakers et al. 2018; Riley et al. 2018; Greif et al. 2019).

The strongest statistical constraints[18] on NS masses are derived by timing radio pulsars in (compact) binaries, and rely on our well-established understanding of relativistic orbital dynamics. Every EOS function (corresponding to a parameter vector for a parameterized model) permits stable spacetime solutions with a maximum gravitational mass—associated with a specific central density—beyond which no stable solutions can exist. High-mass NSs with tight constraints can therefore effectively exclude[19] a subset of EOS function space, barring strong contention with future analyses of independently acquired data. The most informative pulsars in this regard are PSR J0348+0432, with mass $2.01 \pm 0.04\ M_\odot$ (Antoniadis et al. 2013, where the mass is derived by combining pulsar timing and models of the white dwarf companion), and PSR J1614−2230 with mass $1.908 \pm 0.016\ M_\odot$ (Arzoumanian et al. 2018, where the mass comes from Shapiro delay estimation).[20] More recently, Cromartie et al. (2019) have reported a higher—but at present more uncertain—mass of $2.14^{+0.10}_{-0.09}\ M_\odot$ for PSR J0740+6620. We note, however, that the Cromartie et al. (2019) measurement is not subject to the systematic uncertainty that should be added to the formal uncertainty on the mass of PSR J0348+0432 due to the latter's dependence on theoretical models of white dwarf evolution.

The radio pulsar timing of compact binaries has yet to deliver a radius constraint, although this is feasible and indeed anticipated, via moment of inertia estimation (Kramer & Wex 2009). There are, however, constraints on radius via X-ray spectral modeling of transiently accreting and bursting NSs (see, e.g., Steiner et al. 2013; Özel et al. 2016; Nättilä et al. 2017; Shaw et al. 2018; Baillot d'Etivaux et al. 2019); we refer the reader to Miller (2013) and Özel & Freire (2016) for detailed reviews that include an explanation of these X-ray modeling techniques and associated uncertainties. NS mass and tidal deformability estimates are now also being reported based on the first binary NS merger gravitational wave event, GW170817 (Abbott et al. 2017, 2018; De et al. 2018). These can be translated, usually by means of universal relations or EOS model assumptions, into constraints on mass and radius (see, e.g., Abbott et al. 2018; Annala et al. 2018; De et al. 2018; Most et al. 2018; Tews et al. 2018b). Generally, assuming that both NSs have the same EOS, it is found that their radii are nearly equal and (for the 68% credible interval) have the common value 11.9 ± 1.1 km.

NASA's *Neutron Star Interior Composition Explorer* (*NICER*; Gendreau et al. 2016), a soft X-ray telescope installed on the *International Space Station* (*ISS*) in 2017, was developed in part to estimate masses and radii of NSs using pulse-profile modeling of nearby rotation-powered millisecond pulsars (MSPs). Pulse-profile modeling is a technique that probes (approximations to) general relativistic effects on thermal emission from hot regions on the stellar surface (Bogdanov et al. 2019b); these effects are, predominantly, local radiation beaming[21] *due to the bulk motion* of material on the rotationally deformed surface,[22] and subsequent ray propagation on the exterior spacetime. Ray propagation includes the canonical *bending* of light, gravitational redshift, and the increasingly small imprints of rotational metric deformation: frame-dragging, a finite mass quadrupole moment, and higher-order (mass and current) multipole moments. As the star spins, the flux and spectrum of X-ray emission registered by a distant observer is modulated in a periodic manner: we can determine the rotational phase evolution of pulsars precisely and build up a pulse profile (X-ray counts per rotational phase bin per detector channel) by phase-folding X-ray events according to an ephemeris.[23] The mapping of surface emission into the pulse profile detected by a distant observer, via relativistic ray-tracing through the spacetime of a rapidly rotating (and hence oblate) star, is well understood (Pechenick et al. 1983; Miller & Lamb 1998; Poutanen & Gierliński 2003; Poutanen & Beloborodov 2006; Cadeau et al. 2007; Morsink et al. 2007; Bauböck et al. 2013; AlGendy & Morsink 2014; Psaltis & Özel 2014; Nättilä & Pihajoki 2018; Vincent et al. 2018). Thus, given a model for the surface emission (e.g., a geometrically thin atmosphere of some chemical and ionic composition together with a local comoving effective temperature field as a function of surface coordinates), one calculates the expected pulse profile for a given exterior spacetime solution and a given instrument. By coupling such light-curve models to statistical sampling software via efficient software implementations, we can use Bayesian inference to derive posterior probability distributions for spacetime parameters such as mass and equatorial radius directly from pulse-profile data.

For the pulse-profile modeling technique to deliver tight constraints on mass and radius, rapid spin ($\gtrsim$100 Hz) is desirable (Psaltis et al. 2014; Miller & Lamb 2015; Stevens et al. 2016), and one needs high-quality phase- and energy-resolved pulse profiles with time resolution $\leqslant 10\ \mu$s and a large number of photons. The precise number of photons needed to deliver constraints on mass and radius at levels of a few percent—and by extension tight constraints on EOS models—depends on the geometry of a given source, but is $\sim 10^6$ pulsed photons (Lo et al. 2013; Psaltis et al. 2014; Miller & Lamb 2015). For the brightest of the rotation-powered MSPs targeted by *NICER*, it is feasible to collect sufficient data with observation times $\sim$1 Ms. The hot regions on rotation-powered MSPs in theory arise as

[18] Or *measurements*, or *estimates*; in any case, this means some probabilistic measure that is a function of, or otherwise pertains to, model parameters. See Section 2.3 for the probabilistic measures that we consider in this present work.

[19] In a Bayesian context, by truncating the mass likelihood function only far in the tails, leading to a finite but small marginal posterior density for EOSs that do have substantially smaller maximum supported masses.

[20] Note that PSR J1614−2230 was initially reported as having mass 1.97 ± 0.04 (Demorest et al. 2010); the inferences have since been updated via analysis of newly acquired data.

[21] Note that local effective gravity in local comoving frames (instantaneously inertial during rotation) also enters calculation of *atmospheric* beaming of radiation emergent from the local comoving photosphere.

[22] Where for statistical applications the surface is either self-consistently computed via matching to a numerical interior solution to the field equations, or is embedded via a quasi-universal relation in an ambient spacetime solution (for an overview see, e.g., Riley et al. 2018, and references therein).

[23] Note a key difference to the X-ray spectral modeling mentioned two paragraphs earlier: pulse-profile modeling involves phase-resolved spectroscopy; spectral modeling is phase-averaged, and does not fully leverage the temporal dimension of information provided by the star's rotation.

magnetospheric currents—including return currents—deposit energy in the surface layers of the star; the resulting surface radiation field is a priori highly uncertain (Harding & Muslimov 2001; Gralla et al. 2017; Bauböck et al. 2019). *NICER* pulse-profile modeling can therefore also help to constrain the characteristics of the hot regions.

In this Letter we undertake pulse-profile modeling of *NICER X-ray Timing Instrument* (*XTI*) observations of the rotation-powered MSP PSR J0030+0451. Discovered as a radio pulsar by Lommen et al. (2000) and then identified as an X-ray pulsar (Becker et al. 2000), PSR J0030+0451 has a spin frequency of 205 Hz and lies at a distance of 325 ± 9 pc (Arzoumanian et al. 2018). There are no independent prior constraints on either mass or radius. Our analysis uses the *X-ray Pulsation Simulation and Inference* package (*X-PSI*[24] `v0.1`; Riley & Watts 2019). *X-PSI* is a software package for Bayesian modeling of astrophysical X-ray pulsations generated by the rotating, radiating surfaces of relativistic compact stars. *X-PSI* couples X-ray pulsation likelihood functionality to open-source statistical sampling software for use on high-performance computing systems; we apply nested sampling (Skilling 2006) in our analysis (refer to Appendix A). The work presented here is based on usage of a 500,000 core-hour grant on the Dutch national supercomputer Cartesius.[25]

Section 2 outlines the modeling choices and introduces details specific to this analysis, including issues associated with the PSR J0030+0451 surface radiation field parameterization, instrument response, prior definition and implementation, and the consequences for computational efficiency of posterior sampling. In particular we restrict this analysis to models with two distinct hot regions with various structures. While our choices are physically motivated, it is important to emphasize that our inferences are conditional upon these choices. Posterior[26] inferences for the models are presented in Section 3, including the inferred posterior probability distributions for the spacetime parameters (mass, radius, and their combination into compactness), surface radiation field parameters (e.g., heating distribution and resulting temperature field), and instrument parameters. The Bayesian evidence for each model is reported, and we also summarize the computational resources required for each parameter estimation run. We also compare our inference to predictions derived via earlier study of PSR J0030+0451 using *XMM-Newton* (Bogdanov & Grindlay 2009). Sections 2 and 3 are long and detailed; in Section 2.1 we provide a brief overview of some of the key aspects from those sections, to help orient the reader. In Section 4 we discuss the implications of our results for our understanding of dense matter, pulsar emission mechanisms, and stellar evolution. We conclude with a discussion of future work for PSR J0030+0451: variations in the model that should be considered, tests and cross-checks, and the potential for improving the constraints for this source via longer observations or more in-depth analysis.

2. Modeling Procedure

2.1. Executive Summary of Modeling Procedure and Inferences

This Letter (and its companions) are the first pulse-profile modeling analyses to emerge from the *NICER* mission. We have therefore provided (in Sections 2 and 3) a very detailed description of the methodology, the flow of the analysis, and the results. Since this is lengthy, we summarize the key aspects in this subsection.

The pulse-profile modeling technique requires us to define a model for the data-generating process, incorporating the physics that we initially assume to be most important. For a given choice of parameters, this model can be used to generate synthetic pulse-profile data sets. The model in part defines the likelihood function (the probability of the data as a function of parameters); the model also defines the prior probability distribution of parameters entering in the likelihood function. The posterior probability distribution of the model parameters (conditional on the observed data) is then sampled during the inference process. We must also pay attention to model complexity, in order to keep the computational load tractable.

In this Letter we assume that there are two separate hot regions on the stellar surface; this choice was motivated by the presence of two distinct pulses in the observed (phase-folded) pulse-profile. However, we considered a number of different possible configurations for the shapes and temperature functions of the hot regions: circular spots, annuli (rings, both centered and off-centered), and crescents; with one or two temperature components. These choices were motivated by contemporary theories for pulsar surface heating distributions as a result of magnetospheric return currents. We tested configurations where we insisted that the two hot regions were antipodal and identical; and where the hot regions were completely independent and potentially non-antipodal. We then assumed a geometrically thin fully ionized hydrogen atmosphere model (`NSX`, Ho & Heinke 2009), which characterizes the beaming and spectrum of the emergent thermal radiation (see, e.g., Zavlin et al. 1996, for details).

To propagate the emergent radiation toward the observer via relativistic ray-tracing, we use the Oblate Schwarzschild plus Doppler approximation of Morsink et al. (2007) for the NS spacetime. This is sufficiently accurate for our analysis, given the rotation rate of PSR J0030+0451. We define a joint prior distribution of mass and radius (the key parameters specifying the spacetime) that facilitates the subsequent inference of EOS model parameters (Riley et al. 2018; Raaijmakers et al. 2019). For the distance to the source, we use the (Gaussian-distributed) value inferred from radio observations (Arzoumanian et al. 2018) as a prior in our modeling. We then need to model the instrument response matrix (which includes both the effective area and the way in which incident photons of a given energy are assigned to specific detector energy channels). We develop a parameterized model that includes both energy-independent and energy-dependent components. The former attempts to capture absolute calibration uncertainty; for the latter we base our parameterization on residuals derived from *NICER* observations of the Crab Nebula and pulsar (Ludlam et al. 2018). We also assume a non-source background component, which we treat as a rotational phase-independent channel-by-channel contribution, rather than invoking a specific physics-driven spectral model. There are no prior constraints on either observer inclination or interstellar absorption for PSR J0030+0451, so we adopt a wide and diffuse prior for both parameters.

Note that Miller et al. (2019) have made an independent analysis of the same data set using different modeling choices and methodology. The choices we have made in this Letter

[24] https://github.com/ThomasEdwardRiley/xpsi

[25] https://userinfo.surfsara.nl/systems/cartesius

[26] Appendix A provides an overview of the methodology used for posterior computation, and of the format used to present the posterior information.

differ in several regards from those made by Miller et al. (2019); some of the most notable differences are in the models for the hot region configurations and the instrumental response, and the specification of the prior on distance.

During the inference analysis reported in Section 3 we considered a sequence of increasingly complex models for the shape and temperature function of the hot regions. All of the other aspects of the modeling described above are shared between models. Model assessment and comparison then enabled the identification of a superior configuration. We use a combination of performance measures: the evidence (the prior predictive probability of the data); graphical posterior predictive checking (to verify whether or not a model generates synthetic data without obvious residual systematic structure in comparison to the real data); visualization of the combined signals from the hot regions; Kullback–Leibler (KL) divergences (a measure of the parameter-by-parameter information gain of the posterior over the prior); background-marginalized likelihood functions (useful in combination with evidence to assess whether additional model complexity is helpful); model tractability (posterior computational accuracy being higher for less-complex models); and cross-checking of the inferred background against earlier analysis of PSR J0030+0451 with *XMM-Newton*.

Before beginning our analysis, we had mapped out an initial route through the model space of different heating configurations. This was modified as we progressed, informed by the results of each stage. We began with the simplest model, with single-temperature circular spots. Having the spots be antipodal and identical was quickly ruled out due to large residuals between model and data. Relaxing the requirement that the spots be identical and antipodal largely resolved this issue. We then moved to a more complex model where each hot region consisted of a circular spot—a *core*—and a surrounding annulus with an independently determined temperature. This model was superior to the simpler one, based on the evidence, but appeared to be overly complex: one hot region was dominated by a small hot circular spot, with negligible emission in the *NICER* waveband from the cooler annulus; for the other, emission was dominated by a hot annulus, with a much cooler core making almost no contribution. Simplifying the model such that one hot region was a single-temperature circular spot and the other a single-temperature annulus (with a centered, non-emitting core) produced congruent inferences at lower computational cost. At this point (after assessing the contribution from this component, and our remaining computational resources), we elected to restrict the model for one of the hot regions to be a single-temperature circular spot. The other was restricted to a single temperature, but we increased the complexity of the shape, testing two additional models: an annulus with an off-centered non-emitting core, and a crescent.

The superior configuration to emerge from this sequence of models, in terms of the performance measures listed above, was the final one: one hot region a small circular spot (sufficiently small that we would be insensitive to shape changes), and the other was an extended thin crescent. The results that we report in the abstract for the mass and radius of PSR J0030+0451 are those associated with this configuration.

2.2. Data Pre-processing

The *NICER XTI* data set $\boldsymbol{d}$ associated with the rotation-powered MSP PSR J0030+0451 is necessarily a product of pre-processing, and its curation is largely described in Bogdanov et al. (2019a). However, there are a number of details that are specific to each data set and so we record a summary of these details below. The raw *XTI* event data are publicly available via the *NICER* archive (accessible via HEASARC[27]). The processed data set $\boldsymbol{d}$ may be found in the persistent repository of Bogdanov et al. (2019c).

For this analysis we consider only the detector channel[28] subset [25, 300)—meaning channels 25 through 299 inclusive—nominally corresponding to 0.25–3 keV. Below channel 25, there is increased "optical loading" contamination (electronic noise due to ambient light), and there is greater uncertainty in the detector readout triggering efficiency for valid X-ray events. Above channel 300 the soft thermal emission from PSR J0030+0451 becomes negligible relative to the non-source background.

For PSR J0030+0451 we use 49 out of the 52 active detectors (excluding the three detectors that are frequently "hot," i.e., prone to excess electronic noise) and only *NICER* pointings subtending an angle $>80°$ to the direction of the Sun. In addition to the standard filtering criteria applied to *XTI* events, we excluded times where the planetary K-index $K_P \geqslant 5$, and excluded regions in the *NICER* orbit where the cutoff rigidity (the COR_SAX parameter) was less than 1.5. We further screened for occurrences of elevated background and eliminated all 16 s time intervals in which the 0.25–8.00 keV count rate exceeded 3 counts s^{-1}, yielding an integrated exposure time of $T_{\rm exp}$: $=\sum_\ell \Delta t_\ell = 1,936,864$ s, where each Δt_ℓ is the time interval for the ℓth exposure.

Harnessing the flux and timing stability of PSR J0030+0451, the entire event data set in each detector channel is phase-folded coherently according to the best available radio pulsar timing solution from Arzoumanian et al. (2018) and using two approaches to check for consistency: using the TEMPO2 (Hobbs et al. 2006) `photons` plug-in and the PINT[29] `photonphase` tool. Differences of $\lesssim 1\ \mu$s as a phase-offset are observed, but are deemed negligible for the present analysis as such an offset corresponds to $\lesssim 0.02\%$ of the total phase, or less than 0.7% of a bin width. The resulting folded event list, obtained with the PINT `photonphase` tool, is summarized as count data in a set of rotational phase intervals and detector channels. We display in Figure 1 the count data for channels in the interval [25, 300), nominally corresponding to the energy range 0.25–3.00 keV. We reserve the remaining details of data-space definition for Section 2.4.3, wherein we formalize the likelihood function applied in this specific work.

2.3. Generative Modeling

We begin the description of our modeling process by outlining useful mathematical objects that are assigned statistical meaning, and which can interface with open-source computational machinery. In Section 2.4, we build upon this conceptual groundwork and assign astrophysical meaning to such objects.

[27] https://heasarc.gsfc.nasa.gov/

[28] Conventionally termed a pulse-invariant (PI) channel, or alternatively a charge pulse amplitude (or height) channel. Note the distinction between *channel*, which is only indicative of photon energy in units of 10 eV, and incident photon *energy intervals* that map probabilistically to the channel set via the redistribution matrix, a standard calibration product provided by the instrument team.

[29] https://github.com/nanograv/PINT

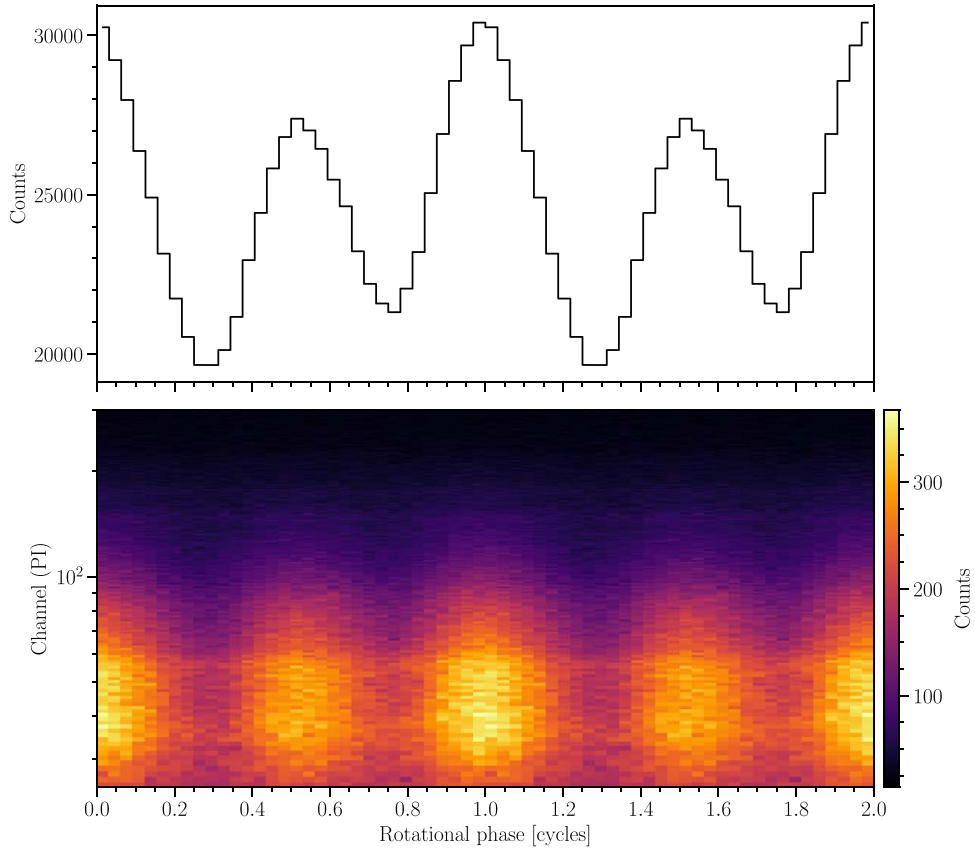

Figure 1. Phase-folded PSR J0030+0451 event data split over two rotational cycles for clarity: we use 32 phase intervals (bins) per cycle and the count numbers in bins separated by one cycle—in a given channel—are identical. The total number of counts is given by the sum over all phase-channel pairs. The top panel displays the pulse-profile summed over the contiguous subset of channels [25, 300). The bottom panel displays the phase-channel resolved count numbers for channel subset [25, 300). For likelihood function evaluation (see Section 2.4.3) we group all event data registered in a given channel into phase intervals spanning a single rotational cycle. Moreover, we do not indicate the count-number noise in the top panel to avoid confusion: the observed events are viewed as fixed random variates that do not have errors, and whose parameterized joint sampling distribution is to be modeled (see Section 2.3).

There exists an inherent degree of freedom as to the precise definition of a *model*. We consider a *generative* model for the X-ray data set $\boldsymbol{d}$ curated for PSR J0030+0451. Moreover, we opt to define a generative model as the union of the following components: (i) a data space $\mathscr{D}$ in which a data set $\boldsymbol{d} \in \mathscr{D}$ exists as a fixed vector of numbers; (ii) an abstract model space $\mathscr{M}$ of elements, such that each element completely specifies a joint sampling distribution on space $\mathscr{D}$ (i.e., the sampling distribution can be evaluated conditional on the element); (iii) a joint probability distribution defined on space $\mathscr{M}$ that is not conditional on data vector $\boldsymbol{d}$. Such a model is considered as generative because one can define a Bayesian joint distribution on the joint space of $\mathscr{D}$ and $\mathscr{M}$: the data vector and a model vector are both interpreted as (finite-dimensional) multivariate random variables, and in order to simulate (or generate) data sets, one can jointly draw random variates to populate the vector elements.

The model space $\mathscr{M}$ is in general a discrete-continuous mixed space, meaning that its elements form a discrete-continuous mixed set; it follows that one could in principle identify each element as a model. Ultimately, however, one can distinguish continuous subsets of $\mathscr{M}$ as models, which is perhaps more common. To formalize the framework that we are working in further, let us define a discrete-continuous mixed space $\mathscr{M}$ as a union $\bigcup_{m \in \mathscr{F}} \mathcal{M}_m$, where $\mathscr{F} \subset \mathbb{N}$ is the space of a discrete parameter m—a flag or label—and where each $\mathcal{M}_m$ may be considered as a model within $\mathscr{M}$. Let each model $\mathcal{M}_m$ define a continuous space $\Theta_m \subseteq \mathbb{R}^{n_m}$ such that $\mathscr{M}$ defines a space given by the union of Cartesian products

$$\Theta := \bigcup_{m \in \mathscr{F}} (\{m\} \times \Theta_m). \tag{1}$$

The number of dimensions of the space Θ_m is given by n_m; a parameter vector $\boldsymbol{\theta} \in \Theta_m \subseteq \mathbb{R}^{n_m}$ then has n_m elements. We thus consider each space in the union $\mathscr{M}$ as a model: unless explicitly stated otherwise, we hereafter consider a model as an element in a discrete set, where each element has an associated continuous parameter space Θ_m (among other constructs, e.g., probability measures such as a joint prior density distribution).

Working within the scope of a given model $\mathcal{M}_m$ with continuous parameter space Θ_m, the prior support $\mathcal{S}_m \subseteq \Theta_m$ is a (compact) subset of $\mathbb{R}^{n_m}$ on which the joint prior density is finite. The target distribution is the joint posterior density distribution, denoted by $\pi(\boldsymbol{\theta} \mid \boldsymbol{d}, \mathcal{M}_m)$, which is related to the joint prior density distribution, $p(\boldsymbol{\theta} \mid \mathcal{M}_m)$, via the probability identity (Bayes' theorem)

$$\begin{aligned} \pi(\boldsymbol{\theta} \mid \boldsymbol{d}, \mathcal{M}_m) p(\boldsymbol{d} \mid \mathcal{M}_m) &= p(\boldsymbol{\theta}, \boldsymbol{d} \mid \mathcal{M}_m) \\ &= p(\boldsymbol{d} \mid \boldsymbol{\theta}, \mathcal{M}_m) p(\boldsymbol{\theta} \mid \mathcal{M}_m), \end{aligned} \tag{2}$$

where $p(\boldsymbol{d} \mid \boldsymbol{\theta}, \mathcal{M}_m)$ is the likelihood function for model $\mathcal{M}_m$. The likelihood function is the sampling distribution on the space $\mathscr{D}$ evaluated at the fixed data vector $\boldsymbol{d}$, as a function of $\boldsymbol{\theta}$, conditional on model $\mathcal{M}_m$; the normalization of the posterior is

the prior predictive probability[30] $p(\boldsymbol{d} \mid \mathcal{M}_m)$ of the data conditional on model $\mathcal{M}_m$. We document the techniques implemented for posterior computation in Appendix A. It is necessarily the case that for construction of a generative model, a joint prior distribution injects a finite quantity of information about the elements of the model space. From a Bayesian perspective, models and parameters are random variables, whose joint prior distribution strictly encodes the information available before acquisition of—and computation given—data. Hereafter we do not need to typeset the symbol Θ (with or without a subscript) to represent a space, and thus we explicitly free it for a different use.

The model space that we consider is some mixture of $\mathscr{M}$-complete and $\mathscr{M}$-open (Vehtari & Ojanen 2012): we do not believe the true data-generating process exists in $\mathscr{M}$, nor do we believe that an element in $\mathscr{M}$ is the closest approximation (to the true data-generating process) that is achievable and tractable (in the future) given more resources (i.e., both cognition and computing time). However, we proceed as though we can imagine a true data-generating process to physically exist—i.e., is plausibly the product of simple physical laws and initial conditions—and that parameterized approximations can in principle approach the real process arbitrarily closely, at least in terms of predictive performance. Moreover, we view the model space for this specific work as effectively the best available to us given current resources, and consider it plausible that it is sufficiently rich to predict features in the procured X-ray event data. A subset of continuous parameters are shared by all models in the discrete set: these are considered to be of an (effectively) fundamental physical nature, such as the distance to a source system and parameters controlling the exterior spacetime solution of a compact star in general relativistic gravity. On the other hand, parameters are also defined that are of an overtly phenomenological nature and are intended to approximate reality only insofar as: (i) predicting—via interplay with the (almost) fundamental parameters—features observed in data, and (ii) supporting future development of physics models that are considered more realistic but crucially remain tractable for statistical falsification.

When we increment model complexity, it is intended to be in an intuitive and natural manner: we generally do so by breaking a form of symmetry, forming nested relationships between models (see Section 2.5 and then Section 2.5.7). Nevertheless, the form of the simplest model and the increments in complexity are ultimately of a subjective nature and exhibit a degree of arbitrariness—different practitioners would have defined their model spaces differently.

The discrete set of models that we condition on was determined partly out of consideration for available resources. Given that posterior computation cost generally increases with prior predictive complexity,[31] we consider it justified to organize a set of increasingly costly problems wherein each is an extension of the former. The salient advantage in this respect is facilitating robustness: by monitoring and analyzing sampling processes operating on gradually more difficult problems, tractability can be gauged for subsequent problems given available computing resources. Moreover, if a pair of models form an exact or approximate nested relationship then we expect the posterior parameter inferences to be consistent with that of the simpler model if the additional complexity is unhelpful.

Aside from resource management, and conditioned on the assumption that posterior computation is sufficiently accurate, one can pose the question of how much complexity is useful to capture structure in observational data. In a Bayesian framework one can in principle estimate prior predictive probabilities of data conditional on a model. It is generally argued that Occam's razor is inherent to prior predictive probability integrals: predictive complexity is penalized if predictions are not *expected* to be at least as commensurate with the data as a simpler (or nested) model. The interpretation of prior predictive probabilities is often fraught with problems, principally sensitivity to prior definition. In this work the joint prior distribution defined for the continuous parameters of each model is not rigorously chosen according to an information-theoretic criterion, nor to accurately quantify belief for overtly phenomenological parameters. However, the prior choices are viewed as being weakly informative[32] for most parameters of interest in the absence of existing constraints, and are viewed as being consistent between models.

As acknowledged above, a widely held view is that evidence estimation[33] does not solve the problem of model comparison. In order to evaluate model performance we thus employ both a form of graphical posterior-predictive checking, and prior predictive probabilities that hereafter we will refer to simply as *evidences*—a less accurate but canonical descriptor of $p(\boldsymbol{d} \mid \mathcal{M})$. If the evidence increases, it is generally accurate to conclude that additional complexity is warranted; if evidence does not increase, however, graphical posterior predictive checking on local modes is useful for determining whether or not facets of the higher-complexity model are a promising avenue to pursue in model development—i.e., if the likelihood function maxima are larger.

2.4. Overarching Definitions

In this section we describe model aspects that are generally shared between all models in the discrete set $\mathscr{M}$. These model facets are in some cases described in detail elsewhere in the *NICER* literature (Bogdanov et al. 2019a, 2019b, 2019c) and thus we are brief where possible. Due to the large number of symbols required to describe the models in this Letter, the symbols used to describe geometric variables shared with Bogdanov et al. (2019b) are different; Table 1 provides symbol translation from Bogdanov et al. (2019b), the theory in which underpins the present work.

2.4.1. Source

The pulsed sources are assumed to be thermally emitting, rotating hot surface regions of PSR J0030+0451.

Parameterization. The exterior spacetime solution is approximated as follows: we embed in each temporal hyperslice of an ambient Schwarzschild spacetime, a (quasi-universal) oblate two-surface, such that the geometric center coincides with the origin of the Schwarzschild coordinate chart (Morsink et al. 2007). The coordinate equatorial radius is

[30] The scalar expectation of the likelihood function with respect to the prior $p(\boldsymbol{\theta} \mid \mathcal{M}_m)$, commonly referred to as the evidence or fully marginal likelihood.

[31] Which is easily proven for (non-dynamic) nested sampling processes (see Appendix A for an outline of the sampling procedure).

[32] Also known as *vague* or *diffuse*.

[33] For calculation of Bayes' factors.

Table 1
Translation of Symbols for Angle Variables Typeset in *both* this Work and Bogdanov et al. (2019b)

Symbol	Description	Bogdanov et al. (2019b)
i	Earth inclination to pulsar rotation axis	ζ
Θ	colatitude of center of a circular hot spot[a]	θ_c
ζ, ψ	angular radius of a circular hot spot[b]	$\theta_{\rm spot}$
ϕ	pulsar rotational phase[c]	ϕ

Notes.
[a] We also use the symbol Θ, with subscripts, to denote the colatitudes of hot regions whose shapes are more complex than circular spots.
[b] We also use these symbols to parameterize hot regions with more complex shapes, such as rings with outer angular radius ζ and inner angular radius ψ.
[c] We also use the symbol ϕ, with subscripts, to denote the azimuthal coordinates of hot regions.

denoted by $R_{\rm eq}$, and the circumference of the equator is $2\pi R_{\rm eq}$; the total mass in the ambient spacetime is denoted by M. The polar axis of the Schwarzschild chart is defined as the pulsar rotational axis. Rotational deformation of the metric away from spherical symmetry is neglected; the current dipole and mass quadrupole moments of the exterior metric enter at first- and second-order in dimensionless angular velocity $\bar{\Omega}$ (Hartle 1967) but are sufficiently small—regardless of the EOS—that they can be neglected in pursuit of a tractable likelihood function (Morsink et al. 2007), especially during initial modeling and in a context where we do not expect the likelihood function to be sensitive to the finiteness of these moments. The perturbations, at constant baryon number, to both the total mass and circumferential radius of a nonrotating star are second-order in $\bar{\Omega}$ (Hartle 1967), and are thus small for a spin of 205 Hz (see also Section 4.2) but are implicitly accounted for. The perturbation to the polar coordinate radius is second-order in $\bar{\Omega}$, and the surface oblateness is controlled by an EOS-insensitive constraint equation (as is the effective gravity along the surface; Morsink et al. 2007). These small changes in the shape of the stellar cross-section induce tilt to the surface, which affects the rays that connect spacetime events at the surface to an observer; together with the change in the projected surface area of a tilted surface, and the change in effective gravity, the effect on light-curves manifests at first-order in $\bar{\Omega}$. Crucially, there is a performance floor for light-curve integration demarcated by a spherically symmetric exterior spacetime solution: embedding an oblate surface in such an ambient spacetime results in negligible increase in computation time per call to a light-curve integrator. We therefore are not concerned about quantifying the difference in our statistical inferences due to inclusion of oblateness over a spherical surface—more resources are required to quantify this rigorously than to simply account for oblateness.

A distant, static, and fictitious[34] instrument (see Section 2.4.2) is located at radial coordinate D, and subtends colatitude—hereafter termed inclination—denoted by i. Interstellar light–matter interaction is described by absorption within a column of material. The attenuation factor is parameterized solely by the column density $N_{\rm H}$ of neutral hydrogen and we assume relative abundances for the interstellar medium from Wilms et al. (2000); we implement the `tbnew`[35] model to precompute a set of lookup tables for attenuation as a function of photon energy.

In each model the spatial dependence of the surface radiation field is of a phenomenological nature: the aim is to introduce sufficient complexity so as to represent the basic notion of pulsar surface heating due to energy deposition by magnetospheric currents (in the vicinity of the magnetic poles). We are largely ignorant of spatial structure in the surface radiation field because the star is not spatially resolved; moreover, it is intractable for us to consider more self-consistent numerical models of the surface radiation field, in part due to the expense of statistical computation. In the simplest case the radiation field is constructed by filling two closed simply connected regions on the surface—which do not mutually overlap—with radiating material;[36] these regions may be interpreted to each result from magnetospheric polar cap heating. We only compute a radiative signal from these hot regions, and therefore in the context of each of our models, *hot region* can be viewed as synonymous with *radiating region*.

For all models a geometrically thin (and thus plane-parallel) fully ionized hydrogen `NSX` atmosphere is invoked for the radiating material (Ho & Lai 2001; Ho & Heinke 2009). The radiation field is precomputed and represented as a lookup table for cubic polynomial interpolation of specific intensity, $I_E/k_{\rm B}T_{\rm eff}^3$, with respect to four variables defined in a surface local comoving frame: effective temperature, $T_{\rm eff}$; effective gravity; photon energy, $E/k_{\rm B}T_{\rm eff}$; and the cosine of the ray zenith angle (to surface normal). A quasi-universal relation for surface effective gravity[37] is adopted from AlGendy & Morsink (2014) in order to evaluate local radiation field intensities. We do not explicitly compute emission from the stellar surface exterior to the closed regions (i.e., as a function of source parameters controlling the exterior radiation field),[38] but the phase-invariant background model that we invoke in all cases

[34] A notion borne from the nature of the event-data pre-processing (see, e.g., Riley & Watts 2019, for details pertaining to *X-PSI*).
[35] https://pulsar.sternwarte.uni-erlangen.de/wilms/research/tbabs/

[36] Note that although a cooler radiating hydrogen atmosphere should exist globally over the stellar surface (as observed for PSR J0437−4715, Durant et al. 2012; Guillot et al. 2016; Gonzalez-Caniulef et al. 2019, and PSR J2124−3358, Rangelov et al. 2017), we make no explicit reference to it when defining our likelihood function—i.e., we do not compute any radiative signal from the atmosphere exterior to the closed regions. The atmosphere cannot be globally uniform because local heating by magnetospheric currents will affect the local temperature and ionization degree; effective gravity also varies due to rotation. Reference to the global atmosphere is implicit due to the fluid properties required for containment of hot material in the closed regions.
[37] Equatorially reflection-symmetric.
[38] Such computation is supported by *X-PSI* with specialization to ensure (almost) exact areas as described above (see also Bogdanov et al. 2019b), but requires a choice of surface radiation field (e.g., atmosphere ionization degree and chemical composition). We therefore opt to capture the *non-pulsed* fraction of emission from the stellar surface exterior to the regions via our default background treatment. If evidence for unmodeled soft pulsed emission arises a posteriori one could then consider explicit computation of such emission.

can capture non-pulsed components of surface and off-surface emission (see Section 2.4.3).

Let us hereafter refer to the geometric configuration of the infinitesimal radiating surface elements simply as the *shape* of a hot region—including both exterior and interior boundaries. In more complex models each hot region is constructed using additional shape parameters and in some cases a second temperature component. We consider the shape and temperature of a hot region to result from the interaction of *two* closed regions—hereafter *members*. The members partially or wholly[39] overlap, and one member takes precedence when evaluating local radiation intensities along rays (null geodesics) that connect spacetime events on the rotating surface to a distant observer. We term one member as *ceding*, and the other as *superseding*. As discussed in the appendix of Bogdanov et al. (2019b), the *X-PSI* implementation (referred to as the AMS code in Bogdanov et al. (2019b)) of a radiating region is specialized for fast likelihood function evaluation when said function is a callback for sampling processes: while numerical approximations are necessary in general, it is relatively inexpensive to ensure that the proper area of each finite-element (discretized) radiating region is computed to a precision that (almost) exactly matches their mathematical definition.[40] When two members overlap to form a hot region (i) the area of a discretely represented superseding member is (almost) exact; and (ii) the area the discretely represented, *non-superseded subset* of a ceding member is also (almost) exact. The subset that is not superseded can itself be simply connected or non-simply connected depending on the model (where the set of configurations assigned finite prior density is model dependent). For the precise details of the hot regions, refer forward to Sections 2.5.1 through 2.5.7.

We opt for two disjoint hot regions: the two distinct pulses visible in the phase-folded event data (Figure 1) are suggestive of two such regions being widely separated. Initially, we impose parity in the complexity of each hot region—i.e., an equal number of shape parameters and temperature components. We then consider models in which the hot regions have unequal complexities because it becomes clear that increasing the complexity of a particular hot region is unwarranted. In all cases we define the support of the joint prior so as to exclude limiting configurations in which the hot regions overlap; the reason being that extension of scope to such configurations requires specification and implementation[41] of additional logical conditions for a complete order of precedence in local radiation intensity evaluation. For a subset of models we impose antipodal symmetry of the hot regions, in order to crudely represent a heating distribution that is consistent with symmetry in the physical mechanisms driving surface X-ray emission, such as a dominantly or perfectly centered-dipolar field configuration. A magnetic field with finite higher-order structure is viewed as a closer approximation of physical reality; we represent this case crudely by breaking antipodal symmetry and defining additional parameters for a secondary hot region that are not derived from parameters of a primary hot region. However, self-consistent coupling of the magnetosphere to the surface radiation field is beyond the scope of this work, partly due to the associated increase in complexity of efficient model implementation for posterior computation.

We consider models with three or more mutually disjoint and separated radiating regions to be a logical extension of the model space if it is deemed that incrementally increasing the complexity of only two such regions is yielding insufficient advancement in posterior predictive performance—i.e., is not satisfactorily capturing observed structure in data for the resource expenditure—when approaching or extrapolating to the limit of what is considered computationally tractable by a group executing posterior computation. A salient advantage of such an approach is that it is more exhaustive with ideas for two hot regions and incrementally breaks symmetries; an apparent disadvantage is that some small set of conceivable closely related models with equal (continuous parameter) dimensionality are not applied.[42] It is, however, necessary to be selective—inherent to which is subjectivity and arbitrariness.

The above choices for surface radiation field configuration are somewhat consistent with the notion of the source being a rotation-powered X-ray pulsar with two relatively small hot regions that are disjoint. Therefore, we consider the proposed model space to be logically structured and a reasonable representation of widely held conceptions of such stars that are yet to be falsified statistically.

Whether or not such a model space is tractable given algorithm properties and computing resources is highly sensitive to the choice of parameterization for posterior computation, especially in phenomenological contexts. If degeneracies plague the problem at hand, it may be considered an indicator that either (i) the model is simply ill-defined, leading to forms of invariance of the parameterized sampling distribution on the space of the data; (ii) the model is needlessly or at least *unhelpfully* complex for describing observations, because despite (physical) parameters having a finite effect on forward data-generation, one is ultimately insensitive to such model structure. Usually this equates—at least in part—to transforming away nonlinear likelihood function degeneracies where possible. A number of sophisticated open-source sampling software packages efficiently handle linear degeneracies, even in multi-modal contexts, but nonlinear degeneracy remains fiendish: certain sampling algorithms can perform accurately,[43] but coupled with an expensive (numerical) likelihood function and moderately high-dimensional sampling spaces, still require massive computing resources.

As we highlight in Section 2.5 (where we provide more precise definitions of surface radiation field structure), the choice of parameterization of a (largely phenomenological) hot region plays a crucial role in sampling-space definition. In Appendix A we summarize the techniques adopted for posterior computation: we opt to perform nested sampling (Skilling 2006). The natural space for nested sampling is usually that of a unit hypercube, which maps to an equal-dimensional physical parameter space according to an inverse transformation derived from a joint (prior) probability distribution on the physical space (e.g., Feroz et al. 2009). Given that nested sampling algorithms tend to operate in such a native space, a parameterization that approaches optimality involves

[39] Such that one member is a superset of the other.

[40] The overall numerical accuracy remains implementation dependent.

[41] Efficient finite-element representations.

[42] For example, configurations in which three single-temperature regions are disjoint.

[43] At reduced efficiency relative to simpler contexts—see the MultiNest sampler cited in Appendix A.

both the physical parameterization *and* the inverse transformation from the native to physical space, and is such that continuous likelihood function degeneracies, if existent, manifest effectively linearly in the native space.

Usually a joint prior distribution is chosen to be weakly informative—or "flat"—in the context of the likelihood function, and in some cases is defined as an absolutely flat density function with respect to a joint space. It follows that the mapping from the parameter space to the native sampling space will then approximately preserve the linear degeneracy of a posterior mode. An exception to this occurs if the boundary of the support of the joint prior satisfies some set of non-trivial constraint equations.[44]

Priors. We define the joint prior density distribution $p(M, R_{\rm eq})$ to be *jointly* flat with compact support: a prophylactic choice that eases future use of samples on the $(M, R_{\rm eq})$-subspace for computing an approximative marginal likelihood function, which in turn can be used for estimation of interior source-matter properties—principally EOS parameters (see Riley et al. 2018; Riley & Watts 2019). We also choose the boundary of prior support to be close to maximally inclusive in regards to theoretical EOS predictions: we impose hard bounds $M \in [1,\ 3]\,M_\odot$, and impose that $R_{\rm eq} \in [3r_g,\ 16]$ km, where $r_g = r_g(M) = GM/c^2$ is the gravitational radius.

Although we allow the boundary of the prior support to extend down to the photon sphere of the ambient spacetime solution, when computing pulse profiles we only integrate over the *primary* images (along rays with angular deflection $\leqslant\pi$) of radiating elements subtended on the sky of the instrument. For a spherical star of radius $R < 3.52r_g(M)$, multiple images of parts of the star will be visible (Pechenick et al. 1983; Bogdanov et al. 2019b) requiring that light from the primary, secondary, and higher-order images be included—at additional computational expense—in an exact calculation of the flux; this issue, and how it pertains to oblate stars, is discussed in more detail elsewhere (Bogdanov et al. 2019b). From a computational statistics perspective, one could view the inclusion of one or more higher-order images as a modeling refinement to be made if, a posteriori, a rotating star is favored to be sufficiently compact: e.g., a substantial fraction of posterior mass lies at $R_{\rm eq}/r_g(M) \lesssim 3.6$. The parameter inference reported in this work favors much less compact stars a posteriori (refer forward to Figure 19), so multiple imaging is not deemed important. However, when images are neglected, the issue of choosing the most appropriate support for a joint prior distribution of M and $R_{\rm eq}$ remains an open problem for statistical modeling.

A typical likelihood function for pulse-profile modeling will express many modes of dependence on the compactness $r_g(M)/R_{\rm eq}$, and will generally be more sensitive to this combination than to M (or $R_{\rm eq}$) individually. We ensure the mapping from the parameter space to the native space preserves such linear degeneracy between M and $R_{\rm eq}$. In Appendix B we provide implementation details for the joint density $p(M, R_{\rm eq})$.

Finally, there exists a constraint on the distance of the PSR J0030+0451 system (Arzoumanian et al. 2018) that we adopt—in approximation—as an informative prior.

[44] An example of trivial constraint equations here are those that generate a (hyper-)rectangular support boundary in parameter space.

2.4.2. Instrument

In defining a generative model, the data space is constructed by phase-folding X-ray events in each detector channel and grouping those events into a uniform set of phase intervals (bins) to curate a set *count* numbers, typically with cardinality $\mathcal{O}(10^3)$. The conditional joint sampling distribution of these count numbers is always constructed in terms of a phase-energy-resolved signal that is generated during a *single* rotation of the source. Together with an appropriate nuisance background model (see Section 2.4.3), it follows that the instrument in such an analysis represents the temporal-mean operation of all detectors collectively in response to the incident radiation field from the source during the observation time intervals. We reserve a more elaborate discussion on these modeling facets for Section 2.4.3 (and also refer the reader to Riley & Watts 2019).

For every model we invoke the instrument response model: the on-axis `v1.02` ancillary response function (ARF) and an updated version of the `v1.02` redistribution matrix file (RMF; private communication from James Steiner, see Hamaguchi et al. 2019, for details of the updates) to generate a reference (or nominal) response matrix $\mathcal{R}^\star$ derived from microphysical knowledge. Let detector channels increment with row number i, and energy intervals increment with column number j, such that an element of the reference response matrix is denoted by $\mathcal{R}^\star_{ij}$. We use this reference matrix as a basis for a parameterized family of response matrices, and aim to compute (for each model) a joint posterior density distribution of continuous source parameters and continuous instrument (response matrix) parameters. It is well founded to parameterize the instrument because despite its synthetic nature, we do not consider its microphysical operation to be sufficiently *known*;[45] nevertheless, we define far fewer parameters for the instrument than for the source. While the following model ensures that operational uncertainty is included, the continuum of response models and the associated prior density distribution does not attempt to rigorously represent uncertainty in microphysical knowledge; given a close approximation to the radiation field incident on the telescope, we would expect the model to be conservative in terms of *prior* predictive performance.

We parameterize the response matrix using a calibration product derived from observations of a calibration source. For this work we use instrumental residuals derived from *NICER* observations of the Crab. These residuals are derived using the observations and following the procedure outlined in Ludlam et al. (2018), modified to use the appropriate number of detectors, ARF, RMF, and Sun-angle cut consistent with the PSR J0030+0451 data set (refer to Section 2.2). We acknowledge that the Crab is a remarkably different source to PSR J0030+0451: the expected operation of *NICER* (and X-ray instruments in general) in response to incident radiation fields is a function of its properties. The Crab exhibits a very different spectrum to PSR J0030+0451, being harder, more absorbed, and subject to astrophysical features; the Crab is also an extended source, not a point source, and is much brighter than the rotation-powered MSPs targeted by *NICER*.

The calibration product is a channel-by-channel vector $\mathscr{R}$ of ratios of observed Crab count numbers to count numbers derived

[45] In-flight astrophysical calibration sources, for instance, are in practice far brighter than science targets, and operation is conditional on the radiation field incident on the detectors.

using a theoretical incident spectrum and the reference response matrix $\mathcal{R}^\star$. Let the vector elements $\mathscr{R}_i := \mathcal{C}_i/(\mathcal{R}^\star \cdot \mathcal{F})_i$: in words, the element-wise division of an *observed* count vector $\mathcal{C}$ from some calibration source, by a vector $\mathcal{R}^\star \cdot \mathcal{F}$ where $\mathcal{F}$ is a vector of photon *fluences* (in the set of energy intervals inherent to the definition of $\mathcal{R}^\star$) computed given some theoretical model of said calibration source during the calibration observations. Note that the calibration product is derived from observations of a single chromatic source and thus is not resolved over elements of the matrix, only over the set of channels; therefore we apply the ratio $\mathscr{R}_i$ for the ith channel to all elements $\mathcal{R}^\star_{ij}$. The theoretical model is uncertain in the lowest 10 channels that we consider: the Crab is highly absorbed so that there is less data at low energies, and the telescopes used to generate the reference spectra for the residuals also perform poorly in this regime. In this work we therefore assume that $\mathscr{R}_i$ for $i \in [25, 35)$ is equal to $\mathscr{R}_{35}$.

We choose to construct the response matrix as a continuous three-parameter family, where the parameters are denoted by *NICER* α, *NICER* β, and *NICER* γ where possible, but reduced to the aliases α, β, and γ, respectively, for clarity of mathematical expressions. First we give the definition, and then we offer an interpretation in words. The parameterized matrix is defined as

$$\begin{aligned}\mathcal{R}_{ij}(\alpha, \beta, \gamma; \mathscr{R}, \mathcal{R}^\star) &:= (1-\beta)\gamma\mathcal{R}^\star_{ij} + \beta\alpha\mathscr{R}_i\mathcal{R}^\star_{ij} \\ &\equiv \gamma\mathcal{R}^\star_{ij} + \beta\underbrace{[\alpha\mathscr{R}_i\mathcal{R}^\star_{ij} - \gamma\mathcal{R}^\star_{ij}]}_{\text{calibration shift}} \\ &\equiv \mathcal{R}^\star_{ij}\underbrace{[\gamma + \beta(\alpha\mathscr{R}_i - \gamma)]}_{\eta_i}. \end{aligned} \tag{3}$$

In general an additional condition must be invoked: $\mathcal{R}_{ij}(\alpha, \beta, \gamma) := 0$ if $[(1-\beta)\gamma\mathcal{R}^\star_{ij} + \beta\alpha\mathscr{R}_i\mathcal{R}^\star_{ij}] \leqslant 0$ for $(\alpha, \beta, \gamma) \in \mathcal{S}_{(\alpha,\beta,\gamma)}$, where $\mathcal{S}_{(\alpha,\beta,\gamma)}$ is the joint prior support on the (α, β, γ)-subspace.[46] We note, however, that this parameterization exhibits a finite degree of degeneracy.

The parameter α scales the calibration vector $\mathscr{R}$, and manifests to target the assumption that the vectors $\mathcal{C}$ and $\mathcal{F}$ are *known*: in regards to $\mathcal{C}$, the assumption that the temporal-mean operation of the instrument between calibration and science observations is invariant (including, e.g., pointing vector relative to source line of sight and the flux-dependent effects); and in regards to $\mathcal{F}$, the assumption that the expectation of the incident radiation field from the Crab during the calibration observations is known. Thus, the parameter α represents the product of dimensionless element-invariant scaling factors applied, respectively, to vectors $\mathcal{C}$ and $\mathcal{F}$. The support of α is such that $\mathcal{S}_\alpha = \{\alpha: \alpha \in \mathbb{R}^{>0} \wedge 1 - \epsilon_\alpha \leqslant \alpha \leqslant 1 + \epsilon_\alpha\}$ where $0 < \epsilon_\alpha < 1$; the prior density function allocates mass mostly to the near vicinity of unity.

The parameter γ is an element-invariant scaling factor applied to the reference matrix $\mathcal{R}^\star$ alone. The reason that we choose $\alpha \neq \gamma$ is that γ operates on $\mathcal{R}^\star$, and thus because $\mathscr{R}$ is a function of $\mathcal{R}^\star$ (via the element-wise vector division written above), γ cancels. The support of γ is such that $\mathcal{S}_\gamma = \{\gamma: \gamma \in \mathbb{R}^{>0} \wedge 1 - \epsilon_\gamma \leqslant \gamma \leqslant 1 + \epsilon_\gamma\}$ where $0 < \epsilon_\gamma < 1$; the prior density function allocates mass mostly to the near vicinity of unity.

The parameter β is a weighting factor between matrices with elements $\gamma\mathcal{R}^\star_{ij}$ and $\alpha\mathscr{R}_i\mathcal{R}^\star_{ij}$—i.e., the element-invariant coefficient of the element-dependent calibration shift away from the $\gamma\mathcal{R}^\star$ matrix. Thus β may be interpreted as the degree to which the calibration vector $\mathscr{R}$ is used to modify the reference matrix $\mathcal{R}^\star$. Note that the prior support for a weighting parameter such as β is the unit interval $\beta \in [0, 1]$. We consider the limit $\beta \to 0$ as a useful safeguard against erroneous calibration—e.g., artifacts may be introduced by invoking a calibration source to which the instrument responds appreciably differently than it does to PSR J0030+0451. As $\beta \to 0$, $\mathcal{R}_{ij}(\alpha, \beta, \gamma) \to \gamma\mathcal{R}^\star_{ij}$, capturing a simple element-invariant scaling of $\mathcal{R}^\star$. On the other hand, in the limit $\beta \to 1$, we have $\mathcal{R}_{ij}(\alpha, \beta, \gamma) \to \alpha\mathscr{R}_i\mathcal{R}^\star_{ij}$.

Priors. To demonstrate the properties of the family of response matrices defined above, we (i) define a joint probability density distribution $p(\alpha, \beta, \gamma)$ that could be plausibly viewed as a *weak* prior on its compact support given that the instrument is an artificial system that has been closely studied, and (ii) then visualize the distribution in terms of derived properties (such as total effective area as a function on energy interval). Let $\alpha \sim N(1, 0.1)$ truncated such that $\alpha \in [0.5, 1.5]$; $\beta \sim U(0, 1)$; $\gamma \sim N(1, 0.1)$, truncated such that $\gamma \in [0.5, 1.5]$. In Figure 2 we display the prior distribution of the total on-axis effective area as a function of energy.

2.4.3. Likelihood Functions and Background

In the *X-PSI* documentation (Riley & Watts 2019) we offer a more complete overview of the supported class of generative models than is appropriate for this work—instead we adapt the *X-PSI* documentation to provide a summary. A generative model for raw on-board event data is eschewed by subsuming a non-parameterized portion of the modeling within a data pre-processing phase. In this work, a pulsar radio timing solution is invoked to transform events into a simpler time domain: a fictitious instrument, which is static (or Eulerian) and distant in the (Schwarzschild) spacetime of the source, is implicitly constructed to register events against the elapsed natural number rotations of the star, which is a clock related to the Schwarzschild coordinate time simply by an affine transformation. In all models we condition on the phase-resolved specific flux signal (incident on the instrument) generated by precisely *one* rotation of the star: accurate computation of such a signal, even when invoking spacetime spherical symmetry, is approaching the limit of what we consider tractable at present in terms of likelihood function callback cost for sampling processes in $\mathcal{O}(10)$-dimensional spaces.

In the context of a model for the joint probability distribution of observed events (see Riley & Watts 2019),[47] phase-folding said events is equivalent to computing one (average) rotational pulse and replicating it over the many rotational cycles in order to evaluate the likelihood function. It follows that, in this limit, no information is lost by transforming events to the unit interval because the underlying information content in the model is not summarized for comparison to data. In each instrument channel we choose to group events into a set of uniform-width phase intervals (bins) that are subsets of the unit interval, and define the data space as $\mathscr{D} := \mathbb{N}^{I \times K}$, where $I \in \mathbb{N}$

[46] Alternatively, one might define the joint prior support such that if for $(\alpha, \beta) = (\alpha', \beta', \gamma')$ the inequality is true for any (i, j), then the joint density is locally zero at $(\alpha', \beta', \gamma')$.

[47] Leading to an unbinned likelihood function.

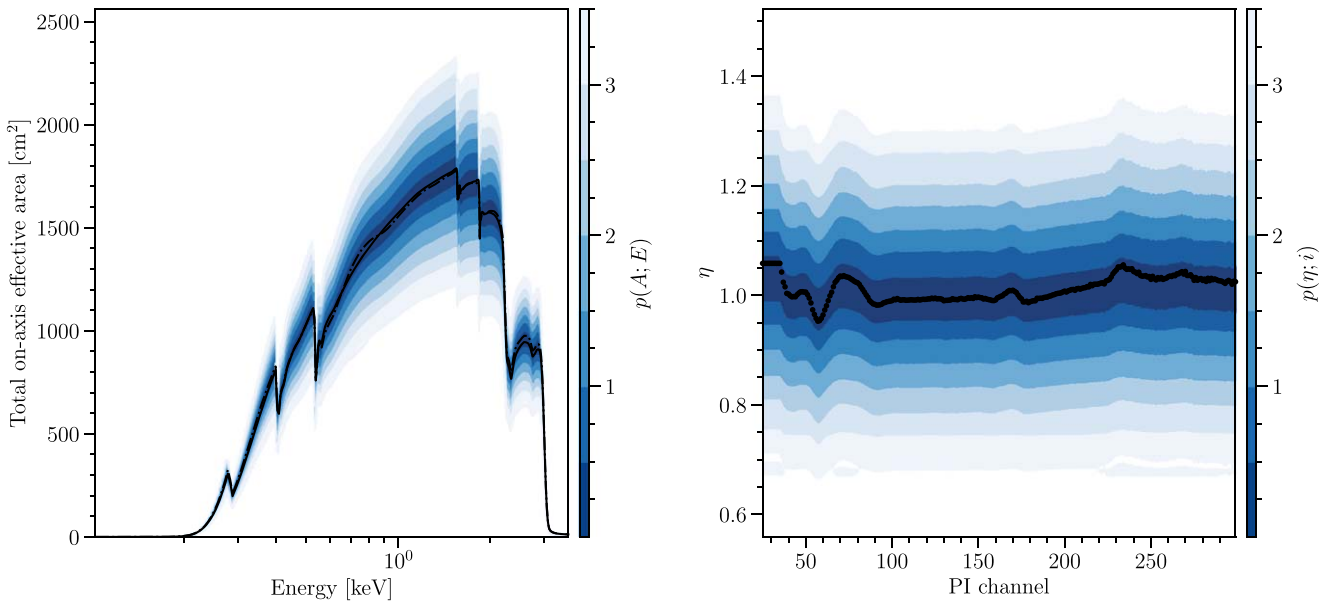

Figure 2. In the left panel we display marginal conditional prior probability density distributions of total on-axis effective area A as a function of energy (integrated over uniform intervals of width 5×10^{-3} keV), summed over the contiguous channel subset [25, 300). Note that the total *NICER* effective area at energies $\gtrsim$3 keV in particular is far greater than shown here. The prior $p(A; E)$ is represented by the blue contours. At energy E a set of (one-dimensional) highest-density credible intervals are estimated for $A = A(\alpha, \beta, \gamma)$; the credible intervals are connected as a function of energy, such that, e.g., the second-darkest band encodes the energy-dependence of the estimated 68.3% highest-density credible interval. We give the marginal prior distributions for the parameters α, β, and γ in Table 2. Note that the posterior information shown is not that of the joint distribution of effective areas over energy intervals: the effective areas are coupled by a functional form with three parameters. The range of the energy intervals is determined based on the RMF of the reference matrix $\mathcal{R}^\star$ and on the curated data set in the contiguous set of channels [25, 300), where these channels are summed over. The solid curve is that of the reference matrix $\mathcal{R}^\star$ (with $\gamma = 1$); the dashed–dotted curve is that of the calibrated matrix $\mathcal{R}_{ij} = \mathscr{R}_i \mathcal{R}^\star_{ij}$ (with $\alpha = 1$). In the right panel we display as black points the elements of the vector $\mathscr{R}$ of multipliers supplied for instrument parameterization based on the Crab as a calibration source. The prior $p(\eta; i)$, where i enumerates channels and η is defined in Equation (3), is represented by the blue contours; the probabilistic information is otherwise congruent in nature to that described for the left panel.

is the number of channels over which the folded events are distributed, and $K \in \mathbb{N}$ is the number of phase intervals; we choose $K = 32$ and $I = 275$ corresponding to channel subset [25, 300). Information loss is an inherent consequence of compression of events into a smaller set of summary quantities, but the phase resolution is sufficiently high here to mitigate our concern about the use of a binned likelihood function instead of an unbinned likelihood function. The conditional joint sampling distribution on the space $\mathscr{D}$ is assumed to be purely Poissonian and separable over channels: the *NICER* instrument exhibits sufficiently high-resolution event-timing capabilities for the Poissonian nature of the incident radiation field to be effectively conserved as an event arrival process in the on-board time domain (see Riley & Watts 2019, for a more explicit set of arguments pertaining to this matter).

Let the likelihood function for phase-folded and binned events be defined by (see also Miller & Lamb 2015)

$$L(\boldsymbol{\theta}, \boldsymbol{B}) \coloneqq p(\{\boldsymbol{d}_i\}_{i=1,\ldots,I} \mid \boldsymbol{\theta}, \{B_i\}) = \prod_{i,k} p(d_{ik} \mid \boldsymbol{\theta}, B_i), \quad (4)$$

where $i \in [1, I]$ enumerates channels of the instrument; each $\boldsymbol{d}_i$ is a data vector associated with the ith channel, constituted by count numbers $\{d_{ik}\}_{k=1,\ldots,K}$ where k enumerates phase intervals $\phi_k \subset [0, 1]$; B_i is the (nuisance) background count-rate parameter in the ith channel; and $\boldsymbol{\theta}$ are the continuous source parameters that constitute the sampling space, and on which source expected count numbers $s_{ik}(\boldsymbol{\theta})$ are dependent. Each B_i is defined as the expectation of a homogeneous—i.e., time invariant—Poisson arrival process: up to a known constant,

$$\ln L(\boldsymbol{\theta}, \boldsymbol{B}) = -2\sum_{i,k} d_{ik} \ln\left[s_{ik}(\boldsymbol{\theta}) + B_i\left(\sum_\ell \Delta t_\ell\right)\int_{\phi_k} d\phi\right] - s_{ik}(\boldsymbol{\theta}) - B_i\left(\sum_\ell \Delta t_\ell\right)\int_{\phi_k} d\phi. \quad (5)$$

Such background treatment is the default for *NICER* parameter estimation work and *X-PSI* (for implementation details see Appendix B of Riley & Watts 2019), and is based on Miller & Lamb (2015). In reality, the statistical properties of backgrounds do not exhibit time invariance, but exhibit long-term variation over the $\mathcal{O}(1)$ year observation epoch of MSPs target by the *NICER* mission, especially due to factors such as dynamical space weather (Bogdanov et al. 2019a). However, any background emission processes—and dynamical emission processes in the local vicinity of PSR J0030+0451—that are not harmonically coupled to the surface X-ray emission will *decohere* over the unit phase interval whose boundary is periodic. It follows that event phase-folding enables invocation of phase-invariant channel-by-channel (background) count-rate terms.

The background below $\sim$3 keV for *NICER* observations of PSR J0030+0451 observations consists of (Bogdanov et al. 2019a) (i) cosmic energetic particle events and diffuse X-ray emission over the $\sim$30 arcmin^2 field of view (Arzoumanian et al. 2014); (ii) many nearby X-ray point sources in the field

that make a small total contribution relative to the targeted MSP; and (iii) solar system contamination, including optical loading (pointing Sun-angle dependent), and high-energy non-cosmic particles and radiation. Considering a proper subset of detector channels and filtering background events during the pre-processing phase acts to reduce background contribution, but some subset of background events survive and must be modeled (Bogdanov et al. 2019a).

The source terms $s_{ik}(\boldsymbol{\theta})$ in Equation (5) are then derived as follows. Let $F(\phi, E; \boldsymbol{\theta})$ denote the incident specific photon flux from the source as a function of rotational phase ϕ. The function $F(\phi, E; \boldsymbol{\theta})$ is evaluated numerically at a regular discrete set of points in the joint space of energy and phase, as an approximating two-dimensional integral over the solid angle of the image of the source subtended on the sky of a point in the vicinity of the distant static instrument; given the discrete representation, a continuous representation is constructed via spline interpolation in *X-PSI*.

Let the symbol $\mathcal{R}_{\ell ij}(\hat{r})$ denote a temporal-mean point-source response matrix invoked for the ℓth observing interval, which is dependent on the radial coordinate unit vector $\hat{r}$ in the Schwarzschild chart at the location of the instrument—i.e., the pointing of the telescope relative to the source. The response matrix with elements

$$\mathcal{R}_{ij}(\hat{r}) = \sum_{\ell} \frac{\Delta t_{\ell}}{\left(\sum_{\ell} \Delta t_{\ell}\right)} \mathcal{R}_{\ell ij}(\hat{r}) := \mathcal{R}_{ij}(\alpha, \beta, \gamma) \tag{6}$$

is the exposure-time-weighted mean response matrix that is modeled as the matrix defined in Equation (3) and Section 2.4.2.

The source contribution to the expected number of counts is given by

$$\begin{aligned} s_{ik}(\boldsymbol{\theta}) &= \textstyle\sum_{\ell,j} \mathcal{R}_{\ell ij}(\hat{r}) \Delta t_{\ell} \int_{\phi_k \times \boldsymbol{E}_j} F(\phi, E; \boldsymbol{\theta}) dE d\phi \\ &= \textstyle\sum_j \left[\left(\sum_{\ell} \Delta t_{\ell}\right) \underbrace{\int_{\phi_k \times \boldsymbol{E}_j} F(\phi, E; \boldsymbol{\theta}) dE d\phi}_{\boldsymbol{F}_{jk}(\boldsymbol{\theta})} \right] \\ &\quad \times \textstyle\sum_{\ell} \frac{\Delta t_{\ell}}{\left(\sum_{\ell} \Delta t_{\ell}\right)} \mathcal{R}_{\ell ij}(\hat{r}). \end{aligned} \tag{7}$$

A matrix of source count numbers may thus be evaluated as the dot-product[48]

$$\boldsymbol{s}(\boldsymbol{\theta}) = \left(\sum_{\ell} \Delta t_{\ell}\right) \mathcal{R}(\alpha, \beta, \gamma) \cdot \boldsymbol{F}(\boldsymbol{\theta}), \tag{8}$$

where $\boldsymbol{F}(\boldsymbol{\theta})$ is a matrix of phase-integrated incident photon fluxes.[49] Note that the elements of the matrix $\boldsymbol{F}(\boldsymbol{\theta})$ may be approximated using instantaneous fluxes at points *within* the finite phase intervals instead of explicitly integrating over those intervals, provided that the intervals are determined to be sufficiently small.

We numerically marginalize the likelihood function given by Equation (5) over the subspace of nuisance background parameters $\boldsymbol{B}$ in order to improve tractability of the sampling process. The target distribution (the posterior) for sampling is written conditional on model $\mathcal{M} \subset \mathscr{M}$ as

$$\begin{aligned} \pi(\boldsymbol{\theta} \mid \boldsymbol{d}, \mathcal{M}) = \int \pi(\boldsymbol{\theta}, \boldsymbol{B} \mid \boldsymbol{d}, \mathcal{M}) d\boldsymbol{B} \propto p(\boldsymbol{\theta} \mid \mathcal{M}) \\ \times \underbrace{\int L(\boldsymbol{\theta}, \boldsymbol{B}) p(\boldsymbol{B} \mid \mathcal{M}) d\boldsymbol{B}}_{L(\boldsymbol{\theta})}, \end{aligned} \tag{9}$$

where $L(\boldsymbol{\theta}) = p(\boldsymbol{d} \mid \boldsymbol{\theta}, \mathcal{M})$ is the marginal likelihood function supplied as a callback for a sampling process, and the joint prior density distribution $p(\boldsymbol{\theta}, \boldsymbol{B} \mid \mathcal{M})$ is separable with respect to $\boldsymbol{\theta}$ and $\boldsymbol{B}$. The joint prior distribution $p(\boldsymbol{B} \mid \mathcal{M})$ is equivalent for all models: jointly flat and separable. Crucially, such a phenomenological background model exhibits a large prior complexity; for instance, the joint density at a background count rate vector $\boldsymbol{B}$, where the variation between channels is always small relative to the limiting instrument count rate, is equivalent to the joint density at a vector $\boldsymbol{B}$ whose elements exhibit vast channel-to-channel variations. It follows that a joint flat, separable prior is not considered representative of our prior belief. However, we consider—without proof—the prior to be weakly informative because (i) the conditional likelihood function (given a fixed source vector) exhibits a large curvature relative to the prior density function; (ii) the source photon flux signal always has few extrema in the joint space of energy and phase; and (iii) a posteriori the conditional likelihood function maxima do not wildly fluctuate as a function of channel because such structure does not exist in the data set. Nevertheless, if one were to compare, based on prior predictive performance, the models that we consider in this work with a model invoking a background component with far lower complexity, one should not be surprised if the former are strongly disfavored.

In general, the support of $p(\boldsymbol{B} \mid \mathcal{M})$ is compact and bounds can be specified on a channel-by-channel basis to truncate the marginalization integrals. Lower bounds may be derived, for example, from calibration observations of nearby fields that exclude the PSR J0030+0451 and are otherwise devoid of bright sources. Upper limits may, for example, be based on distinct *NICER* observations of the field containing PSR J0030+0451.

For this work, however, we define the lower bound as zero for each channel, and we eschew definition of an upper bound in each channel because the posterior is considered integrable: non-diverging on joint compact support, and the conditional likelihood function—$L(\boldsymbol{\theta}, \boldsymbol{B})$ for fixed $\boldsymbol{\theta}$—asymptotes to zero at large background count rates. If a set of sufficiently high upper bounds *were* specified (e.g., based on *NICER* count rate limits), the associated normalizing constant for the joint prior, equal to the reciprocal of the products of those bounds, would not modulate relative probability measures defined on $\mathscr{M}$.[50] We therefore do not view the improperness of the above prior as a misdemeanor, but it does mean that we should not describe our model as *generative* in the strictest sense.

[48] An approximation in many ways, one being the discrete representation of an instrument that responds in a continuous manner to input.

[49] In the *X-PSI* implementation phase integration is performed using splines after a dot-product operation on a matrix of instantaneous incident photon fluxes.

[50] The raw event count rate during the exposures used to curate the data set for this work is known to be far below limiting and thus the conditional likelihood function is always relatively small for near-limiting background count rates. A set of upper bounds defined in this limit therefore truncates the evidence integral in a regime where model-dependent sensitivity is negligible.

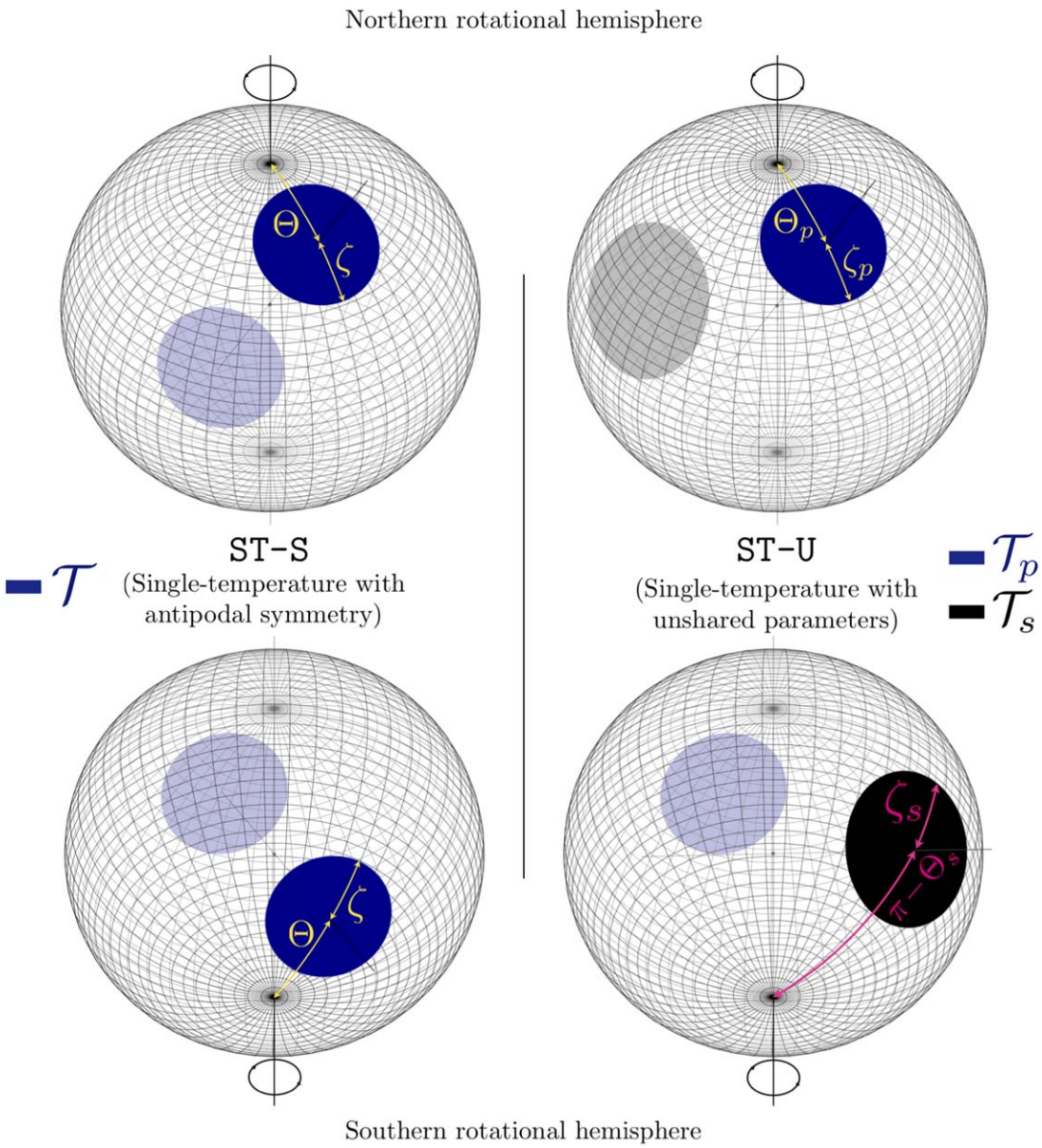

Figure 3. Schematic diagrams of models with single-temperature regions: ST-S defined by antipodal symmetry of the primary and secondary regions, and ST-U defined by the primary and secondary regions not sharing any parameters. Note that the two-surface shown is spherical: the hot regions are defined in spherical coordinates on a (unit) sphere and projected onto the rotationally distorted (oblate) spheroid representing the two-surface of the star, such that the proper areas of the regions are only implicitly defined. To construct the ST-U diagram from the ST-S diagram we displaced the secondary region (defined by having a center colatitude $\Theta_s \geqslant \Theta_p$) away from the antipode of the center of the primary region (with center colatitude Θ_p), decreased ζ_s such that $\zeta_s < \zeta_p$, and assigned the secondary region a distinct temperature parameter. Note that no numeric relationship is implied between the effective temperatures of material within each member—indeed, the prior is separable with respect to the temperatures ($\mathcal{T}_p$ and $\mathcal{T}_s$), and the support includes combinations $\mathcal{T}_s \leqslant \mathcal{T}_p$ and $\mathcal{T}_s > \mathcal{T}_p$. For clarity we display for ST-S a projection showing the southern rotational hemisphere; in subsequent diagrams we omit such a projection when antipodal symmetry applies.

The numerical marginalization operation implemented is described in Appendix B of the *X-PSI* documentation (Riley & Watts 2019).

2.5. Model-specific Definitions

The surface heating distribution by realistic magnetospheric (return) currents remains uncertain. The global magnetic field may be more complex than a simple dipole (at least in the near vicinity of the surface), while the mapping between currents and surface temperature field is not well determined by existing theoretical models (Harding & Muslimov 2001, 2011; Timokhin & Arons 2013; Philippov et al. 2015a; Gralla et al. 2017; Lockhart et al. 2019). We thus consider a set of simplified models that are representative of the various theoretical possibilities, albeit restricting our analysis to models with two distinct hot regions. We allow for the possibility of the hot regions being non-antipodal and non-identical (Pavlov & Zavlin 1997; Bogdanov et al. 2007, 2008; Bogdanov 2013); we also consider various hot-region shapes, including circles, rings, and crescents filled with material of uniform local comoving temperature.

While our choices are physically motivated, it is important to emphasize that our inferences are conditional upon these choices. However, posterior computation is computationally intensive and scales with model complexity. The work

presented here is based on usage of a 500,000 core-hour grant on the Dutch national supercomputer Cartesius; we thus find it pragmatic to disseminate information to the community at this point. Further exploration of model variants or execution of higher-resolution calculations requires additional resource allocation on high-performance systems, building upon the information offered here as guidance. In particular, it will be important to explore the sensitivity of marginal posterior estimates of fundamental physical parameters of interest—i.e., exterior and interior spacetime parameters—to expansion of the space of models that we have had the resources to consider.

In this section we detail the properties that distinguish the models in our model space. For each model we give the parameterization details and any remarkable prior details; notes on the *support* of the joint prior distribution are given where appropriate. We also discuss the existence of (continuous linear and nonlinear) degeneracy in posterior modes for a given parameterization, which we interpret as one indicator of unnecessary complexity for a surface radiation field with phenomenological spatial structure. For each model whose associated posterior distribution we compute, we provide a summary table containing a more precise definition of the joint prior distribution; these tables may be found in Section 3 and in Appendix C.

2.5.1. Single-temperature Regions with Antipodal Symmetry (ST-S) and with Unshared Parameters (ST-U)

Parameterization. The primary hot-region (refer to the leftmost panel of Figure 3) is simply connected and encloses radiating material—a fully ionized hydrogen NSX atmosphere with effective temperature $\mathcal{T}$. The boundary of the region is *circular*: i.e., given a *center* point on the surface with colatitude Θ_p and azimuth ϕ_p (in a spherical coordinate basis whose polar axis is defined as the stellar rotation axis), the boundary is the locus of points that are equidistant[51] in angular space from the center point.

Hereafter we use the alias ST-S, parsed as *Single-Temperature-Shared*. The surface radiation field associated with the secondary hot region is derived exactly by applying antipodal symmetry to the primary region: there are no free parameters associated with the secondary region.

Similarly, we use the alias ST-U, parsed as *Single-Temperature-Unshared*. The primary region (refer to the rightmost panel of Figure 3) definition is retained from ST-S as defined above. The secondary region, however, is now endowed with distinct parameters—i.e., the region is *not* derived from the primary region under antipodal symmetry. The parameters of the secondary region have an otherwise equivalent meaning—in terms of surface radiation field specification—to their primary-region counterparts.

Degeneracy. We note that a discrete degeneracy—multimodality—can in principle arise for a source such as PSR J0030+0451, but may only be weak when there is detectable asymmetry between the two component pulses over the course of one rotational cycle. There may exist two phase solutions, each corresponding to a distinct mapping between hot regions (distinguished by colatitude) and the pulse components in the event data. For instance, the primary (lower-colatitude) region could in principle generate either of the component pulses, while the secondary region generates the other. Fortunately, a number of open-source sampling software packages are designed to handle multi-modality efficiently (at least in the absence of nonlinear degeneracy). If the asymmetry between the component pulses is clear, the posterior mass in one mode may be entirely dominant.

Priors. For ST-S, we eliminate a region-exchange degeneracy by imposing a constraint $\Theta_p \leqslant \pi/2$ on the prior support. The primary region is uniquely defined as the region whose center subtends the smallest colatitude, Θ_p, to the rotational axis, if the region colatitudes are different.

For ST-U, we eliminate a region-exchange degeneracy by imposing a constraint $\Theta_p \leqslant \Theta_s$ on the support of the joint prior distribution. The primary region is uniquely defined as the region whose center subtends the smallest colatitude, Θ_p, to the rotational axis, if the region colatitudes are different; the regions are distinguishable when $\Theta_p = \Theta_s$ according to the subset of parameters that controls their physical manifestation. The joint prior support is such that the two regions cannot overlap but otherwise are not restricted to be antipodally symmetric.

2.5.2. Concentric Single-temperature Regions with Antipodal Symmetry (CST-S) and with Unshared Parameters (CST-U)

Parameterization. The primary hot region (see the leftmost panel of Figure 4) is a non-simply connected annulus (or ring) with outer angular radius ζ, which contains material with effective temperature $\mathcal{T}$. The non-radiating *hole* with angular radius ψ is concentric (in angular coordinates) with the radiating annulus. We thus recover the shape defined for the ST-S and ST-U variants in the limit $\psi \to 0$ (which is at the boundary of the prior support).

A generally useful way to distinguish the hole and the annulus—in particular for further increments in complexity—is as follows. Recall the term *member* from Section 2.4.1: consider two simply connected partially overlapping member regions, each wholly filled with radiating material, but impose the logical condition that when evaluating radiating intensities at a spacetime event on the stellar surface, one member—the hole—takes precedence if the event falls within its boundary. In this case (for the models here described), let the temperature of the material in the hole be (effectively) zero so that no signal need be computed for the hole. The statements in Section 2.4.1 pertaining to the proper areas in finite-element representations of radiating regions apply here: the annulus is a subset of a (simply connected circular) ceding member that is *not superseded* by the hole when evaluating local radiation intensities, and its proper area is computed (almost) exactly. These constructions are useful for further extension of the model.

Hereafter we use the alias CST-S, parsed as *Concentric-Single-Temperature-Shared*. For CST-S, the surface radiation field associated with the secondary region is derived exactly by applying antipodal symmetry to the primary region: there are no free parameters associated with the secondary region. The annuli share an outer angular radius ζ, and the holes share a fractional angular radius f such that the hole angular radii are $\psi := f\zeta$.

Similarly, we use the alias CST-U, parsed as *Concentric-Single-Temperature-Unshared*. For CST-U, the primary region (refer to the rightmost panel of Figure 4) definition is retained

[51] The ambient spacetime is static, and with respect to a Schwarzschild chart, the points are equidistant in angular coordinates. However, when projected from a spherical two-surface onto that of a rotationally deformed (oblate) spheroid, the spacelike separation—on a Schwarzschild temporal hyperslice—between the center point and boundary points is *not* invariant.

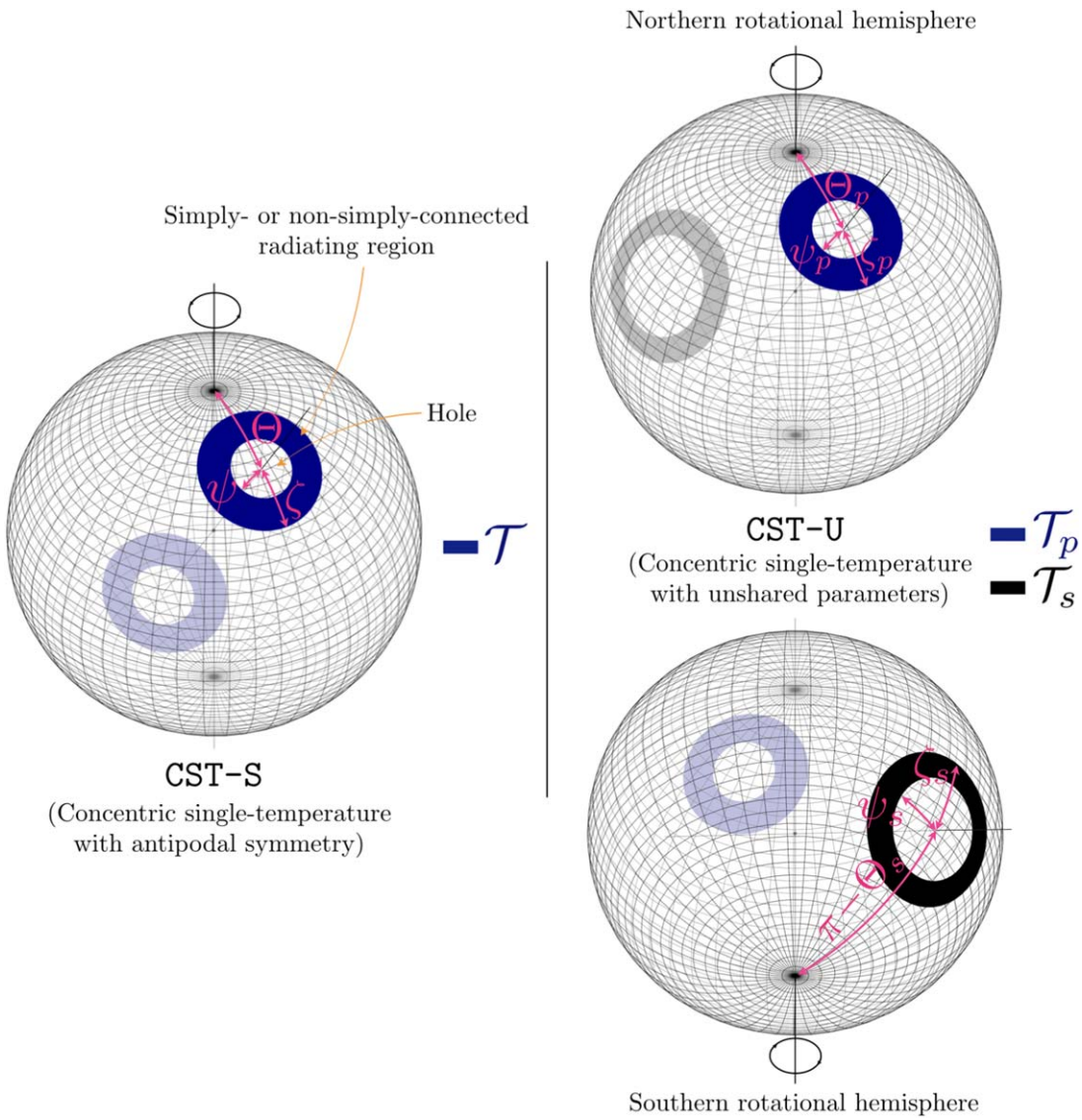

Figure 4. Schematic diagrams of models with concentric single-temperature regions: `CST-S` defined by antipodal symmetry of the primary and secondary regions, and `CST-U` defined by the primary and secondary regions not sharing any parameters.

from `CST-S` as defined above. The secondary region, however, is now endowed with distinct parameters—i.e., it is *not* derived from the primary region under antipodal symmetry. The parameters of the secondary region have an otherwise equivalent meaning—in terms of surface radiation field specification—to their primary-region counterparts.

Degeneracy. We now consider the continuous degeneracy labeled I in Figure 5. When the angular extent of a radiating region is small, the signal generated by that region—as registered by a distant detector that does not spatially resolve (image) the star—is insensitive to its shape (detailed spatial structure). Sensitivity is here a measure in terms of the likelihood: i.e., the *total* variation of the parameterized joint sampling distribution of a set of random variables,[52] in response to motion along a certain set of curves[53] in parameter space, is small as summarized by the scalar likelihood. It follows that if the shape is parameterized with more than a single degree of freedom, the likelihood function is degenerate with respect to shapes that satisfy a constraint on the solid angle subtended by the radiating region at the center of the star, and thus which satisfy a constraint on the proper area of the radiating region.

The degeneracy is not in this instance exact, but holds approximately. Consider a ceding member of angular extent $\cos\zeta \lesssim 1$ and hole with angular extent $\cos\psi > \cos\zeta$: the degeneracy is such that the solid angle, $\varpi(\zeta, \psi) = \cos\psi - \cos\zeta$, of the hot region (the annulus), is approximately $\varpi = 1 - \cos\tilde{\psi}$, where $\zeta = \tilde{\psi}$ is the angular radius in the limit $\psi \to 0$. In other words, the relative size—and indeed existence—of the hole is at most weakly constrained on small angular scales. This degeneracy in the (ζ, ψ)-subspace is nonlinear for $\zeta \to \tilde{\psi}$, but linearizes for increasing $\zeta > \tilde{\psi}$; however, with increasing ζ the signal generated by the region evolves away from that generated in the limit $\zeta \to \tilde{\psi}$ with $\psi \to 0$. Note that if the superseding member is not concentric with the ceding

[52] And whose number usually exceeds the number of parameters.

[53] Where those curves may more generally together generate m-dimensional surfaces in an n-dimensional space where usually $n > m$—if $m = n$ then no facet of the model is constrainable and the model is arguably not useful unless it can meaningfully tested in some other manner.

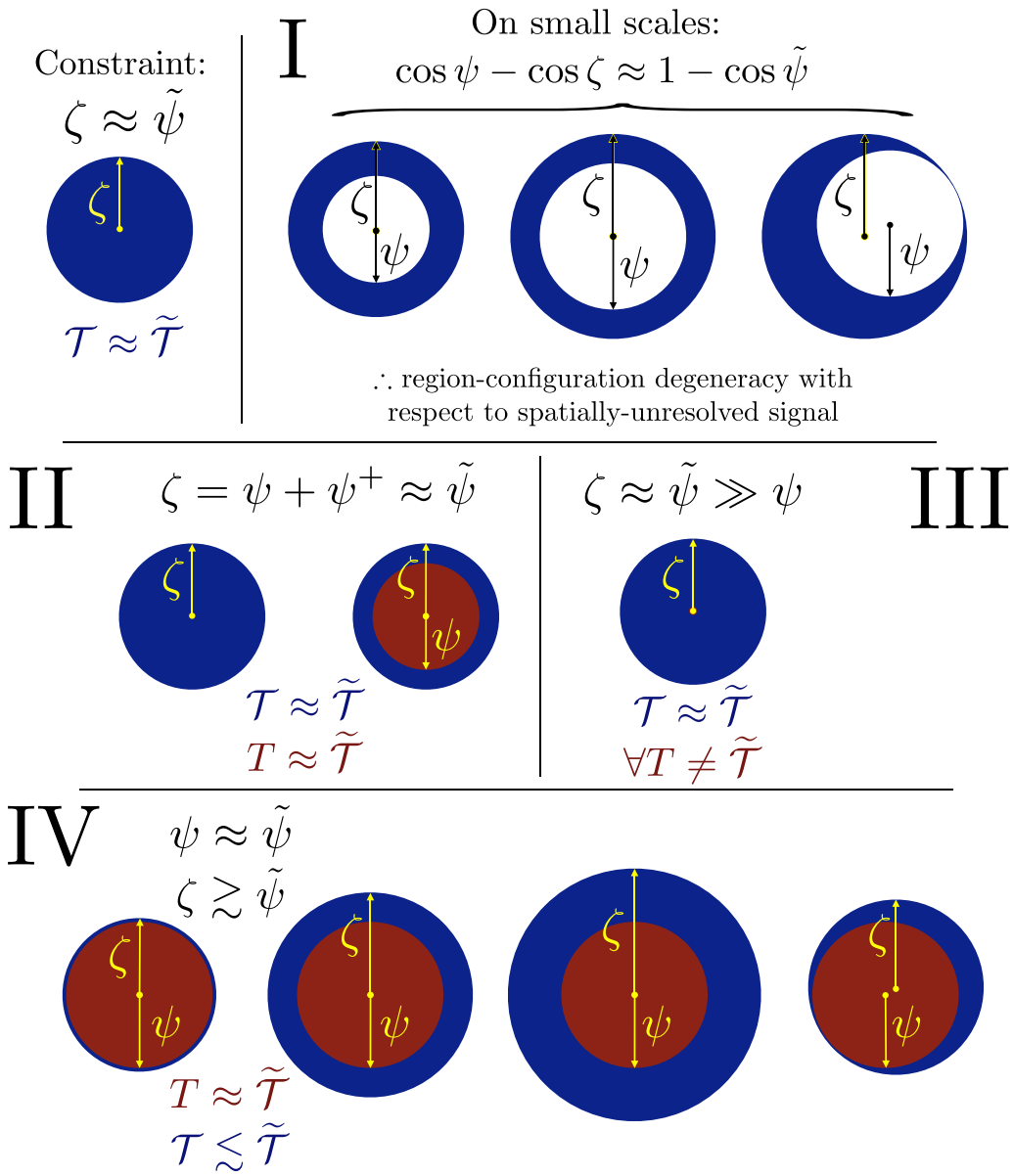

Figure 5. Schematic diagram of (approximate and exact) continuous degeneracies between hot-region structure parameters with respect to the energy-phase-resolved signal incident on a distant telescope. Degeneracy type I is discussed in detail in Section 2.5.2, while types II through IV are discussed in Section 2.5.3; here we focus on defining the components of the diagram. In all cases, let us suppose that there exists a strong posterior constraint on the (coordinate) solid angle ϖ subtended by a component of a hot region (at the stellar origin) with temperature $\tilde{\mathcal{T}}$. Type I—we consider a hot region with a single-temperature component, and represent such a region as simply connected with a strongly constrained radius $\zeta = \tilde{\psi}$. If the angular extent of the headed region is sufficiently small that we are insensitive (in the absence of spatial imaging power) to structural details other than solid angle ϖ, then we can introduce a hole of angular radius ψ such that the hot region has the topology of a ring and a likelihood function degeneracy $\varpi = \cos\psi - \cos\zeta =$ const. manifests (on small angular scales). Similar arguments can be made for other parameterized structural modifications to the hot region. Type II—let us consider a hot region constructed from an annulus and a hole (concentric or eccentric), each filled with material of local comoving temperature $\mathcal{T}$ and T, respectively. Let us assume a strong constraint on the outer angular radius $\zeta = \tilde{\psi}$ of the annulus, where $\tilde{\psi}$ is now not restricted to small angular scales; let us further assume a strong constraint on the structure of the hot region as simply connected circular with uniform temperature $\tilde{\mathcal{T}}$, where only one temperature component is useful. It follows that degeneracy manifests for $\mathcal{T} \approx T \approx \tilde{\mathcal{T}}$ and $\psi + \psi^{+} \approx \tilde{\psi}$, where $\psi^{+} := \zeta - \psi$. Type III—as type I, but in the limit that $\zeta \gg \psi$, such that the signal generated by the hole, whose temperature is degenerate over a range dependent on ψ, is effectively turned off. Type IV—the signal generated by the hole now satisfies the constraints assumed for type II—i.e., $T \approx \tilde{\mathcal{T}}$ and $\psi \approx \tilde{\psi}$—while the solid angle, temperature, and coordinates of the annulus exhibit degeneracy with respect to configurations that effectively turn off the signal generated by the annulus.

member, and the overlap is only partial, the form of the degeneracy—the constraint equation satisfied—has additional dependence on the coordinates of the center of the hole relative to the center of the ceding member.

It is important to be aware of such degeneracy for the purpose of efficient posterior computation—inherent to which is accuracy. In our case, if the type of signal that is superior for describing the event data is generated by radiation from a localized region on the star, the constraint on the solid angle of the region can be viewed as dragging a posterior mode through parameter space along the type I degeneracy direction. Thus, with this parameterization, nonlinearity will exist that will reduce efficiency to some degree.[54]

[54] Which can only be robustly learned during computation.

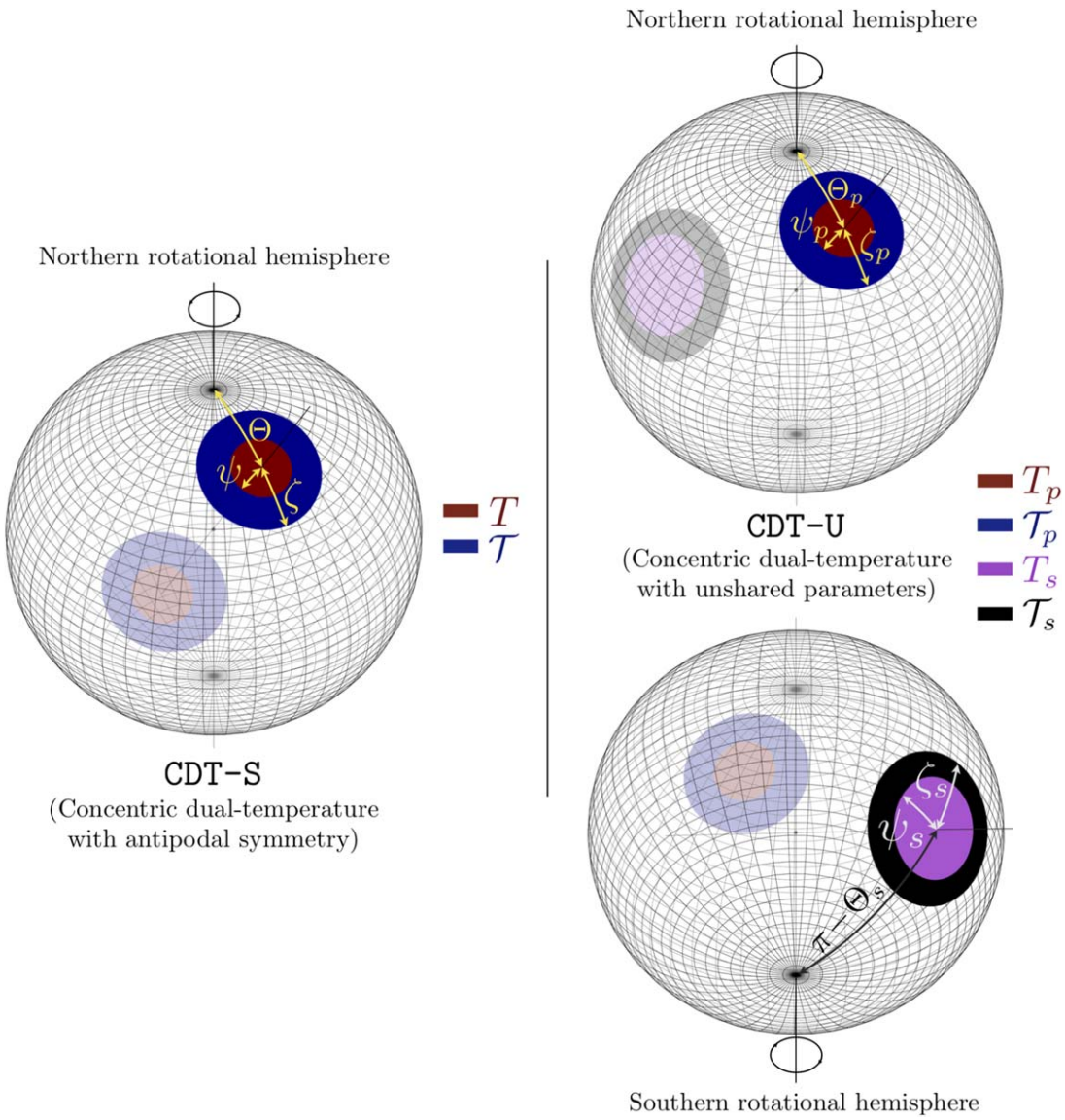

Figure 6. Schematic diagrams of models with concentric dual-temperature regions: `CDT-S` defined by antipodal symmetry of the primary and secondary regions, and `CDT-U` defined by the primary and secondary regions not sharing any parameters. To construct the `CDT-U` diagram from the `CDT-S` diagram we displaced the secondary region (defined by having a center colatitude $\Theta_s \geqslant \Theta_p$) away from the antipode of the center of the primary region (with center colatitude Θ_p), decreased ζ_s such that $\zeta_s < \zeta_p$ while leaving $\psi_s = \psi_p$, equivalently meaning $f_s > f_p$, and assigned distinct colors to the hole and annulus of the secondary region. We retained the caveat that no numeric meaning is implied regarding the effective temperature of the material in the members—indeed, the prior is separable with respect to all temperatures (T_p, $\mathcal{T}_p$, T_s, $\mathcal{T}_s$), and the support includes combinations $\mathcal{T}_s \leqslant T_s$ and $\mathcal{T}_s > T_s$.

If the posterior predictive performance is maximal for signals that are generated by localized emission, and degenerate posterior structure is observed, then clearly the most effective manner in which to achieve efficiency increase is to *reduce* the complexity of the structure of the radiating region. One thus inserts a simpler model into the model space, with the caveat that while estimation of ulterior model parameters should be insensitive to this reduction in complexity, the evidence may not be.

Alternatively, working with an integral summary variable such as the solid angle ϖ of the (uniform temperature) radiating region is useful from the perspective of eliminating degeneracy by parameterizing directly in terms of variables to which we are statistically sensitive. On the other hand, the mapping from ϖ to variables that directly control the shape of the radiating regions can behave undesirably, and can thus complicate the action of extending models.

One potential avenue for efficiency improvement by linearizing the degeneracy, is to sample in the space of $(\cos\zeta, \cos\psi)$, which will eliminate the emergent small-scale nonlinear degeneracy. The cost is complication of the joint prior definition and implementation: in this case, a singularity[55] exists in the mapping for $\psi \to 0$, which is the boundary at which the radiating region reduces to being simply connected as for both `ST-S` and `ST-U`. If we define finite joint prior density $p(\zeta, \psi)$ at points where $\psi = 0$, the joint density $p(\cos\zeta, \cos\psi)$ is divergent (although integrable, possibly in closed form).

Priors. An issue to be aware of is that the mapping from the native sampling space—that of the unit hypercube—would need to avoid introducing nonlinearity, otherwise the effort to

[55] Note that Taylor-expanding on small angular scales to work in the joint space of (ζ^2, ψ^2) by definition cannot bypass the singularity.

improve efficiency may be in vain (see the discussion in Section 2.4.1 regarding implementation of the joint prior distribution of M and $R_{\rm eq}$).

We define the prior as separable on the joint space of f and ζ. Specifically, we condition on $f \sim U(0,\ 1)$ and $\zeta \sim U(\epsilon_\zeta, \pi/2 - \epsilon_\zeta)$ where $\epsilon_\zeta \ll \pi/2$. For posterior computation, in order to ease prior implementation, we opt to transform the prior onto the joint space of ψ and ζ and accept the nonlinear degeneracy in the limit $\zeta \to \tilde{\psi}$ for small $\tilde{\psi}$. The chosen joint prior is not separable on this chosen space, but remains straightforwardly implementable.

For CDT-U, we eliminate a region-exchange degeneracy by imposing a constraint $\Theta_p \leqslant \Theta_s$ on the support of the joint prior distribution. The primary region is uniquely defined as the region whose center subtends the smallest colatitude, Θ_p, to the rotational axis; the regions are distinguishable when $\Theta_p = \Theta_s$ according to the subset of parameters that controls their physical manifestation. The joint prior support is such that the two regions cannot overlap but otherwise are not restricted by antipodal symmetry. Note that imposing that the regions are non-overlapping modifies the marginal prior density $p(\zeta)$—and thus $p(\psi)$—by redistributing prior mass to lower angular radii.

2.5.3. Concentric Dual-temperature Regions with Antipodal Symmetry (CDT-S) and with Unshared Parameters (CDT-U)

Parameterization. We extend the CST models by filling the *holes* (the superseding members) with radiating material at finite temperature and evaluating the signal generated by both the superseding and ceding members. The hot region is simply the union of the members together with an order of precedence, and can be considered to have two heated *subregions* with distinct temperatures, each of which generates a *component* of the signal.

Hereafter we use the alias CDT-S, parsed as *Concentric-Dual-Temperature-Shared*. For CDT-S, the surface radiation field associated with the secondary region is derived exactly by applying antipodal symmetry to the primary region: there are no free parameters associated with the secondary region. The annuli share an outer angular radius ζ, and the holes share a fractional angular radius f such that the hole angular radii are given by $\psi := f\zeta$.

Similarly, we use the alias CDT-U, parsed as *Concentric-Dual-Temperature-Unshared*. For CDT-U, the primary region (see the rightmost panel of Figure 6) definition is retained from CDT-S. The secondary region, however, is now endowed with distinct parameters—i.e., it is *not* derived from the primary region under antipodal symmetry. The parameters of the secondary region have an otherwise equivalent meaning—in terms of surface radiation field specification—to their primary-region counterparts. It follows that parameter vectors that correspond to, e.g., the primary region having a hotter annulus while the secondary region has a hotter hole, are assigned finite local joint prior density.

Degeneracy. Introducing a second temperature component also introduces degenerate structure in the likelihood function—a fundamental problem with such phenomenological descriptions of the surface radiation field. We now consider the continuous degeneracies labeled I, II, III, and IV in Figure 5.

Degeneracy of type I manifests on small angular scales when the temperature T of the superseding member is small relative to the temperature $\mathcal{T}$ of the ceding member. In this case, the signal from the superseding member is dominated and we effectively recover the structure from the CST models; the reader should imagine the hole in panel I of Figure 5 as colored and labeled $T \ll \mathcal{T}$.

Degeneracy of type II manifests because the temperatures of the ceding and superseding members can be approximately and exactly equal. Thus, given a strong constraint on the temperature, the solid angle ($\varpi \approx 1 - \cos\zeta$) constraint on the radiating region can be satisfied $\forall\, \psi \leqslant \zeta$. Note that unlike degeneracy of type I, degeneracy of type II can be exact (for $T = \mathcal{T}$) and exists invariantly of angular scale. The smaller the solid angle constraint, the weaker the constraint on topology of the hotter subregion (annulus or hole), and thus degeneracy of type II should be present. On larger angular scales, the signal offers a much stronger constraint on topology: if the hottest subregion is ring-like,[56] degeneracy of type II cannot be present a posteriori.[57]

Degeneracy of type III manifests because the smaller the superseding member is in relation to the ceding member, the greater the dominance of the signal from the ceding member, and thus the greater the range of values T can assume while leaving the signal approximately invariant. Thus, given a strong constraint on the temperature and solid angle ($\varpi \approx 1 - \cos\zeta$) of the dominant component, the constraint can be satisfied $\forall\, \psi \ll \zeta$. Again note that unlike degeneracy of type I, the existence of degeneracy of type II is insensitive to angular scale. However, if there is a strong constraint on the topology of the subregion that dominates the joint signal, and that subregion is ring-like, degeneracy of type II will not be present a posteriori.

We now consider degeneracy IV and its implications for sampling. Suppose that the signal can be dominated by that from a simply connected subregion: if the superseding member satisfies both a temperature constraint and a solid angle constraint ($\varpi \approx 1 - \cos\psi$), the ceding member then forms an annulus whose width ψ^+ and whose temperature $\mathcal{T}$ can together assume a wide range of values. In Figure 5 we illustrate the case of $\mathcal{T} \ll T$ for varying ζ (and, in the last cartoon, for a shift of the center of the ceding member in angular space).[58] The superseding member need only be described by four parameters, while the non-superseded subset of the ceding member is described by five parameters, three of which are shared with the superseding member. If the ceding member is relatively cool, then the signal it generates is dominated by that of a much hotter superseding member; the signal is then degenerate with respect to $\mathcal{T}$. Crucially, if one writes the properties of the superseding member in terms of that of the ceding member, nonlinear degeneracy can arise in what otherwise may appear to be a natural parameterization, as we show below.

For posterior computation (see Appendix A for methodology) we explicitly consider a parameter space in which the superseding member is constructed using the minimal number

[56] Formed by imposing a relatively large, cooler superseding member (effectively a hole).

[57] Here we assume a unimodal posterior distribution, but more generally, the degeneracy will not be present for a *local* mode in which the topology is strongly constrained as ring-like.

[58] Note that a less important degeneracy occurs, which we do not illustrate: the annulus is arbitrarily hotter ($\mathcal{T} > T$) but $\psi^+ \to 0$ so that the superseding member also dominates the signal. In the $T \approx \mathcal{T}$ transition zone—which coincides with the type II degeneracy—ζ approximately satisfies the solid angle constraint.

of parameters necessary, which eliminates needless *nonlinear* degeneracy. For example, if we work in the joint space of f and ζ, the local direction of approximate signal invariance—which emerges when the superseding member with angular radius ψ is dominant—is *not* everywhere a basis vector, but is given by the gradient of $f = \psi/\zeta$ for constant $\psi \in \mathbb{R}^+$: $\partial f/\partial\zeta = -\psi/\zeta^2$, so the direction is $(1, -\psi/\zeta^2)$ at point (ζ, f). This degeneracy is linearized by working in the joint space of ψ and ζ, or alternatively, in the joint space of ψ and the angular annular width $\psi^+ := \zeta - \psi$.

We note that unlike degeneracy of type I, the existence of degeneracy of type IV is insensitive to angular scale. However, if there exists a strong constraint on the topology of the heated subregion that dominates the signal, and that subregion is ring-like, degeneracy of type IV will not be present a posteriori—in the same vein that degeneracy of types II and III are absent. This does not mean that the posterior modes are devoid of degeneracy if the hot regions are both constrained to be ring-like: the temperature of a superseding member can assume a wide range of values (in logarithmic space) lower than that of the ring, because the additional complexity beyond that of a non-radiating hole (i.e., devoid of heated material) is unwarranted. However, the degeneracy is linear and thus handled straightforwardly.

In many cases, degeneracies are characterized by allowing one temperature component (a heated subregion) to dominate the signal, while one temperature—or the solid angle subtended at the stellar origin by a subregion—assumes relatively low values. In these cases the degeneracy is not expected to be particularly problematic because it will be effectively linear, parallel to basis vectors of the parameter space, and truncated by the boundary of the prior support. Thus, provided that the mapping from the native sampling space to the parameter space preserves this behavior, nested sampling efficiency may not be affected as adversely as when posterior modes exhibit strong nonlinear degeneracy.

For instance, consider degeneracy such as type IV: let the angular scale be sufficiently large for the dominant component to be constrained to be simply connected. The degenerate subsets of the (ψ, ζ)- and $(\psi, \mathcal{T})$-subspaces will be linear and orthogonal to the $\hat{\psi}$ basis vector. The notable source of efficiency reduction for type IV will be the boundary of the degenerate subset of the $(\zeta, \mathcal{T})$-subspace: while there will be a hard lower limit on $\mathcal{T}$, the boundary is otherwise dependent on combinations of parameters and will not conform trivially to common nested-sampling active-point bounding algorithms.

On the other hand, if degeneracy of type I arises and the hole is filled with material of temperature T, we incur a nonlinear degeneracy in the (ζ, ψ)-subspace, *and* non-trivial boundaries of the degenerate subsets of the (ζ, T) and (ψ, T)-subspaces. In this case the potential for efficiency reduction is greater.

It is interesting to note that degeneracy can also arise when one temperature component does *not* dominate the signal. Let us suppose that two components with distinct temperatures are favored a posteriori, where those components both contribute non-negligibly to the total signal. We implement a numerical geometrically thin atmosphere where the effective temperature and effective gravity control the local comoving specific intensity as a function of photon energy and direction (i.e., control the spectrum and beaming); it follows that if a hot region exhibits small angular extent, two components (subregions) can in principle generate signals that are commensurate in total count rate, provided that the solid angles subtended by the subregions at the stellar origin have appropriate relative sizes. For the CDT models, a *discrete* degeneracy—multi-modality—can then arise on small angular scales: pairs of configurations of the components generate approximately the same total signal. In one configuration the hole hosts a particular component, while in the alternate configuration that component is hosted by the annulus; the relative solid angles subtended by the hole and annulus depend on which component is hosted. However, for a more complex model where the superseding and ceding members are not defined as concentric (see Figure 5, and Section 2.5.5 and beyond), it is clear that (approximate) continuous degeneracies would also arise and thus complicate matters.

We should also be aware of the relative prior masses associated with subsets of parameter space over which the signal is approximately invariant, governed roughly by the dimensionality of the degeneracy. Degeneracy of types II and III generally occupy a subset of parameter space with smaller prior mass than that of type I and IV, the former two being effectively to one-dimensional,[59] and the latter two being effectively two-dimensional. Note that the type I degeneracy is effectively two-dimensional *because* we fill the hole from the CST models with material whose temperature is finite and a model parameter.

Priors. We retain almost all prior definitions from the CST models (Section 2.5.2). We again transform the prior onto the joint space of ψ and ζ in order ensure a more optimal parameterization for our sampling algorithm of choice, as highlighted above. Crucially, we need to transform from the native space to the parameter space in a manner that preserves linearity of degeneracy IV. We achieve this by inverse sampling the marginal prior density $p(\psi)$ and the condition prior density $p(\zeta \mid \psi)$; we give these transforms in Appendix B. In some cases we opt to transform to the joint space of ψ and ψ^+ space in post-processing for optimality of kernel density estimation when ψ^+ approaches a boundary—e.g., due to degeneracy of type IV.

2.5.4. Interlude: On Degeneracy and Complexity

General. The continuous degeneracies discussed in Sections 2.5.2 and 2.5.3, when in mutual existence, generally form a connected structure in parameter space. These degeneracies could be characterized in more detail, and also with reference to ulterior parameters (including those of the other hot region). We do not study the degeneracies further here for lack of a clear way to simultaneously linearize each of them via transformation.

We instead observe a fundamental aspect of the modeling process *on a source-by-source basis*: it is judicious to evaluate the utility of additional complexity *on a region-by-region basis*, if a posteriori one infers localized emission and/or that a single-temperature component per hot region suffices in describing a particular pulse component in the phase-folded event data. In practice, this could include the following: (i) design a model space with increments in complexity, moving toward more sophisticated region topologies and/or boundaries, and/or an additional temperature component as warranted by the data; (ii) insert models into one's model space

[59] An unillustrated degeneracy, characterized by a hotter ring in the limit $\psi^+ \to 0$, is also effectively one-dimensional.

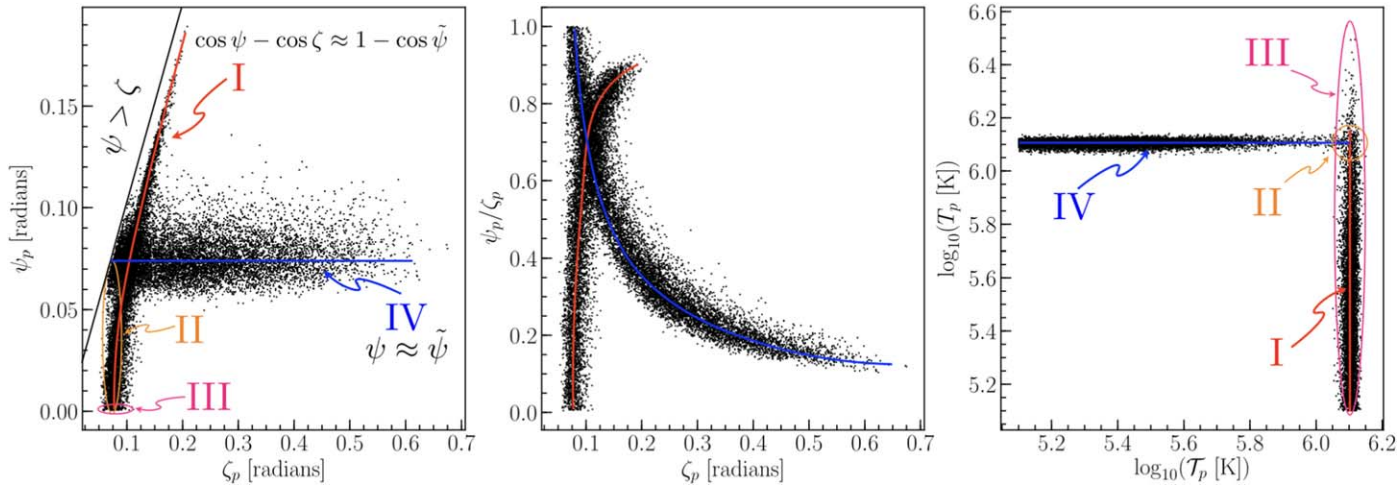

Figure 7. Conditional on CDT−U, we display points (nested samples) $\{\boldsymbol{\theta}_k\}$ that reported (background-marginalized) likelihood function values $L(\boldsymbol{\theta}_k) > L'$, where $\max_k \ln L(\boldsymbol{\theta}_k) - \ln L' \lesssim 13$; the choice of threshold L' is somewhat arbitrary beyond needing a large enough number of points to clearly resolve the form of the degeneracies. We display these points in a selection of two-dimensional spaces to focus on the degeneracies that emerge upon application of CDT−U. These degeneracies pertain to the structure of the primary (lower-colatitude) hot region, which generates a signal describing a particular pulse component visible in Figure 1; the hot region exhibits a small angular extent on the stellar surface, and we are statistically insensitive to the additional complexity offered by a CDT cap over a ST cap. In the left panel we show the points in the joint space (ζ_p, ψ_p)—i.e., in the joint space of the angular radii of the ceding and superseding members. We indicate which type of degeneracy illustrated in Figure 5 corresponds to which structure in parameter space; the curves (blue and red) each correspond to a constraint equation. Types II and III occupy far smaller prior masses than types I and IV, so we choose to indicate the structures associated with the former types with ellipses; in a finite-sample context these structures are allocated points more sparsely, in proportion to the associated prior mass in the full n-dimensional parameter space. Note that the region $\psi_p > \zeta_p$ is not a subset of the CDT−U prior support. In the center panel we display the points in the joint space of (ζ_p, f_p), where $f_p := \psi_p/\zeta_p$; our sampling processes (refer to Appendix A for details) were executed in a space in which likelihood function isosurfaces are structured nonlinearly as suggested in this center panel, leading to reduced posterior computation efficiency and higher nested-sampling error. In Sections 2.5.2 and 2.5.4 we discuss the interpretation and treatment of degeneracy: in hindsight, higher efficiency would have been achieved if we had worked in a joint space that linearized degeneracy of type IV. In the right panel we display the corresponding structures in a joint space trivially related to $(\mathcal{T}_p, T_p)$—i.e., in the joint space of the effective temperatures of the material enclosed by the ceding and superseding members. The points displayed here are a composite set from two sampling processes, where due to reduced efficiency and increased nested-sampling error, neither process individually resolved all of the degenerate structure present.

that reduce region complexity, if it is apparent a posteriori that a model with unhelpful complexity was first applied; or (iii) reduce region complexity as in point (ii), while increasing the complexity of another facet of the model, based for example on graphical posterior predictive checking.

To provide an example, suppose that a posteriori, given CDT−U, hot region $\mathcal{A}$ is degenerate with respect to multiple parameters controlling its surface radiation field, while hot-region $\mathcal{B}$ is only degenerate with respect to temperature of one relatively cool component. Specifically, suppose $\mathcal{A}$ is constrained to have a small angular extent and a single-temperature component, while offering satisfactory posterior predictive performance in comparison to a particular pulse component. Continuous degeneracies of type I and IV are then clear in the posterior distribution. Additionally, suppose that the secondary region has a strong constraint on its topology, with its dominant component being ring-like with moderate angular extent. On the basis of this inference, one might argue that it is justified to modify the model space: one proceeds to define a model wherein the complexities of $\mathcal{A}$ and $\mathcal{B}$ are unequal. In doing so one can reduce or redistribute complexity while improving computational efficiency. For the aforementioned example, one may define a model ST+CST, parsed as *Single-Temperature + Concentric-Single-Temperature*, which is intermediary in relation to ST−U and CST−U: $\mathcal{A}$ has one simply connected component, while $\mathcal{B}$ has one non-simply connected component (which can reduce to a simply connected component). The dimensionality of the parameterization is then $n = 9$, reduced from the CDT−U value of $n = 12$. One could also define additional models that increase the complexity of $\mathcal{B}$ (see Sections 2.5.5 and 2.5.6).

As a brief second example: if, given CDT−U, $\mathcal{B}$ was constrained to have *two* temperature components, one could instead define a model ST+CDT with dimensionality $n = 10$. One could then proceed to increment the complexity of $\mathcal{B}$.

An important remark here is that the performance of $\mathcal{A}$ cannot strictly be decoupled from the performance of $\mathcal{B}$ in relation to their respective target pulse components: the regions exist on the same rotating two-surface and share an ambient spacetime solution. It follows that the complexity of one region can in principle affect our conclusions about the level of complexity of the other. Such conclusions cannot be based solely on the existence of degenerate structure in the joint posterior distribution of the region parameters. If $\mathcal{A}$ exhibits degenerate structure while $\mathcal{B}$ does not, the structure may manifest—at least in part—*because* the complexity of $\mathcal{B}$ is insufficient.

A more robust basis for breaking parity between the hot-region complexities would be the existence of degenerate structure, *and* satisfactory posterior predictive performance of *both* regions in comparison to their respective pulse components. A practical basis for breaking parity, given the existence of efficiency-reducing degenerate structure a posteriori, may be resource availability and management.

Modeling PSR J0030+0451. For the source we focus on in this work, degeneracy emerged upon application of CDT−U. We display the corresponding structures, in parameter space, in Figures 7 and 8. In summary, the primary region was constrained to have a small angular extent and one dominant temperature component, and could generate data structurally consistent with a pulse component visible in the phase-folded event data (Figure 1); the primary region thus here corresponds

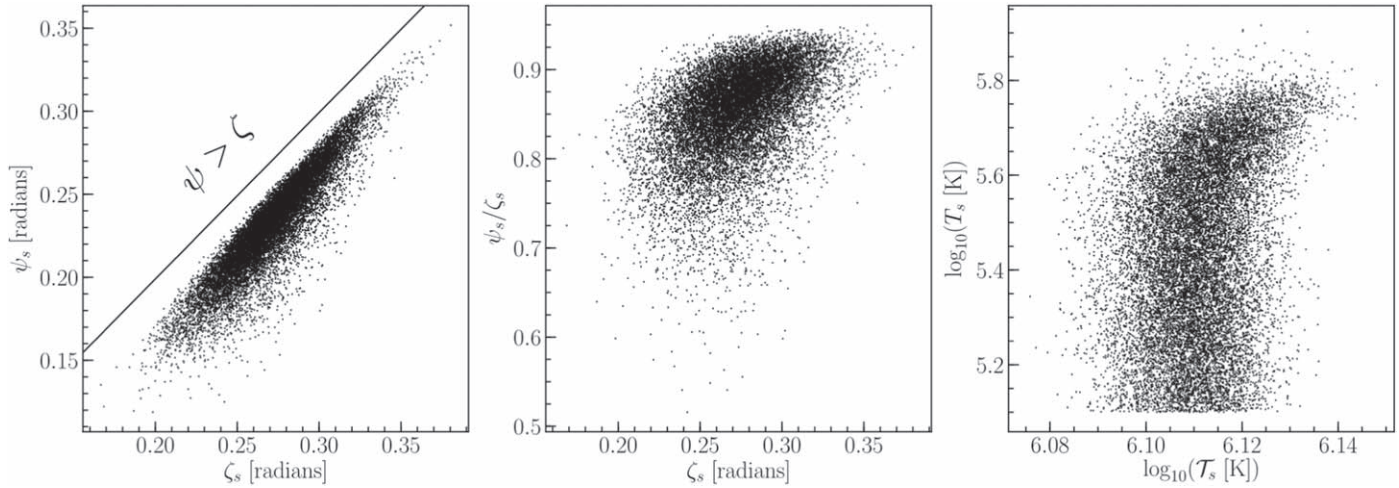

Figure 8. As for Figure 7, conditional on CDT−U, we display points (nested samples) $\{\boldsymbol{\theta}_k\}$ that reported (background-marginalized) likelihood function values $L(\boldsymbol{\theta}_k) > L'$, where $\max_k \ln L(\boldsymbol{\theta}_k) - \ln L' \lesssim 13$. We display these points in a selection of two-dimensional spaces to focus on the secondary (higher-colatitude) hot region. The secondary region exhibits a larger angular extent on the stellar surface than the primary region and, in contrast, we are statistically sensitive to the topology of the secondary region while being statistically insensitive to the additional complexity offered by a CDT cap over a CST cap. In other words, we do not strongly require the material in the hole to radiate when considering the *NICER* waveband.

to region $\mathcal{A}$ above. Degeneracy of types I and IV arose and dominated in prior mass (and by extension, in posterior mass). The nonlinear degeneracies in the native nested-sampling space also suppressed the efficiency of the sampling processes. We therefore now have grounds to design and apply models that break the parity in complexity between hot regions. We redistribute complexity from the primary region to the secondary region, such that the dimensionality of the parameter space does not exceed that of CDT−U. In Appendix D we define models that preserve parity between regions—a brief continuation of the above scheme for model extension.

In Sections 2.5.5 and 2.5.6 we explain how the complexity of a solitary hot region is extended. In Section 2.5.7 we briefly summarize and provide diagrams of the relevant models formed from two disjoint hot regions with unequal complexities. In Section 2.5.7 we then provide diagrams summarizing the relationships between all models considered in the scope of this work.

2.5.5. Eccentric Single- and Dual-temperature Regions (EST and EDT)

Parameterization. We extend the CST and CDT hot-region types by not requiring the ceding and superseding members to be concentric. For a CST region, the superseding member was a hole in a ceding member, devoid of radiating material; for a CDT region, the superseding member was similarly a hole, but filled with radiating material. For both CST and CDT regions, the *non-superseded* subset of the ceding member was a radiating annulus with concentric inner- and outer-boundaries; now the radiating annulus is *eccentric*. Further we require—via the joint prior support—that the ceding member is strictly a superset of the superseding member; in other words, the superseding member is a hole in the ceding member, again forming an annulus or ring.[60]

We illustrate these hot-region structures in the topmost panels of Figure 9; we also alluded to such configurations in Figure 5 and in Sections 2.5.2 and 2.5.3. Hereafter we use the aliases EST and EDT, respectively parsed as *Eccentric-Single-Temperature* and *Eccentric-Dual-Temperature*.

An additional two parameters must be defined to specify the eccentricity as the great-circle segment separating the centers of the members: the magnitude and direction of the offset. To do so, we consider a spherical coordinate basis such that: (i) the polar axis subtends an angle Θ to the stellar rotation axis; (ii) the southern rotational pole subtends angle $\pi - \Theta$ to the polar axis, and has azimuth *zero* (such that the northern rotational pole has azimuth π radians). The azimuth of the annulus center, φ, in the rotated basis uniquely selects the great circle and direction of the offset (depicted in Figure 9). We choose define the magnitude of the angular separation as a fraction ε of the *difference* $\psi^+ := \zeta - \psi \equiv \zeta(1 - f)$ between the angular radii of the hole and annulus (see Section 2.5.3). The magnitude of the angular offset between the centers—equal to the colatitude of the annulus center in the rotated spherical coordinate basis defined above—is thus $\vartheta := \varepsilon\psi^+$.[61]

Degeneracy. In a similar vein to the CDT parameterization, optimality of the parameterization for an EDT region should be considered. By this point in the modeling process, we have a handle on a region-by-region basis whether the additional complexity offered by an EST or EDT region is a justified modeling step. Nevertheless, one can construct the sampling space using the minimum number of parameters need to fully control the superseding member. The parameter vector for the regions is thus of the form $\boldsymbol{\nu} = (\psi, \Theta, \phi, \zeta, \varepsilon, \varphi)$, and the mapping from the native sampling space to the parameter space is formed in part using the marginal density $p(\psi)$ and the conditional density $p(\zeta \mid \psi)$.

[60] The hole reduces to a point at the boundary of the prior support for an EST region, while for a EDT region the hole is not permitted to reduce to a point. Also note that because the ceding and superseding members are circular, their boundaries may intersect at a maximum of one point.

[61] An alternative is to parameterize in terms of the fraction of the sum of their angular radii such that $\vartheta := \varepsilon(1 + f)\zeta$; it is this combination that is the limit of zero partial overlap when the superseding member lies partially exterior to the ceding member (see Section 2.5.6). In order to impose that the superseding member is a hole in the ceding member, we would then require the support constraint that $\varepsilon(1 + f)\zeta + f\zeta \leqslant \zeta$ and thus that $\varepsilon \leqslant (1 - f)/(1 + f)$.

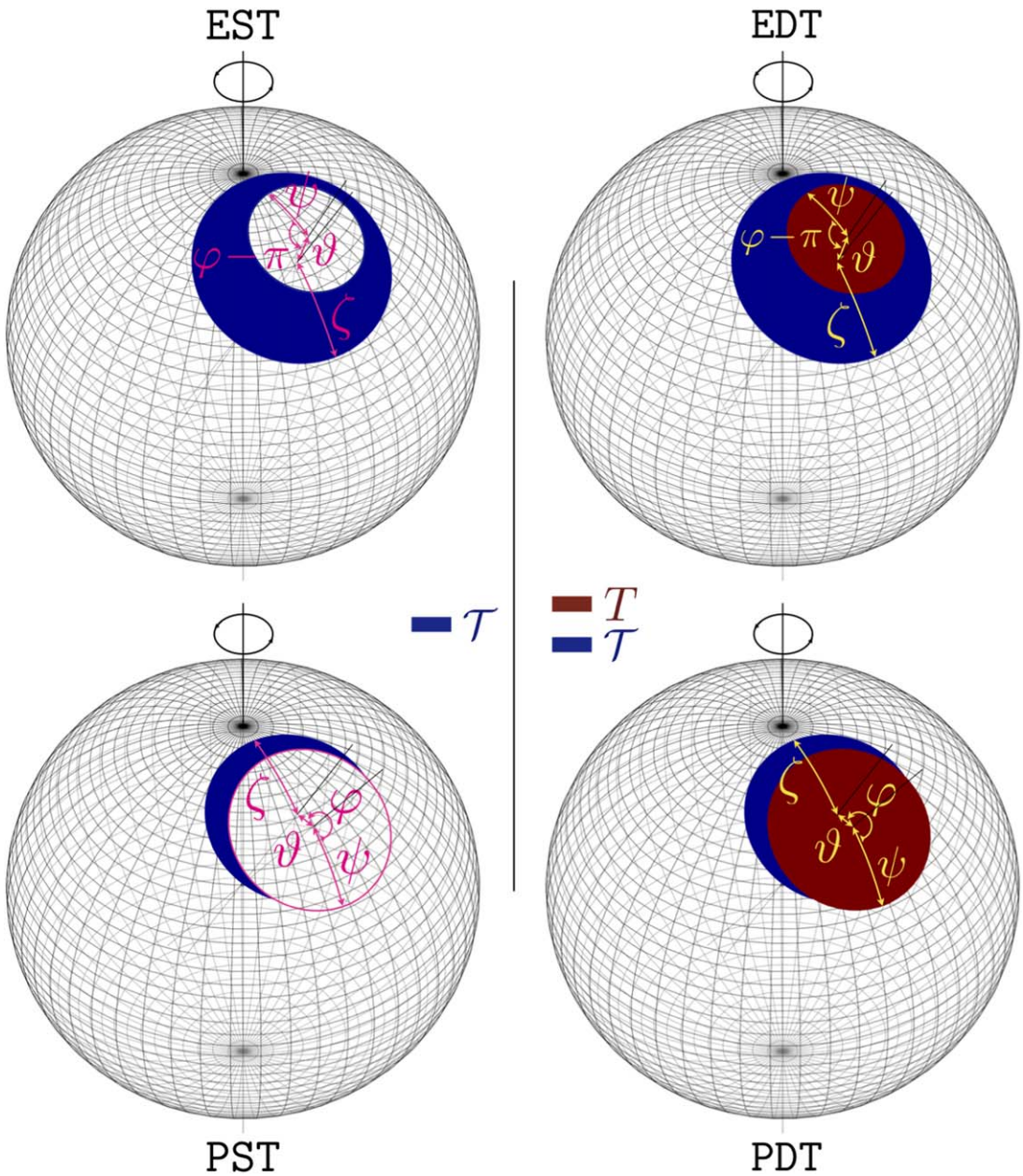

Figure 9. Schematic diagrams of solitary hot regions beyond the CST and CDT complexity levels, as described in Sections 2.5.5 and 2.5.6. We delineate the boundary of the superseding member for the PST region.

Priors. As for the CDT type of region (Sections 2.5.3), joint prior support is such that the material within the annulus may exhibit an effective temperature $\mathcal{T} < T$ or $\mathcal{T} \geqslant T$. Moreover, when an EST/EDT region shares the stellar surface with another hot region $\mathcal{C}$, the joint prior support does not include configurations wherein $\mathcal{C}$ overlaps with the ceding (annular) region of the EST/EDT region. Note that a continuous set of coordinate singularities exist in the mapping $(\varepsilon, \varphi) \mapsto (\Theta', \phi')$, where the coordinates (Θ', ϕ') are the colatitude and azimuth of the center of the annulus in a spherical coordinate system with polar axis defined as the stellar rotation axis. The mapping is singular for all points $(\varepsilon, \varphi) = (0, \varphi)$ at the boundary of the prior support, such that by defining a finite joint prior density at such singular points the joint density at $(\Theta', \phi') = (\Theta, \phi)$ diverges. We consider the spherical coordinates (ϑ, φ) to be more natural for increasing complexity and thus we display density functions with respect to (ε, φ) to avoid difficulty in representing density functions accurately.

2.5.6. Protruding Single- and Dual-temperature Regions (PST and PDT)

Parameterization. We extend the EST and EDT hot-region types by not requiring the ceding member be a strict superset of the superseding member. In other words, the superseding member need not be a hole in the ceding member, leading to radiating component with the topology of a ring. If the superseding member is *not* a hole nor a point, and the boundaries of the ceding and superseding members intersect at two points, then the *non-superseded* subset of the ceding member is simply connected *and* has a non-circular boundary: it cannot therefore always be considered an annulus, and can

assume a crescent- or arc-like morphology.[62] Note that we do not increase complexity here by incrementing the dimensionality of parameter spaces defined for the EST and EDT regions. We nevertheless choose to distinguish between EST/EDT and PST/PDT in view of a symmetry being broken: that of the circularity of the outer boundary of the region. The superseding member can also now subtend the larger (coordinate) solid angle at the stellar origin, and in the limit that the member boundaries touch at a point, the hot region is simply connected, with a boundary that is either circular or union of two circular subregion boundaries.

We illustrate these hot-region structures in the bottommost panels of Figure 9; we also alluded to such configurations in Sections 2.5.2 and 2.5.3. Hereafter we use the aliases PST and PDT, respectively parsed as *Protruding-Single-Temperature* and *Protruding-Dual-Temperature*: the superseding member can protrude from the ceding member, for parameter vectors within the joint prior support.

We modify the EST (and thus EDT) parameterization in order to permit the superseding member to: (i) protrude[63] from the ceding member; and (ii) subtend a larger (coordinate) solid angle at the stellar origin than the ceding member. Let us denote the angular radius of the *largest* member as ξ. Let us then consider the interval $f \in [\epsilon_f, 2-\epsilon_f]$, where ϵ_f is some small number: when $f \leqslant 1$ the angular radii of the superseding and ceding members are, respectively, $\psi = f\xi$ and $\zeta = \xi$, as in the EDT variants. However, when $f > 1$, the angular radii of the superseding and ceding members are, respectively, $\psi = \xi$ and $\zeta = (2-f)\xi$. The angular radii are thus piecewise in f, and are continuous at the transition point $f = 1$. It follows that the interval for the angular radius ξ of the largest member considered in the previous variants can be maintained, while the member that is largest switches. If one varies f through the interval $f \in [\epsilon_f, 2-\epsilon_f]$ while all other parameters are fixed, the solid angle subtended by the superseding member increases to match that of the ceding member; at the $f = 1$ transition the superseding member stops expanding, and for f increasing beyond unity, the solid angle subtended by the ceding member decreases.

We choose to define the magnitude of the angular separation as a fraction[64] $\varkappa$ of a combination of the angular radii of the superseding and ceding members. For $f \leqslant 1$, the combination is the *sum* of the angular radii of the superseding and ceding members, $\psi = f\xi$ and $\zeta = \xi$, respectively, for $f \leqslant 1$: $\vartheta(\xi, f \leqslant 1, \varkappa) := \varkappa(1+f)\xi = \varkappa(\psi+\zeta)$. It is this combination that is the limit of zero partial overlap between the members when the superseding member lies partially exterior to the ceding member. We define the prior support for $\varkappa$ simply as the unit interval: we permit only configurations wherein the members partially overlap (including at a point), with maximum separation $\vartheta = \psi + \zeta$.

We require the angular separation ϑ as piecewise in f: for $f > 1$, we let $\vartheta(\xi, f > 1, \varkappa) := \psi - \zeta + 2\varkappa\zeta = (f-1)\xi + 2\varkappa(2-f)\xi$. Note that the minimum separation here with respect to $\varkappa$, for fixed ξ and fixed f, is $\vartheta = \psi - \zeta$, equivalent to the transition from the ceding member being *partially superseded* to being *wholly superseded*; the minimum separation for the subinterval $f \leqslant 1$ is zero. The maximum separation (with respect to $\varkappa$ for fixed ξ and fixed f) is $\vartheta = \psi + \zeta$, which is equivalent to the expression for the maximum separation for $f \leqslant 1$. Note that at the transition $f = 1$, the piecewise components of $\vartheta(\xi, f, \varkappa)$ continuously match at a value of $2\varkappa\xi$.

The coordinates of the center of the ceding member remain written in terms of those of the center of the superseding member. We cannot define a pair of coordinates as being associated with the *larger* member (in the same vein that ξ is directly associated with the larger constituent) without generally introducing a discontinuous transition with respect to the configuration of the members at $f = 1$.

Note that the above prescription is equivalent in principle to defining a binary discrete parameter (with associated uniform prior probability mass function) that controls which member ξ in turn directly controls, and thus which member f directly controls, where the upper bound of the prior support of f remains as unity. In this equivalent alternative, the piecewise definitions of ϑ and the angular radii are required, but are recast with respect to the binary parameter. However, extension of the support of a continuous parameter to include these configurations eases posterior computation.

Degeneracy. The two clear exact degeneracies beyond those considered above[65] are: (i) equal temperatures where the superseding member is wholly enclosed by the ceding member, leading to three-dimensional degeneracy in the subspace of (f, $\varkappa$, φ); and (ii) the superseding member *wholly supersedes* the ceding member ($\varkappa = 0$ for $f \geqslant 1$), leading to a two-dimensional degeneracy in the (f, φ)-subspace. There are also discrete member-exchange degeneracies for a given region when the temperatures are equivalent.

Priors. The joint prior support is again such that the material within the ceding member may exhibit an effective temperature $\mathcal{T} < T$ or $\mathcal{T} \geqslant T$. Moreover, when a PST/PDT region shares the stellar surface with another hot region $\mathcal{C}$, the joint prior support could be defined to exclude configurations wherein $\mathcal{C}$ overlaps with the PST/PDT region. We note that due to choice of parameterization and prior support, the prior density function for the angular separation between the ceding and superseding members has changed from the corresponding EST/EDT density function.

2.5.7. Overview of the Model Space

In Figure 10 we provide a diagram of the relationships between the models—spanning the discrete model space—that impose equal complexities. A subset of these models are based on the extensions defined in Sections 2.5.5 and 2.5.6; diagrams of EDT-S, EDT-U, PDT-S, and PDT-U are given in Appendix D because we do not compute posterior distributions that are jointly conditional on these models and the event data.

We also define models wherein an ST region shares the stellar surface with a higher-complexity hot region. We provide diagrams of ST+EST and ST+PST in Figure 11. We provide diagrams of ST+EDT and ST+PDT in the online figure set associated with Figure 11. In Figure 12 we illustrate the relationships between these models. Note that these models

[62] It is now particularly clear why we supplant the *hole* and *annulus* descriptors with those in terms of simply connected *members* and evaluation precedence as noted in Section 2.4.1: one member is distinguished from the other simply by which takes precedence when evaluating radiation intensities along a ray (null geodesic) connecting the stellar surface to a distant observer.

[63] Or partially overlap with the ceding member.

[64] Equal to the colatitude of the center of the ceding member in the rotated spherical coordinate basis defined above.

[65] The degeneracies considered above should at this stage be of little to no concern if computation of the simpler (nested) models has *not* indicated that the complexity thus far introduced is unhelpful.

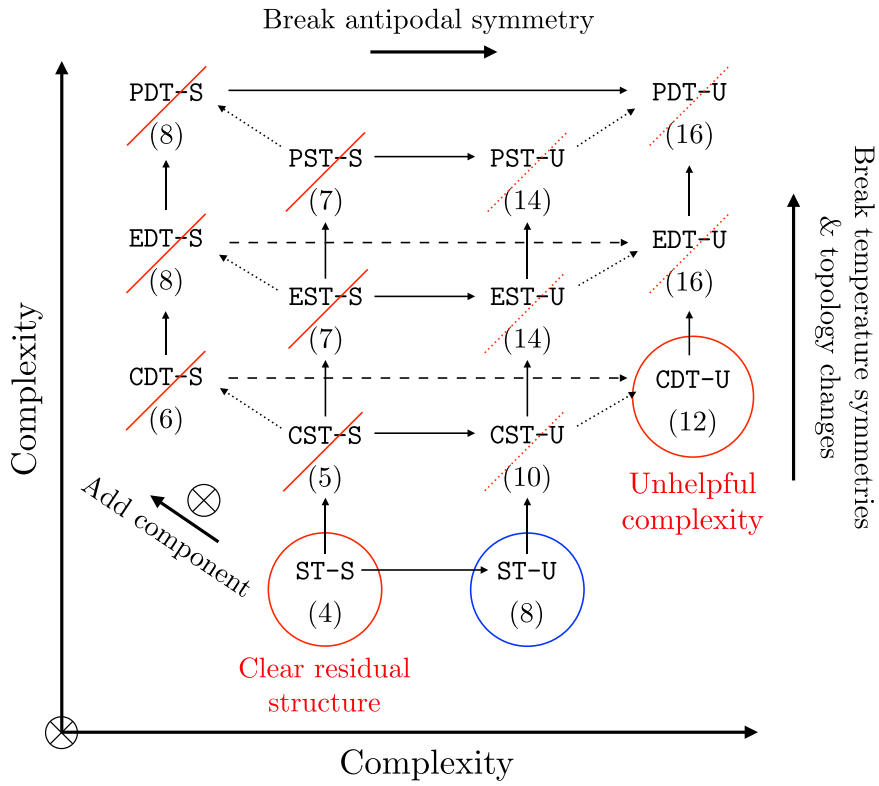

Figure 10. Diagram of relationship between a subset of models $\{\mathcal{M}\}$, where each $\mathcal{M} \subset \mathscr{M}$ and $\mathscr{M}$ is the model space as defined in Section 2.3. The models are ST-S and ST-U (Section 2.5.1), CST-S and CST-U (Section 2.5.2), CDT-S and CDT-U (Section 2.5.3), EDT-S and EDT-U (Appendix D), and PDT-S and PDT-U (Appendix D). The integers in parentheses are the number of continuous parameters controlling the hot regions; to obtain the total number of parameters constituting the sampling space for each model, add 8 to these numbers—corresponding to the vector (M, $R_{\rm eq}$, i, D, $N_{\rm H}$, α, β, γ) shared between all models. Prior predictive complexity increases with dimensionality and/or prior support expansion; complexity increments are achieved by breaking symmetries, allowing the morphology and topology of the radiating regions to change, and adding a second component with parameterized temperature. Solid arrows between model nodes delineate a nested relationship between models: the model at the tail is nested within the model at the head, the latter of which has greater complexity. Adding arrows head-to-tail at a node conserves such relationships—i.e., the model at the tail of the resultant arrow is nested within the more complex model at the head. The dashed arrows are in the background (visualize a third dimension of the graph as indicated by $\otimes$). The dotted arrows between single- and dual-temperature models indicate that the nested relationship is weaker: in the single-temperature models no material (or material with zero temperature) fills the superseding member and thus no signal is generated, whereas for the dual-temperature models we fill the superseding member with material of finite temperature $T \gtrsim \mathcal{O}(10^5)$ K, and a signal is thus physically generated and computed. The blue ring indicates the simplest model that can generate data that is visually comparable to the real data set (refer to Section 3 for discussion). The red annotations are to denote where we learn that a given model is not performing adequately or has unhelpful complexity. A strikethrough denotes that a model was not applied: (i) a solid strikethrough denotes that the model is considered as being incapable of generating synthetic event data that resembles the real *XTI* event data, based on performance of a simpler model with which some degree of symmetry is shared; (ii) a dotted strikethrough denotes that the model is considered to include unhelpful complexity for at least one hot region.

with unequal complexities exist within the scope of those models present in Figure 10.

When the hot regions are distinguishable by complexity level we can label the regions as *primary* and *secondary* according to that complexity: let the higher-complexity region be *secondary*. Our application of CDT-U suggested that evolving the lower-colatitude (primary) region from ST to CDT did not yield any improvement in describing the event data; the lower-colatitude region in this case describes the pulse component in the event data (Figure 1) that peaks at ∼0.5 rotational cycles. Moreover, for both ST+CST and ST+CDT, the secondary region is formed (not necessarily by trivial union) from two members—one or both of which radiate—that are concentric and thus share a single colatitude parameter. Therefore, for ST+CST and ST+CDT it is reasonable to retain the constraint on the prior support that $\Theta_p \leqslant \Theta_s$—i.e., that the colatitude of the *center* of the ST region is at most the colatitude of the *center* of the CST/CDT region.[66]

Notably, we cannot consider a model with an EST/EDT or PST/PDT region as nested within CDT-U, and there is thus not an obvious ordering of regions in colatitude that can be applied based on the CDT-U posterior information. We therefore do not impose such a constraint on the prior support, meaning that the order of the regions in model names ST+EST, ST+EDT, ST+PST, and ST+PDT does *not* indicate an order in colatitude.

Based on the CDT-U posterior information we are now interested in models wherein we couple the lower-complexity (primary) region to the pulse component in the event data (Figure 1) that peaks at ∼0.5 rotational cycles. We consider a practical reason to identify a particular hot region with a particular pulse component in the phase-folded event data: to ease posterior computation by focusing sampling resolution in the vicinity of such configurations. If we do not opt for this coupling, a local posterior mode (or modes) can absorb sampling resolution, despite contributing relatively low posterior mass and thus being ultimately uninteresting for both parameter estimation and evidence estimation; such a local mode is characterized by the ST region describing the pulse component at approximately zero rotational cycles (Figure 1).

[66] A model wherein the CST or CDT region is at *higher* colatitude can be continuously connected to to this model by simply by forgoing the constraint on the prior support that $\Theta_p \leqslant \Theta_s$.

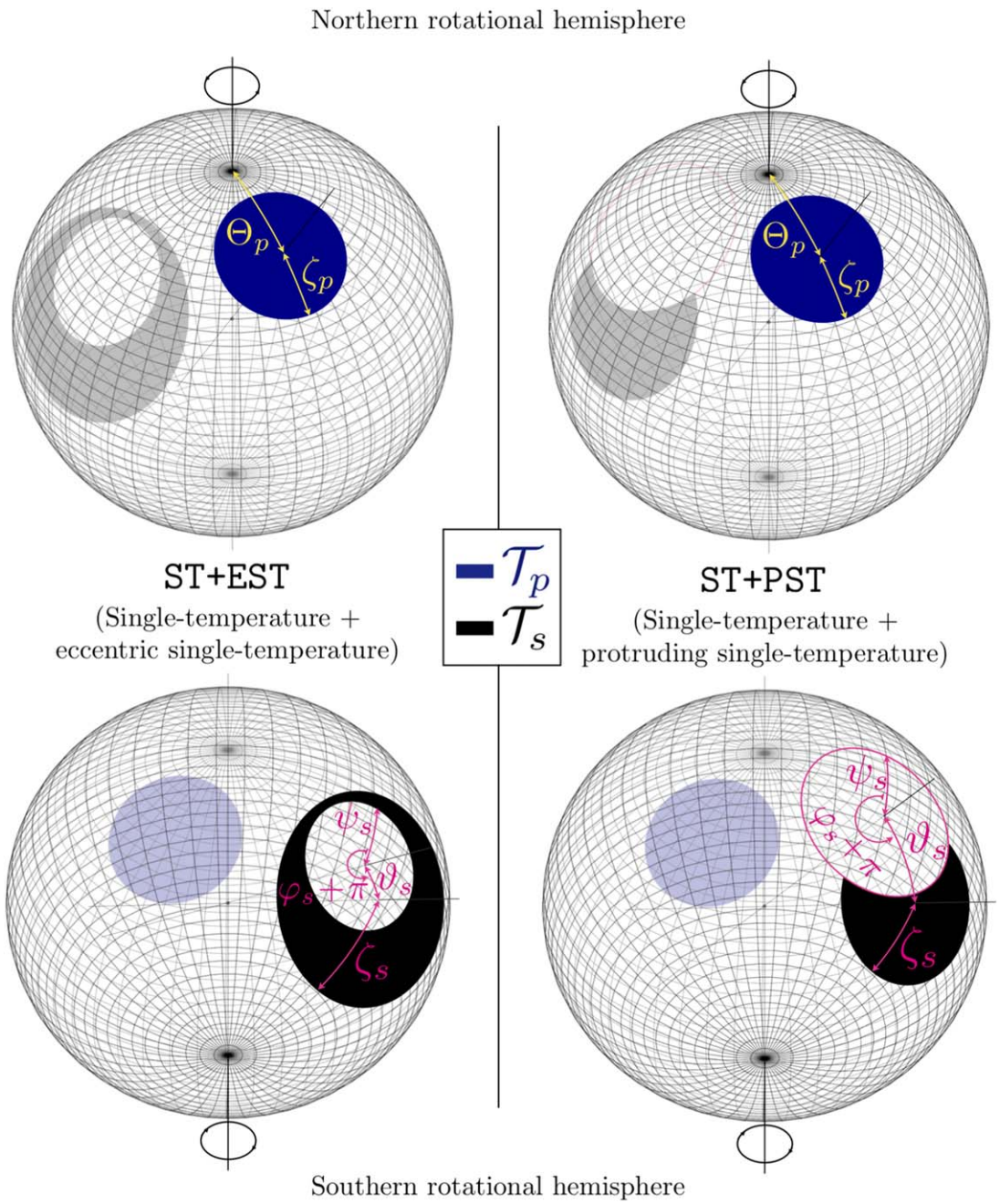

Figure 11. Schematic diagrams of models wherein an ST region shares the stellar surface with a higher-complexity EST or PST region.

Mitigating such an effect may then require additional active points and/or activation of the mode-separation MultiNest sampling variant (refer to Appendix A).

To intentionally couple the hot regions to pulse components, we restrict the prior support for the ST region to an interval $\phi_p \in [a, b]$ where $(b - a) < 1$ (such that the boundary of the support is not periodic with respect to ϕ_p). Remarkably, while such restriction may not affect parameter estimation,[67] the evidence does clearly depend on changes to the prior support, especially for weakly informative priors whose density does *not* fall to negligible values at the changing boundary of the support. It follows that in order to compare models based on evidences, we should obtain a lower bound on the evidence of, e.g., ST+EST, by accounting for the increased prior mass in the posterior mode due to contraction of the ST phase support.

We reserve the remaining prior implementation details for Appendix B.2.

3. Inferences

In this section we provide (posterior) summary information about each model applied and compare them. Tables giving numerical information for all but one model are available in Appendix C. Numerical files associated with the nested sample sets may be found in the persistent repository of Riley (2019). As regards model comparison, there is no clear maximally optimal measure for relative model performance (and certainly not for performance in an absolute sense). We deem ST+PST

[67] Provided that (i) the dominant posterior mode corresponds to a ST primary region, and (ii) that the marginal prior density $p(\phi_p)$ remains weakly informative relative to the likelihood function

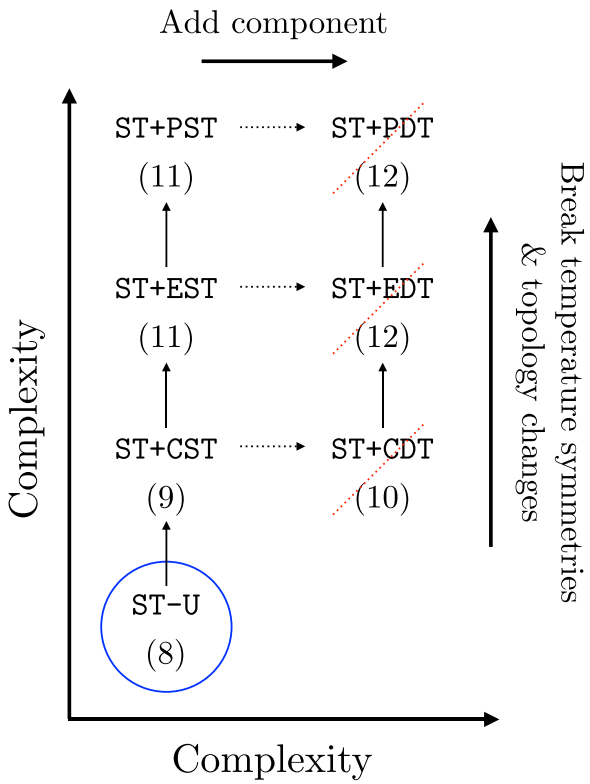

Figure 12. Diagram of relationship between dual-hot-region models with unequal complexities, constructed via extension of ST-U. These models exist within the scope of those displayed in Figure 10.

to be superior considering the following mixture of measures, both quantitative and qualitative.

Posterior predictive performance. Our crude graphical posterior predictive checking procedure suggests that even ST-U can generate synthetic event data that is structurally commensurate with the *XTI* event data—at least in the channel subset [25, 300). For reference, see Appendix A.2.1, together with Figure 13 and the associated figure set. Absent are obvious systematic differences in the (Poisson) standardized residuals over phase-channel intervals. Nevertheless, one could study the residual differences for modeling background event arrival processes, instrument operation, or noise properties of the event data—e.g., whether the event arrival processes could detectably deviate from being Poissonian (see also Figure 23). For the purpose of constructing a model that can simply generate event data that is similar to PSR J0030+0451 under visual inspection, ST-U is competitive with all higher-complexity models.

Visualization. In Figures 14 and 15 (and the associated online figure sets) we display, in posterior-expected form, various signals (derived quantities) generated by the hot regions; the reader can thus get a handle on the source contribution to the model displayed in Figure 13 (center panel). In Figure 16 we display the model-to-model evolution of the posterior-expected count-rate signals generated. To aid visualization, we provide in Figures 17 and 18 schematics of the hot regions on the surface that generate the aforementioned signals.

Evidence. We report evidence estimates in Tables 2 through 6. For the family of models that we have considered, the evidence strongly favors (adopting the guidelines of Kass & Raftery 1995) a model wherein antipodally reflection symmetry is *not* imposed; in other words, ST-S, and by extrapolation any such model with the -S extension (refer to Figure 10), is considered to be strongly disfavored. Moreover, for all computed models that do not impose antipodal reflection symmetry, posterior modes contain configurations characterized by both hot regions being located in the same rotational hemisphere—the opposite rotational hemisphere to the Earth direction. We also conclude that at least one region should be modeled with more complexity than offered by a single-temperature simply connected circular (ST) region; in other words, there is deemed sufficient evidence to disfavor ST-U. However, there is insufficient evidence to resolve between CDT-U, ST+CST, ST+EST, and ST+PST, especially when considering the evidence not as a scalar estimator, but as a random variable with a (simulated) distribution for estimating error intervals. The estimated error intervals (defined to contain 90% of evidence estimates based on nested sampling process realizations) typically overlap for these models, while the expected log-evidences are within $\sim$2 units.

Kullback–Leibler divergence. We report global and marginal divergence estimates in Tables 2 through 6, and in Figures 19–21. Information gain from prior to posterior is defined as a divergence integral over some subset of parameter dimensions: it is a non-negative real scalar measure of the difference between normalized density functions (see Appendix A.2.4 for a more detailed description). The larger the number, the larger the information gain, while a minimum divergence of zero indicates that the density functions are identical. The global information gain—the divergence integral over all dimensions—is comparable for all models. Based on comparison of parameter-by-parameter divergence estimates, and visual comparison of the marginal prior and posterior density functions hence summarized, we consider the joint prior distribution to be weakly informative in the context of the the likelihood function for most source parameters; the main exception is the distance, which is strongly prior-dominated. The other parameters whose marginal posterior distributions are entirely prior-dominated are the two of the instrument parameters, α and γ (refer to Figures 21 and 22). These informative prior distributions are however shared by all models, as are the improper flat prior density functions described in the background treatment (refer to Section 2.4.3). Note that more information is gained about the instrument parameter β—the weighting factor between two response matrices—and we can conclude that the instrument manifests a posteriori as a mixture weighted appreciably toward the nominal response for all posterior computations; we reserve discussion on why the instrument calibration may not be accurate for Section 4.1.3.

Likelihood function. We generally refrain from reporting parameter vector point measures such as the maximum a posteriori vector or the maximum likelihood vector for the purpose of formal quantitative model comparison (see Appendix A.2.1 for reasoning). We note, however, that the background-marginalized likelihood function exhibits the largest values in any posterior *typical set* (by $\sim$4 natural logarithmic units), across all models, for ST+PST. It follows that a subset of the additional complexity introduced by ST+PST is helpful—and suggestive of avenues for future modeling—while a subset of the complexity is unhelpful, leading to only commensurate evidence relative to ST+EST. In other words, the (background-marginalized) likelihood

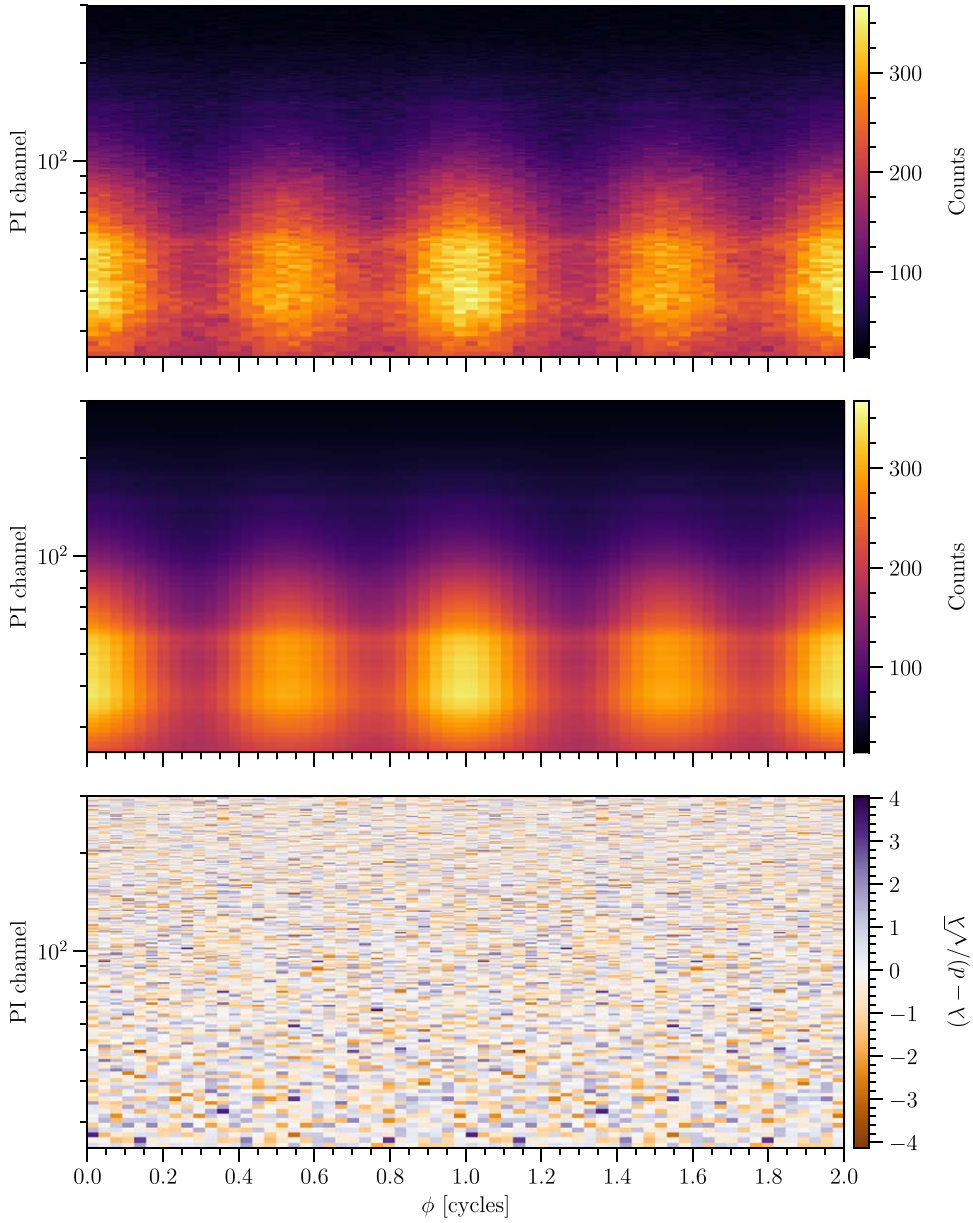

Figure 13. Count data $\{d_{ij}\}$, posterior-expected count numbers $\{\lambda_{ij}\}$, and (Poisson) residuals for ST+PST. Note that we split the count numbers in the upper two panels over two rotational cycles, such that the information on phase interval $\phi \in [0, 1]$ is identical to the information on $\phi \in (0, 2]$; our data sampling distribution, however, is defined as the (conditional) joint probability of all event data grouped into phase intervals on $\phi \in [0, 1]$. We display the standardized (Poisson) residuals in the bottom panel: the residuals for the rotational cycle $\phi \in [0, 1]$ were calculated in terms of all event data on that interval (as for likelihood definition), and simply cloned onto the interval $\phi \in (1, 2]$. In Appendix A.2.1 we elaborate on the information displayed here. The complete figure set (6 images) is available in the online journal, for the ST+PST, ST+EST, ST+CST, ST−U, ST−S, and CDT−U models.

(The complete figure set (6 images) is available.)

function, over a subset of the additional prior support, is at most commensurate with the prior expectation of the likelihood function for the other models; globally, the model does not therefore improve as measured solely by the evidence.

Tractability and complexity. Posterior computation accuracy and reproducibility are generally higher as the models become less complex. The ST+CST, ST+EST, and ST+PST models redistributed complexity based on the performance of CDT−U in pursuit of *helpful* complexity and thus higher-efficiency resource consumption. We demonstrate in Figure 16 that effectively all of the improvement of CDT−U over ST−U is captured by the intermediary ST+CST. As a consequence, ST+PST in particular exhibited substantial improvement in regard to the (background-marginalized) likelihood function in the posterior mode, while reducing the number of parameters by limiting the complexity of one hot region; it follows that it should be clearly preferred over CDT−U.

We remark that although the complexity of one hot region was ultimately limited at the ST-level, this does not mean that the signal generated by that region is fixed or performs maximally in some absolute sense. Indeed, the signal generated by one region cannot be decoupled (as stated in Section 2.5.4) from the signal generated by the other for the purpose of statistical inference: (i) the regions are restricted to exist on the

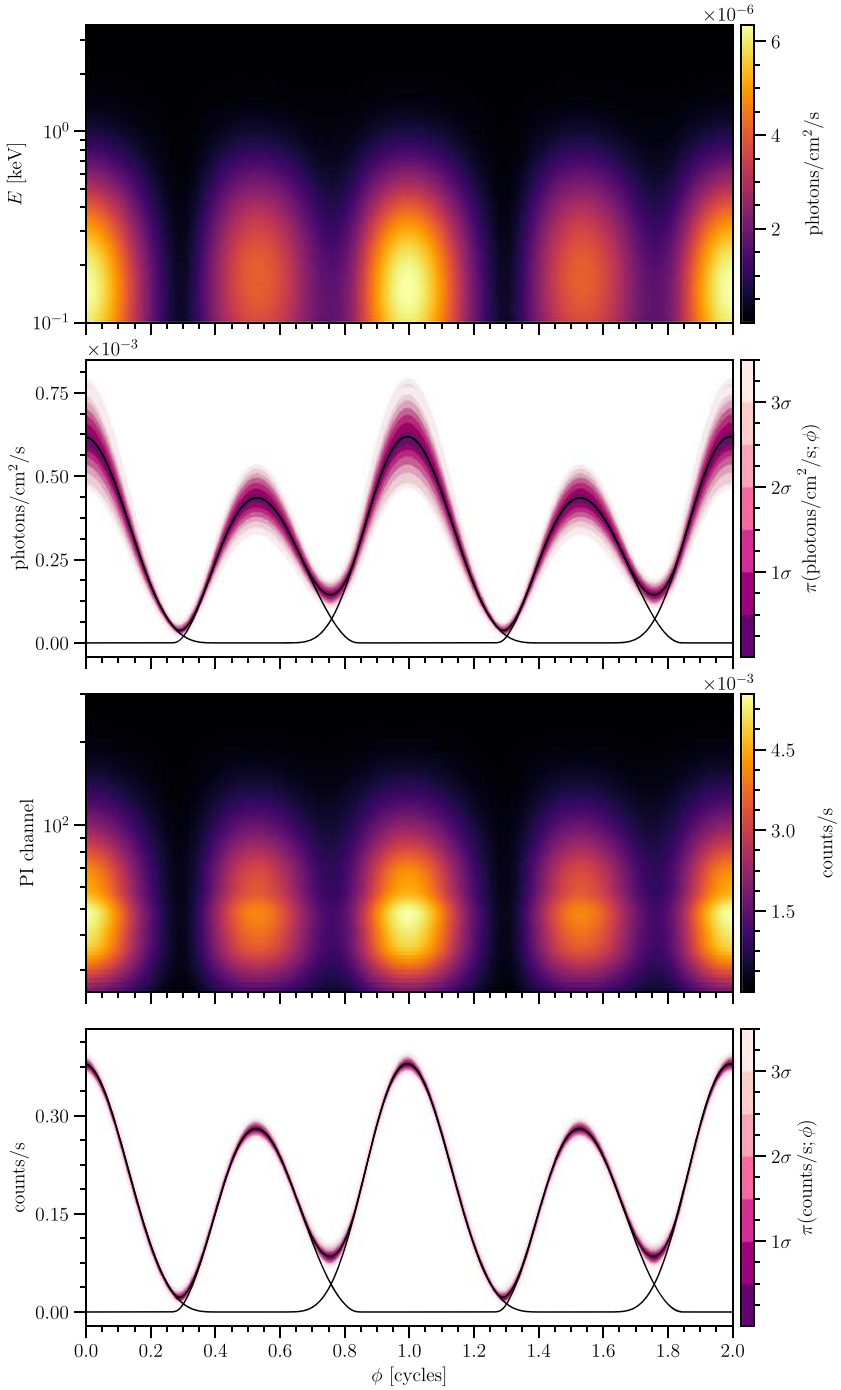

Figure 14. The posterior-expected signal for ST+PST, both incident on the instrument (top and top-middle) and as registered by the instrument (bottom-middle and bottom). The signal in the top panel has been integrated over the linearly spaced instrument energy intervals, and is effectively proportional to the specific photon flux. The black count-rate curves are the posterior-expected signals generated by each hot region separately, and in combination. We also represent the conditional posterior distribution of the incident photon flux (top-middle) and count-rate (bottom) at each phase as a set of one-dimensional highest-density credible intervals, and connect these intervals over phase via the contours; these distributions are denoted by π (photons cm^{-2} s^{-1}; ϕ) and π (counts s^{-1}; ϕ). Note that the fractional width of the credible interval at each phase is usually higher for π (photons cm^{-2} s^{-1}; ϕ) than for π (counts s^{-1}; ϕ) because of the variation permitted for the instrument model; in combination, the signal registered by the instrument is more tightly constrained. To generate the conditional posterior bands we apply the *X-PSI* package, which in turn wraps the fgivenx (Handley 2018) package. The complete figure set (6 images) is available in the online journal.

(The complete figure set (6 images) is available.)

same two-surface within an ambient spacetime; and (ii) for some subset of rotational phases, and for the configurations that report higher (background-marginalized) likelihood values, the images of both regions are simultaneously visible (a posteriori) and registered by the instrument in combination. As a result, upon examination of Figure 16, we observe that the posterior-expected count-rate signal generated by the ST region evolves along the ST−U, ST+CST, ST+EST, and ST+PST sequence,

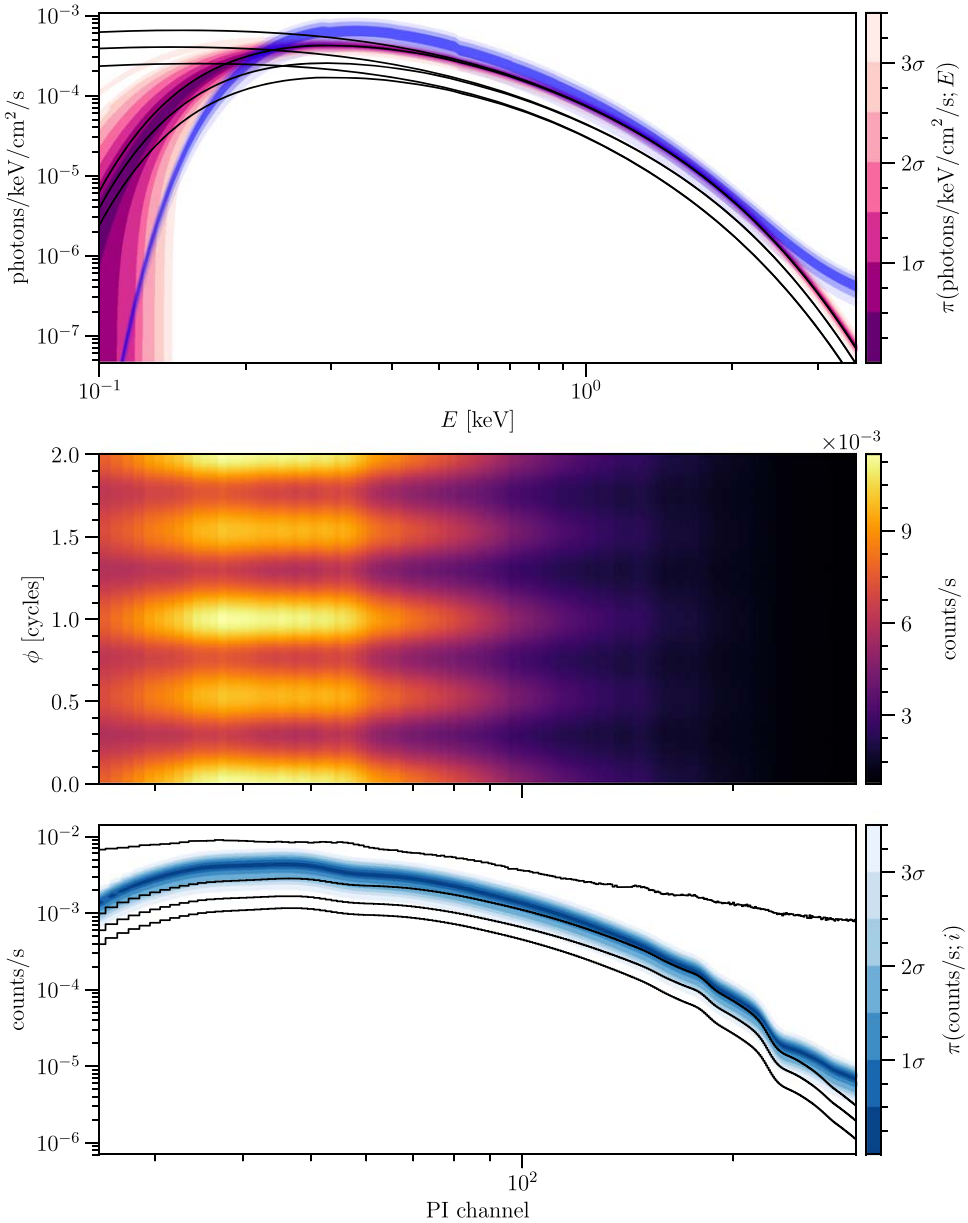

Figure 15. The posterior-expected spectrum for ST+PST, both incident on the instrument (top) and as registered by the instrument (middle and bottom). The black count-rate curves are the posterior-expected spectra generated by each hot region separately, and in combination. In the top panel we display as black curves the incident photon specific flux spectra both with and without interstellar absorption. We represent the conditional posterior distribution π (photons keV^{-1} cm^{-2} s^{-1}; E) of the absorbed incident photon specific flux at each energy as a set of one-dimensional highest-density credible intervals, and connect these intervals over phase via the contours (top); the energies displayed are those spanning the waveband of channel subset [25, 300). The credible intervals fan-out at the lowest energies because (i) conditional on event data for channel subset [25, 300), we are relatively insensitive to the details of the signal for $E \in [0.1, 0.2)$; and (ii) the interstellar attenuation factor is stronger the lower the photon energy, and thus the incident signal varies strongly as a function of the neutral hydrogen column density—a free parameter that operates as an exponent. In the top panel we overlay the incident absorbed spectrum inferred by Bogdanov & Grindlay (2009) based on a phase-averaged analysis of low-background *XMM* observations; the blue band denotes the estimated fitting uncertainty on this spectrum, at each energy, as a Gaussian with fractional standard deviation $\sigma/\mu = 0.15$, and the three opacity levels indicate intervals 1σ through 3σ. There is additional systematic *XMM* flux calibration uncertainty at the $\sim$10%-level that is not included here. In the middle panel we display the background-marginalized posterior-expectation of the source count-rate signal, plus the background count-rate terms that maximize the conditional likelihood function; the signal is equivalent to that displayed in the middle panel of Figure 13. In the bottom panel we display the posterior-expected count-rate spectra generated by the hot regions in combination and individually; we opt not to render the conditional posterior count-rate distribution for each channel because it is too narrow about the expected spectrum to be useful. Moreover, the topmost black step function is the phase-average of the center panel—it is effectively, but not exactly, the observed count-number spectrum divided by the total exposure time $T_{\rm exp}$. We combine the *XMM*-derived count-rate spectrum (and its associated uncertainty) with the marginal *NICER* instrument posterior on parameters α, β, and γ to simulate a conditional probability distribution π (counts s^{-1}; i) for the count-rate in the ith channel; these conditional distributions are connected via the contours in a manner congruent to the top panel described above. The complete figure set (6 images) is available in the online journal.

(The complete figure set (6 images) is available.)

both at phases where the non-ST region is invisible, and at phases where both regions are simultaneously visible. The reader should not therefore interpret our decision to limit the complexity of one region to ST as a statement that an ST region is forecasted to be sufficient for the purpose of future modeling efforts nor that exploration of different models will

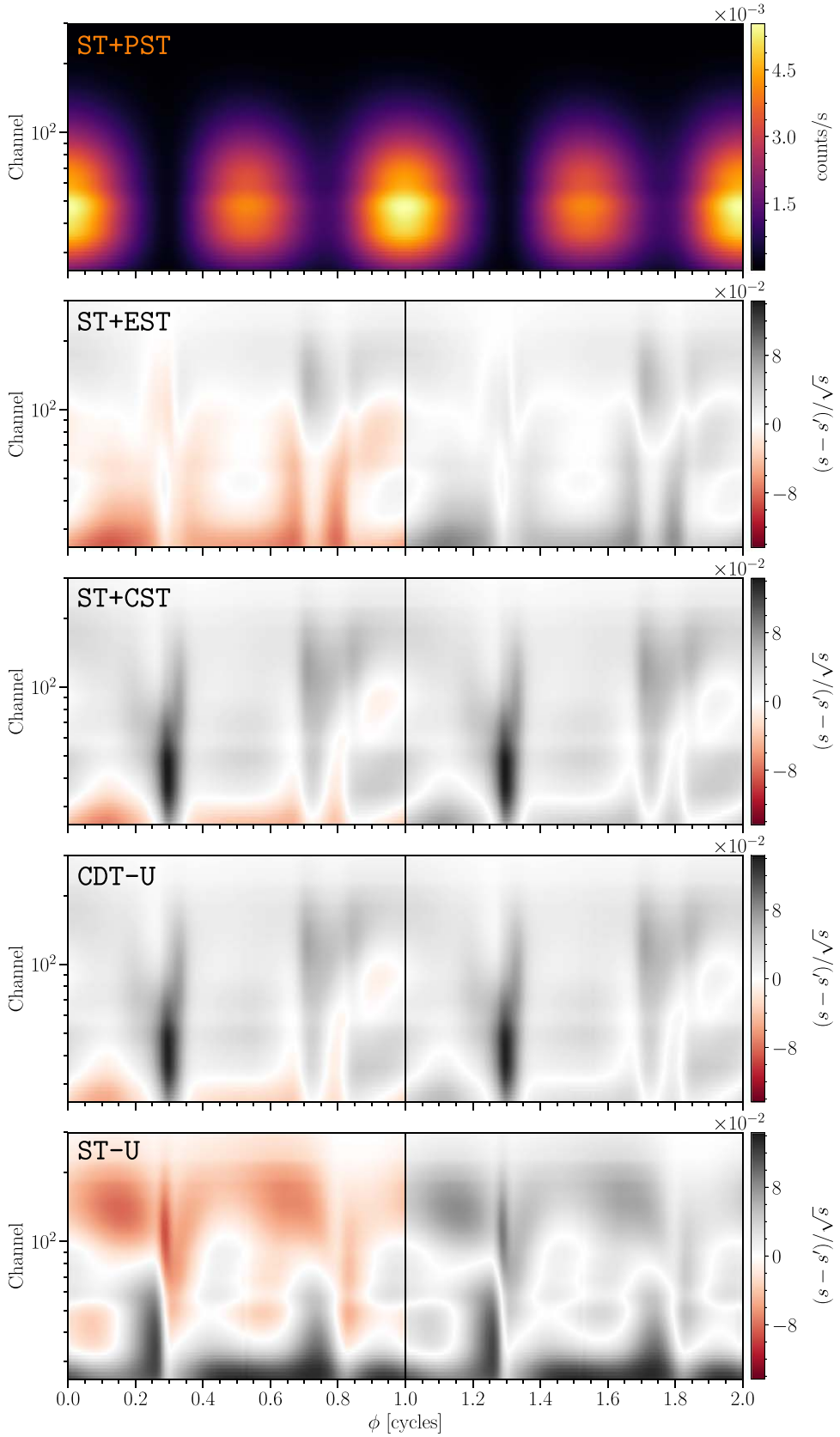

Figure 16. Top panel: the posterior-expected channel-by-channel source count rate signal generated as a function of rotational phase by ST+PST surface emission: $s \coloneqq \mathbb{E}_{\pi(\boldsymbol{\theta})}[g(\boldsymbol{\theta})]$, where $g(\boldsymbol{\theta})$ is a map from parameter space to the corresponding count rate signal. Others panels: the difference between signal s (for ST+PST) and the posterior-expected signal conditional on some other model: let $s' \coloneqq \mathbb{E}_{\pi(\boldsymbol{\theta})}[h(\boldsymbol{\theta})]$, where $h(\boldsymbol{\theta})$ is a map from parameter space to a count-rate signal conditional on some model other than ST+PST. The signals s and s' represent Poissonian arrival processes; we therefore opt to display the difference as $(s - s')/\sqrt{s}$, and scale the signals by $T_{\rm exp}/32$. A grayscale value is then locally representative of the absolute change (shown exclusively on the phase interval $\phi \in [1, 2]$), in units of the Poisson standard deviation, within a phase interval of width $1/32$ cycles as defined during event data pre-processing.

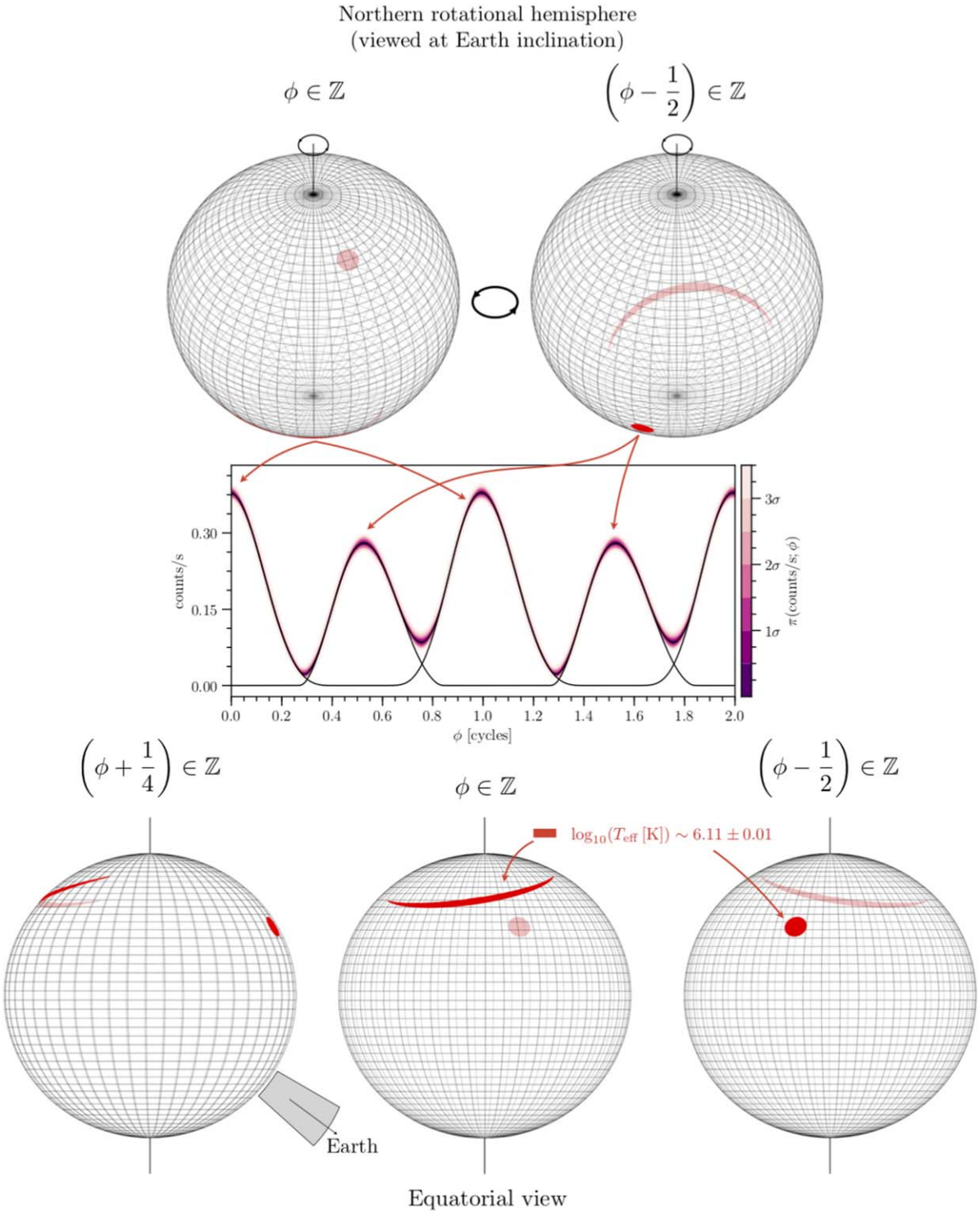

Figure 17. Top panel: schematic diagram of a surface heating configuration—and Earth inclination—representative of those corresponding to points in the ST+PST posterior mode. The configuration rendered here corresponds to the sample that reported the highest background-marginalized likelihood function value across all models (among the values reported by the set of all nested samples). We project the hot regions onto a (unit) sphere and view from the Earth inclination with no ambient gravitational field. The regions are constrained to exist in the same hemisphere, but with remarkably different morphologies. The hot regions are approximately equal in effective temperature and thus we define a new temperature symbol T_{eff} that is common to both. We also display the channel-summed count rate pulse generated by the source emission and indicate which region generates which component; we refer the reader to Figure 14, where this signal is also displayed, for more information. Bottom panel: note that we impose (via the prior support) that the Earth inclination lies within the northern rotational hemisphere, but an identical configuration (in terms of the physics that we consider and thus signal generation) is given via an equatorial reflection of both the Earth direction and radiating regions; we render this alternative configuration as viewed from the equatorial plane, and display the Earth inclination (but not azimuth) as the shaded angular interval bounded by the 16% and 84% quantiles in marginal posterior mass (see Figure 21 and Table 2 for the numerical interval).

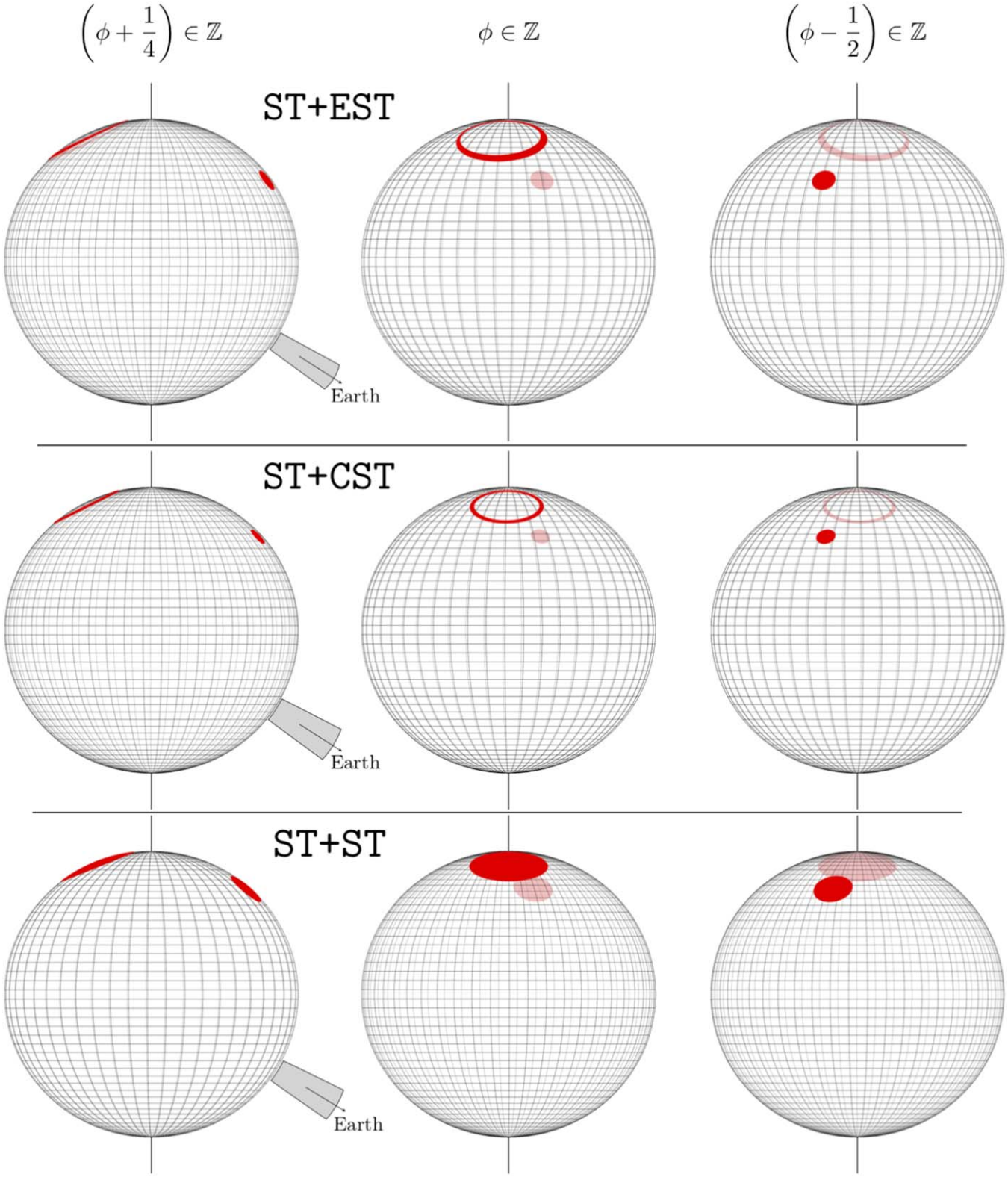

Figure 18. Surface heating configurations conditional on ST+ST (equivalent to ST-U), ST+CST, and ST+EST. For each model the hot regions correspond to the sample assigned the greatest posterior weight and is thus representative, being a draw from the posterior typical set. For each model we display the Earth inclination (but not azimuth) as an angular interval bounded by the 16% and 84% quantiles in marginal posterior mass.

fail to yield improvement; indeed, one could even consider models such as PST-U given that our modeling route for one region was based on CDT-U.

Telescope cross-checking. In Figure 15 we display the posterior information for the phase-integrated spectrum generated by the ST+PST hot regions; corresponding figures for the other models may

Table 2
Summary Table for ST+PST

Parameter	Description	Prior (Density and Support)	$\widehat{\mathrm{CI}}_{68\%}$	$\widehat{D}_{\mathrm{KL}}$
P (ms)	Coordinate spin period	$P = 4.87$,[a] fixed	⋯	⋯
M ($M_\odot$)	Gravitational mass[b]	$M \sim U(1, 3)$[c]	$1.34^{+0.15}_{-0.16}$	$1.26^{+0.02}_{-0.02}$
R_{eq} (km)	Coordinate equatorial radius[d]	$R_{\mathrm{eq}} \sim U[3r_g(1), 16]$[e]	$12.71^{+1.14}_{-1.19}$	$0.78^{+0.02}_{-0.02}$
	Compactness condition	$R_{\mathrm{eq}}/r_g(M) > 3$		
	Compactness condition[f]	$R_{\mathrm{polar}}(M, R_{\mathrm{eq}}, \Omega) \geqslant 3r_g(M)$		
	Enforce elliptical two-surface cross-section	function of $(M, R_{\mathrm{eq}}, \Omega)$		
Θ_p (radians)	ST region center colatitude[g]	$\Theta_p \sim U(0, \pi)$	$2.23^{+0.10}_{-0.10}$	$2.98^{+0.02}_{-0.02}$
ϕ_p (cycles)	ST region initial phase (from Earth)	$\phi_p \sim U(a, a + 0.2)$[h]	$0.46^{+0.00}_{-0.00}$	$4.44^{+0.03}_{-0.04}$
ζ_p (radians)	ST region angular radius	$\zeta_p \sim U(0, \pi/2)$	$0.09^{+0.01}_{-0.01}$	$4.62^{+0.03}_{-0.03}$
Θ_s (radians)	PST region superseding center colatitude	$\Theta_s \sim U(0, \pi)$	$2.91^{+0.05}_{-0.05}$	$3.85^{+0.03}_{-0.03}$
ϕ_s (cycles)	PST region initial phase (from Earth antipode)	$\phi_s \sim U(-0.5, 0.5)$, periodic[i]	$-0.59^{+0.04}_{-0.04}$	$2.43^{+0.02}_{-0.02}$
ψ_s^+ (radians)	PST region angular radii difference[j]	$\xi_s \sim U(0, \pi/2)$, $\psi_s^+ = \psi_s^+(\xi_s, f_s)$[k]	$-0.01^{+0.02}_{-0.02}$	$3.16^{+0.03}_{-0.03}$
ψ_s (radians)	PST region superseding angular radius	$f_s \sim U(0, 2)$, $\psi_s = \psi_s(\xi_s, f_s)$	$0.47^{+0.13}_{-0.13}$	$1.52^{+0.03}_{-0.02}$
$\varkappa_s$	PST region ceding fractional angular offset	$\varkappa_s \sim U(0, 1)$	$0.10^{+0.05}_{-0.03}$	$2.67^{+0.05}_{-0.05}$
φ_s (radians)	PST region ceding azimuthal offset	$\varphi_s \sim U(0, 2\pi)$	$0.71^{+0.10}_{-0.10}$	$2.28^{+0.03}_{-0.03}$
	Non-overlapping hot regions[l]	function of Θ_p through φ_s above		
$\log_{10}(\mathcal{T}_p\,(\mathrm{K}))$	ST region NSX effective temperature	$\log_{10}\mathcal{T}_p \sim U(5.1, 6.8)$, NSX limits	$6.11^{+0.01}_{-0.01}$	$5.29^{+0.03}_{-0.03}$
$\log_{10}(\mathcal{T}_s\,(\mathrm{K}))$	PST region NSX effective temperature	$\log_{10}\mathcal{T}_s \sim U(5.1, 6.8)$, NSX limits	$6.11^{+0.01}_{-0.01}$	$5.75^{+0.03}_{-0.02}$
i (radians)	Earth inclination to rotation axis	$i \sim U(0, \pi/2)$	$0.94^{+0.11}_{-0.10}$	$1.91^{+0.02}_{-0.02}$
D (kpc)	Earth distance	$D \sim N(0.325, 0.009)$[m]	$0.33^{+0.01}_{-0.01}$	$0.07^{+0.01}_{-0.01}$
N_{H} ($10^{20}\mathrm{cm}^{-2}$)	Interstellar neutral H column density	$N_{\mathrm{H}} \sim U(0, 5)$	$0.78^{+0.17}_{-0.16}$	$2.86^{+0.03}_{-0.03}$
NICER α	Calibrated matrix scaling	$\alpha \sim N(1, 0.1)$, $\alpha \in [0.5, 1.5]$	$0.99^{+0.08}_{-0.09}$	$0.04^{+0.01}_{-0.01}$
NICER β	Reference-to-calibrated matrix weighting	$\beta \sim U(0, 1)$	$0.19^{+0.17}_{-0.12}$	$0.96^{+0.02}_{-0.03}$
NICER γ	Reference matrix scaling	$\gamma \sim N(1, 0.1)$, $\gamma \in [0.5, 1.5]$	$0.98^{+0.08}_{-0.08}$	$0.08^{+0.01}_{-0.01}$
	Sampling process information[n]			
	Number of free parameters:[o] 19			
	Number of runs:[p] 1			
	Number of live points: 10^3			
	Inverse hypervolume expansion factor:[q] 0.8			
	Termination condition: 10^{-1}			
	Evidence:[r] $\widehat{\ln \mathcal{Z}} = -36368.28^{+0.49}_{-0.46}$			
	Global KL divergence: $\widehat{D}_{\mathrm{KL}} = 68.9^{+0.9}_{-0.8}$ bits			
	Number of core[s] hours: 42453			
	Likelihood evaluations: 78343018			
	Nested replacements: 57972			
	Weighted posterior samples:[t] 20177			

Notes. We provide (i) the parameters that constitute the sampling space, with symbols, units, and short descriptions; (ii) any notable derived or fixed parameters; (iii) the joint prior distribution, including hard truncation bounds and constraint equations that define the hyperboundary of the support; (iv) one-dimensional (marginal) 68.3% credible interval estimates symmetric in posterior mass about the *median* ($\widehat{\mathrm{CI}}_{68\%}$); and (v) KL divergence estimates in *bits* ($\widehat{D}_{\mathrm{KL}}$) representing prior-to-posterior information gain (a scalar with an associated error calculated as the 68.3% distributional interval about the median with respect to sampling process realizations; see Appendix A.2.4 for high-level description of the divergence). Constraint equations in terms of two or more parameters result in *marginal* distributions that are not equivalent to those inverse-sampled.

[a] Arzoumanian et al. (2018).
[b] Interpreted as a rotationally perturbed mass monopole moment (e.g., Hartle 1967), but the perturbation is small for the spin frequency of PSR J0030+0451 (see Section 4.2).
[c] Hard lower bound based loosely on plausible astrophysical formation channels (see, e.g., Strobel et al. 1999).
[d] An alternative two-dimensional space of $g(M, R_{\mathrm{eq}})$ and $h(M, R_{\mathrm{eq}})$—where $g \neq h$—on which we could choose to specify a joint flat prior density distribution is that of $g := M$ and $h := R_{\mathrm{eq}}/r_g(M)$.
[e] The function $r_g(M)$ denotes the gravitational radius explicitly in dimensions of length.
[f] The coordinate polar radius of the source two-surface, R_{polar} $(M, R_{\mathrm{eq}}, \Omega)$, is a quasi-universal function adopted from AlGendy & Morsink (2014), where $\Omega := 2\pi/P$ is the coordinate angular rotation frequency. This compactness condition, together with the elliptical surface requirement below are unimportant for the $P \sim 5$ ms spin period of PSR J0030+0451, and therefore we ignore these constraints in Tables 3 through 7.
[g] Note that for parameters where a lower bound of zero would correspond to absence of pulsations, we use some small finite number as a lower bound.
[h] Where $\phi_p = a$ is an arbitrary phase dependent on event data pre-processing. We set $a = 0.35$.
[i] The periodic boundary is admitted and handled by MultiNest. However, this is an unnecessary measure because we straightforwardly define the mapping from the native sampling space to the space of ϕ_s such that the likelihood function maxima are not in the vicinity of this boundary.
[j] The difference is defined as $\psi_s^+ := \zeta_s - \psi_s$, where ζ_s is the angular radius of the ceding member that radiates where it is not superseded.
[k] See Section 2.5.6.
[l] Refer to Appendix B.2.4.
[m] Constructed to approximate the information in the measurement (statistical information) reported by Arzoumanian et al. (2018). The support $D \in [0.235, 0.415]$ is equivalent to the interval $\mu \pm 10\sigma$.
[n] Refer to Appendix A for definitions.
[o] In the sampling space; the number of background count-rate parameters is equal to the number of channels defined by the data set.
[p] The mode-separation MultiNest variant was deactivated, meaning that isolated modes are not evolved independently and nested sampling threads contact multiple modes.
[q] For this sampling process, nor any such process reported in this work, we did *not* activate constant-efficiency MultiNest active-point bounding variant.
[r] Defined as the prior predictive probability $p(\boldsymbol{d} \mid \mathtt{ST} + \mathtt{PST})$. We report the interval about the median containing ±45% of 10^3 joint bootstrap-weight replications for the combined run. Note, however, that in order to complete the reported evidence for comparison to models other than those defined in this work, upper bounds for the background parameters need to be specified as described in Section 2.4.3.
[s] Intel® Xeon E5-2697Av4 (2.60 GHz; Broadwell) processors on the SURFsara Cartesius supercomputer. Note that these are physical cores—i.e., hyper-threading technology is not invoked.
[t] Excludes samples with important weight smaller than 10^{-6} times the largest such weight among samples.

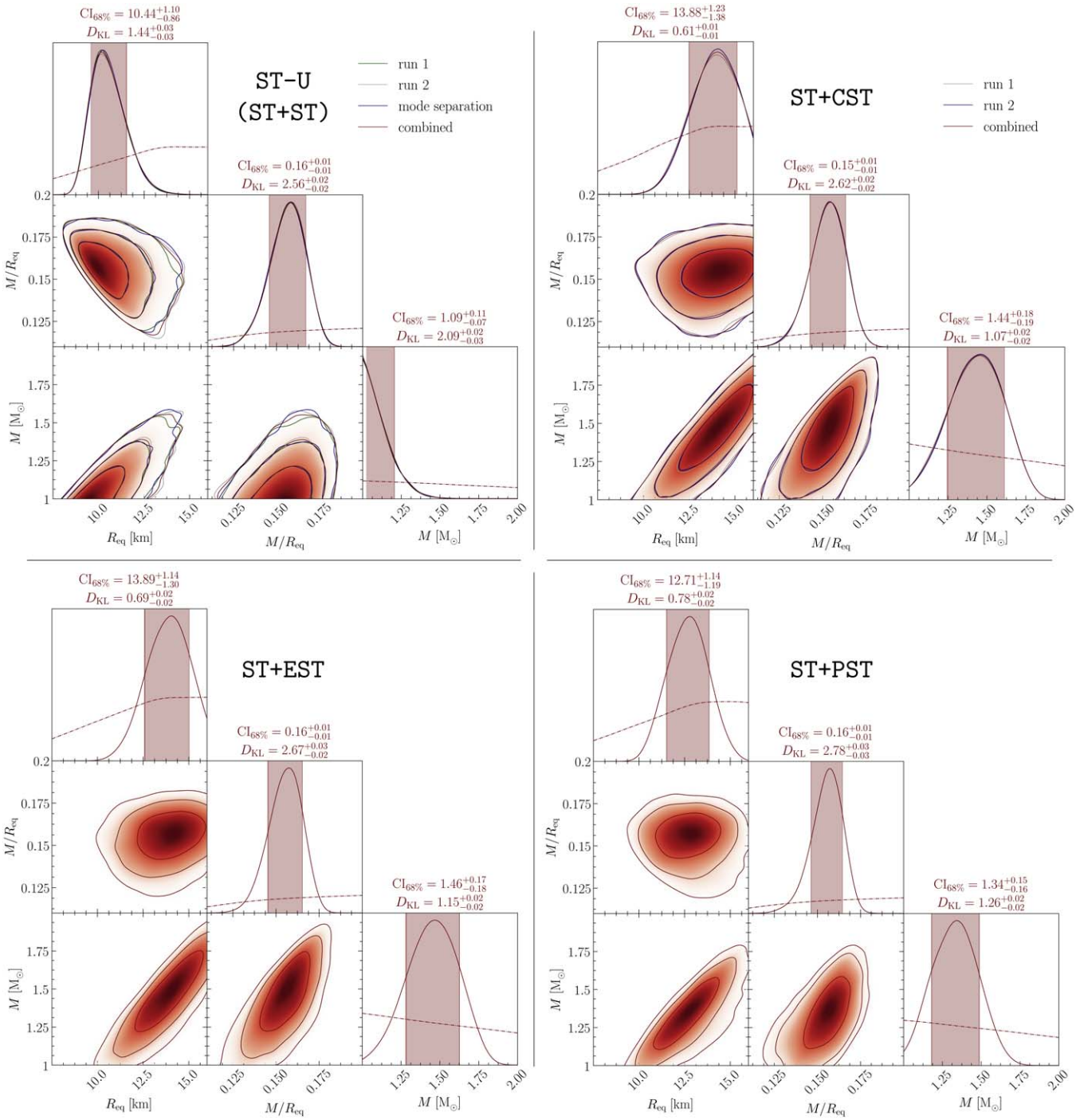

Figure 19. One- and two-dimensional marginal posterior density distributions for the MSP spacetime parameters conditional on the each in the sequence ST−U, ST+CST, ST+EST, and ST+PST. From leftmost to rightmost in each panel, the parameters are equatorial radius, (equatorial) compactness, and gravitational mass. We display the marginal prior density distributions for each parameter as the dashed–dotted functions. For the less expensive ST−U and ST+CST models we executed two production runs and combined them, while for each of ST+EST and ST+PST we executed a single production run. We also display an ST−U run in which the mode-separation MultiNest variant was activated, but because neither the theory nor the software exists for combining such a sampling process with runs in default mode (where sampling threads can migrate between posterior modes), it is not included in the combined run. The mode-separation run allocated ∼one-third of the sampling resolution (i.e., sampling threads, or active points) to a second posterior mode with negligible local mass; this mode corresponds to a distinct phase configuration, with the hot regions—which are distinguished by their order in colatitude—transposed in their coupling to the pulse components visible in the phase-folded event data. We report the KL divergence, D_{KL}, from prior to posterior in bits for each parameter, together with an error interval containing 68.3% of $\widehat{D}_{\mathrm{KL}}$ estimates based on simulated nested sampling process realizations. The shaded credible intervals $\mathrm{CI}_{68\%}$ for each parameter are symmetric in marginal posterior mass about the median, containing 68.3% of the mass; the (barely discernible) darker intervals at the $\mathrm{CI}_{68\%}$ boundaries contain 68.3%, respectively, of the 15.85% and 84.15% quantiles in posterior mass, again based on simulated nested sampling process realizations. The credible regions in the off-diagonal panels, on the other hand, are uniquely the highest-density—and thus the smallest possible—credible regions, containing 68.3%, 95.4%, and 99.7% of the posterior mass. In Appendix A we provide additional information regarding posterior kernel density estimation, error analysis, and the estimators displayed here. The complete figure set (7 images) is available in the online journal.

(The complete figure set (7 images) is available.)

be found in the online figure set. We overlay a model PSR J0030+0451 spectrum, derived via analysis of low-background low-signal-to-noise ratio phase-integrated *XMM* observations (see Bogdanov & Grindlay 2009); this spectrum is considered as a guiding upper bound for all emission in the *NICER* waveband from the PSR J0030+0451 system. The ST−U, CDT−U, ST+CST, ST+EST, and ST+PST models do not violate this condition in channels [25, 300) spanned by the event data considered, nor at incident photon energies that couple strongly to this channel subset; the ST−S model clearly violates this condition. The *XMM*-derived model is more uncertain than shown at low energies in Figure 15, due to unresolved likelihood function degeneracy between $N_{\rm H}$ and the thermal components. The *XMM* spectral analysis also included a power-law component, which is subsumed into the phase-invariant (background) terms in our analysis of *NICER* data (see the topmost *black* count-rate step function in the *bottom* panel of Figure 15); the discrepancy at higher energies is thus accounted for. Nevertheless, a pertinent question remains regarding how much of the signal generated by surface emission is captured by the phase-invariant count-rate terms; these terms combine linearly with the signals from the hot regions and are intended to parameterize the background contribution. We refer the reader to Section 4.1 for more detailed discussion on this topic.

Marginalization. For parameters that are shared between discrete models $\{\mathcal{M}_m\}$, where $\mathcal{M}_m \subset \mathscr{M}$, we could in principle marginalize over the discrete parameter m (see Appendix C of Riley & Watts 2019, for a formulation consistent with Section 2.3), provided we accept a marginal prior mass distribution of m. If two or more models are competitive, the marginal joint posterior distribution of the shared parameters is not dominated by the information from a single model. As stated above, we cannot distinguish between four of the highest-evidence models (ST+PST, ST+EST, ST+CST, and CDT−U). Moreover, for ST+CST, ST+EST, and ST+PST, the marginal joint posterior distribution of the shared spacetime parameters of interest is only mildly sensitive to model choice—i.e., the compactness constraints are commensurate, while the mass and radius are only weakly constrained individually, and the joint credible regions exhibit high partial overlap. For ST+PST, the marginal joint posterior distribution of the shared spacetime parameters discernibly evolves, but the mass and radius remain weakly constrained individually. Given that m labels models that are often (approximately) nested and which differ only in phenomenological complexity, we opt not to marginalize shared parameters over those models; instead, we report headline parameter estimates for ST+PST, which exhibits the largest background-marginalized likelihood function values in any posterior typical set.

4. Discussion

In this section we highlight how our inferences may be sensitive to the modeling assumptions made, and discuss the implications of our inferences for both dense matter physics and NS astrophysics.

4.1. Modeling Assumptions

The inferences that we report are conditional upon a number of modeling assumptions. These assumptions were physically motivated, and reassuringly there are no obvious large discrepancies or structures in the pulse-profile residuals to indicate a major problem. Nonetheless, the sensitivity of our results to these assumptions should be explored in future work, given additional computational resource allocations. With regard to the MSP, the biggest model-dependencies are (i) the atmosphere (see Section 4.1.1); (ii) the treatment of phase-invariant components of the total signal (see Section 4.1.2); and (iii) the assumption there exist two disjoint hot regions, each of which is radiatively contiguous and has a temperature field that is adequately represented by one of the models described in Section 2 (see 4.1.2). The instrument model (see Section 4.1.3) is of less concern.

4.1.1. Atmosphere

Two properties that could affect the atmosphere models used in our analyses are chemical composition (hydrogen as opposed to helium) and ionization state (fully versus partially ionized). In this Letter we have considered only a hydrogen composition: hydrogen would dominate the composition of matter accreted from the interstellar medium (Blaes et al. 1992), while matter accreted from a binary companion star would be predominantly hydrogen or helium. There are other processes that may drive changes in composition. For instance: hydrogen would result from spallation (Bildsten et al. 1992), diffusive nuclear burning could convert hydrogen to helium (Chang & Bildsten 2003, 2004), and significant pulsar wind excavation could make visible an underlying heavy element layer (Chang & Bildsten 2004). If the atmosphere were in fact dominated by helium, we could expect changes because helium atmospheres radiate differently from those of hydrogen. For example, hydrogen and helium model specific intensities, at an atmosphere effective temperature of 10^6 K (the approximate inferred temperature for the hot regions for this source), have fractional differences of at most 2%–5% at 0.5–1 keV in the (maximal) forward direction (Bogdanov et al. 2019c).

Regarding ionization state, our atmosphere models are constructed assuming the atmospheric plasma is fully ionized, such that the dominant opacity in regimes of interest is that due to electron free–free absorption (Ho & Lai 2001). While opacity tables for partially ionized matter exist (Iglesias & Rogers 1996; Badnell et al. 2005; Colgan et al. 2016), they do not cover the full range of energies and temperatures needed for our analysis. However, the hydrogen neutral fraction in the atmosphere at 10^6 K is low, and a comparison of our fully ionized hydrogen atmosphere model with that constructed using the OP (Badnell et al. 2005) opacity table yields specific intensity fractional differences of at most 1%–2% at 0.5–1 keV in the (maximal) forward direction at an atmosphere effective temperature of 10^6 K (Bogdanov et al. 2019c). The importance of including partial ionization, in comparison to developing other aspects of the model (e.g., Section 4.1.2), is not clear; but partially ionized models will be part of future re-analysis as updated opacity tables become available.

4.1.2. Surface Heating Estimation and Treatment of Phase-invariant Components

Predicting the MSP surface temperature field from ab initio[68] calculations of energy deposition by magnetospheric currents is, as described in Section 2, notoriously challenging. In this work we have assumed that there are only two distinct hot regions, motivated by the fact that there appear to be two pulsed components in the pulse profile. If the (surface) field

[68] Terminology adopted from the series of studies by Philippov et al. (2015a, 2015b) and Philippov & Spitkovsky (2018) on pulsar magnetospheric simulations.

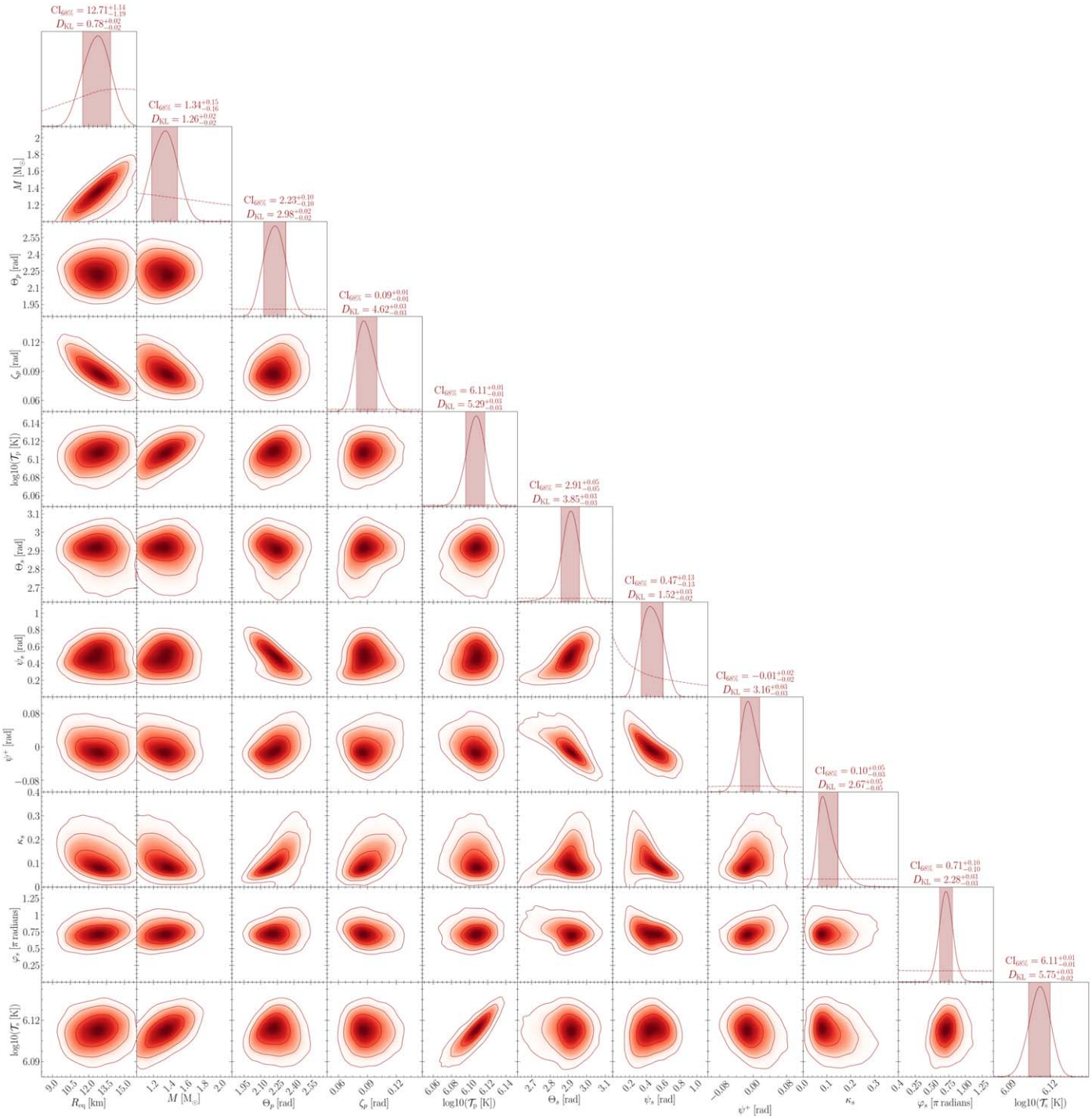

Figure 20. One- and two-dimensional marginal posterior density distributions for the MSP parameters conditional on ST+PST. From leftmost to rightmost: equatorial radius R_{eq}; gravitational radius M; ST center colatitude Θ_p; ST angular radius ζ_p; ST NSX effective temperature $\log_{10}\mathcal{T}_p$; PST superseding member center colatitude Θ_s; PST superseding angular radius ψ_s; PST superseding member angular radius difference $\psi_s^+ = \zeta_s - \psi_s$; where ζ_s is the angular radius of the ceding member; PST ceding member fractional angular offset $\varkappa_s$ (labeled as κ_s); PST ceding member azimuthal offset φ_s; and PST ceding NSX effective temperature $\log_{10}\mathcal{T}_s$. For descriptions of the information displayed, refer to Figure 19; note that here we display the marginal posterior density distribution for each parameter as a single solid function due to the number of panels. We choose not to display joint posterior distributions for all pairs of model parameters because the number of panels is prohibitive; moreover, the posterior azimuthal separation of the ST and PST regions is displayed in Figure 21. The complete figure set (6 images) is available in the online journal.

(The complete figure set (6 images) is available.)

structure involves higher-order multipoles,[69] additional polar caps—and thus additional disjoint surface heating—may be possible, and/or more complicated polar cap topologies (such as ring-like) may be possible. We have also assumed specific forms for each hot region; the true temperature field is more complex, and both the physical complexity and our statistical sensitivity to such complexity should be investigated further. In lieu of a physical emission model for the stellar surface exterior

[69] With respect to some coordinate system that simplifies vector spherical harmonic field expansion; this coordinate system will generally be rotated and displaced from the system with stellar spin axis defined as the polar axis.

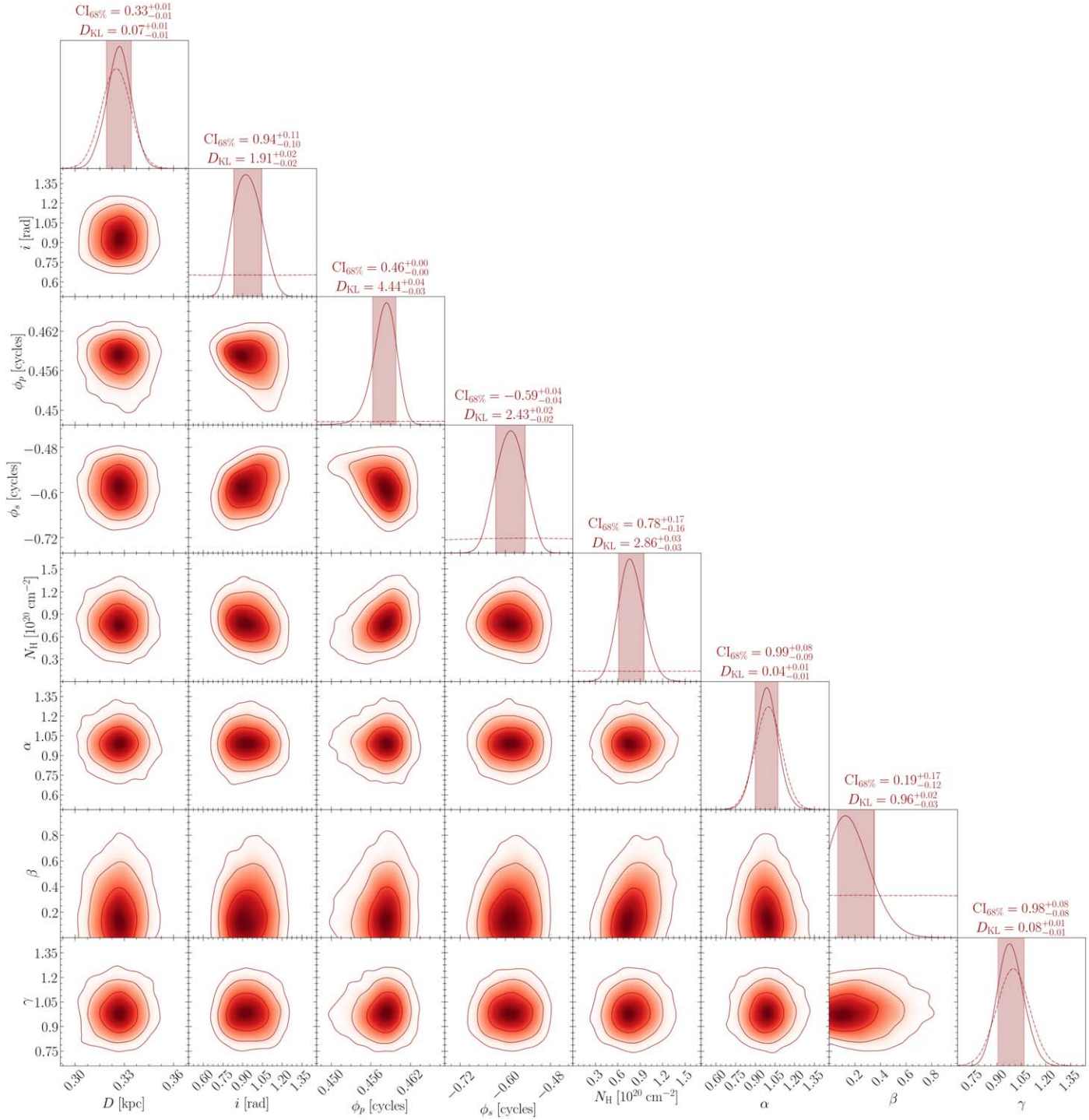

Figure 21. One- and two-dimensional marginal posterior density distributions for parameters pertaining mostly to the MSP observation, conditional on ST+PST. From leftmost to rightmost: distance D; Earth inclination i; ST center azimuth (phase) relative to Earth direction ϕ_p; PST superseding member center azimuth (phase) relative to Earth antipode ϕ_s; interstellar neutral hydrogen column density N_{H}; and *NICER* instrument parameters α, β, and γ. For descriptions of the information displayed, refer to Figure 19; note that here we display the marginal posterior density distribution for each parameter as a single solid function due to the number of panels. The complete figure set (6 images) is available in the online journal.

(The complete figure set (6 images) is available.)

of the hot regions, we subsumed the non-pulsed component of any such emission (which is expected a priori to be dominant if hot regions with smaller angular extent are favored) within phase-invariant count-rate terms; however, this would be a minor concern on the premise that outside of the footpoints of open magnetic field lines at the polar caps, there is no energetically comparable heating to which we are sensitive when observing with *NICER*.

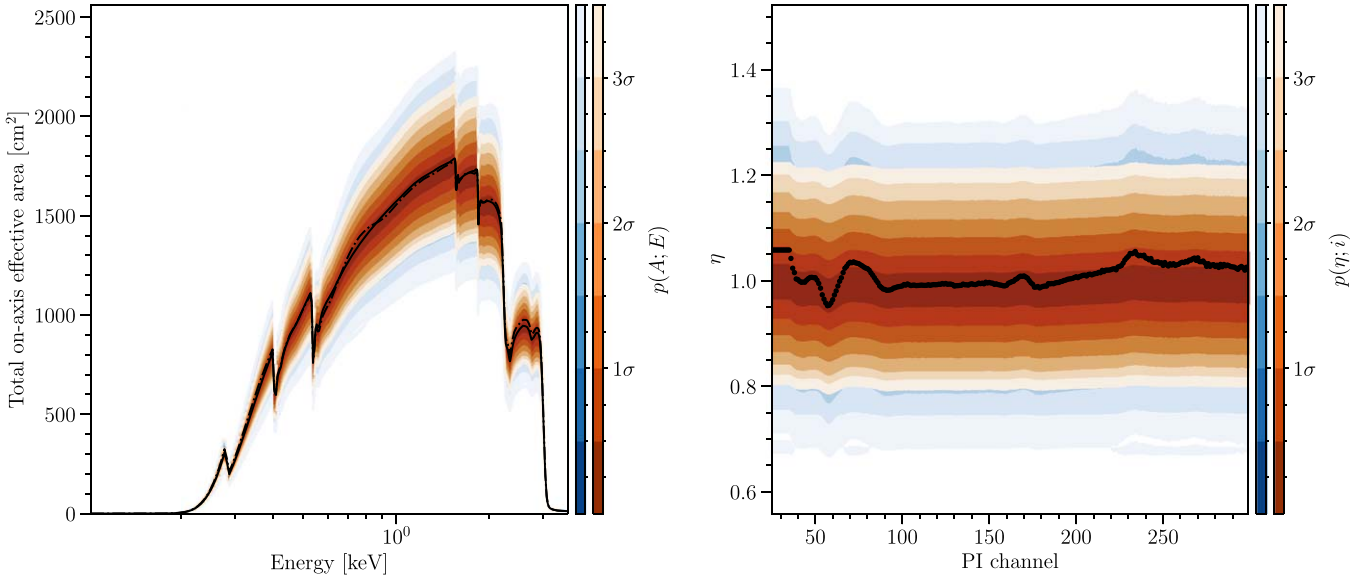

Figure 22. We update the instrument prior (displayed in Figure 2) conditional on ST+PST. The conditional posterior distributions are represented by the orange bands; the conditional prior distributions are displayed in blue to indicate information gain about the instrument, and the black lines and points are equivalent to those in Figure 2. The complete figure set (6 images) is available in the online journal.

(The complete figure set (6 images) is available.)

All emission from sources other than the hot regions—a combination of astrophysical and instrumental—was left free in our models in the form of a set of phase-invariant count-rate terms (background parameters), one per channel, which we collected under the envelope of *background contribution* (refer to Section 2.4.3). Moreover, an improper joint flat prior was implemented that was separable with respect to these background parameters; no upper bounds (or lower bounds) were defined for the prior support, in lieu of a physical (generative) model for the total contribution from the hot regions (and thus surface if emission exterior of the regions is considered unimportant). Such a model would need to account for the combined (phase-invariant) signal attributed to off-surface emission and any astrophysical backgrounds in the field of view, in the *NICER* waveband, based on previous observations of PSR J0030+0451 and/or theoretical modeling.

Remarkably, by neglecting any physical (generative) model for the total counts attributed to *all* surface emission, the phase-invariant terms can even capture emission from the hot regions. One can reason that by permitting the phase-invariant terms to capture all or most of the phase-invariant signal components, there may then exist *background-marginalized* likelihood function maxima corresponding to signals that are (i) dominated by phase-invariant terms over a fraction of a rotational cycle, and (ii) elsewhere found to describe the pulse-profile adequately (in combination with the phase-invariant terms). Near pulse minima, the hot region contribution can be entirely dominated in linear combination with the phase-invariant terms, if the regions are both close to the visible limb of the star, or even partially or wholly non-visible. Such a heating configuration may exhibit systematic bias in the sense that (i) it is not considered an adequate approximation of the configuration inferred when physical limits are modeled for the contribution from the stellar surface (or specifically the hot regions), or (ii) that a configuration alluded to in point (i) is not encompassed by a given posterior credible region boundary. On the other hand, it could be viewed that our treatment of the phase-invariant component of the total signal is in some aspects conservative: posterior credible regions may be appreciably larger than if such physical limits on surface contribution are imposed. In the *X-PSI* documentation (Riley & Watts 2019) a simple parameter estimation workflow is demonstrated using the same default background treatment implemented in this present work; while there is no evidence for systematic bias nor credible region inflation in that specific case (where the true data-generating process is known), guarantees cannot be made universally.

Upon examination of Figure 14 we see that the combined signal from the hot regions falls to near zero at its minimum—such that the fractional amplitude of the signal is near unity—and is thus *not inconsistent* with a phase-invariant component of the combined signal being subsumed in the background. Further, examination of Figure 15, in which we cross-check the ST+PST region spectrum with a PSR J0030+0451 spectrum inferred by Bogdanov & Grindlay (2009), further suggests that a fraction of the contribution from the hot regions is subsumed in the background. Interestingly, Bogdanov & Grindlay (2009) inferred a spectrum with two thermal components of different temperatures.[70]

We attribute the discrepancy to a number of factors. First, the *XMM* photon event set had size $\mathcal{O}(10^4)$, nearly two orders of magnitude smaller than the number of *NICER* events used in this work. Second, it is known that Bogdanov & Grindlay (2009) did not fully resolve degeneracy between the thermal components and the neutral hydrogen column density N_{H}. Lastly, *XMM* is an imaging telescope: the background signal

[70] Note that Bogdanov & Grindlay (2009) explicitly calculate the phase-resolved signal generated by rotating single-temperature circular hot spots, and then phase-average; it is thus not the case that the discrepancy is explained by *our* rotating circular hot spots (refer to ST-U), whose effective temperatures are commensurate, mimicking a dual-temperature *incident* spectrum due to relativistic rotation.

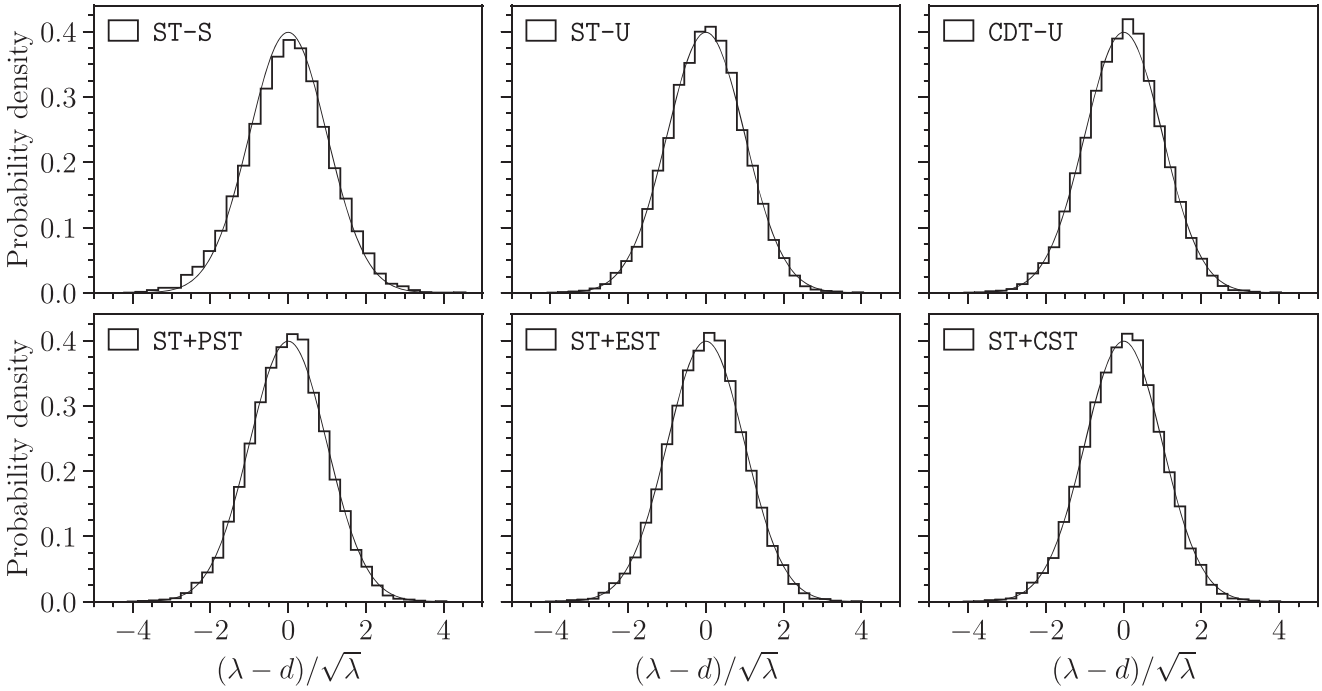

Figure 23. Summary of the two-dimensional residual panels in the online figure set associated with Figure 13. For each model we identify the sample (parameter vector) $\hat{\boldsymbol{\theta}}_{\mathrm{BMML}}$ that reported the highest background-marginalized likelihood function value among identified posterior modes, together with the background count-rate vector $\hat{\boldsymbol{B}}_{\mathrm{CML}}$ that maximizes the conditional likelihood function given $\hat{\boldsymbol{\theta}}_{\mathrm{BMML}}$. Given the expectations $\mathbb{E}[x_{ij}] = \lambda_{ij}(\hat{\boldsymbol{\theta}}_{\mathrm{BMML}}, \hat{\boldsymbol{B}}_{\mathrm{CML}})$, we evaluate the residuals $(\lambda - d)/\sqrt{\lambda}$ for each phase-channel interval, where $\{d_{ij}\}$ are variates of independent Poisson-random variables $\{x_{ij}\}$. We display in each panel the distribution of these random variates (the real count numbers). The minimum number of expected counts in any phase-channel interval is $\sim$30, and thus the $\{x_{ij}\}$ drawn from the sampling distribution are, approximately, identically and normally distributed if transformed as $y \coloneqq (\lambda - x)/\sqrt{\lambda}$. The smooth black distribution in each panel is a normal distribution. The data sampling-distributions for the ST-U model and models higher in complexity do not exhibit systematic structural inaccuracies in the context of the variates: there are no clear signs of noise-model inaccuracy or over-fitting, nor are there clear signs of residual correlations in, e.g., Figure 13. These models can thus perform adequately as point-measure predictors of structure in the real count-number data. The residuals conditional on the ST-S model are distributed with larger variance than unity (normal): more weight is visible in the wings, and less in the near vicinity of zero.

(The complete figure set (3 images) is available.)

was well determined by imaging nearby source-free regions of the sky, and was subsequently used to impose that the surface hot spots generate the remaining signal from the imaged (point-source) MSP. Such a model is distinctly different from those we consider here for *NICER*, a non-imaging telescope; we do not impose (e.g., via some informative background prior) the signal to be generated by the surface hot regions. As a result, we may inaccurately subsume a cooler contribution from the hot regions into the phase-invariant likelihood terms as suggested above; Bogdanov & Grindlay (2009), on the other hand, may miss some non-diffuse radiative component(s) in the near vicinity of the surface of PSR J0030+0451, and thus require their hot spots to generate additional cooler emission than they do in physical reality.

With these considerations in hand, we conclude that without further work, it is unclear which inferred signal is more physically accurate. Indeed, the existence and treatment of additional X-ray emission by PSR J0030+0451—or from its circumstellar vicinity—in the *NICER* waveband is considered an open question for future modeling. Moreover, the sensitivity of parameter estimation to requiring a certain phase-invariant contribution specifically from the hot regions could be investigated with newly allocated computing resources.

A (superficially) straightforward alternative to a full physical generative model of the non-pulsed surface and off-surface emission would be to define bounds—upper in particular—on the prior support of the channel-by-channel background count-rate parameters (refer to related discussion on limits in Section 2.4.3). One must then address the question of how. One option is to move the difficulty of defining a prior density for the background to another level in a Bayesian hierarchy via a hyperparameter (e.g., the upper bound of a flat density function) and a corresponding hyperprior for each channel; each hyperparameter and background parameter pair must then be jointly numerically marginalized over to ensure sampling is tractable in a lower-dimensional parameter space. Another option would be to define a conditional prior distribution for each background parameter, where the upper limit of the support is a function of the source parameters—e.g., some fraction of the phase-average source counts in a channel.

We did not consider at the outset of this work the possibility of jointly modeling *NICER* and *XMM* event data—a strategy both tractable and arguably more rigorous given that we do not have likelihood function information nor posterior information from Bogdanov & Grindlay (2009) that is compatible as a prior information to be updated conditional on the *NICER* data. We could thus consider constructing a joint likelihood function over observations with both telescopes (requiring definition of at least one more nuisance parameter). On the other hand, the

NICER event data comprise far more photons than do the *XMM* data, and so inferences may be dominated by the (background-marginalized) *NICER* likelihood function. There are, however, good prospects for improving our understanding of the *NICER* background (particle radiation and diffuse sky terms; see Section 2.4.3 and Bogdanov et al. 2019a), even without new input from *XMM* observations or other imaging capabilities.

Observations with a future high-time resolution soft X-ray spectroscopic imaging telescope, such as the *Athena X-ray Observatory* (Nandra et al. 2013), would be synergistic with archival *NICER* data—and/or observations with a future large-area soft spectroscopic timing telescope such as the *enhanced X-ray Timing and Polarimetry mission* (*eXTP*; Zhang et al. 2019; Watts et al. 2019) or the *Spectroscopic Time-Resolving Observatory for Broadband Energy X-rays* (*STROBE-X*; Ray et al. 2019). The high-sensitivity (read large-area) imaging capabilities of *Athena* (with $\sim 5''$–$10''$ angular resolution[71]) and its two instruments, the *X-ray Integral Field Unit* (*X-IFU*; 10 μs time resolution[72]) and the *Wide Field Imager* (80 μs time resolution), will permit modeling of the background emission not originating from the line of sight of the PSR J0030+0451[73] system (as permitted by the point-spread function) in a similar manner to Bogdanov & Grindlay (2009) for *XMM* (and also Bogdanov 2013, for PSR J0437−4715). Furthermore, the microcalorimeter spectral resolution of *X-IFU* ($\sim$2.5 eV resolution for photons energies <7 keV) will permit precise measurements of various edges of the interstellar medium (e.g., oxygen K edge at 0.55 keV, iron L edge at 0.72 keV), thereby enabling derivation of independent tight constraints on the hydrogen column density $N_{\rm H}$ for a given MSP. Archival *NICER* MSP data, on the other hand, will remain valuable far into the future because the principal *NICER* mission science objectives focus purely on MSPs; *NICER* will have compiled $\mathcal{O}(10^6)$ s integrated exposures on the primary MSP targets, meaning that despite the smaller total effective area, the size of the event data set will be synergistic with an advanced multi-faceted mission such as *Athena* whose science objectives are broader. Consequently, observations with the *Athena* instruments will enable us to jointly model data sets, and make definitive progress on disentangling the signal generated by surface hot regions from the complicated phase-invariant emission detected by *NICER* (or a future non-imaging telescope).

4.1.3. Instrument

We implemented a specific instrument response model (Section 2.4.2): a simple ad hoc parameterization designed to combine several available calibration products and thus account for both energy-independent (absolute flux calibration) and energy-dependent uncertainty. Sensitivity to our choice of astrophysical calibration source, the Crab, also needs further study; it is known that operation in response to an incident radiation field is a function of its properties (see Section 2.4.2). Future study could explore whether using different calibration sources affects inferences. Another interesting question may be posed as to how the posterior information about this instrument model evolves as we update our knowledge via analysis of other sources (MSPs and otherwise).

As our understanding of the *NICER* instrument improves, it should be possible to improve on this model. One option might be to adopt a more sophisticated approach based on Lee et al. (2011) and Xu et al. (2014) to estimating the uncertainty in instrumental response for *Chandra*. At present such a sophisticated approach may be unjustified because computational expense would be amplified by increasing the complexity of the instrument model instead of—or in addition to—the complexity of model astrophysical sources whose nature is more uncertain.

4.2. Mass and Radius Constraints in Context

For ST+PST, the inferred mass M and equatorial radius $R_{\rm eq}$ are $1.34^{+0.15}_{-0.16}\,M_\odot$ and $12.71^{+1.14}_{-1.19}$ km, where the credible interval bounds are approximately the 16% and 84% quantiles in marginal posterior mass, given relative to the median. The marginal credible intervals may thus be considered as 1σ intervals (containing 68.3% of the posterior mass), where $\sigma_M/M \sim 11\%$ and $\sigma_R/R \sim 9.2\%$. For completeness, and to assist comparison with results derived using other methods, we also give the values for the 90% credible interval ($M = 1.34 \pm 0.24\ M_\odot$, $R_{\rm eq} = 12.71^{+1.83}_{-1.85}$ km) and the 95% credible interval ($M = 1.34^{+0.28}_{-0.27}\,M_\odot$, $R_{\rm eq} = 12.71^{+2.15}_{-2.14}$ km). The (equatorial) compactness $GM/R_{\rm eq}c^2 = 0.156^{+0.008}_{-0.010}$ is more tightly constrained than both M and $R_{\rm eq}$ individually, at the $\sim$6% level; the 90% credible interval is $GM/R_{\rm eq}c^2 = 0.156^{+0.013}_{-0.017}$, and the 95% credible interval is $GM/R_{\rm eq}c^2 = 0.156^{+0.015}_{-0.021}$.

The effect of a rotation rate of 200 Hz on NSs is a small deformation of the star into an oblate spheroid. The deformation enters in two ways. A star rotating at 200 Hz will have an equatorial radius that is at most 2% larger than a nonrotating star with the same mass for the stiffest equations of state, with smaller increases in radius for soft equations of state (Cook et al. 1994).[74] The polar radius will be smaller than the equatorial radius, an effect that depends on the equatorial radius, mass, and spin, with very little dependence on the EOS (AlGendy & Morsink 2014, and references therein); for the a posteriori most probable exterior spacetimes inferred in this present work, the polar radius is $\sim$1% smaller than the equatorial radius. Rotation also increases the mass of a star compared to a nonrotating star with the same number of baryons, but this is at most a 0.2% effect for the rotation-powered pulsars observed by *NICER*. The effect of rotation on the location of the innermost stable circular orbit (ISCO) is larger (van Doesburgh et al. 2018): the (prograde) ISCO typically ranges from $5.6r_g$–$5.8r_g$ for stars spinning at 200 Hz for most theoretical equations of state, compared to the Schwarzschild ISCO radius of $6r_g$. The 95% compactness

[71] Refer to Bogdanov et al. (2019a) for an *XMM* image of the PSR J0030+0451 field; *Athena* promises to improve on the *XMM* point-spread function half-energy width by a factor of $\sim$1.5–3.

[72] Similar to that expected for the *eXTP Spectroscopic Focusing Array* ($\sim$10 μs), but not as good as spectro-timing dedicated missions, like *NICER* or *STROBE-X* with $\sim$0.1 μs time resolution. Note that event time-tagging resolution offered by *X-IFU* will still achieve a level of $\sim$1/500 of the spin period of PSR J0030+0451.

[73] And other MSPs targeted by a mission such as *NICER*.

[74] Note that a one-parameter sequence of nonrotating stars deforms into a sequence of stars rotating at some rate, but a unique deterministic map between the central densities that parameterize those sequences does not exist. This reflects the absence of a unique physical mode for stars to evolve in rotation rate. For comparative purposes, one often considers sequences—parameterized by rotation rate—that conserve a quantity such as total mass, total baryon number, or central density. In the accompanying Letter of Raaijmakers et al. (2019), it is the central density that is explicitly defined as a model parameter (to be marginalized out), and which is held constant for comparison of nonrotating stars to rotating stars in the context of likelihood function evaluation.

credible interval corresponds to equatorial radii in the range of $5.84r_g$–$7.41r_g$, meaning that the most probable stellar surfaces[75] have radii close to or larger than the radius of the ISCO, and thus that the innermost permitted stable orbit is typically at (or just exterior to) the surface.

In this subsection we proceed to discuss how the constraints derived in this work compare to existing constraints on mass, radius, and compactness derived using other methods and independent observations. We also consider prospects for improving *NICER* constraints on PSR J0030+0451. When comparing radii, it should be remembered that most of the published radius determinations using other methods have assumed that the star is spherical. For luminosity radius determinations of rapidly rotating NSs (spins of a few hundred Hz), systematic errors of 5% could be introduced (Bauböck et al. 2015), although other systematic errors may well dominate over an inaccurate treatment of rotational surface and metric deformation.

The present constraints on the radius are consistent with the previous radius lower limit for this pulsar, $R_{\rm eq} > 10.7$ km (95% confidence, assuming a 1.4 $M_\odot$ NS), obtained from early pulse-profile modeling of *XMM* data (Bogdanov & Grindlay 2009). It is also in agreement with the radii inferred from *XMM* observations of other MSPs: $R_{\rm eq} > 11$ km (3σ confidence) for PSR J0437−4715 (Bogdanov 2013); and $R_{\rm eq} > 7.8$ km (68% confidence) for PSR J2124−3358 (Bogdanov et al. 2008). However, these early light-curve models only considered uniform-temperature circular hot spots, neglected stellar oblateness, and we consider the statistical computation described in this Letter as more advanced.

Early constraints on the NS radius were obtained from the X-ray spectroscopic modeling of the thermal emission originating from the entire surface of isolated NS RX J1856.5−3754 (Burwitz et al. 2001; Drake et al. 2002; Pons et al. 2002). However, uncertainties due to the distance and due to the calculations of radiative transfer in the magnetized atmosphere hindered an accurate radius constraint for this NS (Ho et al. 2007). More robust constraints, on the other hand, can be extracted from the X-ray spectra of quiescent low-mass X-ray binaries (qLMXBs) hosted in globular clusters. Not only are their distances known to better than ∼10% precision, but their purely thermal emission is thought to emerge from non-magnetic NS atmosphere models (similar to the NSX model used in the present work) in order to estimate the apparent radius $R_\infty = R_{\rm eq}(1+z) = R_{\rm eq}(1-2GM/R_{\rm eq}c^2)^{-1/2}$. However, the degeneracy between $R_{\rm eq}$ and M in the estimation of R_∞ precluded obtaining useful constraints on the EOS (e.g., Webb & Barret 2007; Heinke et al. 2006, 2014; Guillot et al. 2011), due to the typical shapes of the M–$R_{\rm eq}$ confidence contours that made them compatible with many families of EOS. These results prompted the simultaneous analysis of a set of sources.

In these combined analyses, the degeneracy between M and $R_{\rm eq}$ was lifted by assuming a parameterized shape for the EOS, either a toy-model (constant-radius EOS, as a simplistic representation of nucleonic EOS) or an analytical representation using polytropes. A handful of qLMXBs in globular clusters (up to seven) and of Type-I X-ray bursters (four or five) have been combined to produce constraints on the EOS and/or the radii of NSs (given the assumed EOS shape). Early works using only qLMXBs produced rather small NS radii, $R_{\rm eq} \approx 9$–10 km with ∼10%–15% uncertainties (90% credible interval; Guillot et al. 2013; Guillot & Rutledge 2014; Guillot 2016), but the addition of new data and the use of more recent globular cluster distance measurements resulted in higher values, $R_{\rm eq}$ in the 9.9–11.2 km range for a 1.5 $M_\odot$ NS (2σ credible interval; Bogdanov et al. 2016). Combining qLMXBs and Type-I X-ray bursts, other works have found radii in a wide range of values: $R_{\rm eq} \approx 10.4$–12.9 km (95% credible interval; Steiner et al. 2010, 2013), $R_{\rm eq} \approx 10.5$–12.7 km (90% credible interval; Lattimer & Steiner 2014), and $R_{\rm eq} \approx 9.8$–11.4 km (95% credible interval, Özel et al. 2016), for a 1.4 $M_\odot$ NS. However, these analyses may have been affected by systematics, such as those due to the modeling of piled-up X-ray photons in the *Chandra* data[76]—which was not considered for all qLMXBs in these early analyses—or those due to the choice of atmospheric composition for qLMXBs (generally H versus He). The mass–radius constraints extracted from Type-I X-ray bursts are dependent on the color-correction factors used (between the measured blackbody temperatures and the modeled effective temperatures of the burning atmospheres), which have been debated in the literature (e.g., Suleimanov et al. 2011a; Güver et al. 2012; Güver & Özel 2013; Kajava et al. 2014). These issues cast doubt on the robustness of the error intervals reported in these early works.

Nättilä et al. (2017) recently analyzed Type-I X-ray bursts from 4U 1702−429 by fitting bursting atmosphere models directly to spectra during the cooling tail of the bursts, hence avoiding the use of color-correction factors. These authors found $R_{\rm eq} = 12.4 \pm 0.4$ km and $M = 1.9 \pm 0.3\,M_\odot$ (68% credible interval), although the posterior distributions also allow smaller radii ∼10 km for higher masses ∼2.1 $M_\odot$.

Steiner et al. (2018) considered the effects of pile-up on qLMXB spectra, the possibility of pure helium atmospheres (instead of pure hydrogen atmospheres), as well as non-uniform surface temperature distributions. They obtained constraints on polytropic EOS via Bayesian inference of mass–radius probability distributions of seven NS qLMXBs. These constraints translate to a NS radius in the 10.0–14.4 km range (95% credible interval, assuming a 1.4 $M_\odot$ NS), when considering all of the models tested.

More recently, a physically justified parameterization of the EOS was proposed as an alternative to polytropes (Margueron et al. 2018a, 2018b). In that work, the EOS is a meta-model expressed as a Taylor expansion of nuclear physics parameters, and was applied to a combined spectral analysis of seven qLMXBs to directly extract values of nuclear physics parameters $L_{\rm sym}$, $K_{\rm sym}$, and $Q_{\rm sat}$ (Baillot d'Etivaux et al. 2019). Radius estimates were also derived: $R_{\rm eq} = 12.35 \pm 0.37$ km (2σ credible interval) assuming a 1.45 $M_\odot$ NS.

The cold emission from the MSP PSR J0437−4715 is detectable in the far ultraviolet (Durant et al. 2012) and in the soft X-ray band (0.1–0.3 keV; Guillot et al. 2016), and its mass and distance are known precisely from radio timing (Reardon et al. 2016). Applying NS atmosphere models[77] has permitted estimation of this pulsar's radius: $R_{\rm eq} = 13.1 \pm 0.8$ km (68%

[75] Which in this present work are only embedded in the ambient spacetime while neglecting rotational metric deformation (see Section 2.4.1) and are thus not self-consistently computed with global numerical solutions to the field equations given interior conditions (including an EOS).

[76] It was shown that an unmodeled pile-up fraction as low as ∼1% could affect the radius estimated via modeling of spectral data by as much as 10% (Bogdanov et al. 2016).

[77] Similar but not identical to the atmosphere models used in our *NICER* analysis—the models used in Gonzalez-Caniulef et al. (2019) incorporated various effects that are important at lower temperatures such as partial ionization and plasma frequency effects.

credible interval; Gonzalez-Caniulef et al. 2019). We note that this was a phase-averaged spectral analysis, wherein the emission is assumed to originate from the $\sim 10^5$ K stellar surface exterior to the (heated) polar cap regions.

An indirect method to constrain NS radii is to use emission features from an inner accretion disk in accreting LMXBs. Narrow emission lines, such as Fe K, arising from this rotating material are asymmetrically broadened—to which there is a strong relativistic contribution based upon proximity of the inner disk to the NS surface (Fabian et al. 2000). The accretion disk must truncate at the stellar surface or at a larger radius: spectral modeling of these emission lines enables derivation of a statistical constraint on the inner radius of the (prograde) disk *in units of* the gravitational radius or the spin-dependent ISCO radius (Cackett et al. 2008, 2010; Miller et al. 2013; Degenaar et al. 2015; Ludlam et al. 2017). To do so, an approximative ambient spacetime solution (e.g., Schwarzschild or Kerr) is typically invoked—as in this present work—but without the embedding of a NS surface.[78] The constrained inner radius can then be translated into a lower limit on the stellar compactness for that particular NS.

Ludlam et al. (2017) inferred, for two LMXB systems, inner radii that are consistent with the disks extending down to the ISCOs of their respective ambient spacetimes. In the absence of a constraint on the NS mass that is independent[79] of the inner radius of the disk, a mass merely has to be assumed to obtain an upper limit on the stellar radius. For example, suppose that the 4U 1636−53 system contains a nonrotating[80] minimally compact NS (i.e., disk truncation by surface): for a mass of 1.4 $M_\odot$, the upper limit on the stellar radius would lie close to the Schwarzschild ISCO, at 12.4–13.1 km (1σ confidence interval; Ludlam et al. 2017), which is not inconsistent with the constraint derived conditional on the *NICER* data.[81] Lastly, if the surface of an NS in the 4U 1636−53 system does *not* approximately truncate the disk—and is thus more compact than the ISCO—and/or the (prograde) ISCO is more compact due to NS rotation, the NS could only be viewed as inconsistent with our compactness estimate for PSR J0030+0451 if the following are true: (i) the NS masses are both tightly constrained and happen to be highly commensurate, and (ii) the NSs do not occupy a segment of the mass–radius sequence along which the radius is highly sensitive to increasing mass due to EOS softening or phase transitions (e.g., Drago et al. 2014; Alford & Han 2016; Alford & Sedrakian 2017). However, one mass is unconstrained (disk modeling) while the other is constrained at the ∼10%-level (*NICER* pulse-profile modeling).

Overall, these recent publications have estimated NS radii in the range of 12–14 km, which is compatible with our PSR J0030+0451 radius estimate. We note that equating accurately measured radii of distinct NSs should elicit agreement if (i) the EOS is shared from core to crust, meaning that perturbative effects attributed to crust composition, temperature, and magnetic field strength are sufficiently small in the context of measurement precision; (ii) the EOS is of a nucleonic composition that supports NSs with similar radii over a wide range in mass (0.8 to $\sim 2.0\ M_\odot$); and (iii) differences due to spin-dependent rotational deformations are accounted for or are small enough to justify neglecting (see the discussion in the second and third paragraphs of Section 4.2, and in Raaijmakers et al. 2019). For other families of EOS, such as those involving quarks or hyperons in hybrid stars (e.g., Zdunik & Haensel 2013) or baryon resonances (Drago et al. 2014), the radius may be (highly) sensitive to increasing mass. In such cases, we would expect to find NSs whose radii differ by several km, reinforcing the importance of jointly estimating both the radius and the mass of each member of a population of NSs.

Constraints on NS masses and tidal deformabilities are now also being reported based on the first binary NS merger gravitational wave event, GW170817 (Abbott et al. 2018, 2019). These can be translated into constraints on mass and radius. The inferred values vary somewhat depending on modeling and prior assumptions. Abbott et al. (2018), for example, employed two methods: the first, which did not assume that both stars had the same EOS, yielded radii of $10.8^{+2.0}_{-1.7}$ and $10.7^{+2.1}_{-1.5}$ km for the two stars, with masses in the range 1.16–1.62 $M_\odot$; the second, which assumed a common EOS, yielded a radius of 11.9 ± 1.4 km for both stars and masses in the range 1.18–1.58 $M_\odot$ (all results 90% credible intervals). De et al. (2018), who also assume a common EOS, report radii of $10.7^{+2.1}_{-1.6} \pm 0.2$ km and masses in the range 1.12–1.67 $M_\odot$ (90% credible interval). Constraints taking into account additional information tend to support slightly larger mean values for the radius, and smaller uncertainties, e.g., those derived from the electromagnetic counterpart ($12.4^{+1.1}_{-0.4}$ km, 2σ confidence interval; Most et al. 2018); and those invoking a theoretical minimum (Tews et al. 2017) for neutron matter pressure ($11.4^{+1.9}_{-0.8}$ km, 90% credible interval marginalizing over mass; T. Zhao & J. M. Lattimer 2019, in preparation). The results of Abbott et al. (2018) and De et al. (2018), which employ the assumption that both stars share the same EOS, suggest that the radii of the two stars are nearly equal despite the fact that the mass ratio of the stars could lie between 0.7 and 1.0 with almost uniform probability. Let us make the assumption that PSR J0030+0415 also has the same radius as the binary members to well within the posterior uncertainty on each star: the radius reported in this Letter, inferred from *NICER* data, is more consistent with values in the upper ranges emerging from the gravitational wave analysis of GW170817. Larger radii would only be consistent with mass ratios closer to unity. It follows that if the three stars have nearly the same radius, and if the mass ratio of GW170817 was near its lower limit of 0.7, the common radius should be at the lower end of the *NICER* range. Electromagnetic observations might suggest relatively large amounts of dynamical ejecta, which would favor mass ratios considerably less than unity (Radice et al. 2018).

What are the prospects for improving constraints on mass and radius for PSR J0030+0451? Unfortunately we cannot obtain an independent constraint on the mass for PSR J0030+0451 because it is not in a binary, unlike some of *NICER*'s other MSP targets. Our model of the *NICER* background (particle radiation and diffuse sky terms) is, however, expected to improve without needing to wait for input from other telescope missions; understanding this background accurately will prove crucial, as discussed in Section 4.1.2, and may well

[78] The real surface could thus in principle enclose the ISCO associated with the ambient spacetime solution.

[79] For example, via a binary mass function together with classification of the companion star.

[80] Or at least a small dimensionless spin, despite the 581.0 Hz spin frequency (Ludlam et al. 2017, and references therein).

[81] Where as discussed above the rotational deformation of the surface is small for PSR J0030+0451.

impact mass–radius estimation. A longer total exposure time could also certainly be accumulated (and indeed the *NICER* team anticipate doing this). Previous studies that have examined how posterior estimation of mass and radius is sensitive to factors such as geometry, spin rate, and the number of source counts in the event data, indicate that constraining power increases as the square root of the number of counts (Lo et al. 2013; Psaltis et al. 2014). However, those studies all assumed a single circular single-temperature hot spot, not a more complex hot region configuration such as those we have considered and inferred here. While it is likely that gathering more data will improve the joint constraint on mass and radius (without reference to an EOS model), the precise observing time required to achieve a given level of precision cannot be estimated robustly without further study.

Our report here is encouraging in terms of prospects for other *NICER* targets such as PSR J0437−4715: the pulsar mass is constrained independently to within a few percent via radio pulsar timing because it is in a binary system (Reardon et al. 2016). If such a constraint had been available for PSR J0030 +0451, it is clear that we could have obtained a comparable posterior uncertainty on the inferred radius of a few percent.

4.3. EOS Implications

One of the primary goals of mass–radius inference is to use posterior information[82] to infer the properties of the dense matter EOS, if such information is deemed sufficiently likelihood-dominated to warrant the study. Studies have utilized joint mass–radius posteriors inferred from X-ray spectral modeling of bursting and quiescent NSs (Steiner et al. 2010, 2013; Özel et al. 2016; Raithel et al. 2017). Moreover, studies have utilized mass and tidal deformability constraints derived from analysis of the NS binary merger event GW170817 (Abbott et al. 2018; Annala et al. 2018; Lim & Holt 2018; Malik et al. 2018; Most et al. 2018; Tews et al. 2018b; Carson et al. 2019; Li & Sedrakian 2019; Montaña et al. 2019), and consideration is already being given to combining constraints from electromagnetic and gravitational wave analysis (Kumar & Landry 2019; McNeil Forbes et al. 2019; Weih et al. 2019).

Given a suitable model for the EOS (see, e.g., Read et al. 2009; Raithel et al. 2016; Lindblom 2018; Tews et al. 2018a) there are two approaches to EOS inference: one is to jointly infer the EOS parameters (and central densities) directly from the data (e.g., pulse-profile data); the other is to jointly infer EOS parameters from per-source nuisance-marginalized likelihood functions of exterior-spacetime parameters (e.g., gravitational mass and equatorial radius). The former approach is *at least* as computationally intensive as the direct mass–radius inference reported in this Letter; the latter approach is less computationally intensive *given* archival likelihood function information about exterior spacetime parameters (Riley et al. 2018). In any case, care is required in both overall approach and the selection of (interior source matter and exterior spacetime) model parameterization and priors (Carney et al. 2018; Raaijmakers et al. 2018; Riley et al. 2018; Greif et al. 2019; Landry & Essick 2019). For our analysis here we deliberately defined a joint flat prior density function for M and $R_{\rm eq}$, with the intention that the posterior density function can be invoked as a likelihood function marginalized over all nuisance parameters. We explore the dense matter EOS implications of the inferred mass, radius, and compactness for PSR J0030 +0451 in an accompanying Letter (Raaijmakers et al. 2019), following the approach to EOS inference outlined in Greif et al. (2019).

4.4. Implications of the Surface Heating Configuration

We constructed a sequence of simple models for the properties of the two hot regions, nevertheless motivated by (numerical) pulsar theory. We considered models in which the regions were related via antipodal reflection symmetry with respect to the stellar origin, and models that do not impose such symmetry, meaning that their properties and location were described with distinct parameters (with the restriction that the regions cannot overlap). The models included simply connected circular and crescent regions, and rings (whose hole and annulus are concentric or eccentric), each filled with single-temperature material. The models also included annular (ring) regions whose concentric hole is filled with material of finite temperature distinct from that of the material in the annulus.

We were able to rule out the hot regions being antipodal and identical based on clear systematic structure in the residuals between data and model a posteriori; moreover, a model wherein the regions are both assumed to be simply connected circular single-temperature spots was strongly disfavored. We inferred that the regions are configured to exist in the same rotational hemisphere: one region subtends an angular extent of only a few degrees (in spherical coordinates with origin at the stellar center) but whose other structural details we are insensitive to; the other region is far more azimuthally extended,[83] in the form of a narrow hot crescent. The inferred effective temperature of the `NSX` atmosphere was remarkably consistent across all models considered—for both regions—at $\sim 1.3 \times 10^6$ K. The `ST+PST` model exhibited the largest background-marginalized likelihood function values in the typical set of a posterior mode. Figure 17 renders a representative configuration from the posterior mode, and Table 2 reports the marginal credible intervals for the hot-region parameters. Note that `ST+PST` includes within prior support, configurations wherein the regions are similar or even congruent in shape, and a priori favors (albeit weakly) smaller angular extents—the heating asymmetry is emergent in spite of this.

One of the principal astrophysical questions arising is how such a heating configuration can occur. It appears to be incompatible with magnetospheric current heating at the footpoints of a simple near-centered dipole magnetic field, and is likely to require some higher-order multipole structure (Barnard & Arons 1982; Gralla et al. 2017; Lockhart et al. 2019). We now need to determine the type of field configuration required, the magnitude of the different moments, and whether this is feasible on physical grounds. Consideration will also need to be given to how magnetospheric currents actually map to temperature fields on the stellar surface. We note that there are clear similarities between the inferred `ST+PST` configuration and the current heating distribution contemporaneously derived by Lockhart et al. (2019, see their Figure 6 in particular) via quadrupolar extension of the magnetic field, considering that the heating ring is asymmetric

[82] Strictly, likelihood information (Riley et al. 2018).

[83] In spherical coordinates with polar axis coincident with the stellar rotation axis.

with respect to the dipole axis, and closely resembles a large-scale arc-like hot region. There are, however, also some differences: Lockhart et al. (2019) restricted their study to configurations where the center of the heated ring is antipodal to the heated spot (both of which emit as approximate blackbodies), an assumption that would need to be relaxed to recover our preferred configuration.

There are also implications for pulsar emission in wavebands other than the X-ray (see the reviews by Grenier & Harding 2015; Cerutti & Beloborodov 2017). *If a multipolar field structure is required to explain the surface temperature field, how does this affect radio and gamma-ray emission generated further out in the magnetosphere? Could the multipole structures persist out to the point where emission in these wavebands is thought to happen?* Quadrupole fields fall off faster than dipole fields, as the inverse fifth power of the radius, but the radius beyond which the field is predominantly dipolar would depend on the ratio of quadrupole to dipole components. Most current models of radio and gamma-ray emission assume that the field structure is a centered dipole (e.g., Radhakrishnan & Cooke 1969; Gil et al. 1984; Kijak & Gil 2003; Dyks & Harding 2004; Johnson et al. 2014), and this would need to be revisited.

There are also questions pertaining to stellar evolution. NSs are born with a field structure that could be quite complex as a result of the supernova process (Ardeljan et al. 2005; Obergaulinger & Aloy 2017) but various diffusive evolutionary processes can subsequently modify field structure even for isolated NSs (Reisenegger 2009; Viganò et al. 2013; Mitchell et al. 2015; Gourgouliatos & Hollerbach 2018). In addition, rotation-powered MSPs are thought to go through an extended period of accretion-induced spin-up to reach the observed spin rates. The accretion process may also act to modify the field structure (Romani 1990; Melatos & Phinney 2001; Payne & Melatos 2004). It remains to be determined whether a complex multipolar field structure could emerge and survive from birth, or be generated during the accretion process. If such a field structure is present or evolves during the accretion phase, there will also be implications for the spin-up process and for X-ray emission during that phase of NS evolution. If the magnetic field were to channel accreting material onto two magnetic polar caps on the same hemisphere, for example, this would certainly affect the emission from accreting MSPs (Long et al. 2007, 2008; Patruno & Watts 2012). Whether the star is even visible as an accreting pulsar will depend not only on the geometry of the hot regions where accreting material impacts the star, but also on whether the observer views the hemisphere containing the polar caps or the other one. The flow at the inner-edge of the accretion disk, a strong source of potentially variable X-ray emission, would also be affected by a multipolar field structure. Finally, extremely off-center dipoles or strong non-centered multipole fields, for instance, will produce asymmetries in the Poynting flux of low-frequency radiation parallel to the spin axis, with consequences that could include a large space velocity (Harrison & Tademaru 1975). Lommen et al. (2006) found that PSR J0030+0451 has a relatively low transverse space velocity—a property that is potentially in contention with a field far from that of a centered dipole—although since PSR J0030+0451 is isolated its space velocity would also depend on how the binary was disrupted after the spin-up phase. Discussion on some of these issues is reserved for an accompanying Letter (Bilous et al. 2019). However, further work on the implications of the inferred configuration for pulsar field structure, emission mechanisms, and stellar evolution is certainly required. It is clear that the mass and radius inferred for PSR J0030+0451 depend strongly on the surface radiation field models (including prior support) that we have explored. Further study may show that our models are either not general enough or too general (for example with respect to the prior support). For example, we may find that temperature gradients in the hot regions cannot be neglected; or that field stability considerations impose a minimum angular separation between the polar caps—and possibly, by extension, the hot regions—larger than found in our analysis; or that no magnetospheric model can generate a heating configuration in which one region is a small-scale spot while the other an azimuthally extended crescent.

There are a number of computational aspects for pulsar theorists to consider when developing surface heating models suitable for statistical inference. We were only able to consider the configurations offered uniquely by `ST+PST` as we approached the limit of our computational resource allocation; we can therefore provide stronger guarantees about the accuracy of the posterior computation for the lower-complexity models with more than one run (`ST-U` and `ST+CST`). In the future, we suggest that more resources be devoted to models at the `ST+PST`-level of complexity, in particular for work on (i) parameterization of hot regions with more complex topologies and/or boundaries, (ii) their efficient numerical resolution for likelihood function evaluation, and (iii) exploration of the associated parameter space via sampling or other methods.

We also suggest that additional resources be devoted to research avenues such as self-consistent theory and computation of surface heating by magnetospheric currents, for the purpose of statistical computation. A question may be posed as to the generation of highly non-dipolar surface temperature fields—e.g., arc- or ring-like heating distributions—which can be (i) parameterized such that approximate representations find compromise between accuracy and complexity, capturing the facets considered most crucial to signal generation, perhaps as a sequence of models increasing in complexity; and (ii) built into efficient software implementations. Progress on such fronts should encourage a bridge to form between phenomenological efforts and more self-consistent theory for the purpose of efficient statistical computation, and may also offer a way in which to connect distinct theoretical models (in an approximative manner) on a continuous space.

4.5. Pulse-profile Modeling for Other Types of NS

NICER is the first mission designed specifically to use the pulse-profile modeling technique to infer the mass and radius of NSs. As a soft X-ray telescope with an effective area of less than a square meter, it is optimized for applying the technique to MSPs, which have soft, stable pulse profiles meaning we can use multiple exposures taken over a long baseline to accumulate a sufficient number of events to statistically probe MSP physics. However, the technique can also be applied to other NSs with emission modulated by rapid rotation: accretion-powered pulsars and thermonuclear burst oscillation sources.

In accretion-powered pulsars (see Patruno & Watts 2012, for a review), accreting material is channeled by the magnetic field onto the magnetic polar caps and the pulsed emission has two main components: thermal emission from the heated vicinity of

the accretion impact zones, and nonthermal emission from the shock in the accretion funnel (Poutanen & Gierliński 2003). A third pulsed component may arise due to reflection from the accretion disk (Wilkinson et al. 2011). Thermonuclear burst oscillations (see Watts 2012, for a review) are generated by rotational modulation of global asymmetries that form in a surface radiation field during thermonuclear (Type-I X-ray) bursts; such a burst occurs in the ocean of an accreting NS, driven by unstable burning of accreted hydrogen, helium, or carbon (see, e.g., Galloway et al. 2008). The precise mechanism driving the *detectable* asymmetry (oscillations) is not clear: possibilities include disrupted flame spread (Spitkovsky et al. 2002; Cavecchi et al. 2013), large-scale waves in the burning ocean (Heyl 2004; Piro & Bildsten 2005; Chambers et al. 2019), or patterns triggered by convection (Garcia et al. 2018).

Accretion-powered pulsations and thermonuclear burst oscillations are radiatively harder ($\sim$1–30 keV) than the pulsations of MSPs. Accumulating the requisite number of photons for tight constraints, in a realistic observing time, also requires a telescope with an effective area of several square meters (Watts et al. 2016; Watts 2019). Several mission concepts are currently being developed for large-area broadband X-ray timing telescopes that would access a larger, fainter population of MSPs than we can observe with *NICER*, and fuel pulse-profile modeling for accretion-powered pulsars and thermonuclear burst oscillators: these include the *eXTP* (Watts et al. 2019; Zhang et al. 2019), and the *STROBE-X* (Ray et al. 2019). For an idea of the constraints that can be delivered by pulse-profile modeling and inference using existing data, see the Salmi et al. (2018) analysis of *Rossi X-ray Timing Explorer* observations of the accretion-powered MSP SAX J1808.4−3658.

Our uncertainty toward surface heating physics affects pulse-profile modeling not only for rotation-powered MSPs, but also accretion-powered pulsars and thermonuclear burst oscillators. Although the general mechanism that gives rise to the pulsed components in accretion-powered pulsars is clear, the surface *and off-surface* temperature field and local comoving beaming function—particularly from the accretion-funnel shock—are a priori highly uncertain for any given source. Thermonuclear burst emission has a well-understood (local comoving) beaming function due to the sub-surface thermal origin (Suleimanov et al. 2011b), but the mechanism for generating asymmetries in the global surface radiation field, which in turn generate such rotational oscillations, remains highly uncertain. Reducing the remaining theoretical uncertainties, and developing physically motivated parameterized models of the surface temperature field, will be important. However, our analysis of *NICER* data provides an important real-world demonstration that pulse-profile modeling is a viable technique for constraining masses and radii of NSs, and that the analysis machinery can operate on somewhat flexible models, with weakly informative priors, for both source and background emission.

5. Conclusion

We reported on pulse-profile modeling efforts for the rotation-powered millisecond X-ray pulsar PSR J0030+0451, conditional on *NICER* data. We focused on PSR J0030+0451, a challenging source due to the absence of an independent constraint on the gravitational mass (compared to *NICER*'s other primary target PSR J0437−4715). Nevertheless, PSR J0030+0451 was selected as the optimal source to demonstrate simultaneous inference of gravitational mass and equatorial radius given weakly informative priors, and to develop our analysis procedures.

The mass and radius each have marginal posterior 68% credible interval half-widths at the $\sim$9%–11% level, conditional on the *NICER XTI* event data. These constraints are consistent with those emerging from both gravitational wave analysis and X-ray spectral modeling, and are expected to improve with further exposure. The compactness is constrained more tightly, at the $\sim$6% level. Prospects for *NICER* delivering tight constraints for rotation-powered MSPs where the mass is known independently to uncertainties of a few percent are clearly excellent.

In addition to inferring properties of the spacetime (mass, radius, and compactness), we were also able to infer the properties of the thermally emitting hot regions that we assume generate the pulsations. For the specific set of models that we considered, the inferred configuration has both hot regions in the same rotational hemisphere, with one hot region being a small spot and the other an azimuthally extended narrow crescent. Models wherein the hot regions are antipodal are strongly disfavored, implying a complex offset dipolar and multipolar field structure that, if accurate, has major implications for both pulsar emission and stellar evolution.

We thank the anonymous referees for their suggested improvements to this work. This work was supported in part by NASA through the *NICER* mission and the Astrophysics Explorers Program. T.E.R., A.L.W., and A.V.B. acknowledge support from ERC Starting grant No. 639217 CSINEUTRONSTAR (PI: Watts). A.L.W. would also like to thank Ralph Wijers for environmental support. This work was sponsored by NWO Exact and Natural Sciences for the use of supercomputer facilities, and was carried out on the Dutch national e-infrastructure with the support of SURF Cooperative. This research has made extensive use of NASA's Astrophysics Data System Bibliographic Services (ADS) and the arXiv. R.M.L. acknowledges the support of NASA through Hubble Fellowship Program grant *HST*-HF2-51440.001. S.G. acknowledges the support of the Centre National d'Études Spatiales (CNES). W.C.G.H. appreciates use of computer facilities at the Kavli Institute for Particle Astrophysics and Cosmology. S.M.M. thanks NSERC for support. J.M.L. acknowledges support from NASA through Grant 80NSSC17K0554 and the U.S. DOE from grant DE-FG02-87ER40317.

Facility: NICER (Gendreau et al. 2016).

Software: Python/C language (Oliphant 2007), GNU Scientific Library (GSL; Gough 2009), NumPy (van der Walt et al. 2011), Cython (Behnel et al. 2011), SciPy (Jones et al. 2001), OpenMP (Dagum & Menon 1998), MPI (Forum 1994), *MPI for Python* (Dalcín et al. 2008), Matplotlib (Hunter 2007; Droettboom et al. 2018), IPython (Perez & Granger 2007), Jupyter (Kluyver et al. 2016), TEMPO2 (`photons`; Hobbs et al. 2006), PINT (`photonphase`; https://github.com/nanograv/PINT), MultiNest (Feroz et al. 2009), PyMultiNest (Buchner et al. 2014), *GetDist* (https://github.com/cmbant/getdist), *nestcheck* (Higson 2018; Higson et al. 2018, 2019), *fgivenx* (Handley 2018), *X-PSI* (`v0.1`; https://github.com/ThomasEdwardRiley/xpsi; Riley & Watts 2019).

Appendix A
Posterior Computation

Here we describe how we derived posterior inferences conditional on the models defined in Section 2.

A.1. Nested Sampling

We implemented nested sampling using the open-source software MultiNest[84] (Feroz & Hobson 2008; Feroz et al. 2009, 2013; Buchner et al. 2014). For a subset of model nodes in Figures 10 and 12 we executed two production runs—i.e., we generated two realizations of a particular stochastic sampling process—with the following resolution settings: the number of *active* (or *live*) points was 10^3; the bounded-hypervolume expansion factor was (at least[85]) 0.3^{-1}; the termination condition as a function of iteration number i was, schematically,

$$\ln(\widehat{\mathcal{Z}}_i + \widehat{\Delta\mathcal{Z}}_i) - \ln(\widehat{\mathcal{Z}}_i) < x \Longrightarrow \frac{\widehat{\mathcal{Z}}_i}{\widehat{\mathcal{Z}}_i + \widehat{\Delta\mathcal{Z}}_i} > e^{-x}, \quad (10)$$

where $\widehat{\mathcal{Z}}_i$ is an estimator for the evidence integral up to iteration i over estimated prior mass $(1 - \widehat{X}_i)$, and $\widehat{\Delta\mathcal{Z}}_i$ is an estimator for the *maximum remaining* contribution to the evidence over the complementary estimated prior mass $\widehat{X}_i$. As $x \to 0$, $e^{-x} \to 1^-$ and the estimated amassed evidence entirely dominates the estimated remaining evidence; we generally set $x = 10^{-1}$, which is five times smaller than suggested by Feroz et al. (2009).[86] The number of active points is chosen to be a number that is larger than will be typically reported in the literature for similar dimensional problems (perhaps with simpler distributional structure), or recommended by the authors of MultiNest, for a compromise between resource consumption and accuracy. The hypervolume expansion factor is, for all but one run,[87] greater than the number recommended by the authors of MultiNest for accurate evidence estimation. The combination of a number of active points—which is between 40 and 80 times larger than the dimensionality of the sampling space—and the recommended expansion factor, targets posterior computation with an implementation-specific error[88] that is smaller than the error due to the inherent stochasticity of Monte Carlo sampling.

The *constant-efficiency* MultiNest bounding variant should in general be avoided where tractability is not compromised to reduce risk of under-sampling when a hyper-ellipsoidal decomposition does not conform well to likelihood level hypersurfaces; we did not use this bounding variant. However, in the higher-dimensional contexts that we are approaching in this work, it could be useful to activate this bounding variant if integration is forecasted to consume too many computing resources (e.g., the acceptance fraction drops too low below 10^{-3} when using a high-performance system and an expensive likelihood function). Imposing a target acceptance fraction may be useful for initial exploratory runs in order to probe for configurations with high (marginal) likelihood—a weak indicator of potential model performance if future efforts achieve greater computational efficiency. When *constant-efficiency* mode is activated the evidence estimates should be assumed to be positively biased unless importance nested sampling is also activated (which can consume an appreciable fraction of the memory on a typical supercomputer node for $\sim 10^8$ likelihood function evaluations). The acceptance fraction decaying to such levels is indicative that the minimum-bounding hyper-ellipsoidal decomposition does not conform sufficiently well to the nested likelihood function level hypersurfaces, resulting in (i) a large excess of hypervolume exterior to the likelihood surface but within the bounding union of ellipsoids, and/or (ii) the union of bounding ellipsoids exhibits a large fractional overlap. In such cases one could construct an alternative parameterization of the problem that is more tractable with the MultiNest bounding algorithm (in the native sampling space), or use an alternative (nested) sampling algorithm.

The mode-isolation sampling variant was *not* activated unless stated otherwise. This variant isolates the evolution of local modes whose hyper-ellipsoidal clustering decompositions are mutually non-overlapping; upon isolation, the active points of sampling threads constituting each mode cannot migrate between modes at subsequent iterations—they are locked in, which can alleviate premature mode deactivation. Sampling resolution, however, can be absorbed by unimportant modes, which is undesirable. The mode separation sampling variant generates distinct statistics for each mode and labels actives points according to mode association.

With the above settings, among ulterior numerical settings for marginal likelihood function evaluation, *X-PSI* typically executes $\mathcal{O}(10^7)$ marginal likelihood function evaluations in $O(10^4)$ core hours via MultiNest.

A.2. Summary of Information Presentation

We now summarize how we opt to present probabilistic information in the form of figures and tables. We condition on a set of model variants that are treated in effectively the same manner, and the information presentation is consistent for these models; we thus here describe the information once. Figures and tables are displayed in the main body—see Section 3—for the model we deem to perform best considering both prior and posterior predictive measures and checks; we refer the reader to Table 2 and Figures 13 through 21 for reference.

A.2.1. Graphical Posterior-predictive Checking

In a figure such as Figure 13 we display salient information for assessing performance of a model in isolation. Our generative modeling process is fundamentally built on the statement that we do not believe the true data-generating process exists within the model space considered (refer to Section 2.3); however, the models may, for the purpose of generating data, be deemed adequate approximations. We aim

[84] MultiNest `v3.11` can be located at https://github.com/farhanferoz/MultiNest with SHA1-hash 4b3709c. PyMultiNest `v2.6` can be located at https://github.com/JohannesBuchner/PyMultiNest SHA1-hash 5d8c103.

[85] A *lower bound* for reasons pertaining to the implementation of the joint prior distribution; the lower bound itself is numerically transformed into an appropriate MultiNest setting in order to achieve at least this desired expansion factor. Further detail is beyond the scope of this description (refer to Riley & Watts 2019).

[86] The minimum tolerance used for any process was $x = 10^{-3}$ to confirm that termination was not premature.

[87] The `ST+PST` model was implemented as we were exhausting our computational resources and thus we lowered resolution—increased the nested-sample acceptance fraction—to ensure completion of an exploratory run—see Table 2.

[88] The error due to not sampling from the entire prior hypervolume subject to a given likelihood function constraint.

to graphically approximate an answer to the question: *does the model generate,* a posteriori, synthetic data that emulates structure in the real event data?

Graphical posterior predictive checking here relies on the power of human identification of systematic structural differences, which if physically characterized can drive future model development toward better-performing approximations. Structural differences include spectro-temporal correlations between random variates assumed to be statistically independent (e.g., the ST-S version of Figure 13 in the online figure set), and inaccurate noise modeling leading to under- or over-estimation of the variance of random variables; the latter also may manifest due to excessive, non-physical predictive complexity (over-fitting). In the *top* panel of such a figure we display the data set for convenience. In the middle panel we choose to display the posterior-mean Poisson expected count numbers:

$$\lambda_{ij} \coloneqq \mathbb{E}_{\pi(\boldsymbol{\theta})}[c_{ij}(\boldsymbol{\theta})] = \int_{\mathcal{S}} c_{ij}(\boldsymbol{\theta}, B_i)\pi(\boldsymbol{\theta}, B_i \mid \boldsymbol{d})d\boldsymbol{\theta} \approx \sum_k w_k c_{ij}(\boldsymbol{\theta}_k), \tag{11}$$

where $\boldsymbol{\theta}_k \sim \pi(\boldsymbol{\theta} \mid \boldsymbol{d})$ are samples with normalized importance weights w_k drawn from the background-marginalized posterior density $\pi(\boldsymbol{\theta} \mid \boldsymbol{d})$, and $\mathcal{S}$ is the prior support. Crucially, we do not sample the joint posterior distribution $\pi(\boldsymbol{\theta}, \boldsymbol{B} \mid \boldsymbol{d})$ because of prohibitive scaling of expense with dimensionality;[89] therefore, in order to compute a data-space posterior-mean quantity, we opt to maximize the *conditional* likelihood function $L(B_i; \boldsymbol{\theta}_k)$ with respect to each background count-rate parameter B_i, generating an estimator $\widehat{B}_i$, such that $c_{ij}(\boldsymbol{\theta}_k) \coloneqq c_{ij}(\boldsymbol{\theta}_k, \widehat{B}_i)$. In the *bottom* panel we display standardized residuals between data count numbers and the quantities λ_{ij}, where we define Poisson-random variables $x_{ij} \sim p(x_{ij} \mid \lambda_{ij})$. We consider the set of figures associated with Figure 13 as *graphical posterior-checking* plots. If no clear systematic structure manifests during posterior predictive checking and the posterior-predictive distribution is well approximated by a sampling distribution conditional on a parameter vector, we consider the model to be appropriate for predicting future observations against which the model may be falsified.

Bayesian global performance measures—such as the evidence—are useful for determining the utility of increments in the complexity of a generative model. However, while being a target of our posterior computation, prior predictive probabilities are known to not be universally robust and can be sensitive to prior choices and parameterization, especially in phenomenological contexts. Thus in order to assess performance and identify model features that conform well to data structure, it is necessary—and natural—to also visually inspect predictions a posteriori. We consider other measures such as the expected posterior utility (i.e., power for future statistical falsification) beyond the scope of this work (Vehtari & Ojanen 2012).

In this work we refrain as much as possible from invoking *point measures*—based on parameter vector point estimates—to quantitatively summarize and compare models. The reason we do this is twofold: (i) a point estimate is usually the parameter vector that is estimated to globally optimize some quantity, and subsequent to estimation all information encoded by the posterior distribution is not explicitly regarded; and (ii) the target of our statistical computation (nested sampling) is not any particular point measure, but instead to draw samples from the posterior *typical set* for the purpose of estimating posterior integrals. It follows that stronger guarantees can be made about the accuracy of statistical estimators that are posterior integrals than can be made about those which are point estimates; we therefore view integral estimators as generally more helpful and robust than point estimators.

As an example, consider the canonical estimation of the parameter vector that globally maximizes the likelihood function conditional on some model. In our case, our posterior computation does not target accurate maximization, and we are forced to marginalize over the phase-invariant (background) count-rate parameters in order to define a nested-sampling space whose dimensionality is not prohibitive. We thus do not guarantee that the sample (parameter vector) $\hat{\boldsymbol{\theta}}_{\mathrm{BMML}}$ that reported the highest *background-marginalized* likelihood function value among identified posterior modes, together with the background count-rate vector $\hat{\boldsymbol{B}}_{\mathrm{CML}}$ that maximizes the *conditional* likelihood function given $\hat{\boldsymbol{\theta}}_{\mathrm{BMML}}$, is an adequate estimator of the joint vector $(\boldsymbol{\theta}, \boldsymbol{B})_{\mathrm{ML}}$ that globally maximizes the likelihood function. In Figure 23 we consider the joint vector $(\hat{\boldsymbol{\theta}}_{\mathrm{BMML}}, \hat{\boldsymbol{B}}_{\mathrm{CML}})$: empirically we see that all but one model (ST-S) has, within prior support, parameter vectors that perform adequately as point-measure predictors of structure in the real count-number data.

A.2.2. Parameter Kernel Density Estimation and Credible Regions

We applied the post-processing module of the *X-PSI* package (v0.1; Riley & Watts 2019). *X-PSI* wraps—combines and adds functionality—to several other packages for statistical computation: relevant here for Gaussian kernel density estimation (KDE) is *GetDist*.[90] We do not use *GetDist* to compute numerical one-dimensional credible intervals on each parameter, but *GetDist* is used whenever KDE is necessary for post-processing (posterior) samples into estimators: for calculation of the plotted one- and two-dimensional density functions, for calculation of the plotted two-dimensional (joint) credible regions, and for one-dimensional KL divergence estimation where both the marginal posterior and marginal prior density functions need to be estimated from samples.

GetDist can execute smoothing using either a manual Gaussian kernel bandwidth or an automatic optimized bandwidth. For all parameters and models, for simplicity and consistency, we invoke a manual bandwidth of 0.4 times the

[89] If our set of samples was drawn from the joint posterior distribution $\pi(\boldsymbol{\theta}, \boldsymbol{B} \mid \boldsymbol{d})$ we could better approximate the expectation integral in Equation (11), or at greater cost, approximate the posterior-predictive probability mass distribution in data space:

$$p(x_{ij} \mid \boldsymbol{d}) = \int p(x_{ij} \mid \boldsymbol{\theta}, B_i)\pi(\boldsymbol{\theta}, \boldsymbol{B} \mid \boldsymbol{d})d\boldsymbol{B}d\boldsymbol{\theta} \approx \sum_k w_k p(x_{ij} \mid \boldsymbol{\theta}_k, B_{i,k}),$$

whose expectation $\mathbb{E}[x_{ij}]$ and variance $\mathbb{V}[x_{ij}]$ are indicators of residual structure in the data relative to the model a posteriori. The posterior predictive distribution may also be constructed by jointly generating samples from the Bayesian joint distribution: $\boldsymbol{x}_k \sim p(\boldsymbol{x} \mid \boldsymbol{\theta}_k, \boldsymbol{B}_k)$ and $(\boldsymbol{\theta}_k, \boldsymbol{B}_k) \sim \pi(\boldsymbol{\theta}, \boldsymbol{B} \mid \boldsymbol{d})$.

[90] https://github.com/cmbant/getdist. Specifically, tag v0.3.1, with some minor plotting customization locatable at https://github.com/ThomasEdwardRiley/getdist/tree/customization, with SHA1-hash 61f69d0. The technical KDE notes for *GetDist* are located at https://cosmologist.info/notes/GetDist.pdf.

estimated parameter standard deviations, based on the *GetDist* guidelines for choosing analysis settings. Moreover, *GetDist* performs various smoothing corrections to avoid smoothing bias as one attempts to mitigate finite-sample noise: (i) smoothed-density correction near hard one-dimensional parameter bounds defined through the prior support, with capability to estimate a finite local density function gradient; and (ii) iterative multiplicative bias-correction to the estimated density function to nullify over-smoothing. Density estimation near non-trivial prior support boundaries in two parameters does not account for the local boundary, but this is not problematic for our work here. We roll with the default bias-correction settings: a linear boundary kernel (in both one- and two-dimensional spaces) and zeroth-order multiplicative bias-correction (a single application with no iterations).

A.2.3. Error Analysis for Statistical Estimators

Two frameworks now require distinction: (i) the parametric probabilistic framework of the generative model (a Bayesian context) for the data; and (ii) a non-parametric probabilistic framework that operates with realizations of a stochastic sampling process, which in turn operates on a deterministic target probability distribution defined in the parametric framework given data and a generative model (e.g., Skilling 2006; Higson et al. 2018). The sampling process has a mixture of known and approximated properties, including fixed non-physical settings. Estimators derived from the process output are stochastic and we are interested in their distributions.

The purpose of executing some number of computationally expensive *repeats* is for error analysis—specifically the estimation of implementation-specific error (Higson et al. 2019) pertaining to sampling from the joint prior subject to a likelihood function constraint (a more thorough review of error analysis techniques may be found in Riley & Watts 2019). One way to approach this problem is to compute posterior marginal density functions for many bootstrapped realizations of each stochastic run and then graphically probe for the manifestation of implementation-specific error (Higson et al. 2019).

X-PSI wraps the package *nestcheck*[91] (Higson 2018; Higson et al. 2018, 2019) to access existing error analysis routines. As an example of application in this work, consider Figure 20: in the associated online figure set, where we supply a higher-resolution version of each panel, we display the marginal posterior density distributions for each parameter as a set of shaded error bands. The shaded bands represent the distribution of posterior density, at each parameter value, based on simulated nested sampling process realizations; the posterior density function is estimated for each realization with *GetDist* as described above in Appendix A.2.2. The colorbar denotes the percentage of realizations spanned by a band with a given shade, where each band connects intervals (at each parameter value) containing the highest *realization* density of *posterior density*. Note that the colorbar is not associated with the shaded joint density distributions in the off-diagonal plots. The contours in the on-diagonal panels thus encode information on the variation of the parameter kernel density estimator due to the inherent stochasticity of each of sampling processes; the estimator distributions are connected as a function of each respective parameter to delineate the behavior of the probability mass. If the member processes are deemed to exhibit consistency under visual inspection, the combined process may be invoked to estimate distributions of estimators.

We apply *nestcheck* routines to bootstrap re-sample threads and simulate weights for the following: the one-dimensional quantiles in posterior mass for each parameter, which are in turn used to report the credible intervals; the global and parameter-by-parameter KL divergences; and the evidence. The numerical values we report are in some cases (`ST-S`, `ST-U`, and `ST+CST`) derived by combining two realizations into a single realization with $\mathcal{O}(10^3)$ active points (sampling threads), if the runs are considered sufficiently consistent and exhibit sufficient resolution for our purposes here. However, due to computational expense we could only afford *at most* two runs, and for both `ST+EST` and `ST+PST` we were limited to a single run with $\mathcal{O}(10^3)$ active points. Moreover, note that processes executed by the mode-separation algorithm are incompatible with the notion of process combination: the theory nor software implementation exists at the time of writing, and therefore we only display such a run—when relevant and available—in the posterior figures, but do not use it to calculate numerical estimators.

A.2.4. Estimating Posterior Information Gain

In a Bayesian context, the KL divergence (Kullback & Leibler 1951) can be applied as a non-negative real scalar[92] measure of posterior information *gain* about a parameter—or jointly about parameters—of a generative model, conditioned on the data set; it is also known via information-theoretic interpretation as *relative entropy*. Equivalently it is the *posterior-expected additional* number of bits necessary to encode the value of a parameter sample for lossless communication between agents, *if* the (marginal) prior distribution is invoked to design an optimal encoding. Alternate interpretations exist to satiate a variety of readers—e.g., Shlens (2014).

KL-divergence maximization is central to an information-theoretic—but often in practice intractable—definition of a minimally informative prior via reference to the generative model, but without reference to the data (via data-space marginalization). While we cannot feasibly determine the maximal KL divergence with respect to the space of all proper prior density functions, the number of bits of information gain is a useful indicator of the degree to which the likelihood function dominates the information encoded in the posterior. The KL divergence has, as an example, recently been applied by The LIGO Scientific Collaboration et al. (2019) to probe posterior information gain and sensitivity to prior assumptions.

For continuous symbols, the KL divergence is defined in the limit that a discrete symbol becomes a continuous subset of $\mathbb{R}^n$; in practice, of course, computer representation of the reals is discrete. Given the existence of a known optimal prior encoding, the number of additional bits for lossless communication of a posterior sample at a given precision is, in the context of our inference problem, far less than the number of bits required to store the sample. Mathematically, in units of

[91] Specifically, tag `v0.2.0`, with customization to support use of *GetDist* KDE, locatable at https://github.com/ThomasEdwardRiley/nestcheck/tree/feature/getdist_KDE with SHA1-hash 4555df0.

[92] And thus parameterization invariant.

bits:

$$D_{\mathrm{KL}}(\pi \,||\, p) = \int_{\mathcal{S}} \pi(\boldsymbol{\theta} \mid \boldsymbol{d}) \log_2 \left[\frac{\pi(\boldsymbol{\theta} \mid \boldsymbol{d})}{p(\boldsymbol{\theta})} \right] d\boldsymbol{\theta} \approx \sum_k w_k \log_2 \left[\frac{\pi(\boldsymbol{\theta}_k \mid \boldsymbol{d})}{p(\boldsymbol{\theta}_k)} \right], \tag{12}$$

where $\boldsymbol{\theta}_k \sim \pi(\boldsymbol{\theta} \mid \boldsymbol{d})$ are samples with normalized importance weights w_k drawn from the background-marginalized density $\pi(\boldsymbol{\theta} \mid \boldsymbol{d})$. Computation of a single scalar divergence for the n-dimensional joint posterior is straightforwardly given by

$$\begin{aligned} D_{\mathrm{KL}}(\pi \,||\, p) &= \int_{\mathcal{S}} \pi(\boldsymbol{\theta} \mid \boldsymbol{d}) \log_2 \left[\frac{\pi(\boldsymbol{\theta} \mid \boldsymbol{d})}{p(\boldsymbol{\theta})} \right] d\boldsymbol{\theta} \\ &= \int_{\mathcal{S}} \pi(\boldsymbol{\theta} \mid \boldsymbol{d}) \log_2 \left[\frac{1}{\mathcal{Z}} \frac{p(\boldsymbol{d} \mid \boldsymbol{\theta})\, \cancel{p(\boldsymbol{\theta})}}{\cancel{p(\boldsymbol{\theta})}} \right] d\boldsymbol{\theta} \\ &= -\log_2 \mathcal{Z} + \int_{\mathcal{S}} \pi(\boldsymbol{\theta} \mid \boldsymbol{d}) \log_2 L(\boldsymbol{\theta}) d\boldsymbol{\theta} \\ &\approx -\log_2 \mathcal{Z} + \sum_k w_k \log_2 L(\boldsymbol{\theta}_k). \end{aligned} \tag{13}$$

It is more useful, however, to compute a marginal divergence for each parameter, yielding a handle on which parameters the (marginal) likelihood function is most insensitive to in the context of the (marginal) prior, and thus to which prior assumptions global posterior inferences may be most sensitive. The parameters that exhibit the lowest marginal posterior information gain are those for which prior assumptions are generally more important to be aware of and should thus be an accurate representation of prior belief. Divergence estimation for each parameter (or jointly for $m < n$ parameters) requires more involved post-processing because kernel density estimation is performed for evaluation of the quotient of marginal densities appearing in the integrand.

Note that if the marginal KL divergence for some parameter θ is small (relative to the divergences of other parameters) but the divergence is close to the theoretical maximum expected divergence, the prior exists in the minimally informative limit while being relatively informative. For example, if the Fisher information for θ is everywhere relatively small—meaning the experiment is at most a weak probe of the parameter—the marginal posterior for θ should be dominated even by a minimally informative prior, but posterior inferences about other parameters should be insensitive to all information about θ. If, on the other hand, the likelihood function is a useful probe of θ while the marginal divergence is relatively small, the global posterior may be sensitive to prior information about θ. In practice, we determine that the parameters that typically exhibit the smallest divergences—pulsar distance D and *NICER* instrument parameters α and γ—are assigned marginal priors that are not weakly informative in the context of the likelihood function; moreover, we do not need to calculate Fisher information to understand that the likelihood function itself is a useful probe of these parameters, which exhibit degeneracies with other pulsar parameters. Therefore, we conclude that small divergences in these cases do indicate that our global posterior inferences are strongly conditional on these prior assumptions.

Appendix B
Prior Transforms

For nested sampling we aim to transform from a native sampling space—a unit hypercube $\mathcal{H} = [0, 1]^n$—to a (physical) parameter space $\mathbb{R}^n$ according to an inverse transformation of the joint prior density distribution $p(\boldsymbol{\theta})$ defined on $\mathbb{R}^n$ (typically with some compact support). We thus require implementation of a mapping $\boldsymbol{x} \mapsto \boldsymbol{\theta}$ where $\boldsymbol{x} \in \mathcal{H}$ and $\boldsymbol{\theta} \in \mathbb{R}^n$. In this appendix we give the prior transforms implemented in order to facilitate reproduction of the sampling processes, and also to provide a demonstration of some of the necessary architectural work for parameter estimation via nested sampling.

In this work we provide a summary table for each model; as an example, refer to Table 2. Within each table the joint prior density function $q(\boldsymbol{\theta})$ and its support $\mathcal{S}$ are reported. Here we give a prescription for drawing a sample from a given prior: (i) draw a sample for each parameter according to the listed sampling distribution $p(\boldsymbol{\theta})$ with support $\mathcal{S}^\dagger \subset \mathbb{R}^n$—using one-dimensional inverse sampling—to generate a candidate vector $\widetilde{\boldsymbol{\theta}} \in \mathbb{R}^n$; (ii) systematically evaluate the constraint equations to determine whether $\widetilde{\boldsymbol{\theta}} \in \mathcal{S} \subset \mathbb{R}^n$ or whether $\mathcal{S} \not\ni \widetilde{\boldsymbol{\theta}} \in \mathbb{R}^n$; and (iii) accept the candidate sample if $\widetilde{\boldsymbol{\theta}} \in \mathcal{S}$, otherwise reject the sample. The form—i.e., the relative marginal density at two values of parameter θ—is, for a subset of parameters, not given by the one-dimensional distribution $\theta \sim q(\theta)$ (whose definition in some cases, as the distance D, requires explicitly stated truncation bounds) explicitly written in the prior column: the set of constraint equations defining the joint compact support $\mathcal{S}$ often non-trivially modulate the density distribution $q(\theta)$ if θ appears in constraint equations jointly with some subset of the other parameters. If the joint prior is separable with respect θ to then by definition $p(\theta) \equiv q(\theta)$.

B.1. Gravitational Mass and Equatorial Radius

We defined our joint prior distribution of gravitational mass and equatorial radius in Section 2.4.1. We apply a technique from Appendix E of Riley & Watts (2019): inverse sampling of a joint flat density function $q(M, R_{\mathrm{eq}})$ with a trivial rectangular boundary $M \in [M_a, M_b]$ and $R_{\mathrm{eq}} \in [R_a, R_b]$, and subsequent rejection only if $R_{\mathrm{eq}} \notin [3r_g, 16]$ km.[93] In this case, let $\mathcal{H} = [0, 1] \times [0, 1]$ and let the support of $q(\boldsymbol{\theta}) = q(M, R_{\mathrm{eq}})$ be $\mathcal{S}^\dagger \subset \mathbb{R}^2$. The mapping is then $\mathcal{H} \to \mathcal{S}^\dagger$, $\boldsymbol{x} \mapsto \boldsymbol{\theta}$, where $\mathcal{S}^\dagger \supset \mathcal{S}$. For $(M, R_{\mathrm{eq}}) \in \mathcal{S}$, the joint prior density $p(M, R_{\mathrm{eq}}) \propto q(M, R_{\mathrm{eq}})$ because the constraint equation in compactness is dependent only on M and R_{eq}, and not on any ulterior source parameters. Such a procedure is also summarized in the preamble of Appendix B above.

A standard transform (in the context of the nested sampling software) on the other hand would take the form $\mathcal{H} \to \mathcal{S}$, $\boldsymbol{x} \mapsto \boldsymbol{\theta}$. To construct such a map, one may write $p(M, R_{\mathrm{eq}}) = p(R_{\mathrm{eq}} \mid M) p(M)$ where

$$p(M) = \int_{3r_g(M)}^{R_b} p(M, R_{\mathrm{eq}}) dR_{\mathrm{eq}} \propto R_b - 3r_g(M). \tag{14}$$

[93] Strictly speaking, we also impose several ulterior constraint equations. However, for the spin of PSR J0030+0451 these constraint equations are unimportant for defining the prior support on the joint space of M and R_{eq}.

Then define $\boldsymbol{x} := (x_M, x_R)$ where

$$x_M(M) = \int_{M_a}^{M} p(M')dM' \tag{15}$$

and

$$\begin{aligned} x_R(R_{\rm eq}; M) &= \int_{3r_g(M)}^{R_{\rm eq}} p(R'_{\rm eq} \mid M) dR'_{\rm eq} \\ &= \int_{3r_g(M)}^{R_{\rm eq}} \frac{p(M, R'_{\rm eq})}{p(M)} dR'_{\rm eq} = \frac{R_{\rm eq} - 3r_g(M)}{R_b - 3r_g(M)}. \end{aligned} \tag{16}$$

Inverting, one has

$$R_{\rm eq}(x_R; M) = x_R R_b + 3(1 - x_R) r_g(M), \tag{17}$$

and similarly one obtains a nonlinear function $M(x_M)$.

The problem with such a standard transformation is clear from inspection of $x_R(R_{\rm eq}; M)$. The common $(M, R_{\rm eq})$ degeneracy in pulse-profile modeling is linear due to sensitivity to compactness $M/R_{\rm eq}$. Therefore, requiring a constant compactness $r_g(M)/R_{\rm eq} = $ const. implies

$$x_R(R_{\rm eq}; M) = \frac{\text{const.} - 3}{R_b/r_g(M) - 3}, \tag{18}$$

where $M = M(x_M)$, meaning that $x_R = x_R(x_M; M/R_{\rm eq})$ is generally a nonlinear function. An optimal mapping would preserve the linearity of the degeneracy, and thus we do not opt for a standard transformation where $\mathcal{H} \to \mathcal{S}$, $\boldsymbol{x} \mapsto \boldsymbol{\theta}$; instead we inverse sample with rejection as described above.

B.2. Hot Regions

The joint prior distribution for the parameters of the members comprising both hot regions is non-trivial to implement, requiring a number of considerations. Moreover, the difficulty scales with the complexity of the hot regions. Here we break down the implementation into a series of steps.

B.2.1. Parameter Space

The joint parameter space for the members may be denoted $\boldsymbol{\nu} = (\Theta_p, \phi_p, \zeta_p, \Theta_s, \phi_s, \zeta_s, \ldots)$, where the six parameters explicitly written are inherent to every model wherein antipodal reflection symmetry is *not* imposed, and any ulterior parameters depend on the model. For `ST-U`, these six parameters are sufficient.

B.2.2. Region-exchange Degeneracy

If the two hot regions sharing the stellar surface are of equivalent complexity, the prior support for the coordinates of the regions can be defined so as to avoid degeneracy of the likelihood function under exchange of the region positions.

For regions related via antipodal reflection symmetry, the prior support for the colatitude of the regions can be defined such that only at (or near to) the support boundary are there configurations wherein a pair of regions mutually map onto one another via a rotation about the stellar rotation axis. The same condition applies if the regions are *not* related via antipodal reflection symmetry, but have equivalent complexities—e.g., `ST-U` meaning two `ST` regions. For instance, for `ST-U`, we can impose that $\Theta_p \leqslant \Theta_s$, where Θ_p and Θ_s are, respectively, the colatitudes of the centers of the primary and secondary `ST` regions.

If the regions are not related via antipodal reflection symmetry and do *not* have equivalent complexities—e.g., `ST+CST` or `ST+EST`—then by definition it is not true that an arbitrary point in parameter space yields exactly the same system configuration as distinct point in parameter space due to region exchange. Indeed, region exchange degeneracy may only be exist for a subset of parameter space, and thus one need not impose a joint constraint on the prior support for the colatitudes of the regions.

B.2.3. Ceding- and Superseding-member Radii

As highlighted in Section 2.5.3, it is advisable to define one's native nested-sampling space in order to linearize certain continuous degeneracies where possible.

The angular extent of the regions are remarkable in this respect for models constituted by at least one region at the `CST` complexity level or beyond—i.e., when a hot region is constituted by a superseding member and a ceding member, each with an angular radius. While it is not clear how to fully linearize degeneracy of type I illustrated in Figure 5 (see Section 2.5.2), the important[94] degeneracy of type IV can be linearized by working with the joint space of ψ and ζ, the radii of the superseding and ceding members, respectively (see Section 2.5.3). Although such a choice may be appear obvious in isolation, it may not be the space on which one chooses to intuitively define a joint prior density distribution.

Transforms for a CST or an `EST` *region*. If the superseding member subtends smaller angular extent than the ceding member, it is useful to consider $\psi := f\zeta$ where $f \in [\epsilon_f, 1]$ for small (or zero) ϵ_f. Moreover, it is common to invoke uniform prior density distributions for parameters with the intention of choosing a weakly informative prior but without rigorous proof. We therefore consider a flat separable density for f and ζ, such that $q(f, \zeta) = q(f)q(\zeta)$ where $f \sim U(\epsilon_f, 1)$ and $\zeta \sim U(\epsilon_\zeta, \pi/2 - \epsilon_\zeta)$ for small (or zero) ϵ_ζ. More generally, one might choose $\zeta \in [\epsilon_\zeta, b_\zeta]$; in our case $b_\zeta := \pi/2 - \epsilon_\zeta$. We then require the marginal density function $q(\psi)$ and the conditional density function $q(\zeta \mid \psi)$ in order to define a map $\mathcal{H} \to \mathcal{S}^\dagger$, where $\mathcal{H} = [0, 1] \times [0, 1]$ and where $\mathcal{S}^\dagger$ indicates that the support $\mathcal{S}$ of $p(\psi, \zeta)$, after all considerations in this appendix (see Appendix B.2.4), will be such that $\mathcal{S}^\dagger \supset \mathcal{S}$.

We must now consider the size of ϵ_f and ϵ_ζ: these limits determine the boundary of the prior support in the joint space of ψ and ζ. For a single-temperature hot region, we simply choose $\epsilon_f = 0$, such that either the superseding or ceding member can subtend zero angular extent at the boundary of the support; for a dual-temperature region one might choose a small finite value for ϵ_f given that it is filled with material of finite temperature. Given the choice $\epsilon_f = 0$ the choice of ϵ_ζ is unimportant for deriving the prior distributions of interest.

The joint density $q(\psi, \zeta)$ is given by

$$q(\psi, \zeta) = q(f, \zeta) \left| \frac{\partial f}{\partial \psi} \right| = \zeta^{-1} q(\psi/\zeta) q(\zeta). \tag{19}$$

[94] In terms of prior mass in comparison to that associated with other degenerate structures.

The marginal density function $q(\psi)$ is thus given by

$$q(\psi) = \int \zeta^{-1} q(\psi/\zeta) q(\zeta) d\zeta \propto \begin{cases} \int_{\epsilon_\zeta}^{b_\zeta} \zeta^{-1} d\zeta & \text{if } \psi \leqslant \epsilon_\zeta \\ \int_{\psi}^{b_\zeta} \zeta^{-1} d\zeta & \text{if } \epsilon_\zeta < \psi \leqslant b_\zeta; \end{cases} \tag{20}$$

and further that

$$q(\psi) \propto \begin{cases} \ln(b_\zeta/\epsilon_\zeta) & \text{if } \psi \leqslant \epsilon_\zeta \\ \ln(b_\zeta/\psi) & \text{if } \epsilon_\zeta < \psi \leqslant b_\zeta. \end{cases} \tag{21}$$

Now define $\boldsymbol{x} := (x_\psi, x_\zeta)$ where the mass

$$x_\psi(\psi) := \int_0^\psi q(\psi') d\psi' \propto \begin{cases} \psi \ln(b_\zeta/\epsilon_\zeta) & \text{if } \psi \leqslant \epsilon_\zeta \\ \psi - \epsilon_\zeta - \psi \ln(\psi/b_\zeta) & \text{if } \epsilon_\zeta < \psi \leqslant b_\zeta; \end{cases} \tag{22}$$

note that $x_\psi(\psi)$ is continuous at $\psi = \epsilon_\zeta$, and that $x_\psi \to 1^-$ as $\psi \to b_\zeta^-$ because $q(\psi/\zeta)q(\zeta) = (b_\zeta - \epsilon_\zeta)^{-1}$ where the joint density $q(f, \zeta)$ is finite. The function $\psi(x_\psi)$ is not obviously obtainable in closed form for $\psi > \epsilon_\zeta$, and thus we interpolate to perform the transformation $x_\psi \mapsto \psi$.

We now require the conditional density $q(\zeta \mid \psi)$:

$$q(\zeta \mid \psi) = \frac{q(\psi, \zeta)}{q(\psi)} = \begin{cases} \zeta^{-1}/\ln(b_\zeta/\epsilon_\zeta) & \text{if } (\psi \leqslant \epsilon_\zeta) \wedge (\epsilon_\zeta \leqslant \zeta \leqslant b_\zeta) \\ \zeta^{-1}/\ln(b_\zeta/\psi) & \text{if } (\epsilon_\zeta < \psi \leqslant b_\zeta) \wedge (\psi < \zeta \leqslant b_\zeta). \end{cases} \tag{23}$$

Then define the mass

$$x_\zeta(\zeta; \psi) := \int_{a(\psi)}^{\zeta} q(\zeta' \mid \psi) d\zeta' = \begin{cases} \ln(\zeta/\epsilon_\zeta)/\ln(b_\zeta/\epsilon_\zeta) & \text{if } (\psi \leqslant \epsilon_\zeta) \wedge (\epsilon_\zeta \leqslant \zeta \leqslant b_\zeta) \\ \ln(\zeta/\psi)/\ln(b_\zeta/\psi) & \text{if } (\epsilon_\zeta < \psi \leqslant b_\zeta) \wedge (\psi < \zeta \leqslant b_\zeta). \end{cases} \tag{24}$$

The function $\zeta(x_\zeta; \psi)$ is written in closed-form as

$$\zeta(\boldsymbol{x}) = \begin{cases} \epsilon_\zeta \exp(x_\zeta \ln(b_\zeta/\epsilon_\zeta)) & \text{if } (\psi \leqslant \epsilon_\zeta) \wedge (\epsilon_\zeta \leqslant \zeta \leqslant b_\zeta) \\ \psi(x_\psi) \exp(x_\zeta \ln(b_\zeta/\psi)) & \text{if } (\epsilon_\zeta < \psi \leqslant b_\zeta) \wedge (\psi < \zeta \leqslant b_\zeta). \end{cases} \tag{25}$$

Transforms for a PST region. If the superseding member can subtend a *larger* angular extent than the ceding member we consider the parameters $f \in [\epsilon_f, 2 - \epsilon_f]$ for small (or zero) ϵ_f and $\xi \in [\epsilon_\xi, b_\xi]$ for small ϵ_ξ. If $f \leqslant 1$, we define $\zeta = \xi$ and $\psi = f\zeta$, while if $f > 1$ we define $\psi = \xi$ and $\zeta = (2 - f)\psi$. We consider a flat separable joint density for f and ξ: $f \sim U(\epsilon_f, 2 - \epsilon_f)$ and $\xi \sim U(\epsilon_\xi, b_\xi)$. We again require the marginal density function $q(\psi)$ and the conditional density function $q(\zeta \mid \psi)$ in order to define a map $\mathcal{H} \to \mathcal{S}^\dagger$, where $\mathcal{H} = [0, 1] \times [0, 1]$ and where $\mathcal{S}^\dagger$ indicates that the support $\mathcal{S}$ of $p(\psi, \zeta)$, after all considerations in this appendix (see Appendix B.2.4), will be such that $\mathcal{S}^\dagger \supset \mathcal{S}$.

The joint density $q(\psi, \zeta)$ is piecewise with respect to f, given by

$$q(\psi, \zeta) = q(f, \xi) \left| \frac{\partial(f, \xi)}{\partial(\psi, \zeta)} \right| = \begin{cases} \zeta^{-1} q(f) q(\xi) & \text{if } f \leqslant 1 \\ \psi^{-1} q(f) q(\xi) & \text{if } f > 1. \end{cases} \tag{26}$$

We must now consider the size of ϵ_f and ϵ_ξ: these limits determine the boundary of the prior support in the joint space of ψ and ζ. For a PST region, we simply choose $\epsilon_f = 0$, such that either the superseding or ceding member can subtend zero angular extent at the boundary of the support; for a PDT region one might choose a small finite value for ϵ_f given that it is filled with material of finite temperature. Given the choice $\epsilon_f = 0$ the choice of ϵ_ξ is unimportant for deriving the prior distributions of interest.

In order to construct a map $\mathcal{H} \to \mathcal{S}^\dagger$, we aim to obtain the joint density $p(\psi, \zeta)$ in the conditional form $p(\psi, \zeta) = p(\zeta \mid \psi) p(\psi)$. The marginal density function $p(\psi)$ is given by

$$q(\psi) = \int_0^\psi \psi^{-1} q(f) q(\xi) d\zeta + \int_\psi^{b_\xi} \zeta^{-1} q(f) q(\xi) d\zeta. \tag{27}$$

If $\psi < \epsilon_\xi$, then: for $f > 1$, $q(\xi = \psi) = 0$; and for $f \leqslant 1$, $q(\xi = \zeta) = 0$ for $\zeta < \epsilon_\xi$. It follows that

$$q(\psi) \propto \begin{cases} \int_{\epsilon_\xi}^{b_\xi} \zeta^{-1} d\zeta & \text{if } \psi < \epsilon_\xi \\ \int_0^\psi \psi^{-1} d\zeta + \int_\psi^{b_\xi} \zeta^{-1} d\zeta & \text{if } \epsilon_\xi \leqslant \psi \leqslant b_\xi, \end{cases} \tag{28}$$

and further that

$$q(\psi) \propto \begin{cases} \ln(b_\xi/\epsilon_\xi) & \text{if } \psi < \epsilon_\xi \\ 1 + \ln(b_\xi/\psi) & \text{if } \epsilon_\xi \leqslant \psi \leqslant b_\xi. \end{cases} \tag{29}$$

Now define $\boldsymbol{x} := (x_\psi, x_\zeta)$ where the mass

$$x_\psi(\psi) := \int_0^\psi q(\psi') d\psi' \propto \begin{cases} \psi \ln(b_\xi/\epsilon_\xi) & \text{if } \psi < \epsilon_\xi \\ 2(\psi - \epsilon_\xi) - \psi \ln(\psi/b_\xi) & \text{if } \epsilon_\xi \leqslant \psi \leqslant b_\xi; \end{cases} \tag{30}$$

note that $x_\psi(\psi)$ is continuous at $\psi = \epsilon_\xi$, and that $x_\psi \to 1^-$ as $\psi \to b_\xi^-$ because $q(f)q(\xi) = (b_\xi - \epsilon_\xi)^{-1}/2$ where the joint density $q(f, \xi)$ is finite. The function $\psi(x_\psi)$ is not obviously obtainable in closed form for $\psi > \epsilon_\xi$, and thus we interpolate to perform the transformation $x_\psi \mapsto \psi$.

We now require the conditional density $q(\zeta \mid \psi)$:

$$q(\zeta \mid \psi) = \frac{q(\psi, \zeta)}{q(\psi)} = \begin{cases} \zeta^{-1}/\ln(b_\xi/\epsilon_\xi) & \text{if } (\psi < \epsilon_\xi) \wedge (\epsilon_\xi \leqslant \zeta \leqslant b_\xi) \\ \psi^{-1}/[1 + \ln(b_\xi/\psi)] & \text{if } (\epsilon_\xi \leqslant \psi \leqslant b_\xi) \wedge (0 \leqslant \zeta \leqslant \psi) \\ \zeta^{-1}/[1 + \ln(b_\xi/\psi)] & \text{if } (\epsilon_\xi \leqslant \psi \leqslant b_\xi) \wedge (\psi < \zeta \leqslant b_\xi). \end{cases} \tag{31}$$

Then define the mass

$$x_\zeta(\zeta;\,\psi) \coloneqq \int_{a(\psi)}^{\zeta} q(\zeta' \mid \psi)\,d\zeta' = \begin{cases} \ln(\zeta/\epsilon_\xi)/\ln(b_\xi/\epsilon_\xi) & \text{if } (\psi < \epsilon_\xi) \wedge (\epsilon_\xi \leqslant \zeta \leqslant b_\xi) \\ \dfrac{\zeta}{\psi}[1 + \ln(b_\xi/\psi)]^{-1} & \text{if } (\epsilon_\xi \leqslant \psi \leqslant b_\xi) \wedge (0 \leqslant \zeta \leqslant \psi) \\ [1 + \ln(\zeta/\psi)][1 + \ln(b_\xi/\psi)]^{-1} & \text{if } (\epsilon_\xi \leqslant \psi \leqslant b_\xi) \wedge (\psi < \zeta \leqslant b_\xi). \end{cases} \tag{32}$$

The function $\zeta(x_\zeta;\,\psi)$ is written in closed form as

$$\zeta(\boldsymbol{x}) = \begin{cases} \epsilon_\xi \exp(x_\zeta \ln(b_\xi/\epsilon_\xi)) & \text{if } (\psi < \epsilon_\xi) \wedge (\epsilon_\xi \leqslant \zeta \leqslant b_\xi) \\ x_\zeta \psi(x_\psi)[1 + \ln(b_\xi/\psi)] & \text{if } (\epsilon_\xi \leqslant \psi \leqslant b_\xi) \wedge (0 \leqslant \zeta \leqslant \psi) \\ \psi(x_\psi)\exp(x_\zeta[1 + \ln(b_\xi/\psi)] - 1) & \text{if } (\epsilon_\xi \leqslant \psi \leqslant b_\xi) \wedge (\psi < \zeta \leqslant b_\xi). \end{cases} \tag{33}$$

B.2.4. Non-overlapping Hot Regions

We implicitly define the support $\mathcal{S}$ of the joint density $p(\boldsymbol{v})$, where $\boldsymbol{v} = (\Theta_p, \phi_p, \zeta_p, \Theta_s, \phi_s, \zeta_s, \ldots)$ is the vector of parameters controlling both hot regions sharing the stellar surface, by imposing a constraint equation in terms of $\boldsymbol{v}$: we require that the regions are *non-overlapping*. More explicitly: two radiating regions associated with distinct regions cannot overlap—if they were to overlap, additional logical conditions would be required to specify an order of precedence for intensity evaluation at spacetime events at the stellar surface.

For single-temperature regions with a single member—i.e., simply connected and circular—one need only determine whether the ceding members, with their simple (circular) boundaries, overlap; the same condition is true if there exists a superseding member that is a *hole* in a ceding member—i.e., ST, CST, or EST. For dual-temperature hot regions, whose boundary is always constituted by a maximum of two simple (circular) boundaries, one need only determine whether any pair of members—from two distinct regions—overlap. However, for a PST region the boundary of the radiating region is more unwieldy for evaluating whether or not the radiating region of the PST region overlaps with another region sharing the stellar surface; in this case we simply define an overlap condition only in terms of the simple boundary of the ceding member, a subset of which is superseded by non-radiating surface.

To derive the joint prior density $p(\boldsymbol{v})$ and its support $\mathcal{S}$, we (i) define $q(\boldsymbol{v})$ as a product of density functions, (ii) inverse sample as $\mathcal{H} \rightarrow \mathcal{S}^\dagger$, $\boldsymbol{x} \mapsto \boldsymbol{v}$, and (iii) accept the sample $\tilde{\boldsymbol{v}}$ if the regions are determined to be non-overlapping. Algorithmically, we identify a set of pairs of members with simple boundaries whose center coordinates and angular radii are defined by vector $\tilde{\boldsymbol{v}}$, and evaluate via a spherical coordinate transformation whether or not the angular separation of the member centers is at least equal to the sum of the angular radii. If any of the pairs of members overlap, then $\tilde{\boldsymbol{v}} \notin \mathcal{S}$.

As an example, for ST+EST, $\boldsymbol{v} = (\Theta_p, \phi_p, \zeta_p, \Theta_s, \phi_s, \psi_s, \zeta_s, \varepsilon_s, \varphi_s)$ where the coordinates of the center of the ceding member of the EST region is derived from the vector $(\Theta_s, \phi_s, \psi_s, \zeta_s, \varepsilon_s, \varphi_s)$. Overlap is then evaluated for this ceding member in relation to the ST spot whose boundary is derived from the vector $(\Theta_p, \phi_p, \zeta_p)$. The marginal density function for *every* parameter constituting (the space of) vector $\boldsymbol{v}$ is thus modulated by excluding overlaps.

Appendix C
Model Summary Tables

In this appendix we provide posterior summary tables for all models applied to the PSR J0030+0451 event data, other than ST+PST (Table 2). For ST+EST see Table 3. For ST+CST see Table 4. For ST-U see Table 5. For ST-S see Table 6. For CDT-U see Table 7.

Table 3
Summary Table for ST+EST, Introduced in Section 2.5.7 and Illustrated in Figure 11

Parameter	Description	Prior (Density and Support)	$\widehat{\mathrm{CI}}_{68\%}$	$\widehat{D}_{\mathrm{KL}}$
P (ms)	Coordinate spin period	$P = 4.87$, fixed	⋯	⋯
M ($M_\odot$)	Gravitational mass	$M \sim U(1, 3)$	$1.46^{+0.17}_{-0.18}$	$1.15^{+0.02}_{-0.02}$
R_{eq} (km)	Coordinate equatorial radius	$R_{\mathrm{eq}} \sim U[3r_g(1), 16]$	$13.89^{+1.14}_{-1.30}$	$0.69^{+0.02}_{-0.02}$
	Compactness condition	$R_{\mathrm{eq}}/r_g(M) > 3$		
Θ_p (radians)	ST region center colatitude	$\Theta_p \sim U(0, \pi)$	$2.22^{+0.09}_{-0.10}$	$3.01^{+0.03}_{-0.03}$
ϕ_p (cycles)	ST region initial phase (from Earth)	$\phi_p \sim U(a, a + 0.2)$[a]	$0.45^{+0.00}_{-0.00}$	$6.59^{+0.02}_{-0.03}$
ζ_p (radians)	ST region angular radius	$\zeta_p \sim U(0,\pi/2)$	$0.07^{+0.01}_{-0.01}$	$4.78^{+0.03}_{-0.02}$
Θ_s (radians)	EST region hole center colatitude	$\Theta_s \sim U(0, \pi)$	$2.66^{+0.07}_{-0.09}$	$3.36^{+0.02}_{-0.03}$
ϕ_s (cycles)	EST region initial phase (from Earth antipode)	$\phi_s \sim U(-0.5, 0.5)$, periodic	$-0.51^{+0.01}_{-0.01}$	$4.28^{+0.03}_{-0.02}$
ψ_s^+ (radians)	EST region angular radii difference	$\zeta_s \sim U(0, \pi/2)$, $\psi_s^+ := \zeta_s - \psi_s$	$0.03^{+0.01}_{-0.01}$	$2.93^{+0.03}_{-0.03}$
ψ_s (radians)	EST region hole angular radius	$f_s \sim U(0, 1)$, $\psi_s := f_s\zeta_s$	$0.25^{+0.04}_{-0.04}$	$2.29^{+0.02}_{-0.03}$
ε_s	EST region annulus fractional angular offset	$\varepsilon_s \sim U(0, 1)$[b]	$0.45^{+0.45}_{-0.33}$	$0.08^{+0.01}_{-0.01}$
φ_s (radians)	EST region annulus azimuthal offset	$\varphi_s \sim U(0, 2\pi)$	$0.79^{+0.35}_{-0.26}$	$0.64^{+0.06}_{-0.06}$
	Non-overlapping hot-region annuli	function of $(\Theta_p, \Theta_s, \phi_p, \phi_s, \zeta_p, \zeta_s)$		
$\log_{10}(\mathcal{T}_p\,(\mathrm{K}))$	ST region NSX effective temperature	$\log_{10}\mathcal{T}_p \sim U(5.1, 6.8)$, NSX limits	$6.11^{+0.01}_{-0.01}$	$5.03^{+0.03}_{-0.03}$
$\log_{10}(\mathcal{T}_s\,(\mathrm{K}))$	EST region NSX effective temperature	$\log_{10}\mathcal{T}_s \sim U(5.1, 6.8)$, NSX limits	$6.11^{+0.01}_{-0.01}$	$5.60^{+0.03}_{-0.03}$
i (radians)	Earth inclination to rotation axis	$i \sim U(0, \pi/2)$	$1.01^{+0.07}_{-0.07}$	$2.40^{+0.03}_{-0.02}$
D (kpc)	Earth distance	$D \sim N(0.325, 0.009)$	$0.33^{+0.01}_{-0.01}$	$0.02^{+0.01}_{-0.01}$
N_{H} ($10^{20}\mathrm{cm}^{-2}$)	Interstellar neutral H column density	$N_{\mathrm{H}} \sim U(0, 5)$	$0.61^{+0.18}_{-0.16}$	$2.84^{+0.03}_{-0.03}$
NICER α	Calibrated matrix scaling	$\alpha \sim N(1, 0.1)$, $\alpha \in [0.5, 1.5]$	$0.99^{+0.09}_{-0.09}$	$0.02^{+0.01}_{-0.00}$
NICER β	Reference-to-calibrated matrix weighting	$\beta \sim U(0, 1)$	$0.16^{+0.17}_{-0.11}$	$1.07^{+0.03}_{-0.03}$
NICER γ	Reference matrix scaling	$\gamma \sim N(1, 0.1)$, $\gamma \in [0.5, 1.5]$	$0.99^{+0.09}_{-0.09}$	$0.04^{+0.01}_{-0.01}$
	Sampling process information			
	Number of free parameters: 19 Number of runs: 1 Number of live points: 10^3 Inverse hypervolume expansion factor: 0.3 Termination condition: 10^{-1} Evidence:[c] $\widehat{\ln \mathcal{Z}} = -36367.81^{+0.48}_{-0.43}$ Global KL divergence: $\widehat{D}_{\mathrm{KL}} = 62.1^{+0.8}_{-0.8}$ bits Number of core[d] hours: 61210 Likelihood evaluations: 88965106 Nested replacements: 53149 Weighted posterior samples: 17671			

Notes.
[a] Where $\phi_p = a$ is an arbitrary phase dependent on event data pre-processing. We set $a = 0.35$.
[b] If we were to parameterize the eccentricity in terms of the *sum* of angular radii of the superseding (hole) and ceding regions, $\vartheta := \varepsilon(1 + f)\zeta$, a *conditional* prior such as $\varepsilon \mid f \sim U(0, (1 - f)/(1 + f))$ would be necessary, where the upper bound imposes that the radiating region is not simply connected (i.e., is an annulus): $\varepsilon(1 + f)\zeta + f\zeta \leqslant \zeta \Longrightarrow \varepsilon \leqslant (1 - f)/(1 + f)$.
[c] Defined as the prior predictive probability $p(\boldsymbol{d} \mid \mathrm{ST} + \mathrm{EST})$. We report the interval about the median containing $\pm 45\%$ of 10^3 joint bootstrap-weight replications for the combined run.
[d] Intel® Xeon E5-2697Av4 (2.60 GHz; Broadwell) processors on the SURFsara Cartesius supercomputer.

Table 4
Summary Table for ST+CST, Introduced in Section 2.5.7

Parameter	Description	Prior (Density and Support)	$\widehat{\mathrm{CI}}_{68\%}$	$\widehat{D}_{\mathrm{KL}}$
P (ms)	Coordinate spin period	$P = 4.87$, fixed	⋯	⋯
M ($M_\odot$)	Gravitational mass	$M \sim U(1, 3)$	$1.44^{+0.18}_{-0.19}$	$1.07^{+0.02}_{-0.02}$
R_{eq} (km)	Coordinate equatorial radius	$R_{\mathrm{eq}} \sim U[3r_g(1), 16]$	$13.88^{+1.23}_{-1.38}$	$0.61^{+0.01}_{-0.01}$
	Compactness condition	$R_{\mathrm{eq}}/r_g(M) > 3$		
Θ_p (radians)	ST region center colatitude	$\Theta_p \sim U(0, \pi)$	$2.24^{+0.09}_{-0.09}$	$5.14^{+0.03}_{-0.02}$
ϕ_p (cycles)	ST region initial phase (from Earth)	$\phi_p \sim U(-0.5, 0.5)$, periodic	$0.46^{+0.00}_{-0.00}$	$6.66^{+0.03}_{-0.02}$
ζ_p (radians)	ST region angular radius	$\zeta_p \sim U(0, \pi/2)$	$0.07^{+0.01}_{-0.01}$	$4.59^{+0.02}_{-0.02}$
Θ_s (radians)	CST region center colatitude	$\Theta_s \sim U(0, \pi)$	$2.60^{+0.05}_{-0.06}$	$2.79^{+0.02}_{-0.02}$
ϕ_s (cycles)	CST region initial phase (from Earth antipode)	$\phi_s \sim U(-0.5, 0.5)$, periodic	$-0.50^{+0.00}_{-0.00}$	$7.33^{+0.02}_{-0.03}$
ψ_s^+ (radians)	CST region annulus angular width	$\zeta_s \sim U(0, \pi/2)$, $\psi_s^+ := \zeta_s - \psi_s$	$0.04^{+0.01}_{-0.01}$	$2.71^{+0.02}_{-0.02}$
ψ_s (radians)	CST region hole angular radius	$f_s \sim U(0, 1)$, $\psi_s := f_s \zeta_s$	$0.23^{+0.03}_{-0.03}$	$2.52^{+0.02}_{-0.02}$
	Enforce ST and CST colatitude order[a]	$\Theta_s \geqslant \Theta_p$		
	Non-overlapping hot regions	function of $(\Theta_p, \Theta_s, \phi_p, \phi_s, \zeta_p, \zeta_s)$		
$\log_{10}(\mathcal{T}_p\,(\mathrm{K}))$	ST region NSX effective temperature	$\log_{10}\mathcal{T}_p \sim U(5.1, 6.8)$, NSX limits	$6.10^{+0.01}_{-0.01}$	$4.99^{+0.02}_{-0.02}$
$\log_{10}(\mathcal{T}_s\,(\mathrm{K}))$	CST region NSX effective temperature	$\log_{10}\mathcal{T}_s \sim U(5.1, 6.8)$, NSX limits	$6.11^{+0.01}_{-0.01}$	$5.58^{+0.02}_{-0.02}$
i (radians)	Earth inclination to rotation axis	$i \sim U(0, \pi/2)$	$1.02^{+0.07}_{-0.08}$	$2.32^{+0.02}_{-0.02}$
D (kpc)	Earth distance	$D \sim N(0.325, 0.009)$	$0.33^{+0.01}_{-0.01}$	$0.01^{+0.00}_{-0.00}$
N_{H} ($10^{20}\mathrm{cm}^{-2}$)	Interstellar neutral H column density	$N_{\mathrm{H}} \sim U(0, 5)$	$0.62^{+0.19}_{-0.18}$	$2.75^{+0.02}_{-0.02}$
NICER α	Calibrated matrix scaling	$\alpha \sim N(1, 0.1)$, $\alpha \in [0.5, 1.5]$	$0.99^{+0.10}_{-0.10}$	$0.01^{+0.00}_{-0.00}$
NICER β	Reference-to-calibrated matrix weighting	$\beta \sim U(0, 1)$	$0.16^{+0.18}_{-0.11}$	$0.98^{+0.02}_{-0.02}$
NICER γ	Reference matrix scaling	$\gamma \sim N(1, 0.1)$, $\gamma \in [0.5, 1.5]$	$0.99^{+0.09}_{-0.09}$	$0.01^{+0.00}_{-0.00}$
	Sampling process information			
	Number of free parameters: 17			
	Number of runs: 2			
	Number of live points *per run*: 10^3			
	Inverse hypervolume expansion factor: 0.3			
	Termination condition: 10^{-1}			
	Evidence:[b] $\widehat{\ln \mathcal{Z}} = -36368.00^{+0.34}_{-0.33}$			
	Global KL divergence: $\widehat{D}_{\mathrm{KL}} = 62.9^{+0.6}_{-0.5}$ bits			
	Combined number of core[c] hours: 23010			
	Combined likelihood evaluations: 39501475			
	Combined nested replacements: 105264			
	Combined weighted posterior samples: 32839			

Notes.
[a] Based on learning that additional complexity (of the form we consider in our model space) beyond ST is not warranted for the one region, but is warranted for the other region.
[b] Defined as the prior predictive probability $p(\boldsymbol{d} \mid \mathtt{ST} + \mathtt{CST})$. We report the interval about the median containing ±45% of 10^3 joint bootstrap-weight replications for the combined run.
[c] Approximate equal-partition between Intel® Xeon E5-2697Av4 (2.60 GHz; Broadwell) and E5-2690v3 (2.60 GHz; Haswell) processors on the SURFsara Cartesius supercomputer.

Table 5
Summary Table for ST-U, Introduced in Section 2.5.1 and Illustrated in Figure 3

Parameter	Description	Prior (Density and Support)	$\widehat{\mathrm{CI}}_{68\%}$	$\widehat{D}_{\mathrm{KL}}$
P (ms)	Coordinate spin period	$P = 4.87$, fixed	⋯	⋯
M ($M_\odot$)	Gravitational mass	$M \sim U(1, 3)$	$1.09^{+0.11}_{-0.07}$	$2.09^{+0.02}_{-0.03}$
R_{eq} (km)	Coordinate equatorial radius	$R_{\mathrm{eq}} \sim U[3r_g(1), 16]$	$10.44^{+1.10}_{-0.86}$	$1.44^{+0.03}_{-0.03}$
	Compactness condition	$R_{\mathrm{eq}}/r_g(M) > 3$		
Θ_p (radians)	p region center colatitude	$\Theta_p \sim U(0, \pi)$	$2.48^{+0.06}_{-0.06}$	$6.92^{+0.02}_{-0.02}$
Θ_s (radians)	s region center colatitude	$\Theta_s \sim U(0, \pi)$	$2.78^{+0.02}_{-0.02}$	$4.08^{+0.02}_{-0.02}$
ϕ_p (cycles)	p region initial phase (from Earth)	$\phi_p \sim U(-0.5, 0.5)$, periodic	$0.46^{+0.00}_{-0.00}$	$7.51^{+0.02}_{-0.02}$
ϕ_s (cycles)	s region initial phase (from Earth antipode)	$\phi_s \sim U(-0.5, 0.5)$, periodic	$-0.50^{+0.00}_{-0.00}$	$8.05^{+0.02}_{-0.02}$
ζ_p (radians)	p region angular radius	$\zeta_p \sim U(0, \pi/2)$	$0.14^{+0.02}_{-0.02}$	$3.95^{+0.02}_{-0.02}$
ζ_s (radians)	s region angular radius	$\zeta_s \sim U(0, \pi/2)$	$0.29^{+0.04}_{-0.03}$	$2.98^{+0.02}_{-0.02}$
	Eliminate region-exchange degeneracy Non-overlapping hot regions	$\Theta_s \geqslant \Theta_p$ function of $(\Theta_p, \Theta_s, \phi_p, \phi_s, \zeta_p, \zeta_s)$		
$\log_{10}(\mathcal{T}_p\,(\mathrm{K}))$	p region NSX effective temperature	$\log_{10}\mathcal{T}_p \sim U(5.1, 6.8)$, NSX limits	$6.11^{+0.01}_{-0.01}$	$5.53^{+0.03}_{-0.02}$
$\log_{10}(\mathcal{T}_s\,(\mathrm{K}))$	s region NSX effective temperature	$\log_{10}\mathcal{T}_s \sim U(5.1, 6.8)$, NSX limits	$6.10^{+0.01}_{-0.01}$	$5.71^{+0.02}_{-0.02}$
i(radians)	Earth inclination to rotation axis	$i \sim U(0, \pi/2)$	$1.04^{+0.07}_{-0.08}$	$2.38^{+0.02}_{-0.02}$
D (kpc)	Earth distance	$D \sim N(0.325, 0.009)$	$0.33^{+0.01}_{-0.01}$	$0.35^{+0.02}_{-0.02}$
N_{H} ($10^{20}\mathrm{cm}^{-2}$)	Interstellar neutral H column density	$N_{\mathrm{H}} \sim U(0, 5)$	$1.23^{+0.17}_{-0.17}$	$2.82^{+0.02}_{-0.02}$
NICER α	Calibrated matrix scaling	$\alpha \sim N(1, 0.1)$, $\alpha \in [0.5, 1.5]$	$0.96^{+0.10}_{-0.10}$	$0.11^{+0.01}_{-0.01}$
NICER β	Reference-to-calibrated matrix weighting	$\beta \sim U(0, 1)$	$0.23^{+0.23}_{-0.16}$	$0.57^{+0.02}_{-0.02}$
NICER γ	Reference matrix scaling	$\gamma \sim N(1, 0.1)$, $\gamma \in [0.5, 1.5]$	$0.91^{+0.10}_{-0.09}$	$0.56^{+0.04}_{-0.03}$
	Sampling process information			
	Number of free parameters: 16 Number of runs:[a] 2 Number of live points *per run*: 10^3 Inverse hypervolume expansion factor: 0.3 Termination condition: 10^{-3} Evidence:[b] $\widehat{\ln \mathcal{Z}} = -36377.60^{+0.36}_{-0.35}$ Global KL divergence: $\widehat{D}_{\mathrm{KL}} = 63.7^{+0.5}_{-0.5}$ bits Combined number of core[c] hours: 9588 Combined likelihood evaluations: 25346841 Combined nested replacements: 121617 Combined weighted posterior samples: 49481			

Notes.
[a] The mode-separation MultiNest variant was deactivated for these two runs that were combined to compute estimators. Mode separation means that modes are not evolved independently and nested sampling threads contact multiple modes; a mode-separation run was executed and is displayed in Figure 19 and in the figure sets available in the online corresponding to Figures 20 and 21. The theory nor software implementation exists for combining this run with the two reported in the table.
[b] Defined as the prior predictive probability $p(\boldsymbol{d} \mid \mathtt{ST-U})$. We report the interval about the median containing ±45% of 10^3 joint bootstrap-weight replications for the combined run. See the footnote in Table 2.
[c] Approximate equal-partition between Intel® Xeon E5-2697Av4 (2.60 GHz; Broadwell) and E5-2690v3 (2.60 GHz; Haswell) processors on the SURFsara Cartesius supercomputer.

Table 6
Summary Table for ST-S, Introduced in Section 2.5.1 and Illustrated in Figure 3

Parameter	Description	Prior (Density and Support)	$\widehat{\mathrm{CI}}_{68\%}$	$\widehat{D}_{\mathrm{KL}}$
P (ms)	Coordinate spin period	$P = 4.87$, fixed	⋯	⋯
M ($M_\odot$)	Gravitational mass	$M \sim U(1, 3)$	$2.93^{+0.01}_{-0.01}$	$6.75^{+0.03}_{-0.03}$
R_{eq} (km)	Coordinate equatorial radius	$R_{\mathrm{eq}} \sim U[3r_g(1), 16]$	$15.97^{+0.02}_{-0.04}$	$6.11^{+0.04}_{-0.04}$
	Compactness condition	$R_{\mathrm{eq}}/r_g(M) > 3$		
Θ_p (radians)	p region center colatitude	$\Theta_p \sim U(0, \pi/2)$	$1.26^{+0.02}_{-0.02}$	$4.07^{+0.03}_{-0.02}$
ϕ_p (cycles)	p region initial phase (from Earth)	$\phi_p \sim U(-0.5, 0.5)$, periodic	$-0.09^{+0.00}_{-0.00}$	$8.57^{+0.02}_{-0.03}$
ζ (radians)	ST region angular radius (shared)	$\zeta \sim U(0, \pi/2)$	$0.09^{+0.01}_{-0.00}$	$6.55^{+0.02}_{-0.02}$
$\log_{10}(\mathcal{T}(\mathrm{K}))$	ST region NSX effective temperature (shared)	$\log_{10}\mathcal{T} \sim U(5.1, 6.8)$, NSX limits	$6.08^{+0.00}_{-0.00}$	$6.97^{+0.02}_{-0.02}$
Θ_s (radians)	s region center colatitude	$\Theta_s = \pi - \Theta_p$, derived		
ϕ_s (cycles)	s region initial phase	$\phi_s = \phi_p + 0.5$, derived		
i (radians)	Earth inclination to rotation axis	$i \sim U(0, \pi/2)$	$1.23^{+0.02}_{-0.03}$	$3.98^{+0.03}_{-0.02}$
D (kpc)	Earth distance	$D \sim N(0.325, 0.009)$	$0.32^{+0.01}_{-0.01}$	$0.02^{+0.00}_{-0.00}$
N_{H} ($10^{20}\mathrm{cm}^{-2}$)	Interstellar neutral H column density	$N_{\mathrm{H}} \sim U(0, 5)$	$0.02^{+0.03}_{-0.02}$	$5.93^{+0.04}_{-0.04}$
NICER α	Calibrated matrix scaling	$\alpha \sim N(1, 0.1)$, $\alpha \in [0.5, 1.5]$	$1.00^{+0.09}_{-0.09}$	$0.01^{+0.00}_{-0.00}$
NICER β	Reference-to-calibrated matrix weighting	$\beta \sim U(0, 1)$	$0.36^{+0.22}_{-0.19}$	$0.35^{+0.02}_{-0.02}$
NICER γ	Reference matrix scaling	$\gamma \sim N(1, 0.1)$, $\gamma \in [0.5, 1.5]$	$1.01^{+0.09}_{-0.09}$	$0.03^{+0.00}_{-0.00}$
	Sampling process information			
	Number of free parameters: 12			
	Number of runs: 2			
	Number of live points *per run*: 10^3			
	Inverse hypervolume expansion factor: 0.3			
	Termination condition: 10^{-3}			
	Evidence:[a] $\widehat{\ln \mathcal{Z}} = -37211.71^{+0.29}_{-0.31}$			
	Global KL divergence: $\widehat{D}_{\mathrm{KL}} = 51.3^{+0.5}_{-0.5}$ bits			
	Combined number of core[b] hours: 1494			
	Combined likelihood evaluations: 1666483			
	Combined nested replacements: 87488			
	Combined weighted posterior samples: 30202			

Notes.
[a] Defined as the prior predictive probability $p(\boldsymbol{d} \mid \mathtt{ST-S})$. We report the interval about the median containing ±45% of 10^3 joint bootstrap-weight replications for the combined run. See the footnote in Table 2.
[b] Intel® Xeon E5-2697Av4 (2.60 GHz; Broadwell) processors on the SURFsara Cartesius supercomputer.

Table 7
Summary Table for CDT-U, Introduced in Section 2.5.3 and Illustrated in Figure 6

Parameter	Description	Prior (Density and Support)	$\widehat{\mathrm{CI}}_{68\%}$	$\widehat{D}_{\mathrm{KL}}$
P (ms)	Coordinate spin period	$P = 4.87$,fixed	⋯	⋯
M ($M_\odot$)	Gravitational mass	$M \sim U(1, 3)$	$1.44^{+0.17}_{-0.18}$	1.15
R_{eq} (km)	Coordinate equatorial radius	$R_{\mathrm{eq}} \sim U[3r_g(1), 16]$	$13.86^{+1.16}_{-1.26}$	0.68
	Compactness condition	$R_{\mathrm{eq}}/r_g(M) > 3$		
Θ_p (radians)	p region center colatitude	$\Theta_p \sim U(0, \pi)$	$2.24^{+0.08}_{-0.08}$	4.68
ϕ_p (cycles)	p region initial phase (from Earth)	$\phi_p \sim U(-0.5, 0.5)$, periodic	$0.46^{+0.00}_{-0.00}$	6.75
ψ_p^+ (radians)	p region annulus angular width	$\zeta_p \sim U(0, \pi/2)$, $\psi_p^+ := \zeta_p - \psi_p$	$0.08^{+0.16}_{-0.06}$	2.59
ψ_p (radians)	p region hole angu- lar radius	$f_p \sim U(0, 1)$, $\psi_p := f_p\,\zeta_p$	$0.07^{+0.01}_{-0.01}$	5.28
Θ_s (radians)	s region center colatitude	$\Theta_s \sim U(0, \pi)$	$2.61^{+0.05}_{-0.06}$	2.98
ϕ_s (cycles)	s region initial phase (from Earth antipode)	$\phi_s \sim U(-0.5, 0.5)$, periodic	$-0.50^{+0.00}_{-0.00}$	7.38
ψ_s^+ (radians)	s region annulus angular width	$\zeta_s \sim U(0, \pi/2)$, $\psi_s^+ := \zeta_s - \psi_s$	$0.04^{+0.01}_{-0.01}$	5.23
ψ_s (radians)	s region hole angular radius	$f_s \sim U(0, 1)$, $\psi_s := f_s\,\zeta_s$	$0.23^{+0.03}_{-0.03}$	3.66
	Eliminate region-exchange degeneracy Non-overlapping hot-region annuli	$\Theta_s \geqslant \Theta_p$ function of $(\Theta_p,\Theta_s,\phi_p,\phi_s,\zeta_p,\zeta_s)$		
$\log_{10}(\mathcal{T}_p$ (K))	p region annulus NSX effective temperature	$\log_{10}\mathcal{T}_p \sim U(5.1, 6.8)$, NSX limits	$5.43^{+0.23}_{-0.20}$	1.11
$\log_{10}(T_p$ (K))	p region hole NSX effective temperature	$\log_{10}T_p \sim U(5.1, 6.8)$, NSX limits	$6.11^{+0.01}_{-0.01}$	5.06
$\log_{10}(\mathcal{T}_s$ (K))	s region annulus NSX effective temperature	$\log_{10}\mathcal{T}_s \sim U(5.1, 6.8)$, NSX limits	$6.11^{+0.01}_{-0.01}$	5.56
$\log_{10}(T_s$ (K))	s region hole NSX effective temperature	$\log_{10}T_s \sim U(5.1, 6.8)$, NSX limits	$5.47^{+0.19}_{-0.23}$	1.30
i (radians)	Earth inclination to rotation axis	$i \sim U(0, \pi/2)$	$1.02^{+0.07}_{-0.07}$	2.37
D (kpc)	Earth distance	$D \sim N(0.325, 0.009)$	$0.33^{+0.01}_{-0.01}$	0.02
N_{H} (10^{20}cm^{-2})	Interstellar neutral H column density	$N_{\mathrm{H}} \sim U(0, 5)$	$0.70^{+0.19}_{-0.18}$	2.70
NICER α	Calibrated matrix scaling	$\alpha \sim N(1, 0.1)$, $\alpha \in [0.5, 1.5]$	$0.99^{+0.09}_{-0.09}$	0.02
NICER β	Reference-to-calibrated matrix weighting	$\beta \sim U(0, 1)$	$0.16^{+0.17}_{-0.11}$	1.05
NICER γ	Reference matrix scaling	$\gamma \sim N(1, 0.1)$, $\gamma \in [0.5, 1.5]$	$0.99^{+0.09}_{-0.09}$	0.03
	Sampling process information			
	Number of free parameters: 20 Number of runs: 1 Number of live points:[a] 10^3 Inverse hypervolume expansion factor:[b] 0.3 Termination condition: 10^{-1} Evidence:[c] $\widehat{\ln \mathcal{Z}} = -36366.76 \pm 0.21$ Global KL divergence: $\widehat{D}_{\mathrm{KL}} = 64.0$ bits Combined number of core[d] hours: 101917 Likelihood evaluations: 156707329 Nested replacements: 54610 Weighted posterior samples: 17503			

Notes. In this table we only give the numerical details for one completed run. However, we attempted to perform a higher-efficiency higher-resolution second run, without activation of the mode-separation MultiNest sampling algorithm. Our attempt to improve the sampling efficiency by linearizing the degeneracy (type IV in Figures 5 and 7) observed in the first run; however, we failed to fully apply the necessary transformations (later applied to models ST+CST and beyond, as described in Section 2.5.3 and Appendix B.2), and the mapping from the native sampling space to the physical parameter space inadvertently preserved the nonlinearity of the degeneracy. We thus did not attain higher efficiency, which coupled with higher-resolution calculation, meant that this run was nearing—but did not reach—termination according to the standard criterion used for the other sampling processes reported in this work. Due to the low sampling efficiencies being reported, we ceased computation after consumption of ∼160540 core hours in order to preserve resources and redesign our modeling route as described in Sections 2.5.4 and 2.5.7. The highest-likelihood points from the posterior mode in this second run were however utilized, in combination with those from the first run, to map out all of the degenerate posterior structure in Figures 7 and 8. The inefficiency suffered during CDT-U posterior computation served as a stark reminder that we should design our problems as carefully as possible in order to avoid resource wastage, and was the motivation behind considering in detail the question of how much hot-region complexity is helpful. While we could in principle conclude this adjourned run with additional computing resources, we have argued in this work that would not be fruitful do so.

[a] The mode-separation MultiNest variant was activated, meaning that isolated modes are evolved independently and nested sampling threads migrate between multiple modes. A local posterior mode was identified, corresponding to a weaker phase solution in which the primary and secondary hot regions transpose—relative to the global posterior mode—in their coupling to pulse components visible in the phase-folded event data. The number of live points locked into the mode with dominant posterior mass was 637, a number assigned according to the prior mass distribution upon mode separation and under the influence of Monte Carlo noise. The posterior mass ratio (or ratio of local evidences) is estimated to be ∼1100. As stated in Appendix A.2.3, because of activation of mode-separation sampling, we cannot perform error analysis via process bootstrapping, and we would not be able to combine with another run, supposing that one was available. We nevertheless have an error on the log-evidence reported natively by MultiNest. Another consequence of the activation of mode-separation is that sampling resolution was absorbed by the local posterior mode with much lower mass—in other words, the active points were sparser in the dominant mode. In combination with sampling error due to likelihood isosurface nonlinearity, the consequence was that the dominant and degenerate posterior mode—which forms a large connected structure in parameter space as discussed in Section 2.5.4—was not fully resolved. In particular, the type I degeneracy branch (refer to Figures 5 and 7) was not fully resolved, with sampling threads (active points) migrating to and densely populating the type IV branch (again refer to Figure 7) in an unbalanced manner. The second, albeit incomplete, run described in the caption of this table exhibited much improved resolution of the dominant mode (see the points in Figure 7); the resolution remained incomplete, however, which we attribute to sampling error due to the clear nonlinear degeneracy present in the mode.

[b] We decreased the expansion factor to 0.8^{-1} when the acceptance rate decayed to below 5×10^{-4}, which slightly decreased the rate of decay. At this point the process was sampling from the typical set and nearing termination (2×10^4 core hours remaining at low acceptance fraction).

[c] Defined as the prior predictive probability $p(\boldsymbol{d} \mid \mathtt{CDT-U})$.

[d] Intel® Xeon E5-2697Av4 (2.60 GHz; Broadwell) processors on the SURFsara Cartesius supercomputer.

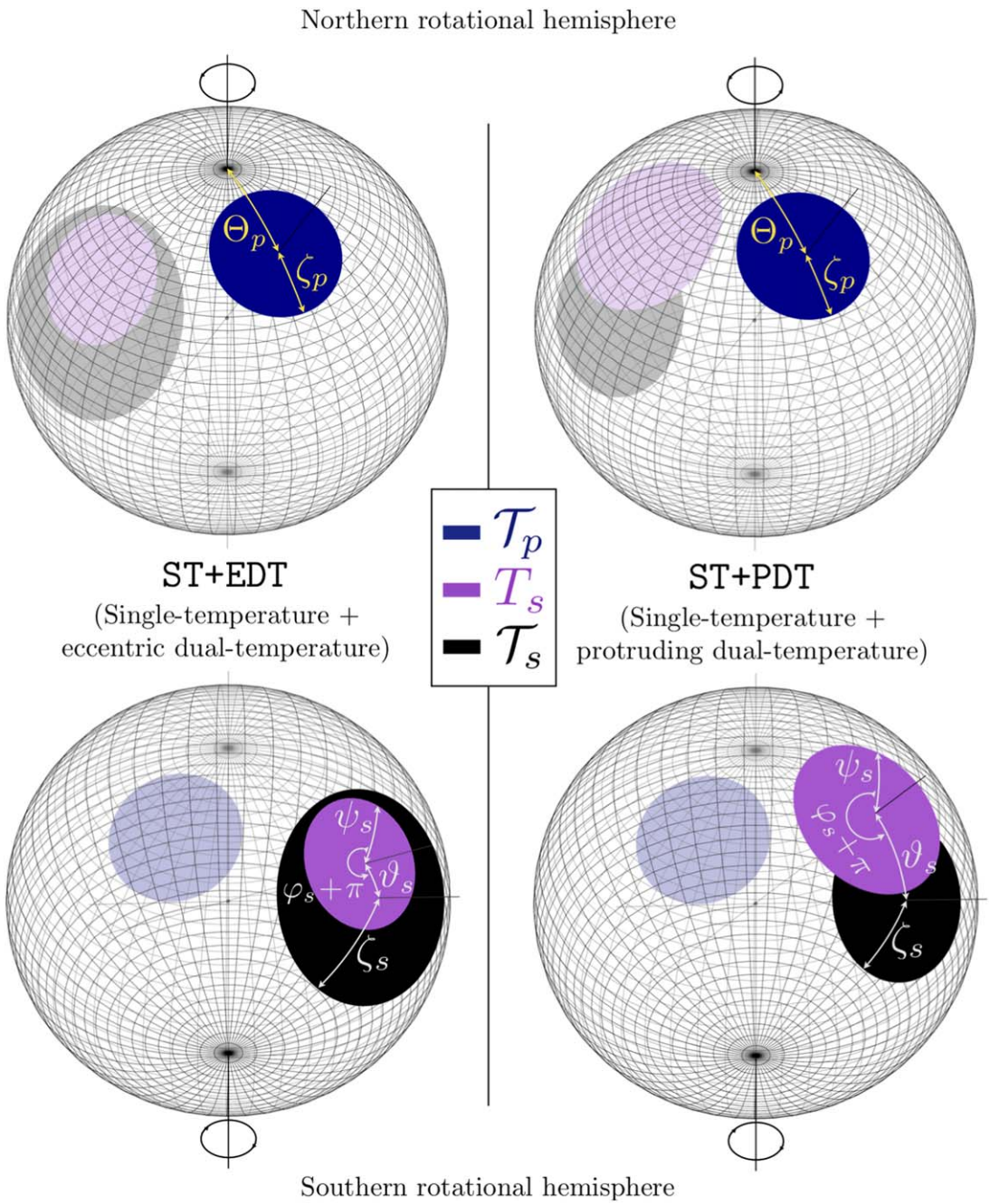

Figure 24. Schematic diagrams of models wherein an ST region shares the stellar surface with a higher-complexity EDT or PDT region. The complete figure set (3 images) is available in the online journal.

(The complete figure set (3 images) is available.)

Appendix D
Supplementary Ideas for Model Extension

We now make note of models within the scope of this work that were either clearly (without need for explicit posterior computation due to the posterior properties of simpler models) not competitive for PSR J0030+0451 or unhelpfully complex in phenomenologically describing the structure of a hot region. Excess complexity does not mean that the modeling has been optimized, but indicates that a particular extension to a model is not warranted because we are insensitive to a subset of parameters (or combinations of parameters), *and* that the signals that maximize the likelihood function are signals that are effectively generated by a simpler (nested) model.

ST+EDT and *ST+PDT*. Obtained via simple extension of ST+EST and ST+PST: let the superseding member (the hole for EST) contain radiating material. Refer to Figure 24.

EDT-S and EDT-U. Refer to the online figure set associated with Figure 24. For EDT-S, the surface radiation field associated with the secondary region is derived exactly by applying antipodal symmetry to the primary region: there are no free parameters associated with the secondary region. Conversely, for EDT-U, the secondary region is endowed with distinct parameters—i.e., it is *not* derived from the primary

region under antipodal symmetry. However, the parameters of the secondary region have an otherwise equivalent meaning—in terms of surface radiation field specification—to their primary-region counterparts. As an example, the azimuth of the center of the secondary ceding member is defined relative to the meridian passing through the center of the secondary hole and through the rotational poles.

*PDT-S*and PDT-U. Refer to the online figure set associated with Figure 24. For PDT-S, the surface radiation field associated with the secondary region is derived exactly by applying antipodal symmetry to the primary region: there are no free parameters associated with the secondary region. Conversely, for PDT-U, the secondary region is endowed with distinct parameters—i.e., it is *not* derived from the primary region under antipodal symmetry. However, the parameters of the secondary region have an otherwise equivalent meaning—in terms of surface radiation field specification—to their primary-region counterparts.

ORCID iDs

T. E. Riley https://orcid.org/0000-0001-9313-0493
A. L. Watts https://orcid.org/0000-0002-1009-2354
S. Bogdanov https://orcid.org/0000-0002-9870-2742
P. S. Ray https://orcid.org/0000-0002-5297-5278
R. M. Ludlam https://orcid.org/0000-0002-8961-939X
S. Guillot https://orcid.org/0000-0002-6449-106X
A. V. Bilous https://orcid.org/0000-0002-7177-6987
D. Chakrabarty https://orcid.org/0000-0001-8804-8946
A. K. Harding https://orcid.org/0000-0001-6119-859X
W. C. G. Ho https://orcid.org/0000-0002-6089-6836
S. M. Morsink https://orcid.org/0000-0003-4357-0575
T. E. Strohmayer https://orcid.org/0000-0001-7681-5845

References

Abbott, B. P., Abbott, R., Abbott, T. D., et al. 2017, PhRvL, 119, 161101
Abbott, B. P., Abbott, R., Abbott, T. D., et al. 2018, PhRvL, 121, 161101
Abbott, B. P., Abbott, R., Abbott, T. D., et al. 2019, PhRvX, 9, 011001
Alford, M., & Sedrakian, A. 2017, PhRvL, 119, 161104
Alford, M. G., & Han, S. 2016, EPJA, 52, 62
AlGendy, M., & Morsink, S. M. 2014, ApJ, 791, 78
Annala, E., Gorda, T., Kurkela, A., & Vuorinen, A. 2018, PhRvL, 120, 172703
Antoniadis, J., Freire, P. C. C., Wex, N., et al. 2013, Sci, 340, 448
Ardeljan, N. V., Bisnovatyi-Kogan, G. S., & Moiseenko, S. G. 2005, MNRAS, 359, 333
Arzoumanian, Z., Brazier, A., Burke-Spolaor, S., et al. 2018, ApJS, 235, 37
Arzoumanian, Z., Gendreau, K. C., Baker, C. L., et al. 2014, Proc. SPIE, 9144, 914420
Badnell, N. R., Bautista, M. A., Butler, K., et al. 2005, MNRAS, 360, 458
Baillot d'Etivaux, N., Guillot, S., Margueron, J., et al. 2019, arXiv:1905.01081
Barnard, J. J., & Arons, J. 1982, ApJ, 254, 713
Bauböck, M., Berti, E., Psaltis, D., & Özel, F. 2013, ApJ, 777, 68
Bauböck, M., Özel, F., Psaltis, D., & Morsink, S. M. 2015, ApJ, 799, 22
Bauböck, M., Psaltis, D., & Özel, F. 2019, ApJ, 872, 162
Baym, G., Hatsuda, T., Kojo, T., et al. 2018, RPPh, 81, 056902
Becker, W., Trümper, J., Lommen, A. N., & Backer, D. C. 2000, ApJ, 545, 1015
Behnel, S., Bradshaw, R., Citro, C., et al. 2011, CSE, 13, 31
Bildsten, L., Salpeter, E. E., & Wasserman, I. 1992, ApJ, 384, 143
Bilous, A. V., Watts, A. L., Harding, A. K., et al. 2019, ApJL, 887, L23
Blaes, O. M., Blandford, R. D., Madau, P., & Yan, L. 1992, ApJ, 399, 634
Bogdanov, S. 2013, ApJ, 762, 96
Bogdanov, S., & Grindlay, J. E. 2009, ApJ, 703, 1557
Bogdanov, S., Grindlay, J. E., & Rybicki, G. B. 2008, ApJ, 689, 407
Bogdanov, S., Guillot, S., Ray, P., et al. 2019a, ApJL, 887, L25
Bogdanov, S., Guillot, S., Ray, P., et al. 2019c, Constraining the Neutron Star Mass-Radius Relation and Dense Matter Equation of State with NICER. I. The Millisecond Pulsar X-Ray Data Set, Zenodo, doi:10.5281/zenodo.3524457
Bogdanov, S., Heinke, C. O., Özel, F., & Güver, T. 2016, ApJ, 831, 184
Bogdanov, S., Lamb, F. K., Mahmoodifar, S., et al. 2019b, ApJL, 887, L26
Bogdanov, S., Rybicki, G. B., & Grindlay, J. E. 2007, ApJ, 670, 668
Buchner, J., Georgakakis, A., Nandra, K., et al. 2014, A&A, 564, A125
Burwitz, V., Zavlin, V. E., Neuhäuser, R., et al. 2001, A&A, 379, L35
Cackett, E. M., Miller, J. M., Ballantyne, D. R., et al. 2010, ApJ, 720, 205
Cackett, E. M., Miller, J. M., Bhattacharyya, S., et al. 2008, ApJ, 674, 415
Cadeau, C., Morsink, S. M., Leahy, D., & Campbell, S. S. 2007, ApJ, 654, 458
Carney, M. F., Wade, L. E., & Irwin, B. S. 2018, PhRvD, 98, 063004
Carson, Z., Steiner, A. W., & Yagi, K. 2019, PhRvD, 99, 043010
Cavecchi, Y., Watts, A. L., Braithwaite, J., & Levin, Y. 2013, MNRAS, 434, 3526
Cerutti, B., & Beloborodov, A. M. 2017, SSRv, 207, 111
Chambers, F. R. N., Watts, A. L., Keek, L., Cavecchi, Y., & Garcia, F. 2019, ApJ, 871, 61
Chang, P., & Bildsten, L. 2003, ApJ, 585, 464
Chang, P., & Bildsten, L. 2004, ApJ, 605, 830
Colgan, J., Kilcrease, D. P., Magee, N. H., et al. 2016, ApJ, 817, 116
Cook, G. B., Shapiro, S. L., & Teukolsky, S. A. 1994, ApJ, 424, 823
Cromartie, H., Fonseca, E., Ransom, S. M., et al. 2019, NatAs, in press (arXiv:1904.06759)
Dagum, L., & Menon, R. 1998, CSE, 5, 46
Dalcín, L., Paz, R., Storti, M., & D'Elía, J. 2008, JPDC, 68, 655
De, S., Finstad, D., Lattimer, J. M., et al. 2018, PhRvL, 121, 091102
Degenaar, N., Miller, J. M., Chakrabarty, D., et al. 2015, MNRAS, 451, L85
Demorest, P. B., Pennucci, T., Ransom, S. M., Roberts, M. S. E., & Hessels, J. W. T. 2010, Natur, 467, 1081
Drago, A., Lavagno, A., & Pagliara, G. 2014, PhRvD, 89, 043014
Drake, J. J., Marshall, H. L., Dreizler, S., et al. 2002, ApJ, 572, 996
Droettboom, M., Caswell, T. A., Hunter, J., et al. 2018, matplotlib/matplotlib v2.2.2, Zenodo, doi:10.5281/zenodo.1202077
Durant, M., Kargaltsev, O., Pavlov, G. G., et al. 2012, ApJ, 746, 6
Dyks, J., & Harding, A. K. 2004, ApJ, 614, 869
Fabian, A. C., Iwasawa, K., Reynolds, C. S., & Young, A. J. 2000, PASP, 112, 1145
Feroz, F., & Hobson, M. P. 2008, MNRAS, 384, 449
Feroz, F., Hobson, M. P., & Bridges, M. 2009, MNRAS, 398, 1601
Feroz, F., Hobson, M. P., Cameron, E., & Pettitt, A. N. 2013, arXiv:1306.2144
Forum, M. P. 1994, MPI: A Message-Passing Interface Standard, Tech. Rep., MPIF, https://www.mpi-forum.org/docs/mpi-1.0/mpi-10.ps
Galloway, D. K., Muno, M. P., Hartman, J. M., Psaltis, D., & Chakrabarty, D. 2008, ApJS, 179, 360
Garcia, F., Chambers, F. R. N., & Watts, A. L. 2018, PhRvF, 3, 123501
Gendreau, K. C., Arzoumanian, Z., Adkins, P. W., et al. 2016, Proc. SPIE, 9905, 99051H
Gil, J., Gronkowski, P., & Rudnicki, W. 1984, A&A, 132, 312
Gonzalez-Caniulef, D., Guillot, S., & Reisenegger, A. 2019, MNRAS, 490, 5848
Gough, B. 2009, GNU Scientific Library Reference Manual (3rd ed.; Network Theory Ltd.)
Gourgouliatos, K. N., & Hollerbach, R. 2018, ApJ, 852, 21
Gralla, S. E., Lupsasca, A., & Philippov, A. 2017, ApJ, 851, 137
Greif, S. K., Raaijmakers, G., Hebeler, K., Schwenk, A., & Watts, A. L. 2019, MNRAS, 485, 5363
Grenier, I. A., & Harding, A. K. 2015, CRPhy, 16, 641
Guillot, S. 2016, MmSAI, 87, 521
Guillot, S., Kaspi, V. M., Archibald, R. F., et al. 2016, MNRAS, 463, 2612
Guillot, S., & Rutledge, R. E. 2014, ApJL, 796, L3
Guillot, S., Rutledge, R. E., & Brown, E. F. 2011, ApJ, 732, 88
Guillot, S., Servillat, M., Webb, N. A., & Rutledge, R. E. 2013, ApJ, 772, 7
Güver, T., & Özel, F. 2013, ApJL, 765, L1
Güver, T., Psaltis, D., & Özel, F. 2012, ApJ, 747, 76
Hamaguchi, K. & NICER Calibration Team 2019, in 14th Workshop of Int. Astronomical Consortium for High Energy Calibration, https://indico2.riken.jp/event/2910/contributions/12756/attachments/8511/10339/NICER-IACHEC-2019.pdf
Handley, W. 2018, JOSS, 3, 849
Harding, A. K., & Muslimov, A. G. 2001, ApJ, 556, 987
Harding, A. K., & Muslimov, A. G. 2011, ApJ, 743, 181
Harrison, E. R., & Tademaru, E. 1975, ApJ, 201, 447
Hartle, J. B. 1967, ApJ, 150, 1005
Hartle, J. B., & Thorne, K. S. 1968, ApJ, 153, 807
Hebeler, K., Lattimer, J. M., Pethick, C. J., & Schwenk, A. 2010, PhRvL, 105, 161102
Heinke, C. O., Cohn, H. N., Lugger, P. M., et al. 2014, MNRAS, 444, 443
Heinke, C. O., Rybicki, G. B., Narayan, R., & Grindlay, J. E. 2006, ApJ, 644, 1090
Heyl, J. S. 2004, ApJ, 600, 939

Higson, E. 2018, JOSS, 3, 916
Higson, E., Handley, W., Hobson, M., & Lasenby, A. 2018, BayAn, 13, 873
Higson, E., Handley, W., Hobson, M., & Lasenby, A. 2019, MNRAS, 483, 2044
Ho, W. C. G., & Heinke, C. O. 2009, Natur, 462, 71
Ho, W. C. G., Kaplan, D. L., Chang, P., van Adelsberg, M., & Potekhin, A. Y. 2007, MNRAS, 375, 821
Ho, W. C. G., & Lai, D. 2001, MNRAS, 327, 1081
Hobbs, G. B., Edwards, R. T., & Manchester, R. N. 2006, MNRAS, 369, 655
Hunter, J. D. 2007, CSE, 9, 90
Iglesias, C. A., & Rogers, F. J. 1996, ApJ, 464, 943
Johnson, T. J., Venter, C., Harding, A. K., et al. 2014, ApJS, 213, 6
Jones, E., Oliphant, T., Peterson, P., et al. 2001, SciPy: Open Source Scientific Tools for Python (http://www.scipy.org/)
Kajava, J. J. E., Nättilä, J., Latvala, O.-M., et al. 2014, MNRAS, 445, 4218
Kass, R. E., & Raftery, A. E. 1995, J. Am. Stat. Assoc., 90, 773
Kijak, J., & Gil, J. 2003, A&A, 397, 969
Kluyver, T., Ragan-Kelley, B., Pérez, F., et al. 2016, in Positioning and Power in Academic Publishing: Players, Agents and Agendas, ed. F. Loizides & B. Schmidt (Amsterdam: IOS Press), 87
Kramer, M., & Wex, N. 2009, CQGra, 26, 073001
Kullback, S., & Leibler, R. A. 1951, Ann. Math. Statist., 22, 79
Kumar, B., & Landry, P. 2019, PhRvD, 99, 123026
Kurkela, A., Fraga, E. S., Schaffner-Bielich, J., & Vuorinen, A. 2014, ApJ, 789, 127
Landry, P., & Essick, R. 2019, PhRvD, 99, 084049
Lattimer, J. M., & Prakash, M. 2016, PhR, 621, 127
Lattimer, J. M., & Steiner, A. W. 2014, ApJ, 784, 123
Lee, H., Kashyap, V. L., van Dyk, D. A., et al. 2011, ApJ, 731, 126
Li, J. J., & Sedrakian, A. 2019, ApJL, 874, L22
Lim, Y., & Holt, J. W. 2018, PhRvL, 121, 062701
Lindblom, L. 2018, PhRvD, 97, 123019
Lo, K. H., Miller, M. C., Bhattacharyya, S., & Lamb, F. K. 2013, ApJ, 776, 19
Lockhart, W., Gralla, S. E., Özel, F., & Psaltis, D. 2019, MNRAS, 490, 1774
Lommen, A. N., Kipphorn, R. A., Nice, D. J., et al. 2006, ApJ, 642, 1012
Lommen, A. N., Zepka, A., Backer, D. C., et al. 2000, ApJ, 545, 1007
Long, M., Romanova, M. M., & Lovelace, R. V. E. 2007, MNRAS, 374, 436
Long, M., Romanova, M. M., & Lovelace, R. V. E. 2008, MNRAS, 386, 1274
Ludlam, R. M., Miller, J. M., Arzoumanian, Z., et al. 2018, ApJL, 858, L5
Ludlam, R. M., Miller, J. M., Bachetti, M., et al. 2017, ApJ, 836, 140
Malik, T., Alam, N., Fortin, M., et al. 2018, PhRvC, 98, 035804
Margueron, J., Hoffmann Casali, R., & Gulminelli, F. 2018a, PhRvC, 97, 025805
Margueron, J., Hoffmann Casali, R., & Gulminelli, F. 2018b, PhRvC, 97, 025806
McNeil Forbes, M., Bose, S., Reddy, S., et al. 2019, PhRvD, 100, 083010
Melatos, A., & Phinney, E. S. 2001, PASA, 18, 421
Miller, J. M., Parker, M. L., Fuerst, F., et al. 2013, ApJL, 779, L2
Miller, M. C. 2013, arXiv:1312.0029
Miller, M. C., & Lamb, F. K. 1998, ApJL, 499, L37
Miller, M. C., & Lamb, F. K. 2015, ApJ, 808, 31
Miller, M. C., Lamb, F. K., Dittmann, A. J., et al. 2019, ApJL, 887, L24
Mitchell, J. P., Braithwaite, J., Reisenegger, A., et al. 2015, MNRAS, 447, 1213
Montaña, G., Tolós, L., Hanauske, M., & Rezzolla, L. 2019, PhRvD, 99, 103009
Morsink, S. M., Leahy, D. A., Cadeau, C., & Braga, J. 2007, ApJ, 663, 1244
Most, E. R., Weih, L. R., Rezzolla, L., & Schaffner-Bielich, J. 2018, PhRvL, 120, 261103
Nandra, K., Barret, D., Barcons, X., et al. 2013, arXiv:1306.2307
Nättilä, J., Miller, M. C., Steiner, A. W., et al. 2017, A&A, 608, A31
Nättilä, J., & Pihajoki, P. 2018, A&A, 615, A50
Nättilä, J., Steiner, A. W., Kajava, J. J. E., Suleimanov, V. F., & Poutanen, J. 2016, A&A, 591, A25
Obergaulinger, M., & Aloy, M. Á. 2017, JPhCS, 932, 012043
Oertel, M., Hempel, M., Klähn, T., & Typel, S. 2017, RvMP, 89, 015007
Oliphant, T. E. 2007, CSE, 9, 10
Özel, F., & Freire, P. 2016, ARA&A, 54, 401
Özel, F., & Psaltis, D. 2009, PhRvD, 80, 103003
Özel, F., Psaltis, D., Güver, T., et al. 2016, ApJ, 820, 28
Patruno, A., & Watts, A. L. 2012, arXiv:1206.2727
Pavlov, G. G., & Zavlin, V. E. 1997, ApJL, 490, L91
Payne, D. J. B., & Melatos, A. 2004, MNRAS, 351, 569
Pechenick, K. R., Ftaclas, C., & Cohen, J. M. 1983, ApJ, 274, 846
Perez, F., & Granger, B. E. 2007, CSE, 9, 21
Philippov, A. A., Cerutti, B., Tchekhovskoy, A., & Spitkovsky, A. 2015a, ApJL, 815, L19
Philippov, A. A., & Spitkovsky, A. 2018, ApJ, 855, 94
Philippov, A. A., Spitkovsky, A., & Cerutti, B. 2015b, ApJL, 801, L19
Piro, A. L., & Bildsten, L. 2005, ApJ, 629, 438
Pons, J. A., Walter, F. M., Lattimer, J. M., et al. 2002, ApJ, 564, 981
Poutanen, J., & Beloborodov, A. M. 2006, MNRAS, 373, 836
Poutanen, J., & Gierliński, M. 2003, MNRAS, 343, 1301
Psaltis, D., & Özel, F. 2014, ApJ, 792, 87
Psaltis, D., Özel, F., & Chakrabarty, D. 2014, ApJ, 787, 136
Raaijmakers, G., Riley, T. E., & Watts, A. L. 2018, MNRAS, 478, 2177
Raaijmakers, G., Riley, T. E., Watts, A. L., et al. 2019, ApJL, 887, L22
Radhakrishnan, V., & Cooke, D. J. 1969, ApL, 3, 225
Radice, D., Perego, A., Hotokezaka, K., et al. 2018, ApJL, 869, L35
Raithel, C. A., Özel, F., & Psaltis, D. 2016, ApJ, 831, 44
Raithel, C. A., Özel, F., & Psaltis, D. 2017, ApJ, 844, 156
Rangelov, B., Pavlov, G. G., Kargaltsev, O., et al. 2017, ApJ, 835, 264
Ray, P. S., Arzoumanian, Z., Ballantyne, D., et al. 2019, arXiv:1903.03035
Read, J. S., Lackey, B. D., Owen, B. J., & Friedman, J. L. 2009, PhRvD, 79, 124032
Reardon, D. J., Hobbs, G., Coles, W., et al. 2016, MNRAS, 455, 1751
Reisenegger, A. 2009, A&A, 499, 557
Riley, T. E. 2019, A NICER View of PSR J0030+0451: Nested Samples for Millisecond Pulsar Parameter Estimation, v1.0, Zenodo, doi:10.5281/zenodo.3386449
Riley, T. E., Raaijmakers, G., & Watts, A. L. 2018, MNRAS, 478, 1093
Riley, T. E., & Watts, A. L. 2019, ApJS, submitted
Romani, R. W. 1990, Natur, 347, 741
Salmi, T., Nättilä, J., & Poutanen, J. 2018, A&A, 618, A161
Shaw, A. W., Heinke, C. O., Steiner, A. W., et al. 2018, MNRAS, 476, 4713
Shlens, J. 2014, CoRR, arXiv:1404.2000
Skilling, J. 2006, BayAn, 1, 833
Spitkovsky, A., Levin, Y., & Ushomirsky, G. 2002, ApJ, 566, 1018
Steiner, A. W., Heinke, C. O., Bogdanov, S., et al. 2018, MNRAS, 476, 421
Steiner, A. W., Lattimer, J. M., & Brown, E. F. 2010, ApJ, 722, 33
Steiner, A. W., Lattimer, J. M., & Brown, E. F. 2013, ApJL, 765, L5
Stevens, A. L., Fiege, J. D., Leahy, D. A., & Morsink, S. M. 2016, ApJ, 833, 244
Strobel, K., Schaab, C., & Weigel, M. K. 1999, A&A, 350, 497
Suleimanov, V., Poutanen, J., Revnivtsev, M., & Werner, K. 2011a, ApJ, 742, 122
Suleimanov, V., Poutanen, J., & Werner, K. 2011b, A&A, 527, A139
Tews, I., Carlson, J., Gandolfi, S., & Reddy, S. 2018a, ApJ, 860, 149
Tews, I., Lattimer, J. M., Ohnishi, A., & Kolomeitsev, E. E. 2017, ApJ, 848, 105
Tews, I., Margueron, J., & Reddy, S. 2018b, PhRvC, 98, 045804
The LIGO Scientific Collaboration, the Virgo Collaboration, Abbott, B. P., et al. 2019, PhRvX, 9, 031040
Timokhin, A. N., & Arons, J. 2013, MNRAS, 429, 20
van der Walt, S., Colbert, S. C., & Varoquaux, G. 2011, CSE, 13, 22
van Doesburgh, M., van der Klis, M., & Morsink, S. M. 2018, MNRAS, 479, 426
Vehtari, A., & Ojanen, J. 2012, Statist. Surv., 6, 142
Viganò, D., Rea, N., Pons, J. A., et al. 2013, MNRAS, 434, 123
Vincent, F. H., Bejger, M., Różańska, A., et al. 2018, ApJ, 855, 116
Watts, A. L. 2012, ARA&A, 50, 609
Watts, A. L. 2019, in AIP Conf. Ser. 2127, Xiamen-CUSTIPEN Workshop on the EOS of Dense Neutron-Rich Matter in the Era of Gravitational Wave Astronomy, ed. A. Li, B.-A. Li, & F. Xu (Melville, NY: AIP) 020008
Watts, A. L., Andersson, N., Chakrabarty, D., et al. 2016, RvMP, 88, 021001
Watts, A. L., Yu, W., Poutanen, J., et al. 2019, SCPMA, 62, 29503
Webb, N. A., & Barret, D. 2007, ApJ, 671, 727
Weih, L. R., Most, E. R., & Rezzolla, L. 2019, ApJ, 881, 73
Wilkinson, T., Patruno, A., Watts, A., & Uttley, P. 2011, MNRAS, 410, 1513
Wilms, J., Allen, A., & McCray, R. 2000, ApJ, 542, 914
Xu, J., van Dyk, D. A., Kashyap, V. L., et al. 2014, ApJ, 794, 97
Zavlin, V. E., Pavlov, G. G., & Shibanov, Y. A. 1996, A&A, 315, 141
Zdunik, J. L., & Haensel, P. 2013, A&A, 551, A61
Zhang, S., Santangelo, A., Feroci, M., et al. 2019, SCPMA, 62, 29502

The Astrophysical Journal, 961:62 (28pp), 2024 January 20 https://doi.org/10.3847/1538-4357/acfb83
© 2024. The Author(s). Published by the American Astronomical Society.
OPEN ACCESS

An Updated Mass–Radius Analysis of the 2017–2018 NICER Data Set of PSR J0030+0451

Serena Vinciguerra[1], Tuomo Salmi[1], Anna L. Watts[1], Devarshi Choudhury[1], Thomas E. Riley[1], Paul S. Ray[2], Slavko Bogdanov[3], Yves Kini[1], Sebastien Guillot[4], Deepto Chakrabarty[5], Wynn C. G. Ho[6], Daniela Huppenkothen[7], Sharon M. Morsink[8], Zorawar Wadiasingh[9,10,11], and Michael T. Wolff[2]

[1] Anton Pannekoek Institute for Astronomy, University of Amsterdam, Science Park 904, 1098XH Amsterdam, The Netherlands; s.vinciguerra@uva.nl
[2] Space Science Division, U.S. Naval Research Laboratory, Washington, DC 20375, USA
[3] Columbia Astrophysics Laboratory, Columbia University, 550 West 120th Street, New York, NY 10027, USA
[4] Institut de Recherche en Astrophysique et Planétologie, UPS-OMP, CNRS, CNES, 9 avenue du Colonel Roche, BP 44346, F-31028 Toulouse Cedex 4, France
[5] MIT Kavli Institute for Astrophysics and Space Research, Massachusetts Institute of Technology, Cambridge, MA 02139, USA
[6] Department of Physics and Astronomy, Haverford College, 370 Lancaster Avenue, Haverford, PA 19041, USA
[7] SRON Netherlands Institute for Space Research, Niels Bohrweg 4, 2333 CA Leiden, The Netherlands
[8] Department of Physics, University of Alberta, 4-183 CCIS, Edmonton, AB, T6G 2E1, Canada
[9] Department of Astronomy, University of Maryland, College Park, MD 20742, USA
[10] Astrophysics Science Division, NASA Goddard Space Flight Center, Greenbelt, MD 20771, USA
[11] Center for Research and Exploration in Space Science and Technology, NASA/GSFC, Greenbelt, MD 20771, USA
Received 2023 July 27; revised 2023 September 7; accepted 2023 September 18; published 2024 January 16

Abstract

In 2019 the NICER collaboration published the first mass and radius inferred for PSR J0030+0451, thanks to NICER observations, and consequent constraints on the equation of state characterizing dense matter. Two independent analyses found a mass of $\sim$1.3–1.4 $M_\odot$ and a radius of $\sim$13 km. They also both found that the hot spots were all located on the same hemisphere, opposite to the observer, and that at least one of them had a significantly elongated shape. Here we reanalyze, in greater detail, the same NICER data set, incorporating the effects of an updated NICER response matrix and using an upgraded analysis framework. We expand the adopted models and also jointly analyze XMM-Newton data, which enables us to better constrain the fraction of observed counts coming from PSR J0030+0451. Adopting the same models used in previous publications, we find consistent results, although with more stringent inference requirements. We also find a multimodal structure in the posterior surface. This becomes crucial when XMM-Newton data is accounted for. Including the corresponding constraints disfavors the main solutions found previously, in favor of the new and more complex models. These have inferred masses and radii of $\sim$[1.4 $M_\odot$, 11.5 km] and $\sim$[1.7 $M_\odot$, 14.5 km], depending on the assumed model. They display configurations that do not require the two hot spots generating the observed X-rays to be on the same hemisphere, nor to show very elongated features, and point instead to the presence of temperature gradients and the need to account for them.

Unified Astronomy Thesaurus concepts: Neutron stars (1108); Nuclear astrophysics (1129); Astronomy data analysis (1858); High energy astrophysics (739); X-ray astronomy (1810)

Supporting material: figure sets

1. Introduction

The Neutron Star Interior Composition Explorer (NICER) is an instrument installed on the International Space Station to detect the soft thermal X-ray emission of rotation-powered millisecond pulsars (MSPs). By modeling this emission, originating from the hot polar caps, we are able to infer neutron star (NS) masses and radii, hence constraining the equation of state (EoS) governing dense and cold matter. So far the NICER collaboration has released results for two sources: PSR J0030+0451 (Miller et al. 2019; Riley et al. 2019) and the high mass pulsar PSR J0740+6620 (Miller et al. 2021; Riley et al. 2021; Salmi et al. 2022).

The X-ray emission of the MSPs that NICER targets is characterized by pulsations generated by return currents heating up the NS surface at the magnetic poles. Special and general relativistic effects on the propagation of radiation ensure that the phase-resolved spectrum of the pulsations carries information about the spacetime surrounding the NS. By modeling all of the relevant relativistic effects, a technique known as pulse profile modeling (PPM), it is possible to infer mass and radius (for a general introduction to PPM, see Bogdanov et al. 2019b, 2021; Watts 2019). As a byproduct of the analysis, PPM also allows us to infer the properties (size, shape, and location) of the hot emitting regions.

In this paper we revisit the first source for which NICER results were released, PSR J0030+0451, using the X-ray Pulse Simulation and Inference (X-PSI)[12] package (Riley et al. 2023). Our analysis is an update to (Riley et al. 2019, hereafter R19), since validated by Afle et al. (2023) who also used X-PSI; the independent analysis of Miller et al. (2019) used a different pipeline.

PSR J0030+0451 is an isolated MSP rotating at $\sim$205 Hz, located at a distance of $\sim$325 pc (Arzoumanian et al. 2018; Ding et al. 2023). The first X-PSI analysis of the NICER data

Original content from this work may be used under the terms of the Creative Commons Attribution 4.0 licence. Any further distribution of this work must maintain attribution to the author(s) and the title of the work, journal citation and DOI.

[12] https://github.com/xpsi-group/xpsi

set for PSR J0030+0451 (R19) found that several models for the size and shape of the hot polar caps could reproduce the data quite well. However, when the models were ranked according to their evidence, the preferred model was one in which emission originated from one small (circular) and one extended (arc-like) hot spot, located in the same rotational hemisphere. An independent analysis of the same data by Miller et al. (2019), using a different parameter estimation code, found qualitatively similar spot shapes and locations on the star, although they used ovals instead of arcs. The shape and location of the hot emitting regions suggested the need for profound changes to the standard picture of the NSs's magnetic field, as they were incompatible with a classical centered dipole (Bilous et al. 2019; Chen et al. 2020; Kalapotharakos et al. 2021).

For the preferred emission pattern and viewing geometry, the mass and radius inferred by R19 for PSR J0030+0451 was $1.34^{+0.15}_{-0.16}\,M_\odot$ and $12.71^{+1.14}_{-1.19}$ km, where the uncertainties, here and throughout this work, are specified at approximately the 16% and 84% quantiles in the 1D marginal posterior (for comparison, Miller et al. 2019 inferred $1.44^{+0.15}_{-0.14}\,M_\odot$ and $13.02^{+1.24}_{-1.06}$ km). The mass and radius posteriors have since been used in a variety of studies to constrain the EoS (see, for example, Raaijmakers et al. 2021; Tang et al. 2021; Biswas 2022; Sabatucci et al. 2022; Rutherford et al. 2023; Sun et al. 2023). The fact that PSR J0030+0451 has an inferred radius similar to that inferred for the $\sim 2.1\,M_\odot$ pulsar PSR J0740+6620 (Fonseca et al. 2021; Miller et al. 2021; Riley et al. 2021; Salmi et al. 2022), despite the much lower inferred mass, is particularly notable (Raaijmakers et al. 2021). The shift in radius as mass increases can be used to distinguish between EoS models (Drischler et al. 2021).

Improving the robustness of the NICER PPM results and updating them whenever possible is therefore crucial for advancing our understanding of the EoS. In a companion paper (Vinciguerra et al. 2023a, hereafter V23a) parameter recovery simulations, tailored to PSR J0030+0451, were carried out to test the reliability of our results for complex hot spot models, and the sensitivity to stochastic fluctuations and inference setups. This study revealed some sensitivity of PPM posteriors to noise, analysis settings and random sampling processes. Their effects are interconnected: depending on the noise realization, specific analysis settings may or may not be sufficient to assert a certain degree of stability in the results and, in general, computationally cheap analysis settings are more prone to variability due to random sampling processes. The other major finding of this work was the presence of a clearly multimodal structure in the posterior. These posterior maxima are often considerably different in terms of associated probabilities, so they do not always appear as clear multimodal structures in the posterior plots. Sometimes they may be present as tails of the distributions, other times they may even be completely obliterated by the main mode. However, their properties can be considerably different, and the application of independent constraints may completely shift their importance.

Due to limitations in the computational resources, the V23a simulation study focused on synthetic data sets based on only two different parameter vectors. This implies that some of its findings may not be general. In particular, comparing the results of V23a with the ones reported in R19, we note some differences that may be tied to the specific choice of parameter vectors. For example, a negligible difference in evidence between different models was found by V23a but not by R19. V23a also reported that different models could recover consistent mass and radius, given a specific synthetic data set; while R19 showed that when analyzing the original NICER data set, presented in Bogdanov et al. (2019a), employing different models drastically changes the inferred mass and radius posterior distributions. In this paper we apply what we have learned from V23a and revisit the PPM for PSR J0030+0451, making a number of improvements over the analysis presented in R19.

X-PSI has undergone a series of major updates since the analysis presented in R19: for example, the surface pattern model suite is more comprehensive, and it is now possible to perform joint analysis with data sets observed by multiple instruments. In R19, the inferred background was checked a posteriori against constraints derived from XMM-Newton observations (Bogdanov & Grindlay 2009). In this paper we include XMM-Newton constraints directly in the inference analysis, as was done for PSR J0740+6620 in Miller et al. (2021), Riley et al. (2021), and Salmi et al. (2022). With more computational resources, we were also able to carry out a wider-range and higher-resolution study. This enables us to explore the robustness of the findings in more depth. Another improvement is to the instrument response model of NICER, which has been updated since the analysis presented in R19. What we present here is the analysis of a revised NICER data set (hereafter B19v006), derived from the one presented in Bogdanov et al. (2019a) and covering the same observations, but modified to be consistent with the latest NICER response matrix. This therefore becomes the baseline to which inference of PSR J0030+0451 data sets containing newer observations should eventually be compared.

Below, for our PPM inferences, we will consider four different models that describe PSR J0030+0451's system, adopting increasingly more complex surface patterns. With NICER-only analyses, we test the sensitivity of the identified posteriors to various assumptions and analysis settings. We also check the impact of random sampling processes, by repeating (multiple times) inferences that are set up identically. Given the various analyses initiated with NICER-only data, we decided to appoint four reference runs, one for each of the adopted models. These are used for the general discussion and have been performed with computationally expensive analysis settings; however, the robustness of our findings is also in this case not always guaranteed. We only performed one production run per model, when jointly analyzing NICER and XMM-Newton data; in this case, there is therefore no need for references. Since joint inferences require considerably higher computing resources, the analysis settings are, most of the time, less optimal compared to the NICER-only case. The corresponding posteriors are therefore not proven to be robust, yet. To help and guide the interpretation of our findings, more details and a wider context are given throughout the text that follows.

In Section 2 we describe the models adopted for this analysis and the most significant upgrades to X-PSI since the R19 analysis. In Section 3 we outline the most relevant properties and changes to the NICER and XMM-Newton data sets that are analyzed. The results of our analysis are then presented in Section 4 and discussed in Section 5. We present our final remarks in Section 6.

2. Methodology: X-PSI Upgrades and Main Setups

In this work, we use the package X-PSI to analyze the X-ray emission produced by PSR J0030+0451 and detected by NICER. NICER data are registered as events (counts) per PI (instrumental-energy) channel, where each event is characterized by a specific detection time. As described in R19, data collected over many ($\mathcal{O}(10^8)$) rotational cycles are folded over the spin period of the MSP of interest, in our case PSR J0030+0451, and are then binned into 32 phase bins. The data analyzed by X-PSI therefore have the form of number of events (counts) per instrumental channel and rotational phase bin.

X-PSI is a software package that performs parameter estimation by modeling the thermal emission generated at the NS surface and detected by NICER, following the methodology described in Bogdanov et al. (2019b), Riley et al. (2019), Bogdanov et al. (2021), and Riley et al. (2021). Each hot spot on the NS surface is modeled by overlapping spherical caps (see Section 2.1 for more details). To account for the potential well and the shape of the NS, our analysis relies on relativistic ray-tracing described by the Oblate Schwarzschild plus Doppler approximation, introduced by Morsink et al. (2007) and AlGendy & Morsink (2014). The final intensity at the observer is then calculated accounting for the effects of the NS atmosphere and the interstellar medium. Such a signal is generated for every parameter vector sampled by MULTINEST (Feroz & Hobson 2008; Feroz et al. 2009, 2019), the algorithm adopted within X-PSI to explore the model parameter space through a nested sampling algorithm (Skilling 2004). This simulation process is essential for our inference analysis, which then compares these synthetic signals against the actual NICER data within a Bayesian framework.

In this work we use X-PSI versions `v0.7` and `v1` (for inference `v0.7.3`, `v0.7.9`, and `v0.7.10`—which differ from one another only by upgrades and minor bug fixes that are not expected to affect the results—and `v1.0.0-v2.0.0` for post-processing). Compared to the version used in R19 (X-PSI `v0.1`) these X-PSI versions incorporate the possibility of multiple images, as described in Section 2.2.3 of Riley et al. (2021). Note that we do not expect this modification to significantly affect our results, since it is relevant for compactness values $C = MR^{-1} > 0.284$ (for brevity, we assume $c = G = 1$) and R19 found negligible posterior probability for compactness above $\sim$0.2 in all tested models (see Figure 19 of that paper).

2.1. X-PSI Models

A summary of the method underlying the analyses performed with X-PSI and its recent upgrades and modifications can be found in Section 2 of V23a. We expand on that overview by presenting below additional analysis specifications that are necessary to introduce the wider range of tests included in this work.

2.1.1. Atmosphere and Interstellar Medium

Throughout this work we assume that the hot spots of PSR J0030+0451 have a fully ionized and nonmagnetic `NSX` hydrogen atmosphere (Ho & Lai 2001; Ho & Heinke 2009). As in Riley et al. (2021), Salmi et al. (2023), and V23a, the intensity of the radiation field is calculated by interpolating it from a table (extended compared to that used in R19), which expresses it for different values of effective temperature, surface gravity, photon energy, and the cosine of emission angle calculated from the surface normal (for more details, see Section 2.4.1 of R19). A detailed discussion of the implications of this choice (and possible alternatives) is presented in Salmi et al. (2023), specifically for PSR J0030+0451 and the data set analyzed here. For the first time, we test the potential impact of adding possible in-band emission from the NS surface, outside the hot spots. For this preliminary test, we still assume a fully ionized hydrogen atmosphere for the hot spots, but model the radiation generated from the remaining part of the surface as blackbody emission, to reduce the corresponding computational cost. Even with this simplification, adding such a component can indeed considerably increase the computational resources required.[13]

The attenuating effects that the interstellar medium has at different energies are simulated with the same precomputed tables, based on the `tbnew` model,[14] used in R19. As outlined in R19, we parameterize the effect of the interstellar medium with a single variable, the neutral hydrogen column density $N_{\rm H}[{\rm cm}^{-2}]$. Other chemical abundances are then assumed from it, following Wilms et al. (2000).

2.1.2. Parameterizations of Hot Spots

To model the thermal emission of the hot spots in the NICER band, we use parameterized models that are motivated by theoretical studies of return currents and polar cap heating in rotation-powered pulsars (Harding & Muslimov 2001, 2011; Timokhin & Arons 2013; Kalapotharakos et al. 2014; Gralla et al. 2017; Lockhart et al. 2019; Kalapotharakos et al. 2021). In particular, we define each hot spot with one or two overlapping spherical caps on the NS surface. One of these components is always emitting at a constant and uniform temperature; the other can also radiate (forming a hot spot with two temperatures) or mask the X-rays of the emitting component (widening the range of possible hot spot shapes to include arcs or rings).

X-PSI analyses of NICER data have always assumed the presence of two nonoverlapping hot spots, motivated by their theoretical connection to the magnetic poles and the data structure of the pulse profile. We refer to these two hot spots as the *primary* and the *secondary*. Within the X-PSI framework we can define different models, given the setup just described. More details about the naming convention adopted for our models and a schematic representation of them are reported in Section 2.3.3 and Figure 1 of V23a.

In this work we adopt nested models that describe the surface patterns with increasing complexity:

1. `ST-U`: where each of the two (single temperature; `ST`) hot spots is described by a single spherical cap. The primary is defined as the hot spot with lower colatitude with respect to the angular momentum vector (spin axis);[15]

[13] Setting what we consider to be an adequate number of cells to present such surface (`sqrt_num_cells=512`), the core hours required for an `ST-U` inference run roughly quadrupled. For the `ST+PST` inference, we had to significantly lower the number of cells (`sqrt_num_cells=64`) and still also set the sampling efficiency to 0.8, to make the run affordable (about twice the core hours required with a similar run, excluding the emission from the remaining part of the NS surface).

[14] https://pulsar.sternwarte.uni-erlangen.de/wilms/research/tbabs/

[15] As in R19, the rotation is defined by the right-hand rule, with the thumb pointing at North.

2. ST+PST: where the primary (ST) is described by a single spherical cap and the secondary (protruding single temperature; PST) by two components, one emitting and one masking (see Figure 2 of V23a). Within this model, for comparison we adopt both the prior used for analyses in R19 and the more Comprehensive Hot spot (CoH) prior described in Section 2.3.4 of V23a. The latter allows for the hot spot described by a single spherical cap to overlap with the masking component of the PST one;
3. ST+PDT: where the primary (ST) is described by a single spherical cap and the secondary (protruding double temperature; PDT) by two components, both emitting; and
4. PDT−U: where each of the two hot spots is described by two emitting spherical caps. The primary is defined as the hot spot with lower colatitude.

The first two are described in detail in V23a; a more detailed explanation of the others is given below. R19 suggested that one of the hot spots was already well represented by our simplest description (i.e., by a circular component with uniform temperature). For this reason, starting from the simplest model here considered, ST−U, we first increase the complexity of the description of only one of the hot spots: first allowing for the creation of different shapes with the ST+PST model, and then allowing two overlapping circular components to emit at different temperatures, with the ST+PDT model. Only the most complex model, PDT−U allows for both hot spots to be described with such complexity. In this project, for the first time within the NICER PPM analyses, we also consider the emission from the remaining portion of the NS surface, introducing the *elsewhere temperature* ($T_{\rm else}$), which can be added to all models.

In Table 1, we briefly list all of the parameters used in this work to describe the ST−U ($+T_{\rm else}$) model. Within our naming convention, the −U, for *unshared*, signifies that the values of model parameters describing one hot spot are completely independent from the other.[16] Subscripts p and s are used to mark when a parameter refers to the primary or the secondary hot spot. The parameters in this table are in general common to all of the models used in this paper; if two components are used to describe a hot spot, then the quantities below refer to either the only emitting spherical cap involved or—if both radiate—to the superseding one. The only exception is the phase ϕ, which refers to the masking component, if present.

When a hot spot is modeled by two spherical caps, we need to define a few more parameters. We divide them into two cases: PST if only one component is emitting and PDT if both of them are. We describe all of these parameters in Table 2. A more detailed explanation of the adopted parameterization in models using PST and PDT hot spots can be found in Section 2.5.6 of R19.

In this work, unlike in R19 and V23a, we coherently incorporate XMM-Newton data into some of our analyses. XMM-Newton is an imaging X-ray telescope. For this reason, it performs better in identifying the photons that are generated by a particular source. Introducing this data set, with associated background, and trying to simultaneously fit both NICER and XMM-Newton data, allows us to better evaluate which fraction of the registered events (for both data sets) actually come from PSR J0030+0451 and which are due to external contributions (see Section 4.2 of Riley et al. 2021 for more details). We describe below how we model uncertainties in the instrument responses of both NICER and XMM-Newton.

[16] With the exception of the imposed condition that they do not overlap.

Table 1
Shared Model Parameters

Symbol	Meaning
M [$M_\odot$]	Mass of the MSP
$R_{\rm eq}$ [km]	Equatorial radius[a] of the MSP
D [kpc]	Distance of the MSP
$\cos(i)$	cos of the inclination angle, the angle between the spin axis and line of sight
$N_{\rm H}$ [cm^{-2}]	Hydrogen column density
$\log_{10}(T_p/{\rm K})$	log of the primary hot spot temperature
$\log_{10}(T_s/{\rm K})$	log of the secondary hot spot temperature
ζ_p [rad]	Angular radius of the primary hot spot
ζ_s [rad]	Angular radius of the secondary hot spot
θ_p [rad]	Colatitude of the primary hot spot
θ_s [rad]	Colatitude of the secondary hot spot
ϕ_p [cycles]	Phase shift of the center of the primary hot spot compared to the reference phase set by the data
ϕ_s [cycles]	Phase shift of the center of the secondary hot spot compared to the reference phase set by the data plus half a cycle
α	(NICER, $\alpha_{\rm XTI}$, or XMM-Newton, $\alpha_{\rm MOS}$) effective area energy-independent scaling factor
β [kpc^{-2}]	distance scaled effective area parameter α/D^2 (used as an alternative to α and D)
$\log_{10}(T_{\rm else}/{\rm K})$	log of the temperature of the remaining surface of the MSP (only adopted in few analyses)

Notes. Definition of the parameters that are common to all models adopted in this work. More detailed descriptions can be found in Section 2.3.3 of V23a.
[a] Hereafter also more simply referred to as radius.

Modeling of the instrument response: When we analyze only the NICER data set B19v006, we use the same parameterization described in Section 2.2 of V23a and summarized below. To model uncertainties in the instrument response, we adopt a variable $\beta\,[{\rm kpc}^{-2}] = \alpha_{\rm XTI} D^{-2}$, where D is the pulsar distance in kiloparsecs and $\alpha_{\rm XTI}$ is the energy-independent factor that scales the reference response matrix, and hence the total effective area, of the NICER X-ray Timing Instrument (XTI). β represents the only combination of $\alpha_{\rm XTI}$ and D to which our analysis is sensitive. When both XMM-Newton and NICER data sets are used, we instead sample from $\alpha_{\rm XTI}$, $\alpha_{\rm MOS}$, and D. As described in Table 1, $\alpha_{\rm MOS}$ represents the energy-independent scaling factor applied to the reference instrument responses of XMM-Newton two cameras: MOS1 and MOS2 (i.e., we assume $\alpha_{\rm MOS} = \alpha_{\rm MOS1} = \alpha_{\rm MOS2}$, which may not actually be the case). We make this parameterization choice to describe the correlation between the NICER and XMM-Newton instrument responses as explained in Section 2.4 of

Table 2
Additional Model Parameters for PST and PDT Hot Spots

Symbol	Meaning	PST	PDT
$\zeta_{o/c}$ [rad]	Radius of the masking /ceding region	✓	✓
$\theta_{o/c}$ [rad]	Colatitude of the masking /ceding region	✓	✓
χ [rad]	Azimuthal offset between the two caps[a]	✓	✓
$\log_{10}(T_c/K)$	Temperature in log of the ceding region	⋯	✓

Notes. Definition of the parameters necessary to describe PST and PDT hot spots. A PST hot spot is characterized by an omitting and an emitting spherical cap, respectively, labeled above with the subscript $_o$ and $_e$. A PDT hot spot is characterized by a ceding and a superseding spherical cap, respectively, labeled with the subscript $_c$ and $_s$. The parameters mentioned in the table with subscripts $_{o/c}$ hence refer to properties of the omitting component, for a PST hot spot, or to the ceding one, for a PDT hot spot. In the presence of two hot spots, additional (initial) subscripts p or s will indicate whether the parameter refers to the primary or the secondary hot spot. For PST parameters, a more detailed description can be found in Section 2.3.4 of V23a.
[a] $\chi/2\pi = \phi_{o/c} - \phi_{e/s}$, where ϕ marks phases and the subscripts clarify the corresponding component.

Table 3
Most Relevant Parameters Describing MULTINEST Settings

Symbol	Meaning	Range or Scale	Our Default
SE	Sampling Efficiency	Typically $\in (0.1 - 1)$	0.3
ET	Evidence Tolerance	Typically $\leqslant 0.5$	0.1
LP	Live Points	Order hundreds to thousands	1000
MM	Multimode/Mode-separation	on/off	off

Notes. The term "typically" is used to denote values that we have encountered in the literature. By "our default" we mean the default values used in our analysis unless otherwise specified. The MULTINEST advised values are 0.5 for evidence tolerance and 0.3 or 0.8 for sampling efficiency, respectively, if the main goal is evidence calculation or parameter estimation (Feroz & Hobson 2008; Buchner 2021). No formal number of live points have been suggested, likely because an adequate number would depend on the problem at hand. Given the same settings, adopting the mode-separation modality slightly worsens the precision of the final results, as live points no longer move as efficiently. Lower numbers for sampling efficiency and evidence tolerance, and higher numbers of live points, imply higher accuracy in the calculation; however, they also significantly increase the computational resources required.

Riley et al. (2021). As in Salmi et al. (2022), in this work we adopt the *compressed effective area prior* (see Section 4.2 of Riley et al. 2021).

In this paper we chose to apply pretty conservative priors for the α parameters. These are comparable to what was used in R19 and more constraining compared to what was adopted for the headline results of Riley et al. (2021), but still broad enough to allow for follow-up tests, adopting importance sampling, with more restricted priors, which could reflect more accurately the current understanding of NICER and XMM-Newton calibration uncertainties.

2.1.3. Priors and Settings

For this paper we use the same priors and settings introduced in Section 2.2 of V23a. These include a flat prior in the joint mass and radius parameter space, where hard boundaries are applied: the mass is constrained to be in the range $\in (1.0, 3.0)\, M_\odot$, while the radius must be <16 km. Similarly to R19, V23a, and Salmi et al. (2022, 2023), we also limit the compactness and the surface gravity. Differently from R19, we adopt the instrumental PI channels in the range [30, 300) and we consider isotropic priors (flat in cosine) for the inclination angle i and the colatitudes of the hot spots' centers θ_p and θ_s.

Priors describing the additional emitting component in the ST+PDT and PDT-U models are constrained by the overlapping condition, which imposes overlaps between the superseding and the ceding spherical caps. These priors are therefore coupled to the value of the parameters describing shape and location of the superceding component. These dependencies are similarly implemented as for the ST+PST model, starting from the angular radius of the ceding region ζ_c (see Section 2.5.6 of R19 for more details). When used, the temperature of the additional elsewhere component $\log_{10}(T_{\rm else}/{\rm K})$ is sampled uniformly between the bounds (5.0, 6.5).

In this work, as well as in V23a, we use both *high-resolution* (HR) and *low-resolution* (LR) X-PSI settings (the specific parameters, that define such settings, and their values are presented in Section 2.3.1 of V23a). The latter allows us to run complex models, while saving significant computational resources. According to the results presented in V23a, no significant changes are expected in the results adopting the low-resolution settings. Below we test whether this hypothesis holds also in the case of the real NICER data.

2.1.4. MULTINEST

X-PSI needs to be coupled with a sampling program. In this work, we use PyMultiNest (Buchner et al. 2014), a library that allows us to interface easily with MULTINEST. MULTINEST is a Bayesian inference technique and a program that targets the estimation of the evidence. Doing so, it explores the parameter space, and so allows for parameter estimation. More details are given in Section 2.4 of V23a; in Table 3 we summarize the most relevant settings for the analyses performed in this work. Our default starting MULTINEST settings are as follows: sampling efficiency 0.3; evidence tolerance 0.1; live points 1000; and multimode/mode-separation off (SE 0.3, ET 0.1, LP 1000, MM off). The sampling efficiency initially set is then modified within X-PSI to account for the effective unit hypercube volume of the prior space considered in the analysis.

2.2. Test Cases

The main goal of this paper is to establish a baseline for the analysis of the upcoming new PSR J0030+0451 data sets and their interpretation. It is supported by the simulations carried out in V23a. To achieve this goal we first set up a few exploratory runs, aiming to test the robustness of the solutions found by R19. We first try to reproduce those results, with the new setup we describe here. Then we investigate the effect of background constraints, by including the XMM-Newton data

Table 4
Collection of Inference Runs Performed for This Work and the Corresponding Properties and Settings

Model	X-PSI Settings	SE	ET	LP	MM	XMM-Newton	N
ST-U	HR	0.3	0.1	10^3	off	no	3
	HR	0.3	0.1	3×10^3	off	no	1
	HR	0.3	0.1	6×10^3	off	no	1
	HR	0.3	0.1	10^4	off	no	1
	HR	0.1	0.1	10^3	off	no	1
	HR	0.8	0.1	10^3	off	no	1
	HR	0.3	0.001	10^3	off	no	3
	HR	**0.3**	**0.1**	**10^4**	**on**	**no**	**1**
	HR	0.3	0.1	10^4	on	yes	1
ST-U+$T_{\rm else}$	HR	0.3	0.1	10^3	off	no	1
ST+PST	HR	0.3[a]	0.1	10^3	off	no	3
	LR	0.3	0.1	10^3	off	no	2
	HR	0.3	0.1	10^3	on	no	1
[b]	LR	0.3	0.1	10^3	off	no	1
[b]	**LR**	**0.3**	**0.1**	**10^4**	**on**	**no**	**1**
[b]	LR	0.8	0.1	10^3	off	yes	1
ST+PST+$T_{\rm else}$[b]	LR	0.3	0.1	10^3	off	no	1
ST+PDT	LR	0.8	0.1	10^3	off	no	1
	LR	0.8	0.1	10^3	on	no	1
	LR	**0.8**	**0.1**	**10^4**	**on**	**no**	**1**
	LR	0.8	0.1	10^3	off	yes	1
PDT-U	LR	0.8	0.1	10^3	off	no	1
	LR	**0.8**	**0.1**	**10^4**	**on**	**no**	**1**
	LR	0.8	0.1	10^3	off	yes	1

Notes. The first column represents the name of the hot spot model adopted for the run (see Section 2.1.2 and Section 2.5 of R19). When the conventional model name is followed by $T_{\rm else}$, the run also includes the modeling of the temperature of the rest of the MSP's surface, exterior to the two hot spots. The second column describes whether the run was performed with high (HR) or low (LR) resolution for some of the main X-PSI parameters. The four columns that follow represent the MULTINEST settings as described in Table 3. The seventh column is used to flag inference runs where NICER and XMM-Newton data have been fitted at the same time; and the last column shows how many identical repetitions of the same run were performed to test the impact of random sampling processes. Reference runs for this study are highlighted in bold.

[a] Two of these three runs were resumed with sampling efficiency 0.8, as was done in R19.

[b] These runs were performed adopting the updated CoH prior.

set in our inference runs. We look at the possible presence of multimodal structures in the posterior surface, as well as conceivable shortcomings of the analysis (in light of what was found in V23a).

Given the scope of this paper, we decided to focus most of our tests on the two simplest models ST-U and ST+PST. The latter was identified as the preferred model in R19 (and associated with the headline mass–radius result); the former was found to be the simplest model that could represent the PSR J0030+0451 NICER data without showing clear structures in the residuals. With these two models we test robustness of the obtained inferred parameter values and their dependencies on random sampling processes and analysis settings. We also begin to explore the parameter space of the more and most complex two hot spot models: ST+PDT and PDT-U. Since V23a uncovered the presence of prominent multimodal structures in the posterior surface, for NICER-only analyses, we here perform one inference adopting the mode-separation variant with 10^4 live points for each model; these are our (NICER-only) reference runs. These settings are proven (see Section 4.1.2) to generate stable posteriors when the ST-U model is used; however, this is not necessarily the case for the more complex models, for which a more detailed testing would have been computationally too expensive. For all four models, we also perform a preliminary production run including XMM-Newton data in the analysis.

We summarize all of the runs carried out, and their settings, in Table 4.

3. Data Sets

3.1. NICER B19v006 Data Set

For this work, we use the same data set as in the initial NICER analyses of PSR J0030+0451 (Miller et al. 2019; Riley et al. 2019), with data processing as described in Bogdanov et al. (2019a, hereafter B19). The data set contains 1.936 Ms of exposure time collected over the period 2017 July 24 to 2018 December 9. However, we have recalibrated the gain using the nicerpi tool, updating the calibration to use the gain calibration file 20170601v006. The response matrices matched to this gain solution are in NICER CALDB file xti20200722. Compared to the inferences reported in R19 (which also included energy channels 25–30), analyses of this recalibrated data set need to be limited to energy channels $\geqslant$30, as the procedure adopted to create the updated B19v006 data set from the original B19 one allows for possible calibration errors at these excluded lowest channels. In Section 5.1 we demonstrate that the effects of removing these channels are minor. This is in agreement with the analysis of Miller et al. (2019), which considered only channels $\geqslant$40 and found that this choice did not affect their results.

3.2. XMM Data Set

The XMM-Newton data of PSR J0030+0451 used in this analysis (first presented in Bogdanov & Grindlay 2009) are from two archival observations obtained on 2001 June 19 (ObsID 0112320101) and 2007 December 12 (ObsID 0502290101). We only consider the EPIC MOS1 and MOS2 "Full Frame" mode imaging observations; although they do not possess adequate sampling time to resolve pulsations from PSR J0030+0451, they provide reliable low background phase-averaged source spectra. The EPIC pn data acquired in "Timing" mode, which provide imaging only in one direction of the detector, are not used due to the considerably larger uncertainties in the calibration of the instrument in this observing mode. The data reduction and extraction of the EPIC MOS data were carried out using the Science Analysis Software (SAS)[17] version `xmmsas_20211130_0941`. The event data were screened for instances of high background count rates and the recommended PATTERN ($\leqslant$12 for MOS1/2) and FLAG (0) filters were applied. This resulted in 121.2 ks and 120.9 ks of total effective exposure for MOS1 and MOS2, respectively, from combining both observations.

4. Results

In the following, we present the results of the inference runs described in Section 2.2 and summarized in Table 4. We consider each hot spot model presented in Section 2.1.2, going from the simplest to the most complex. For the simplest, `ST-U` and `ST+PST`, we start with parameter estimation analyses that allow for an easier comparison with the findings of R19 and explore our sensitivity to settings and random sampling processes, as in V23a. The main data and post-processing routines necessary to reproduce our main results are available on Zenodo at doi:10.5281/zenodo.8239000 (Vinciguerra et al. 2023b).

As estimating mass and radius of MSPs is the main science goal of NICER, in this Section we focus in particular on the inferred posterior distributions of these two parameters. We also show posteriors for compactness, since our analysis is expected to be most sensitive to this particular combination of mass and radius.[18] The corner plots reported in most of the figures that follow show the 1D and 2D posterior distributions of these three parameters. As in V23a, R19, Riley et al. (2021), and Salmi et al. (2022), the colored band present in the 1D posterior plots shows the area enclosed within the $\sim$16% and $\sim$84% quantiles of the 1D marginalized posterior distributions (medians and corresponding lower and upper limits are written on top of each 1D posterior), while the contours in the 2D marginalized distributions represent the $\sim$68.3%, 95.5%, and 99.7% credible regions. As explained in Section 4 of V23a, the X-PSI post-processing tools adopt the GetDist[19] KDE to smooth the distribution of the posterior samples. In 2D posterior plots, this may introduce artificial gradients in the density, when sharp cutoffs (more complex than a threshold on a single parameter) are present in the prior. This is, for example, the case for the 2D posterior density plot of radius and compactness (see also footnote 15 of V23a).

In this Section, as well as in the discussion (Section 5), for simplicity in guiding our thoughts, we sometimes refer to a single sample, the maximum likelihood of the particular run or mode that we are considering. We use it as a reference point to describe some of the properties of such a portion of the posterior. However, generalizations need to be carefully evaluated since a single sample cannot fully represent the whole range of possibilities spanned by a posterior mode.[20]

4.1. `ST-U`

4.1.1. Reproducing R19 Results

R19 identified the `ST-U` as the simplest model that could represent the original NICER data set of PSR J0030+0451 analyzed in that paper. The derived 68% credible interval for mass and radius, assuming `ST-U`, were, respectively, $1.09^{+0.11}_{-0.07}\,M_\odot$ and $10.44^{+1.10}_{-0.86}$ km. For that inference, the MULTINEST settings adopted to analyze PSR J0030+0451 were: SE 0.3, ET 0.001, LP 1000, MM off (hereafter, we refer to these as the R19 MULTINEST settings for `ST-U`),[21] with the posteriors of the three tested runs, overlapping (see, e.g., the posteriors of run 1 in the left panel of Figure 1). Within this new framework (which, compared to the analyses of R19, incorporates an updated NICER data set—adapted to the most recent NICER instrument response—as well as upgraded software), we therefore perform three identical and independent analyses using the same MULTINEST settings. The obtained posterior distributions for mass, radius, and compactness are reported in the left corner plot of Figure 1. The variability of the results inferred from these three runs suggests that, in contrast to what was reported in R19, in our current analysis framework (including all of the changes previously described), these settings are insufficient to exhaustively explore the parameter space. For this reason, in the same plot, we also report posterior distributions for the SE 0.3, ET 0.1, LP 10^4, MM on, HR run, which we consider effectively representative of the `ST-U` results in this new framework (see Figure 2). Although we notice a slight increase in the inferred median value of mass and radius as well as in the widths of their posteriors, they are in good agreement with the findings of R19. If instead of focusing on inference runs with 10^4 live points, we focus on the results derived here with MULTINEST settings similar to those adopted in R19, the newly inferred radius and mass posterior distributions are narrower and display considerably larger medians (differences in radius can be $\gtrsim$1 km). We consider the LP $= 10^4$ run to be more robust since it explores the parameter space better and is more stable (see indeed the overlap between posteriors with LP $\geqslant 6\times10^3$ reported in Figure 2 and discussed in Section 4.1.2).

The right corner plot of Figure 1 displays the posterior distributions obtained with our default MULTINEST settings (SE 0.3, ET 0.1, LP 10^3, MM off). Not surprisingly, also in this case, where the accuracy requirement over the evidence estimate is lower, the results exhibit some variability. In addition, in the same plot, we report the findings obtained adopting the `ST-U`+$T_{\rm else}$, which includes the possibility that

[17] The XMM-Newton SAS is developed and maintained by the Science Operations Centre at the European Space Astronomy Centre and the Survey Science Centre at the University of Leicester.

[18] When computing compactness as defined in Section 2 we use the equatorial radius $R_{\rm eq}$.

[19] https://getdist.readthedocs.io

[20] In fact, as in V23a, in one instance we use the maximum posterior sample to highlight spread in the parameter space corresponding to a single posterior mode.

[21] One of the three runs was done with MM set to be on and ET 0.1. However, since the results obtained were very similar to the other two runs, we will hereafter neglect it.

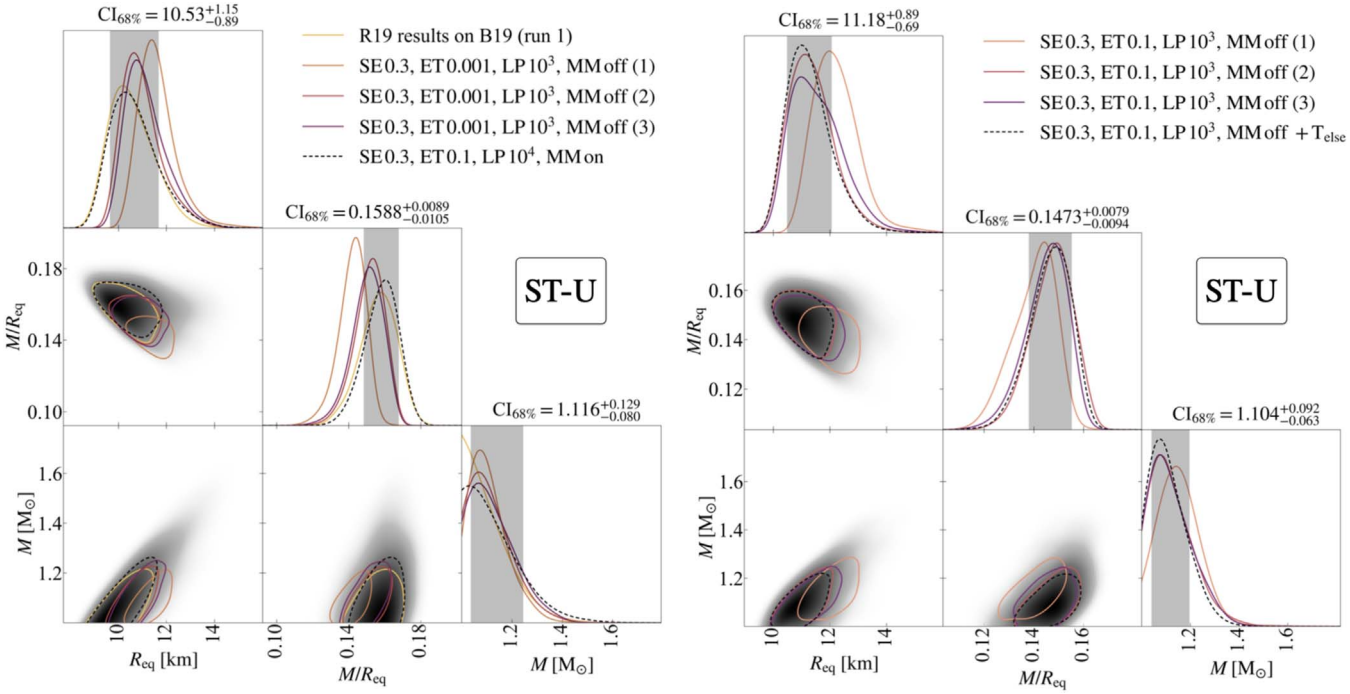

Figure 1. ST−U posterior distributions (smoothed by GetDist KDEs) from nine inference runs, for radius, compactness, and mass. The corner plot on the left shows results for three inference runs with MULTINEST settings identical to those adopted by R19, but obtained in the new X-PSI and data framework described in Sections 2 and 3 (differences listed in Section 5.1). For all of these runs, we adopted the high-resolution X-PSI settings. For comparison, in solid yellow lines we also show the distributions found for run 1, ST−U model, in R19. With the dashed black lines we present posterior distributions for the SE 0.3, ET 0.1, LP 10^4, MM on run, which we consider to be the reference runs for the ST−U model in this work. The corner plot on the right shows the results for three inference runs with our default MULTINEST settings. We also report posterior distributions for the run allowing the whole surface of the MSP to emit (labeled as ST−U+$T_{\rm else}$). Each of the two corner plots shows new posteriors from four inference runs, which use different MULTINEST settings, as reported in the legend (for definitions, see Section 2.1.4). Curves in the representation of the 2D posteriors trace the 68% credible area. On top of the 1D posteriors, we report the 68% credible intervals (representing the area within the 16% and 84% quantiles in the 1D marginalized posterior) starting from the median of the distributions. These values, as well as the colored areas, refer to the two dashed black lines: the run enabling the mode-separation modality, in the left corner plot, and the run adopting the ST−U+$T_{\rm else}$ model, in the right corner plot.

the whole surface of the NS could emit in the NICER sensitivity band. We find that adding this further element in the model produces results consistent with the other inference runs performed with the same settings.

4.1.2. Impact of Analysis Settings

The findings of V23a highlight the importance of MULTINEST settings. For ST−U (computationally the cheapest of our models), we therefore tested the impact of adopting different values of sampling efficiency or evidence tolerance, starting from our default settings (based on the settings adopted for models more complex than ST−U in R19). The inferred posterior distributions are reported in the left corner plot of Figure 2. We report the following: in pink, the results for all three runs with our default settings, and in brown those for the three inference runs, performed with ET 0.001, shown individually in the right and left plot, respectively, of Figure 1.

On the right corner plot, we demonstrate the importance of setting an adequate number of live points to exhaustively cover the model parameter space and derive a stable solution. Again, in pink, we represent parameter estimates for three inference runs adopting our default MULTINEST settings. We then show posterior distributions obtained, respectively, with runs adopting 3k, 6k, and 10k live points, demonstrating the gradual convergence to slightly lower values of radii and larger uncertainties. These results demonstrate that in this setup (and having fixed the sampling efficiency to 0.3 and the evidence tolerance to 0.1) we need a minimum number of live points somewhere in the range (3–6) $\times 10^3$ to guarantee an adequate exploration of the model parameter space.

In both the corner plots, as a reference, we also plot the posterior distributions obtained by the inference run SE 0.3, ET 0.1, LP 10^4, MM on, HR. Adopting the latter as a reference, caveat the low-number statistics, these results hint at the following conclusions:

1. In this new framework, (3×) 10^3 live points are not enough to exhaustively explore the model parameter space;
2. About one in every three runs seems to give a significantly different median value for the radius posterior, both with our default MULTINEST settings and with the variation on the evidence tolerance (ET 0.001);
3. Compared to when we adopt ET 0.001, our default MULTINEST settings (with ET 0.1) seem to lead to a greater variation in the radius and mass medians (but smaller in the compactness); these medians are also in general farther away from the values identified with the reference SE 0.3, ET 0.1, LP 10^4, MM on, HR inference run;
4. However, our default settings seem to also recover wider posteriors compared to their ET 0.001 counterparts; wider posteriors, again compared to the ET 0.001 runs, are also recovered with the ST−U reference run;
5. Changing the value of sampling efficiency does not seem to significantly affect the median value of the posteriors;

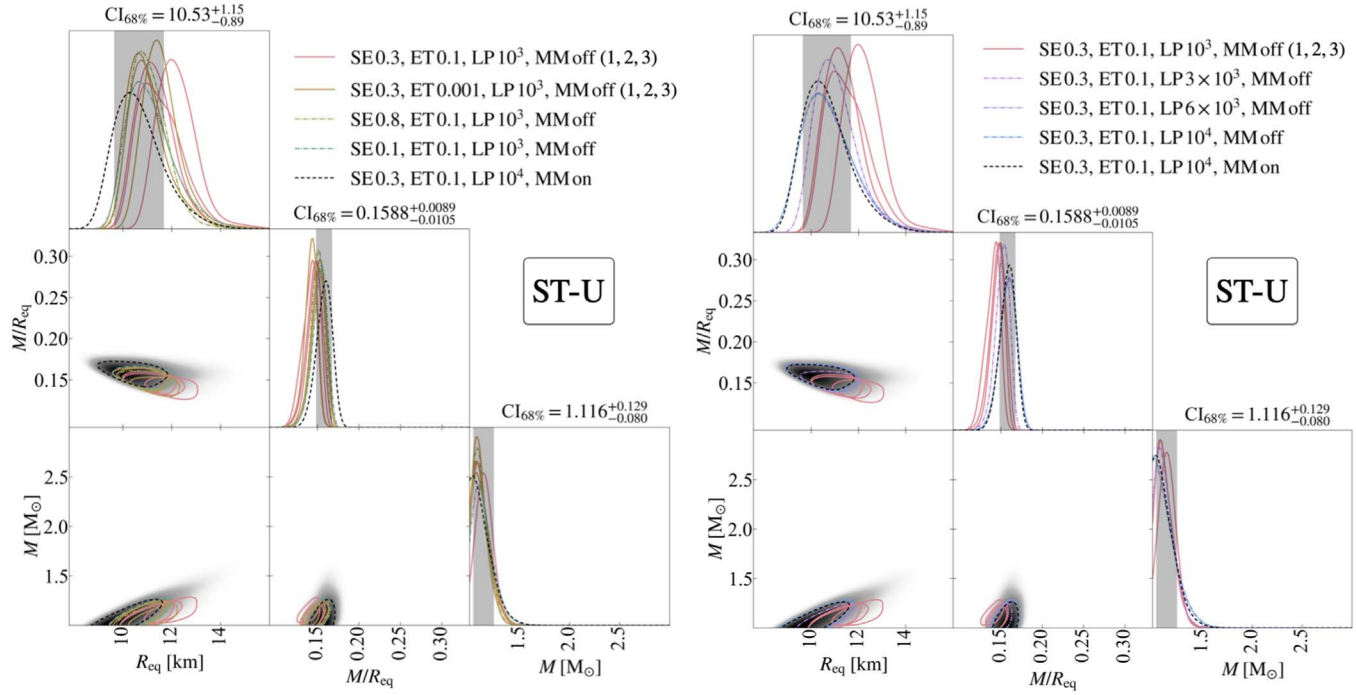

Figure 2. ST−U posterior distributions (smoothed by GetDist KDEs) from 16 runs, for radius, compactness, and mass. This figure highlights the effects of adopting different MULTINEST settings (for all of these runs, we adopted the high-resolution X-PSI settings). On the left plot, we show results for nine ST−U inference runs: they illustrate, for the specific problem at hand, what is the effect of changing evidence tolerance or sampling efficiency, compared to our default settings. The corner plot on the right instead shows the effect of increasing the number of live points. As a reference, in both corner plots, we also report with dashed black lines the posterior distributions obtained with the SE 0.3, ET 0.1, LP 10^4, MM on run; numbers on top of the 1D posteriors, as well as shaded areas, refer to this inference run. See the caption of Figure 1 for further details.

however, when lowering it to 0.1, the widths of the posterior distributions increase, approaching the values obtained if one adopts a higher number of live points; and

6. Given the appearance of a bias toward higher radius values when 10^3 live points are used, multiple runs with this setting seem unlikely to deliver the same result as one would obtain from a single run with a higher number of live points.

4.1.3. Model Exploration

The different mass and radius values obtained for the sequence of nested surface pattern models analyzed in R19 already suggested the presence of multiple modes in the likelihood surface. In this work, we highlight and expand on these findings. We focus here on the posterior distributions obtained with the SE 0.3, ET 0.1, LP 10^4, MM on, HR ST−U inference run. Here we find three modes in the posterior, with considerably different inclinations and hot spot locations (configuration corresponding to the main one reported in panel (A) of Figure 3). Interestingly, they show the same hot spot configuration modes as found in V23a when analyzing with the ST−U model a synthetic data set produced with the ST+PST model (see Figure 8 of V23a for a visual representation). As in that case, the two secondary solutions have similar likelihood and local evidence values, but they perform considerably worse than the main identified mode (the maximum likelihood geometry, for the equivalent run but with MM off, is reported in panel (A) of Figure 3). They also differ considerably from it in inferred mass and radius (means and standard deviations associated with them are reported in Table 5).

From the right corner plot of Figure 2, we can compare the mass, radius, and compactness posterior distributions of this inference run to those obtained adopting the same MULTINEST settings but disabling the mode-separation. When we enable the mode-separation, the posteriors are slightly narrower but otherwise they are very similar to each other: the 68% credible intervals for the PSR J0030+0451 radius, with and without the activation of the mode-separation, are, respectively, $10.53^{+1.15}_{-0.89}$ km and $10.60^{+1.28}_{-0.96}$ km; while for the mass they are $1.12^{+0.13}_{-0.08}\,M_\odot$ and $1.12^{+0.15}_{-0.09}\,M_\odot$. While the latter lets the live points freely and more optimally explore the parameter space, the former, our reference run for ST−U NICER-only analyses, allows us to identify modes in the inferred posterior, even when not visible by eye.

4.1.4. Joint Analysis of NICER and XMM-Newton Data

In the left corner plot of Figure 4, we report the main findings from the joint NICER and XMM-Newton inference analysis. They refer to the SE 0.3, ET 0.1, LP 10^4, MM on, HR run, performed with the setup described in Section 2. The configuration associated with the maximum likelihood sample from its posterior distribution is shown in panel (C) of Figure 3.

The 1D posteriors for mass, radius, and compactness all move to larger values. In particular, the distribution clearly reaches the radius upper boundary of 16 km. Because our analysis is particularly sensitive to the compactness, this radius upper limit is expected to indirectly constrain the mass posterior as well. The plot suggests that the peak of the radius posterior would correspond to even larger radii than allowed by our (physically motivated) prior. There is, however, an elongated tail of the posterior involving considerably lower

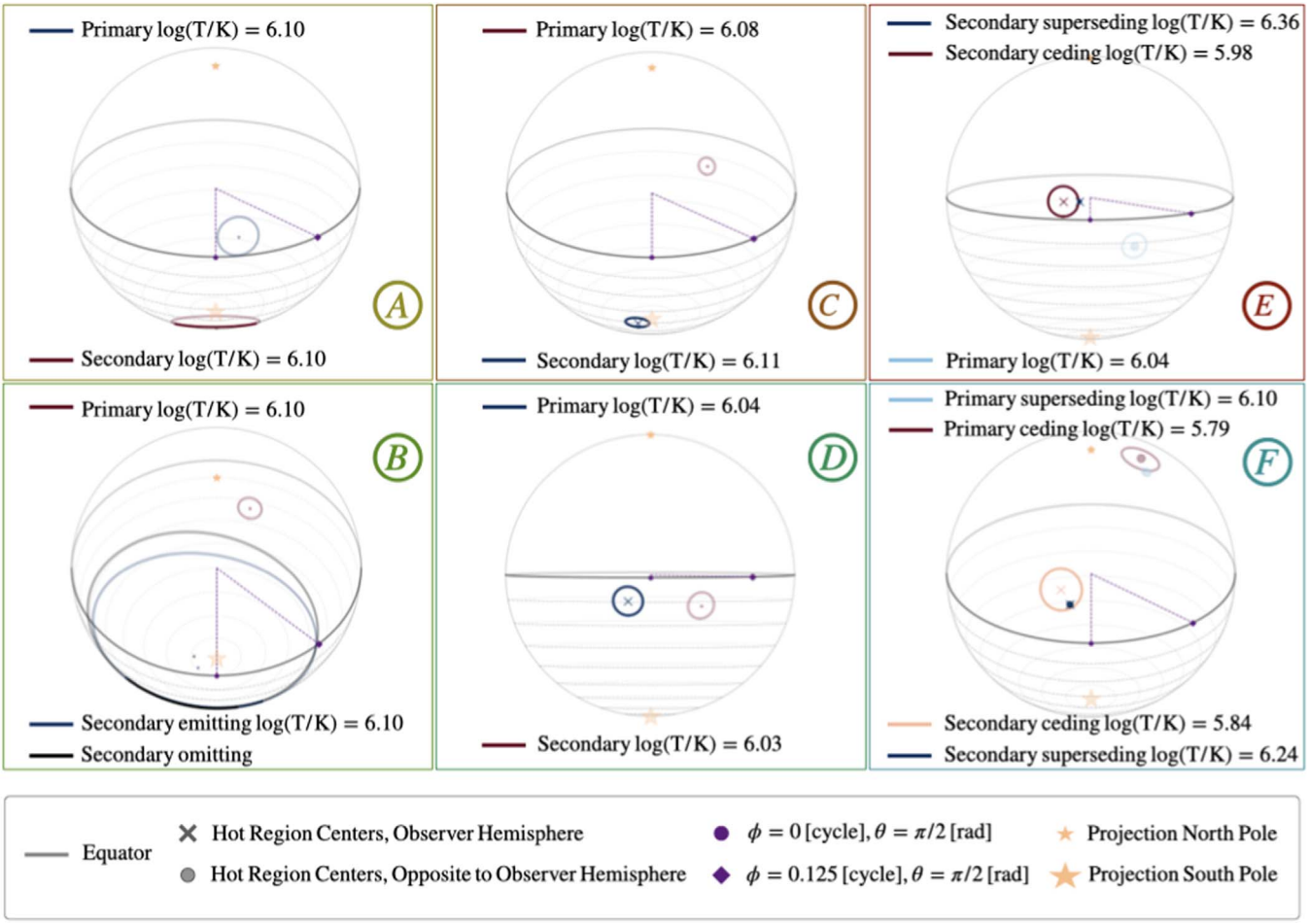

Figure 3. Representation of the main geometrical modes found with the analyses presented in this study. The surface patterns are shown from the observer point of view (i.e., according to the inferred inclination of the specific sample considered), at phase zero of the data. Hot spots on the same (opposite) hemisphere compared to the observer are plotted with full (dimmed) colors and a cross (circular) marker at the center. The color of the hot spot components changes from blue to red from the highest to the lowest temperature of the considered surface pattern (with higher precision compared to the temperature reported in the legend). Black is used for masking components. In all cases, we show, as a reference point, the hot spot geometry associated with the maximum likelihood sample of that specific mode within the considered inference run. Although this single sample cannot capture the whole set of possible variations present in a mode, we hope in this way to provide a simplified but more concrete indication of the configurations belonging to the mode. Panels (A) and (B) refer to the configurations associated with the main mode of `ST-U` (SE 0.3, ET 0.1, LP 10^4, MM off, HR) and `ST+PST` (SE 0.3, ER 0.1, LP 10^4, MM on, LR) models, NICER-only analyses. Panels (C), (D), (E), and (F) refer to the configurations found in joint NICER and XMM-Newton inferences. Panels (C) and (D) are representative of the main (C) and secondary (D) modes derived adopting the `ST-U` model (SE 0.3, ER 0.1, LP 10^4, MM on), while panels (E) and (F) refer to the main mode found with `ST+PDT` and `PDT-U` models (SE 0.8, ER 0.1, LP 10^3, MM off) (for these last two, low-resolution, LR, X-PSI settings have been adopted).

radii. The posteriors belonging to this tail are also characterized by considerably lower masses (see the 2D posterior distribution of mass and radius), in closer agreement with what was found as the main mode when only the NICER data was analyzed. This tail in the radius posterior of the joint NICER and XMM-Newton inference corresponds to the secondary mode found by the sampler, whose configuration is reported in panel (D) of Figure 3. The average and standard deviation of this secondary peak in the posterior, as well as of the main peak, are reported in the last two columns of Table 5. Both modes show a compactness posterior distribution that peaks at considerably higher values compared to the results obtained when only NICER data are analyzed. Including the XMM-Newton data in the inference process limits the contribution of the background (see Figure 5), compared to what is inferred from NICER data alone. To offset the reduction in the unpulsed background, the inferred compactness increases, creating a larger unpulsed signal arising from the star (although with the opposite effect, the same logic was applied to explain the findings from joint NICER and XMM-Newton analyses also in Riley et al. 2021 and Salmi et al. 2022 for PSR J0740+6620). The same trend emerges for both `ST-U` and `ST+PST` models.

The higher radius and compactness values yield lower angular radii describing the two hot spot sizes and allow the hot spot at higher colatitude (closest to the pole) to move slightly closer to the equator. The colatitudes of the hot spots are however not tightly constrained, and this leads to a visible bimodal structure in the posterior of the parameters describing the hot spot properties (see Figure 6). This is due to the ambiguity of the primary and secondary labels associated with the hot spots.[22,23] Since the MSP radius inferred through the

[22] For models that adopt the same complexity to describe both hot spots, we label as primary the hot spot with lower colatitude. This implies that ambiguity on the hot spot associated with a specific label arises if there is a significant posterior mass (see footnote 23) for similar colatitude values for both the hot spots (this chance increases with broader posteriors).

[23] Note that this is not the same as the posterior of the pulsar mass parameter (or the mass posterior).

Table 5
Table Describing the Main Properties of the Three Modes Identified Adopting the ST-U Model

	NICER			NICER & XMM	
	Mode 1	Mode 2	Mode 3	Mode 1	Mode 2
R_{eq} [km]	10.7 ± 1.0	15.5 ± 0.4	15.5 ± 0.4	14.9 ± 1.0	11.4 ± 1.1
M [$M_\odot$]	1.1 ± 0.1	1.6 ± 0.1	1.6 ± 0.1	1.9 ± 0.2	1.4 ± 0.2
max (log ($\mathcal{L}$))	−35735	−35758	−35757	−42661	−42666
log ($\mathcal{E}$)	−35788	−35810	−35808	−42714	−42718
Configuration	Panel (A), Figure 3	Middle panel of Figure 8, V23a	Rightmost panel of Figure 8, V23a	Panel (C), Figure 3	Panel (D), Figure 3

Note. The first two rows show means and standard deviations of mass M and equatorial radius R_{eq} posterior distributions; the last two show the corresponding maximum log-likelihood and local log-evidence values.

secondary mode peaks at values only marginally larger than the one found with NICER-only data, the hot spots' angular radii still decrease, but not as much as for the main posterior mode (see Figure 6). The configurations arising from the main mode of the joint NICER and XMM-Newton inference show temperatures and inclination that are very similar to those found in the main mode when analyzing NICER-only data. This is not the case for the secondary mode, which points to a more edge-on configuration, with the cosine of inclination compatible with zero. In this new setting, hot spots are located close to the equator and characterized by significantly lower temperatures.

4.1.5. Analysis of XMM-Newton Data Only

The XMM-Newton data of PSR J0030+0451 was first analyzed in Bogdanov & Grindlay (2009) in an attempt to extract information about the NS radius. In this analysis, which employed a frequentist approach, a fixed mass of $M = 1.4\,M_\odot$ was assumed and just R was allowed to vary. Only two circular hot spots were considered with a configuration equivalent to the ST-U model. In addition, the pulse profile obtained from the XMM-Newton EPIC pn (used in Bogdanov & Grindlay 2009, but not in this work; see Section 3.2) instrument was fit in only two broad energy bands (0.3–0.7 keV and 0.7–2 keV). Due to the limited photon statistics of the XMM-Newton data, this analysis resulted in only a lower limit on the neutron star radius of $R > 10.7$ km (95% confidence) and very broad constraints on the spot locations and geometry, which are generally consistent with the configurations reported in panels (C) and (D) of Figure 3.

Using the pipeline and procedures outlined in this paper, analysis of only the XMM-Newton data yields only very weakly constrained hot spot properties and 68% credible intervals of $R_{eq} = 11.3 \pm 2.5$ km and mass $M = 1.6^{+0.4}_{-0.3}\,M_\odot$. These are broader than the values quoted in Bogdanov & Grindlay (2009), likely because some of the assumptions have been relaxed and no timing information has been used. They are also much wider than the posterior distributions derived from NICER data, as expected due to the much smaller XMM-Newton exposure time, effective area, time, and energy resolution.

4.2. ST+PST

4.2.1. Reproducing R19 Results and Analyzing the Impact of Settings

For ST+PST, R19 reported credible intervals for mass and radius, respectively, of $1.34^{+0.15}_{-0.16}\,M_\odot$ and $12.71^{+1.14}_{-1.19}$ km. These results were obtained from a run adopting the following MULTINEST settings: SE 0.3 (0.8), ET 0.1, LP 10^3, MM off, where the sampling efficiency was increased to 0.8 when resuming the analysis. In Figure 7, we report posterior distributions derived analyzing B19v006 with the ST+PST model in the new inference framework (see Section 2 for more details). The green lines on the left corner plot show results for the runs that match as much as possible the analysis settings adopted in R19. We notice that there is some scatter among these posterior distributions. In particular the major outlier only finds the secondary mode of the posterior surface (see Sections 4.2.2 and 5 for context and discussion over its multimodality); this resembles the mode found for ST-U and is therefore characterized by smaller radii and masses. The other two runs still present some scatter, suggesting that these MULTINEST settings are now (given the various changes to channel choices, instrument response, etc. compared to R19) inadequate to explore the model parameter space. Compared to the credible intervals presented in R19, the new posteriors show slightly higher values (likely due to the difference in channels, as the same trend was found in preliminary analyses and attributed for the ST-U model to the removal of data in channels 25–30) and similar uncertainties. The only HR run with SE 0.3-only is the inference run, which identifies, as its main mode, the secondary (ST-U-like) mode (1D and 2D posteriors for mass, radius, and compactness are represented in Figure 7 by the green outlier); the computational cost of this analysis was three to four times the cost of the two other HR runs.

The same corner plot also shows the effect of lowering the resolution of X-PSI settings; the green curves show the only posteriors obtained with high resolution for models more complex than ST-U. The yellow lines represent distributions, derived with low resolution but with the other settings directly comparable to those obtained with high resolution. Note that the two outliers are produced with the same fixed MULTINEST and Python seeds. Excluding the outlier (which is again connected to the identification of the secondary mode), the low-resolution runs seem to converge to slightly more stable solutions located at slightly smaller radii and masses and are characterized by marginally larger posteriors, when the mode favored by the evidence[24] is identified (see Section 4.2.2). The

[24] I.e., the mode identified with more adequate MULTINEST settings. That mode is indeed clearly significantly contributing to the estimation of the evidence, as when identified the evidence significantly increases.

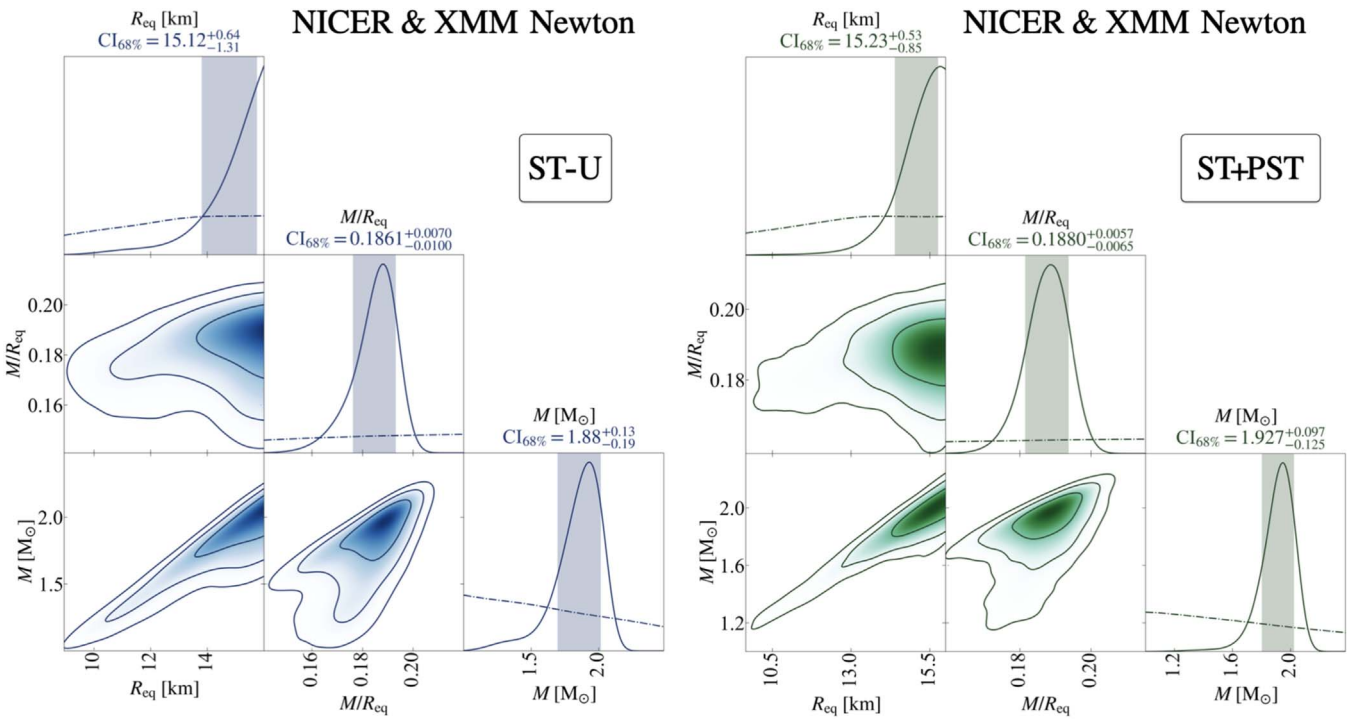

Figure 4. Posterior distributions (smoothed by GetDist KDEs) of radius, compactness, and mass from joint NICER and XMM-Newton inference runs: left and right corner plots, respectively, obtained adopting the ST−U and the ST+PST model. With the dashed lines here we show the prior distributions. In the 2D posteriors, we plot three curves, defining the 68%, 95%, and 99% credible area. Analyses settings for the depicted runs are displayed in Table 4 (see ST−U and ST+PST entries with "yes" in the XMM-Newton column). See caption of Figure 1 for further details.

behavior is different when only the secondary mode is explored by the sampler; comparing the two outliers in the 1D radius plot, indeed, the high-resolution run produces much narrower posteriors, peaking at significantly lower values. We use also low resolution for our new reference ST+PST run, obtained increasing the number of live points to 10^4 and enabling the mode-separation option of MULTINEST. We report the corresponding posterior with a black dashed line in the same left corner plot of Figure 7. Compared to the results found with the other low-resolution runs (where the number of MULTINEST live points was 10^3), these distributions slightly widen and move toward lower values of mass and radius. Similar widening of the posteriors, with increasing number of MULTINEST live points, was also found in Riley et al. (2021) for PSR J0740+6620 and could indicate a broader true posterior distribution. The 68% credible intervals of mass and radius derived from our new reference inference are: $1.37 \pm 0.17\ M_\odot$ and 13.11 ± 1.30 km (as reported on top of the 1D posteriors in the left corner plot of Figure 7), largely in agreement with the findings of R19. The hot spot configuration corresponding to the maximum likelihood sample of this analysis is reported in panel (B) of Figure 3. Our current tests do not guarantee that these analysis settings are sufficient to adequately explore the model parameter space.

In the right corner plot of Figure 7, we show posterior distributions derived from each of the low-resolution runs, reported with yellow lines in the left panel. We also report in ocher the posterior identified by Riley et al. (2019) for the ST+PST model. The outlier, depicted in the right corner plot with blue lines, is found by a replica of an inference run with our default MULTINEST settings. Hence the different results can be attributed solely to the randomness present in the sampling process. The occurrence of such outlier, however, suggests that the number of live points chosen for these inferences is not sufficient to effectively explore the model parameter space. The black dashed curves represent the results obtained when introducing the elsewhere temperature to the ST+PST model and are presented in more detail in Section 4.2.2.

The other three inference runs show posterior distributions almost perfectly overlapping, despite the differences in MULTINEST settings (the yellow lines show the results obtained enabling the mode-separation option) and in the prior (the green curves outline distributions derived from runs adopting the updated ST+PST CoH prior). With this plot and the associated inference runs, we demonstrate that, in analyzing the NICER data B19v006, introducing the updated ST+PST CoH prior leads to no significant difference in the inferred posterior distributions and evidence estimation. We can draw the same conclusion for the effect of adopting the mode-separation MULTINEST option, even though limited to the specific case here considered.

4.2.2. Model Exploration

Our mode-separation inference runs highlight the multimodal structure present in the posterior surface of this specific model, given the chosen B19v006 data set (although we expect all PSR J0030+0451 NICER data sets to exhibit similar behavior). As briefly mentioned in the previous Section, there are two prominent modes in the posterior, which differ in local log-evidence by a factor of ∼5.5. The maximum likelihood samples belonging to the two modes actually differ by a much larger value (>10 in log-likelihood), from which we can deduce that the prior space supporting the secondary mode is considerably larger than that supporting the main mode. This also explains why a relatively low number of live points can

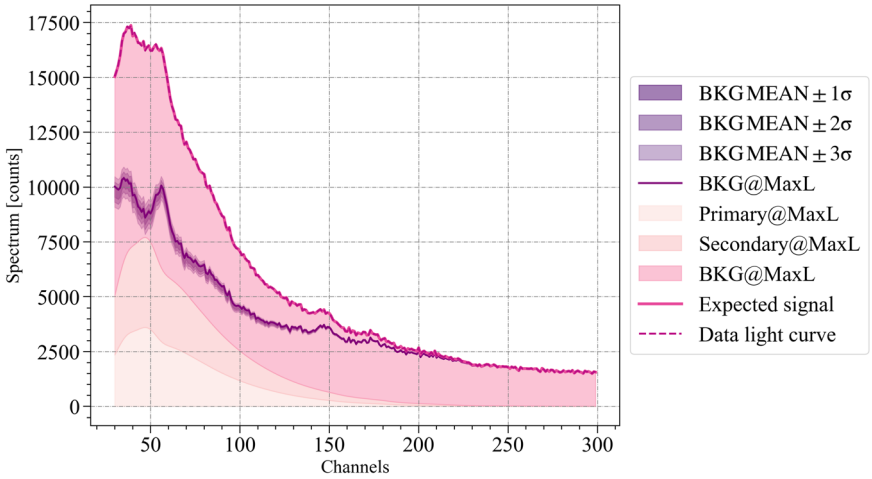

Figure 5. Spectrum of NICER data and its inferred composition, according to the maximum likelihood sample of our X-PSI analysis. Data are plotted with a dashed magenta line; the total signal expected is shown with a solid pink line; the background (BKG) that maximizes the likelihood for the (background-maginalized) maximum likelihood posterior sample (MaxL, in the legend) is plotted with a purple solid line. The contribution of the primary hot spot, the secondary hot spot, and the background, again associated with the maximum likelihood sample, are reported on top of each other with pink-shaded regions, increasingly more intensely colored. The purple shades show from darker to lighter color the average background ±1, 2, or 3 standard deviations, calculated over 200 randomly selected posterior samples from the equal weight MULTINEST output file. The inference runs for this figure concern the joint NICER and XMM-Newton analysis, performed with the X-PSI `PDT-U` model. The complete figure set (8 images) is available, for the `ST-U`, `ST+PST`, `ST+PDT`, and `PDT-U` models for both NICER-only analyses (reference runs highlighted in bold in Table 4) and joint inferences for NICER and XMM-Newton data sets (analysis settings reported in Table 4, corresponding to "yes" entries in the XMM-Newton column).

(The complete figure set (8 images) is available.)

result in the identification of the secondary mode as the main one. An illustrative hot spot geometry associated with the main mode is rendered, taking as example the maximum likelihood sample, in panel (B) of Figure 3. The secondary mode resembles, also in the inferred background, the main mode identified with the `ST-U` model and reported in panel (A) of the same Figure. The omitting component is always associated with the smaller, closer-to-the-equator, hot spot (labeled as primary in panel (A) of Figure 3). The location and size of the masking element can vary significantly within the identified mode. Analyzing the SE 0.3, ET 0.1, LP 10^3, MM off, LR run that missed the main mode, but found this secondary one (whose mass, compactness, and radius posterior are represented with blue lines in the right corner plot of Figure 7), we notice that, while the maximum likelihood sample of this run depicts the primary as a ring, the maximum posterior sample represents it as an almost circular hot spot, where the omitting component barely touches the emitting one. This spread in the `PST` hot spot characteristics suggests, as found in V23a, that we are only very weakly sensitive to the small details of the hot spot shapes. In this case, it seems that we are mostly sensitive to the location and the overall emitting area of the `PST` hot spot: there is indeed a clear correlation between the size of the masking spherical cap and its distance from the center of the emitting one.

Both primary and secondary modes deliver a very similar inferred background (see Figure 13 of V23a, for a comparison between the background associated with `ST+PST` and `ST-U` main solutions) and compactness values, despite the differences in the inferred mass and radius (comparable compactness values are also deduced with our reference `ST-U` analysis). In other aspects these two solutions are quite different from each other. In particular the difference in the inferred observer inclination, estimated by the two modes, yields changes in the hot spot location and sizes, such that they are still observable at the right phases (a more detailed discussion on the effect of different inclinations can be found in Section 5.2.1 of V23a). These considerations highlight the presence of significant, and sometimes nontrivial, degeneracies in our model parameter spaces.

In the right plot of Figure 7, we show the effect of allowing the rest of the surface of the star (the part not covered by the two hot spots) to emit blackbody radiation characterized by a finite, homogeneous temperature (`ST+PST`+$T_{\rm else}$). This inference also uses the updated CoH prior, however, as mentioned above, we do not expect this choice to have a significant impact on the final results. The credible intervals on top of the 1D plots refer to the results of this inference. The configuration found for this model, with these MULTINEST and X-PSI settings, resembles that obtained with the `ST-U` model and represented, for the maximum likelihood sample of that inference run, in panel (A) of Figure 3. The mask is again associated with the hot spot being closer to the equator (labeled as primary in panel (A)) and changes its shape to rings and crescents (both maximum likelihood and posterior exhibit ring-like shapes for this secondary hot spot).

Allowing all of the surface of the MSP to emit introduces more uncertainty on the background and increases uncertainty on the inferred compactness. We find an almost flat posterior support for elsewhere temperatures below $\sim 10^{5.6}$ K, likely due to the negligible contribution of blackbody radiation of such low temperatures within NICER band (for comparison, the temperatures of the two emitting components are $T_{\rm p} \sim T_{\rm s} \sim 10^{6.1}$ K). This additional component can explain part of the unpulsed emission that is otherwise mostly attributed to the background and to higher compactness values (Riley et al. 2021; Salmi et al. 2022). This degeneracy between these three modeled components ($T_{\rm else}$, background, and compactness), and between $T_{\rm else}$ and the hydrogen column density (whose 68% credible interval has indeed increased and widened,

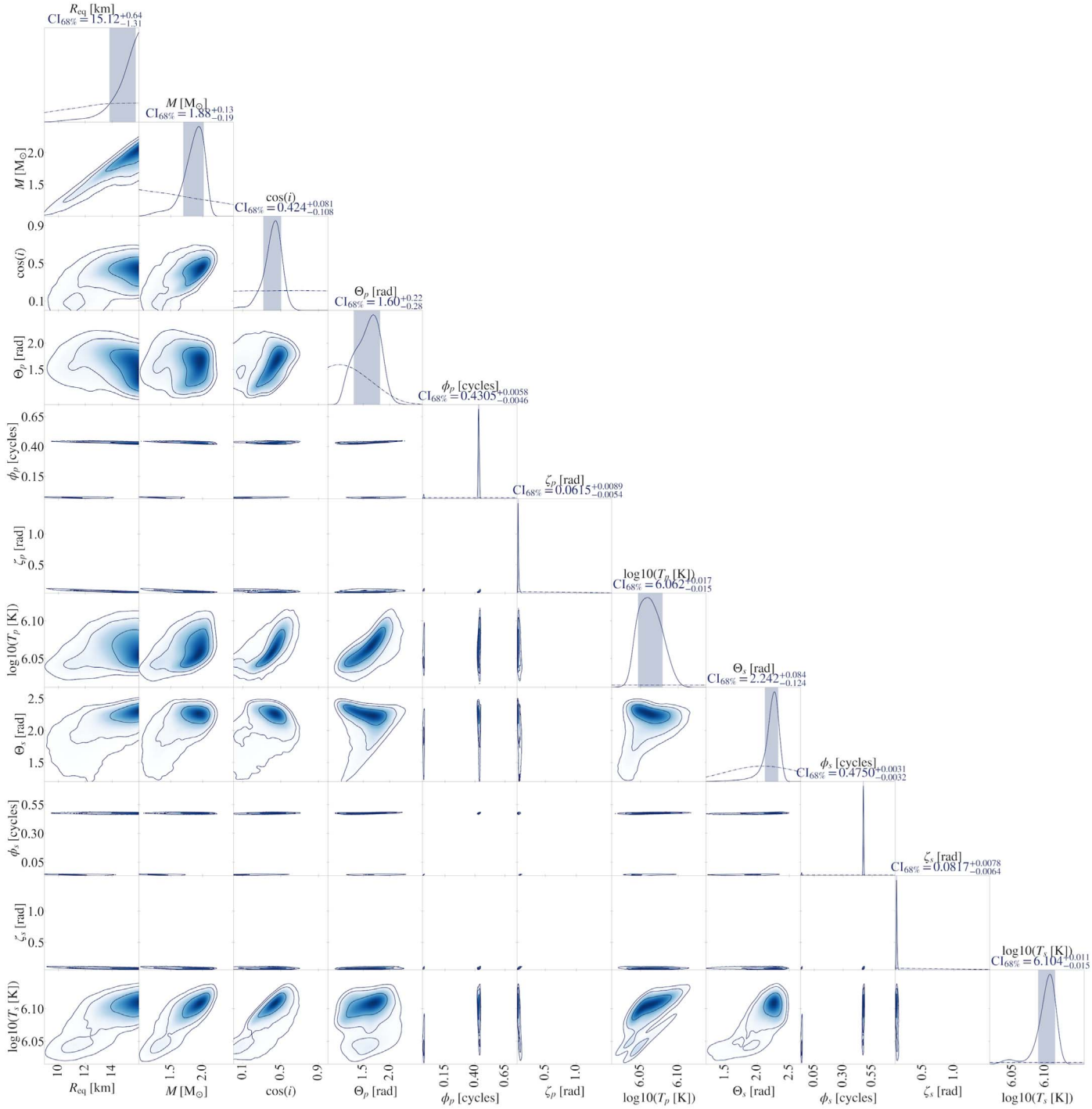

Figure 6. Corner plot based on the joint analysis of NICER and XMM-Newton data sets, carried out with the ST−U model. This image includes the posterior distributions (smoothed by GetDist KDEs) for the parameters describing mass, radius, and the hot spot properties inferred for PSR J0030+0451's system. In the marginalized 1D posteriors, we show with dashed lines our corresponding priors. The complete figure set (8 images) is available, for the ST−U, ST+PST, ST+PDT, PDT−U models for both NICER-only analyses (reference runs highlighted in bold in Table 4) and joint inferences for NICER and XMM-Newton data sets (analysis settings reported in Table 4, corresponding to "yes" entries in the XMM-Newton column). Tables 1 and 2 show the meaning of the adopted parameter labels. The multimodal structure of the posterior, described in Section 4.1.4, is clearly visible here. In particular the bimodality in the 2D posteriors, including the radius, shows the main mode (configuration corresponding to its maximum likelihood sample shown in panel (C) of Figure 3) and a secondary one (configuration corresponding to its maximum likelihood sample shown in panel (D) of Figure 3). For more general details about the plots in this figure set, see Figure 1.

(The complete figure set (8 images) is available.)

compared to the runs without $T_{\rm else}$ that identified as main mode the ST−U-like mode), generates the aforementioned uncertainties, which are, e.g., visible comparing the blue with the black dashed lines in the right corner plot of Figure 7. The slight cut in high compactness values, in combination with the increased uncertainties, yields a posterior that peaks at larger radii (compared to the other runs, which identified the ST−U like mode as the main mode). Overall, the most prominent change

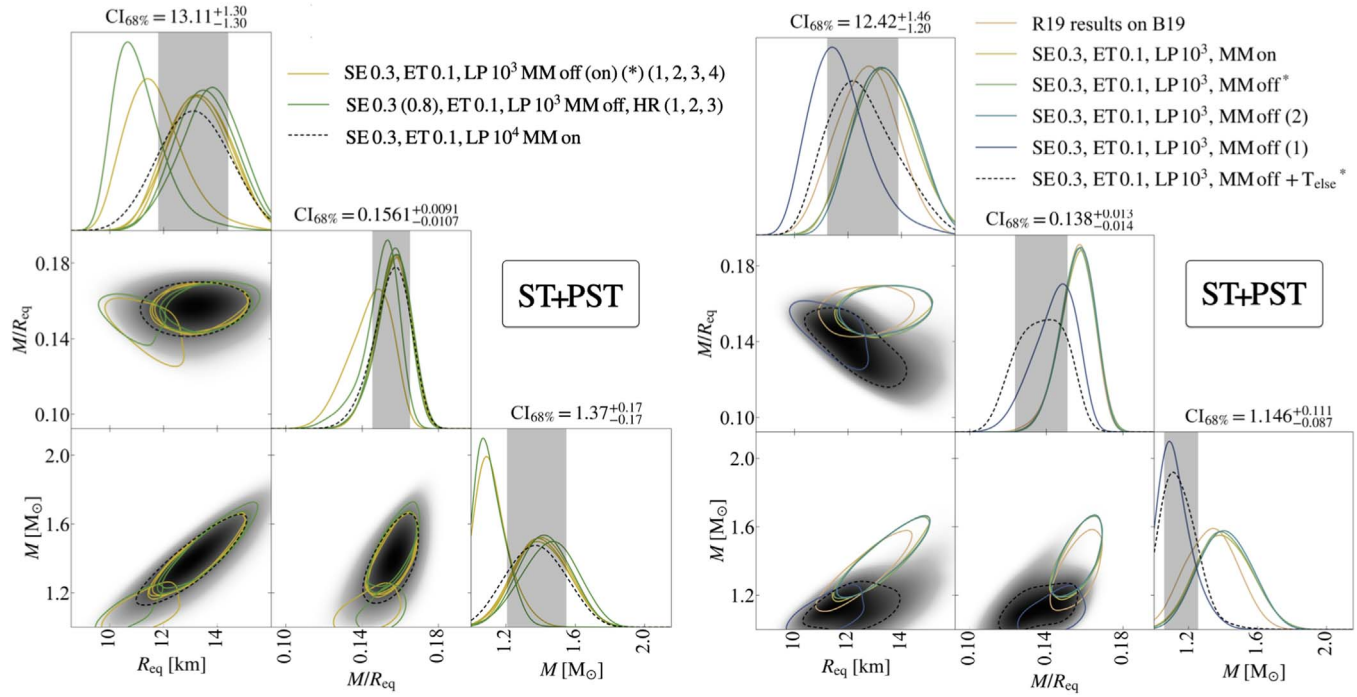

Figure 7. ST+PST posterior distributions (smoothed by GetDist KDEs) from 14 runs, for radius, compactness, and mass. This figure highlights the effects of adopting different MULTINEST settings. The corner plot on the left shows the effect of adopting different (low or high) X-PSI resolution settings. The green curves represent the posterior distributions inferred from the analyses that adopt high resolution (HR in the legend); the yellow ones are derived from low X-PSI resolution setting (our default for models more complex than ST−U). These latter have slightly different MULTINEST settings, as marked with settings in parentheses, but show very similar behaviors and are individually plotted on the right panel. The two outliers (one at HR, green, and one at LR, yellow) have been obtained fixing MULTINEST and Python random seeds to the same values. With black dash lines, we also report the posterior distributions obtained with the SE 0.3, ET 0.1, LP 10^4, MM on run; numbers on top of the 1D posteriors, as well as shaded areas refer to this inference. On the right panel, instead, we show new results for five ST+PST inference runs, with low X-PSI resolution, adopting our default MULTINEST settings, the only exception being the second run from the top of the list, for which we enabled the mode-separation. Similar MULTINEST settings have also been adopted in R19 (although higher X-PSI settings were, in that case, used). The ST+PST posteriors found in R19 are here shown in brown for comparison. This plot tests the following: the variability due to the randomness of the sampling process, given the specific analysis settings; the effect of updating the model prior, to allow the primary hot spot to overlap with the masked part of the secondary (CoH, runs marked in the legend with *); and the effect of introducing emission from all of the MSP surface (see run including T_{else} in the legend). The black dashed lines represent the posterior distributions obtained when allowing the entire surface of the MSP to emit. Shaded areas and numbers on top of the 1D posterior distribution refer to the credible regions and intervals of this inference. See the caption of Figure 1 for further details. *: runs adopting the updated CoH ST+PST prior, as explained in Section 2.3.4 of V23a.

generated by the elsewhere temperature is the broadening of the posteriors (in addition to doubling the computational time).

4.2.3. Joint Analysis of NICER and XMM-Newton Data

We report the mass, compactness, and radius posterior distributions obtained adopting the ST+PST model in a joint NICER and XMM-Newton inference analysis in the right corner plot of Figure 4. These results were obtained by a SE 0.8, ET 0.1, LP 10^3, MM off, LR run in terms of X-PSI settings.

As is immediately clear, comparing the two corner plots of Figure 4, this ST+PST inference run leads to radius, compactness, and mass posterior distributions very similar to those derived with the ST−U model. The radius posterior is again truncated close to its peak by our prior cut at 16 km. This impacts the inferred mass distribution, which appears to be then driven by constraints on the compactness. The similarities are not confined to these parameters; indeed, the inferred hot spot geometries are also almost identical (as can be seen in Figure 6), and therefore resemble the configuration depicted in panel (C) of Figure 3. As shown in panel (C), both hot spots have small sizes and similar temperatures. Small sizes lead to (type I, as explained in R19) degeneracies, when we assume complex hot spot geometries (i.e., when the hot spot is described by two components, as it is the case for our PST hot spot). In practice, the inferred small sizes of the hot spots imply a small sensitivity to their shape. Therefore, this yields weak constraints on the omitting component, which, given the similarities between the two hot spots, can be assigned to either of them. Since in this case we define the PST hot spot as secondary, this ambiguity gives rise once again to visible bimodality in the posterior distributions of the parameters describing the properties of the two hot spots (see, again, Figure 6).

As described in Section 4.1.4, to jointly explain both the phase-resolved NICER data and the XMM-Newton data, it is necessary to increase the contribution of PSR J0030+0451 to the total counts. An increase of the unpulsed emission from the MSP can be produced by higher compactness values, as inferred here.

The similarities in the mass and radius posteriors with those obtained with the ST−U model extend to the tails of these distributions. They thus hint at the presence of a secondary mode, again characterized by lower radius and mass values (respectively, ∼11 km, and $\sim 1.4\,M_\odot$). The samples belonging to these tails display again (see panel (D) of Figure 3, for a qualitative representation) higher inclination, with both hot spots increasing slightly in size and migrating toward the equator, compared to the main mode. Also in this case, we find configurations in which the location of the ST and PST hot spots alternate. Depending on the size of the omitting component (which is not well constrained), the emitting region masked by it may slightly increase its size, to compensate for

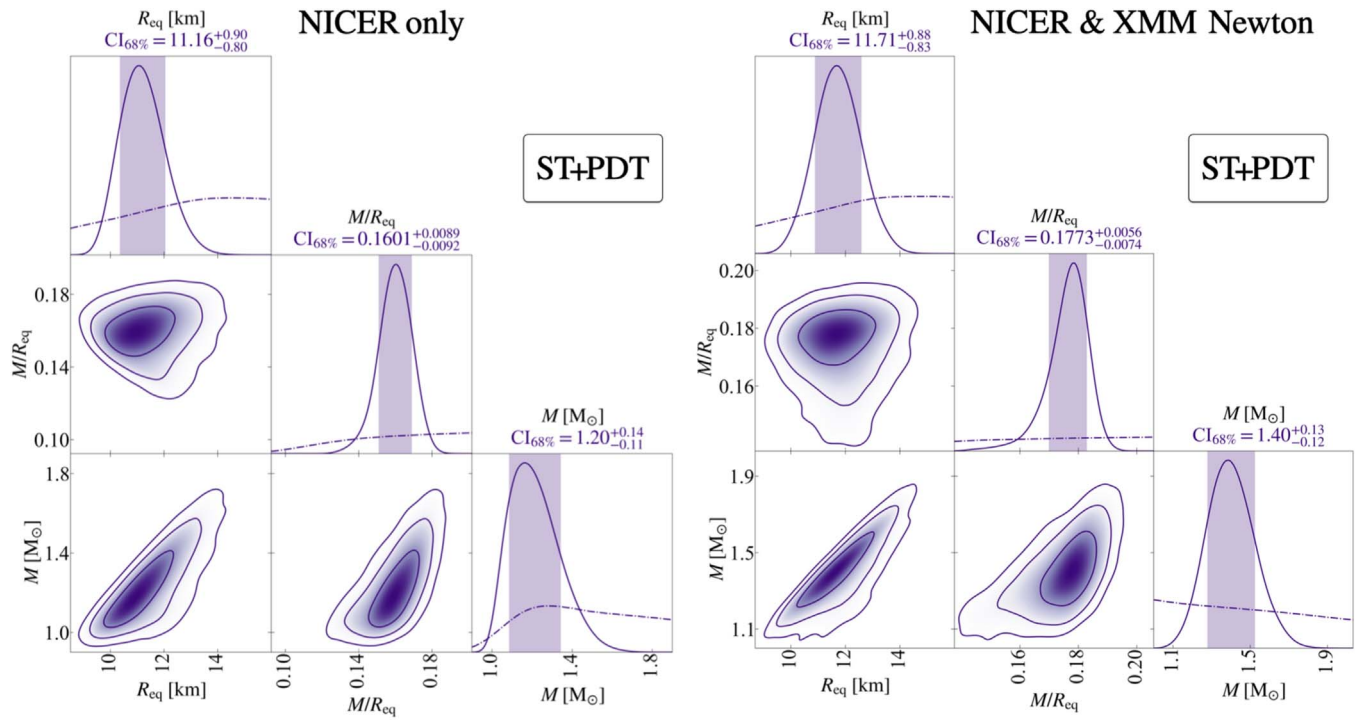

Figure 8. ST+PDT posterior distributions (smoothed by GetDist KDEs) of radius, compactness, and mass for two inference runs. We show results obtained with the analysis of NICER-only data (left), and derived by the joint analysis of NICER and XMM-Newton data (right). For more details about the plot, see Figure 4.

the otherwise decreased emission. This spread over the possible properties of the omitting region highlights again our weak sensitivity to the details of hot spot shapes.

4.3. ST+PDT

4.3.1. Model Exploration

In Figure 8, we show the posterior distributions inferred for mass, radius, and compactness, adopting the ST+PDT model (a more complex model than the ST+PST model used for the headline result in R19, which was not explored in that paper). The left corner plot refers to the results derived with the SE 0.8, ET 0.1, LP 10^4, MM on, LR run, analyzing only the B19v006 NICER data set. The inferred 68% credible intervals for mass and radius are $1.20^{+0.14}_{-0.11}\,M_\odot$ and $11.16^{+0.90}_{-0.80}$ km. This model therefore identifies quite a narrow peak in radius. The associated hot spot configuration and temperatures resemble the one reported in panel (E) of Figure 3. The bulk of the inferred posteriors describe hot spot patterns, mass, and radii similar to those identified as secondary mode in the joint analysis of NICER and XMM-Newton data sets with the ST−U model.[25] We find considerable differences, however, in the two temperatures associated with the PDT hot spot, compared to the temperatures associated with ST emitting regions derived with the combined NICER and XMM-Newton analyses. Similar emission to the $\log_{10}(T_s/\mathrm{K}) \sim 6$ ST hot spot in the ST−U model is often modeled here, as a PDT hot spot, with one component slightly colder ($\sim 10^{5.9-6.0}$ K) and larger and one tiny but very hot ($\sim 10^{6.3-6.4}$ K). The peak of the posterior identifies the ceding region with the small hot spherical cap; however, there is some posterior mass that also associates it with the cold and more extended component. This bimodality is also visible, in the 95% credible area contours, in the 2D posterior distributions of the parameters describing the properties of the secondary hot spot (see Figure set 6). Unlike the results derived from the ST−U and ST+PST models in joint NICER and XMM-Newton analyses, the posterior distributions identified with ST+PDT show no bimodality generated by label ambiguity. This means that there is a significant preference for the location of the PDT hot spot; i.e., the data are better represented if one specific emitting region (the first visible, in our representation of the data; see Figure 9) is described by two components with different temperatures.

With the SE 0.8, ET 0.1, LP 10^4, MM on, LR run, we also find a secondary mode. This mode shows a maximum likelihood that differs from that of the main mode by ∼4 in log. The differences in local evidences are slightly larger, ∼6 in log. The secondary mode identifies configurations resembling (with some variation) the main mode identified with the ST−U model when analyzing NICER-only data. In this case, the dual temperature hot spot may be associated with either of the two emitting regions. The temperature of the superseding component of the PDT hot spot remains of the same order as that found with the ST−U model $\log_{10}(T_s/\mathrm{K}) \sim 6.1$ and is similar to the temperature associated with the ST hot spot. The ceding component is considerably colder $\log_{10}(T_{c,s}/\mathrm{K}) \sim 5.2 - 5.6$. The resemblance to the ST−U NICER-only case also includes the mass and radius posteriors, which cluster around $\sim 1.1\,M_\odot$ and ∼10.5 km, slightly lower than the values for the ST+PDT main mode.

In Section 5.4, we will elaborate on the adequacy of the coverage of the model parameter space during the inference analyses presented in this Section.

4.3.2. Joint Analysis of NICER and XMM-Newton Data

The effect of introducing XMM-Newton data into the inference process, when adopting the ST+PDT model, is

[25] Note that the ST+PST model also shows similar posterior samples in its tails, suggesting the presence of a secondary mode.

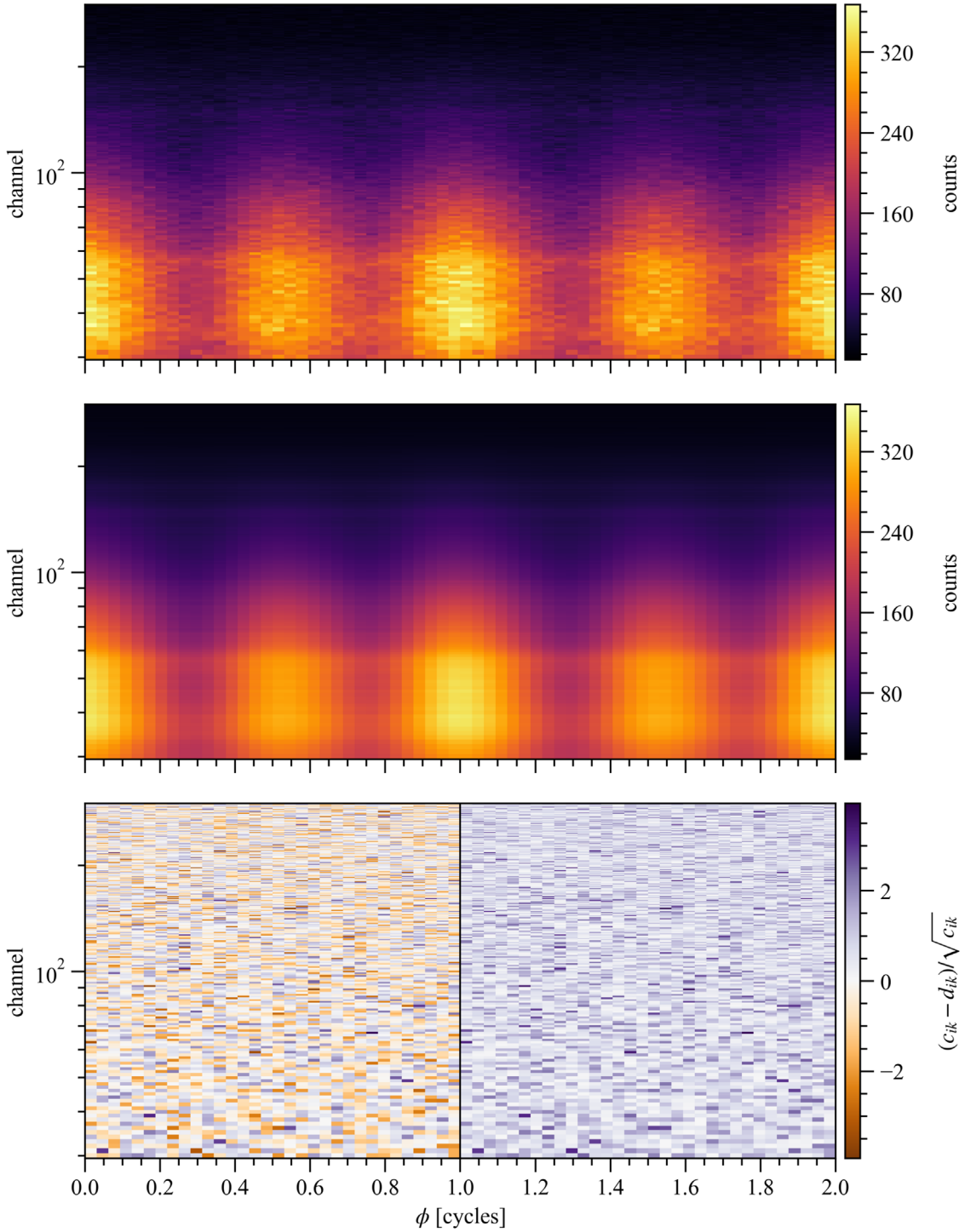

Figure 9. The three panels represent from top to bottom: data counts, posterior counts expected for the PDT-U model, and residuals as a function of cycle phase (on the x-axis) and NICER instrument channel (on the y-axis). Residuals are defined as the difference in counts between data and expectations, weighted by the corresponding Poisson standard deviation (as expressed on the associated color axis): d_{ij} are count data for the ith phase bin and j^{th} channel, c_{ij} the corresponding posterior-expected count numbers. Expected counts are evaluated considering 200 posterior samples, inferred jointly analyzing NICER and XMM-Newton data. More details about this Figure can be found in the caption of Figure 13 and in R19. The complete figure set (8 images) is available, for the ST-U, ST+PST, ST+PDT, and PDT-U models for both NICER-only analyses (reference runs highlighted in bold in Table 4) and joint inferences for NICER and XMM-Newton data sets (analysis settings reported in Table 4, corresponding to "yes" entries in the XMM-Newton column).

(The complete figure set (8 images) is available.)

shown in the right corner plot of Figure 8. The reported posterior distributions were derived from an SE 0.8, ET 0.1, LP 10^3, MM off, LR run. In panel (E) of Figure 3, we show the hot spot geometry of the identified maximum likelihood sample.

For the first time, coherently adding the XMM-Newton data set in the inference process does not yield solutions that are visibly different from those obtained analyzing only NICER data. As with other models, the introduction of the XMM-Newton data

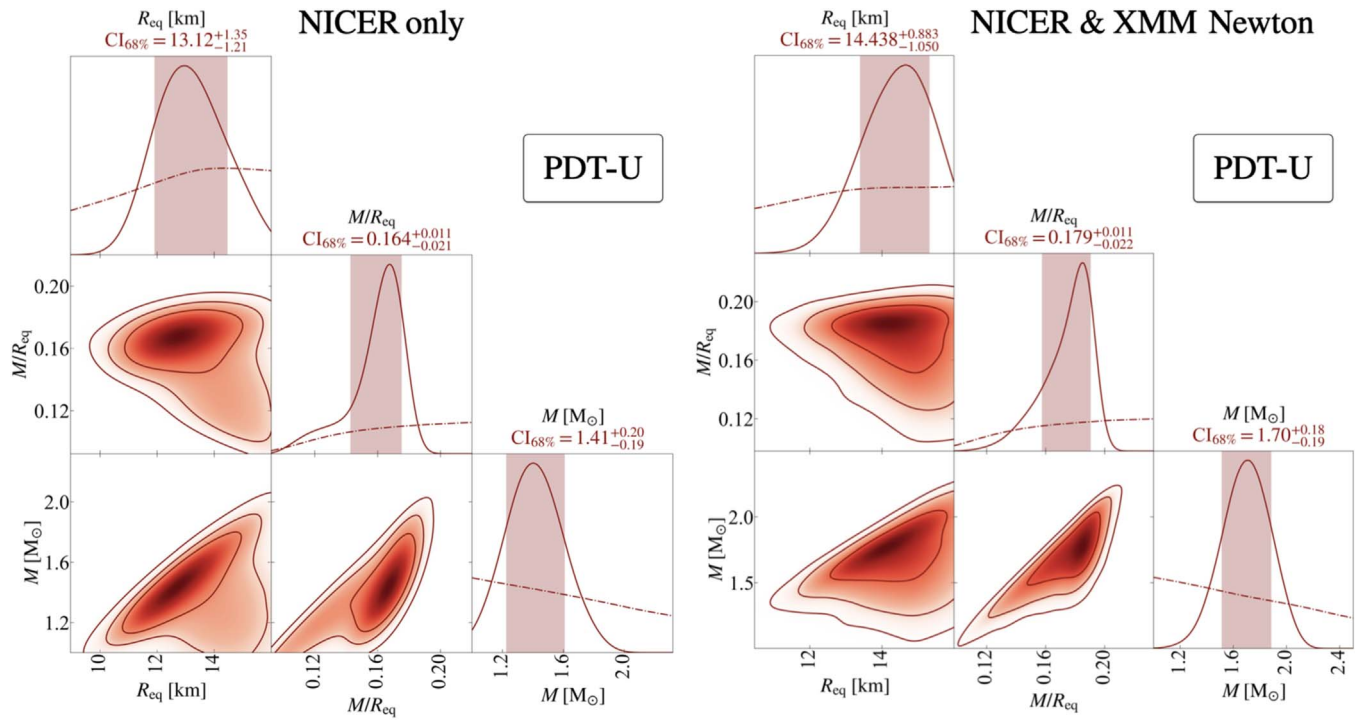

Figure 10. PDT−U posterior distributions (smoothed by GetDist KDEs) of radius, compactness, and mass for two inference runs. We show results obtained with analysis of NICER-only data (left) and derived by the joint analysis of NICER and XMM-Newton data (right). For more details about the plot, see Figure 4.

constrains the background to slightly lower values than otherwise inferred. In this case, we also see an increase in the compactness, although the difference is significantly smaller when compared to the other models. The properties of the pulsed emission are then recovered by increasing both mass (whose 68% credible interval is now $1.40^{+0.13}_{-0.12}\,M_\odot$) and radius (whose 68% credible interval is now $11.71^{+0.88}_{-0.83}$ km). Indeed for both of these parameters the posterior mass at higher values has considerably increased, while the posterior volume for the lowest values has significantly reduced, compared to analysis of the NICER-only data.

Looking at the posterior distributions of the hot spot parameters (see Figure set 6), only the configuration assigning very high temperature to the superseding component of the PDT hot spot has been identified by this joint NICER and XMM-Newton analysis (instead of the predominant alternative found with NICER-only data, where the tiny hot spherical cap was the ceding component and hence partially hidden by a cooler and larger component). There is also a significant anticorrelation between the sizes of the hot spots (particularly of the ST and the superseding component of the PDT hot spot) and inferred mass and radius of PSR J0030+0451. Most likely, this correlation can be explained by the necessity of a similar emitting area, which requires a lower angular radius of the hot spot if the MSP has a larger radius. It is not clear if this is a consequence of the introduction of the XMM-Newton data, or if it is caused by the low number of live points adopted to explore the large ST+PDT parameter space. Indeed, as also reported in Table 4, the ST+PDT joint NICER and XMM-Newton analysis was performed with a considerably lower number of live points (10^3), compared to the corresponding NICER-only inference. Similarly to the NICER-only inference, the uncertainty over the colatitude of the ST hot spot allows it to be located on either the same or the opposite hemisphere as the observer. In this joint analysis, two distinct peaks are present in the 1D colatitude posterior; however, this could again be due to the relatively low number of live points enabled to explore the parameter space.

4.4. PDT−U

4.4.1. Model Exploration

We analyze the revised NICER PSR J0030+0451 data set with an SE 0.8, ET 0.1, LP 10^4, MM on, LR inference run. In the left corner plot of Figure 10, we report the radius, compactness, and mass posterior distributions derived adopting the X-PSI PDT−U model. We find relatively wide posteriors and hence large 68% credible intervals; the estimated mass and radius are, respectively, $1.41^{+0.20}_{-0.19}\,M_\odot$ and $13.12^{+1.35}_{-1.21}$ km. Uncertainties and values resemble those inferred with the ST+PST model, when XMM-Newton data are not included.

From the posterior distributions of the parameters describing the geometry and hot spot properties of the system (see corresponding corner plot in Figure set 6), we note the presence of three distinct modes. These were also identified through the mode-separation MULTINEST option. The main mode is characterized by a hot spot configuration similar to that reported in panel (F) of Figure 3. The solutions with the highest likelihood values from this inference run belong to this mode and have relatively low mass ($\sim$1–1.3 $M_\odot$) and quite high radius ($\gtrsim$15 km), populating most of the lower tail of the observed 1D compactness posterior distribution. However, this mode also extends to and dominates other parts of the parameter space, spanning a relatively wide range in compactness. This spread includes considerably smaller radii and significantly higher masses.

Within this mode, both hot spots are characterized by a cold and large ceding component and a hot, small superseding component. The secondary hot spot (as for all of the X-PSI models ending with −U, this refers to the hot spot with higher colatitude) typically coincides with the surface area

generating the first emission peak recorded in the NICER data, according to our representation (see Figure 9). The secondary hot spot is characterized by both the hottest ceding (with average and standard deviation $\log_{10}(T_{c,s}/\mathrm{K}) \sim 5.86 \pm 0.04$ versus $\log_{10}(T_{c,p}/\mathrm{K}) \sim 5.7 \pm 0.1$ of the primary) and superseding component (with average and standard deviation $\log_{10}(T_s/\mathrm{K}) \sim 6.23 \pm 0.03$ versus $\log_{10}(T_p/\mathrm{K}) \sim 6.08 \pm 0.03$ of the primary). In contrast to what was found for the models analyzed in R19, both hot spots are typically located in the hemisphere directly facing the observer (as shown panel (F) of Figure 3). There is however some spread on their exact location and in the inferred inclination (average and standard deviation of $\cos(i) \sim 0.3 \pm 0.2$); in particular, if the observer inclination compared to the rotation axis approaches $\sim 0°$, the hot spots tend to move toward the equator, to maintain the observed pulsed emission. Slight variations within this main mode also dominate the tails seen in the 2D posterior distributions reported in the left corner plot of Figure 10.

Given the relatively similar colatitude values inferred for the two hot spots and their uncertainties, it is natural to expect a bimodality due to the ambiguity of the primary and secondary labels. The posterior distributions of the parameters describing the hot spot properties clearly show this feature. The secondary mode shows again, for both hot spots, a colder and larger ceding component and a hot, very small superseding component. The temperature ranges characterizing the hot spot components are similar to the main mode, but the warmer hot spot is now labeled as the primary. Still, the warmer hot spot is responsible for the first emission peak, given the definition of phase zero in the data set that we use. However, this secondary mode, formally identified also thanks to the mode-separation MULTINEST option, additionally displays slightly different overall features. Both hot spots are now more typically located in the hemisphere opposite to the observer, whose inclination compared to the rotation axis is now favored at slightly higher angles (with average and standard deviation of $\cos(i) \sim 0.2 \pm 0.1$).

The average and standard deviation of mass and radius posterior samples associated with this secondary mode are $1.46 \pm 0.16\, M_\odot$ and 12.6 ± 0.9 km, and therefore populate the main posterior peak of the compactness. Although these values do not significantly differ compared to the one inferred from the main mode, in this case, these are also representative of the highest likelihood posterior samples.

The maximum likelihood associated with samples belonging to the secondary and the main mode, respectively, differ by only 2 in units of log-likelihood, while the difference in local evidence amounts to ~ 3 units in log. The background associated with these main two modes displays some variability, but it is considerably smaller than that inferred for the ST-U and ST+PST solutions.

Our inference run also identified a third mode, which is visible in some of the 2D posterior distributions corresponding to the parameters describing the hot spot properties. Its contribution is however marginal, as confirmed by the best likelihood values associated with this mode. They are worse by about ~ 9 units in log compared to those associated with the main mode (the difference in local evidence is about ~ 8 units in log). This third mode is the PDT-U representation of the main ST-U mode that was found when analyzing only NICER data. Similarly to that case, the inferred posterior samples cluster around mass and radius values of $1.15 \pm 0.10\, M_\odot$ and 10.7 ± 0.9 km, expressed as average values with standard deviation uncertainties. As expected given this resemblance, the background associated with samples belonging to this mode is considerably higher than that inferred from the other two modes.

The overall posterior distributions of this third mode feature hot spot configurations similar to the main ST-U solutions and their corresponding solution within the ST+PST model parameter space (in that context, describing the secondary mode). As in the latter case, the primary, and now also the secondary, exhibits some variation in terms of the relation between the two components, in particular in the characterization of the cold ceding component (average and standard deviation of $\log_{10}(T_{c,p/s}/\mathrm{K}) \sim 5.5 \pm 0.3$ for both hot spots). Focusing instead on the maximum likelihood solutions belonging to this mode, the complexity introduced to describe the hot spot leads to the presence of a very small ($\zeta_s \sim 0.04$ rad) and hot ($\log_{10}(T_{c,s}/\mathrm{K}) \sim 6.6$) ceding component, almost completely masked by the superseding one.

4.4.2. Joint Analysis of NICER and XMM-Newton Data

In the right corner plot of Figure 10, we show the posterior distributions of radius, compactness, and mass inferred by the joint analysis of NICER and XMM-Newton data sets. These results were obtained through the SE 0.8, ET 0.1, LP 10^3, MM off, LR run.

Again, the main effect of introducing XMM-Newton data in the analysis consists of increasing the fraction of photons recorded by NICER, assigned to the emission from PSR J0030 +0451. Consequently, posterior samples that are associated with high background are here considerably downplayed, and the compactness distribution shifts toward slightly higher values. In this case, however, the identified solutions that can reproduce both data sets are qualitatively similar to those obtained analyzing only NICER data; more specifically belonging to the main and secondary modes of the NICER-only run. The same two modes originate from the bimodality structure clearly visible in some of the posterior distributions describing the properties of the two hot spots (see Figure set 6). Samples associated with the least prominent mode of the NICER-only inference, on the other hand, are unable to represent the data given the additional information provided by XMM-Newton.

In panel (F) of Figure 3, we show, as example, the hot spot configuration associated with the maximum likelihood sample of the joint NICER and XMM-Newton inference run. The geometry of the system is qualitatively representative of the main mode of the posterior, which resembles the main mode inferred with only NICER data. The maximum likelihood samples reach quite high values for the radius, typically $\gtrsim 15$ km. However, now the associated masses are considerably larger, and cluster around 1.2–1.5 $M_\odot$. The secondary mode (whose qualitative characteristics are described in Section 4.4.1) also migrates toward higher masses, once XMM-Newton data are included in the analysis. The maximum likelihood samples belonging to this mode show masses around $\sim$(1.7–2.0) $M_\odot$; the corresponding radius also shifts toward higher values, in the range of $\sim$(13–16) km.

Given the relatively high values of radius associated with both modes, we decided to inspect the solutions that form the posterior mass for equatorial radii <12.5 km. The samples populating this part of the parameter space exhibit characteristics belonging to both modes. At least one of the hot spots

Table 6
Sixty-eight percent Credible Intervals for Mass and Radius for Different Inference Analyses Adopting ST−U and ST+PST Models

	R19 ST−U	Test 1 ST−U	Test 2 ST−U	Test 3 ST−U	Reference ST−U	R19 ST+PST	Reference ST+PST
R_{eq} [km]	9.58–11.54	9.94–11.49	9.54–11.56	9.68–11.91	9.64–11.68	11.52–13.85	11.81–14.41
M [$M_\odot$]	1.02–1.20	1.03–1.17	1.023–1.199	1.03–1.26	1.04–1.25	1.28–1.49	1.2–1.54

Notes. "R19" refers to the results reported in R19, "Reference" to the reference results presented in this paper, and "Test 1–3" to findings of preliminary analyses of the original data set used in R19. Tests 1–3 check for, in order: the effect of the new X-PSI framework and priors (for more details, see Section 2.1.3); the effect of different MULTINEST settings (for more details, see Section 2.1.4); and finally, the effect of channels (25, 30). Note that each change is implemented in addition to the previous one(s).

(usually the primary) is often located in the hemisphere facing the observer, behavior associated with the main mode. However, the observer inclination with respect to the spin axis is quite large, a characteristic more often associated with the secondary mode.

Medians and 68% credible intervals estimated for mass and radius according to the joint analysis of NICER and XMM-Newton data sets are $1.70^{+0.18}_{-0.19}\,M_\odot$ and $14.44^{+0.88}_{-1.05}$ km, respectively. The constraint coming from XMM-Newton data shifts the compactness, mass, and radius values toward slightly higher distribution.

5. Discussion

In this Section we discuss and contextualize the results presented in Section 4.

5.1. Comparison with R19 Results

The results outlined in Sections 4.1.1 and 4.2.1 are in good agreement with the analyses presented in R19, when using the same ST−U and ST+PST models. A few small changes arise due to the differences in setup compared to that adopted in R19:

1. Instrument response: for this study we adopt the latest general NICER instrument response (the one used for the analysis of PSR J0740+6620 in Riley et al. 2021; Salmi et al. 2022, 2023);
2. Data sets: as presented in Section 3, the data set analyzed here, B19V006, has been derived from the same event list defined in Bogdanov et al. (2019a), but accounting for the new instrument response;
3. NICER channel range used: in this work [30:300), in R19 [25:300);
4. Priors on cos(i) and colatitudes: here isotropic and thus sampled from a uniform prior in cosine, in R19 uniformly sampled in angle;
5. Different modeling of instrument uncertainties: as outlined in Section 2.1.2, compared to this study, R19 used two additional parameters to model uncertainties in the instrument response, dealing with the Crab calibration (Ludlam et al. 2018);
6. Updates to the X-PSI pipeline: in this analysis we use X-PSI v0.7 and v1.0, whereas R19 used v0.1. For full details of changes, see the CHANGELOG file in the X-PSI GitHub repository (see footnote 12); and
7. Settings: both in relation to the X-PSI pipeline and MULTINEST (see in particular differences in live points), as discussed in Sections 2.1.3 and 2.1.4.

One particularly relevant change, observed in the results, concerns the widening of the credible intervals associated with some of the model parameters, including the MSP mass and radius. We see this increase for both ST−U and ST+PST models. For the least computationally expensive model, ST−U, we investigated separately the effects of the different elements listed above. In Table 6, we show the 68% credible intervals for mass and radius starting from what was reported in R19 and ending with our reference results. In between we show the results of preliminary analyses that consequently implement the following changes,[26] starting with the analysis of the old B19 data set and original response matrix, as used in R19, and finishing with the inference presented in the work for ST−U NICER-only reference cases.

1. Test 1: new version of X-PSI, new modeling of uncertainties on instrument response, new priors;
2. Test 2: the effect of different MULTINEST settings and in particular of increasing the number of live points; and
3. Test 3: the effect of changing the lowest considered channel from 25–30. Only the columns marked "reference" show results for the new data sets, analyzed with the corresponding updated NICER response matrix.

Adopting the new X-PSI framework, including the updated modeling of instrument uncertainties and priors, has the effect of shrinking the credible intervals when the same MULTINEST settings are used. This can be explained by the fact that there are fewer parameters associated with the model. This reduces the space of possible solutions and hence the range of radii associated with them.

Increasing the live points has the effect of increasing (asymmetrically) the credible interval. Although this was already pointed out for PSR J0740+6620 in Riley et al. (2021) and Salmi et al. (2022, 2023), for PSR J0030+0451 this behavior seems at odds with the findings of R19. There the authors performed three inference runs with 1000 live points. All of them generated well-overlapping contours, leading to the conclusion that a higher number of live points would not have influenced the results (unless other modes, with much smaller width but much higher likelihood were also present). This seems not to be the case in the new framework for the ST−U model. Similarly, Afle et al. (2023) tested the dependence of the ST+PST model on the number of live points. When they increased the number of live points from 1000 to 4000, they found only a very small increase in the size of the credible regions (for instance, the 1σ radius interval increased by 0.1 km).

Reducing the range of channels at low nominal energies also slightly widens the credible intervals. This highlights the

[26] Each change is implemented in addition to the previous one(s).

important role played by events in the low-energy tail of NICER's sensitivity range, where the thermal emission from the hot spots is expected to peak. Since with test 3, we are losing part of the information used previously, the widening is not surprising.

Moving from the B19 to the updated B19v006 data set and the new instrument response slightly reduces the credible intervals once all of the changes mentioned above have been incorporated in the analysis framework. They are however overall still marginally wider than the original values published in R19.

Comparing the R19 results for the ST+PST model and the credible intervals of our new reference inference analysis, we find similar results, for likely similar reasons (see also Afle et al. 2023).

In general, to obtain robust results in the new analysis framework and with the updated B19v006 data set, we require more computationally expensive MULTINEST settings (not all combinations have been tested, but, e.g., adopting a larger number of live points seems necessary to obtain stable posteriors). In particular our various ST-U and ST+PST analyses (including the ones presented in Sections 4.1.2 and 4.2.1) demonstrate that, in the presence of a multimodal structure in the posterior, adopting an insufficient number of live points has not only the effect of underestimating the posterior widths, but it can also lead to significant biases.

5.2. Comparison with Findings from Simulations

The simulation tests performed in V23a have highlighted expected and unexpected dependencies and behaviors of the results of our analyses. In this Section we comment on the most relevant ones, relating them to our findings based on the analysis of the B19v006 updated NICER data set for PSR J0030+0451.

5.2.1. The Multimodal Structure of Our Posteriors

In V23a, the authors revealed the presence of multimodal structures in the posterior surface;[27] this is common to both real data and simulations. The presence of such structure is often clear only when the multimode/mode-separation setting of MULTINEST is activated or after inspecting tails of the posterior distributions. Due to the differences in posterior mass between the various modes, only for some cases is the multimodal structure prominent enough to be perceptible by eye in the marginalized posterior distributions. In both data and simulations, we clearly see very similar pulses and background generated by considerably different hot spot configurations, MSP, and interstellar properties. Multiple models and corresponding parameter vectors can reproduce NICER data without visibly impacting the quality of the residuals. This seems to differ from the case of PSR J0740+6620, where, with the tight mass, distance, and inclination priors, a single and stable mode was identified, for both the ST-U and the ST+PST model, that was well constrained in both the MSP radius and in its hot spot geometry.

More and higher-quality data, in addition to external constraints, could mitigate the challenges in the analysis of PSR J0030+0451's NICER data set posed by this multimodal structure of the posterior surface. For example, as we see when we introduce XMM-Newton data, if we had a stringent and reliable background estimate for NICER, that may lead solutions to a different portion of the parameter space and be less susceptible to multimodality.

The various modes characterizing the posterior surfaces often display different widths of the credible intervals. Moreover, as shown in V23a, posterior widths are quite sensitive to the specific noise realization. It is therefore complicated to predict in advance the evolution of credible intervals once further data and constraints are included in the analysis. If however, the main identified mode is unchanged, we expect, with some scatter, that uncertainties in the 2D posterior distribution of mass and radius will decrease with exposure time or the square root of it, depending on how strong the correlation between the two is in that specific analysis (see Lo et al. 2013; Psaltis et al. 2014; Miller & Lamb 2015).

5.2.2. Data versus Simulations

In addition to the multimodal structure, and just as in some of the analyses based on the synthetic data and reported in V23a, analysis of actual NICER data also shows some variability in the results depending on the analysis settings. However, comparing the results outlined in this paper with the findings from the simulations of V23a, we also notice some differences.

1. Here, as in R19, the inferred mass and radius change depending on the adopted hot spot model, while for the simulations, presented in V23a, it did not matter whether the ST-U or ST+PST model was used: the resulting posterior distributions found with these two models for mass, radius, and compactness were in any case very similar to each other.
2. Adopting the HR or LR X-PSI settings has a visible, although not significant, effect on the posterior distributions of mass and radius (as shown by comparing the green, HR, and the yellow, LR, lines in the left panel of Figure 7), a difference that was not observed in the analyses of synthetic data presented in V23a.
3. Comparing the evidences obtained for NICER-only analyses when adopting different models, we see a significant preference for more complex hot spot shapes. For the two cases tested in V23a, instead, this evidence difference reduced to a factor of a few in log-evidence, not enough to draw a decisive conclusion.

The origin of this different behavior for real data versus simulations could be due to a combination of several factors. The analyzed synthetic data may not cover a representative part of the parameter space; indeed in V23a, only one parameter vector per model was considered. If significantly more computational resources were available, it would be possible to produce and analyze multiple synthetic data sets, which would better sample the posterior inferred from real data (instead of limiting injected parameters to maximum likelihood samples). The different nature of the considered data may also generate some discrepancies in our findings. The simulations are based on synthetic data generated assuming the same physical processes and simplifications later adopted in the inference analyses. However, real data may contain physics that is not accounted for in our models: for example, hot spots are unlikely to have such simple shapes and will very likely display some temperature gradients. Normally we assume that the quality of our data is insufficient for these pieces of missing

[27] We expect the presence of very similar modes and, in general, multimodal structure also in the likelihood surface, given the mostly uninformative priors adopted for the PPM analyses of PSR J0030+0451.

Table 7
Summary of the Results for the Reference NICER-only Inferences and the Joint NICER and XMM-Newton Runs

NICER-only							
Model	Mass [$M_\odot$]	Radius (km)	$\log(\mathcal{E})$	$\max(\log(\mathcal{L}))$	$\max(\log(\mathcal{L}_{\rm N}))$	$\max(\log(\mathcal{L}_{\rm N\&XMM}))$	Core Hours
ST−U	$1.12^{+0.13}_{-0.08}$	$10.53^{+1.15}_{-0.89}$	−35788	−35735	⋯	−42950	11462
ST+PST	$1.37^{+0.17}_{-0.17}$	$13.11^{+1.30}_{-1.30}$	−35778	−35722	⋯	−42942	133970
ST+PDT	$1.20^{+0.14}_{-0.11}$	$11.16^{+0.90}_{-0.80}$	−35779	−35729	⋯	−42705	33069
PDT−U	$1.41^{+0.20}_{-0.19}$	$13.12^{+1.35}_{-1.21}$	−35777	−35721	⋯	−42659	74333
NICER and XMM-Newton							
Model	Mass [$M_\odot$]	Radius (km)	$\log(\mathcal{E})$	$\max(\log(\mathcal{L}))$	$\max(\log(\mathcal{L}_{\rm N}))$	$\max(\log(\mathcal{L}_{\rm N\&XMM}))$	Core Hours
ST−U	$1.88^{+0.13}_{-0.19}$	$15.12^{+0.64}_{-1.31}$	−42714	−42661	−35760	⋯	41219
ST−U[a]	1.35 ± 0.16	11.44 ± 1.14	−42718	−42666	−35769	⋯	⋯
ST+PST	$1.93^{+0.10}_{-0.13}$	$15.12^{+0.64}_{-1.31}$	−42711	−42662	−35761	⋯	84620
ST+PDT	$1.40^{+0.13}_{-0.12}$	$11.71^{+0.88}_{-0.83}$	−42684	−42625	−35730	⋯	3261
PDT−U	$1.70^{+0.18}_{-0.19}$	$14.44^{+0.88}_{-1.05}$	−42677	−42617	−35723	⋯	12421

Notes. Uncertainties represent the 68% credible intervals starting from the median of the marginalized 1D posterior distribution. For NICER-only analyses, we report medians, credible intervals, evidences $\mathcal{E}$, maximum likelihood values $\log_{\max}\mathcal{L}_{\rm N}$ (in a joint NICER and XMM-Newton framework $\log_{\max}\mathcal{L}_{\rm N\&XMM}$), and core hours associated with the run with MULTINEST settings: SE 0.3, ET 0.1, LP 10^4, MM on. The $\log_{\max}\mathcal{L}_{\rm N}$ marks the maximum likelihood values of the run identified by the line. The joint NICER and XMM-Newton inference runs are performed with MULTINEST settings: SE 0.8, ET 0.1, LP 10^3, MM off, except for the ST−U case, the only model for which we could perform a SE 0.3, ET 0.1, LP 10^4, MM on run. All of the inference analyses, apart from those using the ST−U model, assume low resolution in terms of X-PSI settings (see Section 2.3.1 of V23a). For ST−U and ST+PST models, R19 reported, respectively, a mass of $1.09^{+0.11}_{-0.07}\,M_\odot$ and $1.34^{+0.15}_{-0.16}\,M_\odot$ and a radius of $10.44^{+1.10}_{-0.86}$ km and radius of $12.71^{+1.14}_{-1.19}$ km.

[a] Secondary mode of the NICER and XMM-Newton run with SE 0.3, ET 0.1, LP 10^4, MM on (in this specific case, to describe mass and radius posterior, we use means and standard deviations, and we report the value of the local evidence, as calculated by MULTINEST).

physics to affect the outcome of the analysis; but this is something that should be tested in more detail.

5.3. Model Comparison and the Effect of Including Constraints from XMM-Newton

We report the main results for each model considered in this study in Table 7. The first four rows of the table refer to NICER-only reference inferences (settings of reference runs are highlighted in bold in Table 3); while the last five show results for joint NICER and XMM-Newton analyses (see specific settings in Table 4, for entries with XMM-Newton data included). From left to right, we report in each column the following: (i) adopted model, 68% credible interval for (ii) mass and (iii) radius, (iv) natural logarithm of evidence, (v) natural logarithm of the maximum likelihood, (vi) only for joint NICER and XMM-Newton analyses—natural logarithm of the maximum likelihood within the NICER-only framework, (vii) only for NICER-only inferences—natural logarithm of the maximum likelihood within the joint NICER and XMM-Newton framework (assuming $\alpha_{\rm XTI} = \alpha_{\rm MOS1} = \alpha_{\rm MOS2} = 1$, with β defining the distance), and (viii) core hours necessary to compute the run. The second row in the joint NICER and XMM-Newton block refers to the secondary ST−U mode, identified in the ST−U inference run, whose main results are summarized in the row just above. This mode is particularly interesting since a similar configuration is also found adopting the ST+PDT model, and it resembles the main findings for PSR J0740+6620. In this case only, in the fourth column, we report the local evidence; for all other rows, we refer to the global evidence.

We highlight the implications of our findings, summarized in Table 7, in the following subsections.

5.3.1. NICER-only Analyses

The first four rows of Table 7 summarize the results of the NICER-only inference runs. As in R19, the evidence clearly disfavors the ST−U model, but does not display a clear preference for any of the more complex models. However, while the analysis settings for all NICER-only runs whose results are displayed in the table are the same, this does not necessarily imply the same accuracy in the evidence evaluation, since the dimension of the parameter space increases with the complexity of the model. Hence, how well each model explored the parameter space would ideally need to be checked in more detail to corroborate our findings. Note, for example, that the maximum likelihood value found for the ST+PST model is higher than that identified in our reference ST+PDT inference run. Since the ST+PST model is approximately contained in the more complex ST+PDT model, this likely implies that our reference ST+PDT run has not adequately explored the parameter space.[28,29] This has implications for the estimated evidence, whose value is therefore likely underestimated.

[28] Another possibility could be that the prior mass (see footnote 29) of this mode is too small for MULTINEST to consider it relevant for the evidence estimation. This latter hypothesis is however unconvincing, since a detailed look into the posterior samples showed no solution similar to the one found in ST+PST, and hence the total contribution of this mode has at least not been accurately estimated by MULTINEST.

[29] Note again that this is not the same as mass prior, but represents instead the volume of the prior.

Exclusively in terms of mass and radius posteriors, two main classes of solutions are present: $M \sim 1.1$–$1.2\,M_\odot$ and $R_{\rm eq} \sim 10.5$–11.1 km; or $M \sim 1.4\,M_\odot$ and $R_{\rm eq} \sim 13$ km.[30] The former seems to be slightly more asymmetric and narrower than the latter (given the same adopted settings, which, however, again do not guarantee the same quality of the uncovered posterior).

The newly introduced ST+PDT and PDT-U models, which were not studied in R19, show significant posterior mass for configurations with at least one of the hot spots on the same hemisphere as the observer. These geometric configurations were not found in R19.

5.3.2. Joint NICER and XMM-Newton Analyses

We focus now on the entries of Table 7 corresponding to joint NICER and XMM-Newton analyses.

Evidence. Unlike for the NICER-only analyses, for the joint inferences, the evidence indicates a significant preference for the PDT-U model. Both ST-U and ST+PST models are strongly disfavored, with similar evidence values differing from the best one by factors of ∼40 in log units. The difference between PDT-U and ST+PDT is milder (about 7–8 in log units), but still decisive. If we assume that including XMM-Newton data introduces unbiased constraints, the substantial shift in solution(s) driven by the additional XMM-Newton data, compared to those reported in R19, shows that the PSR J0030+0451 NICER results need to be interpreted carefully. This implies that, for this source, whose data are clearly characterized by a prominent multimodal structure, further constraints could once again significantly modify the results of our inference.

Radii inferred with ST-U and ST+PST models. For the NICER and XMM-Newton joint analyses, the new main solutions identified with the ST-U and ST+PST models are very similar to each other, in mass and radius as well as in hot spot configurations. Some of the similarities, especially in terms of mass and radius, could be caused by the radius posteriors' tendency of reaching the upper limit of the prior and consequently constraining the mass through inferences on the compactness. We also highlight that such high radius values are difficult to reconcile with constraints posed by other observations, such as the inferred tidal deformability from gravitational waves (see, e.g., Abbott et al. 2018, 2019) and from the analysis of NICER (and XMM-Newton) PSR J0740+6620 data (Miller et al. 2021; Riley et al. 2021; Salmi et al. 2022).

Hot spot complexity. Introducing the masking component that distinguishes the ST+PST model from the simplest ST-U one does not improve our ability to represent both NICER and XMM-Newton data. Looking at the corresponding geometrical parameter posterior distributions (see Figure set 6), there is a clear degeneracy due to the small size of both hot spots (degeneracy of type I, as described in R19). This generates ambiguity in the association of the ST and PST labels with the hot spots (i.e., either hot spot could in principle be represented with or without the omitting component). On the other hand, when we introduce an emitting component via the ST+PDT model, its association with the hot spot, which we see first in the data is strongly favored, and the associated evidence and maximum likelihood values improve drastically. Introducing a second emitting component also for the other hot spots, as present in the PDT-U model, further improves the quality of our results.

Similarities in the tails of the posteriors. Further examinations of the posterior distributions derived with the ST+PST model reveal that the configurations populating the tails at low radii are likely forming a secondary mode, as was the case for the joint NICER and XMM-Newton ST-U analysis. These secondary modes display similar geometries (being viewed almost from the equator and with almost antipodal hot spots), masses, and radii as the main ST+PDT mode. As we will discuss further in Section 5.3.5, this configuration is of particular interest because it could potentially better explain the gamma-ray emission associated with PSR J0030+0451; moreover, it would be similar to the geometry found for PSR J0740+6620 (which we may expect if the underlying magnetic field and its history are similar).

5.3.3. Transitioning from NICER-only to Joint NICER and XMM-Newton Analyses

In this Section we briefly outline the main effects that we observe in our findings, transitioning from analyzing only the NICER data to jointly considering both NICER and XMM-Newton data sets. We however remind the reader that, as more extensively discussed in Section 5.4, inferences of NICER-only data were performed with better (and more computationally expensive) MULTINEST settings, compared to the joint instrument analyses (the joint analyses generally required a larger number of core hours, given the same settings, to reach the termination condition set by the evidence tolerance).

We start by noting that possible differences in the results were already anticipated in R19 (see the discussion in Section 4.1.2 of that paper). Introducing XMM-Newton data has the general effect of decreasing the inferred background, leading to higher compactness values (following the same logic presented in Riley et al. 2021; Salmi et al. 2022). This is in general true for all models, which, although in different ways, always reach higher compactness by shifting the posteriors of both masses and radii toward higher values. However, the findings obtained adopting the ST-U and ST+PST models are those mostly affected by the change. Indeed the ST-U and ST+PST NICER-only analyses identify, as main modes, solutions that are only supported by higher background levels, compared to the broader background support for the ST+PDT and PDT-U main modes.

For the ST+PDT and PDT-U models, introducing XMM-Newton data into the analyses has the effect of reducing the background support for the main modes identified with NICER-only inferences, while still maintaining them as the most probable configurations (now characterized by slightly narrower posteriors, looking, e.g., at radius and mass, as a consequence of the restricted background support of the same mode).[31]

Instead, solutions found with ST-U and ST+PST in the NICER-only inferences are downplayed by the introduction of the constraints posed by XMM-Newton data, which, jointly with NICER data, can now be better represented by a completely different mode. As mentioned in Section 5.3.2,

[30] These two groups of mass and radius values do not, however, reflect the hot spot configurations associated with them, which show a greater variety.

[31] Again, however, the main mode, identified by the ST+PDT model in NICER-only analyses, is very unlikely to be the one containing the highest likelihood values (see reasoning in Section 5.3.1).

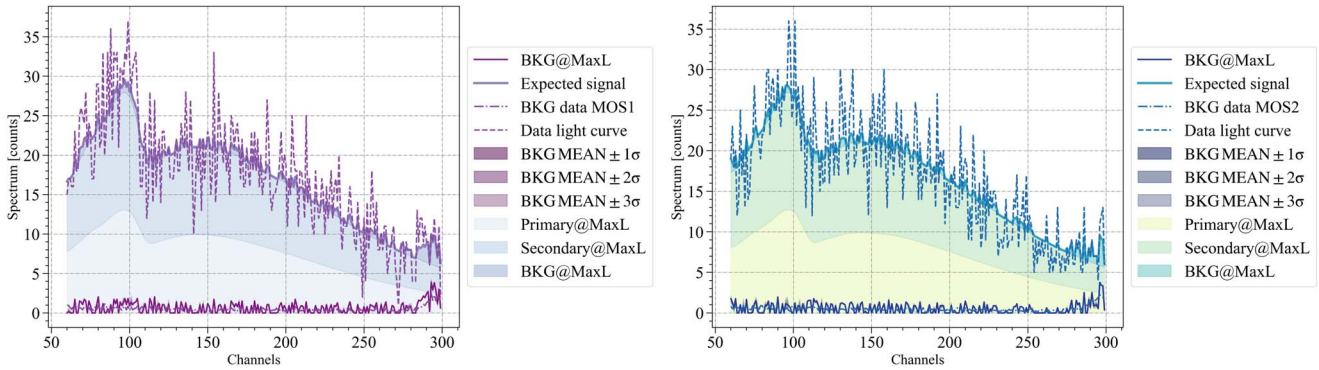

Figure 11. Example showing how our PDT−U maximum likelihood (MaxL, in the legend) solution, obtained in the joint NICER and XMM-Newton analysis, represents XMM-Newton PSR J0030+0451 and background (BKG) data, for MOS1 (left panel) and MOS2 (right panel). The plot shows similar quantities as Figure 5, but for the XMM-Newton MOS1 and MOS2 total and background data sets. The dashed–dotted line (magenta, for MOS1 and light blue, for MOS2) shows the background data used in our analysis; the inferred background is plotted with a solid line (in magenta for MOS1 and dark blue for MOS2). Given its low value, the uncertainties (shown with shaded areas, purple for MOS1, and dark blue for MOS2) are almost imperceptible. The dashed, more scattered line shows the total on-source data, for MOS1 on the left and MOS2 on the right; the solid line (purple for MOS1 and blue for MOS2) is the inferred expected signal. We display the contribution of the primary, the secondary, and the background associated with the maximum likelihood sample, adding them (in this order) on top of each other with areas of different intensities of blue, for MOS1, green for MOS2.

both ST−U and ST+PST models favor solutions with high radius values ($R_{\rm eq} \sim 15$–16 km), and hot spot configurations resembling panel (C) of Figure 3, for the main bulk of the posteriors.

Introducing XMM-Newton data and constraints does not significantly affect the ratio between $\alpha_{\rm XTI}$ and the distance squared, or the β parameter in NICER-only analyses (representing the only distance and $\alpha_{\rm XTI}$ combination to which the analysis is sensitive), which remains between ∼8.4 and 8.9.

Transitioning to joint analyses has different effects on the inferred column density, depending on the assumed model. This is most likely an indirect consequence of changes (for ST−U and ST+PST), or the absence of changes (for ST+PDT and PDT−U), in the identified main mode. For both ST−U and ST+PST, the inferred $N_{\rm H}$ posterior shifts from peaking at specific values ($\sim 1.48 \times 10^{20}$ and 0.9×10^{20} cm^{-2}) to be completely consistent with zero (i.e., clearly limited at $\sim 0.1 \times 10^{20}$ cm^{-2} by the lower limit of our prior). For the ST+PDT analyses, introducing XMM-Newton data does not significantly affect the $N_{\rm H}$ posterior, which clusters around 0.7×10^{20} cm^{-2}. Similarly for PDT−U, the joint analysis points toward an inferred $N_{\rm H}$ posterior only marginally different from what was found in NICER-only inferences, with median values changing from 1.58×10^{20} to 1.48×10^{20} cm^{-2}. Given the different estimates of $N_{\rm H}$ that the various models provide, it is clear that strong constraints would considerably help our analyses and improve our interpretation of their results. In future analyses, we plan to include a more realistic prior on the $N_{\rm H}$, based on literature. We hope to find up-to-date estimates in particular of its lower limit, as this would greatly benefit our analyses.

Finally, introducing XMM-Newton does not seem to significantly affect the quality of the NICER residuals (which are still good; see Figure set 9), while the XMM-Newton data are also well represented (for an example, see panels in Figure 11). From Table 7, we can see that the maximum likelihood for NICER-only drops considerably if we use the maximum likelihood solution identified in the joint analysis for the ST−U and ST+PST models (with a drop of about 30 in log likelihood).

However, this is not the case for ST+PDT and PDT−U. The former shows a similar maximum likelihood value to that found in the corresponding ST+PDT NICER-only analysis; while for the latter, the best-fitting solution has an NICER likelihood comparable to the overall best solution from the NICER-only inferences (and therefore very close to the one identified with the ST+PDT NICER-only analysis).[32]

5.3.4. New versus Old Favored Configurations

As mentioned in Section 5.3.2, overall we find that the NICER and XMM-Newton data sets can be jointly well described by the solutions identified with both ST+PDT and PDT−U models. Interestingly, compared to what was found for the models and data analyzed in R19, in neither case is there a need for elongated hot spots or for both the hot spots being located in the same hemisphere (see panels (E) and (F) of Figure 3). For both models, the PDT hot spot(s), i.e., the ones described by two emitting elements, are characterized by a larger cooler component and a much hotter and smaller one. This hints at the presence of temperature gradients, to which our analysis is apparently sensitive. We believe this should motivate investigations aimed at characterizing the sensitivity and robustness of our findings to more realistic physical properties of the MSP surface hot spots. We also note that for both models, the overall dimensions of the two hot spots are comparable and that they are almost antipodal (at least in phase). These characteristics resemble the configuration found by analyzing NICER-only observations and jointly the NICER and XMM-Newton data for PSR J0740+6620. In particular, the solutions identified with ST+PDT show even more similarities with the findings for PSR J0740+6620, including the high inclination ($\cos(i) \sim 0.1$) and the relatively low radius value of $R_{\rm eq} \sim 12$ km. As mentioned previously, very similar solutions are also found in the tail of the joint NICER and XMM-Newton posteriors derived with the ST−U and ST+PST models, as secondary modes.

[32] Here we compare maximum likelihood values to have a rough estimate on what is worsening in matching the data, required to include the XMM-Newton constraints.

5.3.5. New Favored Configurations in Relation to Gamma-Ray Constraints

The hot spot configurations found with ST+PDT and as a secondary mode of the ST−U (and ST+PST) joint NICER and XMM-Newton inferences are, interestingly, more consistent with the gamma-ray emission associated with PSR J0030+0451. Kalapotharakos et al. (2021) considered multipolar field geometries consistent with the mass, radius, and viewing geometry (inclination ∼50°) results of R19 and Miller et al. (2019), under the assumption the hot spots correspond to open field line regions. Open field lines were identified by integration from the surface to the light cylinder in either static vacuum or force-free models, with corresponding identified surface regions assumed to be uniform in temperature. Only bolometric light curves were considered in Kalapotharakos et al. (2021). The offset dipoles and quadrupoles resulted in a variety of surface patterns qualitatively different in shape but consistent in position with R19 and Miller et al.'s (2019) highest likelihood shapes.

However, Kalapotharakos et al. (2021) also found degeneracies, i.e., a multimodal likelihood surface, when only the X-rays were considered. A key aspect of the force-free models of Kalapotharakos et al. (2021) was that they allowed for the computation of gamma-ray emitting regions, beyond the light cylinder in the current sheet. This high-altitude field region's morphology is most sensitive to the global dipolar field geometry and orientation relative to the spin axis. A key novel aspect in Kalapotharakos et al. (2021) was the computation of synchronous (in absolute phase, relative to the radio) X-ray and gamma-ray pulse profiles with multipolar fields–this involved correcting for light travel times and different emitting regions in curved spacetime. Of the force-free models considered in Kalapotharakos et al. (2021), only one (model RF4_11) seems to describe both the X-rays and gamma-rays well in phase alignment. This model's X-ray hot spots are circular and are reminiscent of models and modes D and E of Figure 3 in this work. The study by Kalapotharakos et al. (2021) implies that a self-consistent treatment of both X-rays and gamma-rays will reduce parameter degeneracies and identify the correct hot spot modes and viewing geometry for PSR J0030+0451. Such an investigation is planned. Note that seeing both radio and gamma-rays from a pulsar generally limits the viewing geometry (the radio is from magnetic polar regions, while the gamma-rays are from equatorial current sheets). These visibility regions cut across almost orthogonally in the space of dipole inclination angle and spin axis viewing direction (see, for example, Corongiu et al. 2021).

5.4. Caveats

In this Section we list the major caveats and assumptions that affect the analyses presented here.

Atmosphere state and composition. For the analyses in this paper, we have assumed a fully ionized hydrogen atmosphere. While this assumption is quite standard, and well motivated, it can have a substantial impact on the parameter posteriors that we recover, as discussed and described in detail in Salmi et al. (2023).

Simplification of the hot spot properties. Here, as in all NICER studies so far, we adopt models that greatly simplify the physics characterizing the hot spots. The underlying assumption is that our data and relative uncertainties are not sensitive enough to such details for us to need to account for them. Degeneracies, in the analyses presented both here and in V23a, show that we are not sensitive, e.g., to the direction of arcs, if thin and elongated, or even to the presence of a structure more complex than a circle, if the hot spot is small enough (see, e.g., label ambiguity in the ST+PST joint NICER and XMM-Newton analysis). However, the jump in evidence and maximum likelihood values obtained when introducing a second emitting component per hot spot suggests that our analyses are in fact sensitive to temperatures and, likely, temperature gradients (considering indeed the usually very small size of the hotter component).

Priors. Priors are particularly important in our inference analyses, as they drive the MULTINEST exploration of the parameter space and sometimes they clearly impact the range of our credible intervals. That is, for example, the case for the radius posteriors inferred in the ST−U and ST+PST joint NICER and XMM-Newton analyses, where our hard upper limit clearly modifies the natural 1D posterior distribution of that mode, truncating it at 16 km and thus skewing the higher radius end of the credible interval. Priors also play a crucial role in the evidence and yet their definition always, at least partially, relies on arbitrary choices: first through the chosen parameterization to describe the problem, and second through their practical implementation, which often includes approximations, simplifications, and arbitrary cutoff values. Thankfully, when the posterior is data-dominated, the impact of these choices is heavily suppressed. However, any time that we use the evidence, we should keep in mind that priors are crucial to evaluate it. As noted, our reference ST+PDT in NICER-only analysis missed exploring an important part of the parameter space, since the solution for ST+PST is also in the ST+PDT parameter space and has a better likelihood. However, it is also possible that MULTINEST did not pick such a solution because its supporting prior volume is too small (if, for example, it required temperatures very close to the prior lower bounds) when put in the higher dimension parameter space describing the ST+PDT model. It should be stressed that MULTINEST explores the parameter space with the aim of computing the evidence, through definitions of isolikelihood contours (Feroz & Hobson 2008; Feroz et al. 2009, 2019).

Use and interpretation of XMM-Newton data. Introducing XMM-Newton data could lead to biases if the underlying assumptions are not correct, e.g., if the assumption on cross calibrations is incorrect, or other astrophysical contamination is present at the pulsar sky location without being accounted for in our models.

However, while we should keep this in mind and test for alternatives when possible, we think it is a crucial procedure to cross-check the compatibility of our findings with other observations, given the large amount of data increasingly available. Hence, independently of the outcome, we believe including XMM-Newton data and constraints promotes correct scientific practice. Cross checks are especially important for NICER sources like PSR J0030+0451, which lack independent information to coherently incorporate in priors (unlike for PSR J0740+6620, and other NICER sources like PSR J0437−4715, where radio constraints can considerably inform our analyses and reduce the prior parameter space associated with masses and inclination).

Adequacy of the analysis settings. The data quality for PSR J0030+0451 is very high, which increases the

computational cost of this type of analysis.[33] Given the computational resources available to us, we could not fully test how well the parameter space was explored for the most complex models; analyses adopting ST−U and focusing on NICER-only data were the only exception. With the various tested settings, it was possible to prove that in this case our reference run had reached a converged state (although a significantly higher number of live points could potentially still reveal unexplored and relevant portions of the parameter space). The exploratory runs, which adopt an increasingly higher number of live points, also proved that merging the results of multiple inference runs with lower live points is not always equivalent to a single run with higher live points (e.g., merging all of our ST−U runs with LP 10^3 would have converged to a radius about ∼1 km higher than what we find with a more adequate amount of live points (6–10) × 10^3). Indeed, contrary to expectations, we find, as also shown to a lesser extent for PSR J0740+6620 in Riley et al. (2021) and Salmi et al. (2022), that a lower number of live points does not only underestimate the width of a mode, but also slightly biases it. In our ST−U NICER-only cases, for example, we see systematically higher median values when only 10^3 live points are used. However, further checks are still needed; e.g., it is yet unclear if decreasing the evidence tolerance to 0.001 would have an effect when a high number of live points is employed. For the more complex models, we cannot guarantee an exhaustive exploration of the parameter space given its increased dimension and the hence increased computational cost.[34] This is particularly true for the joint NICER and XMM-Newton inference, whose requirements in terms of analysis settings had to be lowered to render them computationally tractable. As suggested in V23a, future analyses of upgraded data sets, targeting a new headline inference of mass and radius for PSR J0030+0451, will need adequate studies to address whether settings are appropriate, given the data and the model framework. More tailored techniques may also be employed to assess robustness in the obtained posterior and the adequacy of the adopted models. The robustness of the findings for the ST+PST, ST+PDT, and PDT−U models, both for NICER-only inferences and joint NICER and XMM-Newton analyses, needs more extensive testing, and this will be considered in our computational budget requests for future analysis.

Correct interpretation of evidence. In the presence of a highly multimodal structure of the posterior surfaces, it is important to reflect on what should be inferred from evidence values. In particular, if one model is preferred by the evidence, it does not necessarily imply that the radius posterior associated with its main mode is also favored. We also point out that, in this context, preferences in terms of posteriors seem to be naturally driven by their correspondent local evidence. However this is also an arbitrary choice. Moreover, the evidence depends on the priors that, as we mention above, are defined with some arbitrary components. For these reasons, there may be contexts, especially in presence of multimodal structures in the posterior, where the solutions identified by the evidence and those corresponding to the maximum likelihood or maximum posterior samples are significantly different. Among our reference runs, this happens for mass and radius only for the PDT−U inferences. For both the NICER-only and the joint NICER and XMM-Newton analyses, the maximum likelihood sample lies in the tail of the 2D mass and radius distribution (see Figure 10), respectively, with [$M_{\max\ \mathcal{L}} \sim 1.05\ M_\odot$, $R_{\mathrm{eq,max}\ \mathcal{L}} \sim 15.7$ km] and [$M_{\max\ \mathcal{L}} \sim 1.1\ M_\odot$, $R_{\mathrm{eq,max}\ \mathcal{L}} \sim 14.8$ km].

The evidence calculation, performed through MULTINEST in our analyses, is useful, as it allows us to compare various models through their relative difference (where a model with higher evidence $m1$ is preferred compared to other, $m2$, by a factor e^{Δ}, where $\Delta = \log(\varepsilon_{m1}) - \log(\varepsilon_{m2})$). Tables 5 and 7 show the absolute values of evidences and maximum likelihoods obtained in our analyses. The low-likelihood values are due to the small Poisson probability of getting, in each phase bin and channel, a specific count (the one registered by the data) and to the high total number of the 2D bins (32 phase × 270 channels). The evidence is then calculated as the integral, over the whole parameter space, of the likelihood weighted by the prior.

6. Conclusions

In this paper we analyzed the reprocessed NICER data set for PSR J0030+0451, B19v006. We adopted four different models to describe increasing complexity in the hot spot shapes: ST−U, ST+PST, ST+PDT, and PDT−U. The former two were both found in R19 to well represent the data (i.e., they had no suspicious structure in the residuals); however, the more complex model ST+PST was favored by the evidence. According to this model, PSR J0030+0451 is an MSP characterized by a mass of about ∼1.3 $M_\odot$ and a radius of ∼13 km. Both hot spots were located in the same hemisphere, opposite to the observer, and one of them had an elongated shape. ST+PDT and PDT−U are two additional models tested for the first time for PSR J0030+0451. They allow for an additional emitting component to describe one, for ST+PDT, or both of the hot spots, for PDT−U.

In this work we upgraded the data set release that was described in 2019 using an updated instrument response, and also coherently included XMM-Newton data in our analyses. Compared to R19, we here also adopted more extensive analysis settings in our main inferences. However, we were able to check the robustness of the obtained posterior distributions only for the simplest ST−U model. The computational resources necessary to test the adequacy of the analysis setting for inferences adopting more complex models were instead prohibitive. With this caveat in mind (see also Section 5.4), below we summarize the main takeaway points of our inferences.

1. Analyzing the updated NICER data set, with new settings and an upgraded pipeline, we produce results consistent with what was found and reported in R19.
2. Based on ST−U tests, compared to the analyses of R19, the reprocessed data and new framework seem to require a larger number of MULTINEST live points to ensure the robustness of the inferred posterior distributions.
3. Introducing XMM-Newton, and hence indirectly incorporating background constraints, considerably affects the PSR J0030+0451 findings.

[33] For the same settings, the analysis of PSR J0740+6620 NICER data, which have a much lower quality than for PSR J0030+0451, required considerably fewer core hours. This is one of the reasons why that source has been analyzed with better MULTINEST settings: a much larger amount of live points and a lower sampling efficiency.

[34] This implies that we cannot guarantee that significant posterior shifts and changes would not appear in case of repeated inference runs with the same analysis settings.

4. Joint analyses can require a considerable amount of computing resources, while reducing MULTINEST and X-PSI settings to make the analysis computationally tractable can have significant effects on the final findings. To produce robust results, analyses of future data sets will require the allocation of more computational resources and/or a considerable speed-up of the parameter estimation procedure.
5. In joint NICER and XMM-Newton inferences, ST−U and ST+PST give rise to very similar solutions (but very different from the corresponding ones identified with NICER-only data), which lead to very large masses and very high radii (which would be in strong tension with the results from GW170817), the latter hitting the edge of our hard-cut prior at 16 km.
6. Both ST+PDT and PDT−U models, with the latter being significantly preferred by the evidence, are able to reproduce both NICER and XMM-Newton data, without invoking elongated shapes for hot spots or requiring them both to be located in the same hemisphere. The hot spot configurations found with these two models are likely in better agreement with the PSR J0030+0451 gamma-ray emission and resemble the findings of PSR J0740+6620, especially for the solutions associated with the ST+PDT model. Radii and masses estimated during the preliminary joint NICER and XMM-Newton runs, presented in this work, for ST+PDT and PDT−U are, respectively, $R_{\rm eq} \sim 11.5$ km, $M \sim 1.4\,M_\odot$ and $R_{\rm eq} \sim 14.5$ km, $M \sim 1.7\,M_\odot$. However, more targeted and detailed studies are needed to assess the robustness of these findings.
7. The configurations identified by the ST+PDT and PDT−U models, and how well they seem to describe the data, suggest the presence of gradients of temperature in the hot spot. It is therefore crucial to check what would be the impact of such gradients on our parameter recovery, through more realistic simulations.
8. Our findings also suggest that our analysis is only weakly sensitive to small details describing the hot spots (e.g., for the secondary mode found for the ST+PST NICER-only analyses, the omitting component can assume different sizes and location, as long as the area of the effectively emitting regions maintains a similar size).
9. Different models and parameter vectors are currently in good agreement, given the quality of the residuals, with the B19v006 data and constraints. If this situation does not change in the future, it could be useful to provide a more informative (constrained) prior for PSR J0030+0451's radius, based on other robust observations, such as estimates of the tidal deformability from gravitational waves and/or constraints from other NICER sources. One could also develop more adequate procedures to deal with multimodal solutions for follow-up equation-of-state studies.
10. It appears that more factors complicate the analysis of NICER PSR J0030+0451 data compared to PSR J0740+6620. One reason could be PSR J0740+6620's high inclination and general intrinsic hot spot configuration. It could also be due to the quality of the data, since for PSR J0740+6620 (which is faint in X-ray), we know that most NICER photons actually come from the background. The tight constraints on mass and inclination coming from radio observations, thanks to PSR J0740+6620's parameters and geometry, are also extremely helpful for the analysis of that source.
11. Constraints from other studies and observables would be very useful, for example, from PSR J0030+0451's gamma-ray pulse profile or NICER background estimates.

6.1. Summary

In summary, we analyzed the PSR J0030+0451 data set, described in Bogdanov et al. (2019a), with the most updated instrument response and found, with an updated analysis and modeling framework, results compatible with the findings reported in R19. Our in-depth analysis, however, reveals a complicated structure of the likelihood surface that is difficult to explore extensively, given our current computational resources. We introduce constraints posed by the XMM-Newton X-ray observations of PSR J0030+0451. This suggests that there may be no need for both hot spots to be located on the same hemisphere, nor for elongated shapes, as long as multiple temperatures can be assigned to a single hot spot.

Given the inference analyses conducted for this work (and noting the caveats outlined in Section 5.4), there is a significant preference, in terms of evidence values, for the most complex model tested (PDT−U), which can seemingly well represent both NICER-only and joint NICER and XMM-Newton data. The radius and mass associated with this solution are $14.44^{+0.88}_{-1.05}$ km and $1.70^{+0.18}_{-0.19}\,M_\odot$. However, we find that ST+PDT also well reproduces both NICER-only and joint NICER and XMM-Newton data. It does so with a hot spot configuration that resembles PSR J0740+6620, and radius estimation is more in line with the value currently inferred for that source. The ST+PDT model yields a radius and mass of $11.71^{+0.88}_{-0.83}$ km and $1.40^{+0.13}_{-0.12}\,M_\odot$ for PSR J0030+0451.

This in-depth re-analysis of the 2017–2018 NICER data set indicates that PSR J0030+0451 is a complex source to model. Due to the multimodal nature of the solution space, it is a source for which additional constraints—on the background, or on the system geometry—will be important in determining a robust inference of mass and radius. This study provides a more comprehensive baseline to support in-progress analysis of new, larger NICER data sets for this source, including benchmarking of the computational resources that need to be allocated to ensure robust results.

Acknowledgments

The authors thank Evert Rol and Martin Heemskerk for technical assistance and Phil Uttley for useful discussions. This work was supported in part by NASA through the NICER mission and the Astrophysics Explorers Program. S.V., T.S., A.L.W., D.C., Y.K., and T.E.R. acknowledge support from ERC Consolidator grant No. 865768 AEONS (PI: Watts). This work was sponsored by NWO Domain Science for the use of the national computer facilities. NICER work at NRL is supported by NASA. S.B. acknowledges support through NASA grant 80NSSC22K0728. S.G. acknowledges the support of the CNES. W.C.G.H. acknowledges support through grant 80NSSC23K0078 from NASA. S.M.M. acknowledges support from NSERC Discovery grant RGPIN-2019-06077. A portion of the results presented was based on observations obtained with XMM-Newton, an ESA science mission with instruments and contributions directly funded by ESA Member States and NASA. This research has made use of data and software

provided by the High Energy Astrophysics Science Archive Research Center (HEASARC), which is a service of the Astrophysics Science Division at NASA/GSFC and the High Energy Astrophysics Division of the Smithsonian Astrophysical Observatory. We acknowledge extensive use of NASA's Astrophysics Data System (ADS) Bibliographic Services and the ArXiv.

ORCID iDs

Serena Vinciguerra https://orcid.org/0000-0003-3068-6974
Tuomo Salmi https://orcid.org/0000-0001-6356-125X
Anna L. Watts https://orcid.org/0000-0002-1009-2354
Devarshi Choudhury https://orcid.org/0000-0002-2651-5286
Thomas E. Riley https://orcid.org/0000-0001-9313-0493
Paul S. Ray https://orcid.org/0000-0002-5297-5278
Slavko Bogdanov https://orcid.org/0000-0002-9870-2742
Yves Kini https://orcid.org/0000-0002-0428-8430
Sebastien Guillot https://orcid.org/0000-0002-6449-106X
Deepto Chakrabarty https://orcid.org/0000-0001-8804-8946
Wynn C. G. Ho https://orcid.org/0000-0002-6089-6836
Daniela Huppenkothen https://orcid.org/0000-0002-1169-7486
Sharon M. Morsink https://orcid.org/0000-0003-4357-0575
Zorawar Wadiasingh https://orcid.org/0000-0002-9249-0515
Michael T. Wolff https://orcid.org/0000-0002-4013-5650

References

Abbott, B. P., Abbott, R., Abbott, T. D., et al. 2018, PhRvL, 121, 161101
Abbott, B. P., Abbott, R., Abbott, T. D., et al. 2019, PhRvX, 9, 031040
Afle, C., Miles, P. R., Caino-Lores, S., et al. 2023, arXiv:2304.01035
AlGendy, M., & Morsink, S. M. 2014, ApJ, 791, 78
Arzoumanian, Z., Brazier, A., Burke-Spolaor, S., et al. 2018, ApJS, 235, 37
Bilous, A. V., Watts, A. L., Harding, A. K., et al. 2019, ApJL, 887, L23
Biswas, B. 2022, ApJ, 926, 75
Bogdanov, S., Dittmann, A. J., Ho, W. C. G., et al. 2021, ApJL, 914, L15
Bogdanov, S., & Grindlay, J. E. 2009, ApJ, 703, 1557
Bogdanov, S., Guillot, S., Ray, P. S., et al. 2019a, ApJL, 887, L25
Bogdanov, S., Lamb, F. K., Mahmoodifar, S., et al. 2019b, ApJL, 887, L26
Buchner, J., 2021 MultiNest, GitHub, https://github.com/JohannesBuchner/MultiNest
Buchner, J., Georgakakis, A., Nandra, K., et al. 2014, A&A, 564, A125
Chen, A. Y., Yuan, Y., & Vasilopoulos, G. 2020, ApJL, 893, L38
Corongiu, A., Mignani, R. P., Seyffert, A. S., et al. 2021, MNRAS, 502, 935
Ding, H., Deller, A. T., Stappers, B. W., et al. 2023, MNRAS, 519, 4982
Drischler, C., Han, S., Lattimer, J. M., et al. 2021, PhRvC, 103, 045808
Feroz, F., & Hobson, M. P. 2008, MNRAS, 384, 449
Feroz, F., Hobson, M. P., & Bridges, M. 2009, MNRAS, 398, 1601
Feroz, F., Hobson, M. P., Cameron, E., & Pettitt, A. N. 2019, OJAp, 2, 10
Fonseca, E., Cromartie, H. T., Pennucci, T. T., et al. 2021, ApJL, 915, L12
Gralla, S. E., Lupsasca, A., & Philippov, A. 2017, ApJ, 851, 137
Harding, A. K., & Muslimov, A. G. 2001, ApJ, 556, 987
Harding, A. K., & Muslimov, A. G. 2011, ApJ, 743, 181
Ho, W. C. G., & Heinke, C. O. 2009, Natur, 462, 71
Ho, W. C. G., & Lai, D. 2001, MNRAS, 327, 1081
Kalapotharakos, C., Harding, A. K., & Kazanas, D. 2014, ApJ, 793, 97
Kalapotharakos, C., Wadiasingh, Z., Harding, A. K., & Kazanas, D. 2021, ApJ, 907, 63
Lo, K. H., Miller, M. C., Bhattacharyya, S., & Lamb, F. K. 2013, ApJ, 776, 19
Lockhart, W., Gralla, S. E., Özel, F., & Psaltis, D. 2019, MNRAS, 490, 1774
Ludlam, R. M., Miller, J. M., Arzoumanian, Z., et al. 2018, ApJL, 858, L5
Miller, M. C., & Lamb, F. K. 2015, ApJ, 808, 31
Miller, M. C., Lamb, F. K., Dittmann, A. J., et al. 2019, ApJL, 887, L24
Miller, M. C., Lamb, F. K., Dittmann, A. J., et al. 2021, ApJL, 918, L28
Morsink, S. M., Leahy, D. A., Cadeau, C., & Braga, J. 2007, ApJ, 663, 1244
Psaltis, D., Özel, F., & Chakrabarty, D. 2014, ApJ, 787, 136
Raaijmakers, G., Greif, S. K., Hebeler, K., et al. 2021, ApJL, 918, L29
Riley, T. E., Choudhury, D., Salmi, T., et al. 2023, JOSS, 8, 4977
Riley, T. E., Watts, A. L., Bogdanov, S., et al. 2019, ApJL, 887, L21
Riley, T. E., Watts, A. L., Ray, P. S., et al. 2021, ApJL, 918, L27
Rutherford, N., Raaijmakers, G., Prescod-Weinstein, C., & Watts, A. 2023, PhRvD, 107, 103051
Sabatucci, A., Benhar, O., Maselli, A., & Pacilio, C. 2022, PhRvD, 106, 083010
Salmi, T., Vinciguerra, S., Choudhury, D., et al. 2022, ApJ, 941, 150
Salmi, T., Vinciguerra, S., Choudhury, D., et al. 2023, ApJ, 956, 138
Skilling, J. 2004, in AIP Conf. Proc. 735, Bayesian Inference and Maximum Entropy Methods in Science and Engineering, ed. R. Fischer, R. Preuss, & U von Toussaint (Melville, NY: AIP)
Sun, X., Miao, Z., Sun, B., & Li, A. 2023, ApJ, 942, 55
Tang, S. P., Jiang, J. L., Han, M. Z., Fan, Y. Z., & Wei, D. M. 2021, PhRvD, 104, 063032
Timokhin, A. N., & Arons, J. 2013, MNRAS, 429, 20
Vinciguerra, S., Salmi, T., Watts, A. L., et al. 2023a, ApJ, 959, 55
Vinciguerra, S., Salmi, T., Watts, A. L., et al. 2023b, An updated mass-radius analysis of the 2017-2018 NICER data set of PSR J0030+0451, v1.0.0, Zenodo, doi:10.5281/zenodo.8239000
Watts, A. L. 2019, in AIP Conf. Proc. 2127, Xiamen-CUSTIPEN Workshop on the Equation of State of Dense Neutron-Rich Matter in the Era of Gravitational Wave Astronomy, ed. A. Li, B-A Li, & F. Xu (Melville, NY: AIP), 020008
Wilms, J., Allen, A., & McCray, R. 2000, ApJ, 542, 914

The Astrophysical Journal Letters, 918:L28 (31pp), 2021 September 10 https://doi.org/10.3847/2041-8213/ac089b
© 2021. The American Astronomical Society. All rights reserved.

The Radius of PSR J0740+6620 from NICER and XMM-Newton Data

M. C. Miller[1], F. K. Lamb[2,3], A. J. Dittmann[1], S. Bogdanov[4], Z. Arzoumanian[5], K. C. Gendreau[5], S. Guillot[6,7], W. C. G. Ho[8], J. M. Lattimer[9], M. Loewenstein[5,10,11], S. M. Morsink[12], P. S. Ray[13], M. T. Wolff[13], C. L. Baker[14], T. Cazeau[5], S. Manthripragada[15], C. B. Markwardt[16], T. Okajima[5], S. Pollard[5], I. Cognard[17,18], H. T. Cromartie[19,29], E. Fonseca[20,21,22,23], L. Guillemot[17,18], M. Kerr[24], A. Parthasarathy[25], T. T. Pennucci[26,27], S. Ransom[26], and I. Stairs[28]

[1] Department of Astronomy and Joint Space-Science Institute, University of Maryland, College Park, MD 20742-2421 USA; miller@astro.umd.edu
[2] Illinois Center for Advanced Studies of the Universe and Department of Physics, University of Illinois at Urbana-Champaign, 1110 West Green Street, Urbana, IL 61801-3080, USA
[3] Department of Astronomy, University of Illinois at Urbana-Champaign, 1002 West Green Street, Urbana, IL 61801-3074, USA
[4] Columbia Astrophysics Laboratory, Columbia University, 550 West 120th Street, New York, NY 10027, USA
[5] X-Ray Astrophysics Laboratory, NASA Goddard Space Flight Center, Code 662, Greenbelt, MD 20771, USA
[6] IRAP, CNRS, 9 avenue du Colonel Roche, BP 44346, F-31028 Toulouse Cedex 4, France
[7] Université de Toulouse, CNES, UPS-OMP, F-31028 Toulouse, France
[8] Department of Physics and Astronomy, Haverford College, 370 Lancaster Avenue, Haverford, PA 19041, USA
[9] Department of Physics and Astronomy, Stony Brook University, Stony Brook, NY 11794-3800, USA
[10] Department of Astronomy, University of Maryland, College Park, MD 20742-2421, USA
[11] Center for Research and Exploration in Space Science and Technology, NASA/GSFC, Greenbelt, MD 20771, USA
[12] Department of Physics, University of Alberta, 4-183 CCIS, Edmonton, AB T6G 2E1, Canada
[13] Space Science Division, U.S. Naval Research Laboratory, Washington, DC 20375, USA
[14] Applied Engineering and Technology Directorate, NASA Goddard Space Flight Center, Greenbelt, MD 20771, USA
[15] Instrument Systems and Technology Division, NASA Goddard Space Flight Center, Greenbelt, MD 20771, USA
[16] Astrophysics Science Division, NASA Goddard Space Flight Center, Greenbelt, MD 20771, USA
[17] Station de Radioastronomie de Nançay, Observatoire de Paris, CNRS/INSU, Université d'Orleans, F-18330, Nançay, France
[18] 9 Laboratoire de Physique et Chimie de lEnvironnement, CNRS, 3A Avenue de la Recherche Scientifique, F-45071, Orléans Cedex 2, France
[19] Cornell Center for Astrophysics and Planetary Science and Department of Astronomy, Cornell University, Ithaca, NY 14853, USA
[20] Department of Physics, McGill University, 3600 rue University, Montréal, QC H3A 2T8, Canada
[21] McGill Space Institute, McGill University, 3550 rue University, Montréal, QC H3A 2A7, Canada
[22] Department of Physics and Astronomy, West Virginia University, P.O. Box 6315, Morgantown, WV 26506, USA
[23] Center for Gravitational Waves and Cosmology, West Virginia University, Chestnut Ridge Research Building, Morgantown, WV 26505, USA
[24] Space Science Division, Naval Research Laboratory, Washington, DC 20375 5352, USA
[25] Max-Planck-Institut für Radioastronomie, Auf dem Hügel 69, D-53121 Bonn, Germany
[26] National Radio Astronomy Observatory, 520 Edgemont Road, Charlottesville, VA 22903, USA
[27] Institute of Physics, Eötvös Loránd University, Pázmány P.s. 1/A, 1117 Budapest, Hungary
[28] Department of Physics and Astronomy, University of British Columbia, 6224 Agricultural Road, Vancouver, BC V6T 1Z1, Canada
Received 2021 March 13; revised 2021 June 1; accepted 2021 June 4; published 2021 September 8

Abstract

PSR J0740+6620 has a gravitational mass of $2.08 \pm 0.07\,M_\odot$, which is the highest reliably determined mass of any neutron star. As a result, a measurement of its radius will provide unique insight into the properties of neutron star core matter at high densities. Here we report a radius measurement based on fits of rotating hot spot patterns to Neutron Star Interior Composition Explorer (NICER) and X-ray Multi-Mirror (XMM-Newton) X-ray observations. We find that the equatorial circumferential radius of PSR J0740+6620 is $13.7^{+2.6}_{-1.5}$ km (68%). We apply our measurement, combined with the previous NICER mass and radius measurement of PSR J0030+0451, the masses of two other $\sim 2\,M_\odot$ pulsars, and the tidal deformability constraints from two gravitational wave events, to three different frameworks for equation-of-state modeling, and find consistent results at ∼1.5–5 times nuclear saturation density. For a given framework, when all measurements are included, the radius of a $1.4\,M_\odot$ neutron star is known to ±4% (68% credibility) and the radius of a $2.08\,M_\odot$ neutron star is known to ±5%. The full radius range that spans the $\pm 1\sigma$ credible intervals of all the radius estimates in the three frameworks is 12.45 ± 0.65 km for a $1.4\,M_\odot$ neutron star and 12.35 ± 0.75 km for a $2.08\,M_\odot$ neutron star.

Unified Astronomy Thesaurus concepts: X-ray sources (1822); Millisecond pulsars (1062); Neutron stars (1108); Neutron star cores (1107)

1. Introduction

Neutron stars are unique laboratories for the study of dense matter. Their cores consist of matter that is believed to be catalyzed to the ground state, at a few times nuclear saturation density (a mass density $\rho_s \approx 2.7$–$2.8 \times 10^{14}\,\mathrm{g\,cm^{-3}}$, or a baryonic number density $n_s \approx 0.16\ \mathrm{fm^{-3}}$). The combination of high density and the expected large neutron–proton asymmetry in neutron star cores cannot be duplicated in laboratories. Hence, observations of neutron stars can provide us with a valuable window into an otherwise inaccessible realm of nuclear physics.

Over the last several years great strides have been made in neutron star observations, and thus in our understanding of the equation of state (EOS: pressure as a function of energy density) of neutron star matter at high densities (see, e.g., Pavlov & Zavlin 1997; Bhattacharyya et al. 2005; Steiner et al. 2010; Miller 2013; Miller & Lamb 2016; Özel et al. 2016;

[29] NASA Hubble Fellowship Program Einstein Postdoctoral Fellow.

Nättilä et al. 2017 for earlier perspectives). Three neutron stars have a gravitational mass established to be $M \sim 2\,M_\odot$: PSR 1614–2230 with $M = 1.908 \pm 0.016\,M_\odot$ (the uncertainties here and below are for the 68% credible region) (Demorest et al. 2010; Fonseca et al. 2016; Arzoumanian et al. 2018); PSR J0348+0432 with $M = 2.01 \pm 0.04\,M_\odot$ (Antoniadis et al. 2013); and PSR J0740+6620 with $M = 2.08 \pm 0.07\,M_\odot$ (Cromartie et al. 2020; Fonseca et al. 2021). The existence of such high-mass neutron stars indicates that the EOS of neutron star matter is relatively hard, i.e., that it yields high pressures at a few times ρ_s. The lack of a clear signature of tidal deformation in gravitational wave observations of GW170817 (Abbott et al. 2017, 2018; De et al. 2018) and GW190425 (Abbott et al. 2020a) indicates that the EOS is not too hard. When taken together, these high measured masses and the upper limits on the tidal deformability derived from these gravitational wave observations have already narrowed significantly the range of allowed EOS models. The neutron star radius and mass measurements made using data from the Neutron Star Interior Composition Explorer (NICER) are potentially even more informative.

The first simultaneous measurements of the mass and radius of a neutron star made using NICER data were those of the millisecond pulsar PSR J0030+0451, which was determined to have a gravitational mass of $M \approx 1.44 \pm 0.15\,M_\odot$ and an equatorial circumferential radius of $R_e \approx 13 \pm 1$ km (Miller et al. 2019; Riley et al. 2019; compare with the 11.9 ± 1.4 km radius inferred for the two $\sim 1.4\,M_\odot$ neutron stars in the gravitational wave event GW170817; Abbott et al. 2018; De et al. 2018). Assuming that systematic errors in the NICER measurements are unimportant, and hence that the fractional uncertainty of each of these measurements decreases as the inverse square root of the observing time devoted to each pulsar, we expect these uncertainties to become ∼30%–40% smaller within the next few years. A precision this high will improve significantly our understanding of neutron star matter. It is also important to determine whether the masses and radii, and the EOS of neutron star matter, determined using NICER observations of other neutron stars are consistent with those determined using NICER observations of PSR J0030+0451.

In particular, it is valuable to measure the radii of higher-mass neutron stars. Such stars have higher central densities than a $\sim 1.4\,M_\odot$ star, which means that a radius measurement will probe the EOS in a higher-density regime. For example, whereas the measurement of the radius of a $1.4\,M_\odot$ star has its greatest impact on our understanding of matter at 1.6 times nuclear saturation density, the measurement of the radius of a $2.0\,M_\odot$ star tells us primarily about matter at 2.2 times nuclear saturation density (see Section IV.D of Drischler et al. 2021; see also Xie & Li 2020 for additional perspectives on the importance of radius measurements for high-mass neutron stars). As pointed out in the context of the $\sim 1.9\,M_\odot$ pulsar PSR J1614−2230, even a low-precision radius measurement of a high-mass pulsar, or indeed even a solid lower limit to the radius, will be useful in the construction of more accurate EOS for dense matter (Miller 2016).

Here we report our analysis of X-ray data for the $\sim 2.1\,M_\odot$ pulsar PSR J0740+6620, which has a rotational frequency of 346.53 Hz (Cromartie et al. 2020). In contrast to PSR J0030+0451, which is an isolated neutron star, PSR J0740+6620 is in a binary and therefore we have independent measurements of the mass and orbital inclination. This improves the precision of the fits. The challenge presented by PSR J0740+6620 is that its NICER count rate is only ∼5% that of PSR J0030+0451. As a result, counts in NICER data from PSR J0740+6620 are dominated by sources unassociated with the pulsar, to a far greater degree than is true for PSR J0030+0451. This significantly reduces the modulation fraction and harmonic structure in the X-ray pulse waveform, which in turn reduces the information we have about the emitting regions (which we henceforth call "spots") and the mass and radius of the star. If we had precise and reliable information about the background in NICER observations we could use this to improve our mass and radius estimates, but at present we need to turn to other sources of information.

In this Letter we therefore present an analysis of PSR J0740+6620 based on both NICER and X-ray Multi-Mirror (XMM-Newton) data. The NICER data provide information about the modulated emission from the star, which is produced from hot spots on the star as the star rotates. The XMM-Newton data have a far smaller rate of background counts than the NICER data and are therefore informative about the total flux from the star. Combined, the NICER and XMM-Newton data sets thus yield an improved measurement of the modulation fraction and the harmonic structure from PSR J0740+6620, and hence improve the precision with which we can measure the radius. In particular, stronger gravitational lensing allows more of the star to be visible, which lowers the modulation of the signal. Since gravitational lensing depends on the ratio of mass to radius, for fixed mass, an increase in the pulsed fraction means that a larger radius will be inferred if all other parameters are fixed.

In Section 2 we describe the selection of the NICER and XMM-Newton data, including blank-sky XMM-Newton data that have been accumulated over the duration of its mission and that help us refine further our estimate of the stellar flux. In Section 3 we discuss our analysis methods. These are based on the approaches described in previous NICER papers (Bogdanov et al. 2019, 2021; Miller et al. 2019), but are augmented here by the extra data sets and our inclusion of background information from the XMM-Newton blank-sky observations. In Section 4 we present our analysis results including tests of the adequacy of our models; we find that the radius of PSR J0740+6620 is $R_e = 13.7^{+2.6}_{-1.5}$ km at 68% credibility. We also describe several differences between our analysis and that in the parallel paper Riley et al. (2021), in Section 4.6. In Section 5 we present the implications of our PSR J0740+6620 analysis, combined with our previous results on PSR J0030+0451 and other data, for the EOS of cold dense matter. Our conclusions are in Section 6. We present our full corner plots and tables of posteriors in the appendices. Samples from our full posterior probability distributions are available at https://zenodo.org/record/4670689.

2. Observations

2.1. Data Used

We base our analysis of PSR J0740+6620 on NICER event data that included individual event times, event energies, and event pulsation phase. Our observing strategy and data reduction resulted in a data set with very low noise properties, as was necessary because of the faintness of this pulsar.

Our analysis of the X-ray data on PSR J0740+6620 comes from a series of 215 observations obtained with NICER XTI collected between 2018 September 21 and 2020 April 17, with

a net exposure time of 1602.68 ks (after all filtering was applied, as described below). The final event data were obtained using the following filtering criteria: (i) we only included ObsIDs when all 52 NICER detectors were active; (ii) we excluded events with energies outside the range 0.3–3.0 keV; (iii) we excluded events from DetID 34 (which frequently exhibits elevated count rates compared to the average); (iv) we only considered time intervals when PSR J0740+6620 was situated at least 80° from the Sun to minimize optical loading and scattered solar X-ray background photons; and (v) we rejected data obtained at low cut-off rigidities (COR_SAX < 5) to minimize particle background contamination. The filtered events were assigned pulse phases using the PSR J0740+6620 ephemeris from Fonseca et al. (2021). This event list ultimately consisted of 7334 separate good time intervals (GTIs). We then searched this event list for the pulsar signal. If the events in a particular GTI did not increase the pulsar signal to noise we rejected that GTI. The pulsar detection significance was highest in the energy range 0.31 to 1.18 keV. Ultimately, after all filtering and other exclusions were finished, we ended up with 521,004 NICER XTI events. The details of the NICER observations and pulse detection for PSR J0740+6620 can be found in Wolff et al. (2021).[30]

We use the latest available calibration products, namely the nixtiref20170601v002 redistribution matrix file and the nixtiaveonaxis20170601v004 ancillary response file (ARF). For the latter, the effective areas per energy channel were corrected by a factor of 51/52 to account for the removal of all events from DetID 34. The response properties of NICER incorporated in these calibration products represented the best effort by the instrument modeling team that were available in August 2020 when the analysis presented here was begun.

PSR J0740+6620 was also targeted with XMM-Newton on three separate occasions: 2019 October 26 (ObsID 0851181601), 2019 October 28 (ObsID 0851181401), and 2019 November 1 (ObsID 0851181501) as part of a Director's Discretionary Time program. All three European Photon Imaging Camera (EPIC) instruments (pn, MOS1, and MOS2) were operated in "Full Frame" imaging mode with the "Thin" filters in the optical path. Due to the long detector read-out times (73.4 ms for EPIC-pn and 2.6 s for EPIC-MOS1/2), the data do not permit a pulse-phase-resolved analysis. Data summed over phase are used in the analysis that follows. The XMM-Newton data were processed with the Science Analysis Software (SAS[31]) using the recommended procedures. We employed the recommended event grade PATTERN and FLAG values that ensured only real photon events recorded by the instruments were included in our analysis ($\leqslant 12$ for MOS1/2 and $\leqslant 4$ for pn). All three of these XMM-Newton observations were obtained while the satellite was in a part of its orbit that suffered from intense particle flaring effects. Only 6.8 ks of the total 20.8 ks of EPIC-pn exposure had sufficiently low background to be used in our analysis, and only 18.0/18.7 ks of the total 26.7/34.3 ks of MOS1/2 exposures could be utilized. A circular extraction region of radius 25″ centered on the radio timing position of PSR J0740+6620 was used to produce clean source event lists. The XMM-Newton instrument response files specific to the PSR J0740+6620 observations were then generated using the rmfgen and arfgen tools in SAS.

Under normal observing circumstances, one uses regions near the target source in the instrument image plane from the same observations to estimate the observational background. In our case, however, due to the short durations of these observations, very few background counts were available to estimate the background. As an alternative, we obtained representative background estimates with longer exposures from the blank-sky event files provided by the XMM-Newton Science Operations Centre. The blank-sky images were filtered in the same manner as the PSR J0740+6620 images and the background was extracted from the same location on the detector image plane as the pulsar. The resulting background spectrum was then rescaled so that the exposure times and pixel-area factors matched those of the PSR J0740+6620 exposures.

2.2. Calibration of the Instruments

The effective area of the NICER XTI is determined primarily using observations of the Crab pulsar and nebula. The energy-dependent residuals in the fits to the Crab spectrum are typically at the level of $\lesssim 2\%$.[32] The calibration accuracies for the XMM-Newton EPIC-MOS and EPIC-pn cameras are determined to better than 3% and 2% (at 1σ), respectively.[33] However, in the absence of a suitable absolute calibration source, the uncertainties in the absolute energy-independent effective areas that we use for the NICER XTI and the three XMM-Newton detectors are estimated to be no more than $\pm 10\%$ (e.g., Figure C2 in Ricci et al. 2021; see Section 3.7 for further discussion).

3. Methods

Our approach to modeling the X-ray data is largely the same as it was in Miller et al. (2019), except that for our analysis of PSR J0740+6620 we used both NICER and XMM-Newton data, and we used blank-sky observations to estimate the non-source counts in the XMM-Newton data. In Section 3.1 through Section 3.3, we summarize briefly the approaches used in Miller et al. (2019), and refer the reader to that paper for details and tests of our procedures. In Section 3.4 we discuss the new aspects of our fitting procedure, which include analyzing multiple data sets and incorporating independent estimates of the background made using the XMM-Newton data. We conclude this section with short discussions of our parameter estimation procedure in Section 3.5 (which is the same as was described in Miller et al. 2019), our choice of energy channels in Section 3.6 (which is different from the choice made in Miller et al. 2019 because we are using an updated energy calibration for NICER and because we also use XMM-Newton data in our analysis), and the effects of a possible difference in the absolute calibration of NICER and XMM-Newton in Section 3.7.

[30] See https://heasarc.gsfc.nasa.gov/docs/nicer/mission_guide/ for the standard definitions of the observational terms used in this section.

[31] The XMM-Newton SAS is developed and maintained by the Science Operations Centre at the European Space Astronomy Centre and the Survey Science Centre at the University of Leicester.

[32] See https://heasarc.gsfc.nasa.gov/docs/heasarc/caldb/nicer/docs/xti/NICER-xti20200722-Release-Notesb.pdf for further details.

[33] See in particular Table 1 in https://xmmweb.esac.esa.int/docs/documents/CAL-TN-0018.pdf.

3.1. Modeling the Emission from the Stellar Surface

The soft X-ray emission from old, non-accreting pulsars such as PSR J0740+6620 is believed to be generated when particles with large ($\gg$100) Lorentz factors are produced in pair cascades and deposit their energy deep in the atmosphere of the neutron star (Tsai 1974; Harding & Muslimov 2001, 2002; Bogdanov et al. 2007; see Bauböck et al. 2019 and Salmi et al. 2020 for explorations of the consequences for the beaming pattern of emission from the stellar surface if significant energy is in particles with lower Lorentz factors). The specific intensity as a function of the angle between the photon propagation direction and the local surface normal depends on the assumed composition, the ionization state, and the strength (and potentially the orientation) of the surface magnetic field at the point of emission.

We follow Miller et al. (2019) in assuming that the atmosphere is pure hydrogen and that the magnetic field can be neglected. We now discuss this in more detail.

Composition of the upper atmosphere. The surface gravity of a neutron star is great enough that the lightest element present is expected to float to the top within seconds to minutes (based on extrapolations of the calculations in Alcock & Illarionov 1980). As hydrogen is also the most abundant element in the universe and PSR J0740+6620 likely underwent prolonged accretion to reach its current rotational frequency, it is probable that the atmosphere is pure hydrogen (Blaes et al. 1992; Wijngaarden et al. 2019, 2020). Note that there are some accreting neutron star binaries in which the transferred matter is thought to have little to no hydrogen (such as 4U 1820−30; see, e.g., Strohmayer & Brown 2002), but such binaries have extremely short orbital periods (e.g., Stella et al. 1987 find that the orbital period of 4U 1820−30 is just 685 s). Thus the binary is very compact and as a result the hydrogen envelope is believed to have been completely stripped off. In contrast, the binary containing PSR J0740+6620 has an orbital period of 4.77 days (Cromartie et al. 2020) and the companion could therefore have had a significant hydrogen envelope. Even if the accreted elements were primarily heavier than hydrogen, spallation might create enough hydrogen to dominate the atmosphere (Bildsten et al. 1992; Randhawa et al. 2019).

Ionization fraction. The hot spots on PSR J0030+0451 were inferred to have effective temperatures (i.e., the temperature of a blackbody that would produce a bolometric photon flux equal to the bolometric photon flux produced by the model atmosphere we are considering, which is not a blackbody) $kT_{\rm eff} > 0.1$ keV (Miller et al. 2019; Riley et al. 2019), which implies that essentially all atmospheric hydrogen is completely ionized. The fits we find for PSR J0740+6620 have effective temperatures $kT_{\rm eff} \gtrsim 0.08$ keV for both spots, which also implies nearly full ionization. However, the atmospheric densities are high enough that some neutral atoms may be present. We therefore performed fits using the NSX code for model atmospheres assuming full ionization (Ho & Lai 2001) and also with partial ionization (Ho & Heinke 2009; see Badnell et al. 2005 for the relevant opacity tables). We find no significant difference in the inferred mass and radius between the results obtained using our two different ionization assumptions. This is consistent with previous work (Lo et al. 2013; Miller & Lamb 2015), which finds that in analyses of phase-channel X-ray data such as is collected using NICER, even if the assumptions used in the fit deviate from the properties of the star there is no significant bias in the mass and radius if the fit appears to be statistically good (as measured by, e.g., χ^2/dof or other standard statistics). Here we report only on runs that allow for the possibility of partial ionization.

Effect of the magnetic field on the soft X-ray emission from the stellar surface. Using Equation (12) of Contopoulos & Spitkovsky (2006), assuming a magnetic field inclination of $\pi/2$ and $\alpha = 0$ for the magnetic field configuration, the period $P = 0.00289$ s and period derivative $\dot{P} = 1.219 \times 10^{-20}$ of PSR J0740+6620 (Cromartie et al. 2020) imply that for a centered dipole the polar magnetic field at the surface is $B \approx 3 \times 10^8$ G. The electron cyclotron energy at that field strength is $\approx$3 eV, which has a small effect on atomic structure (Lai 2001; Potekhin 2014) and is $\sim$100 times lower than the lowest energies we consider in our fits. The spot configuration resulting from our analysis is close enough to a centered dipole that it is plausible that the effects of the field on radiative transfer are negligible. For example, in our best fit the two spots are separated by $\approx$2 radians on the surface. The chord length is therefore $\approx \sin(1) \approx 0.84$ times smaller than a diameter, so if the magnetic field is a dipole centered between the two spots then the field strength at the surface is $\approx 1/0.84^3 \approx 1.7$ times larger than it would be if the field were centered at the center of the star. Thus in this example the surface magnetic field at the spots would increase only to $\approx 5 \times 10^8$ G. We follow Miller et al. (2019) in noting that if the field is strong enough to change significantly the spectrum and beaming pattern, then fits assuming a negligible field would likely be statistically poor and/or would yield unreasonable parameter values. Therefore the good quality of our fits could be considered an argument in favor of our assumption that the field can be neglected. However, this conclusion is not certain and a rigorous resolution of this question would require the construction, and use in fits, of atmospheric models with a fine grid of magnetic field strengths and orientations to the local surface normal. Such models are challenging to compute at the required $B \sim 10^9$–10^{10} G because at those field strengths Coulomb and magnetic effects are comparable to each other.

3.2. Our Approach to Modeling the Soft X-Ray Waveform

Our modeling of the NICER pulse waveform of PSR J0740+6620 builds on the modeling of the waveform of PSR J0030+0451 discussed in Miller et al. (2019); see Bogdanov et al. (2019, 2021) for detailed descriptions of how we computed pulse waveforms and tested their accuracy. The waveform of PSR J0740+6620 has two clear peaks and therefore cannot be modeled using a star with a single circular hot spot. Unlike for PSR J0030+0451, and possibly related to the faintness of PSR J0740+6620 and hence the much smaller number of counts in its pulse waveform, we find that a model with two uniform circular hot spots produces a waveform that adequately fits the data, and that adding complexity to the temperature pattern on the stellar surface does not improve the fit. For example, adding a third hot spot to the model or allowing the spots to be oval rather than circular did not improve the fit. We therefore fit the NICER and XMM-Newton data for PSR J0740+6620 using a pulse waveform produced by two uniform-temperature circular spots.

Once the number of spots to be considered and their allowed shapes (e.g., oval or circular) are specified, our spot modeling algorithm automatically explores the full parameter space, to find the configurations with the highest likelihoods (see Miller et al. 2019). The algorithm not only considers configurations in

Table 1
Primary Parameters of the Pulse Waveform Models Considered in This Work

Parameter	Definition	Assumed Prior
$c^2R_e/(GM)$	Inverse of stellar compactness	3.2–8.0
M	Gravitational mass	$\exp[-(M - 2.08\,M_\odot)^2/2(0.09\,M_\odot)^2]$
θ_{c1}	Colatitude of spot 1 center	0 to π radians
$\Delta\theta_1$	Spot 1 radius	0–3 radians
$kT_{\rm eff,1}$	Spot 1 effective temperature	0.011–0.5 keV
$\Delta\phi_2$	Spot 2 longitude difference	0–1 cycles
θ_{c2}	Colatitude of spot 2 center	0 to π radians
$\Delta\theta_2$	Spot 2 radius	0–3 radians
$kT_{\rm eff,2}$	Spot 2 effective temperature	0.011–0.5 keV
$\theta_{\rm obs}$	Observer inclination	1.44–1.62 radians
N_H	Neutral H column density	$0–20 \times 10^{20}$ cm^{-2}
d	Distance	$\exp[-(d - 1.136\,{\rm kpc})^2/2(0.2\,{\rm kpc})^2]$, $d \geqslant 1.136$ kpc
		$\exp[-(d - 1.136\,{\rm kpc})^2/2(0.18\,{\rm kpc})^2]$, $d \leqslant 1.136$ kpc
$A_{\rm XMM}$	XMM-Newton effective area divided by nominal area	0.9–1.1

Note. Except where noted, the prior is flat over the given range.

which the spots are disjoint or in contact, but also configurations in which they partially or completely overlap. This allows the algorithm to model approximately spots with temperature gradients, if these are favored by the data, by allowing spots with different temperatures to partially or completely overlap. This is done by assigning a number to each of the spots. For example, for the two-spot model used here, the spots are labeled 1 and 2. Points on the stellar surface that are covered by both spots are assumed to emit with the effective temperature of the lower-numbered spot. This labeling, and the precedence given to the emission by the lower-numbered spot, is not related to any other property of the spot. For example, the effective temperature of spot 1 could be either higher or lower than the effective temperature of spot 2. This approach is highly flexible, and can be generalized to any number of spots (see Miller et al. 2019 for details). For example, in addition to the best-fit solution we feature in this work, our algorithm also found a lower-likelihood solution with a large, crescent-shaped emitting region that it modeled using a spot with a temperature so low that it is essentially dark lying on top of a hotter spot. This solution is disfavored by a Bayes factor greater than 3000 as measured by MultiNest (see Section 3.5), so we have set it aside for the purposes of this work.

Section 4 of Miller et al. (2019) reported the results of an analysis of synthetic NICER pulse waveform data constructed assuming two, uniform-temperature, circular hot spots, and separately, an analysis of synthetic data assuming two, uniform-temperature, oval hot spots. In both cases, the values of the model parameters inferred from the analysis was consistent with those assumed in constructing the synthetic pulse waveform data. As another test of our analysis algorithm, in Section 4.1 we report a joint analysis of synthetic NICER and XMM-Newton pulse waveform data sets that were generated using the hot-spot model that we found provides a good description of the actual NICER and XMM-Newton data on PSR J0740+6620. This analysis includes analyses of four separate data sets, each with a realistic background.

3.3. Waveform Models

The parameters used in the pulse waveform modeling we report here are listed and defined in Table 1, with their assumed priors. We assume that the effective temperature is uniform over a given spot.

Because PSR J0740+6620 is in a binary system, we have additional information on some of the parameters, beyond that provided by the NICER and XMM-Newton data. In particular, Fonseca et al. (2021) find that at 68% credibility the mass is $M = 2.08^{+0.072}_{-0.069}\,M_\odot$, the distance is $1.136^{+0.174}_{-0.152}$ kpc, and our line of sight makes an angle of $87\overset{\circ}{.}5 \pm 0\overset{\circ}{.}17$ to the orbital axis of the system.

We caution that other lines of evidence imply that PSR J0740+6620 has a lower mass. Prominent among these is that there is an observationally established correlation between the white dwarf mass and the orbital period in white dwarf binaries (Tauris & Savonije 1999; Tauris & van den Heuvel 2014), which would suggest a strong upper limit of $2\,M_\odot$ to the mass of PSR J0740+6620. If the mass is indeed less than our current best estimate, the main effect will be to decrease our estimate of the radius. Although it is not generally true that the compactness $GM/(Rc^2)$ is measured to better fractional precision than the radius (see Section 4 of Bogdanov et al. 2021), this is true for PSR J0740+6620 because, as we discuss in more detail below, the most important information about the radius comes from the modulation fraction. A star that is more compact will deflect light rays coming from its surface by a larger angle, allowing a given observer to see more of the surface, which reduces the modulation fraction the observer sees. As a result, this estimate of the radius of PSR J0740+6620 is roughly proportional to its mass. Because the fractional uncertainty in the compactness of PSR J0740+6620 is large, even an estimated mass of (for example) $1.8\,M_\odot$ would produce a radius posterior that largely overlaps the posterior we report here. For example, if the centroid of the mass prior were $1.8\,M_\odot$ rather than $2.08\,M_\odot$, and the fractional prior mass uncertainties were the same as for our standard mass priors, then our $\pm 1\sigma$ radius range would be 10.6–14.1 km rather than 12.2–16.3 km.

We use the radio observations of Fonseca et al. (2021) to impose a Gaussian prior on the mass of $M = 2.08 \pm 0.09\,M_\odot$, where we have linearly added an estimated systematic error of $0.02\,M_\odot$ to the mass estimate from Fonseca et al. (2021; E. Fonseca, personal communication), and an asymmetric Gaussian prior probability distribution (see Table 1 for the

functional form) centered at $d = 1.136$ kpc with 68% cumulative probability points at $d = 0.956$ kpc and $d = 1.336$ kpc, where we have placed the 68% cumulative probability points 0.03 kpc further from the central value than the quoted statistical uncertainty, to reflect the 0.03 kpc estimated systematic error (E. Fonseca, personal communication).

Our analysis depends on the inclination of our line of sight to the pulsar's rotational axis. Millisecond pulsars such as PSR J0740+6620 are believed to be recycled by accreting matter from their companion stars (see, e.g., Bhattacharya & van den Heuvel 1991). Consequently, the orientation of their rotational axis is thought to be determined by the angular momentum of the matter accreted from the companion; accretion of this matter is expected to gradually align the pulsar's rotational axis with the orbital axis of the system. However, this alignment is not expected to be perfect, and the current rotational axis of the pulsar may therefore be tilted by a few degrees relative to the orbital axis of the binary system. For the analyses reported here, we have adopted a prior on the angle between the observer's line of sight and the pulsars rotation axis that is flat within 5° of the best estimate of the system's orbital inclination, which is 87°.5, and zero outside this range. We find that the inferred mass and radius of PSR J0740+6620 are insensitive to the precise value of the orbital inclination with this range (see the corner plots in the Appendices and the discussion in Section 4.4).

3.4. Our Waveform Modeling Procedure

For PSR J0030+0451 we had only NICER data to analyze. In contrast, for PSR J0740+6620 we also had XMM-Newton imaging data from pn, MOS1, and MOS2. We therefore need to model all four data sets jointly. Once we have full models including backgrounds for all four data sets, then the log likelihood of the data given the model is simply the sum of the log likelihoods of each of the individual data sets. Thus

$$\ln \mathcal{L}_{\rm tot} = \ln \mathcal{L}_{\rm NICER} + \ln \mathcal{L}_{\rm XMM-pn} + \ln \mathcal{L}_{\rm XMM-MOS1} + \ln \mathcal{L}_{\rm XMM-MOS2}. \quad (1)$$

In writing the total log likelihood this way, we are assuming that the data sets are uncorrelated with each other. This assumption is clearly justified for the independent NICER and XMM-Newton data. It is also reasonable for the three XMM-Newton data sets because the pn, MOS1, and MOS2 cameras are all separately mounted and read out on XMM-Newton; there is no plausible mechanism that would link counts in one detector with counts in another detector.

For each individual data set we compute the log likelihood by summing the log Poisson likelihood of the data given the model in all of the phase bins and energy channels, neglecting the log factorial term that is common to all models. That is, if we have broken the data into bins ϕ_i in rotational phase, and energy channels E_j, and in each phase-channel bin the model predicts m_{ij} counts (a positive real number) and d_{ij} counts are observed (a non-negative integer) then the Poisson likelihood of the data given the model in that phase-channel bin is $[m_{ij}^{d_{ij}}/d_{ij}!]e^{-m_{ij}}$. However, the factor $1/d_{ij}!$ is common to all models and hence can be neglected in both parameter estimation and model comparison. The log likelihood we use is therefore

$$\ln \mathcal{L} = \sum_{\phi_i}\sum_{E_j}(d_{ij}\ln m_{ij} - m_{ij}), \quad (2)$$

where there is an implied sum over all four instruments. The NICER data have 32 phase bins. In contrast, for each of the three XMM-Newton data sets, we have only one bin in the rotational phase because the timing resolution is insufficient to divide the data further.

We now discuss the two components of the calculation of m_{ij} for each phase-channel bin in each data set: the computation of the model counts from the spots for each of the four instruments, which is straightforward, and the incorporation of phase-independent background counts, which is more involved and requires different treatments for the NICER and for the XMM-Newton data.

3.4.1. Calculation of the Model Counts from the Spots

Suppose that we are considering a particular parameter combination, i.e., we have some combination of M, R_e, $\theta_{\rm obs}$, …, to assess. Given the specified observation time, this gives us a spots-only waveform that is unique up to an arbitrary definition of the time corresponding to phase 0. As described in Section 3.4 of Miller et al. (2019), once we have a candidate waveform that includes both the contribution from the spots and the contribution from the phase-independent background, we marginalize over the overall phase by assuming that near the peak the likelihood as a function of phase, $\mathcal{L}(\phi)$, can be approximated by a Gaussian in the phase.[34] We only need to carry out this process for the NICER data, because the XMM-Newton data have only one phase.

3.4.2. Inclusion of Unmodulated Background

By "background" we mean any X-ray counts that are not contributed by the spots. This could include space weather, optical loading, resolved or unresolved background or foreground sources, the instruments themselves, or, in the case of a binary such as PSR J0740+6620, the companion star (e.g., interactions of the neutron star particle wind with the companion star could produce X-rays). What these have in common is that those X-rays are not modulated at the rotational frequency of the star and hence with enough exposure time they contribute equally at all rotational phases.

Miller et al. (2019) therefore treated all non-stellar X-rays with a single approach, which we adopt here for the NICER data: for each energy channel independently we allow there to be a phase-independent component of any magnitude. We therefore do not assume any particular spectral form for the non-stellar emission, but in practice this results in an estimated background that varies smoothly with energy channel. The assumption of independence between channels means that, as with the phase, we fit a Gaussian to the likelihood of each energy channel as a function of added background, and can then analytically integrate the likelihood to marginalize over the background. See Miller et al. (2019) for more details. We also note (see Section 4.2 for a more thorough discussion) that future analyses may be able to incorporate estimates of the

[34] This is equivalent to fitting a parabola to $\ln \mathcal{L}(\phi)$ near the peak of the log likelihood. Note that the likelihood for a given phase need not be Gaussian for this approximation to be useful.

NICER background rather than letting the background be completely free.

The XMM-Newton data must be treated differently, because there is only one phase bin, in contrast to the 32 rotational phase bins that we use for the NICER data. To understand why, suppose that we treat the XMM-Newton background, for any instrument, in the same way that we treat the NICER background: each energy channel (with its single phase) can have added to it any number of background counts. Then the best model for the XMM-Newton data would have zero counts from the spots, and the background would equal the observed number of counts. This would automatically maximize the log likelihood. The NICER data are not driven to this pathological fit because there is clear modulation in the data; a phase-independent, background-only fit cannot reproduce this modulation.

Therefore, we instead assume that the blank-sky background is a Poisson realization of the full XMM-Newton background. Each of the XMM-Newton instruments has had, throughout the course of the mission, significant exposure to portions of the sky with no known X-ray sources (see Section 2). The total blank-sky count rate in the XMM-Newton energy channels of interest is ∼20%–30% of the count rate in our XMM-Newton observations of PSR J0740+6620, so incorporation of this background is expected to make a meaningful difference to our analysis. We note that there are other possible contributions than the blank sky to the phase-independent background. For example, as mentioned above, the interaction of the pulsar wind with the binary companion could produce X-rays. Because the total count rate is fixed, if the background is larger then the estimated total count rate from the neutron star is reduced. As a result, the modulation fraction is increased because the modulated count rate is fixed by the NICER observations. In turn, this would increase the inferred radius for PSR J0740+6620. In our treatment we effectively assume that these other contributions can be neglected.

Even with hundreds of thousands of seconds of total exposure time, the total number of counts from the blank-sky observations is too small in many of the energy channels to use Gaussian statistics. Therefore we need to use Poisson statistics. Our approach to the pn, MOS1, and MOS2 backgrounds is as follows.

Consider some particular XMM-Newton energy channel n for one of the three instruments. Suppose that the blank-sky observation had duration $T_{\rm back}$ and yielded $b_{\rm back}$ counts. If the prior on the background counts is flat, then the Poisson probability distribution for the time-averaged number of counts $b_{\rm avg}$ for an interval $T_{\rm back}$ is

$$P(b_{\rm avg})db_{\rm avg} = (1/b_{\rm back}!)b_{\rm avg}^{b_{\rm back}}\exp(-b_{\rm avg})db_{\rm avg}. \quad (3)$$

Now suppose that for the XMM-Newton instrument under consideration the PSR J0740+6620 observation has a duration of $T_{\rm obs}$. Then a given $b_{\rm avg}$ implies an expected number of counts $b_{\rm obs} = b_{\rm avg}(T_{\rm obs}/T_{\rm back})$ counts in that observation. Then because $b_{\rm avg} = (T_{\rm back}/T_{\rm obs})b_{\rm obs}$, Equation (3) implies that the normalized probability distribution for $b_{\rm obs}$ is

$$P(b_{\rm obs})db_{\rm obs} = (1/b_{\rm back}!)[b_{\rm obs}(T_{\rm back}/T_{\rm obs})]^{b_{\rm back}}\exp \times [-b_{\rm obs}(T_{\rm back}/T_{\rm obs})](T_{\rm back}/T_{\rm obs})db_{\rm obs}. \quad (4)$$

If the energy channel had d observed counts in our PSR J0740+6620 observation, then the probability of obtaining that in a model with m expected counts is

$$p(d|m) = m^d/d!\,\exp(-m). \quad (5)$$

If in our model we have s expected counts from the spots, then given a background b we expect a total number of counts $m = s + b$. Setting $b = b_{\rm obs}$ as above, we find that the final likelihood of the data d given the spot counts s and the distribution $P(b_{\rm obs})db_{\rm obs}$ is

$$p(d|s, \text{back}) = \int_0^\infty [(s + b_{\rm obs})^d/d!]\exp \times [-(s + b_{\rm obs})]P(b_{\rm obs})db_{\rm obs}. \quad (6)$$

We find that we achieve sufficient precision for this integral by (1) setting a scale for $b_{\rm obs}$ that is $T_{\rm obs}/T_{\rm back}$ if $b_{\rm back} = 0$, or $b_{\rm back}(T_{\rm obs}/T_{\rm back})$ otherwise, and (2) performing a Simpson's rule integration from 0 to 6.8 times that scale, in intervals of 0.1 times that scale.

3.5. Parameter Estimation and Model Evaluation

As in Miller et al. (2019), we began our sampling of parameter space using the publicly available nested sampler MultiNest (Feroz et al. 2009), typically with 1000 live points, a target efficiency of 0.01 (with variable efficiency), and a tolerance of 0.1. The inverse of the efficiency parameter determines the factor by which the bounding hyperellipsoids constructed by MultiNest are expanded before samples are drawn from within them (see Section 5.2 of Feroz et al. 2009). Lower efficiency means more thorough sampling, and better accommodation of isolikelihood surfaces that are not well-described by ellipsoids. We chose an efficiency of 0.01, which is more than an order of magnitude below the standard recommendation, because we found in early tests that when we fixed the number of live points to 1000 and used efficiencies of 0.1 and 0.03 the $\pm 1\sigma$ credible regions for the radius were, respectively, 45% and 22% narrower than for our efficiency = 0.01 runs, and thus that the sampling at these higher efficiencies with 1000 live points was incomplete.

MultiNest is designed to estimate the Bayesian evidence for a model, and can also provide a quick characterization of parameter space. However, the purpose of nested samplers such as MultiNest is to compute the evidence; convergence of that calculation does not guarantee convergence of the posteriors of the parameters. Studies have shown that nested samplers of this type can give incorrectly small credible regions if isolikelihood surfaces cannot be well-represented by overlapping hyperellipsoids (Buchner 2014, 2021; Nelson et al. 2020). This appears be the case for our PSR J0740+6620 parameter estimation; we found that the parameter space was not completely explored even at the lowest efficiencies and largest number of live points that we employed. As one example, when we used MultiNest to analyze just the NICER data with 1000 live points, a target efficiency of 0.01, and a tolerance of 0.1, the ±1 standard deviation range in the radius posterior had 67% of the width we obtained using parallel-tempered emcee (see the next paragraph). When we used 3000 live points, a target efficiency of 0.01, and a tolerance of 0.1 the width increased, but only to 79% of the emcee width.

We therefore use a kernel density estimate of the MultiNest posteriors to produce the initial positions of the walkers, which we find expedites convergence, especially for multi-modal posteriors, in the parallel-tempered Markov chain Monte Carlo

(MCMC) sampler PT-emcee that is included in the publicly available emcee package, version 2.2.1 (Foreman-Mackey et al. 2013). Because MCMC samplers are designed to satisfy detailed balance, there is a theoretical expectation that the samples will represent the posterior. For the PT-emcee runs we had 1000 walkers per parallel-tempering temperature rung; exploratory runs with 2000 walkers per rung produced results that were consistent with what we report here. We started with five temperature rungs, but found that the number of rungs was not critical and reduced the number to two later in the sampling.

3.6. Choice of Energy Channels

In their analysis of the PSR J0030+0451 data, Miller et al. (2019) used only NICER energy channels 40 and above, because they found that inclusion of lower-energy channels biased the inferred distance. For our analysis of the PSR J0740+6620 data we use the updated 2020 July NICER response (see https://heasarc.gsfc.nasa.gov/docs/heasarc/caldb/nicer/). With this response there does not appear to be any bias in distance or other quantities when we use data down to energy channel 30. Analysis of the NICER data showed that the detection significance is optimized when we use channels up to 118 (see Section 2.1), but there is also an excess of counts relative to the background up to channel ∼150. We used a range between these (channels 30 through 123 inclusive), but exploratory runs including channels up to 150 did not produce palpably different results. Given that the width of the NICER channels is 0.001 keV, our energy channel choice corresponds approximately to photon energies between 0.3 keV and 1.23 keV. For the XMM-Newton data, we used channels 57−299 inclusive for pn, channels 20−99 inclusive for MOS1, and channels 20−99 inclusive for MOS2.

3.7. Relative Normalization of NICER and XMM-Newton

In addition to the uncertainty in the energy-dependent response of an instrument, there is inevitably some uncertainty in the overall response. That is, the overall normalization of the response is not known perfectly. A conservative upper limit on the fractional uncertainty of the relative normalization between NICER and the three XMM-Newton instruments is ∼10%.[35] The three XMM-Newton instruments are thought to have the same overall normalization to ∼2–3%, which are differences small enough to be neglected. Errors in the overall normalization of NICER are absorbed in the >15% half-width of our prior on the distance. However, there is still a question of whether the overall normalizations of NICER and XMM-Newton could affect our fits.

To explore this, we report in Section 4.2 an additional fit in which we add one more parameter: $A_{\rm XMM}$, which is a single number that multiplies the ARFs of all three XMM-Newton instruments that we consider. We explore the consequences of allowing $A_{\rm XMM}$ to be between 0.9 and 1.1, i.e., the largest possible range. We therefore account for a possible inaccuracy in the ARF of NICER by the freedom in the fit to the distance to the source, and for an additional independent inaccuracy of the ARF of the XMM-Newton instruments using $A_{\rm XMM}$. We find that introduction of the parameter $A_{\rm XMM}$ does not produce a significant change in the posteriors of any of our parameters (for example, the radius limits are changed by at most 0.1 km) and the value of $A_{\rm XMM}$ that we infer is consistent with 1.

[35] For the cross-calibration as of December 2018 see the lower panel of Figure C2 in Ricci et al. (2021). For the cross-calibration as of November 2020 see slide 7 of http://iachec.org/wp-content/presentations/2020/NICER-CrossCal-IACHEC-Markwardt-2020b.pdf and note in particular that in the energy range relevant to our analyses, 0.3–1 keV, the flux inferred from 3C 273 agrees between NICER and XMM-Newton to better than 4%.

4. Results of the Analysis of the NICER and XMM-Newton Pulse Waveform Data

Our joint fit of our two-circular-spot model to the NICER and XMM-Newton data yields an equatorial circumferential radius of $R_e = 13.7^{+2.6}_{-1.5}$ km at 68% credibility for PSR J0740+6620. In this section we describe how we reach this conclusion. In Section 4.1 we demonstrate that our method produces statistically expected results when we fit our model to a synthetic data set that is drawn from a good fit to the PSR J0740+6620 data including backgrounds, and is therefore realistic. In Section 4.2 we present our fits to just the NICER data on PSR J0740+6620, and to the NICER and XMM-Newton data combined. We show that although the radius posteriors in the two analyses have significant overlap, inclusion of the XMM-Newton data favors larger radii. In Section 4.3 we show that our sampling of the parameter space has converged. In Section 4.4 we address the effects of priors, and show that other choices for the upper limit of the radius and the allowed range of the observer inclination have little effect on the -1σ radius, which is particularly important in EOS inference (see Section 5). In Section 4.5 we address the adequacy of our model. We show that our model provides acceptable fits to the phase-channel NICER data, the bolometric NICER data, and the XMM-Newton data from all three cameras. There is therefore no indication that our model for the PSR J0740+6620 data is deficient. Finally, in Section 4.6 we note some differences between our analysis method and that of Riley et al. (2021), and suggest which of those differences could be important in producing different radius posteriors between the two groups.

In this section we consider values of $R_{\rm eq}c^2/(GM)$ up to 8.0, which corresponds to a radius ∼24 km at $M \sim 2\,M_\odot$. We find that the radius posterior does not have significant probability near this boundary, and thus that this boundary does not bias our radius estimates. When we explore the implications of results for the EOS in Section 5, we include information from nuclear theory and previous measurements.

4.1. Fits to Synthetic NICER and XMM-Newton Data

Joint analyses of NICER and XMM-Newton data have not previously been performed in the context of neutron star mass and radius estimation. It is therefore important to demonstrate that our method yields the expected results when similar synthetic data are analyzed, because for synthetic data we know the parameter values used to construct the data and can therefore judge the quality of the fit.

To generate the data we started from a good model of the PSR J0740+6620 NICER and XMM-Newton data, including all backgrounds. We then produced the synthetic data by drawing integer numbers of counts from our (in general non-integer) model expectation in each phase-channel bin for NICER, and in each energy channel for each of the three XMM-Newton cameras. We emphasize that this leads to synthetic data with fully realistic backgrounds; previous synthetic data analyses (e.g., Lo et al. 2013; Miller & Lamb 2015; Miller et al. 2019; Bogdanov et al. 2021) have instead

Table 2
Verification of Fits to Synthetic NICER and XMM-Newton Data

Sampler	$\pm1\sigma$ (68.3%)	$\pm2\sigma$ (95.4%)	±3 σ (99.7%)
PT-emcee	6	11	12
MultiNest (Nlive = 1000, efficiency = 0.01)	4	7	9
MultiNest (Nlive = 2000, efficiency = 0.01)	4	8	11

Note. Results of fits to synthetic J0740-like NICER and XMM-Newton data using parallel-tempered emcee and two different settings of MultiNest. The right three columns show the number of parameters, out of 12, for which the values assumed in constructing the synthetic data are within the $\pm1\sigma$, $\pm2\sigma$, and $\pm3\sigma$ credible regions. The PT-emcee results are consistent with statistical expectations (see Appendix A for the full posteriors). In contrast, the credible regions for both MultiNest runs are too narrow, although with more live points the sampling is more thorough.

typically used power-law backgrounds. This is therefore the most realistic synthetic data test that has been performed in the radius estimation context.

The results of our analysis of the synthetic data are summarized in Table 2, and more detail on our PT-emcee analysis is shown in Table 5 and Figure 14 in Appendix A. We see that the PT-emcee sampling yields results that are entirely consistent with statistical expectations. In contrast, MultiNest sampling with Nlive = 1000 and an efficiency of 0.01 is not adequate; for example, three of the 12 parameters have $\pm3\sigma$ credible regions that exclude the parameter value used to construct the data. The MultiNest sampling with Nlive = 2000 and an efficiency of 0.01 is better but the credible regions are still too narrow: one of the 12 true parameter values is excluded at $>3\sigma$, and four of the 12 are excluded at $>2\sigma$. It is possible that, with more live points and/or lower efficiency, MultiNest analysis of our synthetic data would lead to the statistically expected outcomes, but results such as these form part of our motivation to use PT-emcee to determine posterior probabilities.

In summary, even with realistic backgrounds and even when analyzing jointly the NICER and XMM-Newton synthetic data, our analysis method yields statistically acceptable results.

4.2. The Mass and Radius of PSR J0740+6620

In this section we present fits to (1) just the NICER data (see Table 6 and Figure 15 in Appendix B for the best fit and uncertainties, the left-hand panels of Figure 1 for the mass and radius posteriors), (2) the NICER data and the data from the three XMM-Newton instruments, assuming the nominal calibration for XMM-Newton (see Table 7 and Figure 16 in Appendix C for the best fit and uncertainties, and the right-hand panels of Figure 1 for the mass and radius posteriors), and (3) the NICER data and the data from the three XMM-Newton instruments, with an additional energy-independent factor $0.9 < A_{\rm XMM} < 1.1$ that multiplies the effective area of the XMM-Newton instruments (see Table 8 and Figure 17 in Appendix D for the best fit and uncertainties). The Appendices have the full corner plots for each of the three fits. In all cases we use atmosphere tables for pure hydrogen that accommodate partial ionization.

Figure 2 shows a representative spot pattern. We note that because the observer inclination is very close to the rotational equator, there is a near-symmetry between spots in the northern hemisphere (which we define to be the hemisphere of the observer) and the southern hemisphere. In addition, because the spots do not overlap, their labeling (i.e., which is spot 1 and which is spot 2) can be swapped without affecting the solution, unlike what would be the case if the spots overlapped. Thus there is an approximate four-fold degeneracy in the solution.

The inclusion of XMM-Newton data increases the radius estimates: for example, with the NICER data alone the $\pm1\sigma$ range in radius is 10.382 km to 13.380 km, whereas when we add the XMM-Newton data the range becomes 12.209 km to 16.326 km. This is because the prime source of information about the compactness is the modulation fraction (see Miller 2016). The NICER data are dominated by background counts, which means that from that data set alone it could be that the modulation fraction is low. If other parameters such as the observer inclination and spot locations are fixed, then because light deflection increases with increasing compactness $GM/(R_e c^2)$, for a more compact star the light from spots is spread out more and thus the modulation fraction is reduced. As a result, the NICER data alone can be fit with very compact stars. But when the XMM-Newton data are included, we have a measure of the total flux from the star. This total flux is significantly less than that in the NICER data, because those data include significant background. Thus, the modulation fraction is higher than it appears to be from the NICER data alone, and hence the compactness of the star must be lower. Because the mass is known with some precision, a lower compactness implies a larger radius.

We also note that, for the same reason, if reliable information about the non-spot NICER flux were included in the NICER data then the inferred radius would increase. That is, any information that places an upper limit on the flux from the spots, whether it comes from observations of the source (in our case, using XMM-Newton) or a model of some part of the the non-spot flux (which we would obtain with a background model), increases the inferred modulation fraction and thus increases the inferred radius. Hence analysis of only the NICER data on PSR J0740+6620, if augmented with NICER background data that (critically) have reliable estimates of the field-to-field variance as well as statistical uncertainties, is likely to result in an inferred radius that is close to the radius inferred when we also use XMM-Newton data. The 3C50 NICER background model of Remillard et al. (2021) is a good step in this direction, but the variance between the background in different sky pointings is not well understood.

We stress that, despite the clear shift of the radius posterior distribution to larger radii when the XMM-Newton data are included, this distribution is still broadly consistent with that obtained using the NICER data alone, even without background information. One indication of this is that there is a substantial overlap between the two $\pm1\sigma$ ranges. To quantify this overlap we can compute, e.g., the Bhattacharyya coefficient (Bhattacharyya 1943)

$$BC(p, q) = \int \sqrt{p(x)q(x)}\,dx \tag{7}$$

for two normalized probability distributions $p(x)$ and $q(x)$. $BC = 1$ for identical distributions, whereas $BC = 0$ for

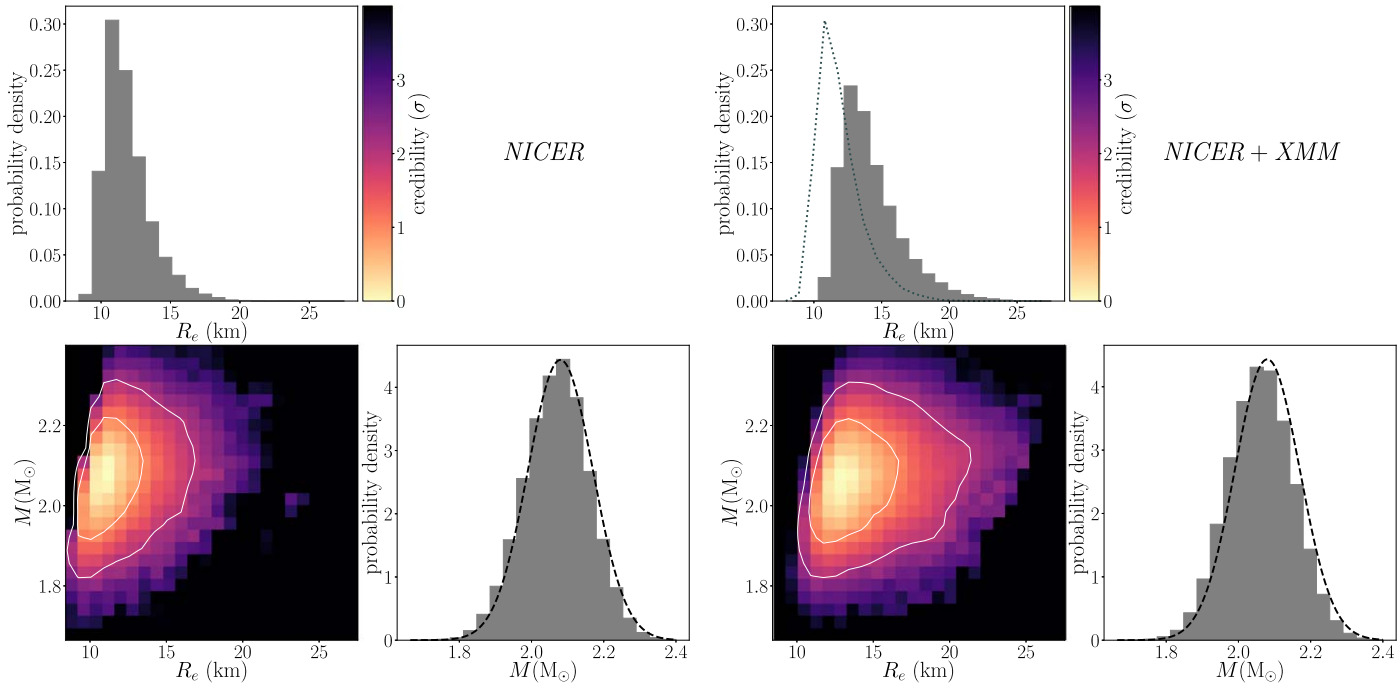

Figure 1. Comparison of the $M-R_e$ corner plots obtained using two circular spots, fit to only the NICER data (left panels) and to both the NICER and the XMM-Newton data with the nominal XMM-Newton calibration (right panels). All of the results that we present use pure hydrogen model atmospheres that allow for the possibility of partial ionization. The mass prior is represented by the dashed line in each of the one-dimensional mass posterior plots. In the mass–radius plots, brighter colors indicate higher posterior probability densities; the inner contour in these plots contains 68.3% of the posterior probability whereas the outer contour contains 95.4%. In the NICER+XMM-Newton one-dimensional radius posterior plot, the dotted line shows the posterior obtained using only the NICER data. The two radius posteriors have substantial overlap, but the effect of including the XMM-Newton data is to increase the favored radius by roughly 2 km.

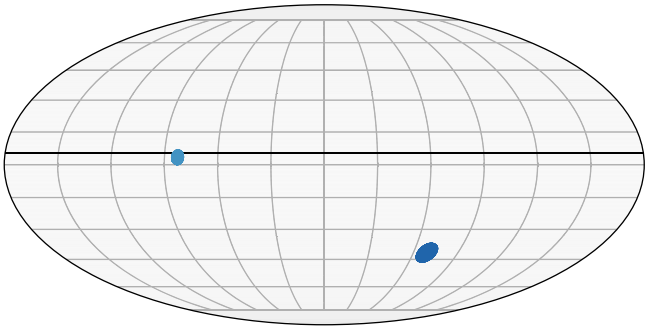

Figure 2. Spot locations for a representative fit, in an equal-area Mollweide projection. The horizontal bar indicates the colatitude of the observer. Because we observe from close to the rotational equator, and because the spots do not overlap, there is an approximate four-fold degeneracy in solutions.

distributions with zero overlap. In our case, $BC = 0.77$ when p is the radius posterior using only the NICER data and q is the radius posterior when the XMM-Newton data are also included, and when we represent those distributions using histograms with bin widths of 0.1 km. For context, $BC = 0.77$ for two unit-variance Gaussians whose centers are separated by roughly 1.5 times their standard deviations. This indicates that there is a significant overlap between the two distributions.

4.3. Convergence of Sampling

As we discussed in Section 3.5, we started our PT-emcee sampling of the posterior using an initial distribution of points that had previously been obtained by using MultiNest (with Nlive = 1000 and efficiency = 0.01) to sample the posterior; as usual, MultiNest had run until the evidence estimate converged. The left panel of Figure 3 shows the evolution of the -1σ, median, and $+1\sigma$ values of the radius posterior as our PT-emcee sampling of the NICER+XMM-Newton data using the nominal calibration progressed, starting with the initial parameter distribution provided by MultiNest. Each point in this plot indicates the estimates of these three radii given by a single set of 20,000 samples; the individual sets are contiguous and non-overlapping. The evolution shown was computed using approximately 1700 such sample sets; we show another view of the progressive mass–radius sampling in Figure 4. The left panel in Figure 3 shows that as the sampling by PT-emcee proceeded, the values of all three characteristic radii increased rapidly at first, indicating that the sampling achieved by MultiNest was insufficient and that the estimated values of the parameters it provided were inaccurate. Eventually the values of the three parameters ceased increasing and begin wandering up and down stochastically by small amounts, indicating that the PT-emcee estimates of the three radii had converged.

The dashed vertical line indicates the beginning of the sample sets that we used to construct our final posterior distributions (a total of 10^7 samples). The effective number of independent samples can be estimated by dividing the total number of samples by the average integrated autocorrelation time. Using typical methods for calculating the autocorrelation time for each walker (e.g., Sokal 1997) yields an estimate of $\sim$4 iterations, suggesting a total of $\sim 2.5 \times 10^6$ independent samples. From sample set to sample set in the converged part of the evolution, the median, $\pm 1\sigma$, and $\pm 2\sigma$ radii vary with a standard deviation of only a few hundredths of a kilometer.

The right panel of Figure 3 shows the evolution of the three radii in our PT-emcee sampling of the model for the NICER +XMM-Newton data when a calibration parameter is included. Again we show the three radius values computed using

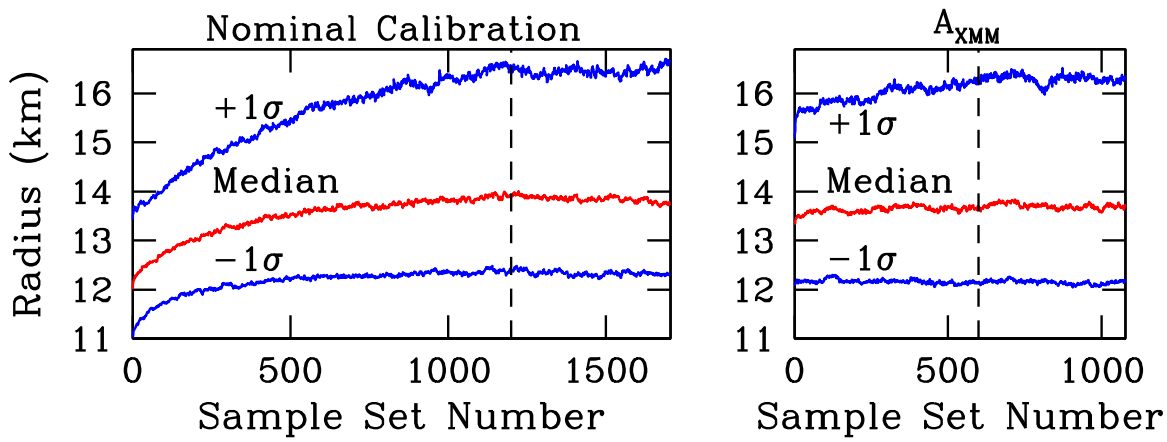

Figure 3. Evolution of the -1σ, median, and $+1\sigma$ values of the radius posterior as our PT-emcee sampling of the NICER+XMM-Newton data progressed. Each point in the plots indicates the estimated values of these three radii given by a single set of 20,000 contiguous, non-overlapping samples. The number of sets included in each estimate is shown by the numbers on the horizontal axis. Left: evolution of these three radii as sampling proceeds, starting from the final posterior distribution provided by MultiNest, and assuming the nominal ratio of the NICER overall effective area relative to that of XMM-Newton. As sampling proceeded, all three radii increased rapidly and then converged to values that are larger, with a broader spread, than was obtained from the MultiNest sampling. The sample sets to the right of the dashed vertical line were used to construct the final posterior distribution from this run (a total of 10^7 samples), which is what we used in our parameter estimation. Right: evolution of the three radii as sampling proceeds, starting with a kernel density estimate of the posterior distribution obtained at the end of the previous run, but now including the overall effective area $A_{\rm XMM}$ of XMM-Newton as a parameter in the fit. The change in the treatment of the effective area produced a small shift in the values of these three radii relative to their final values in the left panel. As sampling progressed, the three radii rapidly approached the values they had at the end of the run shown in the left panel. The 10^7 samples to the right of the dashed vertical line were used to construct the posterior distribution for this run. See the main text for more details.

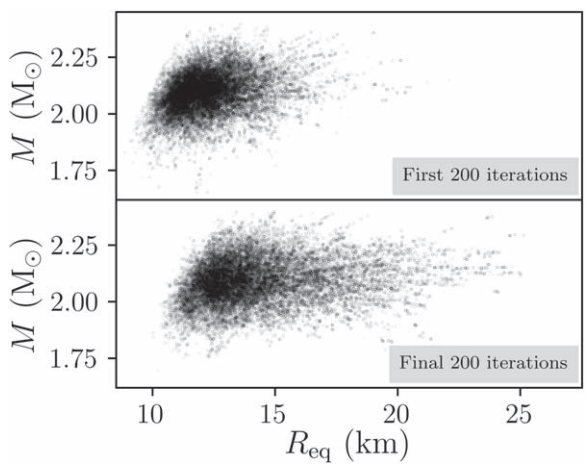

Figure 4. Another view of the evolution of the sampling in our analysis of the NICER and XMM-Newton data on PSR J0740+6620. The top panel shows the positions of the walkers in mass–radius space during the first 200 iterations of our PT-emcee sampling; these points were drawn from the posterior of an Nlive = 1000, efficiency = 0.01 MultiNest run, using a kernel density estimate. The bottom panel shows the positions of the walkers during the final 200 iterations, after the PT-emcee sampling had converged. These panels correspond to the beginning and end of the left panel of Figure 3, and demonstrate the difference in the sampling between the two stages.

contiguous and non-overlapping sets of 20,000 samples. This sampling was initiated using kernel density estimation based on 10% of the final posterior samples from the PT-emcee analysis of NICER+XMM-Newton data performed using the nominal XMM-Newton calibration. As a result, the initial values of the three radii did not match perfectly the final values of the three radii in the left panel, indicating that the initial posterior distribution in the right panel does not quite match the final posterior distribution from the run shown in the left panel. However, as Figure 3 shows, these three radius estimates rapidly approached the values they had at the end of the run shown in the left panel, indicating that as the PT-emcee sampling progressed, the posterior distribution converged quickly to the final posterior distribution in the run shown in the left panel.

We note that both our MultiNest and our PT-emcee analyses of only the NICER data, and of the NICER+XMM-Newton data that were performed using the nominal XMM-Newton calibration, assumed a mass prior of $2.11 \pm 0.09\,M_\odot$, consistent with a preliminary radio-based mass measurement. The posterior function that was sampled to produce the three radius values plotted in the left panel of Figure 3 was computed assuming this prior. However, the posterior function that was sampled to produce the three radius values plotted in the right panel assumed a different mass prior of $2.08 \pm 0.09\,M_\odot$, consistent with the current radio-based mass measurement. As a result, the radius values plotted in the right panel of the figure differ by about 1.5% from the radius values plotted in the left panel. The numbers in the tables and figures that summarize the posteriors produced by our analyses of the NICER-only and the NICER+XMM-Newton data assuming the nominal calibration have been re-weighted using the updated mass.

4.4. Effect of Priors

As summarized in Table 3, our posteriors are robust against several different choices of priors. In Table 3 we compare the $\pm 1\sigma$ and median radii when we analyze the NICER and XMM-Newton data using our standard priors with the $\pm 1\sigma$ and median radii when we (1) include a parameter $A_{\rm XMM}$ that models the relative calibration of NICER and XMM-Newton (as discussed before, our flat prior $0.9 \leqslant A_{\rm XMM} \leqslant 1.1$ is broader that the expected uncertainty around $A_{\rm XMM} = 1$ by a factor ~ 2), and (2) restrict our inclination prior to being flat within $\pm 0\overset{\circ}{.}5$ of the radio measurement, rather than our standard $\pm 5^\circ$. In each case the -1σ radius (which has especially important implications for the EOS; see Section 5) is close to our standard value. For comparison we also show in this table the $\pm 1\sigma$ radii

Table 3
Summary of Inferred Radii Using Different Priors

Prior	-1σ (km)	Median (km)	$+1\sigma$ (km)
NICER+XMM-Newton (featured result)	12.209	13.713	16.326
NICER+XMM-Newton, $A_{\rm XMM}$	12.153	13.705	16.298
NICER+XMM-Newton, $\theta_{\rm obs}$ = radio	12.236	13.750	16.416
NICER only	10.382	11.512	13.380

Note. Comparison of the -1σ, median, and $+1\sigma$ radii inferred using different priors on the NICER+XMM-Newton data sets, and for the NICER-only analysis. See the text for details and note that the top, boldfaced numbers are from the analysis that we use in Section 5 for our EOS inference. When the NICER and XMM-Newton data sets are analyzed jointly the -1σ radius, which is particularly important for EOS analysis (see Section 5), is robust against different priors.

when we use only the NICER data, with no assumed knowledge of the NICER background.

4.5. Adequacy of the Models

As in Miller et al. (2019), we performed χ^2 tests to assess the adequacy of our models in describing the data. This is a one-way test: if $\chi^2 \sim$ dof for dof degrees of freedom this does not guarantee that the model is correct, but if χ^2 is sufficiently larger than dof that the probability is very low, it indicates that the model is deficient. We focus on the results of the joint fit to the NICER and XMM-Newton data using the nominal XMM-Newton calibration, given that the XMM-Newton data refine the solution substantially and that allowance for a shift in the effective area of XMM-Newton does not make a significant difference to the posterior credible regions.

In Figure 5 we show the value of χ over each of the NICER phase-channel bins we used in our analysis, for our best fit to the NICER+XMM-Newton data. There are no obvious patterns, and the $\chi^2/$dof is $2912.37/2901$ for the NICER data alone, which has a probability of 0.437 if the model is correct. In Figure 6 we compare to the data our bolometric model waveform for our best fit, and also display the residuals. Here $\chi^2/\mathrm{dof} = 21.85/18$ (probability of 0.239) for the NICER data alone.

Our final comparison to the NICER data is in Figure 7, which compares the non-spot background in our best model (black line) with the blank-sky NICER background inferred using the 3C50 model of Remillard et al. (2021). Because the 3C50 model is for a blank sky, i.e., directions where there are no known sources, it should provide a lower limit to the background in the direction of a particular source such as PSR J0740+6620. Indeed, we see that our estimated background counts, while consistent with the 3C50 model at energy channels ≈80 and higher, are above the model at lower energy channels. This is likely to be due to particular sources within the NICER field of view that can be identified in the XMM-Newton image of the field (see Wolff et al. 2021).

Our model is therefore a good fit to the NICER data.

In Figure 8 we compare our best NICER+XMM-Newton model with the XMM-Newton data. Because there are few counts per energy channel, we evaluated the quality of our fit by generating 10^5 synthetic data sets by performing Poisson draws using our best model (including the blank-sky counts) in every energy channel in all three instruments. We then compared our model to the J0740 data, and placed that in the context of the comparison of our model to the synthetic data sets, in two ways.

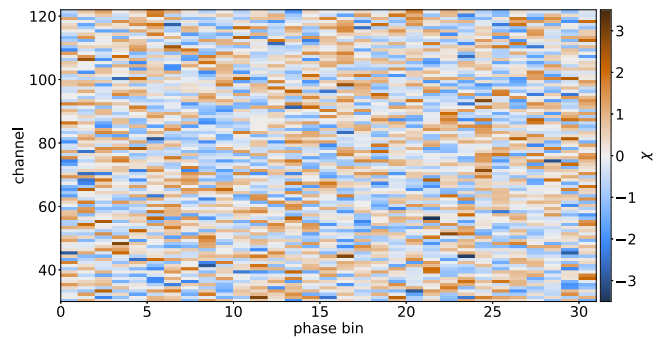

Figure 5. Value of χ in each of the 3008 NICER phase-energy bins (32 phase bins and 94 energy channels), for the best fit of our energy-resolved waveform model to the NICER+XMM-Newton data. As is expected for a good fit, no patterns in the values of χ are evident as a function of phase or energy. The $\chi^2/$dof is $2912.37/2901$, which has a probability of 0.437 if the model is correct.

1. We computed the total log likelihood of all three XMM-Newton data sets for PSR J0740+6620 given our model. We also computed the distribution of the total log likelihoods of each synthetic data set given our model. The total log likelihood of the real data is at the 75th percentile of the log likelihoods from the synthetic set (98th percentile for the pn data alone, 17th percentile for the MOS1 data alone, and 12th percentile for the MOS2 data alone).
2. We also calculated the Kolmogorov–Smirnov (K-S) probability that the cumulative counts in our model, as a function of the energy channel, are drawn from the same distribution as the PSR J0740+6620 data. We then calculated the distribution of the K-S probabilities for the synthetic data set. We found that the K-S probability for the XMM-Newton pn data on PSR J0740+6620 is at the 10th percentile of the corresponding probabilities for the synthetic data sets, the K-S probability for the MOS1 data on PSR J0740+6620 is at the 50th percentile, and the K-S probability for the MOS2 data on PSR J0740+6620 is at the 31st percentile.

As a final check, we note that the XMM-Newton DDT data have 94 counts in the pn camera in the energy range we investigate, 59 counts in the MOS1 camera, and 67 counts in the MOS2 camera. In our best fit, we have respectively 114.88 counts (1.95 standard deviations high), 49.85 counts (1.30 standard deviations low), and 59.78 counts (0.93 standard deviations low). Neither the total count numbers nor the comparisons with synthetic data indicate a problem. Thus, at least based on these tests, our model is fully consistent with all three XMM-Newton data sets.

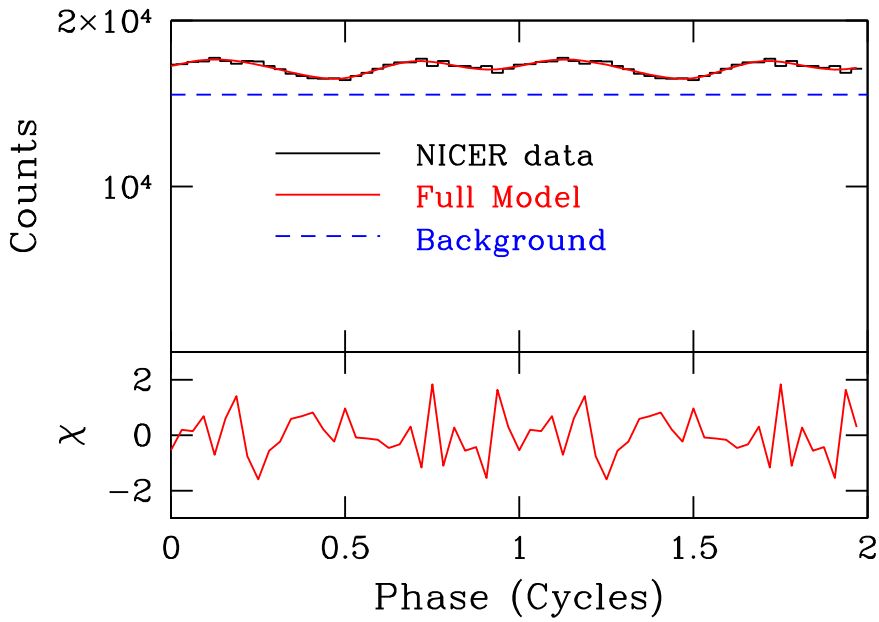

Figure 6. Top: comparison of the 32-phase bolometric waveform constructed using the NICER data on PSR J0740+6620 with the bolometric waveform model that best fits the NICER+XMM-Newton data. The dashed blue line shows the unmodulated background that was added to the counts produced by the two hot spots as part of the fitting procedure (see Section 3.4.2). Bottom: resulting value of χ as a function of phase. The χ^2/dof is 21.85/18, which has a probability of 0.239 if the model is correct.

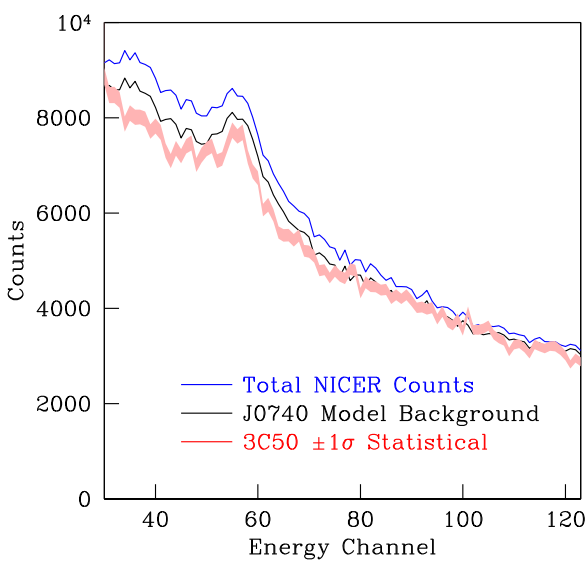

Figure 7. Inferred non-spot counts as a function of NICER energy channel in our best model (black line) compared with the $\pm 1\sigma$ range of the 3C50 background model (pink band) of Remillard et al. (2021). For comparison, we also show the total NICER counts per channel (blue line). Above channel 80 our inferred background is consistent with the 3C50 model. The excess in our inferred background at lower energies is likely due to the presence of other sources in the NICER field, which can be seen in XMM-Newton images.

4.6. Potentially Important Differences between Our Analysis and That of Riley et al. (2021)

The parallel analysis of the NICER and XMM-Newton data by Riley et al. (2021) finds a smaller credible interval for the radius estimate and, most important for the inferred constraints on the EOS, a value for the radius at the -1σ contour that is $\approx$0.8 km smaller than the value we report here. There are a number of differences between their analysis procedure and ours. For example, Riley et al. (2021) assume that the inclination of the observer's line of sight to the pulsar's rotational axis is identical to the measured inclination of the observer's line of sight to the orbital axis of the binary system, whereas we allow the inclination of the observer's line of sight to the pulsar's rotational axis to differ by as much as $\pm 5°$ from the measured inclination of the observer's line of sight to the orbital axis. However, as we have discussed in Section 4.4, this difference between the priors on the inclination of the observer's line of sight to the pulsar's rotational axis used in the two analyses does not produce a significant difference in the value of the radius at the -1σ credibility contour. Another unimportant difference is the ionization fraction of our hydrogen atmospheres: we use tables that allow for the possibility of partial ionization, whereas Riley et al. (2021) used atmospheres with fully ionized hydrogen. As we indicate in Section 3.1, we found negligible changes in the radius posteriors when we used fully ionized hydrogen atmospheres.

There appear to be four differences in the analysis procedures used by the two groups that could contribute to the difference of $\approx$0.8 km in the values of the radius at the -1σ credibility contour that the two groups report in their headline results ($R = 12.2$ km at -1σ reported here and $R = 11.4$ km at -1σ reported by Riley et al. 2021).

1. We allow the relative calibration between NICER and XMM-Newton to deviate by up to $\pm 10\%$ from its nominal value, a deviation that is a factor $\sim$2 times larger than the measured deviation (again see slide 7 of http://iachec.org/wp-content/presentations/2020/NICER-CrossCal-IACHEC-Markwardt-2020b.pdf and focus in particular on the energy range 0.3–1 keV that is relevant for the present analysis; here the deviation is $<4\%$). In contrast, Riley et al. (2021) allow the relative calibration to deviate by several tens of percent, which is many times larger than the measured deviation; for example, in their best fit, $A_{\rm XMM}$ is effectively equal to 0.574. Elsewhere in their paper, Riley et al. show that when they restrict the relative calibration to a range consistent

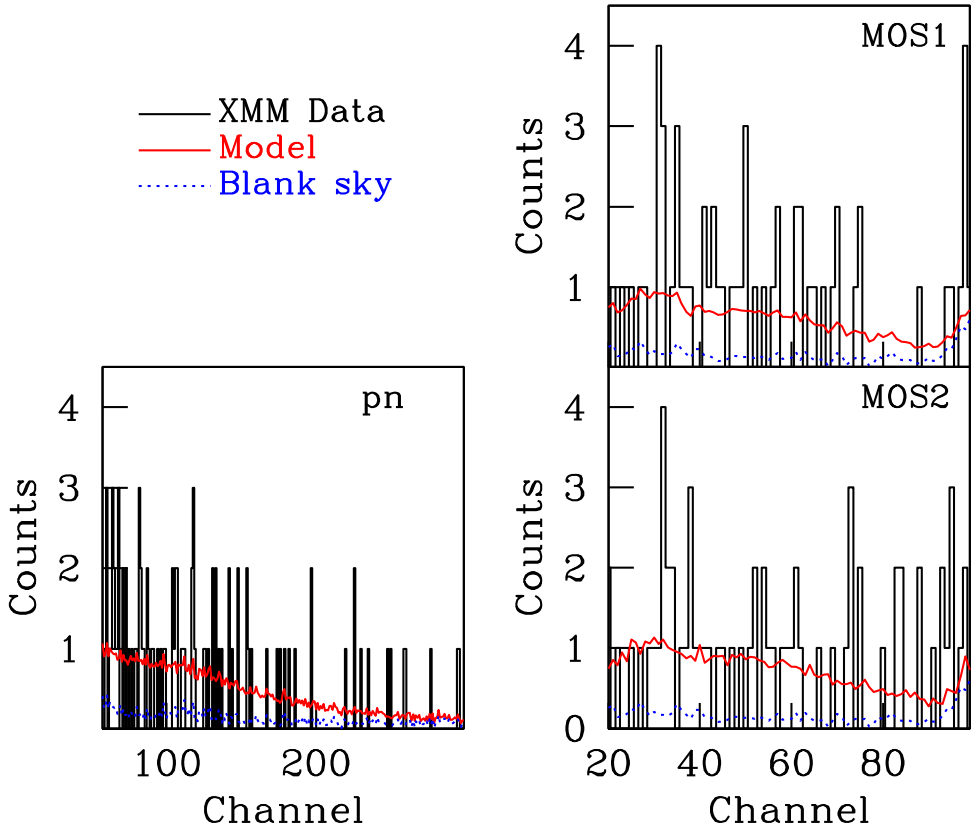

Figure 8. Comparison of the data from the three XMM-Newton cameras (labeled at the top of each plot) with our best NICER+XMM-Newton model. In each plot the black histogram is the data, the dotted blue line is the blank-sky background scaled to the duration of the observations, and the red line is the best model including the background. In each case the energy channel range is the range we use in our analysis. As described in the text, our model provides a good fit to the data.

with the measured range, they find $R = 11.75$ km at the -1σ contour. Thus, when they require the relative calibration between NICER and XMM-Newton to have a value consistent with the measured values, the difference between their value of the radius estimate at the -1σ contour and our value is reduced by almost a factor of two.

2. When estimating the radius of PSR J0740+6620, we allowed $R_{\rm eq}c^2/(GM)$ to be as large as 8.0 (corresponding to $R_{\rm eq} \approx 24.5$ km at $M = 2.08\,M_\odot$) and found that the posterior radius probability density is negligible near this boundary. Hence, this choice for the boundary of our search volume did not affect our estimate of the radius of PSR J0740+6620. In contrast, when Riley et al. estimated the radius of PSR J0740+6620, they sampled the radius parameter space only at radius values <16 km. To investigate the results we would have found if we had sampled the radius parameter space only at $R < 16$ km as they did, we required $R < 16$ km in a test analysis and found $R = 12.06$ km, 13.28 km, and 14.82 km at the -1σ contour, the median value, and the $+1\sigma$ contour. Even when we imposed $R < 16$ km and also allowed the relative calibration factor $A_{\rm XMM}$ to vary freely in the range $0.9 < A_{\rm XMM} < 1.1$, a factor >2 deviation larger than its measured value, we found that this had only a very small effect on the position and width of the credible interval of the radius, which changed only slightly to $R = 12.00$ km, 13.28 km, and 14.80 km at the -1σ contour, the median value, and the $+1\sigma$ contour. Thus, these two differences between our analysis procedure and the analysis procedure used by Riley et al. (the different breadths of the allowed deviation of the relative calibration of the NICER and XMM-Newton instruments and artificially limiting or not limiting the sampling of the radius parameter volume) account for ≈0.55 km of the 0.8 km difference between the value of the radius at the -1σ contour reported by Riley et al. and the value of the radius at the -1σ contour that we found.
3. We used PT-emcee to thoroughly sample the multi-dimensional posterior, using MultiNest only to create an initial rough sample that we then used to speed up the sampling using PT-emcee. In our analysis of synthetic pulse waveform data constructed to mimic the actual NICER and XMM-Newton data (see Section 4.1), we found that when we used only MultiNest, even with values of the MultiNest parameters chosen to try to achieve thorough sampling, the credible regions it generated were too small, i.e., they too often failed to include the values of the pulse waveform parameters that had been used to generate the synthetic pulse waveform data. In contrast, when we used PT-emcee we found credible regions that were consistent with the values of the parameters chosen when generating the synthetic data (see Table 2 for more details). Figure 3 shows the detailed evolution of the -1σ, median, and $+1\sigma$ radii throughout the course of our PT-emcee sampling. Riley et al. used only MultiNest for all of their analyses and found that their posteriors continued to broaden with more thorough sampling for all of the live point numbers that they explored.

4. We treated the distribution of the blank-sky counts in each energy channel as a realization of a Poisson distribution for the observed number of counts. Riley et al. instead assumed a flat prior for the distribution of the blank-sky counts in each energy channel, centered on the flux implied by the observed number of counts with a variety of widths equal to various multiples of the standard deviation of the observed number of counts.

5. Implications for the EOS

Our aim is to combine multiple lines of data relevant to the properties of cold, catalyzed, dense matter, using a Bayesian procedure that is both statistically rigorous and computationally practical. In this section we divide our approach into two subtasks: (1) likelihood computation and parameter estimation for a given EOS family (Section 5.1), and (2) different approaches to generating candidate EOSs (Section 5.2). Finally, we show in Section 5.3 that with the inclusion of the mass and radius estimates for PSR J0030+0451 and PSR J0740+6620, the constraints on the EOS depend relatively weakly on the EOS parameterization assumed in the analysis, up to a few times nuclear saturation density.

5.1. Statistical Method

There is a growing number of papers on EOS inference from astronomical and/or laboratory data (e.g., Agathos et al. 2015; Lackey & Wade 2015; Alvarez-Castillo et al. 2016; Margalit & Metzger 2017; Annala et al. 2018; Most et al. 2018; Radice et al. 2018; Rezzolla et al. 2018; Riley et al. 2018; Tews et al. 2018; Greif et al. 2019; Kiuchi et al. 2019; Landry & Essick 2019; Shibata et al. 2019; Capano et al. 2020; Cierniak & Blaschke 2020; Dietrich et al. 2020; Landry et al. 2020; Li & Magno 2020; Raaijmakers et al. 2020; Pang et al. 2020; Zhang & Li 2020; Essick et al. 2020b; Xie & Li 2021). Here we follow the procedure described in Miller et al. (2020). Their procedure is fast and flexible enough to incorporate multiple types of data.

To elaborate, suppose that we have i different types of measurements, which might include laboratory experiments, or the measurement of a high mass from a pulsar, or the measurement of a tidal deformability, a radius, a moment of inertia, and so on. Suppose also that for measurement type i we have $j = 1, 2, \ldots, j(i)$ independent measurements of that type; these could be different measurements of the same source, or measurements of different sources.[36] We wish to evaluate a set k of EOSs; in the next section we discuss the selection of k. If the likelihood of data set (i,j) given EOS k is $\mathcal{L}_k(i, j)$, then the likelihood of all of the data sets given EOS k is simply the product of the likelihoods:

$$\mathcal{L}_k = \prod_i \left[\prod_{j=1}^{j(i)} \mathcal{L}_k(i, j)\right]. \tag{8}$$

Note that in some cases one may need to marginalize over extra parameters. As discussed in Section 2 of Miller et al. (2020), there are some parameters that are expected to be the same for all neutron stars (such as the parameters that describe the EOS beyond nuclear saturation density, given that we expect the EOS to be unique at such densities), some that can differ between neutron stars but are the same for any observation of a given neutron star (such as the distance, observer inclination, stellar mass and radius, and central density), and some that could vary between different observations of a given neutron star (such as the absorbing column if the star is in a binary and there is a significant wind). It would be incorrect to marginalize over parameters separately for different data sets that share those parameters; we do not perform such marginalizations in Equation (8). In contrast, marginalization can be performed for a likelihood applying to a given data set, over parameters that apply only to that data set. For example, to compute the likelihood of a NICER posterior in mass and radius for a given neutron star it is necessary to integrate over the prior for the central density, which applies to that star and is not the same for all EOSs because different EOSs have different maximum stable central densities.

Given the calculation of the likelihood $\mathcal{L}_k$ of the full set of data assuming a specific EOS k (see Miller et al. 2020 for more details), then as usual in a Bayesian analysis the posterior probability P_k of the EOS is proportional to the prior probability q_k of the EOS times the likelihood:

$$P_k \propto q_k \mathcal{L}_k. \tag{9}$$

We could use this procedure to compare individual EOSs from the literature. However, our primary goal is to produce a posterior probability distribution for, say, the pressure P as a function of the total energy density ϵ or of the number density n of baryons. To do this, we simply calculate the pressure at specified ϵ or n for each EOS k, weight it by $\mathcal{L}_k$, and then sum over all k to find the final distribution of P at a given ϵ or n.

For each specific EOS selected from a given EOS family we need to compute the likelihood of all relevant data sets for that EOS. We largely follow the procedure of Miller et al. (2019) in our treatment of our data sets. In particular, we apply kernel density estimation (other methods exist, e.g., random forest regressors; see Hernandez Vivanco et al. 2019) to produce an estimated continuous probability distribution from our discrete samples. When we do so, we use the standard bandwidth from Silverman (1986) for our samples in mass and tidal deformability, but multiply this bandwidth by 0.1 for our mass–radius samples because we found previously that the standard bandwidth significantly broadened the radius posterior (see Miller et al. 2019 for more details, and Essick et al. 2020a for a more detailed approach to selecting the bandwidth). We modify the procedure of Miller et al. (2020) in two ways.

1. In Miller et al. (2019, 2020) the prior on the central density was flat between the density that produces a 1 $M_\odot$ star and the density that produces the maximum-mass non-rotating neutron star for the EOS under consideration. Because the central density changes rapidly near the maximum mass, this gives relatively greater prior weight to higher-mass stars. Here our prior on the central density is instead quadratic in the central density between the 1 $M_\odot$ density, $\rho_{\rm min}$ and the maximum-mass density $\rho_{\rm max}$. That is, we select uniformly in $0 \leqslant x \leqslant 1$, where the central density is $\rho_c = \rho_{\rm min} + x^2(\rho_{\rm max} - \rho_{\rm min})$. This

[36] For example, here we present our radius measurements, which are based on X-ray data, using a prior on the mass given by radio observations. This prior, however, is obtained by starting with a flat mass prior and then updating the mass distribution using the radio data. Thus our procedure is equivalent to starting with a flat mass prior and then computing the joint likelihood of the radio and X-ray data given candidate masses and radii.

produces a more even prior distribution on the masses. However, we assign zero prior weight to any densities between $\rho_{\rm min}$ and $\rho_{\rm max}$ that produce unstable stars; in this way we explicitly treat EOSs that have two stable ranges of central density separated by an unstable range of central density (these are sometimes called "twin stars"), when they arise. In practice, the different prior distribution for the central density does not change the EOS posteriors significantly compared with the approach in Miller et al. (2019).

2. Because we include the high-mass binary merger GW190425 (Abbott et al. 2020a) in our analysis, and the total mass of the binary is high enough that one of the compact objects might have been a black hole, we treat tidal deformabilities differently than in Miller et al. (2019, 2020) (although we also note that the large distance to and high mass of GW190425 mean that it adds only a small amount of information). Our approach is to select the central density of the lower-mass star, up to the central density such that the implied mass of the other star equals that of the lower-mass star. Given the mass of the lower-mass star, and given that the chirp mass (equal to $(m_1 m_2)^{3/5}/(m_1+m_2)^{1/5}$ for stellar masses m_1 and m_2 in a binary) is known with high precision, we know the mass of the higher-mass object to the precision that we know the chirp mass. We marginalize over the chirp mass as in Equation (15) of Miller et al. (2020). If for the EOS and central density under consideration the higher-mass object is a neutron star, then we compute the tidal deformabilities of both stars, using the same EOS, following the prescription of Hinderer (2008; see the erratum at Hinderer 2009). If instead for the EOS and central density under consideration the higher-mass object is a black hole, then we assume that its tidal deformability is zero (Binnington & Poisson 2009; Damour & Nagar 2009). Note that for rotating black holes the tidal deformability may not be exactly zero (see Chia 2020; Le Tiec & Casals 2021; Le Tiec et al. 2021 for an ongoing discussion), but it is small enough that the difference from zero is not important for our calculations.

To implement our analysis, we need a mechanism to select a set of EOSs. We now discuss our three different approaches to this selection.

5.2. EOS Models

There exist many different nuclear physics computations of the EOS of cold, catalyzed matter both below and above nuclear saturation density. It is usually agreed that our understanding of matter below saturation density is fairly good, based on the idea that we can perform laboratory experiments that probe this density regime. One caveat is in order: the matter that can be examined in laboratories has roughly equal numbers of neutrons and protons (the most asymmetric stable nuclei, such as ^{208}Pb, have roughly 50% more neutrons than protons). In contrast, neutron star matter in the vicinity of saturation density is more than 90% neutrons. Thus although from the standpoint of density the regime is familiar, theoretical arguments not directly supported by experiment are necessary to extrapolate to very asymmetric matter.

Nonetheless, we will follow standard procedure and assume that we know the EOS up to a threshold density, which we take to be half of saturation density because this is approximately the crust–core transition density (Hebeler et al. 2013). Note that some calculations suggest that different treatments of the crustal EOS could introduce radius uncertainties as large as 0.3 km (Fortin et al. 2016; Gamba et al. 2020). Below half of nuclear saturation density we use the QHC19 EOS (Baym et al. 2019). Above half of nuclear saturation density, we then need to model the EOS, where there are well motivated and carefully constructed models, but where these models have not been validated by laboratory measurements.

A necessary output of our EOS analysis is an understanding of how strongly our conclusions depend on the type of EOS model that we employ. Therefore, in the rest of this section we discuss the three EOS model families that we use in our analysis. First we present two parameterizations which have been widely used in the literature. We then turn our attention to a newer method using Gaussian processes (GPs) that was introduced in this context by Landry & Essick (2019).

5.2.1. Parametric Models

The most common approach to EOS inference has used parameterized models. That is, we assume that there is some set of parameters α that completely describe the EOS at high densities. Given priors on α, we can generate a large number of sample EOSs for which we then compute the likelihood of the assembled data. As discussed above, this allows us to compute posteriors for $P(\epsilon)$ or $P(n)$. The two parameterizations we use are as follows.

Piecewise polytrope. In this model, above a number density $n = n_s/2$ the pressure is given by a series of polytropes: $P = K_1 n^{\Gamma 1}$ for $n_s/2 \leqslant n \leqslant n_2$, $P = K_2 n^{\Gamma_2}$ for $n_2 \leqslant n \leqslant n_3$, and so on, where the coefficients K_i are chosen to ensure continuity of pressure between density segments. Variants of this model differ in the number of segments, the priors on the polytropic indices Γ_i, and whether the transition densities n_1, n_2, …are fixed or can vary. We use the following assumptions (compare with Miller et al. 2019, which used the same assumptions except for restricting the first polytropic index to the range [2, 3]): the polytropic index from $n_s/2$ to $n_2 \in [3/4,\ 5/4]n_s$ is $\Gamma_1 \in [0,\ 5]$; from n_2 to $n_3 \in [3/2,\ 5/2]n_s$ is $\Gamma_2 \in [0,\ 5]$; from n_3 to $n_4 \in [3,\ 5]n_s$ is $\Gamma_3 \in [0,\ 5]$; from n_4 to $n_5 \in [6,\ 10]n_s$ is $\Gamma_4 \in [0,\ 5]$; and from n_5 to ∞ is $\Gamma_4 \in [0,\ 5]$ (all priors are uniform in the listed range). When Γ is close to zero, the pressure is nearly independent of the density, which is what one expects near a phase transition and which can produce the twin stars discussed earlier. If at some density below n_5 the implied adiabatic sound speed $c_s = (dP/d\epsilon)^{1/2} > c$, the speed of light, then we set $dP/d\epsilon = c^2$ at that density.

Spectral parameterization. A different parameterization was introduced by Lindblom (2010, 2018). In this approach, the polytropic index is a continuous function of the pressure, $\Gamma(P)$:

$$\Gamma(P) = \exp\left(\sum_i \gamma_i x^i\right). \tag{10}$$

Here $x \equiv \log(P/P_0)$ and P_0 is the pressure at $n_s/2$. We follow Abbott et al. (2018), Carney et al. (2018), and Miller et al. (2019) in expanding to $O(x^3)$, and in using uniform priors $\gamma_0 \in [0.2,\ 2]$, $\gamma_1 \in [-1.6,\ 1.7]$, $\gamma_2 \in [-0.6,\ 0.6]$, and $\gamma_3 \in [-0.02,\ 0.02]$. As with the piecewise polytrope, if $c_s > c$ at

some density then we set $c_s = c$ at that density. Unlike the piecewise-polytropic parameterization, the spectral parameterization with these ranges of γ_i cannot easily simulate a phase transition. However, in other ways it is more flexible, with fewer parameters, than the piecewise-polytropic model.

5.2.2. Models Using Gaussian Processes

A newer approach to EOS modeling using GPs was introduced in Landry & Essick (2019) (see also the subsequent work in Landry et al. 2020; Essick et al. 2020a, 2020b). Because this method is currently less commonly used in the community than the parametric approach, we will summarize it in more detail.

The essence of GP estimation of a function f (see Rasmussen & Williams 2006 for an excellent introduction) is that we would like to have the outcome of our analysis be the joint probability density for the function values $f(\boldsymbol{x})$ at inputs $\boldsymbol{x}$ (which we can represent as x_i), which we assume to be a multivariate Gaussian distribution with means $\boldsymbol{\mu} = \mu_i$ and covariance matrix $\Sigma = \Sigma_{ij}$. That is, we would ultimately like to obtain

$$f(\boldsymbol{x}) \sim \mathcal{N}(\boldsymbol{\mu}, \Sigma), \tag{11}$$

where $\mathcal{N}$ indicates a normal distribution.

A key assumption made in GP estimation is that correlations between the function values f_i, f_j at inputs x_i, x_j can be represented using a covariance kernel K that is a function of x_i and x_j. That is, if our joint distribution is

$$f_i | x_i \sim \mathcal{N}(\langle f_i \rangle, \Sigma(f_i, f_j)), \tag{12}$$

where $\langle f_i \rangle$ is the expectation value for f at x_i and $\Sigma(f_i, f_j)$ is the covariance matrix, then we assume we can write $\Sigma(f_i, f_j) = K(x_i, x_j)$.

It is reasonable to assume that when x_i and x_j are closer to each other, K is larger. Given that covariance matrices are symmetric, it also must be that $K(x_i, x_j) = K(x_j, x_i)$ for any x_i and x_j. A common and much more drastic simplification is to assume that K depends on only the distance between the points: $K(x_i, x_j) = K(|x_i - x_j|)$. We use a Gaussian kernel, which in this context is called a "squared-exponential kernel":

$$K_{\rm se}(x, x') = \sigma^2 \exp\left(-\frac{(x - x')^2}{2\ell^2}\right), \tag{13}$$

which has the properties listed above. Here the hyperparameter σ determines the strength of the overall correlation and the hyperparameter ℓ gives the correlation length scale. For example, $\ell \to 0$ would mean that all of the points are independent of each other, and $\sigma \to 0$ would mean that there is negligible variance.

Transformation of dependent variable. There is one additional important qualitative aspect of the analysis of EOS using GPs. A true Gaussian has a domain of $-\infty$ to $+\infty$. However, if we think about an EOS as $\epsilon(P)$, then because ϵ is non-negative it cannot range from $-\infty$ to $+\infty$. We could instead use $\log(\epsilon)$ as a function of $\log(P)$, because if we express ϵ in some units, e.g., cgs units, $\log(\epsilon)$ can range from $-\infty$ to $+\infty$. However, this approach is also sub-optimal because it could lead to unstable ($dp/d\epsilon < 0$) or acausal ($dp/d\epsilon > c^2$) EOS. In principle one could simply discard such EOSs when they are drawn from the GP, but this would be inefficient.

Therefore, we follow Lindblom (2010) and Landry & Essick (2019) in defining a new variable:

$$\phi \equiv \ln\left(c^2 \frac{d\epsilon}{dP} - 1\right). \tag{14}$$

Because the adiabatic speed of sound c_s is given by $c_s^2 = dP/d\epsilon$, at the boundary of thermodynamic stability ($c_s^2 \to 0$), $\phi \to +\infty$, and at the boundary of causality ($c_s^2 \to c^2$), $\phi \to -\infty$. Thus if we construct a GP in $\phi(\log P)$, all values of ϕ correspond to stable and causal EOSs.

The next choice we need to make is how closely we wish to follow tabulated EOSs in our function $\phi(\log P)$. Landry & Essick (2019) define two approximate limits: the "model-informed" EOS prior, in which the GP is strongly conditioned on a set of EOSs proposed in the literature, and the "model-agnostic" EOS prior, in which the GP is only loosely related to existing EOS proposals. The model-agnostic approach is much less computationally demanding and is less biased by existing EOSs, so it is the path that we follow.

We then need to choose the parameters that describe our GP. Landry & Essick (2019) note that it is advantageous to look for approximate trends in the function we wish to model (here $\phi(\log P)$) and then to produce a GP for the residuals. We find from sets of tabulated EOS (e.g., those at the CompOSE website https://compose.obspm.fr/table/families/3/) that in the log pressure range of interest ($\log_{10} P$ (erg cm^{-3}) $\sim$ 32–36) the trend is roughly linear. We use $\phi_0 = 5.5 - 2.0(\log_{10} P - 32.7)$ as our approximate trend, but construction of the GP does not require an exact fit. For our kernel, we use the squared-exponential kernel of Equation (13) and, based on the spread between the EOS above in the $\log_{10} P$(erg cm^{-3}) $\sim$ 32–36 range, we choose $\sigma = 1$ and $\ell = 1$.

We note that the GP framework allows for substantial flexibility beyond our particular choice (see, e.g., Essick et al. 2020a). For example, although $\sigma = 1$ and $\ell = 1$ matches well most existing EOSs in the density range that has a discernible impact on the maximum mass, radius, and tidal deformability of neutron stars, when combined with our $\phi_0 = 5.5 - 2.0(\log_{10} P - 32.7)$ trend it leads to sound speeds approaching the speed of light at densities several times nuclear saturation density. A different choice of hyperparameters, e.g., a larger σ, would not necessarily require such high sound speeds; see for example Figure 2 of Landry et al. (2020).

5.3. EOS Results

The constraints we obtain on the EOS at different densities depend both on the EOS model and priors and on the data sets that we include. Here we present the EOS constraints for each of our three models, with progressive incorporation of more data. We also plot the distributions of mass versus radius and the maximum mass for non-rotating neutron stars for different amounts of data and using the GP model. For a given EOS and central density, we solve the Tolman–Oppenheimer–Volkoff equation (Oppenheimer & Volkoff 1939; Tolman 1939) to obtain the mass and radius. Thus for the purpose of calculating stellar structure we implicitly treat the star as non-rotating. This is an excellent approximation at the 346.53 Hz rotation frequency of this pulsar (Cromartie et al. 2020), because this is only $\sim$20% of the mass-shedding frequency and thus the expected deviation from the structure of a non-rotating star is much smaller than our measurement precision (e.g., see

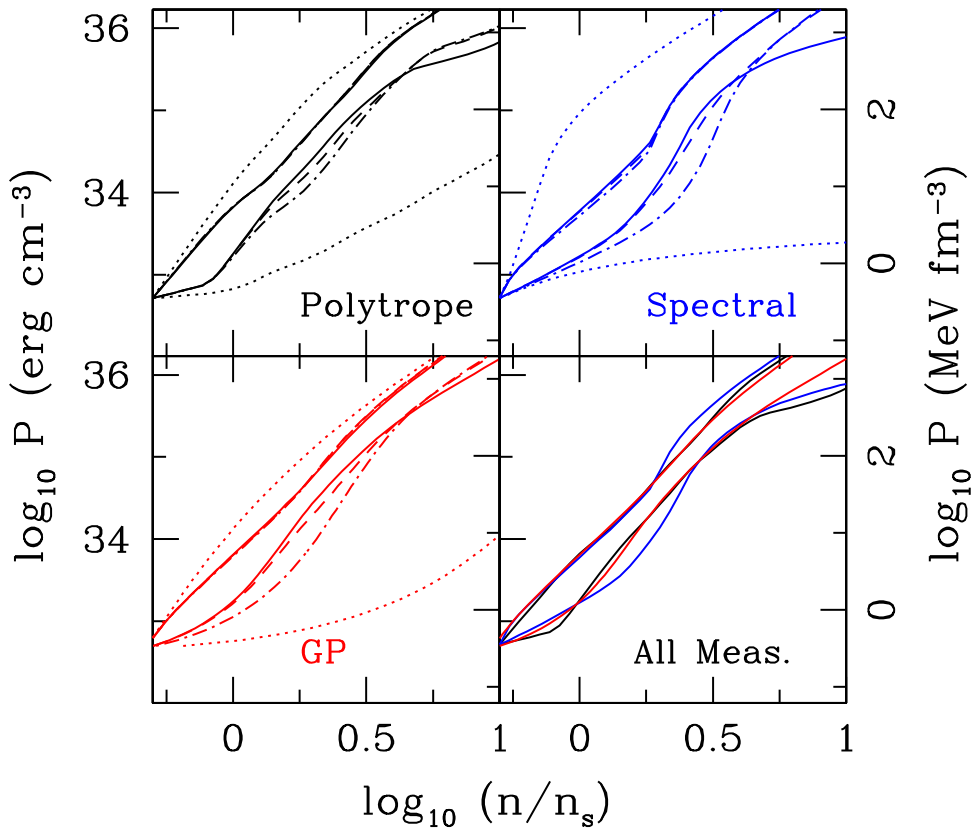

Figure 9. Comparison of the pressure ranges as a function of number density for the three EOS models described in the text, as a function of the data sets included in the analysis. For each line type and color in each panel, the lower line shows the 5th percentile, and the upper line shows the 95th percentile, of the pressure as a function of density. Colors indicate the EOS model used in the analysis: black for a piecewise-polytrope model (see the first part of Section 5.2.1), blue for the spectral model (see the second part of Section 5.2.1), and red for a model based on Gaussian processes (see Section 5.2.2). We show the results for our priors (dotted lines in each panel); our priors plus symmetry energy measurements, the existence of three high-mass pulsars, and two tidal deformability upper limits (dashed–dotted lines in each panel); those plus the mass–radius posteriors on PSR J0030+0451 from Miller et al. (2019) (dashed lines in each panel); and finally all of those plus the mass–radius measurement of PSR J0740+6620 that we report here (solid lines in each panel). The lower right panel shows the full set of constraints, including our PSR J0740+6620 radius measurement, for each of our three EOS families. Inclusion of the masses and radii of PSR J0030+0451 and PSR J0740+6620 tightens significantly the EOS models in the vicinity of $n/n_s \sim 1.5$–5 [$\log_{10}(n/n_s) \sim 0.2$–0.7]. This indicates that with the NICER and XMM-Newton data added, in this density range the posterior is now dominated by the data rather than by the priors.

Figure 13 of Miller et al. 2019; at this mass and rotation frequency, the radius increase is at most 0.2 km compared with a non-rotating star).

In Figure 9 we show, for each EOS model, the middle 90% range for the pressure as a function of number density when we incorporate successively more constraining measurements. The upper left panel shows the results using the piecewise-polytropic model, the upper right panel shows the results using the spectral model, and the lower left panel shows the results using the GP model. Our first constraints (dotted lines) use only the prior for each EOS model. The next constraints include a Gaussian prior of $S = 32 \pm 2$ MeV for the symmetry energy at nuclear saturation density (see Tsang et al. 2012),[37] the existence of three high-mass pulsars (Antoniadis et al. 2013; Arzoumanian et al. 2018; Cromartie et al. 2020), and the tidal deformability posteriors from gravitational wave observations of GW170817 (Abbott et al. 2017, 2018; De et al. 2018) and GW190425 (Abbott et al. 2020a). Other constraints on the symmetry energy are possible; for example, Drischler et al. (2020) find a tighter range for the symmetry energy of $S = 31.7 \pm 1.1$ MeV and analyses of PREX-II data (Adhikari et al. 2021; Reed et al. 2021; Yue et al. 2021) suggest a higher symmetry energy of $S \approx 38 \pm 4$ MeV. The third set of constraints also includes the mass–radius posteriors from the Miller et al. (2019) analysis of NICER data on PSR J0030+0451. Finally, the last set of constraints also includes our mass–radius posteriors for PSR J0740+6620. The lower right panel collects the final set of constraints for all three EOS models. In each case, we only display the results for our fit to both the NICER and the XMM-Newton data using the nominal XMM-Newton calibration. When we include our mass–radius posteriors for PSR J0740+6620, we use only the masses of PSR 1614–2230 and PSR J0348+0432 in our high-pulsar-mass data, i.e., we do not double-count the high mass of PSR J0740+6620.

Several trends are evident in this figure.

1. The 5%–95% pressure range at densities $n \approx (1.5 - 5)n_s$, after incorporation of all measurements, has been tightened substantially compared with the prior range and now depends relatively weakly on the EOS model. For example,

[37] The symmetry energy S is the difference between the total energy per nucleon of pure neutron matter and $E_{\rm sym}$, the energy per nucleon of symmetric nuclear matter. Here we approximate S using $\epsilon/n - m_n c^2$. Given that the matter at nuclear saturation density is not pure neutrons, $\epsilon/n - m_n c^2$ could be a few percent different from S (see Lattimer & Prakash 2016 for a discussion). However, the inclusion of an S constraint has only a minor effect; for example, with our constraint, the full $\pm 1\sigma$ range of radii at $M = 1.4\,M_\odot$ over all three EOS frameworks is 11.8–13.1 km, whereas without any S constraint the range is 11.6–13.0 km.

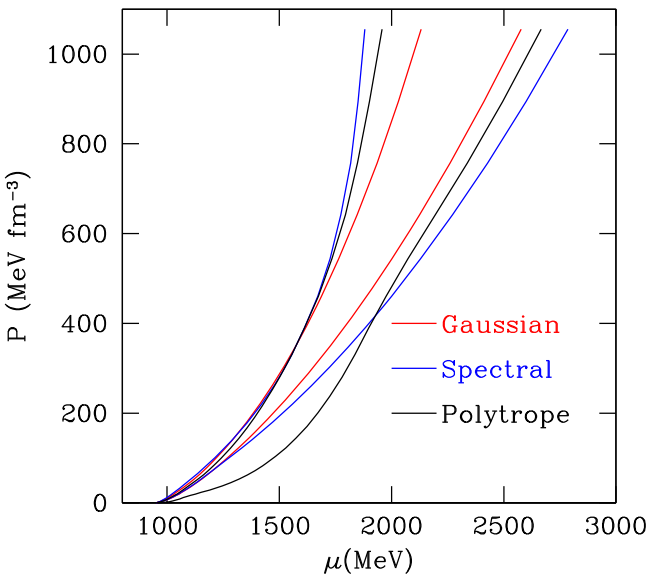

Figure 10. The 5th to 95th percentile range of the pressure as a function of the baryon chemical potential, including the neutron rest mass-energy, for all three of our models of the EOS: the red line is for the Gaussian process EOS, the blue line is for the spectral EOS, and the black line is for the piecewise-polytropic EOS. Here we include all measurements: symmetry energy, high-mass pulsars, tidal deformability from gravitational wave measurements, and measurements of the mass and radius of PSR J0030+0451 and PSR J0740+6620.

using the priors the maximum difference in the 5th percentile of the log pressure in this density range, among all three EOS frameworks, is 0.61; after incorporation of all data, the maximum difference has dropped to 0.34. For the 95th percentile, the maximum difference in the log pressure among all our EOS frameworks in this density range has dropped from 0.86 to 0.21. This is encouraging, because it means that for this density range the posterior is now dominated by the data rather than by the priors.

2. This convergence of constraints requires the NICER data on PSR J0030+0451 and the NICER+XMM-Newton data on PSR J0740+6620. Without these data, the pressure ranges differ significantly among the three models.
3. As expected, there is much less convergence at higher densities ($\gtrsim 5 n_s$) and at lower densities ($\lesssim 1.5\, n_s$). This is because low and high densities contribute less to the radius, mass, and tidal deformability of neutron stars. See Lattimer & Prakash (2007, 2016), Xie & Li (2020), and Drischler et al. (2021) for the detailed theoretical context.
4. Finally, we note that the constraining power of our measurement of PSR J0740+6620 comes entirely from the strong lower limit on its radius. Other measurements, particularly the non-detection of tidal deformability from GW170817, already strongly exclude radii as large as even our $+1\sigma$ value of >16 km. However, the evidence that the -1σ radius is $\gtrsim 12$ km, and that the -2σ radius is $\gtrsim 11$ km, adds significantly to our understanding of dense matter.

In Figure 10 we present another view of the EOS, after all measurements are incorporated. Here we show the pressure versus the baryon chemical potential $\mu = (\epsilon + P)/n$ (including the baryon rest mass-energy) for all three of our EOS models.

In Figure 11 we present the 5th to 95th percentile range, and the 25th to 75th percentile range, of the radius as a function of mass, using our GP model, for the same set of measurements as in Figure 9. In this figure we also plot (faint lines) representative mass–radius relations drawn from our set of EOSs, where in each panel the probability of drawing an individual EOS is proportional to its statistical weight given the measurements considered in that panel. Here we only plot masses below the 95th percentile of the maximum gravitational mass of a non-rotating neutron star, given the measurements being considered. The radius and mass of PSR J0030+0451, and our current measurement of the radius of PSR J0740+6620, tighten the allowed radius significantly at all neutron star masses greater than $1.0\, M_\odot$. See Table 4 for details. In particular, the $\pm 1\sigma$ radius range at $M = 1.4\, M_\odot$, spanning all three EOS frameworks, is just 11.79–13.11 km, or $\pm 5.3\%$. In addition, although the direct measurement that we report of the radius of PSR J0740+6620 has a $\pm 1\sigma$ range of $\approx$12.2–16.3 km, when we include other measurements the $\pm 1\sigma$ range, spanning all three EOS frameworks, narrows to 11.60–13.11 km at $M = 2.08\, M_\odot$. This is dramatically improved compared with the prior $\pm 1\sigma$ range of 10.47–14.27 km over all of our EOS frameworks.

In Figure 12 we see that the maximum mass range shifts slightly to smaller values when we include our radius measurement of PSR J0740+6620; see Table 4 for details. As the table shows, the maximum mass range still has a significant dependence on the EOS framework. In a given EOS framework, there is a weak positive correlation between the radius at $M = 2.08\, M_\odot$ and the maximum mass of a non-rotating star; one reflection of this is that when our analysis of the NICER and XMM-Newton data of PSR J0740+6620 is included, the maximum mass decreases and the $+1\sigma$ radius at $M = 2.08\, M_\odot$ also decreases slightly in two of the three EOS frameworks. As one implication of the slightly lowered maximum mass, consider the lighter object in the gravitational wave coalescence GW190814, which has a best mass estimate of $2.59\, M_\odot$ (Abbott et al. 2020b). Using our GP EOS model, without our PSR J0740+6620 measurement, there is a 12.1% probability that this object is a slowly rotating neutron star. With our PSR J0740+6620 measurement, the probability drops to 7.5%.

In Figure 13 we show the inferred 5th and 95th percentile curves for the sound speed squared as a function of number density, for our results including our PSR J0740+6620 analysis. For comparison we also show the results for our particular GP EOS framework, using only our priors. This figure shows that the sound speed c_s is not very well constrained compared to the pressure. This is expected, because $c_s^2 = dP/d\epsilon$ and thus the sound speed is related to the slope of the pressure. A comparison of the prior to the final posterior of the sound speed for the GP EOS shows that the data are not constraining beyond $\sim 4 n_s$ but do tighten the allowed range significantly at lower densities. In particular, the increase in the 5th percentile of c_s^2/c^2, compared with the prior, at densities $\sim$2–4n_s, is common to all three EOS frameworks.

6. Conclusions

NICER measurements of PSR J0030+0451 and PSR J0740+6620, complemented with XMM-Newton measurements of PSR J0740+6620, have reduced the uncertainty about the EOS of high-density, cold catalyzed matter. This is especially true in the density range $n \sim 1.5$–$5 n_s$. These two radius measurements

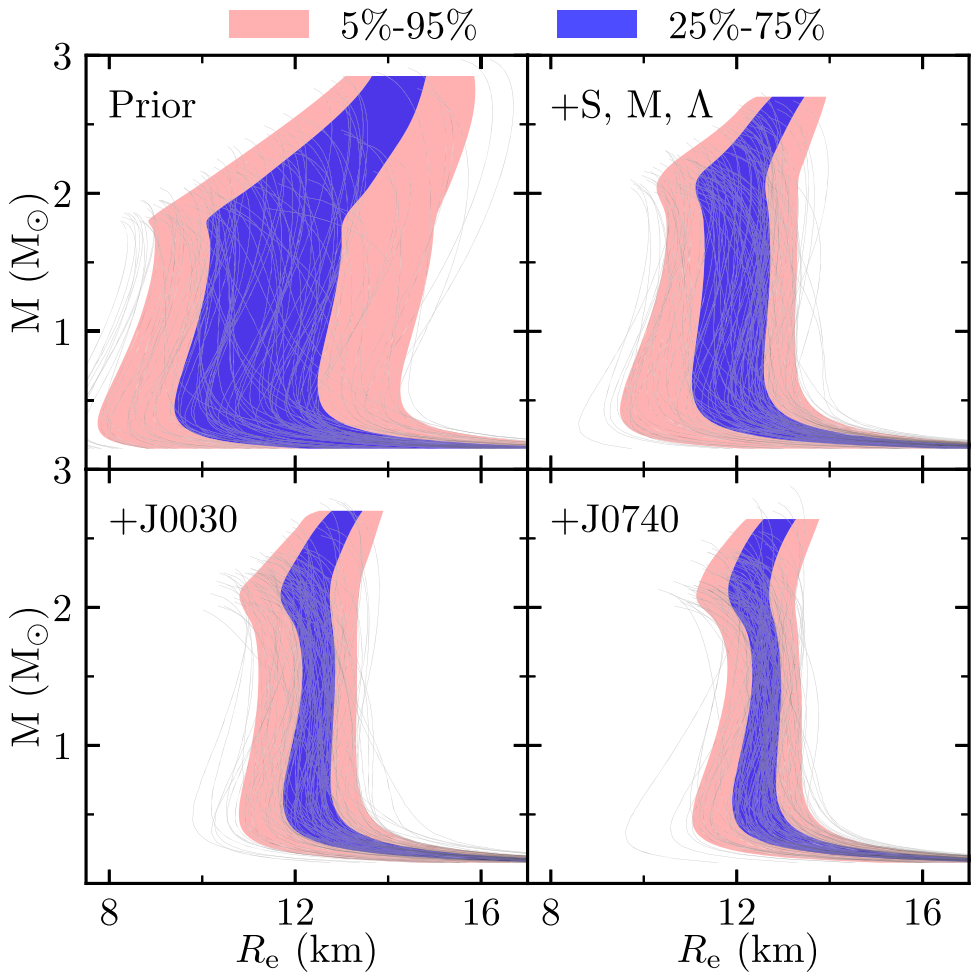

Figure 11. The 25th to 75th percentile range (blue shading) and the 5th to 95th percentile range (pink shading) of the radius as a function of mass, for non-rotating neutron stars. The faint lines show the mass–radius relations of representative individual EOS (see the text for details). At each mass only EOSs that can reach that mass contribute to the radius posterior; thus at high masses, which require hard EOSs, the radii become larger. We use the Gaussian process EOS model for the same progression of measurements as in Figure 9, where S is the symmetry energy, M refers to the high masses of three pulsars, and Λ indicates the gravitational wave measurements of tidal deformability for GW170817 and GW190425. In each panel, we only include masses below the 95th percentile of the maximum mass for non-rotating neutron stars (see Figure 12 for a closer investigation of the maximum mass). See Table 4 for details of how our radius bounds change between EOS models and when including different observations. The agreement between the methods, particularly at the $\pm 1\sigma$ level, is another indication of improving convergence between models.

Table 4
Summary of Maximum Mass and Radii at 1.4 $M_\odot$ and 2.08 $M_\odot$

EOS Model	Measurements	$M_{\max}$ ($M_\odot$)			R_e(1.4 $M_\odot$), km			R_e(2.08 $M_\odot$), km		
		-1σ	Median	$+1\sigma$	-1σ	Median	$+1\sigma$	-1σ	Median	$+1\sigma$
Gaussian	S, M, Λ	2.12	2.27	2.52	10.92	12.23	12.93	10.80	11.97	12.86
	+J0030	2.13	2.30	2.54	11.88	12.51	13.02	11.39	12.27	12.95
	+J0740	2.08	2.23	2.47	12.17	12.63	13.11	11.60	12.28	12.88
Spectral	S, M, Λ	2.28	2.55	2.88	10.41	11.43	12.40	10.79	11.81	12.97
	+J0030	2.39	2.78	2.93	11.52	12.22	12.67	11.56	12.77	13.11
	+J0740	2.23	2.74	2.92	11.79	12.30	12.84	11.83	12.78	13.11
Piecewise	S, M, Λ	2.13	2.37	2.64	11.26	12.32	12.89	11.04	12.21	12.90
polytrope	+J0030	2.14	2.41	2.65	11.95	12.47	12.94	11.42	12.35	12.94
	+J0740	2.09	2.27	2.61	12.16	12.56	13.01	11.67	12.36	12.91

Note. Maximum gravitational masses and equatorial circumferential radii at $M = 1.4\ M_\odot$ and $M = 2.08\ M_\odot$ (the best estimate of the mass of PSR J0740+6620), all at $\pm 1\sigma$ for nonrotating stars, inferred using our three EOS frameworks with three different sets of measurements. The S, M, Λ set includes constraints on the symmetry energy, the high masses of three pulsars, and the two LIGO/Virgo tidal deformability measurements. The +J0030 set also includes the Miller et al. (2019) measurement of the radius and mass of PSR J0030+0451. The +J0740 data add our measurement of the radius of PSR J0740+6620. We see that the radius estimates tighten with addition of more data, and in particular that the final $\pm 1\sigma$ radius range for a 2.08 $M_\odot$ star, spanning all three EOS frameworks (11.60–13.11 km), is very similar to the final $\pm 1\sigma$ radius range for a 1.4 $M_\odot$ star, spanning all three EOS frameworks (11.79–13.11 km).

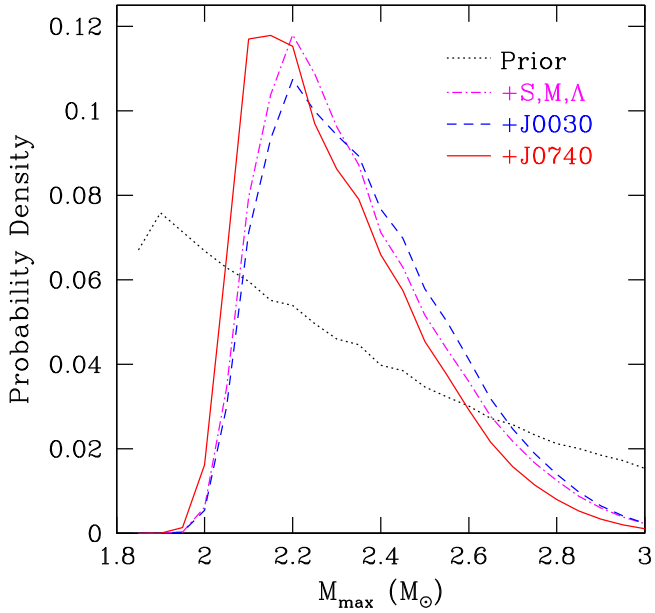

Figure 12. Posterior probability distribution for the maximum gravitational mass of a non-rotating neutron star, normalized in each case so that the integral of the probability density in the $M_{\rm max} = 1.8$–$3.0\,M_\odot$ range is 1. The highest maximum mass allowed in our analysis was $3.0\,M_\odot$. We use the Gaussian process model for the same progression of measurements as in Figure 9, where S is the symmetry energy, M refers to the high masses of three pulsars, and Λ indicates the gravitational wave measurements of tidal deformability for GW170817 and GW190425. See Table 4 for details of how our maximum mass bounds change between EOS models and when including different observations.

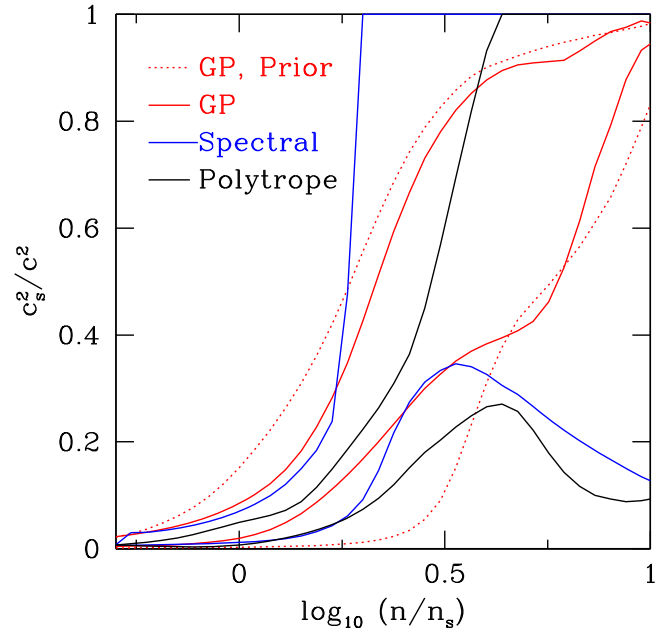

Figure 13. The 5th to 95th percentile range of the sound speed squared (in units of c^2), for all three of our models of the EOS: the red line is for the Gaussian process (GP) EOS, the blue line is for the spectral EOS, and the black line is for the piecewise polytropic EOS. The solid lines show the results when we include all measurements: symmetry energy, high-mass pulsars, tidal deformability from gravitational wave measurements, and measurements of the mass and radius of PSR J0030+0451 and PSR J0740+6620. The dotted line shows our GP results using only our priors. Because $c_s^2 = dP/d\epsilon$, the sound speed is the slope of the pressure-density relation and is therefore not as well constrained as the relation itself. We see from this plot that in our particular GP EOS framework the sound speed automatically approaches the speed of light at high densities; the prior dominates at densities $\gtrsim 4n_s$ (other choices of GP hyperparameters need not lead to this behavior; see for example Figure 2 of Landry et al. 2020). However, the rise in the 5th percentile of the sound speed, compared with the prior, at densities $\sim$2–$4n_s$, is common to all three EOS frameworks.

also shift slightly the credible region for the maximum gravitational mass of a non-rotating neutron star.

Most importantly, our new measurement narrows significantly the inferred radius range for $1.4\,M_\odot$ neutron stars. For instance, prior to our measurement, when we used our GP EOS model, inclusion of nuclear data, information about neutron star tidal deformability from the gravitational wave event GW170817, and our previous mass and radius measurement of PSR J0030+0451 had constrained the radius to 11.2–13.3 km at 90% credibility and 11.9–13.0 km at 68% credibility. When we also include our PSR J0740+6620 measurement, these ranges shrink to 11.8–13.4 km (90%) and 12.2–13.1 km (68%). That is, as expected, the main effect of our PSR J0740+6620 measurement is to increase the lower limit to the radius. Indeed, even when we consider the radius range spanned by all three of our EOS models, the range is 11.8–13.1 km at 68% credibility, for a fractional uncertainty of $\pm 5.3\%$. This is broadly consistent with previous radius estimates based both on nuclear theory and tidal deformabilities inferred from gravitational wave observations (Abbott et al. 2017, 2020a; De et al. 2018) and on the NICER mass and radius estimates for PSR J0030+0451 (Miller et al. 2019; Riley et al. 2019): the total radius range spanned by all the computed $\pm 1\sigma$ radius bounds, prior to our measurement of the radius of PSR J0740+6620, for $1.4\,M_\odot$ neutron stars is $\approx$11–13.5 km (e.g., Alvarez-Castillo et al. 2000; Dietrich et al. 2020; Greif et al. 2020; Jiang et al. 2020; Li et al. 2020, 2021; Zhao & Lattimer 2020; Essick et al. 2020b; Biswas et al. 2021; Han et al. 2021; Selva et al. 2021; Sen & Guha 2021).

Data are still being taken actively; for example, it is likely that by the end of the NICER mission the exposure times on PSR J0030+0451 and PSR J0740+6620 will roughly double compared with those used in current analyses, and an analysis of NICER data on PSR J0437−4715 (which has the highest X-ray flux of any non-accreting neutron star) is in progress. This gives reason for optimism that future NICER observations, and in the coming years more gravitational-wave observations of tidal deformability, will provide even clearer insight into a realm of matter which cannot be explored in laboratories.

This work was supported by NASA through the NICER mission and the Astrophysics Explorers Program. The authors acknowledge the University of Maryland supercomputing resources (http://hpcc.umd.edu) that were made available for conducting the research reported in this Letter. The authors also thank Felix Fuerst for facilitating the XMM-Newton director's discretionary time observations of PSR J0740+6620, and Brad Cenko for early Swift observations. MCM thanks the Radboud Excellence Initiative for supporting his stay at Radboud University and was supported in part by NASA ADAP grant 80NSSC21K0649. MCM also thanks Gordon Baym, Cecilia Chirenti, and Sanjay Reddy for comments on an earlier version of this manuscript. W.C.G.H. appreciates use of computer facilities at the Kavli Institute for Particle Astrophysics and Cosmology and acknowledges support through grant 80NSSC20K0278 from NASA. T.T.P. is a NANOGrav Physics Frontiers Center Postdoctoral Fellow funded by the

National Science Foundation award number 1430284. I.H.S. is supported by an NSERC Discovery grant and by the Canadian Institute for Advanced Research. Support for H.T.C. was provided by NASA through the NASA Hubble Fellowship Program grant #HST-HF2-51453.001 awarded by the Space Telescope Science Institute, which is operated by the Association of Universities for Research in Astronomy, Inc., for NASA, under contract NAS5-26555. S.M.M. thanks the Natural Sciences and Engineering Research Council of Canada for funding. Portions of this work performed at NRL were funded by NASA. The authors acknowledge the use of NASA's Astrophysics Data System (ADS) Bibliographic Services and the arXiv.

Facility: NICER (Gendreau et al. 2016), XMM-Newton (Strüder et al. 2001; Turner et al. 2001), Swift (Gehrels et al. 2004).

Software: emcee (Foreman-Mackey et al. 2013), MultiNest (Feroz et al. 2009), Python and NumPy (Oliphant 2007), Matplotlib (Hunter 2007), Cython (Behnel et al. 2011), schwimmbad (Price-Whelan & Foreman-Mackey 2017), and the XMM-Newton Scientific Analysis System (SAS, Gabriel et al. 2004).

Appendix A
Posterior Distributions from Analysis of Synthetic J0740-like NICER and XMM-Newton Data

Table 5 and Figure 14 show the best fit and uncertainties for a two-circle fit to a synthetic NICER plus XMM-Newton data set which mimics the actual data on PSR J0740+6620.

Table 5
Fits to Synthetic NICER and XMM-Newton Data

Parameter	Median	-1σ	$+1\sigma$	-2σ	$+2\sigma$	Assumed value
R_e (km)	13.933	12.344	17.396	11.342	22.215	13.378
GM/c^2R_e	0.221	0.177	0.248	0.139	0.267	0.230
M ($M_\odot$)	2.081	1.991	2.174	1.895	2.261	2.080
θ_{c1} (rad)	1.618	0.892	2.341	0.583	2.602	1.820
$\Delta\theta_1$ (rad)	0.121	0.078	0.180	0.051	0.259	0.061
$kT_{\rm eff,1}$ (keV)	0.085	0.076	0.097	0.068	0.111	0.107
θ_{c2} (rad)	1.574	0.881	2.313	0.586	2.604	2.280
$\Delta\theta_2$ (rad)	0.121	0.078	0.179	0.050	0.262	0.086
$kT_{\rm eff,2}$ (keV)	0.085	0.076	0.097	0.068	0.111	0.100
$\Delta\phi_2$ (cycles)	0.554	0.422	0.578	0.409	0.592	0.422
$\theta_{\rm obs}$ (rad)	1.526	1.467	1.585	1.444	1.610	1.463
N_H (10^{20} cm^{-2})	3.067	1.377	4.389	0.302	4.915	0.226
d (kpc)	1.211	1.025	1.400	0.840	1.598	1.099

Note. The one-dimensional credible intervals for each of the parameters in a pulse waveform model with two possibly different uniform circular spots, obtained by jointly fitting the model to synthetic NICER data (in channels 30–123) and synthetic XMM-Newton data that together mimic the actual NICER and XMM-Newton data. The rightmost column lists the parameter values that were used to generate the synthetic data. These values were taken from a model that gives a good fit to the actual PSR J0740+6620 data. The synthetic data were then generated by Poisson draws from the fluxes predicted by that model, including the background fluxes it predicts. Consistent with statistical expectations, six of the 12 $\pm1\sigma$ credible intervals, 11 of the 12 $\pm2\sigma$ credible regions, and all (12 of 12) of the $\pm3\sigma$ credible regions contain the values of the model parameters that were assumed in generating the synthetic data.

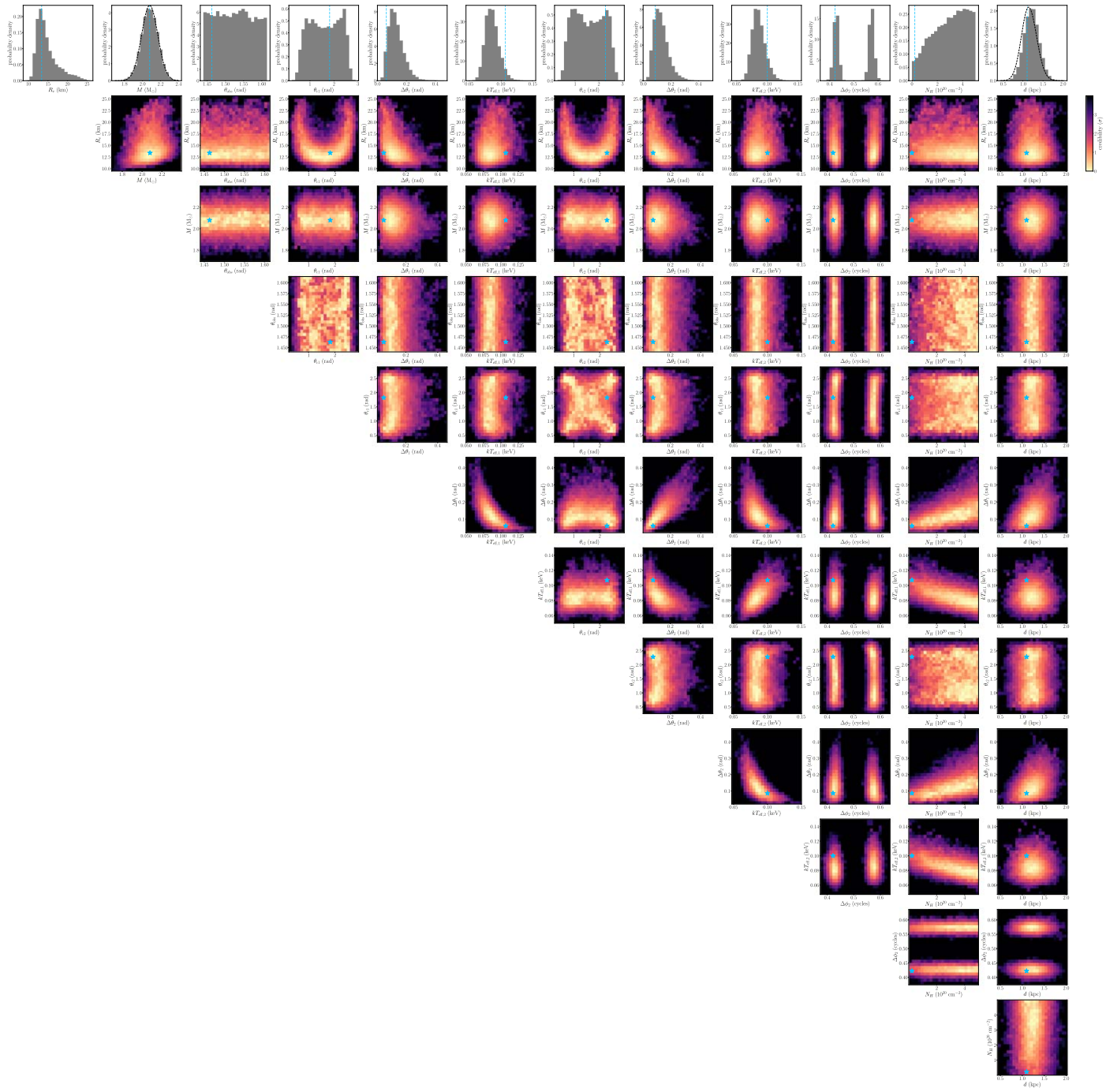

Figure 14. Posterior probability density distributions for a model with two uniform circular spots that is fit jointly to the synthetic NICER and XMM-Newton data. The dotted lines in the one-dimensional plots for gravitational mass and distance indicate the priors that we applied. The vertical dashed lines in the one-dimensional plots indicate the value of the associated parameter that was assumed in the construction of the synthetic data. Similarly, the star symbols in the two-dimensional plots show the assumed values of both parameters. In this and the other corner plots in the appendices, brighter colors in the two-dimensional plots indicate higher posterior probability densities.

Appendix B
Posterior Distributions from Analysis of Only NICER Data

Table 6 and Figure 15 show the best fit and uncertainties for a two-circle fit to just the NICER data on PSR J0740+6620.

Table 6
Fits to Only NICER Data

Parameter	Median	-1σ	$+1\sigma$	-2σ	$+2\sigma$	Best fit
R_e (km)	11.512	10.382	13.380	9.642	16.256	11.008
GM/c^2R_e	0.266	0.229	0.293	0.188	0.308	0.278
M ($M_\odot$)	2.072	1.978	2.159	1.885	2.247	2.071
θ_{c1} (rad)	1.655	0.667	2.541	0.292	2.858	0.494
$\Delta\theta_1$ (rad)	0.329	0.205	0.541	0.132	0.899	0.328
$kT_{\rm eff,1}$ (keV)	0.072	0.064	0.079	0.057	0.087	0.078
θ_{c2} (rad)	1.582	0.641	2.510	0.310	2.847	1.803
$\Delta\theta_2$ (rad)	0.326	0.204	0.539	0.132	0.854	0.208
$kT_{\rm eff,2}$ (keV)	0.072	0.064	0.079	0.057	0.087	0.079
$\Delta\phi_2$ (cycles)	0.527	0.441	0.560	0.422	0.578	0.550
$\theta_{\rm obs}$ (rad)	1.528	1.468	1.586	1.444	1.610	1.535
N_H (10^{20} cm^{-2})	1.833	0.599	3.414	0.094	4.667	0.858
d (kpc)	1.213	1.025	1.407	0.843	1.596	1.086

Note. One-dimensional credible regions, and best fit, obtained by fitting a model with two possibly different uniform circular spots to only the NICER data, using energy channels 30–123. These credible regions may be compared with the regions in Table 7, where both NICER and XMM-Newton data are analyzed. The analysis here was performed using a free background in each NICER energy channel; as discussed in Section 4.2, future incorporation of reliable background models for NICER will likely increase the NICER-only radius to values more comparable to what we infer when we also use XMM-Newton data.

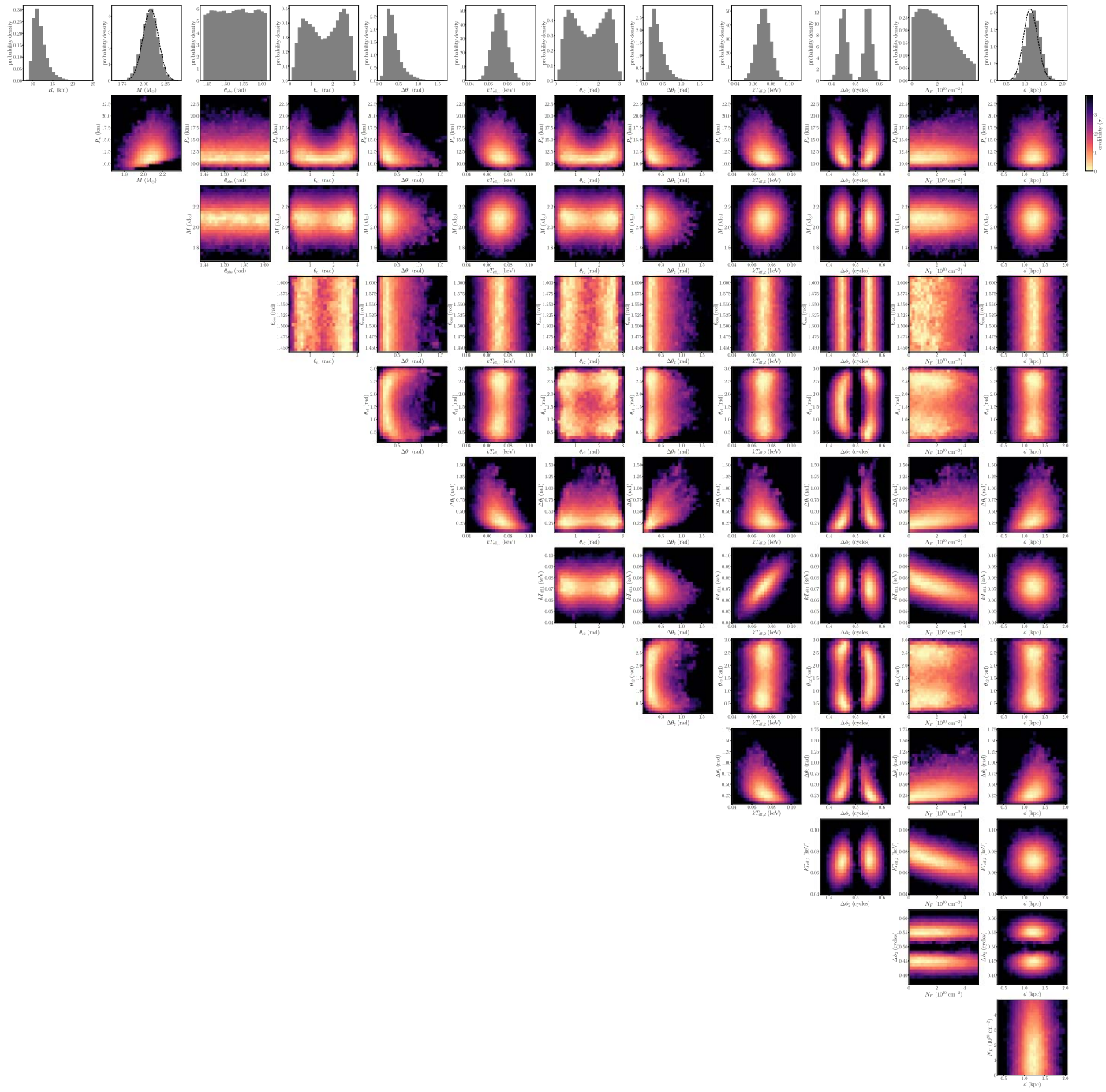

Figure 15. Posterior probability density distributions for a model with two uniform circular spots that is fit to only the NICER data. Note that because the observer inclination is close to the equator, there is a near-degeneracy between spots in the northern hemisphere and spots in the southern hemisphere. The dotted lines in the one-dimensional plots for gravitational mass and distance indicate the priors that we applied.

Appendix C
Posterior Distributions from Analysis of NICER and XMM-Newton Data

Table 7 and Figure 16 show the best fit and uncertainties for a two-circle fit to the NICER plus XMM-Newton data on PSR J0740+6620.

Table 7
Fits to NICER and XMM-Newton data

Parameter	Median	-1σ	$+1\sigma$	-2σ	$+2\sigma$	Best fit
R_e (km)	13.713	12.209	16.326	11.243	20.051	13.823
GM/c^2R_e	0.222	0.187	0.249	0.151	0.267	0.221
M ($M_\odot$)	2.062	1.971	2.152	1.883	2.242	2.067
θ_{c1} (rad)	1.600	0.900	2.319	0.586	2.631	0.834
$\Delta\theta_1$ (rad)	0.098	0.065	0.145	0.044	0.219	0.087
$kT_{\rm eff,1}$ (keV)	0.094	0.083	0.105	0.073	0.118	0.098
θ_{c2} (rad)	1.612	0.917	2.297	0.572	2.618	1.223
$\Delta\theta_2$ (rad)	0.096	0.064	0.143	0.042	0.213	0.066
$kT_{\rm eff,2}$ (keV)	0.094	0.083	0.106	0.073	0.120	0.103
$\Delta\phi_2$ (cycles)	0.558	0.422	0.579	0.409	0.592	0.577
$\theta_{\rm obs}$ (rad)	1.527	1.467	1.586	1.444	1.610	1.561
N_H (10^{20} cm^{-2})	1.137	0.315	2.549	0.043	4.174	0.006
d (kpc)	1.215	1.027	1.404	0.852	1.593	1.151

Note. One-dimensional credible regions, and best fit, obtained by jointly fitting a model with two possibly different uniform circular spots to channels 30–123 of the NICER data and to the XMM-Newton data on PSR J0740+6620. This analysis used the nominal calibration of NICER and XMM-Newton. These credible regions may be compared with the regions in Table 6, where only NICER data are analyzed.

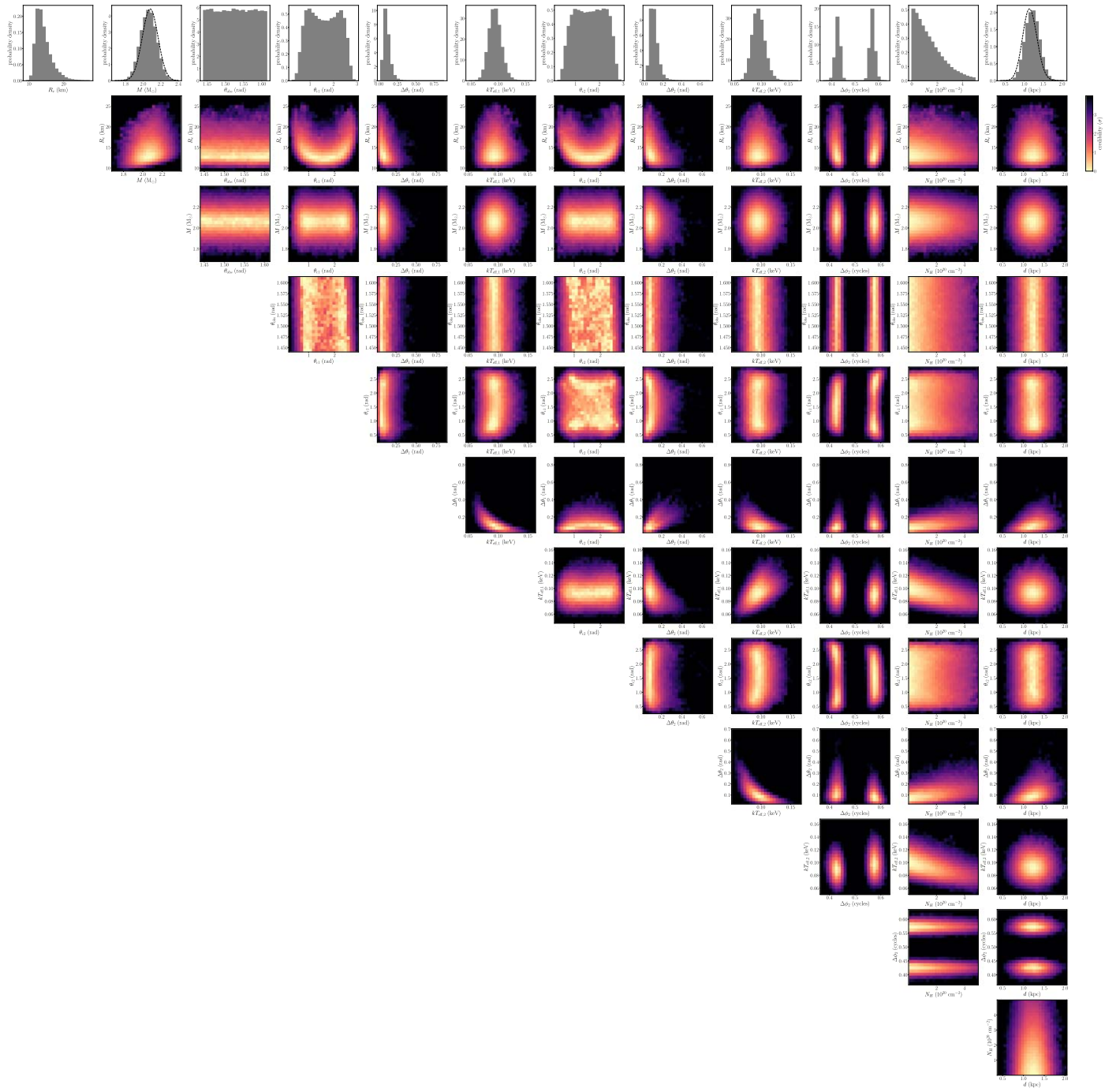

Figure 16. Posterior probability density distributions for a model with two uniform circular spots that is fit to the NICER and XMM-Newton data, using the nominal calibration for NICER and XMM-Newton. The dotted lines in the one-dimensional plots for gravitational mass and distance indicate the priors that we applied.

Appendix D
Posterior Distributions from Analysis of NICER and XMM-Newton Data with an XMM-Newton Calibration Parameter

Table 8 and Figure 17 show the best fit and uncertainties for a two-circle fit to the NICER plus XMM-Newton data on PSR J0740+6620, in which we have added a parameterized normalization for the XMM-Newton calibration.

Table 8
Fits to NICER and XMM-Newton Data with a Parameterized Normalization for the XMM-Newton Calibration

Parameter	Median	-1σ	$+1\sigma$	-2σ	$+2\sigma$	Best fit
R_e (km)	13.705	12.153	16.298	11.140	20.199	13.524
GM/c^2R_e	0.223	0.187	0.250	0.151	0.270	0.227
M ($M_\odot$)	2.064	1.973	2.154	1.882	2.244	2.082
θ_{c1} (rad)	1.635	0.895	2.324	0.575	2.634	2.399
$\Delta\theta_1$ (rad)	0.097	0.064	0.144	0.042	0.214	0.106
$kT_{\rm eff,1}$ (keV)	0.095	0.084	0.107	0.074	0.120	0.098
θ_{c2} (rad)	1.647	0.910	2.327	0.573	2.632	1.876
$\Delta\theta_2$ (rad)	0.097	0.065	0.143	0.044	0.212	0.076
$kT_{\rm eff,2}$ (keV)	0.095	0.084	0.106	0.074	0.119	0.102
$\Delta\phi_2$ (cycles)	0.551	0.422	0.578	0.409	0.591	0.571
$\theta_{\rm obs}$ (rad)	1.525	1.467	1.586	1.444	1.610	1.536
N_H (10^{20} cm^{-2})	1.081	0.293	2.489	0.040	4.116	0.033
d (kpc)	1.209	1.023	1.403	0.845	1.599	1.206
$A_{\rm XMM}$	0.969	0.919	1.043	0.902	1.090	0.917

Note. One-dimensional credible regions, and best fit, obtained by jointly fitting a model with two possibly different uniform circular spots to channels 30–123 of the NICER data and to the XMM-Newton data on PSR J0740+6620. Here we add a parameter, $A_{\rm XMM}$, which is the energy-independent ratio of the XMM-Newton effective area to its nominal value. These credible regions are nearly identical to those in Table 7, where we assumed the nominal effective area.

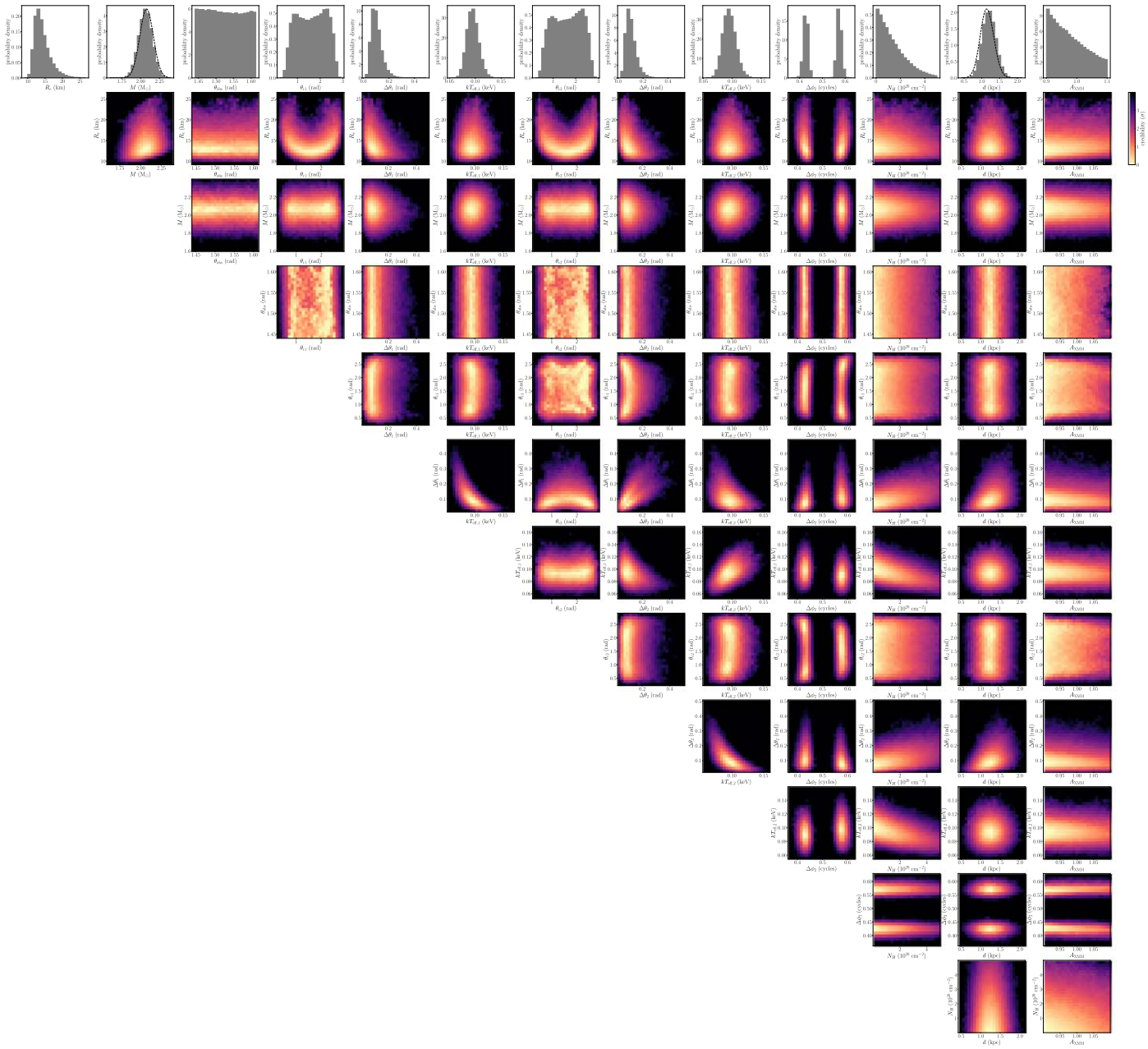

Figure 17. Posterior probability density distributions for a model with two uniform circular spots that is fit to the NICER and XMM-Newton data, where we allow the XMM-Newton effective area to be multiplied by an energy-independent parameter $A_{\rm XMM}$. The dotted lines in the one-dimensional plots for gravitational mass and distance indicate the priors that we applied. Here the prior on $A_{\rm XMM}$ was flat between 0.9 and 1.1; this range is roughly twice as broad as has been measured, as can be seen from slide 7 of http://iachec.org/wp-content/presentations/2020/NICER-CrossCal-IACHEC-Markwardt-2020b.pdf, which shows that in the energy range relevant to our analyses, 0.3–1 keV, the flux inferred from 3C~273 agrees between NICER and XMM-Newton to ∼4%. Examination of this corner plot suggests that the preference for smaller $A_{\rm XMM}$ within this limited range is likely due to more spot sizes and configurations being allowed when the XMM-Newton data are deweighted.

ORCID iDs

M. C. Miller https://orcid.org/0000-0002-2666-728X
F. K. Lamb https://orcid.org/0000-0002-3862-7402
A. J. Dittmann https://orcid.org/0000-0001-6157-6722
S. Bogdanov https://orcid.org/0000-0002-9870-2742
K. C. Gendreau https://orcid.org/0000-0001-7115-2819
S. Guillot https://orcid.org/0000-0002-6449-106X
W. C. G. Ho https://orcid.org/0000-0002-6089-6836
J. M. Lattimer https://orcid.org/0000-0002-5907-4552
M. Loewenstein https://orcid.org/0000-0002-1661-4029
S. M. Morsink https://orcid.org/0000-0003-4357-0575
P. S. Ray https://orcid.org/0000-0002-5297-5278
M. T. Wolff https://orcid.org/0000-0002-4013-5650
C. B. Markwardt https://orcid.org/0000-0001-9803-3879
T. Okajima https://orcid.org/0000-0002-6054-3432
I. Cognard https://orcid.org/0000-0002-1775-9692
H. T. Cromartie https://orcid.org/0000-0002-6039-692X
E. Fonseca https://orcid.org/0000-0001-8384-5049
L. Guillemot https://orcid.org/0000-0002-9049-8716
M. Kerr https://orcid.org/0000-0002-0893-4073
A. Parthasarathy https://orcid.org/0000-0002-4140-5616
T. T. Pennucci https://orcid.org/0000-0001-5465-2889
S. Ransom https://orcid.org/0000-0001-5799-9714
I. Stairs https://orcid.org/0000-0001-9784-8670

References

Abbott, B. P., Abbott, R., Abbott, T. D., et al. 2017, PhRvL, 119, 161101
Abbott, B. P., Abbott, R., Abbott, T. D., et al. 2018, PhRvL, 121, 161101
Abbott, B. P., Abbott, R., Abbott, T. D., et al. 2020a, ApJL, 892, L3
Abbott, R. & LIGO Scientic Collaboration, & Virgo Collaboration 2020b, ApJL, 896, L44
Adhikari, D., Albataineh, H., Androic, D., et al. 2021, PhRvL, 126, 172502
Agathos, M., Meidam, J., Del Pozzo, W., et al. 2015, PhRvD, 92, 023012
Alcock, C., & Illarionov, A. 1980, ApJ, 235, 534
Alvarez-Castillo, D., Ayriyan, A., Barnaföldi, G. G., Grigorian, H., & Pósfay, P. 2000, EPJST, 229, 3615
Alvarez-Castillo, D., Ayriyan, A., Benic, S., et al. 2016, EPJA, 52, 69
Annala, E., Gorda, T., Kurkela, A., & Vuorinen, A. 2018, PhRvL, 120, 172703
Antoniadis, J., Freire, P. C. C., Wex, N., et al. 2013, Sci, 340, 448
Arzoumanian, Z., Baker, P. T., Brazier, A., et al. 2018, ApJ, 859, 47
Badnell, N. R., Bautista, M. A., Butler, K., et al. 2005, MNRAS, 360, 458
Bauböck, M., Psaltis, D., & Özel, F. 2019, ApJ, 872, 162
Baym, G., Furusawa, S., Hatsuda, T., Kojo, T., & Togashi, H. 2019, ApJ, 885, 42
Behnel, S., Bradshaw, R., Citro, C., et al. 2011, CSE, 13, 31
Bhattacharya, D., & van den Heuvel, E. P. J. 1991, PhR, 203, 1
Bhattacharyya, A. 1943, Bull. Calcutta Math. Soc., 35, 99
Bhattacharyya, S., Strohmayer, T. E., Miller, M. C., & Markwardt, C. B. 2005, ApJ, 619, 483
Bildsten, L., Salpeter, E. E., & Wasserman, I. 1992, ApJ, 384, 143
Binnington, T., & Poisson, E. 2009, PhRvD, 80, 084018
Biswas, B., Char, P., Nandi, R., & Bose, S. 2021, PhRvD, 103, 103015
Blaes, O. M., Blandford, R. D., Madau, P., & Yan, L. 1992, ApJ, 399, 634
Bogdanov, S., Dittmann, A. J., Ho, W. C. G., et al. 2021, ApJL, 94, L15
Bogdanov, S., Lamb, F. K., Mahmoodifar, S., et al. 2019, ApJL, 887, L26
Bogdanov, S., Rybicki, G. B., & Grindlay, J. E. 2007, ApJ, 670, 668
Buchner, J. 2014, S&C, 26, 383
Buchner, J. 2021, arXiv:2101.09675
Capano, C. D., Tews, I., Brown, S. M., et al. 2020, NatAs, 4, 625
Carney, M. F., Wade, L. E., & Irwin, B. S. 2018, PhRvD, 98, 063004
Chia, H. S. 2020, arXiv:2010.07300
Cierniak, M., & Blaschke, D. 2020, EPJST, 229, 3663
Contopoulos, I., & Spitkovsky, A. 2006, ApJ, 643, 1139
Cromartie, H. T., Fonseca, E., Ransom, S. M., et al. 2020, NatAs, 4, 72
Damour, T., & Nagar, A. 2009, PhRvD, 80, 084035
De, S., Finstad, D., Lattimer, J. M., et al. 2018, PhRvL, 121, 091102
Demorest, P. B., Pennucci, T., Ransom, S. M., Roberts, M. S. E., & Hessels, J. W. T. 2010, Natur, 467, 1081
Dietrich, T., Coughlin, M. W., Pang, P. T. H., et al. 2020, Sci, 370, 1450
Drischler, C., Furnstahl, R. J., Melendez, J. A., & Phillips, D. R. 2020, PhRvL, 125, 202702
Drischler, C., Han, S., Lattimer, J. M., et al. 2021, PhRvC, 103, 045808
Essick, R., Landry, P., & Holz, D. E. 2020a, PhRvD, 101, 063007
Essick, R., Tews, I., Landry, P., Reddy, S., & Holz, D. E. 2020b, PhRvC, 102, 055803
Feroz, F., Hobson, M. P., & Bridges, M. 2009, MNRAS, 398, 1601
Fonseca, E., Cromartie, H. T., Pennucci, T. T., et al. 2021, arXiv:2104.00880
Fonseca, E., Pennucci, T. T., Ellis, J. A., et al. 2016, ApJ, 832, 167
Foreman-Mackey, D., Hogg, D. W., Lang, D., & Goodman, J. 2013, PASP, 125, 306
Fortin, M., Providência, C., Raduta, A. R., et al. 2016, PhRvC, 94, 035804
Gabriel, C., Denby, M., Fyfe, D. J., et al. 2004, in ASP Conf. Ser. 314, Astronomical Data Analysis Software and Systems (ADASS) XIII, ed. F. Ochsenbein, M. G. Allen, & D. Egret (San Francisco, CA: ASP), 759
Gamba, R., Read, J. S., & Wade, L. E. 2020, CQGra, 37, 025008
Gehrels, N., Chincarini, G., Giommi, P., et al. 2004, ApJ, 611, 1005
Gendreau, K. C., Arzoumanian, Z., Adkins, P. W., et al. 2016, Proc. SPIE, 9905, 99051H
Greif, S. K., Hebeler, K., Lattimer, J. M., Pethick, C. J., & Schwenk, A. 2020, ApJ, 901, 155
Greif, S. K., Raaijmakers, G., Hebeler, K., Schwenk, A., & Watts, A. L. 2019, MNRAS, 485, 5363
Han, M.-Z., Jiang, J.-L., Tang, S.-P., & Fan, Y.-Z. 2021, arXiv:2103.05408
Harding, A. K., & Muslimov, A. G. 2001, ApJ, 556, 987
Harding, A. K., & Muslimov, A. G. 2002, ApJ, 568, 862
Hebeler, K., Lattimer, J. M., Pethick, C. J., & Schwenk, A. 2013, ApJ, 773, 11
Hernandez Vivanco, F., Smith, R., Thrane, E., et al. 2019, PhRvD, 100, 103009
Hinderer, T. 2008, ApJ, 677, 1216
Hinderer, T. 2009, ApJ, 697, 964
Ho, W. C. G., & Heinke, C. O. 2009, Natur, 462, 71
Ho, W. C. G., & Lai, D. 2001, MNRAS, 327, 1081
Hunter, J. D. 2007, CSE, 9, 90
Jiang, J.-L., Tang, S.-P., Wang, Y.-Z., Fan, Y.-Z., & Wei, D.-M. 2020, ApJ, 892, 55
Kiuchi, K., Kyutoku, K., Shibata, M., & Taniguchi, K. 2019, ApJL, 876, L31
Lackey, B. D., & Wade, L. 2015, PhRvD, 91, 043002
Lai, D. 2001, RvMP, 73, 629
Landry, P., & Essick, R. 2019, PhRvD, 99, 084049
Landry, P., Essick, R., & Chatziioannou, K. 2020, PhRvD, 101, 123007
Lattimer, J. M., & Prakash, M. 2007, PhR, 442, 109
Lattimer, J. M., & Prakash, M. 2016, PhR, 621, 127
Le Tiec, A., & Casals, M. 2021, PhRvL, 126, 131102
Le Tiec, A., Casals, M., & Franzin, E. 2021, PhRvD, 103, 084021
Li, A., Jiang, J.-L., Tang, S.-P., et al. 2020, arXiv:2009.12571
Li, A., Miao, Z., Han, S., & Zhang, B. 2021, ApJ, 913, 27
Li, B.-A., & Magno, M. 2020, PhRvC, 102, 045807
Lindblom, L. 2010, PhRvD, 82, 103011
Lindblom, L. 2018, PhRvD, 97, 123019
Lo, K. H., Miller, M. C., Bhattacharyya, S., & Lamb, F. K. 2013, ApJ, 776, 19
Margalit, B., & Metzger, B. D. 2017, ApJL, 850, L19
Miller, M. C. 2013, arXiv:1312.0029
Miller, M. C. 2016, ApJ, 822, 27
Miller, M. C., Chirenti, C., & Lamb, F. K. 2020, ApJ, 888, 12
Miller, M. C., & Lamb, F. K. 2015, ApJ, 808, 31
Miller, M. C., & Lamb, F. K. 2016, EPJA, 52, 63
Miller, M. C., Lamb, F. K., Dittmann, A. J., et al. 2019, ApJL, 887, L24
Most, E. R., Weih, L. R., Rezzolla, L., & Schaffner-Bielich, J. 2018, PhRvL, 120, 261103
Nättilä, J., Miller, M. C., Steiner, A. W., et al. 2017, A&A, 608, A31
Nelson, B. E., Ford, E. B., Buchner, J., et al. 2020, AJ, 159, 73
Oliphant, T. E. 2007, CSE, 9, 10
Oppenheimer, J. R., & Volkoff, G. M. 1939, PhRv, 55, 374
Özel, F., Psaltis, D., Güver, T., et al. 2016, ApJ, 820, 28
Pang, P. T. H., Dietrich, T., Tews, I., & Van Den Broeck, C. 2020, PhRvR, 2, 033514
Pavlov, G. G., & Zavlin, V. E. 1997, ApJL, 490, L91
Potekhin, A. Y. 2014, PhyU, 57, 735
Price-Whelan, A. M., & Foreman-Mackey, D. 2017, JOSS, 2, 357
Raaijmakers, G., Greif, S. K., Riley, T. E., et al. 2020, ApJL, 893, L21
Radice, D., Perego, A., Zappa, F., & Bernuzzi, S. 2018, ApJL, 852, L29
Randhawa, J. S., Meisel, Z., Giuliani, S. A., et al. 2019, ApJ, 887, 100
Rasmussen, C. E., & Williams, C. K. I. 2006, Gaussian Processes for Machine Learning (Cambridge, MA: MIT Press)
Reed, B. T., Fattoyev, F. J., Horowitz, C. J., & Piekarewicz, J. 2021, PhRvL, 126, 172503
Remillard, R. A., Loewenstein, M., Steiner, J. F., et al. 2021, arXiv:2105.09901
Rezzolla, L., Most, E. R., & Weih, L. R. 2018, ApJL, 852, L25
Ricci, C., Loewenstein, M., Kara, E., et al. 2021, arXiv:2102.05666
Riley, T. E., Raaijmakers, G., & Watts, A. L. 2018, MNRAS, 478, 1093
Riley, T. E., Watts, A. L., Bogdanov, S., et al. 2019, ApJL, 887, L21
Riley, T. E., Watts, A. L., Ray, P. S., et al. 2021, arXiv:2105.06980
Salmi, T., Suleimanov, V. F., Nättilä, J., & Poutanen, J. 2020, A&A, 641, A15
Selva, G., Roca-Maza, X., & Colò, G. 2021, Symmetry, 13, 144
Sen, D., & Guha, A. 2021, MNRAS, 504, 3354
Shibata, M., Zhou, E., Kiuchi, K., & Fujibayashi, S. 2019, PhRvD, 100, 023015
Silverman, B. W. 1986, Density Estimation for Statistics and Data Analysis (London: Chapman Hall/CRC)
Sokal, A. 1997, Monte Carlo Methods in Statistical Mechanics: Foundations and New Algorithms (Boston, MA: Springer)
Steiner, A. W., Lattimer, J. M., & Brown, E. F. 2010, ApJ, 722, 33
Stella, L., Priedhorsky, W., & White, N. E. 1987, ApJL, 312, L17
Strohmayer, T. E., & Brown, E. F. 2002, ApJ, 566, 1045
Strüder, L., Briel, U., Dennerl, K., et al. 2001, A&A, 365, L18
Tauris, T. M., & Savonije, G. J. 1999, A&A, 350, 928
Tauris, T. M., & van den Heuvel, E. P. J. 2014, ApJL, 781, L13
Tews, I., Margueron, J., & Reddy, S. 2018, PhRvC, 98, 045804
Tolman, R. C. 1939, PhRv, 55, 364
Tsai, Y.-S. 1974, RvMP, 46, 815
Tsang, M. B., Stone, J. R., Camera, F., et al. 2012, PhRvC, 86, 015803
Turner, M. J. L., Abbey, A., Arnaud, M., et al. 2001, A&A, 365, L27
Wijngaarden, M. J. P., Ho, W. C. G., Chang, P., et al. 2019, MNRAS, 484, 974
Wijngaarden, M. J. P., Ho, W. C. G., Chang, P., et al. 2020, MNRAS, 493, 4936

Wolff, M. T., Guillot, S., Bogdanov, S., et al. 2021, arXiv:2105.06978
Xie, W.-J., & Li, B.-A. 2020, ApJ, 899, 4
Xie, W.-J., & Li, B.-A. 2021, PhRvC, 103, 035802
Yue, T.-G., Chen, L.-W., Zhang, Z., & Zhou, Y. 2021, arXiv:2102.05267
Zhang, N.-B., & Li, B.-A. 2020, ApJ, 893, 61
Zhao, T., & Lattimer, J. M. 2020, PhRvD, 102, 023021

The Astrophysical Journal, 941:150 (23pp), 2022 December 20 https://doi.org/10.3847/1538-4357/ac983d
© 2022. The Author(s). Published by the American Astronomical Society.
OPEN ACCESS

The Radius of PSR J0740+6620 from NICER with NICER Background Estimates

Tuomo Salmi[1], Serena Vinciguerra[1], Devarshi Choudhury[1], Thomas E. Riley[1], Anna L. Watts[1], Ronald A. Remillard[2], Paul S. Ray[3], Slavko Bogdanov[4], Sebastien Guillot[5], Zaven Arzoumanian[6], Cecilia Chirenti[7,8,9,10], Alexander J. Dittmann[7,11], Keith C. Gendreau[6], Wynn C. G. Ho[12], M. Coleman Miller[7], Sharon M. Morsink[13], Zorawar Wadiasingh[9,14,15], and Michael T. Wolff[3]

[1] Anton Pannekoek Institute for Astronomy, University of Amsterdam, Science Park 904, 1090GE Amsterdam, The Netherlands; t.h.j.salmi@uva.nl
[2] MIT Kavli Institute for Astrophysics & Space Research, MIT, 70 Vassar Street, Cambridge, MA 02139, USA
[3] Space Science Division, U.S. Naval Research Laboratory, Washington, DC 20375, USA
[4] Columbia Astrophysics Laboratory, Columbia University, 550 West 120th Street, New York, NY 10027, USA
[5] Institut de Recherche en Astrophysique et Planétologie, UPS-OMP, CNRS, CNES, 9 avenue du Colonel Roche, BP 44346, F-31028 Toulouse Cedex 4, France
[6] X-Ray Astrophysics Laboratory, NASA Goddard Space Flight Center, Code 662, Greenbelt, MD 20771, USA
[7] Department of Astronomy and Joint Space-Science Institute, University of Maryland, College Park, MD 20742-2421, USA
[8] Astroparticle Physics Laboratory NASA/GSFC, Greenbelt, MD 20771, USA
[9] Center for Research and Exploration in Space Science and Technology, NASA/GSFC, Greenbelt, MD 20771, USA
[10] Center for Mathematics, Computation, and Cognition, UFABC, Santo André, SP 09210-170, Brazil
[11] Theoretical Division, Los Alamos National Laboratory, Los Alamos, NM 87545, USA
[12] Department of Physics and Astronomy, Haverford College, 370 Lancaster Avenue, Haverford, PA 19041, USA
[13] Department of Physics, University of Alberta, 4-183 CCIS, Edmonton, AB, T6G 2E1, Canada
[14] Department of Astronomy, University of Maryland, College Park, Maryland 20742, USA
[15] Astrophysics Science Division, NASA Goddard Space Flight Center, Greenbelt, MD 20771, USA
Received 2022 July 20; revised 2022 September 11; accepted 2022 September 23; published 2022 December 19

Abstract

We report a revised analysis for the radius, mass, and hot surface regions of the massive millisecond pulsar PSR J0740+6620, studied previously with joint fits to NICER and XMM-Newton data by Riley et al. (2021) and Miller et al. (2021). We perform a similar Bayesian estimation for the pulse-profile model parameters, except that instead of fitting simultaneously the XMM-Newton data, we use the best available NICER background estimates to constrain the number of photons detected from the source. This approach eliminates any potential issues in the cross-calibration between these two instruments, providing thus an independent check of the robustness of the analysis. The obtained neutron star parameter constraints are compatible with the already published results, with a slight dependence on how conservative the imposed background limits are. A tighter lower limit causes the inferred radius to increase, and a tighter upper limit causes it to decrease. We also extend the study of the inferred emission geometry to examine the degree of deviation from antipodality of the hot regions. We show that there is a significant offset to an antipodal spot configuration, mainly due to the non-half-cycle azimuthal separation of the two emitting spots. The offset angle from the antipode is inferred to be above 25° with 84% probability. This seems to exclude a centered-dipolar magnetic field in PSR J0740+6620.

Unified Astronomy Thesaurus concepts: X-ray astronomy (1810); Neutron stars (1108)

Supporting material: animation, figures sets

1. Introduction

Determination of the masses and radii of a set of neutron stars (NSs) provides direct insight into the equation of state (EOS) of matter at supranuclear densities (Lattimer 2012; Oertel et al. 2017; Baym et al. 2018; Tolos & Fabbietti 2020; Yang & Piekarewicz 2020; Hebeler 2021). This is the primary science goal of NASA's Neutron Star Interior Composition Explorer (NICER; Gendreau et al. 2016), an X-ray telescope installed on the International Space Station (ISS). NICER aims to measure masses and radii of rotation-powered millisecond X-ray pulsars using the technique of pulse-profile modeling (PPM; see Watts et al. 2016; Bogdanov et al. 2019; Watts 2019; Bogdanov et al. 2021 and references therein). PPM exploits relativistic effects that leave a measurable signature on rotationally modulated emission from the hot ($\sim 10^6$ K) magnetic polar caps of the pulsars. By modeling the relativistic effects, such as gravitational light-bending, Doppler boosting, aberration, time delays, and the effects of rotationally induced stellar oblateness, we are able to infer not only the mass and radius but also the geometric surface properties of the pulsar, in effect making a map of the hot emitting regions. Those regions are heated by the flow-back of particles that are accelerated in the magnetosphere. The bombarding particles are likely ultra-relativistic and produced in single photon magnetic pair cascades, originating at the open field line region where field lines connect the pulsar to its light cylinder (see, e.g., Ruderman & Sutherland 1975; Arons 1981; Harding & Muslimov 2001).

To date the NICER collaboration have reported results for two pulsars: PSR J0030+0451 (Miller et al. 2019; Riley et al. 2019) and the high-mass pulsar PSR J0740+6620 (Miller et al. 2021a; Riley et al. 2021a, hereafter R21).[16] The results have pointed to non-antipodal magnetic polar cap geometries (suggesting a complex magnetic field structure; Bilous et al. 2019;

Original content from this work may be used under the terms of the Creative Commons Attribution 4.0 licence. Any further distribution of this work must maintain attribution to the author(s) and the title of the work, journal citation and DOI.

[16] Each source is analyzed by two independent teams within the collaboration, each with their own PPM code and analysis pipeline.

Miller et al. 2019; Chen et al. 2020; Kalapotharakos et al. 2021), and are starting to restrict dense matter models (for a small selection of recent papers, see, for example Legred et al. 2021; Li et al. 2021; Miller et al. 2021a; Pang et al. 2021; Raaijmakers et al. 2021; Tang et al. 2021; Annala et al. 2022; Biswas 2022).

The pulse profiles are formed by recording the energy and arrival times by the individual NICER Focal Plane Modules (FPMs), and rotation phases are assigned via a previously observed pulsar ephemeris (obtained from radio timing) for every detected event. We then sum the total number of events in each energy and phase bin (see for example Figure 1 of R21). Because the NICER pulsar sources are assumed to be extremely stable rotators, pulse profiles can be built up over weeks or even years of observations, in order to obtain the required high signal-to-noise ratio.

The resulting pulse profile consists of pulsed and unpulsed components. The hot spots can produce both pulsed and unpulsed emission, with unpulsed emission likely generated if a spot overlaps the rotational pole, if the viewing angle is close to the rotational pole, or if the compactness is high enough and the geometry is such that parts of the spots remain in view as the star rotates. The unpulsed component also has background contributions from instrumental noise, particles, the cosmic X-ray background, and other astrophysical sources in the field of view (FoV).[17] It is crucial for the NS parameter estimation to accurately determine the relative contributions to the unpulsed emission from the background and the hot spots. If, for example, the background is underpredicted, the hot spots will be incorrectly assigned a larger unpulsed component, possibly leading to an incorrect prediction of a larger gravitational lensing effect caused by a larger compactness ratio, M/R. This issue is most important for very faint pulsars with a pulsed signal that is only slightly larger than the background, such as PSR J0740+6620.

Having an independent constraint on the unpulsed background thus provides useful input to the inference analysis. At the time of the 2019 analysis of PSR J0030+0451 (Miller et al. 2019; Riley et al. 2019), NICER background models were not sufficiently well developed to be used in the inference process. Instead, the inferred NICER phase-averaged source spectrum was compared a posteriori to a phase-averaged source spectrum derived independently from XMM-Newton observations (for which the background is empirically determined and better constrained from the observations, because XMM-Newton focuses photons and images the region of interest). These results indicated that the NICER PPM analysis might be attributing slightly too much of the unpulsed component to the non-source background (see Figure 15 of Riley et al. 2019; and Figure 12 of Miller et al. 2021a).

In the 2021 analysis of PSR J0740+6620, a different approach was taken: we performed simultaneous inference of both the phase-resolved NICER data set and a smaller phase-averaged XMM-Newton data set, using a blank-sky estimate of the astrophysical background as an additional constraint on the XMM-Newton fit. This was an indirect method of constraining the non-source contribution to the unpulsed component in the NICER pulse profile. However it had a large effect, shifting the median posterior radius upwards by ∼1 km (compared to an analysis using NICER data alone), by excluding higher compactness solutions (Miller et al. 2021a; R21). The inferred NICER background was compared a posteriori to the NICER background model estimates that existed at the time, and was found to be in reasonable agreement (see Figure 15 of R21).

One disadvantage of using XMM-Newton to provide a background constraint is that one has to take into account both the absolute uncertainty in X-ray flux calibration and the cross-calibration uncertainty from instrument to instrument. While we made an attempt to capture this in our previous analysis by including energy-independent calibration model parameters, we did not take into account any potential energy-dependent cross-calibration effects.

Thanks to intensive work by the NICER instrument team, there are now reliable NICER background estimates that can be used directly in the PPM inference pipeline to constrain the non-source contribution to the unpulsed component in the pulse profile. In this paper, we update the R21 analysis of PSR J0740+6620, using these constraints as an alternative to relying on XMM-Newton. We apply both the space weather (SW) background estimate (Gendreau 2020) to the original NICER data from Wolff et al. (2021), and the 3C50 background estimate using a new 3C50-filtered data set (Remillard et al. 2022). We find that the results are consistent with those presented in R21, and explore and refine the procedure to be used for NICER background estimates in future analyses. In Appendix B, an independent analysis is presented using the 3C50 data set based on the codes and methods from Miller et al. (2021a).

The remainder of this paper is structured as follows. In Section 2, we introduce the different data sets and background estimates used for PSR J0740+6620. In Section 3, we present the modeling procedure to obtain NS parameter constraints using PPM, with the help of those data and estimates. In Section 4, we show the results and compare them to the previously published NS parameter constraints. We also analyze the spot geometry of the best-fitting samples and perform more simulations to quantify the likely deviation from an antipodal spot configuration. We discuss the implications arising from our results in Section 5 and conclude in Section 6.

2. Data Analysis and Background Modeling

In this section, we summarize the three event data sets and background estimates used in the analysis presented in this paper.

2.1. Previous Data Set with Space Weather Background Estimate

We start by using the same X-ray event data described in Wolff et al. (2021) and used by R21, Miller et al. (2021a), which we will refer to as the W21 data set. This filtered data set has 1.60268 Ms of exposure accumulated over the period 2018 September 21 through 2020 April 17. The data set contains thousands of individual good time intervals (GTIs), which are filtered based on the sorting method of Guillot et al. (2019) without any additional GTI consolidation. We note that Essick (2022) raised questions about the GTI sorting method. We investigated and found that using this GTI sorting method for PSR J0740+6620 is not an issue (see Essick 2022). The idealized model considered in Essick (2022) is a poor representation of NICER data for which the non-pulsar background contributes the majority of accumulated counts and is not constant. This means that, in practice, the GTI

[17] NICER has a 6' non-imaging FoV.

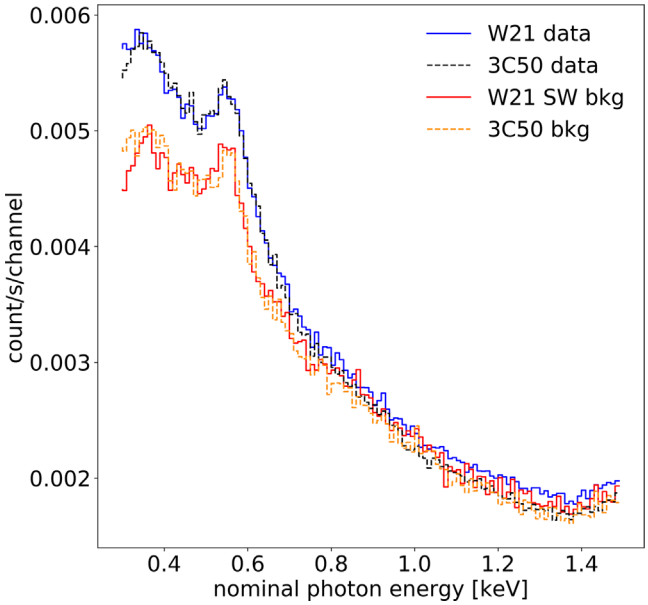

Figure 1. NICER count-rate spectrum of PSR J0740+6620 as a function of detector channel nominal photon energy (i.e., the PI value from the event file divided by 100). The blue solid and the black dashed step functions represent the spectrum for W21 and 3C50 data sets, respectively. The former is the same as used in R21, Miller et al. (2021a). The space weather background estimate (specific for the W21 data) is shown with a red solid step function, and the 3C50 background estimate (specific for the 3C50 data) is shown with an orange dashed step function.

sorting procedure does not significantly alter the count-rate distribution of the pulsed emission in the data set analyzed in Miller et al. (2021a), R21 and, as a consequence, does not introduce a measurable bias in the inferred NS radius.

For this work, we have also generated a background estimate using the SW background estimator (Gendreau 2020). This estimator is based only on environmental conditions when the data were taken. The parameters are the cosmic ray cutoff rigidity (the COR_SAX parameter) and the planetary K index (K_p, characterizing the magnitude of geomagnetic storms). The estimated background for an observation is constructed using spectra from blank-sky observations obtained within the same ranges of those two parameters. When combined with the COR_SAX > 2 cut[18] used to create this data set (which excludes the regions of highest and most-variable background), this method has been shown to be very reliable. When averaged over many GTIs, a background lower limit of 0.9 times the SW estimate is believed to be a safe prior to impose in the modeling. We note that this choice is based on extensive experience applying the SW model to a larger number of data sets, while it remains subject to more-rigorous study of the systematic errors (overprediction or underprediction) in the SW model. Other assumptions for the lower limit can affect the inferred results, as mentioned in Section 4.1.

The count-rate spectrum for the W21 data set and the SW background are shown in Figure 1 in comparison to the corresponding 3C50 data and background estimate, which are introduced next.

[18] Note that there is an error in R21 where it incorrectly specifies the filter criterion as COR_SAX > 5.

2.2. 3C50 Data and Background Model

An alternative, empirical model to estimate the NICER background, known as the 3C50 model (Remillard et al. 2022), uses three non-source count rates within the on-source GTIs to select and rescale background components from the model's libraries. The full description of the 3C50 data and background model used in this work is presented in Appendix A.

2.3. XMM-Newton EPIC

As a part of our analysis, we use the same XMM-Newton data as in R21 (see Section 2.1.2. of that paper) pre-processed correspondingly. The three EPIC instruments (pn, MOS1, and MOS2) were employed to get phase-averaged spectral information, with effective exposure times of 6.81, 17.96, and 18.7 ks, respectively. In addition, blank-sky observations were used to constrain the background contribution in the XMM-Newton data, as in R21; see Section 2.5.2. of that paper.

3. Modeling Procedure

The modeling procedure is largely shared with that of Riley et al. (2019), Bogdanov et al. (2019), R21, and Bogdanov et al. (2021). In this section, we summarize that methodology and report the new model components in more detail. For all posterior computations, we use the X-ray Pulse Simulation and Inference (X-PSI) code, version `v0.7.10` (Riley et al. 2022), which belongs to the same `v0.7` framework as used by R21.[19] The analysis files may be found in the persistent repository on Zenodo[20] including the data products, the numeric model files, scripts, and Jupyter notebooks in the Python language to produce the results and figures of this article using the X-PSI framework, and posterior sample files.

3.1. Radiation from Source to Telescope

We model the energy-resolved X-ray pulses using the PPM technique with the "Oblate Schwarzschild" approximation (see, e.g., Miller & Lamb 1998; Nath et al. 2002; Poutanen & Gierlinski 2003; Morsink et al. 2007; Lo et al. 2013; AlGendy & Morsink 2014; Bogdanov et al. 2019; Watts 2019). The choices for prior probability density functions (PDFs) of the model parameters follow those presented in R21. Mass, inclination, and distance priors we obtain from the generalized least-squares (GLS) algorithm determining timing model parameters from wide-band radio timing data (Fonseca et al. 2021). These priors were also used for the production analysis in R21, although not in the exploratory analysis shown, e.g., in Figure 5 of that paper. For relativistic ray-tracing, multiple imaging was still allowed to enable exploration of high compactness solutions due to the very high mass known from the radio timing ($2.08 \pm 0.07\ M_\odot$ from Fonseca et al. 2021). The interstellar attenuation of X-rays is again accounted for by neutral hydrogen column density $N_{\rm H}$, based on the state-of-the-art `TBabs` model (Wilms et al. 2000, updated in 2016), and having a conservative prior of $N_{\rm H} \sim U(0, 10^{21})$ cm^{-2}.

3.2. Surface Hot Regions

The surface hot regions are modeled using similar methods to R21, our main model being again `ST-U`

[19] https://github.com/xpsi-group/xpsi
[20] doi:10.5281/zenodo.6827537

(*Single-Temperature-Unshared*), with two circular hot regions with uniform effective temperature of the atmosphere (Riley et al. 2019). In this model, the spots are not restricted to an antipodal reflection symmetry. However, to further study the deviation from antipodal symmetry, and to check how much worse antipodal models would perform, we also consider antipodal models (see Section 4.4). In this examination, we use both the model `ST-S` (*Single-Temperature-Shared*) from Riley et al. (2019) where both hot spots share the same temperature and spot size, and a new model version `ST-Ua` (*Single-Temperature-Unshared-antipodal*) where the spot parameters (size, temperature) are unshared but the spot centers are fixed to be antipodal. For the priors of the hot region parameters, we follow R21 and use a flat PDF of the cosine of each hot region center colatitude (unlike in Riley et al. 2019).

For the atmosphere model, determining the specific intensity emitted from the NS surface, we restrict ourselves to using only the fully ionized hydrogen model `NSX` (Ho & Lai 2001). The sensitivity to atmosphere composition, using helium instead of hydrogen, was shown to be negligible in the radius of PSR J0740+6620 for the models and data considered in R21, although with some small changes in the properties of the hot regions. Other uncertainties related to the atmosphere model choice are discussed and treated in Bogdanov et al. (2021) and in T. Salmi et al. (2022, in preparation). As in R21, we assume that the surface exterior to the hot regions is not radiating.

3.3. Instrument Response Models

For the NICER W21 data set, we use the instrument response files described in Section 2.4 of R21. For the 3C50 GTIs, a singular response file is used, and it is calculated as the sum of the individual responses for the 50 FPMs selected for that data set.

For the joint analysis with XMM-Newton, we use the restricted effective-area uncertainty of R21. The overall scaling factor (for each instrument) is defined as a product of a shared scaling factor and a priori statistically independent telescope-specific scaling factor. For the restricted uncertainty, a standard deviation of 3%[21] was assumed for each telescope-specific scaling factor and 10% for the shared scaling factor (Ishida et al. 2011; Madsen et al. 2017; Plucinsky et al. 2017), resulting in about 10.4% uncertainty in the overall scaling factor as in Section 4.2 of R21. We have also explored the sensitivity to the cross-calibration uncertainty by performing low-resolution runs with two other choices for uncertainties, which are shown in Section 4.3.2. The least restricted uncertainty corresponds to the initial scaling of R21 with 10% uncertainty in both telescope-specific and shared scaling factors, leading to the 15% uncertainty in the overall scaling factors. The most restricted case (more than in Section 4.2 of R21) applies 5% shared scaling factor uncertainty and 3% telescope-specific uncertainty leading to 5.8% uncertainty in the overall scaling factors. For the NICER analysis without XMM-Newton, we assume ±15% uncertainty in the effective area of the instrument, by using a free energy-independent effective-area scaling parameter as in R21. We checked (for a few of our runs) that importance-sampling the scaling parameter prior from ±15% to ±10.4% has only negligible effects on the posteriors of the other parameters. For example, the credible interval for radius remains the same with better than 0.1% accuracy.

[21] See heasarc.gsfc.nasa.gov/docs/heasarc/caldb/nicer/docs/xti/NICER-xti20200722-Release-Notesb.pdf and xmmweb.esac.esa.int/docs/documents/CAL-TN-0018.pdf for further details.

Table 1
Summary of the Model Cases

Case	NICER[a]	NICER +BKG[b]	XMM+BKG[c]
1	YES	NO	NO
2	YES	NO	YES
3	NO	YES	NO
4	NO	YES	YES

Notes.
[a] Analysis without any prior NICER background information.
[b] NICER analysis where NICER background (BKG) estimates are applied.
[c] Analysis where XMM-Newton data with XMM-Newton background information are applied.

3.4. Likelihood Function and Background

In this section, we present how the likelihood function is calculated using different constraints for the background. We consider four different cases, which are summarized in Table 1.

The first and second cases, when applied to the W21 data set, are identical to those applied in R21. We apply the first and second cases also to the 3C50 data set using the same methodology. In these cases, the uncertainty in the NICER background is numerically marginalized by integrating the likelihood over statistically independent background variables $\{\mathbb{E}[b_{\rm N}]\}$ that are allowed to range from $\{0\}$ to an unspecified set of upper bounds $\{\mathcal{U}\}$ (see Appendix B.2 in Riley 2019, for details). Here $b_{\rm N}$ denotes the background count rate at a specific NICER energy channel. For the second case when XMM-Newton data is applied, specified limits are used for the XMM-Newton background variables $\{\mathbb{E}[b_{\rm X}]\}$, where $b_{\rm X}$ is the background count rate at a specific XMM-Newton energy channel. The lower and upper bounds for the support are $\mathscr{L} := \max(0, \mathscr{B}_{\rm X} - n\sqrt{\mathscr{B}_{\rm X}})$ and $\mathscr{U} := \mathscr{B}_{\rm X} + n\sqrt{\mathscr{B}_{\rm X}}$, where $\{\mathscr{B}_{\rm X}\}$ is the set of XMM-Newton background count numbers based on the blank-sky observation, and $n = 4$ is the chosen degree of conservatism. These blank-sky count numbers are rescaled with the ratio of the areas of the extraction regions of the blank-sky and PSR J0740+6620 observation, and divided by the exposure time of the blank-sky observation, when converting them to limits for XMM-Newton background variables $\{\mathbb{E}[b_{\rm X}]\}$, as shown in Equation (3) of R21. Note that in R21 and the associated code and results repository (Riley et al. 2021b) this scaling factor (known also as BACK_SCAL factor) was the inverse of the correct value. Since the scaling factor is close to unity for PSR J0740+6620 observations, the effect was anticipated to be minimal, but to be sure, we confirmed this with an additional inference run. The results of this additional run, together with corrected scripts, can be found in an update to the repository (Riley et al. 2021c).

The background-marginalized likelihood function (probability of the data given the model) for the NICER and XMM-Newton data sets, assuming a flat prior density in the

background variables, is then given as

$$p(d_{\rm N}, d_{\rm X}, \{\mathscr{B}_{\rm X}\}|s) \propto \int_{\{0\}}^{\{\mathcal{U}\}} p(d_{\rm N}|s, \{\mathbb{E}[b_{\rm N}]\}, \text{NICER}) \times d\{\mathbb{E}[b_{\rm N}]\} \int_{\{\mathscr{L}\}}^{\{\mathscr{U}\}} p(d_{\rm X}|s, \{\mathbb{E}[b_{\rm X}]\}, \text{XMM}) d\{\mathbb{E}[\mathscr{B}_{\rm X}]\}, \quad (1)$$

where $d_{\rm X}$ is the XMM-Newton count matrix data, $d_{\rm N}$ is the NICER count matrix data, s denotes the pulsar signal parameters, NICER and XMM denote models for the response of the corresponding instrument to incident radiation, and d's followed by brackets show the differentials of the integrals.

The third (and new) case we consider is the analysis of NICER data with tighter lower and upper limits, $\{\mathfrak{L}\}$ and $\{\mathfrak{U}\}$, for the background based on a NICER background estimate. For the fourth case (with XMM-Newton observations included as in Equation (1)), we describe the likelihood as

$$p(d_{\rm N}, d_{\rm X}, \{\mathcal{B}_{\rm N}\}, \{\mathscr{B}_{\rm X}\} \mid s) \propto \int_{\{\mathfrak{L}\}}^{\{\mathfrak{U}\}} p(d_{\rm N} \mid s, \{\mathbb{E}[b_{\rm N}]\}, \text{NICER}) \times d\{\mathbb{E}[\mathcal{B}_{\rm N}]\} \int_{\{\mathscr{L}\}}^{\{\mathscr{U}\}} p(d_{\rm X} \mid s, \{\mathbb{E}[b_{\rm X}]\}, \text{XMM}) d\{\mathbb{E}[\mathscr{B}_{\rm X}]\}, \quad (2)$$

where $\{\mathcal{B}_{\rm N}\}$ is the set of NICER background count rates from the background estimate.[22] We note that $\{\mathcal{B}_{\rm N}\}$ is already defined in count rates directly comparable to the NICER data, and does not need to be rescaled using BACK_SCAL or exposure time factors, unlike $\{\mathscr{B}_{\rm X}\}$.

The integration limits $\{\mathfrak{L}\}$ and $\{\mathfrak{U}\}$ were determined either based on the SW estimate (only lower limit) or on the 3C50 background estimate (either only lower or both lower and upper limits); see Section 2.1 and Appendix A for information about those models. In the case where we used only a lower limit from the NICER background estimates, the upper limits (for each channel) were set to the same unspecified values $\{\mathscr{U}\}$ as in Equation (1). This is motivated by the existence of known sources in the FoV of NICER's observation of PSR J0740 +6620, which are not accounted for in the background estimates (Wolff et al. 2021). However, we also explored the sensitivity of the results to a conservative upper limit in some of our models.

In case of the SW estimate, we considered two different lower limits: one with a factor of 0.9 times the original SW estimate, and the other 0.9 times a smoothed version of the SW estimate. The latter was employed after determining that the original lower limit was forcing the total inferred NICER background to be higher by limiting the background only at the channel 87 (corresponding to nominal energy 0.87 keV), where the background estimate peaks up while the NICER data do not have a similar feature (see Section 4.1 for the inferences). The smoothed and non-smoothed backgrounds are shown in Figure 2. The smoothing of the background estimate was performed using a Savitzky–Golay filter with a window length of 17 (number of coefficients) and a fifth order polynomial,[23]

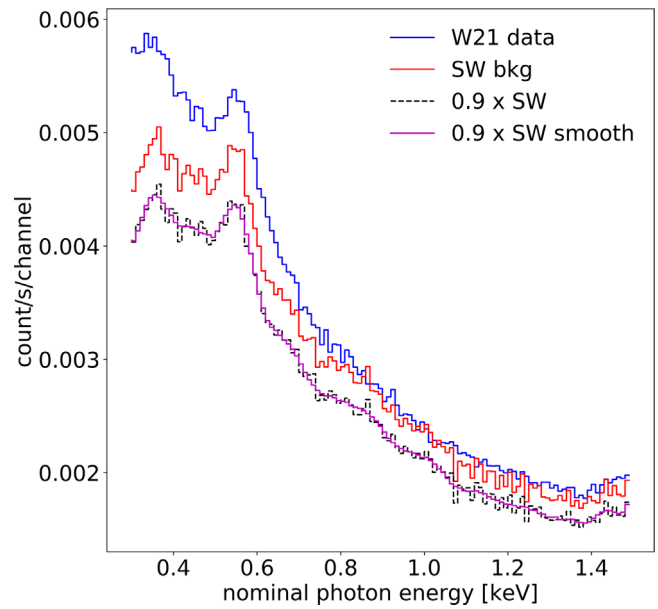

Figure 2. Prior limits for the background of the W21 data set. The count-rate spectrum and the SW background estimate are shown with blue and red step functions as in Figure 1. The black dashed step function is the estimate multiplied with a factor of 0.9, and a smoothed version of that is shown with a magenta step function. These two rescaled estimates were used as lower limits $\{\mathfrak{L}\}$ for the joint prior PDF of the expected count-rate variables $\{\mathbb{E}[b_{\rm N}]\}$ (see Equation (2)).

after restricting the estimate to the energy channels considered for the analysis (from channel 30 to 150). We note that the choice of the smoothing technique and the values for the filter are not based on detailed analysis, but chosen so that the end result approximates a spectrum rebinned to minimize over-sampling (corresponding to averaging over three adjacent energy bins).

In case of the 3C50 background estimate (and 3C50 data), we considered several options for the lower and upper limits of the background variables. As explained in Appendix A.2, the 3C50 background spectrum is accompanied by an estimate of the systematic error that is rescaled based on the background spectrum itself. For the total standard deviation $\sigma_{\mathcal{B}_{\rm N}}$ of the background estimate at a given channel, we use the square root of the quadratic sum of the systematic and statistical errors. The latter come from the convolved statistical errors of the library spectra, and are actually tiny compared to the systematic uncertainty. Given this, we set the lower bound for the background prior to $\mathcal{B}_{\rm N} - n_{\rm l}\sigma_{\mathcal{B}_{\rm N}}$ and the upper bound to $\mathcal{B}_{\rm N} + n_{\rm u}\sigma_{\mathcal{B}_{\rm N}}$, where $n_{\rm l}$ and $n_{\rm u}$ are settings that control the degree of conservatism. We considered cases with ($n_{\rm l} = 3$, $n_{\rm u} = \infty$), ($n_{\rm l} = 3$, $n_{\rm u} = 3$), and ($n_{\rm l} = 2$, $n_{\rm u} = 3$). Here $n_{\rm u} = \infty$ means that the default upper limit $\mathcal{U}$ is used instead, and even using $n_{\rm u} = 3$ is a very conservative choice, because it cuts off only solutions with background almost as high as the data, as seen from Figure 3. The background and its estimated errors are also compared against the energy-integrated pulses for the 3C50 data set in Figure 4 (and in the associated online figure set).

In all of the high-resolution runs for 3C50 presented here, we used a smoothed background estimate, using the same smoothing technique as for the SW estimate. According to our initial lower-resolution runs, smoothing was again required to mitigate a strong dependence on the influence of one or very

[22] The third case corresponds to a similar equation as Equation (2) but without dependence and integration over XMM-Newton background variables.

[23] Coded in Python with spectrum_smooth = scipy.signal.savgol_filter(spectrum, 17, 5).

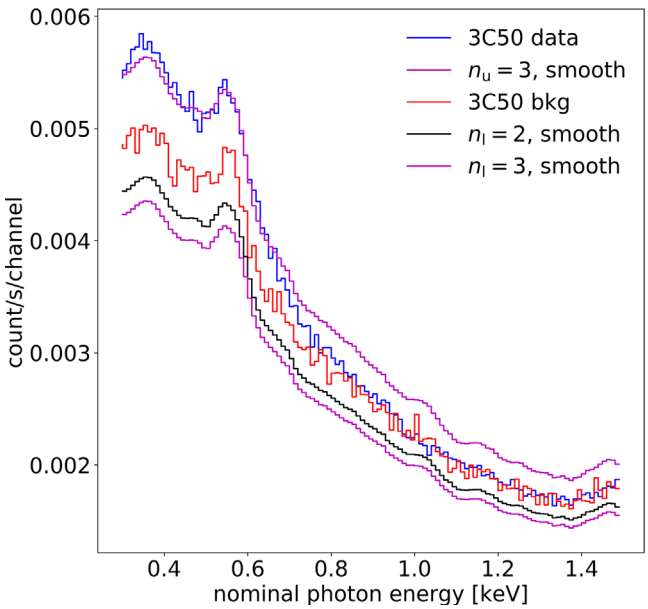

Figure 3. Prior limits for the background of the 3C50 data set. The count-rate spectrum and the 3C50 background estimate are shown with blue and red step functions (corresponding to the black and gray dashed functions in Figure 1). The magenta step functions show the smoothed joint prior PDF lower and upper limits for the expected count-rate variables $\{\mathbb{E}[b_N]\}$ based on 3σ uncertainty (see the equations and main text in Section 3.4). The black step function shows the corresponding 2σ lower limit. The corresponding figure with 2σ and 3σ lower limits based on the minimum of the data and the background estimate (mdb) is shown in the figure set in the online journal (HTML version).

(The complete figure set of 2 images is available.)

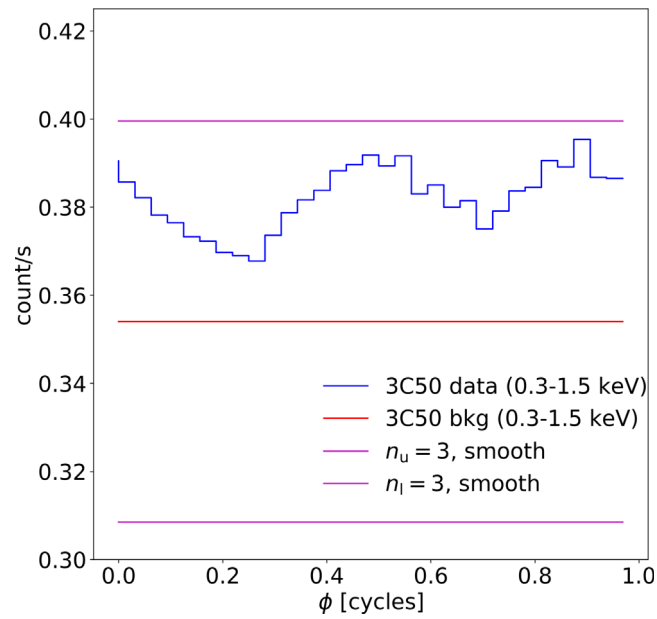

Figure 4. Prior limits for the background of the 3C50 data set for the bolometric pulse profile. The energy-integrated count-rate pulse profile and the 3C50 background estimate are shown with blue and red step functions. The magenta step functions show the smoothed 3σ lower and upper limits for the energy-integrated background, corresponding to those shown in Figure 3. The complete figure set (4 images) for different energy intervals is shown in the online journal (HTML version).

(The complete figure set of 4 images is available.)

few channels. We also checked (with low-resolution runs) that smoothing by averaging over three adjacent bins yields very similar results to the smoothing method used in this paper. However, as seen from Figure 3, the background estimate may still overpredict the background at high-energy channels; therefore we also considered models where the data d_N replaces the background estimate at those channels: in other words, the lower limit was set to $\min(\mathcal{B}_N - n_l\sigma_{\mathcal{B}_N}, d_N - n_l\sigma_{\mathcal{B}_N})$.[24] Hereafter, the models using the minimum function as the lower limit are labeled as *mdb* (minimum of the data and the background).

3.5. Posterior Computation

We use X-PSI to calculate the likelihood function and prior PDFs and then employ nested sampling to compute the posterior samples using MULTINEST (Feroz & Hobson 2008; Feroz et al. 2009; Buchner et al. 2014). The details of the sampling and the resolution settings follow accurately the production calculations of R21: 4×10^4 live points; a bounding hypervolume expansion factor of 0.1^{-1}; and an estimated remaining log-evidence of 10^{-1}. For most of the models, we also performed first a low-resolution run with 4×10^3 live points, where the inferred median NS radius was typically 0.2–0.4 km smaller, and the credible interval was more constrained than in the high-resolution runs. This was also noted in R21, where a small further broadening of the radius posterior was seen even if using 8×10^4 live points. Due to the additional computation expense and the aim of studying mainly the sensitivity of the results to different background modeling choices (which appear more significant than the sensitivity to increasing resolution further), we still consider 4×10^4 live points as a suitable resolution for the main runs of this paper. This resolution is used in all the runs unless stated otherwise (a couple of sensitivity tests referred to as *low-resolution* use

Table 2
Model Parameters

Parameter	Description
M [$M_\odot$]	gravitational mass
R_{eq} [km]	coordinate equatorial radius
Θ_p [radians]	p[a] region center colatitude
Θ_s [radians]	s[a] region center colatitude
ϕ_p [cycles]	p region initial phase[c]
ϕ_s [cycles]	s region initial phase[d]
ζ_p [radians]	p region angular radius
ζ_s [radians]	s region angular radius
$\log_{10}(T_p$ [K])	p region NSX effective temperature
$\log_{10}(T_s$ [K])	s region NSX effective temperature
$\cos(i)$	cosine Earth inclination to spin axis
D [kpc]	Earth distance
N_H [10^{20} cm^{-2}]	interstellar neutral H column density
α_{NICER}	NICER effective-area scaling
α_{XMM}	XMM-Newton effective-area scaling

Notes.
[a] Primary.
[b] Secondary.
[c] With respect to the meridian on which Earth lies.
[d] With respect to the meridian on which the Earth antipode lies.

[24] We note that with this definition of background prior the same data affect both the prior and the likelihood factor when calculating the background-marginalized likelihood.

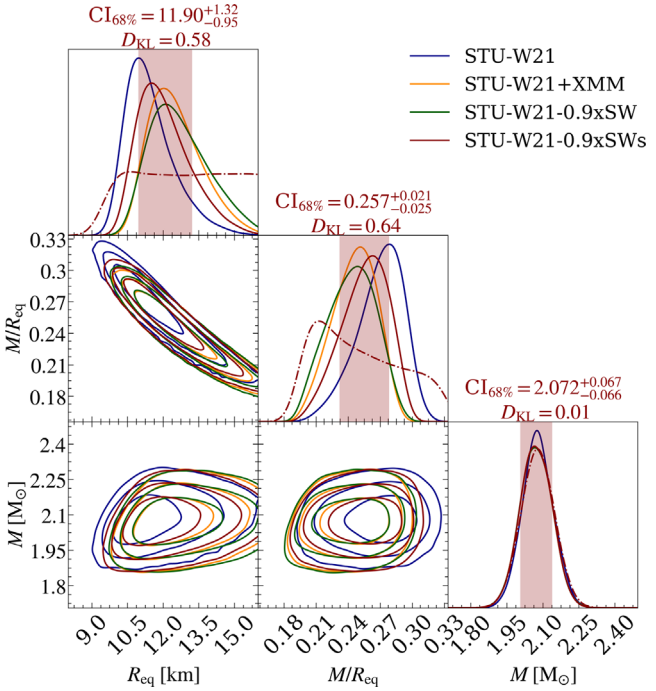

Figure 5. Effect of the SW background estimate on the mass and radius posterior distributions using the W21 data set conditional on the ST−U model. Also, the posteriors for compactness $GM/R_{eq}c^2$ are shown (hereafter and in the figure referred as M/R_{eq}, i.e., assuming $c = 1$ and $G = 1$). Four types of posterior distribution are shown: one conditional on the NICER likelihood function with a smoothed SW background lower bound (STU-W21-0.9xSWs); one similar but with a non-smoothed lower bound (STU-W21-0.9xSW); one conditional on NICER likelihood function without background constraints (STU-W21); and one conditional on the NICER and XMM-Newton likelihood function (STU-W21+XMM). The last two are from R21. The marginal prior PDFs are shown by the dashed–dotted functions. We report the credible intervals and the Kullback–Leibler divergence D_{KL} for the NICER posterior conditional on the smoothed SW estimate lower bound (for the other cases, see Table 6). The shaded intervals contain 68.3% of the posterior mass, and the contours in the off-diagonal panels contain 68.3%, 95.4%, and 99.7% of the posterior mass. See the caption of Figure 5 of R21 for additional details about the figure elements.

4×10^3 live points instead). All our free sampling parameters are shown and described in Table 2.

4. Inferences

In this section, we report our results. First we show the effects of using the SW background estimate in the NICER analysis without applying XMM-Newton data (case (3) from Table 1). Then we present our inference based on the 3C50 filtering of the NICER data, first without using the corresponding background estimate (case (1) from the same table) and then including the estimate using several different methods (case (3)). We also perform a few joint 3C50 and XMM-Newton runs (applying both cases (2) and (4)). We finish the section by showing the results of runs with antipodal models and measuring the degree of non-antipodality of the other runs.

4.1. Effect of the SW Estimate

As explained in Appendix A and Section 3.4, we studied the effect of using the SW estimate as a lower limit for the NICER background, instead of applying a joint NICER and XMM-Newton analysis as in R21, Miller et al. (2021a). The resulting posterior probability distributions for the spacetime parameters (mass, radius, compactness) are shown in Figure 5, using either smoothed or non-smoothed 0.9 times the SW estimate as the lower limit (a summary can be found in Table 6 and Figure 18 in Appendix C). Posteriors are compared against the headline results from R21, which used the joint NICER and XMM-Newton analysis with non-compressed effective-area scaling between the instruments (and the incorrect BACK_SCAL factor), giving a median radius of around 12.4 km (for the compressed scaling, it was 12.7 km). We see that the new NICER-only results, using the SW background information, are consistent with the previous joint NICER and XMM-Newton results, but the median radius depends slightly on whether we use the non-smoothed or smoothed SW estimate (see Section 3.4 for definitions). The former gives 12.5 km and the latter 11.9 km. We interpret this as indicating that XMM-Newton is posing a stricter condition on the background than the 0.9 times the SW lower limit, rather than indicating the non-smoothed version as being more accurate. However, both are higher than the median radius from the previous NICER-only run, which was about 11.3 km.[25]

The increase in the radius, when constraining the background by setting a lower limit, can be understood from the necessity to decrease the unpulsed component emitted from the NS surface, in order to associate a larger fraction of the unpulsed emission with the background. An obvious way to decrease the unpulsed component is to decrease the NS compactness, so that fewer photons can reach the observer by light bending when the radiating spots are seen at high angles. Since the mass of PSR J0740+6620 is tightly constrained by the prior, increasing the radius is the only way to decrease the compactness. As expected, the inferred background with the SW limit applied is consistent with the inferred NICER background from the old joint NICER and XMM-Newton results. This is seen in Figure 6 by comparing the orange lines from the left and right panels, showing the background-constrained results. The green lines show the original NICER-only results, which are the same in both panels. In both cases, the unpulsed NS component is decreased relative to the results inferred if no background constraints are applied. Smoothing the SW estimate affects the constraints, as it eliminates a few noisy peaks present in the SW estimate (e.g., at channel 87), that would otherwise force the entire inferred background to increase.

By inspecting the posterior distributions of the other model parameters, we see only small changes in most of them (the full set of posterior figures for hot region parameters is provided in Section 4.2 of the online journal). This implies that the change in the background can be mainly compensated by adjusting the compactness. The inferred configuration (hot spots located near the equator) remains also very similar to that found in R21. However, we note that constraints especially on the spot colatitudes are not very stringent. That can also be noticed from the animations showing the maximum likelihood and maximum posterior configurations for different runs, presented later in Section 4.4.

Furthermore, no significant difference in the model performance can be detected between the different background treatments. The residuals between the data and best-fit models can be found as part of the online journal figure set in

[25] The 11.3 km radius was obtained by applying importance sampling to include updated mass, inclination, and distance priors and presented in the Appendix of R21.

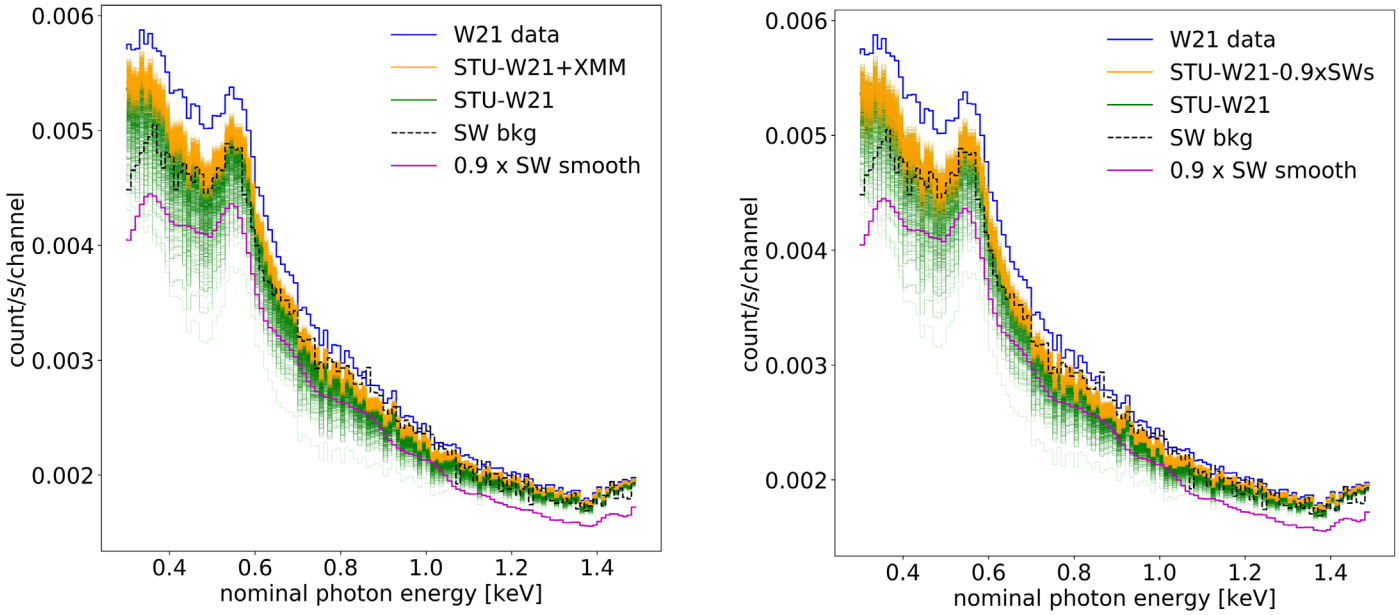

Figure 6. Comparison of the inferred NICER background for the W21 data set based on different models. Left panel: the blue step function is the total NICER count-rate spectrum, the dashed black step function is the SW background estimate, and the magenta step function is the SW estimate multiplied by a factor of 0.9 and smoothed. Orange step functions show 1000 background curves that maximize the likelihood for 1000 equally weighted posterior samples from the previously published joint NICER and XMM-Newton run, as in Figure 15 of R21. The green step functions show the corresponding inferred backgrounds for the previous NICER-only analysis. The orange functions are partly overlapping the green functions. Right panel: same as left panel, except the orange step functions present now the inferred background from the new NICER-only run with the smoothed SW constraint. The complete figure set (6 images), including also the results for the non-smoothed SW constraints, and inferred backgrounds based on the 1000 highest-likelihood samples, is available in the online journal (HTML version).

(The complete figure set of 6 images is available.)

Section 4.4. Posterior distributions for the other parameters (distance, cosine of observer inclination, effective-area scaling factor, and the hydrogen column density) are also included in the figure sets in Section 4.2, and the expected pulse signals for each of the models can be found in the repository of Salmi et al. (2022).

In addition, we explored the sensitivity to the choice of the factor 0.9 with low-resolution inference runs (using the smoothed version of the estimate), and found significant differences if using either 0.85 or 0.95 factor for the lower limit instead. Using 0.85 times SW as the lower limit yields similar results as without any background constraints, and using 0.95 times SW shifts the median radius up to around 13.5 km. However, we think the latter limit potentially biases the results if the SW estimate were overpredicting the background strongly enough at even a few of the considered energy channels. We examine the sensitivity to different cutoffs in the background prior more thoroughly for the 3C50 data in Section 4.3.1.

4.2. Effect of Using 3C50 Data

As explained in Appendix A and Section 3.4, we have analyzed another data set, called 3C50, produced using new filtering and providing improved background constraints. Since the data set itself is different, we first show the parameter constraints without applying the corresponding background estimates (case (1) in Table 1), in the same manner as for the NICER-only analysis in R21 for the W21 data set. The effect on the spacetime parameters, when using 3C50 filtered data (without background information) instead of the W21 data, is shown in Figure 7 (comparing again to the same already published results as in Section 4.1 and in Figure 5), and the parameter values for the new run are given in Table 7. Using the 3C50 data set shifts the posterior distribution on the radius to be more consistent with that inferred previously from the joint NICER and XMM-Newton analysis. The uncertainty is however larger, which is partly expected due to the smaller number of detected counts for the 3C50 data set, which is 594709 instead of 628280 counts in the same energy intervals (see Lo et al. 2013; Psaltis et al. 2014, for discussions of the expected uncertainty as a function of counts and pulse amplitudes). However, that difference cannot fully explain the change, as discussed further in Section 5.1.

The shift of the radius to higher values could be related to the 3C50 data set being cleaner than the W21 data set, and thus genuinely providing a radius estimate closer to the original joint W21 and XMM-Newton result where the background is more constrained. However, we note that the shift is still relatively small compared to the statistical uncertainties in the measured radius. Similarly, a shift to a higher radius with 3C50 data set was also found in the independent analysis presented in Appendix B, using the same PPM code and analysis pipeline as in Miller et al. (2021a).

The parameter constraints in the new 3C50 results are mostly similar to the original joint constraints, as seen from the posterior distributions of the hot region parameters in Figure 8. A notable exception is the relative phase shift produced by the different data filtering procedures. The hot spots are also slightly closer to the equator for the 3C50-only and W21-XMM-Newton runs than for the original W21-only run. However, the 3C50 results differ from both previous results in the sizes and temperatures of the hot spots, predicting slightly colder and larger hot spots. The inferred hydrogen column density $N_{\rm H}$ for the 3C50 filtered data is significantly

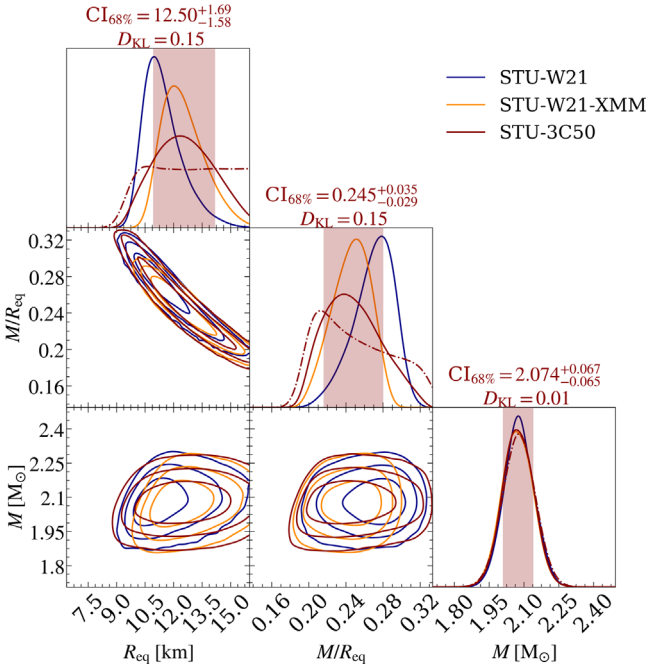

Figure 7. Effect of 3C50 data selection on the mass and radius posterior distributions conditional on the ST-U model. Three types of posterior distribution are shown: one conditional on the NICER likelihood function using 3C50 data set; one conditional on the NICER likelihood function using the W21 data set; one conditional on NICER W21 data and XMM-Newton likelihood function (the latter two are the same as in Figure 5). We report the credible intervals and the divergence estimates for the NICER posterior conditional on the 3C50 data set. See the caption of Figure 5 for additional details about the figure elements.

higher than that in the original results, which is shown in the posterior distributions of other model parameters in Figure 9. This may be explained by the differences in the data sets at the lowest energy channels, where the 3C50 selection has a lower count rate (as seen from Figures 2 and 3) allowing stronger interstellar absorption. The correlation between N_H and R_{eq} could also partly explain why the 3C50 filtering infers a slightly different NS radius (although seen only in the 2D posterior of N_H and R_{eq} for 3C50 case). These parameters are known to be related due to their degeneracy with the temperature, at least in the case of spectral fitting as in Gonzalez-Caniulef et al. (2019).

4.3. Effect of Using 3C50 Data with Background Constraints

4.3.1. 3C50 Data with 3C50 Background Constraints

In addition to the results shown in Section 4.2, we have analyzed the 3C50-filtered NICER data combined with the associated background constraints, as explained in Section 3.4 (the case referred as (3) in Table 1). The spacetime posterior distributions are shown in Figure 10 when using the smoothed 3C50 background limit. In the corresponding online journal figure set, similar posteriors are shown using the modified mdb background estimate mentioned in the end of Section 3.4 (where the background estimate is limited to not exceed the data).

We see clear shifts in the distributions depending on the choices for the background limits; however all of the results are still statistically consistent (the median values and credible intervals for radius for all the runs are shown in Tables 7 and 8, and visualized in Figure 18).

From both posterior figures, we see that constraining the background using a lower limit always causes the radius to increase, and using an upper limit always causes it to decrease (compared to a case where the other limit has not been altered). For example, imposing $n_l = 3$ lower limit shifts the median radius from 12.5 to 13.0 km (in the case of Figure 10). This effect is also similar to that found in the independent analysis of Appendix B. Applying a $n_u = 3$ upper limit in addition alters the median from 13.0 to 12.0 km. In the case of a more restrictive lower limit, $n_l = 2$, the median shifts from 12.0 to 13.1 km. When using the mdb version of the estimate, the effects are similar but generally produce radii that are 0.3−0.7 km smaller, due to the less strict lower limit of the background for a few noisy high-energy channels. In all cases, credible intervals of the radius tighten slightly when tighter background limits are applied. The difference between the 84% quantile and the median value shifts from about $\Delta R^+ = 1.6$ to $\Delta R^+ = 1.4$ km, and the difference between the median and 16% quantile shifts from about $\Delta R^- = 1.7$ to $\Delta R^- = 1.1$ km, when considering the tightest background limits, compared to the results without any background constraints. Clearly, the credible intervals are most affected by the addition of the upper limit for the background.

The changes in the radius can be understood via compactness, as in Section 4.1: higher background leads to a higher radius (for a fixed mass) and vice versa. The inferred backgrounds are presented in Figure 11 for the case with 3σ lower limit and no upper limit for the NICER background. The other cases are shown in the corresponding online journal figure set. We see that setting either lower or upper limits to the background affects the inferred background (the orange step functions) by pushing it either up or down, as expected. In addition, the inferred background (and the radius) is also moderately sensitive to changes in the prior limits in only a few relevant energy channels. This is demonstrated by the difference between the inferred backgrounds when using the smoothed mdb estimate versus the smoothed estimate without the minimum function (e.g., by comparing the Figures 1 and 4 in the online set).

4.3.2. 3C50 Data and Background with XMM-Newton

We have also analyzed the 3C50-filtered NICER data in combination with the same XMM-Newton data set that was used in the previous analysis of R21 (case (2) in Table 1). In addition, we have tried constraining the NICER background using both the XMM-Newton data set and the 3C50 background estimate simultaneously (case (4)). The posterior distributions of spacetime parameters are shown in Figure 12 (and the credible intervals for each run are presented in Table 9 and Figure 18). From there we see that the inclusion of XMM-Newton data shifts the median radius from 12.5 to 12.9 km and narrows the width of the 68% credible interval of radius from 3.3 to 2.2 km. Constraining the NICER background further using the 3C50 estimate does not significantly affect the results, since the background is essentially more restricted using XMM-Newton than providing, for example, background limits of $n_l = 2$ and $n_u = 3$ based on the 3C50 estimate (as seen from the full online set for Figure 11). However, we note that these conclusions can depend on the assumed cross-calibration

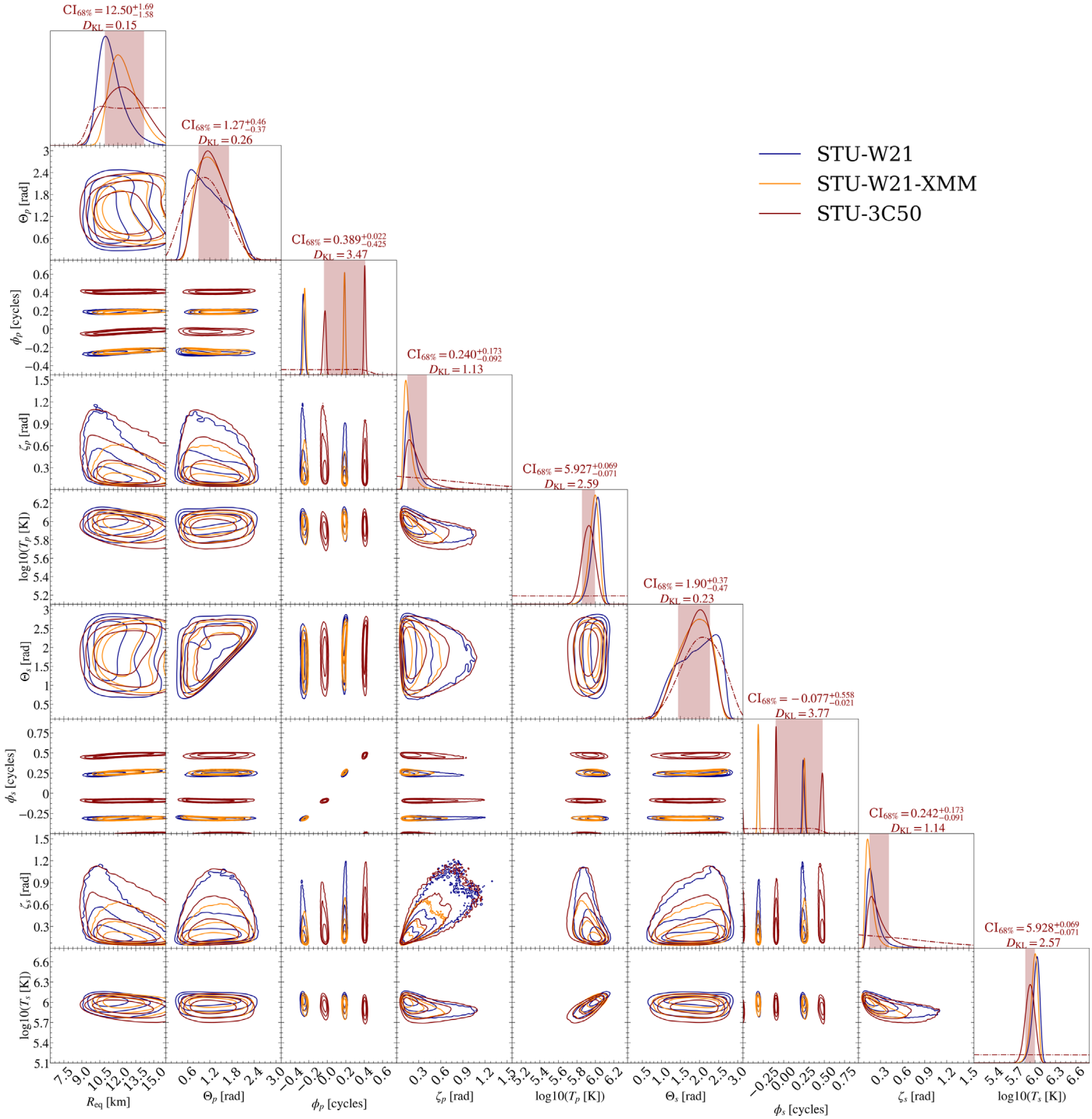

Figure 8. Effect of 3C50 data selection on the hot region parameter posterior distributions conditional on the `ST-U` model. The same types of posterior distributions are shown as in Figure 7, and the shown parameters are described in Table 2. The credible intervals and the divergence estimates are reported for the NICER posterior conditional on the 3C50 data set. The complete figure set (6 images), including also the results based on different background constraints and spot models, is available in the online journal (HTML version).

(The complete figure set of 6 images is available.)

uncertainty between NICER and XMM-Newton, and for other sources or future data sets, the 3C50 uncertainties may be smaller. We use the compressed scaling for cross-calibration as explained in Section 3.3, which yielded an NS radius of $12.71^{+1.25}_{-0.96}$ km in R21, very similar to the 3C50+XMM-Newton results obtained here (and also fairly close to the 3C50+XMM-Newton results of Appendix B). We also tested the sensitivity to the energy-independent cross-calibration uncertainty with low-resolution runs (as mentioned in Section 3.3), but found only relatively small effects on the

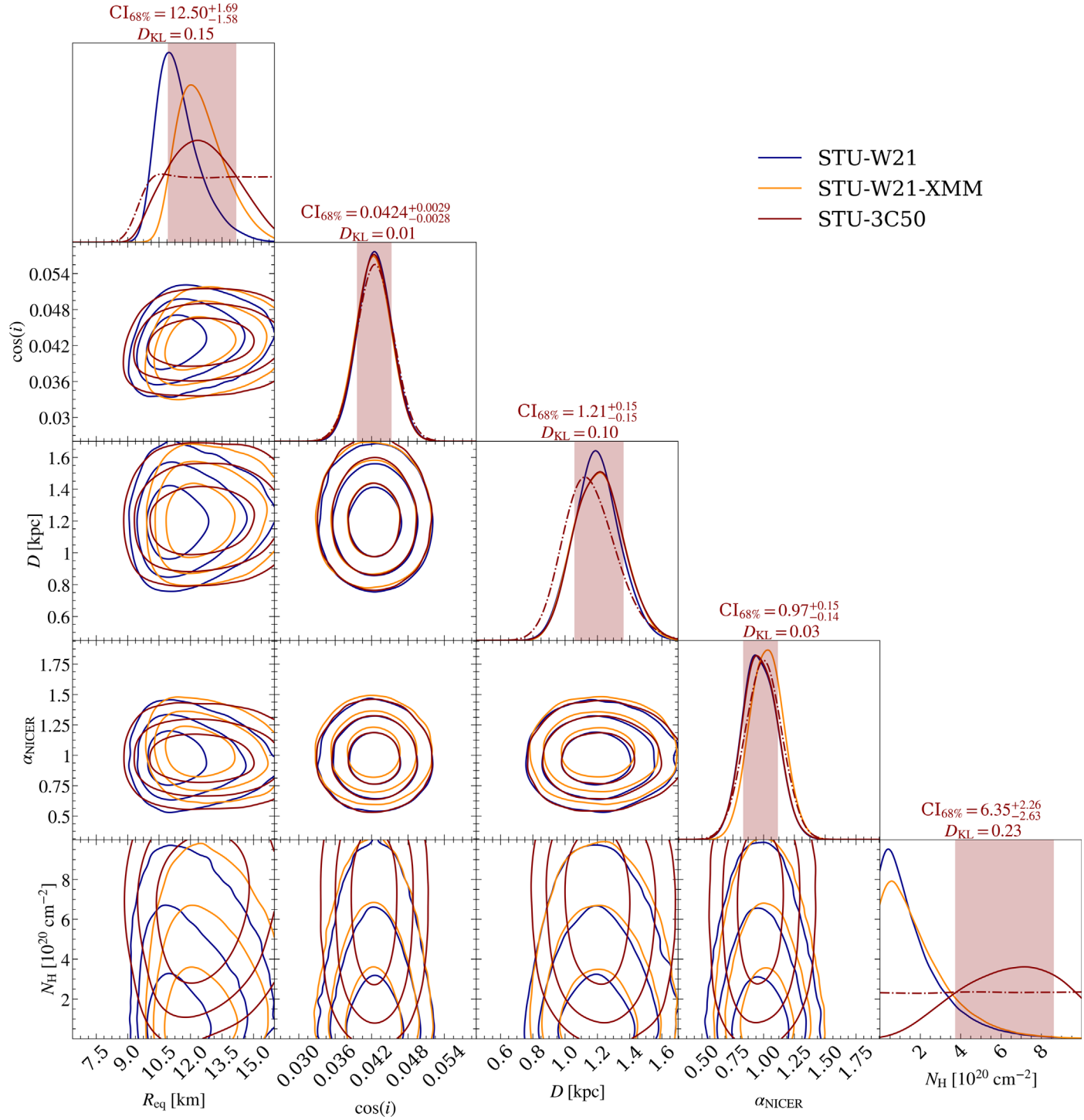

Figure 9. Effect of 3C50 data selection on the additional parameter posterior distributions conditional on the ST-U model. The same types of posterior distributions are shown as in Figure 7, and the shown parameters are described in Table 2. The credible intervals and the divergence estimates are reported for the NICER posterior conditional on the 3C50 data set. The complete figure set (6 images), including also the results based different background constraints and spot models, is available in the online journal (HTML version).

(The complete figure set of 6 images is available.)

inferred parameters (results shown in the online set of Figure 12).

4.4. Effect of Antipodality

As mentioned in Section 3.2, we have also analyzed models with less complexity in the surface hot regions, restricting the spots to be in an antipodal configuration. We applied both the models ST-S and ST-Ua (the former restricting also the temperatures and sizes of the spot to be the same), and compared against the non-antipodal ST-U results for the 3C50 data without background constraints (case (1)), and for the 3C50 data with ($n_l = 3$, $n_u = \infty$) background limits combined with

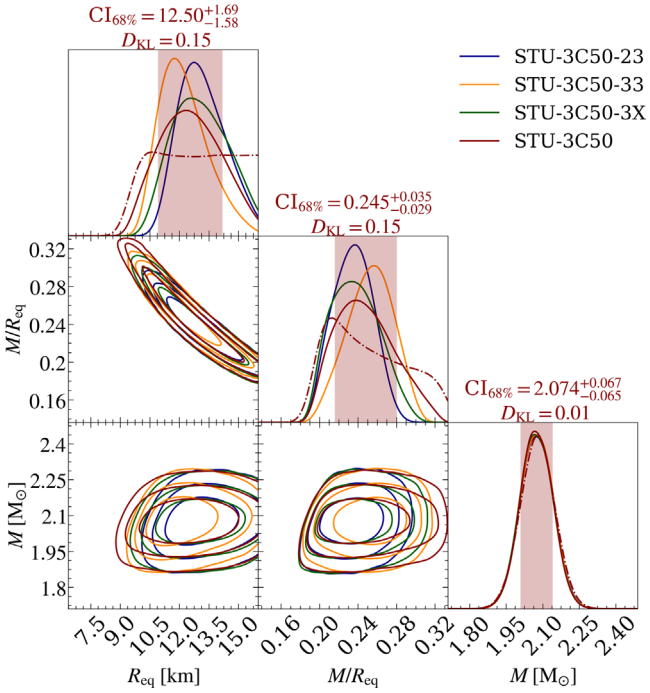

Figure 10. Effect of 3C50 background estimate on the mass and radius posterior distributions. Four types of posterior distribution are shown: one conditional on the NICER likelihood function using the ST−U model and 3C50 data set (same as in Figure 7); one otherwise same but with $n_l = 3$ lower limit for the background (3C50-3X); one otherwise same but with $n_l = 3$ lower and $n_u = 3$ upper limits for the background (3C50-33); and one otherwise same but with $n_l = 2$ lower and $n_u = 3$ upper limits for the background (3C50-23). The credible intervals and the divergence estimates are reported for the NICER posterior conditional on the 3C50 data set as in Figure 7 (for the other cases, see Table 7). See the caption of Figure 5 for additional details about the figure elements. The corresponding posterior results using the lower limits based on the minimum of the data and the background (mdb) are shown in the figure set in the online journal (HTML version).

(The complete figure set of 2 images is available.)

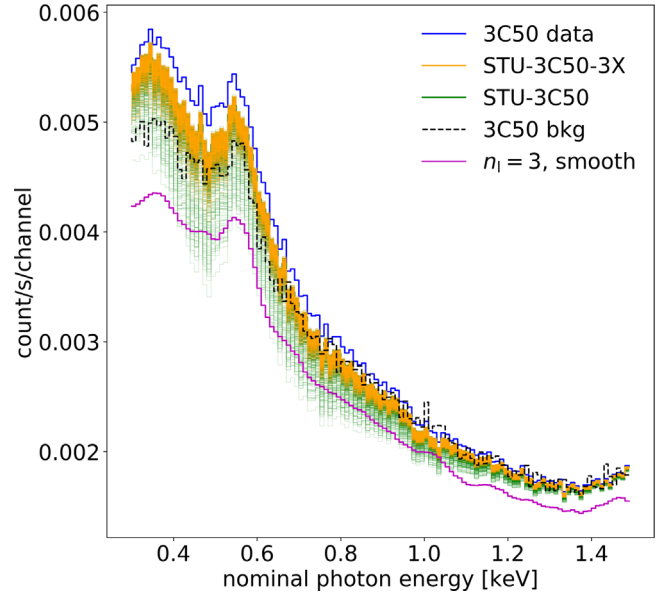

Figure 11. Comparison of the inferred NICER background for the 3C50 data set with and without background constraints. The blue step function is the total NICER count-rate spectrum, the dashed black step function is the 3C50 background estimate, and the magenta step functions show the lower and upper bounds for background support. Orange step functions show 1000 background curves that maximize the likelihood for 1000 equally weighted posterior samples from the 3C50 data analysis when applying $n_l = 3$ lower limit for the NICER background (with no upper limit). The green step functions show the corresponding inferred backgrounds for the 3C50 analysis without applying any background constraints. The complete figure set (11 images) is available in the online journal (HTML version). These include the inferred backgrounds for the other background prior choices for 3C50.

(The complete figure set of 11 images is available.)

XMM-Newton observation (case (4)). The resulting spacetime parameter constraints are shown in Table 10 and in Figure 13 for the background limited case. The residuals for the different cases are shown in Figure 14.

From the figures mentioned above, we see that the inferred radius is consistent with ST−S and ST−U (the former with notably larger credible intervals), but the ST−Ua model predicts a significantly higher radius. However, both of the antipodal models show more residual clustering than ST−U (indicating defects in the model), even though the difference is not enormous. The residuals for ST−Ua are only shown in the online figure set for Figure 14, but they look very similar to those of ST−S. Also, the Bayesian evidence for ST−U is larger than the evidence for either of the antipodal models (see the evidences in Table 10). On the other hand, the evidence for ST−Ua is higher than the evidence for ST−S when the background is not constrained (and ST−Ua is clearly then predicting a background that is too low), and vice versa for the limited background case. This shows that, when the background is forced to be reasonable, adding the freedom of having different temperatures and spot sizes for the two hot regions is not helpful in order to resolve the structures in the residuals. Instead, ST−Ua tends to find significant differences in the temperature and size of the two spots, whereas ST−U (for PSR J0740+6620) finds very similar spot parameters but places the spots in a non-antipodal configuration.

The major reason for antipodal configurations not being adequate for the modeling is the azimuthal offset of the two hot spots, rather than the offset in their colatitudes. The total angular offset of the secondary hot spot center from the antipode of the center of the primary spot one is inferred to deviate more than 25° with more than 84% probability in the case of all ST−U runs performed here (and in R21). The inferred angular sizes of the hot spots peak typically around 10° with a tail in the posterior distribution toward larger spot sizes, being still less than 25° with more than 84% probability (depending slightly on the model). This means there is only a relatively small chance that the antipode of the primary spot center would be enclosed by the secondary hot spot.

In addition, we examined the effect of setting a hard upper limit of 10° on the maximum angular size for the smaller of the hot spots. This prior is somewhat more restrictive than expected from the maximum spot size from a centered-dipole (see, e.g., Gonthier & Harding 1994), but it was chosen to maximize the effect and to account for the fact that the entire polar cap should not actually be uniform in temperature. We tested this with low-resolution runs for 3C50 without any background constraints, because the inferred spot size is the highest for that case (the median of the smaller spot angular radius around 13°.8). We found that, by adding the spot size upper limit, the inferred radius shifted up roughly by 1 km, and the inferred background became also higher. Thus, having a spot size prior changed the results in the same direction as

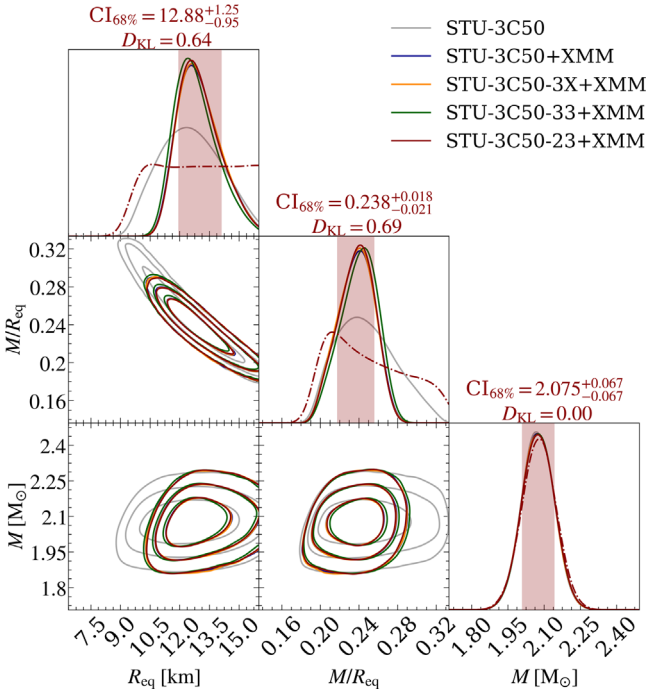

Figure 12. Effect of adding XMM-Newton data to the 3C50 data on the mass and radius posterior distributions conditional on the `ST-U` model. Five types of posterior distribution are shown: one conditional on 3C50; one conditional on 3C50 and the XMM-Newton likelihood function; one conditional on 3C50 with ($n_l = 3$ and $n_u = \infty$) background limits and XMM-Newton likelihood function; one conditional on 3C50 with ($n_l = 3$ and $n_u = 3$) background limits and the XMM-Newton likelihood function; and one conditional on 3C50 with ($n_l = 2$ and $n_u = 3$) background limits and XMM-Newton likelihood function. The credible intervals and the divergence estimates are reported for the NICER posterior conditional on the 3C50 and the XMM-Newton likelihood function (for the other cases, see Table 9). See the caption of Figure 5 for additional details about the figure elements. The complete figure set (2 images), which include also the results with different cross-calibration prior assumptions, is available in the online journal (HTML version).

(The complete figure set of 2 images is available.)

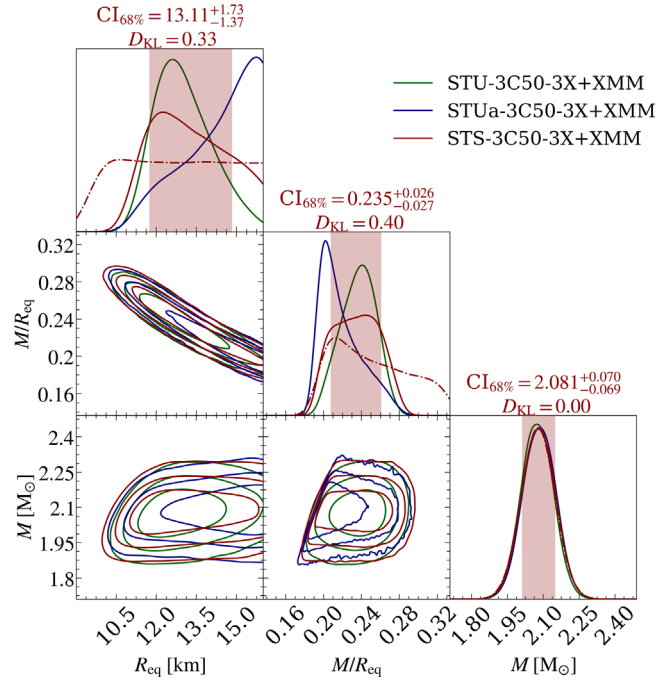

Figure 13. Effect of antipodality on the mass and radius posterior distributions conditional on 3C50 with ($n_l = 3$ and $n_u = \infty$) background limits and XMM-Newton likelihood function. Three types of posterior distribution are shown: one conditional on the `ST-U` model; one conditional on the `ST-Ua` model; and one conditional on the `ST-S` model. The credible intervals and the divergence estimates are reported for the NICER posterior conditional on the `ST-S` model (for the other cases, see Table 10). See the caption of Figure 5 for additional details about the figure elements.

applying a lower bound to the background. However, this prior did not have any significant effects on the offset from antipodality of the spot centers, but of course the chance of the antipode being enclosed within the other spot became even smaller.

The posterior distributions for the latitudinal, longitudinal, and total angular offset are shown in Figure 15. From there we see that colatitudes of the spots are inferred with large uncertainty, being on average closely antipodal. But the phase offset from the antipode is clearly constrained to around 0.1 of the total cycle, which is around 36°. The offset is also similar for both posterior modes, which only differ based on which of the spots (with higher or smaller colatitude) is leading the other spot by 0.4 cycle (these modes were also present in R21). The most likely spot configurations are visualized in the animation of 100 highest-likelihood geometries shown in the online journal version of Figure 16, with separate videos shown for the 2 different posterior modes.

5. Discussion

As shown in Section 4, we found that the results obtained when using NICER background constraints in our analysis are consistent with those obtained previously from joint NICER and XMM-Newton analysis. In the following sections, we discuss the uncertainties in the measured NS radius in more detail, implications for the cross-calibration between NICER and XMM-Newton, and what we can learn from the inferred geometry of the radiating hot spots.

5.1. Radius Uncertainties

Using 3C50-selected NICER data, we found larger statistical uncertainties in the inferred radius compared to the original run with the W21 data set. Applying the 3C50 background constraint improved the radius constraints slightly, the credible intervals becoming comparable to those obtained previously with the joint NICER and XMM-Newton analysis. On the other hand, applying the SW estimate to the W21 data set increased the statistical radius uncertainty, but again produced results closer to the joint NICER and XMM-Newton analysis. This likely implies that the unmeasured systematic uncertainties are reduced when setting reasonable limits for the inferred background. We also found that the results are quite sensitive to the hard cutoffs set for the NICER background prior information and to small features in the background estimates (either by using a smoothed estimate or the mdb estimate that was forced to not exceed the data). All of the 68% credible intervals for the different runs presented here still overlap significantly. But using the new approach, i.e., constraining the NICER background through the SW and 3C50 background estimates, the uncertainty associated with the cross-calibration between NICER and XMM-Newton is avoided.

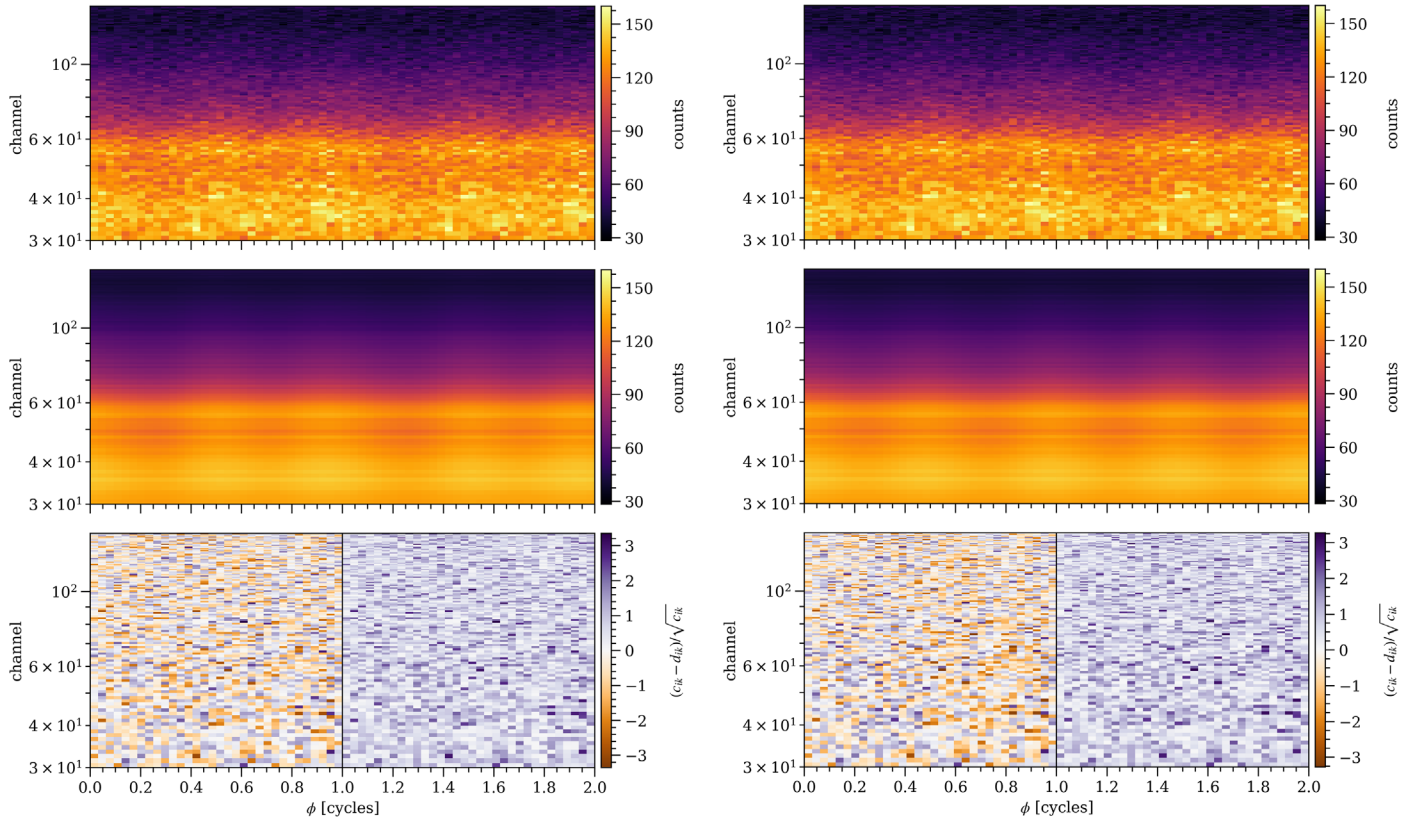

Figure 14. NICER 3C50 count data, posterior-expected count numbers, and (Poisson) residuals for ST−U (left panel) and ST−S (right panel) conditional on 3C50 with ($n_l = 3$ and $n_u = \infty$) background limits and XMM-Newton likelihood function. See Figure 6 of R21 for additional details about the figure elements. The complete figure set (3 images), which includes the corresponding ST−Ua residuals, is available in the online journal (HTML version).

(The complete figure set of 3 images is available.)

If we assume an unconstrained background, we find that the 3C50 data set produces a larger credible interval for the radius compared to W21. But after constraining the background using XMM-Newton, both W21 and 3C50 produce comparably tight radius constraints. Statistical uncertainties depend on source and background counts (see Lo et al. 2013; Psaltis et al. 2014). This implies a dependence of the radius credible interval on exposure time and effective area. Since 3C50 has both a shorter exposure time (1.55569 versus 1.60268 Ms) and lower effective area (3C50 collects data from 50 of the 52 active detectors, W21 from 51 of them), the trend is consistent with expectations. However the difference between the statistical uncertainties of the two data sets (when not including XMM-Newton) is bigger than expected by simply considering these two changes. In particular, based on the square root dependence on the observed counts, one would expect less than 0.1 km broadening in the length of the radius credible interval, instead of the observed broadening of 1 km. However, this is not necessarily surprising: the two data sets rely on two different observing periods and have indeed been built adopting very different approaches (3C50 targeting an estimation of the background and W21 targeting high counts) and procedures, including filtering. Because of the different observing periods, the contribution from a time variable background (like the active galactic nucleus, hereafter AGN, in the FoV) could also be different in the two data sets.

5.2. Implications for the Cross-calibration Uncertainty between NICER and XMM-Newton

Since the results of the new NICER-only analysis are consistent with the joint NICER and XMM-Newton (using either old W21 or new 3C50 NICER data sets), we conclude that there is no evidence for inconsistency in the NICER and XMM-Newton cross-calibration. This is also concluded in the independent analysis of Appendix B. Instead, we found that the constraints obtained by applying NICER background estimates are not restrictive enough to limit the inferred background as tightly as with a simultaneous NICER and XMM-Newton analysis. However, we note this is not necessarily the case for other sources and data sets, and the use of NICER background estimates also provides an independent way to constrain the relative pulse amplitude for the signal from the hot spots, and thus more robustly measure the NS radius. Also, as seen in R21, Miller et al. (2021a), the radius posteriors may slightly depend on the allowed energy-independent cross-calibration uncertainty in the modeling. In the new joint analysis of this paper, we primarily used the compressed scaling uncertainty from R21, and checked with a low-resolution run that further compression did not change the results significantly (as explained in Section 4.3.2). However, energy-dependent cross-calibration effects may also exist, and those were not accounted for in our analysis.

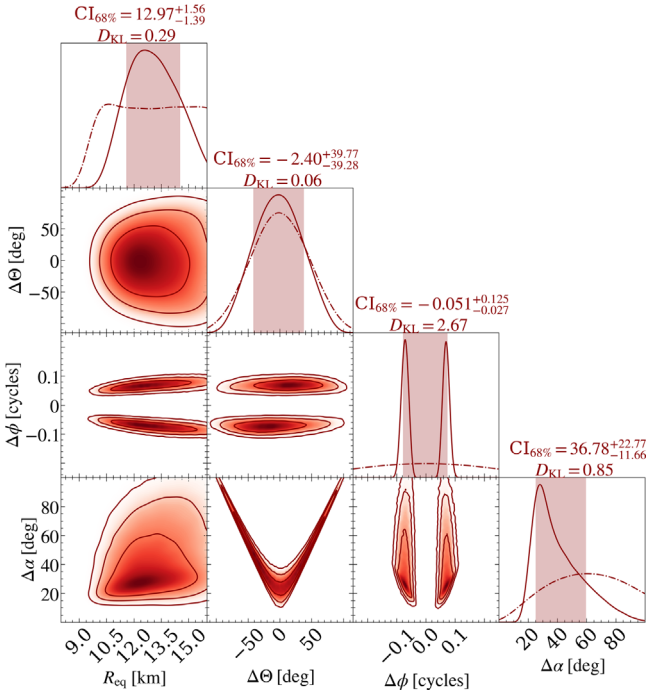

Figure 15. Antipodal offset inferred from the ST−U run based on 3C50 data with $n_l = 3$ background lower limit. Here $\Delta\Theta$ is the offset from antipodality in the hot spot colatitudes, $\Delta\phi$ is the offset from antipodality in the spot azimuths, and $\Delta\alpha$ is the total offset angle from antipode. See the caption of Figure 5 for additional details about the figure elements. The complete figure set (2 figures), which includes the inferred offset also for the run with W21 data set and the smoothed SW background lower limit, is available in the online journal (HTML version).

(The complete figure set of 2 images is available.)

5.3. Deviation from Antipodality

As presented in Section 4.4, we constrained the offset angle from antipodality to be more than 25° with a higher than 84% probability even when allowing the possibility of the two spots having different temperatures and sizes. As shown in Table 10, the evidence difference significantly favors the non-antipodal ST−U model both when including and excluding background prior information. The Bayes factor of ST−U against the best antipodal model is always larger than 10^8, which can be considered as decisive evidence against the antipodal models (Kass & Raftery 1995). This result challenges magnetic field models with a centered-dipolar field structure, even though the inferred configuration is much closer to antipodal than in the case of PSR J0030+0451 (Bilous et al. 2019; Miller et al. 2019; Riley et al. 2019). We also note that deviation arises almost entirely because of the phase difference of the hot spots, offset by 0.1 cycle from being antipodal. For this reason, the simpler models ST−S and ST−Ua explored in this paper were not able to provide as good a description of the data as the less constrained ST−U model. Since, in the ST−U runs, the inferred spot radii and temperatures are almost identical between the two spots, and colatitudes on average antipodal, it may be still possible to fit the data with a less complex model in which temperatures, sizes, and colatitudes are shared or derived between the spots but where each of them would have their own phase parameters.

6. Conclusions

In this paper, we have presented PPM analysis of NICER data of the high-mass pulsar PSR J0740+6620, using the X-PSI simulation and inference code, building on the work previously reported by R21, and using a similar framework as in Miller et al. (2021a), the latter reported in Appendix B. Those previous analyses used XMM-Newton data and background estimates to provide an indirect constraint on the NICER background, and the inferred radius was sensitive to the inclusion of this constraint. In this paper, we have used newly developed NICER background models as a direct constraint during the PPM, so that we no longer have to attempt to model the uncertain cross-calibration between NICER and XMM-Newton. The results, in particular the inferred mass and radius, are consistent with our previous findings and have similar uncertainties. This means that dense matter EOS inference using our previous results does not, at this stage, need to be updated; though the posterior samples derived from our new NICER-only analysis can be downloaded via the associated repository in Salmi et al. (2022).

Constraints are expected to become tighter in the future, as NICER builds up more data on PSR J0740+6620. The procedure outlined in this paper for analyzing NICER data with NICER-only background estimates will be used in future PPM analysis for both PSR J0740+6620 and other NICER sources. Our analysis shows the impact, on an inferred radius and its uncertainties, of having good and well-constrained models for the background emission. The 3C50 model (with background estimates and uncertainties) developed by Remillard et al. (2022) used in this paper is extremely useful for PPM; in the future, we also hope to have better constraints on contributions from unrelated sources in the FoV such as the AGN SDSS J074115.14+662234.9, which as reported by Wolff et al. (2021) also contributes to the NICER background but is not accounted for in the 3C50 model estimates. Given the uncertainty over the AGN contribution at present, our recommendation for anyone wishing to use the updated NICER-only posteriors reported in this paper is to use the 3C50-3X results, for which the inferred mass and radius are $2.073^{+0.068}_{-0.066}\ M_\odot$ and $12.97^{+1.56}_{-1.39}$ km.

The consistency we found between the NICER-only radius posteriors using NICER backgrounds, and the radius posteriors from joint NICER and XMM-Newton analyses, motivates the inclusion of XMM-Newton data in future work. Applying NICER background information separately or on top of XMM-Newton can still be a useful independent precaution. In our case, using both NICER background estimates and XMM-Newton reduced the uncertainty in the radius giving, for the 3C50-3X+XMM case; $M = 2.075^{+0.067}_{-0.067}\ M_\odot$, and $R_{eq} = 12.90^{+1.25}_{-0.97}$ km. Furthermore, we note that the lower limit of 68% credible interval for the radius converges to very similar values also in the case of the corresponding Illinois–Maryland analyses (see Appendix B, and Figure 18 in Appendix C), when both 3C50 and XMM-Newton data are applied, whereas a larger discrepancy appears for the joint W21 and XMM-Newton analysis. This similarity can, at least partly, come from the improved data selection leading to smaller sensitivity on the background modeling. The difference in the 68% upper limit can still be attributed to the different choices in the radius prior and modeling procedures as discussed in Section 4.6 of Miller et al. (2021a) and Section 4.4 of R21.

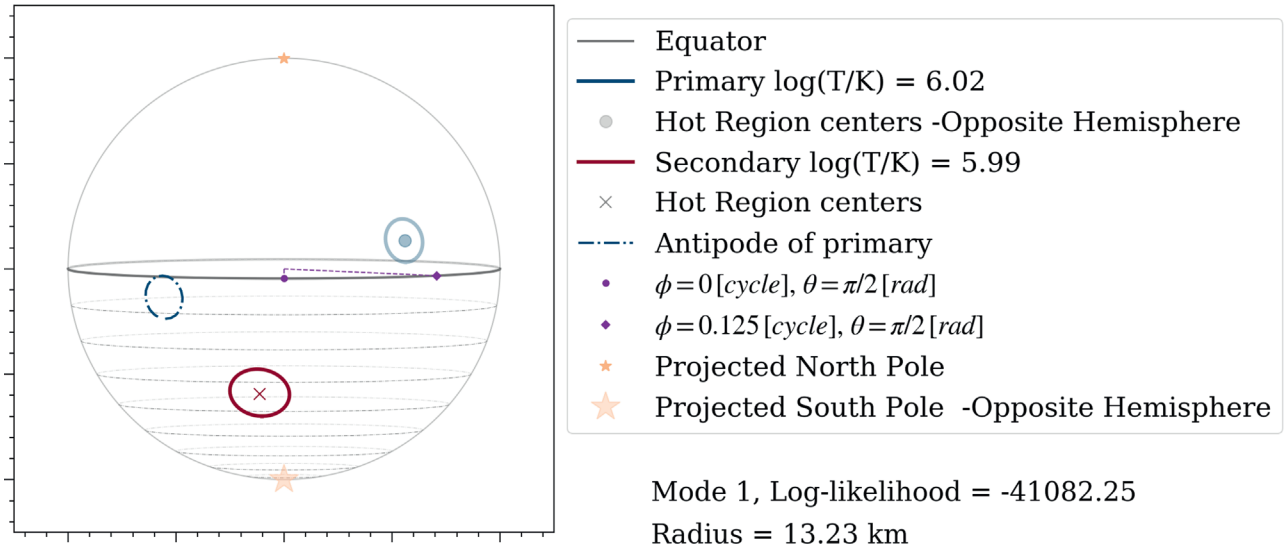

Figure 16. Geometry configuration for STU-3C50-3X+XMM run (see Figures 12 and 13 for description) corresponding to the nested sample with maximum likelihood. The viewing angle represents the Earth inclination to the spin axis. The full animation set with 100 best samples, in the order of decreasing likelihood is shown in the online journal (HTML version) separately for the two different posterior modes (where the primary, i.e., lower colatitude spot is either around 0.4 cycle ahead or behind the secondary spot). The animation shows a large variation between the best-fitting geometries. More inferred configuration samples for different runs, also ordered based on maximum posterior weight instead of maximum likelihood, are available in Salmi et al. (2022).

(An animation of this figure is available.)

We also reported an extended analysis of the degree to which the inferred hot spot (magnetic polar cap) geometry deviates from a purely antipodal configuration. The degree to which the hot regions deviate from a purely antipodal configuration is of importance to those modeling multiwavelength pulsar emission and pulsar magnetic field evolution (Bilous et al. 2019; Chen et al. 2020; Kalapotharakos et al. 2021). A purely antipodal configuration, even one where the hot regions can have different sizes and temperatures, can be ruled out with a high degree of certainty. The degree of offset of the central points of the polar caps is at least 25° with 84% probability. This excludes, with high confidence, a centered-dipolar field configuration for PSR J0740+6620, implying that multipolar or non-centered-dipolar fields might be common in millisecond pulsars, as PSR J0740+6620 is already the second object showing evidence for this.

This work was supported in part by NASA through the NICER mission and the Astrophysics Explorers Program. T.S., S.V., D.C., T.E.R., and A.L.W. acknowledge support from European Research Council (ERC) Consolidator grant (CoG) No. 865768 AEONS (PI: Watts). This work was sponsored by the Nederlandse Organisatie voor Wetenschappelijk Onderzoek (NWO) Domain Science for the use of the national computer facilities. A major part of the work was carried out on the HELIOS cluster including dedicated nodes funded via the abovementioned ERC CoG. S.G. acknowledges the support of the Centre National d'Etudes Spatiales (CNES). W.C.G.H. acknowledges support through grant 80NSSC22K0397 from NASA. S.M.M. thanks NSERC for research support. The material is based upon work supported by NASA under award number 80GSFC21M0002 (Z.W.). A.J.D. was supported in part by LANL/LDRD under project number 20220087DR. The Los Alamos Unlimited Release (LA-UR) number is LA-UR-22-28454. M.C.M. and A.J.D. were supported in part by NASA ADAP grant 80NSSC21K0649. Part of this work was performed at the Aspen Center for Physics, which is supported by U.S. National Science Foundation grant PHY-1607611. Some of the resources used in this work were provided by the NASA High-End Computing (HEC) Program through the NASA Center for Climate Simulation (NCCS) at Goddard Space Flight Center. NICER research at Naval Research Laboratory (NRL) is supported by NASA. A.L.W. would like to thank Anatoly Spitkovsky for prompting us to look in more detail at the question of non-antipodality.

Appendix A
3C50 Data and Background Model

Here we describe both the data analysis steps and the filtering steps that define a set of GTIs that we refer to, hereafter, as the 3C50 data set. There is substantial overlap with other NICER data sets for PSR J0740+6620, but the selection criteria are designed to produce a background spectrum with reliable uncertainty estimates, in any range of photon energy. We also note that the GTI sorting method from Guillot et al. (2019), used to maximize the pulsed signal significance, was not used when filtering the new 3C50 data. Therefore, the new filtering can not produce any biases in the pulsation amplitude as suggested by Essick (2022) for the original sorting method (see Section 2.1).

The 3C50 background model (Remillard et al. 2022) uses three non-source count rates within the on-source GTIs to select and rescale background components from the model's libraries. The spectra in the libraries are derived from observations of seven fields (named "BKGD_RXTE") selected in the Rossi X-ray Timing Explorer era (Jahoda et al. 2006) to contain no detected sources with the existing instrumentation at that time.[26] These blank-sky observations are the same as used

[26] We note that none of these seven blank-sky regions have been observed with modern X-ray imaging instruments (except eROSITA). There are no detected second ROSAT Source Catalog (2RXS; Boller et al. 2016) sources within 8′ of the NICER pointed positions of these fields, except for "BKGD_RXTE_3", which has two 2RXS sources (19 and 12 c s^{-1}) within ∼4′ and ∼4′.4.

by the SW model in Section 2.1. They show that the in-band background rate, i.e., the rate of events that cannot be distinguished from X-ray events from the science target, can vary by several orders of magnitude, and they mainly originate from interactions between the silicon drift detectors and the various types of charged particles encountered in the space environment.

Appendix A.1 describes the methods used to limit the systematic error during the initial data analyses and also to screen the background-subtracted spectra to avoid intervals when the background prediction has poor quality. Then in Appendix B, the large archive of final GTI selections for PSR J0740+6620 is divided into eight consecutive time intervals, with exposure time ∼214 ks in each interval. These data represent eight trials to measure the source intensity, choosing evaluations in three energy bands. The net count rate for PSR J0740+6620 is 0.028 c s^{-1} at 0.3–2.0 keV, with no detection at 2–4 or 4–12 keV. Similar analyses are conducted for six additional rotation-powered pulsars, with the following conclusions. The mean and rms values are consistent with steady emission for each target, over the 5 yr lifetime of NICER, as expected for this source class. Furthermore, the rms measures in each energy band reveal common uncertainty values that scale proportionally with the shape of the average background spectrum. These rms results imply a systematic uncertainty that scales (1σ) as roughly 2% of the average background spectrum, under the condition that the screening steps are imposed.

A.1. Data Processing and Filtering of Good Time Intervals

For any NICER target observed over different epochs of the data-processing and calibration pipeline, archived data must be brought to a uniform gain calibration by running the HEASARC tool *nicerl2* on each observation. This task reruns the NICER data pipeline to determine the time and equivalent photon energy of each recorded event, producing the *unfiltered* and *cleaned* event lists within GTIs that establish selection windows for the calibrated event lists. The pipeline uses an embedded task, *nimaketime*, to define GTIs while applying filters for a variety of geometric constraints, e.g., the pointing offset from the target, presence in the South Atlantic Anomaly, and minimum angles to the Earth limb and to the solar-illuminated Earth limb. There are also rate constraints that specify maximum frequencies of overshoot-flagged events and undershoot-flagged events, and a maximum for the relationship between the overshoot rate and the magnetic shielding index, known as the cutoff rigidity, i.e., the COR_SAX column in the NICER filter files (see the documentation for "nimaketime" in the NASA HEASARC ftools web pages). In the present investigation, we adopted all of the default settings for geometric filters. However, the three rate filters were effectively disabled by specifying impossibly high values for each (i.e., 15000) on the *nicerl2* command line. The reason for this is to modestly increase the initial, overall exposure time, with the intent to filter for data quality at later stages of analysis.

After reprocessing is finished, an explicit list of GTI times can be made by running *nimaketime* on each observation, using the same combination of filter parameters, i.e., adopting default values for geometric parameters and disabling values for rate parameters. However, when defining our GTIs, two additional steps were employed to facilitate the background estimation process.

The goal is to limit the dynamic range of values for the 3C50 model parameters within any GTI, so that non-linearities inherent in the background behavior might be reduced. First, it was found that transitions in orbit day versus night can reduce the effectiveness of the *nz* parameter (count rate at below 0.25 keV) for predicting the soft X-ray excess tied to optical light loading, when such transitions occur within a GTI. Furthermore, the reflections in advance of ISS sunrise and lingering detector noise after ISS sunset can broaden the effects of the day–night transition to a range of ±30 s from the transition time. To avoid integrating the *nz* parameter over such conditions, *nimaketime* was run twice with added constraints, SUNSHINE=1 and SUNSHINE=0, respectively, and then combining all of the results into one table.

A second step to improve background predictability is a response to the fact that NICER background count rate and spectral shape routinely vary in complex ways over the course of the ISS orbit, and also from orbit to orbit. It is therefore prudent to limit the orbital phase duration of each time interval for which a background prediction will be made. On the other hand, the 3C50 model parameters for the stage (1) library (i.e., *ibg* and *hrej*; see Section 3.1 of Remillard et al. 2022 for definitions) suffer from low count rates, creating an opposing motivation to integrate as long as possible, to limit the effects of Poisson noise. Given the four passages between the Earth equator and the highest polar latitudes (52°) in the ISS orbit (92 minutes), we choose a target and maximum GTI of 300 and 450 s, respectively. Intervals of duration (dt) longer than 450 s are subdivided into N GTIs, with $N = int(dt/300 + 0.5)$, where *int* denotes an integer value. Finally, we choose to ignore GTI when the gap time is 2 s or less. Such gaps may be caused by packet losses or noise in *nimaketime* selection parameters, and the isolated, brief gaps can be integrated over without significant consequences. To implement our choices for GTI definition, we use a customized C program to read the initial GTI table and then output the final table, while ignoring brief gaps, masking mission elapsed time values within 30 s of a SUNSHINE transition in consecutive GTIs, and dividing long GTIs into pieces of roughly 300 s. The final GTI table is indexed, and the index number is included in the file names of all downstream data products based on a given GTI.

For PSR J0740+6620, we applied these steps to NICER data collected through between 2018 September 21 and 2021 December 28 (observation IDs, hereafter ObsIDs, 1031020101 through 4031020407), yielding 9907 GTIs and a total exposure of 2.79 Ms. This is the starting point for application of the 3C50 background model. For every GTI, the extractions of spectra and 3C50 model parameters values are made on the basis of 50 selectable FPMs, while ignoring FPMs 14 and 34, as explained in Remillard et al. (2022; in contrast, the W21 data set events did not exclude detector (14)). The model parameter values are used to generate a 3C50 prediction of the background spectrum, again per GTI, and the difference between the raw extraction and the 3C50 background spectrum is the background-subtracted spectrum used for subsequent filtering considerations.

Screening criteria use background-subtracted spectra (noted as parameters with subscript "net"), per GTI, in diagnostic energy bands, as described in Remillard et al. (2022). The criteria are designed to flag and ignore the GTIs that have an obviously poor background prediction. For faint, non-accreting pulsars, such as PSR J0740+6620, we extend the types of

Table 3
Pulsar Data Sets Filtered for 3C50 Background Model

Pulsar Name (1)	ObsID Start (2)	ObsID End (3)	Initial Ms (4)	Selected Ms (5)	Subset (6)	0.3–2.0 keV Rate (rms)[a] (7)	2–4 keV Rate (rms) (8)	4–12 keV Rate (rms) (9)
J0030+0451	1060020101	4060020511	3.078	1.984	9	0.234 (0.018)	−0.0077 (0.005)	−0.0015 (0.010)
J0614-3329	1030050106	5030050307	1.250	0.726	6	0.062 (0.016)	−0.0112 (0.008)	−0.0100 (0.011)
J0740+6620	1031020101	4031020407	2.790	1.713	8	0.028 (0.020)	−0.0042 (0.010)	−0.0061 (0.011)
J1231-1411	1060060101	5060060656	3.130	1.730	8	0.163 (0.019)	−0.0131 (0.006)	−0.0094 (0.008)
J1614-2230	0060310101	4060310289	1.049	0.572	5	0.216 (0.018)	−0.0030 (0.003)	0.0063 (0.007)
B1821-24[b]	1070010101	5070010449	1.139	0.789	6	0.666 (0.020)	0.0747 (0.008)	0.0236 (0.010)
B1937+21	1070020101	5070020735	2.562	1.079	6	−0.085 (0.015)	0.0044 (0.007)	−0.0013 (0.012)

Notes.
[a] Rate is measured in counts per second.
[b] B1821-24 was not filtered for the 2–4 keV band.

filters in the interest of reducing systematic uncertainty in the background estimation. The list of filters and the fraction of remaining exposure time, in parentheses, for the case of PSR J0740+6620, are given as follows. The selection fractions are scaled to the initial set of GTIs with a total exposure 2.79 Ms. We first remove GTIs that have 3C50 parameter measurements beyond the model limits (0.998). Then, for better 3C50 parameter statistics, we select GTIs with exposure time greater than 200 s (0.968). To avoid noise contamination in strong sunlight, we select GTIs with $nz < 220$ c s^{-1} (0.856). Because the 3C50 model performs best at normal–low count rates, presumably due to the lack of identified metrics for background contributions from trapped and precipitating particles in the local space environment, we further select GTIs with $ibg < 0.2$ c s^{-1} (0.790). Extending the filters described in Remillard et al. (2022), we apply $|hbg_{\rm net}| < 0.05$ (0.777) and $|S0_{\rm net}| < 0.15$ (0.728).

Consistent with the overall result that there is no detection of PSR J0740+6620 with NICER above 2.0 keV, we use the in-band energy ranges at 2–4 (C band) and 4–12 keV (D band) to select $|D_{\rm net}| < 0.3$ (0.686) and $|C_{\rm net}| < 0.1$ (0.614). The use of $D_{\rm net}$ and $C_{\rm net}$ filters has to be self-consistent with the final, deep FoV spectrum of a given target. Filter limits were chosen to reject the wings of the probability distribution in each of these bands, assuming that such outliers arise from inaccurate background predictions. If the filter limits are within an order of magnitude of the net flux in that band, then the filtering step is suspended. Finally, for the simplicity of using one response file for these data, we select from the remainder only those GTIs in which all 50 selected FPMs are operating (0.558). This completes the definition of the 3C50 data set (1.55569 Ms final exposure) used in this investigation. The source intensity is 0.028 c s^{-1} at 0.3–2.0 keV, and there is no detection at 2–4 or 4–12 keV.

The sum of the raw spectra for the 3C50 data set and the sum of the 3C50 model background predictions for the same time intervals are shown in Figure 1. The difference between raw and background spectra is referred to as the average FoV spectrum for PSR J0740+6620, and the possibility of contributions from other sources in the NICER FoV must be considered before treating the FoV spectrum as the average pulsar spectrum. The same time intervals for GTIs in the 3C50 data set were used to derive the average 3C50 pulse profile for PSR J0740+6620, using the same steps applied to other data sets.

A.2. Quantifying Systematic Uncertainty in the Background Spectrum

The group of non-accreting X-ray pulsars with large exposure times in the NICER archive (currently, 1–3 Ms per target) offers an important opportunity to measure the systematic limits on the accuracy of NICER background models. The ability to assume that the average source intensity is constant over the timescale of many years is another key condition. For each target, we divide the exposure time into subsets of 100–200 ks, average the background-subtracted spectra for each subset, and finally use the rms scatter for each subset group, in selected energy bands, to search for evidence of systematic limits that span the group of such pulsars. We stress that the average background spectrum is always tied to a specific list of GTIs, with substantial variations that depend on data selection criteria. Background measurements and model results, alone, do not offer a control needed to anchor uncertainty analyses. On the other hand, deep background-subtracted spectra for invariable X-ray sources, examined as a series of 100+ ks exposures with negligible statistical error, might reveal systematic limits in the background model, given a uniform set of filtering steps. The net count rate for such pulsars is fainter than the average background level, giving rise to the expectation that systematic uncertainties would produce the same rms variations in 100–200 ks subsets, for a given energy band, regardless of the pulsar brightness. However, we note that the assumption for this method is that there are no variable sources in the FoV.

Filtering efforts were conducted for 7 pulsars with Ms accumulated exposures in the NICER archive, and the results are given in Table 3. For each pulsar, the data were divided into a number of subsets (column (6) in Table 3), yielding 100–200 ks exposures in each sample. The selection steps are the same as that described above for PSR J0740+6620, except for two differences. For the tabulated results, the last step, i.e., the restriction to a uniform set of 50 active FPMs, was not imposed, while the spectra are linearly scaled to 50 FPMs for the small percentage of GTIs where one or more normally selected FPMs were not operating. The selected exposure time for PSR J0740+6620 is then 1.71 Ms, rather than the 1.556 Ms noted for data used in the present investigation. Despite this difference, the average net count rates for PSR J0740+6620 in the 3 given energy bands (columns (7)–(9) in Table 3) are the same, in either case, for the number of significant digits reported. The second difference in selection steps is that

B1821-24 was not filtered for the *C* band (2.4 keV, column (8) in Table 3), where a significant detection is found. This result can be seen as a corroboration of the filtering methods, since B1821-24 is a relatively bright pulsar with a non-thermal spectrum that continues above 2 keV (Rowan et al. 2020). The net count rates (columns (7)–(9) in Table 3) are background-subtracted averages and rms values for the given range in photon energy, in units counts per second, scaled to 50 FPMs. For example, we note that the C-band count rate for PSR J0740+6620 is 0.028 c s^{-1}.

The rms values shown in Table 3 are similar across all pulsars, for each of the chosen energy bands. This invites interpretation as a measurement of systematic limits for the accuracy of 3C50 model predictions, for 100–200 ks exposure times, given the filtering efforts described herein. We adopt the average rms values in counts per second as estimates for the 3C50 background uncertainty (1σ): 0.018 (0.3–2.0 keV), 0.007 (2–4 keV), and 0.010 (4–12 keV). The ratios in these energy bands scale as follows: 1, 0.39, 0.56. On the other hand, the background spectrum for the 1.55569 Ms data set for PSR J0740+6620 shows integrated values of 0.4207, 0.1246, and 0.2401 c s^{-1}, in the same energy bands, scaling as 1.0, 0.30, 0.57. This implies that the spectral shapes of the rms measurements for pulsar subsets and the background spectrum for PSR J0740+6620 are quite similar. We interpret this as evidence that the systematic uncertainty in the 3C50 model can be pictured as a normalization uncertainty on the final background spectrum. The uncertainty array (versus spectral bin), for the purposes of pulsar pulse-phase modeling, is then estimated as the rescaled values (by factor 0.018/0.4207) of the 3C50 background spectrum for PSR J0740+6620.

Appendix B
An Independent Analysis of the 3C50 Data Set and Background Estimates

Herein we describe analyses of the 3C50 data set and associated background estimates using the same PPM code and analysis pipeline as in Miller et al. (2021a), which we refer to subsequently as the Illinois–Maryland analyses. We investigate all combinations of inclusion and exclusion of both XMM data and NICER background estimates in conjunction with the 3C50-selected NICER data set. We provide an independent confirmation that the radius inferences from 3C50 data and background estimates are consistent with previous analyses of NICER and XMM data, and that the calibrations of NICER and XMM do not appear inconsistent with one another.

B.1. Methodology

We utilize the PPM models and code previously applied to PSR J0740+6620 in Miller et al. (2021a), the details and underlying assumptions of which are further described in Miller et al. (2019), Bogdanov et al. (2019), and Bogdanov et al. (2021). As in Miller et al. (2021a), we perform Bayesian parameter inference using the parallel-tempered Markov Chain Monte Carlo (MCMC) sampler in version 2.2.1 of the emcee package (Foreman-Mackey et al. 2013). We drew the initial walker positions for each analysis from a kernel density estimate of the posterior probability distributions from the analyses of Miller et al. (2021a), using the samples archived in

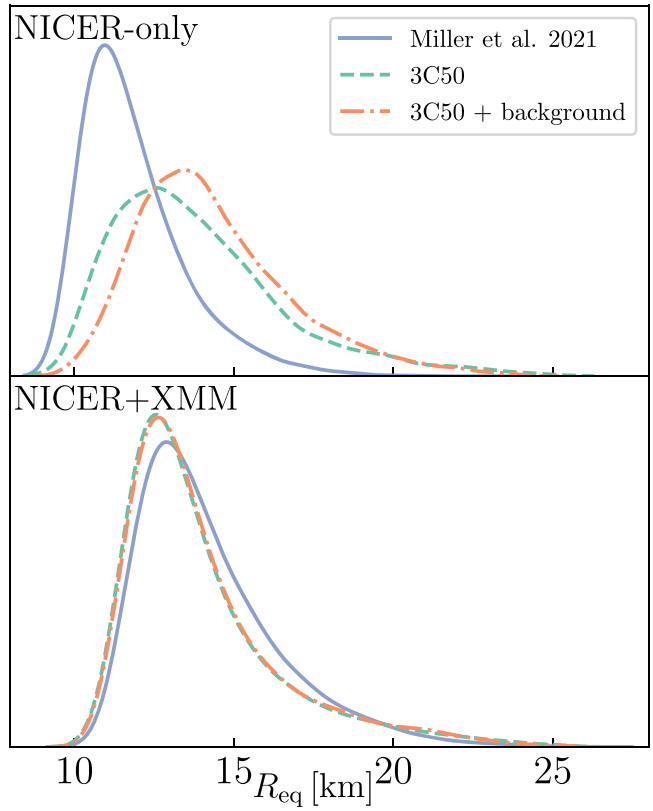

Figure 17. The 1D posterior probability density of the equatorial circumferential radius of PSR J0740-6620 inferred using the Illinois–Maryland analysis pipeline. Each line is an averaged shifted histogram (e.g., Scott 1985) of the posterior samples from the converged portion of an MCMC analysis. Blue solid lines illustrate the results from Miller et al. (2021a), which analyzed the W21 data set. Green dashed lines illustrate the results from analyses that used the 3C50-selected NICER data, but did not incorporate the 3C50 background estimate as a lower limit; and orange dashed–dotted lines illustrate results from analyses, which used the 3C50-selected NICER data set and incorporated the 3C50 background estimate, with uncertainties, as a lower limit on the NICER background. The top panel includes results from analyses of NICER data alone, while the bottom panel includes results derived using both NICER and XMM data.

Table 4
Best-fit, Median, and ±68.3% Credible Interval Values ($\pm CI_{68\%}$) of the Equatorial Circumferential Radius (Given in Kilometers) of PSR J0740+6620 from the Analysis of Various Data Sets, Using Only NICER Data

NICER Data Set	Best Fit	Median	$-CI_{68\%}$	$+CI_{68\%}$
W21	11.008	11.512	10.381	13.380
3C50	10.265	13.383	11.350	16.354
3C50+bkg	12.849	13.959	12.097	16.747

Table 5
Best-fit, Median, and ±68.3% Credible Interval Values ($\pm CI_{68\%}$) of the Equatorial Circumferential Radius (Given in Kilometers) of PSR J0740+6620 from the Analysis of Various Data Sets, Using Both NICER and XMM Data

NICER Data Set	Best Fit	Median	$-CI_{68\%}$	$+CI_{68\%}$
W21	13.823	13.713	12.209	16.326
3C50	11.933	13.310	11.940	16.107
3C50+bkg	12.918	13.362	11.980	16.177

Miller et al. (2021b). We use the termination criterion described in Section 4.3 of Miller et al. (2021a), accruing 10^7 post-convergence samples during each analysis.

When including 3C50 background estimates, we first produce a smoothed model count spectrum using a cubic smoothing spline, smoothed such that the spline has a frequency response of 0.5 over a wavelength of 10 bins following the algorithm introduced by Cook & Peters (1981). To take into account systematic field-to-field uncertainty in the 3C50 background predictions, we introduce an energy-independent rescaling factor β_{3C50} in the Illinois–Maryland analyses, by which we multiply the 3C50 background spectrum. Based on Appendix A.2, we use for this parameter a Gaussian prior with a mean of 1 and a standard deviation of 0.0461, a conservative estimate of the total uncertainty. On top of the smoothed and rescaled background spectrum predicted by the 3C50 model, we marginalize over additional possible background contributions (such as other X-ray sources within NICER's FoV; see Wolff et al. 2021) as described in Section 3.4.1 of Miller et al. (2021a). In all analyses using XMM data, we used the nominal telescope response, without allowing for any variation in the effective area (see, for comparison, Section 4.4 of Miller et al. 2021a).

B.2. Results

We present the inferred radii from the Illinois–Maryland analyses of the available X-ray data for PSR J0740+6620 in Figure 17. The maximum-likelihood, median, and 68% credible interval equatorial radius values derived from each analysis are presented in Tables 4 and 5 for our NICER-only and NICER+XMM analyses respectively. Some differences between the X-PSI and Illinois–Maryland results are expected based on a number of choices made over the course of each set of analyses, including the details of the 3C50 background implementation in addition to those described in Section 4.6 of Miller et al. (2021a) and Section 4.4 of R21. However, there are a number of common trends between the results reported in this Appendix and those derived using the X-PSI framework.

In the Illinois–Maryland analyses not incorporating XMM data, the results of which are shown in the upper panel of Figure 17, we find that inclusion of the 3C50 data alone pushes the inferred equatorial radii to higher values, relative to the NICER-only analysis of the W21 data, into closer agreement with the results from the NICER+XMM fit to the W21 data. This shift is likely the result of the more stringent data selection cuts when constructing the 3C50 data set, described in Appendix A, resulting in a lower background and thus a higher fraction of modulated emission, and is similar to the results presented in Figure 7. Furthermore, inclusion of background constraints in the fits only to NICER data shifts the equatorial radius posterior to yet higher values, a similar effect to including XMM data in the analysis of the W21 data set, along the same lines as the results discussed in Section 4.3.1. As in Section 4.2, we find that the posteriors derived from the 3C50 NICER data set, without incorporating XMM data, are broader than those derived from the W21 data set.

In the Illinois–Maryland analyses, which incorporate both NICER and XMM data, the results of which are presented in the lower panel of Figure 17, we observe that including 3C50 background constraints makes a much smaller difference than in the NICER-only case, similar to the results presented in Section 4.3.2. However, we do find that including both XMM data and a 3C50-derived NICER background estimate results in a very slight shift of the equatorial radius posterior to higher values. As shown in Table 5, the 68% credible regions become very slightly wider in both analyses of the 3C50 data set compared to the results from Miller et al. (2021a), although to a lesser extent than in the analogous NICER-only analyses.

Appendix C
Mass and Radius Credible Intervals for Different Runs Using X-PSI

We summarize the inferred results of radius and mass credible intervals using the X-PSI framework using different approaches for the background modeling in Tables 6–10. The radius intervals are also visualized in Figure 18 for both X-PSI and Illinois–Maryland results.

Table 6
Summary Table for Different Runs with W21 NICER Data Set Including SW Background Estimate without Smoothing and with Smoothing

Parameter	W21			W21+XMM			W21-0.9xSW			W21-0.9xSWs		
M [$M_\odot$]	$2.078^{+0.066}_{-0.063}$	0.01	2.125	$2.072^{+0.066}_{-0.067}$	0.01	2.070	$2.072^{+0.066}_{-0.068}$	0.01	1.99	$2.072^{+0.067}_{-0.066}$	0.01	1.99
R_{eq} [km]	$11.29^{+1.20}_{-0.81}$	0.72	10.90	$12.39^{+1.30}_{-0.98}$	0.58	11.02	$12.53^{+1.47}_{-1.10}$	0.45	11.78	$11.90^{+1.32}_{-0.95}$	0.58	11.26

Note. We show the 68.3% credible intervals around the median $\widehat{\mathrm{CI}}_{68\%}$, Kullback–Leibler divergence D_{KL} representing prior-to-posterior information gain, and the maximum likelihood nested sample $\widehat{\mathrm{ML}}$ of mass and radius. See Figure 5 for more details.

Table 7
Similar to Table 6, but with Different 3C50 Runs Using Smoothed Background Spectra

Parameter	3C50			3C50-3X			3C50-33			3C50-23		
M [$M_\odot$]	$2.074^{+0.067}_{-0.065}$	0.01	2.061	$2.073^{+0.068}_{-0.066}$	0.01	2.101	$2.076^{+0.067}_{-0.067}$	0.01	2.153	$2.076^{+0.068}_{-0.067}$	0.0	2.071
R_{eq} [km]	$12.50^{+1.69}_{-1.58}$	0.15	13.35	$12.97^{+1.56}_{-1.39}$	0.29	12.66	$12.09^{+1.41}_{-1.08}$	0.45	12.64	$13.05^{+1.36}_{-1.11}$	0.50	13.66

Note. See Figure 10 for the model name descriptions.

Table 8
Similar to Table 7, but with Using the Minimum Function for the Lower Bound of the Background

Parameter	3C50			3C50-3X-mdb			3C50-33-mdb			3C50-23-mdb		
M [$M_\odot$]	$2.074^{+0.067}_{-0.065}$	0.01	2.061	$2.074^{+0.067}_{-0.066}$	0.01	1.974	$2.077^{+0.067}_{-0.066}$	0.01	2.112	$2.076^{+0.067}_{-0.067}$	0.0	1.909
$R_{\rm eq}$ [km]	$12.50^{+1.69}_{-1.58}$	0.15	13.35	$12.69^{+1.66}_{-1.46}$	0.23	12.76	$11.73^{+1.39}_{-1.05}$	0.48	10.64	$12.35^{+1.38}_{-1.03}$	0.51	13.11

Note. See second figure in Figure Set 10 for more details.

Table 9
Similar to Table 7, but with Joint 3C50 and XMM-Newton Runs

Parameter	3C50+XMM			3C50-3X+XMM			3C50-33+XMM			3C50-23-XMM		
M [$M_\odot$]	$2.075^{+0.067}_{-0.067}$	0.01	2.119	$2.075^{+0.067}_{-0.067}$	0.01	2.132	$2.076^{+0.067}_{-0.067}$	0.01	1.972	$2.075^{+0.067}_{-0.067}$	0.0	1.934
$R_{\rm eq}$ [km]	$12.89^{+1.26}_{-0.97}$	0.61	13.59	$12.90^{+1.25}_{-0.97}$	0.62	13.23	$12.71^{+1.25}_{-0.94}$	0.64	12.00	$12.88^{+1.25}_{-0.95}$	0.64	12.80

Note. See Figure 12 for more details.

Table 10
Similar to Table 7, but with Different Runs Using Antipodal Hot Spots

Parameter	STS-3C50			STUa-3C50			STS-3C50-3X+XMM			STUa-3C50-3X+XMM		
M [$M_\odot$]	$2.076^{+0.070}_{-0.068}$	0.0	2.166	$2.054^{+0.071}_{-0.066}$	0.08	2.138	$2.082^{+0.070}_{-0.069}$	0.0	2.314	$2.085^{+0.068}_{-0.070}$	0.01	1.926
$R_{\rm eq}$ [km]	$11.73^{+2.18}_{-1.45}$	0.14	13.45	$15.57^{+0.31}_{-0.59}$	2.13	15.95	$13.11^{+1.73}_{-1.37}$	0.33	15.12	$14.65^{+0.97}_{-1.84}$	0.59	15.93
$\widehat{\ln \mathcal{Z}}$	-16024.67 ± 0.02			-16018.03 ± 0.02			-20593.12 ± 0.02			-20597.28 ± 0.02		

Notes. We also show the log-evidences $\widehat{\ln \mathcal{Z}}$[a] to compare the model performance between `ST-U`, `ST-Ua`, and `ST-S`.[b] For more details, see Figure 13 and Section 4.4.

[a] The evidence is defined as the prior predictive probability, $p(d_{\rm N}, d_{\rm X}, \{\mathcal{B}_{\rm N}\}, \{\mathscr{B}_{\rm X}\}|\texttt{ST} - \texttt{S})$. Note that the evidences for models with different background limits are not comparable.

[b] For STU-3C50 $\widehat{\ln \mathcal{Z}}=-15997.60 \pm 0.02$, and for STU-3C50-3X+XMM, $\widehat{\ln \mathcal{Z}}=-20564.85 \pm 0.02$.

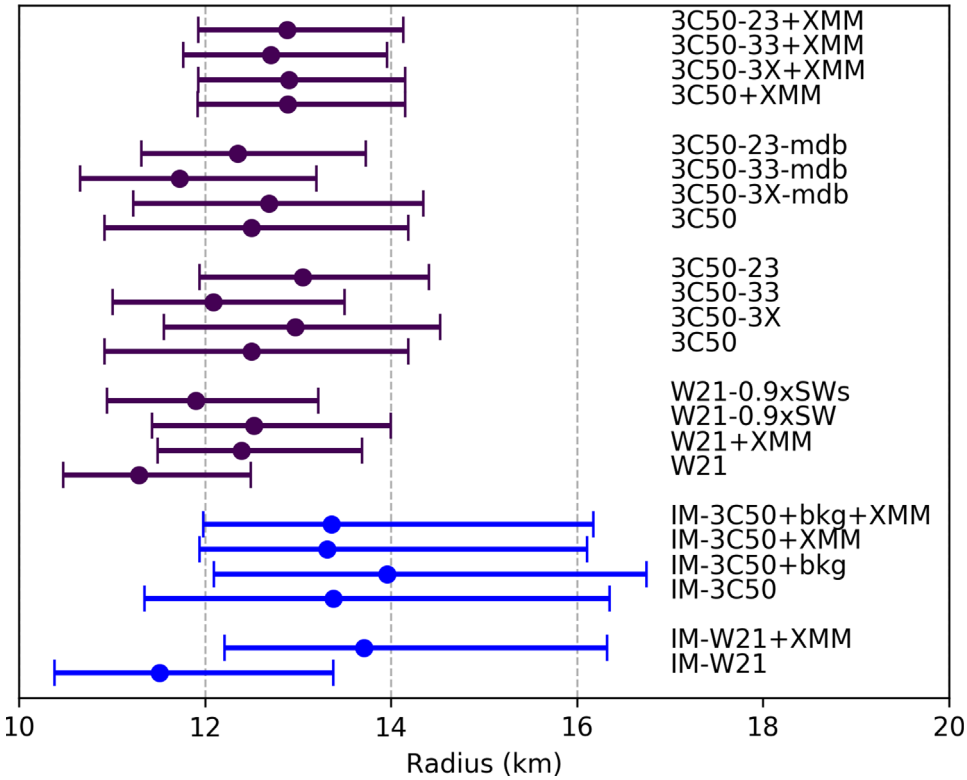

Figure 18. Summary of the medians and 68.3% credible intervals for radius using two circular hot spot model `ST-U` with different data sets and treatments for the background modeling. Purple dots and lines correspond to the results obtained using X-PSI with models described in Tables 6–9 and the associated figures in Section 4. Blue dots and lines correspond to the results obtained using the independent Illinois–Maryland code with the models described in Appendix B, Table 4, and Table 5.

ORCID iDs

Tuomo Salmi https://orcid.org/0000-0001-6356-125X
Serena Vinciguerra https://orcid.org/0000-0003-3068-6974
Devarshi Choudhury https://orcid.org/0000-0002-2651-5286
Thomas E. Riley https://orcid.org/0000-0001-9313-0493
Anna L. Watts https://orcid.org/0000-0002-1009-2354
Ronald A. Remillard https://orcid.org/0000-0003-4815-0481
Paul S. Ray https://orcid.org/0000-0002-5297-5278
Slavko Bogdanov https://orcid.org/0000-0002-9870-2742
Sebastien Guillot https://orcid.org/0000-0002-6449-106X
Cecilia Chirenti https://orcid.org/0000-0003-2759-1368
Alexander J. Dittmann https://orcid.org/0000-0001-6157-6722
Keith C. Gendreau https://orcid.org/0000-0001-7115-2819
Wynn C. G. Ho https://orcid.org/0000-0002-6089-6836
M. Coleman Miller https://orcid.org/0000-0002-2666-728X
Sharon M. Morsink https://orcid.org/0000-0003-4357-0575
Zorawar Wadiasingh https://orcid.org/0000-0002-9249-0515
Michael T. Wolff https://orcid.org/0000-0002-4013-5650

References

AlGendy, M., & Morsink, S. M. 2014, ApJ, 791, 78
Annala, E., Gorda, T., Katerini, E., et al. 2022, PhRvX, 12, 011058
Arons, J. 1981, ApJ, 248, 1099
Baym, G., Hatsuda, T., Kojo, T., et al. 2018, RPPh, 81, 056902
Bilous, A. V., Watts, A. L., Harding, A. K., et al. 2019, ApJL, 887, L23
Biswas, B. 2022, ApJ, 926, 75
Bogdanov, S., Lamb, F. K., Mahmoodifar, S., et al. 2019, ApJL, 887, L26
Bogdanov, S., Dittmann, A. J., Ho, W. C. G., et al. 2021, ApJL, 914, L15
Boller, T., Freyberg, M. J., Trumper, J., et al. 2016, A&A, 588, A103
Buchner, J., Georgakakis, A., Nandra, K., et al. 2014, A&A, 564, A125
Chen, A. Y., Yuan, Y., & Vasilopoulos, G. 2020, ApJL, 893, L38
Cook, E. R., & Peters, K. 1981, Tree-Ring Bulletin, http://hdl.handle.net/10150/261038
Essick, R. 2022, ApJ, 927, 195
Feroz, F., & Hobson, M. P. 2008, MNRAS, 384, 449
Feroz, F., Hobson, M. P., & Bridges, M. 2009, MNRAS, 398, 1601
Fonseca, E., Cromartie, H. T., Pennucci, T. T., et al. 2021, ApJL, 915, L12
Foreman-Mackey, D., Hogg, D. W., Lang, D., & Goodman, J. 2013, PASP, 125, 306
Gendreau, K. 2020, NICER Background Estimator Tools, https://heasarc.gsfc.nasa.gov/docs/nicer/tools/nicer_bkg_est_tools.html
Gendreau, K. C., Arzoumanian, Z., Adkins, P. W., et al. 2016, Proc. SPIE, 9905, 99051H
Gonthier, P. L., & Harding, A. K. 1994, ApJ, 425, 767
Gonzalez-Caniulef, D., Guillot, S., & Reisenegger, A. 2019, MNRAS, 490, 5848
Guillot, S., Kerr, M., Ray, P. S., et al. 2019, ApJL, 887, L27
Harding, A. K., & Muslimov, A. G. 2001, ApJ, 556, 987
Hebeler, K. 2021, PhR, 890, 1
Ho, W. C. G., & Lai, D. 2001, MNRAS, 327, 1081
Ishida, M., Tsujimoto, M., Kohmura, T., et al. 2011, PASJ, 63, S657
Jahoda, K., Markwardt, C. B., Radeva, Y., et al. 2006, ApJS, 163, 401
Kalapotharakos, C., Wadiasingh, Z., Harding, A. K., & Kazanas, D. 2021, ApJ, 907, 63
Kass, R. E., & Raftery, A. E. 1995, Journal of the American Statistical Association, 90, 773
Lattimer, J. M. 2012, ARNPS, 62, 485
Legred, I., Chatziioannou, K., Essick, R., Han, S., & Landry, P. 2021, PhRvD, 104, 063003
Li, J. J., Sedrakian, A., & Alford, M. 2021, PhRvD, 104, L121302
Lo, K. H., Miller, M. C., Bhattacharyya, S., & Lamb, F. K. 2013, ApJ, 776, 19
Madsen, K. K., Beardmore, A. P., Forster, K., et al. 2017, AJ, 153, 2
Miller, M. C., & Lamb, F. K. 1998, ApJL, 499, L37

Miller, M. C., Lamb, F. K., Dittmann, A. J., et al. 2019, ApJL, 887, L24
Miller, M. C., Lamb, F. K., Dittmann, A. J., et al. 2021a, ApJL, 918, L28
Miller, M. C., Lamb, F. K., Dittmann, A. J., et al. 2021b, NICER PSR J0740+6620 Illinois-Maryland MCMC Samples, v1, Zenodo, doi:10.5281/zenodo.4670689
Morsink, S. M., Leahy, D. A., Cadeau, C., & Braga, J. 2007, ApJ, 663, 1244
Nath, N. R., Strohmayer, T. E., & Swank, J. H. 2002, ApJ, 564, 353
Oertel, M., Hempel, M., Klahn, T., & Typel, S. 2017, RvMP, 89, 015007
Pang, P. T. H., Tews, I., Coughlin, M. W., et al. 2021, ApJ, 922, 14
Plucinsky, P. P., Beardmore, A. P., Foster, A., et al. 2017, A&A, 597, A35
Poutanen, J., & Gierlinski, M. 2003, MNRAS, 343, 1301
Psaltis, D., Ozel, F., & Chakrabarty, D. 2014, ApJ, 787, 136
Raaijmakers, G., Greif, S. K., Hebeler, K., et al. 2021, ApJL, 918, L29
Remillard, R. A., Loewenstein, M., Steiner, J. F., et al. 2022, AJ, 163, 130
Riley, T. E. 2019, PhD thesis, Univ. Amsterdam, https://hdl.handle.net/11245.1/aa86fcf3-2437-4bc2-810e-cf9f30a98f7a
Riley, T. E., Watts, A. L., Bogdanov, S., et al. 2019, ApJL, 887, L21
Riley, T. E., Watts, A. L., Ray, P. S., et al. 2021a, ApJL, 918, L27
Riley, T. E., Watts, A. L., Ray, P. S., et al. 2021b, A NICER View of the Massive Pulsar PSR J0740.6620 Informed by Radio Timing and XMM-Newton Spectroscopy: Nested Samples for Millisecond Pulsar Parameter Estimation, v1.0.0Zenodo, doi:10.5281/zenodo.4697625
Riley, T. E., Watts, A. L., Ray, P. S., et al. 2021c, A NICER View of the Massive Pulsar PSR J0740.6620 Informed by Radio Timing and XMM-Newton Spectroscopy: Nested Samples for Millisecond Pulsar Parameter Estimation, v1.0.1Zenodo, doi:10.5281/zenodo.5735003
Riley, T. E., Choudhury, D., Salmi, T., et al. 2022, JOSS, submitted
Rowan, D. M., Ghazi, Z., Lugo, L., et al. 2020, ApJ, 892, 150
Ruderman, M. A., & Sutherland, P. G. 1975, ApJ, 196, 51
Salmi, T., Vinciguerra, S., Choudhury, D., et al. 2022, The Radius of PSR J0740.6620 from NICER with NICER Background Estimates, v1.0.0, Zenodo, doi:10.5281/zenodo.6827537
Scott, D. W. 1985, AnSta, 13, 1024
Tang, S.-P., Jiang, J.-L., Han, M.-Z., Fan, Y.-Z., & Wei, D.-M. 2021, PhRvD, 104, 063032
Tolos, L., & Fabbietti, L. 2020, PrPNP, 112, 103770
Watts, A. L. 2019, in AIP Conf. Ser. 2127, Xiamen-CUSTIPEN Workshop on the EOS of Dense Neutron-rich Matter in the Era of Gravitational Wave Astronomy, ed. A. Li, B.-A. Li, & F. Xu (Melville, NY: AIP), 020008
Watts, A. L., Andersson, N., Chakrabarty, D., et al. 2016, RvMP, 88, 021001
Wilms, J., Allen, A., & McCray, R. 2000, ApJ, 542, 914
Wolff, M. T., Guillot, S., Bogdanov, S., et al. 2021, ApJL, 918, L26
Yang, J., & Piekarewicz, J. 2020, ARNPS, 70, 21

The Astrophysical Journal, 974:295 (19pp), 2024 October 20 https://doi.org/10.3847/1538-4357/ad5f1e
© 2024. The Author(s). Published by the American Astronomical Society.
OPEN ACCESS

A More Precise Measurement of the Radius of PSR J0740+6620 Using Updated NICER Data

Alexander J. Dittmann[1,2], M. Coleman Miller[1], Frederick K. Lamb[3,4], Isiah M. Holt[1,5], Cecilia Chirenti[1,6,7,8], Michael T. Wolff[9], Slavko Bogdanov[10], Sebastien Guillot[11], Wynn C. G. Ho[12], Sharon M. Morsink[13], Zaven Arzoumanian[5], and Keith C. Gendreau[5]

[1] Department of Astronomy and Joint Space-Science Institute, University of Maryland, College Park, MD 20742-2421, USA; dittmann@umd.edu
[2] Theoretical Division, Los Alamos National Laboratory, Los Alamos, NM 87545, USA
[3] Illinois Center for Advanced Studies of the Universe and Department of Physics, University of Illinois at Urbana-Champaign, 1110 West Green Street, Urbana, IL 61801-3080, USA
[4] Department of Astronomy, University of Illinois at Urbana-Champaign, 1002 West Green Street, Urbana, IL 61801-3074, USA
[5] X-Ray Astrophysics Laboratory, NASA Goddard Space Flight Center, Code 662, Greenbelt, MD 20771, USA
[6] Astroparticle Physics Laboratory, NASA Goddard Space Flight Center, Greenbelt, MD 20771, USA
[7] Center for Research and Exploration in Space Science and Technology, NASA Goddard Space Flight Center, Greenbelt, MD 20771, USA
[8] Center for Mathematics, Computation, and Cognition, UFABC, Santo André, SP 09210-170, Brazil
[9] Space Science Division, U.S. Naval Research Laboratory, Washington, DC 20375-5352, USA
[10] Columbia Astrophysics Laboratory, Columbia University, 550 West 120th Street, New York, NY 10027, USA
[11] Institut de Recherche en Astrophysique et Planétologie, UPS-OMP, CNRS, CNES, 9 avenue du Colonel Roche, BP 44346, F-31028 Toulouse Cedex 4, France
[12] Department of Physics and Astronomy, Haverford College, 370 Lancaster Avenue, Haverford, PA 19041, USA
[13] Department of Physics, University of Alberta, Edmonton, AB, T6G 2E1, Canada
Received 2024 January 24; revised 2024 June 7; accepted 2024 June 18; published 2024 October 18

Abstract

PSR J0740+6620 is the neutron star with the highest precisely determined mass, inferred from radio observations to be $2.08 \pm 0.07\,M_\odot$. Measurements of its radius therefore hold promise to constrain the properties of the cold, catalyzed, high-density matter in neutron star cores. Previously, Miller et al. and Riley et al. reported measurements of the radius of PSR J0740+6620 based on Neutron Star Interior Composition Explorer (NICER) observations accumulated through 2020 April 17, and an exploratory analysis utilizing NICER background estimates and a data set accumulated through 2021 December 28 was presented in Salmi et al. Here we report an updated radius measurement, derived by fitting models of X-ray emission from the neutron star surface to NICER data accumulated through 2022 April 21, totaling ∼1.1 Ms additional exposure compared to the data set analyzed in Miller et al. and Riley et al., and to data from XMM-Newton observations. We find that the equatorial circumferential radius of PSR J0740+6620 is $12.92^{+2.09}_{-1.13}$ km (68% credibility), a fractional uncertainty ∼83% the width of that reported in Miller et al., in line with statistical expectations given the additional data. If we were to require the radius to be less than 16 km, as was done in Salmi et al., then our 68% credible region would become $R = 12.76^{+1.49}_{-1.02}$ km, which is close to the headline result of Salmi et al. Our updated measurements, along with other laboratory and astrophysical constraints, imply a slightly softer equation of state than that inferred from our previous measurements.

Unified Astronomy Thesaurus concepts: Millisecond pulsars (1062); Neutron stars (1108); Nuclear astrophysics (1129); Neutron star cores (1107)

1. Introduction

The cores of neutron stars consist of cold matter that is believed to be catalyzed to its ground state at a few times nuclear saturation density (saturation corresponds to a baryon number density $n_s \approx 0.16\,\mathrm{fm}^{-3}$, equivalent to a mass density $\rho_s \approx 2.7 \times 10^{14}\,\mathrm{g\,cm}^{-3}$). Laboratories are unable to replicate the extremely high densities, and likely very high neutron–proton asymmetries, present in neutron star cores. Thus, observations of neutron stars provide unique insights about the nature of dense matter. Notably, the densities in neutron star cores partially bridge the gap between the regime $\rho \lesssim \rho_s$ probed by nuclear experimentation (e.g., Danielewicz et al. 2002; Adhikari et al. 2021) and the regime $\rho \gg \rho_s$ where perturbative quantum chromodynamics is currently able to make predictions about the nature of nuclear matter (e.g., Bedaque & Steiner 2015; Hoyos et al. 2016; Ecker et al. 2017).

In recent years, observations of neutron stars have added considerably to our knowledge of the equation of state (EOS; pressure as a function of energy density) of cold matter—matter in which the thermal energies of the particles are much smaller than their Fermi energies—at high densities (e.g., Pavlov & Zavlin 1997; Bhattacharyya et al. 2005; Özel et al. 2016b; Nättilä et al. 2017; Miller 2021).

Three neutron stars have precisely measured masses $\sim 2\,M_\odot$: PSR J1614-2230, with $M = 1.937 \pm 0.014\,M_\odot$ (Demorest et al. 2010; Fonseca et al. 2016; Arzoumanian et al. 2018; Agazie et al. 2023); PSR J0348+0432, with $M = 2.01 \pm 0.04\,M_\odot$ (Antoniadis et al. 2013); and PSR J0740+6620, with $M = 2.08 \pm 0.07\,M_\odot$ (Cromartie et al. 2020; Fonseca et al. 2021), where the quoted uncertainties denote the 68% credible regions. Observations of such massive neutron stars can rule out EOS that predict appreciably lower maximum stable masses. Additionally, observations of the gravitational-wave

Original content from this work may be used under the terms of the Creative Commons Attribution 4.0 licence. Any further distribution of this work must maintain attribution to the author(s) and the title of the work, journal citation and DOI.

event GW170817 have provided constraints on the tidal deformability of inspiraling neutron stars (e.g., Abbott et al. 2017, 2018; De et al. 2018; Abbott et al. 2020a), ruling out EOS that would cause neutron stars to have relatively high radii at a given mass. Observations of the kilonovae following binary neutron star mergers may also place upper limits on the maximum stable mass of nonrotating neutron stars (e.g., Margalit & Metzger 2017; Rezzolla et al. 2018; Pang et al. 2021).

The Neutron Star Interior Composition Explorer (NICER) can make phase- and energy-resolved measurements of the thermal X-ray pulses produced by some rotating neutron stars. These can be used to constrain the masses and radii of these stars, and thus the neutron star EOS (e.g., Özel et al. 2016a; Watts et al. 2016). The first mass and radius constraints derived from modeling NICER X-ray pulse profiles were reported in two independent analyses of the energy-resolved pulse profile of PSR J0030+0451: Miller et al. (2019) measured its mass and equatorial radius to be $1.44^{+0.15}_{-0.14}\,M_\odot$ and $13.02^{+1.24}_{-1.06}$ km, respectively, while Riley et al. (2019) measured its mass and radius to be $1.34^{+0.15}_{-0.16}\,M_\odot$ and $12.71^{+1.14}_{-1.19}$ km. Later, a pair of independent analyses of NICER and XMM-Newton data constrained the radius of PSR J0740+6620 to be $13.7^{+2.6}_{-1.5}$ km (Miller et al. 2021) and $12.39^{+1.30}_{-0.98}$, km (Riley et al. 2021), providing unique insight into the EOS, given the higher-density material present in the core of such a massive neutron star.[14] The incorporation of XMM-Newton observations is particularly useful when analyzing NICER data on PSR J0740+6620, given the faintness of the source and the crowded field of view, because the imaging data provided by XMM-Newton constrain the phase-averaged stellar flux and the nonstellar astrophysical background (Wolff et al. 2021). Models of the spurious X-ray counts caused by particle interactions with the NICER detectors (e.g., Remillard et al. 2022) can also provide valuable information about the actual astrophysical flux, and can provide similar constraints in practice to the inclusion of XMM-Newton data (e.g., Salmi et al. 2022).

Here we present a new measurement of the equatorial radius of PSR J0740+6620, incorporating previous NICER and XMM-Newton observations as well as an additional ∼1.1 Ms of NICER data. We outline our data selection and processing procedures in Section 2 and describe our methodology in Section 3. The results of our X-ray data analysis are presented in Section 4 and their implications are discussed in Section 5. We summarize our conclusions in Section 6 and report our full posteriors in Appendices B and C. The posterior samples from our analyses are available on Zenodo via doi:10.5281/zenodo.10215109.

2. Data

The present analysis of the pulse profile of PSR J0740+6620 uses NICER event data collected between 2018 September 21 (ObsID 1031020101) and 2022 April 21 (ObsID 5031020445). These NICER data add roughly 2 yr of data to the set presented in Wolff et al. (2021) and analyzed in Miller et al. (2021) and Riley et al. (2021). The net exposure time of the resulting data set (after application of the filtering procedure described below) was 2733.81 ks, in comparison to the 1602.68 ks net exposure time of the observations analyzed in Miller et al. (2021) and Riley et al. (2021).

We utilized NICER event data processed using the xti20210707 calibration release and HEASoft version 6.30.1 to extract events (NASA High Energy Astrophysics Science Archive Research Center 2014). NICER event data were filtered to minimize the background signal resulting from high-energy particles interacting with the NICER X-ray Timing Instrument (XTI). We rejected events obtained at low cosmic-ray cutoff rigidities (COR_SAX < 2). We excluded all events from NICER XTI detector 34 because it exhibited anomalously high levels of noise compared to the others, and in some time intervals we excluded data recorded by detector 14 for the same reason. We did not explicitly exclude data based on the angle between NICER's pointing direction and the Sun. Rather, we limited our event extractions to time intervals where the maximum "undershoot rate" (the detector reset rate) was below a set threshold. This limited contamination by the accumulation of optical photons ("optical loading"), which leads to spectral broadening of low-energy electronic noise that would otherwise be confined below ≈0.2 keV, and negatively affects both the detector gain and spectral resolution. Holding all other data-reduction choices constant, we compared the significances with which pulsations were detected (as quantified by the Z_2^2 test; see Buccheri et al. 1983) for data selected by requiring maximum undershoot rate limits of 50, 100, 150, and 200 counts per second (cps). The 100 cps undershoot rate limit produced the most significant detection and was therefore used in our subsequent analysis. Unlike in Wolff et al. (2021), we did not employ the Good Time Interval (GTI) sorting method of Guillot et al. (2019), which might have biased the resulting radius measurements by up to ∼10% (under simplified assumptions; Essick 2022), but in practice by $\lesssim$1% (see also Salmi et al. 2022). Because our data-selection procedure is based on the optical-photon-induced detector reset rate, we expect any biases potentially introduced by our consideration of pulsation detection significance to be even smaller than the $\lesssim$1% bias in previous analyses.

We analyzed data from NICER pulse-invariant channels 30 through 123 inclusive, which correspond to a calibrated photon energy range of 0.3–1.24 keV. We folded the waveform observed in each NICER energy channel on the spin period of the pulsar to produce a pulse profile at each energy for subsequent analysis. In our analyses incorporating XMM-Newton data, we used the same XMM-Newton data sets and channel ranges as Miller et al. (2021): channels 57 through 299 (inclusive) for the European Photon Imaging Camera (EPIC) pn instrument and channels 20 through 99 (inclusive) of the EPIC MOS1 and MOS2 instruments.

3. Methods

Our approach to modeling the X-ray data is similar in most aspects to the procedures outlined in Miller et al. (2019) and Miller et al. (2021). We review our models of emission from the stellar surface in Section 3.1 and our pulse profile models in Section 3.2. We then describe our parameter-estimation procedure in Section 3.3, which is generally similar to that described in Miller et al. (2021).

[14] See, for example, Section 4.6 of Miller et al. (2021) for a summary of the differences between these two works. Subsequent analyses of the PSR J0740+6620 data resolved some of the differences between these estimates, as noted in Section 3.3 of Salmi et al. (2022).

3.1. Modeling X-Ray Emission from the Stellar Surface

PSR J0740+6620 emits soft X-rays that are modulated on the rotational period of the neutron star (Wolff et al. 2021). The accepted model for soft X-ray emission in old, nonaccreting pulsars such as PSR J0740+6620 is that particles with large ($\gg$100) Lorentz factors, produced by magnetospheric pair cascades (e.g., Timokhin & Harding 2015; Tolman et al. 2022), penetrate deep into the neutron star's atmosphere, where their interaction with the atmosphere heats it (Tsai 1974; Harding & Muslimov 2001, 2002; Bogdanov et al. 2021).[15] The dependence of the specific intensity of the radiation emerging from the atmosphere on the angle between the direction of propagation and the local normal to the surface depends on the atmospheric composition, which we expect to be pure hydrogen or, less probably, pure helium (see Section 3.1.1); the ionization state (see Section 3.1.2); and the strength and orientation of the stellar magnetic field, which we assume has a negligible effect on the specific intensity emerging from the atmosphere of PSR J0740+6620 (see Section 3.1.3).

3.1.1. Upper Atmosphere Composition

Calculations in Alcock & Illarionov (1980) suggest that the strong surface gravity of neutron stars causes the lightest elements present in their atmospheres to rise to the surface within seconds or minutes. Because PSR J0740+6620 is expected to have accreted a substantial quantity of matter from its binary companion to reach its current spin frequency, the prevalence of hydrogen in the outer layers of the envelopes of stars like its companion suggests that PSR J0740+6620's upper atmosphere is likely to consist of pure hydrogen (see, e.g., Blaes et al. 1992; Wijngaarden et al. 2019, 2020). Although some neutron stars in X-ray binaries are thought to have accreted little or no hydrogen (see, e.g., 4U 1820-30; Strohmayer & Brown 2002), such binaries have very short periods (685 s for 4U 1820-30; Stella et al. 1987), implying that the neutron star and its companion are very close to one another and that the companion's envelope has been completely stripped of hydrogen. The orbital period of the system containing PSR J0740+6620 is 4.77 days (Cromartie et al. 2020), suggesting that the pulsar's companion had a significant hydrogen envelope when its envelope was accreting onto PSR J0740+6620. There is some evidence that the companion of PSR J0740+6620 may now be a cool helium atmosphere white dwarf (e.g., Beronya et al. 2019; Echeveste et al. 2020). Even if little hydrogen was accreted onto PSR J0740+6620, spallation may have created enough hydrogen to dominate the atmospheric composition (Bildsten et al. 1992; Chang & Bildsten 2004; Randhawa et al. 2019). For the sake of completeness, we performed analyses using helium (Ho & Heinke 2009) as well as hydrogen model atmospheres, but consider them less likely to accurately represent the surface composition of PSR J0740+6620 a priori.

[15] If particles with Lorentz factors $\lesssim$100 contribute significantly to atmospheric heating, the resulting emission pattern may be relatively limb-brightened compared to predictions in the deep-heating approximation (Bauböck et al. 2019; Salmi et al. 2020, 2023). The resulting reduction in the pulsed emission fraction could confound the influence of spacetime curvature; underestimating the degree of shallow heating is therefore expected to cause the underestimation of R/M.

3.1.2. Ionization Fraction

The analyses of PSR J0740+6620 presented in Miller et al. (2021), Riley et al. (2021), and Salmi et al. (2022) inferred that the emitting regions of the stellar surface had temperatures $k_b T_{\rm eff} \gtrsim 0.07$ keV. In spite of these high temperatures, atmospheric densities may be sufficient to create an appreciable neutral hydrogen fraction via recombination. We therefore performed two sets of analyses using tabulated atmospheric data generated by the NSX code, one assuming complete ionization (Ho & Lai 2001) and a second allowing for partial ionization (Ho & Heinke 2009).[16] We report results from both sets of analyses, although we consider the fully ionized models to be more reliable because of systematic uncertainties in the partially ionized hydrogen atmosphere models due to the incomplete coverage of the temperature, density, and energy ranges relevant to neutron star atmospheres in the opacity tables that are currently available (Bogdanov et al. 2021).

3.1.3. Surface Magnetic Fields

Sufficiently strong magnetic fields can significantly affect radiative transfer of X-rays through neutron star atmospheres (e.g., Ho & Lai 2003; Ho et al. 2003). Using the measured spin period ($P = 0.00289$ s) and period derivative ($\dot{P} = 1.219 \times 10^{-20}$) of PSR J0740+6620 (Cromartie et al. 2020) along with Equation (12) of Contopoulos & Spitkovsky (2006) assuming $\alpha = 0$ (i.e., that the closed field line region extends to the light cylinder) and a magnetic field inclination of $\pi/2$, we estimate a surface magnetic field strength of $B \approx 3 \times 10^8$ G if the field configuration is a centered dipole. Miller et al. (2021) inferred that the centers of emitting regions were separated on the surface by $\approx$2 radians in the best-fit model and were thus not antipodal. The chord length between the two spots was therefore $\approx \sin(1) \approx 0.84$ times the diameter, suggesting a surface magnetic field strength $\approx 0.84^{-3} \approx 1.7$ times larger than that of a centered dipole, i.e., a surface magnetic field strength $B \approx 5 \times 10^8$ G. This field strength would have only a small effect on atomic structure (Lai 2001; Potekhin 2014) and the corresponding electron cyclotron energy is only $\approx$6 eV, much smaller than the typical thermal energies we infer for particles in the atmosphere of PSR J0740+6620. Therefore, we use nonmagnetic atmosphere models throughout the present work. However, we caution that we have not rigorously tested this assumption, which would require the construction of grids of model atmospheres with magnetic fields covering the range $B \sim 10^9 - 10^{10}$ G, an especially challenging task due to the comparable strengths of Coulomb and magnetic effects.

3.1.4. X-Ray Propagation from Surface to Detector

We model the propagation of light in the vicinity of the pulsar using the oblate Schwarzschild approximation (e.g., Miller & Lamb 1998; AlGendy & Morsink 2014; Bogdanov et al. 2019; Silva et al. 2021), which takes into account the oblate shape and Doppler boosts resulting from the rapidity of the spins of millisecond pulsars, but treats the exterior spacetime as Schwarzschild; the oblate Schwarzschild approximation typically results in fractional systematic errors $\lesssim$0.1% for pulsars rotating at frequencies of a few hundred hertz (Bogdanov et al. 2019; Silva et al. 2021). We account for the absorption of X-rays in the interstellar medium using the

[16] See Badnell et al. (2005) for the relevant opacity tables.

`TBabs` model (Wilms et al. 2000). We convert our model photon spectra reaching the telescope to model count spectra, as would be registered by the NICER detectors, using a version of the NICER response matrix constructed to match that used over the course of a set of GTIs comprising each data set (see Section 2). The XMM-Newton data are treated similarly, using response matrices generated by the XMM-Newton Scientific Analysis System tools "arfgen" and "rmfgen" relevant to the individual CCDs where the pulsar source image fell during the observations for the EPIC-pn and EPIC-MOS instruments (Gabriel et al. 2004; SAS Development Team 2014).

3.2. Pulse Profile Modeling

Our approach to modeling the NICER pulse profile of PSR J0740+6620 is the same as that described in Miller et al. (2021), which built upon the approach discussed in Miller et al. (2019). Detailed descriptions of our pulse profile generation procedure and tests of its accuracy are given in Bogdanov et al. (2019) and Bogdanov et al. (2021). The X-ray pulse profile of PSR J0740+6620 has two clear peaks separated by ∼0.4 in phase (Wolff et al. 2021), and is therefore incompatible with emission from a single circular emitting region of uniform temperature (hereafter we use the term "spot" to refer to X-ray-emitting regions of uniform temperature). While modeling the pulse profile of PSR J0030+0451 necessitated oval (Miller et al. 2019) or crescent (Riley et al. 2019) spots, Miller et al. (2021) and Riley et al. (2021) found that emission from two circular spots, although not antipodal ones, was sufficient to describe the X-ray pulse profile of PSR J0740+6620, with no evidence for more complicated spot geometries; however, we have not rigorously explored this possibility with the present data set.

3.2.1. Model Parameters

Having specialized our models to a pair of circular spots, we construct them as follows. Each spot ($i = 1, 2$) is characterized by an effective temperature ($kT_{\mathrm{eff},i}$), where k is Boltzmann's constant, an angular radius ($\Delta\theta_i$), and a colatitude ($\theta_{\mathrm{c},i}$). We allow the two spots to have an arbitrary phase offset, measured in rotational cycles from one spot center to the other ($\Delta\phi$). Furthermore, we characterize the star using its gravitational mass (M) and inverse stellar compactness ($c^2R_e/(GM)$), where R_e is its equatorial circumferential radius. We also model the observer inclination to the pulsar spin axis (θ_{obs}), the neutral hydrogen column density between NICER and PSR J0740+6620 (N_{H}), and the distance from NICER to PSR J0740+6620 (D). We allow arbitrary overlaps, or lack thereof, between spots. This is accomplished by labeling the spots "1" and "2," and assigning any overlapping regions the effective temperature of the lower-numbered spot. This allows, for example, the creation of a single crescent-shaped spot by covering a hotter spot with another so cool that the latter emits virtually no radiation.

The full set of parameters used in our analyses is listed in Table 1, along with the priors we assume for each parameter. For most parameters we use a flat prior, defined as having a uniform nonzero probability density between an upper and lower bound (inclusive) and zero probability density outside of those bounds. Because PSR J0740+6620 is in a binary system, we are able to incorporate additional informative priors. Specifically, Fonseca et al. (2021) reported based on Shapiro delay measurements that the mass of PSR J0740+6620 was $2.08^{+0.072}_{-0.069}\,M_\odot$, that the distance to the pulsar was $1.136^{+0.174}_{-0.152}$ kpc, and that the angle between our line of sight and the orbital axis of the system was $87.5° \pm 0.17°$, all at 68% credibility.

We use these radio-timing-derived measurements to place priors on the mass, distance, and observer inclination in our analysis. We implement a Gaussian prior on the gravitational mass of the pulsar, with a median of $2.08\,M_\odot$ and standard deviation of $0.09\,M_\odot$, where we have linearly added an estimate of the systematic error in the Shapiro delay measurement (E. Fonseca, personal communication). We implement an asymmetric quasi-Gaussian distance prior, which has a probability distribution that falls off at different rates above and below the mode, according to the functional form listed in Table 1. This distribution is based on the results presented in Fonseca et al. (2021) and includes an additional, linearly added estimate of the systematic error of 0.03 kpc (E. Fonseca, personal communication).

Radio observations are able to constrain the angle between the observer's line of sight and the orbital axis of the binary system, but our analysis depends on the angle between the observer's line of sight and the rotational axis of PSR J0740+6620. Accretion from their companion stars is thought to be the primary mechanism for the spin-up of millisecond pulsars such as PSR J0740+6620 (e.g., Bhattacharya & van den Heuvel 1991). Accordingly, the spin axis of the pulsar should gradually align with the orbital axis of the system. However, it is unlikely that the alignment is perfect, and thus the pulsar spin axis may be tilted a few degrees with respect to the orbital axis of the binary system. Thus, we have adopted a flat prior on the angle between the observer's line of sight and pulsar spin axis centered at 87.5°, which is the best estimate of the orbital inclination of the binary, with a width of 5°.[17]

3.2.2. Pulse Profile Models

Given values for the set of model parameters described in Section 3.2.1, a stellar rotation period (which is known to high precision from radio observations; e.g., Cromartie et al. 2020; Fonseca et al. 2021), a neutron star atmosphere model, and a specified observation time, we can generate a spots-only pulse profile. However, to compare these model pulse profiles with data, it is necessary to account for nonspot (or "background") contributions to the observed X-ray counts, which are not modulated on the spin period of the pulsar. To compare with NICER data it is also necessary to select a starting rotational phase for the pulse profile. We are then able to calculate the log likelihood of the available data sets given a particular model. When we incorporate information from various XMM-Newton instruments, the overall log likelihood is simply the sum of the log likelihoods for the data given the model for each data set, i.e.,

$$\log \mathcal{L}_{\mathrm{tot}} = \log \mathcal{L}_{\mathrm{NICER}} + \log \mathcal{L}_{\mathrm{XMM-pn}} + \log \mathcal{L}_{\mathrm{XMM-MOS1}} + \log \mathcal{L}_{\mathrm{XMM-MOS2}} \quad (1)$$

for analyses of NICER data along with XMM-Newton imaging data from the pn, MOS1, and MOS2 instruments, or

[17] Miller et al. (2021) found that the inferred radius of PSR J0740+6620 was insensitive to the observer inclination within this range, and in an exploratory analysis we found that broadening the inclination prior further also did not affect our radius measurement.

Table 1
The Primary Model Parameters, and Their Corresponding Priors, for the Pulse Profile Models Considered in This Work

Parameter	Definition	Assumed Prior
$c^2R_e/(GM)$	Inverse stellar compactness at equator	3.2 to 8.0
M	Gravitational mass	$\exp[-(M - 2.08\,M_\odot)^2(0.09\,M_\odot)^{-2}/2]$
$\theta_{c,1}$	Colatitude of spot 1 center	0 to π radians
$\Delta\theta_1$	Angular radius of spot 1	0 to 3 radians
$kT_{\rm eff,1}$	Effective temperature of spot 1	0.011 to 0.5 keV
$\theta_{c,2}$	Colatitude of spot 2 center	0 to π radians
$\Delta\theta_2$	Angular radius of spot 2	0 to 3 radians
$kT_{\rm eff,2}$	Effective temperature of spot 2	0.011 to 0.5 keV
$\Delta\phi$	Longitudinal offset between spots 1 and 2	0 to 1 cycles
$\theta_{\rm obs}$	Observer inclination to stellar rotation axis	1.44 to 1.62 radians
$N_{\rm H}$	Neutral H column density	0 to 2×10^{21} cm^{-2}
D	Distance	$\exp[-(D - 1.136\ {\rm kpc})^2(0.20\ {\rm kpc})^{-2}/2]$, $D \geqslant 1.136$ kpc
		$\exp[-(D - 1.136\ {\rm kpc})^2(0.18\ {\rm kpc})^{-2}/2]$, $D \leqslant 1.136$ kpc

Note. Except where noted, the prior is uniform across the given range and zero elsewhere. We place no additional restrictions on the potential values for each parameter.

$\log \mathcal{L}_{\rm tot} = \log \mathcal{L}_{\rm NICER}$ for analyses of NICER data alone. The straightforward summation of the terms in Equation (1) assumes that the different terms are uncorrelated, which is valid for data from NICER and the different instruments mounted on XMM-Newton (Strüder et al. 2001; Turner et al. 2001).

We compute the log likelihood corresponding to each data set by summing the Poisson log likelihoods of the data given the model for each energy channel (E_j) and phase (ϕ_k). Given an observed number of counts d_{jk}, which is a nonnegative integer, and a predicted number of counts m_{jk}, which is a positive real number, the Poisson likelihood of the data given the model is $m_{jk}^{d_{jk}} e^{-m_{jk}} \big/ d_{jk}!$. However, the factor $1/d_{jk}!$ is shared by all models, and can thus be neglected. The log likelihood we use is therefore $\log \mathcal{L} = \sum_{\phi_k}\sum_{E_j}(d_{jk} \log m_{jk} - m_{jk})$, where NICER data are analyzed over 32 phases and the XMM-Newton data that we use are resolved only in energy, with a single time-averaged phase.

As previously mentioned, observed pulsar X-ray pulse profiles may include contributions not modulated on the spin period of the pulsar, from sources such as particle background, optical loading, and both resolved and unresolved sources in the telescope field of view, among others. We analytically marginalize over a phase-independent background parameter for each NICER energy channel, as described in Section 3.4 of Miller et al. (2019). Concerning the XMM-Newton background, we take previously measured XMM-Newton blank-sky background spectra to be a Poisson realization of the actual XMM-Newton background, and calculate the probability of the data given the spot counts and the distribution of possible background counts, as described in Section 3.4.2 of Miller et al. (2021).

3.3. Bayesian Parameter Estimation

We adopt a hybrid sampling approach that utilizes an initial suite of nested sampling (Skilling 2004) analyses followed by a suite of Markov Chain Monte Carlo (MCMC) analyses for the purpose of refining our posterior inferences. To wit, each of the initial nested sampling analyses, which we carry out using the MultiNest package and its Python bindings (Feroz et al. 2009; Buchner 2016a), is able to sample the parameter space globally, identify multiple modes if they exist, and approximate the Bayesian evidence for each mode.[18,19] The evidence ($\mathcal{Z}$), which is the average of the likelihood $\mathcal{L}$ over the normalized prior π, is given by the following integral over the model parameters θ:

$$\mathcal{Z} = \int \mathcal{L}(\boldsymbol{\theta})\pi(\boldsymbol{\theta})d\boldsymbol{\theta}, \tag{2}$$

and can be used to compare models, where the model with the highest evidence is preferred.

Basic nested sampling algorithms such as MultiNest, while often relatively fast, produce a very limited number of posterior samples during each analysis and provide neither theoretical nor practical convergence guarantees.[20] Therefore, following each nested sampling analysis we used the posterior probability distribution inferred from that analysis to initialize an MCMC analysis, which we continued until the posterior distribution appeared to be stationary, and we were able to obtain approximately 10^6 independent posterior samples from the stationary distribution.

3.3.1. Nested Sampling Analyses

We began our analysis using the publicly available MultiNest algorithm (Feroz et al. 2009; Buchner 2016a), which begins by randomly sampling a number of points (a user-specified number of "live points," $N_{\rm live}$) from the prior. Subsequently, MultiNest sequentially replaces the lowest-likelihood point with a higher-likelihood point. Proposals for these higher-likelihood points are drawn from within the region bounded by an approximation of the isolikelihood surface corresponding to the likelihood of the point to be replaced. A larger number of live points will lead to more thorough sampling of the parameter space, all other parameters being equal. MultiNest constructs approximate isolikelihood surfaces using multiple hyperellipsoids constructed to envelop the set of live points. If these minimal bounding hyperellipsoids contain a

[18] https://github.com/farhanferoz/MultiNest
[19] http://github.com/JohannesBuchner/PyMultiNest
[20] Other nested sampling packages do allow users to target posterior rather than evidence accuracy, and allow for further sampling after the convergence of an initial nested sampling of the parameter space (e.g., Speagle 2020; Buchner 2021).

volume smaller than the expectation value of the remaining prior volume, the bounding ellipsoids are expanded until the overlap-corrected enclosed volume matches the expected remaining prior volume (Feroz et al. 2009, Section 5.2). However, if the true isolikelihood surface is not described accurately by the (possibly expanded) hyperellipsoids encompassing a given set of live points, MultiNest can draw samples from a biased region of parameter space, resulting in biased estimates of the posterior and Bayesian evidence (e.g., Buchner 2016b; Nelson et al. 2020; Buchner 2023; Lemos et al. 2023; Dittmann 2024). The MultiNest algorithm attempts to ameliorate this shortcoming through an "efficiency" parameter, which is the inverse of a factor used to further increase the hypervolume of the MultiNest bounding ellipsoids (e.g., an efficiency value of $\epsilon = 0.1$ multiplies by 10 the target volume for the expanded hyperellipsoids). However, this procedure is still not guaranteed to encompass the intended isolikelihood surface.[21]

Previous analyses of NICER data have found that MultiNest rarely produces converged posterior estimates. For example, Miller et al. (2021) reported that a MultiNest analysis of an earlier PSR J0740+6620 data set using $N_{\rm live} = 1000$ and $\epsilon = 0.01$ systematically underestimated the stellar radius and its uncertainty. Analyzing the same data set, Riley et al. (2021) found that the settings $\epsilon = 0.1$ and $N_{\rm live} = 4 \times 10^4$ underestimated the width of the inferred radius posterior compared to a run with the same efficiency and twice as many live points. Moreover, Miller et al. (2021) showed, by performing MultiNest inferences and comparing the number of parameters inferred to fall within the $\pm(1, 2, 3)\sigma$ credible intervals with statistical expectations, that MultiNest systematically underestimated the width of credible intervals, although less significantly when more live points and lower sampling efficiencies were used. Analyzing NICER data for PSR J0030+0451, Vinciguerra et al. (2024) found that analyses using $\epsilon = 0.3$ and $N_{\rm live} = 10^3$ often overestimated the median stellar radius and underestimated the width of the posterior distribution compared to higher-resolution analyses using $\epsilon = 0.1$, $N_{\rm live} = 10^3$ and $\epsilon = 0.3$, $N_{\rm live} = 10^4$; in some cases, the posteriors estimated by lower-resolution analyses strongly excluded the median from higher-resolution analyses (Vinciguerra et al. 2024). Despite these shortcomings, MultiNest is in our experience able to provide a suitable starting point for subsequent MCMC analyses using orders of magnitude fewer computational resources than would initializing an MCMC analysis using uniform samples drawn from the prior.

Based on these considerations and a series of convergence tests, our adopted MultiNest settings were $\epsilon = 0.01$ and $N_{\rm live} = 4096$. In each analysis we enabled MultiNest to evaluate multiple modes. Because our parameter inferences do not rely on the capacity of MultiNest to estimate posteriors with high accuracy, these settings were sufficient for our preliminary nested sampling analysis.

3.3.2. Markov Chain Monte Carlo Analyses

Following the completion of each nested sampling analysis, we used the posterior probability distribution estimates it produced to draw initial walker positions for an MCMC analysis using the `emcee` package (Foreman-Mackey et al. 2013) and the affine-invariant "stretch" proposal of Goodman & Weare (2010).[22] Because the proposal distribution utilized used in this analysis satisfies detailed balance, the distribution of walker positions will converge to and provide samples from the stationary posterior distribution. In principle, the convergence of each chain of walkers to the stationary distribution may take an arbitrarily long time if the walkers are initialized very far from equilibrium, which is why we use a preliminary nested sampling analysis to generate initial walker positions that more accurately approximate the posterior distribution.

Each analysis used 4096 walkers, for which we drew initial positions by resampling a Gaussian kernel density estimate of the corresponding MultiNest-derived posterior distributions. We performed MCMC sampling until we had collected $\sim 10^6$ effective samples (in practice $\sim 10^7$ samples, because our analyses had proposal acceptance fractions of ~ 0.1 and autocorrelation times of ~ 10 iterations). We judged the sampling to be converged when over the aforementioned $\sim 10^7$ MCMC iterations we observed no secular variation in the 1st, 16th, 50th, 84th, or 99th percentiles.

4. Pulse Profile Modeling Results

We first present in Section 4.1 the different modes identified during the initial stage of our analysis, assess the thoroughness of that preliminary nested sampling stage, and report approximate evidences for each atmosphere model and data set analyzed. Subsequently, we report in Section 4.2 the mass and radius inferences from each data set and atmosphere model combination. We assess the goodness-of-fit of our models in Section 4.3, and compare our results with those of Salmi et al. (2024) in Section 4.4.

4.1. Inferred Emitting Region Geometries

Miller et al. (2021) identified two emitting region geometries that were capable of reproducing the observed pulse profile and spectrum of PSR J0740+6620: One was a crescent (or lunate) configuration formed by an extremely cool circular spot eclipsing a hotter spot; the other consisted of two fairly small spots with similar temperatures, well separated in azimuth. Both spot configurations are also allowed by the priors used in this work (Table 1).

Figure 1 shows illustrative schematic examples of both configurations. Miller et al. (2021) found that the configuration with two fairly small spots was favored by a Bayes factor of ~ 3000 over the lunate configuration. When only the updated NICER data are considered, we find that either spot configuration can provide good fits, depending on the assumed atmospheric composition and whether or not we also consider the XMM-Newton data.

Table 2 shows the spot configurations that provided good fits to each data set under each assumed atmosphere model. We also include in Table 2, for each data set, the log evidence for each model relative to the fit assuming a fully ionized hydrogen atmosphere to the same data set.[23] For example, the logarithm of the Bayesian evidence for our fully ionized helium fit to only the NICER data was ≈ 1.33 larger than the logarithm of the Bayesian evidence for the fully ionized hydrogen fit to the

[21] For example, Lemos et al. (2023) found that a value $\epsilon \leqslant 10^{-3}$ was necessary for MultiNest to produce unbiased Bayesian evidence estimates when performing cosmological inferences, and that $\epsilon \leqslant 10^{-2}$ was necessary to recover the true value (within MultiNest's error estimates) of a simple high-dimensional Gaussian likelihood. See Dittmann (2024) for a thorough investigation into the accuracy of MultiNest's posterior and evidence estimates.

[22] https://github.com/dfm/emcee

[23] Throughout this work we use the natural logarithm unless otherwise denoted by a subscript.

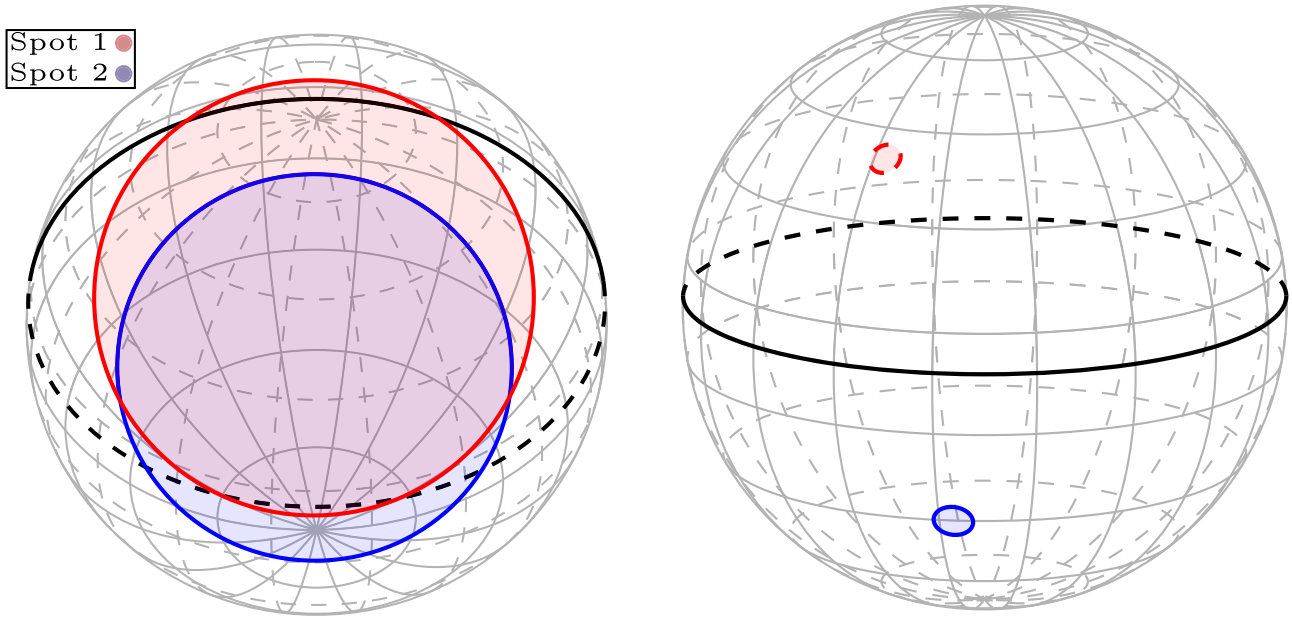

(a) Lunate spot configuration (b) Dual-spot configuration

Figure 1. Examples of the two spot configurations identified during our analysis of the updated data set for PSR J0740+6620 able to produce good fits to the NICER data. The black circle denotes the colatitude of the observer line of sight. Dashed lines indicate features on the side of each sphere opposite the observer. To reiterate, in our models regions that overlap emit with the temperature of the "lowest-number" spot; accordingly, emission from the configuration shown in panel (a), for which the temperature of "spot 1" tends toward the lower end of our prior, effectively comes from the protruding crescent of "spot 2."

Table 2
The Inferred Spot Configuration(s) and Log Bayes Factors for Each Data Set and Each Atmosphere Model Considered in This Work

Data Set	Atmosphere	Lunate Spot	Dual Spot	$\Delta \log Z$
NICER	H_{full}	✓	⋯	⋯
NICER	$H_{partial}$	✓	✓	−0.11
NICER	He_{full}	✓	⋯	1.33
NICER+XMM	H_{full}	⋯	✓	⋯
NICER+XMM	$H_{partial}$	⋯	✓	1.0
NICER+XMM	He_{full}	⋯	✓	2.08

Notes. In the second column, subscripts indicate whether each atmosphere model assumed full ionization or allowed for partial ionization. Check marks (✓) indicate which spot configurations provided good fits to each data set under the assumptions of a particular atmosphere model. For each data set (NICER and NICER+XMM), we report the evidence for each model (including all identified modes) relative to the evidence obtained using that data set assuming the fully ionized hydrogen atmosphere, which we consider to be the most astrophysically relevant atmosphere (see Section 3).

same data set. Given the sensitivity of the evidence to priors, and the potential for appreciable systematic errors in evidences estimated by MultiNest, no atmosphere model is significantly favored over another.

When only the available NICER data are considered, the preferred mode depends on the assumed atmospheric composition and conditions: While the fully ionized hydrogen and helium atmosphere models overwhelmingly favor the lunate configuration, the partially ionized hydrogen atmosphere models favor both configurations. However, when the XMM data—which constrain the stellar count rate and nonstellar background—are included, the data prefer models with two smaller, near-antipodal spots.

Before attempting to sample any of the posteriors more thoroughly, we first verified that our initial nested sampling analyses were thorough enough to identify the most significant mode, and that each did not find one mode or the other only by chance. The first test to which we subjected our nested sampling results was to evaluate the best fit from an analysis that identified only one mode using the data and atmospheric model of analyses which found other modes. Taking the best fits from our fully ionized hydrogen atmosphere analyses as an example, when we apply the (lunate) best-fit parameters from our analysis of the NICER data alone to the joint NICER and XMM-Newton data set, we find a log likelihood ∼400 lower than for the (dual-spot) best joint fit to the NICER and XMM-Newton data. Similarly, the log likelihood of the best fit found analyzing the NICER data alone assuming a helium atmosphere was ∼600 lower than the log likelihood of the best fit found in the joint analysis of NICER and XMM-Newton data. This analysis thus suggests that the XMM-Newton data strongly disfavor the lunate spot configuration. For comparison, the model that best fits the NICER data only, using the partially ionized hydrogen atmosphere tables, which is the smaller, near-antipodal spot configuration, gives a NICER+XMM log likelihood only ∼35 lower than the best fit for this model found in the joint NICER and XMM-Newton analysis.

Based on the comparisons above, and additional tests discussed in Appendix A, we believe that our MultiNest analyses have sampled parameter space thoroughly enough to identify the relevant modes in each analysis. Because we are able to sample each posterior further using MCMC techniques, we do not need to rely on the often-questionable convergence of the posterior estimates reported by MultiNest. Instead, we require only that the different modes identified by MultiNest be assigned roughly the correct weights.[24] In practice, the two modes present in $\Delta\phi$

[24] In principle, various MCMC implementations are able to properly sample multimodal posteriors, including by allowing walkers to move from one mode to another. Although our requirement that MultiNest be able to adequately identify each mode certainly accelerated our subsequent MCMC analysis, that requirement was not strictly necessary.

Table 3
Summary of Inferred Equatorial Radii

Data Set	Atmosphere Model	-2σ	-1σ	Median	$+1\sigma$	$+2\sigma$
NICER	H_{full}	9.60	10.54	12.48	16.54	21.84
NICER	$H_{partial}$	9.72	10.59	11.95	14.46	18.32
NICER	He_{full}	9.62	10.56	12.72	17.39	22.55
NICER +XMM	H_{full}	10.99	11.79	12.92	15.01	18.57
NICER +XMM	$H_{partial}$	10.94	11.76	12.99	15.36	19.75
NICER +XMM	He_{full}	10.98	11.82	13.07	15.52	20.50

Notes. A comparison of the -2σ, -1σ, median, $+1\sigma$, and $+2\sigma$ constraints on the equatorial radius of PSR J0740+6620 (measured in kilometers), using different data sets and atmospheric models. When we include only the NICER data, the inferred stellar radius and especially its upper limit depend on the model atmosphere assumed. However, when we also include the XMM-Newton data, which constrain the spectra of the stellar flux and the nonstellar background, we find more consistent results across different assumed model atmospheres.

for the smaller-spot configurations (see Appendix C), which are a result of the near-reflection symmetry due to the observer's inclination being so close to the rotational equator of the star, have very little effect on the radius or mass posteriors. Thus, the only capability of MultiNest on which we rely is its ability to differentiate between the lunate and near-antipodal configuration for each data set and atmosphere model, a capability our analyses have demonstrated.

4.2. Mass and Radius Constraints

After we completed our preliminary nested sampling analyses, we initialized a series of MCMC analyses to thoroughly sample each posterior. We discuss the results in this section.

Unsurprisingly, given the faintness of PSR J0740+6620, we are able to infer little about the stellar mass, although we systematically infer masses very slightly lower than the median value of our prior (e.g., $2.06\,M_\odot$ rather than $2.08\,M_\odot$). We present the credible regions for the equatorial radius of PSR J0740+6620 derived from each of our analyses in Table 3, the posterior probability distributions of the mass and equatorial radius derived from our analyses assuming a fully ionized hydrogen atmosphere in Figure 2, and a comparison of the present constraints on the equatorial radius to those derived in Miller et al. (2021) in Figure 3.

We find that, when the constraints provided by XMM-Newton data are included, the radii we infer from analyses utilizing differing neutron star atmosphere models are consistent with one another: The -1σ values range only from 11.76 to 11.82 km and the $+1\sigma$ values range from 15.01 to 15.52 km. In contrast, when we analyze the NICER data alone, we find that the constraints on the stellar radius vary much more between our analyses. This is largely due to the faintness of PSR J0740+6620 and the presence of other sources within the field of view of NICER when it is observing PSR J0740+6620, as shown in Wolff et al. (2021). Because the number of phase-dependent counts in the pulse profile of PSR J0740+6620 is much smaller than the number of phase-independent counts, the NICER data alone allow a wide range of emitting region geometries and values of the stellar compactness, which limits the precision of the resulting constraints on the radius of the pulsar. When the XMM-Newton imaging data are included, the stellar and background fluxes are better constrained.

A general trend illustrated in Table 3 and Figure 3 is that in each analysis, when the XMM-Newton data are included, the lower limits on the stellar radius increase. Because the XMM-Newton observations constrain the number of nonstellar counts in the star's pulse profile, the inferred fractional modulation in the profile increases when the XMM-Newton data are included, placing a strong upper bound on the stellar compactness. The XMM-Newton data also constrain the total flux from the stellar surface and its spectrum, and when we assume the atmosphere is fully ionized hydrogen or helium we find that, compared to fitting the NICER data alone, including the XMM-Newton data places more stringent upper limits on the stellar radius. As shown in Appendices B and C, the maximum-likelihood radius is also slightly reduced. When we instead assume the atmosphere is partially ionized hydrogen, we find that the upper limits on the radius are more lenient when the XMM-Newton data are included, as previously found in Miller et al. (2021), which used these same model atmospheres.

If we compare our results to those presented in Miller et al. (2021), temporarily restricting ourselves to the model atmospheres used in that work, we find a 68% credible interval for the equatorial radius that is narrower (only 83% as wide) when the NICER and XMM-Newton data are jointly fit. On the other hand, when we fit the NICER data alone we find no improvement over Miller et al. (2021). We have not rigorously determined why this is the case. One clear difference is that our current analyses have identified support for lunate modes in our NICER-only analyses, which tend to support larger-radius configurations (see Tables 2 and 3, and Appendices B and C). Miller et al. (2021) did not find evidence for these modes. We find that including the XMM-Newton data excludes models with those modes, possibly due to the information about the total stellar X-ray flux provided by these data. This may explain why the analyses that include the XMM-Newton data find lower upper limits on the equatorial radius. A possible but less likely explanation is the different data-selection choices made in this work.

We find that fits which assume a fully ionized helium atmosphere infer slightly larger values of the stellar radius than the corresponding fits which assume either a partial or fully ionized hydrogen atmosphere. Similar though much stronger trends have been noted in analyses of the PSR J0030+0451 NICER data (Miller et al. 2019; Salmi et al. 2023). These trends are likely due to differences between the emergent spectra and the beaming patterns produced by the two model atmospheres, which are larger for neutron stars that emit X-rays from larger fractions of their surfaces. Previous analyses of the NICER data on PSR J0740+6620 assuming an ionized helium atmosphere that were reported in Riley et al. (2021) and Salmi et al. (2023) did not show any appreciable differences between the results for the helium and hydrogen atmospheres used in these works. However, both works assumed an a priori upper limit on the stellar radius of 16 km, which reduced the variation of the upper limits they derived from their posteriors.

4.3. Adequacy of the Fits

As in Miller et al. (2019) and Miller et al. (2021), we performed several tests to assess the adequacy of the fits we obtained. Here we consider only the maximum-likelihood

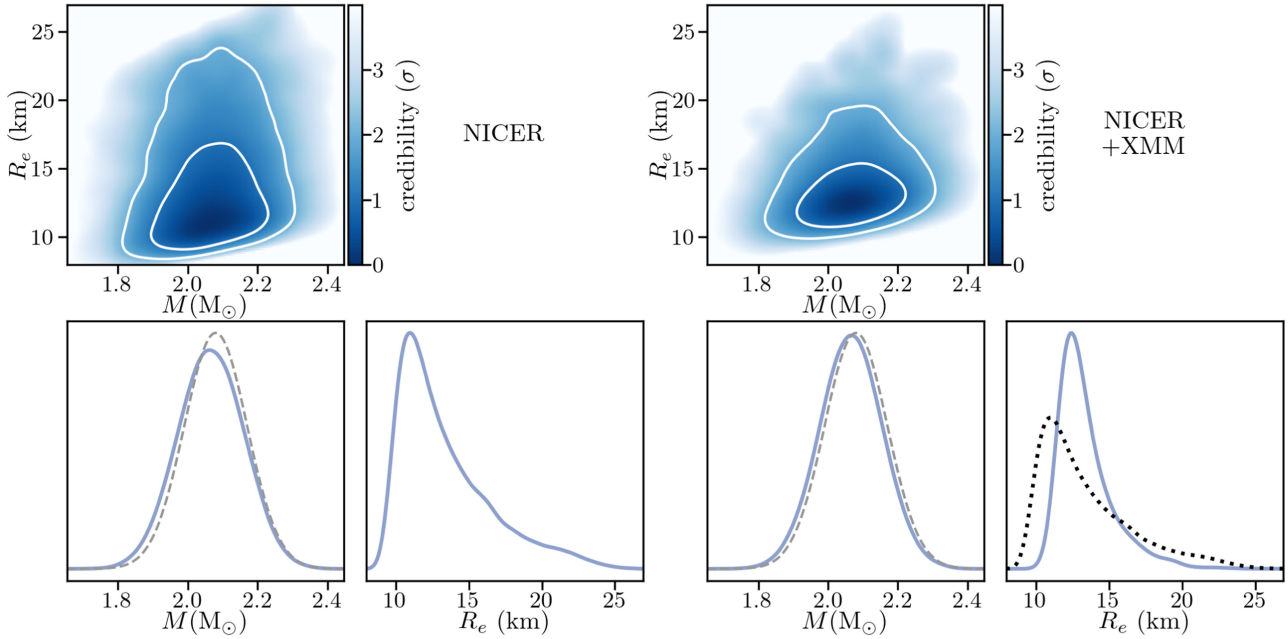

Figure 2. A comparison of the M, R_e, and joint M–R_e posterior probability distributions for PSR J0740+6620 inferred by analyzing the NICER data only (left panels) and the NICER and XMM-Newton data analyzed jointly (right panels). The results shown here assume a fully ionized, purely hydrogen atmosphere, which we consider the most likely atmosphere for the reasons explained in Section 3.1. The solid curve in each bottom-left panel shows the one-dimensional probability distribution for the stellar mass inferred from these data sets; the mass prior derived from Fonseca et al. (2021) is shown by the dashed gray line. The color shading in the two-dimensional M–R_e plots illustrates the shapes of the minimum-area credible regions; the overplotted white lines show the 1σ and 2σ contours outside which $\sim$31.7% and $\sim$4.6% of the posterior mass of each distribution lies. The solid curve in the bottom-right panel on the left shows the probability density of the equatorial radius inferred by analyzing only the NICER data. The solid curve in the bottom-right panel on the right shows the probability density inferred by jointly analyzing the NICER and XMM-Newton data; the black dotted curve in this panel shows the probability density inferred by analyzing the NICER data alone.

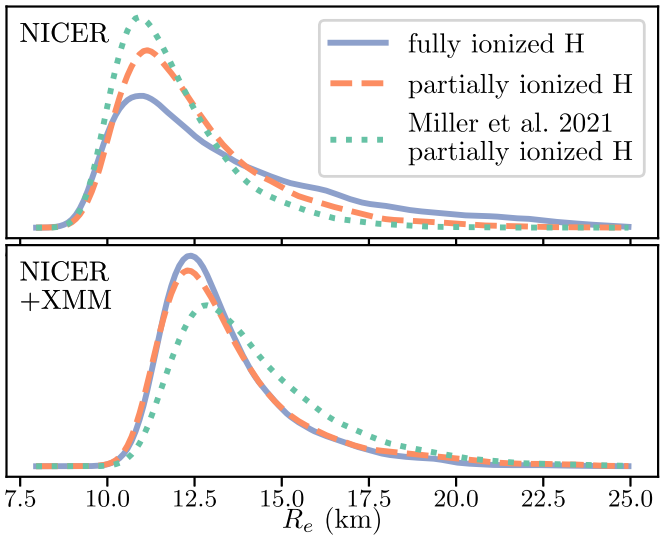

Figure 3. Radius posteriors obtained when only the NICER data are used (top panel) and when the NICER and XMM-Newton data are both used (bottom panel). The solid blue lines show the posterior for a fully ionized hydrogen atmosphere, whereas the dashed orange lines are for a partially ionized hydrogen atmosphere. The dotted green lines show the posterior reported by Miller et al. (2021), who assumed a partially ionized hydrogen atmosphere. The results obtained here using only the NICER data depend on the atmospheric model, because different spot patterns are favored by the different models (see Figure 1). However, when both the NICER and XMM-Newton data are used, the posterior is almost independent of the atmospheric model assumed.

parameters from our joint analysis of the NICER and XMM-Newton data, assuming a fully ionized hydrogen atmosphere.

We first performed a standard χ^2 test comparing our best-fit phase- and energy-resolved pulse profile model to the NICER data and found the ratio of the resulting χ^2 to the number of degrees of freedom (dof) of 2818.8/2901. The probability of finding a value of χ^2 this high or higher for this many degrees of freedom using the correct model is 86%. Figure 4 shows the resulting signed residuals in each phase and energy bin. There is no evidence for clustering or systematic trends. Although this test cannot show that the model being used is correct, this value of χ^2 shows that this model is not obviously deficient.

We have also checked the ability of our analysis to reproduce the bolometric pulse profile. This is a nontrivial test, because our Bayesian analysis fits an energy-resolved pulse profile model to the energy- and phase-resolved NICER data. Because the χ^2 statistic is nonlinear, it is possible to significantly over- or underestimate the total flux at a particular phase, even though the pulse phase–energy channel residuals are negligible, causing the residuals obtained by comparing the model bolometric pulse profile to the observed bolometric profile to be significant. We find that the χ^2/dof obtained by comparing this bolometric pulse profile model to the observed bolometric pulse profile is 28.8/27. The probability of finding a value of χ^2 this high or higher given the correct model is $\sim$37%.[25] We show the bolometric fit in Figure 5, which also shows the size of the background relative to the X-ray emission from the pulsar.

Figure 6 compares the observed energy spectra predicted by our model of a fully ionized hydrogen atmosphere that best fits the combined NICER and XMM-Newton data with the spectra observed by the MOS1, MOS2, and pn detectors on XMM-Newton in the energy channels used in our analysis. Because

[25] Because it is not clear a priori how many of our model parameters influence the bolometric pulse profile, we used synthetic data tests to determine that the effective number of parameters is $\approx$5. These tests were suggested by Serena Vinciguerra during discussions within the NICER Light Curves working group.

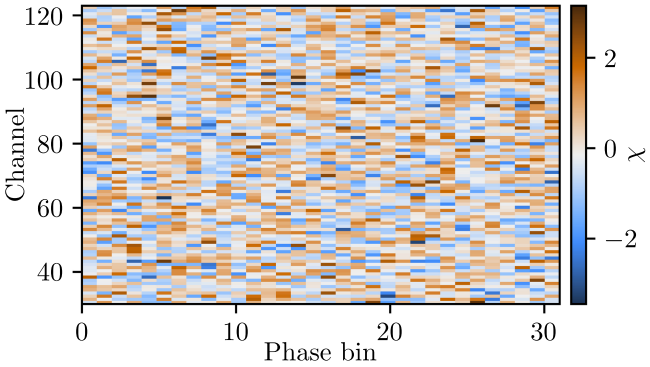

Figure 4. The value of $\chi_i = (m_i - d_i)/\sqrt{m_i}$, where m_i is the predicted number of model counts and d_i is the number of observed counts in phase-channel bin i, for each of the 3008 NICER phase–energy bins considered in this study (32 bins in rotational phase and 94 energy channels), for the energy-resolved pulse profile model that best fits the NICER and XMM-Newton data, assuming a fully ionized hydrogen atmosphere. No patterns in the values of χ are evident, as expected of a good fit. For this fit, $\chi^2/\mathrm{dof} = 2818.8/2901$, where $\chi^2 = \sum \chi_i^2$. The probability of finding $\chi^2 \geqslant 2818.8$ for 2901 degrees of freedom is ∼86% if the model is correct.

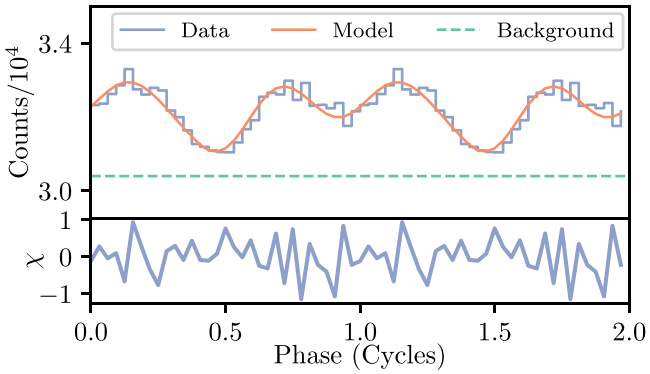

Figure 5. Top: a comparison of the bolometric NICER pulse profile (in 32 bins, plotted in blue) to the bolometric pulse profile from our best fit to the combined NICER and XMM-Newton data set, shown in orange. The dashed green line plots the unmodulated background in our best fit, which was added to the pulse profile generated by the two hot spots, as described in Section 3.2.2. Bottom: bolometric residuals, χ, as a function of phase. For our best fit, we find a bolometric χ^2/dof of 28.8/27, which has a probability of 37% if the model is correct.

very few counts were recorded in each energy channel, we evaluated the quality of the fit by generating a set of 10^5 synthetic data sets by Poisson sampling the spectrum predicted by our best-fit model in each channel of each instrument. We then computed the log likelihood for each synthetic data set and instrument, and compared it to the log likelihood of the actual data given our model. We found the total log likelihood of the real data was at the 78th percentile, that the log likelihood of the real pn data alone was at the 99th percentile, and that the log likelihoods of the real data for MOS1 and MOS2 were at the 15th and 4th percentiles, respectively. The overall fit to the XMM data is therefore good, the fit to the pn data is anomalously good, and the fits to the MOS1 and MOS2 data are relatively bad. Miller et al. (2021) observed the same trend, although to a lesser extent.

4.4. Differences between Our Results and Those of Salmi et al. (2024)

An independent analysis of the data analyzed in this paper is presented in Salmi et al. (2024), which reports a radius

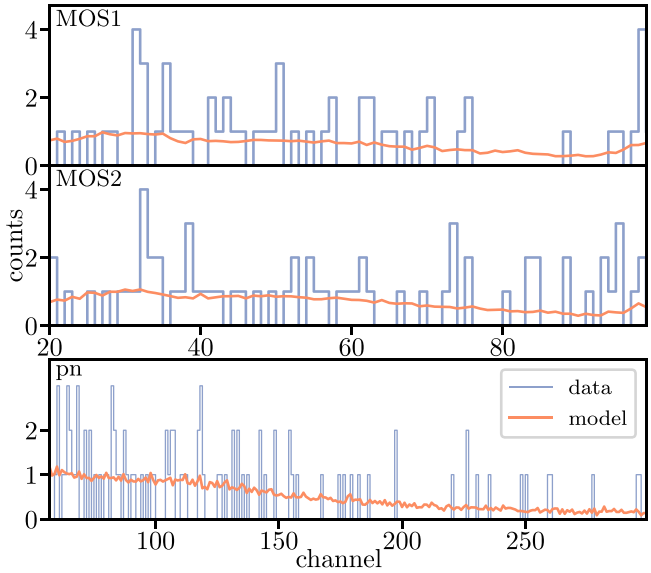

Figure 6. Comparison of the observed energy spectra predicted by our model of a fully ionized hydrogen atmosphere that best fits the combined NICER and XMM-Newton data with the spectra observed by the MOS1, MOS2, and pn detectors on XMM-Newton in the energy channels used in our analysis. Each panel shows the spectrum observed by the indicated XMM-Newton detector in blue as a histogram and the spectrum predicted by the best-fit model in orange. The model provides acceptable fits to all three observed spectra.

measurement of $12.49^{+1.28}_{-0.88}$ km (68% credibility). This radius measurement overlaps with our measurement of $12.92^{+2.09}_{-1.13}$ km, particularly at the -1σ point in the posterior distribution, which is especially important for constraining the dense-matter EOS, because larger radii are disfavored by the current gravitational-wave observations of binary neutron star mergers (e.g., Abbott et al. 2017; De et al. 2018). However, substantial discrepancies remain between the median values and uncertainties in these two measurements. As we demonstrate below, these discrepancies are due largely to the different methods used to sample the posterior, the different priors assumed for the equatorial radius (Salmi et al. 2024 imposed a hard upper limit of 16 km on the equatorial radius), and the different methods used to model the XMM-Newton data.[26] For reference, the results of both our preliminary nested sampling analyses and our converged MCMC analyses are provided in Appendix A.

4.4.1. Analyses of the NICER Data Alone

For our initial, preliminary analysis of the data we used MultiNest, which Salmi et al. (2024) use exclusively for their parameter estimation. We can therefore make a nearly apples-to-apples comparison of some of our preliminary results with their final results in some cases. As we now discuss, our results are consistent with those of Salmi et al. (2024) when we use the same sampling methodology, consider only the NICER data, and employ the same radius prior.

[26] Although we have imposed priors on the stellar mass and the inclination angle between the stellar rotation axis and observer line of sight that are broader than those imposed by Salmi et al. (2024) in order to account for systematic errors in the Shapiro delay mass measurement and the possibility of a slight spin–orbit misalignment, we have determined that these priors make negligible contributions to the differences between our results and those of Salmi et al. (2024). Given that we have found that the new data analyzed here place tighter upper limits on the stellar radius, the upper limit of 16 km placed on the radius by Salmi et al. (2024) should have a smaller effect than it had in previous analyses.

Consider first analyses that assume a fully ionized hydrogen atmosphere. Our preliminary, MultiNest analysis of only the NICER data gave an estimate for the equatorial radius of $12.15^{+2.3}_{-1.51}$ km; the corresponding absolute and fractional widths of the $\pm 1\sigma$ interval are 3.81 km and 31%. The final radius estimate quoted in Salmi et al. (2024) for this same case is slightly smaller, namely, $11.29^{+1.13}_{-0.81}$ km, while the absolute and fractional widths of the $\pm 1\sigma$ interval are almost a factor of 2 smaller, namely, 1.94 km and 17%. If we now discard all posterior samples with $R_e > 16$ km to mimic the radius prior assumed in Salmi et al. (2024), our radius estimate becomes $11.98^{+1.9}_{-1.4}$ km, and the absolute and fractional widths of the $\pm 1\sigma$ interval become 3.28 km and 27%. We note, however, that the lunate spot mode was enormously favored over the dual-spot configuration for this data set and atmosphere model in our analysis, and that the analysis of Salmi et al. (2024) was precluded from finding this mode by their constraint that each spot have an angular radius less than $\pi/2$ and that the spots were not allowed to overlap.

Consider now the preliminary, MultiNest results we obtained assuming a partially ionized hydrogen atmosphere and the final results Salmi et al. (2024) obtained assuming a fully ionized hydrogen atmosphere. If we again discard from our analysis all samples with $R_e > 16$ km, our radius estimate becomes $11.47^{+1.2}_{-0.91}$ km, and the absolute and fractional widths of the $\pm 1\sigma$ interval become 3.28 km and 27%. If we then also discard all samples with spot angular radii larger than 0.4 radians, which effectively eliminates the lunate spot mode, we obtain a radius estimate of $11.36^{+0.97}_{-0.81}$ km and the absolute and fractional widths of the $\pm 1\sigma$ interval become 1.78 km and 16%, in agreement with the result reported by Salmi et al. (2024).

4.4.2. Analyses of the NICER and XMM-Newton Data

Our preliminary joint analysis of the NICER and XMM-Newton data using MultiNest and assuming a fully ionized hydrogen atmosphere gave a radius estimate of $12.70^{+1.48}_{-0.97}$ km. Using a prior as above to exclude radii greater than 16 km reduced the estimated radius to $12.66^{+1.37}_{-0.94}$ km. Because the lower bounds on the radius provide the most information about the EOS, it is useful to compare the value of the radius at the -1σ point in the posterior distribution obtained by various analyses. In our preliminary analysis we obtained 11.72 km, whereas Salmi et al. (2024) found 11.61 km when analyzing the same data. Based on the above comparison of analyses that use only the NICER data, this difference, as well as some of the differences in the reported widths of the credible regions, appears to be due largely to differences in the treatment of the XMM-Newton data. As one example, we treated the distribution of blank-sky counts in each energy channel as a realization of a Poisson process, whereas Salmi et al. (2024) followed Riley et al. (2021) in assigning a flat prior for the distribution of blank-sky counts in each channel with bounds chosen to be a few times larger than the statistical uncertainty in the number of blank-sky counts, clipped to maintain positivity. Although notable, the differences in the assumed radius prior and in the treatments of the XMM-Newton data are insufficient to explain the difference between the width of our radius posteriors and those of Salmi et al. (2024).

Another significant difference between our analysis and that of Salmi et al. (2024) is the statistical sampling method employed. Although MultiNest is often suitable for exploring the parameter space, numerous studies have shown that it can be unreliable when used for parameter estimation, as discussed in Section 3.3.1. Appendix A shows that using MultiNest for parameter estimation tends to underestimate the widths of radius credible regions, and that these are typically biased toward low radii.

To derive converged results, we performed MCMC sampling, using our initial MultiNest results only to select the initial positions of the walkers. Over the course of the MCMC sampling, the radius credible interval expanded from the initial, MultiNest-derived interval of $12.70^{+1.48}_{-0.97}$ to $12.92^{+2.09}_{-1.13}$ km.[27] In Section 4.3 of Salmi et al. (2024), the authors report an additional MultiNest analysis that used a lower sampling efficiency ($\epsilon = 10^{-3}$) than the efficiency they used to obtain the headline result featured in the abstract of their paper. A lower efficiency allows MultiNest to better sample the parameter space. The additional analysis gave a radius of $12.55^{+1.37}_{-0.92}$, in better agreement with our result than the headline result of Salmi et al. (2024), despite the different treatments of the XMM data and radius prior in these two analyses.

The headline result of Salmi et al. (2024, $R_e \approx 12.49^{+1.28}_{-0.88}$ km) is only very slightly narrower than the value reported in Riley et al. (2021, $R_e \approx 12.39^{+1.30}_{-0.98}$ km), despite the inclusion of about 50% more data.[28] Adopting instead the results presented in Section 4.3 of Salmi et al. (2024), which used a MultiNest sampling efficiency that is expected to better sample the parameter space, their radius estimate using the present data is $12.55^{+1.37}_{-0.92}$ km, very slightly broader than the result reported in Riley et al. (2021). In contrast, our radius estimate improved from $13.71^{+2.61}_{-1.50}$ km in Miller et al. (2021) to $12.92^{+2.09}_{-1.13}$ km in the present work. Overall, the differences between the results obtained in different analyses have diminished as NICER has accumulated more data.

5. Discussion

As discussed in Section 2, we have analyzed an additional 1.1 Ms of NICER data on PSR J0740+6620, in addition to the NICER and XMM-Newton data analyzed in Miller et al. (2021). Analysis of these NICER and XMM-Newton data improves the precision of the constraint on the radius of this neutron star from $13.71^{+2.61}_{-1.50}$ to $12.92^{+2.09}_{-1.13}$ km, reducing the fractional uncertainty in the radius from ∼30% to ∼25%. This more precise measurement of the radius incrementally improves the constraints on the EOS of dense matter. We expect the EOS to be further constrained by analysis of the additional data on PSR J0740+6620 that is currently being collected. Although measurements of the radius of PSR J0740+6620 made using NICER still depend somewhat on the procedure used to analyze the data (see Section 4.4), the consequences of using different procedures have become less significant as the amount of NICER data has increased.

[27] Figure 3 of Miller et al. (2021) provides an illustrative example of the expansion of the initial, MultiNest-determined credible regions over the course of more thorough MCMC sampling.

[28] This is not quite a fair comparison because the headline results of Riley et al. (2021) used an unrealistically broad prior on the relative calibration between NICER and XMM-Newton, which strongly affected the inferred radius. Section 4.1 of Salmi et al. (2024) presents a more detailed comparison to Riley et al. (2021). It is also worth noting that the headline results of Salmi et al. (2024) used $\epsilon = 0.01$, whereas Riley et al. (2021) used $\epsilon = 0.1$.

5.1. Equation of State Constraints

Our current radius measurement is more precise than that of Miller et al. (2021), which was based on the data collected through 2020 (see Miller et al. 2021). For example, the value of the equatorial radius at the $+1\sigma$ point in the posterior distribution has decreased from 16.32 to 14.34 km, and the radius width at $\pm 1\sigma$ is now 3.22 km, which is 78% of the 4.12 km width reported in Miller et al. (2021). This improvement is almost exactly what is expected under the assumption that the radius uncertainty scales as the inverse square root of the exposure time, because $\sqrt{1602.68\ \mathrm{ks}/2733.81\ \mathrm{ks}} \approx 0.77$.

However, this decrease has a relatively minor effect on our EOS inferences, because in making these inferences we also include other results that bear on the properties of cold, catalyzed matter at densities above the saturation density of nuclear matter. In particular, the upper bound placed on the tidal deformability of neutron stars with moderate masses by the observations of GW170817 (Abbott et al. 2017, 2018; De et al. 2018) disfavors large stellar radii, so equatorial radii $\gtrsim$14 km already had low posterior weight. Our new constraints on the radius of PSR J0740+6620 can be viewed as being in better agreement with current tidal deformability measurements.

In this section, we update our EOS constraints based on our new measurement of the radius of PSR J0740+6620. Our method is described in detail elsewhere (Miller et al. 2019, 2020, 2021). In brief:

1. We assume that we know the EOS below a threshold density, which we take to be half the saturation density of nuclear matter, because this is roughly the density of the transition between the solid crust and the fluid core (Hebeler et al. 2013). We use the QHC19 EOS of Baym et al. (2019) below this density, but the mass, radius, tidal deformability, and other stellar properties we derive are insensitive to the low-density EOS.
2. We then extend the EOS to higher densities. There are many frameworks for such extensions, but for the most direct comparison with previous work we use the Gaussian-process approach that was introduced in this context by Landry & Essick (2019). We use the same set of 100,000 realizations of a high-density EOS that were used in Miller et al. (2021), so any differences between the results we obtain here and our previous results are due to the new measurement rather than to different samples in the EOS space. Our particular Gaussian-process sampling of possible equations of state does not explicitly take into account the possibility of phase transitions, but initial studies suggest that phase transitions (or, more generally, complex variations of the sound speed with density) are neither favored nor disfavored by current data (Mroczek et al. 2023a, 2023b; Essick et al. 2023). As discussed in Miller et al. (2021), this prior on the sound speed tends toward the speed of light at very high densities.
3. The EOS constraints presented here also impose a Gaussian prior on the nuclear symmetry energy at nuclear saturation density $S = 32 \pm 2$ MeV, (Tsang et al. 2012), take into account the existence of the three high-mass pulsars (Antoniadis et al. 2013; Arzoumanian et al. 2018; Fonseca et al. 2021), and make use of the tidal deformability posteriors from the gravitational-wave observations of GW170817 (Abbott et al. 2017, 2018; De et al. 2018) and GW190425 (Abbott et al. 2020b).

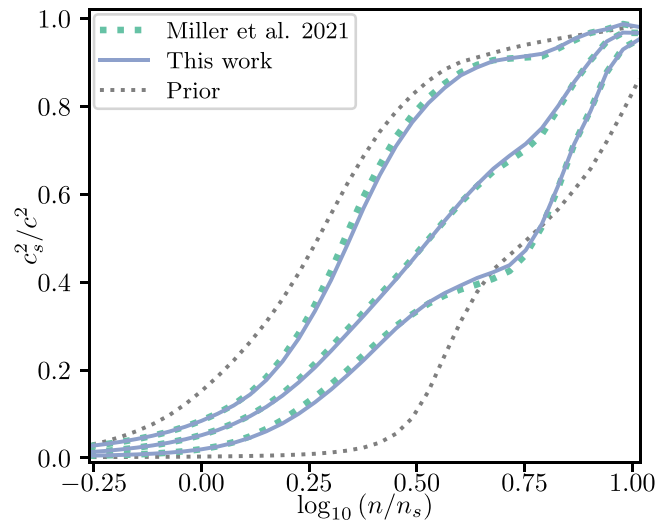

Figure 7. The constraints we infer on the square of the sound speed in dense matter using the results obtained in this paper. At a given baryonic number density (shown here in units of the nuclear saturation density $n_s = 0.16\ \mathrm{fm}^{-3}$), the lower line shows the 5th percentile of the squared sound speed, the upper line shows the 95th percentile, and the middle line shows the median value of the squared sound speed. The dotted green lines show the constraints inferred by Miller et al. (2021), whereas the solid blue lines show the constraints obtained using the results presented in this paper. The dotted black lines show the prior 5th and 95th percentiles of our EOS samples. We find a slightly lower sound speed at densities below $n \lesssim 3n_s (\log_{10} n/n_s \lesssim 0.5)$ and slightly tighter overall constraints on the sound speed in the density range from $n \sim 3 - 5n_s$ ($\log_{10} n/n_s \sim 0.5 - 0.7$) than those found by Miller et al. (2021).

Figure 7 shows how the constraints on the square of the sound speed in dense matter are revised when the additional NICER results obtained in this paper are included in the analysis. The details of this analysis and the priors we used can be found in Section 5.3 and Figure 13 of Miller et al. (2021). Table 4 and Figure 8 show how the inferred maximum gravitational mass of a nonrotating neutron star (M_{TOV}) and the circumferential radius of a nonrotating neutron star of fiducial gravitational mass 1.4 $M_\odot$ are revised when our current results are included. All the inferences in Table 4 include the current measurements of the masses of the three high-mass pulsars, the gravitational-wave-inferred limits on the tidal deformability of neutron stars, and the current experimental constraints on the nuclear symmetry energy (see Section 5.3 of Miller et al. 2021 for details).

We find evidence for a slightly softer EOS and consequent reduction of the maximum mass and fiducial radius, but the changes are relatively small. The high values for the radius of PSR J0740+6620 that are more disfavored by the present NICER data than by the previous data are also disfavored by the gravitational-wave observations. However, as the slight improvements in Figure 7 suggest, the NICER data have begun to exclude high stellar radii independent of the constraints provided by gravitational-wave data. We have included, in Table 4 and Figure 8, a forecast of how the constraints on the equatorial radius of a 1.4 $M_\odot$ neutron star and the maximum mass of a nonrotating neutron star might tighten using twice the present data on PSR J0740+6620, or equivalent measurements of another pulsar. However, we caution that the precise values of the constraints on the equatorial radius of a 1.4 $M_\odot$ neutron star and the maximum mass of a nonrotating neutron star depend more strongly on the details of a given EOS parameterization than do the EOS constraints themselves, as

Table 4
Updated Maximum Mass and Fiducial Radius

Quantity	Data Set	-1σ	Median	$+1\sigma$
$M_{\rm TOV}$ ($M_\odot$)	Miller et al. (2021)	2.08	2.23	2.47
$M_{\rm TOV}$ ($M_\odot$)	This work	2.08	2.22	2.44
$M_{\rm TOV}$ ($M_\odot$)	Projected	2.08	2.19	2.37
$R_e(1.4\,M_\odot)$ (km)	Miller et al. (2021)	12.17	12.63	13.11
$R_e(1.4\,M_\odot)$ (km)	This work	12.09	12.57	13.06
$R_e(1.4\,M_\odot)$ (km)	Projected	12.07	12.46	12.85

Notes. Comparison of the -1σ, median, and $+1\sigma$ points in the posterior distributions of the maximum gravitational mass of a nonrotating neutron star ($M_{\rm TOV}$) and the equatorial circumferential radius of a fiducial nonrotating 1.4 $M_\odot$ neutron star (R_e) inferred by Miller et al. (2021) using the PSR J0740+6620 data then available and the values we infer here after including an additional 1.1 Ms of NICER data. The improvements achieved by using the larger present data set are relatively small because other information, notably that provided by the gravitational waves produced by the double neutron star coalescence event GW170817, plays an important role in both analyses and by itself disfavors the high radii that are more disfavored by the present NICER data set than by the earlier NICER data set. The table also shows a projection of the constraints on $M_{\rm TOV}$ and $R_e(1.4\,M_\odot)$ that could potentially be achieved using twice the presently analyzed NICER data on PSR J0740+6620.

shown in Table 4 of Miller et al. (2021). Thus, additional NICER observations will continue to improve our knowledge of the properties of dense matter; for example, our projections suggest that doubling the current exposure time on PSR J0740 would by itself reduce the uncertainty of the radius of a fiducial 1.4 $M_\odot$ pulsar to ∼80% of its present value, at least based on the set of EOS that we currently consider.

5.2. Future Prospects

The X-ray faintness of PSR J0740+6620 makes measurement of its radius using NICER challenging. Based on the data analyzed here, which yield an uncertainty in the radius of ±∼12%, and assuming the uncertainty is proportional to the inverse of the square root of the observing duration, more than 12 Ms of NICER data would be required to achieve an uncertainty of ±∼5%. Although it is unlikely that NICER will be able to collect such a large quantity of data on PSR J0740+6620, even including the data from ∼2−3 Ms of additional observations could appreciably improve the constraints on the EOS of dense matter, as Table 4 shows.

Future X-ray timing missions such as STROBE-X (Ray et al. 2019), which would have an effective area ∼2 m^2 at 1.5 keV, or eXTP (Zhang et al. 2019) should be able to provide estimates of the radii of even faint pulsars like PSR J0740+6620 with a precision of a few percent or better. Given the paucity of counts observed by XMM-Newton and the apparent discrepancy between the XMM-Newton pn and MOS1/MOS2 data (see Section 4.3), additional imaging observations of PSR J0740+6620 may further improve our knowledge of the flux from the pulsar and the background flux, and therefore decrease the limit on the radius of PSR J0740+6620.

6. Conclusions

The present NICER observations, which include approximately 1.1 Ms of data in addition to the ∼1.6 Ms of data that was previously available, have improved the constraints on the radius of PSR J0740+6620 from $13.71^{+2.61}_{-1.50}$ km (Miller et al. 2021) to $12.92^{+2.09}_{-1.13}$ km. These additional data have also reduced the effects of using different analysis methods. Being able to obtain results that are insensitive to the analysis methods used is particularly important when analyzing data on faint sources such as PSR J0740+6620 (see, e.g., Section 4.4 and Salmi et al. 2024). Although the improvements in estimates of the mass and radius of PSR J0740+6620 presented here are incremental, these new estimates provide further information about the properties of matter at supranuclear densities. They imply that the EOS of cold, dense matter is slightly softer than was implied by the previously available data. Future NICER observations will provide even more information about the EOS.

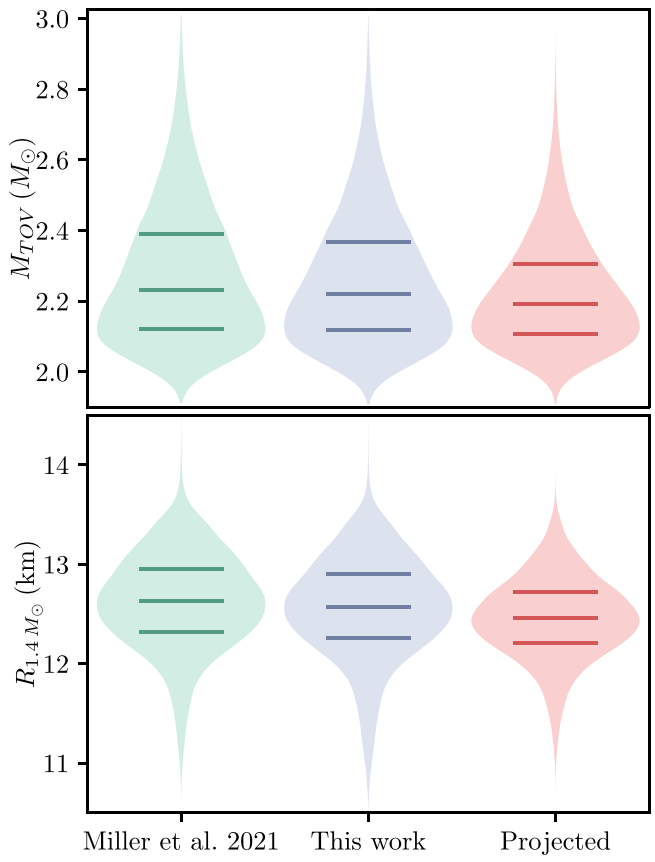

Figure 8. The posterior distributions (shaded regions) and the 25th, 50th, and 75th percentiles of these distributions (horizontal lines) for the maximum stable gravitational mass of a nonrotating neutron star (top panel) and the circumferential radius of a nonrotating 1.4 $M_\odot$ neutron star (bottom panel) inferred from the current constraints on the EOS of neutron star matter. The results reported by Miller et al. (2021) are shown in green, the constraints based on the updated measurements presented in this work are shown in blue, and the projected constraints that might follow from analysis of an additional ∼2.7 Ms of NICER data on PSR J0740+6620 are shown in red.

Acknowledgments

A.J.D. and M.C.M. were supported in part by NASA ADAP grant Nos. 80NSSC21K0649 and 80NSSC20K0288. Part of this work was performed at the Aspen Center for Physics, which is supported by a U.S. National Science Foundation grant No. PHY-1607611. Some of the resources used in this work were provided by the NASA High-End Computing (HEC) Program through the NASA Center for Climate Simulation (NCCS) at Goddard Space Flight Center. A.J.D. gratefully acknowledges the support of LANL/LDRD under

project number 20220087DR. The LA-UR number is LA-UR-24-20120. The authors acknowledge the University of Maryland supercomputing resources (http://hpcc.umd.edu) that were made available for conducting the research reported in this paper, as well as the YORP and ASTRA clusters administered by the Center for Theory and Computation within the University of Maryland Department of Astronomy. We are particularly thankful to Tuomo Salmi and Serena Vinciguerra for useful discussions.

S.B. acknowledges funding from NASA grant Nos. 80NSSC20K0275 and 80NSSC22K0728. S.G. acknowledges the support of the Centre National d'Etudes Spatiales (CNES). W.C.G. H. acknowledges support through grant No. 80NSSC23K0078 from NASA. S.M. acknowledges support from NSERC Discovery Grant RGPIN-2019-06077. Portions of this work performed at the Naval Research Laboratory were supported by NASA.

We acknowledge extensive use of NASA's Astrophysics Data System (ADS) bibliographic services and arXiv.

Facilities: NICER, XMM

Software: `emcee` (Foreman-Mackey et al. 2013), MultiNest (Feroz et al. 2009), matplotlib (Hunter 2007), numpy (van der Walt et al. 2011), scipy (Virtanen et al. 2020), PyMultiNest (Buchner 2016a), PGF/Ti*k*Z (http://sourceforge.net/projects/pgf/), PINT (Luo et al. 2019, 2021), XMM-Newton SAS (Gabriel et al. 2004; SAS Development Team 2014), HEASoft (NASA High Energy Astrophysics Science Archive Research Center 2014).

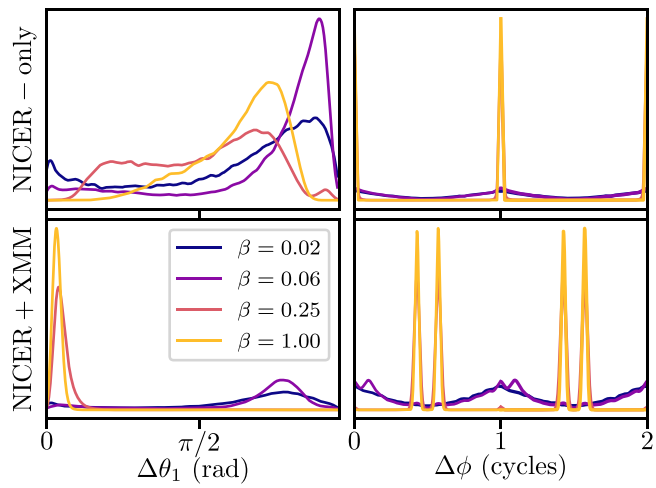

Figure 9. A demonstration, from our analyses using a fully ionized helium atmosphere model, that MultiNest explored subdominant modes in each analysis thoroughly enough to assign them appreciable mass at intermediate stages of the analysis. We accomplish this by tempering the likelihood function to place less weight on samples acquired at later times in the analysis. The top panels present effective posteriors from the analysis of NICER data alone, and the bottom panels show results from the joint analysis of NICER and XMM-Newton data. The lightest yellow lines plot the inferred posterior, while the others plot effective posteriors, tempered to varying degrees. The left panels present probability distributions for the angular radius of the first spot, and the right panels present distributions for the separation between spots; in both analyses, the subdominant mode was thoroughly explored before being abandoned for higher-likelihood ground.

Appendix A
Assessing the Thoroughness of Our Nested Sampling Analyses

In Section 4.1, we found that the best-fitting parameter values from our analysis of NICER data alone, using fully ionized hydrogen and helium atmosphere models, which produce a lunate spot configuration, were drastically disfavored by differences in log likelihood of >400 when the XMM-Newton data were included. On the other hand, the best-fitting parameters from our NICER-only analysis using neutron star atmosphere models consisting of hydrogen that could be partially ionized, which describe a mode with separate and much smaller emitting regions, gave a log likelihood ∼35 smaller than the lunate spot configuration. While this first analysis strongly suggested that the lunate configurations that are capable of fitting the NICER data alone are disfavored when the XMM-Newton data are included, the possibility remained that comparably good fits exist for that or other spot configurations which differ from the maximum-likelihood configurations identified during the analyses of NICER data alone. To check whether these modes were explored by our analyses, we reanalyzed the nested samples produced by MultiNest using a tempered likelihood function $L' = L^{\beta}$ for $\beta \in [1, 0]$, such that $\beta = 1$ generates samples from the posterior and $\beta = 0$ generates samples from the prior, using the procedure suggested in Wolfe et al. (2023) to initialize parallel-tempered MCMC runs using nested sampling analyses.

To make things explicit, nested sampling determines a set of samples i and the prior volumes w_i associated with each likelihood isocontour. Given a likelihood function L, these prior volumes can be used to calculate the evidence as $Z \approx \sum w_i L_i$, after which the points can be used as weighted posterior samples with weights $p_i = w_i L_i / Z$. Because the prior volume of each sample is independent of the likelihood function itself as long as the order between points is preserved, we are free to reweight samples according to $p_{i,\beta} = L_i^{\beta} w_i / Z_{\beta}$. For example, using $\beta \sim 1/100$, the differences observed earlier between points in different modes can be smoothed over. Thus, plotting effective quasi-posteriors with $0 \leqslant \beta \leqslant 1$ can inform us whether certain regions of parameter space were favored over the prior, and explored during sampling, before the highest-likelihood regions dominated the sampling.[29]

Figure 9 illustrates the aforementioned analysis for two parameters, namely, the angular radius of the first spot and the phase offset between the two spots, for fits using fully ionized hydrogen atmospheres to the NICER data alone and to both the NICER and XMM-Newton data. Considering first the fits to only the NICER data, the results show that the mode with a large first spot, and spots separated by ∼zero rotational cycles, clearly dominates the posterior. However, after tempering the likelihood by a factor of $\beta \lesssim 0.06$, we observe substantial quasi-posterior mass at small spot angular radii and at intermediate phased offsets, suggesting that these families of modes were explored early in the analysis before the far-higher-likelihood points belonging the lunate mode were identified. Similarly, while the posterior from the joint analysis of NICER and XMM data is comprised almost entirely by configurations with small, nearly antipodal spots, before honing in on these much-higher-likelihood solutions the analysis thoroughly explored the crescent-shaped configurations, which better suit the NICER data without the flux constraints from the data provided by XMM-Newton.

Although this analysis indicates that MultiNest was able to identify the various spot configurations capable of describing the present NICER and XMM-Newton data analyzed here, with

[29] However, this does not prove that the parameter space was thoroughly explored, or that the tempered likelihood surface is accurately or precisely characterized by this analysis, as it would be in an MCMC analysis of the tempered posterior.

the settings used in this work it was unable to produce accurate posterior inferences. Table 5 lists the 68% uncertainty and median values of the equatorial radius for each of our preliminary nested sampling analyses and our converged MCMC analyses. In every case, MultiNest estimated a posterior that was both erroneously narrow and biased toward low radii. We also list in Table 5 the radius credible regions obtained after placing various cuts on our posterior samples to simulate the effects of imposing the priors used in Salmi et al. (2024). The posterior distributions resulting from these constraints agree better with the MultiNest-derived results reported in Salmi et al. (2024).

Table 5
The Equatorial Radii Inferred by Our Various Analyses

Data Set	Atmosphere Model	Nested Sampling	Nested Sampling $R_e < 16$ km	Nested Sampling $R_e < 16$ km $\Delta\theta_i < 0.4$	MCMC	MCMC $R_e < 16$ km	MCMC $R_e < 16$ km $\Delta\theta_i < 0.4$
NICER +XMM	H_{full}	$12.704^{+1.484}_{-0.970}$	$12.661^{+1.368}_{-0.942}$	$12.661^{+1.368}_{-0.942}$	$12.922^{+2.089}_{-1.129}$	$12.756^{+1.495}_{-1.020}$	$12.756^{+1.495}_{-1.021}$
NICER +XMM	$H_{partial}$	$12.754^{+1.656}_{-1.039}$	$12.692^{+1.454}_{-1.004}$	$12.692^{+1.454}_{-1.004}$	$12.992^{+2.364}_{-1.228}$	$12.760^{+1.534}_{-1.074}$	$12.760^{+1.534}_{-1.074}$
NICER +XMM	He_{full}	$12.773^{+1.657}_{-1.048}$	$12.705^{+1.442}_{-1.008}$	$12.705^{+1.442}_{-1.007}$	$13.067^{+2.455}_{-1.248}$	$12.812^{+1.560}_{-1.076}$	$12.814^{+1.562}_{-1.073}$
NICER	H_{full}	$12.150^{+2.305}_{-1.507}$	$11.984^{+1.881}_{-1.394}$	N/A	$12.475^{+4.062}_{-1.938}$	$11.856^{+2.302}_{-1.481}$	N/A
NICER	$H_{partial}$	$11.479^{+1.232}_{-0.922}$	$11.465^{+1.216}_{-0.914}$	$11.365^{+0.970}_{-0.811}$	$11.946^{+2.512}_{-1.361}$	$11.781^{+1.946}_{-1.247}$	$11.804^{+1.826}_{-1.191}$
NICER	He_{full}	$12.552^{+2.816}_{-1.799}$	$12.211^{+2.039}_{-1.567}$	N/A	$12.723^{+4.666}_{-2.159}$	$11.877^{+2.351}_{-1.514}$	N/A

Notes. The median and 68% credible regions for the equatorial radius (in kilometers) derived from both our preliminary nested sampling analyses (using MultiNest), and from our MCMC analysis after convergence (using `emcee`). For the sake of comparison with other works, such as Riley et al. (2021) and Salmi et al. (2024), we also report the credible regions resulting from each analysis after imposing an upper limit of 16 km on the radius. Because some of our analyses identified lunate spot configurations which were neither significant after incorporating XMM-Newton data nor allowed by the priors used in Salmi et al. (2024), we also include the radius constraints after eliminating these solutions by requiring the angular diameters of both spots to be less than 0.4 radians. As this table shows, our preliminary, MultiNest-derived results are typically biased toward smaller radii, and often have erroneously small uncertainties.

Appendix B
Posterior Distributions from Analysis of Only NICER Data

Table 6 lists the median, $\pm 1\sigma$, and $\pm 2\sigma$ points in the posterior distributions obtained by fitting our models to only the NICER data, assuming a fully ionized hydrogen atmosphere, and the resulting maximum-likelihood values for each of the parameters in these models. We display the complete corner plot of the posteriors from these same analyses in Figure 10.

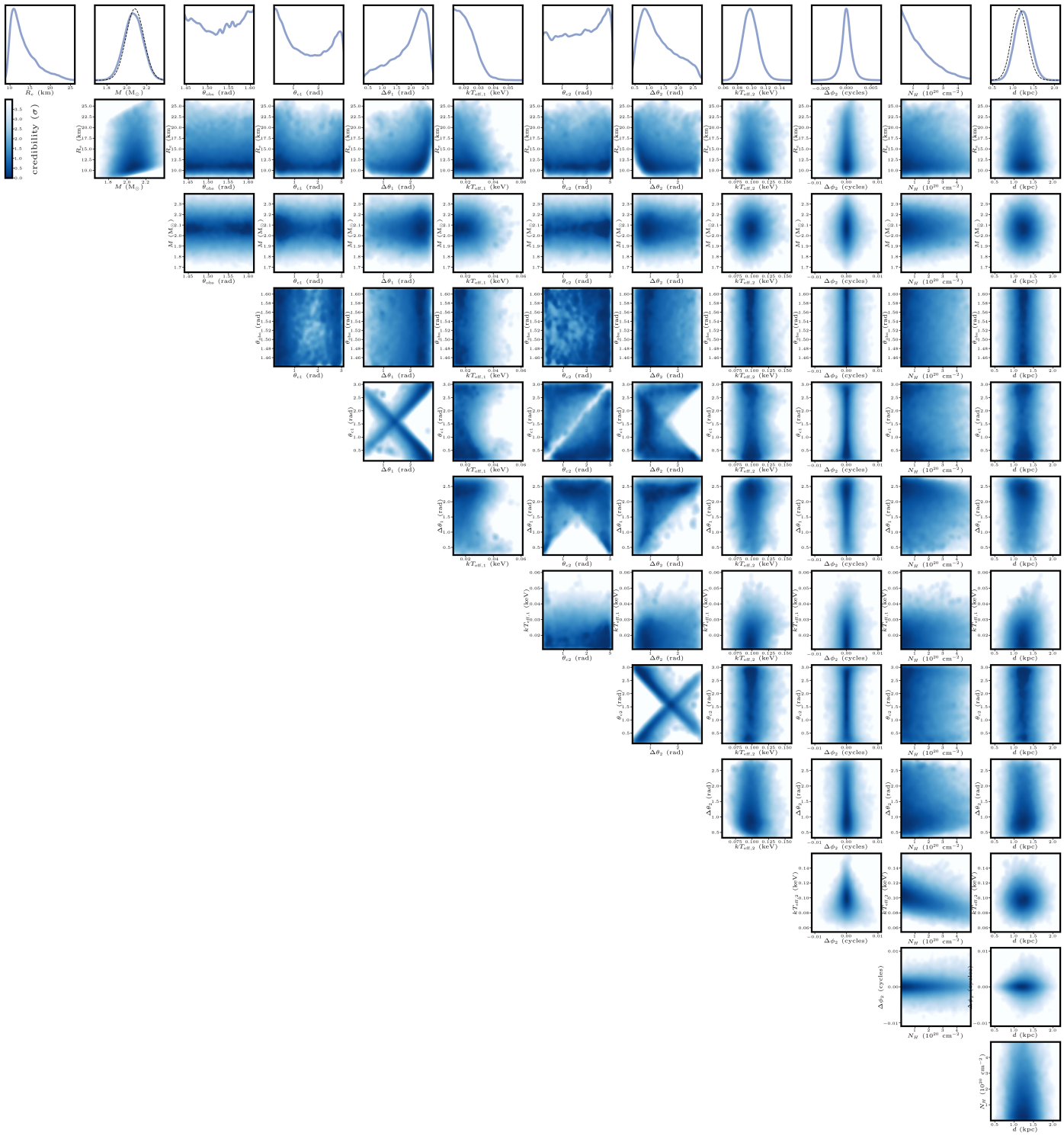

Figure 10. Posterior probability density distributions from our analysis of NICER data alone, using a fully ionized hydrogen atmosphere model. In the one-dimensional plots of the distance to and gravitational mass of the pulsar, dashed lines indicate the priors that we applied.

Table 6
Fits to Only NICER Data

Parameter	Median	-1σ	$+1\sigma$	-2σ	$+2\sigma$	Maximum Likelihood
R_e (km)	12.475	10.537	16.538	9.602	21.840	11.731
GM/c^2R_e	0.245	0.185	0.289	0.140	0.308	0.259
M ($M_\odot$)	2.066	1.972	2.161	1.878	2.252	2.058
θ_{c1} (rad)	1.331	0.384	2.632	0.149	2.972	1.680
$\Delta\theta_1$ (rad)	2.096	1.266	2.485	0.552	2.671	1.159
$kT_{\rm eff,1}$ (keV)	0.020	0.014	0.028	0.011	0.036	0.021
θ_{c2} (rad)	1.718	0.629	2.677	0.193	2.980	2.907
$\Delta\theta_2$ (rad)	1.167	0.719	1.993	0.490	2.570	0.617
$kT_{\rm eff,2}$ (keV)	0.098	0.088	0.109	0.078	0.122	0.107
$\Delta\phi_2$ (cycles)	0.003	0.000	1.000	0.000	1.000	1.000
$\theta_{\rm obs}$ (rad)	1.528	1.467	1.589	1.444	1.610	1.471
N_H (10^{20} cm^{-2})	1.056	0.273	2.524	0.037	4.182	0.063
d (kpc)	1.228	1.039	1.423	0.861	1.619	1.116

Notes. A comparison of the -2σ, -1σ, median, $+1\sigma$, and $+2\sigma$, and maximum-likelihood values inferred from our analysis of NICER data for PSR J0740+6620. These results were derived under the assumption of a fully ionized pure hydrogen atmosphere.

Appendix C
Posterior Distributions from Analysis of Both NICER and XMM-Newton Data

Table 7 lists the median, $\pm1\sigma$, and $\pm2\sigma$ points in the posterior distributions obtained by fitting our models to both the NICER data and XMM-Newton data, assuming a fully ionized hydrogen atmosphere, and the resulting maximum-likelihood values for each of the parameters in these models. We display the complete corner plot of the posteriors from these same analyses in Figure 11.

Table 7
Fits to NICER and XMM-Newton Data

Parameter	Median	-1σ	$+1\sigma$	-2σ	$+2\sigma$	Maximum Likelihood
R_e (km)	12.922	11.793	15.010	10.992	18.574	11.541
GM/c^2R_e	0.236	0.204	0.257	0.165	0.272	0.250
M ($M_\odot$)	2.066	1.976	2.155	1.886	2.246	1.958
θ_{c1} (rad)	1.573	0.946	2.222	0.641	2.546	1.387
$\Delta\theta_1$ (rad)	0.101	0.072	0.140	0.051	0.199	0.092
$kT_{\rm eff,1}$ (keV)	0.095	0.085	0.104	0.076	0.114	0.106
θ_{c2} (rad)	1.578	0.957	2.220	0.640	2.531	1.980
$\Delta\theta_2$ (rad)	0.100	0.073	0.138	0.052	0.193	0.112
$kT_{\rm eff,2}$ (keV)	0.095	0.085	0.104	0.077	0.114	0.099
$\Delta\phi_2$ (cycles)	0.553	0.424	0.576	0.413	0.587	0.428
$\theta_{\rm obs}$ (rad)	1.529	1.469	1.587	1.444	1.610	1.539
N_H (10^{20} cm^{-2})	0.953	0.255	2.209	0.034	3.871	0.023
d (kpc)	1.205	1.020	1.397	0.844	1.588	1.297

Notes. A comparison of the -2σ, -1σ, median, $+1\sigma$, and $+2\sigma$, and maximum-likelihood values inferred from our joint analysis of NICER and XMM-Newton data for PSR J0740+6620. These results were derived under the assumption of a fully ionized pure hydrogen atmosphere.

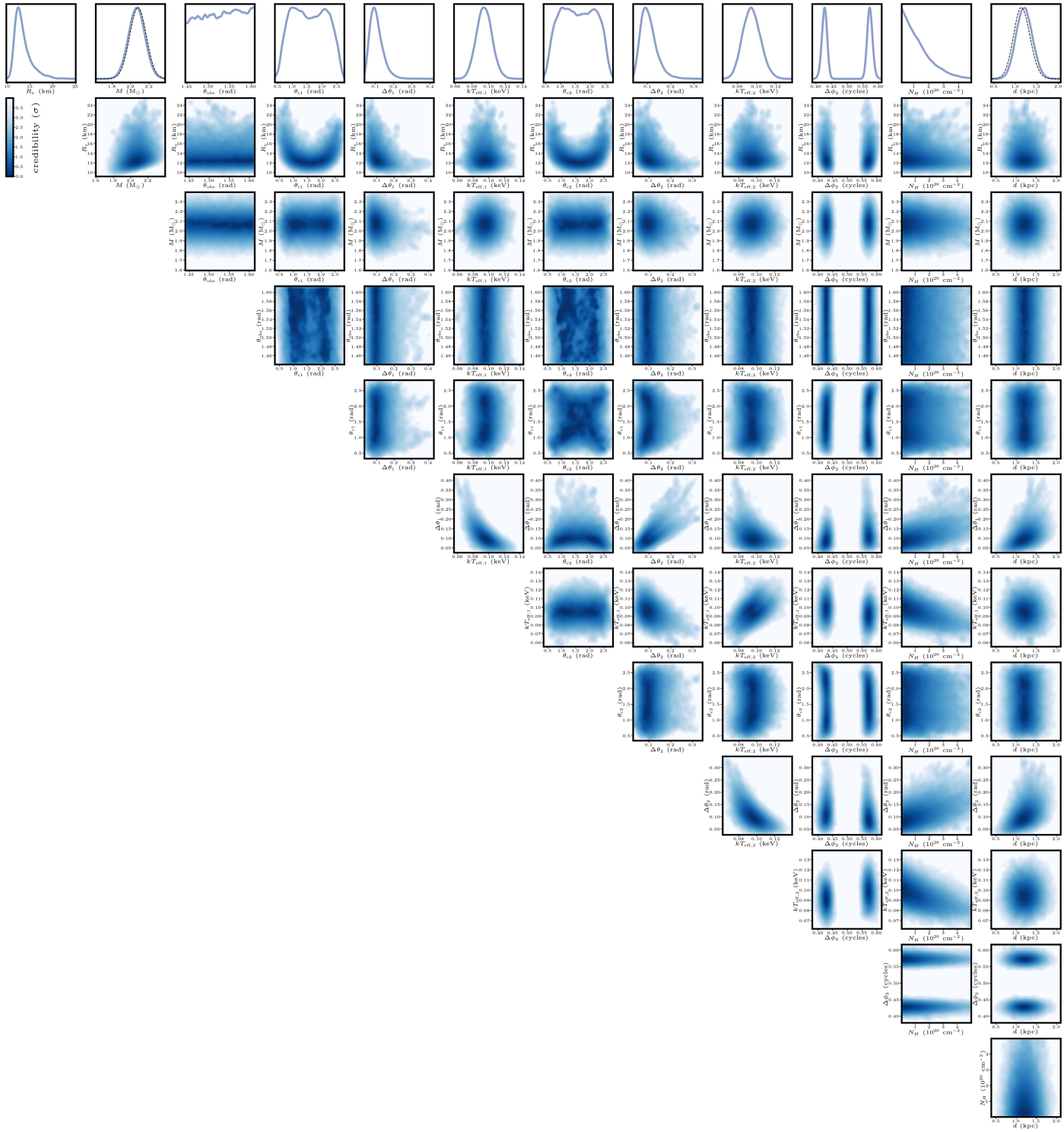

Figure 11. Posterior probability density distributions from our joint analysis of NICER and XMM-Newton data, using a fully ionized hydrogen atmosphere model. In the one-dimensional plots of the distance to and gravitational mass of the pulsar, dashed lines indicate the priors that we applied.

ORCID iDs

Alexander J. Dittmann https://orcid.org/0000-0001-6157-6722
M. Coleman Miller https://orcid.org/0000-0002-2666-728X
Frederick K. Lamb https://orcid.org/0000-0002-3862-7402
Isiah M. Holt https://orcid.org/0000-0002-3097-942X
Cecilia Chirenti https://orcid.org/0000-0003-2759-1368
Michael T. Wolff https://orcid.org/0000-0002-4013-5650
Slavko Bogdanov https://orcid.org/0000-0002-9870-2742
Sebastien Guillot https://orcid.org/0000-0002-6449-106X
Wynn C. G. Ho https://orcid.org/0000-0002-6089-6836
Sharon M. Morsink https://orcid.org/0000-0003-4357-0575
Keith C. Gendreau https://orcid.org/0000-0001-7115-2819

References

Abbott, B. P., Abbott, R., Abbott, T. D., et al. 2017, PhRvL, 119, 161101
Abbott, B. P., Abbott, R., Abbott, T. D., et al. 2018, PhRvL, 121, 161101
Abbott, B. P., Abbott, R., Abbott, T. D., et al. 2020a, CQGra, 37, 045006
Abbott, B. P., Abbott, R., Abbott, T. D., et al. 2020b, ApJL, 892, L3
Adhikari, D., Albataineh, H., Androic, D., et al. 2021, PhRvL, 126, 172502
Agazie, G., Alam, M. F., Anumarlapudi, A., et al. 2023, ApJL, 951, L9
Alcock, C., & Illarionov, A. 1980, ApJ, 235, 534
AlGendy, M., & Morsink, S. M. 2014, ApJ, 791, 78
Antoniadis, J., Freire, P. C. C., Wex, N., et al. 2013, Sci, 340, 448
Arzoumanian, Z., Baker, P. T., Brazier, A., et al. 2018, ApJ, 859, 47
Badnell, N. R., Bautista, M. A., Butler, K., et al. 2005, MNRAS, 360, 458
Bauböck, M., Psaltis, D., & Özel, F. 2019, ApJ, 872, 162
Baym, G., Furusawa, S., Hatsuda, T., Kojo, T., & Togashi, H. 2019, ApJ, 885, 42
Bedaque, P., & Steiner, A. W. 2015, PhRvL, 114, 031103
Beronya, D. M., Karpova, A. V., Kirichenko, A. Y., et al. 2019, MNRAS, 485, 3715
Bhattacharya, D., & van den Heuvel, E. P. J. 1991, PhR, 203, 1
Bhattacharyya, S., Strohmayer, T. E., Miller, M. C., & Markwardt, C. B. 2005, ApJ, 619, 483
Bildsten, L., Salpeter, E. E., & Wasserman, I. 1992, ApJ, 384, 143
Blaes, O. M., Blandford, R. D., Madau, P., & Yan, L. 1992, ApJ, 399, 634
Bogdanov, S., Dittmann, A. J., Ho, W. C. G., et al. 2021, ApJL, 914, L15
Bogdanov, S., Lamb, F. K., Mahmoodifar, S., et al. 2019, ApJL, 887, L26
Buccheri, R., Bennett, K., Bignami, G. F., et al. 1983, A&A, 128, 245
Buchner, J., 2016a PyMultiNest: Python interface for MultiNest, Astrophysics Source Code Library, ascl:1606.005
Buchner, J. 2016b, S&C, 26, 383
Buchner, J. 2021, JOSS, 6, 3001
Buchner, J. 2023, StSur, 17, 169
Chang, P., & Bildsten, L. 2004, ApJ, 605, 830
Contopoulos, I., & Spitkovsky, A. 2006, ApJ, 643, 1139
Cromartie, H. T., Fonseca, E., Ransom, S. M., et al. 2020, NatAs, 4, 72
Danielewicz, P., Lacey, R., & Lynch, W. G. 2002, Sci, 298, 1592
De, S., Finstad, D., Lattimer, J. M., et al. 2018, PhRvL, 121, 091102
Demorest, P. B., Pennucci, T., Ransom, S. M., Roberts, M. S. E., & Hessels, J. W. T. 2010, Natur, 467, 1081
Dittmann, A. J. 2024, arXiv:2404.16928
Echeveste, M., Novarino, M. L., Benvenuto, O. G., & De Vito, M. A. 2020, MNRAS, 495, 2509
Ecker, C., Hoyos, C., Jokela, N., Fernández, D. R., & Vuorinen, A. 2017, JHEP, 2017, 31
Essick, R. 2022, ApJ, 927, 195
Essick, R., Legred, I., Chatziioannou, K., Han, S., & Landry, P. 2023, PhRvD, 108, 043013
Feroz, F., Hobson, M. P., & Bridges, M. 2009, MNRAS, 398, 1601
Fonseca, E., Cromartie, H. T., Pennucci, T. T., et al. 2021, ApJL, 915, L12
Fonseca, E., Pennucci, T. T., Ellis, J. A., et al. 2016, ApJ, 832, 167
Foreman-Mackey, D., Hogg, D. W., Lang, D., & Goodman, J. 2013, PASP, 125, 306
Gabriel, C., Denby, M., Fyfe, D. J., et al. 2004, in ASP Conf. Ser. 314, Astronomical Data Analysis Software and Systems (ADASS) XIII, ed. F. Ochsenbein, M. G. Allen, & D. Egret (San Francisco, CA: ASP), 759
Goodman, J., & Weare, J. 2010, CAMCS, 5, 65
Guillot, S., Kerr, M., Ray, P. S., et al. 2019, ApJL, 887, L27
Harding, A. K., & Muslimov, A. G. 2001, ApJ, 556, 987
Harding, A. K., & Muslimov, A. G. 2002, ApJ, 568, 862
Hebeler, K., Lattimer, J. M., Pethick, C. J., & Schwenk, A. 2013, ApJ, 773, 11
Ho, W. C. G., & Heinke, C. O. 2009, Natur, 462, 71
Ho, W. C. G., & Lai, D. 2001, MNRAS, 327, 1081
Ho, W. C. G., & Lai, D. 2003, MNRAS, 338, 233
Ho, W. C. G., Lai, D., Potekhin, A. Y., & Chabrier, G. 2003, ApJ, 599, 1293
Hoyos, C., Jokela, N., Rodríguez Fernández, D., & Vuorinen, A. 2016, PhRvD, 94, 106008
Hunter, J. D. 2007, CSE, 9, 90
Lai, D. 2001, RvMP, 73, 629
Landry, P., & Essick, R. 2019, PhRvD, 99, 084049
Lemos, P., Weaverdyck, N., Rollins, R. P., et al. 2023, MNRAS, 521, 1184
Luo, J., Ransom, S., Demorest, P., et al., 2019 PINT: High-precision pulsar timing analysis package, Astrophysics Source Code Library, ascl:1902.007
Luo, J., Ransom, S., Demorest, P., et al. 2021, ApJ, 911, 45
Margalit, B., & Metzger, B. D. 2017, ApJL, 850, L19
Miller, M. C. 2021, in Timing Neutron Stars: Pulsations, Oscillations and Explosions, ed. T. M. Belloni, M. Méndez, & C. Zhang (Heidelberg: Springer), 1
Miller, M. C., Chirenti, C., & Lamb, F. K. 2020, ApJ, 888, 12
Miller, M. C., & Lamb, F. K. 1998, ApJL, 499, L37
Miller, M. C., Lamb, F. K., Dittmann, A. J., et al. 2019, ApJL, 887, L24
Miller, M. C., Lamb, F. K., Dittmann, A. J., et al. 2021, ApJL, 918, L28
Mroczek, D., Coleman Miller, M., Noronha-Hostler, J., & Yunes, N. 2023a, JPhCS, 2536, 012006
Mroczek, D., Miller, M. C., Noronha-Hostler, J., & Yunes, N. 2023b, arXiv:2309.02345
NASA High Energy Astrophysics Science Archive Research Center, 2014 HEAsoft: Unified Release of FTOOLS and XANADU, Astrophysics Source Code Library, ascl:1408.004
Nättilä, J., Miller, M. C., Steiner, A. W., et al. 2017, A&A, 608, A31
Nelson, B. E., Ford, E. B., Buchner, J., et al. 2020, AJ, 159, 73
Özel, F., Psaltis, D., Arzoumanian, Z., Morsink, S., & Bauböck, M. 2016a, ApJ, 832, 92
Özel, F., Psaltis, D., Güver, T., et al. 2016b, ApJ, 820, 28
Pang, P. T. H., Tews, I., Coughlin, M. W., et al. 2021, ApJ, 922, 14
Pavlov, G. G., & Zavlin, V. E. 1997, ApJL, 490, L91
Potekhin, A. Y. 2014, PhyU, 57, 735
Randhawa, J. S., Meisel, Z., Giuliani, S. A., et al. 2019, ApJ, 887, 100
Ray, P. S., Arzoumanian, Z., Ballantyne, D., et al. 2019, arXiv:1903.03035
Remillard, R. A., Loewenstein, M., Steiner, J. F., et al. 2022, AJ, 163, 130
Rezzolla, L., Most, E. R., & Weih, L. R. 2018, ApJL, 852, L25
Riley, T. E., Watts, A. L., Bogdanov, S., et al. 2019, ApJL, 887, L21
Riley, T. E., Watts, A. L., Ray, P. S., et al. 2021, ApJL, 918, L27
Salmi, T., Choudhury, D., Kini, Y., et al. 2024, ApJ, 974, 294
Salmi, T., Suleimanov, V. F., Nättilä, J., & Poutanen, J. 2020, A&A, 641, A15
Salmi, T., Vinciguerra, S., Choudhury, D., et al. 2022, ApJ, 941, 150
Salmi, T., Vinciguerra, S., Choudhury, D., et al. 2023, ApJ, 956, 138
SAS Development Team, 2014 SAS: Science Analysis System for XMM-Newton observatory, Astrophysics Source Code Library, ascl:1404.004
Silva, H. O., Pappas, G., Yunes, N., & Yagi, K. 2021, PhRvD, 103, 063038
Skilling, J. 2004, in AIP Conf. Proc. 735, 24th Int. Workshop on Bayesian Inference and Maximum Entropy Methods in Science and Engineering, ed. R. Fischer, R. Preuss, & U. V. Toussaint (Melville, NY: AIP), 395
Speagle, J. S. 2020, MNRAS, 493, 3132
Stella, L., Priedhorsky, W., & White, N. E. 1987, ApJL, 312, L17
Strohmayer, T. E., & Brown, E. F. 2002, ApJ, 566, 1045
Strüder, L., Briel, U., Dennerl, K., et al. 2001, A&A, 365, L18
Timokhin, A. N., & Harding, A. K. 2015, ApJ, 810, 144
Tolman, E. A., Philippov, A. A., & Timokhin, A. N. 2022, ApJL, 933, L37
Tsai, Y.-S. 1974, RvMP, 46, 815
Tsang, M. B., Stone, J. R., Camera, F., et al. 2012, PhRvC, 86, 015803
Turner, M. J. L., Abbey, A., Arnaud, M., et al. 2001, A&A, 365, L27
van der Walt, S., Colbert, S. C., & Varoquaux, G. 2011, CSE, 13, 22
Vinciguerra, S., Salmi, T., Watts, A. L., et al. 2024, ApJ, 961, 62
Virtanen, P., Gommers, R., Oliphant, T. E., et al. 2020, NatMe, 17, 261
Watts, A. L., Andersson, N., Chakrabarty, D., et al. 2016, RvMP, 88, 021001
Wijngaarden, M. J. P., Ho, W. C. G., Chang, P., et al. 2019, MNRAS, 484, 974
Wijngaarden, M. J. P., Ho, W. C. G., Chang, P., et al. 2020, MNRAS, 493, 4936
Wilms, J., Allen, A., & McCray, R. 2000, ApJ, 542, 914
Wolfe, N. E., Talbot, C., & Golomb, J. 2023, PhRvD, 107, 104056
Wolff, M. T., Guillot, S., Bogdanov, S., et al. 2021, ApJL, 918, L26
Zhang, S., Santangelo, A., Feroci, M., et al. 2019, SCPMA, 62, 29502